System Simulation in Buildings 2018

December 10 – 12, 2018

Proceedings of the Tenth International Conference

Organised by :
The Thermodynamics Laboratory
Aerospace & Mechanical Engineering Department
University of Liège

Campus du Sart-Tilman
Bâtiment B49 – Parking P33
B-4000 Liège, Belgium

2019

Atelier des Presses

System Simulation in Buildings 2018

Université de Liège - Atelier des Presses
Chemin des Amphithéâtres - Bât B7a
4000 Liège (Belgique)

Ouvrage mis en page par l'auteur
Imprimé en Belgique

D/2021/13.315/1
ISBN : 978-2-930772-30-1

Organised by :
The Thermodynamics Laboratory
Aerospace & Mechanical
Engineering Department
University of Liège

System Simulation in Buildings 2018

Proceedings of the Tenth International Conference

Atelier des Presses

SYSTEM SIMULATION IN BUILDINGS 2018

Proceedings of the Tenth International Conference

Organized by:

The Thermodynamics Laboratory
Aerospace & Mechanical Engineering Department
University of Liège

December 10-12, 2018

Organization Committee

Vincent Lemort
Conference Chairman
Thermodynamics Laboratory
University of Liege
vincent.lemort@uliege.be

Philippe André
Scientific Committee Chairman
BEMS - Arlon
University of Liege
p.andre@uliege.be

Frédéric Ransy
Conference Secretary
Thermodynamics Laboratory
University of Liege
frederic.ransy@uliege.be

Scientific Committee

BERTAGNOLIO Stephane (Belgium)

BRAUN James (USA)

CORGNATI Stefano (Italy)

CUEVAS BARRAZA Cristian (Chile)

DE PAEPE Michel (Belgium)

DEWALLEF Pierre (Belgium)

FISSORE Adelqui (Chile)

FRERE Marc (Belgium)

HEISELBERG Per (Denmark)

HELSEN Lieve (Belgium)

JIANJUN Xia (China)

KUMMERT Michael (Canada)

LEBRUN Jean (Belgium)

MADJIDI Madjid (Germany)

MASY Gabrielle (Belgium)

QUOILIN Sylvain (Belgium)

SAELENS Dirk (Belgium)

STABAT Pascal (France)

THOMAS Sébastien (Belgium)

STEPHAN Wolfram (Germany)

XIAOHUA Liu (China)

ZOUGHAIB Assaad (France)

Table of Contents

hot water
Cristian Cuevas – Universidad de Concepción (Chile)

- ***P18: Experimental Characterization of Fault Impacts on the Functioning Variables of Inverter Driven Heat Pumps***
  Derek Noël – EDF & Ecole des Mines de Paris (France)

SIXTH SESSION – INTEGRATION OF COLLECTIVE HEATING SYSTEMS IN BUILDINGS

- ***P19: An energetic comparison between collective heating systems and individual heating systems in apartment buildings***
  Margot De Pauw – Kenniscentrum Energie Thomas More Geel (Belgium)

- ***P20: Hydronic integration of heat pumps in collective heating system of buildings***
  Freek Van Riet – UAntwerpen (Belgium)

- ***P21: Solar and Heat Pump Systems: parallel vs series configurations analysis***
  Javier Vega – Universidad de Concepción (Chile)

SEVENTH SESSION – BUILDING ENERGY SIMULATION 2

- ***P22: Assessment of the Energy Performance of building facades through different testing conditions and analysis techniques***
  Gabrielle Masy – UCL (Belgium)

- ***P23: Impact of air-conditioning waste heat on air temperature in Paris during heat waves***
  Brice Tremeac – CNAM (France)

- ***P24: Validation of a BES model of an all-air HVAC educational building***
  Bart Merema – KU Leuven (Belgium)

EIGHTH SESSION – BUILDING ENERGY SIMULATION 3

- ***P25: Connecting Thermal Building Simulation to Computational Fluid Dynamics - an experience report for TRNSYS and FDS***
  Madjid Madjidi – University of Applied Sciences Munich (Germany)

- ***P26: A new approach to model transport delay in branched pipes***
  Freek Van Riet – UAntwerpen (Belgium)

NINTH SESSION – ENERGY STORAGE IN BUILDINGS

- ***P27: Thermodynamic simulation of quasi-isothermal compressed air energy storage***
  Ghady Dib – INSA de Lyon (France)

- ***P28: Development and Evaluation of a Rule-Based Heuristic Control Strategy for Ice Storage Systems in Residential Buildings***
  Aaron Tam – Purdue University (USA)

- ***P29: Towards a subsurface predictive-model environment to simulate aquifer thermal energy storage for demand-side management applications***
  Tanguy Robert – University of Liege (Belgium)

- ***P30: Optimized control for standing column wells in cold climate***
  Camille Beurcq – Polytechnique Montréal (Canada)

- ***P31: Development of sophisticated heat pump heating systems considering different storage technologies: A comparative simulation study***
  Christian Vering – RWTH Aachen University (Germany)

TENTH SESSION – NON-CONVENTIONAL HVAC SYSTEMS

- ***P32: Numerical investigation of energy potential and performance of a residential building-integrated solar micro-cogeneration system***
  Simon Martinez – Université de La Rochelle (France)

- ***P33: Cascading implementation of a magnetocaloric heat pump for building space heating applications***

Hicham Johra – Aalborg University (Denmark)

- ***P34: Simulation of solar collectors with two low temperature heat engines for buildings applications***
  Vaclav Novotny – Czech Technical University in Prague (Czech Republic)

- ***P35: Dynamic modelling and control strategy of a heating system based on wood pellet boiler-stove***
  Van Long Lê – CENAERO (Belgium)

- ***P36: Evaluation of micro Combined Heat and Power systems in the Walloon residential sector through dynamic simulation***
  Vincent Cousin – University of Liege (Belgium)

CONCLUSIONS

Foreword

This 10th International Conference on System Simulation in Buildings gathered delegates from 15 different countries who had the opportunity, through 36 presentations and 2 keynotes, to share the latest findings of their research work. Some of the works presented were conducted in the frame of projects from the International Energy Agency's Energy in Buildings and Communities Programme.

On behalf of the organizing committee I would like to thank:

- The authors who accepted to write interesting papers and to submit them to a reviewing process.
- All the reviewers for the time they devoted to criticizing the papers in order to help authors improving them.
- All participants for the fruitful discussions we had.
- Our conference secretary Frederic Ransy and our laboratory secretary Isabelle Cosyns for their large efforts when organizing this event

I hope that the dissemination of these proceedings will contribute to the development of affordable new low-carbon HVAC technologies in the current context of energy transition, by tackling some of the technical challenges and highlighting the scientific opportunities.

I wish you a pleasant reading.

Vincent Lemort

Chairman of SSB 2018

Liege, May 2019

List of Participants

Queralt Altes Buch	ULiege	Belgium
Philippe André	ULiege	Belgium
Alessio Antonini	University of L'Aquila	Italy
Cleide Aparecida Silva	JCJ Energetics	Belgium
Alessia Arteconi	Universita Politecnica delle marche	Italy
Romain Baiwir	ULiege	Belgium
Stéphane Bertagnolio	Emerson Commercial & Residential Solutions	Belgium
Camille Beurcq	Polytechnique Montréal	Canada
Odile Cauret	EDF R&D	France
John Clauß	Norwegian University	Norway
Cristian Cuevas	Universidad de Concepción	Chile
Camila Dávila	ULiege	Belgium
Elisabeth Davin	ULiege	Belgium
Margot De Pauw	Kenniscentrum Energie Thomas More Geel	Belgium
Bertrand Dechesne	ULiege	Belgium
Arno Dentel	Technische Hochschule Nürnberg	Germany
Kevin R. Deutz	EDF R&D	France
Ghady Dib	INSAVALOR	France
Rémi Dickes	ULiege	Belgium
Olivier Dumont	ULiege	Belgium
Antoine Fabre	ARMINES	France
Samuel Gendebien	Von Karmann Institute	Belgium
Kamel Ghali	American University of Beirut	Lebanon
Sebastian Gonzato	Imperial College London	U.K.
Jules Hannay	JCJ Energetics	Belgium
Lieve Helsen	KU Leuven	Belgium
Hicham Johra	Aalborg University	Norway
Filip Jorissen	KU Leuven	Belgium
Michaël Kummert	Polytechnique Montréal	Canada
Long Le-Van	CENAERO	Belgium
Jean Lebrun	JCJ Energetics	Belgium
Vincent Lemort	ULiege	Belgium
Francesco Lombardi	Politecnico di Milano	Italy
Madjid Madjidi	Munich University of Applied Sciences	Germany
Charlotte Marguerite	CENAERO	Belgium
Simon Martinez	UNIVERSITE DE LA ROCHELLE-LaSIE	France
Gabrielle Masy	UCL	Belgium
Bart Merema	KU Leuven	Belgium
Rasha Mustapha	MINES PARISTECH	France
Derek Noël	EDF R&D	France
Vaclav Novotny	Czech Technical University	Czech

		Republic
Antoine Parthoens	ULiege	Belgium
Julien Quinten	UMons	Belgium
Sylvain Quoilin	ULiege	Belgium
Frédéric Ransy	ULiege	Belgium
Thibaut Résimont	ULiege	Belgium
Tanguy Robert	University of Liège	Belgium
Romuald Rullière	INSAVALOR	France
Pascal Stabat	ARMINES	France
Wolfram Stephan	Technische Hochschule Nürnberg ieg	Germany
Sébastien Thomas	SECO group	Luxembourg
Brice Tréméac	Conservatoire National des Arts et Métiers Laboratoire du Froid	France
Anke Uytterhoeven	KU Leuven	Belgium
Freek Van Riet	UAntwerpen	Belgium
Javier Vega	ULiege	Belgium
Ivan Verhaert	UAntwerpen	Belgium
Christian Vering	RWTH Aachen University	Germany
Eric Winandy	Emerson Climate Technologies	Belgium
Ying Xie	Tsinghua University	China
Davide Ziviani	Purdue University	USA
Assaad Zoughaib	MINES PARISTECH	France

First Session
Buildings Energy Simulation 1

Modeling framework for the simulation and control of greenhouse climate

Queralt Altes-Buch[1]*, Vincent Lemort[1]

[(1)] University of Liege, Energy Systems Research Unit – Thermodynamics Laboratory, Department of Mechanical and Aerospace Engineering, Liege, Belgium

[*] Corresponding author: qaltes@uliege.be

ABSTRACT

This work presents an open-source modeling framework for the purpose of greenhouse climate simulation. To that end, a greenhouse climate model and a crop yield model are implemented, based on the literature. Moreover, climate control system models are developed for the control of heating, ventilation, CO_2 enrichment and supplementary lighting. Climate controllers aim at maintaining an indoor climate that has been designed to optimize crop growth. In this work, the indoor climate is computed by the climate model and the crop growth is defined by the yield model. To establish optimal growth conditions, a strategy is defined to select optimal temperature and CO_2 set-points. The models are written in the Modelica language, thus enabling to simulate their integration with other thermal systems. The use of the models is illustrated in a case study. To that end, the models are coupled and run for a simulation time period equivalent to a growing cycle for tomato crop in mild-climate conditions. Results for the thermal consumption of the greenhouse, the harvest rate of the crop are presented. The control variables and the indoor climate variables and flows are illustrated. The obtained results and profiles are in accordance with the literature, thus ensuring the physical behavior of the model and the proper functioning of the proposed control strategies.

Keywords: Climate control, Climate model, Crop yield model, Greenhouse

1. INTRODUCTION

In the European context, energy consumption by agriculture only accounted for 2.7% of final energy consumption in the EU-28 in 2016 (2018a). The Netherlands was the country with the highest share, with a 7.4% of its final energy consumption. Although the average energy consumption by agriculture of the EU-28 decreased about 18.6% from 1996 to 2016, it has increased in some countries. The utilized agricultural area (UAA) is used as a common denominator for the comparison of the results across different countries. In fact, the Netherlands was the country with the highest use in energy by agriculture per ha UAA between 1996 and 2016 (2018b). This was due to intensive farming. According to the Farm Structure Survey, although greenhouses covered only the 0.5% of the total UAA in the Netherlands in 2013, they represented about 79% of the total energy consumption by agriculture (2018c).

Agriculture, as an energy consumer, contributes to the depletion of non-renewable energy sources and to global warming, for instance through CO_2 emissions from fossil fuel combustion gases. It is therefore important to study energy-saving options not only for greenhouses but also, in the current context of energy transition, for a higher-scale system with integrated district heating and electrical production. The goal of this work is to implement a model able to simulate the complex flows in a greenhouse to facilitate the future study of energy integration of greenhouses with other energy systems. To that end, this work implements:

- A detailed model of a greenhouse climate, including the modeling of heat, vapor and CO_2 flows, to simulate the indoor climate and energy consumption of a greenhouse given its specific design, outdoor conditions and a specific control. The modeling of heating systems is also included.
- A crop yield model, to account for the needs of the crop and the flows related to plant transpiration and photosynthesis. These flows influence the indoor climate and thus, the energy consumption.
- Climate control system models to regulate heating, ventilation, CO_2 enrichment and supplementary lighting in the greenhouse. A control strategy for the thermal screen is also proposed.

This paper presents a detailed description of the mentioned models. In order to illustrate the capabilities of the modeling framework, the greenhouse, the crop yield and the climate control system models are coupled and run simultaneously for a real case study. Results for the case study are presented and discussed. The models are written in the Modelica language and are run within the Dymola simulation platform. The Modelica language has the asset of being flexible and it allows simulating system integration through the connection with other components such as thermal generators. The models are released as open-source, thus ensuring a proper reproducibility and reusability of this work (Pfenninger et al., 2017).

2. METHODS

2.1 Greenhouse climate model

A greenhouse climate model is a model that describes the indoor climate of a greenhouse resulting from the greenhouse design, the outdoor climate and a specific control. In greenhouses, the indoor climate is characterized by the temperature, the vapor pressure of water (i.e. the relative humidity) and the CO_2 concentration of the air. Together with the temperature of the heating pipes, the indoor climate constitutes the climate controller feed-back quantities. However, in order to attain the desired climate, the variables with an indirect influence on the climate also need to be modeled. These are mainly the characteristics relative to the canopy and the envelope (i.e. the cover, the floor and the thermal screen). The canopy temperature has an impact on its photosynthesis and transpiration, which decrease the CO_2 concentration and increase the vapor content of the air, respectively. Evaporation or condensation at surfaces may occur depending on the water vapor pressure difference with respect to the air. The temperature of the envelope influences the vapor pressure of water of the air, which is decreased by condensation at the cover and at the thermal screen. The thermal screen is a membrane used to reduce the energy requirement to heat the greenhouse (waved line in Fig. 1). When drawn, thermal losses to the outside are reduced by 38 to 60%, depending on the nature of its material (Bailey, 1988). Given the porous nature of the screen, air and moisture is exchanged through its fabric. Air exchange with the outside decreases the partial vapor pressure and the CO_2 concentration of the air, which can be increased by supplementary CO_2 supply. The here above mentioned variables are stated in Fig. 1.

Greenhouse climate models have been the object of a substantial literature. While many models have been developed (Bot, 1983; De Zwart, 1996; Impron et al., 2007; Luo et al., 2005; van Ooteghem, 2010), most of them can only be used for a single location and for a specific greenhouse structure and climate. Recently, a more generic greenhouse climate model (Vanthoor, 2011) combining the work of Bot, 1983 and De Zwart, 1996 was developed. The model was validated for a range of climates and greenhouse designs. For the purpose of this work, the model (Vanthoor, 2011) has been implemented in the Modelica language, thus

enabling system integration through the connection with other components such as thermal generators.

It should be noted that, when the screen is drawn, the air of the greenhouse is divided in two zones, i.e. below and above the screen. The model assumes the climate of each zone to be homogeneous. For the rest of the manuscript, the zones below and above are going to be referred as main and top air zones, respectively. The model includes the energy and mass balances to compute all the mentioned variables. These are energy balances on the main and top air zones, canopy, heating pipes, cover, floor and thermal screen; and mass balances of vapor and CO_2 on the main and top air zones. The vapor pressure of water at a surface is defined by the saturated vapor pressure at its temperature. The entirety of the balances are described in Altes-Buch et al., 2018 and follow the structure of equations 1-3. Since no spatial differences in temperature, vapor pressure of water and CO_2 concentration are considered, all the model flows are described per square meter of greenhouse floor. For the main air zone, the temperature, vapor pressure of water and CO_2 concentration are described by:

$$c_{Air}\dot{T}_{Air} = p_{SunAir} + \dot{q}_{cnv,UpAir} + \dot{q}_{cnv,LowAir} + \dot{q}_{cnv,CanAir} - \dot{q}_{cnv,AirFlr} - \dot{q}_{cnv,AirCov} - \dot{q}_{cnv,AirScr} - \dot{q}_{cnv,AirTop} - \dot{q}_{cnv,AirOut} \quad [\mathrm{W\ m^{-2}}] \quad (1)$$

$$c_{VP_{Air}}\dot{P}_{v,Air} = \dot{m}_{v,CanAir} - \dot{m}_{v,AirCov} - \dot{m}_{v,AirScr} - \dot{m}_{v,AirTop} - \dot{m}_{v,AirOut} \quad [\mathrm{kg\ m^{-2}\ s^{-1}}] \quad (2)$$

$$c_{CO2_{Air}}\dot{CO2}_{Air} = \dot{m}_{c,ExtAir} - \dot{m}_{c,AirCan} - \dot{m}_{c,AirTop} - \dot{m}_{c,AirOut} \quad [\mathrm{mg\ m^{-2}\ s^{-1}}] \quad (3)$$

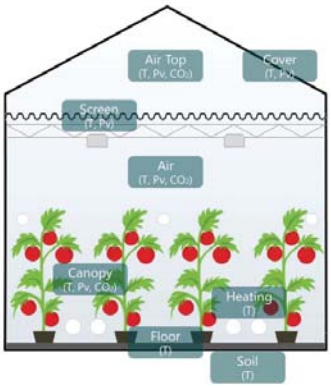

Fig. 1: Graphical representation of the state variables (T: temperature, P_v: vapor pressure of water, CO_2: CO_2 concentration) of the greenhouse climate model.

The majority of the flows distinguished in a greenhouse originate from convection at surfaces, ventilation processes, conduction at the soil and long-wave infrared radiation (FIR). Forced flows such as the short-wave radiation from the sun, latent heat flows or the sensible heat from supplementary lighting are also considered. A graphical representation of all the flows encountered in a greenhouse is shown in Fig. 2.

2.1.1 Heat flows

Convection and conduction

Convective heat flows at surfaces are function of the heat exchange coefficient (U_{ij}) and are described by:

$$\dot{q}_{cnv,ij} = U_{ij}(T_i - T_j) \qquad [\mathrm{W\ m^{-2}}] \quad (4)$$

Typically, convective processes in greenhouses are governed by free convection. In this case, the Nusselt (Nu) number describing the convective exchange process can be defined as a function of the Rayleigh (Ra) number (Balemans, 1989). The heat exchange coefficients are therefore modeled based on the Nu-Ra relation, as presented in De Zwart, 1996. In other cases, the convective heat exchange can be considered to be forced. This is the case of the outer side of the greenhouse cover, where convection is driven by wind speed. For the pipes situated close to the canopy and the floor, the heat exchange is considered to be hindered, compared to a pipe in free air. The heat exchange coefficients of these forced processes are modeled by experimental results (Bot, 1983). The whole heat exchange coefficients are presented in Table 1.

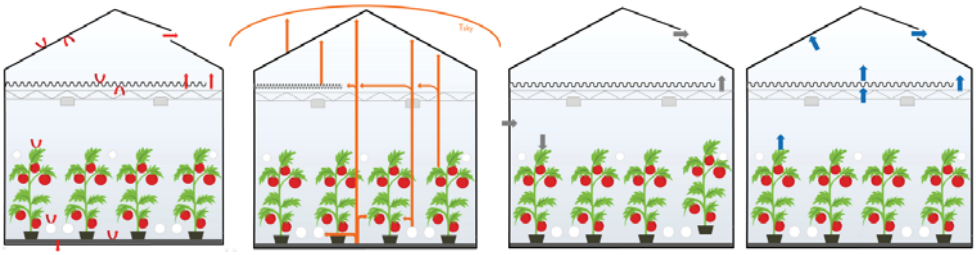

(a) (b) (c) (d)

Fig. 2: Graphical representation of the flows present in a greenhouse related to: (a) convection and conduction, (b) long-wave radiation, (c) CO_2 and (d) vapor.

The only conductive flow considered in greenhouse modeling is the conduction through the greenhouse soil. The soil under the greenhouse floor represents a big thermal capacity with a poor thermal conductivity. The floor surface can show temperature variations of 10 K during a day. To be able to describe the temperature gradient, the soil is modeled in several layers. The heat flow between the layers is described by equation 4, using the last heat exchange coefficient from Table 1.

Table 1: Heat exchange coefficients for convective and conductive heat flows

Heat exchange coefficients U_{ij} [W m^{-2} K^{-1}]	**Sources**
$U_{CanAir} = 2\ \alpha_{LeafAir}\ LAI$	(De Zwart, 1996)
$U_{AirFlr} = \begin{cases} 1.7(T_{Flr} - T_{Air})^{0.33} & \text{if } T_{Flr} > T_{Air} \\ 1.3(T_{Air} - T_{Flr})^{0.25} & \text{if } T_{Flr} \le T_{Air} \end{cases}$	(De Zwart, 1996)
$U_{AirScr} = 1.7u_{Scr}\lvert T_{Air} - T_{Scr}\rvert^{0.33}$	(De Zwart, 1996)
$U_{ScrTop} = 1.7u_{Scr}\lvert T_{Scr} - T_{Top}\rvert^{0.33}$	(De Zwart, 1996)
$U_{AirCov} = 1.7(T_{Air} - T_{Cov})^{0.33}\cos(\varphi)^{-0.66}$	(De Zwart, 1996)
$U_{TopCov} = 1.7\left(T_{Top} - T_{Cov}\right)^{0.33}\cos(\varphi)^{-0.66}$	(De Zwart, 1996)
$U_{CovOut} = \begin{cases} (2.8 + 1.2v_w)\frac{1}{\cos(\varphi)} & \text{if } v_w < 4\ m\ s^{-1} \\ 2.5v_w^{0.8}\frac{1}{\cos(\varphi)} & \text{if } v_w \ge 4\ m\ s^{-1} \end{cases}$	(Bot, 1983)

$$U_{HinderedPipeAir} = 1.99\,\pi\,\phi_{Pipe}\,l_{Pipe}\left|T_{Pipe} - T_{Air}\right|^{0.32} \quad \text{(Bot, 1983)}$$

$$U_{FreePipeAir} = 1.28\,\pi\,\phi_{Pipe}^{0.75}\,l_{Pipe}\left|T_{Pipe} - T_{Air}\right|^{0.25} \quad \text{(De Zwart, 1996)}$$

$$U_{So(j-1)So(j)} = \frac{2}{h_{So(j-1)}/\lambda_{So(j-1)} + h_{So(j)}/\lambda_{So(j)}}$$

Ventilation

The ventilation processes in a greenhouse are mainly driven by natural ventilation between the inside and outside air and between the main and top air zones. Convective flows caused by ventilation processes are modeled based on the air exchange rate f_{ij} between two air volumes *i* and *j*, as described by:

$$\dot{q}_{vent,ij} = \rho_{Air}\,c_{p,Air}\,f_{ij}(T_i - T_j) \quad [\text{W m}^{-2}] \quad (5)$$

The air ventilation between the main and top air zones is caused by two mechanisms: the air through the openings in the fabric of the screen and the air through a gap when the screen is opened. Balemans, 1989 studied the temperature driven air exchange through fully closed screens ($u_{Scr} = 1$) and derived a fitted function through experimental data. When the screen is open ($u_{Scr} < 1$), the air exchanged through the gap, caused by density difference, will dominate the exchange through the screen. This exchange was theoretically modeled by Miguel, 1998 using the Navier-Stokes equation. Combining the air flow through the screen and through the gap, the total air ventilation rate between the air and top zones is described by:

$$f_{AirTop} = u_{Scr}K_{Scr}\left|T_{Air} - T_{Out}\right|^{0.66} + \frac{1-u_{Scr}}{\bar{\rho}_{air}}\sqrt{0.5\bar{\rho}_{air}W(1-u_{Scr})g\left|\rho_{Air} - \rho_{Top}\right|} \quad [\text{m}^3\,\text{m}^{-2}\,\text{s}^{-1}] \quad (6)$$

The air ventilation flow caused by natural ventilation with the outside air through the roof windows depends mainly on the windows opening (u_{vent}), and is influenced by the wind pressure coefficient and the coefficient of energy discharge caused by friction at the windows. It is described by Boulard and Baille, 1993:

$$f_{AirOut} = \frac{u_{vent}A_{Roof}C_d}{2A_{Flr}}\sqrt{g\frac{h_{vent}}{2}\frac{T_{Air} - T_{Out}}{\bar{T}} + C_w v_w^2} \quad [\text{m}^3\,\text{m}^{-2}\,\text{s}^{-1}] \quad (7)$$

The ventilation of the greenhouse is influenced by the leakage rate through the greenhouse structure, which is dependent on the wind speed and the leakage coefficient of the greenhouse, characteristic of its structure. It can be described by:

$$f_{leakage} = \begin{cases} 0.25c_{leakage} & \text{if } v_w < 0.25 \\ c_{leakage}\,v_w & \text{if } v_w \geq 0.25 \end{cases} \quad [\text{m}^3\,\text{m}^{-2}\,\text{s}^{-1}] \quad (8)$$

Long-wave radiation

The long-wave infrared radiation flows are modeled by the Stefan-Boltzmann equation:

$$\dot{q}_{rad,ij} = A_i\epsilon_i\epsilon_j F_{ij}\sigma(T_i^4 - T_j^4) \quad [\text{W m}^{-2}] \quad (9)$$

The emission coefficients are characteristic of the surfaces and the view factors of the greenhouse elements are described in De Zwart, 1996. The exchange with the sky, whose

temperature is estimated from meteorological data by an approach proposed in (De Zwart, 1996), is also considered.

Short-wave radiation

Short-wave radiation in a greenhouse can be originated from the sun or from supplementary lighting. Although the contribution of supplementary lighting is very small during summer, in winter it can double the sun input through a day and thus, have an important impact on crop growth.

The solar radiation incident in a greenhouse can be split in three spectral parts: ultra violet (UV, from 0.3 to 0.4 μm), visible light (from 0.4 to 0.7 μm) and near infrared light (NIR, from 0.7 to 3 μm). The visible light has an interest for biological growth and is referred as photosynthetically active radiation (PAR) in greenhouse modeling. The fraction of UV is 6-10% and of PAR is 45-60% of the global radiation (Coulson, 1975). However, for plant growth it is common to assign 50% to PAR, neglect the UV and assign the other 50% to NIR (De Zwart, 1996). Besides the spectral division, the solar radiation can be divided in direct and diffuse radiation. As done in Vanthoor, 2011, the solar model of this work is simplified by making no distinction between diffuse and direct solar radiation and by assuming that the transmission coefficient of the greenhouse cover does not depend on the solar angle.

The radiation from the sun is partially absorbed by the cover and partially transmitted inside the greenhouse. Part of the transmitted radiation is later absorbed by the canopy and the floor. The PAR and NIR absorbance coefficients of the canopy and the floor depend on their reflection coefficients and on the leaf area index (LAI), defined as the leaf area per unit of ground area, i.e. of greenhouse floor. The rest of the sun radiation is absorbed by the construction elements and then released as long-wave radiation to the air.

Latent heat flows

In the thermal model there are four latent heat flows related to: condensation at the screen and cover, and evaporation at the screen and the canopy leaves. These flows are described by:

$$\dot{q}_{lat,ij} = \Delta H \, M_{v,ij} \qquad [\text{W m}^{-2}] \quad (10)$$

Sensible heat from supplementary lighting

Only part of the electric consumption of the supplementary lighting is converted to short-wave radiation. For a high intensity discharge lamp e.g., high pressure sodium (HPS) lamps, 17% of the electrical power is converted to NIR and 25% to visible light (Urban and Urban, 2010). Thus, 58% is released to the greenhouse air.

2.1.2 Vapor flows

The vapor exchange coefficients for condensation and evaporation at the screen and the cover are linearly related to their convective heat exchange coefficients by a conversion factor. The vapor flow from the air to a component is described by:

$$\dot{m}_{v,ij} = \begin{cases} 0 & \text{if } P_{v,i} < P_{v,j} \\ 6.4 \cdot 10^{-9} \, U_{ij}(P_{v,i} - P_{v,j}) & \text{if } P_{v,i} \geq P_{v,j} \end{cases} \qquad [\text{kg m}^{-2}\,\text{s}^{-1}] \quad (11)$$

By allowing a mass flow rate from the upper surface of the screen to the top air compartment, the model assumes that the screen is capable of transporting water through its fabric. Water is transported from the lower side to the upper and storage of water in the screen is neglected. Therefore, evaporation from the upper side is only possible when condensation takes place at the lower side.

Mass transfer also occurs in ventilation processes, i.e. between the main and top air zones, and between these and the outside air. The computation of the mass flow from an air exchange by ventilation is described by:

$$\dot{m}_{v,ij} = \frac{M_{Water} f_{ij}}{R}\left(\frac{P_{v,i}}{T_i} - \frac{P_{v,j}}{T_j}\right) \quad [\text{kg m}^{-2}\text{ s}^{-1}] \quad (12)$$

The vapor flow from the canopy to the greenhouse air originates from a phase interface somewhere inside the cavities of a leaf. The resistance to vapor transport from the canopy leaves to the greenhouse air is made of an internal resistance and a boundary layer resistance (Stanghellini, 1987). According to the latter, the canopy transpiration can be defined as:

$$\dot{m}_{v,CanAir} = \frac{2\,\rho_{Air}\,c_{p,Air}\,LAI}{\Delta H\,\gamma(r_b + r_s)}\left(P_{v,Can} - P_{v,Air}\right) \quad [\text{kg m}^{-2}\text{ s}^{-1}] \quad (13)$$

2.1.3 CO_2 flows

In the greenhouse, there are three CO_2 flows associated to the ventilation processes and two forced flows, i.e. the canopy consumption and the CO_2 enrichment. The CO_2 flow accompanying an air flow is function of the air flow rate and can be described by:

$$\dot{m}_{c,ij} = f_{ij}\left(CO_{2,i} - CO_{2,j}\right) \quad [\text{mg m}^{-2}\text{ s}^{-1}] \quad (14)$$

The CO_2 flow from the air absorbed by the canopy depends on the canopy photosynthesis rate and respiration processes and is described by the crop yield model.

2.2 Crop yield model

A dynamic tomato crop yield model was implemented to account for the effects of the indoor climate on crop growth and thereby on the harvested dry matter. Although crop growth is related to photosynthesis, most of the existent crop models directly relate these two with the absence of a carbohydrate buffer. The function of the buffer is to store the carbohydrates from the photosynthesis (inflow) and to distribute them to the plant organs (outflow). It has a maximum capacity, above which carbohydrates cannot be stored anymore, and a lower limit, below which the carbohydrate outflow stops. Thus, the in- and out-flows depend on the level of carbohydrates in the buffer and thereby, may not be simultaneous. An approach based on not considering the buffer neglects the non-simultaneous character of the flows. For example, it can neglect the crop growth after dusk, when photosynthesis stops but there may still be carbohydrate distribution if the buffer level is higher than its lower limit. The presence of a carbohydrate buffer is thus important when modeling crop growth.

Models with a common carbohydrate buffer are available in the current literature (e.g. Dayan et al., 1993; Heuvelink, 1996; Linker et al., 2004; Marcelis et al., 1998; Seginer et al., 1994). In this work, a recent yield model developed and validated for a variety of temperatures (Vanthoor, 2011) has been implemented. The model computes the carbohydrates distribution flows in the presence of a buffer, as shown in Fig. 3. To that end, the model applies carbohydrates mass balances on the buffer, fruits, stems and leaves. The mass balance on the buffer is defined by:

$$\dot{C}_{Buf} = \dot{m}_{C,AirBuf} - \dot{m}_{C,BufFruit} - \dot{m}_{C,BufLeaf} - \dot{m}_{C,BufStem} - \dot{m}_{C,BufAir} \quad [\text{mg m}^{-2}\text{ s}^{-1}] \quad (15)$$

The description of the whole balances can be found in Altes-Buch et al., 2018. The inputs of the model are the canopy instantaneous temperature, the CO_2 concentration of the greenhouse

air and the PAR absorbed by the canopy. Their values are retrieved from the greenhouse climate simulation model, in which T_{Can} and $CO2_{Air}$ are state variables and PAR_{Can} is a function of the global irradiation and the transmission coefficient of the greenhouse cover. The model takes also into account the 24 hour mean temperature of the canopy (T_{Can}^{24}). The main outputs of the model are the harvested tomato dry matter (DM_{Har}), the LAI and the air CO_2 flow absorbed by the canopy.

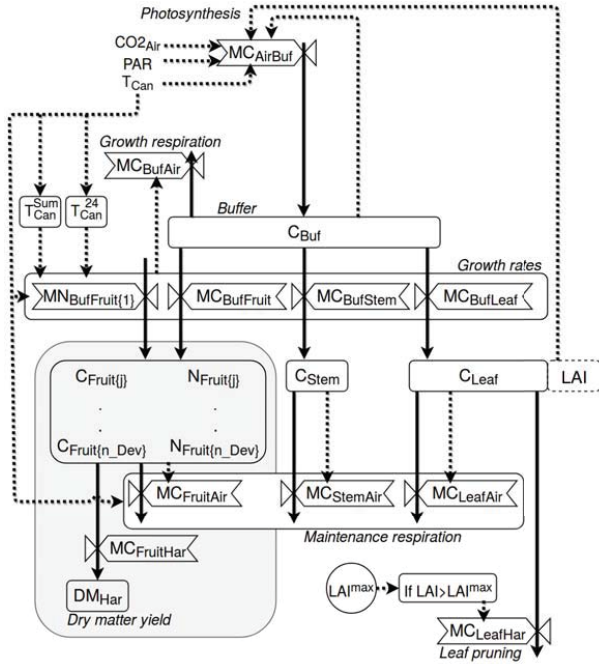

Fig. 3: Schematic representation of the crop yield model. Boxes define state variables (blocks), semi-state variables (dotted blocks) and carbohydrate flows (valves). Arrows define mass flows (solid lines) and information flows (dotted lines). For the purpose of readability, the grey box is a simplified scheme of the mass flow rates related to fruit development. A more detailed scheme of the latter can be found in Vanthoor, 2011.

2.3 Climate control

Greenhouses have high requirements on indoor climate control. The climate controller adjusts heating, ventilation and CO_2 supply to attain the desired climate. In this work, several control systems are developed, based on the control strategies proposed in the literature.

2.3.1 Set-points definition for temperature and CO_2

The determination of set-points is at the top of the functionality of the climate controller. Temperature set-points differ from day-time to night-time and are sometimes adapted to the level of radiation. CO_2 is supplied during daylight to enhance photosynthesis. As measured in Nilsen et al., 1983, different combinations of CO_2 concentration and air temperature lead to different photosynthesis rates. Although a sharp reduction in photosynthesis is measured at non-optimal temperatures, similar values are measured for close-to-optimal temperatures (i.e. optimal temperature ±5ºC). Therefore, temperature and CO_2 set-points can be optimized not only in terms of crop growth but also in terms of energy use. In fact, the definition of temperature set-points for optimal crop growth and energy use has been the subject of a

substantial literature (e.g. Elings et al., 2006; Aaslyng et al., 2003 ; Dieleman et al., 2006 ; Dieleman et al., 2005). However, since this work does not focus on climate set-points optimization, no innovative control is proposed. Instead, the strategy proposed in Aaslyng et al., 2003 is implemented in Python and the set-points are inputted as a time-series "txt" file in the model. This strategy consists in minimizing energy consumption while maintaining a crop growth close to the maximal growth rate by:

i) computing a 2-D array of photosynthesis rates for a range of CO_2 and temperature values at a given PAR,
ii) selecting the pairs of CO_2 and temperature that ensure at least 80% of the photosynthesis rate (being 100% the maximum value of the 2-D array), and
iii) defining the temperature and CO_2 set-point ($T_{Air,SP}$ and $CO_{2,Air,SP,th}$) as the pair in ii) with the lowest temperature.

In this work, a PI controller is responsible for adjusting the heating power output by varying the mass flow rate of the heating pipes according to the difference between the air temperature set-point and the actual value. The control strategy for CO_2 is based on a maximal supply rate, defined by the capacity of the CO_2 enrichment system. This capacity is function of the CO_2 source, which is commonly a combination of fossil fuel combustion gases and CO_2 stored in liquid phase. While respecting the enrichment capacity, the supply rate is adapted to attain the CO_2 set-point. However, in high ventilation conditions, CO_2 enrichment is commonly reduced due to the high exchange rate to the outside air. To take this into account, the theoretical CO_2 set-point proposed by the control strategy is modified so that it decreases proportionally with the increase in the ventilation rate. This is done as defined by equations 16 and 17.

$$CO_{2,Air,SP} = f(u_{vent})\left(CO_{2,Air,SP,th} - CO_{2,ExtMin}\right) + CO_{2,ExtMin} \quad \text{[ppm]} \quad (16)$$

$$f(u_{vent}) = \begin{cases} 1 - {u_{vent}}/{u_{vent_{Max}}} & \text{if } u_{vent} < u_{vent_{Max}} \\ 0 & \text{if } u_{vent} \geq u_{vent_{Max}} \end{cases} \quad \text{[-]} \quad (17)$$

2.3.2 Supplementary lighting

The most popular lamp type for commercial supplementary lighting in horticulture is high pressure sodium (HPS) lamps. HPS lamps are the most efficient in the PAR spectrum range, with an emission highly concentrated between 500 and 650 nm. HPS lighting is not designed for frequent cycling because it dramatically reduces lamp lifespan. Thus, regardless of the control method, it is best to set up constraints to operate lighting for extended periods. The implemented control strategy for the lighting is based on the following:

- *Lighting window*: allow lights to be turned on between $h_{illu,min,ON}$ and $h_{illu,max,ON}$ (e.g. 5 AM and 10 PM).
- *Lighting set-point*: allow lights to be turned on during the lighting window if light levels decrease below $I_{illu,ON}$ (e.g. 40 Wm^{-2}) and to be turned off when light levels increase above $I_{illu,OFF}$ (e.g. 120 Wm^{-2}).
- *Light accumulation*: turn off lights or do not allow turning them on if the daily accumulated light exceeds $I_{acc,max}$ (e.g. 5 kWh).
- *Proving time*: light levels must be below the set-point for at least $t_{illu,proving}$ (e.g. 30 minutes).
- *Minimum on time*: to prevent cycling, lights must remain on for minimum $t_{illu,min,ON}$ (e.g. 2 hours) once they are turned on, regardless of other conditions.

The strategy sets up a time window for lighting, during which a lighting set-point condition is applied. The proving time and minimum on time strategies are implemented to prevent cycling.

2.3.3 Windows aperture

Windows in the greenhouse can be opened either for dehumidification or for cooling the greenhouse. Excessive humidity can cause fungal diseases or physiological disorders (Grange and Hand, 1987). Humidity in greenhouses is controlled by means of a strategy related to a constraint rather than a specific set-point (De Zwart, 1996). The constraint is based on allowing a maximum value of relative humidity in the air, commonly set at 85%. The most common technique for dehumidification is the combination of ventilation and heating. Although this technique is energy consuming and thus expensive, dehumidifying systems based on refrigerant cycles, e.g. heat pumps, have not proved to be economically feasible (Urban and Urban, 2010). Windows are also used for cooling the air in the case of excessive temperatures, since they have a negative impact on the harvest rate. For example, in Vanthoor, 2011 the harvest rate at daylight temperatures of 40ºC was 54.5% of that at 25ºC. Moreover, temperatures above 25ºC can penalize fruit quality e.g. size and color (Urban and Urban, 2010). In this work, a proportional (P) controller is used to select the opening of the windows according to the following:

- *Air sanitation*: A maximum value $RH_{vent,ON}$ is allowed for humidity.
- *Air cooling*: A maximum value $T_{vent,ON}$ is allowed for air temperature.

2.3.4 Thermal screen closure

As previously mentioned, thermal losses to the outside can be reduced from 38% to 60% by using a thermal screen (Bailey, 1988). This capability of reducing thermal losses is defined by the screen material, which is selected according to the climate of the region. In fact, depending on the nature of the screen, the light transmission coefficient can vary from 15% to 88%. Thus, when drawn, the screen reduces considerably the transmitted light above the canopy. The most conventional method to operate the screen is therefore to deploy it at sunset, when heating demand becomes significant, and remove it at sunrise, to profit from the available sun light. The removal of the screen must be operated progressively to avoid a thermal shock. A way of further reducing energy consumption is to deploy the screen before sunset or to delay the removal until after sunrise. However, this implies a loss of crop production caused by a reduction on the available light. A good approach would be to study the threshold between energy saving and production loss in order to define the optimal deployment and removing times. However, estimating the reduction of plant growth is a complex task that, although it has been the object of some studies (e.g. Aaslyng et al., 2003; Bailey, 1988), it commonly has many uncertainties and thereby requires many assumptions. A simpler approach is to define the deployment of the screen in function of the outside irradiation. In fact, the photosynthetic activity of the plant achieves its maximal potential about one hour after sunrise and diminishes just before sunset (Grisey and Brajeul, 2007). In Dutch-conditions, deploying the screen after 50 Wm^{-2} (instead of 5 Wm^{-2} usually practiced) allows to decrease energy consumption by an extra 3% without penalizing crop growth (Dieleman and Kempkes, 2006). Depending on the night, a small temporary opening of the screen may be necessary to regulate humidity or temperature. As defined by equation 6, screen gaps increase the air exchange between the main and top air zones and therefore decrease temperature and humidity.

In this work, the developed screen control strategy is based on the following:

- *Opening/closing set-point*: the screen is opened (closed) if irradiation increases (decreases) above (below) a certain value $I_{Scr,ON}$ ($I_{Scr,OFF}$) (e.g. 35 Wm^{-2}).
- *Opening/closing time*: the screen is opened progressively by 1% per minute (with an interval pause of 3 minutes) followed by a full opening after 30%. This approach has proven not to generate cold air flows on top of the canopy (Grisey and Brajeul, 2007). As proposed by the latter, the opening percentage and pause time is adapted to the outside weather. The time to fully open the screen is about 45 min to 60 min in cold days and 30 min in mild days.
- *Humidity gap*: the screen is opened in steps of 1% (with an interval of 3 min) up to a maximum of 4% if relative humidity exceeds its set-point. This approach is similar to the one proposed in Dieleman and Kempkes, 2006.

3. SIMULATION

3.1 Case study

The dynamic model of greenhouse climate is used to simulate the indoor climate of a greenhouse for tomato crop. The model is parameterized based on a real case study of a greenhouse in the Netherlands, whose design parameters were published in Vanthoor, 2011. The considered greenhouse structure is that of a Venlo-type greenhouse, typical for mild-temperature conditions. The cover is made of a single glass layer and the considered floor area is 1.4 ha. The greenhouse is only ventilated naturally through the windows on both wind and leeside of the roof. The greenhouse is heated by means of pipe heating and is equipped with a CO_2 enrichment system as well as a movable thermal screen. Any type of cooling equipment is considered. The design parameters related to greenhouse construction, ventilation, heating, CO_2 enrichment and supplementary lighting are presented in Table 2.

The tomato yield model is run simultaneously with the greenhouse climate model. The crop initial conditions are established by the case study and are presented in Table 3. The climate controller actions are based on the strategies presented in section 2.20, whose inputs are presented in Table 3. The simulation period starts in December 10th and ends in November 22nd, being equivalent to a growing period for tomato in mild-climate conditions. Data for a typical meteorological year (TMY) in Brussels is used to describe the outdoor conditions, namely air temperature, relative humidity, pressure, wind speed and global irradiation.

For the purpose of comparison, several simulations are performed:

- *G*: Simulation with the design and control parameters presented in Table 2 and Table 3.
- *G2*: Simulation similar to *G* but with an opening and closing of the screen at sunrise and sunset ($I_{Scr,ON} = I_{Scr,OFF} = 5\ Wm^{-2}$).
- *G-Scr*: Simulation of a greenhouse without thermal screen.

Table 2: Greenhouse design parameters for the case study

Greenhouse design parameters	Parameter	Value	Unit
Construction			
Mean greenhouse cover slope	φ	25	º
Surface of the cover including side-walls	A_{Cov}	$1.8 \cdot 10^4$	m^2
Surface of the greenhouse floor	A_{Flr}	$1.4 \cdot 10^4$	m^2
Height at which the screen is installed	h_{Air}	3.8	m
Mean height of the greenhouse	h_G	4.2	m

Cover			
FIR emission coefficient	$\epsilon_{Cov,FIR}$	0.85	-
NIR reflection coefficient	$\rho_{Cov,NIR}$	0.13	-
PAR reflection coefficient	$\rho_{Cov,PAR}$	0.13	-
NIR transmission coefficient	$\tau_{Cov,NIR}$	0.85	-
PAR transmission coefficient	$\tau_{Cov,PAR}$	0.85	-
Specific heat capacity	$c_{p,Cov}$	$0.84 \cdot 10^3$	J K^{-1} kg^{-1}
Density	ρ_{Cov}	$2.6 \cdot 10^3$	kg m^{-3}
Thickness	h_{Cov}	$4 \cdot 10^{-3}$	m
Thermal screen			
FIR emission coefficient	$\epsilon_{Scr,FIR}$	0.67	-
NIR reflection coefficient	$\rho_{Scr,NIR}$	0.35	-
PAR reflection coefficient	$\rho_{Scr,PAR}$	0.35	-
NIR transmission coefficient	$\tau_{Scr,NIR}$	0.6	-
PAR transmission coefficient	$\tau_{Scr,PAR}$	0.6	-
Specific heat capacity	$c_{p,Scr}$	$1.8 \cdot 10^3$	J K^{-1} kg^{-1}
Density	ρ_{Scr}	$0.2 \cdot 10^3$	kg m^{-3}
Thickness	h_{Scr}	$0.35 \cdot 10^{-3}$	m
Screen flux coefficient	K_{Scr}	$0.05 \cdot 10^{-3}$	m^3 m^{-2} $K^{-0.66}$ s^{-1}
Floor			
FIR emission coefficient	$\epsilon_{Flr,FIR}$	1	-
NIR reflection coefficient	$\rho_{Flr,NIR}$	0.5	-
PAR reflection coefficient	$\rho_{Flr,PAR}$	0.65	-
Thermal conductivity	λ_{Flr}	1.7	W m^{-1} K^{-1}
Specific heat capacity	$c_{p,Flr}$	$0.88 \cdot 10^3$	J K^{-1} kg^{-1}
Density	ρ_{Flr}	2300	kg m^{-3}
Thickness	h_{Flr}	0.02	m
Soil			
Thermal conductivity	λ_{So}	0.85	W m^{-1} K^{-1}
Volumetric heat capacity	$\rho c_{p,So}$	$1.73 \cdot 10^6$	J K^{-1} m^{-3}
Canopy			
Convective heat exchange coefficient	$\alpha_{LeafAir}$	5	W m^{-2} K^{-1}
FIR emission coefficient	$\epsilon_{Can,FIR}$	1	-
Ventilation properties			
Specific roof ventilation area	A_{Roof}/A_{Flr}	0.1	m^2
Ventilation discharge coefficient	C_d	0.75	-
Ventilation global wind pressure coefficient	C_w	0.09	-
Greenhouse leakage coefficient	$c_{leakage}$	$1 \cdot 10^{-4}$	-
Vertical dimension of a single vent opening	h_{vent}	0.68	m
Heating system			
External pipe diameter	$\emptyset_{pipe}$	51	mm
Pipe length per greenhouse square meter	l_{pipe}	1.875	m m^{-2}
CO_2 enrichment			
Capacity of the external CO_2 source	ϕ_{ExtCO2}	7.5	mg m^{-2} s^{-1}
Supplementary lighting (HPS)			
Capacity of the lamps	$P_{el,illu}$	100	W m^{-2}

Table 3: Initial crop conditions and climate control inputs for the case study

	Parameter	Value	Units
Crop conditions			
LAI maximum	LAI_{max}	2.7	$m^2\ m^{-2}$
LAI at the start growing period	LAI_0	0.3	$m^2\ m^{-2}$
Carbohydrate weight of leaves	C_{Leaf}	$40 \cdot 10^3$	mg $\{CH_2O\}\ m^{-2}$
Carbohydrate weight of stems and roots	C_{Stem}	$30 \cdot 10^3$	mg $\{CH_2O\}\ m^{-2}$
Climate control			
CO_2 enrichment			
Minimum CO_2 concentration enrichment	$CO_{2,ExtMin}$	390	ppm
Maximum ventilation for CO_2 enrichment	$u_{vent,Max}$	0.3	-
Supplementary lighting			
Start of light window	$h_{illu,min,ON}$	5	AM
End of light window	$h_{illu,max,ON}$	10	PM
Light set-point for turning ON lights	$I_{illu,ON}$	40	$W\ m^{-2}$
Light set-point for turning OFF lights	$I_{illu,OFF}$	120	$W\ m^{-2}$
Light accumulation set-point	$I_{acc,max}$	5	kWh
Proving time	$t_{illu,proving}$	1800	s
Minimum ON time	$t_{illu,min,ON}$	7200	s
Windows			
Ventilation set-point for air sanitation	$RH_{vent,ON}$	85	%
Ventilation set-point for air cooling	$T_{air,vent,ON}$	26	ºC
Thermal screen			
Opening set-point	$I_{Scr,OFF}$	50	$W\ m^{-2}$
Closing set-point	$I_{Scr,ON}$	50	$W\ m^{-2}$

3.2 Results

The overall thermal consumption after the simulation period for every case is presented in Table 4. If we compare the consumptions after one winter day we can observe that, as expected, the use of a thermal screen results in a reduced thermal consumption, being in G 41% lower than in G-Scr. This value is in agreement with (Bailey, 1988), who stated the savings could go between 38 and 60%, and with (Grisey and Brajeul, 2007), who attribute savings between 35-40% for non-aluminized screens such as the one used in this simulation. The screen control set-point in G (i.e. 50 Wm^{-2}) enabled savings in thermal consumption up to 11% more than using G2's set-point (i.e. 5 Wm^{-2}). When comparing the consumptions after the whole simulation period, the savings are attenuated, since in summer the thermal screen is barely used. After the whole simulation period, the use of the screen enabled reducing the overall thermal consumption by 18% and the screen set-point in G (i.e. 50 Wm^{-2}) resulted in saving an extra 1.3%. Due to light loss, the harvested dry matter in G is 1.1% lower than in G2. Although the computed overall saving is in agreement with Dieleman and Kempkes, 2006, by using the screen set-point of 50 Wm^{-2} they obtain energy savings of 3% with a production loss of 0.5%. The variation on these values is mainly due to the different type of thermal screen used in both studies and the implemented control strategy. The control strategy of the screen could therefore be improved to further decrease the consumption. The computed total harvested dry matter (Table 4) overestimated the values simulated for two Dutch greenhouses in Vanthoor, 2011. However, it should be noted that their simulation period was shorter (from December to October). The overestimation on yield could also be explained by

a higher 24-hour mean canopy temperature (20.24 in this work, compared to 18.2 in Vanthoor, 2011), the differences on the used set-point strategy (unknown in Vanthoor, 2011) and/or a possible higher global radiation in the TMY used for this simulation.

Table 4: Consumption and harvest results for the three simulations (G, G2, G-Scr)

Description	G	G2	G-Scr	Units
Consumption after a winter day	1.956	2.203	3.328	kWh m^{-2}
Consumption after the simulation period	368.8	373.7	451.3	kWh m^{-2}
Harvested DM after the simulation period	4.61	4.66	4.68	kg m^{-2}

The differences in the screen operation during a winter day for both treatments G and G2 are shown in Fig. 4. In a winter day as such, global outside radiation is very low, being above 50 Wm^{-2} only from 12:51 to 14:34 (see irradiation plot). The screen in G is therefore open only for less than two hours, whereas in G2, the screen is open for more than six hours (from 10:21 until 17:01) (see control value plot). The PAR absorbed by the canopy ($I_{PAR,SunCan}$) is lower in G, since having the screen deployed implies a lower light transmittance coefficient. However, this decrease on absorbed PAR decreases crop growth only by 1% over the whole simulation period (Table 4) and is therefore negligible. In cold days the solar contribution, being low, is not enough to heat up the indoor air to the set-point. Thus, once the screen is opened, the main and top air zones are mixed, the air temperature decreases and as a consequence, the heating demand increases. The heating demand in G2 is therefore much higher than in G because of its earlier screen opening, as it can be seen in the heat flow plot. In fact, by comparing the instant heating demand curves, differences up to 75 Wm^{-2} are encountered. In cold sunny days, this difference is attenuated due to the higher heat gain from the sun.

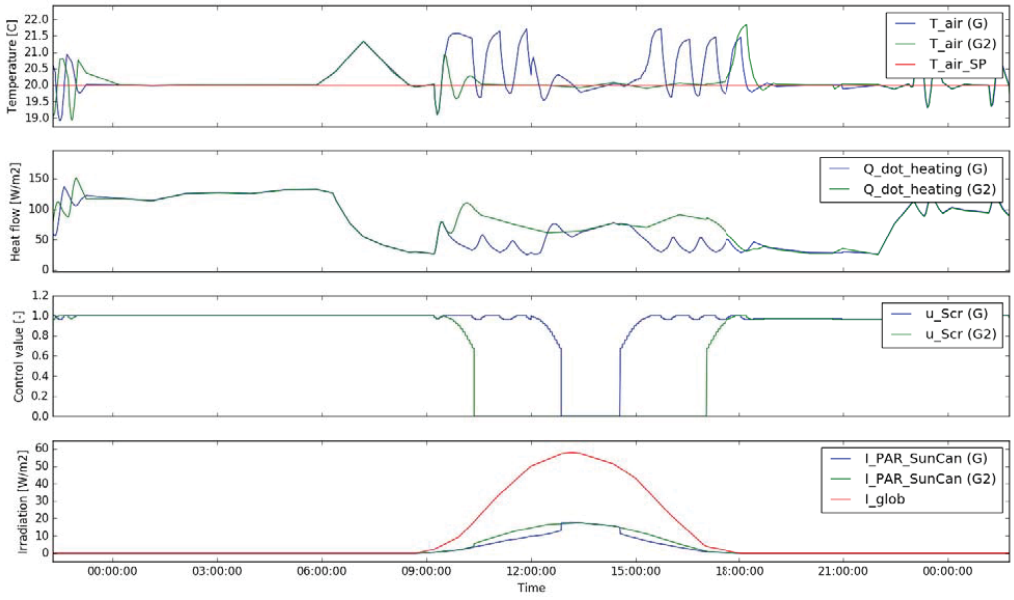

Fig. 4: Comparison of the indoor temperature, heating demand, screen control and absorbed PAR by the canopy for simulations G and G2 in January 27.

Fig. 5 compares the indoor climate and the climate control variables for three cold and warm days. The irradiation plot shows the importance of supplementary lighting in winter days, in which it can double the total accumulated light from the sun. By looking at the lighting profile, it can be seen that lighting is used constantly during the *lighting window* in winter. However, lighting is barely used in summer, except for cloudy days (e.g. the 22nd of July in Fig. 5).

In the control variables plot, it can be seen that in winter the screen is used every day and there is almost no ventilation, whereas in summer, ventilation is used constantly and the screen is always open. The control actions are therefore consistent with mitigating losses in cold days and cooling down the indoor air in warm days. As stated by equation 16, high ventilation rates imply a decrease on the CO_2 concentration set-point of the air with respect to the theoretical set-point. This can be seen in the CO_2 plot, where the CO_2 concentration is equal to the theoretical set-point in winter and much lower in summer.

The gaps opened by the screen to control humidity can be seen in the control variables plot. These gaps cause an increase on the air flow rate between the main and top air zones, and thereby a decrease on the humidity of the main air zone. However, temperature is also decreased. This can be seen in the left temperature plot, where temperature fluctuations are synchronized with the screen gaps. Since temperature fluctuations are kept in ±1.5K difference from the set-point, it is assumed that they do not penalize crop growth.

In *Fig. 6*, the CO_2 concentrations of the air zones and the main CO_2 flows in the greenhouse are presented for two cold (left) and warm (right) days. As expected, the CO_2 concentration in the top zone is lower than in the main zone when the screen is closed. However, when the screen is open, the air zones are mixed and their concentration is therefore equal. In warm days the screen is always open, whereas in cold days it is only open for some hours after midday (i.e. when solar gain is acceptable), as previously shown in Fig. 4. It can be noticed that the CO_2 concentration reaches values up to 1200 ppm in cold days, in which ventilation is limited. In summer, on the contrary, ventilation is enhanced and can reach high flow rates, as it can be seen in the right CO_2 flow plot ($\dot{M}_{c,AirOut}$). Thus, the CO_2 concentration of the air in warm days is much lower, being almost equal than the CO_2 concentration of the outside air.

When the screen is deployed, some fluctuations in the CO_2 concentration of the top air zone are present. This is due to the screen gaps opened for humidity control. The higher exchange between the air and top zones implies a decrease in the CO_2 concentration of the main zone, which is compensated by an increase in CO_2 enrichment. It should be noted that the CO_2 enrichment flow at night is null, since the canopy does not consume CO_2 at this point.

The vapor pressure of water (*Fig. 7*), controlled by the screen opening, presents a similar oscillating behavior. This occurs in cold days, since in warm days the screen is always open. In this case, the vapor pressure of water is only controlled by natural ventilation. This control may not be sufficient because, as previously shown in Fig. 5, relative humidity in the greenhouse may stay above the set-point for several hours, even with the windows fully open. It should be highlighted that the canopy transpiration flow (function of the air temperature, CO_2 concentration, vapor pressure of water and PAR absorbed by the canopy) can reach high values in summer. For example, during the 24th of July, $\dot{M}_{v,CanAir}$ was up to three times higher than in cold days or than in the 22nd of July. This is due to the high solar gain and the excessive air temperature in the greenhouse (as shown in Fig. 5).

The obtained profiles of temperature, CO_2 concentration and vapor pressure of water of the indoor air are similar to those presented in Vanthoor, 2011, where a greenhouse is simulated for the summer and winter period in The Netherlands. In Vanthoor, 2011, the air CO_2

concentration profile is only presented for summer period. Therefore, the temperature and CO_2 concentration profiles are also compared to the results presented De Zwart, 1996, in which a greenhouse is simulated in The Netherlands. The simulation results are plotted for three winter days. Although the maximum CO_2 value reached in the indoor air is different because of the different CO_2 supply capacities used in both works, the obtained profiles are very similar.

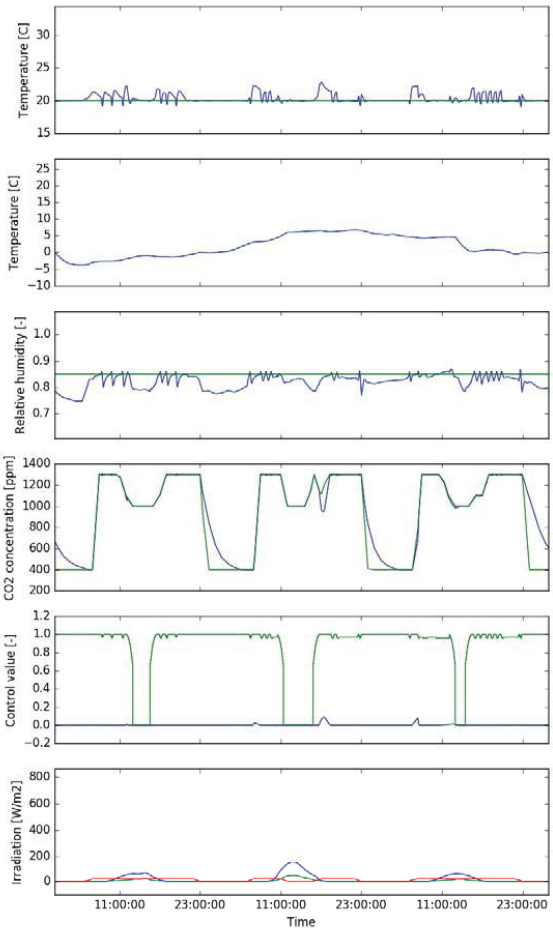
Temperature [C]
30
25
20
15
Temperature [C]
25
20
15
10
5
0
−5
−10
Relative humidity [-]
1.0
0.9
0.8
0.7
CO2 concentration [ppm]
1400
1200
1000
800
600
400
200
Control value [-]
1.2
1.0
0.8
0.6
0.4
0.2
0.0
−0.2
Irradiation [W/m2]
800
600
400
200
0
11:00:00
23:00:00
11:00:00
23:00:00
11:00:00
23:00:00
Time

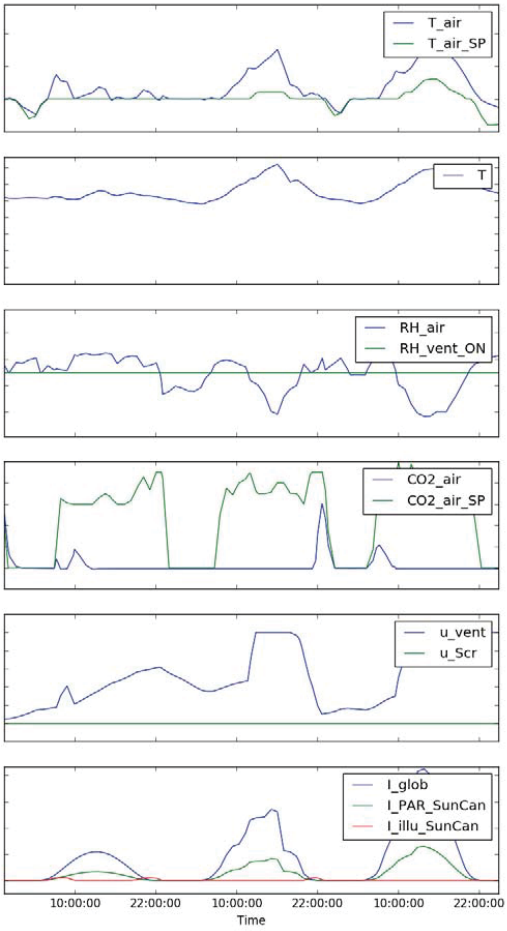

Fig. 5: Comparison of the indoor climate and control variables in simulation G during three cold (22nd-24th January, left) and warm (22nd-24th July, right) days.

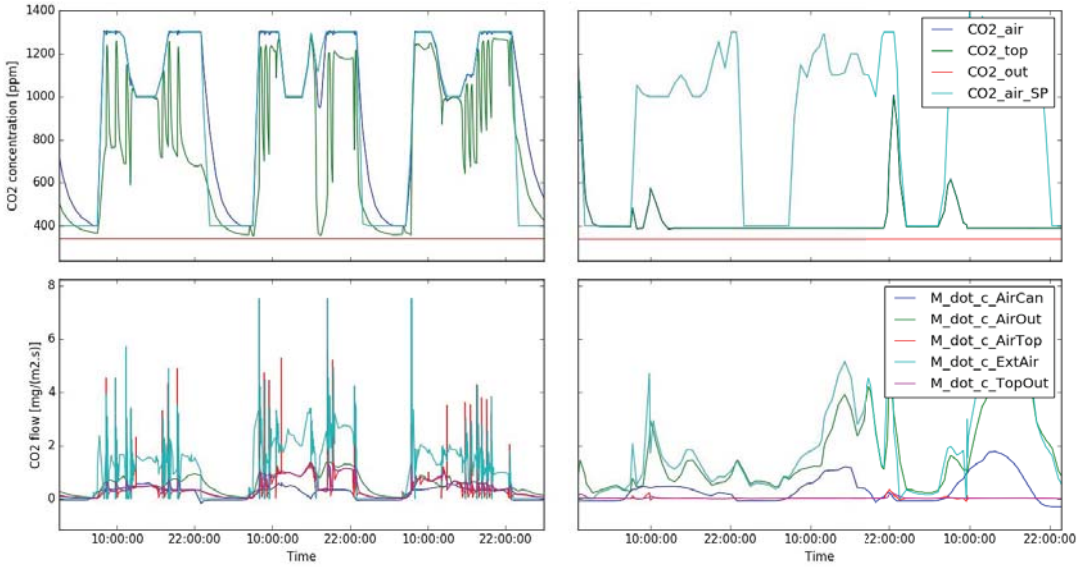

Fig. 6: Comparison of the CO_2 concentrations of the air zones and the main CO_2 flows in the greenhouse in simulation G during three cold (22nd-24th January, left) and warm (22nd-24th July, right) days.

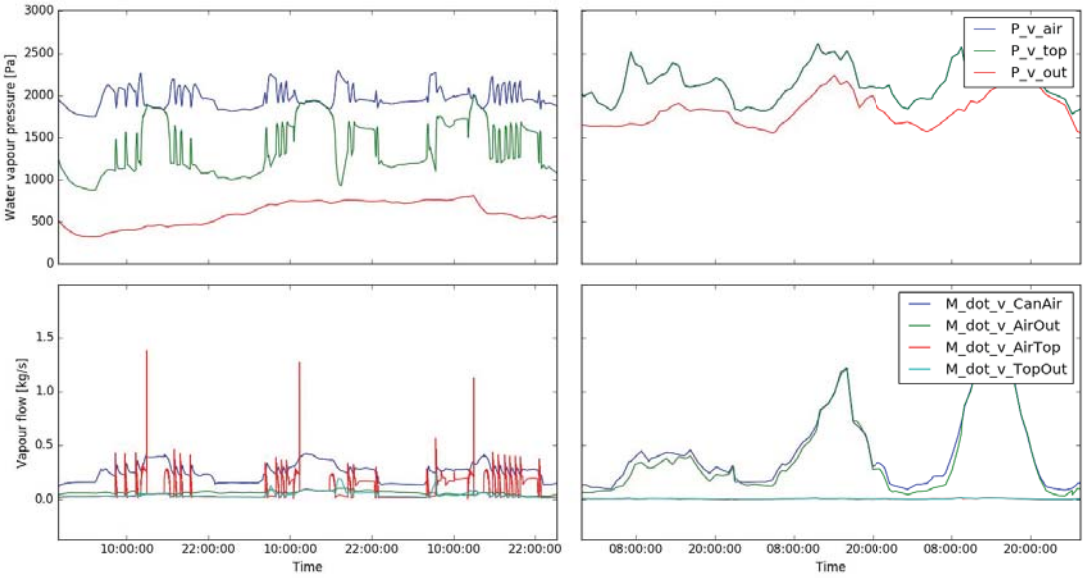

Fig. 7: Comparison of the vapor pressure of water from the different air zones and the main vapor flows in the greenhouse in simulation G during three cold (22nd-24th January, left) and warm (22nd-24th July, right) days.

4. CONCLUSION

The presented modeling framework filled the gap of an inexistent open-source platform for the simulation of greenhouse climate and crop yield including climate control systems. It

should be noted that the models can be used for a wide range of purposes, such as the optimal control of the greenhouse actuators, the optimal sizing of the HVAC appliances or the optimal integration of the units in district heating and/or the power system. The models are parametric, thus ensuring its use for a range of greenhouse designs, climates and cultivation crops. The models are released as open-source in order to ensure a proper reproducibility and reusability of this work (Download from: https://github.com/queraltab/Greenhouses-Library). A detailed description of each model and the required information to run the models is provided in Altes-Buch et al., 2019.

For the purpose of climate control, several control systems are developed to regulate heating, ventilation, CO_2 enrichment, supplementary lighting and the movable screens in greenhouses. The proposed control strategies are designed based on a literature review. The strategies are then tested in a case study, which is also used to exemplify the use of the greenhouse climate and the tomato yield models. To that end, the models are run for three cases with different screen control strategies. The computed thermal consumption in every case is in agreement with the results presented in the literature (Bailey, 1988; Dieleman and Kempkes, 2006; Grisey and Brajeul, 2007). Although the screen control strategy was proved to function properly, it could be optimized to further decrease the thermal consumption. The harvested dry matter computed in the crop yield model is a bit overestimated with respect to the values presented in Vanthoor, 2011. However, the differences in both simulations could justify the overestimation, as discussed in section 4.2. Moreover, the computed profiles of air temperature, CO_2 concentration and vapor pressure of water, illustrated for cold and warm days, are very similar to profiles presented in the literature (De Zwart, 1996; Vanthoor, 2011). This not only ensures the physical representation of the flows by the implemented greenhouse model, but also the proper functioning of the proposed control strategies for CO_2 enrichment and humidity control.

ACKNOWLEDGMENTS

The authors thank the Walloon Region of Belgium, which has funded this research in the context of the EcoSystemePass project (convention nº 1510610).

NOMENCLATURE

Subscripts

Air	Greenhouse main air zone	lat	Latent
b	Boundary	Leaf	Leaves
Buf	Carbon buffer	Out	Outside air
c	CO_2	Pipe	Pipe heating system
C	Carbohydrate	rad	Long-wave infrared radiation
Can	Canopy	Roof	Roof ventilation
cnv	Convection	s	Stomata
Cov	Cover	Scr	Thermal screen
Ext	External source of CO_2	So(j)	The 'j'th soil layer
Flr	Floor	Stem	Stem and roots
Fruit	Fruit	Top	Greenhouse top air zone
Glob	Global radiation	v	Vapor
Har	Harvest	vent	Ventilation
illu	Supplementary lighting	w	Wind

Remaining symbols

α	Absorption coefficient	-
γ	Psychometric constant	Pa K^{-1}
ϕ	Diameter	m

ϵ	FIR emission coefficient	-
ρ	Density or reflection coefficient	kg m^{-3}, -
λ	Thermal conductivity	W m^{-1} K^{-1}
τ	Transmission coefficient	-
σ	Stefan-Boltzmann constant	W m^{-2} K^{-4}
ΔH	Latent heat of evaporation of water	J kg^{-1}
A	Area	m^2
c	Capacity of the associated component	
C	Carbohydrate amount	mg {CH_2O} m^{-2}
c_p	Specific heat capacity	J kg^{-1} K^{-1}
$CO2$	Carbon dioxide concentration	mg m^{-3}
DM	Dry matter	mg {DM} m^{-2}
f	Air flow rate	m^3 m^{-2} s^{-1}
F	View factor	-
h	Thickness or vertical dimension	m
l	Length per square meter	m m^{-2}
$\dot{m}$	Mass flow (vapor, CO_2) averaged per square meter of greenhouse floor	kg m^{-2} s^{-1}, mg m^{-2} s^{-1}
P	Pressure	Pa
$\dot{q}$	Heat flow averaged per square meter of greenhouse floor	W m^{-2}
r	Resistance	s m^{-1}
T	Temperature	K
u	Climate control variable	-
U	Heat exchange coefficient	W m^{-2} K^{-1}
v	Speed	m s^{-1}
W	Width	m

REFERENCES

Aaslyng, J.M., Lund, J.B., Ehler, N., and Rosenqvist, E. (2003). IntelliGrow: a greenhouse component-based climate control system. Environ. Model. Softw. *18*, 657–666.

Altes-Buch, Q., Quoilin, S., and Lemort, V. (2018). Modeling and control of CHP generation for greenhouse cultivation including thermal energy storage. In Proceedings of the 31st International conference on Efficiency, Cost, Optimization, Simulation and environmental impact of energy systems, (Guimaraes, Portugal).

Altes-Buch, Q., Quoilin, S., and Lemort, V. (2019). Greenhouses: A Modelica Library for the Simulation of Greenhouse Climate and Energy Systems. In Proceedings of the 13th International Modelica Conference, (Regensburg, Germany).

Bailey, B.J. (1988). Control strategies to enhance the performance of greenhouse thermal screens. J. Agric. Eng. Res. *40*, 187–198.

Balemans, L. (1989). Assessment of criteria for energetic effectiveness of greenhouse screens. Agricultural University.

Bot, G.P.. (1983). Greenhouse climate : from physical processes to a dynamic model. Wageningen University.

Boulard, T., and Baille, A. (1993). A simple greenhouse climate control model incorporating effects of ventilation and evaporative cooling. Agric. For. Meteorol. *65*, 145–157.

Coulson, K.L. (1975). Solar and Terrestrial Radiation (Elsevier).

Dayan, E., van Keulen, H., Jones, J.W., Zipori, I., Shmuel, D., and Challa, H. (1993). Development, calibration and validation of a greenhouse tomato growth model: I. Description of the model. Agric. Syst. *43*, 145–163.

De Zwart, H.F. (1996). Analyzing energy-saving options in greenhouse cultivation using a simulation model. Wageningen University.

Dieleman, J.A., and Kempkes, F.L.K. (2006). Energy screens in tomato: determining the optimal opening strategy. Acta Hortic. 599–606.

Dieleman, J., Meinen, E., Marcelis, L.F.M., Zwart, and Van Henten, E.J. (2005). Optimisation of CO2 and Temperature in Terms of Crop Growth and Energy Use. Acta Hortic. *691*.

Dieleman, J.A., Marcelis, L.F.M., Elings, A., Dueck, T.A., and Meinen, E. (2006). Energy Saving in Greenhouses: Optimal Use of Climate Conditions and Crop Management. Acta Hortic. 203–210.

Elings, A., Zwart, H.F. de, Janse, J., Marcelis, L.F.M., and Buwalda, F. (2006). Multiple-day temperature settings on the basis of the assimilate balance: a simulation study. Acta Hortic.

Grange, R.I., and Hand, D.W. (1987). A review of the effects of atmospheric humidity on the growth of horticultural crops. J. Hortic. Sci. *62*, 125–134.

Grisey, A., and Brajeul, E. (2007). Serres chauffées: réduire ses dépenses énergétiques (Centre technique interprofessionnel des fruits et légumes (CTIFL)).

Heuvelink, E. (1996). Tomato growth and yield : quantitative analysis and synthesis. phd. Heuvelink.

Impron, I., Hemming, S., and Bot, G.P.A. (2007). Simple greenhouse climate model as a design tool for greenhouses in tropical lowland. Biosyst. Eng. *98*, 79–89.

Linker, R., Seginer, I., and Buwalda, F. (2004). Description and calibration of a dynamic model for lettuce grown in a nitrate-limiting environment. Math. Comput. Model. *40*, 1009–1024.

Luo, W., Feije de Zwart, H., DaiI, J., Wang, X., Stanghellini, C., and Bu, C. (2005). Simulation of Greenhouse Management in the Subtropics, Part I: Model Validation and Scenario Study for the Winter Season. Biosyst. Eng. *90*, 307–318.

Marcelis, L.F.M., Heuvelink, E., and Goudriaan, J. (1998). Modelling biomass production and yield of horticultural crops: a review. Sci. Hortic. *74*, 83–111.

Miguel, A.A.F. (1998). Transport phenomena through porous screens and openings : from theory to greenhouse practice /. Wageningen University.

Nilsen, S., Hovland, K., Dons, C., and Sletten, S.P. (1983). Effect of CO2 enrichment on photosynthesis, growth and yield of tomato. Sci. Hortic. *20*, 1–14.

van Ooteghem, R.J.C. (2010). Optimal Control Design for a Solar Greenhouse. IFAC Proc. Vol. *43*, 304–309.

Pfenninger, S., DeCarolis, J., Hirth, L., Quoilin, S., and Staffell, I. (2017). The importance of open data and software: Is energy research lagging behind? Energy Policy *101*, 211–215.

Seginer, I., Gary, C., and Tchamitchian, M. (1994). Optimal temperature regimes for a greenhouse crop with a carbohydrate pool: A modelling study. Sci. Hortic. *60*, 55–80.

Stanghellini, C. (1987). Transpiration of greenhouse crops : an aid to climate management. Wageningen University.

Urban, L., and Urban, I. (2010). La production sous serre: La gestion du climat (Lavoisier).

Vanthoor, B.H.E. (2011). A model-based greenhouse design method. PhD thesis. Wageningen University.

(2018a). Eurostat (online data code: nrg_100a).

(2018b). Eurostat (online data code: apro_acs_a).

(2018c). CBS StatLine: Energieverbruik; land- en tuinbouw.

Questions and Answers:

Did you consider rain and wind in your model?

Queralt Altes Buch:

Rain is not considered. Wind yes, in the computation of the exchange coefficient of convection on the cover with the outside air and also in the computation of the air ventilation rate through the cover's windows.

***

Does your model take into account the stomata of the plant? We know that if the climate conditions are not the optimal, the crop stomata may close itself and stop crop growth?

Queralt Altes Buch:

Yes. For example, the crop transpiration model takes into account the effects of the stomata by means of a resistance to vapor transport. This resistance is a function of the temperature, CO2 concentration and humidity content of the indoor air, as well as the level of short-wave radiation.

Equivalent wall method for dynamic modelling of thermal bridges in low-energy building: application and parametric study

J. Quinten[1]*, V. Feldheim[1]

(1) University of Mons, Faculty of Engineering, Thermal and Combustion Unit

Rue de l'Epargne 56, 7000 Mons, Belgium

ABSTRACT

This paper presents a mixed method to determine a 1-D three-layer wall having the same thermal behaviour as a multidimensional thermal bridge. It is based on the calculations of thermal resistance, heat capacity, structure factors and an objective function using heat fluxes in harmonic conditions. The method is applied to five different 2-D thermal bridges. Accuracy of their 1-D equivalent wall is checked in various conditions (solar heat flux, meteorological data, period of the year, constant or variable indoor temperature). Results are very satisfactory since the error on the integral of inner heat flux over the study period is always lower than 0.65% (except in one case) and the average error on inner heat flux is always lower than 1 W/m.

Keywords: thermal bridge, building energy simulation, equivalent wall, dynamic heat conduction, low-energy building.

1. INTRODUCTION

Currently, scarcity and cost of fossil fuels increase and we are facing more and more problems due to pollutants emissions. The European Union has then set energy savings and greenhouse gases reduction targets of 20% by 2020, from the 1990 levels. As the building sector represents about 40% of the total energy consumption of the European Union, many energy efficiency measures are taken in this domain. Simulations are performed to evaluate, predict or improve energy performance of new buildings thanks to numerical tools. Their accuracy must be improved as the building energy consumption becomes lower and lower.

This work focuses on the dynamic modelling of thermal bridges and multidimensional details of low-energy buildings. A thermal bridge is a 2-D or 3-D part of the building envelope where the otherwise uniform thermal resistance is significantly modified by full or partial penetration of the building envelope by materials with a different thermal conductivity and/or change in thickness of the fabric and/or a difference between internal and external areas, such as it occurs at wall/floor/ceiling junctions (EN ISO 10211, 2007). They may be responsible for 4% up to 39% of the heat losses of a building (39% for a highly insulated building with a bad treatment of thermal bridges) (Martin et al., 2011) and they can cancel the time lag benefits of a heavy wall (Carpenter, 2001).

In most of the building energy software packages, the heat flux is considered as being 1-D and the heat conduction problem is solved by using 1-D time series models (Karambakkam et al., 2005). The steady-state additional heat loss of the 2-D/3-D detail, compared to a 1-D calculation, is easy to take into account via its thermal transmittance[1]. However, its real dynamic and multidimensional effects cannot be considered.

Some studies have highlighted this problem. An ASHRAE project (Enermodal Engineering Limited, 2001) demonstrated that the results obtained with a simplified 1-D calculation are

[1] For a 2-D detail, the linear thermal transmittance Ψ [W/mK]. For a 3-D detail, the punctual thermal transmittance χ [W/K].

inaccurate. According to Martin et al. (2011), the use of a simple method based on a stationary characteristic has no sense in order to evaluate the building energy demand and the accuracy of simple models depends on the inertia of each thermal bridge and is not good in all cases. According to Viot et al. (2015), there is no accurate simplified method for the heat flux study in dynamic conditions and they propose to use a reduced model. According to Ascione et al. (2012), approximate models of thermal bridges induce inaccurate results for the evaluation of building energy performance.

These different works have shown that a 1-D simple model cannot accurately predict the thermal behaviour of a 2-D or 3-D geometry, mainly if there is a large disparity in thermal conductivity and thermal mass of elements. According to Kosny et al. (2002), the part of the wall that is not influenced by multidimensional details (region of 1-D heat flux) only corresponds to 50-80% of the total area of the opaque walls. Therefore, it is necessary to develop a simple model accurately evaluating the impact of dynamic effects of multidimensional details on the building energy performance and easy to integrate into existing building energy software.

A review of existing methods dedicated to the consideration of the dynamic thermal aspects of multidimensional geometry has been performed in a previous paper (Quinten et al., 2016). Those methods have been compared and we have selected the equivalent wall method, which is easy to integrate into existing building simulation programs using a layer-by-layer description of the wall. In this previous paper, we have proposed a new equivalent wall method – the mixed method – mixing the use of structure factors and harmonic heat fluxes calculation and a first version of this method has been successfully applied to a 2-D thermal bridge.

In this paper, we present first the principle of the equivalent wall method, the theory needed to understand the methodology and the different steps of our mixed method. Then, five 2-D thermal bridges are presented and their equivalent walls are determined by using the mixed method. Afterwards, accuracy of the equivalent walls, in terms of heat flux, is checked for various boundary conditions. The results are analysed and discussed. The paper ends with the perspectives and the conclusion.

2. METHOD

2.1 Equivalent wall principle

Principle of the equivalent wall method is to replace a 2-D or 3-D geometry by a 1-D multilayer wall (Fig. 1) having the same static and dynamic thermal behaviours. For each layer, the thermal resistance R_m and the heat capacity C_m must be defined and the value of thickness e_m, thermal conductivity k_m, specific heat capacity c_m and density ρ_m are deduced and introduced into the building energy software.

According to Martin et al. (2012) and Kosny et al. (2002), a three-layer equivalent wall is the optimum. Using more layers leads to a more accurate equivalent wall but the calculation needs more time and computational resources. For a three-layer equivalent wall, six parameters (R_1, R_2, R_3, C_1, C_2 and C_3) are to be determined.

We assume that the thermal properties are constant (no dependence on temperature) and the materials are isotropic. Phase changing materials are not considered and radiative and convective phenomena are not modelled but standard heat transfer coefficients are used.

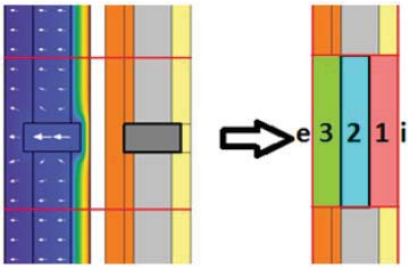

Figure 1: Equivalent wall principle.

2.2 Mixed method

The multidimensional detail (initial wall) and its equivalent wall must have a similar or very close behaviour. To ensure that, some relevant characteristics must be identical for both walls. For our mixed method, we use the principles of the structure factors method (Kossecka et al., 1997) and of a harmonic method (Xiaona et al., 2008).

The total resistance R, the total heat capacity C and the structure factors (ϕ_{ii}, ϕ_{ie} and ϕ_{ee}) are five numbers characterising the thermal behaviour of a structure: structures with these same five numbers have similar dynamic characteristics even if they are quite different in details (Kosny et al., 2002). That imposes four relations and six parameters are to be determined: an infinity of 1-D three-layer walls may respect those conditions. The best solution, the "best equivalent wall", minimises an objective function, comparing the response, in terms of heat flux, to a harmonic signal of environment temperature of each possible solution to that of the initial wall.

In this section, we present the theory and equations about the structure factors, the harmonic analysis and the methodology of our mixed method.

2.2.1 Structure factors

The dimensionless structure factors ϕ_{ii}, ϕ_{ie} and ϕ_{ee} are positive numbers and represent the fractions of heat stored in wall volume, in transition between two different steady states, which are transferred across each wall surface (Kossecka et al., 1997). Examples of values of structure factors are given by Kosny et al. (2002). They depend on the wall's thermal structure: for example, the quantity ϕ_{ii} is comparatively large if most of the thermal mass is located near the interior surface and most of the resistance belongs to the outer part located near the exterior surface. The maximal value of ϕ_{ii} and ϕ_{ee} is 1.The maximal value of ϕ_{ie} is 0.25, when the whole thermal mass of negligible resistance is in the centre and the whole resistance is distributed symmetrically on both sides of it. There is a relation between the structure factors (Eq. 1):

$$\phi_{ii} + 2\phi_{ie} + \phi_{ee} = 1 \tag{1}$$

For a multidimensional geometry, the structure factors can be calculated from the temperature field inside the structure (Eqs. 2-4), in steady-state condition with the outside temperature T_e equal to 1 and the inside temperature equal to 0 (in this case, T is a dimensionless temperature) (Kossecka, 1997).

$$\phi_{ii} = \frac{1}{C}\int_V \rho c\big(1 - T(x,y,z)\big)^2 \, dV \tag{2}$$

$$\phi_{ie} = \frac{1}{C}\int_V \rho c\big(1 - T(x,y,z)\big) \times \big(T(x,y,z)\big)\, dV \tag{3}$$

$$\phi_{ee} = \frac{1}{C}\int_V \rho c\big(T(x,y,z)\big)^2\, dV \tag{4}$$

$$C = \int_V \rho c\, dV \tag{5}$$

For a 1-D geometry, the structure factors can be calculated from simple relations depending on the values of R_m and C_m . For a 1-D three-layer wall, those relations become Eqs. 6-8 (Carpenter, 2001). R_i and R_e are the surface heat transfer resistances (inside and outside).

$$\phi_{ii} = \frac{1}{R^2 C} \times \begin{pmatrix} C_1 \times \left(\frac{R_1^2}{3} + R_1 \times (R_2 + R_3 + R_e) + (R_2 + R_3 + R_e)^2\right) \\ +C_2 \times \left(\frac{R_2^2}{3} + R_2 \times (R_3 + R_e) + (R_3 + R_e)^2\right) \\ +C_3 \times \left(\frac{{R_3}^2}{3} + R_3 \times R_e + {R_e}^2\right) \end{pmatrix} \tag{6}$$

$$\phi_{ie} = \frac{1}{R^2 C} \times \begin{pmatrix} C_1 \times \left(-\frac{R_1^2}{3} + \frac{R_1 \times R}{2} + R_i \times (R_2 + R_3 + R_e)\right) \\ +C_2 \times \left(-\frac{R_2^2}{3} + \frac{R_2 \times R}{2} + (R_i + R_1) \times (R_3 + R_e)\right) \\ +C_3 \times \left(-\frac{R_3^2}{3} + \frac{R_3 \times R}{2} + (R_i + R_1 + R_2) \times R_e\right) \end{pmatrix} \tag{7}$$

$$\phi_{ee} = \frac{1}{R^2 C} \times \begin{pmatrix} C_1 \times \left(\frac{R_1^2}{3} + R_1 \times R_i + {R_i}^2\right) \\ +C_2 \times \left(\frac{R_2^2}{3} + R_2 \times (R_i + R_1) + (R_i + R_1)^2\right) \\ +C_3 \times \left(\frac{R_3^2}{3} + R_3 \times (R_i + R_1 + R_2) + (R_i + R_1 + R_2)^2\right) \end{pmatrix} \tag{8}$$

With:

$$R = R_i + R_1 + R_2 + R_3 + R_e \tag{9}$$

$$C = C_1 + C_2 + C_3 \tag{10}$$

$$R_m = \frac{e_m}{k_m} \tag{11}$$

$$C_m = \rho_m \times c_m \times e_m \tag{12}$$

2.2.2 Harmonic heat flux

Any signal over time can be expressed as a sum of harmonics (of different amplitudes Am, periods P and phases α: see Eq. 13).

$$T(t) = T_{av} + \sum_n Am_n \times \sin\left(\frac{2\pi t}{P_n} + \alpha_n\right) \quad (13)$$

That can be done for hourly data of the outdoor temperature over a year. By summing some particular harmonics, it is possible to approximatively reconstitute a simple signal of realistic outdoor temperature. By selecting the harmonics of Tab. 1 for the Brussels climate[2] (Belgium) and adding the average temperature (T_{av} = 9.73°C), we obtain a quite good approximation of the real climate (Meteonorm data) (see Fig. 2).

Table 1: Combination of harmonics: amplitude and phase (Brussels climate).

P [h]	Am [°C]	α [rad]
8760	7.60	0.35
4380	0.58	-1.29
1095	0.76	0.72
876	1.37	1.29
730	1.21	1.19
584	1.26	0.65
273.75	0.70	1.13
24	2.65	1.26
12	0.62	0.97

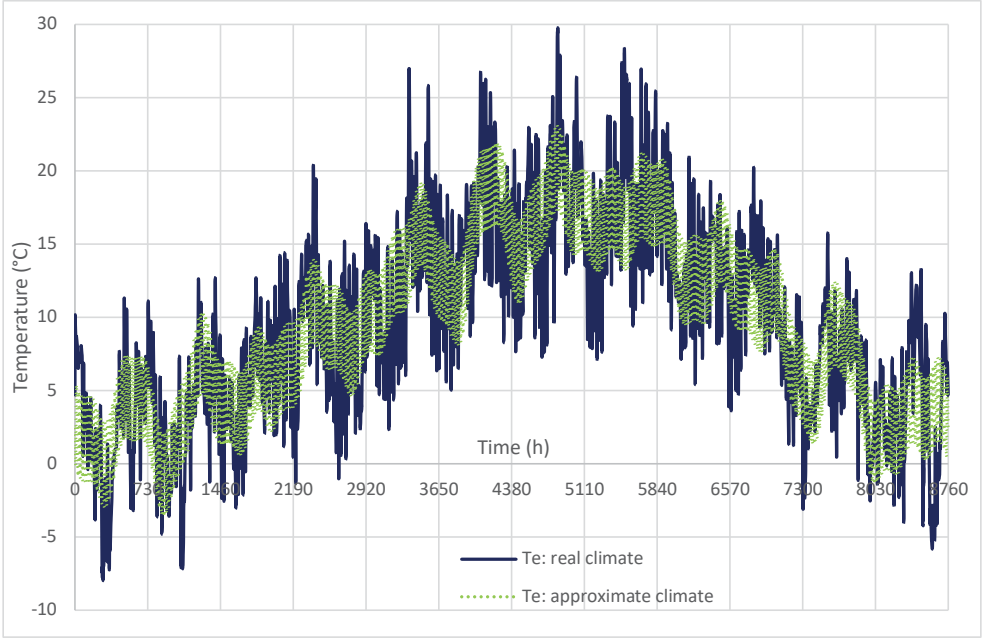

Figure 2: Outdoor temperature of Brussels: approximation with harmonics vs real data (time = 0 corresponds to the 1st January at 00:00).

This harmonic approximate climate of Brussels, a simple function, constitutes our "test" climate for the outdoor temperature in the determination of the equivalent wall. For the indoor

[2] Meteorological data of the Uccle (Brussels Region) station are used.

temperature, a sinus function is used (Am = 1°C, P = 24h, α = π). For this analysis, only the variable part of the signal is considered.

The response of a wall (in terms of heat flux) to a sum of sinus signals is the sum of the responses to each sinus signal, since the problem is linear. Thanks to the Pipes' theory (1957) in the Laplace's domain which can be applied in the frequency domain, it is possible to evaluate analytically the response of a 1-D wall to a sinus signal.

By considering a 1-D three-layer wall and a sinus solicitation of period P, Eqs. 14-18 are deduced in the frequency domain (heat fluxes are considered positive from outdoor to indoor).

$$\begin{bmatrix} T_e \\ q'_e \end{bmatrix} = M \times \begin{bmatrix} T_i \\ q'_i \end{bmatrix} \tag{14}$$

$$M = \begin{bmatrix} M_{1,1} & M_{1,2} \\ M_{2,1} & M_{2,2} \end{bmatrix} = \begin{bmatrix} 1 & R_e \\ 0 & 1 \end{bmatrix} \times \begin{bmatrix} D_3 & B_3 \\ G_3 & D_3 \end{bmatrix} \times \begin{bmatrix} D_2 & B_2 \\ G_2 & D_2 \end{bmatrix} \times \begin{bmatrix} D_1 & B_1 \\ G_1 & D_1 \end{bmatrix} \times \begin{bmatrix} 1 & R_i \\ 0 & 1 \end{bmatrix} \tag{15}$$

$$D_m = cosh\left(\sqrt{\frac{2 \times \pi \times C_m \times R_m \times j}{P}}\right) \tag{16}$$

$$B_m = sinh\left(\sqrt{\frac{2 \times \pi \times C_m \times R_m \times j}{P}}\right) / \sqrt{\frac{2 \times \pi \times C_m \times j}{R_m \times P}} \tag{17}$$

$$G_m = \sqrt{\frac{2 \times \pi \times C_m \times j}{R_m \times P}} \times sinh\left(\sqrt{\frac{2 \times \pi \times C_m \times R_m \times j}{P}}\right) \tag{18}$$

For a three-layer wall and a unit sinus solicitation of outdoor temperature, the heat flux q_i' through the inner surface of the 1-D structure is calculated with Eq. 19:

$$q_i'\left(\frac{2\pi j}{P}\right) = \frac{1}{M_{1,2}\left(\frac{2\pi j}{P}\right)} \rightarrow q_i'(t) = Am'_{ie}(P) \times sin\left(\frac{2\pi t}{P} + \alpha'_{ie}(P)\right) \tag{19}$$

For a three-layer wall and a unit sinus solicitation of indoor temperature, the heat flux q_i' through the inner surface of the 1-D structure is calculated with Eq. 20:

$$q_i'\left(\frac{2\pi j}{P}\right) = -\frac{M_{1,1}\left(\frac{2\pi j}{P}\right)}{M_{1,2}\left(\frac{2\pi j}{P}\right)} \rightarrow q_i'(t) = Am'_{ii}(P) \times sin\left(\frac{2\pi t}{P} + \alpha'_{ii}(P)\right) \tag{20}$$

In this work, we only focus on the heat flux through the inner surface of the wall as it is used in the energy balance of the building.

2.2.3 Steps of the methodology

Our mixed method is decomposed into two main steps: determination of the characteristics of the real 2-D/3-D geometry and determination of the equivalent wall. There are some operations for each step and they are summarized on Fig. 3:

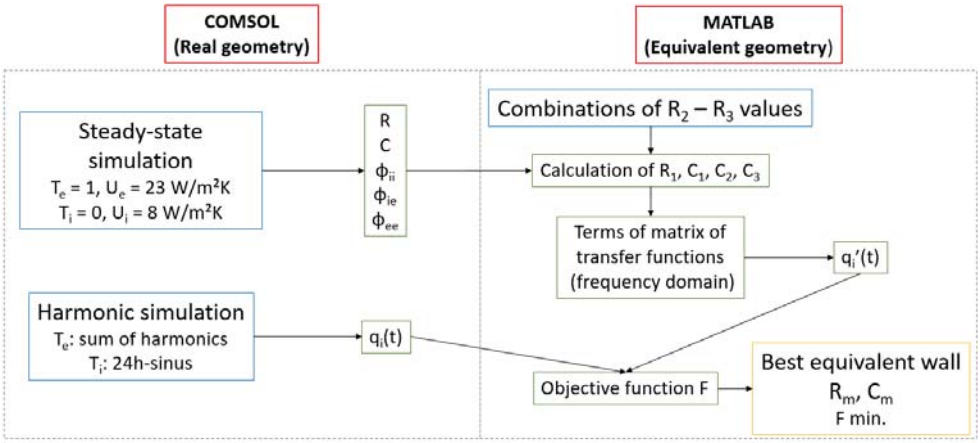

Figure 3: Mixed method: methodology.

1) Determination of the characteristics of the real 2-D/3-D geometry (for numerical simulations, the COMSOL Multiphysics software is used):
   a. A steady-state simulation is performed (T_e = 1, U_e = $1/R_e$ = 23 W/m²K, T_i = 0, U_i = $1/R_i$ = 8 W/m²K) to evaluate the structure factors (Eqs. 2-4), the thermal resistance and the heat capacity (Eq. 5) of the real wall.
   b. A dynamic simulation is performed to evaluate the heat flux $q_i(t)$ through the inner surface of the real wall over time, considering the boundary conditions detailed in Section 3.2.2.: only the variable part of the signals compared to 0°C is considered here (24h-sinus indoor temperature: -1 to 1°C, sum of some harmonics representative of the Brussels climate for the outdoor temperature). The time step is 1h.
2) Elaboration of the equivalent wall (MATLAB scripts are used):
   a. A large number of combinations of R_2-R_3 values are tested (exhaustive method). For each combination, the values of R_1, C_1, C_2 and C_3 are calculated to ensure Eqs. 6-7 and 9-10.
   b. For each combination, the heat flux $q_i'(t)$ through the inner surface of the corresponding 1-D wall is evaluated, considering the boundary conditions detailed in Section 3.2.2. (time step of 1h). Contribution of each harmonic in terms of heat flux is calculated with Eqs. 14-20.
   c. For each combination, the objective function F is calculated (Eq. 21). The equivalent wall corresponds to the set of R_1, R_2, R_3, C_1, C_2, C_3 values leading to the lowest value of F.

$$F = \sqrt{\sum_{t=400h}^{t=2000h} (q_i(t) - q_i'(t))^2} \; with \; \Delta t = 1h \qquad (21)$$

The dynamic simulation starts at t = 0h (1st January at 00:00), but the evaluation of the function F begins at t = 400h to avoid the influence of initial conditions. More details about the study of the objective function F are available in a PhD thesis (Quinten, 2018).

A reference surface area of the 1-D equivalent wall (S_{ref}) must be defined. In most cases it is the projected external surface of the initial wall. Properties of the 2-D/3-D details are then adapted to the 1-D calculation:

- Thermal resistance [K/W] is multiplied by the area S_{ref} ;

- Heat capacity [J/K] is divided by the area S_{ref} ;
- Heat flux [W] is divided by the area S_{ref} ;
- Surface heat transfer coefficients are multiplied by the relation “real area/reference area”, to ensure the heat flux conservation:
  - $U_{i,equivalent} = U_{i,initial} \times \frac{S_i}{S_{ref}}$
  - $U_{e,equivalent} = U_{e,initial} \times \frac{S_e}{S_{ref}}$

3. SIMULATION

The mixed equivalent wall method is applied to five 2-D thermal bridges. In this section, geometry and materials of those thermal bridges are first detailed. Then, accuracy of each case is checked by comparing the heat flux through the thermal bridge and through its equivalent wall under various conditions: different meteorological data, different periods of the year, constant or variable indoor temperature, with or without solar heat flux.

Dynamic simulations are performed with the COMSOL Multiphysics software, using a finite elements method. Maximal mesh size is 10 mm, except in the corners (maximal size: 0.5 mm). Cubic shape functions are used. It has been verified a good accuracy is reached with those settings (error on heat flux is less than 0.01%).

3.1 2-D thermal bridges

The studied details come from the website of the thermal bridges section of the *Passive House Platform* in Belgium, a non-profit organization participating in the development and the realisation of exemplary buildings. In each case, we assume the bricks are perfectly joined, without cement, and the vapour barriers and rain screens are not modelled.

3.1.1 TB1: Intermediate floor – exterior wall (heavy structure)

TB1 is a junction between an intermediate floor and an external wall in a heavy structure, with external insulation (Fig. 4). Its materials are listed in Tab. 2. The mesh used leads to 91.8 10^3 degrees of freedom.

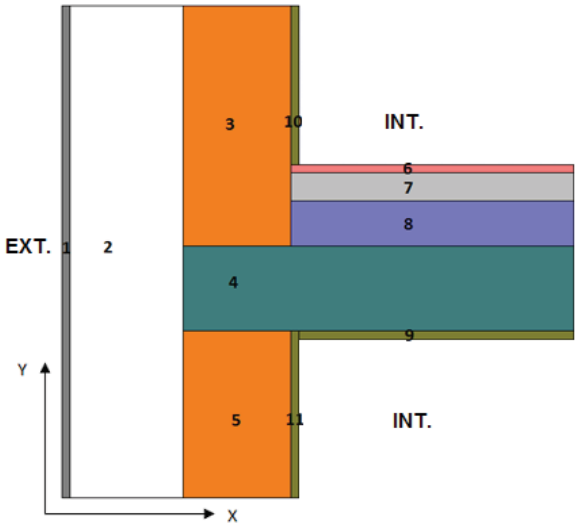

Figure 4: TB1 – Geometry.

Table 2: TB1 – Materials.

N°	Material	L_X [mm]	L_Y [mm]	k [W/mK]	ρ [kg/m³]	c [J/kgK]
1	Mortar	15	870	0.3	1100	1000
2	Expanded PS	200	870	0.034	20	1450
3	Brick	190	425	0.26	850	1000
4	Reinforced concrete	705	150	2.2	2400	1000
5	Brick	190	295	0.26	850	1000
6	Tiling	515	15	1	2000	1000
7	Light concrete	515	50	0.41	1200	1000
8	Concrete	515	80	0.8	1800	1000
9	Plaster	500	15	0.52	1300	1000
10	Plaster	15	280	0.52	1300	1000
11	Plaster	15	295	0.52	1300	1000

3.1.2 TB2: Corner (heavy structure)

TB2 is a corner in a heavy structure, with external insulation (Fig. 5). Its materials are listed in Tab. 3. The mesh used leads to 82.9 10^3 degrees of freedom.

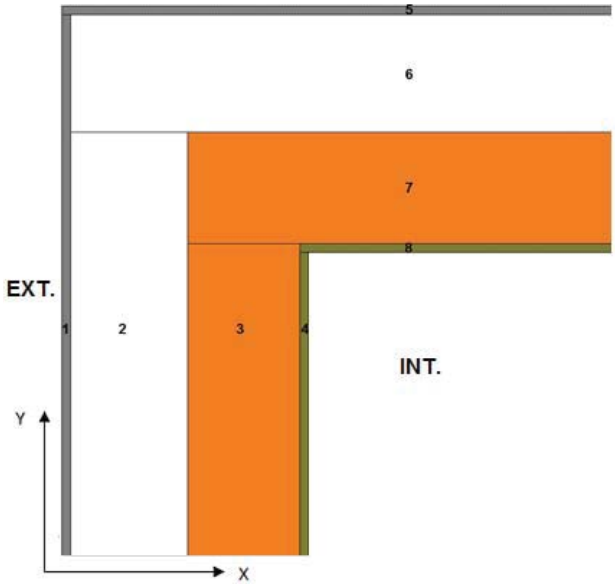

Figure 5: TB2 – Geometry.

Table 3: TB2 – Materials.

N°	Material	L_X [mm]	L_Y [mm]	k [W/mK]	ρ [kg/m³]	c [J/kgK]
1	Mortar	15	935	0.93	1100	1000
2	Expanded PS	200	735	0.034	20	1450
3	Brick	190	545	0.26	850	1000
4	Plaster	15	530	0.52	1300	1000
5	Mortar	950	15	0.93	1100	1000

n°	Material	L_X [mm]	L_Y [mm]	k [W/mK]	ρ [kg/m³]	c [J/kgK]
6	Expanded PS	935	200	0.034	20	1450
7	Brick	735	190	0.26	850	1000
8	Plaster	545	15	0.52	1300	1000

3.1.3 TB3: Intermediate floor – exterior wall (light structure)

TB3 is a junction between an intermediate floor and an external wall in a light structure, with internal insulation (Fig. 6). Its materials are listed in Tab. 4. The mesh used leads to 80.5 10^3 degrees of freedom.

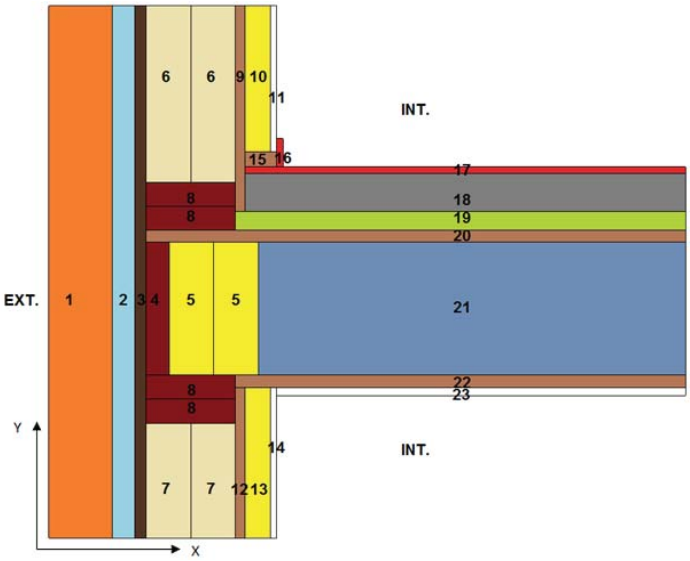

Figure 6: TB3 – Geometry.

Table 4: TB3 – Materials.

N°	Material	L_X [mm]	L_Y [mm]	k [W/mK]	ρ [kg/m³]	c [J/kgK]
1	Brick	100	840	1.1	1800	1000
2	Poorly ventilated air space	35	840	0.085	1.2	1004
3	Fibreboard of wood	18	840	0.048	270	2068
4	Wood	36	210	0.13	500	1880
5	PUR	70	210	0.023	30	1400
6	PUR + wood (10%)	70	278.5	0.0337	77	1448
7	PUR + wood (10%)	70	181.5	0.0337	77	1448
8	Wood	140	38	0.13	500	1880
9	OSB panel	15	324.5	0.13	650	1880
10	PUR	40	230.5	0.023	30	1400
11	Plasterboard	10	230.5	0.2	700	1000
12	OSB panel	15	237.5	0.13	650	1880
13	PUR	40	237.5	0.023	30	1400

n°	Material	L_X [mm]	L_Y [mm]	k [W/mK]	ρ [kg/m³]	c [J/kgK]
14	Plasterboard	10	237.5	0.2	700	1000
15	OSB panel	50	24	0.13	650	1880
16	Tiling	10	45	1	2000	1000
17	Tiling	692	10	1	2000	1000
18	Concrete	692	60	0.6	1300	1000
19	Acoustic insulation	707	30	0.6	300	1880
20	OSB panel	847	18	0.13	650	1880
21	Air + wood (13%)	671	210	0.5313	66	1118
22	OSB panel	707	20	0.13	650	1880
23	Plaster	642	12.5	0.52	1300	1000

3.1.4 TB4: Internal wall – external wall (heavy structure)

TB4 is a junction between an internal wall and an external wall in a heavy structure, with internal insulation (Fig. 7). Its materials are listed in Tab. 5. The mesh used leads to 114 10^3 degrees of freedom.

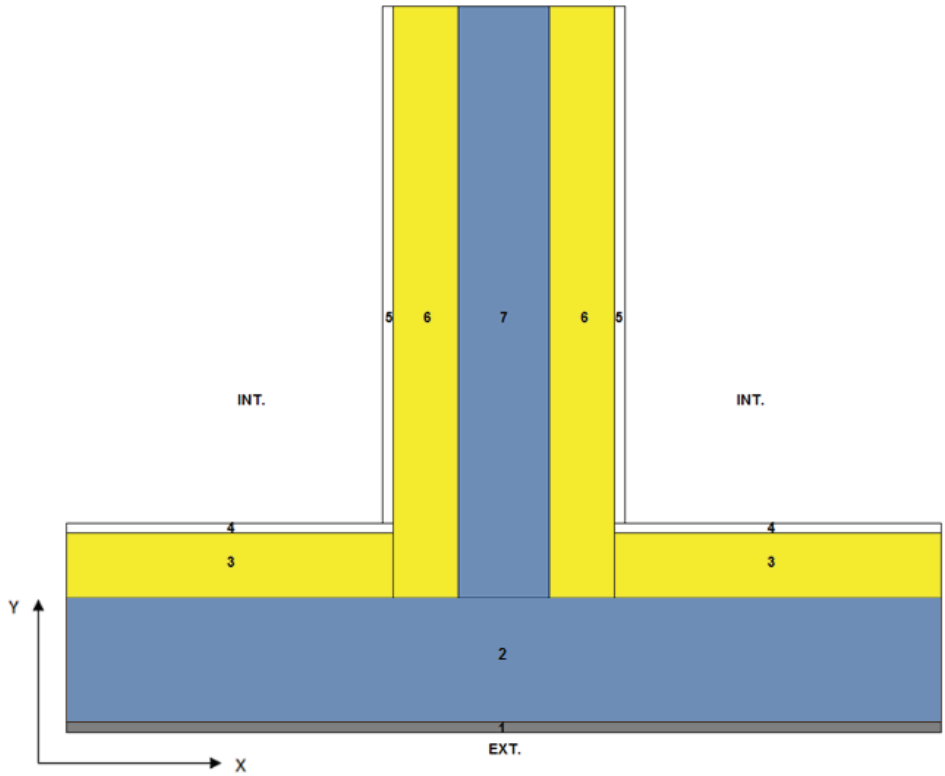

Figure 7: TB4 – Geometry.

Table 5: TB4 – Materials.

N°	Material	L_X [mm]	L_Y [mm]	k [W/mK]	ρ [kg/m³]	c [J/kgK]
1	Mortar	1340	15	0.93	1100	1000
2	Hollow heavy concrete	1340	190	1.357	1300	1000
3	PUR	500	100	0.023	40	1450
4	Plaster	500	15	0.52	1300	1000
5	Plaster	15	790	0.52	1300	1000
6	PUR	100	905	0.023	40	1450
7	Hollow heavy concrete	140	905	1.273	1400	1000

3.1.5 TB5: Window frame – external wall (light structure)

TB5 is a junction between a window frame and an external wall in a light structure (Fig. 8). Its materials are listed in Tab. 6. The mesh used leads to 74.0 10^3 degrees of freedom.

Table 6: TB5 – Materials.

N°	Material	L_X [mm]	L_Y [mm]	k [W/mK]	ρ [kg/m³]	c [J/kgK]
1	Wood (siding)	819	35	0.13	600	1880
2	Wood	419	35	0.13	600	1880
3	Wood	360	35	0.13	600	1880
4	Wood	40	35	0.13	600	1880
5	Wood	4	35	0.13	600	1880
6	Wood	16	107	0.13	600	1880
7	Rain screen	823	4	0.04	240	2100
8	Fibreboard of wood	823	33	0.05	350	1880
9	Cellulose	700	280	0.039	35	2110
10	Cellulose	50	100	0.039	35	2110
11	Wood	50	90	0.13	600	1880
12	Draughtproofing	29	80	0.35	1200	1300
13	Wood	44	80	0.13	600	1880
14	Wood	36	80	0.13	600	1880
15	OSB panel	20	200	0.13	650	1880
16	PS panel	30	218	0.045	20	1450
17	Plaster (Fermacell)	10	288	0.32	1100	1000
18	OSB panel	770	18	0.13	650	1880
19	Mineral wool	770	60	0.05	50	1880
20	Plaster (Fermacell)	800	10	0.32	1100	1000
21	Wood	30	60	0.13	600	1880

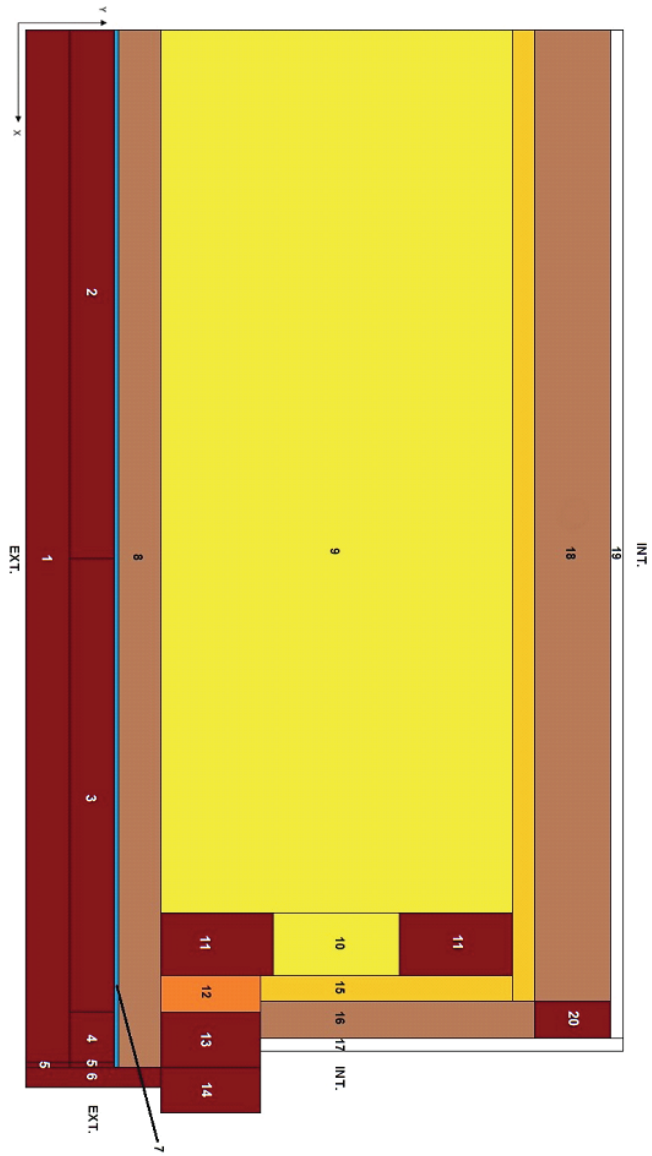

Figure 8: TB5 – Geometry.

3.1.6 Thermal bridges and equivalent walls properties

Table 7: Properties of thermal bridges and equivalent walls

		TB1	**TB2**	**TB3**	**TB4**	**TB5**
U_{1D}	[W/m²K]	0.146	0.146	0.141	0.213	0.116
Ψ	[W/mK]	0.00421	-0.0639	0.0509	0.1314	0.0517
R	[mK/W]	6.30	4.66	5.92	2.40	5.41
C	[kJ/mK]	692	269	349	597	163
$e_{ext.\ wall}$	[m]	0.42	0.42	0.358	0.32	0.475
S_i	[m²/m]	2.15	1.06	1.76	2.55	1.15
S_e	[m²/m]	1.06	1.9	0.84	1.34	0.97
S_{ref}	[m²/m]	1.06	1.06	0.84	1.34	0.83
Φ_{ii}	-	0.921	0.688	0.426	0.158	0.295
Φ_{ie}	-	0.025	0.084	0.048	0.096	0.091
Φ_{ee}	-	0.029	0.144	0.478	0.650	0.523
R_1	m²K/W	0.160	0.600	0.153	$9\ E^{-16}$	0.518
R_2	m²K/W	5.35	3.70	4.71	2.71	3.89
R_3	m²K/W	1.06	0.492	$8\ E^{-7}$	0.392	$2\ E^{-19}$
C_1	[kJ/m²K]	624	201	160	26.3	44.7
C_2	[kJ/m²K]	9.12	20.7	82.1	117	75.4
C_3	[kJ/m²K]	19.9	31.4	173	303	73.7
F	[W/m²]	3.1	5.6	0.35	11	7.7

Properties of the thermal bridges and their equivalent walls are listed in Tab. 7.

External walls of each thermal bridge are well insulated, their U-values comply with the actual standard in Belgium ($U_{1D,max}$ = 0.24 W/m²K). Thermal transmittance value Ψ is low for each thermal bridge except for *TB4*, where the internal insulation is interrupted by hollow heavy concrete. For *TB2*, an external corner, this value is negative, as taking into account the external surface of this detail in the calculation overestimates the heat losses (in cold period).

Structure factors values are quite different for each 2-D detail. ϕ_{ii} is largely dominant for *TB1* (external insulation), all the thermal mass is inside (bricks and concrete floor). ϕ_{ii} is still dominant for *TB2* (corner, with external walls almost similar to that of *TB1*), but its dominance is less significant since only internal bricks have thermal mass: there is no concrete and ϕ_{ie} and ϕ_{ee} become not negligible. For *TB3*, ϕ_{ii} and ϕ_{ee} have the same order of magnitude as the thermal mass is divided between the external bricks and the concrete under the tilling (inside) and the central wooden structure with insulation has no thermal mass (ϕ_{ie} is low). For *TB4*, ϕ_{ee} is high due to the external hollow heavy concrete and the central hollow block of intermediate wall increases ϕ_{ie}. For *TB5*, there is no material with a high thermal mass, the greatest massive layer is the external one (70 mm of wood): ϕ_{ee} is greater than ϕ_{ie} and ϕ_{ii}, and disparity of structure factors values is less than for *TB4*.

The values of R_1, R_2, R_3, C_1, C_2 and C_3 are the parameters of the equivalent wall in each case and F is the value of the objective function: it is lower for *TB3* and higher for *TB4* and *TB5*.

3.2 Parametric study

A high number of simulations with different boundary conditions are performed to evaluate the robustness of the equivalent walls use, for the five thermal bridges (*TB1* to *TB5*). Those boundary conditions are different from those used for the calculation of equivalent walls: real hourly meteorological data are used. More simulations are performed for the most

problematic thermal bridges (*TB4* and *TB5*). Initial condition is 20°C into all the geometry and the time step is 1h. The reference heat flux is the heat flux related to the 2-D thermal bridges.

Table 8: Parametric study – Simulation information and results.

TB	T_i (°C)	City	q_{sol}	Period (10^3 h)	E_{int} (%)	ε_{av} (W/m)	ε/q
1	20	Brussels	No	0-2	0.002	0.025	0.0096
1	20	Brussels	Yes	0-2	0.004	0.060	0.028
1	19-21	Brussels	Yes	0-2	0.024	0.065	0.010
1	**20**	**Moscow**	**Yes**	**0-2**	**0.002**	**0.077**	**0.021**
2	20	Brussels	Yes	0-2	0.005	0.110	0.038
2	19-21	Brussels	Yes	0-2	0.002	0.195	0.061
3	20	Brussels	No	0-2	0.053	0.021	0.0075
3	20	Brussels	Yes	0-2	0.056	0.051	0.022
3	19-21	Brussels	Yes	0-2	0.042	0.044	0.011
3	20	Moscow	Yes	0-2	0.056	0.067	0.017
4	20	Brussels	No	0-2	0.012	0.41	0.060
4	20	Brussels	Yes	0-2	0.029	0.76	0.13
4	20	Brussels	Yes	2-4	0.14	0.90	0.43
4	20	Brussels	Yes	4-6	0.18	0.89	0.73
4	20	Brussels	Yes	6-8	0.63	0.76	0.27
4	19-21	Brussels	Yes	0-2	0.055	0.68	0.12
4	20	Moscow	No	0-2	0.009	0.58	0.052
4	**20**	**Moscow**	**Yes**	**0-2**	**0.045**	**0.93**	**0.097**
4	20	Kathmandu	No	0-2	0.073	0.55	0.17
4	19-21	Kathmandu	No	0-2	0.008	0.28	0.075
4	20	Quito	No	0-2	0.079	0.32	0.12
4	20	Quito	Yes	0-2	0.16	0.60	0.44
4	19-21	Quito	No	0-2	0.038	0.30	0.094
4	19-21	Quito	Yes	0-2	0.023	0.41	0.14
5	20	Brussels	No	0-2	0.037	0.09	0.030
5	20	Brussels	Yes	0-2	0.024	0.24	0.096
5	20	Brussels	Yes	2-4	0.099	0.36	0.39
5	20	Brussels	Yes	4-6	0.18	0.36	0.66
5	20	Brussels	Yes	6-8	0.11	0.29	0.23
5	**19-21**	**Brussels**	**Yes**	**0-2**	**2.6**	**0.28**	**0.11**
5	20	Moscow	No	0-2	0.035	0.12	0.024
5	20	Moscow	Yes	0-2	0.055	0.32	0.074
5	20	Kathmandu	No	0-2	0.001	0.24	0.17
5	20	Kathmandu	Yes	0-2	0.14	0.74	**1.3**
5	19-21	Kathmandu	No	0-2	0.09	0.21	0.13
5	19-21	Kathmandu	Yes	0-2	0.39	0.78	0.58
5	20	Quito	No	0-2	0.016	0.13	0.11
5	20	Quito	Yes	0-2	0.070	0.27	0.44
5	19-21	Quito	No	0-2	0.12	0.15	0.11
5	19-21	Quito	Yes	0-2	0.15	0.30	0.25

In Tab. 8, some information and results about each simulation can be found:

- T_i: indoor temperature is constant (20°C) or a sinus signal of a 24h-period (variation between 19 and 21°C) is considered ;

- City: the climate of the city is used (hourly meteorological data from Meteonorm);

    - The materials and the construction techniques are different for each region. The studied thermal bridges do not necessarily correspond to structures encountered in each region.
- q_{sol}: consideration or not of the solar heat flux (solar absorption = 100%) ;
- Period: the simulation period, t = 0h corresponds to 1st January 00:00 and a duration of 2000h is similar to around 12 weeks.
- E_{int}: the relative error on the temporal integral value of heat flux (rectangle rule) [%];
- ε_{av}: the average error on the inner heat flux [W/m];
- $\varepsilon/q = \frac{\int_{t_0}^{t_f} |\varepsilon_i(t)|}{\int_{t_0}^{t_f} |q_i(t)|}$: the integral of absolute error divided by the integral of absolute heat flux.

Heat flux over time is illustrated for three cases: TB1-20-Moscow-q_{sol}, TB4-20-Moscow-q_{sol} and TB5-19/21-Brussels-q_{sol} on Fig. 9, 10 and 11 respectively.

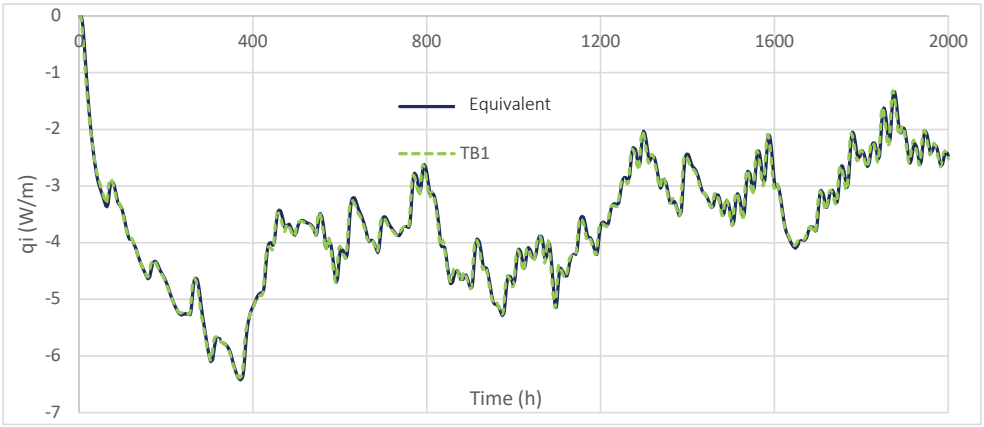

Figure 9: TB1: 20°C, Moscow, q_{sol}: Heat fluxes comparison.

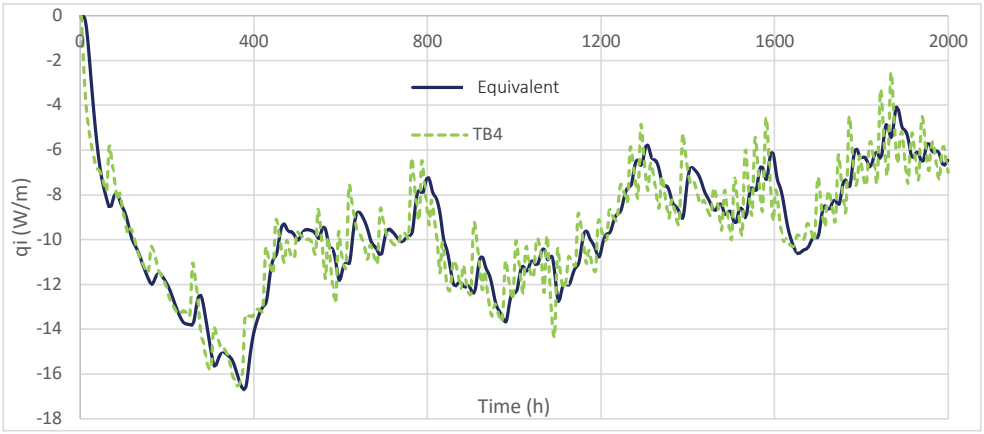

Figure 10: TB4: 20°C, Moscow, q_{sol}: Heat fluxes comparison.

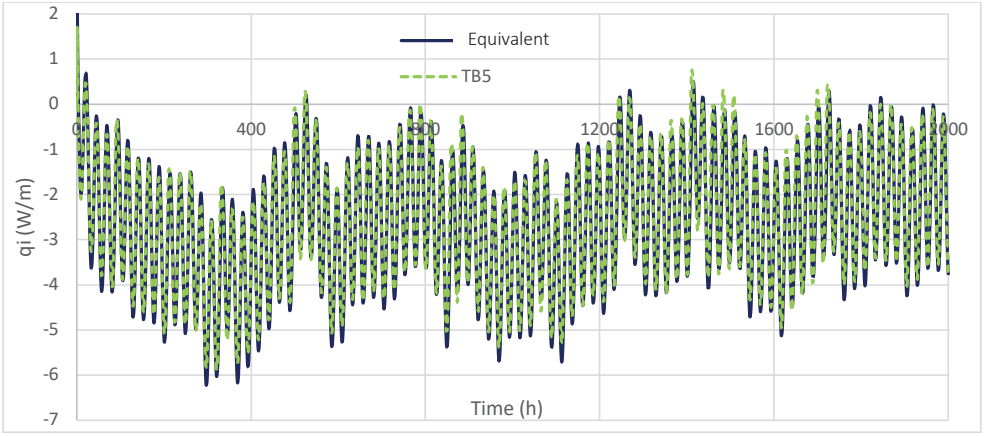

Figure 11: TB5: 19-21°C, Brussels, q_{sol}: Heat fluxes comparison.

4. DISCUSSION AND RESULT ANALYSIS

For studied cases of Tab. 8, results are very accurate for *TB1* (for example, see Fig. 9), *TB2* and *TB3* and satisfactory for *TB4* and *TB5*: in consequence, the parametric study is mainly concentrated on *TB4* and *TB5*. That corresponds to the two equivalent walls (*TB4* and *TB5 cases*) having the greatest values of the objective function F (see Tab. 7).

In each case, value of integrated heat flux over time is accurately estimated: error is always lower than 0.65% except in one case (*TB5*, 19-21°C, Brussels, see Fig. 11) where it reaches 2.6% but the average error has the same order of magnitude as the other ones. Average error is always less than 1 W/m (maximal average error is 0.93 W/m, in this case heat flux mainly varies between 4 and 16 W/m, see Fig. 10).

Concerning the influence of each parameter, we can make the following observations:

- Average error varies little with the type of indoor temperature (constant or sinus). Results are satisfactory in each case. Value of ε/q is often lower for a sinus indoor temperature, as inner heat flux reaches higher values in this case.
- Average error and ε/q value are multiplied by 2-3 on average when the solar heat flux is considered. When it is taken into account, inner heat flux of initial wall varies more and that of equivalent wall can be less reactive (it is the case for *TB4* and *TB5*) even if evolution over time is similar on average (see Fig. 10 for example). Accuracy remains acceptable in the worst cases, the differences are due to a time lag and different oscillations amplitudes.
- Whatever the climate (Brussels, Moscow, Kathmandu, Quito), average error remains quite similar in each case.
- The best results are obtained for the period 0h-2000h. For the other periods of the year (2000h-4000h, 4000h-6000h, 6000h-8000h), order of magnitude of average error is quite similar (maximal factor is 1.5). Nevertheless, value of ε/q can be high for other periods (maximum is 0.73) as values reached by heat fluxes are lower.
- High values of ε/q can be reached in some cases. Average error is quite significant compared to average heat flux: this is mainly due to a time lag or a difference in oscillations amplitudes. As previously said, the average evolution of inner heat flux over time is however respected.

The goal of this analysis was to confirm the accuracy of equivalent walls in other conditions than those of the "test" climate used for their determination (24h-sinus indoor temperature and outdoor temperature is a sum of harmonics representative of the Brussels climate). That has been done by using hourly meteorological data, different climates and types of indoor temperature and by considering or not the solar heat flux. For each case, the results are satisfactory and validate our method: error on energy transferred across the inner surface during the studied period is limited to few percent (< 3%) and error on instantaneous heat flux is limited to few watts by metre of length (< 4 W/m) in the worst case.

For two of the five studied 2-D thermal bridges (*TB4* and *TB5*), the results could be better. On average, the heat flux evolution over time is similar for the thermal bridge and its equivalent wall but there can happen a time lag or a difference in oscillations amplitude, mainly when the solar heat flux is considered. Classically, evolution of inner heat flux of these equivalent walls is less reactive to the solar heat flux. There is no clear relationship between the properties (R, C, ϕ, Ψ, U_{1D}) of a thermal bridge and this lower precision.

In a PhD thesis (Quinten, 2018), we have highlighted that in the *TB4* and *TB5* structures, there are thermal phenomena at different speeds governed by very different time constants. This difference of dynamics is difficult to model with a 1-D structure, even a four-layer equivalent wall does not lead to very good results. A solution could be to use two 1-D equivalent walls in parallel, each one having its own dynamics (two very different dynamics are then possible).

In this PhD, we have also proved that the accuracy of the equivalent wall is largely better than a classic 1-D calculation of a 2-D/3-D detail.

With common computer specifications (8 Go-RAM, Intel® Core i5-2400 CPU 3.10 GHz), the different steps of the mixed method take less than 2h for multidimensional geometry with around 10^5 degrees of freedom (steady-state simulation: less than 1min, dynamic simulation: up to 65min, determination of the equivalent wall: 30min, calculation of the thermal properties of each layer: a few seconds). Drawing time is not considered in the total time of the method as it depends on the experience of the user and the complexity of the geometry and it is unavoidable for any modelling.

5. CONCLUSION

This work focuses on a method of equivalent wall allowing to take easily into account the multidimensional details in building energy simulation software considering a 1-D conductive heat flux. It is a reduced model method, where the multidimensional geometry is replaced by a 1-D three-layer wall having a similar thermal behaviour.

We have presented a new mixed method where the equivalent wall must have the same thermal resistance, heat capacity and structure factors as the multidimensional detail. Moreover, it minimizes an objective function, comparing the heat flux through its inner surface and through the inner surface of the 2-D/3-D geometry in harmonic conditions. The theory and the relations linked to those conditions have been presented in this paper.

This method has been applied to five 2-D thermal bridges to determine their equivalent walls. The accuracy, in terms of inner heat flux, of those equivalent walls has been verified in various conditions: hourly meteorological data of different climates, different periods of the year, for a variable or constant indoor temperature and by considering or not the solar heat flux. Results are very satisfactory since the error on the integral of inner heat flux over the study period is always less than 0.65% (except in one case) and the average error on inner heat flux is always lower than 1 W/m.

The equivalent walls of two of the five thermal bridges lead to not perfect results, mainly when the solar heat flux is considered, as thermal phenomena occur with very different time constants. However, on average, the heat flux evolution over time is similar.

Future work deals with the application of the method to thermal bridges of a building with the aim to evaluate the impact of using this method to study the energy performance of the building, compared to a classic 1-D consideration. For buildings with a high number of thermal bridges, there is a need to reduce the calculation time of the equivalent wall: an improvement of the optimisation method to define the equivalent wall (currently an exhaustive method), an automation of the process (now, data obtained from numerical simulations in COMSOL are manually extracted and introduced into the Matlab scripts) and an inventory of details or some rules to determine the properties of the equivalent wall are the main ideas to reduce this calculation time. Finally, to improve the accuracy of the equivalent walls of thermal bridges with thermal phenomena at very different speeds, the use of two 1-D equivalent walls in parallel could be a solution.

REFERENCES

Ascione, F., Bianco, N., de'Rossi, F., Turni, G., and Vanoli, G.P., 2012. *Different methods for the 19ulfill19 of thermal bridges into energy simulation programs: Comparisons of accuracy for flat heterogeneous roofs in Italian climates*. Applied Energy, vol. 97, pp. 405-418.

Carpenter, S., 2001. *Advances in 19ulfill19 thermal bridges in building envelopes*. Enermodal Engineering Limited, Kitchener (Canada).

Enermodal Engineering Limited, 2001. *Modeling two- and three-dimensional heat transfer through composite wall and roof assemblies in hourly energy simulation programs*. ASHRAE 1145-TRP Final Report, Part I, Part II, Library of Wall Assemblies.

European Committee for Standardization, 2007. *EN ISO 10211:2007 – Thermal bridges in building constructions – Heat flows and surface temperature – Detailed calculations*.

Karambakkam, B. K., Nigusse, B., and Spitler, J.D., 2005. *A one-dimensional approximation for transient multidimensional conduction heat transfer in building envelopes*. Proceedings of the 7th Symposium on Building Physics in the Nordic Countries, The Icelandic Building Research Institute, Reykjavik (Iceland).

Kosny, J., and Kossecka, E., 2002. *Multidimensional heat transfer through complex building envelope assemblies in hourly energy simulation programs*. Energy and Buildings, vol. 34, pp. 445-454.

Kossecka, E., and Kosny, J., 1997. *Equivalent wall as a dynamic model of the complex thermal structure*. Journal of Thermal insulation and Building Envelopes, vol. 20, pp. 249-268.

Martin, K., Erkoreka, A., Flores, I., Odriozola, M., and Sala, J.M., 2011. *Problems in the calculation of thermal bridges: Application to wood-frame buildings*. Energy and Buildings, vol. 43, pp. 529-535.

Pipes, L.A., 1957. *Matrix analysis of heat transfer problems*. Journal of the Franklin Institute, vol. 263, No. 3.

Quinten, J., and Feldheim, V., 2016. *Dynamic 19ulfill19 of multidimensional thermal bridges in building envelopes: Review of existing methods, application and new mixed method*. Energy and Buildings, vol. 110, pp. 284-293.

Quinten, J., 2018. *Dynamic 20ulfill20 of thermal bridges: Impact on the energy performance of low-energy buildings*. PhD Thesis, University of Mons (Belgium), Faculty of Engineering, Thermal Engineering and Combustion Unit.

Viot, H., Sempey, A., Pauly, M., and Mora, L., 2015. *Comparison of different methods for calculating thermal bridges: Application to wood-frame buildings*. Building and Environment, vol. 93, pp. 339-348.

Xiaona, X., Jianjun, X., and Yi, J., 2008. *A new approach to compute heat transfer of ground-coupled envelope in building thermal simulation software*. Energy and Buildings, vol. 40, pp. 476-485.

NOMENCLATURE

Am	heat flux amplitude, $W.m^{-2}$
C	heat capacity, $J.K^{-1}$ or $J.K^{-1}.m^{-2}$(1-D)
c	specific heat capacity, $J.kg^{-1}.K^{-1}$
E	error on integral of heat flux, $\%$
e	thickness, m
F	objective function, W/m^{-2}
j	imaginary unit
k	thermal conductivity, $W.m^{-1}.K^{-1}$
L	length, mm
P	period, s or h
q	heat flux, $W.m^{-2}$ or $W.m^{-1}$
R	thermal resistance, $m^2.K.W^{-1}$(1-D)
S	surface, m^2
x,y,z	spatial coordinates
T	temperature, $°C$
t	time, s or h
U	heat transfer coefficient, $W.m^{-2}.K^{-1}$
V	volume, m^3

Greek symbols

α	phase shift, rad
ε	error on heat flux, W/m
ϕ	structure factor
ρ	density, $kg.m^{-3}$
ψ	thermal transmittance, $W.m^{-1}.K^{-1}$

Subscripts

av	average
e	exterior/outside/outdoor
I	interior/inside/indoor
m	m-th layer
ref	reference
sol	solar

Study on the Krylov Subspace Method for Computationally Efficient Building Energy Simulations

Donghun Kim[1]* and James E. Braun[1]

[(1)]School of Mechanical Engineering, Purdue University, West Lafayette, IN, United States

ABSTRACT

Developing a computationally efficient but accurate building energy simulation (BES) model is important in order to accelerate building design optimizations, and development and evaluation of advanced control algorithms where a number of iterations over a long simulation period are required. For this purpose, identification approaches that develop simplified models from building simulation datasets could replace detailed energy simulation software. However, those approaches require extensive computational time at the front to generate the necessary data sets and train the model to provide both reliability and high accuracy. An alternative approach that utilizes model order reduction methods to directly reduce the number of differential equations is attractive in order to avoid the pre-simulation requirement. The balanced truncation method has been applied to the building science field for this purpose, but it can not be practically applied to a large-scale building with many zones due to computational and data storage requirements. To overcome the problem, this paper introduces the Krylov subspace method for model order reduction to the building science field, and investigates its performance for a large multi-zone building in terms of both accuracy and computation times.

Keywords: reduced order building envelope model, Krylov subspace method, moment matching

1. INTRODUCTION

Computationally efficient but accurate building energy simulation models that could replace high fidelity building energy simulation tools such as TRNSYS (Klein et. Al. 2004) and EnergyPlus (Crawley et. Al. 2000) are useful for many building applications particularly when a number of iterations of monthly or annual simulations are required. Many researchers have investigated black-box modelling approaches that include classical system identification methods and machine learning techniques to replace detailed energy simulation software. However, these inverse modelling approaches require extensive computational time on the front end to generate the necessary data sets for training the model to ensure both reliability and high accuracy.

Model order reduction methods (MOR) that convert a high dimensional linear time invariant (LTI) system model to a reduced-order LTI model (ROM) are attractive, since the MOR techniques completely eliminate the pre-simulation period for training by exploiting information contained in the original model. The balanced truncation method (B.C. Moore,

1981) is one of the most popular MOR techniques. It truncates dynamic states that are hardly controllable and hardly observable detected by the singular values of the Hankel operator calculated by balancing the observability and controllability Gramians of the original LTI system. It has been widely applied in the building science field (Del Barrio et. Al. 2000, Goyal and Barooah, 2012, Kim and Braun, 2012), because the generated ROM preserves original system properties, such as stability, controllability and observability, and it provides a way of estimating errors associated with the ROM. Despite these desired characteristics, the computational cost to generate a ROM is significant, because the balancing process needs to solve two matrix equations, i.e. the *Lyapunov equations* of the full-order system. Also, the computation cost for generating a ROM increases with $O(n^3)$ where n is the state dimension.

For a large-scale building, it is not unusual to have the state dimension higher than 10^3. For example, consider a 30-zone building where each zone has 6 surfaces and each surface consists of an average of 3 different wall layers. With two temperature nodes for each layer, the state dimension for the building becomes at least 1110 $(30 \times (6 \times 3 \times 2 + 1))$. Since the computation time for the balanced truncation method increases cubically with the state dimension, it may not be feasible to apply the MOR method for large-scale buildings, especially when parametric studies or optimization for design are needed.

Surprisingly, very few MOR methods that can systematically handle high dimensional buildings have been developed or introduced to the building science field. In this paper, we introduce a MOR method, the *Krylov subspace* method, to overcome the challenge for large-scale buildings, and investigate feasibility and performance of the MOR method for a 59-zone case study building.

2. METHODOLOGY

2.1 Linear Time Invariant Representation of Building Envelope System

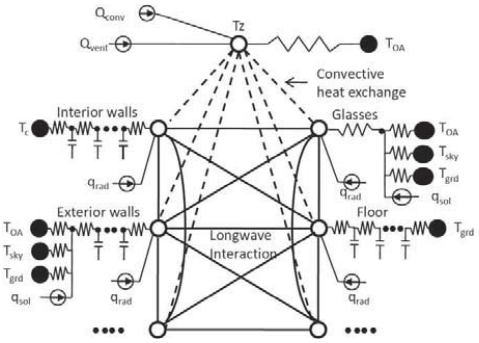

Figure 1: Considered thermal network

The first and essential step to generate a ROM is to construct a reliable LTI model for a building envelope system. The model should be sufficiently accurate when compared with building energy simulation software.

The formula introduced by Kim and Braun (2012, 2015) which converts a complex building thermal network (see Figure 1) to an LTI system quadruple (A, B, C, D) was adopted in this

study and is briefly summarized in this section. Some of important assumptions used to construct the full order model are:

- The temperature of each surface or surface segment and of its cross section is uniform.
- A room is well-stirred.
- Each wall emits or reflects diffusely and is gray and opaque.
- Air is nonparticipating media to radiation.
- Heat transfer is one dimensional.
- Conduction between window and window frame is neglected (1-D assumption).

For clarification, fundamental energy balance equations are shown in this paper.

A finite volume formulation is used to describe the heat conduction through walls. For any j[th] node in a wall except the first and last nodes, an energy balance leads to

$$\rho_j^i C_j^i w_j^i \frac{dT_j^i}{dt} = h_{cd}^L |_j^i \, T_{j-1}^i - (h_{cd}^L |_j^i + h_{cd}^R |_j^i) T_j^i + h_{cd}^R |_j^i \, T_{j+1}^i \qquad (1)$$

where $h_{cd}{}^L |_j^i = \frac{k^L |_j^i}{w^L |_j^i}$,

ρ_j^i= density at j[th] node in i[th] wall,

C_j^i= specific heat capacity at j[th] node in ith wall,

w_j^i= width of control volume of j[th] node in ith wal,

$k^L |_j^i$= thermal conductivity at left surface of the jth node in ith wall, and

$w^L |_j^i$= distance from the "j-1"th node to the jth node in ith wall.

For any i[th] outside wall (connected to the outdoor air) belonging to an individual zone, the heat balance equation at the surface is

$$\rho_1^i C_1^i w_1^i \frac{dT_1^i}{dt} = h_{cv,ex}^i (T_a - T_1^i) + h_{cd}^R |_1^i (T_2^i - T_1^i) + \alpha_1^i q_{SW}^i + q_{LW}^i \qquad (2)$$

where T_1^i represents the wall temperature of the first node which is set to be an outside surface of the wall. $q_{SW}^i, q_{LW}^i, h_{cv,ex}$ and T_a represent short wavelength solar irradiation, net long wavelength radiation exchange with the environment, convective heat transfer coefficient at the outside surface of a wall and outdoor air temperature, respectively.

With the assumptions that the outside surface is gray and diffuse and the air is a non-participating radiation media, net long wavelength interactions with the environment can be expressed as

$$q_{LWR}^i = \sigma \varepsilon_1^i F_{sky}^i (T_{sky}^4 - T_1^{i4}) + \sigma \varepsilon_1^i F_{grd}^i (T_{grd}^4 - T_1^{i4}) \qquad (3)$$

where σ, ε and F are the Stefan-Boltzmann constant, emittance and view factor, respectively.

Using a linear approximation of the long-wave heat exchange term gives

$$\rho_1^i C_1^i w_1^j \frac{dT_1^i}{dt} = -(h_{cv,ex}^i + h_{cd}^R \,|_1^i + h_{rad,ex}^i) T_1^i + h_{cd}^R \,|_1^i \, T_2^i + q_1^i \tag{4}$$

where

$h_{rad,ex}^i = 4\sigma \dot{U}_1^i (F_{sky}^i \overline{T}_{sky}^3 + F_{grd}^i \overline{T}_{grd}^3)$, $q_1^i = h_{cv,ex}^i T_a + 4\sigma \dot{U}_1^i (F_{sky}^i \overline{T_{sky}^3 T_{sky}} + F_{grd}^i \overline{T_{grd}^3 T_{grd}}) + \alpha_1^i q_{SWR}^i$, $\overline{T}_{sky} = \frac{T_{sky} + T_1}{2}$ and $\overline{T}_{grd} = \frac{T_{grd} + T_1}{2}$.

The mean temperatures for long-wave exchange between the surface and sky and surface and ground are assumed to be the same for all outside surfaces.

For the i[th] wall, the energy balance equation for the inside surface is

$$\rho_n^i C_n^i w_n^j \frac{dT_n^i}{dt} = h^i{}_{cv,in}(T_z - T_n^i) + h_{cd}^L \,|_n^i \, (T_{n-1}^i - T_n^i) - q_{net,rad}^i \tag{5}$$

where $q_{net,rad}$ is net radiative flux out of the inside wall.

The radiosity method is utilized to express the net flux under the assumption that the walls are gray, diffuse and opaque. The same linearization method used in Eqn. (4) is employed. It results in

$$\vec{q}_{net,rad} = \tilde{A}^{-1}[\tilde{B}' \vec{T}_n - \vec{h}_o] \tag{6}$$

where,

$$\tilde{A}_{ij} \equiv \frac{\delta_{ij}}{\dot{U}_j} - \frac{\rho_j}{\dot{U}_j} F_{ij}, \; \tilde{B}'_{ij} = 4\sigma(\delta_{ij} - F_{ij})\overline{T}^3$$

F_{ij} is view factor from i[th] to j[th] surface, δ is the Kronecker delta, ρ is reflectance and $\vec{h}_o$ is external radiative source. In Eqn. (6), radiosity does not appear explicitly, which is convenient for building simulation. Since the i[th] component of $\vec{h}_o$ represents an external radiative source acting on the i[th] surface, the effects of internal sources and transmitted solar energy through windows are treated in a consistent manner. For any shaped room, the net radiative flux can be explicitly calculated as a function of surface temperatures if the view factors and the external radiative sources are known.

Equations of (1), (4) and (5) for all temperature nodes for all walls and the zone air energy balances are collected to construct a full-order building LTI model which has the following standard form.

$$\begin{aligned} \dot{x}(t) &= Ax(t) + Bu(t) \\ y(t) &= Cx(t) + Du(t) \end{aligned} \tag{7}$$

where $A \in R^{n \times n}, B \in R^{n \times m}, C \in R^{p \times n}, D \in R^{p \times m}$ and (m, p) are the numbers of inputs and outputs, respectively. For more detailed descriptions and the LTI formation, refer to Kim and Braun (2015).

2.2 Introduction of moment matching problem and Krylov subspace method

Essential ideas and important points of the moment matching problem and the Krylov subspace method are presented in this Section. It is assumed that the system quadruple of (A, B, C, D) in Eqn. (7) is available.

The problem definition of MOR for an LTI system is to construct lower order system matrices $(A_r, B_r, C_r D_r)$ of Eqn. (9) from the original system of Eqn. (8).

$$G_o : \begin{cases} \dot{x}(t) = Ax(t) + Bu(t) \\ y(t) = Cx(t) + Du(t) \end{cases} \tag{8}$$

$$G_r : \begin{cases} \dot{x}_r(t) = A_r x_r(t) + B_r u(t) \\ y(t) = C_r x_r(t) + D_r u(t) \end{cases} \tag{9}$$

where $x(t) \in \mathrm{R}^n, x_r(t) \in \mathrm{R}^r$ and $r << n$. In other words, we want to reduce the state dimension from n to r while maintaining the original input-output relation as much as possible.

To explain the moment matching (MM) problem, consider the *Laurent series* expansion of a transfer function $G(s) = C(sI - A)^{-1}B + D$ in the neighbourhood of s_0 in a complex plane.

$$G(s) = \eta_0(s_0) + \eta_1(s_0)(s - s_0) + \cdots + \eta_k(s_0)(s - s_0)^k + \cdots, \tag{10}$$

where η_j is called the j[th] *moment* of G at s_0. It is assumed that there are no poles within a neighbourhood of s_0. The MM problem is to construct (A_r, B_r, C_r, D_r) such that the first k moments of G_r, denoted as $\eta_{r,0}(s_0), \eta_{r,1}(s_0), \cdots, \eta_{r,k-1}(s_0)$, *exactly* match those of G_o, i.e. $\eta_{o,0}(s_0), \eta_{o,1}(s_0), \cdots, \eta_{o,k-1}(s_0)$.

Since the moments have different expressions of the system quadruple (A, B, C, D), i.e.

$$\begin{aligned} &\eta_0(0) = D, \quad \eta_j(0) = CA^{(j-1)}B, \\ &\eta_0(\infty) = -D, \ \eta_j(\infty) = -CA^{-j}B, \\ &\eta_0(s_0) = -D, \ \eta_j(s_0) = -C(A - s_0 I)^{-j}B, \end{aligned} \tag{11}$$

the MM problem becomes one of finding (A_r, B_r, C_r, D_r) such that

$$C_r A_r^{(j-1)} B_r = CA^{(j-1)}B \ \ (\forall j \in \{1, 2, \cdots, k\}) \text{ if } s_0 = 0, \tag{12}$$

$C_r A_r^{-j} B_r = CA^{-j}B \ \ (\forall j \in \{1, 2, \cdots, k\})$ if $s_0 = \infty$, and

$C_r (A_r - s_0 I)^{-j} B_r = C(A - s_0 I)^{-j} B \ (\forall j \in \{1, 2, \cdots, k\})$ if $s_0 \notin \{0, \infty, \Lambda(A)\}$, where $\Lambda(A)$ is the spectrum of A.

The MM problems at $s_0 = 0, s_0 = \infty$ and $s_0 \notin \{0, \infty, \Lambda(A)\}$ are known as *partial realization*, *Padé approximation* and *rational interpolation* problems, respectively.

The Krylov subspace method (KM) is one of the most numerically efficient and stable algorithms for the MM problems. The KM seeks a lower dimensional subspace namely the Krylov subspace where 1) original dynamics are projected onto and 2) partial moments of the projected dynamic system equate to those of the original dynamic system.

In order to show how the KM works, consider the partial realization problem for a single input system, that is $B \in R^{n\times 1}$. The main idea of the KM may be described in the following three steps.

1. Given the system tuple (A, B, C), define the Krylov subspace as follows.

$$\mathrm{K} \coloneqq span\,col\left[B, AB, \cdots, A^{-k}B\right] \tag{13}$$

   where *span col* represents the column span, i.e. K is the space spanned by column vectors of the matrix $\left[B, AB, \cdots, A^{-k}B\right]$.

2. Define $V \in R^{n\times k}$ as a basis (in the form of a matrix) of K and choose any $W^T \in R^{k\times n}$ as a left inverse of V, i.e. $W^TV = I$. Then, construct the reduced order system matrices (A_r, B_r, C_r, D_r) by the *Petrov-Galerkin projection* with V and W. That is,

$$A_r = W^TAV,\quad B_r = W^TB,\quad C_r = CV,\quad D_r = D. \tag{14}$$

3. Consider the first moment of G_r at $s_0 = \infty$. It is $\eta_{r,1}(\infty) = C_rB_r = (CV)(W^TB)$. Since $span col[B] \subset \mathrm{K}$ from the definition of the Krylov subspace (see the 1st step, Eqn. (13)), B can be expressed as $B = V\zeta$ for some ζ. Therefore, $C_rB_r = (CV)(W^TB) = (CV)(W^TV\zeta) = CV\zeta = CB$. The biorthorgonal condition of $W^TV = I$ is used in the derivation. This shows the first moments of G_r and G_o are equal. By applying the same process in this step, it can be shown that the KM method is able to match up to the k[th] moment.

For the rational interpolation problem, the steps are the same as above except for the definition of the Krylov subspace in the 1st step. This is because moments are expressed differently as indicated in Eqn. (11). For the rational interpolation, it is;

$$\mathrm{K} = span\,col[(s_0I - A)^{-1}B, (s_0I - A)^{-2}B, \cdots, (s_0I - A)^{-k}B]. \tag{15}$$

The remaining problem for the KM is how to construct V and W in a numerically efficient manner in the 2nd step. Ideally, the *Gram-Schmidt process* (or QR factorization) can be applied to form a basis of the Krylov subspace, but it is not numerically reliable since $(s_0I - A)^{-j}B$, for the rational interpolation problem as an example, converges very quickly to the largest eigenvector as the exponent j increases, resulting in a badly conditioned matrix. To understand this numerical issue, it is helpful to recall that the *Power method* approximates the largest eigenvalue and eigenvector of a matrix. Therefore, for generating a numerically reliable basis V of a Krylov subspace, the *Arnoldi or Lanczos algorithms* are typically used rather than the QR (Householder, 2006). Like the QR factorization, the methods sequentially generate an orthonormal basis for an updated column vector (for single input systems) by perpetually projecting it onto the subspace spanned by previous orthonormal basis. However, for those methods, the updated vector is not the multiplication of the matrix power of $(s_0I - A)^{-j}$ with B, but is the multiplication of $(s_0I - A)^{-1}$ with the latest orthogonal basis.

The Arnoldi algorithm for the rational interpolation problem for a single input system can be expressed as follows (Antoulas, 2005).

$Solve\ (A - s_0 I)v_1 = B$
$v_1 \leftarrow v_1 / \| v_1 \|$
$Solve\ \ (A - s_0 I)w = v_1$
$V \leftarrow v_1$
$p_1 = (I - VV^T)w$
$for\ \ j = 1, 2, \cdots, k-1$
$\quad v_{j+1} = p_j / \| p_j \|$
$\quad Solve\ \ (A - s_0 I)w = v_{j+1}$
$\quad V \leftarrow [V, v_{j+1}]$
$\quad p_{j+1} = (I - VV^T)w$
end

v_j represents the j[th] orthonormal basis obtained from the j[th] Krylov sequence, i.e. $(s_0 I - A)^{-j} B$.

For the Arnoldi algorithm, W is equal to V. Since V as a result of the Arnoldi algorithm is an orthonormal basis for a Krylov subspace, the biorthonormality condition of $W^T V = I$ in the 2[nd] step is automatically satisfied.

2.3 Krylov method for building applications

For building applications, the Krylov subspace method should handle general multi-input multi-output (MIMO) systems because building dynamics are driven by various indoor and outdoor heat sources and have a number of outputs which could be zone air temperatures or heating/cooling loads depending on the application. The Arnordi algorithm is preferable for building applications compared with the Lanczos algorithm because of the difficulty and complexity of the Lanczos procedure for general MIMO systems that are non-symmetric and have different numbers of inputs and outputs, i.e. $m \neq p$, (Gucercin, 2003).

For the MIMO case, one may attempt to extend the Anordi algorithm for SISO systems by simply treating the matrix B as a block of vectors. In this case, the updated coordinate, v_j , will be a matrix rather than a vector. However, this approach could fail because it may yield rank deficiency and redundancy in the projection matrices (Gucercin, 2003). More precisely, the resulting V may be not a full rank such that $V^T V \neq I$. Therefore, modification(s) of the Arnordi algorithm must be made for an appropriate deflation of V for MIMO systems. We adopt the method proposed by Boley (1994) to overcome this challenge. In this method, block vectors are updated without considering rank deficiency and the deflation is made by using the Gram-Schmit process and a rank revealing process at each iteration of the Arnodli procedure. We present the following algorithm which is a modified version of Boley's algorithm.

$$
\begin{aligned}
&Solve\ (A - s_0 I)v_1 = B \\
&v_1 \leftarrow qr(v_1) \\
&Solve\ \ (A - s_0 I)w = v_1 \\
&V \leftarrow v_1 \\
&p_1 = (I - VV^T)w \\
&for\ \ j = 1, 2, \cdots, k' - 1 \\
&\quad v_{j+1} = qr(p_j) \\
&\quad Solve\ \ (A - s_0 I)w = v_{j+1} \\
&\quad V \leftarrow [V, v_{j+1}] \\
&\quad p_{j+1} = (I - VV^T)w \\
&end
\end{aligned}
$$

where the operator *qr* acts on a matrix and extracts only linearly independent column vectors after the QR factorization of the matrix. The presented algorithm is mathematically the same as Boley's method but numerically more efficient because it avoids an internal iteration which requires a number of matrix multiplications. The modification is helpful to further reduce the computation time for obtaining V.

3. CASE STUDY RESULTS

3.1 Description of case study building

The validity of the full-order LTI model representation discussed in Section 2 has been evaluated for a number of buildings. TRNSYS and Modelica Buildings' library were used to compare dynamic responses. Previous case study results can be found in Kim et. Al. (2013) and Kim and Braun (2015).

A case study for a multi-zone (59-zone) commercial building located at the Philadelphia Navy Yard is presented to test feasibility and performance with respect to the accuracy and computational requirements of the KM. Figure 1 shows an external view of the building. Some characteristics used in the modeling include:

- 55,000 square feet of total floor area.
- 3 occupied floors with a basement and attic spaces and a total of 59 zones.
- 18 different types of layers used for wall construction that primarily consist of concrete, insulation board, plaster board, and brick.
- 6 different types of walls various combinations of the layer types.
- Ground boundary temperature modeled as a time varying signal.
- TMY2 weather data for Philadelphia.
- Values of 17.77[W/m^2-K] and 3.05[W/m^2-K] were used for convective heat transfer coefficients at the outside and inside surfaces, respectively.

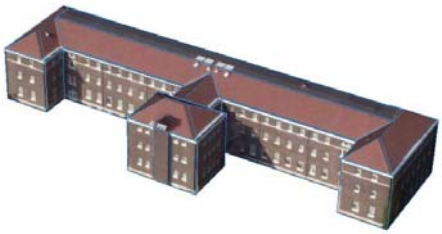

Figure 2: External view of a case study building (3D Google Map)

In order to construct a full order LTI system for the building, average values of effective sky temperature, ground surface temperature and mean external wall temperatures are needed for linearization of the radiation heat transfer coefficient and are determined prior to simulation. The average ground temperature was taken as the average annual air temperature. The average sky and air temperature were determined from the TMY2 weather file, whereas the mean external wall temperature was set to 15ºC.

3.2 Discussion and result analysis

The original LTI model (G_o) with the state dimension over 1500 for the 59 zones was developed using the formulation described in Section 2. There are 144 inputs and 59 outputs. The rational interpolation algorithm presented in Section 3.3 was applied to G_o with $s_0 \approx 0$, resulting in a ROM (G_r) with the state dimension of around 500.

The time required to generate a ROM for a large-scale building and simulation time compared with that of an original LTI model are of interest, because it could answer whether the KM is feasible for building applications involving parametric studies and design optimization.

Table 1. Computational time for generating G_o and G_r for a 59-zone building

	Full LTI System Construction (G_o)	ROM Construction (G_r)
Computational time [sec]	4.47	11.82
Number of states	1625	498

Table 2. Computational time comparison between G_o and G_r for a one-year simulation

G_o	G_r	Computation time savings [%]
54.32 [sec]	1.09 [sec]	97.98

Table 1 shows the computational time to generate G_o and G_r. All computation times are based on a quarter-core 3.10 GHz with 3.16GB memory desktop computer. It took less than 5 sec to build the entire system matrices and the memory required to save the system matrix was 243.4 KB utilizing sparsity of the matrix. The construction time for the KM was about 12 sec. The

number of states was reduced by about a factor 3 from G_o. A one-year simulation time comparison between G_o and G_r is provided in Table 2. For this case study, the computational requirements were about 55 sec for G_o and 1 sec for G_r, respectively. Note that the computation was reduced by more than a factor of 50 (98 % savings) compared to the linearized building model which is already numerically efficient and stable. Compared with commercial building energy simulation tools, the savings potential would be much greater. These indicate that there are significant computation time savings potential utilizing the KM for building simulations of large-scale buildings, if G_r is accurate enough.

Sample model output comparisons are shown in Figure 3 to Figure 5. Figures 3, 4 and 5 show example comparisons of total building load profiles for peak heating days, mild days, and peak cooling days, respectively. The setpoints for all zones were set to 22 ºC in calculating buildings loads. For all cases, G_r predicts total building loads with negligible errors.

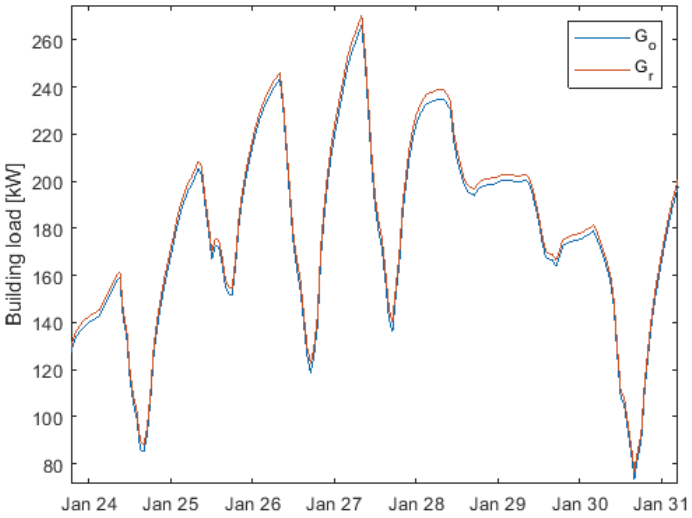

Figure 3: Load comparisons between full-order and reduced-order models for a heating period (heating (+), cooling (-))

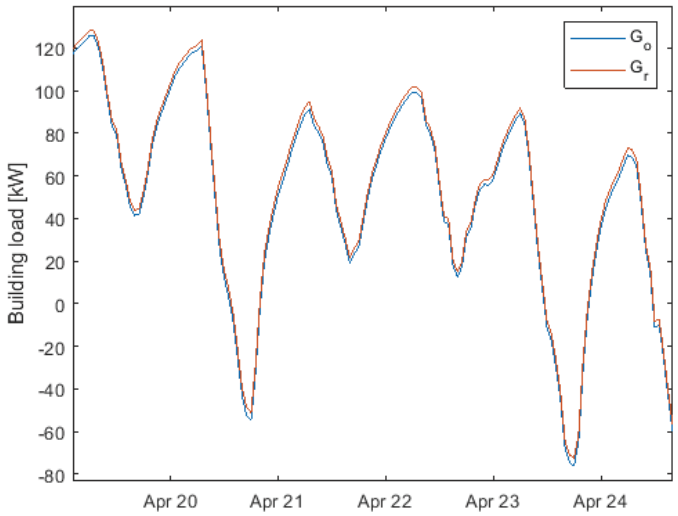

Figure 4: Load comparisons between full-order and reduced-order models for a mild period (heating (+), cooling (-))

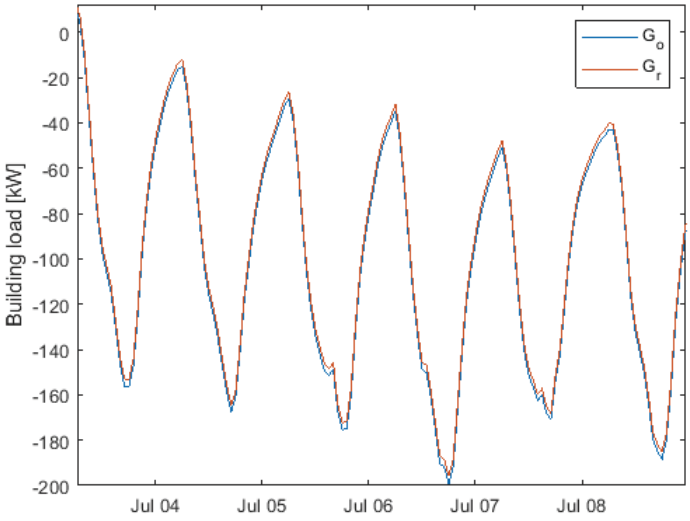

Figure5: Load comparisons between full-order and reduced-order models for a cooling period (heating (+), cooling (-))

Table 3. Comparisons of Predicted Building Loads

	G_r	G_o	|Relative ERR| [%]
Peak heating load [kW]	266.17	270.29	1.54
Peak cooling load [kW]	199.27	195.92	1.69
Annual heating load [MWh]	554.90	570.65	2.84
Annual cooling load [MWh]	193.83	184.63	4.75

Table 3 summarizes comparisons of predicted heating and cooling loads. It is a bit surprising that errors associated heating and cooling loads are somewhat high despite of the accuracy of G_r shown in Figure 3-5. To analyze it, the distribution of errors, which is defined by the load calculated from G_r subtracted by that of G_o, is shown in Figure 6, and its mean and standard deviation are provided in Table 4. It indicates G_r slightly overestimates building loads around 3 kW for almost all simulation times. Through parametric study, the differences were found to be associated with the treatment of windows in the full LTI model. It is expected that these differences could be mostly eliminated by using a consistent approach for the windows. Nonetheless, the ROM clearly captures major dynamics of building load. Nonetheless, G_r provides comparable accuracy for annual heating/cooling loads and peak heating/cooling loads.

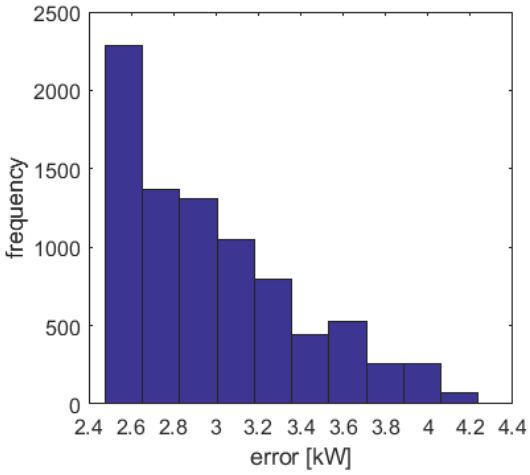

Figure 6: histogram of building load calculation errors (hourly sampled for one-year simulation)

Table 4. Mean and standard deviation errors (kW) comparison of G_o and G_r for one-year simulation

MEAN ERROR [kW]	STD ERR [kW]
3.11	0.44

3.3 Further discussion

In this paper, the presented method was used to calculate only sensible building loads. This is because moisture dynamics occur within the surfaces of a zone which results in decoupled dynamics as long as there is no convective flow coupling between zones. In this case, the KM is not very attractive since the state dimension for the moisture dynamics for an individual zone is small and the balanced truncation method can be applied.

The proposed method and any other MOR methods for LTI systems is not able to accurately reduce detailed zonal air flow coupling or infiltration models in which the amount of air flow is driven by the pressure difference, because the detailed models form nonlinear algebraic equations. However, an approximated flow coupling could be considered by a linearization, e.g. fixed air flow exchange rate.

It is of interest how an integrated ROM and HVAC model performances in terms of accuracy and computational speed. We refer to a previous paper (Kim et. Al. 2013) for a case study which compares the integrated model with TRNSYS and Modelica Buildings Library (Wetter et. Al. 2014).

4. CONCLUSIONS

The balanced truncation method which is one of the most popular and reliable model order reduction methods in the literature is computationally very demanding for application to large-scale buildings. This paper introduced an alternative method, the Krylov subspace method, to the building science field that can effectively and reliably reduce high dimensional building dynamics. To deal with a general multi-input and multi-output structure for various building applications, a suitable algorithm from the literature of control and numerical analysis was identified, modified and applied. A case study for a 59-zone building was carried out. In this study, the lower order model gave results that were close to those predicted by the original full order model with about a factor of 50 reduction in computational time compared to a full-order model. The computational requirements for generating the ROM are small enough such that this approach would be useful for general building simulations, particularly when considering parametric studies and optimization for design.

ACKNOWLEDGEMENTS

This work was supported by the Center for High Performance Buildings (CHPB) at Purdue University under the grant number of CHPB-32-2018.

REFERENCES

Antoulas, A.C., 2005. Approximation of large-scale dynamical systems (Vol. 6). *SIAM*.

Boley, D. L. (1994). Krylov space methods on state-space control models. *Circuits, Systems and Signal Processing*,13(6), 733-758.

Crawley, D. B., Pedersen, C. O., Lawrie, L. K., & Winkelmann, F. C. (2000). EnergyPlus: energy simulation program. *ASHRAE journal*, 42(4), 49.

Del Barrio, E. P., Lefebvre, G., Behar, P., & Bailly, N. (2000). Using model size reduction techniques for thermal control applications in buildings. *Energy and Buildings*, 33(1), 1-14.

Goyal, S., & Barooah, P. (2012). A method for model-reduction of non-linear thermal dynamics of multi-zone buildings. *Energy and Buildings*, 47, 332-340.

Gugercin, S. (2003). Projection methods for model reduction of large-scale dynamical systems (Doctoral dissertation, Rice University).

Householder, A. S. (2006). Principles of numerical analysis. *Courier Corporation.*

Isaacson, E., & Keller, H. B. (1994). Analysis of numerical methods. *Courier Corporation.*

Kim, D., & Braun, J. E. (2012). Reduced-order building 14ulfill14g for application to model-based predictive control. *Proceedings of SimBuild*, 5(1), 554-561.

Kim, D. & Braun, J.E. (2015). A General Approach for Generating Reduced-Order Models for Large Multi-Zone Buildings. *Journal of Building Performance Simulation*. 8(6), 435–448.

Kim, D., Zuo, W., Braun, J. E., & Wetter, M. (2013). Comparisons of building system 14ulfill14g approaches for control system design. *In Proceedings of the 13th International Conference of the International Building Performance Simulation Association* pp. 3267-3274.

Klein, S. A., Beckman, W. A., Mitchell, J. W., Duffie, J. A., Duffie, N. A., Freeman, T. L., ... & Urban, R. E. (2004). TRNSYS 16–A TraNsient system simulation program, user manual. *Solar Energy Laboratory*. Madison: University of Wisconsin-Madison.

Moore, B. (1981). Principal Component Analysis in Linear Systems: Controllability, Observability, and Model Reduction, *IEEE Transactions on Automatic Control*, Vol. 26, No. 1, pp 17–32.

Wetter, M., Zuo, W., Nouidui, T. S., & Pang, X. (2014). Modelica buildings library. *Journal of Building Performance Simulation*, 7(4), 253-270.

Positive Energy Houses, envelope and systems integrated optimization by means of dynamic simulations

P. Abrahams[1*], C. Scheuren[1], P. André[1]

(1) BEMS Université de Liège, Arlon Campus Environnement, Luxembourg

ABSTRACT

In the framework of the Interreg IV-A Greater Region project called « VallEnergie » four projects of residential houses with "positive energy performance" were analysed. The main purpose of the study was to define the optimal choices in terms of envelope and energy system in the building in order to reach the high performance level of a "Positive Energy House" (PEH in this paper). The first step was to determine what was meant by the term "Positive Energy House" and to define criteria used to characterize energy and comfort performance of such house.

The concept of « Positive Energy house » defined in the project had to be in adequacy with European definition, therefore a complete state of the art of NZEB concept in Europe was carried out. The collected information was used to establish the specifications document of "PEH" in concertation with the project consortium. By means of TRNSYS17 software different sets of variants were assessed by thermal dynamic simulations and compared in order to define the optimal choice of insulation strategy and heating, DHW and Renewable Energy production systems configuration to reach the PEH performance as defined in the specification document of "VallEnergie" project. The paper will present the selected hypotheses of the simulation models, describe the applications that were developed in TRNSYS and discuss the results of the different variants.

Keywords: Positive Energy Houses, NZEBs, System simulation, Dynamic simulation, TRNSYS.

1. INTRODUCTION

The 20-20-20 EU's strategy aims at a triple reduction objective in terms of annual primary energy consumption and greenhouse gases (GHG) and also to reach a 20% share in renewables in the European energy consumption. In this context new standards of construction have been developed because buildings represent a high potential for a significant reduction of GHG emissions and energy use. Indeed, buildings (residential and commercial) represent around 40% of the global final energy consumption and are responsible about 36% of the total CO2 emissions in EU (European Parliament, 2012). These standards are aimed at ambitious requirements for energy performance in the building sector and were introduced in the Energy Performance of Buildings Directive (EPBD, 2010/31/EC) that imposes Members States to define a national definition for "nearly Zero Energy Buildings" (nZEB). As mentioned in article 2 of EBPD the term "nZEBs" means buildings with a very high energy performance and the low amount of residual energy should be covered by renewable sources and as possible produced on-site or nearby (EU, 2010).

Because all buildings have to be nZEB by 31 December 2020 the standard has gradually been implemented across EU in the last few years. But already some Members States went further in the requirements with the "Net Zero Energy Buildings" (NZEB) which are buildings with a net annual energy balance equal to 0. In other words, these buildings have a net energy consumption calculated on an annual basis which is roughly equal to the renewable energy produced on-site or nearby.

In Belgium the Brussels-Capital Region defined its own definition for NZEB or so called "Positive Energy Building". A "zero energy" building has to show a very high energy performance and cover its demand by means of renewables sources. Furthermore only its primary energy needs for heating, cooling, domestic hot water (DHW), lighting and auxiliary electricity (ventilation, circulating pump, etc…) in normalized situation are taken into account as mentioned in the Vademecum of PHPP of Brussels-Capital Region (Vandenberghe & VanLoon, 2013). If the owner of this building also decides to compensate the residual needs for domestic consumptions (household appliances, electric vehicle, etc…) by means of renewables produced on-site or nearby thus this building will become a "positive energy" one. Fig. 1 illustrates the difference between each term.

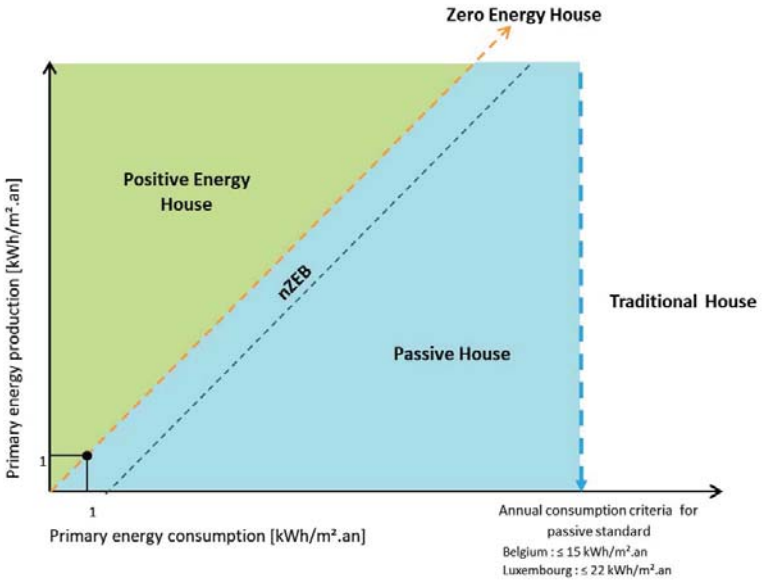

Figure 1: Differences between a positive energy house, nZEB, passive house and traditional house

The Interreg IV-A Greater Region project VallEnergie was developed with the objective of developing solutions to achieve energy autonomy in the Attert valley in Belgium near the Luxembourg border. This project focused on new renewable energy concepts and more specifically for the residential sector with the study of four PEH projects (2 Belgian houses and 2 Luxemburgish houses). Therefore, specifications were drawn up in order to determine the definition of the positive energy house concept including the constructive and technical criteria expected for this type of construction. Based upon these specifications, simulation variants on the envelope and system choices were conducted using TRNSYS software. As a result of the simulations, it was possible, in consultation with the architects of the project, to define the optimal solution in terms of constructive and technical criteria (envelope and energy systems) for building PEH meeting the specifications pre-established. This paper presents the hypotheses, methodology for simulations and the main results of the study.

2. METHODOLOGY AND SIMULATIONS

2.1 Common hypotheses and simulation variants

2.1.1 Four houses project

The Belgian side of the VallEnergie project concerned two semi-terraced houses with each other. The energy performance of the houses was first evaluated in the PEB software (Energy Performance Building standard in Belgium). This evaluation helped to design in TRNSYS the houses models with more accuracy thanks to tremendous information from the PEB report and architect's inputs. In the Luxemburgish side there was also two projects of semi-terraced PEH but in different location. The first house was a case of demolition of an old annex and reconstruction of three passive houses in its place. For the study only one of these houses was selected for simulations. The energy performance of the second house didn't be primarily assessed only the architect's plans were available. There were no information concerning the wall composition thus the information was taken from the first Luxemburgish house. The four houses are respectively called A, B for Belgian houses and C, D for Luxemburgish houses. An important quantity of results were generated but only the results for one of the 4 models will be presented in this article, namely the Belgian house model A.

Fig. 2 shows the floor plan (ground floor and first floor (right) as well as the zoning strategy (left) defined in the TRNSYS simulations).

Fig 2: Floor plans and zoning strategy of the simulated house

The main characteristics of the four houses are shown in Table 1.

Table 1: Main characteristic of the PEH in VallEnergie project

	A	B	C	D
Location	Belgium		Luxembourg	
Type	New construction		Demolition and New construction	New construction
Construction Type	Massive / heavy	Light		
Construction material	Brick	Wood		
Insulation material	Graphite enriched EPS	Cellulose		
Glazing	Triple			
Ventilation type	Dual flow CMV			
Infiltration rate (vol/h)	0.6			
Occupancy (pers.)	4			
Temperature setpoint ($°C_{night}/°C_{day}$)	16/20			
Living surface (m²)	120	127	142	140

2.1.2 General hypotheses

Some hypotheses in the study were common for the four house models in TRNSYS. It notably concerned: occupancy profiles, temperature setpoints, heating period, internal gains, infiltration rate and ventilation system, (Abrahams, Rogiest, & André, 2015). Impact of certain parameters on the energy performance of the models was evaluated. Thus the influence of the set temperature or the internal gains on the annual consumption for heating was analyzed for one of the 4 houses of the project – here the Belgian house A. Results are shown in Table 2. The reference model used to compare results had an unlimited power heating system able to cover instantaneously the heating needs of the house.

Table 2: Influence of temperature setpoint and internal gains on the annual heating consumption for Belgian house model A.

Setpoint temperature influence on annual heating consumption (final energy)			
	Setpoint 16°C/19°C	**Setpoint 16°C/20°C**	**Setpoint 16°C/21°C**
Annual heating consumption (kWh/yr)	1414	1696	2001
Relative variation	-17 %	-	+18 %
Artificial lighting influence on annual heating consumption (final energy)			
	With artificial ligthing gain	**Without artificial lighting gain**	
Annual heating consumption (kWh/yr)	1696	1858	
Relative variation	-	+9.5%	
Domestic appliances influence on annual heating consumption (final energy)			
	With domestic appliances gain	**Without domestic appliances gain**	
Annual heating consumption (kWh/yr)	1696	1842	
Relative variation	-	+8.6%	
Internal gains influence on annual heating consumption (final energy)			

	With internal gains	Without internal gains
Annual heating consumption (kWh/yr)	1696	3077
Relative variation	-	+81%

As shown in Table 2 in either case, a 1°C change in the setpoint temperature in a house with high energy performance such as model A generates an increase or a reduction of the annual energy consumption for heating around 17 to 18%. The artificial lighting also seems to have a significant impact on such a building. A total absence of artificial lighting will cause an increase around 9.5% of the annual heating consumption in house A. The value is almost similar for domestic appliances gains impact on annual energy consumption. In general, a model without any internal gains (occupancy, lighting, domestic appliances) will consume around 81% more energy than with internal gains. These simulations demonstrate the importance of the choice of starting assumptions and their influence on the results.

2.1.3 Simulation tool

TRNSYS (version 17) was used to perform the dynamic simulations reported in this paper. The building was simulated using Type 56 allowing a multizone approach. The model was the object of a deep validation work performed in the IEA Annex 58 project. In this project, the model was compared to detailed measurements performed in the test houses located in Holzkirchen. The results obtained in this validation exercise were very good (Strachan et al, 2016).

2.1.4 Envelop variants

In order to determine the optimal solution in terms of envelope which will make it possible to respect the criteria imposed by the specifications of the project, a series of simulation were carried out. The parameters selected for envelope simulation concerned: the choice of wall composition and in particular insulation type and thickness, orientation of the building, type of solar protection and their control, value of the glazing g factor.

Some other variants on the architectural configurations of house models were also simulated thanks to the TRNSYS 3D plugin. For example, the window recess (see Figure 3) impact on building performance was analyzed. Most of the time this architectural detail is not taken into account in simulations. For this purpose, a shading element around windows was designed in order to reproduce the window offset in the wall. The window recess influences the quantity of solar gains that enter the zone through the glazing. Thus a model with and without window recess was simulated in order to know its impact on energy performance and summer thermal comfort. Results are shown in *4.1.1*.

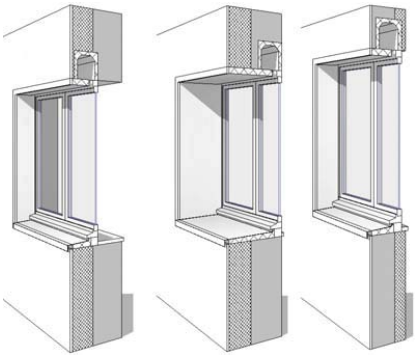

Figure 3: Examples of Window offset in the wall (source: http://revit-memo.blogspot.com)

2.1.5 System variants

Once the envelope configurations for the house models have been fixed, the work has then started to study the system variants for the production of heating, domestic hot water and renewables. Different combinations between systems were simulated to obtain an optimal energy solution for the houses, see Table 3. These combinations had to 6ulfill the PEH energy performance requirements and also to meet some financial constraints due to the target public of the construction project.

Table 3: Simulation variants for systems combinations

System variant	Heating production	DHW production	RE production
Variant n°1 – V1			
V1a	Electrical heating	Electric tank	PV panels
V1b	Electrical heating	Solar tank	PV + thermal solar panels
V1c	Electrical heating	Solar tank + HP	PV + thermal solar panels
Variant n°2 – V2			
V2a	Wood pellet stove	Electric tank	PV panels
V2b	Wood pellet stove	Solar tank	PV + thermal solar panels
V2c	Wood pellet stove	Solar tank + HP	PV + thermal solar panels
V2d	Wood pellet stove + electric heating	Solar tank + HP	PV + thermal solar panels
Variant n°3 – V3			
V3	Hot pulsed air	-	-
Variant n°4 – V4			
V4a	HP + radiators	Solar tank + HP	PV + thermal solar panels
V4b	HP + radiators	Solar tank + HP	PV panels

As shown in Table 3 there were four heating systems analysed by dynamic simulations in TRNSYS. For the electrical heating the TRNBuild interface of TRNSYS software was used with the classic heating type manager. The wood pellet stove was emulated thanks to a PID controller (Type23 in TRNSYS) with parameters set from (Georges, et al., 2014). The model of this wood pellet stove is a simplified one and the simulations were run in order to define the power emitted by convection by the wood stove. This power is transformed into an internal gain to be applied in the room where the stove is placed. The radiative part is distributed between the walls of the room according to view factors. Nevertheless, simulations demonstrated that this radiative power could be neglected compared to the convective one

because it represented less than 1% of the global emitted power from the stove. The third system – a heating by hot air distribution in house – required a preliminary work that consisted in evaluated first the demand of the houses thanks to a heating system able to instantly supply energy to the house (for a temperature set point set at 20°C by day and 16°C by night). The second step was to compute the supply temperature in order to reach 20°C in house (1), (2). Indeed, the power is related to the supply temperature by the formula:

$$P = Cp \times \rho air \times Q \times (Tsupply - Tambient) \quad (1)$$

$$Tsupply = Tambient + \frac{P}{Cp \times Q \times \rho air} \quad (2)$$

The last heating system was a heat pump (HP). The coefficient of performance (COP) of the HP was computed thanks to simulations and the thermal power was determined thanks to the computed COP of HP. A system of equations was used in order to introduce Carnot equations for the COP computation. Once again the simulation of the HP was based on computation and not on real simulation of the system itself.

For the DHW production three configurations were simulated: a classic tank with electrical resistance, a solar tank connected to the solar thermal panels with an auxiliary electrical resistance and the same solar tank but in which the electrical resistance was replaced by the HP. Finally, the photovoltaic (PV) electricity production was also estimated for each house and simulated thanks to the Type 94a in Simulation Studio (TRNSYS environment). Four kinds of PV panels were tested by changing the parameters of this type.

3. RESULTS ANALYSIS AND DISCUSSION

3.1.1 Envelope simulations results

All the four house models of the project presented a very high envelop performance with a U-value for external wall between 0.101 and 0.113 W/m²K. For each model the minimal insulation thickness needed to achieve passive requirements was determined by means of TRNSYS simulations (see Figure and Table 4). To obtain the minimal value of thickness insulation the maximal amount of annual energy demand of each building allowed by the passive standard was computed. This value is shown by the dot line on Figure as an example given for one of the four house models – house A. The insulation layer was increased by 5 cm in each simulation. All results are given in Table 4.

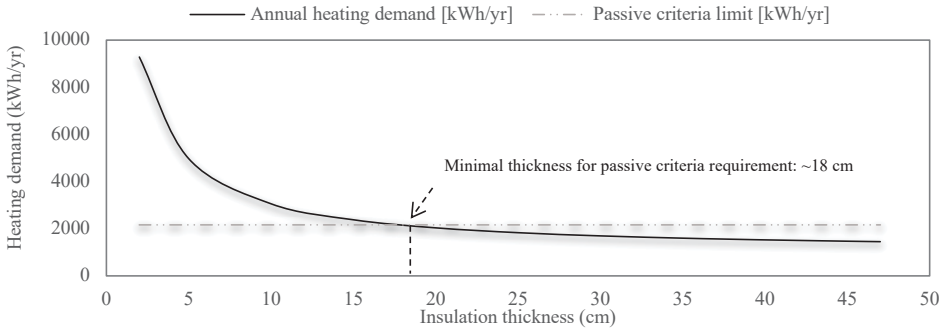

Figure 4: House model A – insulation thickness – graphite enriched EPS [cm]

Table 4: Determination of minimal insulation thickness for each house models

	Model A	Model B	Model C	Model D
Annual heating demand – passive limit (kWh/yr)	2164	2346	3165	2673
Insulation material	Graphite enriched EPS	Cellulose		
Minimal insulation thickness (cm)	18	19	8	9

The difference between Belgium and Luxembourg is mainly explained by the heating consumption requirement for passive standard which is different in each country. Indeed for Belgium the annual heating specific consumption has to be lower or equal than 15kWh/m².yr whereas Luxembourg criteria imposes a value lower or equal than 22kWh/m².an (Chambre des métiers Luxembourg, 2014). Another aspect shown in Figure is the limited impact of the additional thickness after a certain insulation level on the annual heating consumption. The real gain is on the very first insulation centimeters. For house model A it seems that after 20cm of graphite enriched EPS the impact on energy needs is lowered. For the window recess simulations, the depth of window offset has an impact on the operative temperature as shown in Figure . Results are given for a simulation period between the 15th of July and the 15th of August (summer).

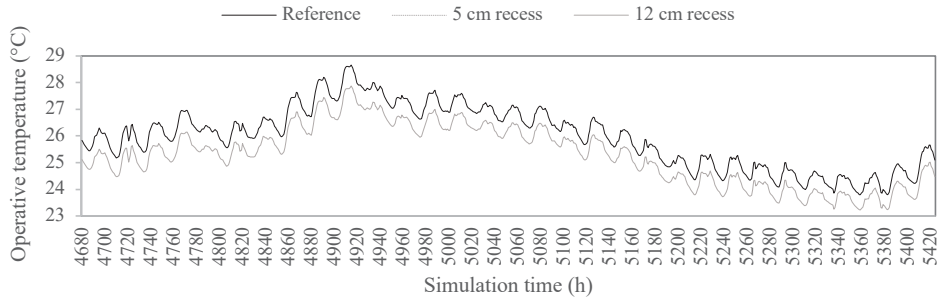

Figure 5: Internal air temperature in one thermal zone in house model A, with or without window recess simulation

In black the model without window recess show a higher temperature during summer than the model with 5cm (dot line) and 12 cm (light grey) of window offset in the wall. As calculated in 6a the overheating is reduced by 3% to 5% thanks to the window recess. While the offset of window in the wall has a positive impact on thermal comfort in summer it is also responsible of an increase of energy consumption in winter. Indeed, as shown in Figure 6b the offset of window in the wall has an impact on the yearly energy demand of building.

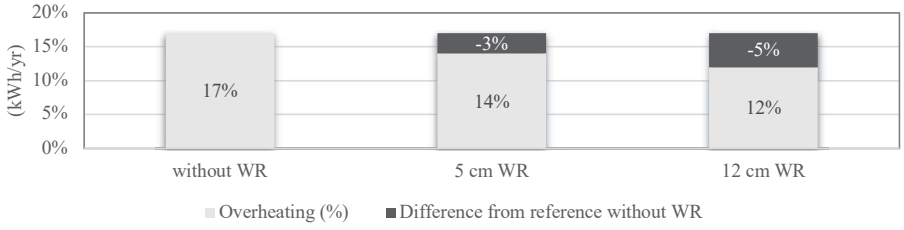

a)

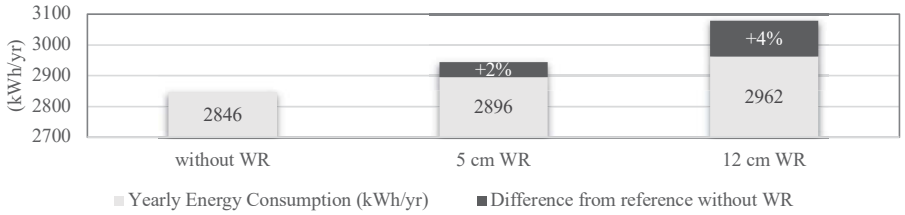

b)

Figure 6: a) Overheating reduction by window recess ; b) Yearly energy consumption increase due to window recess

Due to the high level of performance to be achieved by the houses, the impact of construction details such as window embrasure, on the results must be taken into account. Indeed, before considering the energy systems to be integrated into the houses of the project, it was first necessary to look at the good design and implementation of the envelope of the buildings themselves. This envelope must therefore be designed in such a way that heat losses are reduced to the minimum so that the building's demand is as low as possible. The simulations showed the importance of taking into account constructive details such as the window recess depth. Indeed, if it increases the annual consumption of the house will be impacted. In the case of a classical embrasure of about 12 cm, the impact on annual consumption is 4%. This value is not negligible for high energy standards. Simulations in TRNSYS were useful to highlight such a parameter to be taken into account in building simulation.

3.1.2 Systems simulations results

As there were a tremendous number of results for the complete study of the four houses and each variants of system combinations, only results for Belgian house model A will be presented in this section. A synthesis was done to define by each system combination which kind of energy performance level the house model is able to reach, see Table 5.

Table 5: Energy performance level reached by house model A in TRNSYS in function of energy systems combinations.

System variant	Heating / DWH production	RE production	Energy performance level
V1a	Electrical heating / Electric tank	PV panels	PASSIVE
V1b	Electrical heating / Solar tank	PV + thermal solar panels	PASSIVE
V1c	Electrical heating / Solar tank + HP	PV + thermal solar panels	PASSIVE
V2a	Wood pellet stove / Electric tank	PV panels	PASSIVE
V2b	Wood pellet stove / Solar tank	PV + thermal solar panels	PASSIVE
V2c	Wood pellet stove / Solar tank + HP	PV + thermal solar panels	PEH
V2d	Wood pellet stove + electric heating / Solar tank + HP	PV + thermal solar panels	PEH
V3	Hot pulsed air	-	N.A

V4a	HP + radiators / Solar tank + HP	PV + thermal solar panels	PEH
V4b	HP + radiators / Solar tank + HP	PV panels	PEH

The electrical solution in house A (electric convectors and boiler) is one of the systems combinations that did not allow the house to fulfil the PEH requirements as set in the project. Indeed, the global annual energy balance of the house is not compensated by the local renewable energy production as required in the specifications of the project.

For the variant with the wood pellet stove the only combination that permits to the house to become a PEH is the solution that combined the stove and auxiliary electric heating for the heating system and the solar tank and heat pump for DHW production. In this case the global annual energy balance of the house is negative which means the house is able on one year to produce more energy that it consumes. But the results are mitigated for the wood stove simulations because of discomfort issues in the living room as shown in Figure 7. If the control of temperature is set on the air temperature of the living room the stove is unable to heat the other rooms (room 2 called "Chambre 2" on the graph) that are on the 1st floor. To counter this comfort issue it was decided to control the stove on the air room temperature of room 2. This control had a positive impact on the mean air temperature on the 1st floor where the setpoint is better maintained but the air temperature in the living room, where the stove is placed, is too high and sometimes exceeds the temperature of 30°C in winter. The results are to be taken with caution because the wood stove model used for simulations was a simplified one. Moreover, the control of the setpoint in the room at the 1st floor was not reflecting the real control of a stove.

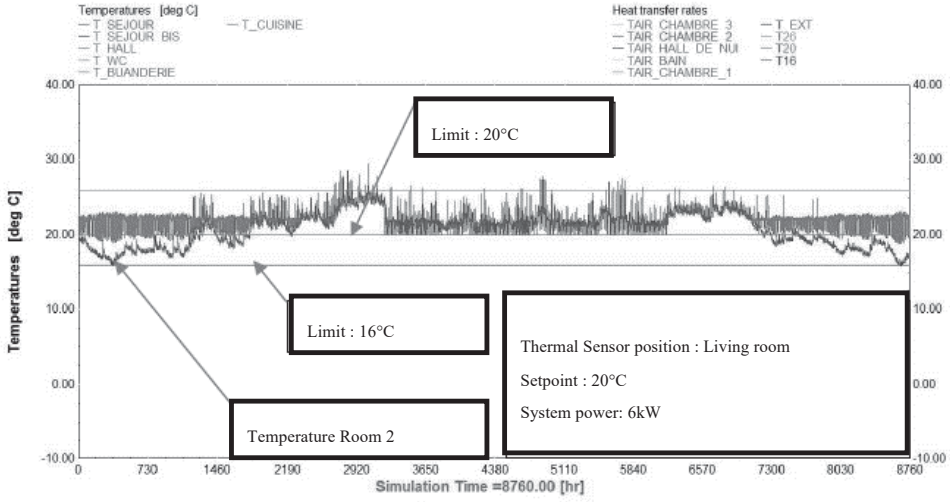

a) Wood pellet stove simulation: control of temperature set on the living room temperature

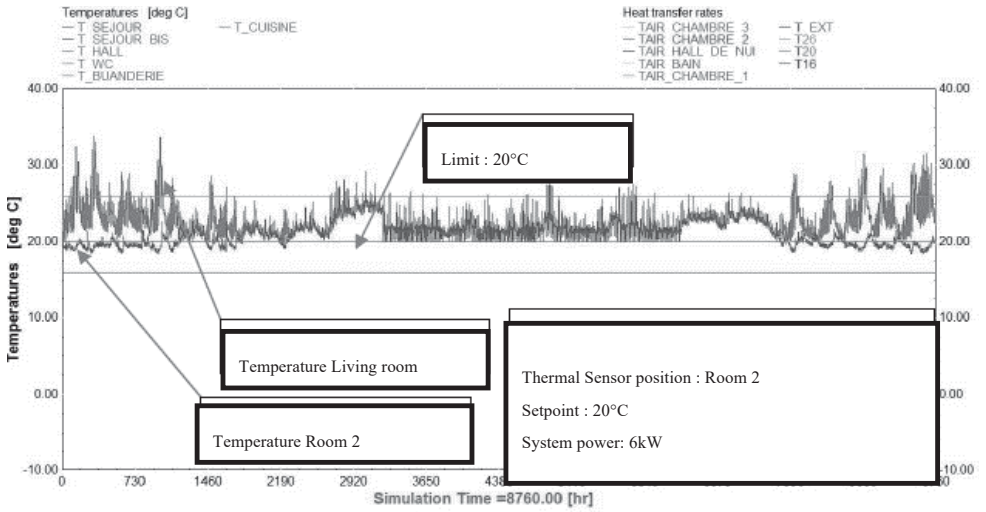

b) Wood pellet stove simulation: control of temperature set on the night room 2 temperature

Figure 7: Simulations results for wood stove system – Air room temperature analyse for comfort evaluation

The third system which was the distribution in the house of warm air by the ventilation system was immediately rejected because of too high supply temperature (more than 80°C in the coldest winter days). At least the best solution that was adopted for the project was the combination between a heat pump with distribution by radiators and a solar tank with auxiliary heating provided by a heat pump. The local RE production was ensured by PV panels. Thanks to this systems combinations the house A was able to completely fulfil the project requirements in terms of energy performance, comfort and construction costs.

4. CONCLUSIONS

To achieve the energy and cost specifications of the project each house had to show a very high performance. Therefore, the first point of attention was the reduction of thermal losses by the building envelop. Therefore, the first step of the house models study was to optimize the envelop and analyse conception choice by means of dynamic simulations. The minimal insulation thickness was defined thanks to TRNSYS simulations and a cost evaluation shown that the additional thickness is expensive compared to the gain on thermal loss diminution. Another aspect highlighted by simulations was the importance of architectural details consideration. Some details in envelop design as the window recess have an impact on results. Most of the time this detail is not simulated in TRNSYS although the 3D plugin integrated to the software allows such a simulation.

The second part of the study consisted in comparing several energy systems combinations in order to select the optimal solution to achieve the PEH standards as specified in the specifications document of the VallEnergie project. Due to large number of simulations most of the models used for energy systems were simplified or emulated in TRNSYS. The variant system selected for the house was confirmed by architects and the Belgian houses are now under construction.

5. REFERENCES

Abrahams, P., Rogiest, C., & André, P. (2015). *Rapport d'étude Simulations dynamiques de maisons à énergie positive (E+) avec le logiciel TRNSYS 17*. Arlon, Belgium.

Chambre des métiers Luxembourg. (2014). *Performance énergétique des bâtiments*. *Les avis de la chambre des métiers*. Retrieved from http://www.veolia.com/veolia/ressources/documents/1/1391,batiments_energetique.pdf

EU. (2010). Directive 2010/31/EU of the European Parliament and of the Council of 19 May 2010 on the energy performance of buildings (recast). *Official Journal of the European Union*, 13–35. https://doi.org/doi:10.3000/17252555.L_2010.153.eng

European Parliament. (2012). Directive 2012/27/EU of the European Parliament and of the Council of 25 October 2012 on energy efficiency. *Official Journal of the European Union Directive*, (October), 1–56. https://doi.org/10.3000/19770677.L_2012.315.eng

Georges, L., Skreiberg, Y., & Novakovic, V. (2014). On the proper integration of wood stoves in passive houses under cold climates. *Energy and Buildings*, *72*, 87–95. https://doi.org/10.1016/j.enbuild.2013.12.023

Strachan, P.; Svehla, K.; Kersken, M.; Heusler, I. (2016). Empirical validation of common building energy simulation models based on in situ dynamic data. IEA Annex 58 Subtask 4a final report.

Vandenberghe, A., & VanLoon, S. (2013). Vade-mecum résidentiel. *Pmp*, 115. Retrieved from http://www.maisonpassive.be/IMG/pdf/vade-mecum-pdf_hd.pdf

Wallonie Energie SPW. (2018). *Méthode de détermination du niveau de consommation d'énergie primaire des unités résidentielles*. Retrieved from https://energie.wallonie.be/servlet/Repository/annexe-a1---per-modif.-ecodesign-2018---coordination-(fr).pdf?ID=49412&saveFile=true

6. ACKNOWLEDGEMENTS

This work has been performed in the framework of the VallEnergie project which was funded by the European Union and the Walloon Region through the FEDER and the Interreg IV-A Greater Region program.

7. NOMENCLATURE

DHW: Domestic Hot Water

EPBD: Energy Performance of Buildings Directive

EU: European Union

GHG: Greenhouse Gases

HP: Heat Pump

N.A: Not Applicable

nZEB: nearly Zero Energy Building

NZEB: Net Zero Energy Building

PEH: Positive Energy House

PV: Photovoltaic

RE: Renewable Energy

TRNSYS: Transient System Simulation Tool

Questions and Answers:

Were the doors opened during the simulations with the wood stove?

Pauline Abrahams:

Yes. The simulation took into account the door opening in the house model by simulating a coupling airflow between zones. The air flow between the zones was calculated on the basis of research works studying the estimated air flows at the level of the interior openings in the buildings.

***

And is it normal that the temperature in the furthest areas didn't match the setpoint even if the doors were opened?

Pauline Abrahams:

Yes, because the air coupling between adjacent zones was not sufficient for an optimal mixing of the internal air. Increasing this air flow rate was also not realistic.

***

Which kind of emission system was simulated for the simulation with the wood stove?

Pauline Abrahams:

It was an emission system with electric radiators to compensate losses in areas furthest from the stove.

THIRD SESSION
PLENARY SESSION

Emerging trends in HVAC&R

Eric Winandy

Director Integrated Solutions at Emerson Commercial & Residential Solutions

Questions and Answers

Madjid Madjidi:

Do you also work on hybrid chillers which include compressors in absorption loops?

Eric Winandy:

No we don't, we have looked at the technology combining vapour compression and absorption.
We concluded it has some potential in niche applications but decided not to pursue.

***

Lieve Helsen:

Some places become hotter and hotter. Can we rely on current approaches and technologies to cool these buildings over high DT?

Eric Winandy:

A lot can already be done with existing technologies, combining Solar PVs and AC systems for example.

But as seen in the presentation, new breakthrough technologies might help in the future like the radiative cooling material.

***

Vincent Lemort:

Is there any commercial opportunities and interest for mixing propane and CO2 to limit the problem of high pressure and flammability?

Eric Winandy:

To what we have observed so far, we don't see an immediate interest. Pressure and flammability are for sure challenges that even if moderated by their mixture, they remain a hurdle.
Flammability for example is an issue even if limited. For example PED does not make any difference, it is either non-flammable or it is flammable...

***

Assaad Zoughaib:

In the disruptive technologies, some are not in direct competition with the Vapour compression technology.

Eric Winandy:

Yes we agree, the list established by DOE mentions very different technologies for different applications. Some of them are competitive to VCC, some are complementary.

***

Filip Jorissen:

What are the limitations and/or requirements of simulations tools? Do current tools satisfy these requirements?

Eric Winandy:

Not a strong opinion on that part since we use broad use tools like Dymola, Python, EES etc, not dedicated tools already coded for our applications.

SECOND SESSION

DISTRICT HEATING NETWORKS

Economic and environmental comparison of a centralized and a decentralized heating production for a district heating network implementation

Thibaut Résimont[1]*, Queralt Altes-Buch[1], Kevin Sartor[1], Pierre Dewallef[1]

(1) Energy Systems Research Unit, Aerospace & Mechanical Engineering Department, University of Liège, Liège, Belgium

ABSTRACT

District heating networks seem to be a promising solution for heating delivery by using a centralized production unit instead of local gas boilers or heat pumps in each house. The use of several available heat sources, like waste incinerators for example, enables to reduce global primary energy consumption and to have a better control on pollutants emissions and greenhouse gases emissions than with a local heating production. The main drawback of district heating networks is the consequent initial investment cost for pipes and substations. It is thus interesting to achieve a fair comparison between a centralized heating production unit including a district heating network and a decentralized one with heating units in each house. The comparison is based on the *IEA EBC Annex 60* case study made up of a small neighborhood of 24 dwellings combined with a greenhouse characterized by specific energy consumption profiles. For the centralized heating production, a waste incinerator and a gas boiler are considered as heating sources while gas boilers or heat pumps are taken into account for a decentralized heating production. In both cases, an economic and environmental study is achieved to determine the optimal scenario between a centralized and a decentralized heating production.

Keywords: District Heating Network (DHN), Dynamic modelling, Economic and environmental analysis

1. INTRODUCTION

In the frame of a worldwide environmentally-friendly policy looking for energy efficient solutions in order to reduce pollutants emissions and primary energy consumption, district heating technology exhibits some advantages compared to a decentralized heating production technology for the heating and cooling sector. 4th generation district heating systems enable the use of various combined heat and power (CHP) technologies from centralized heat pumps to residual heat from industrial processes or waste incinerators for example. Combined with thermal storages at strategic points along the network, this district system could be a promising solution for efficient energy models at an urban scale including renewable energies (UNEP, 2015). However, despite its existence since the 14th century (Rezaie et al., 2012), district heating is not widely developed in central Europe even though there is a large potential to harness. Indeed, in Eastern Europe for instance, district heating projects are more developed and have proven the technical feasibility and economic viability of this technology. Within the European Union, there are more than 5000 district heating systems in operation today with more than 40% in countries like Denmark, Sweden, Finland, Poland, Estonia, Latvia and Lithuania. On the other hand, there is a very small part of the heating demand which is covered by district heating in countries in Western Europe and especially in Belgium (Frederiksen et al., 2013). With an European policy for the short-term and mid-term scope

based on smart, efficient and sustainable heating and cooling systems (EUROPA, 2016), there is an increasing interest for projects in district heating with some new ones including the use of waste heat from incinerators or industrial processes. A local example in Liège (Belgium) is the waste incineration plant of *Intradel* which manages waste produced by more than 900,000 habitants and burns 370,000 tons per year of municipal waste. This energy could be valorized at a city scale such that a district heating network project (EcoSystèmePass project) is currently in progress for the 2020 horizon.

The main issue for the development of district networks is the large initial investment cost for required pipes and substations. Investments in district heating projects are generally limited by budget constraints and by a fear of underestimating the total costs for the project. The implementation of a simulation tool able to fulfill accurately some criteria as the assessment of the heating losses and pressure losses would be a solution to a current lack on the district heating network market. Currently, district heating networks are generally sized based on rules of good practice by quasi steady-state simulations. To take into account dynamic phenomena which have an impact on thermal and hydraulic losses, dynamic models would be useful as a basis for a decision tool. In the literature, many conventional dynamic models where pipes are modelled by finite volume elements can be found. However, these models are limited to small-scale networks because of their lack of numerical robustness for large district heating networks. Sartor et al. (2015) illustrated numerical problems related to conventional finite volume approaches developed by Gabrielaitiene et al. (2001) and many others. The development and validation of more adequate pipes components for a large scale application would therefore be useful to quantify as accurately as possible the physical behavior of a district heating network. These components with a stronger numerical robustness leading to an affordable computation time would answer to the current lack of simple dynamic models on the district heating network market. Based on these components, a simple simulation tool could be developed to assess economic and environmental criteria related to district heating networks.

2. THE SYSTEM MODEL

The case study used in this paper, depicted in Fig. 1, to assess the economic profitability to combine a waste incinerator to a district heating network is based on a test case developed by the *IEA Annex 60* (IEA, 2018). An additional heat demand of a 1,000 m^2 greenhouse is located at a distance of 100m of the heat source at the beginning of the network.

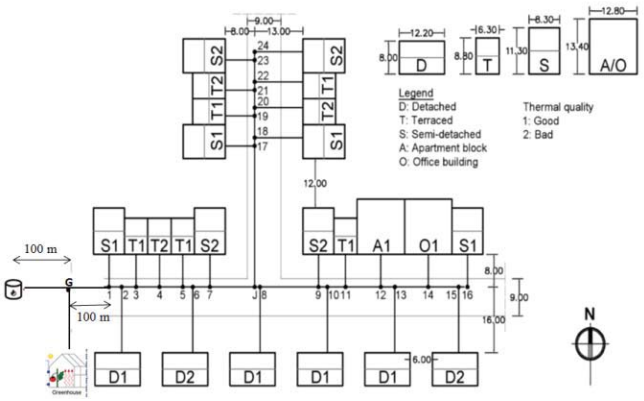

Figure 1: Sketch of the case study used in this paper based on the IEA Annex 60 Neighbourhood Case Study (IEA, 2018).

This case study is based on the *EcoSystemePass* project (cf. *Acknowledgements*) which aims to connect a greenhouse and a neighborhood of a few dwellings to a waste incinerator. Based on this configuration, it is required to model physically the components for each part of the network.

3.1. District Heating Network (DHN) model

The modelling of the whole system requires the modelling of each component of the district heating network including the heat source, the pipes, the substations and the dwellings. This modelling can become quickly complex because of the large amount of partial differential equations in the mathematical model (even for a small network). Dynamic effects have to be taken into account in the dwellings but also in pipes where there are thermal inertia phenomena and a heat wave propagation time. For sake of simplicity, the detailed models of the dwellings and the greenhouse are not presented in this paper. The interested reader can refer to Résimont et al. (2018) and Altes-Buch et al. (2018) for an overview of the physical modelling used to determine hourly heating demands of the dwellings and the greenhouse. For the network modelling, these heating load profiles are used as inputs and a fixed temperature difference at the primary side of the substations is prescribed to determine the required mass flow rates in each substation. Assuming an ideal heat source able to provide any required mass flow rate without limitations for a prescribed temperature set point, the main remaining components to model are the pipes. The graphical model of the network developed in the dynamic simulation software *Dymola* is proposed in Fig. 2.

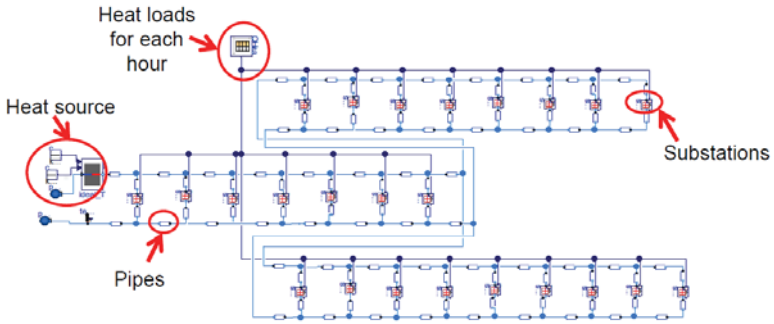

Figure 2: Thermo-hydraulic model of the district heating network developed in the dynamic simulation software Dymola

3.1.1. Pipes model

Pipes are used as connectors between the heating source and the substations and can reach a length of several hundreds or thousands of meters in large district networks. The main result is a heat wave propagation time from the heating source to the farthest points in the network of a few minutes (assuming a mean water velocity around 1 m/s in the pipes). Dynamic phenomena have thus a significant influence on the water temperature level in the pipes. Usual finite volume numerical methods dividing the pipes in discrete cells are commonly used for the thermo-hydraulic modelling of flows in pipes. However, these methods require large computational times proportional to the level of discretization of the pipes. A balance between a fair computation time and an accurate solution has thus to be found even though this compromise involves some limitations (Sartor et al., 2015). In the literature, an alternative pipe model, proposed by Van Der Heijde et al. (2017), is used to find an efficient solution both in terms of computation time and accuracy. This model is based on a plug flow method where a delay time function is used to compute the residence time Δt of the fluid in the pipes. Overlooking about axial diffusion along the pipes and assuming a constant heat capacity of the pipes C_V [J/K] as well as a constant thermal resistance R_{th} [K/W] between the pipes and its surroundings, an analytical expression of the temperature at the outlet of the pipe can be directly deduced by Eq. (1). This equation is deduced from a combination of the energy and continuity equation. For a detailed physical explanation of the model and its mathematical development, the reader can refer to Van Der Heijde et al. (2017).

$$T_{out} = T_{sur} + (T_{in} - T_{sur}).\,\mathrm{e}^{-\frac{\Delta t}{R_{th}C_V}} \quad (1)$$

Equation (1) shows that the temperature at the outlet of the pipes is only dependent on the inlet temperature T_{in} [°C], the surroundings temperature T_{sur} [°C] and the thermal properties of the pipes C_V and R_{th}. This simple method has already been validated on other test cases and provides fair computation times for large scale district networks. Indeed, for this case study, dynamic simulations over a reference year get a computation time around only 3 hours compared to simulations of several days with finite volume methods. These relatively low computation times are also an advantage for operation planning on a day-to-day basis in order to predict the heating load profile as a function of daily weather conditions and to have a better instantaneous control monitoring over the entire network.

3.2. Heating source modelling

Centralized heating units usually run at full-load regime on a daily basis because they feed district heating networks with a global heating demand quite uniform over the day. Due to the different types of heating profiles related to various kinds of dwellings, the global heating consumption is fairly distributed over the day. This effect is represented in Fig.3.

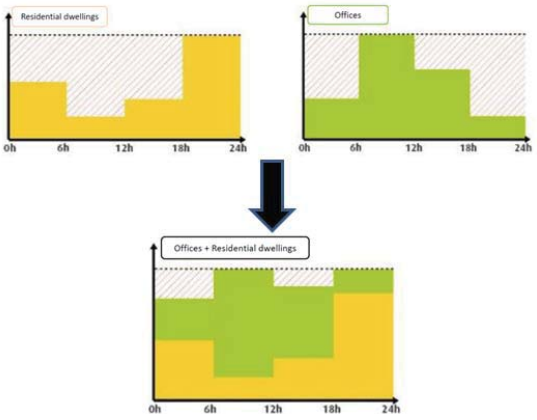

Figure 3: Combination of the heating demand profiles of two types of dwellings (offices and residential dwellings)

As can be observed in Fig.3, the combination of both heating load profiles with offices, which have a significant heating consumption mainly during working hours, and residential dwellings whose the consumption is shifted during morning and evening periods, enables to have a global heating load profile more or less uniform over the day. This is the main advantage of centralized production enabling to run at full-load conditions most of the time such that a constant boiler efficiency can be considered all over the year.
About decentralized heating units for local production, a variable load regime has to be taken into account, both for gas boilers and heat pumps, such that a variable efficiency/COP regime is used in this model. For the gas boiler, a variable efficiency included between 85 and 100% for respectively minimum and maximum heating loads is assumed. This efficiency varies linearly with the heating load, as represented in Fig. 4.

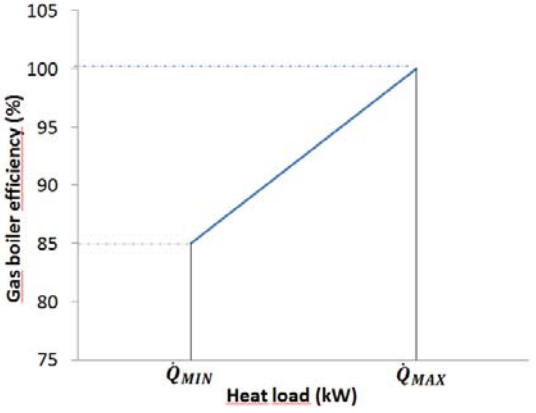

Figure 4: Variation of the gas boiler efficiency with the heating load

The gas boiler efficiency can be expressed mathematically as a linear function of the minimum and maximum efficiencies $\eta_{min/max}$ and the heating demand $\dot{Q}_{heat}$:

$$\eta(\dot{Q}_{heat}) = \eta_{min} + \frac{\eta_{max} - \eta_{min}}{\dot{Q}_{max} - \dot{Q}_{min}} . \dot{Q}_{heat} \quad (2)$$

The average thermal efficiency $\bar{\eta}_{th}$ of the gas boiler is defined by integrating the required heating power $\dot{Q}_{heat}$ divided by the primary energy consumption $\dot{Q}_{prim,ener}$ all over the year on an hourly basis:

$$\bar{\eta}_{th} = \frac{\int_1^{8760} \dot{Q}_{heat}\, dt}{\int_1^{8760} \dot{Q}_{prim,ener}\, dt} = \frac{\int_1^{8760} \dot{Q}_{heat}\, dt}{\int_1^{8760} \frac{\dot{Q}_{heat}}{\eta(\dot{Q}_{heat})}\, dt} \quad (3)$$

Concerning the COP of a heat pump, in addition to the influence of the part-load regime, it also varies with the temperature of the heat source as shown in Figure 5 (Ransy et al., 2017). The modelling of the heat pump is based on three polynomial laws developed by Bolther et al. (1999) in order to determine the COP and the full heating load capacity as a function of the heating source temperature, the required outlet temperature of the water and the part-load ratio for an air to water heat pump. Parameters for the polynomial laws are identified from manufacturers' data such that each heat pump has specific parameters values and are based on nominal conditions. These nominal conditions are prescribed for the sizing of the machine. Nominal temperatures of 7°C and 35°C are respectively set up for the evaporator and the condenser of the heat pump. In this case study, a water set point temperature of 50°C and an air temperature based on weather data on an hourly basis are taken into account.

In this case study, reference heat pumps chosen for the performance assessment are *Daikin Altherma 4kW* heat pumps whose polynomial coefficients have been identified and are summarized in Table 1.

Table 1: Heat pump parameters for a Daikin Altherma 4kW heat pump

Parameters	**Value**
C_0 (-)	0.949
C_1 (-)	-8.05
C_2 (-)	111.09
D_0 (-)	0.968
D_1 (-)	0.0226
D_2 (-)	-0.0063
K_1 (-)	0
K_2 (-)	0.67
COP_n (-)	3.9505
$\dot{Q}_n$(kW)	5

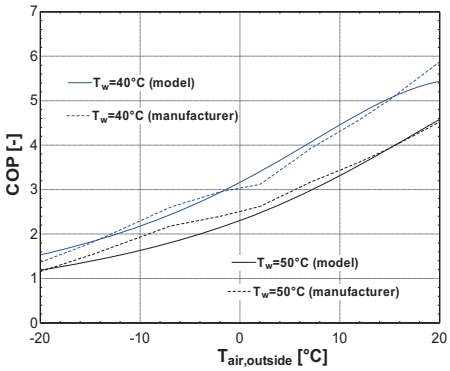

Figure 5: Variation of the COP of the heat pump with the outdoor temperature (Ransy et al., 2017)

The 3 polynomial laws mentioned above are represented by the following set of equations.

$$EIRFT = \frac{COP_n}{COP_{fl}} = C_0 + C_1.\Delta T + C_2.\Delta T^2 \quad (4)$$

$$\text{with } \Delta T = \frac{T_{air,out}}{T_w} - \left(\frac{T_{air,out}}{T_w}\right)_n \quad (5)$$

$$CAPFT = \frac{\dot{Q}_{fl}}{\dot{Q}_n} = D_0 + D_1.\left(T_{air,out} - T_{air,out,n}\right) + D_2.\left(T_w - T_{w,n}\right) \quad (6)$$

$$EIRFPLR = \frac{\dot{W}_{pl}}{\dot{W}_{fl}} = K_1 + (K_2 - K_1).PLR + (1 - K_2).PLR \quad (7)$$

$$\text{with } PLR = \frac{\dot{Q}_{heat}}{\dot{Q}_{fl}} \quad (8)$$

The first one is used to determine the COP at full load of the heat pump for a prescribed air temperature and a water set point temperature. The second one is an illustration of the maximum available heating capacity of the heat pump compared to the nominal heating load capacity. A computation of the heat pump performance at part-load operation is achievable using the third polynomial law represented by Eq. (7). For details about this polynomial model, the reader can refer to Bolther et al. (1999). Based on these 3 equations, an assessment of a mean COP over the year is computed by Equation (9) where $\dot{W}_{elec,HP}$ is the electrical consumption of the compressor of the heat pump.

$$\overline{COP} = \frac{\int_1^{8760} \dot{Q}_{heat}\, dt}{\int_1^{8760} \dot{W}_{elec,HP}\, dt} = \frac{\int_1^{8760} \dot{Q}_{heat}\, dt}{\int_1^{8760} \frac{\dot{Q}_{heat}}{COP(\dot{Q}_{heat})}\, dt} \quad (9)$$

About the centralized waste incineration, the bottleneck of this technology concerns pollutants emissions which have to be taken into account for prospective additional deNO$_x$ units. A set of chemical equations modelling pollutants emissions from waste combustion is thus proposed in the next section to assess the prospective need to install a treatment unit for pollutants emissions.

3.2.1. Model for pollutants emissions assessment from waste incineration

A combustion model based on the waste chemical species composition is put in place by using the general combustion equation based on waste composition from the Phyllis 2 database (2018) presented in Table 2.

Table 2: Typical municipal waste composition

Atomic species	Mass fraction (%)
C	25.5
H	3.8
O	14.22
N	0.6
S	0.2
Inerts	24.68
Water	31

The general combustion equation for waste of generic chemical formula $C_m H_n O_x N_y S_z$ is based on Sartor et al. (2014) model validated for a large range of combustion furnaces:

$$C_m H_n O_x N_y S_z + x_w\ H_2O + (1+e)\kappa(O_2 + \beta N_2 + \gamma H_2O) \rightarrow \Delta_1 H_2 + \Delta_2 O_2 + \Delta_3 H_2O + \Delta_4 CO + \Delta_5 CO_2 + \Delta_6 OH + \Delta_7 H + \Delta_8 O + \Delta_9 N_2 + \Delta_{10} N + \Delta_{11} NO + \Delta_{12} NO_2 + \Delta_{13} CH_4 + \Delta_{14} SO_2 + \Delta_{15} SO_3 \quad (10)$$

regarding a combustion air made up mainly of nitrogen, oxygen and water (rare species like Argon are neglected). x_w is the molar fraction of water in the fuel and e represents the excess air related to the combustion. β and γ are the respective ratios between molar fractions of nitrogen and oxygen and of water and oxygen in wet air. $\kappa = m + \frac{n}{4} - \frac{x}{2} + z$ and Δ_i are the molar coefficients of each products species. Indexes *m, n, x, y* and *z* are computed from the waste mass composition in Table 2. For instance, for carbon atoms, the index *m* is computed by the following equation:

$$m = \frac{Mass\ fraction\ of\ C\ in\ \boldsymbol{dry}\ fuel\ [\%]}{100.\ Molar\ mass\ of\ C} \quad (11)$$

The same approach is applied to compute indexes *n, x, y* and *z*. It is important to notice that mass fractions taken into account in (11) are based on the *dry* composition of waste *without* water fraction in the fuel. Molar coefficients Δ_i of the products species are determined by mass conservation on the 5 different atomic species (C, H, O, N, S). Having 15 combustion products for only 5 mass conservation equations, there are 10 additional formation/dissociation equations to include in the model to obtain a determined system. These 10 formation/dissociation equations are based on the model developed by Sartor et al. (2014). The interested reader can refer to Sartor et al. (2014) for a complete description of the chemical model of the combustion process.

The main point to focus on in this combustion model is the NO_x emissions which can be an important source of pollution in combustion processes using fuels with a non-negligible nitrogen content. In combustion processes, the main part of emissions of nitrogen oxides are NO molecules even though NO is converted into NO_2 in the atmosphere. For NO formation, there are 2 main formation mechanisms (Flagan et al., 1988), namely the thermal NO and the fuel NO. It can be noticed that there is a third formation process, the prompt NO, which can be neglected herein because this formation mechanism requires very high temperature combustion processes (Fenimore, 1971). The model from Sartor et al. (2014) is thus used in order to determine NO_x emissions and compare them to European limits for a prospective installation of a deNOx unit.

3.3. Economic assessment

In order to determine the optimal configuration to minimize costs for a prescribed heating production unit, it is necessary to define a comparison factor which illustrates a global cost related to the heating technology and type of heating distribution (centralized or decentralized). A cost of heating (COH) can be defined similarly to the levelized cost of electricity (LCOE). This cost is expressed by Eq. (12) and includes four main terms. This generic equation takes into account heat losses over the district network for centralized heating production with a factor ε_{DHN}, standing for the thermal network efficiency, including heat losses over the network in the total energy production.

$$COH\ [€/MWh] = \frac{1}{\varepsilon_{DHN}}.\left(\underbrace{\frac{C.\psi+U_{fix}}{P_i.\tau_e}}_{\text{CAPEX}} + \underbrace{\frac{y_F}{\bar{\eta}_{th}}}_{\text{Fuel cost}} + \underbrace{u_{var}}_{\text{OPEX}} - \underbrace{(y_{el}+\tau_{GC}.y_{GC}).\frac{\bar{\eta}_{el}}{\bar{\eta}_{th}}}_{\text{Electricity resale price + assignment of green certificates}}\right) \quad (12)$$

CAPEX stand for the initial investment cost taking into account a depreciation rate ψ corresponding to the evolution of the initial investment cost over the lifetime of the project. C corresponds to the investment cost for the technology (€/year), P_i is the installed power of the technology (MW) with an equivalent operating time τ_e (h). This equivalent operating time, expressed by Eq. (13), is the ratio between the total heating consumption over one year $\dot{Q}_{heat,1\ year}$ and the installed heating power P_i.

$$\tau_e = \frac{\dot{Q}_{heat,1year}}{P_i} \quad (13)$$

OPEX include variable costs for operation and maintenance. They are generally set up from database and can take into account electricity prices. About the electricity consumption, this cost component is important to take into account in the OPEX. For heat pumps technology, the fuel cost is free but the electricity consumed by the compressor of the heat pump system has a non-negligible part in the total COH. This cost component for a heat pump, with an average coefficient of performance $\overline{COP}$, is expressed by Eq. (14).

$$u_{var} = \frac{Electricity\ price\ (\frac{€}{MWh})}{\overline{COP}} \quad (14)$$

The cost of heating also includes the fuel cost y_F taking into account an average thermal efficiency $\bar{\eta}_{th}$ specific to each type of production. For a centralized production, electricity resale prices y_{el} (€/MWh) over the network as well as the assignment of a number τ_{GC} of green certificates at a price y_{GC} (€) for some technologies are also part of the total cost of heating. In Belgium, green certificates are subsidies which are granted for the production of 1 MWh_{el} without CO_2 emissions, i.e. corresponding to CO_2 savings of 456kg.

4. RESULTS

4.1. Dwellings heating requirements

For the modelling of the district heating network, hourly heating profiles of the different dwellings have to be included in the model. Based on the mathematical models developed for the dwellings and the greenhouse (Résimont et al. & Altes-Buch et al., 2018), these heating load profiles are represented in Fig. 6.

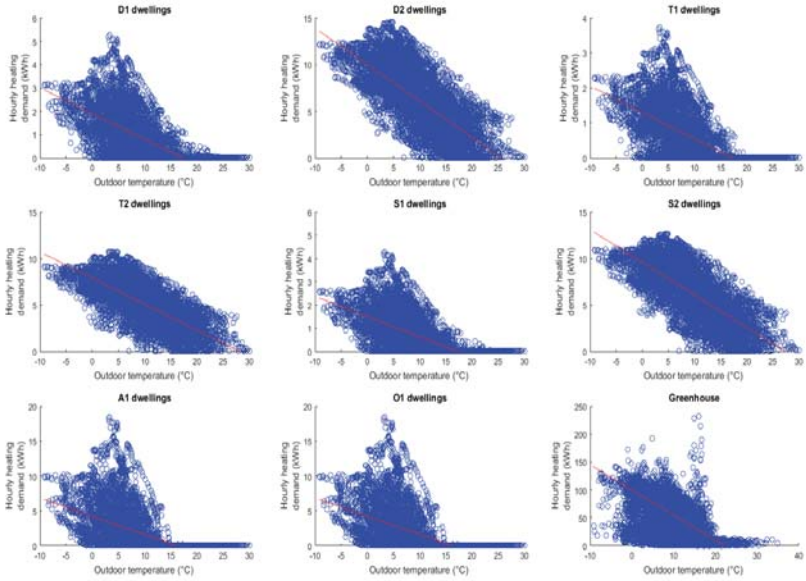

Figure 6: Heating load profiles for the different dwellings

It can be observed from Fig. 6 that the heating consumption is very variable over the year (even for a same outdoor temperature because of inertia effects in the dwellings) such that local heating production units have to run most of the time at part-load regime. Heating demands are logically higher for poorly insulated dwellings (type 2) than for well-insulated dwellings (type 1) because of their different thermal properties. About the greenhouse heating consumption, the heating demand is important even for temperatures above 15°C. This is due to the variable set point associated to the greenhouse which determines the hourly heating demand. This set point is not totally dependent on outdoor temperatures because even for high outdoor temperatures, crops in the greenhouse can require larger heating demands (especially during nights where radiation heat losses in the greenhouse are substantial).
In order to cover heating requirements all over the year with decentralized heating units, it is necessary to install decentralized heating units with a nominal power greater than the peak heating demand over the year. These nominal powers are detailed in Table 3.

Table 3: Nominal installed heating power for each type of dwellings in the case of a decentralized heating production unit

Type of dwellings	**Installed power (kW)**
Greenhouse	240
D1	5
D2	15
T1	5
T2	15
S1	5
S2	15
A1	20

O1	20
Total	**480**

From these results, a total thermal power of 480 kW_{th} has to be installed in the dwellings and the greenhouse for a decentralized heating production.

4.2. Cost of heating (*without* the allocation of green certificates)

In this study, four cases including centralized and decentralized heating production units are taken into account:

1. Combination of a centralized CHP waste incinerator for base load production with backup gas boilers for peak heating production
2. Use of a centralized CHP natural gas boiler
3. Decentralized heat pumps in each dwelling
4. Decentralized natural gas boilers in each dwelling

Considering a project lifetime of 20 years, a discount rate of 5% per year, a cost for pipes of 300€ per meter of pipes, a value of 65€ for each allocated green certificate and based on data from Table 4, a comparison of the cost of heating for all the scenarios mentioned above is presented in Fig. 7. The heat losses ratio 1-ε_{DHN}, which will influence the total heating production at the power plant, is around 8.5% for respective supply and return operating temperatures of 90°C and 60°C.

Table 4: Cost data for the different technologies (Energy Danish Agency, 2018)

Technology	**C (€/kW)**	**U_{fix} (€/kW/y)**	**u_{var} (€/MWh)**	**Fuel price y_F (€/MWh)**	**Electricity price y_{el} (€/MWh)**	**Thermal efficiency η_{th} (%)**	**Electrical efficiency η_{el} (%)**	**COP (-)**	**CO_2 emissions (kg/MWh_{th})**
Waste incinerator	200	54	5.6	0	110	70	20	/	149
Centralized natural gas boiler	120	80	4.5	35	110	45	40	/	198
Decentralized air-water heat pump	1000	285	0	0	110	/	/	2.31[3]	0[4]
Decentralized natural gas boiler	320	20	0	35	110	87.03[5]	/	/	198

[3] Computed from Eq.(11)
[4] There are indirect CO_2 emissions due to the electricity consumption of the heat pumps
[5] Computed from Eq.(5)

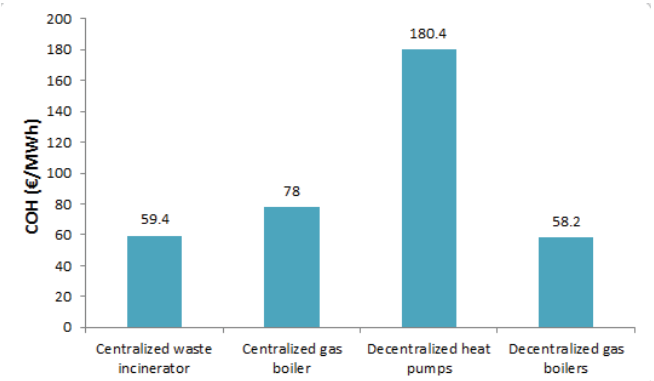

Figure 7: COH for the different studied technologies without the allocation of green certificates

Two heating technologies stand out as economically profitable heating production units to minimize the cost of heating. These two technologies are a centralized heating production using waste incineration as the main heat source and a decentralized heating production unit with gas boilers in each house. It can be noticed from Fig.7 that the use of a centralized gas boiler or decentralized heat pumps in each house has a more significant cost of heating such that these technologies are excluded from an economic point of view. The choice of a centralized or a decentralized heating technology based only on an economical criterion can be filled up by an environmental analysis of the pollutants and greenhouse gases emissions for each technology. In the case of a centralized production, the pollutant model described in Section 3.2.1.can be used to determine NO_x and SO_x emissions due to the waste combustion and the prospective cost of an additional deNO_x unit. Moreover, based on data in Table 4, a comparison of CO_2 emissions from the different units can be established to determine the most environmentally-friendly heating technology in terms of greenhouse gases. This analysis is achieved in the next section.

4.3. CO_2 and NO_x emissions

4.3.1. CO_2 emissions

Considering a mean value of CO_2 emissions of 320 kg/MWh_{el} for the electricity production (Energie+, 2018) in the Belgium power station park and including the electricity consumption of the heat pumps in the CO_2 balance sheet, a comparison of CO_2 emissions for the four different technologies is summarized in Fig.8.

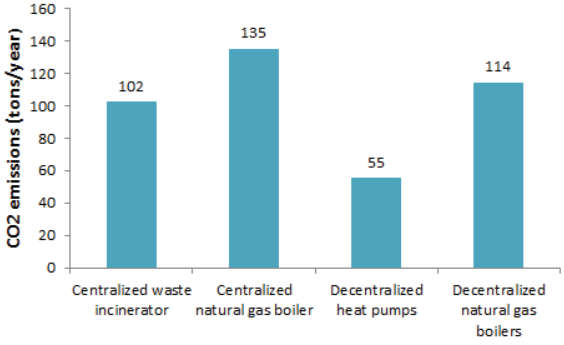

Figure 8: CO_2 emissions in tons per year for the different studied technologies

In terms of CO_2 emissions, the most suitable solution to minimize the total amount of carbon dioxide is the heat pump technology. Despite using electricity during the compression phase of the heat pump which has an indirect impact on the CO_2 emissions, there are no direct CO_2 emissions with this type of technology. However, the large cost of heating of this technology excludes it as an economically optimal solution. The best compromise from an economic and environmental point of view seems therefore to be the centralized waste incineration unit which emits less CO_2 than decentralized gas boiler units. It can be noticed that CO_2 emissions concerning the transport of the waste are not taken into account here in this CO_2 assessment. CO_2 emissions for this heating technology are thus slightly underestimated. However, greenhouse gases from waste transport are emitted no matter that waste are burnt or recycled by after such that there is no direct leverage on this environmental comparison.

Even though there are additional heat losses over the network for centralized heating production, waste incinerators in a district heating scenario stay thus economically and environmentally competitive compared to decentralized heating units. The main bottleneck of the waste incineration technology is the NO_x pollutants emissions which have an influence on the cost of heating due the additional cost of a deNO_x unit.

4.3.2. NO_x emissions from waste incineration

From the annual heating load profile over the year of the neighborhood depicted in Fig.9, the sizing of the centralized heating plant unit can be achieved by installing a nominal power covering the maximum heating demand over the year. For the studied neighborhood, this nominal heating power is of 450 kW_{th} such that the nominal mass flow rate related to this heating power can be directly deduced by Eq. (15).

$$\dot{m}_{waste} = \frac{\dot{Q}_{heat,tot}}{\eta_{comb}.LHV_{waste}} \tag{15}$$

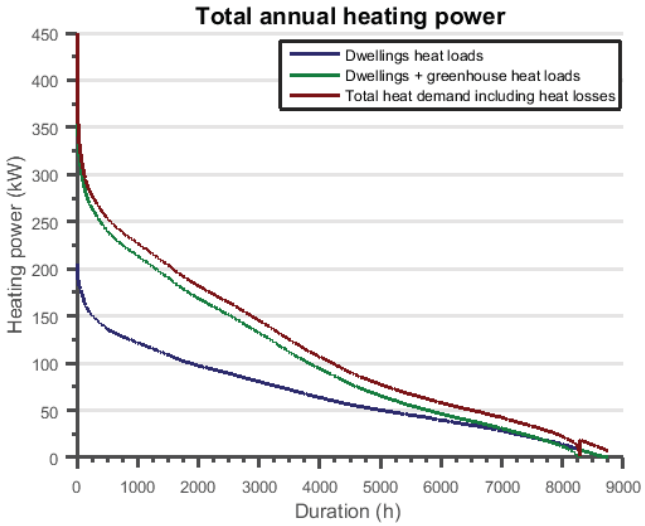

Figure 9: Annual heating consumption over the network

Pollutants emissions are based on combustion parameters summarized in Table 5 for a waste incinerator.

Table 5: Standard combustion parameters for a waste incineration.

Parameters	Value
Lower Heating Value of waste (MJ/kg)	11.71
Combustion efficiency η_{comb} (%)	70
Excess air e (-)	1.5
Air temperature (°C)	15
Relative humidity (%)	50
Combustion pressure (Pa)	101325
Volume of the combustion chamber (m^3)	30

Based on data from Table 5, a nominal waste mass flow rate of 138.34 kg/h is computed and is thus used in the combustion model to compute NO_x emissions at a nominal point. These emissions are compared to European legislation in terms of pollutants restricting NO_x emissions to 400 mg/Nm^3 for plants with a nominal power less than 50 MWth (Directive 2010/75/UE du Parlement Européen et du conseil, 2010). These emissions standards are based on a combustion air with an O_2 content of 6%. In this case study, NO_x emissions are estimated to 1511 mg/Nm^3 with parameters from Table 5. This value is much higher than European standards such that a deNO_x unit has to be installed. Assuming a deNO_x cost around 100€/kW of power installed (European Commission Joint Research Centre, 2017) for small-scale power plants, the additional cost related to NO_x treatment for the 450 kW waste incinerator would be of 45,000€. The cost of heating for the waste incineration technology is thus increased and is computed to 62.7€/MWh. This cost of heating is slightly larger than the cost of decentralized gas boilers in each house such that the choice of a decentralized production could be promoted from a purely economic point of view. However, the cost of heating with waste incineration could be decreased with the allocation of green certificates.

4.4. Cost of heating *with* the allocation of green certificates

The allocation of green certificates for the energy production with CHP heating units involves a decrease of the cost of heating. Considering a value of 65€ (value of a green certificate on the Belgian market) for each allocated green certificate, the cost of heating for the waste incineration technology with the allocation of one or two green certificates is depicted in Fig.10.

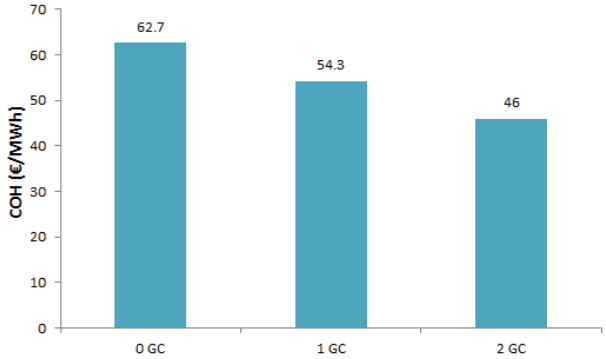

Figure 10: COH for the different studied technologies with the allocation of green certificates

The allocation of green certificates for heating production with the waste incineration technology can decrease the cost of heating around 26.5%. With the allocation of 2 green certificates (legal limit in Belgium to allocate green certificates per MWh), the waste incineration technology becomes distinctly the most profitable solution for heating production.

5. CONCLUSION

In this paper, a generic thermal, economic and environmental model has been implemented to assess the profitability of a district heating network using a centralized heating unit compared to a decentralized heating production with production units in each house. After a description of the mathematical models used in the study to determine heating demands and pollutants emissions, a comparison of 4 scenarios including centralized and decentralized solutions has been achieved to choose the most profitable one. An economic analysis defining a cost of heating as the main key performance indicator has shown a trend about the two most profitable scenarios for a minimization of the cost of heating. These two scenarios include a centralized heating production using a waste incinerator as heating source and a decentralized one using natural gas boilers in each dwelling.

A complementary approach to determine the most environmentally-friendly solution based on greenhouse gases and pollutants emissions led to the conclusion that in terms of CO_2 emissions, centralized waste incineration units enable to achieve some CO_2 savings compared to decentralized gas boiler units. The main weakness of this technology remains the NO_x emissions which are consequent due to the chemical fuel composition containing a non-negligible amount of nitrogen. Additional deNO_x units have thus to be taken into account in the economic profitability analysis of the system. Nevertheless, despite these consequent NO_x emissions, the centralization of the heating production with adequate technologies to control accurately pollutants emissions from these heating units is an additional benefit for a centralized heating production compared to a decentralized one.

Finally, taking into account the prospective allocation of green certificates with centralized CHP units, it has been shown that the cost of heating with a waste incineration unit becomes clearly more profitable than decentralized gas boilers for heating production.

NOMENCLATURE

Physical quantities

c	specific heat, J/(kg K)
C	*investment cost, €/kW*
C_V	*lumped thermal capacitance, J/K*
COP	*Coefficient Of Performance for a heat pump, -*
e	*combustion excess air, -*
G	*Gibbs free energy, J/kg*
h	enthalpy, J/kg
k_i	*rate constant of a chemical reaction i, m³/(mol.s)*
K_P	*equilibrium constant of a chemical reaction, -*
LHV	*Lower Heating Value*, MJ/kg
$\dot{m}$	mass flow rate, kg/s
$\dot{Q}$	heat flow, W
R	perfect gas constant, J/mol.K
R_{th}	thermal resistance, K/W
s	entropy, J/kg.K
t_{res}	residence time of the combustion products in the combustion chamber, s
T	temperature, K or °C
V	volume, m^3
$\dot{V}$	volumetric flow rate, m^3/s
$\dot{W}$	electrical production, W
x_w	*molar fraction of water in the fuel, -*
Δt	residence time of the fluid in the pipes, s
ΔT	*temperature difference at the primary side of the substations, K or °C*

Greek symbols

α	ratio between real and at equilibrium NO concentrations, -
β	*nitrogen/oxygen molar fraction in combustion air, -*
γ	water/oxygen molar fraction in combustion air, -
Δ_i	molar coefficients of each combustion product, -
ε_i	percentage of conversion of fuel-N into NO, %
$\varepsilon_{\mathrm{DHN}}$	*heat losses ratio, -*
η	efficiency, -
τ_{NO}	characteristic time for NO formation, s

Subscripts and superscripts

comb	Combustion
e	Equilibrium
el	Electrical
ex	Exhaust
fg	Flue Gases
fix	Fixed

fl	Full Load
F	Fuel
GC	Green Certificate
in	Indoor
n	Nominal
pl	Part-Load
prim	Primary
out	Outdoor
su	Supply
sur	Surroundings
th	Thermal
var	Variable
w	Water

Other symbols

CHP	*Combined Heat and Power*
COH	*Cost Of Heating*
DHN	District Heating Network
PLR	*Part Load Ratio*

ACKNOWLEDGEMENTS

Financial support from *FEDER Tropical Plant Factory* project is duly acknowledged in the frame of this paper.

REFERENCES

UNEP – the official web site of the United Nations Environment Programme. District Energy in Cities: Unlocking the full potential of energy efficiency and renewable energy. – Available at: <http://staging.unep.org/energy/districtenergyincities>.[accessed 23.1.2018].

Rezaie B., Rosen MA, 2012. *District heating and cooling: Review of technology and potential enhancements.* Applied Energy ;93:2-10.

Frederiksen S., Werner S., 2013. *District heating and cooling*. Studentlitteratur, Lund.

EUROPA - the official web site of the European Union. *Communication From The Commission To The European Parliament, The Council, The European Economic And Social Committee And The Committee of The Regions. An EU Strategy on Heating and Cooling* – Available at: <https://ec.europa.eu/energy/sites/ener/files/documents/1_EN_ACT_part1_v14.pdf>.[accessed 11.4.2018].

IEA EBC Annex 60 – the official website of the *Annex 60* project of the IEA. Description of reference "Annex 60 Neighborhood Case" – Available at: <http://www.iea-annex60.org/downloads/Annex60_2_2_ReferenceCaseStudy-v1.0.pdf> [accessed 22.10.2018].

Gabrielaitienė I, Kačianauskas B, Sunden B. 2003. *Application of the Finite Element Method for Modelling of District Heating Network.* J Civ Eng Manag. 2003, 9(3), 153–62.

Résimont T., Sartor K., Dewallef P., 2018. *Thermo-Economic Evaluation of a Virtual District Heating Network Using Dynamic Simulation.* ECOS 2018: Proceedings of the 31th International Conference on Efficiency, Cost, Optimization, Simulation and Environmental Impact of Energy Systems, Guimaraes, Portugal.

Altès Buch Q., Quoilin S., Lemort V., 2018. *Modeling and control of CHP generation for greenhouse cultivation including thermal energy storage*. ECOS 2018: Proceedings of the 31th International Conference on Efficiency, Cost, Optimization, Simulation and Environmental Impact of Energy Systems, Guimaraes, Portugal.

Sartor K., Thomas D., Dewallef P., 2015. A comparative study for simulation of heat transport in large district heating network. ECOS 2015: Proceedings of the 28th International Conference on Efficiency, Cost, Optimization, Simulation and Environmental Impact of Energy Systems; Pau, France.

Van Der Heijde B., Fuchs M., Ribas C., Schweiger G., Sartor K., Basciotti D., Müller D., Nytsch-Geusen C., Wetter M., Helsen L., 2017. Dynamic equation-based thermo-hydraulic pipe model for district heating and cooling systems. Energy Convers Manage 2017, 151, 158-169.

Savola T., Keppo I., 2005. *Off-design simulation and mathematical modeling of small-scale CHP plants at part loads.* Applied thermal engineering, vol.25, no 8-ç, P.1219-1232.

Flagan R.C., Seinfeld J.H., 1988. *Fundamentals of air pollution engineering*. Prentice Hall.

Ransy F., Gendebien S., Lemort V., 2017. *Performances d'une mini pompe à chaleur réversible fonctionnant sur l'air extrait : étude numérique et expérimentale*. XIIIème Colloque Interuniversitaire Franco-Québécois sur la Thermique des Systèmes. Saint-Lô, France.

Bolther A., Casari R., Fleury E., Marchio D., Millet J., 1999. *Méthode de calcul des consommations d'énergie des bâtiments climatisés « consoclim »*. Ecole des Mines, Paris.

Phyllis2, database for biomass and waste, *https://www.ecn.nl/phyllis2*, Energy Research Centre of the Netherlands. [accessed 08.6.2018].

Sartor K., Restivo Y., Ngendakumana P., 2014. *Prediction of SO_x and NO_x emissions from a medium size biomass boiler.* Biomass and Bioenergy 2014; 65 91-100.

Fenimore CP, 1971. *Formation of nitric oxide in premixed hydrocarbon flames*. Proceedings of the 13th International Symposium on Combustion. Pittsburgh, P.373-380.

Hanson R.K., Salimian S., 1984. *Survey of rate constants in the N/H/O system*. In: Gardiner W.C. (eds). Combustion Chemistry. Springer, New York, NY.

Vermeulen I., Block C., Vandecasteele C., 2012. *Estimation of fuel-nitrogen oxide emissions from the element composition of the solid or waste fuel.* Fuel Processing Technology, Vol 94, PP.75-80.

Directive 2010/75/UE du parlement européen et du conseil du 24 novembre 2010 relative aux émissions industrielles (prévention et réduction intégrées de la pollution).

European Commission Joint Research Centre, *Reference document on best available techniques for large combustion plants* - – Available at: <https://ec.europa.eu/jrc/en/publication/eur-scientific-and-technical-research-reports/best-available-techniques-bat-reference-document-large-combustion-plants-industrial>[accessed 13.4.2018].

Energy Danish Agency. Technology Data for Energy Plants – Available at: < https://ens.dk/sites/ens.dk/files/Analyser/technology_data_catalogue_for_el_and_dh_-_aug_2016_upd_oct18.pdf >.[accessed 05.11.2018].

Energie+ - Outil d'aide à la décision en efficacité énergétique des bâtiments tertiaires – Available at : <https://www.energieplus-lesite.be/>[accessed 08.6.2018].

Questions and Answers:

Filip Jorissen:

Typically, the gas boiler efficiency increases at part-load and yours does not?

Thibaut Résimont:

Indeed, the boiler efficiency increases at part-load: it is my mistake. However, this assessment of the part-load efficiency has for main goal to assess the average efficiency over the year such that the average gas boiler efficiency is just slightly underestimated and does not affect significantly the final results of the study.

***

Filip Jorissen:

Do you use the Annex 60 pipe model?

Thibaut Résimont:

The pipe model used in this study is the model developed in the IBPSA Modelica library in the framework of the Annex 60 study.

***

Assaad Zoughaib:

What could be the economical result for scenario mixed centralized and decentralized?

Thibaut Résimont:

To assess this scenario, I think that the use of an optimization platform with a mixed-integer programming model would be necessary to determine the best synergies between centralized and decentralized heating units in a district heating network.

***

Assaad Zoughaib:

Is modelling the best tool for designing the DH architectures?

Thibaut Résimont:

No, I think that the modelling is the best way to perform control over a district heating network but for the design, an optimization approach has to be used with the objectives to minimize the costs under some environmental constraints. The following of my work will be based on the development of an optimization platform able to provide best scenarios for DH architectures.

***

Freek Van Riet:

Did you look at the effect of smoothing of the outlet temperature by taking the average of multiple outgoing plugs during a single timestep? Especially for large networks, this smoothing will occur (of course still less than when using a Finite Volume approach)

Thibaut Résimont:

No, I did not look at this effect. The pipe model used has been validated for large district heating networks and even with these smoothing effects, I think that this plug flow model is more reliable than the finite volume model.

***

Ivan Verhaert:

How did you attribute the 'environmental costs' of the waste incinerator within the grid as the alternatives (because it is still there)?

Thibaut Résimont:

I consider the most pessimistic case where the waste incinerator would be built only for the heating production. However, in reality, it is true that this waste incinerator is already there such that environmental costs would be lower than those presented during the presentation.

***

Ivan Verhaert:

Any reference on the demand profiles for offices & residential?

Thibaut Résimont:

The demand profiles are based on the Annex 60 Case Study developed by the International Energy Agency. A report about this study is available online.

***

Ivan Verhaert:

Difference between 480 & 450 kW is low. Did you include DHW?

Thibaut Résimont:

This weak difference between the centralized and decentralized total installed power is justified by the fact that the modelling of the dwellings in the district heating network includes only space heating demand. Domestic Hot Water is not taken into account in the modelling.

***

Madjid Madjidi:

Do you consider condensation in the boiler exhaust air? Then it could reach even more than 100%

Thibaut Résimont:

No, I take into account the most pessimistic case where we can reach a maximum efficiency of 100% for gas boilers. However, we could have made a sensitivity analysis about the gas boiler efficiency on the cost of heating.

Impact and detection of malfunctions on district heating networks

Antoine Fabre[1]*, Cong-Toan Tran[1], Bruno Duplessis[1], Pascal Stabat[1]

[(1)] MINES ParisTech, PSL Research University, CES - Centre for Energy efficiency of Systems, 60 boulevard St Michel 75006, Paris, France

ABSTRACT

European and French energy policies require increasing the use of renewable energy in the energy mix. In this context, district heating networks will play an important role because they allow to massively integrating renewable energies. In the case of geothermal energy, district heating networks should work with the lowest possible return primary temperature to improve its use. In practice, this may be not achieved due to the malfunctions of the networks. Indeed, the priority of network operators is to ensure customer comfort at the expense of malfunction problem solving, especially since the fault does not necessarily impact the comfort and fault detection is are difficult to detect. The objectives of this paper are to study the impact of common malfunctions and to propose a method to detect them. A focus will be done on common malfunctions such as damaged valves and fouled heat exchangers. A dynamic thermal hydraulic model of district heating systems including secondary side using Dymola/Modelica is developed. In order to study their impact, malfunctions are simulated on a generic district heating network with several types of substation. Results show that damaged valves lead to a higher primary return temperature as well as a decrease in the renewable energy share of the network energy mix without impacting customer comfort.

Keywords: District heating network modeling, Malfunctions, Geothermal energy, fault detection

1. INTRODUCTION

The residential and service sectors currently represent 45% of France final energy consumption, 60% of that are for space heating (Ministère de la Transition Ecologique et Solidaire, 2014). To face the climate change issues, it seems crucial to tackle this end-use consumption. District Heating (DH) systems can help reducing fossil energy consumption and greenhouse gas emissions by increasing the share of renewable energies in the energy mix (Lund et al., 2014). EU and France have enacted the development of DH systems through European Energy Efficiency Directive and French “Energy Transition” law (Ministère de la Transition Ecologique et Solidaire, 2015).

In order to fulfill European and French objectives, innovative DH systems have to be developed in the coming years. Besides, the extension of the current DH networks must be undertaken as well as the improvement of their performance (Rezaie & Rosen, 2012).

A key point of the DH system performance is the difference between the supply and return primary temperatures. Indeed, by increasing the temperature difference, the demand can therefore be covered with a smaller water flow rate. This allows reducing heat losses through distribution pipes and pump electric consumption. It must also increase the renewable energy share in the energy mix of the network. However, the optimal performance may be not

achieved because of different faults in the DH system can increase the return temperature. Due to the complexity of the latter, the possible causes of faults are numerous; they can impact the user comfort and/or the return temperature (Zinko et al., 2005). Generally, a problem leading to a lack of comfort for the customer is treated by DH operators by increasing the pressure or the supply temperature of their network. Therefore, these solutions only address the consequences of a fault and may tend to downgrade the DH system performance. The lack of efficient tools to detect fault sources and the lack of time prevent DH operators to correctly fix malfunctions (Gadd & Werner, 2015). Thus, this paper tries to determine the impact of common malfunctions on the DH system in order to develop performance indicators able to detect the origin of malfunctions.

1.1 Detection and cause of malfunctions of DH networks

While DH system operators have carried out many works to improve the performance of heat generation systems, few studies have focused on the improvement of substations and secondary systems linked to DH systems. Operational experience on existing networks reveals that a substantial number of substations are troublesome. As an example, among 135 substations of the DH network in Helsingborg and Ängelholm, only 26% of them worked correctly when 3 types of malfunctions are considered: poor substation control, unsuitable heat load pattern and low average annual temperature difference (Gadd & Werner, 2015). The criteria used to identify malfunctions are:

- Irregular oscillations of the water flow rate in a substation or a bad correlation between outside temperature and hourly heat load
- The correlation between the type of customers (multi-family dwellings, trade buildings, industrial demands ...) and heat load patterns. For example a trade building with no time-clock operation is considered as defective.
- A substation with a primary temperature difference $\Delta T < 45°C$ is considered as faulty.

The problem of insufficient primary ΔT concerns 68% of the tested substations but the criterion used in the study is quite severe: if the threshold is set to 35°C for primary ΔT then only 23% of the substations are defective. It should be noted that the study focused on two types of malfunction. Indeed, a low average annual temperature difference is just a consequence of a fault. Hence, this study only gives information on the detection of the malfunctions but not on their origins.

Moreover, a study of the IEA (International Energy Agency) has defined a list of potential faults on substations according to several studies on DH system in Sweden and South Korea (Zinko et al., 2005). Therefore, 60% of malfunctions are derived from the secondary heating systems, 30% are coming from DHW systems (Domestic Hot Water) and failures of a component (valves, heat exchangers, pumps ...) constitute the last 10%. Furthermore, usual faults have been detected such as:

- Damaged or manually adjusted valves
- Poor substation control (unsuitable water logic, sensor failure)
- Unsuitable secondary systems

Besides, the malfunctions with the strongest impact on primary return temperature have also been identified such as:

- Too old or improperly sized heating systems at the secondary side
- Damaged or manually adjusted valves
- Substation with DHW systems including accumulation

Furthermore, Zinko et al., (2005) have identified potential faults through a control algorithm developed specifically to the Korean networks. The application of this algorithm is limited, because it is based on instantaneous measurements, so the dynamic behaviour of DH systems is not taken into consideration.

1.2 Performance indicators

The substations are a key point of DH network performance. But as shown in the previous part, a significant number of substations may be defective and so downgrade the performance. Hence, performance indicators have been developed in order to check the proper operation of a DH system. Different performance indicators are presented in the literature, in particular those detecting the substations that have the strongest impact on the overall performance of the network. The "excess flow" method enables to set a sequence of inspection of substations through the measurement of annual heat load and the average annual primary temperature difference of each substation (Quiquerez, 2017; Zinko et al., 2005). The main idea is the following: a substation is considered as faulty if its average temperature difference is low enough compared to a reference value. To give more information, the method calculates also an excess flow allowing to quantify the impact of the malfunction on the whole network. To do so, a reference consumed water volume V_{ref} is calculated from the annual heat consumption E and the reference of the average annual temperature difference ΔT_{ref} (see equation 1):

$$V_{ref} = \frac{E}{C\Delta T_{ref}} \tag{1}$$

Then the actual consumed water volume V_{act} is calculated according to the annual heat consumption E and the actual average annual temperature difference ΔT_{act} (see equation 2):

$$V_{act} = \frac{E}{C\Delta T_{act}} \tag{2}$$

Then the reference and the actual water volumes are compared to determine the excess water volume. The more the excess volume is important the more the substation downgrades the network performance.

$$V_{excess} = V_{act} - V_{ref} \tag{3}$$

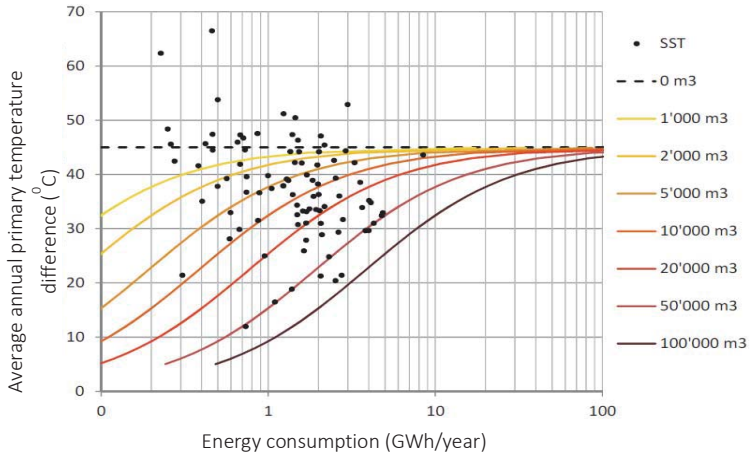

Figure 1: "Excess flow" method applied on a Swiss network (Quiquerez, 2017).

The results of excess flow method can be represented on a graphic such as presented on Figure 1. Each tested substation is represented by a black dot and the curves represent constant excess volume cases. Hence, using the figure one can read the average temperature difference, the energy consumption and the excess volume for each substation. A substation is considered inefficient when it is located below the dotted line (reference case with no excess volume). On the other hand, when a dot is above the reference line, it means that the corresponding substation is more efficient than expected. The graph allows also visualizing the impact of the substations on the overall network performance: the more a substation is right-down, the more its impact is important.

The implementation of the "excess flow" method needs to collect data over a long-time period, what also opens the door for corrective maintenance strategies. Moreover, the main drawback of this method remains the determination of a reference temperature difference ΔT_{ref} which might be adapted to all different configurations.

In order to have a faster and a more accurate detection of malfunction, the method of thermal signature (Gadd & Werner, 2014) have been developed. Historical data of all substations are used to identify a linear correlation between the outdoor temperature and the daily average temperature difference on the primary side of each substation. A range of tolerance is then defined, typically 3 times the standard deviation between historical data and the correlation. When a substation is out of the range, it's considered faulty. The Figure 2 provides an example of thermal signature results. The correlation and range of tolerance are represented by a bold dashed line and by two dotted lines, respectively. A fault is detected when a measurement point is located outside the zone delimited by the dotted lines.

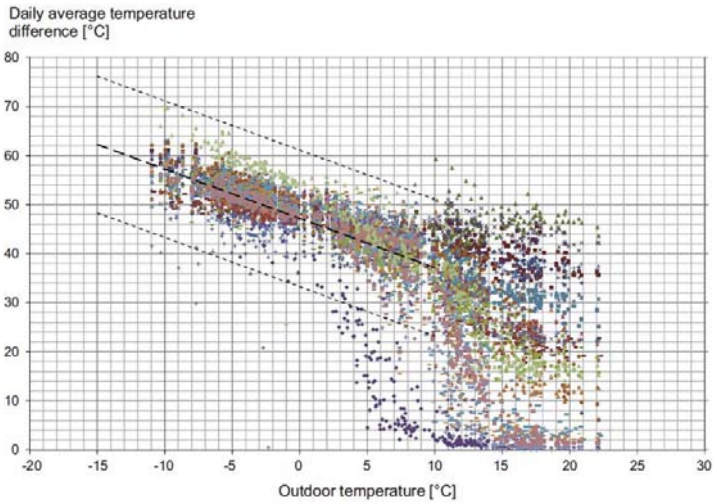

Figure 2: *Thermal signature method (Gadd & Werner, 2014).*

Like the previous indicator, a reference is necessary to define acceptability thresholds. Nevertheless, this method does not work for outside temperatures above 10°C, because beyond this value the heat consumption essentially comes from the DHW demand which is not simply temperature dependent. So this method can be only used for substations supplying space heating system.

These two indicators (excess flow and thermal signature) allow detecting defective substations but not identifying the causes. Moreover, except for the heat exchanger (Gudmundsson, Palsson, & Palsson, 2010), no indicator specific to a component is available in the literature.

1.3 Research motivations

As shown in the previous part, it is necessary to develop new performance indicators and to improve the old ones. Besides, according to the literature, DH system performance often depends on faults in the secondary side. Consequently, development of a DH system model including the secondary side must be undertaken. Finally, the aim of this paper is to assess the impact of common malfunctions to create performance indicators capable of distinguishing each of them. In this study, we focus on the following malfunctions: blocked valves and fouled heat exchanger.

2. METHODOLOGY: DEVELOPMENT OF A NUMERICAL TEST BENCH

Studies on DH system modelling are widely present in the literature and concern various aspects of the system such as the primary network (Bennonysson, 1991; Gabrielaitiene, Bøhm, & Sunden, 2007; van der Heijde et al., 2017; Zheng, Zhou, Zhao, & Wang, 2017), the substations (Brand, Thorsen, & Svendsen, 2012; Johansson, Lauenburg, & Wollerstrand, 2009) and the entire network (Kauko, Kvalsvik, Rohde, Hafner, & Nord, 2017; Li & Svendsen, 2012; Schweiger, Larsson, Magnusson, Lauenburg, & Velut, 2017). In these studies, the secondary side is only modelled by a demand profile at the substation and that is not enough to quantify the network performance in the case of malfunction. However, studies dealing with the secondary side in the literature only focus on the optimization of the couple

"temperature-mass flow rate" so as to reduce the primary return temperature (Lauenburg & Wollerstrand, 2014). To authors' knowledge no overall dynamic DH system model including the full operation of the secondary network has been presented in the literature. In order to study the sources of default on substations, a dynamic model including the secondary side is developed on Dymola/modelica environment. A descriptive scheme of the model is given in Figure 3.

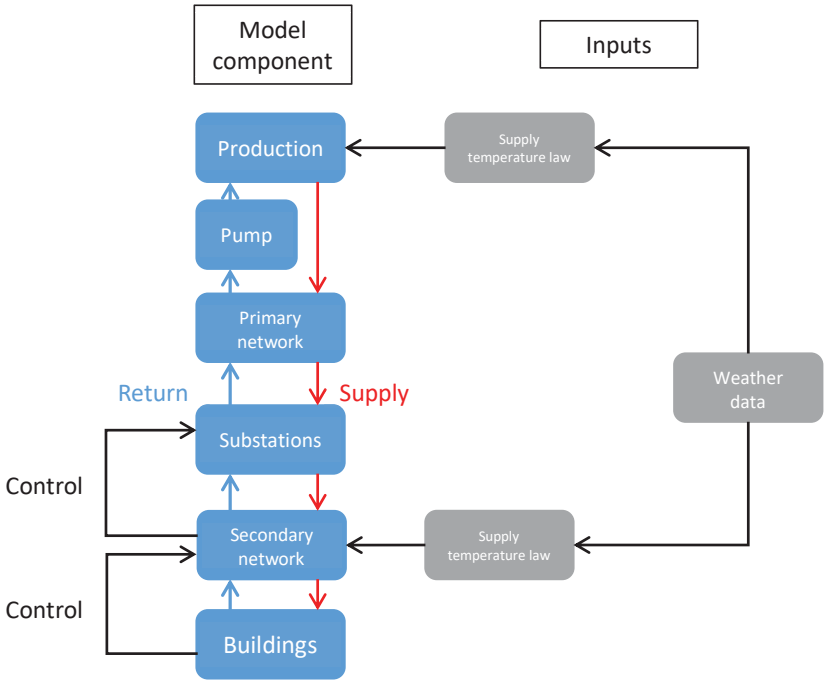

Figure 3: *Descriptive scheme of model operation*

Because the main objective is to study the impact of the malfunction, the substations and the secondary side need to be modelled in detail. By contrast, simplified models for the primary network and the heat generation plant are employed.

2.1 Simulation environment

For this study, the numerical test bench has been developed with the commercial simulation environment Dymola based on the Modelica language (Hilding Elmqvist, 1997). It allows the numerical simulation of dynamic behaviors and complex physical interactions between different physical phenomena (mechanics, hydraulics, thermodynamics, electrical, etc.). Modelica is an open object-oriented language, whose advantages are extensively explained in (Wetter, 2009). It allows users to freely create and share libraries of components.

The user puts components (blocks of Modelica code) on a grid, and the simulation environment (in this case Dymola) translates it into an equation system to be solved. The main characteristic of the Modelica language is its acausal nature; this means that no equation sequence has to be given by the user for numerical solving. This makes the creation of a model fast and easy, yet it can imply solving problems that are a bit more difficult to debug.

2.2 Heat generation model

For this study, a heat generation plant centralized and composed of a geothermal source and a gas boiler (in-series configuration) is considered. This type of plant is common in Ile-de-France region and interesting to be studied since the renewable energy share in the energy consumption is very sensitive to return primary temperature. As observed on typical French DH systems, the supply temperature is set through an outdoor temperature reset control (see Figure 4). The thresholds of supply temperature law are determined given according to observations on a real DH system.

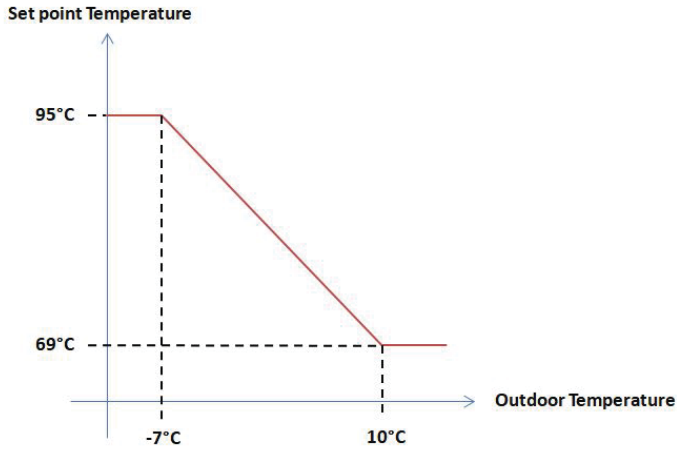

Figure 4: *Example of supply temperature law as a function of outdoor temperature*

The gas boiler is only used when the outlet temperature of the geothermal plant is inferior to the temperature set by the outdoor reset control. The gas boiler efficiency and the geothermal heat exchanger effectiveness are considered constant.

2.3 Primary network model

Two types of modelling are pointed out from the literature: the mathematical modelling based on statistical methods and the physical modelling using network's physical properties (Pálsson, Helge, Bohm, Ravn, & Zhou, 1999; Zheng et al., 2017). Within physical modelling approach, two methods are widely validated by comparison with experimental data: the node method and the element method. For the development of our virtual test bench, the element method is used due to its higher accuracy and its validation in Modelica (del Hoyo Arce et al., 2017; Giraud, Baviere, Vallée, & Paulus, 2015; Kauko et al., 2017; van der Heijde et al., 2017).

The primary network is constituted of pipes insulated with polyurethane foam (thermal conductivity $\lambda_{ins} = 0.025\ W/(m.K)$). The pipes are buried into the ground whose temperature is considered constant ($T_{ground} = 10°C$). In the pipes, heat losses normally depend on the convection between the flow of water and the pipes and also on the conduction through the pipe and insulation. According to (Dalla Rosa, Li, & Svendsen, 2011) the convection losses can be neglected compared to the conduction losses through insulation. Hence, the heat losses $\dot{Q}_{losses}$ are calculated such as (Giraud et al., 2015):

$$\dot{Q}_{losses} = \frac{2\,\pi\,L\,\lambda_{ins}}{\ln\left(\frac{2\,e_{ins}+D}{D}\right)}\left(T_{water} - T_{ground}\right)\ [\mathrm{W}] \quad (4)$$

Where L (m) is the pipe's length, D(m) the pipe's hydraulic diameter, e_{ins} (m) the insulation's thickness. Besides, the pressure losses Δp are calculated according to:

$$\dot{m} = k\sqrt{\Delta p} \quad (5)$$

Where $\dot{m}$ is the mass flow rate and k is a constant calculated from the nominal condition $k = \dot{m}_{nominal}/\sqrt{\Delta p_{nominal}}$ in kg.s^{-1}.Pa$^{-1/2}$. Moreover, a pump controlled by a pressure law with an efficiency of 90% is used. The electric power of the pump is given by:

$$P_{pump} = \frac{\Delta p \dot{V}}{\eta} \quad (6)$$

Where $\dot{V}$ is the volumetric flow rate (m^3/s).

2.4 Substation and secondary side model

The secondary network of a DH system is divided into two sub-systems, the heating system and the DHW system.

2.4.1 Heating system

In order to provide a proper temperature inside the building heated by a set of radiators, two control parameters can be used: the supply temperature and the mass flow rate in the radiators. Hence, 3 control strategies are possible (Gustafsson, Delsing, & van Deventer, 2010):

- Constant mass flow rate and variable supply temperature
- Variable mass flow rate and constant supply temperature
- Variable mass flow rate and supply temperature

A control strategy based on variable mass flow rate and supply temperature is the most popular. The supply temperature is set through an outdoor temperature control and to reach the secondary supply temperature, a valve is installed on the primary supply line before the heat exchanger to regulate the primary mass flow rate (see Figure 5). The valve opening is monitored through a controller that compares the set measured temperature with a target. The latter is defined by a function of the outdoor temperature. On the secondary side, a constant speed pump is sufficient to deliver the required heat. Moreover, in order to satisfy the heat demand a thermostatic valve is used to regulate the pump flow rate (ASHRAE, 2013; Gustafsson et al., 2010). The thermostatic valve is monitored by a proportional controller comparing the indoor temperature with a setpoint value.

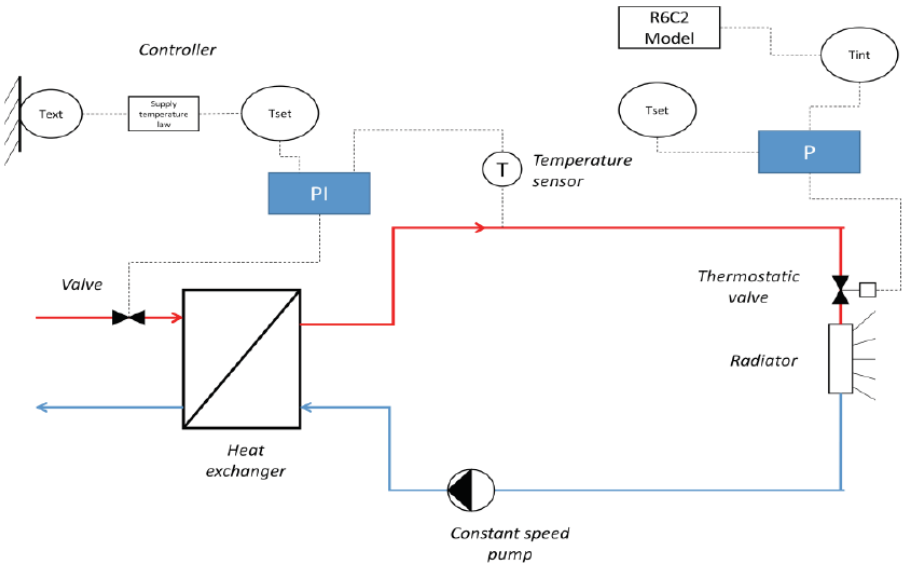

Figure 5: *Scheme of the secondary network (heating) with a thermostatic valve (SST VS)*

It is also possible to monitor the network using a constant flow rate on the secondary side (ASHRAE, 2013; Frederiksen & Werner, 2013). The secondary supply temperature is controlled as in the previous case. However, in this configuration a 3-way valve is placed downstream to the radiator in order to limit the flow passing in the radiator through a by-pass (Figure 6).

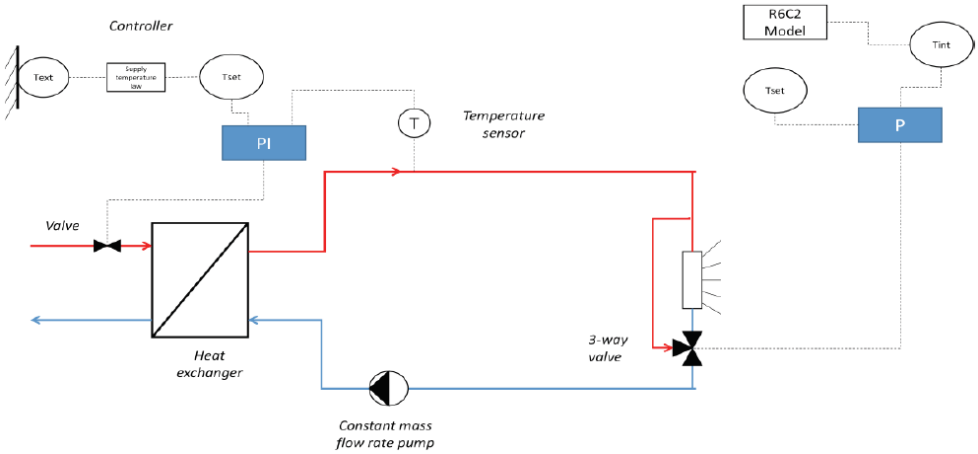

Figure 6: *Scheme of the secondary network (heating system) with a 3-way valve (SST V3V)*

2.4.2 DHW system

As for the case of space heating, the supply temperature of the secondary network is controlled by a valve located on the primary network, but the target value is fixed all the time.

Two configurations are widespread (Frederiksen & Werner, 2013; Yang, Li, & Svendsen, 2016; Yang & Svendsen, 2017). The first one aims to prepare instantaneously hot water

(60 °C) when requested by the customer (Figure 7). It should be noted that when DHW is not requested, there is always a flowrate (controlled by a recirculation pump). That allows avoiding stagnant water to be cooled and preventing the legionella development.

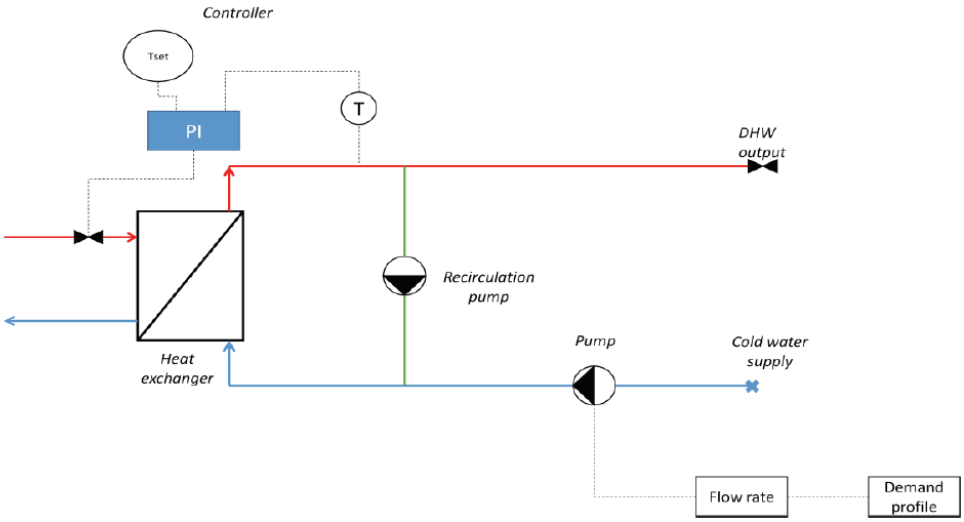

Figure 7: *Scheme of secondary network for instantaneous preparation of DHW (SST DHW instantaneous)*

The second configuration uses a hot water tank (Figure 8). Water temperature is measured at the top of the tank and is controlled via the primary valve. A 3-way valve is used to reduce the water temperature when it is excessively high. A recirculation pump also works for preventing stagnant water.

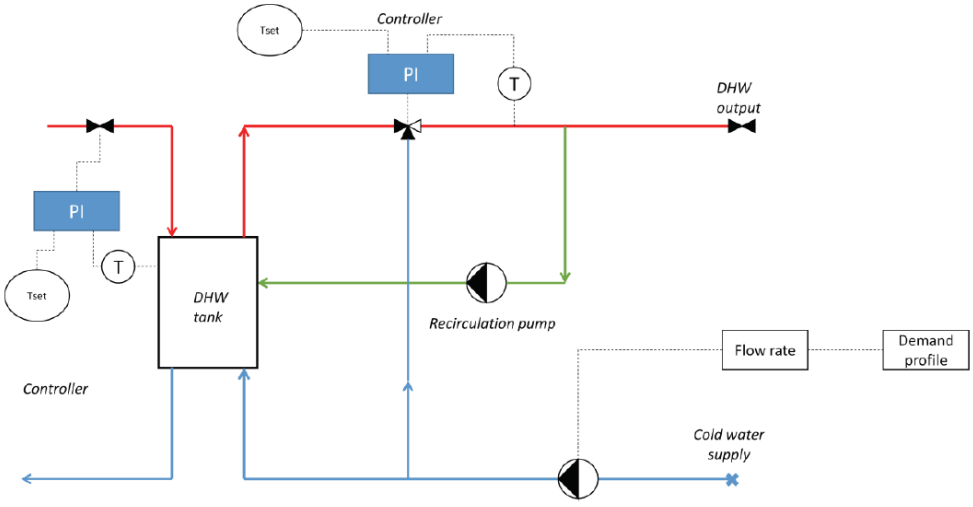

Figure 8: *Scheme of secondary network with hot water tank (SST DHW tank)*

2.5 Demand model

In order to simulate the operation of the secondary network, the thermal behaviour of a building must be modelled. Two types of models are described in the literature: detailed physical models and simplified physical models. The simplified models are preferred here because the detailed models are time-consuming (Greslou, Duplessis, & Stabat, 2015). They are usually represented by a thermal network composed of resistances and capacities. These models are called R_xC_y, where x and y refer the number of resistances and capacities, respectively. Among many models presented in the literature (Fux, Ashouri, Benz, & Guzzella, 2014), the R_6C_2 model is chosen due to its high simplicity-accuracy trade-off (Berthou, 2014). A scheme of the model is given on Figure 9.

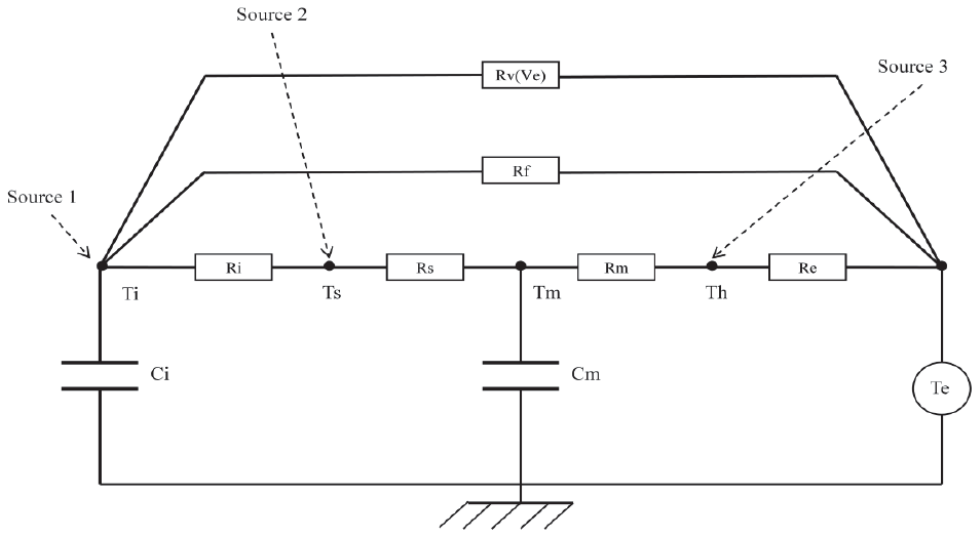

Figure 9: *R_6C_2 model*

The model is described by the following equations:

$$C_i \frac{dT_i}{dt} = \frac{T_s - T_i}{R_i} + \frac{T_e - T_i}{R_f} + \frac{T_e - T_i}{R_v} + source\ 1 \tag{7}$$

$$\frac{T_i - T_s}{R_i} + \frac{T_m - T_s}{R_f} + source\ 2 = 0 \tag{8}$$

$$C_m \frac{dT_m}{dt} = \frac{T_s - T_m}{R_s} + \frac{T_h - T_m}{R_m} \tag{9}$$

$$\frac{T_e - T_h}{R_e} + \frac{T_m - T_h}{R_m} + source\ 3 = 0 \tag{10}$$

The model takes into account the conduction transfers through the walls via the thermal resistances R_m and R_s and through the windows R_f. Besides, the convection is represented by the thermal resistances R_i and R_e. The heat transfer due to mechanical ventilation is modelled by the variable resistance R_v. The heat capacities of the walls and furniture are represented by C_m and C_i, respectively. Then the sources 1, 2 and 3 represent respectively the convective gains due to occupants and heating systems, the radiative internal gain due to occupants and electric appliances, and the solar gain.

3. SIMULATION OF TYPICAL MALFUNCTIONS IN DH NETWORK

For our case study, a DH system is modelled, including 40 substations distributed in 8 groups (Figure 10). The first four of these groups are located at 500 m and the rest at 250 m from the heat generation plant. Each group is composed of 4 substations for space heating and 1 for DHW. The four substation configurations presented in 2.4 are tested.

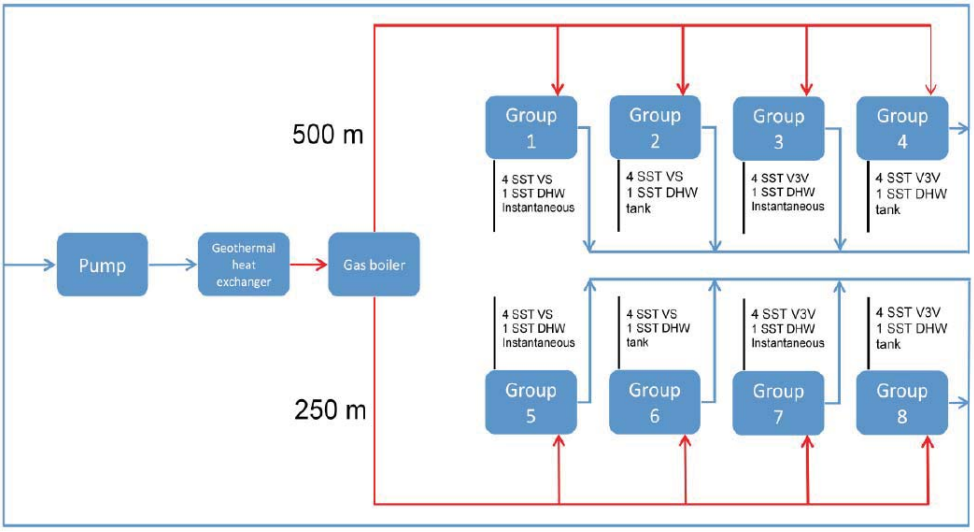

Figure 10: *Descriptive scheme of the DH network model*

Simulations are done over the month of January in Paris area; the weather data are given in Figure 11.

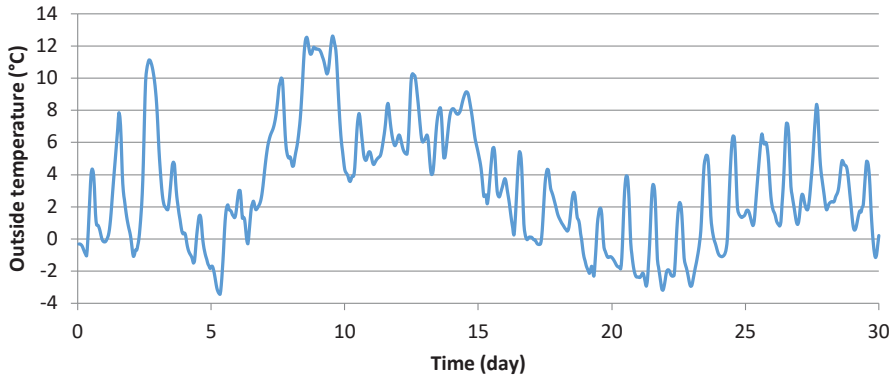

Figure 11: *Evolution of outside temperature during the whole simulation period*

3.1 Impact of the valve fault

The first study deals with the impact of blocked valves on the network performance. In each group, the primary valve of one space heating substation is blocked in a given opening position: 10%, 25%, 50% or 75%. The pressure control on the primary side allows to always satisfying the heating and DHW demands despite the malfunctions, as it appears in the real operation.

As a result (see Figure 12), the total energy consumption keeps nearly constant despite the faults. But, the malfunctions of valve imply a reduction of the share of heat produced by the geothermal plant. In the reference case, the geothermal share is 62.6 % while in the worst case reduced to 48.5 %. Moreover, the pump electric consumption is increased of 10% to 50%.

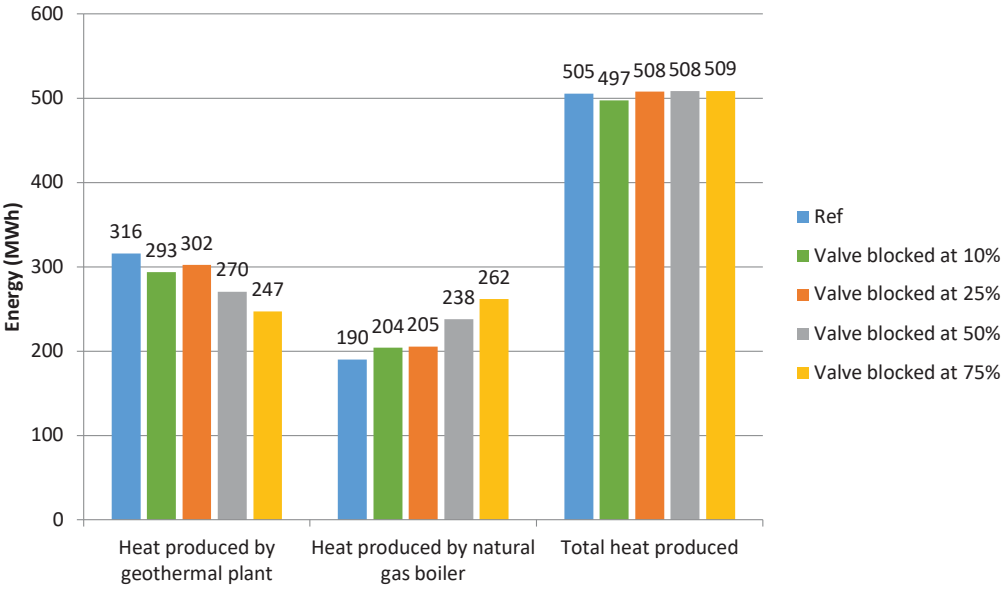

Figure 12: *Energy consumption of the DH network*

The indicators "excess flow" and "thermal signature" are tested, in order to check their ability to detect the malfunction. The results of the excess flow method are presented on Figure 13. For the reference case (blue circle) the substations have low excess flows (around 10 m^3), this means that they operate around the optimal conditions as expected. In the other cases where the valve fault occurs, an important excess flow can be observed. Hence, the method allows identifying the substations which fail to work correctly. However, it cannot specify the fault, because an excess flow can be caused by many other faults.

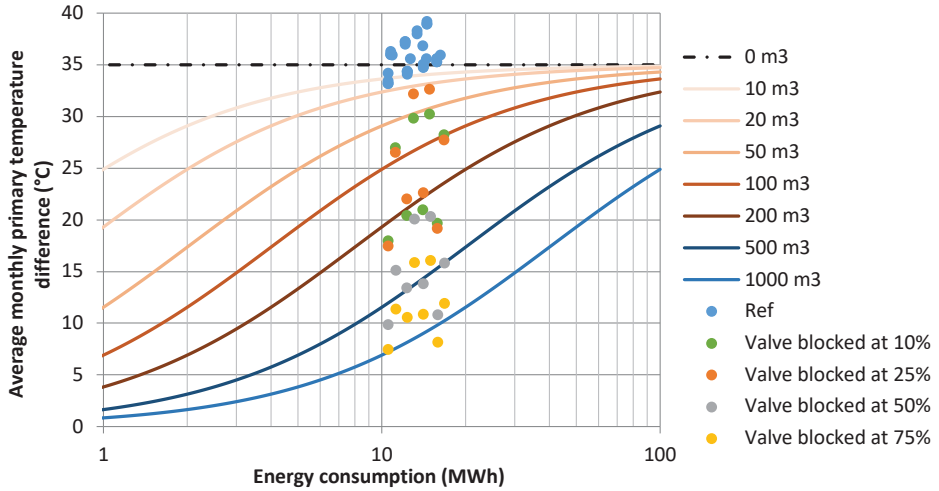

Figure 13: *Fault detection by excess flow method*

Regarding the thermal signature method (Figure 14), one can observe that operation points are clearly out of the range of tolerance in the case of 50% and 75% blockage, within the range for the case of 25 % and very close to the limit in the case of 10%. This observation can be explained knowing that the average valve opening is 20% in the reference case; the further the degree of blockage is from 20%, the more important its impact is.

Hence, the thermal signature indicator is not sensitive enough to detect fault when the degree of blockage is close to the normal operation.

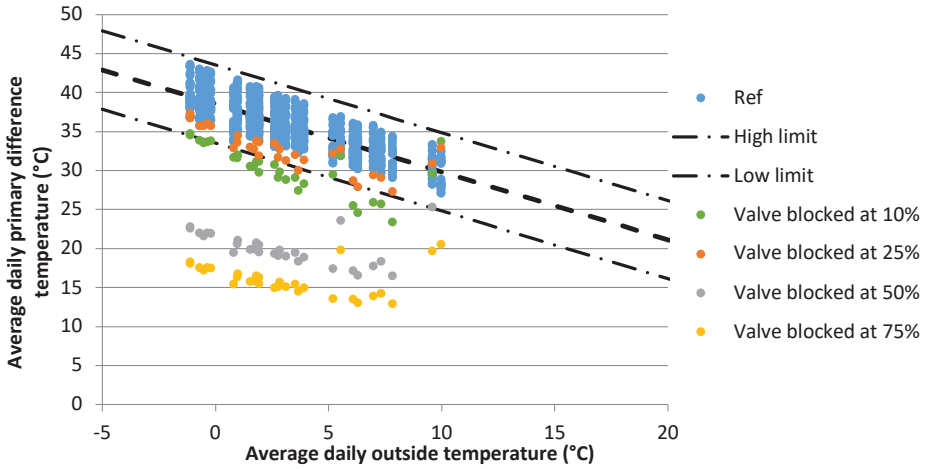

Figure 14: *Fault detection by the thermal signature*

In this context, other indicators must be developed. Figure 15 presents the mass flow rate on the primary side of one substation, for different levels of blockage. It has to be noticed that during day 9, the reduction of the mass flow rate is a consequence of a drop of the demand due to high outside temperatures (see Figure 11). We observe that the mass flow rate on the primary side becomes unstable during a valve malfunction. Moreover, for each case the mass flow rate in the cases of blockage is higher than in the reference case. Indeed, that can be expected for the cases of 25% 50% and 75% of valve opening, those are larger than the mean opening of the reference case (around 20%). Regarding the case of 10% valve opening, the supply pressure of the network has been augmented to maintain the building comfort what involves a mass flow rate rising. It should be noted that the increase in mass flow rate does not actually help detecting faults because the reference value is not necessary known in practice. When the valve blockage occurs, the mass flow rate becomes unstable even in the case where the degree of blockage is close to the normal operation. This behaviour may help detecting faults.

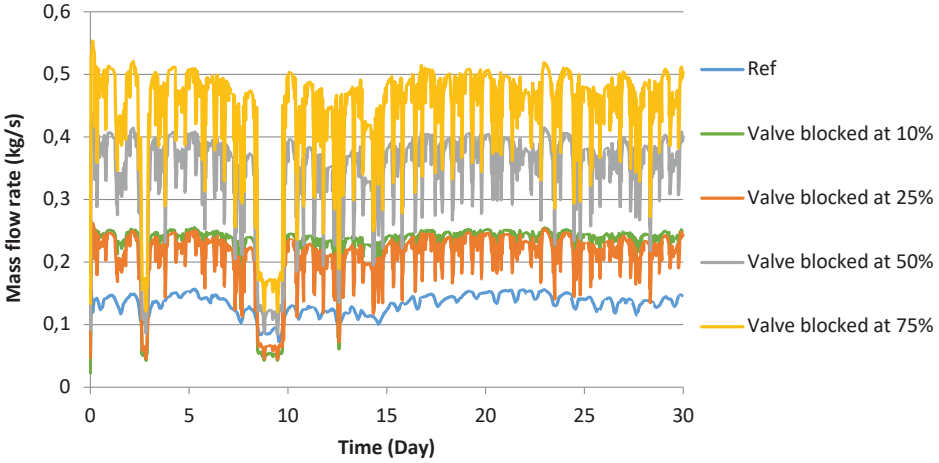

Figure 15: *Evolution of the primary mass flow rate*

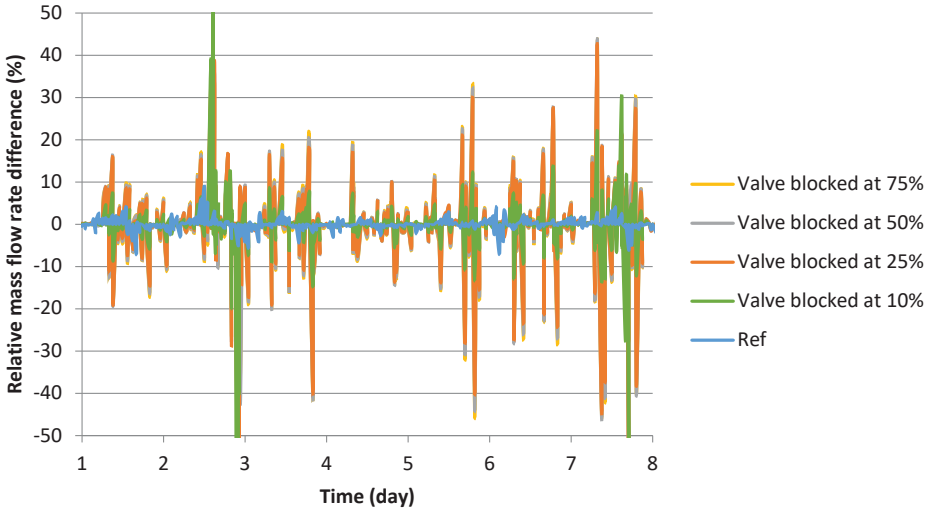

Figure 16: *Evolution of the relative mass flow rate difference*

In order to quantify the mass flow rate instability, a specific indicator is proposed. Figure 16 shows the relative difference between two consecutive mass flow rate measurements (time step of 1 hour):

$$D_{\dot{m}} = \frac{\dot{m}_{t+\Delta t} - \dot{m}_t}{\dot{m}_{t+\Delta t}} \ [\%] \tag{11}$$

Hence, for the reference case, the $D_{\dot{m}}$ is inferior to 10%, contrary to the other cases where $D_{\dot{m}}$ can reach 50%. Therefore a threshold at 10% can be set to detect a blocked valve. The choice of the threshold is quite arbitrary and tests shall be done on real data to justify this choice.

To conclude, an indicator based on mass flow rate instability seems to be a promising solution to detect specifically valve faults.

3.2 Impact of fouled heat exchanger

The second study deals with a malfunction due to a fouled heat exchanger. The latter is modelled via a thermal network composed of 2 resistances in series: one resistance for the convection and other for the impact of fouling. Various degree of fouling are considered and are summarized in the table below:

Case	1 (reference)	2	3	4	5	6	7
$\frac{Fouling\ thermal\ resistance}{Total\ thermal\ resistance}$ [%]	0	1.25	11.2	23.9	38.5	52.1	64.57
Heat exchanger effectiveness	0.9	0.897	0.876	0.841	0.787	0.715	0.642

Table 1: Description of case study

For sake of clarity, only 4 defective substations are represented on Figure 17. We focus only on one malfunctioning substation on Figure 18, 19 and 20, similar results are observed on other faulty substations.

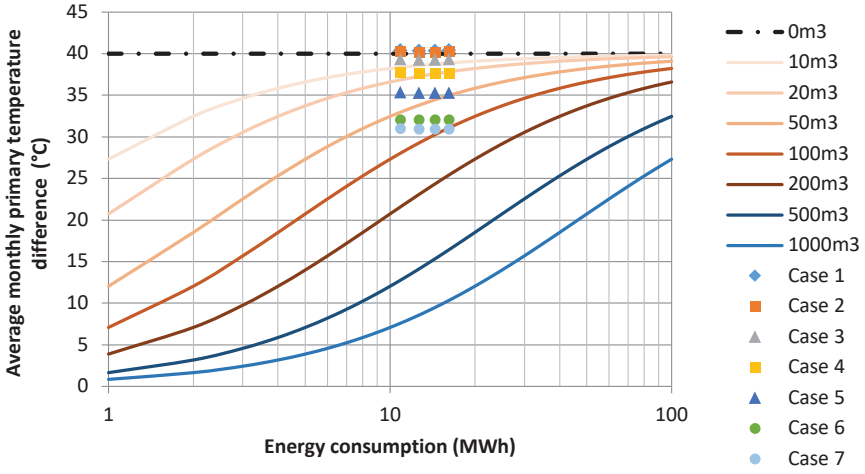

Figure 17: Detection of fouling with the excess flow method

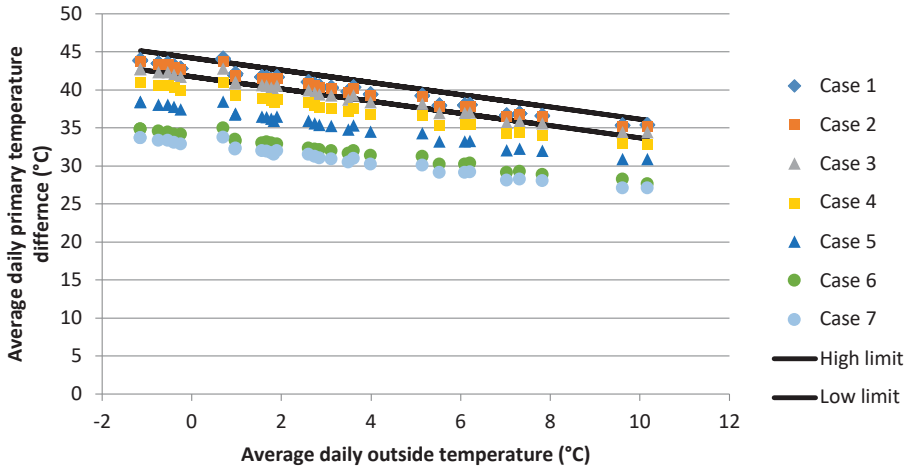

Figure 18: *Detection of fouling with the thermal signature*

The result from the excess flow method (see Figure 17) and the thermal signature (see Figure 18) confirm that these indicators can detect the fouling fault if the fouling is important enough. However, other indicators can be considered. The pinch is a common indicator of the heat exchanger performance. The study shows how the pinch of the heat exchanger is impacted by the fouling. Hence, an indicator similar to the thermal signature (see 1.2) is intoduced on Figure 19 to detect a malfunction due to a fouled heat exchanger.

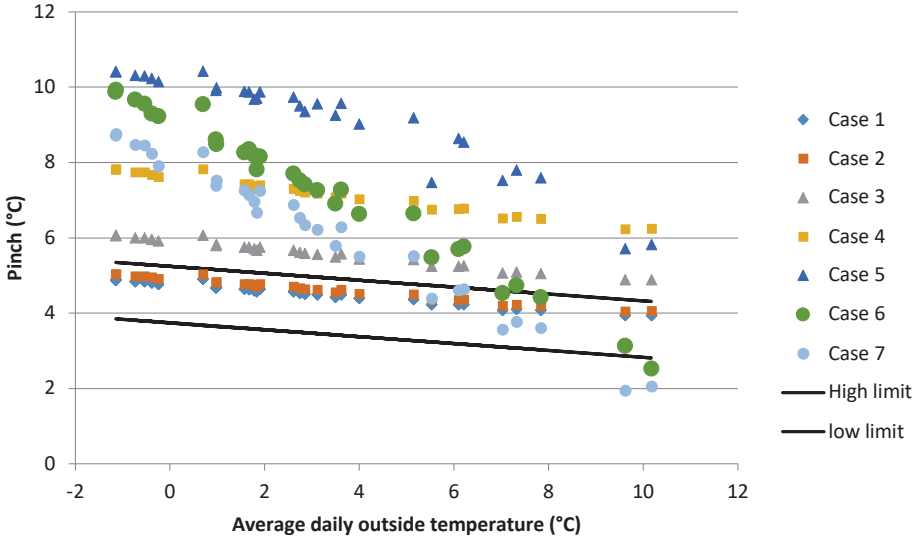

Figure 19: *Detection of fouling with the evolution of the pinch*

Indeed, an average behaviour of the pinch is determined through the case 1 (reference case) and the thresholds are set to ∓ 3 times the standard deviation between the average behaviour and the whole data of the case 1. Regarding the case 3, the indicator detects a troublesome

fouling whereas the heat exchanger effectiveness only decreases from 0.9 to 0.876. In practice, the threshold should be less strict due to the measurement uncertainty. It should be noted that the pinch position is not the same in all cases. Indeed, for cases 1 to 5, the pinch is situated in the cold side of the exchanger whereas for the cases 6 and 7 the pinch is in the hot side. That explains why the pinch in the cases 6 and 7 can be lower than in the reference case when the outside temperature is high.

Furthermore, one can wonder if the pinch can also be used to detect blocked valves. The evolution of the pinch when valves are blocked is presented on Figure 20. The threshold is determined through the reference case data (E=0.9, no blocked valves). The pinch does not allow detecting the fault except the case of 75% valve opening. In this case, the pinch is equal to the difference between the primary inlet temperature and the secondary outlet temperature in contrast to the reference case where the pinch is equal to the temperature difference at the cold side of the heat exchanger. For the other cases, the pinch at the cold side of the heat exchanger what explains the slight increase of the pinch. In this case, contrary to the case of fouled heat exchanger, the pinch decreases. To conclude, this indicator is inefficient to detect blocked valve since the threshold is not exceeded in each case.

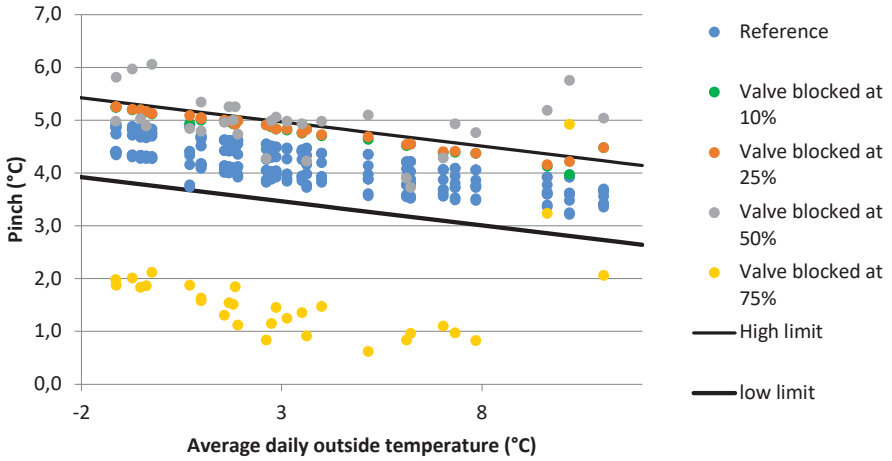

Figure 20: *Detection of a blocked valve with the evolution of the pinch*

4. CONCLUSION

This study proposes a DH system model including the operation of the secondary side. Based on an appropriate simulation tool (Dymola/Modelica), our model allows studying the dynamic behaviour of the network including thermo-hydraulic interactions. This new model enables to evaluate the impact of several malfunctions downgrading the performance of the network. For now, two possible malfunctions have been tested: blocked valve and fouled heat exchanger. The study demonstrates the relevance of the indicators namely, excess flow and thermal signature, to detect substations which malfunction. However, these indicators cannot bring us a clue on the origin of the malfunction. For that reason two indicators have been proposed in this study to detect specific malfunctions. The instability of the mass flow rate enables to detect blocked valves on the network, and the heat exchanger fouling is detected by the evolution of the pinch.

These studies constitute the first step of a global study on the impact and detection of principal malfunctions on the network. To complete the study other malfunctions such as, unsuitable regulation, defecting temperature sensor or unsuitable secondary system linked to DH system will be studied. Moreover, simultaneous malfunctions will also be taken into consideration. Last, in order to validate the studies made by simulation, the developed performance indicators will be tested on real data.

5. ACKNOWLEDGEMENT

The authors would like to thank "L'Agence De l'Environnement et de la Maîtrise de l'Energie"(ADEME) Ile de France for their financial support in these research activities.

6. NOMENCLATURE

E	Energy consumption, J	$\dot{V}$	Volumetric flow rate, m^3/s
V_{ref}	Reference volume m^3	η	Pump efficiency
V_{act}	Actual volume m^3	C_i	Furniture capacity, J/K
V_{excess}	Excess volume m^3	C_m	Wall capacity, J/K
ΔT_{ref}	Reference primary temperature difference, K	R_i	Internal convective thermal resistance, K/W
ΔT_{act}	Actual primary temperature difference, K	R_e	External convective thermal resistance, K/W
C	Thermal capacity $J/(K.m^3)$	R_m	Wall thermal resistance, K/W
λ_{ins}	Insulation thermal conductivity, W/(m.K)	R_f	Windows thermal resistance, K/W
L	Pipe's length, m	R_v	Mechanical ventilation thermal resistance, K/W
D	Pipe diameter, m	T_i	Inside temperature, K
e_{ins}	Insulation thickness, m	T_s	Internal surface temperature, K
T_{water}	Water's temperature, K	T_m	Wall temperature, K
T_{ground}	Ground temperature, K	T_e	Outside temperature, K
$\dot{Q}_{losses}$	Thermal losses, W	T_h	Outside surface temperature, K

$\dot{m}$	Mass flow rate, kg/s	$source\ 1$	Convective gain due to occupants and space heating, W
Δp	Pressure difference, Pa	$source\ 2$	Radiative gain due to occupants and space heating; W
k	Constant, $kg.s^{-1}.Pa^{-1/2}$	$source\ 3$	External solar gain, W
P_{pump}	Pump power, W	$D_{\dot{m}}$	Relative masse flow rate difference, %

7. REFERENCES

AB, D. S. (2014). *Dymola user guide manual* (No. 1).

ASHRAE. (2013). *District heating guide* (Book). NE Atlanta: W. Stephen Comstock.

Bennonysson, A. (1991). *Dynamic modelling and operation optimization of district heating systems*. Technical University of Denmark, Phd Thesis.

Berthou, T. (2014). *Développement de modèles de bâtiment pour la prévision de charge de climatisation et l'élaboration de stratégies d'optimisation énergétique et d'effacement*. MINES ParisTech, Phd Thesis. Retrieved from https://tel.archives-ouvertes.fr/pastel-00935434/document

Brand, M., Thorsen, J. E., & Svendsen, S. (2012). Numerical modelling and experimental measurements for a low-temperature district heating substation for instantaneous preparation of DHW with respect to service pipes. *Energy*, *41*(1), 392–400. https://doi.org/10.1016/j.energy.2012.02.061

Dalla Rosa, A., Li, H., & Svendsen, S. (2011). Method for optimal design of pipes for low-energy district heating, with focus on heat losses. *Energy*, *36*(5), 2407–2418. https://doi.org/10.1016/j.energy.2011.01.024

del Hoyo Arce, I., Herrero López, S., López Perez, S., Rämä, M., Klobut, K., & Febres, J. A. (2017). Models for fast modelling of district heating and cooling networks. *Renewable and Sustainable Energy Reviews*, (June), 1–11. https://doi.org/10.1016/j.rser.2017.06.109

Frederiksen, S., & Werner, S. (2013). *District heating and cooling* (Studentlit). Lund.

Fux, S. F., Ashouri, A., Benz, M. J., & Guzzella, L. (2014). EKF based self-adaptive thermal model for a passive house. *Energy and Buildings*, *68*(PART C), 811–817. https://doi.org/10.1016/j.enbuild.2012.06.016

Gabrielaitiene, I., Bøhm, B., & Sunden, B. (2007). Modelling temperature dynamics of a district heating system in Naestved , Denmark — A case study, *48*, 78–86. https://doi.org/10.1016/j.enconman.2006.05.011

Gadd, H., & Werner, S. (2014). Achieving low return temperatures from district heating substations. *Applied Energy*, *136*, 59–67. https://doi.org/10.1016/j.apenergy.2014.09.022

Gadd, H., & Werner, S. (2015). Fault detection in district heating substations. *Applied Energy*, *157*, 51–59. https://doi.org/10.1016/j.apenergy.2015.07.061

Giraud, L., Baviere, R., Vallée, M., & Paulus, C. (2015). Presentation, Validation and Application of the DistrictHeating Modelica Library, 79–88. https://doi.org/10.3384/ecp1511879

Greslou, O., Duplessis, B., & Stabat, P. (2015). *Analyse de la demande des bâtiments raccordés à un réseau et de leur agrégation, Final report ADEME/ARMINES*. Rapport.

Gudmundsson, O., Palsson, O. ., & Palsson, H. (2010). Analysis of heat transfert in heat exghangers by using the NTU method and empirical relations. In *12th International Symposium on District Heating and Cooling* (pp. 305–308).

Gustafsson, J., Delsing, J., & van Deventer, J. (2010). Improved district heating substation efficiency with a new control strategy. *Applied Energy*, *87*(6), 1996–2004. https://doi.org/10.1016/j.apenergy.2009.12.015

Hilding Elmqvist. (1997). Modelica — A unified object-oriented language for physical systems modeling. *Simulation Practice and Theory*, *5*(6), p32. https://doi.org/10.1016/S0928-4869(97)84257-7

Johansson, P.-O., Lauenburg, P., & Wollerstrand, J. (2009). Improved cooling of district heating water in substations by using alternative connection schemes. In ECOS (Ed.), *22nd International Conference on Efficiency, Cost, Optimization Simulation and Environmental Impact of Energy Systems* (pp. 843–852). Foz do Iguaçu, Parana, Brèsil.

Kauko, H., Kvalsvik, K. H., Rohde, D., Hafner, A., & Nord, N. (2017). Dynamic modelling of local low-temperature heating grids: A case study for Norway. *Energy*, *139*, 289–297. https://doi.org/10.1016/j.energy.2017.07.086

Lauenburg, P., & Wollerstrand, J. (2014). Adaptive control of radiator systems for a lowest possible district heating return temperature. *Energy and Buildings*, *72*, 132–140. https://doi.org/10.1016/j.enbuild.2013.12.011

Li, H., & Svendsen, S. (2012). Energy and exergy analysis of low temperature district heating network. *Energy*, *45*(1), 237–246. https://doi.org/10.1016/j.energy.2012.03.056

Lund, H., Werner, S., Wiltshire, R., Svendsen, S., Thorsen, J. E., Hvelplund, F., & Mathiesen, B. V. (2014). 4th Generation District Heating (4GDH). Integrating smart thermal grids into future sustainable energy systems. *Energy*, *68*, 1–11. https://doi.org/10.1016/j.energy.2014.02.089

Ministère de la Transition Ecologique et Solidaire. (2014). Indicateur de développement durable nationaux 2010-2013, consommation d'énergie des secteurs résidentiel et tertiaire. Retrieved January 1, 2017, from http://www.statistiques.developpement-durable.gouv.fr/indicateurs-indices/li/indicateurs-developpement-durable-nationaux-2010-2013.html

Ministère de la Transition Ecologique et Solidaire. (2015). Loi n°2015-992 relative à la transition énergétique pour la croissance verte. Retrieved from https://www.ecologique-solidaire.gouv.fr/loi-transition-energetique-croissance-verte

Pálsson, H., Helge, V. L., Bohm, B., Ravn, H. F., & Zhou, J. (1999). *Equivalent Models of District Heating Systems*. Rapport.

Quiquerez, L. (2017). *Décarboner le système énergétique à l'aide des réseaux de chaleur:*

état des lieux et scénarios prospectifs pour le canton de Genève. Université de Genève, Phd Thesis. Retrieved from http://archive-ouverte.unige.ch/unige:93380

Rezaie, B., & Rosen, M. A. (2012). District heating and cooling: Review of technology and potential enhancements. *Applied Energy*, *93*, 2–10. https://doi.org/10.1016/j.apenergy.2011.04.020

Schweiger, G., Larsson, P.-O., Magnusson, F., Lauenburg, P., & Velut, S. (2017). District heating and cooling systems – Framework for Modelica-based simulation and dynamic optimization. *Energy*, *137*, 566–578. https://doi.org/10.1016/j.energy.2017.05.115

van der Heijde, B., Fuchs, M., Ribas Tugores, C., Schweiger, G., Sartor, K., Basciotti, D., … Helsen, L. (2017). Dynamic equation-based thermo-hydraulic pipe model for district heating and cooling systems. *Energy Conversion and Management*, *151*(August), 158–169. https://doi.org/10.1016/j.enconman.2017.08.072

Wetter, M. (2009). Modelica-based modelling and simulation to support research and development in building energy and control systems. *Journal of Building Performance Simulation*, *2*(2), 143–161. https://doi.org/10.1080/19401490902818259

Yang, X., Li, H., & Svendsen, S. (2016). Evaluations of different domestic hot water preparing methods with ultra-low-temperature district heating. *Energy*, *109*, 248–259. https://doi.org/10.1016/j.energy.2016.04.109

Yang, X., & Svendsen, S. (2017). Achieving low return temperature for domestic hot water preparation by ultra-low-temperature district heating. *Energy Procedia*, *116*, 426–437. https://doi.org/10.1016/j.egypro.2017.05.090

Zheng, J., Zhou, Z., Zhao, J., & Wang, J. (2017). Function method for dynamic temperature simulation of district heating network. *Applied Thermal Engineering*, *123*, 682–688. https://doi.org/10.1016/j.applthermaleng.2017.05.083

Zinko, H., Lee, H., Kim, B.-K., Kim, Y.-H., Lindkvist, H., Loewen, A., … Wigbels, M. (2005). *Improvement of operational temperature differences in district heating systems*.

Questions and Answers:

Madjid Madjidi:

Could we sort the measured values by the return temperature also (instead of the outdoor temperature)?

Antoine Fabre:

The primary temperature difference could be replaced by the evolution of the return temperature according to the outdoor temperature. Indeed, the outdoor temperature is not the only indicator of the heating consumption of the building but it is the simplest to use.

***

Ivan Verhaert:

Does it work with Domestic Hot Water (DHW)? Because it is dependent on the outdoor temperature?

Antoine Fabre:

Indeed the thermal signature method does not work with DHW substations.

***

Sebastian Gonzato:

What other faults might the excess flow method indicate?

Antoine Fabre:

The excess flow method is able to detect all the faults impacting the return temperature. In fact, practically all the faults.

THIRD SESSION
INTEGRATION OF BUILDINGS IN ELECTRICITY GRIDS

Hybrid heat pump scenarios as a transition towards more flexible buildings

A. Uytterhoeven[1,2]*, G. Deconinck[2,3], A. Arteconi[1,4], L. Helsen[1,2]

(1) KU Leuven, Department of Mechanical Engineering, Division Applied Mechanics and Energy Conversion, Leuven, Belgium.

(2) EnergyVille, Genk, Belgium.

(3) KU Leuven, Department of Electrical Engineering, Division Electrical Energy and Computer Architectures, Leuven, Belgium.

(4) Universita degli Studi eCampus, Novedrate, Italy.

ABSTRACT

The potential of heat pumps (HP) to contribute to a cost-efficient and environmentally-friendly operation of the electric power system is widely acknowledged. Nevertheless, a large-scale implementation of heat pumps in Belgium is lacking today, with applications restricted to new or deeply retrofitted houses. This paper investigates the potential of a more accessible transition scenario, where heat pumps are used to assist, rather than replace, the original heating system in place. The reference heating system considered is a gas boiler (GB) connected to radiators (RAD). To analyse the behaviour of the hybrid system, a model predictive control (MPC) approach is used. Main interests are the achievable heat pump utilisation, as well as the detailed behaviour of the system. Also the impact of the introduction of the heat pump on primary energy use and operational cost for space heating (SH) is illustrated. To ensure a profound analysis, different scenarios are investigated, where the dwelling characteristics, heating system, objective function and energy prices are varied. The results illustrate that under current price conditions in Belgium, minimisation of the primary energy use is the only beneficial scenario leading to a considerable heat pump utilisation. When minimising operational costs, a lower electricity-to-gas price ratio (EGR) is needed to tip the balance.

Keywords: hybrid heat pump, air-to-water heat pump, air-to-air heat pump, thermal energy storage, smart grid, flexibility

1. INTRODUCTION

The potential of heat pumps to contribute to a more cost-efficient and environmentally-friendly operation of the electric power system is widely acknowledged (Forsén, 2005). A first key characteristic is their high energy efficiency. Moreover, they embody a great potential for demand response (DR) when combined with thermal energy storage (TES) (Six, Desmedt, Vanhoudt, & Van Bael, 2011; Arteconi, Hewitt, & Polonara, 2013; Patteeuw, 2016). The TES, which can be provided by, among others, the thermal inertia of the building mass, unlocks the flexibility to shift heat production in time while maintaining thermal comfort of the residents. If the building is heated by a heat pump, the electricity use can hence

be shifted to periods of low electricity prices or high shares of renewable energy sources (Arteconi, et al., 2013; Sweetnam, Fell, Oikonomou, & Oreszczyn, 2018).

Considering that buildings account for over 30% of the global final energy use, of which the majority is used for space heating (SH) and domestic hot water (DHW), heat pumps can be a true game changer in the built environment (IEA & IPEEC, 2015). However, in Belgium, a large-scale implementation of heat pumps is still lacking today (Jespers, Al Koussa, Dams, Renders, & Vingerhoets, 2017). The current implementation of residential heat pumps is mostly restricted to new or deeply retrofitted houses characterised by a high-quality building envelope; in these houses, a heat pump is a logic choice for the main heating system, mostly assisted by a back-up electrical resistance heater (Patteeuw, 2016). With this in mind, the question arises whether it might be possible to enhance a widespread use of heat pumps in the future energy system by implementing a more accessible transition scenario. One possible roadmap is the implementation of heat pumps in existing buildings as a supplementary space heating system, assisting – rather than completely replacing – an existing gas boiler coupled to radiators.

The goal of this paper is to determine which objectives, and, along with that, which signals can increase heat pump utilisation in a hybrid configuration. Furthermore, the impact of the unlocked flexibility on primary energy use and operational costs related to space heating is investigated. This study analyses two alternative hybrid configurations, containing either an air-to-water heat pump (AWHP) or an air-to-air heat pump (AAHP) as supplementary space heating technology. The space heating system is coupled with TES, provided (uniquely) in a passive way by the thermal inertia of the building mass; no additional active buffer tank is present. In order to fully delineate the potential of both transition scenarios, their implementation is investigated in different building types, of different age classes, with different renovation levels. Also different time-varying price profiles for both electricity and gas are considered.

The paper is structured as follows. Section 2 explains the modelling framework, used to mimic the behaviour of the system. Here, all required equations, boundary conditions and assumptions are further elaborated on. This is followed by an in-depth analysis and discussion of the results in Section 3, leading to final conclusions in Section 4.

2. METHODOLOGY

This section describes the research method. First, Section 2.1 elaborates on the investigated systems. Section 2.2 describes the set-up of the modelling framework and the controller, with the imposed objective functions, the constraints, and the additional boundary conditions.

2.1 System description

Generally, hybrid heat pump (HHP) systems are defined as the combination of a ‘conventional’ space heating technology and a heat pump. Consequently, a lot of different combinations are possible. The specific configurations that are studied in this paper are shown in Figure 1. The conventional scenario, where a gas boiler coupled to radiators supplies heat to the building, serves as a reference. In the first hybrid set-up (A), an air-to-water heat pump is installed in series with the conventional set-up, serving as an upstream preheating step; both heat supply systems are hydronic systems in this case. In the second hybrid set-up (B), an air-to-air heat pump is placed in parallel with the gas boiler, serving as an alternative heat supply system; here, water-based and air-based systems are combined. For both hybrid configurations (A and B) the gas boiler is also responsible for covering the full domestic hot

water demand. This is however not further addressed in this paper, since this has no impact on the comparison between the different cases.

To be able to translate these theoretical concepts into practical case studies, their implementation has to be coupled to a specific building. Based on the nominal heat demand for the dwelling considered, a heat pump can then be selected within the constraints of the currently available heat pumps on the market. Note that, where the heat pump selection is a rather meticulous task, the gas boiler selection is not so stringent, since these devices tend to be largely oversized, thereby relaxing their case-specificity.

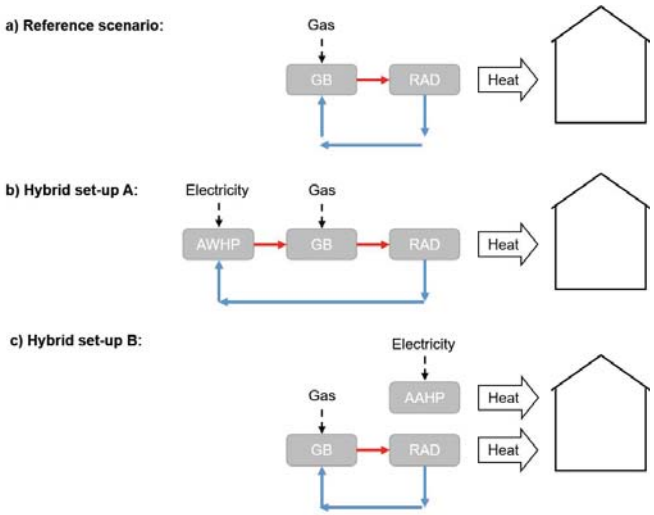

Figure 1 The investigated configurations:(a) reference scenario, where the heat demand is covered by a gas boiler coupled to radiators; (b) hybrid set-up A, where an air-to-water heat pump serves as an upstream preheating step for the gas boiler; (c) hybrid set-up B, where an air-to-air heat pump assists the gas boiler to cover the space heating demand.

Two different dwelling types are studied in this paper, being an old, mildly renovated, detached, single family house, and its new-built, low-energy equivalent. They mainly differ in thermal inertia because of different insulation levels, and in supply temperature of the radiator system, which can have a considerable impact on the heat pump utilisation and its behaviour (in case of the AWHP). The specific characteristics of both dwelling types, summarised in Table 1, are based on the Belgian building stock description developed in the European TABULA project (Cyx, Renders, & Van Holm, IEE TABULA - Typology Approach for Building Stock Energy Assessment, 2011), and the work of Reynders (2015) elaborating thereupon.

A heat loss calculation leads to the design heat demand of the space heating technology and the radiators. In general, autonomous heat pump systems are sized to meet 80% of the design heat demand at a design indoor temperature for the day zone of 20°C, for the night zone of 18°C, a ground temperature of 12°C, and an ambient temperature of -10°C (Code van goede praktijk voor de toepassing van warmtepompsystemen in de woningbouw, 2004). Since a hybrid heat pump does not have to be able to cover the full heat demand, in this case, the sizing is based on 100% of the design heat demand at the same design indoor temperatures and ground temperature, but at a higher ambient temperature of 5°C, called ‘modified design heat demand’. The ambient temperature of 5°C is chosen as a reference, since this is the

tipping point below which the heat pump operation is deteriorating due to the lower ambient temperature as such, and, more important, due to defrosting. At temperatures around 0°C, the relative humidity of the ambient air is rather high, and due to the low air temperature, ice is formed on the outdoor unit. This ice is removed by reverse cycle operation, thereby negatively affecting the performance in this specific temperature window (Daikin Europe N.V., 2018).

Table 2 summarises the resulting design heat demand for both case studies, together with the appropriate heat pumps resulting from a selection process in consultation with Daikin. Note that in all cases, a supplementary gas boiler is still required, since the heat pumps can only cover the heat demand at mild weather conditions.

Table 1 Dwelling characteristics of the considered building types (Reynders, 2015).

	Dwelling type 1	**Dwelling type 2**
Description	Old, mildly renovated, detached, single family house	New-built, low-energy, detached, single family house
Age class	1971-1990	Post 2005
Energy performance measures	- Double glazing - Improved air-tightness - Insulated roof - High temperature radiator (90°C/70°C)	- Double glazing - High air-tightness - Insulated roof - Insulated outer walls - Insulated floor - Heat recuperation on ventilation - Low temperature radiator (45°C/35°C)
Area	238 m²	270 m²
Main U-value (external wall)	0.990 $^{W}/_{m^2K}$	0.403 $^{W}/_{m^2K}$

Table 2 Heat pump selection process, based on the design heat demand of the considered dwellings (Daikin Europe N.V., 2018).

	Dwelling type 1	**Dwelling type 2**
Modified design heat demand	6.4 kW	3.7 kW
Heat pump selection	**AWHP:** Daikin Altherma hybrid with outdoor unit EVLQ08-CV3 **AAHP:** Daikin outdoor unit 4MXS80E (multisplit, coupled to four indoor units: 15/15/15/35)	**AWHP:** Daikin Altherma hybrid with outdoor unit EVLQ05-CV3 **AAHP:** Daikin outdoor unit FTXM35M + RXM25M (split, coupled to one indoor unit)

2.2 Modelling framework

To be able to optimise the operation of the heating system, while taking into account the system behaviour and relevant boundary conditions (such as occupant behaviour, thermal comfort requirements, weather predictions, forecasted electricity prices) a model predictive

control framework has to be set up. At each control time step, an optimal control problem (OCP) is solved for a chosen prediction horizon, deciding when/how the gas boiler and/or the heat pump are/is used to cover the heat demand. Solving the OCP allows exploiting the flexibility as good as possible to reach the goal set by the minimum of the objective function, subject to (in)equality constraints describing the system behaviour and other environmental factors. In the remainder of this section, all equations needed to build up the optimal control problem formulation are discussed in detail. In the equations, j always represents the time index and Δt the corresponding time step, equal to one hour.

2.2.1 Objective function

In this paper, two different objective functions are considered, as shown by Equations (1) and (2). In the first case, the controller aims at minimising the operational cost of the heating system by searching for an optimal heating profile for both the heat pump and the gas boiler. In this case, the electricity and gas consumption need to be multiplied by the corresponding price profiles. In a second case, emphasis is on primary energy use. Since electricity is not primary energy, the electricity consumption of the heat pumps needs to be multiplied by the primary energy factor (PEF), representing (the inverse of) the average efficiency of the electricity generation mix.

Note that in the framework developed also other objective functions are possible, such as minimisation of CO_2 emissions, maximisation of use of electricity originating from renewable energy sources (RES), etc. However, these are not considered further here, since emphasis is on the impact of unlocking flexibility on operational cost and primary energy use.

$$\min \left(\sum_{j=1}^{n} (cost_j^{el} \cdot P_j^{HP} + cost_j^{gas} \cdot P_j^{GB}) \right) \tag{1}$$

$$\min \left(\sum_{j=1}^{n} (PEF \cdot P_j^{HP} + P_j^{GB}) \right) \tag{2}$$

With	n	Time horizon of optimal control problem	$[h]$
	$cost_j^{el}$	Electricity cost as perceived by consumer	$\left[\frac{EUR}{kWh_{el}}\right]$
	P_j^{HP}	Electrical energy used by heat pump[6]	$[kWh_{el}]$
	$cost_j^{gas}$	Gas cost as perceived by consumer	$\left[\frac{EUR}{kWh_{gas}}\right]$
	P_j^{GB}	Primary energy used by gas boiler[1,7]	$[kWh_{prim}]$
	PEF	Primary energy factor	$\left[\frac{kWh_{prim}}{kWh_{el}}\right]$

2.2.2 Constraints

The MPC framework needs a model of the system, being the heating system and building, to predict its behaviour over the prediction horizon. These models are described in Section 2.2.2.1 and 2.2.2.2. Furthermore, the boundary conditions, i.e., the occupant behaviour,

[6] Since a time step of 1 hour is used, we consider $[kWh/h]$.
[7] Since gas is a primary energy source, $[kWh_{gas}] = [kWh_{prim}]$.

thermal comfort requirements, weather conditions, energy prices and primary energy factor are needed. These are elaborated on in Section 2.2.2.3.

2.2.2.1 Heating system model

As already explained in Section 2.1, the buildings are equipped with a heating system combining a gas boiler and a heat pump as heat production units, and radiators as heat emission system. The behaviour of these components, as well as their interaction, are described by underlying equations. Part of these equations is based on the work of Patteeuw (2016).

Gas boiler:

$$\forall j: \dot{P}_j^{GB,sh} \leq \dot{P}^{GB,sh,max} \quad (3)$$

$$\forall j: \dot{P}_j^{GB,sh} \geq 0 \quad (4)$$

$$\forall j: \eta^{GB,sh} \cdot \dot{P}_j^{GB,sh} \leq \dot{Q}_j^{GB \rightarrow RAD,max} \quad (5)$$

With			
	$\dot{P}_j^{GB,sh}$	Power required by gas boiler for space heating	$[kW_{gas}]$
	$\dot{P}_j^{GB,sh,max}$	Maximum power that can be used by gas boiler	$[kW_{gas}]$
	$\eta^{GB,sh}$	Efficiency of gas boiler for space heating	$\left[\frac{kW_{heat}}{kW_{gas}}\right]$
	$\dot{Q}_j^{GB \rightarrow RAD,max}$	Maximum deliverable heat power by gas boiler to considered radiator system	$[kW_{heat}]$

The maximum power that can be used by the gas boiler for space heating, and the efficiency of the gas boiler, are derived from manufacturer data. For the old, partially renovated house, a conventional gas boiler is considered, whereas for the new-built low-energy dwelling – where the radiators operate at lower water temperatures – a more efficient condensing gas boiler is chosen.

The maximum heat power that the radiators can transfer, is defined by the design conditions of the radiator system, and the maximum attainable supply temperature by the gas boiler.

Air-to-water heat pump:

$$\forall j: \dot{P}_j^{AWHP,sh} \leq \dot{P}^{AWHP,sh,max} \quad (6)$$

$$\forall j: \dot{P}_j^{AWHP,sh} \geq 0 \quad (7)$$

$$\forall j: COP_j^{AWHP,sh} \cdot \dot{P}_j^{AWHP,sh} \leq \dot{Q}_j^{AWHP \rightarrow RAD,max} \quad (8)$$

With			
	$\dot{P}_j^{AWHP,sh}$	Power required by AWHP for space heating	$[kW_{el}]$
	$\dot{P}_j^{AWHP,sh,max}$	Maximum power that can be used by AWHP	$[kW_{el}]$
	$COP_j^{AWHP,sh}$	Coefficient of performance of AWHP for space heating	$\left[\frac{kW_{heat}}{kW_{el}}\right]$
	$\dot{Q}_j^{AWHP \rightarrow RAD,max}$	Maximum deliverable heat power by AWHP to considered radiator system	$[kW_{heat}]$

Although aforementioned equations describing the AWHP behaviour seem to be simple, there is one major difficulty that has to be tackled. The maximum power and coefficient of performance (COP) are generally heavily dependent on ambient temperature, water supply

temperature, and compressor frequency, making the optimisation problem highly non-linear. For arguments of computational efficiency, a linear optimisation problem is preferred (Patteeuw, 2016). Since neglecting these dependencies would lead to erratic behaviour of the heat pump, as proven by Verhelst, Logist, Van Impe, & Helsen (2012), an appropriate and well-thought approach is needed here.

To obtain a linear problem, the heat pump is considered to be modulating, but the part-load efficiency as well as the minimum modulation level are neglected. This entails a large simplification, leading to an underestimation of the heat pump performance by neglecting the part-load performance, and an overestimation by neglecting the minimum modulation level. The work of Verhelst et al. (2012) can be used as a first step in justifying this simplification – at least regarding the COP – but extra research is needed to assess the exact influence of this simplification on the decision making process of the controller (MPC), and thus on the heat pump operation.

Neglect of part-load behaviour results in a dependency on ambient temperature and water supply temperature, that still has to be tackled. Since a deterministic simulation model is used as an emulator, based on historic weather measurement data, ambient temperature is a known input. The only remaining variable is thus the temperature of the water leaving the condenser of the heat pump. In order to ensure a linear optimisation problem, this variable should be known beforehand, so that the COP and the maximum power can be calculated prior to solving the optimisation problem. The major difficulty here is that the water supply temperature of the heat pump, which is the intermediate temperature of the water that has left the heat pump but still has to enter the gas boiler, depends on the share of both technologies in the space heating demand. This share is one of the results of the optimisation problem, and cannot be known beforehand. In order to tackle this problem, following methodology is proposed. Figure 2 gives an overview of all important variables, and how they relate to each other.

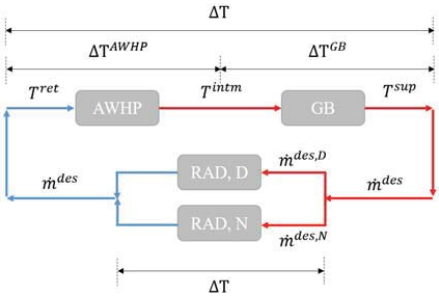

Figure 2 Schematic overview of the heating system in case the air-to-water heat pump and gas boiler are combined to supply heat to the day zone (D) and night zone (N) with radiators.

Based on the results of the optimisation of the reference scenario, being a gas boiler connected to radiators, a first estimation of the heat demand that has to be covered by the hybrid system is obtained. In order to allow the heat pump to shift its operation in time from a DR perspective, the intervals of zero heat demand in the reference case are replaced by the mean heat demand for a time period of one day. Using Equation (9), and assuming that the mass flow rate of water in the system is constant and equal to the design value, the total temperature difference, $\Delta T = \Delta T^{AWHP} + \Delta T^{GB} = T^{sup} - T^{ret}$, can be calculated. Next, the radiator equation, Equation (10), computes the supply temperature to the radiators. Based on ΔT, the return temperature can then also be calculated. Finally, the intermediate temperature of the water leaving the heat pump, T^{intm}, has to be determined, which is done as follows.

Starting from the hypothesis that the heat pump is always maximally utilised, three cases are possible, which are shown in Figure 3:

i) *no heat pump utilisation*: if the return temperature is higher than the maximum temperature that the heat pump can deliver ($T^{AWHP,max}$, generally taken equal to 55°C) the heat pump cannot contribute to space heating, and the intermediate temperature is equal to the return temperature;

ii) *partial heat pump utilisation*: if the return temperature is lower than the maximum temperature of the heat pump, but the supply temperature for the radiators is higher, the intermediate temperature is taken equal to the maximum temperature of the heat pump;

iii) *maximum heat pump utilisation*: if both the return temperature and the supply temperature of the radiators are smaller than the maximum temperature of the heat pump, the intermediate temperature is put equal to the supply temperature.

$$\forall j: \dot{Q}_j^{RAD,Zone,ref} = \dot{m}^{des,Zone} \cdot c_w \cdot \Delta T_j \implies \Delta T_j \tag{9}$$

$$\forall j: \dot{Q}_j^{RAD,Zone,ref} = (UA)_{RAD}^{Zone} \cdot \left(T_j^{sup} - \frac{\Delta T_j}{2} - T_j^{Zone}\right)^n \implies T_j^{sup} \tag{10}$$

With

$\dot{Q}_j^{RAD,Zone,ref}$	Heat power delivered by radiators in corresponding zone (D: day zone, N: night zone) according to reference scenario	$[kW_{heat}]$
$\dot{m}^{des,Zone}$	Design mass flow rate in radiator system of corresponding zone	$\left[\frac{kg}{s}\right]$
c_w	Specific heat of water	$\left[\frac{kJ}{kg\ K}\right]$
ΔT_j	Temperature difference bridged by the heating system ($= T_j^{sup} - T_j^{ret}$)	$[K]$
$(UA)_{RAD}^{Zone}$	Constant overall heat transfer coefficient for radiator system in corresponding zone	$\left[\frac{kW_{heat}}{K}\right]$
T_j^{sup}	Supply temperature to the radiators	$[K]$
T_j^{ret}	Return temperature to the heat pump	$[K]$
T_j^{Zone}	Indoor air temperature in corresponding zone	$[K]$
n	Radiator exponent	$[-]$

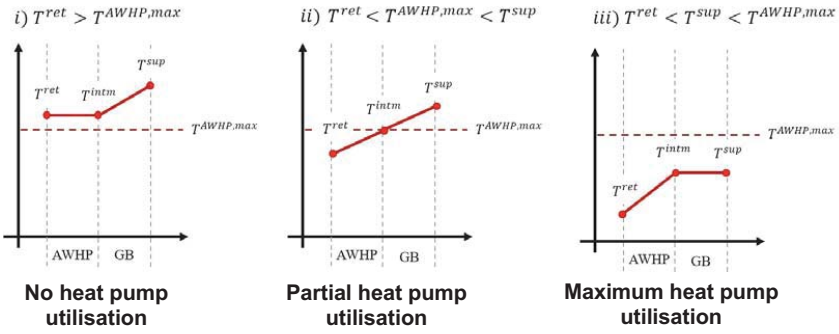

Figure 3 Possible heat pump utilisation, given the supply and return temperature of the heating system and the maximum deliverable water temperature by the heat pump.

Now that all required values are known, the COP and maximum power are calculated for each time step, using Equation (11). To avoid confusion, the nomenclature is in correspondence with Figure 2. The COP correlation is based on the work of Verhelst et al. (2012), but one additional term, containing an arc tangent, is added. This term is introduced to capture the efficiency drop of an air-coupled heat pump around 0°C due to defrosting, as explained in more detail in Section 2.1. The coefficients in the correlations are determined using capacity tables of the selected heat pumps (Daikin Europe N.V., 2018). Their numerical value can be found in Table 3.

$$x = a_0 + a_1 \cdot T_{amb} + a_2 \cdot T_{intm} + a_3 \cdot T_{amb}^2 + a_4 \cdot T_{intm}^2 + \cdots \\ \ldots\ a_5 \cdot T_{amb} \cdot T_{intm} + a_6 \cdot \tan^{-1}(T_{amb}) \quad (11)$$

With			
	x	The required variable, being either the COP or the maximum power of the heat pump	$[-]$ or $[kW_{el}]$
	a_i	The coefficients of the correlation	
	T_{amb}	Ambient temperature	$[K]$
	T_{intm}	Temperature of the water leaving the heat pump	$[K]$

The only remaining undetermined parameter in Equations (6) to (8) is the maximum power that the radiators can accept from the heat pump. As was the case for the gas boiler, this parameter is set by the design variables of the radiator system, and the maximum water temperature that the heat pump can deliver.

Air-to-air heat pump:

For describing the behaviour of an AAHP, Equations (6), (7) and (11) remain valid. In Equation (11), T^{intm} no longer represents a water temperature in this case, but the indoor air temperature. This temperature is again a result of the optimisation problem, but can be approximated by the temperature set-points imposed by the residents to guarantee thermal comfort, see also 2.2.2.3. The coefficients to be used in case of an AAHP can also be found in Table 3.

Table 3 Coefficients in the correlations for the COP and maximum electrical power.

	AIR-TO-WATER HEAT PUMP				**AIR-TO-AIR HEAT PUMP**			
	Dwelling type 1 Altherma hybrid EVLQ08-CV3		**Dwelling type 2** Altherma hybrid EVLQ05-CV3		**Dwelling type 1** Multisplit 4MXS80E		**Dwelling type 2** Split FTXM35M+RXM25M	
	COP	$\dot{\mathbf{P}}^{max}$	**COP**	$\dot{\mathbf{P}}^{max}$	**COP**	$\dot{\mathbf{P}}^{max}$	**COP**	$\dot{\mathbf{P}}^{max}$
$\mathbf{a_0}$	6.428E+00	3.652E-01	7.865E+00	1.013E+00	4.334E+00	2.143E+00	4.274E+00	8.215E-01
$\mathbf{a_1}$	1.783E-01	-3.863E-03	3.903E-01	-3.480E-02	3.593E-02	2.042E-02	6.135E-02	2.858E-03
$\mathbf{a_2}$	-1.248E-01	8.085E-02	-1.473E-01	-9.496E-03	-5.367E-02	1.297E-02	-4.946E-02	3.723E-03
$\mathbf{a_3}$	1.152E-03	-1.260E-05	1.034E-03	7.249E-04	1.738E-03	-5.498E-06	3.493E-03	-5.266E-04
$\mathbf{a_4}$	8.388E-04	-5.456E-04	6.780E-04	5.747E-04	2.431E-04	-3.845E-05	1.044E-04	1.127E-05
$\mathbf{a_5}$	-2.325E-03	8.482E-05	-6.323E-03	-2.888E-04	-9.797E-05	1.568E-05	7.416E-05	5.018E-05
$\mathbf{a_6}$	-5.255E-03	-2.064E-02	-6.600E-02	2.536E-03	2.289E-01	0.000E+00	1.189E-02	8.614E-02

Heat emission system:

When the hybrid configuration combines the gas boiler with an AWHP, only radiators are used, which can be modelled as a thermal capacity, C_{RAD}, at a temperature T_j^{RAD}. Their

behaviour is described by Equation (12), being the linearised equivalent of Equation (10). In addition, Equation (13) is needed to further link the heat sources to the heat emission system.

$$\forall j: C_{RAD}^{Zone} \cdot \frac{T_{j+1}^{RAD,Zone} - T_j^{RAD,Zone}}{\Delta t} = \dot{Q}_j^{heat\ source \rightarrow RAD,Zone} - (UA)_{RAD,lin}^{Zone} \cdot \left(T_j^{RAD,Zone} - T_j^{Zone}\right) \quad (12)$$

With

C_{RAD}^{Zone}	Heat capacity of the radiator in corresponding zone (D: day zone, N: night zone)	$[kJ/K]$
$T_{j(+1)}^{RAD,Zone}$	Radiator temperature in corresponding zone	$[K]$
$\dot{Q}_j^{heat\ source \rightarrow RAD,Zone}$	Heat power delivered by heat source to radiator in corresponding zone	$[kW_{heat}]$
$(UA)_{RAD,lin}^{Zone}$	Constant overall heat transfer coefficient for radiators in corresponding zone[8]	$\left[\frac{kW_{heat}}{K}\right]$
T_j^{Zone}	Indoor air temperature in corresponding zone	$[K]$

$$\forall j: \dot{Q}_j^{RAD,D} + \dot{Q}_j^{RAD,N} = \dot{Q}_j^{heat\ source \rightarrow RAD,D} + \dot{Q}_j^{heat\ source \rightarrow RAD,N} \quad (13a)$$

$$\text{[ref. case or hybrid set-up B]} = \eta^{GB,sh} \cdot \dot{P}_j^{GB,sh} \quad (13b)$$

$$\text{[hybrid set-up A]} = \eta^{GB,sh} \cdot \dot{P}_j^{GB,sh} + COP_j^{AWHP,sh} \cdot \dot{P}_j^{AWHP,sh} \quad (13c)$$

With

$\dot{Q}_j^{RAD,Zone}$	Heat power delivered by the radiators in corresponding zone (D: day zone, N: night zone)	$[kW_{heat}]$
$\dot{Q}_j^{heat\ source \rightarrow RAD,Zone}$	Heat power delivered by heat source to radiator in corresponding zone	$[kW_{heat}]$
$\eta^{GB,sh}$	Efficiency of gas boiler for space heating	$\left[\frac{kW_{heat}}{kW_{gas}}\right]$
$\dot{P}_j^{GB,sh}$	Power required by gas boiler for space heating	$[kW_{gas}]$
$COP_j^{AWHP,sh}$	Coefficient of performance of AWHP for space heating	$\left[\frac{kW_{heat}}{kW_{el}}\right]$
$\dot{P}_j^{AWHP,sh}$	Power required by AWHP for space heating	$[kW_{el}]$

On the other hand, when the hybrid configuration uses an AAHP, the radiators are combined with an air-based system. In this case, Equations (14) and (15) need to be used in addition to Equations (12) and (13b) to capture the emission system's behaviour.

$$\forall j: C_{AIR}^{Zone} \cdot \frac{T_{j+1}^{Zone} - T_j^{Zone}}{\Delta t} = \dot{Q}_j^{AIR,Zone} + (\dots) \quad (14)$$

With

C_{AIR}^{Zone}	Heat capacity of the indoor air in corresponding zone (D: day zone, N: night zone)	$\left[\frac{kJ}{K}\right]$
$T_{j(+1)}^{Zone}$	Indoor air temperature	$[K]$
$\dot{Q}_j^{AIR,Zone}$	Heat power delivered via air in corresponding zone (assumed to be injected in the air node directly)	$[kW_{heat}]$

In Equation (14), focus is on the specific impact of the AAHP on the indoor air temperature. Note that this is not the only factor determining this temperature; all other influencing factors

[8] The value of $(UA)_{RAD}^{Zone}$ used in Equation (12) is not equal to the one used in Equation (10), because of the linearisation.

can be easily derived from Figure 4 and are lumped in the term (…). The more complete and correct expression, explicitly capturing all influences and dependencies, can be found in Equation (16) (Reynders, 2015).

$$\forall j: \dot{Q}_j^{AIR,D} + \dot{Q}_j^{AIR,N} = COP_j^{AAHP,sh} \cdot \dot{P}_j^{AAHP,sh} \quad (15)$$

With

$\dot{Q}_j^{AIR,Zone}$	Heat power delivered via air in corresponding zone (D: day zone, N: night zone)	$[kW_{heat}]$
$COP_j^{AAHP,sh}$	Coefficient of performance of AAHP for space heating	$\left[\frac{kW_{heat}}{kW_{el}}\right]$
$\dot{P}_j^{AAHP,sh}$	Power required by AAHP for space heating	$[kW_{el}]$

2.2.2.2 Building model

The heat power that has to be delivered by the combination of the heat production unit and the heat emission system, is determined by two main factors, the first being the dwelling characteristics and building dynamics presented here, and the second being the boundary conditions, such as occupant behaviour, thermal comfort requirements, weather conditions, energy prices and primary energy factor, elaborated on in Subsection 2.2.2.3.

The dynamic building behaviour is represented by a linear RC-model, shown in Figure 4, and a corresponding state-space model, succinctly presented in vector format by Equation (16). These equations are essential to calculate the instantaneous heat demand and indoor temperatures of the buildings (Reynders, 2015; Patteeuw, 2016).

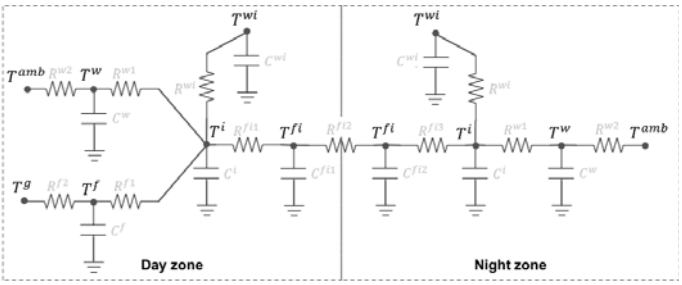

Figure 4 Structure of the 2-zone RC-model, showing all states representing the building structure as a day and night zone, together with the associated thermal capacities and resistances (same indices). Also (part of) the external disturbances are represented. Note that the gain inputs and related parameters are not shown here (adapted from Reynders, 2015).

The model shown in Figure 4 represents a dwelling as two thermal zones: a day zone, consisting of all rooms in which the occupants are active during the day, and a night zone, mainly consisting of bedrooms (Reynders, 2015).

The building structure is characterised by 9 states, being: the temperatures – in both zones – of the indoor air, T_j^i, of the external walls, T_j^w, of the interior walls, T_j^{wi} and of the floor/ceiling, $T_j^{f(i)}$. These states are grouped in the state vector $\bar{T}_j^{sh}$. The inputs for the state space model, represented by the input vector $\bar{U}_j$ in Equation (16), are: the heat power added by the radiators in both zones, and by the air. Finally, the disturbances to the model (which are in fact also inputs), are grouped in the vector $\bar{D}_j$, and can be identified as: the ambient temperature, T_j^{amb}, the ground temperature, T_j^g, the heat gains due to solar irradiation, and the internal heat gains generated by occupants and appliances.

The interaction between all aforementioned variables is expressed by Equation (16). The state space matrices $\boldsymbol{A}_j^{sh}$, $\boldsymbol{B}_j^{sh}$ and $\boldsymbol{E}_j^{sh}$ are based on the thermal resistances and capacitances representing the building structure. Their numerical value for the different dwelling types considered in this study can be found in the work of Reynders (2015).

$$\forall j: \bar{T}_{j+1}^{sh} = \boldsymbol{A}_j^{sh} \cdot \bar{T}_j^{sh} + \boldsymbol{B}_j^{sh} \cdot \bar{U}_j + \boldsymbol{E}_j^{sh} \cdot \bar{D}_j \quad (16)$$

2.2.2.3 Boundary conditions

Occupant behaviour and thermal comfort requirements:

The occupant behaviour determines the internal heat gains and the set-points for the indoor temperature.

In this study, these heat gains and temperature set-points are considered to be fixed, predetermined profiles. The considered profile in this study is based on the StROBe model of Baetens, De Coninck, Jorissen, Picard, Helsen, & Saelens (2015) and Baetens & Saelens (2015). The internal heat gains serve as an input (disturbance) for the state space model. The temperature set-points, on the other hand, determine the minimum temperature bounds $\bar{T}_j^{sh,min}$ for the state vector $\bar{T}_j^{sh}$. Equation (17) is imposed as a hard constraint, thereby guaranteeing that thermal comfort is always met in terms of minimum allowed temperatures.

$$\forall j: T_j^{Zone,min} \leq T_j^{Zone} \quad (17)$$

With	$T_j^{Zone,min}$	Lower bound for indoor air temperature, guaranteeing thermal comfort in corresponding zone (D: day zone, N: night zone)	$[K]$
	T_j^{Zone}	Indoor air temperature in corresponding zone	$[K]$

The general trends in the selected set-point schedule that is used in this work are summarised below. It is important to stress that, since StROBe is based on real-life information, the (stochastic) occupancy profiles are no ideal repetitions of the trends mentioned below, they regularly contain deviations because of the stochastic character.

Table 4 Main trends in considered temperature set-point schedule.

	Set-point high	Set-point low	High set-point period
Day zone	21.5°C	15.5°C	07:00-21:00
Night zone	12°C	12°C	/

For the maximum allowed temperature, an arbitrary value of 50°C is imposed. Because of the minimisation of the effort related to space heating, being either the operational cost or the energy use, the system always tries to stick at the lower temperature bound. Therefore, the upper bound is of minor importance; the only requisite is that it is chosen high enough in order to prevent infeasibilities in warmer periods when indoor temperatures might become rather high (since cooling and solar shading are not considered in this study). Also, it should be different from the lower bound. Indeed, if the zone temperature would always have to be exactly equal to the imposed set-point, the flexibility offered by the heat pump cannot be addressed.

Weather conditions:

Additional factors impacting the heat power demand are the weather conditions, more specifically, the ambient temperature and the solar heat gains. These data are obtained from measurements at the Vliet test building of the KU Leuven Laboratory of Building Physics in

Leuven, Belgium. The reason why measurement data are used instead of typical meteorological year (TMY) data, is twofold. Firstly, since historic energy price profiles are considered, as discussed below, it is important to use weather data of the exact same year (2017 is taken here), to ensure consistency and retention of possible correlations (e.g., electricity prices are generally low when there is a high production by solar photovoltaics (PV) or by wind turbines). Secondly, measurements also contain (more realistic) extreme temperatures, which are not present in TMY data.

Energy prices:

Since one of the objective functions aims at minimising operational cost, also electricity and gas prices are needed to be able to determine the optimal heat power profile.

In a first step, a flat profile for both electricity and gas price is imposed. The exact prices are derived from energy supplier data representative for today's price climate (VREG, 2018; Luminus, 2018; Engie, 2018). Current prices tend to favour the gas boiler over the heat pump, given the significant disproportion between taxes, grid tariffs and VAT charged on electricity and those charged on gas (Claeys & Sourbron, 2017). In order to mitigate this, four different electricity-to-gas price ratios (EGR) are used. Starting from the current price ratio, being 5.4 based on an electricity price of 0.27 EUR/kWh_{el} and a gas price of 0.05 EUR/kWh_{gas} (VREG, 2018), the gas price is relatively increased, until the EGR equals the primary energy factor of electricity. As such, only the energetic difference between electricity and gas remains, rather than an artificial (meaningless) price difference.

In a next step, also time dependency of price profiles is introduced. By progressively exposing consumers to the price variability of the day-ahead market, the heat pump demand response potential is explored. Four different price profile combinations are used:
i) *fix-fix:* a fixed electricity price profile combined with a fixed gas price profile. Here, prices are determined based on energy supplier data, as already described above.
ii) *dn-fix:* a day-night electricity price profile combined with a fixed gas price profile. Again, energy supplier data serve as a reference for the electricity price. The gas price is then determined with the help of the EGR, based on the mean of the day-night profile for electricity.
iii) *var-fix*: a variable electricity price profile combined with a fixed gas price profile. The electricity price is based on the day-ahead price increased by distribution costs. Since this study focusses on the current situation in Belgium, the day-ahead Belpex prices for 2017 are used, being the most recent full-year data available (Entsoe Transparancy Platform). The gas price profile is set up based on the mean electricity price over the previous year (2016 in this case) and the EGR.
iv) *var-var*: a variable electricity price profile combined with a variable gas price profile. In this case, the same reasoning is followed as for the var-fix profile, except that the gas price is based on the mean electricity price over the previous day. Due to the averaging over a whole day, the variations of the gas prices are in general less pronounced than those of the electricity prices.

The resulting price profiles are shown in Figure 5.

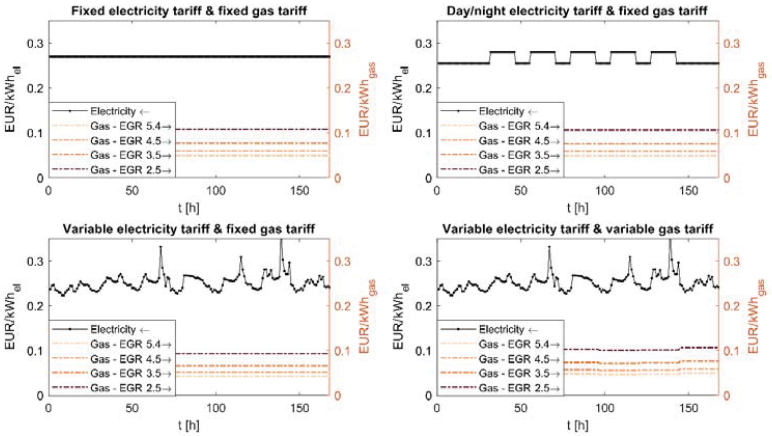

Figure 5 Different energy price profiles perceived by consumers in this study.

Primary energy factor:

The final important boundary condition is the primary energy factor (PEF). This factor represents the electricity supply side mix. In this study, the current prevailing value of 2.5 is used, although discussions are going on to lower this value down to 2.1[9] (Euroheat & Power, 2005-2006; European Parliament, 2016).

3. RESULTS AND DISCUSSION

The scenario analysis, for which the variations are summarised in Table 5, allows identifying the main factors impacting the heat pump utilisation in different hybrid set-ups, consisting either of an AWHP or an AAHP. Firstly, the impact of different objectives, different electricity-to-gas price ratios and different time-varying price profiles on the yearly performance of the hybrid systems, installed in different dwelling types, is investigated. The original heating system, consisting of a gas boiler coupled to radiators, serves as a reference. This reference is used to verify how the flexibility unlocked by the heat pump impacts the primary energy use and the operational cost of the heating system.

In addition, in order to get a more profound insight in the flexibility unlocked, the detailed behaviour of a hybrid heating system, and its exact response to specific external signals – such as the ambient temperature or different price signals – is analysed for one particular illustrative case.

Table 5 Parameters that are varied in the simulations.

Building	Heating system	Objective	EGR	Price profiles
Old, mildly renovated	Gas boiler	Min. cost	EGR1 (5.4)	Fix-fix
New-built, low-energy	Hybrid system with AWHP	Min. energy	↓	Dn-fix
			EGR4 (2.5)	Var-fix
	Hybrid system with AAHP			Var-var

[9] At the time of paper revision the PEF of 2.1 has been approved, however simulations considered a value of 2.5.

3.1 Heat pump utilisation

This section investigates which factors succeed in increasing the heat pump utilisation. Since optimisation of the operation of the hybrid heating system focusses either on the primary energy use or on the operational cost, the variation of these two parameters with increasing heat pump utilisation is also assessed.

Figure 6 depicts the share of the heat pump in the total heat power demand according to the different scenarios described in Table 5.

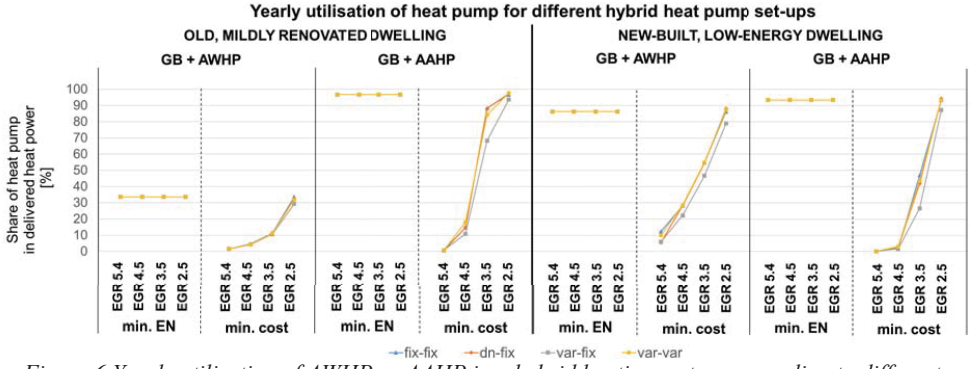

Figure 6 Yearly utilisation of AWHP or AAHP in a hybrid heating system, according to different objectives and different price scenarios, in an old, mildly renovated dwelling, or in a new-built, low-energy dwelling.

Figure 6 shows that minimisation of the primary energy use clearly facilitates the heat pump utilisation. However, a pronounced effect seems to be missing for the AWHP installed in the old dwelling. This is merely a consequence of the technical constraints of the heating system, being the high prevailing water supply temperature of the radiator system, which cannot be delivered by the heat pump. The alternative objective function, minimising operational cost, cannot induce a significant heat pump engagement under current price conditions in Belgium. This changes however when the disproportion between the gas price and electricity price is removed by gradually decreasing the EGR, and thus increasing the gas price compared to the electricity price. When decreasing the value of the EGR until it equals the PEF, the heat pump utilisation converges to the level obtained by minimising primary energy use. Finally, Figure 6 also clearly demonstrates that the specific impact of a certain energy price profile combination is rather limited; all profiles generally induce the same trend. The only profile triggering a slightly differing effect is the var-fix profile, where a variable electricity tariff is combined with a fixed gas tariff based on the mean of the day ahead price of the year before. This is the only profile where the ratio between the electricity and gas price is not always approximately constant. For the considered reference year 2017, the situation is (coincidentally) in favour of the gas boiler, due to a low mean value of the day ahead electricity price for 2016, leading to a relatively low gas price.

As can be seen from Figure 8 and Figure 9, the increasing heat pump participation leads to significant energy savings compared to the reference scenario, where only a gas boiler is in place. For the old, mildly renovated dwelling, relative energy savings of approximately 37% can be achieved in the best case. For the new-built, low-energy dwelling, relative energy savings of almost 30% are possible. These results are promising, certainly given the fact that the applied PEF is on the conservative side. These energy savings are however accompanied by a significant operational cost, which only starts to pay-off for lower EGR values.

When comparing the heating system based on an AWHP and the one using an AAHP, the AAHP clearly outperforms the AWHP in the old house. This is caused by three factors. Firstly, as already mentioned above, the high water supply temperature of the radiator system hampers the engagement of the AWHP, since the heat pump is not able to increase the water temperature above 55°C without considerable performance losses. Secondly, the water supply temperature is subject to far larger variations throughout the year than the indoor temperature. Consequently, for the same degree of heat pump utilisation, the SPF of the AAHP is on average higher than the one for the AWHP, thereby favouring the AAHP. Thirdly, the effect of prices has a huge impact in helping the AAHP compared to the AWHP when minimising the operational cost. Indeed, because of the technical constraints, the gas boiler engagement for the hybrid set-up with the AWHP remains high despite the decreasing EGR. Thereby, the impact of the increasing gas price heavily impairs the added value of this configuration, as is clearly shown in Figure 9. For the new-built house, the differences between the AWHP and AAHP are less pronounced. Although both configurations seem to be equivalent in this case, an important remark has to be made here. Where both hybrid systems are suitable for space heating, which is the focus of this paper, the hybrid system containing an AAHP – or an AWHP if it would be combined with a more appropriate emission system than radiators – also allows cooling. This is becoming an important asset, given the trend of increasing insulation and air-tightness levels, combined with global warming, leading to overheating in summer periods. This is substantiated in Figure 7, where the pronounced overheating in the new-built, well-insulated and air-tight dwelling is clearly observable in case no active cooling is applied. Since the cooling demand strongly correlates with solar radiation, an AAHP coupled to a PV system can serve as a sustainable cooling technology. This is an important factor in favour of the AAHP.

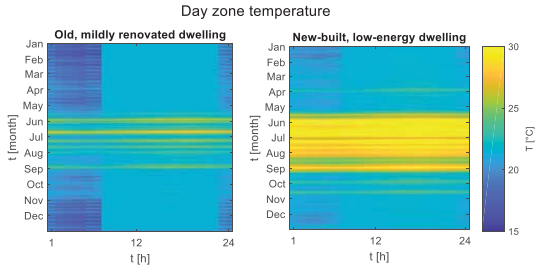

Figure 7 The evolution of the day zone temperature throughout the year for the two dwelling types considered in this study (without active cooling).

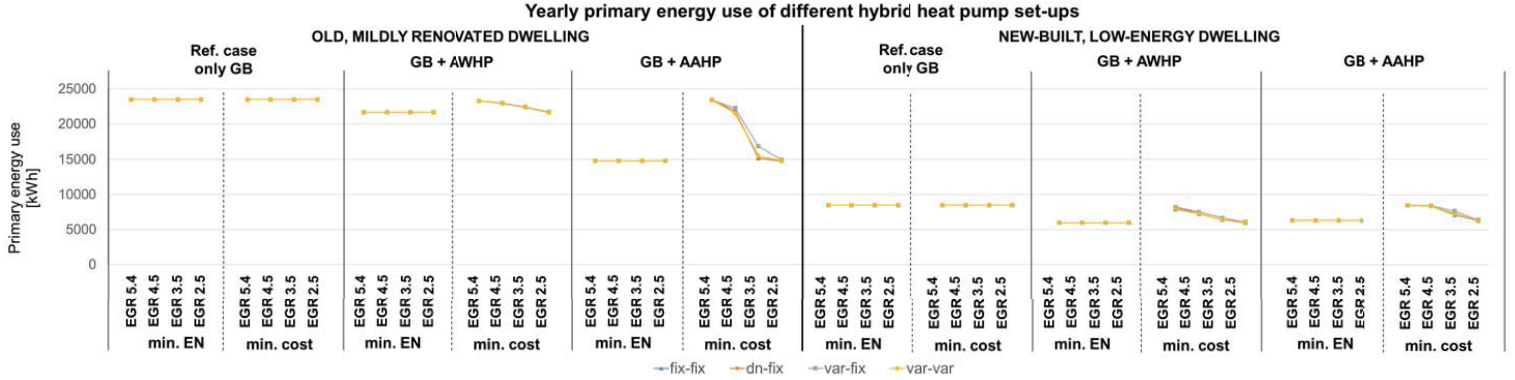

Figure 8 Yearly primary energy use of AWHP or AAHP in a hybrid heating system, according to different objectives and different price scenarios, in an old, mildly renovated dwelling, or in a new-built, low-energy dwelling. The reference heating system that only uses a gas boiler serves as a benchmark.

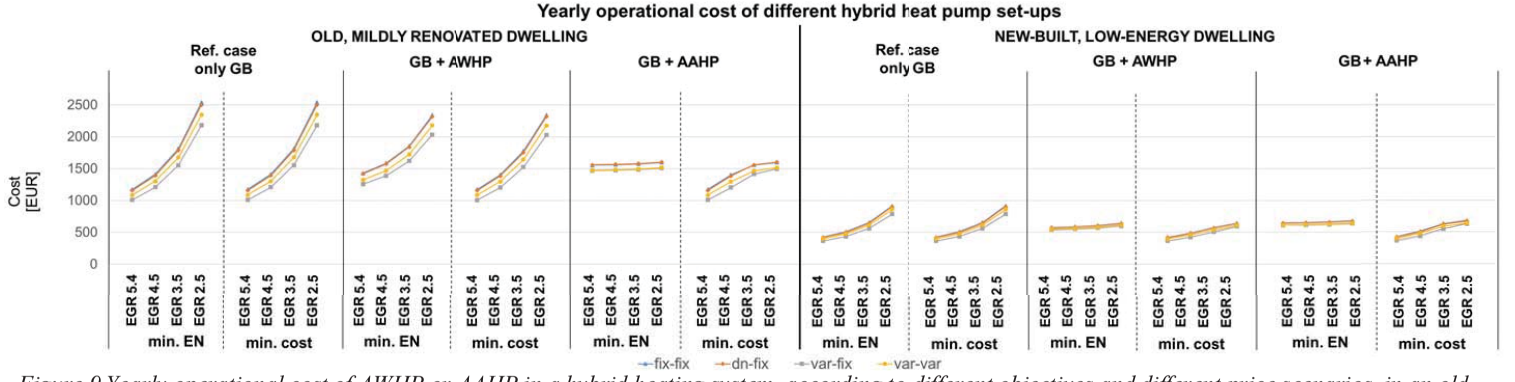

Figure 9 Yearly operational cost of AWHP or AAHP in a hybrid heating system, according to different objectives and different price scenarios, in an old, mildly renovated dwelling, or in a new-built, low-energy dwelling. The reference heating system that only uses a gas boiler serves as a benchmark.

3.2 Detailed behaviour of hybrid system

This section aims at illustrating how the yearly savings on primary energy use and operational cost, described in Section 3.1, are exactly obtained by analysing the unlocked flexibility resulting from heat pump participation. Any combination of parameters from Table 5 could be used as an illustrative case. Here, an AWHP as supplementary heat source in a new-built, low-energy building is considered, subject to a day-night electricity tariff and a fixed gas tariff. The system aims at minimising operational cost.

The operational cost is determined by the multiplication of the energy used by the heating system and the energy prices. Therefore, it is expected that the heat pump tends to shift its operation to periods of high performance and to periods of low electricity costs (being the nights and/or weekend days in case of a day-night tariff). Since the heat pump performance correlates with the ambient temperature, as shown in Equation (11), periods of high performance generally coincide with periods of high outdoor temperatures.

Figure 10 and Figure 11 illustrate that, for a decreasing EGR, the heat pump first starts to substitute the gas boiler in periods of high ambient temperature, and thus high performance. Gradually, the heat pump operation is extended to periods of low electricity prices. Finally, when an EGR of 2.5 is reached, leading to a considerable heat pump engagement, the true added value of the heat pump becomes visible. In this case, the heat pump does not merely substitute the gas boiler anymore, but also starts shifting its operation to the most optimal periods where, initially, the gas boiler was not working.

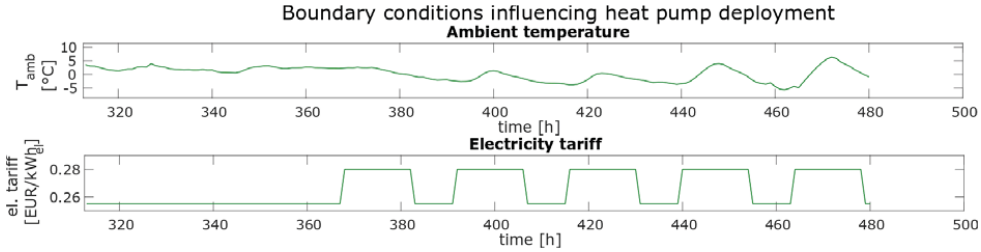

Figure 10 Two important factors influencing the heat pump operation, being i) the ambient temperature, affecting the COP, and ii) the electricity tariff, affecting the operational cost.

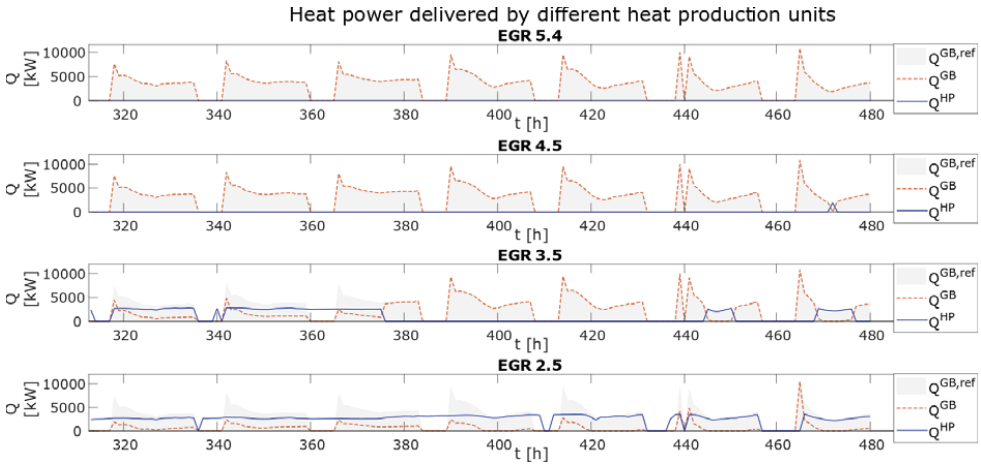

Figure 11 The evolution of the heating profiles delivered by the different heat sources for changing EGR. The grey shaded area is the heating profile when only a gas boiler supplies heat. The red dashed and blue solid curves represent the heating profile of the gas boiler and heat pump respectively.

As can be seen from Figure 12, these effects are made possible by the fact that the zone temperature does not have to strictly follow the set-point, but can deviate from it in a certain predefined temperature band that guarantees thermal comfort.

These results clearly illustrate that hybrid heat pump set-ups can shift operation as a response to external signals, which makes them a suitable technology for demand response.

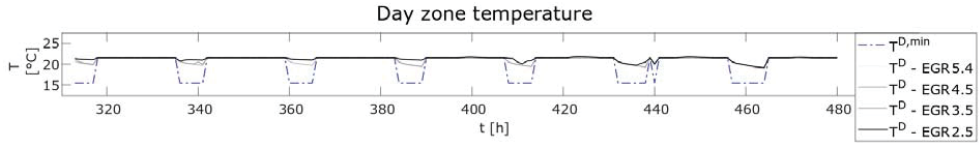

Figure 12 The day zone temperature resulting from the imposed heating profiles shown in Figure 11.

4. CONCLUSION

Two different hybrid heat pump systems, where either an air-to-water heat pump or an air-to-air heat pump serves as a supplementary heat supplier assisting a gas boiler coupled to radiators, are compared for different scenarios. The variable parameters in the scenario analysis are the dwelling characteristics (mainly age class and renovation level), the objective function of the MPC framework optimising the heating system performance, the electricity-to-gas price ratio and the energy price profiles (being a fixed or a variable, market-driven profile).

Of the different objectives, minimisation of primary energy use results in a high heat pump engagement, both for the AWHP and the AAHP. When minimising the operational cost, however, with the current price conditions, the heat pump share in the delivered thermal power is negligible. Lowering the electricity-to-gas price ratio tips the balance, converging to a high heat pump engagement when the price ratio equals the primary energy factor. Changing the specific profile of the electricity and gas price is of minor impact, as long as a rather constant electricity-to-gas price ratio is guaranteed in time. Not only the objective function and the energy prices, but also technical constraints linked to the dwelling characteristics impact the heat pump engagement. This is particularly true in the old, mildly renovated dwelling, where the high water supply temperature of the radiator system impairs the AWHP performance, clearly favouring the AAHP in this case. For the new-built, low-energy house, the differences between the hybrid system based on an AWHP and that based on an AAHP are less pronounced, in case only space heating is considered. However, the cooling potential of the AAHP, together with the overheating tendency of new-built or deeply retrofitted houses with high insulation and air-tightness levels, becomes a great added value.

A detailed analysis of the hybrid system behaviour illustrates that the introduction of a HP (irrespective of the specific type) unlocks flexibility, which can be addressed to shift operation as a response to an external control signal. Therefore, hybrid heat pump set-ups are a good candidate for demand response measures, allowing for savings in – among others – primary energy use or operational cost.

If in hybrid systems the HP would not be sized as a supplementary system, but for full load, MPC allows to further extend the share of heat pump operation, in order to increase the use of RES or decrease CO_2 emissions, e.g. according to a trajectory set by policy makers to reach their goals. This makes both hybrid heat pump systems and MPC enabling technologies for the energy transition.

All results are obtained with an MPC framework using perfect predictions and controlling a building model, not an actual building. Therefore, it has to be stressed that this study is a

theoretical assessment. In order to further consolidate the conclusions given here, a study of the influence of prediction errors, or a field test, are recommended.

ACKNOWLEDGEMENT

The authors acknowledge the support of Daikin Europe in providing access to heat pump performance data. Besides, the advice by Dieter Patteeuw, former post-doctoral researcher at KU Leuven, has been a great help in setting up this study. Finally, the authors are grateful to KU Leuven, for funding this research in the framework of a PhD within the C2 project entitled “Energy storage as a disruptive technology in the energy system of the future”.

REFERENCES

Arteconi, A., Hewitt, N., & Polonara, F. (2013). Domestic demand-side management (DSM): Role of theat pumps and thermal energy storage (TES) systems. *Applied Thermal Engineering, 51*(1-2), 155-165.

Ashrae Handbook. (1977). New-York.

AST, H. (n.d.). *IEA Annex 10 - System simultaion : Thermostactic Valve.* Stuttgart, Germany.

Baetens, R., & Saelens, D. (2015). Modelling uncertainty in district energy simulations by stochastic residential occupant behaviour. *Journal of Building Performance Simulation, 9*(4), 431-447.

Baetens, R., De Coninck, R., Jorissen, F., Picard, D., Helsen, L., & Saelens, D. (2015). OpenIDEAS - an open framework for integrated district energy simulations. *14th Conference of International Building Performance Simulation Association*, (pp. 347-354). Hyderabad, India.

Bouvenot, J.-B., Andlauer, B., Stabat, P., Marchio, D., Flamenta, B., Latoura, B., & Siroux, M. (2014). Gas Stirling engine - CHP boiler experimental data driven model for building energy simulation. *Energy and Buildings 84*, 117-131.

Brandemuehl, M., Gabel, S., & Andersen, I. (1993). A toolkit for secondary HVAC System Energy Calculations. *ASHRAE*.

Braun, J. E.-H. (2006). Assessment of demand limiting using building thermal mass in small commercial buildings. *ASHRAE Transactions*, 112 PART 1, 547-558.

Cabeza, L. F. (2017). Review on sorption materials and technologies for heat pumps and thermal energy storage. *Renewable and Sustainable Energy Reviews, 110*, 3-39.

Candanedo, J., Dehkordi, V., & Lopez, P. (2014). A multi-level architecture to facilitate MPC implementation in commercial buildings: basic principles and case study. *Proceedings of eSim 2014 conference.*

Claeys, B., & Sourbron, M. (2017, May 24). Pas het elektriciteitstarief aan voor meer groene warmte (in Dutch). *De Tijd, Opinion piece*.

Code van goede praktijk voor de toepassing van warmtepompsystemen in de woningbouw (in Dutch). (2004). *Computer software manual*.

Coffey, E. B. (2013). Approximating model predictive control with existing building simulation tools and offline optimization. *Journal of Building Performance Simulation, 6*(3), 220-235.

Commission des Communautés Européennes. (n.d.). *"Etude CIEL" : Maîtrise de la Demande Electrique Campagne de Mesures par usage dans le secteur domestique.*

CSTB. (2012). *Règlementation Thermique 2012 - Règles d'application Th-Bât.* CSTB Edition.

Cyx, W., Renders, N., & Van Holm, M. (2011). *IEE TABULA - Typology Approach for Building Stock Energy Assessment.* Technical report, VITO, Vlaamse instelling voor technologisch onderzoek.

Cyx, W., Renders, N., Van Holm, M., & Verbeke, S. (2011). *IEE TABULA - Typology Approach for Building Stock Energy Assessment.*

Daikin Europe N.V. (2018). Technical data sheets for Altherma EVLQ-CV3, Multisplit 4MXS, Split FTXM35+RXM25. Brussels. Retrieved January 19, 2018, from estranet.daikineurope.com/captab

Deutscher Wetterdienst. (2004). *Testreferenzjahr 2004.* Retrieved 08 02, 2016, from https://www.dwd.de/DE/leistungen/testreferenzjahre/testreferenzjahre.html

Deutsches Institut für Normung. (2016). DIN EN 14825 - Luftkonditionierer, Flüssigkeitskühlsätze und Wärmepumpen mit elektrisch angetriebenen Verdichtern zur Raumbeheizung und -kühlung - Prüfung und Leistungsbemessung unter Teillastbedingungen und Berechnung der saisonalen Arbeitszahl.

Dugaria, S., Moro, L., & Del Col, D. (2015). Modelling heat and mass transfer in a membrane-based air-to-air enthalpy exchanger. *33rd UIT (Italian Union of Thermo-fluid-dynamics) Heat Transfer Conference.*

Elia. (2018, July 6). *Déséquilibre actuel du système*. Retrieved from Elia: http://www.elia.be/fr/grid-data/balancing/desequilibre-actuel-du-systeme

Energiebilanzen AG. (2018). *Evaluation tables from 1990-2017.*

Enertech, ADEME, & Union Européenne. (2008). *Projet REMODECE : Mesure de la consommation des usages domestiques de l'audiovisuel et de l'informatique - Rapport final.*

Engie. (2018, May). Engie Easy Fixed 1y tariffs for electricity and gas. Retrieved May 10, 2018, from https://www.engie-electrabel.be/nl/energie/elektriciteit-gas/prijzen-voorwaarden

Entsoe Transparancy Platform. (n.d.). Day-ahead electricity prices. Retrieved May 10, 2018, from https://transparency.entsoe.eu/transmission-domain/r2/dayAheadPrices/show

Euroheat & Power. (2005-2006). *Ecoheatcool project - Workpackage 3: Guidelines for assessing the efficiency of district heating and district cooling systems.* Technical report, Euroheat & Power. Retrieved March 18, 2018, from https://www.euroheat.org/wp-content/uploads/2016/02/Ecoheatcool_WP3_Web.pdf

European Comission. (2013). *Smarter, greener, more inclusive? Indicators to support the Europe 2020 strategy.* Luxembourg (LU).

European Parliament. (2016, November 19). The primary energy factor for renewables. *Parliamentary questions*. Retrieved June 2, 2018, from http://www.europarl.europa.eu/sides/getDoc.do?type=WQ&reference=E-2016-008892&format=XML&language=EN; http://www.europarl.europa.eu/sides/getAllAnswers.do?reference=E-2016-008892&language=EN

Forsén, M. (2005). *Heat pumps - technology and environmental impact.* Technical report, Swedisch Heat Pump Association, European Heat Pump Association. Retrieved March 12, 2018, from

http://ec.europa.eu/environment/ecolabel/about_ecolabel/reports/hp_tech_env_impact_aug2005.pdf

Gendebien, S., Bertagnolio, S., & Lemort, V. (2013). Investigation on a ventilation heat recovery exchanger: Modeling and. *Energy and Buildings, 62*, 176-189.

Georges, E., Gendebien, S., Bertagnolio, S., Dechesne, B., & Lemort, V. (2013). *Evolution des profils de consommations énergétiques des bâtiments résidentiels en Belgique, suite à l'introduction de nouvelles technologies de chauffage, climatisation et cogénération.* Liège (Belgium).

Händel, C. (2001). Ventilation with heat recovery. *Rheva Journal*.

Henze, G., Felsmann, C., & Knabe, G. (2004). Evaluation of optimal control for active and passive building thermal storage. *International Journal of Thermal Sciences, 43*(2), 173–183.

Henze, G., Le, T., Florita, A., & Felsmann, C. (2006). Sensitivity Analysis of Optimal Building Thermal Mass Control. *Journal of Solar Energy Engineering, 129*(4), 473-485.

Huchuk, B., A. Cruickshank, C., O'Brien, W., & Gunay, H. (2014). Recursive thermal building model training using Ensemble. *Proceedings of eSim 2014 conference.*

Hydro-Québec. (2014, 01 22). *Hydro-Québec demande à ses clients de poursuivre leurs efforts de réduction de la consommation d'électricité en période de pointe et les remercie de leur collaboration.* Retrieved August 01, 2014, from http://cnw.ca/ONjV5

IBPSA-Canada. (2011). *Model predictive control in buildings workshop.* Retrieved September 10, 2014, from http://www.ibpsa.us/conferences

IEA, & IPEEC. (2015). *Building energy performance metrics - Supporting energy efficiency progress in major economies.* Technical report, IEA, IPEEC. Retrieved March 12, 2018, from https://www.iea.org/publications/freepublications/publication/BuildingEnergyPerformanceMetrics.pdf

ISO-1. (2008). ISO 10211:2008 - Thermal bridges in building construction - Heat flows and surface temperatures - Detailed calculations.

ISO-2. (2008, June). ISO 10456: 2008 - Building materials and products - Hygrothermal properties - Tabulated design values and procedures for determining declared and design thermal values.

ISO-3. (2008, April). ISO 13370: 2008 - Thermal performance of buildings - Heat transfer via the groung - Calculation methods.

ISO-4. (2013). ISO 13790: 2013 - Energy performance of buildings - Calculation of energy use for space heating and cooling. *Energy performance of buildings - Calculation of energy use for space heating and cooling*.

ISO-5. (2008). ISO 6946:2008 - Building components and building elements - Thermal resistance and thermal transmittance - Calculation method.

Jespers, K., Al Koussa, J., Dams, Y., Renders, N., & Vingerhoets, P. (2017). *Inventaris hernieuwbare energiebronnen Vlaanderen 2005-2016 (in Dutch).* Technical report, VITO, Vlaams instituut voor technologisch onderzoek. Retrieved March 12, 2018, from

https://www.energiesparen.be/sites/default/files/atoms/files/Inventaris_hernieuwbare_energiebronnen_Vlaanderen_2005-2016_v6.pdf

Kaltschmitt, M., Streicher, W., & Wiese, A. (2013). *Erneuerbare Energien: Systemtechnik, Wirtschaftlichkeit, Umweltaspekte.* Heidelberg: Springer Verlag.

Kelly, G. (1988). Control system simulation in North America. *Energy and Buildings, 10*(3), 193–202.

Keys, W. M., & Crawford, M. E. (1980). *Convective heat and mass transfer* .

Knight, I. (2007). *IEA Annex 42 - The simulation of Building-Integrated Fuel Cell and other cogeneration systems (FC+COGEN-SIM) : Domestic Energy Profiles.* Cardiff (UK).

Koester, S., Falkenberg, M., Logemann, M., & Wessling, M. (2017). Modeling heat and mass transfer in cross-counterflow enthalpy exchangers. *Journal of Membrane Science*, 68-76.

Kummert, M., Leduc , M.-A., & Moreau , A. (2011). Using MPC to reduce the peak demand associated with electric heating. *Model Predictive Control in Buildings Workshop.* Montréal.

Lebrun, J., Ding, X., Eppe, J.-P., & Wasac, M. (1990). Cooling Coil Models to be used in Transient and/or Wet Regimes. Theoretical Analysis and Experimental Validation. *Proceedings of SSB*, (pp. 405-411). Liège.

Lehmann, B., Gyalistras, D., Gwerder, M., Wirth, K., & Carl, S. (2013). Intermediate complexity model for Model Predictive Control of Integrated Room. *Energy and Buildings*(58), 250–262.

Lehrstuhl für Technische Thermodynamik - RWTH Aachen. (2017). SorpLib 3: Adsorption Energy System Library. Aachen.

Leonhardt, C. (2016). *Thermische Speicher mit Phasenwechselmaterialien im Heizsystem.* Aachen.

Leonhardt, C., & Müller, D. (2009). Modelling of Residential Heating Systems using a Phase Change Material Storage System. *Proceedings of the 7th International Modelica Conference.* Como.

Leonhardt, C., & Müller, D. (2010). Latent Heat Storage Devices for Heat Pump and Solar Heating Systems.

Liang, C. (2014). Experiments Investigation of the Parallel-plates Enthalpy Exchangers. *The 6th International Conference on Applied Energy*, (pp. 2699 – 2703).

Luminus. (2018, May). Luminus #BeGreenFix tariffs for electricity and gas. Retrieved May 10, 2018, from https://www.luminus.be/nl/prive/elektriciteit/begreenfix/#tab3; https://www.luminus.be/nl/prive/gas/begreenfix/#tab3

Müller, D., Lauster, M., Constantin, A., Fuchs, M., & Remmen, P. (2016, September). AixLib - An Open-Source Modelica Library within the IEA-EBC Annex 60 Framework. *BauSIM*, pp. 3-9.

Ma, Y., & Borrelli, F. (2011). Hierarchical Predictive Control Energy Efficient Buildings. *Model Predictive Control in Buildings Workshop.* Montreal.

Madson, H., & Holst, J. (1995). Estimation of continuous-time models for the heat dynamics. *Energy and Buildings*, 67-79.

May-Ostendorp, P., Henze, G., Corbin, C., Rajagopalan, B., & Felsmann, C. (2011). Model-predictive control of mixed-mode buildings with rule extraction. *Building and Environment, 46*(2), 428–437.

May-Ostendorp, P., Henze, G., Rajagopalan, B., & Corbin, C. (2013). Extraction of supervisory building control rules from model predictive control of windows in a mixed mode building. *Journal of Building Performance Simulation, 6*(3), 199-219.

Mehrfeld, P. (2016). Reference Building Model. Aachen: E.ON Energy Research Center, Institute for Energy Efficient Buildings and Indoor Climate.

Morari, M., & Lee, J. (1999). Model predictive control: past, present and future. *Computers & Chemical Engineering*, 667–682.

Morisot, O., & Marchio, D. (2002). Simplified Model for the Operation of Chilled Water Cooling Coils Under Nonnominal Conditions. *HVAC&R Research*, pp. 135-158.

Nasif, M. S., Al-Waked, R., Behnia, M., & Morrison, G. (2012). Modeling of Air to Air Enthalpy Heat Exchanger. *Heat Transfer Engineering*, 1010-1023.

Nasif, M., AL-Waked, R., Morrison, G., & Behinia, M. (2010). Membrane heat exchanger in HVAC energy recovery systems, systems energy analysis. *Energy and buildings* , 1833-1840.

Nassif, N., Kajl, S., & Sabourin, R. (2005a). Simplified model-based optimal control of VAV air conditioning system. Montreal: Proceedings of the 9th international building performance simulation association (IBPSA) conference.

Nassif, N., Stainslaw , K., & Sabourin, R. (2005b). Optimization of HVAC control system strategy using two-objective genetic algorithm. *International Journal of HVAC&R Research, 11*(3), 459-486.

Niu, J., & Zhang, L. (2001). Membrane-based Enthalpy Exchanger: material considerations and clarification of moisture resistance. *Journal of Membrane Science*, 179-191.

Oldewurtel, F., Parisio, A., Jones, C., & Morari, M. (2010). Energy efficient building climate control using Stochastic Model Predictive Control and weather predictions. *American Control Conference (ACC)*, (pp. 5100 - 5105). Baltimore, MD .

Oldewurtel, F., Parisio, A., Jonesc, C. N., Gyalistrasa, D., Gwerderd, M., Stauche, V., . . . Moraria, M. (2012). Use of model predictive control and weather forecasts for energy efficient building climate control. *Energy and Buildings* (45), 15–27.

Patteeuw, D. (2016). *Demand response for residential heat pumps in interaction with the electricity generation system.* PhD Thesis, KU Leuven, Belgium.

Prívara, S., Cigler, J., Váňa, Z., Oldewurtel, F., Sagerschnig, C., & Žáčeková, E. (2013). Building modeling as a crucial part for building predictive control. *Energy and Buildings, 56*, 8–22.

Reynders, G. (2015). *Quantifying the impact of building design on the potential of structural storage for active demand response in residential buildings.* PhD Thesis, KU Leuven, Belgium.

Rosato, A., & Sibilio, S. (2012). Calibration and validation of a model for simulating thermal and electric performance of an internal combustion engine-based micro-cogeneration device. *Applied Thermal Engineering 45-46*, 79-98.

Roulet, C.-A., Heidt, F., Foradini, F., & Pibiri, M.-C. (2001). Real heat recovery with air handling units. *Energy and Buildings, 33*(5), 495-502.

Sebai, R., Chouikh, R., & Guizani, A. (2014). Cross-flow membrane-based enthalpy exchanger balanced and unbalanced flow. *Energy Conversion and Management*, 19-28.

Sharma, A., & et al. (2009). Review on thermal energy storage with phase change materials and applications. *Renewable and Sustainable Energy Reviews, 13*(2), 318-345.

Six, D., Desmedt, J., Vanhoudt, D., & Van Bael, J. (2011). Exploring the flexibility potential of residential heat pumps combined with thermal energy storage for smart grids. *21st International Conference on Electricity Distribution*, (pp. 1-4). Frankfurt, Germany.

Stephan, W. (n.d.). *IEA Annex 10 - System simulation : Radiator.* Stuttgart (Germany).

Sturzenegger, D., Gyalistras, D., Semeraro, V., Morari, M., & Smith, R. S. (2014). BRCM Matlab Toolbox: Model Generation for Model Predictive Building Control. *American Control Conference.*

Sweetnam, T., Fell, M., Oikonomou, E., & Oreszczyn, T. (2018). Domestic demand-side response with heat pumps: controls and tariffs. *Building Research & Information*, 1-18.

Swinton, M. C., Moussa, H., & Marchand, R. J. (2001). Commissioning Twin Houses for Assessing the Performance of Energy-Conserving Technologies. Thermal Performance of the Exterior Envelopes of Whole Buildings VIII.

TLK-Thermo GmbH. (2012). *TIL Suite.* Retrieved 11 14, 2018, from https://www.tlk-thermo.com/index.php/de/softwareprodukte/til-suite

Verhelst, C., Logist, F., Van Impe, J., & Helsen, L. (2012). Study of the optimal control problem formulation for modulating air-to-water heat pumps connected to a residential floor heating system. *Energy and Buildings, 45*, 43-53.

Verhelst, C., Sourbron, M., Antonov, S., & Helsen , L. (2011). Towards MPC for office buildings with TABS connected to a GCHP system controller model. *Model Predictive Control in Buildings Workshop.* Montreal.

Viskanta, R., Behnia, M., & Karalis, A. (1977, Nr. 2). Interferometric observations of the temperatur estructure in water cooled or heated from above. *Advances in Water Resources*, pp. 57-59.

VREG. (2018). Hoeveel kost 1 kWh elektriciteit/aardgas? Prijzen voor huishoudelijke afnemers (all in, incl. BTW) (in Dutch). Retrieved May 10, 2018, from https://infogram.com/hoeveel-kost-1-kwh-elektriciteitaardgas-prijzen-voor-gezinnen-all-in-incl-btw-1h9j6qj8ovd54gz

Wang , S., & Xu, X. (2006). Simplified building model for transient thermal performance estimation. *International Journal of Thermal Sciences*(45), 419–432.

Wang, S., & Jin, X. (2000). Model-based optimal control of VAV air-conditioning system using genetic algorithm. *Building and Environment, 35*(6), 471–487.

Wetter, M. (2001). GenOpt® -- A Generic Optimization Program. Proceedings of the 7th IBPSA Conference. Retrieved from http://gundog.lbl.gov/GO/

Wetter, M. (2011). *GenOpt, Generic Optimization Program, User Manual Version 3.1.0.* Retrieved July 01, 2014, from http://gundog.lbl.gov/GO/

Wystrcil, e. a. (2013). Model-based optimization of control strategies for low-exergy space heating systems using an environmental heat source. *13th Conference of International Building Performance Simulation Association.* Chambéry: BS2013.

Zeng, C., Liu, S., & Shukla, A. (2017). A review on the air-to-air heat and mass exchanger technologies for building applications. *Renewable and Sustainable Energy Reviews*, 753-774.

Zhang, L.-Z. (2009). Heat and mass transfer in plate-fin enthalpy exchangers with different plate and fin materials. *International Journal of Heat and Mass Transfer*, 2704-2713.

Questions and Answers:

Kévin Deutz:

How is the heat pump exactly modelled (modulating)? What are the hypotheses in terms of predictions? Is overheating allowed?

Anke Uytterhoeven:

- *The heat pump is assumed to be modulating (i.e., not on/off), and is – as a starting point – characterized by a continuous power function between 0 and 100% (i.e., no minimal power level). Also, at a first stage, no minimal operating times are taken into account.*
- *All predictions are assumed to be perfect.*
- *Overheating is allowed in summer, since no active cooling is incorporated at this point.*

***

M. Kummert:

What is the advantage of an MPC approach vs. a reactive controller "knowing" the current electricity and gas price?

Anke Uytterhoeven:

The main added value of an MPC – that always takes into account a certain prediction horizon for the optimal control – is the inherent capability to anticipate on future events, instead of only reacting to the 'here and now'. For example, if the energy prices will be high in the future at the moment when thermal comfort is required, but are low now, the MPC makes it possible to already start to preheat the building now, in order to avoid very expensive operation at a later point in time. As such, the MPC fulfills the thermal comfort requirements in the most cost optimal way.

***

Freek Van Riet

1) Did you assume the predicted electricity price is correct?

2) Will you look at other hydronic configurations?

Anke Uytterhoeven:

1) In the modelling framework, all predictions (including among others the predicted energy prices, and also weather data and occupancy behavior) are assumed to be perfect.

2) We don't intend to investigate other hydronic configurations at this point. The considered configurations were chosen after extensive discussions with hybrid heat pump manufacturers, in order to ensure that the most practically relevant cases were investigated. It would however be very interesting to compare the chosen configurations with other ones, in order to truly verify (rather than suppose) their practical relevance.

***

Assaad Zoughaib**:**

What is your personal opinion about the role of heat pumps in the future energy system?

Anke Uytterhoeven:

I truly believe that a large scale implementation of heat pumps is the way to go in order to support the energy transition, since this technology is highly energy efficient and sustainable. Moreover it offers flexibility to the electricity system if connected to energy storage. However, I am convinced that it will still take some time and effort, since the discrepancy between the electricity and gas price is currently too high to make the heat pump economically attractive for the end consumer.

***

Vincent Lemort:
In new buildings, DHW need should be predominant or at least quite important. Have you considered heat pump water heaters in connection with gas boilers (the latter ones would be used only for space heating).

Anke Uytterhoeven:

In the proposed modelling framework, the DHW demand is currently fully covered by the gas boiler, so no heat pump water heaters are considered. This can be explained by the fact that the heat pump is assumed to be installed at a later point in time during a renovation, in order to assist – rather than replace – a gas boiler that was already in place. Since this gas boiler was previously sized to be able to cover the peak DHW demand (which is higher than the peak space heating (SH) demand), the heat pump can be sized smaller, and no additional buffer tank is needed. (Note that in practice, a heat pump water heater is indeed mostly combined with a buffer tank. The main reason is that this buffer offers a little bit more operational flexibility, keeping in mind that DHW demand is always prioritized, momentarily disabling the SH operation.)

Using the heat pump for both SH and DHW, and the gas boiler only for SH, could be an interesting concept to be investigated. This would require some adaptations to the system design (sizing of heat pump and gas boiler, and addition of buffer tank), as well as to the control (prioritize the DHW demand over SH), but could also work. However, when thinking about practical relevance, taking into account the current investment and operational costs of a heat pump compared to those of a gas boiler (which is substantially higher in Belgium), a gas boiler is currently still a more attractive option (especially keeping in mind that the COP for DHW production will be lower than for SH, because of the higher water supply temperatures).

***

Sebastian Gonzato:
Isn't the decision that the MPC makes very simple: find out which is cheaper, HP or boiler, then use the cheapest (which would mean optimization could be replaced with a simple logic expression)?

Anke Uytterhoeven:

If the heat pump operation was not flexible, the optimization could indeed be replaced by a simple logic expression for each subsequent time step. However, because the building mass acts as a thermal energy storage, it is possible to decouple the moment when thermal energy is demanded by the end user and the moment when this heat is actually delivered by the heat pump. Consequently, the heat pump electricity consumption becomes flexible and can be shifted in time, in order to anticipate on future events, such as changing electricity prices or changing ambient temperature (influencing the COP). These effects can only be properly taken into account by using an MPC, and thus by making use of optimization.

Heat Pump Ready for Smart Grid – Evaluation of Operation Strategies

Wolfram Stephan[1]*, Arno Dentel[2]

(1) Technische Hochschule Nürnberg, Institut für Energie und Gebäude (ieg), Germany

(2) Technische Hochschule Nürnberg, Energie Campus Nürnberg (encn), Germany

ABSTRACT

For buildings with a photovoltaic-system it is economically worthwhile to increase the self-consumption rate, even to reach a certain degree of autarky. Therefore the self-consumption potential and degree of autarky are important benchmarks when evaluating operation strategies for heat pumps and storage systems.

A single-household building, built in low energy standard, is modelled with TRNSYS and a series of parametric studies are performed.The use of thermal storage can support the operation of an electrical grid or increase the self-consumption of electricity from PV systems.

There are three heat capacities that can be activated: 1. the domestic hot water storage tank, 2. the heating system and the related buffer tank and 3. the thermal mass of the building. Different operating strategies are evaluated. The simulation results show that activating the thermal mass of the building (increasing the room temperatures set points) gives the best benefit. An increase of the self-consumption up to 30% (in February) is possible, but the overall cost benefit is low. As smart grid or PV- orientated strategies always implement a rise of temperature in the heating system or in the building, higher thermal losses and a decrease of the coefficient of performance (COP) is shown.

The results of the simulation studies are transferred to a real project with 8 buildings served with a GCHP and the simulation models are implemented in an emulation test bench.

Keywords: Heat Pump, Smart Grid, Modelling; Optimal Control, TRNSYS Simulation

1. INTRODUCTION

In the recent years, the interest for ground coupled heat pump (GCHP) and for renewable technologies has grown in the field of single-household buildings. Heat pumps, thermal storages and photovoltaic-systems can contribute to the energy transformation of our society. They are able to adapt their consumption to the production of electricity. The components are labelled with “smart grid ready” (BWP 2013). But there is a lack of suitable and simple operation strategies. Building Energy Management Systems (BEMS) are rarely used in single household buildings.

In Germany there are about 40 GW installed PV power. Due to governmental policy the feed in rate decrease rapidly (see figure 1). There again the consumer rate for electricity today is about 25 ct/kWh.

On the other hand, a decrease in investment cost could still encourage individuals to buy PV panels. Moreover, as explained later in this paper, PV panels coupled with specific heating system may lead to benefits, not only from the revenues coming from the sale of electricity, but also from the reduction of electricity consumption during peak loads by storing the surplus energy produced by these panels.

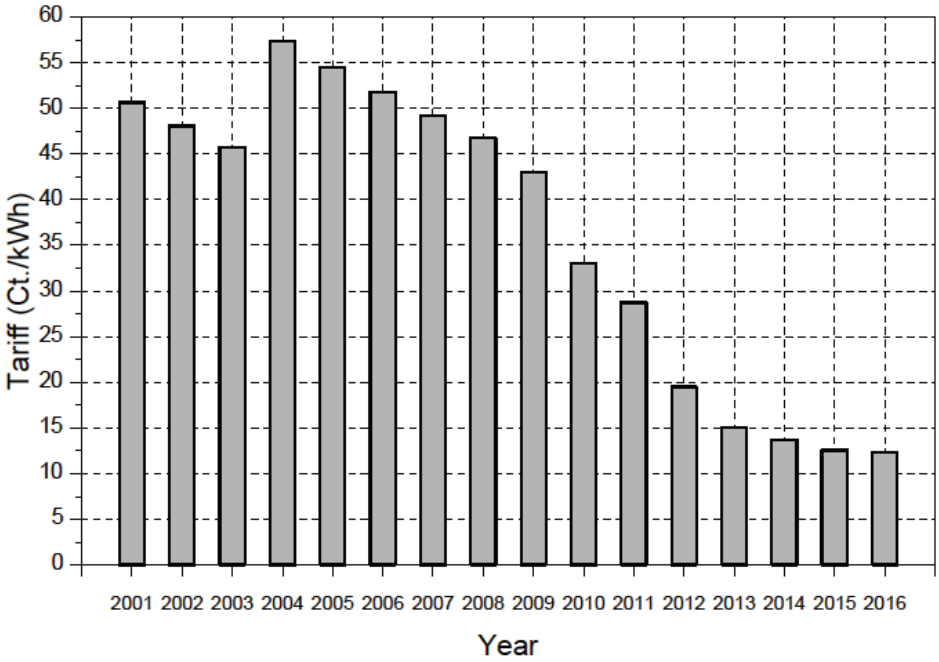

Figure 1: Feed-in tariffs in Germany since 2001

In this paper, we will focus on the heat pump heating system. The heat pump heating system has become popular considerably during the last few years. Indeed, the number of heat pumps installed in Germany has increased from 350,000 in 2008 to 750,000 in 2016.

A parametric study, using TRNSYS as a simulation environment, is performed. The main system configuration (see Figure 2) consists of a heat pump and PV system, serving the electrical consumers, DHW and floor heating system in a single family house.

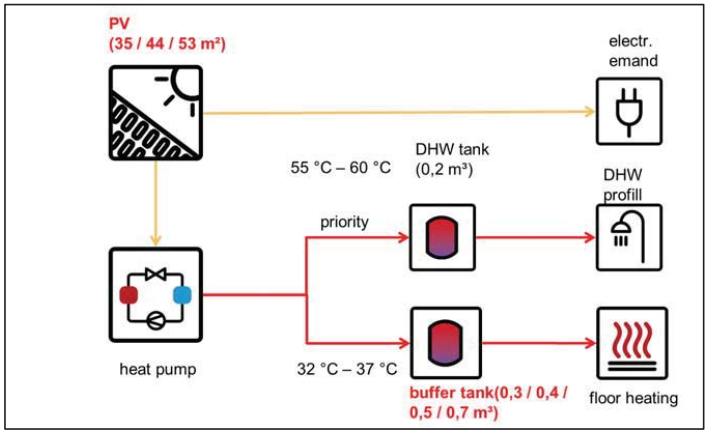

Figure 2: Configuration: heat pump system with PV serving DHW and heating system

Before starting the simulation work some key figures are defined to compare the self - consumption potential and the degree of autarky.

The paper summarizes the work of Conradty (Conradty, 2017), Lorenzi (Lorenzi, 2017) and Dentel & Betzold (Dentel & Betzold, 2017). Conradty worked on the simulation environment and performed the strategy studies. Lorenzi improved the modelling and refined the analysis of the simulation results. The simulation possibilities are used by Dental and Betzold in practical cases.

2. LITERATURE REVIEW

Since 2012 Fisch has published several results optimizing the efficiency of heat pump and PV system with buffer storages (Fisch et al., 2017). This work is mostly inspired by the work of G. Hausladen. He investigated the load management potential considering the heat storage into the building structure. He assessed the influence of several factors such as the type, the mass and the insulation of the building and the heating system (Hausladen, et al., 2017). The load management potential of buildings are further evaluated by Auer (Auer, et.al. 2017).

Both of the following studies assess the self-consumption potential on the basis of the price of electricity. Although this aspect is not taken into account in this work, it is interesting to get an overview of the existing approaches. E. Georges et al. assessed the implementation of a method for an optimal load management (Georges et al., 2016). They analysed the load matching potential (between consumer electricity consumption and local electricity production) and the influence of retail and buy-back tariff by aiming to minimize the electricity cost for the end-user. They obtained significant improvement regarding the load matching and the cost saving.

D. Vanhoudt et al. searched on peak-shaving by the mean of self-consumption (D. Vanhoudt et al., 2013). They implemented a market based multi-agent control system where every device is represented by an agent which consumes or produces electricity and all these needs are organized according their priority. They managed to increase the self-consumption.

Franco and Fantozzi report on experimental analysis of a self consumption strategy for residential building by the integration of PV system and geothermal heat pumps (Franco, A. and Fantozzi, F. (2016b).

Operating strategies are evaluated in the projects SOL2Heat (2017) and PV KWK (2016) and Seiffert reports on the evaluating of thermal comfort in buildings with sophisticated operation strategies (Seiffert. Et.al. 2016).

3. SMART GRID STRATEGIES

Analyzing the PV electricity generation and the electricity consumption shows a discrepancy. On sunny days there is a surplus, the PV production exceed the electrical consumption (see Figure 4).

In a preliminary study a simple smart grid strategy (see Figure 3) is investigated (Conradty, 2018). The set temperatures, i. e. of the room thermostats, are increased if there is a surplus.

With this first strategy (here: increase of room temperature set point by 2 K) a significant reduction of the PV surplus is achieved (see Figure 5).

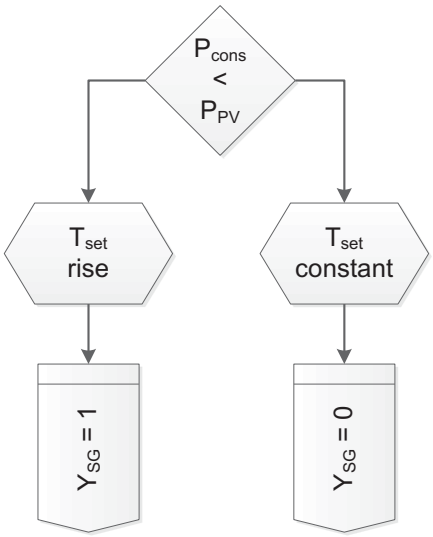

Figure 3: Principle of simple smart grid strategy (Type A)

Mathematically this strategy can be expressed as:

$$T_{set} = T_{set,basic} + \Delta T_{Ceil}\left(\frac{P_{PV} - P_{cons}}{2|P_{PV} - P_{cons}|}\right) \textit{(Equation 1)}$$

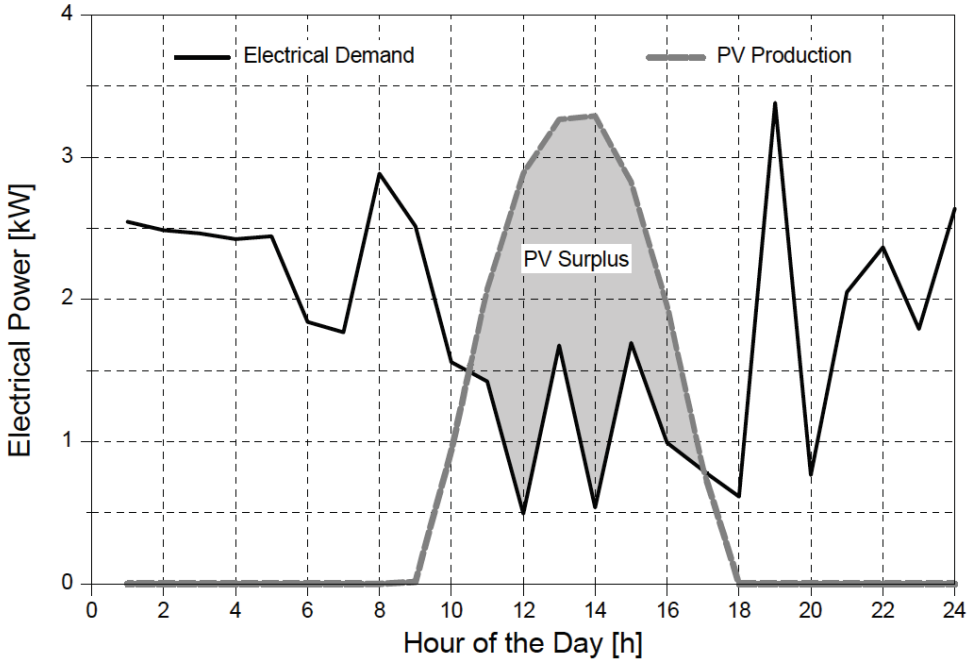

Figure 4: PV production and el. demand, no smart grid strategy, simulation results for a typical sunny day in February.

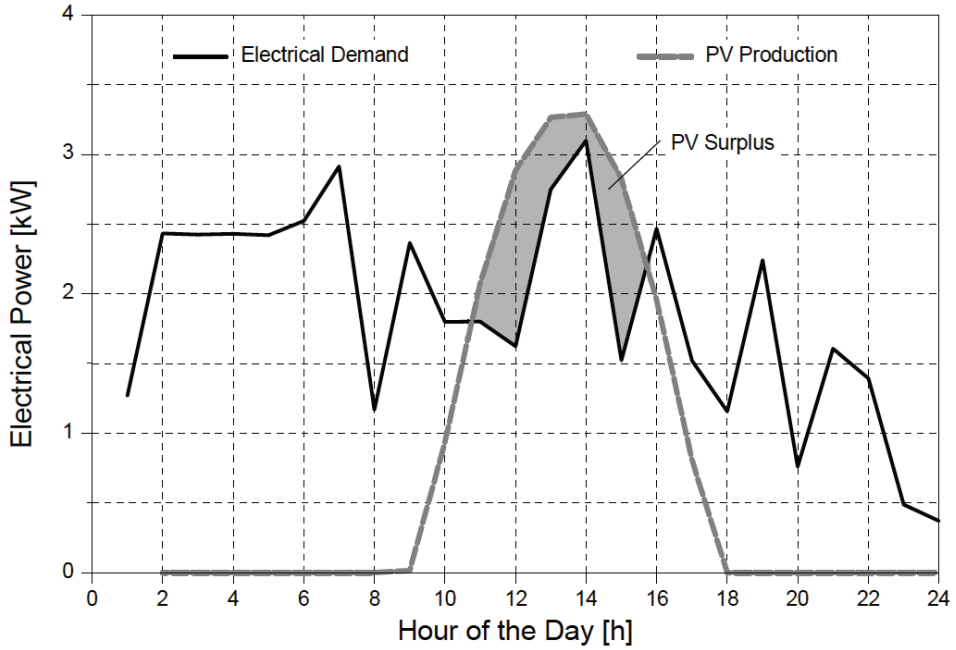

Figure 5 PV production and el. demand, with smart grid strategy, simulation results for a typical sunny day in February.

Results of this preliminary study are shown in Table 1. Here, the room temperature set point is Increased by 2 K is, if a Smart grid Signal occurs (SG_1.1). As the Total demand decrease, the supply cover factor increase.

Table 1: Preliminary results evaluating smart grid strategies

January - February		**Base Case no Smart Grid**	**Smart Grid Case SG_1.1 ↑ 2 K**
Total el. demand	W_{cons}	2049,9 kWh	↓ 10,8 kWh
Feed into the grid	$W_{grid,in}$	244,7 kWh	↓161,8 kWh
Demand from the grid	$W_{grid,dem}$	1681,1 kWh	↓172,5 kWh
PV Self Consumption	W_{sc}	368,8 kWh	↑ 161,8 kWh
Supply cover factor (self-consumption)	γ_s	60,1 %	↑26,4 %
Demand cover factor (autarky)	γ_d	18,0 %	↑ 8,0 %

3.1 Self-Consumption and Autarky

The electricity consumption P_{cons} and the electricity production P_{PV} are the two rates which are evaluated. The electricity rates are usually evaluated in time steps of 15 minutes. The simulation time step is 1 minute.

The following definitions (see Vanhoudt, et.al (2014)) are used:

PV-self-consumption:

$$W_{sc} = \sum \min(P_{cons,} P_{PV}) \cdot dt_{timestep} \qquad \textit{(Equation 2)}$$

Degree of PV self-consumption

The degree of PV self-consumption is expressed with the **PV supply cover factor γs.**

$$\gamma_s = \frac{\sum \min(P_{cons,} P_{PV})}{\sum P_{PV}} \qquad \textit{(Equation 3)}$$

Degree of autarky

The degree of autarky is expressed with the **demand cover factor**

$$\gamma_D = \frac{\sum \min(P_{cons,} P_{PV})}{\sum P_{cons}} \qquad \textit{(Equation 4)}$$

Load Management Potential (see Hausladen et.al. (2015))

$$LM - Potential = If(P_{PV} > P_{cons}) \frac{\sum \min(P_{PV}, P_{cons})}{\sum P_{cons}} \quad (Equation\ 5)$$

The load management potential factor is similar to the demand cover factor, limited to the time when is the Smart Grid signal on. The increase of the load management potential gives an idea of the possibility to shift the electrical load into the period of PV-surplus.

3.2 Strategies and Parameters Evaluated

3.2.1 Simple Smart Grid Strategies (Type A)

Based on the simple strategy described before a parametric study on 9 cases is performed:

- The room temperature set point is increased by a step of ΔT 2K or 4K.
- The heating system supply temperature is increased by ΔT 5K
- The DHW tank temperature is increased by ΔT 5K or 10K
- The heating buffer tank temperature is increased by ΔT 5K /or 10K

Table 2: Overview on parameters for smart grid strategy

SG Strategy	room-temperature	supply-temperature	buffer temperature DHW	h-buffer
SG1.1	+ 2K			
SG 1.2	+ 4 K			
SG 1.3	+ 2 K	+ 5 K		
SG 2.1				+ 10 K
SG 2.2	+ 2 K	+ 5 K		+ 10 K
SG 2.3	+ 2 K	+ 5 K		+ 5 K
SG 3.1			+ 10 K	
SG 3.2	+ 2 K	+ 5 K	+ 10 K	+ 10 K
SG 3.3	+ 2 K	+ 5 K	+ 5 K	+ 5 K

3.2.2 Improved Smart Grid Strategy (Type B)

The improved method is based on the monthly average power consumption. To achieve this, we assume that we know approximately the monthly electricity consumption of the system. The consumption could be assessed either with a simulation program (as it is done here) or according to the building power consumption of the previous years (for an existing building). The method is described with the following equation:

$$T_{set} = T_{set,basic} + \Delta T_{Ceil}\left(\frac{P_{PV} - P_{mean,i}}{2\left|P_{PV} - P_{mean,i}\right|}\right) \quad \textit{(Equation 6)}$$

Where $P_{mean;i}$ is the mean power consumption which has been assessed beforehand for the month i, with I ε P { january, february}. Here, the mean power consumption is calculated according to the basic case. The set point temperatures depend now on the PV power production and the mean power consumption.

$$\begin{aligned}
&\text{if } P_{PV} < P_{meana,i} \text{ then}\\
&\quad T_{set} = T_{set,basic}\\
&\text{if } P_{PV} > P_{meana,i} \text{ then}\\
&\quad T_{set} = T_{set,basic} + \Delta T\\
&\text{endif}
\end{aligned} \quad \textit{(Equation 7)}$$

The characteristic of this method is that the control depends on a fixed value (P_{mean}), contrary to the method A, where the temperature control depends on the real-time power consumption, which is highly variable.

4. EXAMPLE REISDENTIAL BUILDING WITH GCHP

The effects of the smart grid strategies are shown for a typical new single family house. The building is equipped with a mechanical ventilation system with 75% heat recovery, a ground source heat pump and floor heating system.

4.1 The Building

Table 3: Basic information on the building

Type of use	single-family house
Building standard	ENEV 2014
Building structure	two floors
Type of roof	lean-to roof
Dimensions	6.8 m _ 13.25 m
Gross surface area	174.3 m^2
Cubic volume	600.4 m^3
Mean heat transfer coefficient	0,38 W/m^2K
Specific heating demand	50 kWh/m^2a

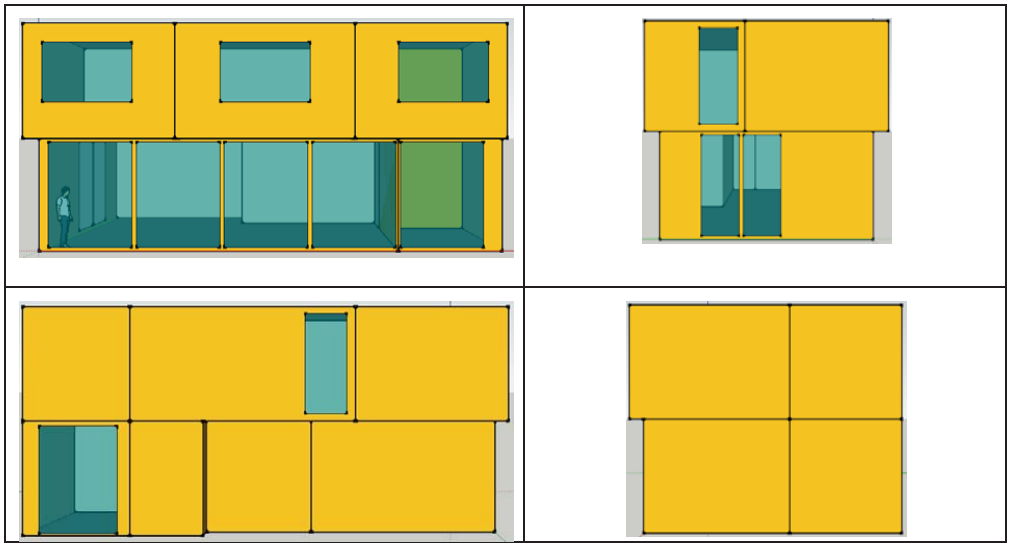

Figure 6: Building view (south, west, north and east)

4.2 The System

For heating a ground source heat pump is used, serving a floor heating system (system temperature: 32°/28°C).

For domestic hot water a 200 liter buffer tank is used and for the heating system a 350 liter buffer tank ensures a minimum running time of the heat pump.

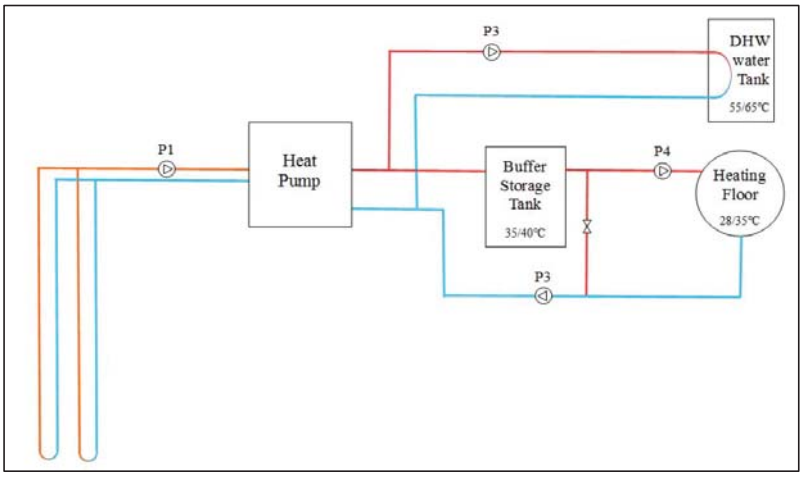

Figure 7: Heating system scheme

4.2.1 Heat Pump System

A one stage heat brine/water heat pump is used.

Type	brine-water
Manufacturer	Dimplex
Brine (concentration)	Monoethylene glycol (25%)
Brine density	1.053 kg/m^3
Brine specific heat	3.8 kJ/kg.K
Min-max flow rate (water side)	0.9 - 1.9 m^3/h
Min flow rate (brine side)	2.6 m^3/h
Heat output (B0/W35)	10.9 kW
COP (B0/W35)	4.91
Electrical consumption (B0/W35)	2.22 kW
Min. pause time	5 minutes
Max no. of starts per hour	3

Figure 8: Heat pump Parameters

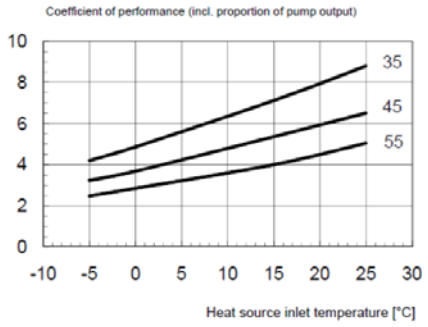

Figure 9: Heat pump COP

The heat pump is coupled with vertical ground heat exchanger in which the brine circulates. Both sides of the heat pump (brine and water sides) are closed loops. There are two boreholes; each 90 m depth. (Double U-Pipe)

4.2.2 Photovoltaic System

The PV panels are implemented in TRNSYS according the data of existing PV panels (see Table 4.

Table 4: PV data

PV panels manufacturer	Heckert Solar
Type	NeMo 60 P 250
Cell type	Polycrystalline (polysilicon)
No. cell per module	60
Module dimensions	991 x 1640 mm
Max. Power (per module)	250 W_p (Standard Test Conditions) 179 W_p (Nominal Operating Cell Temperature)
Module efficiency	15.4 %
Short circuit current I_{sc}	8.79 A (STC) 7.07 A (NOCT)
Open circuit voltage V_{oc}	38.32 V (STC) 34.96 V (NOCT)
Maximum System Voltage VDC	1000 V
Inverter	Kostal Piko 12
Max DC current	36 A (2 x 18 A)
Max voltage VDC	1000 V
Number of modules	48
Total surface area	78.01 m^2
Max. Power	12 kW_p (Standard Test Conditions) 8.59 kW_p (Nominal Operating Cell Temperature)

4.2.3 Basic Control Parameters

Heat pump control:

The heat pump minimum running time is 6 minutes. The basic control is defined with the following parameters:

- The heat pump is switched ON if:
    - The warm water flow rates in the floor heating circuit is non-zero (detailed further below) AND if:
        - The temperature of the buffer tank falls below 35 °C until it exceeds 40 °C.
        - The temperature of the DHW tank falls below 55 °C until it exceeds 65 °C.
- The DHW heating has priority before the buffer tank heating operation.

DHW-Buffer Tank

The temperature is maintained between 55 °C and 65 °C. This is to prevent the proliferation of Legionella bacteria which can cause Legionnaires disease (type of pneumonia).

Supply Temperature

The system is operated according to outside temperature with a max. system temperature of 35°C/28°C at –15 °C ambient temperature.

Floor Heating System

The warm water circulates through the pipes of the floor heating of a given room, if:

- The outside temperature falls below 8 °C (heating limit temperature)

AND

- The air temperature of the room falls under a certain threshold.

The water runs within the pipes until the set point temperature T_{set} of the room is reached. It works basically according an on/off hysteresis control. The set point temperatures are shown in the Table 5.

Table 5: Room set point temperatures

Rooms	Lower / Upper threshold temperatures
Living room	20 / 20.5 °C
Staircase	15 / 15.5 °C
WC	20 / 20.5 °C
Entrance	15 / 15.5 °C
Bathroom	24 / 24.5 °C
Bedroom 1	20 / 20.5 °C
Bedroom 2	20 / 20.5 °C
Coridor	15 / 15.5 °C
Study	20 / 20.5 °C

5. TRNSYS MODEL

A rather sophisticated TRNSYS model is used to simulate the building and the HVAC system.

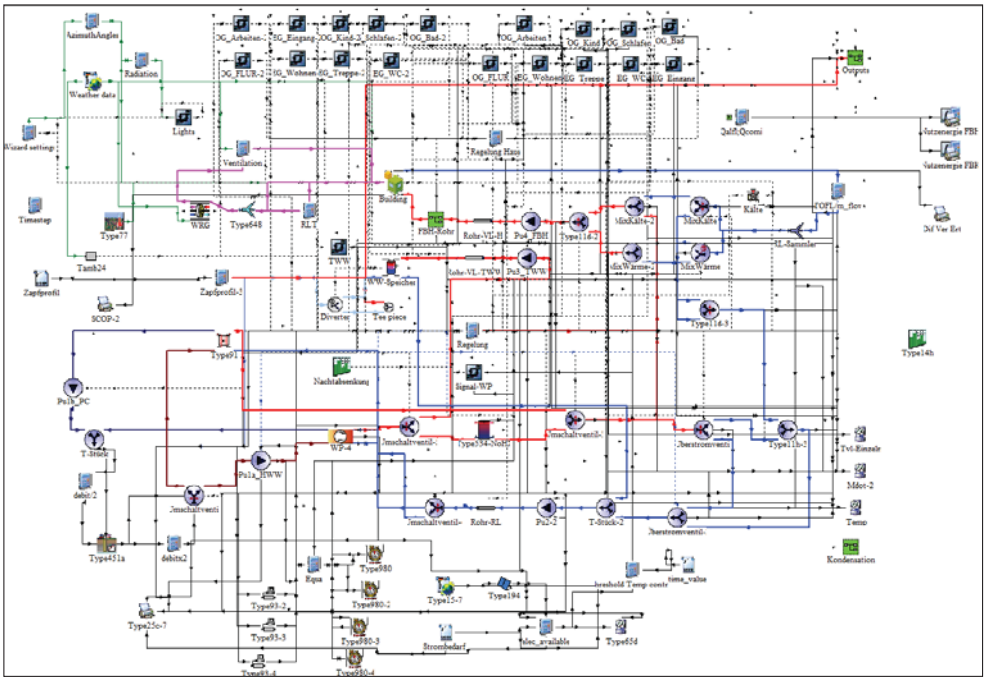

Figure 10: TRNSYS Simulation Studio (single family building with PV, heat pump and Smart Grid operating strategies

In particular some of the Types used are listed in Table 6.

Table 6: Types used in TRNSYS simulation

Component	TRNSYS Type	Remark
Stratified HW tank	Type 64	
Buffer Storage	Type 543	
Ground source heat Exchanger (Borehole)	Type 451a	Instead of Type 557a[10]
Heat Pump	Type 401	Type 4010[11]
Multizone Building	Type 56	
Floor heating	active layer in Type 56	

[10] see (Lorenzi 2017)
[11] see Project Herzobase (Dentel & Betzold 2017)

6. RESULTS

Rising the room temperatures during surplus of PV results in better cover factors, considering self-consumption and autarky (see Table 7).

The simulation results are shown for a 2 period of two month (Jan. –Feb.) and for a cold (29, Jan, - 2. Feb.) and medium (25. March – 31. March) period.

Table 7: Comparision of energy flow and smart grid potentials for SG_1.1, SG_1.2, simulation results

January - February		**Base case**	**SG_1.1 ↑ 2 K**	**SG_1.2 ↑ 4 K**
Total el. demand	W_{cons}	2049,9 kWh	↓ 10,8 kWh	↓6,2 kWh
Feed into the grid	$W_{grid,in}$	244,7 kWh	↓161,8 kWh	↓ 180,8 kWh
Demand from the grid	$W_{grid,dem}$	1681,1 kWh	↓172,5 kWh	↓ 187,0 kWh
PV Self Consumption	W_{sc}	**368,8 kWh**	**↑ 161,8 kWh**	**↑ 180,8 kWh**
Supply cover factor (self-consumption)	γ_s	**60,1 %**	**↑26,4 %**	**↑ 29,5 %**
Demand cover factor (autarky)	γ_d	**18,0 %**	**↑ 8,0 %**	**↑ 8,9 %**
29. Jan. - 4. Feb.				
Total el. demand	W_{cons}	317,3 kWh	↓ 2,0 kWh	↓ 2,7 kWh
Feed into the grid	$W_{grid,in}$	28,0 kWh	↓ 20,0 kWh	↓ 20,6 kWh
Demand from the grid	$W_{grid,dem}$	270,2 kWh	↓ 22,1 kWh	↓ 23,4 kWh
PV Self Consumption	W_{sc}	**47,2 kWh**	**↑ 20,0 kWh**	**↑ 20,6 kWh**
Supply cover factor (self-consumption)	γ_s	**62,7 %**	**↑ 26,7 %**	**↑ 27,5 %**
Demand cover factor (autarky)	γ_d	**14,9 %**	**↑ 6,4 %**	**↑ 6,7 %**
25. March - 31. March				
Total el. demand	W_{cons}	164,7 kWh	↑ 5,6 kWh	↑ 2,0 kWh
Feed into the grid	$W_{grid,in}$	196,3 kWh	↓ 24,4 kWh	↓ 35,4 kWh
Demand from the grid	$W_{grid,dem}$	104,9 kWh	↓ 18,8 kWh	↓ 33,5 kWh
PV Self Consumption	W_{sc}	**59,8 kWh**	**↑ 24,4 kWh**	**↑ 35,4 kWh**
Supply cover factor (self-consumption)	γ_s	**23,3 %**	**↑ 9,6 %**	**↑ 13,9 %**
Demand cover factor (autarky)	γ_d	**36,3 %**	**↑ 13,1 %**	**↑ 20,8 %**

The difference between an increase of the room temperature by 2 K versus 4 K is shown,

For the cold period the differences between the two cases are small. Here the PV power in relation to the demand is low already in the base case a great amount of the PV- energy is covered (62,7%). Better Conditions for loads management are in medium periods.

Supply cover factors (self consumption of PV) of over 80% and an autarky of over 25% are possible in our case. The results could not be generalized, as the cover factors depend on the sizing of the systems.

6.1 Evaluating of the Smart Grid Strategies

6.1.1 Increase of Operative Temperature

The smart grid strategies influence the thermal comfort. The operative temperature, according to DIN ISO 7730, is used as comfort indicator.

The rises of mean daily operative temperatures are compared in Figure 11 for the smart grid strategies shown in Table 2.

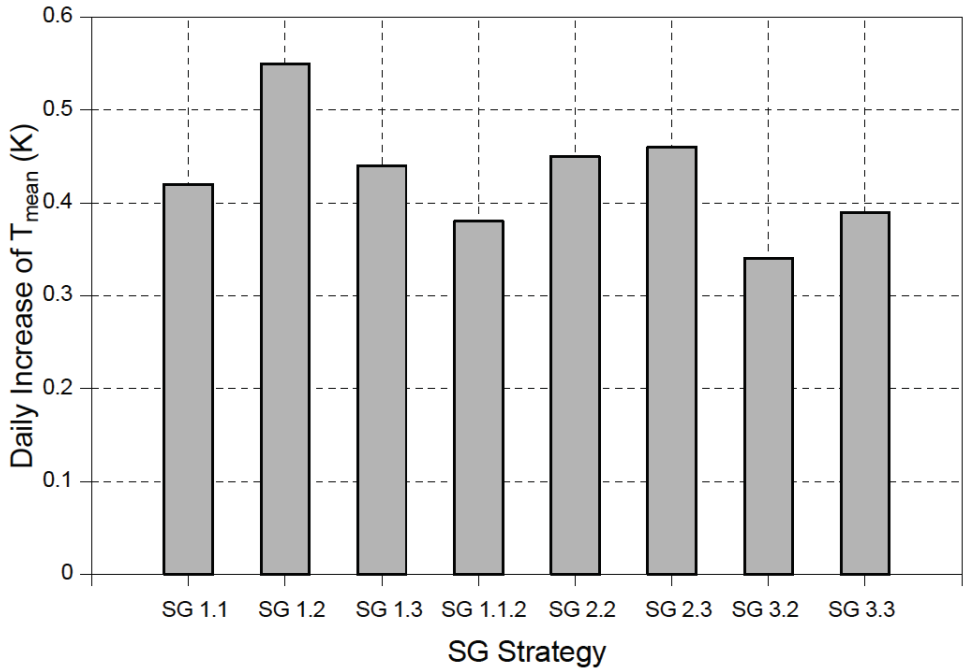

Figure 11: Increase of mean daily operative temperature, comparison of different smart grid strategies, evaluating period Jan.- Febr.

The biggest effect is for SG 1.2 (ΔTset = 4 K), in comparison to SG 1.1 (ΔTset = 2 K) the temperature increase is only 0,13 K . The maximum temperatures are about 0,5 K higher.

6.1.2 Load Management Potential

The increase of the load management potential gives an idea of the possibility to shift the electrical load into the period of PV-surplus.

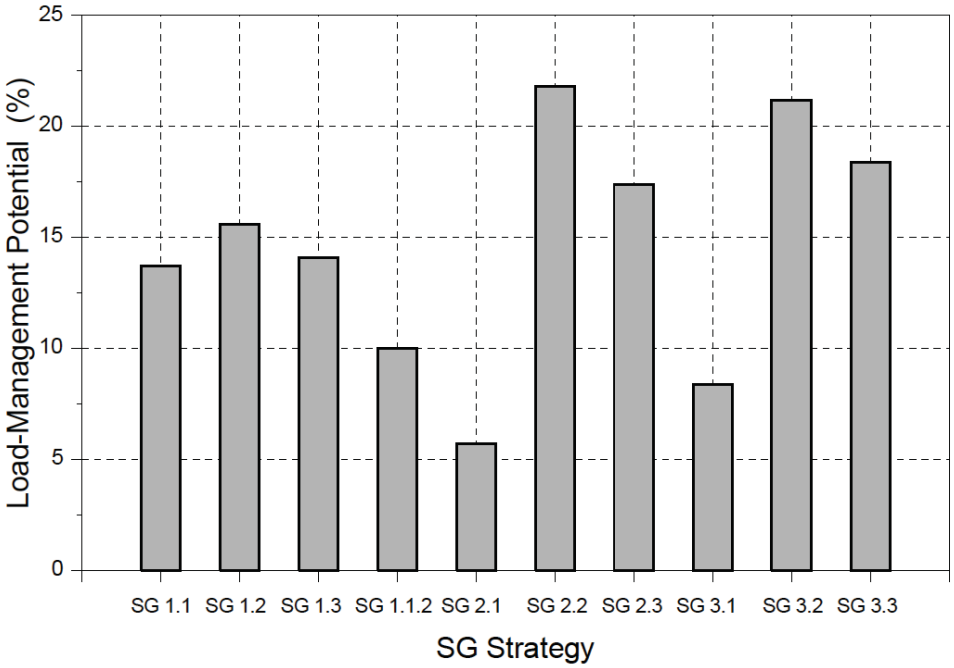

Figure 12: Load-Management potentials for smart grid strategies, evaluating period Jan. - Febr.

The strategies (SG_2.2, SG_2.3, SG_3.2 und SG_3.3) with a combination of room temperature, buffer temperature and system temperature rise have the biggest potential.

The rise of the supply temperature (SG 1.3) has a small effect.

A room temperature set point increase of 4K (SG1.2) shows also a small effect. The temperature rise is limited due to the heating capacities of the floor heating system.

6.1.3 Economical Aspects

Beside the load management the financial aspects have to be evaluated.

Smart grid rates for electricity are only available for consumers over 10 MWh/a. For single family house consumers flat rates are common.

Electrical Rates:

Standard rate: 27,75 [Cent/kWh]

Heat pump rate: 20,01 [Cent/kWh]

(total heating system, inclusive circulation pumps)

Feed in rate: 12,31 [Cent/kWh] (03/2017)

Table 8 shows the total costs and the savings applying a smart grid strategy (see also Figure 13).

Table 8: Electrical consumption costs and savings, evaluating period Jan. - Febr.

Smart Grid Strategy	Total costs [€]	savings [€]
SG_1.1	320,7	14,6
SG_1.2	320,1	15,2
SG_1.3	319,9	15,4
SG_1.1.2	321,6	13,7
SG_2.1	349,0	-13,7
SG_2.2	355,4	-20,1
SG_2.3	330,7	4,6
SG_3.1	345,9	-10,6
SG_3.2	345,6	-10,3
SG_3.3	330,4	4,9

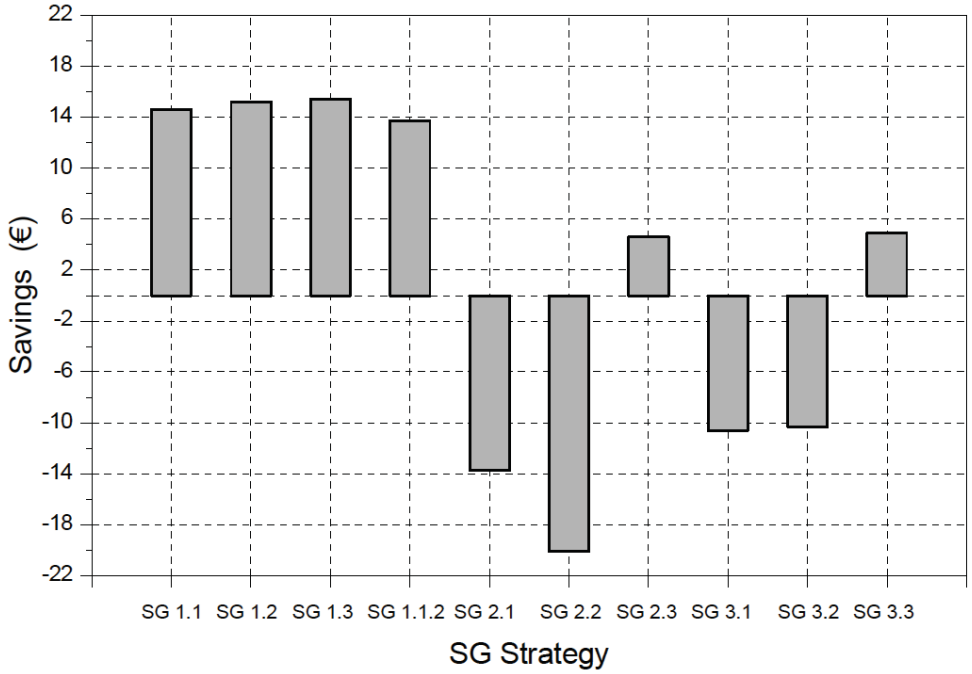

Figure 13: Savings due to smart grid strategies

All strategies (SG_2.1, SG_2.2; SG_3.1, SG_3.2) who increase the buffer tank temperature by ΔTset 10 K have a negative saving. The rising demand, due to higher temperatures which involves higher losses and a lower COP of the heat pump overrides the load management effect.

6.1.4 Results with the improved Smart Grid Strategies (Type B)

As explained in 3.2.2 an improvement of the simple strategies (of Type A) could lead to better results.

The characteristic of the improved method Type B is that the control depends on a fixed value (P_{mean}), contrary to the method A, where the temperature control depends on the real-time power consumption, which is highly variable. This method implements a weather forecast possibility.

The setback of strategy Type A is shown in Figure 14 (left). As soon as solar radiation increases the electrical consumption the set points are increased and the heat pump starts operating.

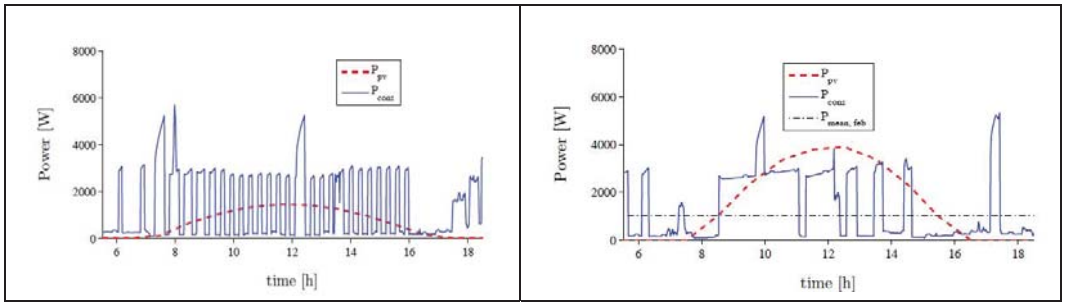

Figure 14: El Power consumption P_{cons} and PV production P_{PV}, Strategy type A (left) Type B (right)

There is no hysteresis implemented. A Strategy Type B, using a forecasted P_{PVmean} -Value as an input for the smart grid signal the behaviour improves and even the supply and demand cover factors increase by 5% (see Table 9).

Table 9: Comparison of the el. energies for strategy Type A and B

		Method A				Method B			
	$\sum P_{pv}$ [kWh]	$\sum P_{cons}$ [kWh]	$\sum P_{sc}$ [kWh]	γ_S	γ_D	$\sum P_{cons}$ [kWh]	$\sum P_{sc}$ [kWh]	γ_S	γ_D
+ 2 K	737	1589	393	53.3 %	24.7 %	1567	438	59.3 %	27.9 %
+ 3 K	737	1598	440	59.6 %	27.5 %	1592	497	67.2 %	31.2 %
+ 4 K	737	1602	453	61.4 %	28.2 %	1602	517	70 %	32.3 %

Remark:

Further improvements are possible using heat pumps with variable speed driven copressors .

7. IMPLENTATION AND TESTING OF SMART GRID STRAGETIES

7.1 ENERGY STORAGE BUILDINGS- HERZO-BASE

The energy balance of the energy storage building Herzo Base [12] (Figure 15) is optimized by Dentel and Betzold using Demand Side Management Strategies (DSM) (see Dentel & Betzold 2017).

Also simulation studies are performed and first real data will be available in 2018/19.

Figure 15: Energy storage buildings „Herzo Base“ (Illustration: © Werbeagentur Jung)

System components used are shown in (Figure 16):

- 2 geothermal modulating heat pumps
- 8 decentral DHW heat pumps
- Thermal und electrical storage systems
- Optimal control strategy

[12] Projekt ”Herzo Base – Energiespeicherhäuser – Ein energieflexibles Gebäudekonzept von morgen” (gefördert BMWI, FKZ 03ET1364A)

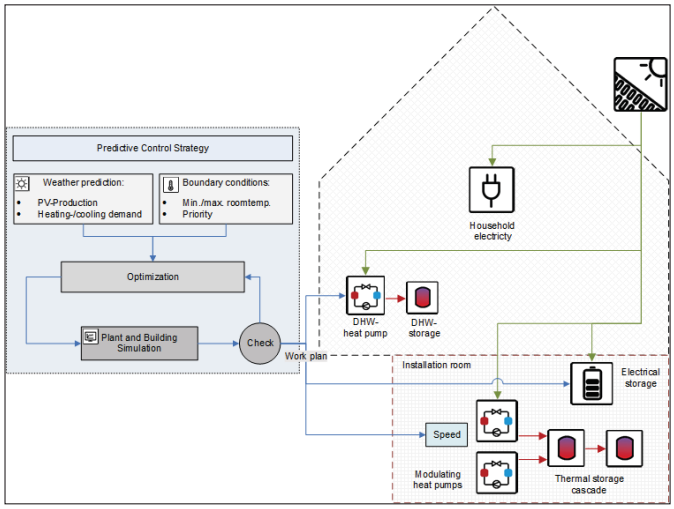

Figure 16: System configuration and control for Energy storage buildings „Herzo Base“

Aim of the optimization is an increase of the self-consumption of PV, of the demand cover factor (autarky) and of the efficiency of the whole system. The thermal mass of the building is not yet considered.

The simulation study shows an increase of the demand cover factor (direct consumption) by 21 %, the grid feed is reduced by 13% and the battery power is reduced.

The higher system temperature decreases the efficiency of the heat pumps (SCOP) from 4.2 to 3.9.

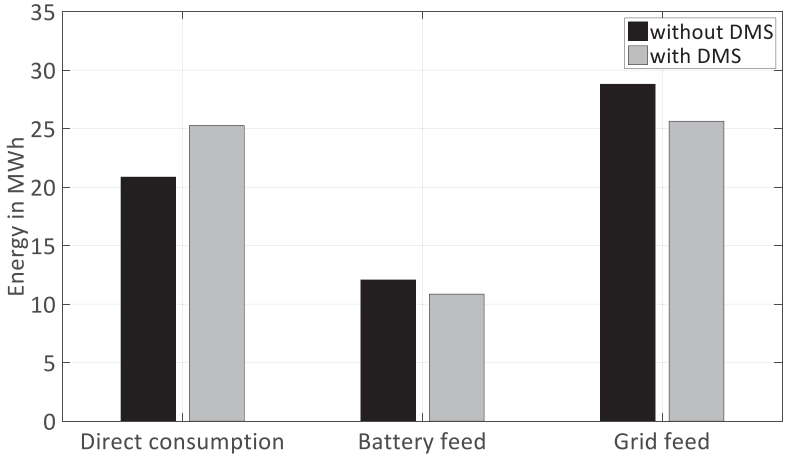

Figure 17: Results of the simulation study for the Energy storage buildings „Herzo Base“

7.2 Emulation Tests

Smart Grid load management strategies can be tested by so called “emulation” in a virtual laboratory. Heat pump, buffer and control are real, the Building and the building systems are simulated. A flexible test environment can be used. Figure 19 explain the principle of emulation environment and distinguish between virtual components or the building and real system components.

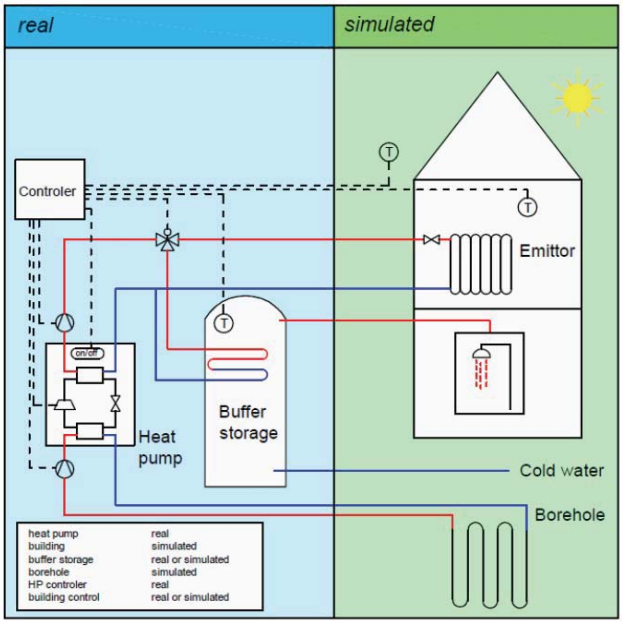

Figure 18: Virtual Building/System and real components in an emulation environment

Such an emulation test bench is available in Nuremberg (see Figure 19 and Figure 20) and is used for improving demand side management strategies (DSM) (see SENSIBLE 2017). With the help of the presented test bench a comparison between different control strategies is done. Model predictive control strategies allow adapting the operation of heat pumps to external influences such as flexible energy tariffs. In the study of Buderus et al. (2017) two model based control approaches are compared. For this purpose, simplified and detailed models of a heat pump and a thermal energy storage device are developed and used with different optimization techniques. These two approaches differ in terms of their application, computing time as well as accuracy. In general, optimization based control strategies allow a shifting of the electrical loads to low price phases. Assuming a stock market based electricity tariff for private households, the resulting cost savings are quite low. Compared to heat led operation the average cost reduction is less than 1 % per day.

Figure 19: Emulation test bench - THN-Rednitzhembach

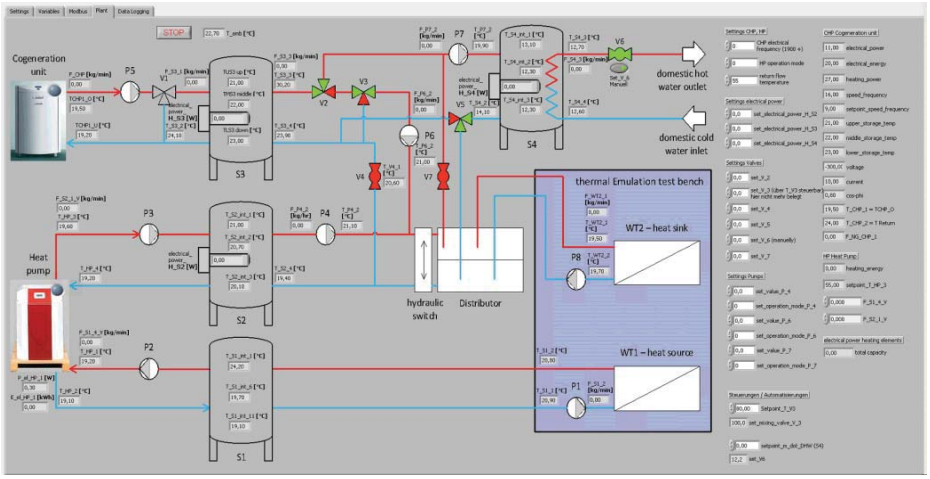

Figure 20: User interface of the Emulation test bench - THN-Rednitzhembach (LABVIEV)

8. CONCLUSION

Simulation studies show that heat pumps, buffer tanks for heating and DHW and the building itself can be used for load management, increasing the self-consumption of PV electricity or following a smart grid signal.

Especially in the heating season the self-consumption of PV electricity can be improved by increasing the set points of the room temperature, but a reduction of the thermal comfort is the consequence. System temperatures should be increased carefully, as higher temperatures result in higher losses and lower COP of heat pumps. In addition the thermal comfort must be guaranteed.

Already simple algorithms work well; implementing weather forecast will improve the strategies in the future.

TRNSYS is a reliable tool for the simulation work and will be also used in an emulation test bench for heat pumps, buffers and cogeneration systems.

According to simulation results a real project (Herzo Base) is operated. First results are available in 2018.

Further work will be done in:

- more sophisticated components (modulating heat pumps, PCM, ..)
- simplified model predictive control
- use of weather forecast
- improving simulation models

REFERENCES

Auer,T., Hammacher, T., Wagner, U. (2017): Gebäude als intelligenter Baustein im Energiesystem Lastmanagement-Potenziale von Gebäuden im Kontext der zukünftigen Energieversorgungsstruktur in Deutschland, Forschungsinitiative Zukunft Bau (Aktenzeichen: SWD-10.08.18.7-15.44, 2017

Buderus, J., Betzold, C., Bordin, S., Kandasamy, K., Dentel, A. (2018): Gegenüberstellung zweier modellbasierter Optimierungen für den Wärmepumpenbetrieb. 7th IBPSA Germany Conference BAUSIM, Karlsruhe, 26.09.-29.09.2018.

BWP (2013): Regularium für das Label „SG Ready“ für elektrische Heizungs- und Warmwasserwärmepumpen, Bundesverband Wärmepumpen e.V., 2013

Conradty, D. (2017): Neue Steuerstrategien zur Optimierung beim Einsatz regenerativer Energien im Bereich der Wohngebäude und Privathaushalte, Bachelorarbeit, März 2017

Dentel, A., Betzold, Ch. (2017): Control Strategies for Geothermal Heat Pump Systems in Combination with Thermal and Electrical Storage Units, 15th IPBSA Building Simulation Conference, San Francisco 10.-12.08.2017

Fisch N., et al. (2016): Netto-Plusenergie-Gebäude mit Stromlastmanagement und Elektro-Mobilität: Forschungsinitiative Zukunft Bau des Bundesinstitutes für Bau-, Stadt- und Raumforschung, Förderkennzeichen: SF-10.08.18.7-11.32, Laufzeit: 01.09.2011 – 01.03.2013, Stand: April, Fraunhofer IRB Verlag; 2016

Fisch N., F. Bockelmann, Th. Wilken, Ch. Kley (2016): Betriebsstrategien für EnergiePLUSGebäude am Beispiel der Berghalde, Forschungsinitiative Zukunft Bau des Bundesinstitutes für Bau-, Stadt- und Raumforschung; Förderkennzeichen SWD – 10.08.18.7-13.33, Laufzeit 08.08.2013 – 10.08.2015 Stand 15.10.2015, Fraunhofer IRB Verlag; 2016

Franco, A., Fantozzi, F. (2016b). Experimental analysis of a self consumption strategy for residential building: The integration of PV system and geothermal heat pump. Renewable Energy 86, 1075-1085.

Georges, E., Braun, J. E., Lemort, V. (2017) A general methodology for optimal load management with distributed renewable energy generation and storage in residential housing, Journal of Building Performance Simulation, 10:2, 224-241.

Hausladen, G. et al. (2016): Lastverhalten von Gebäuden unter Berücksichtigung unterschiedlicher Bauweisen und technischer Systeme: Endbericht – Speicher- und Lastmanagementpotenziale in Gebäuden, Technische Universität München, Forschungsinitiative Zukunft Bau des Bundesinstitutes für Bau-, Stadt und Raumforschung, Aktenzeichen: II 3-F20-11-1-047 / SWD-10.08.18.7-12.4, 7 July 2016.

Lorenzi, S. (2017): Investigation of dierent strategies to improve the performance and the self-consumption potential of a GCHP system with buffer storage and PV panels, master thesis Univ. Liege, July 2017

PV KWK (2017): Intelligente Energiemanagementlösungen und Photovoltaik-Kombisysteme für die optimierte Strom-Wärme-Kopplung im Haus – Teilvorhaben: Gesamtsystem-Charakterisierung SMA Solar Technology AG, Vaillant GmbH; Institute for Automation of Complex Power Systems, RWTH Aachen University BMBF FKZ 13N13297, 2017

Seiffert, J. et.al. (2016): Instationäre gekoppelte energetische und wärmephysiologische Bewertung von Regelungsstrategien für HLK Systeme, BMWi/PTJ (FKZ: 03ET1166A), Abschlussbericht 2016

SENSIBLE (2017): Storage Enabled Sustainable Energy for Buildings and Communities . first results on the nuremberg demonstrator, interim report, Mai 2017, project funded by the European Community, HORIZON 2020 , Grant No 645963

Sol2 Heat (2016): Intelligente Erzeugung und Speicherung von Solarwärme und –Strom zur Realisierung hoher solarer Deckungsanteile, Karlsruhe Institut of Technology KIT; Abschlussbericht, FKZ 0325539A, June 2016

Vanhoudt, D. , Geysen, D. , Claessens, B-, Leemans, F. , Jespers, L. , Van Bael, J. (2014): An actively controlled residential heat pump: Potential on peak shaving and maximization of self-consumption of renewable energy, Renewable Energy, Volume 63, March 2014

NOMENCLATURE

T_{set}	actual set point temperature
$T_{set,basic}$	set point temperature, basic operation
ΔT	Temperature shift, if smart grid signal is on
P_{pv}	electricity power produced by PV
Pcons	total electricity power consumed by the building
$P_{mean,i}$	mean total electricity power demand, forecasted for day i
Y_{SG}	smart grid signal (0/1)
W_{cons}	total electricity energy consumed by the building
$W_{grid,in}$	electricity energy delivered to the grid
$W_{grid,dem}$	electricity energy from the grid
W_{sc}	self consumed pv electricity energy
γs	Supply cover factor (self-consumption)
γd	Demand cover factor (autarky)

Questions and Answers:

John Clauß:

Why do you use water storage tanks with volume of 2800 L for MPC case but a tank with 800 L for the HC case?

Wolfram Stephan:

The HC case has no option for storage the PV surplus and the storage volume of 2000 L is only used for the storage coming from the PV surplus.

***

Gabrielle Masy:

Did you consider consider load shifting in the demand side management for example driers, dishwashers, etc.

Wolfram Stephan:

In our study only thermal (no electricity) capacities are considered.

***

Lieve Helsen:

Did you also look into investment costs? Load control leads to smaller peaks

Wolfram Stephan:

We consider only energy costs. We consider that the heat pumps are sized according the thermal needs, so we consider the same size for all cases.

***

Davide Ziviani:

Was occupant thermal comfort included within MPC strategy? Is the heat pump variable speed?

Wolfram Stephan:

The occupant comfort was not taken in account (possible future work). The heat pump is variable speed.

A generic methodology to evaluate hourly average $CO_{2eq.}$ intensities of the electricity mix to deploy the energy flexibility potential of Norwegian buildings

J. Claußˡ*, S. Stinnerˡ, C. Solli², K. B. Lindberg³,⁴, H. Madsen⁵,⁶, L. Georgesˡ,⁶

(1) Norwegian University of Science and Technology NTNU, Department of Energy and Process Engineering, Trondheim, Norway

(2) NTNU, Property Division, Trondheim, Norway

(3) NTNU, Department of Electric Power Engineering, Trondheim, Norway

(4) SINTEF Building and Infrastructure, Oslo, Norway

(5) DTU Technical University of Denmark, DTU Compute, Copenhagen, Denmark

(6) NTNU, (ZEN-project), Trondheim, Norway

*john.clauss@ntnu.no

ABSTRACT

This work presents a generic methodology to calculate the average $CO_{2eq.}$ intensity of the electricity mix in a bidding zone for every hour. The evaluation is based on the logic of a *multi-regional input-output approach*. The methodology includes the $CO_{2eq.}$ intensities of the electricity imports from neighboring bidding zones. To apply this methodology, input data about electricity generation is here taken from ENTSO-E and $CO_{2eq.}$ emissions per fuel type from the database Ecoinvent. This article demonstrates that it is important to take electricity imports into account when evaluating the $CO_{2eq.}$ intensity in many Scandinavian bidding zones. Correlations between the average $CO_{2eq.}$ intensity in Norway and the electricity spot price, the electricity import from foreign countries and the filling level of the Norwegian water reservoirs are investigated. The average $CO_{2eq.}$ intensity of the Norwegian electricity mix is relatively high during times with electricity imports and low when electricity is generated from hydropower. Making use of the building energy flexibility, a large potential for load shifting and emission reductions can be offered. As ENTSO-E provides 72h forecasts for the electricity generation, the $CO_{2eq.}$ intensity evaluated using this methodology can be applied as a penalty signal in predictive controls of buildings (such as model-predictive control or predictive rule-based control). The paper discusses the applicability of such a $CO_{2eq.}$ intensity as a control signal for the operation of an energy system.

Keywords: building energy flexibility, dynamic $CO_{2eq.}$ intensity, predictive control, Scandinavian power market

1. INTRODUCTION

A low-carbon energy system is required to reduce its environmental impact in the future. The energy use in buildings constitutes a large part of the total energy use. Two ways to achieve a more sustainable system could be to (1) increase the energy efficiency of buildings and (2) de-carbonize the energy supplied to buildings (IEA & Nordic Energy Research, 2016). According to the IEA, the CO_2 price is expected to sharply increase in the future and will thus be a fundamental driver for the transformation of energy systems towards carbon neutrality. Furthermore, an increased interaction between the Norwegian power grid and the "continental" European power grids is expected. Introducing demand side flexibility into the power system may lead to more stable electricity prices in the Norwegian energy grid (IEA & Nordic Energy Research, 2016). In Norway, electricity is mostly generated by hydropower

and since there is a very limited number of fossil fuel power plants for electricity generation, hourly average $CO_{2eq.}$ intensities of the electricity mix are strongly influenced by electricity exchanges with neighboring bidding zones and countries. If the $CO_{2eq.}$ intensity is used as an indicator for the fraction of renewables in the electricity mix, it can be used as a control signal for buildings. By making use of the energy flexibility of a building, energy use can be shifted to times with high fraction of renewables in the electricity mix.

The objective of this work is the development of a methodology for calculating the hourly average $CO_{2eq.}$ intensity of the electricity mix in an interconnected power grid from existing electricity production data sets. This methodology aims to evaluate the average $CO_{2eq.}$ intensities for each bidding zone (BZ) in Scandinavia taking $CO_{2eq.}$ intensities of electricity imports into account. The average $CO_{2eq.}$ intensity includes the emissions of a technology from a life cycle perspective. Electricity losses in the transmission and distribution grid are neglected in this study. The methodology is generic and not restricted to the Norwegian power system. Input data for calculating the $CO_{2eq.}$ intensity of the electricity mix is not readily available. Therefore, this work will provide the calculation methodology as well as will hint on where to retrieve and how to structure the input data in order to apply this methodology

1.1 State-of-the-art for determining average $CO_{2eq.}$ intensities for building energy system control

Usually, the $CO_{2eq.}$ intensity of imports from neighboring countries is assumed to be fixed (i.e. constant in time) when calculating the $CO_{2eq.}$ intensity of the domestic grid mix. For example, the Danish transmission system operator (TSO) Energinet provides hourly data of the average $CO_{2eq.}$ intensity of the electricity consumption in Denmark where imports from Norway are assumed as 0 g/kWh, from Sweden as 40 g/kWh and from Germany as 500 g/kWh (ENERGINET.DK, 2011). Knudsen and Petersen (Dahl Knudsen & Petersen, 2016), Hedegaard et al. (Hedegaard, Pedersen, & Petersen, 2017) and Pedersen et al. (Heidmann Pedersen, Hedegaard, & Petersen, 2017) study the demand response potential for space heating in Danish residential buildings applying hourly average $CO_{2eq.}$ intensities using the data from Energinet. Vandermeulen et al. (Vandermeulen, Vandeplas, Patteeuw, Sourbron, & Helsen, 2017) aim at maximizing the electricity use of residential heat pumps at times of high renewable energy penetration in the Belgian power grid. They use data from the Belgian TSO, Elia, but it is not stated how electricity imports are considered (i.e. if dynamic $CO_{2eq.}$ intensities of the imported electricity are considered). The company “Tomorrow” has launched a website, which shows the average $CO_{2eq.}$ intensity in most European countries in real time (Tomorrow, 2016). They consider trading between bidding zones as well as dynamic $CO_{2eq.}$ intensities in their models (Tomorrow, 2018), but a license is required to get access to the data.

1.2 The Scandinavian power market

NordPool is the leading power market in Europe (NordPoolGroup, 2018b) and operates mainly in Scandinavia, the Baltics, Germany and the UK. It has a day-ahead as well as an intra-day market. NordPool is owned by the Nordic TSOs (Norway, Sweden, Finland and Denmark) and the Baltic TSOs (Estonia, Latvia and Lithuania) (NordPoolGroup, 2018a). Each country can be divided into several bidding zones. As shown in Figure 1, Norway consists of five BZs, each of these zones have physical connections with neighboring bidding zones that enable import and export of electricity. Generally, BZs are created to avoid bottlenecks in the transmission system. By allocating different electricity prices for each BZ, they can help indicating constraints in the transmission system (NordPoolGroup, 2018c).

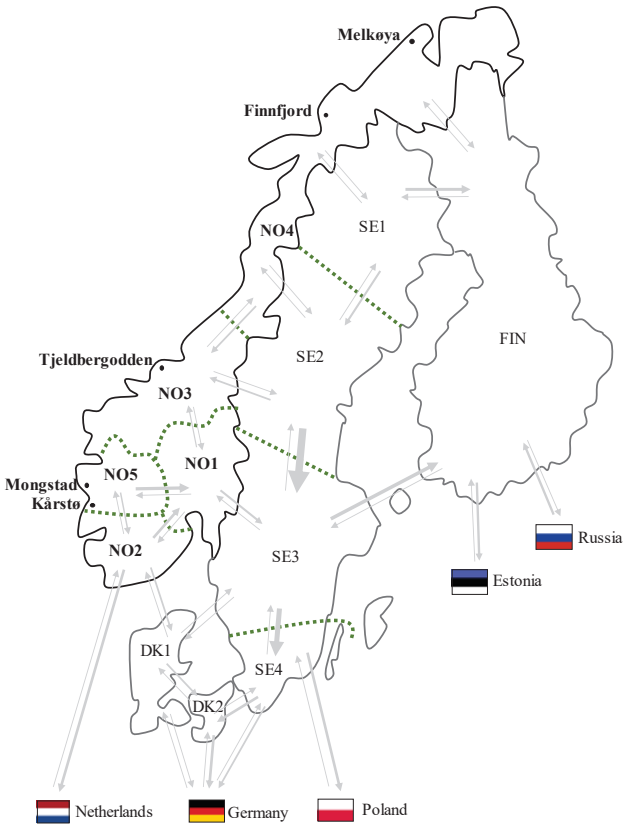

Figure 1: Overview of the Scandinavian power market bidding zones also including gas-fired power plants in Norway (adjusted from (IEA & Nordic Energy Research, 2016)*).*

2. EVALUATION METHOD FOR HOURLY AVERAGE $CO_{2EQ.}$ INTENSITY

This paper compares two scenarios for the calculation of the average $CO_{2eq.}$ intensity of the electricity mix. The calculation methodology is exactly the same, but the input data is treated differently:

(1) Scenario 1: The average $CO_{2eq.}$ intensity of the electricity mix is evaluated using the electricity generation per fuel type (retrieved from ENTSO-E).
(2) Scenario 2: For some gas power plants, the sales of their electricity generation to the grid is limited. Consequently, the second scenario evaluates the average $CO_{2eq.}$ intensity of the electricity mix using the same data as scenario (1) but with additional information on sales licenses of gas power plants. These licenses are granted by NVE (Norwegian water resources and energy directorate).

In the case of Norway, both scenarios lead to significant differences in the average $CO_{2eq.}$ intensity. Both scenarios are compared in section 3.1. As already mentioned, the impact of fossil fuels on the average $CO_{2eq.}$ intensity is very strong since the electricity generation in Norway originates almost entirely from hydropower. The dataset from ENTSO-E contains hourly values for the *total electricity generation per production type within a BZ*. It also includes data for thermal power plants which consume most of the generated electricity onsite. It is necessary to have knowledge about sales licenses of such power plants. As the

electricity is not sold to the electricity grid, it should not be considered in the calculation of the *average $CO_{2eq.}$ intensity of the electricity grid mix* (Scenario 2).

This section presents the sources for the input data, the assumptions made for processing the data and the calculation methodology to evaluate hourly average $CO_{2eq.}$ intensities. Although generic, the calculation methodology is explained using Norway as a particular case.

2.1 Data retrieval

2.1.1 Electricity generation per bidding zone

Electricity generation per production type within a bidding zone can be retrieved from ENTSO-E, which is the European Network of TSOs for Electricity. Each European TSO is asked to provide data to ENTSO-E to promote closer cooperation across the TSOs as well as to promote market transparency. The data can be downloaded after setting up a free user account.

In this work, missing data is handled in the following way: missing data for individual hours are populated with interpolated values based on the hour before and after; missing data for a whole day is populated with data of the previous day. Depending on the case, it can be sufficient to interpolate between hours or to duplicate individual previous hours. It may also be better to include data of the same hours from the day before or day ahead. If the dataset from ENTSO-E is incomplete for specific bidding zones, data may be retrieved from the respective national TSOs. For instance, in the Norwegian case study, the hourly electricity generation per production type for Sweden was obtained from the Swedish TSO because data for Swedish BZs was not available from ENTSO-E.

Pre-processing of the electricity generation data

For Scenario 1, ENTSO-E data for the hourly values of the electricity generation is considered and no further information about sales licenses for individual power plants is considered. The dataset from ENTSO-E remains unchanged regarding the electricity generation, except for treating missing data. Data regarding the hourly electricity imports and exports between BZs is usually provided by the market operator. For the particular case of Norway, data related to electricity imports was taken from both, ENTSO-E and NordPool (Nord Pool Spot, 2016).

Scenario 2 calculates the average $CO_{2eq.}$ intensity of the electricity mix taking information of the power plant fleet into account as well as the sales license of the thermal power plants. In other words, this is representative for the $CO_{2eq.}$ intensity of the electricity mix consumed by households. Norway has a very limited number of thermal power plants which normally are not allowed to sell electricity to the grid by agreement. The thermal power plants with the highest capacities are shown in Figure 1. In Scenario 2, the electricity generation of these power plants is not considered in the evaluation of the $CO_{2eq.}$ intensity, except for the power plant in Mongstad, which sells electricity to the grid. Regarding the other thermal power plants, their electricity generation has been removed from the ENTSO-E data. Nevertheless, data on the electricity generation from these power plants is either logged under the production technology "*fossil gas*" or "*other*" in the ENTSO-E dataset. It is not explained in the ENTSO-E documentation what exactly is considered as "other". The utilization of waste heat from industrial processes is not explicitly considered in any production type of the ENTSO-E dataset. Therefore, it is here assumed that the utilization of waste heat is meant by "other" in the dataset. Furthermore, it is difficult to allocate a CO_2 factor for this production type "other", since the meaning of this category is not specified by ENTSO-E and could be

different in every country. Here, the factor is simply assumed to be the average of the different fossil fuel technologies. Information regarding sales licenses of power plants can usually be obtained from either the TSO, the company owning the power plants or state directorates. It has to be mentioned that this information is here restricted to Norway, the dataset for Scenario 2 remains unchanged for other BZs. Regarding Scenario 2, when electricity is generated from waste heat in Norway, electricity is mostly for self-consumption and therefore the hourly electricity generation from "other" is set to 0.

Structure of the dataset

This paper also describes in detail how the methodology can be implemented into a specific environment, here using Excel and MATLAB. In general, the input data can be arranged in the following matrix:

$$BZ_j = \begin{bmatrix} P_{BZ_j,EGT_1}(t_1) & \cdots & P_{BZ_j,EGT_m}(t_1) \\ \ddots & \vdots & \iddots \\ \vdots & P_{BZ_j,EGT_i}(t_g) & \vdots \\ \iddots & \vdots & \ddots \\ P_{BZ_j,EGT_1}(t_{8760}) & \cdots & P_{BZ_j,EGT_m}(t_{8760}) \end{bmatrix} \quad (1)$$

where

- *i* is the *"index of EGTs"* ranging from 1 to m
- *j* is the *"index of a specific BZ"*
- *g* is the *"hour of the year"* ranging from 1 to 8760 (or 8784)

Matrix BZ (where "BZ" stands for Bidding Zone) includes the electricity generation from each electricity generation technology (EGT_i) at every hour of the year (t_g). EGT_i contains data about the electricity generation from each technology in the BZ, but, by extension, also includes the imports from 1st tier BZs. In other words, imports from other BZs are considered as an EGT in the matrix. For instance, in Excel, one sheet per BZ can be used with each sheet having exactly the same layout. The input data can be arranged in the same way as the data sheets from the ENTSO-E website.

2.1.2 Emission factors per electricity generation technology

The average $CO_{2eq.}$ intensity of a bidding zone depends directly on the CO_2 factor that is associated to each EGT. Two ways of acquiring CO_2 factors of a given EGT are the IPCC report (Krey et al., 2014; Schlömer et al., 2014) or the Ecoinvent database (Ecoinvent, 2016). Ecoinvent provides a vast variety of CO_2 factors for electricity generation from a given fuel type depending on the type of power plant or the specific country. A license is necessary to use Ecoinvent, whereas the IPCC report is available free of charge. An identical CO_2 factor has been applied for each EGT in every country and thus the CO_2 factor is assumed to be independent of the country. Therefore, it is assumed that each power plant using a same EGT has the same CO_2 factor, disregarding the thermal efficiency or the age of the power plant. The choice of the CO_2 factor of an EGT strongly affects the final result of the evaluation. Differences of the CO_2 factors between references mainly result from different allocations of emissions, especially for combined heat-and-power plants. More detailed information regarding emission allocations are given in references (Ecoinvent, 2016; Krey et al., 2014; Schlömer et al., 2014). Regarding annual average $CO_{2eq.}$ intensities of a country, they can be calculated from Ecoinvent or taken from the website of the European Environment Agency (EEA, 2018), for instance. Table 1 gives an overview of typical CO_2 factors for different fuel types. For this work, data from the Ecoinvent database has been used. Here, the phases that are considered in the CO_2 factor of an EGT consider the extraction of fuels, the construction of the power plant including infrastructure and transport as well as its operation and maintenance and the end of use of the power plant. For the sake of simplicity, the CO_2 factor

for *hydro pumped storage* is here assumed constant in time, 62 $gCO_{2eq.}$/kWh. In fact, it is dependent on the $CO_{2eq.}$ intensity of the electricity mix used when pumping water into the storage reservoir. Unlike Norway, this assumption can be critical for bidding zones that usually have a relatively high $CO_{2eq.}$ intensity.

Table 1. Comparison of CO_2 factors per electricity generation technology (EGT) from different references

Electricity generation technology (EGT)	**Emission factor [$gCO_{2eq.}$/kWh_e]**		**Name of EGT in Ecoinvent** (for reproduction purposes)	**Emission factor [$gCO_{2eq.}$/kWh_e]**
	IPCC	**EEA**		**Ecoinvent** (applied here)
Biomass	740	-	Electricity, high voltage {SE}| heat and power co-generation, **wood chips**, 6667 kW, state-of-the-art 2014 | Alloc Rec, U	60[13]
Fossil brown coal/Lignite	820	-	Electricity, high voltage {DE}| electricity production, **lignite** | Alloc Rec, U	1240
Fossil coal-derived gas		-	Electricity, high voltage {DE}| treatment of **coal gas**, in power plant | Alloc Rec, U	1667
Fossil gas	490	-	Electricity, high voltage {DK}| heat and power co-generation, **natural gas**, conventional power plant, 100MW electrical | Alloc Rec, U	529
Fossil hard coal	1001	-	Electricity, high voltage {DK}| heat and power co-generation, **hard coal** | Alloc Rec, U	1266
Fossil oil		-	Electricity, high voltage {DK}| heat and power co-generation, **oil** | Alloc Rec, U	1000
Fossil oil shale		-	No data in Ecoinvent (assumed value)	1000
Fossil peat		-	Electricity, high voltage {FI}| electricity production, **peat** | Alloc Rec, U	1071
Geothermal	38	-	Electricity, high voltage {DE}| electricity production, **deep geothermal** | Alloc Rec, U	95
Hydro pumped storage	24	-	Electricity, high voltage {NO}| electricity production, **hydro, pumped storage** | Alloc Rec, U	62
Hydro run-of-river and poundage	24	-	Electricity, high voltage {SE}| electricity production, **hydro, run-of-river** | Alloc Rec, U	5
Hydro water reservoir	24	-	Electricity, high voltage {NO}| electricity production, **hydro, reservoir**, alpine region | Alloc Rec, U	8
Marine	24	-	No data in Ecoinvent (assumed value - as wind offshore)	18
Nuclear	12	-	Electricity, high voltage {SE}| electricity production, **nuclear**, pressure water reactor | Alloc Rec, U	13
Other		-	No data in Ecoinvent (assumed value - avg. fossil fuels)	979
Other RES		-	No data in Ecoinvent (assumed value - avg. RES)	46
Solar	45	-	Electricity, low voltage {DK}| electricity production, **photovoltaic**, 3kWp slanted-roof installation, single-Si, panel, mounted | Alloc Rec, U	144
Waste		-	Electricity, for reuse in municipal waste incineration only {DK}| **treatment of municipal solid waste**, incineration | Alloc Rec, U	500
Wind offshore	12	-	Electricity, high voltage {DK}| electricity production, **wind**, 1-3MW turbine, **offshore** | Alloc Rec, U	18
Wind onshore	11	-	Electricity, high voltage {DK}| electricity production, **wind**, 1-3MW turbine, **onshore** | Alloc Rec, U	14
Imports from all bidding zones with calculated hourly data	-	0		0
Imports from Russia	-	-	Electricity, high voltage {**RU**}| market for | Alloc Rec, U	862

[13] Assuming that biogenic CO_2 is climate neutral; 100 year spruce rotation assumption and dynamic GWP for climate impact of burning wood; does not consider climate impact from CO_2 from wood combustion

Imports from Estonia	-	762	Electricity, high voltage {**EE**}| market for | Alloc Rec, U	1179
Imports from Poland	-	671	Electricity, high voltage {**PL**}| market for | Alloc Rec, U	1225
Imports from Belgium	-	212	Electricity, high voltage {**BE**}| market for | Alloc Rec, U	365
Imports from Great Britain	-	389	Electricity, high voltage {**GB**}| market for | Alloc Rec, U	762

Strictly speaking, if the constant CO_2 factor considered for pumped hydro storage is much lower than the $CO_{2eq.}$ intensity of the electricity mix when water is pumped into the storage, it would correspond to a "greenwashing" of the electricity mix.

2.2 Calculation methodology

This work evaluates the hourly average $CO_{2eq.}$ intensity of the electricity mix in an interconnected power grid, where hourly average $CO_{2eq.}$ intensities of the electricity mix of the electricity imports are considered for most of the BZs. Constant annual average values for the $CO_{2eq.}$ intensity are allocated to the electricity imports from a few specific countries (Russia, Estonia, Poland, Belgium and Great Britain), here also called boundary BZs. This section provides a step-by-step guidance on how to determine the hourly average $CO_{2eq.}$ intensity of the electricity mix of a bidding zone. Tables are presented in matrix-form for illustration purposes and easier reproduction.

In the present case study, hourly average $CO_{2eq.}$ intensities are calculated for all Norwegian, Swedish and Danish bidding zones as well as for Finland, Germany and the Netherlands. In each BZ, the electricity mix is assumed homogeneous, leading to a same $CO_{2eq.}$ intensity for the entire BZ at each hour of the year. For neighboring countries where the $CO_{2eq.}$ intensities are not evaluated (meaning Great Britain, Belgium, Poland, Estonia and Russia), a yearly-averaged $CO_{2eq.}$ intensity are considered. It is nonetheless reasonable to assume that these countries have a limited impact on the $CO_{2eq.}$ intensity of the Norwegian electricity mix. They either are 2nd tier countries (i.e. which do not have a direct grid connection to Norwegian bidding zones) or have limited electricity export to Norway (which is typically the case for Russia).

Matrix T(t) (where "T" stands for Technology) includes the electricity generation from each generation type (EGT_i) in all BZs and is calculated for each hour of the year (t):

$$T(t) = \begin{bmatrix} P_{BZ_1,EGT_1}(t) & \cdots & P_{BZ_n,EGT_1}(t) \\ \ddots & \iddots & \\ \vdots & P_{BZ_j,EGT_i}(t) & \vdots \\ \iddots & \ddots & \\ P_{BZ_1,EGT_m}(t) & \cdots & P_{BZ_n,EGT_m}(t) \end{bmatrix}$$

where
- i is the *"index of EGTs"* ranging from 1 to m
- j is the *"index of BZs"* ranging from 1 to n

(2)

The size of matrix T(t) depends on the number of EGTs and number of BZs that are considered in a respective study.

The next step is a normalization to 1 MWh by dividing by the total hourly electricity generation (Σ EGT_i) in a bidding zone (BZ_j) (also considering imports) during each hour (t) of the year. This step will be necessary to determine the $CO_{2eq.}$ intensity for 1 MWh of generated electricity in a respective BZ has. Matrix N(t) (where "N" stands for Normalization) is set up as follows:

$$N(t) = \begin{bmatrix} \frac{1}{\sum_i P_{BZ_1,EGT_i}}(t) & 0 & 0 & 0 & 0 \\ 0 & \ddots & 0 & 0 & 0 \\ 0 & 0 & \frac{1}{\sum_i P_{BZj,EGT_i}}(t) & 0 & 0 \\ 0 & 0 & 0 & \ddots & 0 \\ 0 & 0 & 0 & 0 & \frac{1}{\sum_i P_{BZ_n,EGT_i}}(t) \end{bmatrix} \quad (3)$$

where
- i is the *"index of EGTs"* ranging from 1 to m
- j is the *"index of a specific BZ"* ranging from 1 to n

The matrix P(t) (where "P" stands for Production) is the share of electricity generation from each EGT ($P_{EGT,t}$) and the imports on the total hourly electricity generation in a respective BZ, still considering electricity imports as an EGT. Regarding the electricity imports to a BZ, it is distinguished between imports from BZs with a fixed $CO_{2eq.}$ intensity of the electricity mix ($P_{Import,fix,t}$)[14] and imports from BZs with a variable electricity mix ($P_{Import,var,t}$). P(t) considers the share of each EGT in the electricity mix of a specific BZ, but does not consider the share of each EGT in the imports. P(t) is calculated by multiplying T(t) and N(t):

$$P(t) = T(t) \cdot N(t) = \begin{bmatrix} P_{EGT,t} \\ P_{Import,fix,t} \\ P_{Import,var,t} \end{bmatrix} \quad (4)$$

$P_{EGT,t}$ and $P_{Import,fix,t}$ can be combined to $P_{EGT,fix}$:

$$P_{EGT,fix} = \begin{bmatrix} P_{EGT,t} \\ P_{Import,fix,t} \end{bmatrix} \quad (5)$$

The next steps show how to include the share of each EGT in the electricity mix of neighboring BZs into the electricity mix of the BZ in question. In general, the balance between electricity consumption and electricity generation has to be satisfied at all times for each BZ. For each BZ, the sum of import and generation of electricity generated by a specific EGT should be consumed in the BZ or exported. This complies with the logic of a multi-regional input-output (MRIO) framework, which can be used for calculating consumption-based emissions for an entire country or region (Wiebe, 2016). Based on the MRIO approach, the electricity balance can be expressed as

$$M = P_{EGT,fix} + M \cdot P_{Import,var,t}, \quad (6)$$

with *M* (where "M" stands for Mix) as the share of each EGT (and boundary BZ) on the electricity use of BZ *j* and the exports from BZ *j*. Solving equation (6) for *M* is done by

$$M(i,j) = P_{EGT,fix} \cdot \left(I - P_{Import,var,t}\right)^{-1} \cdot \quad (7)$$

where *I* is an identity matrix. *Matrix M (i.j) contains the share of each EGT (i) (and boundary BZ) on the electricity use and exports from BZ (j).* A new matrix is computed for each hour of the year.

The ***average $CO_{2eq.}$ intensity of a BZ for every hour of the year*** is calculated by

$$e_j(t) = \sum_{i=1}^{m} ef_{EGT_i} \cdot M(i,j) \quad (8)$$

[14] These are the boundary BZs where the $CO_{2eq.}$ intensity is given as a boundary condition to the calculation and therefore not calculated (such as Russia, Estonia, Poland, Belgium and Great Britain).

where *t* is the hour of the year, *i* is the *"index of EGTs"* ranging from 1 to m, *j* is the *"index of a specific BZ"* ranging from 1 to n and ef_{EGT_i} is a vector containing the emission factors of the EGTs.

If a different $CO_{2eq.}$ factor should be considered for a same electricity generation technology, but for a different plant efficiency, plant age or country, a new EGT should be defined for each different $CO_{2eq.}$ factor considered.

3. RESULTS

The import from 2nd tier BZs have a lower impact on the average $CO_{2eq.}$ intensity of the target BZs (here Norway) than 1st tier BZs. Therefore, the influence of the direct imports from 1st tier BZs on the average $CO_{2eq.}$ intensities of Norwegian BZs are rather investigated. Average $CO_{2eq.}$ intensities for *Scenario 1* and *Scenario 2* are presented in Figure 2(a) and (b). The case study is done for the year 2015.

3.1 Hourly average $CO_{2eq.}$ intensities for all Norwegian bidding zones

Figure 2(a) shows the calculated $CO_{2eq.}$ intensity for each Norwegian BZ using *Scenario 1*. It can be seen that NO2 has the lowest intensity most of the year, which can be explained by the absence of gas power plants in this BZ. NO2 also shows the highest variations in the hourly average $CO_{2eq.}$ intensities because it is the only Norwegian BZ with direct transmission lines to the Netherlands and Denmark. It can thus reach high peaks during hours of import from these two countries. NO4 has the highest average $CO_{2eq.}$ intensity because a relatively large share of the generation comes from the LNG production plant in Melkøya. Nevertheless, according to its sales license, this power plant generates electricity mostly for self-consumption. The power plant is connected to the grid either to buy electricity from the grid during the start-up of the power plant (e.g. after maintenance) or for frequency control of the grid (i.e. participation to the intra-day market), if required. The average $CO_{2eq.}$ intensities calculated using *Scenario 2* is presented in Figure 2(b). It is evident that the average $CO_{2eq.}$ intensity decreases significantly in all BZs compared to Scenario 1 except for NO2 and NO5.

Figure 2: Hourly average $CO_{2eq.}$ intensity of the electricity mix in Norwegian bidding zones for (a) Scenario 1 and (b) Scenario 2.

In fact, the annual-averaged $CO_{2eq.}$ intensity of NO2 decreases as well but only slightly compared to other BZs. As NO2 does not have fossil fuel power plants, the peaks in NO2 remain similar to Scenario 1 since electricity imports from the Netherlands and Denmark remain unchanged between Scenario 1 and Scenario 2. The average $CO_{2eq.}$ intensities in NO5 remain similar because the thermal power plant in Mongstad is selling its electricity to the grid and is therefore also considered in Scenario 2. The average $CO_{2eq.}$ intensities for SE1, SE4, DK1, Finland and the Netherlands are plotted for comparison in Figure 3. As expected, the Norwegian electricity mix has low average $CO_{2eq.}$ intensities compared to other countries. For instance, it can be seen that the $CO_{2eq.}$ intensity in NO2 is only a fraction of the intensities of other non-Norwegian BZs. Therefore, the average $CO_{2eq.}$ intensity in NO2 is expected to increase during times of electricity imports from the BZs DK1 and NL.

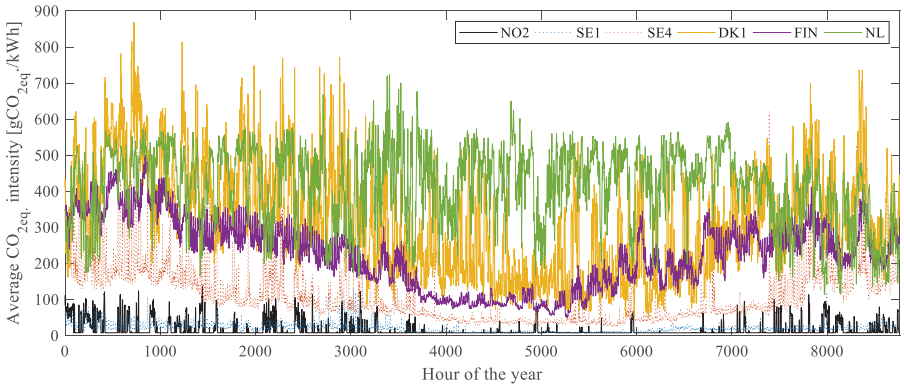

Figure 3: Hourly $CO_{2eq.}$ intensity of the electricity mix for several bidding zones (data of Scenario 2).

Due to the fact that the electricity generation in Norway is almost entirely from hydropower, the impact of imports of fossil fuel-based electricity on the average $CO_{2eq.}$ intensity is very strong. In other countries, for example Finland or the Netherlands, the impact of fossil fuels on the average $CO_{2eq.}$ intensity is lower.

Figure 4 illustrates the dependency of the average $CO_{2eq.}$ intensity on the electricity imports for four Scandinavian BZs: NO2, SE4, DK1 and FIN. It can be seen that the average $CO_{2eq.}$ intensity of NO2 systematically increases with an increasing share of imports in the electricity mix. On the contrary, the dependency is the opposite in SE4. Every time there is a higher fraction of imports, the $CO_{2eq.}$ intensity decreases because electricity is mostly imported from SE3 which has a higher share of renewables in the grid. A fraction of imports normalized by the total electricity use above 1 can occur when a BZ is importing from another BZ while at the same time the total electricity use in this BZ is lower than the total electricity imports (then this BZ imports and exports electricity at the same time). This happens frequently in SE4. Regarding DK1, it can be seen that the average $CO_{2eq.}$ intensity is only slightly dependent on the electricity imports while the average $CO_{2eq.}$ intensity of the Finnish electricity mix is barely influenced by the electricity imports. This clearly shows that the need to account for imports in the evaluation of the average $CO_{2eq.}$ intensity strongly depends on the country.

In the following, a closer look is taken at the average $CO_{2eq.}$ intensities in NO2 because this is the Norwegian BZ with the highest fluctuations in the $CO_{2eq.}$ intensity. Several correlations are investigated: $CO_{2eq.}$ intensity as a function of (a) the hourly electricity use in NO2, (b) the hourly electricity spot price in NO2, (c) the hourly electricity imports from the Netherlands and Denmark to NO2 and (d) the hydropower reservoir level. The investigation considers the average $CO_{2eq.}$ intensity of Scenario 2.

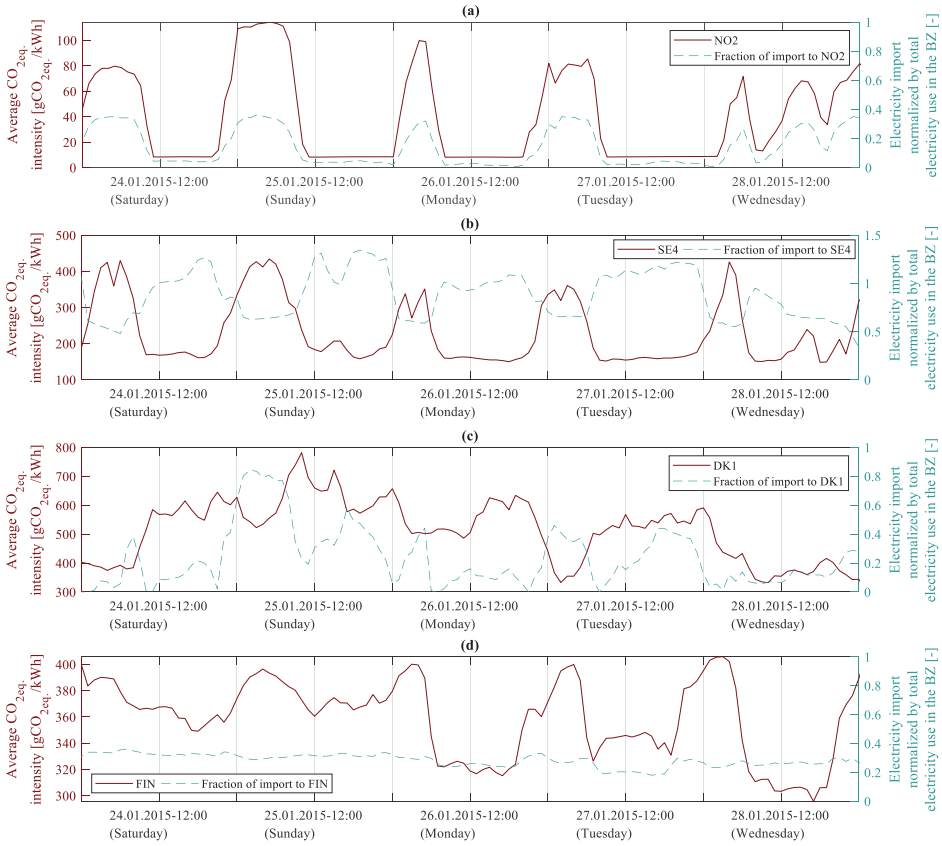

Figure 4. Average $CO_{2eq.}$ intensity and fraction of imports on the total electricity use of a BZ for five exemplary days for 4 Scandinavian BZs: (a) NO2, (b) SE4, (c) DK1 and (d) FIN.

3.2 Correlation of average $CO_{2eq.}$ intensity and electricity use

Figure 5 shows that the average $CO_{2eq.}$ intensity is usually low during times of high electricity use and vice versa. Cheap electricity is usually bought from abroad during periods of low electricity use, while electricity generation using hydropower only starts during periods of higher electricity prices corresponding to periods with higher loads.

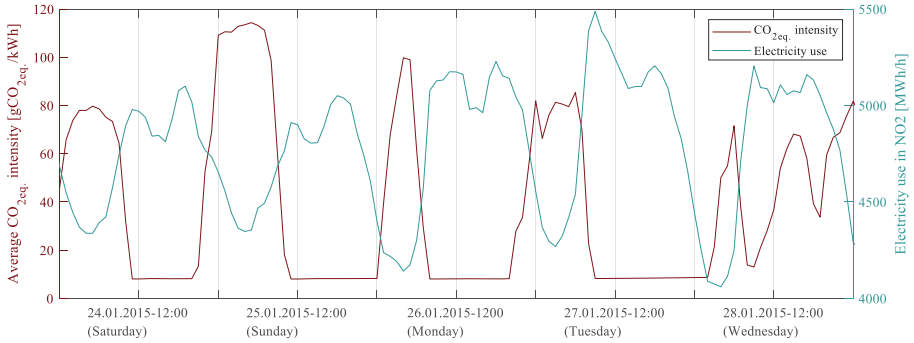

Figure 5: Average $CO_{2eq.}$ intensity and electricity use in NO2 for five exemplary days in January 2015.

This dependency is of importance when discussing the average $CO_{2eq.}$ intensity as a control signal for building energy systems (see section 5).

3.3 Correlation of average $CO_{2eq.}$ intensity and electricity spot price

Figure 6 presents the correlation between the average $CO_{2eq.}$ intensity and the electricity spot price in NO2. It is obvious that low average $CO_{2eq.}$ intensities occur during hours of high prices. High average $CO_{2eq.}$ intensities occur mostly during low-price hours with prices being typically low during night time when the electricity use is low. It should be mentioned that prices are fluctuating daily as well as seasonally. Spot prices during summer time are typically lower than during winter time.

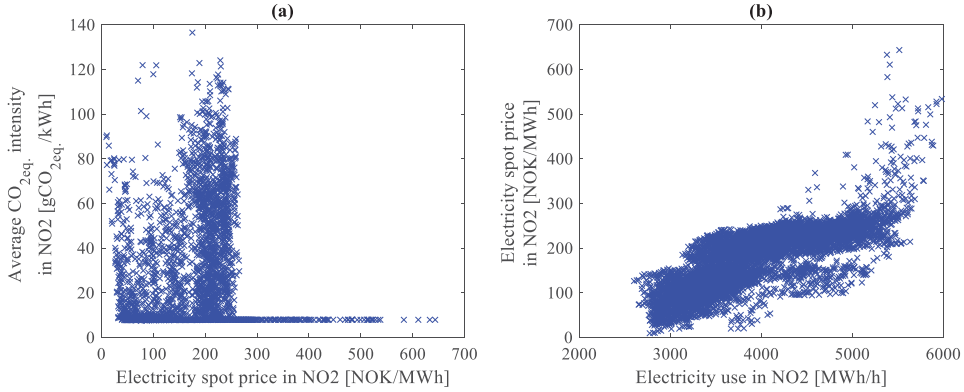

Figure 6: Correlation between (a) the $CO_{2eq.}$ intensity and electricity spot price in NO2 and (b) the electricity spot price and the electricity use in NO2, both in 2015.

Therefore, a same electricity price can be a relatively low price in winter time, but a relatively high price in summer time. It can be seen from Figure 6(a) that there is a clear break at a spot price of about 270 NOK/MWh. Most of the electricity is used when spot prices are between 180 and 280 NOK/MWh (for 2015). As already mentioned, electricity is usually generated from hydropower as soon as the daily electricity demand is relatively high and thus the price as well. Figure 7 presents the spot price in NO2 and the average $CO_{2eq.}$ intensities of all Norwegian BZs for five exemplary days in January 2015.

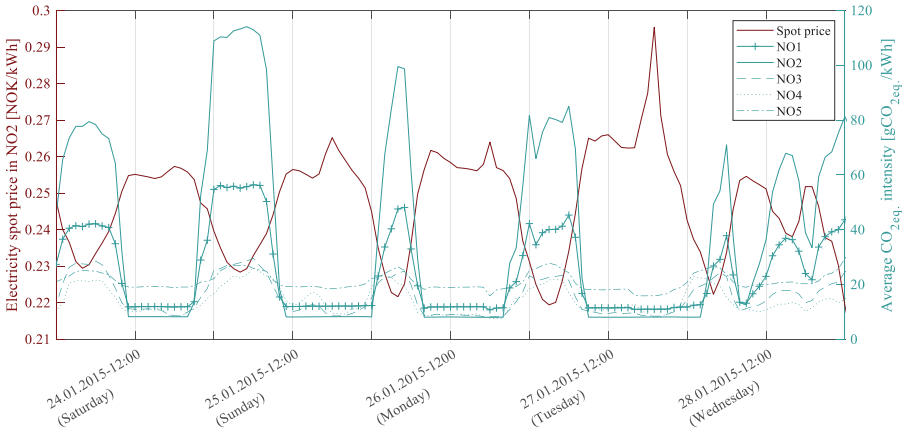

Figure 7: Electricity spot price in NO2 and average $CO_{2eq.}$ intensity in all Norwegian BZs for five exemplary days in January 2015.

As electricity is usually generated from hydropower during periods of high prices, the average $CO_{2eq.}$ intensity is low during these high-price periods typically leading to low $CO_{2eq.}$ intensities in the mornings and early evenings. The average $CO_{2eq.}$ intensity is usually high during night times due to electricity imports from the Netherlands and Denmark. This does not only affect the $CO_{2eq.}$ intensity of NO2 but subsequently impact the intensities of the other Norwegian BZs as a BZ can both import and export at the same time. This shows that it can be important to consider imports from 2nd tier BZs in some cases.

3.4 Correlation of average $CO_{2eq.}$ intensity and imports from DK and NL

The correlation between the average $CO_{2eq.}$ intensity in NO2 and its electricity imports from Denmark and the Netherlands is illustrated in Figure 8. It is evident that the average $CO_{2eq.}$ intensity in NO2 increases with more imported electricity. The different colors show three different ranges of the average $CO_{2eq.}$ intensity of DK1 to show the impact that the imported electricity with certain $CO_{2eq.}$ intensity has on the average $CO_{2eq.}$ intensity in NO2. Generally, the average $CO_{2eq.}$ intensity in NO2 is increased more rapidly if the average $CO_{2eq.}$ intensity of the imported electricity is high.

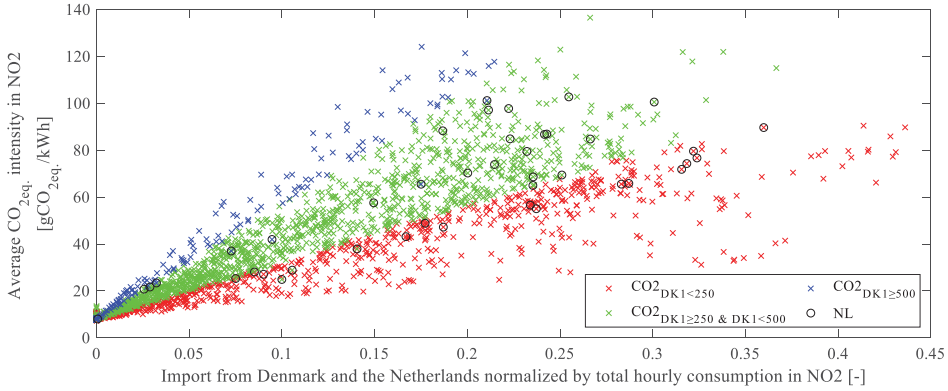

Figure 8: Correlation between the average $CO_{2eq.}$ intensity in NO2 and the electricity imports from NL and DK1 to NO2 in 2015 (colors show different magnitude of $CO_{2eq.}$ intensity of the imported electricity).

Electricity of low average $CO_{2eq.}$ intensity can be imported without increasing the intensity in NO2 significantly. If the share of imports from Denmark is high, but the average $CO_{2eq.}$ intensity in NO2 is still rather low, it indicates that the imported electricity has been generated from less

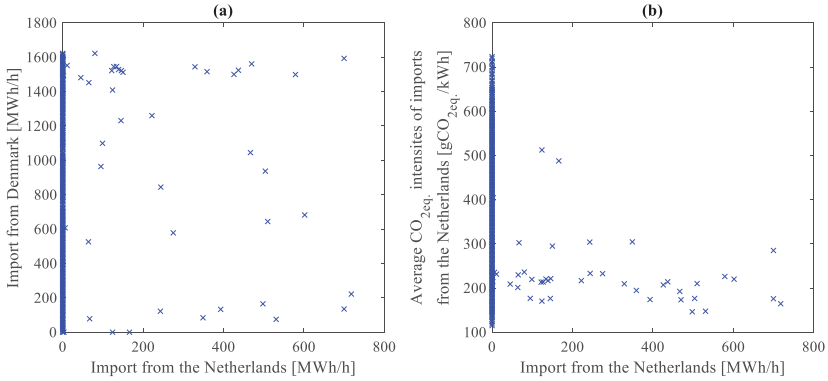

Figure 9: Correlation between (a) the imports from DK1 and imports from NL and (b) the average $CO_{2eq.}$ intensity of the imports from NL and the imports from NL.

carbon-intense technologies, such as wind power. Figure 8 does not directly show whether electricity is generated from wind or fossil fuels in DK1. It is reasonable to believe that the production is most probably from wind if the intensities in NO2 are below 20 $gCO_{2eq.}$/kWh. Figure 9 displays that electricity is imported from the Netherlands almost only in hours when there is also import from Denmark. There are only two hours throughout the whole year when NO2 imported from the Netherlands, but not from Denmark. The average $CO_{2eq.}$ intensity of the electricity imported from the Netherlands is between 150 and 300 $gCO_{2eq.}$/kWh for most of the hours.

3.5 Correlation of average $CO_{2eq.}$ intensity, hydropower reservoir level and total imports

Data for the hydropower reservoir levels in Norway is available with a weekly time resolution. In Figure 10(a), the weekly level of hydropower reservoirs in Norway is shown throughout the year. The level is at its highest at the end of autumn (week 40) when all the snow in the mountains has melted. A high electricity use during winter and shoulder season (Figure 10(b)) leads to depletion of the reservoirs. The filling level of the reservoirs is lowest just before the snow starts to melt in the mountains in spring (week 17) (Figure 10(a)). To find a correlation between weekly reservoir levels and hourly average $CO_{2eq.}$ intensities, these intensities are averaged over one week. Figure 11 shows that there is a positive correlation between the $CO_{2eq.}$ intensity in NO2 and the reservoir level, if the reservoir level is decreasing (winter and spring), but almost no correlation for increasing reservoir levels (summer and autumn). This is also supported by Figure 10(a) showing that there is less electricity import to NO2 when the water reservoir levels are increasing (week 18 to week 40 in 2015).

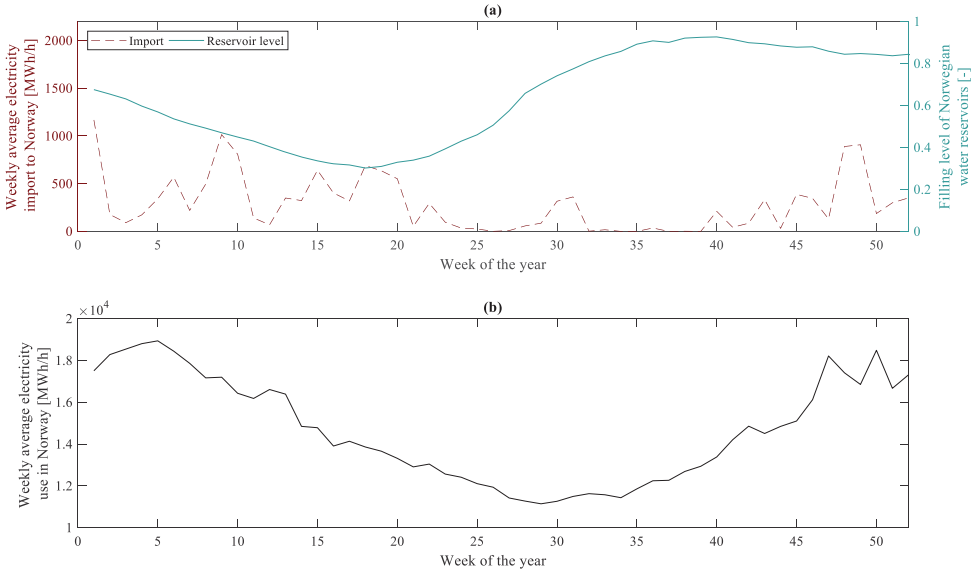

Figure 10: (a) Electricity imports to Norway (MWh/h) and weekly level of the Norwegian water reservoirs (-) and (b) electricity use in Norway (MWh/h) in 2015 (weekly average values).

It has to be pointed out that the management of the hydropower reservoirs is based on a cost-optimal planning depending on (a) the expected future electricity price, (b) the expected precipitations and the resulting expected water level in reservoirs as well as (c) the expected future electricity demands. Within this optimization, the minimum water reservoir level is determined by national restrictions for waterways, while the maximum level that is possible without losing water and thus money is limited by the capacity of the reservoirs. Electricity imports to Norway are necessary in winter and early spring even though the water reservoirs are still rather full because precipitation and thus the water level of reservoirs are not predictable many months ahead. Some water is kept in the reservoirs to ensure electricity supply at all times. As discussed in section 3.3, Norway imports electricity on a daily basis when prices are low and exports when prices are high, independent of the season of the year.

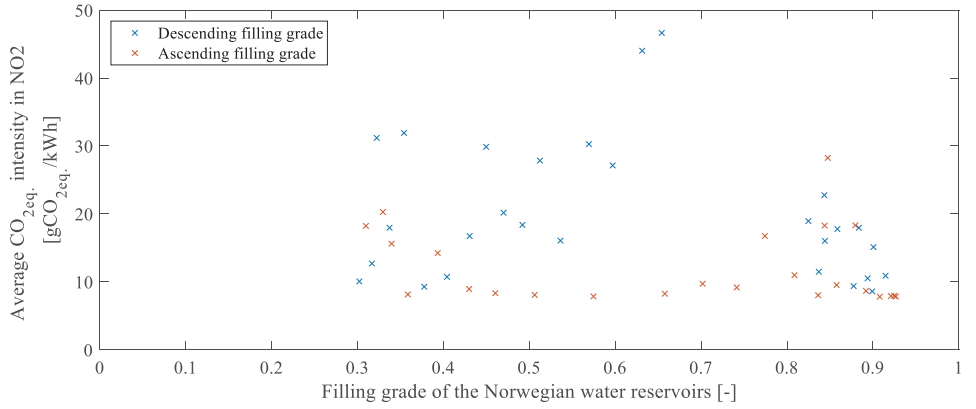

Figure 11: Correlation of $CO_{2eq.}$ intensity in NO2 and the hydropower reservoir level in Norway in 2015 (weekly average values)

4. DISCUSSION: APPLICABILITY IN BUILDING ENERGY SYSTEM CONTROL

In general, a low $CO_{2eq.}$ intensity is an indication for a high share of renewables and/or nuclear electricity generation. The application of the $CO_{2eq.}$ intensity as a control signal for the operation of building energy systems may help to reach the emission targets of the European Union. Even though it is a rather new approach, it has been used in several studies across Europe, for instance in Denmark (Dahl Knudsen & Petersen, 2016; Hedegaard et al., 2017; Heidmann Pedersen et al., 2017; Junker et al., 2018), Belgium (Patteeuw et al., 2015; Vandermeulen et al., 2017) and in Spain (Péan, Salom, & Ortiz, 2018). The control principle is rather straightforward as the basic idea is to avoid the use of electricity at times of high $CO_{2eq.}$ intensities of the electricity mix. This paper focuses on the evaluation of an hourly *average $CO_{2eq.}$ intensity* signal. Although the evaluation of a marginal $CO_{2eq.}$ intensity is not part of the scope, it is briefly mentioned here for the sake of completeness. Compared to an average $CO_{2eq.}$ intensity signal, a marginal $CO_{2eq.}$ intensity signal has the distinction of having stronger emission fluctuations and thus a higher emission savings potential, but a much more advanced methodology is required to calculate these marginal emissions.

Average and marginal $CO_{2eq.}$ intensities are two different concepts. The average $CO_{2eq.}$ intensity is the $CO_{2eq.}$/kWh emitted on average for the entire electricity consumption of the bidding zone, thus resulting from a mix of power plants. The marginal $CO_{2eq.}$ intensity is the $CO_{2eq.}$/kWh emitted for an additional kWh consumed, thus resulting from a single power plant. It may be argued that controlling a building will not affect the overall production but rather a single plant (or limited number of plants) and that marginal $CO_{2eq.}$ intensities are more coherent. Nevertheless, average factors have been extensively used in the past for buildings exporting electricity to the grid, such as Nearly Zero Energy Buildings or Zero Emission Buildings. These buildings often have large photovoltaic systems onsite.

The method proposed computes the average $CO_{2eq.}$ intensity based on the forecast of the electricity generation for the next days. It is a decoupled approach since the interaction between the supply side and the demand side is not considered. If a large number of buildings applies this $CO_{2eq.}$ intensity as a control signal, the overall electric load could be sufficiently affected so that the forecasted generation would not be optimized anymore for this load. For instance, if the $CO_{2eq.}$ signal is low, a large number of buildings may decide to favour consumption during this period of time. If the number of buildings is significant, a strong imbalance will appear between the real and predicted energy consumption. Balancing power would be needed, potentially with a power plant generating electricity with relatively high $CO_{2eq.}$ intensity (such as a coal-fired power plant). The resulting overall $CO_{2eq.}$ emissions can therefore be suboptimal. Ideally, a coupled model is required so that the impact of the demand response control is taken into account in the forecast of the electricity generation and corresponding $CO_{2eq.}$ emissions (Arteconi et al., 2016; Patteeuw et al., 2015).

Consequently, the proposed method suffers some limitations. Nevertheless, the market penetration of demand response in buildings is still limited and the method can be used as long as the number of buildings participating is rather low. Even though limited this approach is representative for most studies in building energy flexibility and, more generally, in building energy performance simulation. For example, regarding the evaluation of zero emission buildings, fixed average $CO_{2eq.}$ intensities of the electricity mix are usually assumed to calculate the emission balance. The use of an hourly average $CO_{2eq.}$ intensity for demand response would then remain coherent with that approach. In the EPBD method, the performance of buildings is evaluated using an average primary energy factor and not a marginal. Finally, the major advantage of the proposed methodology is its simplicity.

In general, a reduction of the energy use as well as the peak load during peak hours are desired to avoid exceeding the capacity of the transmission and/or the distribution grid. Advanced controls, such as predictive rule-based control or model-predictive control, can schedule the operation of energy systems to reduce the peak load. A study on CO_2 emissions of the electricity generation in Europe by (Graabak & Feilberg, 2011) has shown that marginal emissions could actually increase, if load shifting from peak to off-peak hours is performed and if the peak loads are covered by gas power plants. According to the merit order curve, fossil gas has higher marginal costs than hard coal, but reducing peak loads may lead to a lower share of gas power plants in the electricity mix, which will lead to an increase in marginal emissions as coal has a higher $CO_{2eq.}$ intensity than gas.

Norway is a special case in Europe because the electricity generation is almost fully renewable. When controlling a building's electricity use according to the average $CO_{2eq.}$ intensity in Norway, this paper has shown that the electricity consumption will be increased during peak hours, thus causing more stress on the grid. Thus, increased power loads at times of low $CO_{2eq.}$ intensities may amplify already existing peak loads, which could lead to grid congestions and possibly higher electricity prices, according to Figure 6. This would admittedly lead to decreased carbon emissions, but the transmission and distribution grid could get stressed even more. Regarding building HVAC control it is interesting to see that a control based on the average $CO_{2eq.}$ intensity of the electricity mix and a price-based control would lead to contradictory operation periods of the energy system meaning that minimizing operation costs is not compatible with minimizing CO_2 emissions (see Figure 7). This will be different in other countries with more thermal power plants.

5. CONCLUSION

This work presents a generic methodology for evaluating the average $CO_{2eq.}$ intensity of the electricity mix in a bidding zone also considering dynamic $CO_{2eq.}$ intensities of electricity imports from neighboring bidding zones. The method is based on the balance between *electricity production plus imports* and *electricity consumption plus exports.* The balance is satisfied for all BZs at each hour of the year. The methodology complies with the logic of a multi-regional input-output framework. Among possible applications, this $CO_{2eq.}$ intensity signal can be used to control the operation of a building HVAC system in order to minimize the overall $CO_{2eq.}$ emissions.

Input data about the hourly electricity generation per generation technology was retrieved from ENTSO-E. Information on the CO_2 factors of an electricity generation technology was based on Ecoinvent. Comparing the CO_2 factors from Ecoinvent and the IPCC report, it can be seen that these factors are significantly different depending on the assumptions taken for the specific CO_2 factors.

As a particular case of this method, the average $CO_{2eq.}$ intensity in Norway is evaluated as a function of (a) the electricity use in a BZ, (b) the electricity spot price, (c) the electricity import from foreign countries and (d) the filling level of the water reservoirs. In Norway, the average $CO_{2eq.}$ intensities are typically low during peak load hours because flexible hydropower plants prefer to operate at high electricity prices, when the electricity demand is usually high. Therefore, average $CO_{2eq.}$ intensities in Norway are low during high-price hours. The $CO_{2eq.}$ intensity can increase significantly as soon as electricity is imported from neighboring BZs because of a more carbon-intensive electricity generation outside Norway. For the particular case of Norway with high renewable share in the electricity generation, it is shown that it is important to consider electricity imports when evaluating the average $CO_{2eq.}$ intensity. The $CO_{2eq.}$ intensities are correlated to the filling grade of the Norwegian water

reservoirs to a smaller extent. The amount of weekly electricity imports, and thus the average $CO_{2eq.}$ intensity, is to a certain extent correlated to an ascending and descending trend for the Norwegian reservoir level.

This work proves the importance of considering electricity imports and dynamic $CO_{2eq.}$ intensities of these imports when evaluating the average $CO_{2eq.}$ intensity of the electricity mix of a BZ for the case of Norway. It is shown that high electricity demands, high spot prices and low average $CO_{2eq.}$ intensities typically occur simultaneously. These correlations are specific to Norway, while in other countries with a higher share of thermal power plants, the correlations between electricity spot prices, electricity demands and average $CO_{2eq.}$ intensities of the electricity mix can be different.

Lastly, the paper discusses the applicability of a $CO_{2eq.}$ intensity control signal for the operation of building energy systems. The average $CO_{2eq.}$ intensity signal that is determined in this methodology can be applied in predictive controls for building energy systems, such as model-predictive control or predictive rule-based controls, by using the forecast of the hourly electricity generation provided by ENTSO-E. The proposed methodology to evaluate the hourly average $CO_{2eq.}$ intensity is a decoupled approach meaning that the interaction between the supply and demand side is not considered. A coupled approach should be used to take into account these interactions into the forecast of the electricity generation, if a significant number of buildings takes part in the demand response control.

ACKNOWLEDGEMENTS

The authors would like to acknowledge IEA EBC Annex 67 “Energy Flexible Buildings”, IEA HPT Annex 49 “Design and Integration of Heat Pumps for nZEBs” as well as the Research Centre on Zero Emission Neighbourhoods in Smart Cities (FME ZEN). Sebastian Stinner gratefully acknowledges that his contribution was supported by a research grant from E.ON Stipendienfonds im Stifterverband für die Deutsche Wissenschaft (project number T0087/29896/17).

REFERENCES

Arteconi, A., Patteeuw, D., Bruninx, K., Delarue, E., D’haeseleer, W., & Helsen, L. (2016). Active demand response with electric heating systems: Impact of market penetration. *Applied Energy*, *177*, 636–648. https://doi.org/10.1016/j.apenergy.2016.05.146

Dahl Knudsen, M., & Petersen, S. (2016). Demand response potential of model predictive control of space heating based on price and carbon dioxide intensity signals. *Energy and Buildings*, *125*, 196–204. https://doi.org/10.1016/j.enbuild.2016.04.053

Ecoinvent. (2016). www.ecoinvent.org. Retrieved from www.ecoinvent.org

EEA. (2018). Overview of electricity production and use in Europe. Retrieved April 12, 2018, from https://www.eea.europa.eu/data-and-maps/indicators/overview-of-the-electricity-production-2/assessment

ENERGINET.DK. (2011). CO 2 -prognoser. Retrieved from https://www.energinet.dk/-/media/Energinet/El-RGD/El-CSI/Dokumenter/Data/CO2-prognoser.pdf.

Graabak, I., & Feilberg, N. (2011). *CO2 emissions in a different scenarios of electricity generation in Europe. SINTEF Energy Research*.

Hedegaard, R. E., Pedersen, T. H., & Petersen, S. (2017). Multi-market demand response using economic model predictive control of space heating in residential buildings. *Energy and Buildings*, *150*, 253–261. https://doi.org/10.1016/j.enbuild.2017.05.059

Heidmann Pedersen, T., Hedegaard, R. E., & Petersen, S. (2017). Space heating demand

response potential of retrofitted residential apartment blocks. *Energy & Buildings*, *141*, 158–166. https://doi.org/10.1016/j.enbuild.2017.02.035

IEA, & Nordic Energy Research. (2016). *Nordic Energy Technology Perspectives 2016 Cities, flexibility and pathways to carbon-neutrality*. Oslo. Retrieved from http://www.nordicenergy.org/wp-content/uploads/2016/04/Nordic-Energy-Technology-Perspectives-2016.pdf

Junker, R. G., Azar, A. G., Lopes, R. A., Lindberg, K. B., Reynders, G., Relan, R., & Madsen, H. (2018). Characterizing the energy flexibility of buildings and districts. *Applied Energy*, *225*(February), 175–182. https://doi.org/10.1016/j.apenergy.2018.05.037

Krey, V., Masera, O., Blanforde, G., Bruckner, T., Cooke, R., Fish-Vanden, K., Haberl, H., Hertwich, E., Kriegler, E., Müller, D., Paltsev, S., Price, L., Schlömer, S., Uerge-Vorsatz, D., Van Vuuren, D., Zwickel, T. (2014). Annex II: Metrics & Methodology. *Climate Change 2014: Mitigation of Climate Change. Contribution of Working Group III to the Fifth Assessment Report of the Intergovernmental Panel on Climate Change*, 1281–1328. Retrieved from http://www.ipcc.ch/pdf/assessment-report/ar5/wg3/ipcc_wg3_ar5_annex-ii.pdf

Nord Pool Spot. (2016). www.nordpoolspot.com/historical-market-data. Retrieved from www.nordpoolspot.com/historical-market-data

NordPoolGroup. (2018a). NordPool-About us. Retrieved from https://www.nordpoolgroup.com/About-us/

NordPoolGroup. (2018b). NordPool. Retrieved June 13, 2018, from https://www.nordpoolgroup.com/message-center-container/newsroom/exchange-message-list/2018/q2/nord-pool-key-statistics--may-2018/

NordPoolGroup. (2018c). NordPool Bidding Areas. Retrieved April 28, 2018, from https://www.nordpoolgroup.com/the-power-market/Bidding-areas/.

Patteeuw, D., Bruninx, K., Arteconi, A., Delarue, E., D'haeseleer, W., & Helsen, L. (2015). Integrated modeling of active demand response with electric heating systems coupled to thermal energy storage systems, *151*, 306–319. https://doi.org/10.1016/j.apenergy.2015.04.014

Péan, T. Q., Salom, J., & Ortiz, J. (2018). Environmental and Economic Impact of Demand Response Strategies for Energy Flexible Buildings. *Proceedings of BSO 2018*, (September), 277–283.

Schlömer, S., Bruckner, T., Fulton, L., Hertwich, E., McKinnon, A., Perczyk, D., Roy, J., Schaeffer, R., Sims, R., Smith, P., Wiser, R. (2014). Annex III: Technology-Specific Cost and Performance Parameters. *Climate Change 2014: Mitigation of Climate Change. Contribution of Working Group III to the Fifth Assessment Report of the Intergovernmental Panel on Climate Change*, 1329–1356. https://doi.org/https://www.ipcc.ch/pdf/assessment-report/ar5/wg3/ipcc_wg3_ar5_annex-iii.pdf

Tomorrow. (2016). Electricity map Europe. Retrieved April 13, 2018, from https://www.electricitymap.org/?wind=false&solar=false&page=country&countryCode=NO

Tomorrow. (2018). CO2-equivalent Model Explanation. Retrieved May 4, 2018, from https://github.com/tmrowco/electricitymap-contrib/blob/master/CO2eq Model Explanation.ipynb

Vandermeulen, A., Vandeplas, L., Patteeuw, D., Sourbron, M., & Helsen, L. (2017). Flexibility offered by residential floor heating in a smart grid context : the role of heat

pumps and renewable energy sources in optimization towards different objectives . In *12th IEA Heat Pump Conference 2017*. Rotterdam, Netherlands.

Wiebe, K. S. (2016). The impact of renewable energy diffusion on European consumption-based emissions†. *Economic Systems Research*, *28*(2), 133–150. https://doi.org/10.1080/09535314.2015.1113936

Questions and Answers:

Can you clarify/repeat how you treat "Boundary" zones (i.e. zones from which you import)?

John Clauss:

For neighboring countries where the CO2eq. intensities are not evaluated (here called boundary BZ), a yearly-averaged CO2eq. intensity is considered. In our case study, these countries are Great Britain, Belgium, Poland, Estonia and Russia. It is nonetheless reasonable to assume that they have a limited impact on the Norwegian electricity mix. They are either 2nd tier countries (i.e. which do not have a direct grid connection to Norwegian BZs) or have limited electricity export to Norway (which is typically the case for Russia). Furthermore, all other BZs considered in the methodology are BZs for which the average CO2eq. intensity is calculated for every hour of the year.

***

Could you give your comments about marginal vs average emissions?

John Clauss:

Average and marginal CO2eq. intensities are two different concepts. The average CO2eq. intensity is the CO2eq./kWh emitted on average for the entire electricity consumption of the bidding zone, thus resulting from a mix of power plants. The marginal CO2eq. intensity is the CO2eq./kWh emitted for an additional kWh consumed, thus resulting from a single power plant. It may be argued that controlling a building will not affect the overall production but rather a single plant (or limited number of plants) and that marginal CO2eq. intensities are more coherent. Nevertheless, average factors have been extensively used in the past for buildings exporting electricity to the grid, such as Nearly Zero Energy Buildings or Zero Emission Buildings. These buildings often have large photovoltaic systems onsite.

Modelling of a village-scale Multi-Energy System (MES) for the integrated supply of electric and thermal energy

F. Lombardi[1]*, S. Balderrama[2,3], N. Stevanato[1], S. Pistolese[1], E. Colombo[1], S. Quoilin[2,4]

(1) Politecnico di Milano, Department of Energy, Milan, Italy
(2) University of Liege, Energy System Research Unit - Thermodynamics Laboratory, Department of Mechanical and Aerospace Engineering, Liege, Belgium
(3) University Mayor de San Simon, Centro Universitario de Investigación en Energía, Cochabamba, Bolivia
(4) KU Leuven, Smart Energy Systems, Mechanical Engineering Department, Belgium

ABSTRACT

Energy system models for off-grid systems usually tend to focus solely on the provision of electricity for powering simple appliances, thus neglecting more energy-intensive and critical needs, such as water heating. The adoption of a Multi-Energy System (MES) perspective would allow not only to provide comprehensive solutions addressing all types of energy demand, but also to exploit synergies between the electric and thermal sectors. To this end, we expand an existing open-source micro-grid optimisation model with a complementary thermal model and show how the latter allows to achieve optimal solutions that are otherwise restricted.

Keywords: energy system, thermal, electric, modelling, off-grid, rural electrification

1. INTRODUCTION

To meet the challenging targets of climate change mitigation and ensuring affordable access to energy to present and future generations, it is imperative to develop innovative sustainable energy strategies addressing all types of energy demand (Collier, 2018; Lund et al., 2017; Mancarella, 2014). Indeed, electric energy accounts only for about 15% of global total final energy consumption, while much larger shares are associated with transport (29%) and heating (52%) needs (Collier, 2018b). What is more, the smart integration of multiple energy vectors and storage options – usually referred to as "Multi-Energy System" or "Smart Energy System" approach (Lund et al., 2017; Mancarella, 2014) – has been proven to allow for optimal energy system configurations that would remain unexplored within a single-sector domain (Mathiesen et al., 2015a). Indeed, non-electric storage options are typically cheaper than their electric counterparts, and can be supplied by multiple energy vectors (Lund et al., 2016; Mathiesen et al., 2015b). For instance, thermal storage can be fed both by direct heat and by electricity (through heat pumps or resistances) thus ensuring an increased flexibility of the overall system and a significantly higher penetration of renewable sources, or reduction of primary non-renewable energy supply (Good & Mancarella, 2017; Lund et al., 2016).

Adopting such a Multi-Energy System (MES) perspective might prove even more important in the context of off-grid areas, where both electric and thermal energy needs are typically satisfied by non-renewable fuels, associated with an unreliable and expensive supply-chain (International Energy Agency, 2017). In such contexts, increasing the penetration of locally-available renewable sources would imply reducing the dependency on external fuel imports and the economic instability associated with prices fluctuations. Nevertheless, projects regarding access to energy in off-grid villages usually tend to focus solely on the provision of electric energy for powering simple appliances, thus neglecting other energy needs – such as

cooking, space heating and water heating – that are not traditionally satisfied by electricity and that require significantly higher amounts of energy (International Energy Agency, 2017; Mancarella, 2014). This is also owing to the lack of adequate modelling tools allowing to comprehensively analyse multi-energy vectors and storage options at a village-scale. In fact, modelling thermal energy systems for village-scale off-grid contexts requires an increasing effort, in terms of: (i) higher temporal resolution of load curves that may include cooking, space heating and water heating activities (McKenna & Thomson, 2016); and (ii) higher spatial resolution and necessity to include topographic constraints for most energy conversion technologies, in the absence of centralised heat distribution networks (Mancarella, 2014). Indeed, despite the abundance of tools for modelling and optimising off-grid systems, the large majority of them do not allow for a MES perspective, and even when some non-electric energy technologies and loads are allowed, only a restricted and pre-defined set of options is available. Such barriers are exacerbated by the fact that most of these tools are released as closed-source non-modifiable software, preventing adaptability to the context and to users' needs as well as repeatability (Pfenninger et al. 2017). This is the case, for example, of the widespread tools HOMER Energy (HOMER Energy LLC, n.d.), DER-CAM (Mashayekh et al., 2017) and iHOGA (Dufo-López et al., 2011; Dufo-Lòpez, et al., 2016).

As a response to the lack of open-source models for off-grid energy systems optimisation, Balderrama et al. (2016) recently released the open-source MicroGridPy, a Python-based modelling framework conceived for the optimisation of electric micro-grids, including PV panels, diesel generators and batteries. In this study, we expand MicroGridPy by integrating it with a novel complementary high-resolution thermal energy system model, including thermal energy conversion technologies, storage options and back-up systems. The expanded model results in an integrated village-scale MES optimisation tool (MES-Py), which we apply to generate a set of scenarios for the implementation of a sustainable and resilient energy system for the case of the rural village of Toconao, located in the Atacama desert in Chile and totally dependent on imports of diesel-generated electricity and LPG for its energy supply. In particular, we focus on the two most energy-demanding final uses of the village, namely domestic hot water (DHW) and electric appliances for residential and institutional uses. Our analysis aims at investigating the potential benefits, in terms of energy cost, overall system efficiency, penetration of renewables and imports dependency, ensured by the integration of the thermal and electric energy systems, as compared to scenarios in which all energy needs are satisfied by means of traditional fuels or electricity only.

2. CASE STUDY AND SCENARIOS CHARACTERISATION

In the period of June-July 2017, we conducted a field campaign to assess the baseline energy situation of Toconao. The village has a population of about 800 inhabitants, grouped into 332 households. It comprises 32 commercial activities – such as restaurants and small grocery stores –, a public school and 6 public offices. Electricity is supplied by diesel-fired generation units from the near village of San Pedro de Atacama, yet electricity tariffs are more than double the national average and the supply is subject to frequent blackouts, typically lasting for several days and necessitating the reliance on a 320 kW diesel backup generator. LPG bottles, delivered to the village by trucks on a weekly basis, represent instead the main source for the supply of thermal energy for final uses. As for electricity, gas price is significantly higher than the national average due the isolated position of the area. Overall, the village shows a marked dependency on expensive, non-renewable, unreliable and imported primary energy sources. In addition, it is worth noting that an estimated more than half of the total final energy consumption is due to thermal demand – in accordance with the abovementioned global trend –, mostly driven by DHW loads. On the other hand, the area is characterised by a

significant solar energy potential, with a total annual global horizontal irradiation of 2578 kWh/(m^2·year). Figure 1 reports the solar resource trend and the temperature trend in the area.

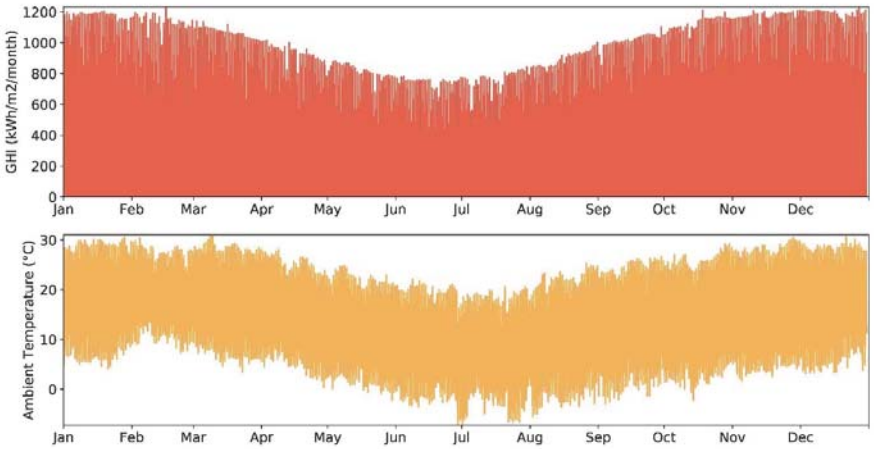

Figure 1 –Global Horizontal Irradiance and ambient temperature trend in Toconao throughout the year.

We propose 4 scenarios (summarised in Figure 2) to analyse how different energy system configurations may improve the energy cost, the overall energy efficiency of the village, the renewables penetration and the dependency on importation, namely:

a) *Traditional energy system*, in which all main energy needs (electric and DHW) are satisfied by means of the current mix of sources and technologies, i.e. diesel generators and LPG boilers;
b) *Conventional micro-grid*, in which a typical hybrid micro-grid (including PV panels, batteries and diesel generators) is installed to supply only purely electric loads, while DHW loads are covered by LPG boilers only. This scenario is defined to represent the mainstream strategy adopted in the framework of off-grid projects, which rarely take into account non-electric loads;
c) *Multi-good micro-grid*, where the hybrid micro-grid is sized in order to meet all the energy needs of the village, hence including DHW loads, which are in this case supplied by means of electric heaters;
d) *Integrated multi-energy system*, where solar thermal collectors, hot water tanks and LPG boilers are coupled with the hybrid micro-grid to serve DHW loads. The micro-grid can also interact with the thermal energy system through electric resistance heating elements installed inside hot water tanks. In this configuration, electricity can be thus stored both directly, in battery banks, and indirectly, in hot water tanks for thermal use.

It is worth specifying that the possibility of cogeneration from the diesel generators is not taken into account within the scenarios due to the absence of a centralised heat distribution network and to the low realism of assuming the construction of such an infrastructure in the context of interest.

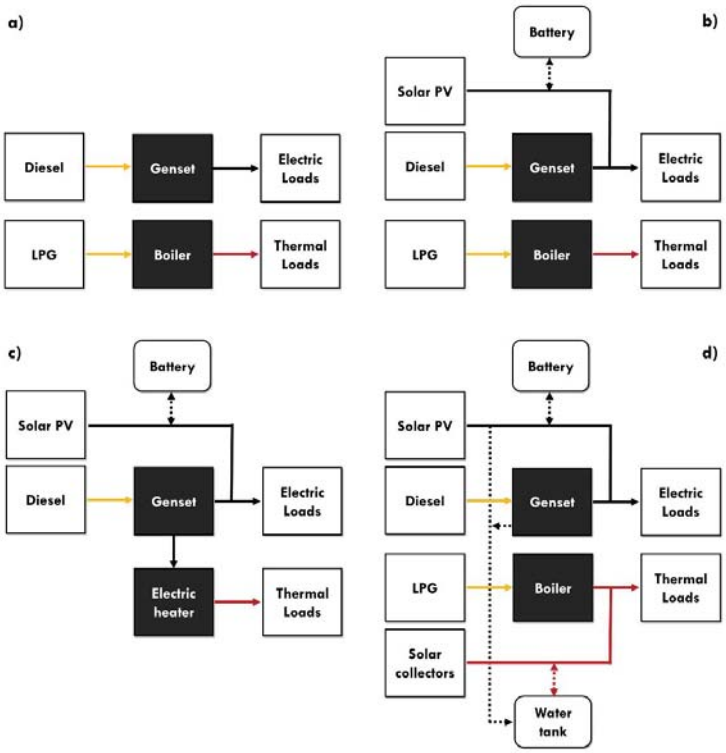

Figure 2 – Schematic summary of the 4 scenarios considered: a) Traditional energy system; b) Conventional micro-grid; c) Multi-good micro-grid; d) Integrated multi-energy system. The conceptual scheme is adapted from Mathiesen et al. (2015).

3. MODELLING APPROACH

3.1 Load profiles

For the generation of load demand profiles we adopt a high-resolution (15-min time-step) stochastic approach that builds on information about appliances ownership and time of use collected via interviews on the field (the inputs are summarised in Table 1). The approach was previously validated and applied in a comparable off-grid context by Mandelli et al. (2016). It is implemented in the MATLAB-based software LoadProGen, which we employ for this study. The model receives the inputs shown in Table 1 for each typology (class) of user considered (e.g. domestic, school, etc.) and subsequently exploits the chosen degree of random variability, in terms of appliance total time and periods of use, in order to generate a random profile for the given class. Each class contributes with its specific profile to the computation of a total profile, aggregating all classes. Load factors and coincidence factors are also indirectly taken into account by means of a specific correlation, as further detailed in Mandelli et al. (2016). To this regard, it is worth specifying that such correlation has been empirically derived based on data about electric load profiles only. In this study, we neglect in a first approximation the potential loss of reliability of the model in its application of the same empirical correlation to both electric and non-electric loads.

i	Type of appliance (e.g. indoor light, TV, fridge, etc.)
j	Specific user class (e.g. domestic, commercial, etc.)
N_j	Number of user within class j
n_{ij}	Number of appliances i within class j
P_{ij}	Nominal power [W] of appliance i within class j
h_{ij}	Functioning time [min], or overall time each appliance i within class j is on during a day
$w_{F,ij}$	Functioning windows, or period(s) during the day when each appliance i within class j can be on
d_{ij}	Functioning cycle [min], i.e. minimum continuous functioning time once appliance ij is on
Rh_{ij}	% random variation of functioning time appliance ij
Rw_{ij}	% random variation of functioning windows appliance ij

Table 1 – Inputs required by the stochastic approach for the generation of load profiles, adapted from Mandelli et al. (Mandelli et al., 2016)

To comply with the formalisation of input data originally conceived for electric loads, we create fictitious thermal appliances with a corresponding nominal power value, which we compute based on data about typical water temperature ranges for DHW applications and average water consumption and duration of each task (Equation 1) (Caleffi, 1999; Fischer et al., 2016).

$$P_{nom,th.task} = \frac{\rho_w V_{w,task} c_{p,w} (T_{DHW} - T_0)}{t_{task}} \; [W_{th}] \tag{1}$$

Where:

- $V_{w,task}[l]$ is the average volume of water consumed for the selected task, derived from reference values available in the literature (ASHRAE, 2015; Widén et al., 2009);
- $\rho_w \; [kg \cdot m^{-3}]$ is the density of liquid water;
- $c_{p,w} \; [kJ \cdot kg^{-1} \cdot K^{-1}]$ is the specific heat of liquid water;
- $T_{DHW} \; [K]$ is the average water temperature for DHW applications (set at 45°C);
- $T_0 \; [K]$ is the temperature of cold water before heating (set at 15°C);
- t_{task} [s] is the average duration of the selected task.

Furthermore, at the difference of electric loads, thermal loads related to different user classes are not aggregated in a single total load profile. In fact, considering the absence of a centralised heat distribution network, thermal loads need to be spatially bound to the site of consumption. Accordingly, we model a separate thermal load profile for each user class, namely: (i) *domestic*, (ii) *commercial activities*, (iii) *school*, and (iv) *public offices*.

Electric load profiles are generated based on 4 different sets of input data, reproducing four specific seasonal behaviours. No seasonality is considered for thermal loads, which are stochastically generated for 365 days based on the same set of input data. Further details about the data and the assumptions made for the creation of electric and thermal loads are provided in Appendix B.

3.2 Multi-Energy System

The MES model ("Multi-Energy Systems Py," 2018) builds on the existing concept developed by Balderrama et al. (2016) for purely electric micro-grids, by adding a

complementary thermal energy system model comprising solar thermal energy conversion technologies (flat-plate solar thermal collectors), thermal storage (hot water tanks) and traditional back-up systems (LPG boilers). Thermal technologies are not connected by any centralised heat distribution network, and thus direct heat consumption remains bound to the site of generation. Nevertheless, the electric and thermal systems are interconnected by means of electric resistance heating elements that are modelled inside hot water tanks, thus allowing a "smart" electric recharge of the thermal storage that gives rise to a more flexible MES, as shown by the sketch in Figure 3. Such electric resistance heating elements are also interpreted as standalone components to model electric heaters in the *Electric energy system* scenario. The main inputs and output of the MES model are summarised in Table 2.

Inputs	***Outputs***
PV panel output	Optimal system size
Solar collector output	NPC, LCOE
Electric load profile	Electric dispatch strategy
Thermal load profile	Thermal dispatch strategy
Economic parameters	

Table 2 – Main inputs and outputs of the Multi-Energy System model.

Further details about the specific technical characteristics of the modelled technologies, and about PV panels and solar collectors outputs, are available in Appendix A – Technology parameters.

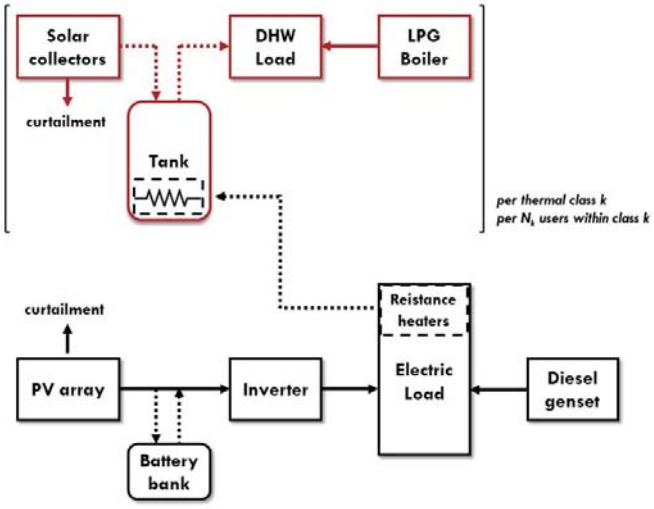

Figure 3 – Schematic of the integrated electric and thermal energy system model. The thermal energy system is not a single centralised entity but rather the aggregate of multiple user-scale individual systems, which are modelled for each user within each user class and only connected through the electricity grid, in the absence of a heat distribution network.

It is worth noting that, while the electric energy system consists of a single entity, the thermal energy system is composed of multiple user-scale energy systems, which reproduce topographically constrained generation and consumption for each user within each user class. In other terms, the model considers each thermal user class *k* (i.e. domestic users, commercial activities, etc.) as a separate system consisting of the aggregate of N_k user-scale subsystems (where N_k is the number of users within the *k*-th class). Indeed, the thermal energy balance (Equation 2) satisfies independently the thermal demand (in this case DHW only) for each thermal user-class *k*, and for each time step *t*. The thermal demand of a user-class ($E_{Th,class\ demand}$) consists in turns of the load profile of a representative user multiplied by the number of users within the class (Equation 3).

$$E_{Th,class\ demand}(k,t) = E_{boiler}(k,t) + E_{Tank_{out}}(k,t) - E_{Curt}(k,t) + E_{lost\ load,th}(k,t) \quad \forall k, \forall t \tag{2}$$

$$E_{Th,class\ demand}(k,t) = E_{th,user\ demand}(k,t) \cdot N_{Users}(k) \quad \forall k, \forall t \tag{3}$$

where E_{boiler} is the energy supplied by the LPG boilers, $E_{Tank_{out}}$ the one supplied by the hot water tank, E_{Curt} is the fraction of the excess energy produced by solar collectors that cannot be stored in the tank and $E_{lost\ load,th}$ is the accepted fraction of unmet thermal load – which we set at 1% for all the scenarios.

On the electrical side, the energy balance (Equation 4) includes the energy generated by PV panels (E_{PV}) and diesel generators (E_{Gen}), the energy flows to and from the battery ($E_{bat,ch}$ and $E_{bat,dis}$), the electric energy that is curtailed (E_{Curt}), the energy supplied to the thermal storage through electric resistance heating elements ($E_{Res,tot}$) and the fraction of accepted unmet load ($E_{lost\ load}$) – set at 1%, as for thermal loads.

$$E_{El,demand}(t) = E_{PV}(t) + E_{Gen}(t) - E_{bat,ch}(t) + E_{bat,dis}(t) - E_{Curt}(t) - E_{Res,tot}(t) + E_{lost\ load}(t) \quad \forall t \tag{4}$$

Where $E_{Res,tot}$ is the cumulative energy absorbed by the electric resistance heating elements of all *n* thermal classes, as shown by Equation 5.

$$E_{Res,tot}(t) = \sum_{k=1}^{n} E_{Res,class}(k,t) \quad \forall t \tag{5}$$

As compared to the original MicroGridPy model, which includes both linear programming (LP) and mixed-integer linear programming (MILP) versions of the code depending on the way the diesel generator is modelled, the novel MES model is based uniquely on a LP configuration. This choice is motivated by the necessity to keep the computational time within a reasonable range while we increase the temporal resolution of the model from the original 1-hour to the current 15-minute.

3.2.1 Electric components

The equations adopted to model the behaviour of the electric components, and thus producing the variables in Equation 4, are kept identical to those already introduced by Balderrama et al.

(2016) for the original MicroGridPy model, in its LP version. The reader is thus referred to the abovementioned study for further details.

3.2.2 Thermal components

3.2.2.1 Solar thermal collectors

The total thermal energy provided by the solar collectors ($E_{SC_{tot}}$) for each class *k* is computed as the energy generated by a single collector (E_{SC}) – which is given as an input to the model – multiplied by the number of solar collectors in the class, N_{SC}.

$$E_{SC_{tot}}(k,t) = E_{SC}(k,t) \cdot N_{SC}(k) \quad \forall k, \forall t \tag{6}$$

Further details about the specific flat-plate collector model used as a reference, and about how the collector output is obtained, are provided in Appendix A – Technology parameters. It is worth noting that $N_{SC}(k)$ is an optimisation variable for each class and is not given as an input. Indeed, it is indirectly taken into account in Equation 2, due to its contribution to the definition of $E_{Tank_{out}}(k,t)$ (Equation 7).

3.2.2.2 Hot water tanks

Hot water tanks provide an option for thermal energy storage within the model, and can be fed by both solar collectors and electric resistance heating elements. The tanks are represented adopting a fully-mixed (or thermal capacity) model (Dumont et al., 2016): for each time-step *t* and for each class *k*, the thermal energy stored in the tank ($E_{SOC_{Tank}}(k,t)$) is computed based on the balance reported in Equation 7. The latter considers the energy stored in the preceding step ($E_{SOC_{Tank}}(k,t-1)$), the energy supplied by solar collectors ($E_{SC_{tot}}$) and by the electrical resistance ($E_{Res,class} \cdot \eta_{Res}$, with η_{Res} = 1), and the energy flow outside the tank ($E_{Tank_{out}}$). Energy losses due to the heat transfer between thermal storage and environment are taken into account by means of an efficiency parameter (η_{tank} = 0.99), following the approach proposed by Duffie and Beckman (2013).

$$E_{SOC_{Tank}}(k,t) = E_{SOC_{Tank}}(k,t-1) \cdot \eta_{tank} + E_{SC_{tot}}(k,t) + E_{Res,class}(k,t) \cdot \eta_{Res} - E_{Tank_{out}}(k,t) \;\; \forall k, \forall t \tag{7}$$

A set of constraints is also defined, as shown in Equations 8,9, and 10. In particular:

- The energy stored in the tank is constrained not to exceed the maximum capacity $C_{SOC_{tank}}$ of the tank, for each class *k*.

$$E_{SOC_{Tank}}(k,t) \leq C_{SOC_{tank}}(k) \quad \forall k, \forall t \tag{8}$$

- The energy stored in the tank is constrained to be kept above a minimum value (defined as depth of discharge, D_{SOC}), defined as a percentage of the nominal tank capacity.

$$E_{SOC_{Tank}}(k,t) \geq C_{SOC_{tank}}(k) \cdot D_{SOC} \quad \forall k, \forall t \tag{9}$$

– The thermal energy flow out of the tank ($E_{Tank_{out}}$) is constrained to be lower than the tank maximum power of discharge ($P_{out,max}$) multiplied by a delta time (Δt) calibrated on the time-step.

$$E_{Tank_{out}}(k,t) \leq P_{out,max}(k) \cdot \Delta_t \quad \forall k, \forall t \tag{10}$$

3.2.2.3 Electric resistance heating elements

Electric resistance heating elements are modelled inside hot water tank to maintain a minimum level of stored thermal energy (i.e. a minimum water temperature) as well as to serve as an additional backup system to satisfy the thermal demand when needed. The decision about the possible switch-on of electric resistances at each time step is a result of the cost-optimisation problem, as it is for LPG boilers, which is provided for each user class independently. The resistance is assumed to have a unitary efficiency (η_{Res}) and the energy provided per unit time-step ($E_{Res,class}(k,t)$) is constrained to not exceed its nominal capacity (C_{Res}), as shown in Equation 11.

$$E_{Res,class}(k,t) \leq C_{Res}(k) \cdot \Delta t \quad \forall k, \forall t \tag{11}$$

3.2.2.4 LPG boilers

LPG boilers act as a backup system connected directly to the thermal load. The thermal energy per unit time-step provided by LPG boilers (E_{Boiler}) is constrained to remain below its nominal capacity value (C_{Boiler}).

$$E_{Boiler}(k,t) \leq C_{Boiler}(k) \cdot \Delta t \quad \forall k, \forall t \tag{12}$$

The model also computes the LPG consumption (LPG_{cons}) dividing the energy supplied by the boilers by their nominal efficiency (η_{boiler}) and the LPG heating value, as shown by Equation 13.

$$LPG_{cons} = \frac{E_{boiler}}{\eta_{boiler} \cdot LHV_{LPG}} \tag{13}$$

3.2.3 Optimisation

The minimised objective function is the total Net Present Cost (NPC) of the energy system, computed in Equation 15.

$$ObjectiveFunction = \min(NPC) \tag{14}$$

$$NPC = Inv + \sum_{n=1}^{N} \frac{YCC}{(1+e)^n} + Cost_{rep} \tag{15}$$

Where Inv is the total investment cost, YCC is the yearly constant cost of the project, N is the project life-time, e is the discount rate factor and $Cost_{rep}$ is the cost of components replacement (in this case defined for batteries only).

The total investment is evaluated by summing the capital costs of all the installed components, computed based on their specific costs (expressed in USD/kW for generation technologies and USD/kWh for storage). Equation 16 reports the detailed calculation of the investment cost, in which fun represents the percentage of the investment that is financed by a bank (or any another entity).

$$Inv = \Bigg[N_{PV} C_{PV} U_{PV} + C_{bat} U_{bat} + N_{gen} C_{gen} U_{gen} + \sum_{k=1}^{n} \left(N_{SC}(k) U_{SC} C_{SC} + U_{Tank} C_{SOC_{tank}}(k) + U_{Boiler} C_{Boiler}(k) + U_{Res} C_{Res}(k) \right) \Bigg] \cdot (1 - fun) \quad (16)$$

YCC is calculated as shown by Equation 17, where $Cost_{O\&M}$ is the cost of operation and maintenance of the system and $Cost_{finan}$ is the fixed-rate loan payment, while the other variables represents cost associated with the use of fossil fuels and the cost of lost the unmet load (LL_{cost}).

$$YCC = Cost_{O\&M} + Cost_{finan} + \sum_{t=1}^{T} Cost_{Diesel}(t) + \sum_{t=1}^{T} Cost_{\mathrm{gas}}(t) + LL_{cost}\,(t) \quad (17)$$

$Cost_{finan}$ in Equation 17 is computed as per Equation 18, where i is the number of years in which the loan has to be paid back and r is the interest rate.

$$Cost_{finan} = \frac{Inv \times fun \times r}{1 - (1 + r)^{-i}} \quad (18)$$

The cost of components replacement is finally computed as per Equation 19, where y is the number of years after which battery is replaced.

$$Cost_{rep} = \frac{C_{bat} U_{bat}}{(1 + e)^{y}} \quad (19)$$

Based on the NPC, the model also evaluates the Levelised Cost of Energy (LCOE) as in Equation 20,

$$LCOE = \frac{NPC}{\sum_{n=1}^{N} \frac{E_{demand}}{(1 + e)^{n}}} \quad (20)$$

where E_{demand} is the total energy demand (electric and thermal) of the system.

An overall system efficiency is also computed as per Equation 21,

$$\eta_{overall} = \frac{E_{demand,net}}{\sum_{j} E_{supply,j}} \quad (21)$$

where $E_{demand,net}$ is the net (i.e. after subtracting the lost load) total energy demand, and $E_{supply,j}$ is the total energy supplied by each *j-th* energy supply technology (such as diesel generators, PV panels, LPG boilers and solar thermal collectors).

4. RESULTS AND DISCUSSION

4.1 Generated load profiles

Figure 4 reports an example of the electric daily load profile for the month of April, generated with a 15-min time step. The profile shows a peak of about 340 kW in the evening (approximately around 6 p.m.), whilst the lighter lines in the background, representing the load in different months (January and August), show that the modelled seasonality entails a marked peak shift towards the later evening hours.

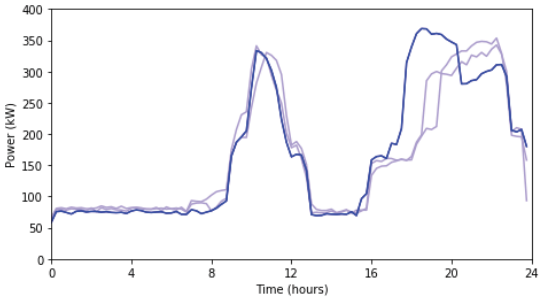

Figure 4 – Example of total electric load profile, referred to the month of April (heavy line), and comparison with profiles in January and August (light lines).

Thermal loads are represented in Figure 5, disaggregated for typical users within each user class. As expected, these are characterised by almost-instantaneous significant peaks, especially as regards the *school* user class.

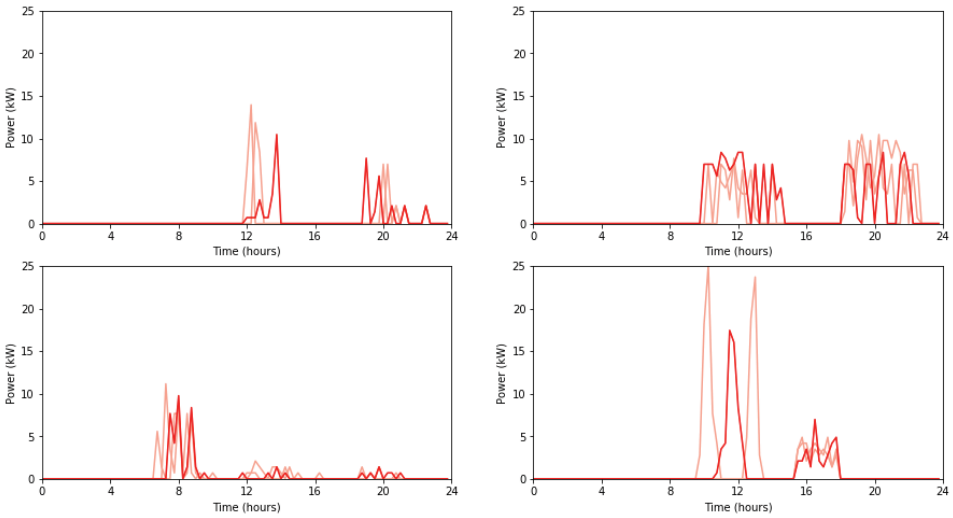

Figure 5 – Example of thermal load profiles for single typical users within each user class: a) domestic; b) commercial activities; c) public offices; and d) school. Heavy lines

represent the load of April 10th, whilst light lines show the load of the day before and the day after as an example of the stochasticity ensured by the model.

The two modelled demands correspond to a Total Final energy Consumption (TFC) of about 3150 MWh/year, with a share of 46% for electricity and 54% for DHW.

4.2 Optimisation results

The MES model provides the optimal energy system configuration for each of the selected scenarios. The results in terms of LCOE, Total Primary Energy Supply (TPES), overall system efficiency, imports dependency and renewables penetration are summarised in Table 3.

	Baseline	**Conventional micro-grid**	**Multi-good micro-grid**	**Integrated multi-energy system**
TPES [MWh]	576	404	434	525
Imports [%TPES]	100%	80.7%	50.6%	33.3%
Renewables [%TPES]	0%	19.3%	49.4%	66.7%
$\eta_{overall}$ **[%]**	47.1%	67.1%	62.5%	51.6%
LCOE [USD/kWh]	0.295	0.254	0.438	0.167

Table 3 – Summary of selected indicators for the four proposed scenarios.

All the proposed scenarios result in an improvement of the energy situation of the village as compared to the baseline situation. The *Conventional micro-grid* configuration, in which thermal needs are still constrained to be satisfied by LPG boilers alone, already allows to achieve a consistent reduction of TPES and a very good overall system efficiency. However, renewables penetration and energy independency are significantly lower than for the *Integrated multi-energy system* case, and are achieved at the expense of a higher LCOE. This highlights how focusing solely on purely electric needs does not allow for the identification of the overall optimal solution. Similarly, the *Multi-good micro-grid* scenario, in which all energy needs (including DHW, through electric heaters) are satisfied by an electric micro-grid, is associated with a much higher LCOE value – even higher than the baseline. In fact, though the system is in this case characterised by a very high penetration of solar PV, the micro-grid size increases significantly as a consequence of the need to manage two different loads with a single and costly storage option. As shown in Table 4, the installed PV capacity is more than twice that of the *Conventional micro-grid* scenario, the battery bank is almost four-fold and the diesel genset capacity is an order of magnitude larger. As expected, this scenario is suboptimal due to the restriction eliminating the possibility of installing LPG boilers or thermal storage.

	Baseline	**Conventional micro-grid**	**Multi-good micro-grid**	**Integrated multi-energy system**
PV panels [kW]	0	394	1096	405
Battery storage [kWh]	0	1110	4263	990
Diesel gensets [kW]	329	144	3719	160
Solar collectors [kW]	0	0	0	1737

Hot water tanks [kWh]	0	0	0	12123
LPG boilers [kW]	5640	5640	0	619
Electric heaters [kW]	0	0	5910	87

Table 4 – Summary of nominal capacities installed for different energy conversion and storage technologies in the four proposed scenarios.

This result also underlines how the idea of satisfying all types of energy demand through electric appliances implies significant complications in terms of system management and dispatch strategy, leading to an unprofitable overreliance on electric storage options and diesel gensets. This can be seen in the graphical representation of the electrical dispatch in Figure 6-c: the electricity production of the *Multi-good micro-grid* far exceeds the pure electric load, as a relevant excess needs to be redirected to electric heaters in order to satisfy also thermal loads. Conversely, the excess electricity conveyed to thermal loads for the *Integrated multi-energy system* scenario represents only a negligible fraction of the total electricity production, i.e. that needed to compensate losses from the storage tanks.

The *Integrated multi-energy system* is the configuration allowing for the lowest LCOE, notwithstanding the need to have thermal energy conversion technologies spatially bound to the site of consumption and the subsequent impossibility to exploit economies of scale. This is a result of the combined presence of a second renewable energy conversion technology (solar collectors) and, moreover, of an additional and more cost-effective energy storage option, i.e. hot water tanks. **Erreur ! Source du renvoi introuvable.**8 shows the thermal e nergy dispatch for representative users within each thermal user class, for the *Integrated multi-energy system*. The contribution of renewable electricity (approximately represented by resistance heaters, which are preferred to LPG when renewable or stored electricity is available) to the heat supply is nonetheless limited, as shown in Figure 7.

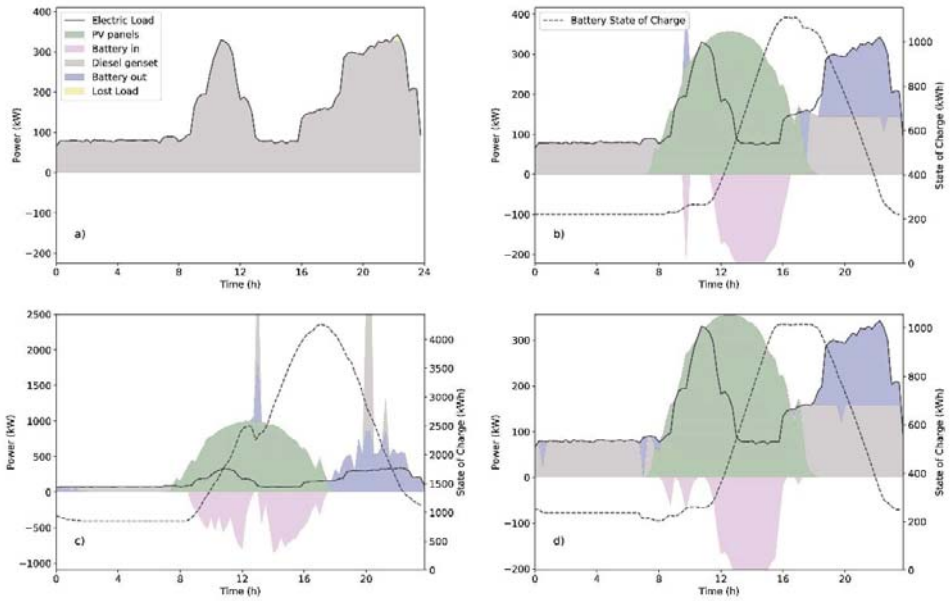

Figure 6 – Electric energy dispatch strategy in the four modelled scenarios, namely: a) Baseline; b) Conventional micro-grid; c) Multi-good micro-grid; d) Integrated multi-energy system. The represented day is May 11th.

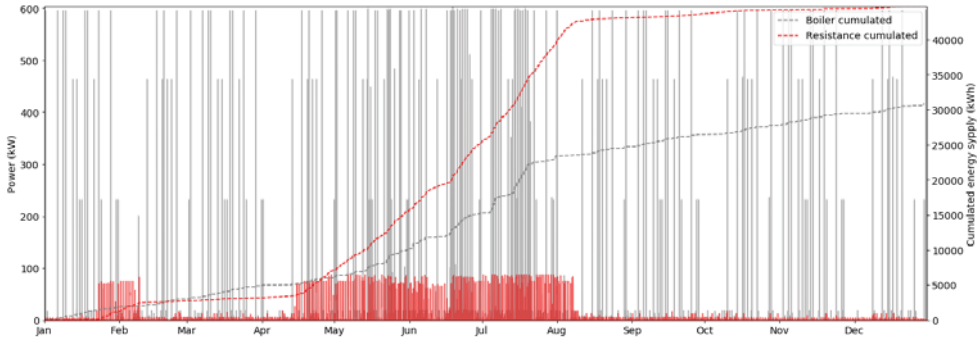

Figure 7 – Instantaneous use of LPG boilers and resistance heaters throughout the year, and cumulative energy supplied by the two technologies.

This is a consequence of the fact PV generation follows the same production pattern of solar collectors, bound to the daily solar irradiance profile. If other renewable sources, with a different daily production profile (such as wind), were exploitable, they could potentially further benefit from the presence of thermal storage, which could be electrically charged and used also during morning and evening peaks.

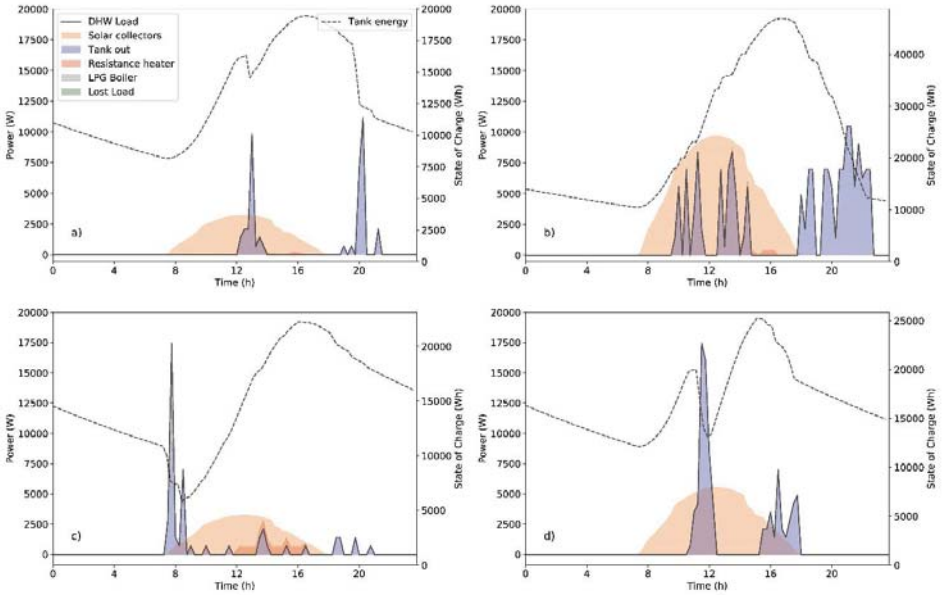

Figure 28 – Example of thermal energy dispatch for representative single users for each of the four modelled user classes. The represented day is May 11th.

CONCLUSION

The study shows that the novel open-source MES optimisation tool that we developed building on the existing MicroGridPy effectively allows for the generation and comparison of multiple integrated thermal and electric energy system configurations for off-grid contexts. In particular, the application of the tool to the Chilean village of Toconao confirms how the integration of multiple energy vectors and storage options allows to identify least-cost optimal solutions that remain unreachable within a single-sector perspective. Indeed, both "micro-grid" configurations proposed (*Conventional* and *Multi-good*) face some limitations as compared to the integrated multi-energy system, either in terms of economic viability or of technical feasibility. A "Multi-Energy" or "Smart Energy System" perspective is thus critical to achieve overall optimal energy systems configurations, especially in relationship with the inclusion of multiple storage options. Potentially, larger benefits might be achieved in cases where different renewable energy sources can be coupled and where even more energy vectors and storage options can be integrated. Furthermore, the link between the electric and thermal sector is in this case limited to the supply of energy to counterbalance heat losses from thermal storage, but it might be improved by considering the use of heat pumps or combined heat and power (CHP) plants.

It is also worth noting how the focus of the present analysis is the comparison of different energy system scenarios from an overall point view. As such, it does not aim at accurately reproducing the physical behaviour of all the modelled technologies, which may be indeed obtained, if needed, by implementing a MILP logic. For instance, MILP would allow better evaluating the choice of installing or not solar thermal collectors on a given building, by binding the decision to a minimum integer number of kW installed per user type, rather than allowing a linear space of optimisation from 0 to infinite that produces less realistic figures (such as having fractions of the unitary nominal collector capacity installed). Also, from a

thermodynamic point of view, the modelling of specific components such as the storage tank might be improved, within a MILP domain, by passing from a fully-mixed model to a multi-node or other types of models that allow to take into account stratification, as well as by adopting a temperature dependent heat loss factor. However, it should be noted that the fully-mixed approach here adopted provides a lower bound of performance and represents hence a conservative approach. This study also highlights the need for appropriate tools for the generation of multi-energy load profiles in off-grid areas and proposes a completely open-source solution that can be freely re-used, adapted and improved.

APPENDIX A – TECHNOLOGY PARAMETERS

PV panels' technical parameters are based on the Yingli YL300P-35b Polycrystalline module, which has a nominal capacity of 300 W per module. The model has been selected due to its availability in the considered region. The PV output has been obtained based on the 5-parameter model – implemented in the modelling language Modelica – presented in Balderrama et al. (2016). The cost is of 1.67 USD/W.

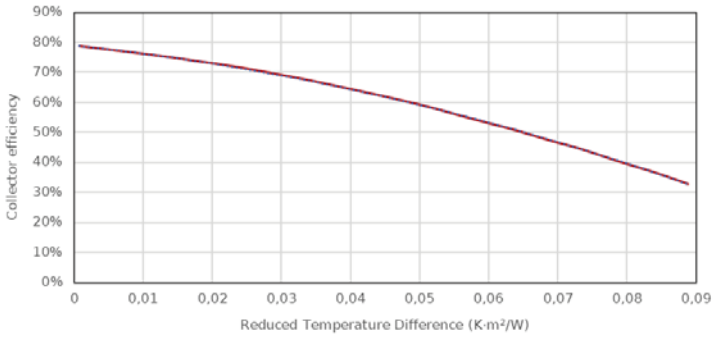

Figure A1 – Solar thermal collector efficiency curve, as a function of the reduced temperature difference. The latter is defined as the difference between (a) the average fluid temperature between inlet and outlet of the collector and (b) the ambient temperature, divided by the radiation incident on the tilted collector surface.

Solar thermal collectors parameters are instead referred to the datasheet of the FP-GV2.15.00, a flat-plate collector with an area of 1.963 m^2, manufacture by First Solares Co., Ltd. The output of the solar collector is obtained by calculating a hourly time-dependent efficiency time series (based on the efficiency curve provided by the datasheet and reported in Figure), and subsequently multiplying the latter for the collector area and the incident radiation (assuming an isotropic sky model) (Duffie & Beckman, 2013). The solar irradiation has been derived from experimental data measured in the field by means of a pyranometer.

The costs of solar thermal collectors and thermal storage are assessed based on the UNEP market assessment for solar water heaters in Chile (UNEP, 2014), which estimates a cost of 1900 USD for a standard solar water heating system composed of a 2-4 m^2 collector area, and 200-300 l tank volume. Assuming also a cost share of 20% for the tank and 80% for the collectors, and average inlet and outlet temperatures to the tank of 15°C and 45°C respectively (the latter used to compute the energy storage capacity (Caleffi, 1999)), we calculate a specific cost for the collectors of 0.55 USD/W and for the hot water tank of 0.043 USD/Wh.

APPENDIX B – LOAD PROFILES DATA

The User types and the corresponding appliances defined within LoadProGen are reported in Table B1 and Table B2. The detailed list of inputs is available in the form of open-source repository ("Multi-Energy Systems Py," 2018).

***User type* name**	**Acronym**	***Users* number**
High-Income households	HI	130
Low Income households	LI	202
Small commercial activities	CA	32
School	SC	1
Public Services	PS	6
Public lighting	PL	1

Table B1 – User types and number of users per each type, as defined within the LoadProGen environment.

	HI	**LI**	**CA**	**SC**	**PS**	**PL**
Electric appliances						
Indoor bulbs	7	1	13	2	12	8
Outdoor bulbs	1	1	2	1	1	6
TV	3	2	4	1	0	1
Phone charger	4	2	5	2	8	5
Fridge	0	1	4	0	3	0
Iron	1	1	1	0	1	0
PC	1	1	1	0	1	18
Radio	1	1	7	0	0	1
Washing Machine	1	0	0	0	0	0
Street lighting	0	0	0	0	0	375
Stadium light	0	0	0	0	0	20
DHW appliances (tasks)						
Sink (generic use)	0	0	6	0	0	0
Sink (dish washing)	2	2	0	0	0	0
Sink (hand washing)	1	1	2	20	2	0
Shower	1	1	2	2	2	0
Food washing	0	0	1	4	1	0

Table B2 – Number of electric appliances or fictitious thermal appliances defined in LoadProGen for each User type.

REFERENCES

ASHRAE. (2015). *2015 ASHRAE Handbook - Heating, ventilation and air-conditioning applications*.

Balderrama, S., Canedo, W., Fernandez, M., Lemort, V., & Quoilin, S. (2016). Techno-economic optimization of isolate micro- grids including PV and Li-Ion Batteries in the Bolivian context. In *The 29th International Conference on Efficiency, Cost, Optimization and Environmental Impact of Energy Systems* (pp. 1–12).

Caleffi, M. (1999). Produzione di acqua calda ad accumulo. *IDRAULICA*, *16*. Retrieved from http://www.caleffi.com/sites/default/files/certification_contracts/idraulica_16_it.pdf [Consultato il 6/6/2016]

Collier, U. (2018a). *Renewable Heat Policies - Delivering clean heat solutions for the energy transition*. Retrieved from http://www.iea.org/publications/insights/insightpublications/Renewable_Heat_Policies.pdf

Collier, U. (2018b). *Renewable Heat Policies - Delivering clean heat solutions for the energy transition*.

Duffie, J., & Beckman, W. (2013). *Solar Engineering of Thermal Processes, 4th ed. Journal of Solar Energy Engineering* (Vol. 116). https://doi.org/10.1115/1.2930068

Dufo-López, R., Bernal-Agustín, J. L., Yusta-Loyo, J. M., Domínguez-Navarro, J. A., Ramírez-Rosado, I. J., Lujano, J., & Aso, I. (2011). Multi-objective optimization minimizing cost and life cycle emissions of stand-alone PV-wind-diesel systems with batteries storage. *Applied Energy*, *88*(11), 4033–4041. https://doi.org/10.1016/j.apenergy.2011.04.019

Dufo-Lòpez, R., Cristòbal-Monreal, I. R., & Yusta, J. M. (2016). Stochastic-heuristic methodology for the optimisation of components and control variables of PV-wind-diesel-battery stand-alone systems, *99*. https://doi.org/10.1016/j.renene.2016.07.069

Dumont, O., Carmo, C., Dickes, R., Emelines, G., Quoilin, S., & Lemort, V. (2016). Hot water tanks : How to select the optimal modelling approach? In *CLIMA 2016*. Retrieved from https://orbi.uliege.be/handle/2268/199778

Fischer, D., Wolf, T., Scherer, J., & Wille-haussmann, B. (2016). A stochastic bottom-up model for space heating and domestic hot water load profiles for German households. *Energy & Buildings*, *124*, 120–128. https://doi.org/10.1016/j.enbuild.2016.04.069

Good, N., & Mancarella, P. (2017). Flexibility in multi-energy communities with electrical and thermal storage: A stochastic, robust approach for multi-service demand response. *IEEE Transactions on Smart Grid*. https://doi.org/10.1109/TSG.2017.2745559

HOMER Energy LLC. (n.d.). HOMER Energy. Retrieved from https://www.homerenergy.com

International Energy Agency. (2017). *Energy Access Outlook 2017 - From poverty to prosperity*. Retrieved from http://www.iea.org/publications/freepublications/publication/WEO2017SpecialReport_EnergyAccessOutlook.pdf

Lund, H., Alberg, P., Connolly, D., & Vad, B. (2017). Smart energy and smart energy systems. *Energy*, *137*, 556–565. https://doi.org/10.1016/j.energy.2017.05.123

Lund, H., Østergaard, P. A., Connolly, D., Ridjan, I., Mathiesen, B. V., Hvelplund, F., … Sorknæs, P. (2016). Energy Storage and Smart Energy Systems. *International Journal of Sustainable Energy Planning and Management*, *11*, 3–14. https://doi.org/10.5278/ijsepm.2016.11.2

Mancarella, P. (2014). MES (multi-energy systems): An overview of concepts and evaluation models. *Energy*, *65*, 1–17. https://doi.org/10.1016/j.energy.2013.10.041

Mandelli, S., Merlo, M., & Colombo, E. (2016). Novel procedure to formulate load profiles for off-grid rural areas. *Energy for Sustainable Development*, *31*, 130–142. https://doi.org/10.1016/j.esd.2016.01.005

Mashayekh, S., Stadler, M., Cardoso, G., & Heleno, M. (2017). A mixed integer linear programming approach for optimal DER portfolio, sizing, and placement in multi-energy microgrids. *Applied Energy*, *187*, 154–168. https://doi.org/10.1016/j.apenergy.2016.11.020

Mathiesen, B. V., Lund, H., Connolly, D., Wenzel, H., Ostergaard, P. A., Möller, B., … Hvelplund, F. K. (2015a). Smart Energy Systems for coherent 100% renewable energy and transport solutions. *Applied Energy*, *145*, 139–154. https://doi.org/10.1016/j.apenergy.2015.01.075

Mathiesen, B. V., Lund, H., Connolly, D., Wenzel, H., Ostergaard, P. A., Möller, B., … Hvelplund, F. K. (2015b). Smart Energy Systems for coherent 100% renewable energy and transport solutions. *Applied Energy*, *145*, 139–154. https://doi.org/10.1016/j.apenergy.2015.01.075

McKenna, E., & Thomson, M. (2016). High-resolution stochastic integrated thermal-electrical domestic demand model. *Applied Energy*, *165*, 445–461. https://doi.org/10.1016/j.apenergy.2015.12.089

Multi-Energy Systems Py. (2018). Retrieved from https://github.com/MicroGridsPy/SSB-2018-material

Pfenninger, S., Decarolis, J., Hirth, L., Quoilin, S., & Staffell, I. (2017). The importance of open data and software : Is energy research lagging behind ? *Energy Policy*, *101*(July 2016), 211–215. https://doi.org/10.1016/j.enpol.2016.11.046

UNEP. (2014). *Solar Water Heating Techscope Market Readiness Assessment*. Retrieved from http://www.in.undp.org/content/dam/india/docs/EnE/solar-water-heating-techscope-market-readiness-assessment.pdf

Widén, J., Lundh, M., Vassileva, I., Dahlquist, E., Ellegård, K., & Wäckelgård, E. (2009). Constructing load profiles for household electricity and hot water from time-use data—Modelling approach and validation. *Energy and Buildings*, *41*(7), 753–768. https://doi.org/10.1016/J.ENBUILD.2009.02.013

Questions and Answers:

Why not considering heat recovery from generator?

Francesco Lombardi:

We consider that even in the most energy intensive buildings (i.e hospitals) cogenerations is impossible due to the lack of a heat distribution system.

***

Are water tanks only for domestic hot water?

Francesco Lombardi:

Yes, space heating is currently not presented in the village, thought is likely that people may start plugging new appliances as time passes.

***

What is the number of optimization variables?

Francesco Lombardi:

We size the nominal capacity of the electric components and in each node for the thermal components. Also, there is the energy flows at each time step.

FOURTH SESSION
VENTILATION AND AIR HANDLING PROCESSES

Model development of a new single room ventilation enthalpy exchanger under wet conditions

A. Parthoens[1]*, S. Gendebien[2], P. Lemaitre[3], V. Lemort[4]

[(1),(2),(4)] Université de Liège, Belgium

[(3)]Certech, Belgium

ABSTRACT

The present paper deals with the model development of an enthalpy exchanger under wet conditions in the frame of single room ventilation. Numerous models take into account simultaneous heat and vapour transfer, but not liquid transfer. This new model takes into account condensation on stale air side, liquid transfer through porous membrane and finally water evaporation on the fresh air side. The involved phenomena depend on each other as the evaporation cools down the membrane, intensifying condensation. A coupling is then necessary, leading to spatial discretization of the exchanger and numerical considerations. An experimental set-up has been used to validate the membrane mass transfer model. The enthalpy exchanger model is then used to simulate performances under different outdoor conditions.

Keywords: Enthalpy exchanger, heat recovery, liquid water recovery

1. INTRODUCTION

1.1 Context

In the frame of energy savings, buildings (new and refurbished) are getting more and more thermally insulated and airtight. As outside air infiltrations are prevented due to the building envelope, ventilation systems are required to ensure a sufficient indoor air quality (Händel, 2001). The relative part of ventilation in the global building consumption is then increasing (Roulet et al., 2001). To fulfill the air renewal, different systems exist, going from simple natural ventilation to more complex systems with heat recovery. The heat recovery allows to decrease the ventilation energy losses by the means of a heat exchanger. Furthermore, beside the sensible heat, it is needed to ensure a good humidity level in the fresh air. This leads to a latent load representing a non-negligible part of the required air conditioning energy (Nasif et al., 2010). To reduce this load, devices that are called enthalpy exchanger, may be implemented to recover humidity in addition to heat.

1.2 State of art

Many works in scientific literature handle these kinds of exchangers. Dugaria et al. (2015) predicted with a 2-dimensional finite difference model sensible, latent and total effectiveness sensibility to membranes' characteristics. Sebai et al. (2014) modelled cross-flow enthalpy exchangers with balanced or unbalanced flow with a control volume method. Zhang (2009) measured latent effectiveness going up to about 70% with a paper-plate and paper-fin exchanger. Niu & Zhang (2001) showed numerically and experimentally the effectiveness evolution of enthalpy exchangers for different membranes and operating conditions. Koester et al. (2017) developed and validated a CFD model of what they called a counter- cross-flow enthalpy exchanger, presenting thermal as well as hydraulic performances of such an exchanger. They reached thermal and latent effectiveness of respectively 95 and 80% for most

advantageous tested conditions. Liang (2014) measured experimentally performances of a parallel-plates enthalpy exchanger. He showed that sensible effectiveness was independent of the relative humidity. However the latent effectiveness increased with it. Many more works are available in the literature and Zeng et al. (2017) made a review of such devices for building applications.

1.3 Motivations

All these publications show the real interest of these enthalpy exchangers. However most of these works consider membranes that are generally fragile such as paper. These are efficient considering heat and mass transfer but cannot be thermoformed and their lifetime is quite short. Furthermore, to the best authors' knowledge, no modelling of liquid water through a membrane exists. This paper tries to fulfill this gap by introducing a new model of liquid water transfer through a porous membrane in the frame of air-to-air enthalpy exchangers. The mass transfer model through the membrane is validated with a specific thermoformed polymer membrane and the simulation results of an enthalpy exchanger are presented for membranes of different permeability.

2. MODEL DESCRIPTION

The wet regime model handles several different aspects. There are first the heat transfer phenomena, with convection between the wall and the air fluxes as well as conduction within the wall. Then, different kinds of mass transfer are considered: moisture condensation in the stale air side as the air is cooled down, liquid water transfer through the membrane due to water partial pressure difference and finally evaporation of this water in the fresh air stream. It is to note that the different phenomena are linked. As the water film evaporates in the fresh air, it induces cooling of the membrane. If the membrane cools down, the condensation process will be intensified.

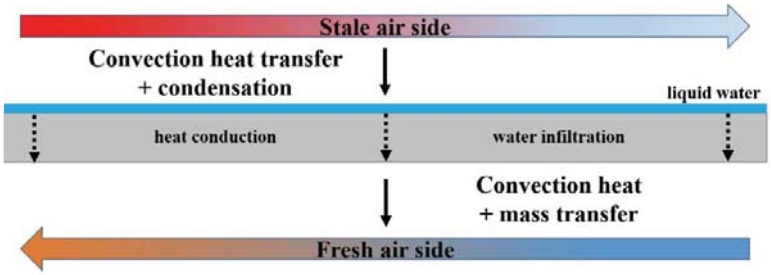

Figure 1: Schematic representation of the membrane and of the main physical phenomena

The global model links different bricks that take into account each of the phenomena. Each of these blocks is described hereafter.

2.1 Convection heat transfer and condensation on the stale air side

While the conditions are such that the stale air cools down when going through the exchanger, the partial pressure of vapour increases. If this pressure reaches the saturation pressure, condensation takes place. The modeling of this process was described and experimentally validated by Gendebien et al. (2013). It is a simplified cooling coil model based on the work of Lebrun et al. (1990), Brandemuehl et al. (1993) and Morisot & Marchio (2002). From this model, the mass flowrate of condensates $\dot{M}_{cond}$ as well as the heat transfer rate can be

evaluated. Lebrun et al. (1990) demonstrated that the total heat transfer rate could be expressed as:

$$\dot{Q}_{tot,st} = \varepsilon_{st} \cdot \dot{C}_{st,fict} \cdot (T_{su,wb,st} - T_{su,f}) \quad (1)$$

with ε_{st} being the effectiveness of the ε-NTU method and

$$\dot{C}_{st,fict} = \dot{M}_{st} \frac{h_{su,st} - h_{ex,st}}{T_{su,wb,st} - T_{ex,wb,st}} \quad (2)$$

This cooling coil model allows to determine the conditions at the outlet of the coil, the amount of condensates but it does not deal with mass transfer through a membrane. To be consistent, adaptations need to be implemented. The latter ones are explained in a following section

2.2 Water and heat transfer through the membrane

As porous membrane is wetted by the condensates, liquid water infiltrates up to the fresh air side. This mass transfer is driven by the difference of the water partial pressure on both sides of the membrane. This relies on two main assumptions:

- The whole system is in steady state,
- The porous membrane is already filled with liquid water (capillary effect is neglected).

As it is a liquid flow through a porous media, an equivalent law of Darcy was used, involving a membrane resistance *R* and a partial water pressure difference.

$$\dot{M}_{w,memb,th} = \frac{\Delta P \cdot A_{wet} \cdot \rho}{R \cdot \mu \cdot \delta} \quad (3)$$

with

$$\Delta P = P_{w,sat}(T_{memb,st}) - P_{w,f} \quad (4)$$

The membrane resistance is a feature of the membrane and should be experimentally determined. Nasif et al. (2012) showed that the membranes could be classified in three different categories. First the membrane resistance (to vapour, not liquid) can be independent of the atmospheric conditions. For the two other categories, the resistance can either increase or decrease with the air humidity ratio. In the frame of this paper, the resistance is considered as constant. The mass flow rate expressed in (3) is a maximum threshold and if the quantity of water available to migrate through the membrane is smaller, it must be taken into account. The water that actually goes from one side of the membrane to the other is then the minimum between the flow rate expressed in (3) and the condensed water flow rate:

$$\dot{M}_{w,memb} = \min(\dot{M}_{cond}, \dot{M}_{w,memb,th}) \quad (5)$$

The heat transfer through the membrane was described using the conduction heat transfer equations with the assumption that the conductivity only depends on the membrane material and not on the water quantity in the membrane. This hypothesis makes sense if the porosity is relatively low and if the membrane is thin. The liquid water reaching the fresh air side is now subject to evaporation.

2.3 Evaporation on the fresh air side

The liquid film arising from the membrane to the fresh air side is confronted to an air stream. A gas in motion in contact with a liquid leads to convective effects. This mass transfer between the wet surface and the air stream was modeled following the Ashrae Handbook

(1977) formalism. The driving force of the water transfer is the humidity ratio difference:

$$\dot{M}_{w,ev,f,th} = h_{mass} \cdot A_{wet} \cdot (\omega_{memb,f} - \overline{\omega}_f) \quad (6)$$

where $\omega_{memb,f}$ is the specific humidity at the membrane level (as there is a liquid film, the air is considered as saturated), $\overline{\omega}_f$ the mean humidity ratio of the fresh air flow and $h_m$is the mass convective coefficient. h_m was computed using the Chilton-Coburn analogy (Nasif et al. 2012):

$$h_{mass} = \frac{h}{\overline{cp}_a} \cdot Le^{-1/3} \quad (7)$$

The Lewis number was set to 1 as the Prandtl and Schmidt numbers are close to the unity for gas mixtures (Keys & Crawford, 1980). Iteration loops were made to predict the fresh air exhaust conditions to deduce the mean specific heat coefficient and humidity ratio, allowing to compute the mass convective transfer coefficient. Similarly to (5), the effective evaporated mass rate is expressed as:

$$\dot{M}_{w,ev,f} = \min(\dot{M}_{w,ev,f,th}, \dot{M}_{w,memb}) \quad (8)$$

The latent heat corresponding to this water evaporation can be written as:

$$\dot{Q}_{lat,f} = \dot{M}_f \cdot h_{fg} \cdot (\omega_{ex,f} - \omega_{su,f}) \quad (9)$$

with h_{fg} being the latent heat of vaporization being set to 2.442 kJ/kg. The sensible heat transfer can be computed from two different ways:

$$\dot{Q}_{sens,f,1} = \varepsilon_f \cdot \dot{C}_{min} \cdot (T_{su,st} - T_{su,f}) \quad (10)$$

$$\dot{Q}_{sens,f,2} = \dot{M}_f \cdot cp_f \cdot (T_{ex,f} - T_{su,f}) \quad (11)$$

The total heat exchange rate on the fresh air side is the sum of the latent and sensible heat flow rates.

2.4 Coupling and discretization

The equations described until here are consistent independently, however, the influence of the evaporation on the fresh air side on the condensation on the stale air side was not taken into account. To fix this, a slight modification of the equations was introduced. The trick used was to consider, for the heat transfer only (not for the mass transfer), the membrane as a fictitious wall that is at a constant temperature. In this formalism, the two air streams are not exchanging heat with each other but with this wall. If the ambient losses are neglected, the idea is applying the energy conservation by iterating on the wall temperature $T_{wall,fict}$ in order to equal the total heat transfer on both sides. The equations (1) and (10) then become:

$$\dot{Q}_{sens,f,1} = \varepsilon_f \cdot \dot{C}_f \cdot (T_{wall,fict} - T_{su,f}) \quad (12)$$

$$\dot{Q}_{tot,st} = \varepsilon_{st} \cdot \dot{C}_{st,fict} \cdot (T_{su,wb,st} - T_{wall,fict}) \quad (13)$$

ε_f and ε_{st} are the effectiveness of respectively the fresh and the stale air side of the ε-NTU method, now considering a semi-isothermal exchanger. As the quantity of evaporated water Eq. (6) impacts the latent Eq.(9) and thus the total heat transfer rate on the fresh air side, it will impact the wall temperature Eq. (12), which will impact the stale air side Eq. (13). The coupling is therefore made.

However, considering this technique at the whole exchanger level, the stale and the fresh air cannot exit the exchanger at a temperature respectively lower and higher than the fictitious wall temperature, leading again to an inconsistency. This is why a spatial discretization of the exchanger had to be made.

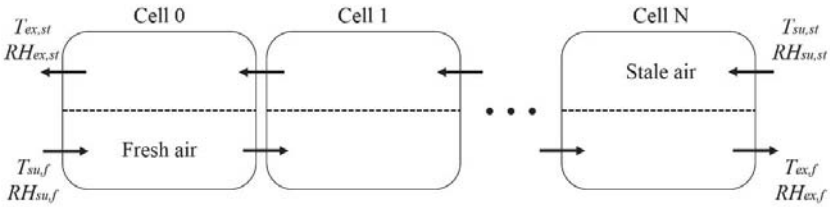

Figure 2: Representation of the special discretization of the enthalpy exchanger

The model described before was applied to each cell and the inputs of the cell *i* are:

$$x_{su,f}[i] = x_{ex,f}[i-1] \quad (14)$$

$$x_{su,st}[i] = x_{ex,st}[i+1] \quad (15)$$

x being either the temperature or the humidity. Guesses on the supply conditions of each cell are made on one side of the exchanger and the model iterates until the convergence of each cell is reached.

2.5 Parametric study of the required number of cells

As the model needs a spatial discretization, the question of the necessary number of cells must be considered. The method envisaged was to draw the model outputs evolution with the number of cells involved. A water resistance tending towards the infinity (i.e. impermeable membrane) was used to compare it with the model without mass transfer validated by Gendebien et al (2015). To see if it is either the number or the size of the cells that is the key parameter, the simulations were done for two exchangers of different sizes. The cells that were considered were are all of the same size fixed with the number of cells. The outputs chosen to check the convergence were the exhaust temperatures and the stale air exhaust humidity.

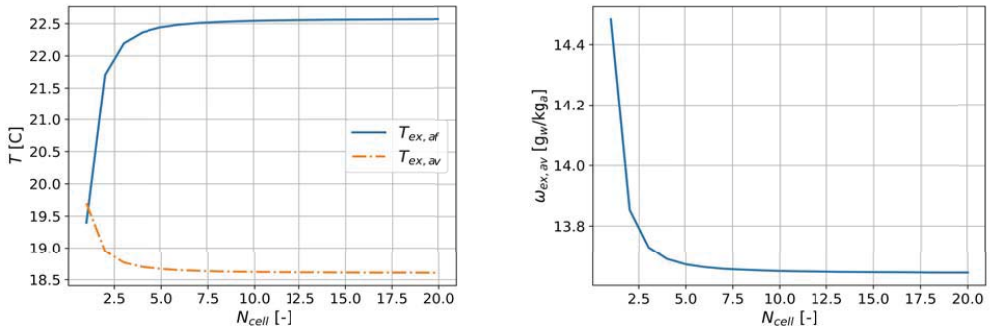

Figure 3: Model outputs versus the number of cells

Obviously, not enough cells will lead to erroneous results. Considering too many cells will lead to a good solution, however the computational time will be much higher. A trade-off should be made to conciliate good results with a reasonable simulation time. Figure 3 suggests that from above 10 cells, refining the discretization will not imply a substantial change in the results. More precisely, Figure 4 shows that from 10 cells, the difference adding new cell is asymptotical to 0. For such an exchanger, using a discretization of 10 cells seems to be the best trade off between the precision the computational time.

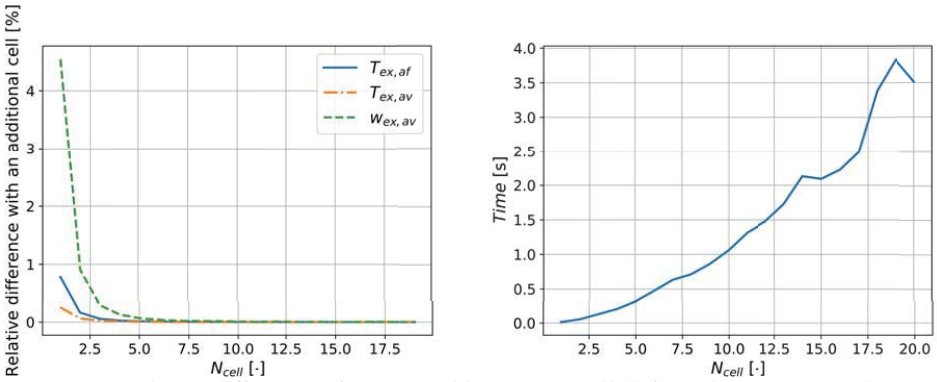

Figure 4: Relative difference of outputs adding a new cell (left) and computational time regarding the number of cell (right)

The simulation time was for simulations conducted with a machine with Intel i7 processor running at 2.5 GHz. The same simulations were achieved for the exact same exchanger and conditions except that rather than having an exchange area of 2 m², it was 4 m². The results showed that the difference of outputs between the 10th and 11th cells was under 0.04%. This revealed that the number of cells is more important than their size. Indeed, for the larger exchanger with the same number of cells, the cells were twice bigger, however, the results were satisfactory. The output difference with the validated model (impermeable) were of 0.40%, 0.72% and 0.70% for respectively $T_{ex,f}$, $T_{ex,st}$ and $\omega_{ex,st}$ considering 10 cells for a 4 m² exchanger.

3. MEMBRANE MODEL VALIDATION

The model validation was achieved in different steps. First, the cooling coil model with condensation developed by Gendebien et al. (2015) had been validated in their paper. Therefore this step is skipped in the frame of this paper.
Then the model of the mass transfer through the membrane was considered. First, the membrane resistance of (3) had to be determined experimentally. The experimental setup is represented in Figure 5.

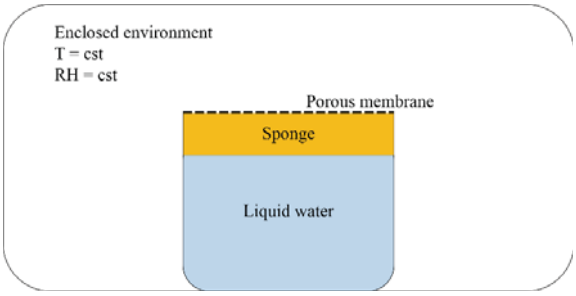

Figure 5: Experimental setup used for the membrane resistance determination

Preliminarily, the membrane was submerged in water for one hour to load all the interstices and to reach steady state conditions. Then, a recipient was filled with liquid water and closed with the membrane. To ensure a permanent contact between the liquid and the membrane, a sponge was added and periodic checks were made to control that the liquid was in contact with the sponge during the whole experiment. This setup was weighted and put in an enclosed

environment where the atmospheric conditions were controlled. The temperature was fixed to 23±0.5°C and the relative humidity to 50 ± 1%. After 24 hours in these conditions, the recipient was weighted a second time. The difference between the two measures corresponded to the water that went through the membrane and that was evaporated to the environment. The mass flow rate and the environmental conditions being known, the membrane resistance *R* could be deduced from a rewriting of (4).
Figure 6 represents the normalized mass flow rate of water transferred through the membrane.

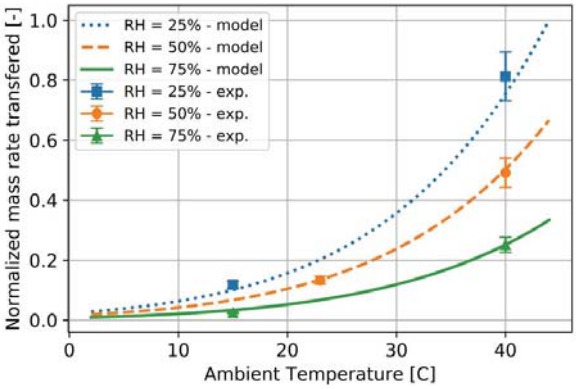

Figure 6: Model validation transfer of water through the membrane

The different curves are the simulation results, varying the temperature and the humidity. If the atmospheric pressure is considered as constant, these two factors totally set the atmospheric conditions. The different markers represent different experimental measurements with a 10% error bar. The membrane resistance was identified with the 40°C and 75% relative humidity point. Figure 6 shows satisfying results for the other points. The membrane model is considered as validated and the assumption of constant membrane resistance (for this specific membrane) is consistent.

4. SIMULATION RESULTS

4.1 Enthalpy exchanger definition

For the simulations, the geometry of the heat exchanger was fixed. A counter-flow exchanger with an exchange surface of 4 m² was considered. This corresponds to an exchanger in single room ventilation units. The design was such that the sensible effectiveness in dry regime with a flow rate of 42 m^3/h is 80%. The thermal conductivity of the membrane was 0.2 W/m/K (i.e. polypropylene) and its thickness was 105 µm.

4.2 Influence of membrane resistance on exchanger effectiveness

The membrane resistance obviously impacts the mass transfer through the membrane for given atmospheric conditions. A parametric study was conducted to see the impact of this resistance on the sensible and latent effectiveness, for both air flows. The conditions were such that the condensation appears at the inlet of the exchanger (i.e. $RH_{su,st}=100\%$) and at a temperature of 20°C. The fresh air was at 15°C and 80% of relative humidity. Before the analysis, the effectiveness should be defined:

$$\varepsilon_{lat,f} = \frac{\dot{M}_f \cdot h_{fg} \cdot (\omega_{ex,f} - \omega_{su,f})}{\dot{M}_{min} \cdot h_{fg} \cdot (\omega_{su,st} - \omega_{su,f})} \quad (16) \qquad \varepsilon_{lat,st} = \frac{\dot{M}_{st} \cdot h_{fg} \cdot (\omega_{su,st} - \omega_{ex,st})}{\dot{M}_{min} \cdot h_{fg} \cdot (\omega_{su,st} - \omega_{su,f})} \quad (17)$$

$$\varepsilon_{sens,f} = \frac{\dot{C}_f \cdot (T_{ex,f} - T_{su,f})}{\dot{C}_{min} \cdot (T_{su,st} - T_{su,f})} \quad (18) \qquad \varepsilon_{sens,st} = \frac{\dot{C}_{st} \cdot (T_{su,st} - T_{ex,st})}{\dot{C}_{min} \cdot (T_{su,st} - T_{su,f})} \quad (19)$$

$$\varepsilon_{tot,f} = \frac{\dot{M}_f \cdot (h_{ex,f} - h_{su,f})}{\dot{M}_{min} \cdot (h_{su,st} - h_{su,f})} \quad (20) \qquad \varepsilon_{tot,st} = \frac{\dot{M}_{st} \cdot (h_{su,st} - h_{ex,st})}{\dot{M}_{min} \cdot (h_{su,st} - h_{su,f})} \quad (21)$$

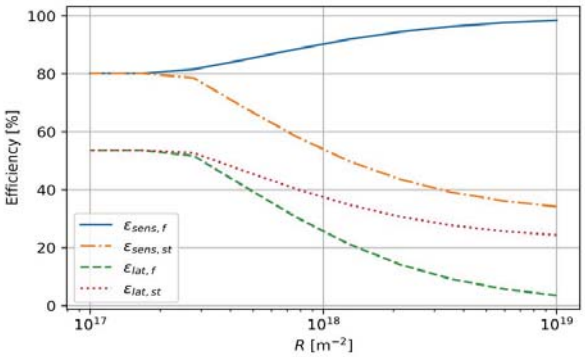

Figure 7: Effectiveness variation regarding the membrane permeability resistance

First, it is to note that for low resistances (high water transfer) constant effectiveness is observed. This means that all the condensed water is transferred through the membrane and evaporated in the fresh air. This case is extreme and should not be considered. Then, as the resistance increases, all effectiveness's decrease, except $\varepsilon_{sens,f}$. This because if less water is transferred and then evaporated, then a larger proportion of the power transferred to the fresh air will be devoted to heating it up. Next, $\varepsilon_{lat,f}$ decreases because if less water is available to evaporate, the exhaust humidity will decrease. Then, if less water evaporates on the fresh air side, the membrane mean temperature will increase. This conducts to a lower sensible heat transfer (smaller temperature difference between the air stream and the membrane) and less condensation as the colder the wall, the higher the condensation. This explains the fall of $\varepsilon_{sens,st}$ and $\varepsilon_{lat,st}$ with the membrane resistance increase.

For the rest of the numerical study, as the resistance is considered constant, it is fixed to a specific value. For the above-mentioned conditions, it was chosen to take a resistance leading to $\varepsilon_{lat,f}$ = 30%, which is consistent with the literature. The matching resistance is $R =$ 7.85E17 m^{-2}.

4.3 Performance mapping

For a deeper understanding of the involved phenomena and coupling of the evaporation and the condensation, different performance maps were drawn, based on simulation results. To build the latter ones, indoor conditions were set to 20°C and 100% HR (to still ensure the condensation from the beginning of the exchanger). Then the outdoor conditions varied from 2 to 18°C and 10 to 90% HR.

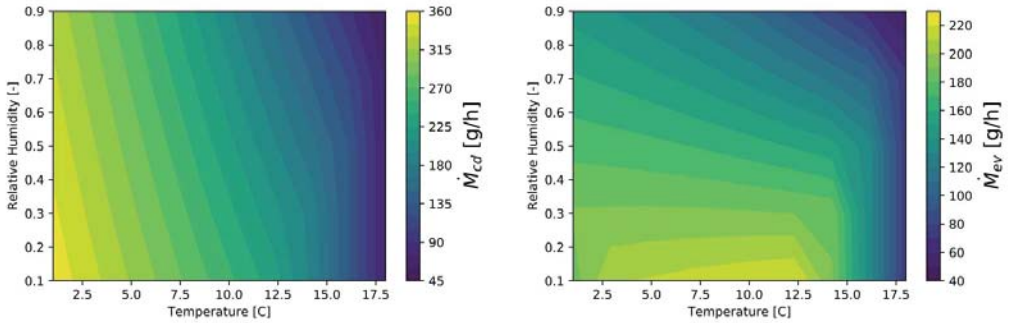

Figure 8: Mass flow rate condensed on the stale air side (left) and evaporated on the fresh air side (right) regarding the fresh air supply temperature and humidity

Looking first at the $\dot{M}_{cd}$ for a constant humidity, the hotter the fresh air, the less the condensation. Intuitively, it is physically consistent. Then for a fixed temperature, the trend is that the condensation is favoured for lower fresh air humidity. If the humidity is low, the water will evaporate more easily, implying a wall cooling.

For a given temperature, as the humidity increases, less water evaporates on the fresh air side. For a fixed humidity, an optimum is observed, resulting on one side on the membrane capacity to transfer water and on the other side on the available quantity of condensates. When the fresh air is cold, it enhances the condensation process. Furthermore, when the air is warmer, the mass transfer is eased but the mass of condensates is limited. The best behaviours result thus from a trade-off.

These phenomena are recovered in the representation of latent effectiveness shown in the next figures. Especially for the fresh air latent effectiveness, the optimum can be easily spotted.

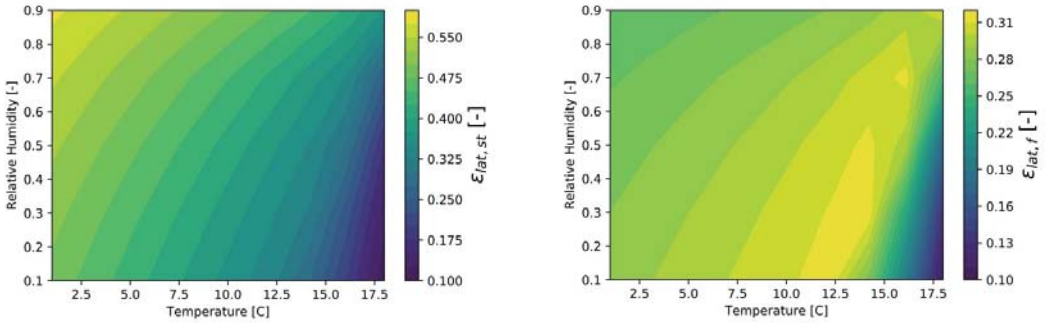

Figure 9: Latent effectiveness (stale air side (left), fresh air side (right)) regarding the outdoor temperature and relative humidity

Then, the sensible effectiveness can be drawn with the same approach.

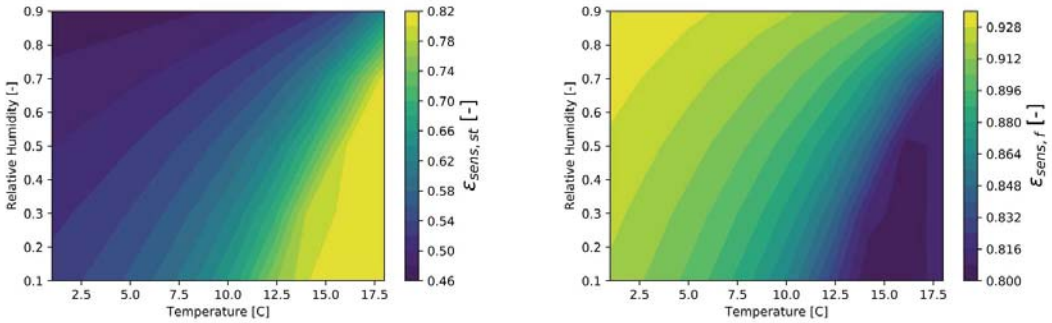

Figure 10: Sensible effectiveness (stale air side (left), fresh air side (right)) regarding the outdoor temperature and relative humidity

For the stale air side, the sensible effectiveness is better while the condensation is low. The combination to have a good sensible effectiveness is hot and dry outdoor air. Hot air limits the condensation and moreover if it is dry, it will enhance evaporation on the fresh air side (giving a colder membrane). Concerning the sensible effectiveness on fresh air side, it is the opposite: it is better for cold and humid air. These conditions are such that the evaporation is limited, leading to a small latent part and thus giving high sensible performances.

To have an idea of the conditions giving a better global heat transfer between the two sides, the same map was drawn for the total heat transfer as well as the total effectiveness (Eq. (20) and (21)).

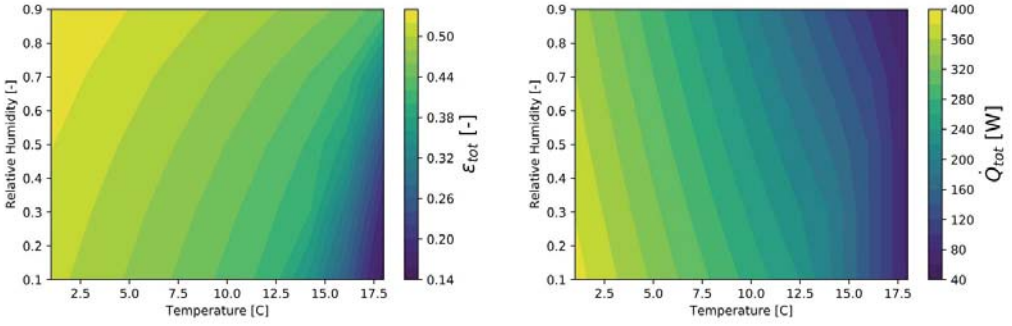

Figure 11: Total effectiveness (left) and total heat transfer (right) regarding the outdoor temperature and relative humidity

To obtain the best total effectiveness, the colder and the more humid the better. A large temperature difference is favourable to high sensible transfer. Then the increase of effectiveness with the humidity can be explained looking at the Eq. (20) and (21). Indeed, for a given temperature, if the supply fresh air humidity is higher, the supply enthalpy will be larger too, decreasing the value of the denominator. Then, to recover a maximum heat power (sensible and latent), the colder and the dryer the best. This combination will lead to a large water condensation on the stale air side and as it is dry, evaporation will be favoured. With the coupling effect, these phenomena will strengthen each other leading to high latent load. Furthermore, with the high temperature difference, the sensible part is also consequent.

5. CONCLUSIONS

This paper attempts to fill a gap in the literature that is the modeling of liquid transfer trough a porous membrane in the frame of air-to-air enthalpy exchangers. The different processes, namely the water condensation, liquid transfer and evaporation were described. As the water evaporation on fresh air side impacts the membrane temperature and thus the condensation process on the stale air side, a coupling between these phenomena was implemented.

The coupling led to the need of special discretization of the enthalpy exchanger to keep physical consistency. The number of cells involved was discussed and it was shown that the number and not the size of the cell was the key parameter. With 10 cells, good numerical results were achieved keeping a reasonable simulation time.

The model of the membrane (not the whole exchanger model) was successfully validated experimentally by measuring the water transfer for different atmospheric conditions

The enthalpy exchanger model under wet conditions was then used to predict the mass transfers, the effectiveness and the exchanged thermal power, for different outdoor conditions. It revealed that to recover maximum heat (sensible and latent), dry and cold conditions are preferred. However to recover a maximum of water in the fresh air flow, an optimum resulting from the ability to transfer water through the membrane and the quantity of condensates available was found.

Acknowledgment

This work was supported by the Walloon Region and the Pole Mecatech [convention 7711].

NOMENCLATURE

QUANTITIES

cp	specific heat capacity, J/kg/K
$\dot{C}$	capacity flowrate, W/K
h	convective coefficient, W/m^2/K or kg/m^2/s
$h_{fg.}$	heat of vaporization, J/kg
Le	Lewis number, -
$\dot{M}$	mass flow rate, kg/s
$\dot{Q}$	heat transfer rate, kg/s
R	membrane resistance, m^{-2}
RH	relative humidity, -

GREEK SYMBOLS

ε	effectiveness, -
δ	thickness, m
Δ	difference, -
ω	specific humidity, kg$_w$/kg$_a$
ρ	density, kg/m^3
μ	dynamic viscosity, Pa.s

6. REFERENCES

Arteconi, A., Hewitt, N., & Polonara, F. (2013). Domestic demand-side management (DSM): Role of theat pumps and thermal energy storage (TES) systems. *Applied Thermal Engineering, 51*(1-2), 155-165.

Ashrae Handbook. (1977). New-York.

AST, H. (n.d.). *IEA Annex 10 - System simultaion : Thermostactic Valve.* Stuttgart, Germany.

Baetens, R., & Saelens, D. (2015). Modelling uncertainty in district energy simulations by stochastic residential occupant behaviour. *Journal of Building Performance Simulation, 9*(4), 431-447.

Baetens, R., De Coninck, R., Jorissen, F., Picard, D., Helsen, L., & Saelens, D. (2015). OpenIDEAS - an open framework for integrated district energy simulations. *14th Conference of International Building Performance Simulation Association*, (pp. 347-354). Hyderabad, India.

Bouvenot, J.-B., Andlauer, B., Stabat, P., Marchio, D., Flamenta, B., Latoura, B., & Siroux, M. (2014). Gas Stirling engine - CHP boiler experimental data driven model for building energy simulation. *Energy and Buildings 84*, 117-131.

Brandemuehl, M., Gabel, S., & Andersen, I. (1993). A toolkit for secondary HVAC System Energy Calculations. *ASHRAE*.

Braun, J. E.-H. (2006). Assessment of demand limiting using building thermal mass in small commercial buildings. *ASHRAE Transactions*, 112 PART 1, 547-558.

Cabeza, L. F. (2017). Review on sorption materials and technologies for heat pumps and thermal energy storage. *Renewable and Sustainable Energy Reviews, 110*, 3-39.

Candanedo, J., Dehkordi, V., & Lopez, P. (2014). A multi-level architecture to facilitate MPC implementation in commercial buildings: basic principles and case study. *Proceedings of eSim 2014 conference.*

Claeys, B., & Sourbron, M. (2017, May 24). Pas het elektriciteitstarief aan voor meer groene warmte (in Dutch). *De Tijd, Opinion piece*.

Code van goede praktijk voor de toepassing van warmtepompsystemen in de woningbouw (in Dutch). (2004). *Computer software manual*.

Coffey, E. B. (2013). Approximating model predictive control with existing building simulation tools and offline optimization. *Journal of Building Performance Simulation, 6*(3), 220-235.

Commission des Communautés Européennes. (n.d.). *"Etude CIEL" : Maîtrise de la Demande Electrique Campagne de Mesures par usage dans le secteur domestique.*

CSTB. (2012). *Règlementation Thermique 2012 - Règles d'application Th-Bât.* CSTB Edition.

Cyx, W., Renders, N., & Van Holm, M. (2011). *IEE TABULA - Typology Approach for Building Stock Energy Assessment.* Technical report, VITO, Vlaamse instelling voor technologisch onderzoek.

Cyx, W., Renders, N., Van Holm, M., & Verbeke, S. (2011). *IEE TABULA - Typology Approach for Building Stock Energy Assessment.*

Daikin Europe N.V. (2018). Technical data sheets for Altherma EVLQ-CV3, Multisplit 4MXS, Split FTXM35+RXM25. Brussels. Retrieved January 19, 2018, from estranet.daikineurope.com/captab

Deutscher Wetterdienst. (2004). *Testreferenzjahr 2004.* Consulté le 08 02, 2016, sur https://www.dwd.de/DE/leistungen/testreferenzjahre/testreferenzjahre.html

Deutsches Institut für Normung. (2016). DIN EN 14825 - Luftkonditionierer, Flüssigkeitskühlsätze und Wärmepumpen mit elektrisch angetriebenen Verdichtern zur Raumbeheizung und -kühlung - Prüfung und Leistungsbemessung unter Teillastbedingungen und Berechnung der saisonalen Arbeitszahl.

Dugaria, S., Moro, L., & Del Col, D. (2015). Modelling heat and mass transfer in a membrane-based air-to-air enthalpy exchanger. *33rd UIT (Italian Union of Thermo-fluid-dynamics) Heat Transfer Conference.*

Elia. (2018, July 6). *Déséquilibre actuel du système*. Récupéré sur Elia: http://www.elia.be/fr/grid-data/balancing/desequilibre-actuel-du-systeme

Energiebilanzen AG. (2018). *Evaluation tables from 1990-2017.*

Enertech, ADEME, & Union Européenne. (2008). *Projet REMODECE : Mesure de la consommation des usages domestiques de l'audiovisuel et de l'informatique - Rapport final.*

Engie. (2018, May). Engie Easy Fixed 1y tariffs for electricity and gas. Retrieved May 10, 2018, from https://www.engie-electrabel.be/nl/energie/elektriciteit-gas/prijzen-voorwaarden

Entsoe Transparancy Platform. (s.d.). Day-ahead electricity prices. Consulté le May 10, 2018, sur https://transparency.entsoe.eu/transmission-domain/r2/dayAheadPrices/show

Euroheat & Power. (2005-2006). *Ecoheatcool project - Workpackage 3: Guidelines for assessing the efficiency of district heating and district cooling systems.* Technical report, Euroheat & Power. Retrieved March 18, 2018, from https://www.euroheat.org/wp-content/uploads/2016/02/Ecoheatcool_WP3_Web.pdf

European Comission. (2013). *Smarter, greener, more inclusive? Indicators to support the Europe 2020 strategy.* Luxembourg (LU).

European Parliament. (2016, November 19). The primary energy factor for renewables. *Parliamentary questions*. Consulté le June 2, 2018, sur http://www.europarl.europa.eu/sides/getDoc.do?type=WQ&reference=E-2016-008892&format=XML&language=EN; http://www.europarl.europa.eu/sides/getAllAnswers.do?reference=E-2016-008892&language=EN

Forsén, M. (2005). *Heat pumps - technology and environmental impact.* Technical report, Swedisch Heat Pump Association, European Heat Pump Association. Consulté le March 12, 2018, sur http://ec.europa.eu/environment/ecolabel/about_ecolabel/reports/hp_tech_env_impact_aug2005.pdf

Gendebien, S., Bertagnolio, S., & Lemort, V. (2013). Investigation on a ventilation heat recovery exchanger: Modeling and. *Energy and Buildings, 62*, 176-189.

Georges, E., Gendebien, S., Bertagnolio, S., Dechesne, B., & Lemort, V. (2013). *Evolution des profils de consommations énergétiques des bâtiments résidentiels en Belgique,*

suite à l'introduction de nouvelles technologies de chauffage, climatisation et cogénération. Liège (Belgium).

Händel, C. (2001). Ventilation with heat recovery. *Rheva Journal*.

Henze, G., Felsmann, C., & Knabe, G. (2004). Evaluation of optimal control for active and passive building thermal storage. *International Journal of Thermal Sciences, 43*(2), 173–183.

Henze, G., Le, T., Florita, A., & Felsmann, C. (2006). Sensitivity Analysis of Optimal Building Thermal Mass Control. *Journal of Solar Energy Engineering, 129*(4), 473-485.

Huchuk, B., A. Cruickshank, C., O'Brien, W., & Gunay, H. (2014). Recursive thermal building model training using Ensemble. *Proceedings of eSim 2014 conference.*

Hydro-Québec. (2014, 01 22). *Hydro-Québec demande à ses clients de poursuivre leurs efforts de réduction de la consommation d'électricité en période de pointe et les remercie de leur collaboration.* Consulté le August 01, 2014, sur http://cnw.ca/ONjV5

IBPSA-Canada. (2011). *Model predictive control in buildings workshop.* Consulté le September 10, 2014, sur http://www.ibpsa.us/conferences

IEA, & IPEEC. (2015). *Building energy performance metrics - Supporting energy efficiency progress in major economies.* Technical report, IEA, IPEEC. Consulté le March 12, 2018, sur https://www.iea.org/publications/freepublications/publication/BuildingEnergyPerformanceMetrics.pdf

ISO-1. (2008). ISO 10211:2008 - Thermal bridges in building construction - Heat flows and surface temperatures - Detailed calculations.

ISO-2. (2008, June). ISO 10456: 2008 - Building materials and products - Hygrothermal properties - Tabulated design values and procedures for determining declared and design thermal values.

ISO-3. (2008, April). ISO 13370: 2008 - Thermal performance of buildings - Heat transfer via the groung - Calculation methods.

ISO-4. (2013). ISO 13790: 2013 - Energy performance of buildings - Calculation of energy use for space heating and cooling. *Energy performance of buildings - Calculation of energy use for space heating and cooling*.

ISO-5. (2008). ISO 6946:2008 - Building components and building elements - Thermal resistance and thermal transmittance - Calculation method.

Jespers, K., Al Koussa, J., Dams, Y., Renders, N., & Vingerhoets, P. (2017). *Inventaris hernieuwbare energiebronnen Vlaanderen 2005-2016 (in Dutch).* Technical report, VITO, Vlaams instituut voor technologisch onderzoek. Consulté le March 12, 2018, sur https://www.energiesparen.be/sites/default/files/atoms/files/Inventaris_hernieuwbare_energiebronnen_Vlaanderen_2005-2016_v6.pdf

Kaltschmitt, M., Streicher, W., & Wiese, A. (2013). *Erneuerbare Energien: Systemtechnik, Wirtschaftlichkeit, Umweltaspekte.* Heidelberg: Springer Verlag.

Kelly, G. (1988). Control system simulation in North America. *Energy and Buildings, 10*(3), 193–202.

Keys, W. M., & Crawford, M. E. (1980). *Convective heat and mass transfer* .

Knight, I. (2007). *IEA Annex 42 - The simulation of Building-Integrated Fuel Cell and other cogeneration systems (FC+COGEN-SIM) : Domestic Energy Profiles.* Cardiff (UK).

Koester, S., Falkenberg, M., Logemann, M., & Wessling, M. (2017). Modeling heat and mass transfer in cross-counterflow enthalpy exchangers. *Journal of Membrane Science*, 68-76.

Kummert, M., Leduc , M.-A., & Moreau , A. (2011). Using MPC to reduce the peak demand associated with electric heating. *Model Predictive Control in Buildings Workshop.* Montréal.

Lebrun, J., Ding, X., Eppe, J.-P., & Wasac, M. (1990). Cooling Coil Models to be used in Transient and/or Wet Regimes. Theoretical Analysis and Experimental Validation. *Proceedings of SSB*, (pp. 405-411). Liège.

Lehmann, B., Gyalistras, D., Gwerder, M., Wirth, K., & Carl, S. (2013). Intermediate complexity model for Model Predictive Control of Integrated Room. *Energy and Buildings*(58), 250–262.

Lehrstuhl für Technische Thermodynamik - RWTH Aachen. (2017). SorpLib 3: Adsorption Energy System Library. Aachen.

Leonhardt, C. (2016). *Thermische Speicher mit Phasenwechselmaterialien im Heizsystem.* Aachen.

Leonhardt, C., & Müller, D. (2009). Modelling of Residential Heating Systems using a Phase Change Material Storage System. *Proceedings of the 7th International Modelica Conference.* Como.

Leonhardt, C., & Müller, D. (2010). Latent Heat Storage Devices for Heat Pump and Solar Heating Systems.

Liang, C. (2014). Experiments Investigation of the Parallel-plates Enthalpy Exchangers. *The 6th International Conference on Applied Energy*, (pp. 2699 – 2703).

Luminus. (2018, May). Luminus #BeGreenFix tariffs for electricity and gas. Consulté le May 10, 2018, sur https://www.luminus.be/nl/prive/elektriciteit/begreenfix/#tab3; https://www.luminus.be/nl/prive/gas/begreenfix/#tab3

Müller, D., Lauster, M., Constantin, A., Fuchs, M., & Remmen, P. (2016, September). AixLib - An Open-Source Modelica Library within the IEA-EBC Annex 60 Framework. *BauSIM*, pp. 3-9.

Ma, Y., & Borrelli, F. (2011). Hierarchical Predictive Control Energy Efficient Buildings. *Model Predictive Control in Buildings Workshop.* Montreal.

Madson, H., & Holst, J. (1995). Estimation of continuous-time models for the heat dynamics. *Energy and Buildings*, 67-79.

May-Ostendorp, P., Henze, G., Corbin, C., Rajagopalan, B., & Felsmann, C. (2011). Model-predictive control of mixed-mode buildings with rule extraction. *Building and Environment, 46*(2), 428–437.

May-Ostendorp, P., Henze, G., Rajagopalan, B., & Corbin, C. (2013). Extraction of supervisory building control rules from model predictive control of windows in a mixed mode building. *Journal of Building Performance Simulation, 6*(3), 199-219.

Mehrfeld, P. (2016). Reference Building Model. Aachen: E.ON Energy Research Center, Institute for Energy Efficient Buildings and Indoor Climate.

Morari, M., & Lee, J. (1999). Model predictive control: past, present and future. *Computers & Chemical Engineering*, 667–682.

Morisot, O., & Marchio, D. (2002). Simplified Model for the Operation of Chilled Water Cooling Coils Under Nonnominal Conditions. *HVAC&R Research*, pp. 135-158.

Nasif, M. S., Al-Waked, R., Behnia, M., & Morrison, G. (2012). Modeling of Air to Air Enthalpy Heat Exchanger. *Heat Transfer Engineering*, 1010-1023.

Nasif, M., AL-Waked, R., Morrison, G., & Behinia, M. (2010). Membrane heat exchanger in HVAC energy recovery systems, systems energy analysis. *Energy and buildings* , 1833-1840.

Nassif, N., Kajl, S., & Sabourin, R. (2005a). Simplified model-based optimal control of VAV air conditioning system. Montreal: Proceedings of the 9th international building performance simulation association (IBPSA) conference.

Nassif, N., Stainslaw , K., & Sabourin, R. (2005b). Optimization of HVAC control system strategy using two-objective genetic algorithm. *International Journal of HVAC&R Research, 11*(3), 459-486.

Niu, J., & Zhang, L. (2001). Membrane-based Enthalpy Exchanger: material considerations and clarification of moisture resistance. *Journal of Membrane Science*, 179-191.

Oldewurtel, F., Parisio, A., Jones, C., & Morari, M. (2010). Energy efficient building climate control using Stochastic Model Predictive Control and weather predictions. *American Control Conference (ACC)*, (pp. 5100 - 5105). Baltimore, MD .

Oldewurtel, F., Parisio, A., Jonesc, C. N., Gyalistrasa, D., Gwerderd, M., Stauche, V., . . . Moraria, M. (2012). Use of model predictive control and weather forecasts for energy efficient building climate control. *Energy and Buildings* (45), 15–27.

Patteeuw, D. (2016). *Demand response for residential heat pumps in interaction with the electricity generation system.* PhD Thesis, KU Leuven, Belgium.

Prívara, S., Cigler, J., Váňa, Z., Oldewurtel, F., Sagerschnig, C., & Žáčeková, E. (2013). Building modeling as a crucial part for building predictive control. *Energy and Buildings, 56*, 8–22.

Reynders, G. (2015). *Quantifying the impact of building design on the potential of structural storage for active demand response in residential buildings.* PhD Thesis, KU Leuven, Belgium.

Rosato, A., & Sibilio, S. (2012). Calibration and validation of a model for simulating thermal and electric performance of an internal combustion engine-based micro-cogeneration device. *Applied Thermal Engineering 45-46*, 79-98.

Roulet, C.-A., Heidt, F., Foradini, F., & Pibiri, M.-C. (2001). Real heat recovery with air handling units. *Energy and Buildings, 33*(5), 495-502.

Sebai, R., Chouikh, R., & Guizani, A. (2014). Cross-flow membrane-based enthalpy exchanger balanced and unbalanced flow. *Energy Conversion and Management*, 19-28.

Sharma, A., & et al. (2009). Review on thermal energy storage with phase change materials and applications. *Renewable and Sustainable Energy Reviews, 13*(2), 318-345.

Six, D., Desmedt, J., Vanhoudt, D., & Van Bael, J. (2011). Exploring the flexibility potential of residential heat pumps combined with thermal energy storage for smart grids. *21st International Conference on Electricity Distribution*, (pp. 1-4). Frankfurt, Germany.

Stephan, W. (n.d.). *IEA Annex 10 - System simulation : Radiator.* Stuttgart (Germany).

Sturzenegger, D., Gyalistras, D., Semeraro, V., Morari, M., & Smith, R. S. (2014). BRCM Matlab Toolbox: Model Generation for Model Predictive Building Control. *American Control Conference.*

Sweetnam, T., Fell, M., Oikonomou, E., & Oreszczyn, T. (2018). Domestic demand-side response with heat pumps: controls and tariffs. *Building Research & Information*, 1-18.

Swinton, M. C., Moussa, H., & Marchand, R. J. (2001). Commissioning Twin Houses for Assessing the Performance of Energy-Conserving Technologies. Thermal Performance of the Exterior Envelopes of Whole Buildings VIII.

TLK-Thermo GmbH. (2012). *TIL Suite.* Consulté le 11 14, 2018, sur https://www.tlk-thermo.com/index.php/de/softwareprodukte/til-suite

Verhelst, C., Logist, F., Van Impe, J., & Helsen, L. (2012). Study of the optimal control problem formulation for modulating air-to-water heat pumps connected to a residential floor heating system. *Energy and Buildings, 45*, 43-53.

Verhelst, C., Sourbron, M., Antonov, S., & Helsen , L. (2011). Towards MPC for office buildings with TABS connected to a GCHP system controller model. *Model Predictive Control in Buildings Workshop.* Montreal.

Viskanta, R., Behnia, M., & Karalis, A. (1977, Nr. 2). Interferometric observations of the temperatur estructure in water cooled or heated from above. *Advances in Water Resources*, pp. 57-59.

VREG. (2018). Hoeveel kost 1 kWh elektriciteit/aardgas? Prijzen voor huishoudelijke afnemers (all in, incl. BTW) (in Dutch). Consulté le May 10, 2018, sur https://infogram.com/hoeveel-kost-1-kwh-elektriciteitaardgas-prijzen-voor-gezinnen-all-in-incl-btw-1h9j6qj8ovd54gz

Wang , S., & Xu, X. (2006). Simplified building model for transient thermal performance estimation. *International Journal of Thermal Sciences*(45), 419–432.

Wang, S., & Jin, X. (2000). Model-based optimal control of VAV air-conditioning system using genetic algorithm. *Building and Environment, 35*(6), 471–487.

Wetter, M. (2001). GenOpt® -- A Generic Optimization Program. Proceedings of the 7th IBPSA Conference. Récupéré sur http://gundog.lbl.gov/GO/

Wetter, M. (2011). *GenOpt, Generic Optimization Program, User Manual Version 3.1.0.* Consulté le July 01, 2014, sur http://gundog.lbl.gov/GO/

Wystrcil, e. a. (2013). Model-based optimization of control strategies for low-exergy space heating systems using an environmental heat source. *13th Conference of International Building Performance Simulation Association.* Chambéry: BS2013.

Zeng, C., Liu, S., & Shukla, A. (2017). A review on the air-to-air heat and mass exchanger technologies for building applications. *Renewable and Sustainable Energy Reviews*, 753-774.

Zhang, L.-Z. (2009). Heat and mass transfer in plate-fin enthalpy exchangers with different plate and fin materials. *International Journal of Heat and Mass Transfer*, 2704-2713.

Questions and Answers:

Assaad Zoughaib*:*

Is the sponge test adapted to measure K? Different driving forces (gravity, capillarity,…)? What about the dry K (Fick law vs Darcy)?

Antoine Parthoens:

The goal of the sponge is to ensure constant contact between liquid and membrane. If the membrane is considered fully loaded, capillarity is not present. Gravity is not taken into account but it could be. Dry R was experimentally tested, giving higher R.

***

Pascal Stabat*:*

Which advantages do you expect from your humidification system compared to classical enthalpy wheels?

Antoine Parthoens:

The exchanger is made of a porous polymer membrane. It allows this latter to be thermoformed. Furthermore this kind of material has a longer lifetime in comparison to classical enthalpy exchangers.

Liquid desiccant cascaded system for indoor air conditioning

Jinane Charara[1], Kamel Ghali[1], Nesreen Ghaddar[1], Rasha Mustapha[2], Assaad Zoughaib[2]

[1] Mechanical Engineering Department, Faculty of Engineering and Architecture, American University of Beirut, P.O. Box 11-0236, Beirut, Lebanon 1107-2020; farah@aub.edu.lb
[2] ARMINES Mines Paristech, PSL Research University, CES - Centre d'efficacité énergétique des systems, Z.I. Les Glaizes – 5 rue Léon Blum 91120 Palaiseau, France; assaad.zoughaib@mines-paristech.fr

1. ABSTRACT

Chilled ceilings combined with displacement ventilation (DV) have gained popularity due to their efficiency in terms of providing thermal comfort and good air quality, with minimal noise and good energy savings. Chilled ceilings can be replaced by liquid desiccant membrane systems integrated with DV system (LDMC-C/DV) to operate at lower ceiling temperatures without facing the risk of condensation. However, a major drawback of the system is that there is no control over the indoor relative humidity. During the system's operation, the combined internal and external loads can exceed the system's capacity leading to uncomfortable indoor conditions. Elevated indoor humidity can jeopardize thermal comfort, affect the occupants' wellbeing and lead to condensation on the ceiling surface in extreme cases. This study proposes to improve occupants' comfort and reduce energy costs by coupling the liquid desiccant membrane chilled ceiling/displacement ventilation (LDMC-C/DV) with an efficient parallel plate Heat and Moisture Membrane Exchanger. The latter system is dedicated to control the relative humidity of the supply air while using the liquid desiccant drawn from the chilled ceiling. A predictive mathematical model of the exchanger system is coupled to the liquid desiccant membrane LDMC-C/DV model. Then a case study that takes into consideration the hot and humid climate of Beirut is performed in order to verify the effectiveness of the system in assuring the standards of indoor spaces. Energy savings compared to a system that uses a conventional vapor compression dehumidifier instead of the membrane exchanger will be investigated.

Keywords: Liquid desiccant membrane, membrane Chilled ceiling, Displacement ventilation, cascaded desiccant system.

2. INTRODUCTION

Meeting the standards of indoor spaces gets increased attention nowadays in terms of air quality and thermal comfort. That is why, the majority of the worldwide end-use energy of the building sector is consumed by heating, ventilation and air conditioning systems (HVAC) (Ramesh et al 2010). The conventional HVAC systems that are widly used are based on the vapour compression cycle (Mckinley et al. 2008). However, these systems consume high grade energy and depend on mixing the fresh air with the contaminated air which may affect the indoor air quality and motivates the search for energy efficient alternatives (Al-Assad et al. 2017).

Displacement ventilation (DV) is one of the efficient alternative ventilation systems that provides high indoor air quality to the space through continuous delivery of 100% fresh air at low level (Itani et al. 2015). In particular, The DV system relies on dividing the indoor space into two zones: a lower cool and fresh air occupied zone, and a contaminated zone above the breathing level of occupants. This flow and temperature stratification drives the contaminants to be exhausted at the ceiling level with high ventilation efficiency (Novocelac et al. 2002). However, in order to assure the thermal comfort of occupants, the supply of fresh air through DV system is limited by a maximum velocity of 0.2 m/s and a minimum temperature of 18°C (ASHRAE Handbook, 2009). These restrictions limit the cooling loads to be not greater than 40 w/m^2 which affects the cooling efficiency of the system in hot and humid climate (Itani et al. 2015)

One of the adopted solutions is to combine the Chilled-Ceiling (CC) with DV system to improve the sensible heat removal by radiation and convection (Mumma 2001, Rees et al. 2002, Dieckmann et al. 2004). Nevertheless, condensation of water vapour on the surface of cooling pipes is a major concern that causes mold growth and potential IAQ problems (Simmonds et al. 2006). Condensation occurs when the temperature of cooling pipes is lower than the dew point temperature of the air at ceiling level (Hoa et al. 2007). To overcome the previous problem, researchers investigated the use of a cooled liquid desiccant membrane at ceiling (Hout et al. 2017; Keniar et al. 2015; Muslamani et al. 2016). The application of semi-permeable membrane allows the transport of moisture from the space to the desiccant solution while preventing any penetration of the hazardous desiccant to indoor air. By that, the combined liquid desiccant membrane CC/DV system is able to achieve an effective radiant cooling without condensation or entrainment of desiccant. Consequently, lower ceiling temperatures could be set, extending the overall heat load removal range of the CC/DV system.

This approach had been studied in several works that aimed to develop a reliable air conditioning system suitable for hot and humid environment. Keniar et al. (2015) proposed a theoretical model that integrated liquid desiccant membrane pipes for dehumidification and regeneration with an indoor space model. Muslmani et al. (2016) developed a mathematical model for a combined liquid desiccant membrane CC and DV system coupled with a parabolic solar collector and a space thermal model. Their results showed that integrating the liquid desiccant membrane CC along with DV is a promising system that saves about half of the electrical power consumed by a conventional CC/DV system. Furthermore, Hout et al. (2017) associated to the previous system a mathematical model for the boundary layer that described accurately the heat and mass transfer through the membrane. They developed several design

charts to determine the suitable air flow rates and desiccant temperatures for different DV supply air temperatures.

In spite of the energy saving that have been achieved in the previous studies compared to the conventional CC/DV system, the implementation of the membrane desiccant technology had only contributed in the sensible load removal. Hout et al. (2017) reported that the relative humidity of the air in the indoor space was very high is many cases. In other words, the liquid desiccant membrane CC/DV system wasn't designed to fulfill the requirements of humidity control. Since the temperature of ceiling is not constrained by the dew point temperature of the air, it could reach lower values without condensation on the ceiling but could create an additional challenge in high relative humidity cases regarding the increasing probability of condensation and mold growth in the room.

Thus, this problem reveals the need for an additional humidity control unit that can be associated to the liquid desiccant CC/DV system. Results of the study of Keniar et al. (2015) stated that the concentration and the temperature of the desiccant solution at the outlet to the indoor space didn't change significantly compared to the inlet values. Thus, the use of an outdoor air heat and moisture membrane exchanger allows to take advantage of the desiccant solution drawn after it passes through the ceiling to control the humidity of DV supply air. Although many configurations of compact membrane exchangers were found in the literature, parallel plates heat and moisture exchangers seems to be a promising system regarding its simple design and high efficiency. The parallel plate configuration is based on alternative streams of liquid desiccant and air flowing in the space between parallel membrane plates.

In this study, a cascaded liquid desiccant system composed of two membrane sub-systems: an indoor membrane chilled ceiling and a compact parallel plate membrane heat and moisture exchanger is proposed. The liquid desiccant solution exiting from the ceiling will be directed to the heat and moisture exchanger in order to reduce the sensible and latent heat of the supply air. The ability of the suggested system to control the humidity and to assure the thermal comfort of the indoor space will be investigated. To achieve that objective, a mathematical model for each component will be adopted and coupled. Then a case study that takes into consideration the hot and humid climate of Beirut will be conducted to show the performance of the cascaded system. Finally, energy consumption of the proposed system will be compared to that of a conventional LDMC-C system.

3. SYSTEM DESCRIPTION

Fig. 1 shows the cascaded system composed of two main subsystems: A liquid desiccant membrane chilled ceiling and a parallel plate membrane heat and mass exchanger. The strong and cooled desiccant is pumped in a closed loop and enters the indoor liquid desiccant membrane chilled ceiling at (a). As the solution flows inside the membrane structure, it absorbs moisture and heat from the zone near the ceiling. The exiting solution at (b) is directed to the inlet of a liquid to air membrane energy exchanger at (c) for supply air dehumidification and cooling. At (d), the desiccant solution is sent to the heating and regeneration section to restore the inlet desiccant concentration. A chiller provides the cooling needs to the solution at (e) through a sensible heat exchanger before it enters to the space.

On the other hand, ambient air enters the system at (1) with the aid of a fan that drives the air through the parallel plate membrane exchanger**.** If the cooling provided by the membrane exchanger cannot assure the adequate supply air temperature, auxiliary sensible cooling coil will be used. The cool and fresh air supplied to the room through the DV system at (3) displaces the warm and contaminated air vertically by natural convection to be exhausted through the exhaust grill at (4).

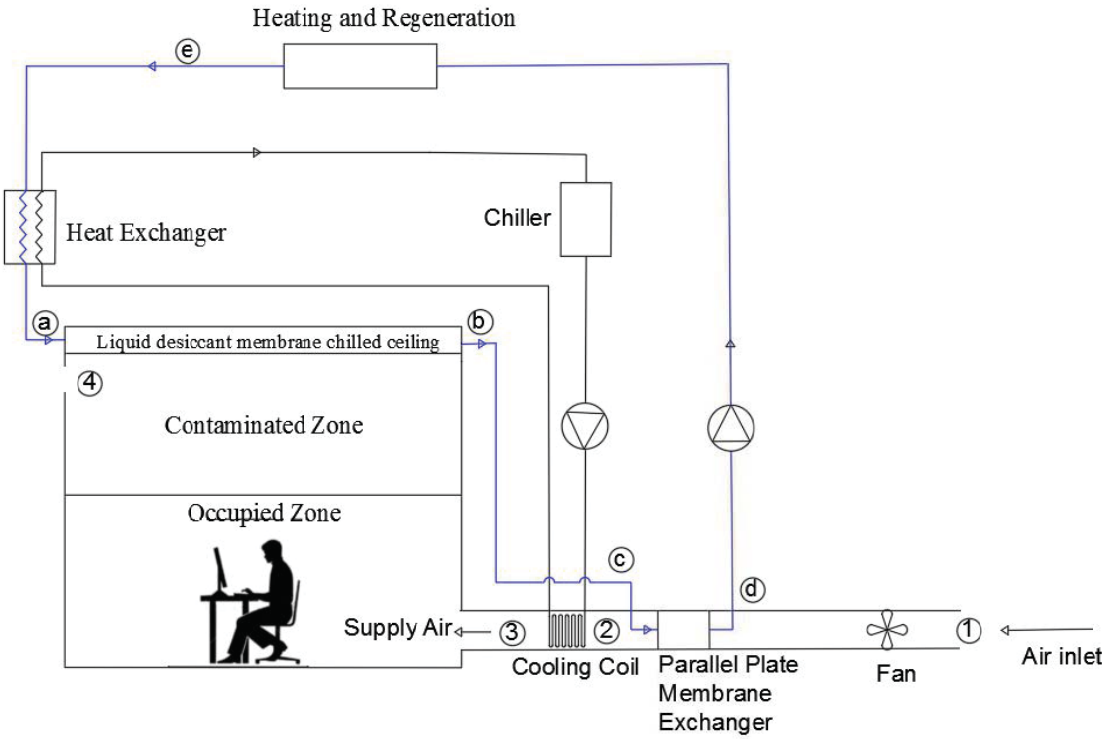

Figure 1: Illustration of the proposed system

4. MODELING APPROACH

To study the performance of the cascaded system, predictive mathematical models for each sub-system are adopted and coupled.

4.1. Indoor Space and Membrane Ceiling Model

In order to predict the conditions inside the space, the steady state integrated model of Hout et al. (2017) will be adopted to calculate the temperature and the humidity in the space. Their model combines a two zones space model with a desiccant membrane ceiling model. In a displacement ventilation system, the lower occupied zone is a comfortable zone with good breathable air quality while the upper unoccupied zone is a contaminated zone where neither IAQ nor thermal comfort is a concern. The model assumes the air movement in the vertical direction and predicts temperature and humidity values in each zone. Moreover, the model takes into consideration the air boundary layer zone created at the ceiling membrane vicinity. The heat and mass balance equation for this zone were treated separately from the upper zone due to the heat and moisture absorption that occurs at ceiling level. On the other hand, the mass and heat equations of the solution side were formulated to predict the temperature and the concentration in the liquid desiccant.

The equations of the boundary layer zone are thoroughly explained in the reference with the following assumptions: 1-D heat and mass diffusion, steady state conditions in the boundary layer zone and in the CC pipes, the axial heat conduction is neglected, constant latent heat of vaporization of water along the ceiling, equal velocity, mass and temperature boundary layer thickness and opposite desiccant and air flows. The energy equation for the both the desiccant and air boundary flows are:

$$-\dot{m}_{sol}\frac{d}{dx}\left(c_{p.sol}T_{sol}\right)+U_c(T_{BL}-T_{sol})+\rho_a h_{fg}U_m(W_{BL}-W_{sol})=0 \quad (1)$$

$$-\dot{m}_{BL}(x)\frac{d}{dx}\left(c_{p.air}T_{BL}(x)\right)+U_c\left(T_{sol}(x)-T_{BL}(x)\right)+\rho_{air}h_{fg}U_m\left(W_{sol}(x)-W_{BL}(x)\right)+$$
$$\dot{m}_{entrained}(x)c_{p,air}T_{air}(x)=0 \quad (2)$$

The first terms of Eqs.(1) and (2) represent the net convective heat flows in the solution and air sides respectively while the second terms account for the sensible heat transferred driven by the difference in temperature in the desiccant and air sides. The third terms represent the latent heat added due to water vapor absorption through the membrane. The last term in Eq (2) represents the convective energy flow of the air entrained from the room to the boundary layer.

The solution mass flow rate, specific heat, temperature and humidity ratio are represented by $\dot{m}_{sol}$,$c_{p.sol}$, T_{sol}, W_{sol} respectively, while T_{BL}, W_{BL} and $c_{p.air}$ are the temperature, and humidity ratio and specific heat in the air boundary layer respectively, h_{fg} is the latent heat of vaporization of water and $\dot{m}_{entrained}$ is the mass flow rate of air displaced from the upper zone to the boundary layer zone. The heat transfer coefficient U and the mass transfer coefficients U_m are calculated using the equations of Hout et al. (2017).

Similarly, the mass transfer equations for the desiccant and air sides are given respectively by

$$-\dot{m}_{sol}\frac{d}{dx}(C_{sol})+\rho_a U_m(W_{BL}-W_{sol})=0 \quad (3)$$

$$-\dot{m}_{BL}(x)\frac{d}{dx}\left(W_{BL}(x)\right)+\rho_{air}U_m\left(W_{sol}(x)-W_{BL}(x)\right)+\dot{m}_{entrained}(x)W_{air}(x)=0 \quad (4)$$

The first terms of Eqs.(3) and (4) represent the net convective moisture flow in the solution and air sides respectively while the second terms account for the vapour added due to the transfer of moisture through the membrane. The last term in Eq (4) represents the convective moisture flow of the air entrained from the room to the boundary layer.

After integrating the equations of the boundary layer zone with a DV space model, equations of the upper contaminated and lower occupied zones were established to solve for the temperature and humidity conditions. Energy and mass conservation for the lower occupied zone at steady state are given respectively by:

$$\dot{m}_S C_{p,air}\left(T_S-T_{air,o}\right)+\sum\left(h_i A_{w,i}\left(T_{W,i}-T_{air,o}\right)\right)+q_{people}+q_{electric}=0 \quad (5)$$

$$\dot{m}_S\left(\omega_S-\omega_{a,o}\right)+\frac{q_{latent}}{h_{fg}}=0 \quad (6)$$

In Eq. (5), the first two terms represent the net convective heat transfer between the supply air and the occupied zone and between the indoor air and the room's wall respectively, while the last two terms represent the sensible heat generated by the electric equipments and occupants respectively. In Eq. (6) the first term represents the net convective moisture transfer between the supply air and the occupied zone while the last term accounts for the rate of moisture generation (kg/s) by occupants.

Energy and mass conservation for the upper unoccupied zone at steady state are given respectively by:

$$\dot{m}_S C_{p,air}T_{air,o}-\int_0^{L_p}\dot{m}_{entrained}(x)C_{p,air}T_{air}dx-\dot{m}_{exhaust}C_{p,air}T_{air}+q_{light}+\sum\left(h_i A_{w,i}\left(T_{W,i}-T_a\right)\right)=0 \quad (7)$$

$$\dot{m}_S\omega_{air,o}-\int_0^{L_p}\dot{m}_{entrained}(x)\omega_a dx-\dot{m}_{exhaust}\omega_{air}=0 \quad (8)$$

In Eq. (7) the first term of the energy balance represents the rate of heat transferred from the lower occupied zone to the upper contaminated zone; the second term represents the rate of heat transfer from the upper zone to the boundary layer zone, while the third term accounts for the rate of heat transferred from the upper zone to the outdoor through the exhaust grill. The fourth term accounts for the energy added due to heat produced by lights. Finally, the last term represents the convective heat transfer between the indoor air space and the upper zone's wall.

Eq. (8) takes into consideration the mass balance for the air transferred from the lower to the upper zone, from the upper zone to the boundary layer zone and air exhausted through the grill.

4.2. Parallel plates heat and moisture membrane exchanger

Parallel Plates heat and moisture membrane exchanger is a liquid to air membrane energy exchanger that uses the liquid desiccant drawn from the ceiling to absorb moisture and heat from the supply air. The mathematical model developed by Mustapha et al. (2017) is adopted to describe the steady state performance of the system with the following assumptions: 1-D heat and mass diffusion, steady state and fully developed conditions in the moist air side and liquid desiccant side, the axial heat conduction and vapor diffusion are neglected, opposite desiccant and air flows and constant mass flow rates for the dry desiccant and dry air.

The flows of moist air and desiccant solution were considered in opposite directions (counter flow). The model solves for the humidity and the temperature of the air in the exchanger and determines the concentration and temperature of the solution in the liquid desiccant passages.

4.3.Models Integration

The indoor space and membrane ceiling model and the heat and mass energy exchanger model are implemented in MATLAB in order to evaluate the effectiveness of the cascaded system in humidity control of the indoor space. The indoor space model uses the conditions of the air supplied through DV and the inlet desiccant solution conditions to predict the temperature and humidity inside the occupied zone, the contaminated zone and the boundary layer zone in addition to the temperature and concentration of the solution flowing inside the ceiling membranes. Therefore, the conditions of the solution at the exit of the ceiling together with the ambient air conditions are considered as an input to the exchanger model to derive the conditions of the supply air.

5. CASE STUDY

In order to verify the effectiveness of the proposed system in humidity control, an indoor office space located in hot and humid Beirut is considered. The office has a 6m x 6m floor dimensions and a height of 2.8m. Consequently, different cases will be considered: case (A) the space is equipped with LDMC-C/DV system without any humidity control method for the supply air, case (B) the space is equipped with the cascaded liquid desiccant membrane system. Then, the thermal energy required by integrated system is compared to the energy required by a Case (C) where a typical vapor compression system is used to dehumidify the DV supply air in a LDMC-C/DV system.

The internal sensible and latent load schedules resulting from the presence of occupants, lighting and electrical equipment in the office in addition to the ambient condition as for a typical day in August in the office are shown in **Table 1**. The maximum number of space occupants is 8 and the space is occupied from 7 a.m. till 7 p.m., where the maximum latent load due to moisture generation from occupants is 400 W.

It is assumed that desiccant membrane covers 90% of the ceiling area and that the membrane exchanger is composed of 30 panels each having a 20 x 20 cm^2 area. For the three cases, the

desiccant solution selected is $CaCl_2$ due to its good ability of moisture absorption (Al-Farayedhi et. al, 2005) with an inlet concentration of 38% w/w and an inlet temperature of 13.5 °C. The membrane material considered is micro porous polypropylene for which the properties can be found in (Hout et al., 2017).

Table 1: Hourly outdoor weather conditions for a day in August and internal sensible and latent loads considered

Time	Outside temperature (°C)	Outside humidity ratio (g/kg)	Internal sensible load (W)	Internal latent load (W)
7:00	24.5	13.145	1000	75
8:00	25.8	13.145	1550	95
9:00	27.3	13.927	1650	150
10:00	28.7	14.807	1650	150
11:00	29.9	15.521	1650	150
12:00	30.7	16.283	1700	300
13:00	31.3	16.673	1700	400
14:00	31.6	16.872	1700	400
15:00	31.6	16.709	1150	300
16:00	31.1	16.435	1050	150
17:00	30.1	15.747	950	100
18:00	29.1	15.091	1050	150

6. RESULTS AND DISCUSSION

6.1.Performance analysis

The performance of the proposed cascaded system (Case B) is first compared to a case where the space is conditioned by a LDMC-C/DV system without any humidity control strategy (Case A). It is worth mentioning that the air temperature in the occupied zone in Case (A) are kept in the comfortable region (24 °C ±0.5) by varying the DV air supply flow rate. However, in Case (B) the flow rate of the desiccant solution exiting from the ceiling and entering to the exchanger is varied in order to maintain a thermally comfortable occupied zone. The results obtained are

represented in **Table 2** and **Table 3**. As shown in **Table 2**, the relative humidity and the humidity ratios in the lower occupied zone in Case (A) are found relatively high which may hindered the comfort of the occupants.

After applying the cascaded system to the same indoor space Case (B), the humidity levels decreased to a considerably acceptable level.

Table 2: Simulation results showing the conditions inside the office after applying the system in Case (A)

			Case (A)			
Time	Flow rate of supply air (L/s)	Flow rate of desiccant solution (L/s)	Temperature of supply air (°C)	Temperature in the occupied zone (°C)	Humidity ratio in the occupied zone (g/kg)	Relative humidity in the occupied zone (%)
7:00	38.65	0.625	20	24.07	8.2	76.80
8:00	85.03	0.625	20	24.40	11.7	61.40
9:00	154.6	0.625	20	24.50	12.6	66.40
10:00	309.2	0.625	20	24.50	13.5	70.55
11:00	355.58	0.625	20	23.90	14.9	70.43
12:00	386.5	0.625	20	24.3	15.3	80.4
13:00	386.5	0.625	20	24.3	15.9	83.2
14:00	386.5	0.625	20	24.4	16	84.2
15:00	100.49	0.625	20	23.60	15.5	85.20
16:00	63.4	0.625	20	23.90	11.4	82.00
17:00	61.8	0.625	20	24.10	10.8	82.30
18:00	61.8	0.625	20	24.20	11.2	81.70

Table 3: Simulation results showing the conditions inside the office after applying the system in Case (B)

				Case (B)			
Time	Flow rate of supply air (L/s)	Flow rate of desiccant solution in the ceiling (L/s)	Flow rate of desiccant solution in the exchanger (L/s)	Temperature of supply air (°C)	Temperature in the occupied zone (°C)	Humidity ratio in the occupied zone (g/kg)	Relative humidity in the occupied zone (%)
7:00	142.8	0.625	0.0625	23.5	24.00	9.8	53.00
8:00	142.8	0.625	0.1375	20.6	24.10	9.5	51.30
9:00	142.8	0.625	0.25	20.3	24.20	9.7	51.70
10:00	142.8	0.625	0.5	20.1	24.10	10	54.00
11:00	142.8	0.625	0.575	20.5	24.25	10.4	55.10
12:00	142.8	0.625	0.625	20.8	24.3	11.19	57.5
13:00	142.82	0.625	0.625	21.09	24.5	11.6	59.1
14:00	142.82	0.625	0.625	21.2	24.6	11.7	59.3
15:00	142.82	0.625	0.1625	22.7	24.02	11.8	63.70
16:00	142.82	0.625	0.15	23.1	23.90	11.3	61.80
17:00	142.82	0.625	0.125	21.2	23.60	10.5	64.40
18:00	142.82	0.625	0.1	23.2	24.00	10.7	58.20

6.2.Energy consumption

In order to evaluate the effectiveness of the proposed system, the energy consumption of case (B) and another system (Case (C)) will be compared. Case (C) represents an (LDMC-C/DV) system where the inlet DV air is cooled and dehumidified using a conventional sub cool-reheat system. The energy analysis is carried out by taking into account the thermal energy consumed by the proposed system (Case (B)) and comparing it to the energy needed by the system in Case (C) to get the same inlet conditions of Case (B). Since the flow rates of the air and the desiccant solution were kept constant in the two cases, the energy consumed by pumps and fans will be constant. Consequently, in case (B), the energy demand is represented by the energy needed to regenerate the desiccant solution and subsequently cool it to the required inlet temperature. On the other hand, the energy required in system (C) is divided into the regeneration energy of the desiccant in the CC and the energy required for sub-cooling and reheating the DV supply air (vapor compression system). The regeneration energy calculations were derived from the work of El-sayed et al. (1993) who developed a model to describe the performance of a packed bed in

a liquid desiccant system. The efficiency of the heat exchanger used to cool the desiccant solution was assumed to be 0.8.

Results of the energy consumption in the two cases are shown in **Table 4.** Over a period of a day, the total energy consumption for the Case (B) was 81.4 kWh for desiccant regeneration and 124.29 kWh for desiccant cooling which result in a total energy demand of 205.69 kWh. However in the Case (C) the total energy required was 236.74 kWh divided as follows: 100.68 kWh for desiccant regeneration, 99.36 kWh for desiccant cooling, 27.34 kWh to sub-cool the DV supply air and 9.36 kWh to reheat the sub-cooled air to the design inlet temperature. This means that the proposed cascaded desiccant membrane system used 13.1 % less energy than the LDMC-C/DV system aided with conventional vapor sub-cool reheat system.

The same strategy was applied for another 3 typical days in the cooling season in Beirut (May, June and July) and the results are stated in **Table 5.**

Table 4: Energy loads for Case (B) and Case (C)

	Case (B)		**Case (C)**			
Time	Desiccant Regeneration Energy (kWh)	Desiccant Cooling Energy (kWh)	Desiccant Regeneration Energy (kWh)	Desiccant Cooling Energy (kWh)	Air Sub-cool Energy (kWh)	Air Reheat Energy (kWh)
7:00	7.9	7.14	8.6	8.28	0.71	0.37
8:00	7.6	8.05	8.67	8.28	1.95	0.90
9:00	7.1	9.42	8.67	8.28	2.47	1.00
10:00	6.07	12.46	8.43	8.28	2.75	1.00
11:00	5.75	13.37	8.39	8.28	2.77	0.92
12:00	5.54	13.98	8.34	8.28	3.47	1.10
13:00	5.54	13.9	8.24	8.28	3.60	1.10
14:00	5.54	13.9	8.19	8.28	3.67	1.10
15:00	7.50	8.36	8.14	8.28	3.08	0.92
16:00	7.56	8.21	8.19	8.28	1.13	0.35
17:00	7.6	7.90	8.43	8.28	0.75	0.25
18:00	7.7	7.60	8.39	8.28	0.99	0.35
Total	81.4	124.29	100.68	99.36	27.34	9.36

Table 5: Total Thermal Energy consumption for the typical days in 4 cooling months in Beirut

The typical day in :	**Total energy consumption in Case (B) (kWh)**	**Total Energy Consumption in Case(C) (kWh)**	Percent of Energy Reduction
May	183.23	198.9	7.9%
June	189.60	205.71	7.8%
July	196.74	221.49	11.2%
August	205.69	236.74	13.1%

7. Conclusion

Liquid desiccant membrane CC/DV system permits lower ceiling temperature without condensation on the ceiling. By that, the system will be hindered by a potential mold growth in the room in high humidity cases which reveals the need for an additional humidity control unit. This project proposes a cascaded system that takes the liquid desiccant solution leaving the indoor space and introduce it in a parallel plate heat and moisture membrane exchanger to control the humidity of the DV supply air. It is intended to prevent the implications imposed by the high humidity inside the space and to reduce the energy consumption compared to a liquid desiccant membrane CC/DV assisted by a conventional vapor compression dehumidification system.

The results show that the system has the potential to ensure a humidity controlled indoor environment while assuring the thermal comfort of occupants. The energy analysis conducted showed that up to 13.1% of energy can be saved during a day while using the cascaded system compared to a LDMC-C/DV system assisted with a conventional DV supply air conditioning system.

REFERENCES

Ramesh, T., Prakash, R., & Shukla, K. (2010). Life cycle energy analysis of buildings: An overview. *Energy and Buildings,42*(10), 1592-1600. doi:10.1016/j.enbuild.2010.05.007

Mckinley, T. L., & Alleyne, A. G. (2008). An advanced nonlinear switched heat exchanger model for vapor compression cycles using the moving-boundary method. *International Journal of Refrigeration, 31*(7), 1253-1264. doi:10.1016/j.ijrefrig.2008.01.012

Al-Assaad, D., Ghaddar, N., & Ghali, K. (2017). Performance of Mixing Ventilation System Coupled With Dynamic Personalized Ventilator for Thermal Comfort. *Volume 1: Aerospace Heat Transfer; Computational Heat Transfer; Education; Environmental Heat Transfer; Fire and Combustion Systems; Gas Turbine Heat Transfer; Heat Transfer in Electronic Equipment; Heat Transfer in Energy Systems*. doi:10.1115/ht2017-4747

Itani, M., Ghali, K., & Ghaddar, N. (2015). Performance Evaluation of Displacement Ventilation System Combined with a Novel Evaporative Cooled Ceiling for a Typical Office in the City of Beirut. *Energy Procedia,75*, 1728-1733. doi:10.1016/j.egypro.2015.07.440

Novoselac, A., & Srebric, J. (2002). A critical review on the performance and design of combined cooled ceiling and displacement ventilation systems. *Energy and Buildings,34*(5), 497-509. doi:10.1016/s0378-7788(01)00134-7 Itani M, Ghali K, Ghaddar N. Increasing energy efficiency of displacement ventilation integrated with an evaporative-cooled ceiling for operation in hot humid climate. Energy and Buildings 2015;105: 26–36.

Keblawi, A., Ghaddar, N., Ghali, K., & Jensen, L. (2009). Chilled ceiling displacement ventilation design charts correlations to employ in optimized system operation for feasible load ranges. Energy and Buildings, 41(11), 1155-1164. doi:10.1016/j.enbuild.2009.05.009

Mumma, S. A. (2001). Ceiling panel cooling systems. *ASHRAE Journal, 43*(11), 28

Rees, S., & Haves, P. (2001). A nodal model for displacement ventilation and chilled ceiling systems in office spaces. Building and Environment, 36(6), 753-762. doi:10.1016/s0360-1323(00)00067-6

Simmonds, P., Chambers, I., Mehlomakulu, B., & Simmonds, C. (2006). Applied Performance of Radiant Ceiling Panels for Cooling. ASHRAE Transactions, 112(1), 368-376

Hao, X., Zhang, G., Chen, Y., Zou, S., & Moschandreas, D. J. (2007). A combined system of chilled ceiling, displacement ventilation and desiccant dehumidification. *Building and Environment,42*(9), 3298-3308. doi:10.1016/j.buildenv.2006.08.020

Hout, M., Ghaddar, N., Ghali, K., Ismail, N., Simonetti, M., Fracastoro, G., Virgone, J., Zoughaib, A. (2017). Displacement ventilation with cooled liquid desiccant dehumidification membrane at ceiling; modeling and design charts. *Energy,139*, 1003-1015. doi:10.1016/j.energy.2017.08.046

Keniar, K., Ghali, K., & Ghaddar, N. (2015). Study of solar regenerated membrane desiccant system to control humidity and decrease energy consumption in office spaces. *Applied Energy,138*, 121-132. doi:10.1016/j.apenergy.2014.10.071

Muslmani, M., Ghaddar, N., & Ghali, K. (2016). Performance of combined displacement ventilation and cooled ceiling liquid desiccant membrane system in Beirut climate. *Journal of Building Performance Simulation,9*(6), 648-662. doi:10.1080/19401493.2016.1185153

Ayoub, M., Ghaddar, N., & Ghali, K. (2006). Simplified Thermal Model of Spaces Cooled with Combined Positive Displacement Ventilation and Chilled Ceiling System. *HVAC&R Research,12*(4), 1005-1030. doi:10.1080/10789669.2006.10391448

Mustapha, R., El Khoury, K., & Assaad, Z. (2017, July). A Hybrid no Frost Refrigeration System Using a Membrane Based Desiccant System. In *30th International Conference on*

Efficiency, Cost, Optimization, Simulation and Environmental Impact of Energy Systems (ECOS 2017).

Al-Farayedhi, Gandhidasan A, Antar, and M S Abdul Gaffar (2005). Experimental study of an aqueous desiccant mixture system: Air dehumidification and desiccant regeneration. *Journal of Power and Energy* . 219, (8), 669 – 680.

Elsayed, M., Gari, H. N., & Radhwan, A. (1993). Effectiveness of heat and Mass transfer in packed beds of liquid desiccant system. Renewable Energy, 3, 661-668.

ACKNOWLEDGMENTS

The authors would like to acknowledge of the financial support from the ERANETMED Project SOL-COOL-DRY: ERANETMED_ENERG-11-138 under ERA-MET Initiative “EURO-MEDITERRANEAN Cooperation through ERANET joint activities of FP7 INITIATIVE ERANETMED. In addition, the support from the Munib and Angela Masri Institute of Energy and Natural resources grant award at the American University of Beirut is also acknowledged

NOMENCLATURE

A	area (m2)
C	concentration of water per desiccant (kg of H_2O/kg CaCl2)
CC	chilled ceiling
C_p	specific heat (J/kg·K)
DV	displacement ventilation
h_{fg}	latent heat of vaporization of the water (J/kg)
IAQ	Indoor Air Quality
LDMC-C	liquid desiccant membrane chilled ceiling
Lp	length of the dehumidifier panel (m)
$\dot{m}$	mass flow rate (kg/s)
T	temperature (℃)
T_{air}	Air temperature (℃)
T_{sol}	Liquid desiccant solution temperature (℃)
U_c	Overall heat transfer coefficient per unit length
U_m	Overall mass transfer coefficient per unit length
W_{air}	Air Humidity ratio ($kg_{H2O}/kg_{dry\ air}$)
W_{sol}	the solution equilibrium humidity ratio ($kg_{H2O}/kg_{dry\ air}$)
w	humidity ratio (kg of H_2O/kg of dry air)
x	distance from the inlet of the membrane (m)

Greek Letters

ρ	density (kg/m^3)

Subscripts

a	room air
air	air stream
k	index representing the orientation of wall
s	Supply
sol	Solution stream
o	outdoor conditions
w	wall
entrained	entrained from the upper zone to the boundary layer zone

Flexible Design of a Hybrid Air Conditioning System

Rasha Mustapha[1]*, Assaad Zoughaib[1]

(1) MINES ParisTech-PSL Research University-CES, Palaiseau, France,

rasha.mustapha@mines-paristech.fr

assaad.zoughaib@mines-paristech.fr

ABSTRACT

Globally, the building sector is the largest energy consumer contributing to about 40% of final energy consumption. For air conditioning, vapor compression systems are the most commonly used technologies with an increasing amount of installed equipment. Yet these systems waste energy when it comes to humidity control inside buildings. Alternative systems, such as hybrid systems, have been studied with the aim of improving energy performance and maintaining thermal comfort with proper indoor air quality. The performance of these systems radically depends on the outside operating conditions where the ratio of latent to sensible load inside the building changes accordingly. In this paper, several architectures of such a hybrid system are proposed for the seasonal air conditioning of an office in a mid-rise building in the south of France. A validated mathematical model is used to assess the performance of each architecture in different months of the year. Results of certain architectures indicate high coefficient of performance (COP) compared to others, depending on the latent to sensible load ratio. This finding would significantly contribute in reducing the energy cost when cleverly implemented in buildings.

Keywords: Hybrid system, liquid desiccant, membrane heat and mass exchangers, seasonal performance.

1. INTRODUCTION

Among the major worldwide energy end use sectors, the building sector including both residential and commercial, contributes to the largest share exceeding the figures of the transportation and the industry (Coulomb, Dupon, & Pichard, 2015). An increase in the population, in the indoor comfort level, in the air quality demands as well as in the time spent inside buildings, leads to a predictive rise in the building energy consumption in the future. For these reasons, efficient energy use in buildings is a significant global objective. The control of heating, ventilation and air conditioning (HVAC) occupies about half of the energy consumed in buildings (Pérez-Lombard, Ortiz, & Pout, 2008), surpassing that associated to lighting, appliances and domestic hot water production. Most of the HVAC operations are handled by conventional vapor compression cycles which are considered to be huge electricity consumers due to their inefficiency in controlling humidity (Giampieri, Ma, Smallbone, & Roskilly, 2018) . These devices can effectively control the sensible loads but when it comes to latent loads, around 20 to 40% of their energy is dissipated to dehumidify the air (Yang, Yan, & Lam, 2014). To lower the humidity levels, the vapor compression cycle (VCC) decreases the temperature of the air below its dew point to remove the moisture by the process of condensation as shown in fig 1. Then to reach the desired supply temperature, air is reheated. Besides wasting energy, the overcooling and reheating processes lead to mold growth and thus poor air quality and uncomfortable indoor conditions.

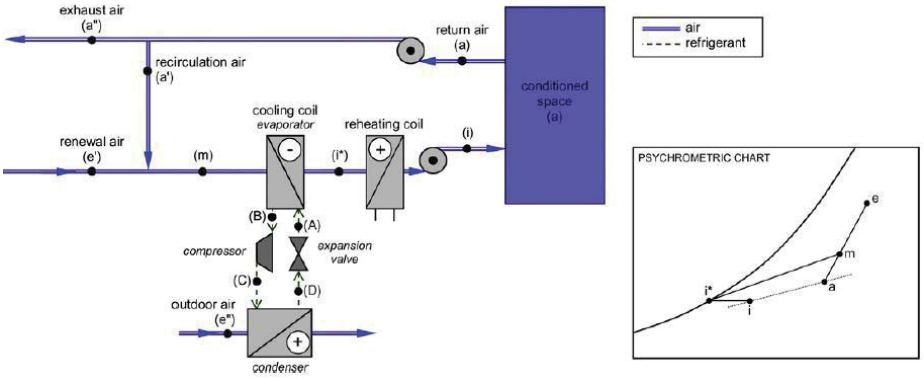

Figure 1: Layout of the traditional air conditioning system (Bergero & Chiari, 2011).

Desiccant technology has proved to be a reliable alternative due to the strong ability of desiccants to handle dehumidification. Desiccants can be of two types: solids and liquids. The solid desiccant system is made of a rotating wheel with a frame of a thin layer desiccant material that may be silica gel, zeolites, aluminas or others (Mohammad, Mat, Sulaiman, Sopian, & Al-abidi, 2013). The cross section of the wheel is divided into the moist air side and the regeneration air side. In one part of the wheel, the process air passes to be dehumidified and simultaneously in the other part hot air is passed to remove the added water from the solid desiccant.

Liquid desiccants are composed of aqueous salt solutions that can be a solution of lithium chloride or calcium chloride or other. A liquid desiccant system is made of two separate exchangers that play the role of a dehumidifier and a regenerator. In each exchanger a transfer of both heat and mass occurs (Fu & Liu, 2017). In the dehumidifier the solution absorbs the humidity of the air while in the regenerator, where hot air is blown over the hot solution, the water vapor moves from the desiccant solution to the air.

As presented by (Rafique, Gandhidasan, & Bahaidarah, 2016) liquid desiccants have shown a number of advantages over solid desiccants due to their flexibility of integration in the systems being in the liquid state and due to their high capacity of absorption. Moreover, liquid desiccants require lower regeneration temperatures than solid desiccants and avoid the problem of pressure drop caused when the process air passes through solid desiccant materials. Due to their conveniences, liquid desiccants have been widely integrated in hybrid systems where the air is usually dehumidified by direct contact with the hygroscopic solution such as in packed bed towers as shown in (Evans, 2016). Some direct contact exchangers (cooling towers) use spraying technology where the fluid that needs to be cooled is dispersed over an upcoming stream of air and the direct contact enables the air to cool the liquid through evaporation and convection. However, when the fluid is a desiccant solution, the direct contact leads to a serious problem of corrosion caused by the carryover of solution droplets by the process air. This problem affects the indoor air quality and to be avoided, a polymer semi porous membrane is installed in the heat and mass exchangers to prevent the salt solution from crossing to the air. At the same time, the membrane should allow and favor the transport of both heat and mass from the air towards the desiccant solution (Huang & Zhang, 2013). The use of membranes in combination with the liquid desiccant systems is greatly important to separate the air from the solution limiting the problems of the liquid desiccant droplets crossover towards the air and thus preventing indoor space corrosion. Fig. 2 shows a sketch of a counter flow membrane based heat and mass exchanger.

Figure 2: Sketch of a counter-flow membrane exchanger.

Combining the desiccant membrane technology with the traditional air conditioning system forms a promising hybrid membrane based liquid desiccant vapor compression system. Research done on the application of these hybrid systems (Mohammad et al., 2013) has shown that they are reliable technologies with encouraging potential energy savings in buildings. These systems are capable of efficiently controlling both temperature and humidity by separating the sensible load and the latent load. Some advantages of hybrid systems include inducing higher evaporating temperature than the traditional system thus leading to a better performance, a lower energy consumption, and a healthier indoor space.

In some studies (Lin, Huang, Wang, & Chua, 2018), the desiccant solution in the dehumidifier is used to do the humidity control contributing at the same time to the temperature reduction of the process air. In other studies (Niu, Xiao, & Ge, 2010), the liquid desiccant is used only to remove the latent load and in order to treat the sensible load, the air is passed by the cooling coil of the vapor compression cycle. Bergero and Chiari (2011) suggested the addition of a storage tank between the regenerator and the dehumidifier of the liquid desiccant cycle so that the change in concentration and temperature inside the tank is always compensated from both cycles.

From the previous cited work, the configuration of the hybrid system and its architecture is offering high efficiency over a range of operating conditions represented by the ratio to the liquid to sensible load. This range of operating conditions is varying from one configuration to another; it is clear that maintaining a high energy efficiency offered by the hybrid system should be offered by a flexible design operating through a whole season in an efficient way. Triggered by the previous research of Bergero and Chiari (2011) and in order to increase the flexibility of the system, in this study two storage tanks are placed in a hybrid membrane based liquid desiccant air conditioning system. One is inserted in the dehumidification cycle and the other in the regeneration cycle. Both tanks are connected together with a heat recovery heat exchanger in between. The aim of this work is to analyze the steady state behavior and to compare the performance of different architectures through a seasonal simulation of an office located in the south of France.

2. GENERAL SYSTEM DESCRIPTION

The hybrid system proposed in this study is similar to the systems mentioned before composed of two main subsystems: a traditional vapor compression cycle and a membrane based liquid desiccant system. The vapor compression cycle consists of a compressor, a condenser, an expansion valve and an evaporator where refrigerant R-134a is the working fluid. The liquid desiccant system is mainly made of a dehumidification cycle and a

regeneration cycle as shown in fig. 3. The first cycle dehumidifies the air; the desiccant solution absorbs moisture from the air through the difference in the vapor pressure between the surface of the desiccant material and the air. It is made up of a dehumidifier, a storage tank and a pump. The dehumidifier is a cross flow heat and mass membrane based exchanger. After absorbing water vapor from the process air, the solution must be reactivated in order to be able to absorb the same amount of water vapor again. Thus its concentration and temperature should be continuously maintained the same at the entry of the dehumidifier. To restore its temperature, the evaporator of the vapor compression cycle is used to cool the desiccant solution before entering the dehumidifier.

To reactivate the desiccant and retain its concentration, regeneration process takes place where the water that is absorbed during the dehumidification process will be removed from the desiccant solution. This occurs by increasing the surface vapor pressure of the desiccant through heating the solution. The regeneration cycle is made of a regenerator (which is also a cross flow membrane heat and mass exchanger), a pump and a storage tank and it uses the excess heat given by the condenser of the vapor compression cycle to increase the temperature of the solution before entering the regenerator. It should be noted that at steady state the mass flow rate of the water that is removed by the dehumidifier is transferred to the regeneration cycle where it is taken by the air passing through the regenerator.

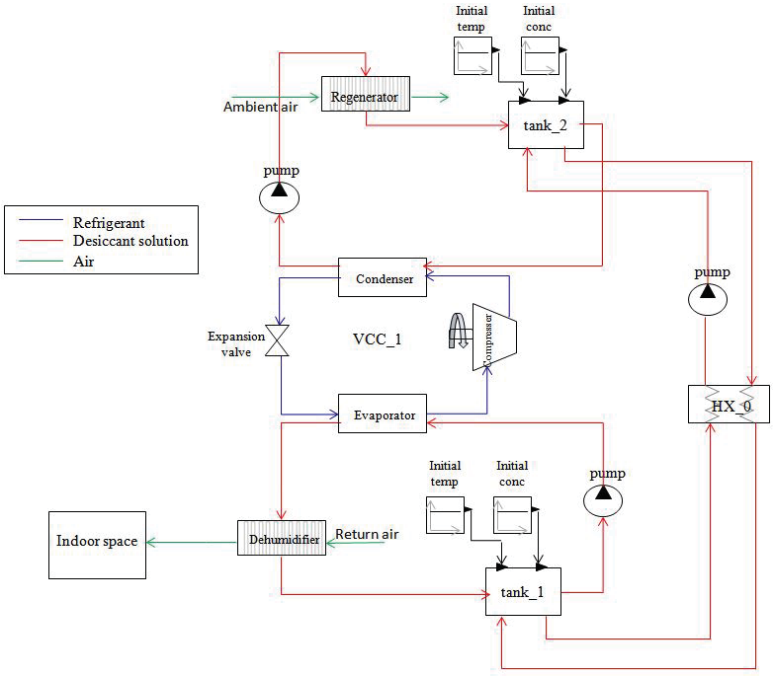

Figure 3: Schematic of the hybrid system with storage tanks.

The storage tank in the first cycle (tank_1) is used to store the diluted solution leaving the dehumidifier which is continuously pumped to the regenerator for reactivation. The tank in the regeneration cycle (tank_2) is for storing the concentrated solution which is again pumped to the first cycle to absorb the water vapor from the air and so on. Before reaching a steady state the concentration of the solution inside the tank of the first cycle decreases with time while that of the second cycle increases. The concentration of the diluted solution present in tank_1 is always adjusted by adding more concentrated solution from tank_2. The starting

temperature and concentration of the solution are specified as initial conditions inside the tanks which are not necessarily equal in both tanks.

The action of preheating the solution before entering the condenser and pre-cooling it before entering the evaporator is very important. It intends to save some of the energy required in the process of regeneration and dehumidification respectively. Thus also a new cycle exists which consists of the two storage tanks: tank_1 and tank_2, a heat exchanger hx_0 and a pump. As the desiccant solution flows from one tank to the other, it passes through a heat exchanger where heat is transferred to or from the solution. The heat exchanger is used to increase the solution's temperature before entering the regeneration cycle and to reduce its temperature before entering the dehumidification cycle. It adds flexibility to the system by allowing us to assign different concentrations and flow rates in the two cycles. The pumps are used to define the mass flow rates of the solution in each cycle that could also be of different values.

The desiccant cycle is able to play the role of both dehumidifying and cooling the air at the same time. The evaporator of VCC_1 is used to cool the desiccant solution which in turn cools and dehumidifies the air simultaneously. A previous study was done by (Mustapha, Khoury, & Zoughaib, 2017) where different architectures were analyzed to find the most efficient among them. The configurations are summarized by whether the solution removes the latent and sensible loads entirely, or the whole latent load and part of the sensible load or only the entire latent load without interfering with the sensible load. In the case where part of the sensible load is removed by the solution, air would pass by another vapor compression cycle in order to reach the desired temperature before entering the indoor conditioned space. The results showed that optimizing the amount of the sensible load removed by the liquid desiccant solution led to an increase in the COP of the system and a decrease in the overall power consumption by around 30%.

In this paper, the flexibility of the proposed system in figure 3 is increased by adding heat exchangers before or after the dehumidifier and the regenerator allowing to exchange sensible heat with room air for the dehumidifier cycle and ambient air for the regenerator cycle.

3.1 Baseline building

A baseline office in Nice (43.3˚N, 5.4˚E), a city in the south of France, is simulated in this study. Nice has a Mediterranean climate with warm spring and autumn and with a hot summer. The office is located on the third floor within a mid-rise building of 5 floors. Each floor is 3 m high and has an area of 100 m^2; it consists of 2 workplaces, an open space, a meeting room, an entrance, a lunchroom and a toilet. The design of the building's envelope is considered as the real case construction. The coefficients of heat transmission U-value of the exterior walls, the interior walls, the roof and the floor are taken from (« EURIMA - U-values in Europe », s. d.). The window to wall ratio is about 20%. The U-value of the glazing is 2 $W/m^2.K$ made of 2 double clear panes of 6 mm each, separated by a 6 mm layer of argon, with a solar heat gain coefficient SHGC of 0.57. Side fins 30 cm depth are installed on the windows. The infiltration rate is considered to be as 0.5 ACH. Schedules of occupancy are specified for every room where generally people are present in the building from 9 to 18 h. The schedules of activity, lighting, office equipment and HVAC system are proposed accordingly. The cooling set point temperature is 24 ˚C and the building is simulated with these conditions using Designbuilder that uses EnergyPlus as an interface tool.

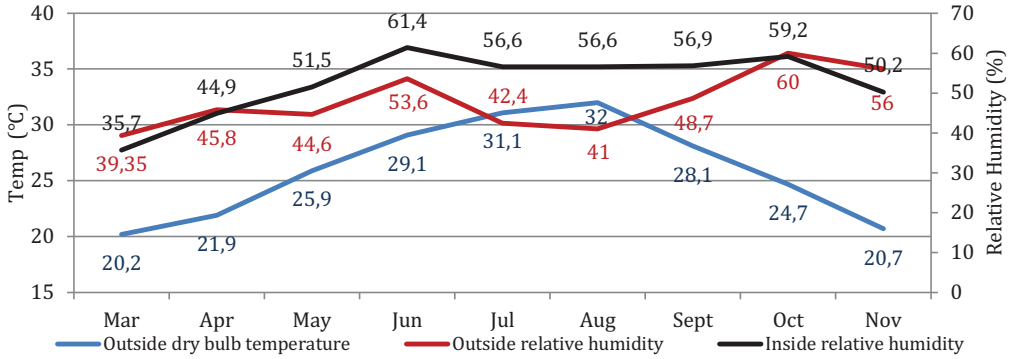

Figure 4: Temperature and relative humidity in each month.

The cooling load is calculated for the months where cooling is needed. In each month the ambient conditions change and so does the relative humidity of the air inside the office. Fig. 4 shows the monthly temperature and relative humidity of the ambient air as well as the monthly indoor air conditions.

The total cooling load inside the office differs from one month to another as shown in fig. 5. It is divided into latent load and sensible load and the role of the desiccant system is to remove the entire latent load and part of the sensible load. The ratio of the latent to sensible load (R) varies from one month to another and its different values are noted also in fig. 5. The most interesting months in terms of (R) are chosen for this study and these months are May, June, August and October. May is chosen because of the low value of the ratio R (15.5%) and June is chosen due to the highest value of R which is equal to 53.8%. August is selected being the month with the highest ambient temperature where R=35.6% and October being a typical month of autumn where cooling is needed to a small extent with a ratio R=45.3%.

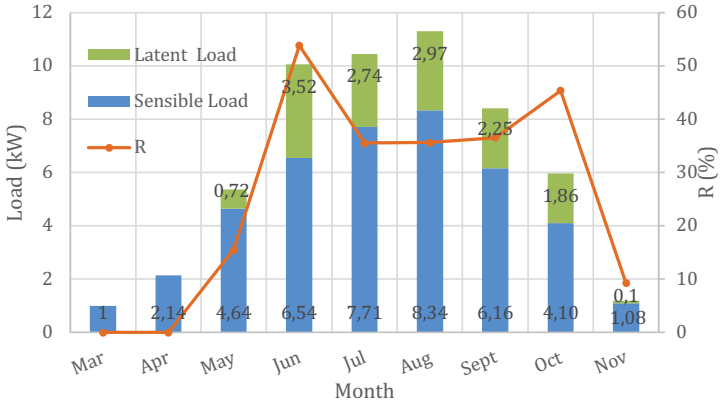

Figure 5: Monthly cooling load distribution.

3.2 Model

A detailed mathematical model is written in Dymola software for the whole system. As mentioned before the dehumidifier and the regenerator are cross flow membrane exchangers. These exchangers are made of several channels where a desiccant solution of lithium chloride (LiCl) is supplied vertically inside the channels (direction of z axis) and the air is supplied

perpendicular to it outside the channels (direction of x axis) in a way that there is no direct contact between the air and the solution as shown in fig. 6. The model is done using discretization method; each of the x axis and the z axis were discretized into 30 segments of equal sizes (Ni=Nj=30). The width of each channel is 1 cm (corresponds to the height where the solution flows) and the distance between two consecutive channels is also equal to 1 cm (corresponds to the height where the air flows). The membranes separating the two fluids are porous polymers with a thickness of 0.157 mm, a thermal conductivity of 0.334 W/m.K, and a mass conductivity of $4.3\text{x}10^{-6}$ kg/m.s. The width (L) and the height (Z) of each of the dehumidifier and the regenerator are proposed and the modeling is done accordingly.

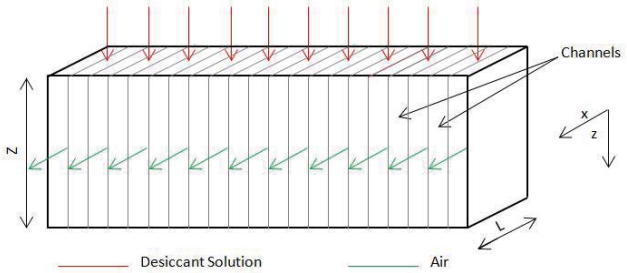

Figure 6: A drawing of a cross flow heat and mass exchanger.

3.2.1. Dehumidifier

The energy and mass equations for the dehumidifier are derived and defined by the following at the steady state:

a) Air side:

Mass conservation equation for water vapor

$$\dot{m}_a \frac{dz}{Z}(Y[i-1,j]-Y[i,j]) - 2A_a\, U_M[i,j](Y[i,j]-Y_s[i,j]) = 0 \tag{1}$$

1.1.1 *Energy conservation equation for moist air*

$$\dot{m}_a \frac{dz}{Z}(C_a[i,j]+C_v[i,j]Y[i-1,j])(T_a[i-1,j]-T_a[i,j]) - 2A_a\, h_{Ta}[i,j](T_a[i,j]-T_{ma}[i,j]) = 0 \tag{2}$$

b) Solution side:

Mass conservation equation for liquid water

$$\dot{m}_a \frac{dx}{L}(X[i,j-1]-Y[i,j]) + 2A_a\, U_M[i,j](Y[i,j]-Y_s[i,j]) = 0 \tag{3}$$

1.1.2 *Energy conservation equation for moist air*

$$\dot{m}_a \frac{dx}{L}(1+X[i,j-1])C_s[i,j](T_S[i,j-1]-T_s[i,j]) + 2A_a U_M[i,j]h_{fg}[i,j](Y[i,j]-Y_s[i,j]) - 2A_s\, h_{Ts}[i,j](T_s[i,j]-T_{ms}[i,j]) = 0 \tag{4}$$

c) Membrane:

Energy conservation equations

$$A_a\, h_{Ta}[i,j](T_a[i,j] - T_{ma}[i,j]) - \frac{K_T}{d}\, A_m(T_{ma}[i,j] - T_{ms}[i,j]) = 0 \quad (5)$$

$$A_s\, h_{Ts}[i,j](T_s[i,j] - T_{ms}[i,j]) + \frac{K_T}{d}\, A_m(T_{ma}[i,j] - T_{ms}[i,j]) = 0 \quad (6)$$

Where $U_M = (\frac{1}{h_{ma}} + \frac{\delta}{k_m} + \frac{1}{h_{ms}})^{-1}$, $dx = \frac{L}{Ni}$ and $dz = \frac{Z}{Nj}$

3.2.2. Storage Tank

The solution entering the storage tank has a temperature and concentration different from that leaving it due to the connection of tank_1 and tank_2. These values change with time and thus the new outlet solution conditions are calculated by the following equations:

$$\frac{dT_{out}}{dt} = \frac{\dot{m}_{s,1} C_{p,avg1}(T_{in,1} - T_o) + \dot{m}_{s,2} C_{p,avg2}(T_{in,2} - T_{out})}{\rho A H C_{p,out}} \quad (7)$$

$$\frac{dC_{out}}{dt} = \frac{\dot{m}_{s,1} C_1 + \dot{m}_{s,2} C_2 - C_{out}(\dot{m}_{s,1} + \dot{m}_{s,2})}{\rho A H} \quad (8)$$

Where H is the height of the tank and A is its area, $C_{p,avg1}$ and $C_{p,avg2}$ are the average specific heat of the solution that is coming from the dehumidifier (or regenerator) and hx_0 respectively. $C_{p,out}$ is the outlet specific heat of the solution at temperature T_{out} and concentration C_{out}.

$$C_{p,avg1=} \frac{C_{p,1} + C_{p,out}}{2} \quad (9)$$

$$C_{p,avg2=} \frac{C_{p,2} + C_{p,out}}{2} \quad (10)$$

$C_{p,1}$ and $C_{p,2}$ being the specific heat of the solution that is coming from the dehumidifier (or regenerator) and hx_0 respectively.

With respect to the other components of the system including the compressor, the condenser, the expansion valve and the evaporator of the vapor compression cycle, the energy and mass equations are well known. The heat exchangers that are added to the system also have predefined equations and thus the energy equations of these components will not be mentioned in this paper.

3.2.3. Membrane exchangers model validation

An experimental validation of the membrane exchangers model using a prototype has been performed and the results showed an acceptable compatibility with the simulations (predicted heat and mass transfer within 20% of the measurements). This proved that the model can be applied in the prediction of the performance of such exchangers, and this work will be presented in details in a later dedicated article in order not to overcharge this paper.

3.3 Configurations

Several simulations are done where the aim is to be able to remove the total cooling load by the hybrid system by using the above model. To be able to treat the latent and sensible loads, three configurations are studied. The first is by placing a heat exchanger before the dehumidifier and a heat exchanger before the regenerator. The second is by placing these heat exchangers after the dehumidifier and the regenerator respectively. The third one is by replacing the heat exchangers of the second configuration by another vapor compression cycle. In all configurations the dehumidifier of the desiccant system removes the entire latent load and part of the sensible load. The remaining sensible load is removed by the heat exchangers in the first two configurations and by the vapor compression cycle in the third configuration. Another configuration exists where both of the latent and sensible loads are entirely removed by the desiccant system without the help of additional equipment. This configuration has a poor flexibility outside the months with high latent to sensible load ratio and failed to prove any seasonal effectiveness because the desiccant system shows high performance in removing latent loads rather than sensible loads. In this case when the dimensions of the dehumidifier are chosen to be able to remove the entire latent load, the sensible load removal would be small. In order to increase the sensible load removal, the mass flow rate of the air in the dehumidifier should be increased. Thus the concentration of the solution increases leading to an increase in the condensation temperature and hence the COP of the system decreases. So due to its very low COP, this configuration is eliminated from our study.

3.3.1 Description

So as mentioned, 3 configurations are studied in order to be able to compare the seasonal performance and the energy consumption of the hybrid system. In the first configuration as in fig. 7, a heat exchanger hx_1 is placed before the dehumidifier and another heat exchanger hx_2 is placed before the regenerator.

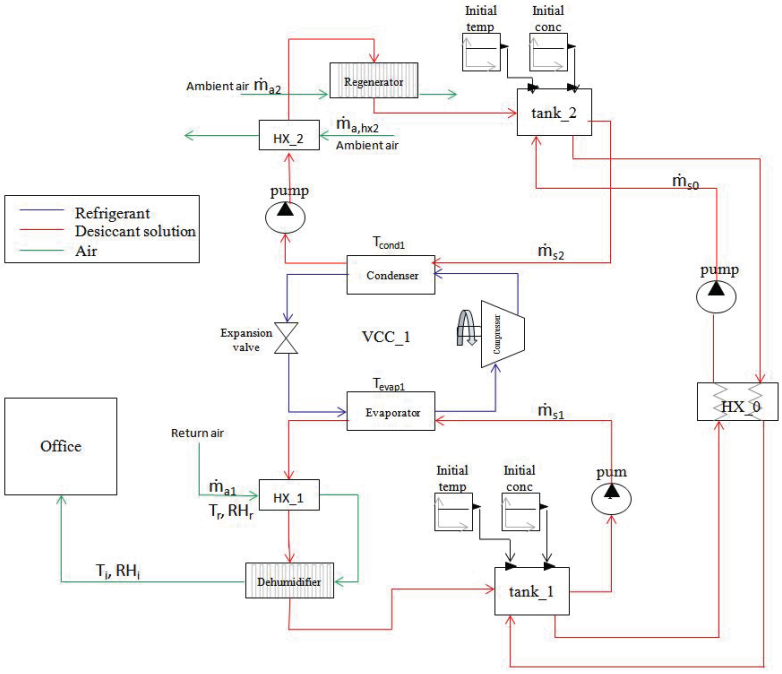

Figure 7: Schematic of the first configuration.

Air that has been recycled from the office enters hx_1 with a given mass flow rate ($\dot{m}_{a1}$) and at the indoor temperature and relative humidity of the office (T_r, RH_r). The dehumidifier not only removes the humidity, but it further cools the air in order to meet the supply conditions. On the solution side, the summation of the sensible load added to the solution in hx_1 and the total load added in the dehumidifier should be equal to the power of the evaporator of the vapor compression cycle. But this is not exactly the case because of the presence of the storage tank tank_1. The solution enters tank_1 at a temperature slightly less than when leaving it and this leads to an additional sensible heat on the solution side. Therefore, the loads added to the solution in the dehumidifier, along with that added in hx_1 and in tank_1 are equal to the load removed from the solution by the evaporator of the vapor compression cycle.

In the regeneration cycle, unlike the case of hx_1 where the air flow is in series with the dehumidifier, the flow rate of the air entering hx_2 is independent of that in the regenerator. The ambient air passing in hx_2 is used to slightly decrease the temperature of the solution. The ambient air passing through the regenerator is used to cool the solution and simultaneously remove some of the water in order to return the solution to its initial concentration. Similar to the case of the dehumidification, the sensible load removed from the solution in hx_2, with the sensible load removed in tank_2 and the total load removed in the regenerator must be equal to the load added to the solution by the condenser of the vapor compression cycle.

After leaving the regenerator, the solution is sent back to the storage tank (tank_2). It is then pumped to tank_1 after being further cooled in hx_0 by the cold solution as explained before. Hx_1 is used to cool the air before being dehumidified and supplied to the room while hx_2 is used to cool the desiccant solution before being regenerated.

Taking as example the month of August, the return air coming from the office is at 24°C and 56% relative humidity which correspond to an absolute humidity of 10.39 g/kg (d.a). When the office is at these return conditions, the supply air of a proposed mass flow rate 2950 m^3/h should be at 15.72 °C and 82.6% relative humidity in order to meet the latent load which is 2.97 kW and the sensible load which is 8.34 kW. In hx_1 air is partially cooled by the cold desiccant solution that leaves the evaporator. After leaving hx_1, the same cooled air now enters the dehumidifier in order to be dried. The air at the entrance of the dehumidifier is at 16 °C and 91.84% relative humidity which correspond to an absolute humidity of 10.39 g/kg (d.a). The dry air leaving the dehumidifier has an absolute humidity of 9.16 g/kg.d.a. The latent load removed by the dehumidifier should be equal to the latent load in the office. Now the air that leaves the dehumidifier has the proper supply conditions and is ready to be delivered to the room with a temperature, a relative humidity and an absolute humidity of 15.72°C, 82.6% and 9.16 g/kg (d.a) respectively.

In the second configuration, as per fig.8, the place of the heat exchangers is changed. This time hx_1 is placed after the dehumidifier and hx_2 after the regenerator. Again the mass flow rate of the ambient air entering the regenerator and that entering hx_2 are not necessarily equal. On the contrary, the same flow rate of the air that enters the dehumidifier is transferred to hx_1. The concept of this configuration is the same as the previous one but here the cooling of the supply air is done after its dehumidification and the cooling of the desiccant solution is done after its regeneration. Hx_1 uses the cold desiccant solution to lower the temperature of air and hx_2 uses the cool ambient air to lower the temperature of the desiccant solution.

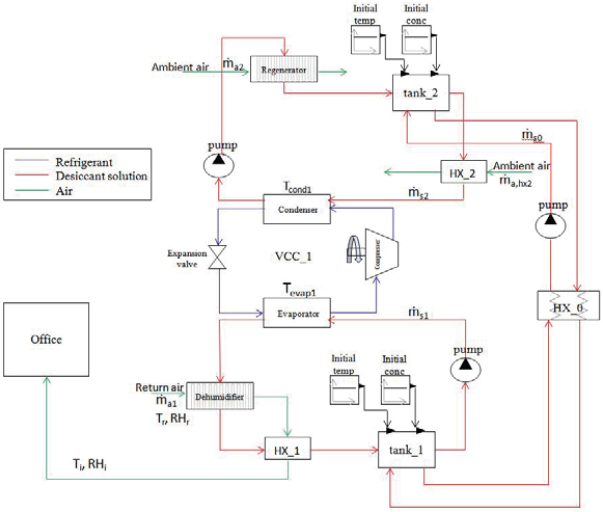

Figure 8: Schematic of the second configuration.

In the third configuration, the heat exchangers of the second configuration are replaced by a second vapor compression cycle VCC_2 as shown in fig. 9. The evaporator of VCC_2 plays the same role as the heat exchanger hx_1 which is to further decrease the temperature of the air before being supplied to the office. At the entrance of the second evaporator the dry air leaving the dehumidifier is mixed with a part of the return air recycled from the room. Mixing the air not only increases the evaporation temperature of VCC_2 and thus the COP of the second vapor compression cycle, but also increases the temperature of the supply air at the inlet of the office as it will be seen later.

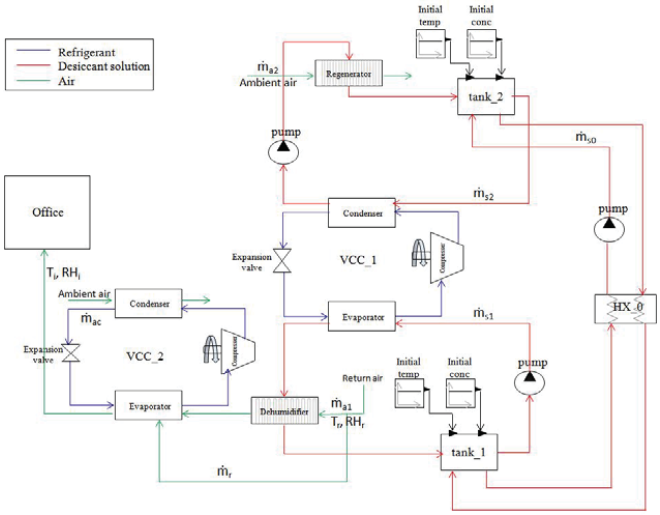

Figure 9: Schematic of the third configuration.

4. RESULTS AND DISCUSSIONS

The different designs of the three configurations, allow simulating 12 models such that for every configuration 4 simulations are done for each of May, June, August and October as

explained before. The ambient air temperature and relative humidity are given to the system as well as the indoor air conditions. The results of the simulations are given at steady state.

4.1 Design of dehumidifier and regenerator

The dimensions of the dehumidifier and the regenerator are changed in a way to be able to remove the entire latent load. Modifying the dimensions of the dehumidifier would cause more critical changes than modifying the dimensions of the regenerator. By adjusting the number of channels, the width (in the direction of the air flow) and the height (in the direction of the solution flow) of these two heat and mass exchangers, we will be consequently changing the amount of latent and sensible loads removed by the system. These dimensions could be different from one configuration to another in order to optimize the system and to find the highest COP possible. However, for a comparative approach, they will be taken the same in all configurations because the aim of this paper is to show the relative flexibility of each design and where its application is the most effective. These dimensions are chosen in a way to be relevant in all the 12 cases and they are presented in table 1.

Table 1: Dimensions of the dehumidifier and regenerators in all configurations.

	Number of Channels	L	Z
Regenerator	50	1	1
Dehumidifier	48	0.5	0.6

4.2 Mass flow rates of air and desiccant solution

The mass flow rates of the air and the solution also play an important role in changing the load removal quantity. The mass flow rates of the air and the solution in hx_2, in the regenerator, in the dehumidifier and in hx_0 are altered in a way to be able to attain the aimed load removal. For the third configuration, the heat exchanger hx_1 is removed and along with the previous initial parameters, we have 2 additional parameters. The first is the mass flow rate ($\dot{m}_r$) of the return air that is mixed with the air leaving the dehumidifier before entering the second evaporator. The second is the mass flow rate of the ambient air ($\dot{m}_{ac}$) that is entering the second condenser. The value of $\dot{m}_r$ is chosen such that the total air mass flow rate that enters the second evaporator is 4000 m^3/h. While the value of $\dot{m}_{ac}$ is selected such that the difference in the inlet and outlet air temperature along the condenser is about 8 °C. These values are summarized for the 3 configurations in table 2.

Table 2: Mass flow rates of air and solution in the system.

Month	$\dot{m}_{a,hx2}$ (m^3/h)	$\dot{m}_{a2}$ (m^3/h)	$\dot{m}_{s2}$ (kg/s)	$\dot{m}_{a1}$ (m^3/h)	$\dot{m}_{s1}$ (kg/s)	$\dot{m}_0$ (kg/s)	$\dot{m}_r$ (m^3/h)	$\dot{m}_{ac}$ (m^3/h)
1st configuration								
May	3000	100	0.6	3100	1.1	0.1	--	--
June	400	4500	5	2900	5	0.1	--	--
August	4000	500	2.4	2950	1.8	0.1	--	--
October	2500	3000	0.8	2050	3.7	0.1	--	--
2nd configuration								
May	4000	50	1	5200	2.5	0.1	--	--
June	1800	1000	3	3900	2.1	0.1	--	--

Month	$\dot{m}_{a,hx2}$ (m^3/h)	$\dot{m}_{a2}$ (m^3/h)	$\dot{m}_{s2}$ (kg/s)	$\dot{m}_{a1}$ (m^3/h)	$\dot{m}_{s1}$ (kg/s)	$\dot{m}_0$ (kg/s)	$\dot{m}_r$ (m^3/h)	$\dot{m}_{ac}$ (m^3/h)
August	7000	600	2	3500	2.2	0.1	--	--
October	4500	500	3	3900	1.6	0.1	--	--
3rd configuration								
May	--	2000	1	500	0.5	0.1	3500	1700
June	--	1750	3	3300	3	0.1	700	1500
August	--	3200	2	2200	0.8	0.1	1800	2500
October	--	1100	3	3100	1.6	0.1	900	1000

4.3 Supply indoor air conditions

The simulations are done with all the previously mentioned parameters. The supply air conditions are calculated and unlike traditional systems, the supply air temperature in these hybrid systems could be of higher values. Generally, in vapor compression cycles, the larger the air mass flow rate that enters the evaporator, the lower is the difference in temperature between the inlet and the outlet air across the evaporator. This is considered a limitation for the conventional systems because if the temperature was not decreased sufficiently to reach values below the dew point, the humidity would not be removed from the air. This problem is avoided by using the desiccant system that allows the proper control of humidity even at higher air mass flow rates and temperatures. The values of the temperature and relative humidity of the supply air (T_i, RH_i) for the 3 configurations are shown in table 3.

Table 3: Calculated temperature and relative humidity of the supply air.

Month	1st configuration			2nd configuration			3rd configuration		
	T_i (˚C)	RH_i (%)	Y_i (g/kg)	T_i (˚C)	RH_i (%)	Y_i (g/kg)	T_i (˚C)	RH_i (%)	Y_i (g/kg)
May	19.6	65.2	9.3	21.4	59.2	9.44	18.65	58.33	7.82
June	17.4	79.8	9.93	19.1	74.5	10.32	18.75	74.5	10.1
August	15.72	82.6	9.16	17	77.7	9.42	16.55	74.63	8.78
October	18.15	76.1	9.93	20.9	67.5	10.46	20.65	67.37	10.27

4.4 Load removal and COP

In addition, the simulations provide the COP of the first compression cycle for the three configurations as well as the COP of the second vapor compression cycle for the third configuration. Figures 10 (a) and 10 (b) show the COP of the vapor compression cycle as well as the load removed by the dehumidifier and by the heat exchanger in the first and second configurations respectively. Figure 10 (c) presents the load removed by the dehumidifier and by the evaporator of the second vapor compression cycle in the third configuration. Figure 10 (d) shows the COPs of the first and second vapor compression cycles and fig. 10 (e) indicates the overall COP of the two cycles in configuration 3 where this overall COP is calculated by equation (11).

$$COP_{overall} = \frac{Q_{evap1} + Q_{evap2}}{W_{comp1} + W_{comp2}} \quad (11)$$

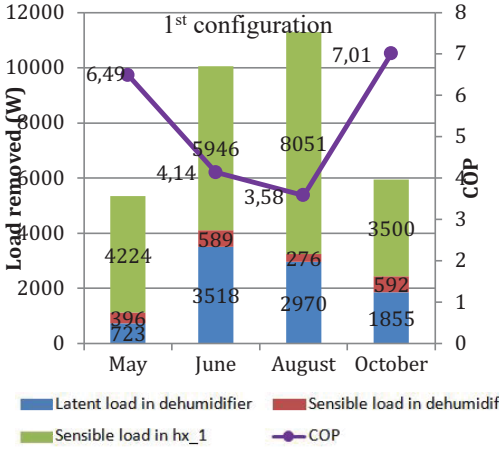

(a)

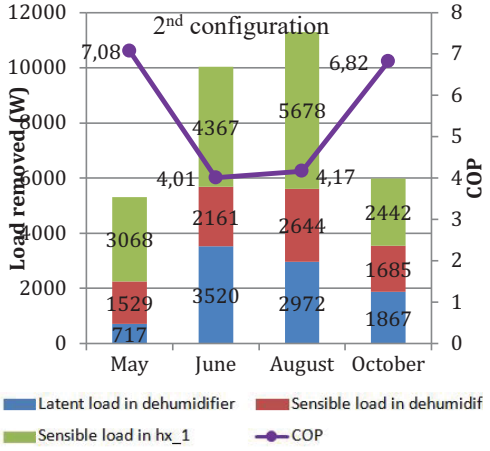

(b)

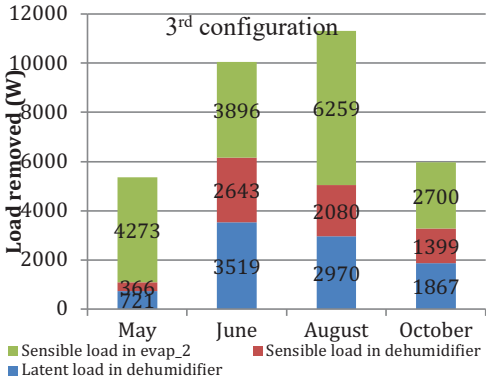

(c)

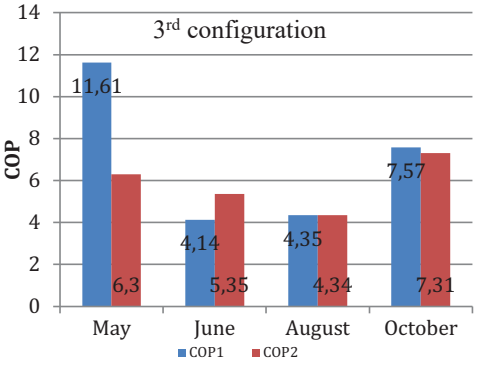

(d)

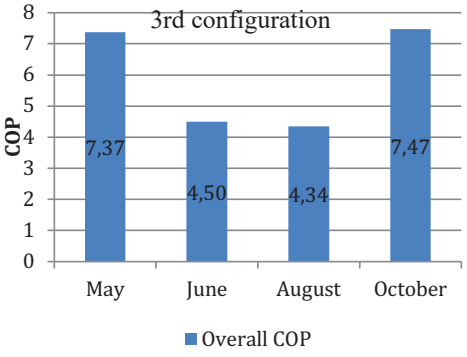

Figure 10: Calculated COP and distribution of cooling load removal in the three configurations.

By comparing the results of the first two configurations, we can notice that the COPs of June and October are higher whenever the heat exchangers are placed before the dehumidifier and the regenerator. While for May and August, these values are higher when the exchangers are placed after. In the third configuration, where another vapor compression cycle is used to reduce the sensible load, the figures of the COPs of all the months are higher than the other configurations. We may say that whenever the ratio of latent to sensible load is high, it is more favorable to reduce first the temperature of the air before passing it to the dehumidifier for dehumidification. Observing the results of the second configurations, we can note that there is a contradiction with the fact that as the ambient air temperature decreases, the COP of the system increases. However, by comparing the results of the simulation done in May and in October, we can recognize that even though the ambient temperature in May is higher than that in October, still the COP of the system in May is higher than that in October. The same can be noticed if we compare June with August. This is because whenever the latent load is higher, in order to increase the latent load removal in the dehumidifier, the evaporation temperature decreases causing the COP to decrease. This analysis can lead to a conclusion that removing the humidity of the air before decreasing its temperature is favored whenever the ratio of latent to sensible load is low.

The evaporation and the condensation temperatures determine the COP of the system and they are highly dependent on the concentration of the solution as well as on the mass flow rates of air in the regenerator, in the exchanger, and in the dehumidifier. The solution concentration in the regenerator as well as the condensation and evaporation temperatures of the vapor compression cycles are shown in table 4.

Table 4: Condensation and evaporation temperatures with percentage concentration of solution.

Month	T_{cond1} (°C)	T_{evap1} (°C)	T_{cond2} (°C)	T_{evap2} (°C)	Concentration in regenerator (%)
1st configuration					
May	34.5	14	--	--	23.26
June	42.7	12	--	--	33
August	44.6	10	--	--	31.53
October	32	13	--	--	24.23
2nd configuration					
May	34	15	--	--	22.6
June	43.5	12	--	--	32
August	40.3	10	--	--	29.55
October	33.6	14	--	--	24.65
3rd configuration					
May	30	18	36.9	15.65	29
June	40.45	10	40.5	15.75	30.44

August	40.25	11	43.2	13.55	32.38
October	32.85	15	36.3	17.65	26.12

When comparing the behavior of the first two configurations in June, we observed that by passing from the first configuration to the second, the amount of latent and sensible loads removed are decreased if no changes are proposed to the air flow rates. The mass flow rate of the regeneration air if decreased, the latent load removal increases while the sensible load removal, is not affected. In order to increase the sensible load control, the mass flow rate of the air in the dehumidifier should be increased which in turn increases the latent load control. These changes cause the concentration of the solution to increase, thus increasing the condensation temperature and reducing the COP of the system. But again to decrease the latent load, the air mass flow rate in hx_2 should be increased which in turn lowers the concentration of the solution thus lowering T_{cond1} and increasing the COP. The COP in the second configuration is lower than that in the first due to the difference in the condensation temperature (affected by the low regeneration air mass flow rate).

The third configuration shows the highest values of COP in each of the four months studied. Yet also these values could be optimized by changing the mass flow rates of the air entering the condenser on one side and of the recycled air entering the evaporator on another side.

More globally, the three proposed configurations are flexible and can operate in a wide range of latent to sensible load ratio. This feature surpasses the proposed systems in literature where the performance is studied and discussed for a critical nominal point or for a tight range of operating conditions.

5. CONCLUSIONS AND PERSPECTIVES

Three different configurations of a flexible hybrid liquid desiccant membrane based system have been proposed and studied in four particular months of a year in a Mediterranean climate. Energy and mass equations were used to do the modeling and the results showed that the ratio of latent to sensible load plays an important role in determining the most relevant application of a certain configuration. The following conclusions can be drawn:

(1) Compared to a vapor compression system, hybrid systems allow using a higher air mass flow rate to achieve higher supply air temperatures and thus higher evaporation temperatures.
(2) The installation of storage tanks in the system increases its flexibility where the concentration of the desiccant solution could be varied between the dehumidification cycle and the regeneration cycle.
(3) Whenever the ratio of latent to sensible load is high, it is more efficient to remove part of its sensible load first and then to dry it by the dehumidifier.
(4) When the ratio of latent to sensible load is low, it is favorable to dehumidify the air first and then send it for further cooling.
(5) Using two vapor compression cycles showed to be the highest performing system for the four studied months.

The results show that the studied systems are promising alternatives for traditional systems where they can significantly improve the performance and decrease the consumption of electricity in buildings. The third configuration where two vapor compression cycles were used revealed its effectiveness in each of the four studied months. However, this

configuration is the most costly among the others, and still it should be proved whether the low running cost would be able to compensate for the high initial cost. Thus a compromise should be reached between the effectiveness of the system and its price. Yet, we cannot generalize those results and give a broad conclusion unless further work is performed with a yearly simulation for all the months where cooling is needed since some months may be penalizing for certain configurations.

ACKNOWLEDGMENTS

The authors would like to acknowledge of the support of ERANETMED Project SOL-COOL-DRY, ID number: ERANETMED_ENERG-11-138 under ERA-MET Initiative "EURO-MEDITERRANEAN Cooperation through ERANET joint activities of FP7 INITIATIVE ERANETMED.

NOMENCLATURE

A	*area, m^2*
C	*concentration, kg/kg*
Cp	*specific heat, J/(kg K)*
COP	*coefficient of performance*
h	*enthalpy, J/kg*
k_m	*mass conductivity of the membrane, kg/m.s*
K_T	*thermal conductivity of the membrane, W/m.K*
L	*width (in the direction of x-axis), m*
$\dot{m}$	*mass flow rate, kg/s*
Ni	*number of discretization in the direction of x-axis*
Nj	*number of discretization in the direction of z-axis*
Q	*load, W*
R	*ratio of latent to sensible load*
$SHGC$	*solar heat gain coefficient*
T	*temperature, K (unless indicated other)*
t	*time, s*
U_M	*overall mass exchange coefficient, $kg/m^2.s$*
VCC	*vapor compression cycle*
W	*work, W*
X	*humidity ratio in the solution: mass of water per kg of dry desiccant, kg/kg*
Y	*humidity ratio in moist air: mass of water vapor per kg of dry air, kg/kg*
Y_s	*moist air equivalent humidity ratio in the solution, kg/kg*
Z	*height (in the direction of z-axis), m*

Greek symbols

ρ	density, kg/m^3

Subscripts

a	air

avg	average
comp	compressor
cond	condenser
d	desiccant
evap	evaporator
i	inlet
m	membrane
ma	membrane-air
ms	membrane-solution
s	desiccant solution
v	vapor

REFERENCES

Bergero, S., & Chiari, A. (2011). On the performances of a hybrid air-conditioning system in different climatic conditions. *Energy*, *36*(8), 5261‑5273. https://doi.org/10.1016/j.energy.2011.06.030

Coulomb, D., Dupon, J., & Pichard, A. (2015). The Role of Refrigeration in the Global Economy. *29th Informatory Note on Refrigeration Technologies; Technical Report; International Institute of Refrigeration: Paris, France*.

EURIMA - U-values in Europe. (s. d.). Consulté 14 mai 2018, à l'adresse https://www.eurima.org/u-values-in-europe/

Evans, P. (2016, octobre 2). How Cooling Towers work. Consulté 15 juin 2018, à l'adresse http://theengineeringmindset.com/how-cooling-towers-work/

Fu, H.-X., & Liu, X.-H. (2017). Review of the impact of liquid desiccant dehumidification on indoor air quality. *Building and Environment*, *116*, 158‑172. https://doi.org/10.1016/j.buildenv.2017.02.014

Giampieri, A., Ma, Z., Smallbone, A., & Roskilly, A. P. (2018). Thermodynamics and economics of liquid desiccants for heating, ventilation and air-conditioning – An overview. *Applied Energy*, *220*, 455‑479. https://doi.org/10.1016/j.apenergy.2018.03.112

Huang, S.-M., & Zhang, L.-Z. (2013). Researches and trends in membrane-based liquid desiccant air dehumidification. *Renewable and Sustainable Energy Reviews*, *28*, 425‑440. https://doi.org/10.1016/j.rser.2013.08.005

Lin, J., Huang, S.-M., Wang, R., & Chua, K. J. (2018). Thermodynamic analysis of a hybrid membrane liquid desiccant dehumidification and dew point evaporative cooling system. *Energy Conversion and Management*, *156*, 440‑458. https://doi.org/10.1016/j.enconman.2017.11.057

Mohammad, A. T., Mat, S. B., Sulaiman, M. Y., Sopian, K., & Al-abidi, A. A. (2013). Survey of liquid desiccant dehumidification system based on integrated vapor compression technology for building applications. *Energy and Buildings*, *62*, 1‑14. https://doi.org/10.1016/j.enbuild.2013.03.001

Mustapha, R., Khoury, K. E., & Zoughaib, A. (2017). A Hybrid no Frost Refrigeration System Using a Membrane Based Desiccant System. Présenté à 30th International Conference on Efficiency, Cost, Optimisation, Simulation and Environmental Impact of Energy Systems (ECOS 2017). Consulté à l'adresse https://hal-mines-paristech.archives-ouvertes.fr/hal-01561415

Niu, X., Xiao, F., & Ge, G. (2010). Performance analysis of liquid desiccant based air-conditioning system under variable fresh air ratios. *Energy and Buildings*, *42*(12), 2457‑2464. https://doi.org/10.1016/j.enbuild.2010.08.027

Pérez-Lombard, L., Ortiz, J., & Pout, C. (2008). A review on buildings energy consumption information. *Energy and Buildings*, *40*(3), 394‑398. https://doi.org/10.1016/j.enbuild.2007.03.007

Rafique, M. M., Gandhidasan, P., & Bahaidarah, H. M. S. (2016). Liquid desiccant materials and dehumidifiers – A review. *Renewable and Sustainable Energy Reviews*, *56*, 179‑195. https://doi.org/10.1016/j.rser.2015.11.061

Yang, L., Yan, H., & Lam, J. C. (2014). Thermal comfort and building energy consumption implications – A review. *Applied Energy*, *115*, 164‑173. https://doi.org/10.1016/j.apenergy.2013.10.062

Questions and Answers:

Is there a way to combine both VCC in the 3rd configuration (in order to investment cost saving)? It would be a machine with several evaporators/condensers and one single compressor.

Rasha Mustapha:

Actually by combining two evaporators or two condensers, it would be the same as the 1st and 2nd configurations since the 2nd evaporator or the 2nd condenser would be acting as heat exchanger. Moreover, the CO of such a cycle would be much lower than a VCC with one evaporator or condenser.

***

Long Van Le:

Could you clarify how better this solution can be compared to the conventional vapor compression cycles in term of indoor air quality and energy saving?

Rasha Mustapha:

In some preliminary studies as the 3rd configuration (2 vapor compression cycles) we were able to reach an improvement on the COP of about 25%. For the indoor air quality by using our system it is possible to reach the desired relative humidity while in conventional VCC the inside relative humidity is a result.

Experimental and numerical investigation on winter performance of hybrid liquid desiccant system

Ying Xie [1,*], Xiaohua Liu [1,*], Tao Zhang [1]

[(1)] Department of Building Science, Tsinghua University, Beijing 100084, China

ABSTRACT

As an energy-efficient approach for the humid air handling process, a hybrid liquid desiccant system was investigated under winter conditions in the present study. The key components of the hybrid system are two counter-flow packed towers as dehumidifier/regenerator and a heat pump cycle as the external cooling/heating source. The prototype of this system was designed and tested and the experimental analysis on the system performance was demonstrated. Then an optimal solution flow rate for the prototype was proposed and chosen based on the experimental results. The system performance expressed by COP_{sys} could be up to 7.8 under partial load winter conditions in Beijing. Moreover, the numerical model of this system was introduced and validated to make further investigation on this system. Based on the simulated results, the influences of crucial parameters such as air inlet parameters were also analyzed. COP_{sys} of the system could reach above 9.2 under partial load winter condition as 0ºC, 1.7g/kg with one compressor operating while COP_{sys} could also be above 7.8 under the more extreme winter outdoor condition as -10ºC, 0.6g/kg with two compressors operating.

Keywords: liquid desiccant system, counter-flow, heat pump

1. INTRODUCTION

With the rapid increase of energy consumptions of air-conditioning system in buildings, liquid desiccant air-conditioning technology has arisen increasing attention for the past few decades (Rafique et al. 2016). Compared to the conventional condensation dehumidification technology, liquid desiccant dehumidification has advantages in sufficient use of renewable and low-grade energy sources, such as solar (Qi et al. 2014) and biomass (Jradi et al. 2014). And the hybrid air-conditioning system with liquid desiccant shows superior dehumidification efficiency and system performance (Mucke et al. 2016).

In recent years, the hybrid heat pump driven liquid desiccant system has gained more and more development and application, which can provide cooling and heating sources for the system simultaneously as an effective alternative without available low-grade heat for desiccant regeneration (Cai et al. 2017). And extensive researches on cross-flow hybrid systems have been performed in previous studies, whose flow pattern has more merits on convenient equipment layout and practical application. A two-stage cross-flow hybrid system was proposed and tested by Liu et al. (2008), with the coefficient of performance of the system up to 5.0 in summer (36 ºC, 26g/kg of outdoor air parameter). However, the research on the field uniformity principle in liquid desiccant dehumidifier/regenerator from Liu et al. (2009) has proved that the counter flow pattern between air and solution would show better performances on heat and mass transfer than the cross flow pattern in dehumidification processes. Then the hybrid system based on counter flow pattern will help to increase the system efficiency further, under the equal input heat and mass transfer area with simpler configuration (Xie et al. 2016). Moreover, the hybrid system could use cooling and heating capacities from the heat pump to achieve dehumidification and regeneration processes simultaneously, which means that the hybrid system could be applied under summer and

winter conditions respectively through the conversion of the four-way valve of the heat pump. And yet, there are plenty of researches on the system performances under summer conditions (Yamaguchi et al. 2011), while lack of studies about the winter conditions.

Therefore, this paper intends to conduct researches on a new type of counter-flow hybrid liquid desiccant system with the indoor exhaust air as the dehumidification air, which can recover heat and moisture from the indoor exhaust air. And the system performance under heating and humidifying conditions in winter will be investigated. A prototype of the system was designed and tested, and then the numerical model for the system was introduced and validated to make further performance analysis. Based on the experimental and simulated results, the effects of the crucial parameters such as solution flow rate and inlet air parameters will be analysed, in order to provide basic data for further reasonable application of liquid desiccant air handling systems.

2. EXPERIMENT INTRODUCTION

2.1 Experimental prototype

The schematic of a hybrid liquid desiccant system is illustrated in Figure 1. The hybrid system could operate throughout the year. It mainly contains two packed towers for regeneration and dehumidification respectively, and heat pump cycles to provide heating and cooling capacities for the air handling processes. Under winter conditions, the outdoor air (a_{in}) is heated and humidified in the regenerator to the supply air (a_{out}) while the indoor exhaust air (r_{in}) is cooled and dehumidified to the exhaust air (r_{out}) in the dehumidifier. The liquid desiccant as an aqueous salt solution circulates between the two packed towers to achieve heat and mass transfer processes with air. Then the evaporator and condenser of the heat pump cycle provide cooling and heating sources for the circulating solution, in order to maintain its dehumidification/regeneration abilities. In addition, adopting a multi-stage heat pump cycle is always seen as an effective way to improve the system performance (Xie et al. 2016). Thus, the prototype of the hybrid system is built with a two-stage heat pump cycle.

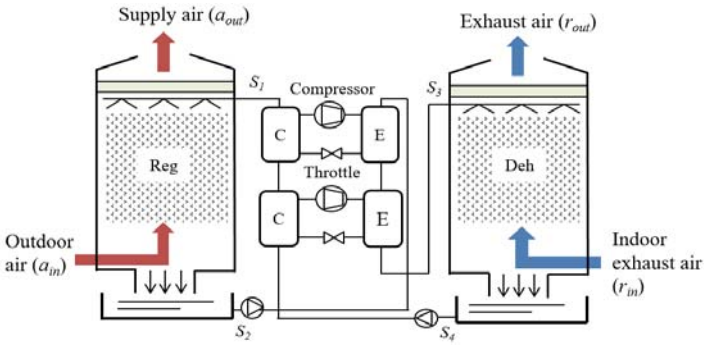

Reg-Regenerator Deh-Dehumidifier C-Condenser E-Evaporator

Figure 1: Schematic diagram of the hybrid liquid desiccant system.

Figure 2 shows the experimental prototype of the hybrid system. The dehumidifier and regenerator are structurally similar, and the size of the packing is 0.8 m×0.968 m×1.2 m (length×width×height). The liquid desiccant is aqueous solution of calcium chloride ($CaCl_2$). Besides, heat transfer areas of the evaporator and condenser are both 4 m^2, and the refrigerant of the compression system is R410A. For experimental measurements, the anemometer and temperature and humidity recorder are used for measuring the air inlet and outlet parameters.

The solution parameters are obtained by the densimeter and temperature recorder. Furthermore, the power consumption of compressor and pumps are measured by a three-phase electric energy meter.

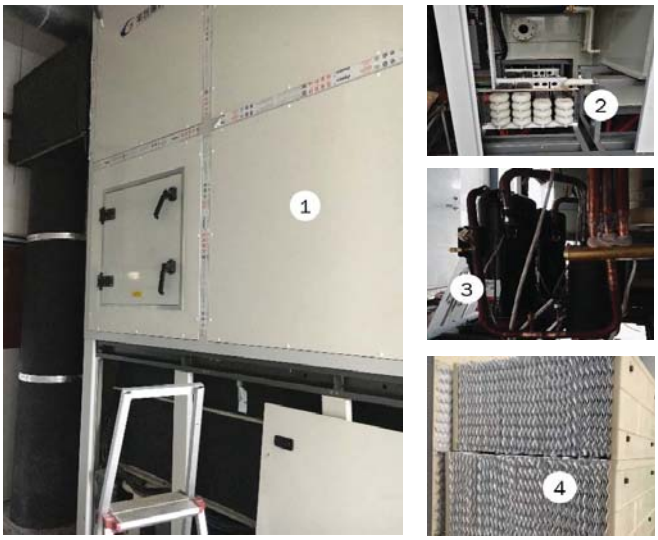

Figure 2: Experimental prototype of the hybrid liquid desiccant system: (1) whole unit; (2) evaporator and condenser; (3) compressor; (4) packing.

2.2 Evaluation indexes

The system performance can be evaluated by the index of the coefficient of performance of the system COP_{sys}, as defined in Eq. (1).

$$COP_{sys} = \frac{Q_a}{P_{sys}} = \frac{m_a(h_{ain} - h_{aout})}{P_{com} + P_{pump}} \quad (1)$$

where Q_a is the heating capacity gained by the outdoor air, which is related to the air flow rate (m_a) and the enthalpy difference between outdoor air (h_{ain}) and supply air (h_{aout}). P_{sys} is the power consumption of the hybrid system, including power consumptions of the compressor (P_{com}) and the circulating pumps (P_{pump}). And the fan power consumption is not included in the equation of the present research considering the different required supply air pressure for different circumstances.

Then performance of the heat pump inside the prototype is evaluated by COP_{hp}, as shown in Eq. (2). Q_c is the heating capacity provided by the heat pump.

$$COP_{hp} = \frac{Q_c}{P_{com}} \quad (2)$$

For this system, the outdoor air is heated and humidified in the regenerator by the higher and diluted solution out of the condenser, and then the heat and moisture will be transfer to the indoor exhaust air through the solution circulating. Therefore, the heating capacity obtained by outdoor air Q_a benefits from not only the heating capacity Q_c provided by the condenser, but also the recovered heating capacity from indoor exhaust air, which is expressed by Q_{hr}

(Xie et al. 2016). Thus, δ is defined as the heat recovery ratio to evaluate the heat recovery performance of the system, as shown in Eq. (3).

$$\delta = \frac{Q_{hr}}{Q_a} = \frac{Q_a - Q_c}{Q_a} \tag{3}$$

3. EXPERIMENTAL RESULTS

The experiments are carried out under 4 partial load outdoor conditions in Beijing. Outdoor air temperature (T_{ain}) was 8.9-11.9℃, and air humidity ratio (ω_{ain}) was 1.4-1.9g/kg; indoor exhaust air temperature (T_{rin}) was 19.0-20.7℃, and air humidity ratio (ω_{rin}) was 4.0-5.1g/kg. The air flow rate was up to 5000m^3/h, and the two air inlet flow rates (m_a and m_r) equalled to each other. Then the prototype only need to operate one compressor to meet the air handling demand. With varying solution flow rate (m_s) from 2.6 m^3/h to 4.2 m^3/h, the system performances were tested and analyzed.

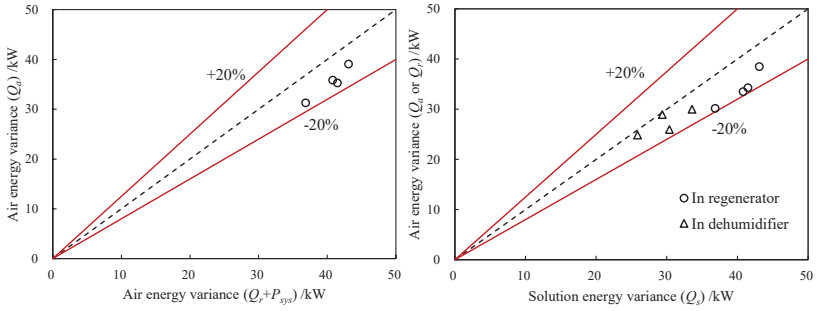

(a) (b)

Figure 3: Energy balance of the experiments: (a) between outdoor air and indoor exhaust air; and (b) between solution and outdoor air.

Considering the principle of energy balance, the differences between energy variance of outdoor air (Q_a+P_{sys}) and that of indoor exhaust air (Q_r) are all within ±20% for the entire system. Furthermore, the differences between the solution energy variance (Q_s) and air energy variance (Q_a or Q_r) for a single packed tower are also within ±20%, as indicated in Figure 3. Q_r is the cooling capacity gained by the indoor exhaust air and Q_s is the total heat obtained by the solution. According to the energy balance of the experiments, whether the energy imbalance rate of the whole system shown in Figure 3(a), or that of the single packed tower shown in Figure 3(b) are all within ±20%, then the experimental results were valid.

3.1 Basic condition

Taking a basic condition to analyse the system performance in details, the experimental results were listed in Table 1 when m_s was 3.0 m^3/h. Outdoor air was heated and humidified by the solution inlet as 24.3℃, 34.7% from 10.7℃, 1.6g/kg to 20.8℃, 8.0g/kg. The solution outlet was 9.8℃, 35.0%. Indoor exhaust air was cooled and dehumidified by the solution inlet as 2.0℃, 35.0% from 20.3℃, 5.1g/kg to 6.2℃, 3.1g/kg. COP_{hp} was 5.9 while COP_{sys} could be 7.8, benefiting from the heat recovery of the system as δ was 0.29.

Table 1: Experimental results about a basic condition of the hybrid system.

Parameter	Data	Parameter	Data

m_a /(m³/h)	4900	m_r /(m³/h)	5200
T_{ain} /(℃)	10.7	T_{rin} /(℃)	20.3
ω_{ain} /(g/kg)	1.6	ω_{rin} /(g/kg)	5.1
T_{aout} /(℃)	20.8	T_{rout} /(℃)	6.2
ω_{aout} /(g/kg)	8.0	ω_{rout} /(g/kg)	3.1
T_e /(℃)	-4.6	T_c /(℃)	30.2
P_{sys} /(kW)	4.9	P_{pump} /(kW)	0.3
Q_a /(kW)	43.1	Q_r /(kW)	33.6
Q_c /(kW)	30.8	Q_{hr} /(kW)	12.3
COP_{hp}	5.9	COP_{sys}	7.8

3.2 Under variable solution flow rate

When m_s varied from 2.6 m³/h to 4.2 m³/h, the supply air temperature (T_{aout}) was 18.0-21.2℃ and air humidity ratio (ω_{aout}) was 7.3-8.0g/kg, meeting indoor air supply demand as depicted in Figure 4. The solution inlet temperature of the regeneration was 18.2-27.9℃, and the solution inlet concentration was 31.0-35.8%. The solution inlet temperature of the dehumidifier was 3.6-2.3℃, and the solution inlet concentration was 31.3-36.1%. For the heat pump performance, the evaporating temperature (T_e) was -4.6- -2.1℃ and the condensing temperature (T_c) was 26.0-34.2℃, while the evaporating and condensing heat transfer efficiencies were 50%~60%. The temperature difference of T_c and T_e would decrease with the increase of m_s. Then the heat pump performance COP_{hp} increased. However, the recovered heating capacity from indoor exhaust air δ decreased significantly. Therefore, there was an optimal solution flow rate for the system and COP_{sys} could be up to 7.8, when m_s was 3.0 m³/h.

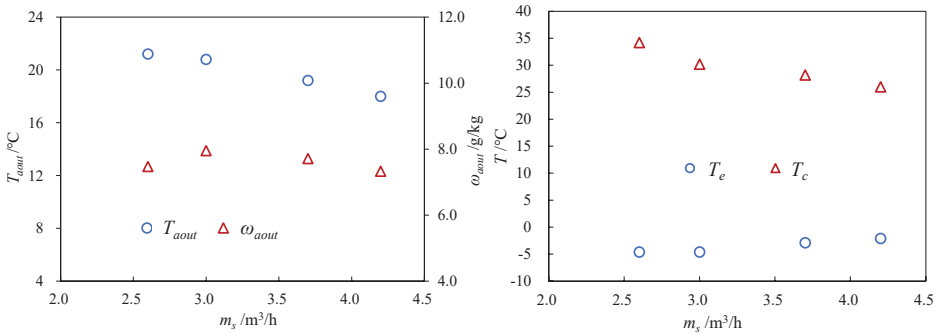

(a) (b)

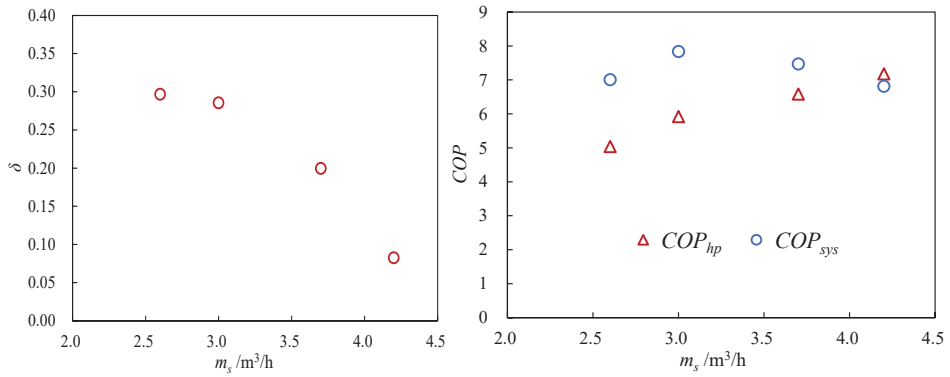

(c) (d)

Figure 4: Experimental results under variable solution flow rate m_s: (a) T_{aout} and ω_{aout}; and (b) T_e and T_c, (c) δ, and (d) COP_{hp} and COP_{sys}.

4. SIMULATION ANALYSIS

In order to further analyze the effects of other crucial parameters such as air inlet parameters on the system performance, a numerical model is utilized to simulate the system performance under various conditions.

4.1 System model

The coupled heat and mass transfer processes between air and solution in the two packed towers with counter-flow configuration have been previously modeled (Liu et al. 2007). Equations of the energy conservation, mass conservation, solute mass conservation and heat and mass transfer can be expressed as Eqs. (4)-(9), respectively.

$$m_a dh_a = d\left(m_s h_s\right) \tag{4}$$

$$dm_s = m_a d\omega_a \tag{5}$$

$$d\left(m_s X\right) = 0 \tag{6}$$

$$\frac{dh_a}{dx} = \frac{NTU_m \cdot Le}{\mathrm{H}}\left[\left(h_a - h_{se}\right) + r\left(\frac{1}{Le} - 1\right)\left(\omega_a - \omega_{se}\right)\right] \tag{7}$$

$$\frac{d\omega_a}{dx} = \frac{NTU_m}{H}\left(\omega_a - \omega_{se}\right) \tag{8}$$

$$Le = \frac{\alpha}{\alpha_m c_{p,m}},\ NTU_m = \frac{\alpha_m A}{m_a} = \frac{\alpha_m aV}{m_a} \tag{9}$$

Given the fact that the brand of the compressors installed in the experimental prototype is Copeland, the compressor can be described by two nine-coefficient empirical formulas of input power P_{com} and cooling capacity Q_e, and all the coefficients can be generated according to the massive data from a software named Copeland Selection Software 6.6 with high accuracy. The two formulas are shown in Eqs. (10)-(11).

$$P_{com} = a_1 + a_2 T_e + a_3 T_e^2 + a_4 T_c + a_5 T_c^2 + a_6 T_e T_c + a_7 T_e^2 T_c + a_8 T_e T_c^2 + a_9 T_e^2 T_c^2 \tag{10}$$

$$Q_e = b_1 + b_2 T_e + b_3 T_e^2 + b_4 T_c + b_5 T_c^2 + b_6 T_e T_c + b_7 T_e^2 T_c + b_8 T_e T_c^2 + b_9 T_e^2 T_c^2 \quad (11)$$

where a_i (i = 1,2,…,9) are 4.035, -0.03368, 0.06015, 0.002395, 0.0008334, -0.001792, 8.581e-06, -2.590e-06, -1.197e-07, and b_i (i = 1,2,…,9) are 36.53, -0.1312, 0.9540, -0.002711, 0.009761, 0.008960, -0.0001962, 2.612e-05, 2.710e-07 respectively.

The evaporator and condenser are evaluated by the heat exchange efficiencies ε_e and ε_c, as defined in Eqs. (12)-(13). T_{s1}, T_{s3}, T_{s2} and T_{s4} are the solution inlet and outlet temperature respectively.

$$\varepsilon_e = \frac{T_{s2} - T_{s3}}{T_{s2} - T_e} \quad (12)$$

$$\varepsilon_c = \frac{T_{s1} - T_{s4}}{T_c - T_{s4}} \quad (13)$$

The heat transfer process between refrigerant and solution is described as Eqs. (14)-(15).

$$Q_e = m_s c_s (T_{s2} - T_{s3}) \quad (14)$$

$$Q_c = P_{com} + Q_e = m_s c_s (T_{s1} - T_{s4}) \quad (15)$$

4.2 Model validation

Figure 5 shows the comparison results of the simulated values by the numerical model with the corresponding experimental parameters. With the same input heat and mass transfer area, air and solution inlet parameters, the simulated results (T'_{aout}, ω'_{aout} and COP'_{sys}) demonstrated good agreement with the experimental results under different conditions, where the discrepancies of these parameters were all within ±10%.

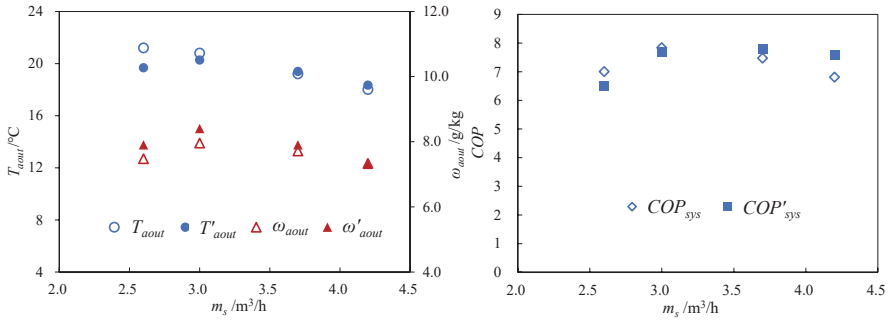

(a) (b)

Figure 5: Comparison between simulated and experimental results about: (a) T_{aout} and ω_{aout}; (b) COP_{sys}.

4.3 Simulated results under variable air inlet parameters

According to the national standard for a heat pump driven liquid desiccant outdoor air processor (GB/T 27943-2011), the outdoor air is 0ºC, 1.7g/kg and the indoor exhaust air is 20ºC, 7.0g/kg under winter normal conditions. And considering the more extreme operating condition, the winter outdoor design parameters in Beijing is -10ºC, 0.6g/kg. From the experimental results above, m_s was set as 3.0 m^3/h, and the indoor exhaust air was set as 20ºC,

7.0g/kg, then the effects of outdoor air parameters (T_{ain} and ω_{ain}) on the system performance would be analyzed by the simulation model.

Firstly, the system model also operated only one compressor under winter normal conditions. When T_{ain} increased from -2ºC to 5ºC and ω_{ain} was 1.7g/kg, T_{aout} increased from 17.0ºC to 18.8ºC and ω_{aout} increased from 7.8 to 8.4g/kg, as shown in Figure 6. Due to the unchanged temperature difference of T_c and T_e, COP_{hp} of the system maintained as 5.2. T_{ain} has little effect on the heat pump performance of the hybrid system, while the heat recovery performance δ decreased significantly from 0.53 to 0.44 with the increase of T_{ain}, due to the decreasing enthalpy difference of outdoor air and indoor exhaust air. Thus, the system performance COP_{sys} would decrease from 10.8 to 9.2.

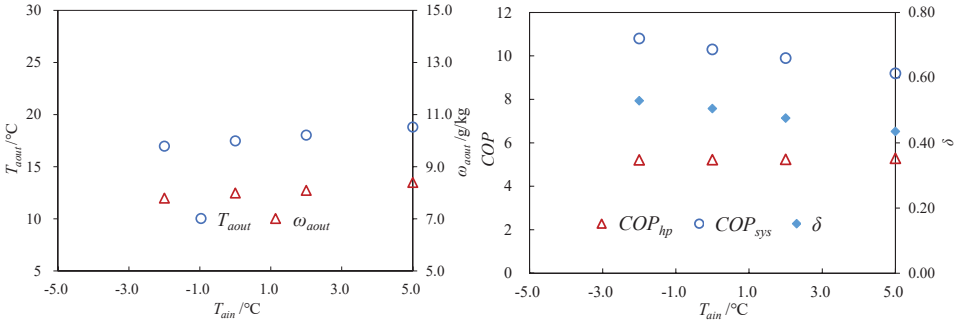

Figure 6: Simulated results under variable outdoor air temperature T_{ain} with one compressor operating: (a) T_{aout} and ω_{aout}; and (b) COP_{hp}, COP_{sys} and δ.

In the same way to analyse the effect of ω_{ain} when T_{ain} was 0ºC, T_{aout} would increase from 17.2ºC to 18.3ºC and ω_{aout} increase from 7.7 to 8.6g/kg with ω_{ain} increasing from 1g/kg to 3.5g/kg. And figure 7 shows that COP_{hp} of the system also remained unchanged as 5.3. However, the heat recovery performance δ also decreased significantly with the increase of ω_{ain}. Then the system performance COP_{sys} would decrease from 10.6 to 9.5. Therefore, variable air inlet parameters have little influence on the heat pump performance but larger influence on the heat recovery performance of the system, resulting in the variable system performance.

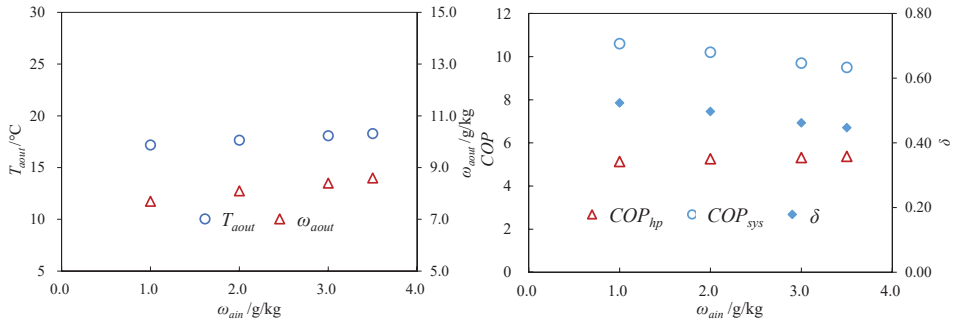

Figure 7: Simulated results under variable outdoor air temperature ω_{ain} with one compressor operating: (a) T_{aout} and ω_{aout}; and (b) COP_{hp}, COP_{sys} and δ.

Considering the hybrid system under winter outdoor design parameters as full load condition, the system model would operate two compressors to meet the air handling demand. When T_{ain} increased from -11ºC to -8ºC and ω_{ain} was 0.6g/kg, T_{aout} was 17.7 ºC -18.6ºC and ω_{aout} was 8.4-8.7g/kg, as shown in Figure 8. Similarly, COP_{hp} of the system maintained as 4.6, while δ decreased from 0.44 to 0.41. Thus, the system performance COP_{sys} would decrease from 8.2 to 7.8.

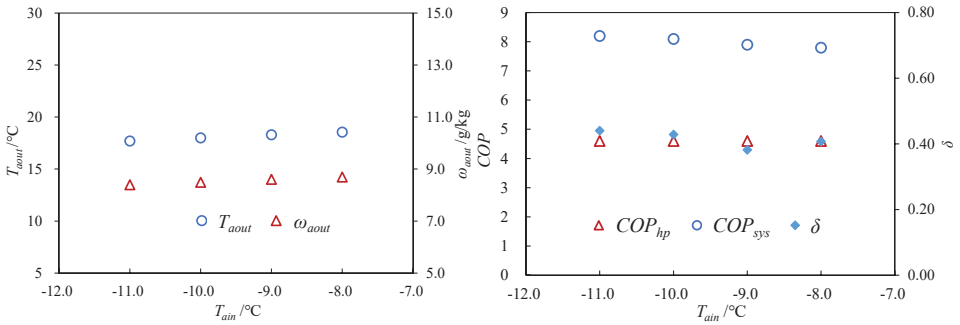

Figure 8: Simulated results under variable outdoor air temperature T_{ain} with two compressors operating: (a) T_{aout} and ω_{aout}; and (b) COP_{hp}, COP_{sys} and δ.

For the effect of ω_{ain} on system performance, T_{aout} was 17.8ºC-18.3ºC and ω_{aout} was 8.4-8.7g/kg with ω_{ain} increasing from 0.3g/kg to 1.2g/kg, when T_{ain} was 0ºC. Figure 9 shows that COP_{hp} of the system also remained as 4.5, and δ also decreased. Then the system performance COP_{sys} would decrease from 8.1 to 7.9.

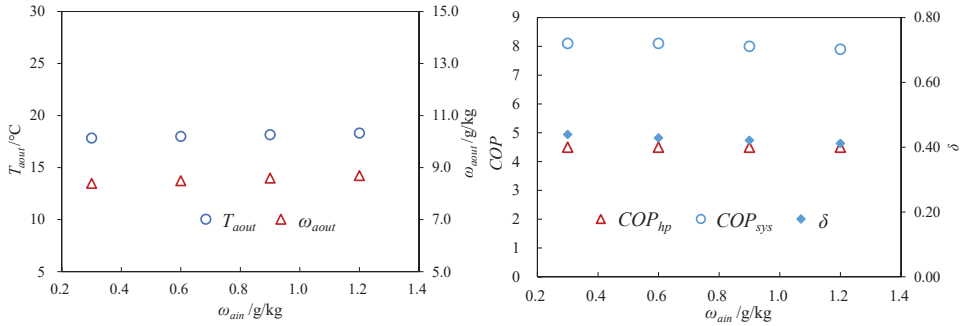

Figure 9: Simulated results under variable outdoor air temperature ω_{ain} with two compressors operating: (a) T_{aout} and ω_{aout}; and (b) COP_{hp}, COP_{sys} and δ.

Therefore, COP_{sys} of the system could reach above 9.2 under partial load winter condition as 0ºC, 1.7g/kg with one compressor operating. T_{aout} and ω_{aout} would be 17.5ºC and 8.0g/kg respectively. While COP_{sys} could also be above 7.8 under the more extreme winter outdoor condition as -10ºC, 0.6g/kg with two compressors operating, and the supply air T_{aout} and ω_{aout} would be 18.0ºC, 8.5g/kg.

5. CONCLUSION

A hybrid liquid desiccant system under winter conditions were tested and simulated in the present study. Based on the aforementioned analysis, the following conclusions can be made:

- Effect of solution flow rate m_s on the performance of the hybrid system was drawn from the experimental results. It is found that there is an optimal m_s for the system. When m_s was 3.0 m^3/h, and the COP_{sys} could reach 7.8 under partial load winter conditions.
- Effects of outdoor air parameters (T_{ain} and ω_{ain}) on system performance were obtained from the simulated results. COP_{sys} of the system could reach above 9.2 under partial load winter condition as 0ºC, 1.7g/kg with one compressor operating while COP_{sys} could also be above 7.8 under the more extreme winter outdoor condition as -10ºC, 0.6g/kg with two compressors operating.

REFERENCES

Rafique M.M., Gandhidasan P., Bahaidarah H.M.S., 2016. Liquid desiccant materials and dehumidifiers – A review. Renewable and Sustainable Energy Reviews.

Qi R.H., Lu L., Huang Y., 2014. Energy performance of solar-assisted liquid desiccant air-conditioning system for commercial building in main climate zones. Energy Conversion and Management.

Jradi M., Riffat S., 2014. Experimental investigation of a biomass-fuelled micro-scale tri-generation system with an organic Rankine cycle and liquid desiccant cooling unit. Energy.

Mucke L., Fleig D., Vajen K., et al., 2016. Hybrid liquid desiccant air-conditioning systems: A conceptual study with respect to energy saving potentials. International Journal of Refrigeration.

Cai D.H., Qiu C.B., Zhang J.Z., et al., 2017. Performance analysis of a novel heat pump type air conditioner coupled with a liquid dehumidification/humidification cycle. Energy Conversion and Management.

Liu S.Q., Jiang Y., Liu X.H., et al., 2008. System principle and performance tests of a heat pump driven two-stage liquid desiccant outdoor air handler (in Chinese). HV&AC.

Liu X.H., Yi X.Q., Chang X.M., et al., 2009. Research on the field uniformity principle in liquid desiccant dehumidifier/regenerator. Acta Energiae Solaris Sinica.

Xie Y., Zhang T., Liu X.H., 2016. Performance investigation of a counter-flow heat pump driven liquid desiccant dehumidification system. Energy.

Yamaguchi S., Jeong J., Saito K., et al., 2011. Masatoshi Harada, Hybrid liquid desiccant air-conditioning system: Experiments and simulations. Applied Thermal Engineering.

Liu X.H., Jiang Y., Xia J.J., et al., 2007. Analytical solutions of coupled heat and mass transfer processes in liquid desiccant air dehumidifier/regenerator. Energy Conversion and Management.

GB/T 27943-2011, 2011. Heat pump driven liquid desiccant outdoor air processor with heat recovery, Beijing: China Standard Press.

ACKNOWLEDGEMENTS

The authors appreciate the support from the National Natural Science Foundation of China (No. 51608296 and No. 51521005).

NOMENCLATURE

a	Specific area of the packing per volume (m^2/m^3)
A	Heat and mass transfer area (m^2)
COP_{hp}	COP of the heat pump (dimensionless)
COP_{sys}	COP of the dehumidification system (dimensionless)
c_s	Specific heat capacity of the solution (kJ/(kg·ºC))
$c_{p,m}$	Specific heat capacity of air (kJ/(kg·ºC))
h	Enthalpy (kJ/kg)
H	Height of the packing (m)
Le	Lewis number (dimensionless)
m	Mass flow rate in cross section (kg/s)
NTU_m	Number of mass transfer units (dimensionless)
P_{com}	Power consumption of the compressor (kW)
P_{pump}	Power consumption of the circulating pumps (kW)
P_{sys}	Power consumption of the system (kW)
Q_a	Heating capacity gained by the outdoor air (kW)
Q_r	Cooling capacity gained by the indoor exhaust air (kW)
Q_e	Cooling capacity of the heat pump (kW)
Q_s	Energy that the solution obtains (kW)
Q_{hr}	Recovered cooling capacity of the system (kW)
r	Latent heat of vaporization (kJ/kg)
T	Temperature (ºC)
V	Volume of heat and mass transfer module (m^3)
x	The location along the solution flow direction (dimensionless)
X	Mass concentration of solution (%)

Greek symbols

α	Heat transfer coefficient between air and desiccant (kW/m^2·ºC)
α_m	Mass transfer coefficient between air and desiccant ($kg/(m^2 \cdot s)$)
δ	Heat recovery ratio (dimensionless)
ε	Heat exchange efficiency (dimensionless)
ω	Humidity ratio (g/kg)

Subscripts

a	Outdoor air
c	Condenser
deh	Dehumidifier
e	Evaporator
h	Enthalpy
m	Mass
r	Indoor exhaust air
reg	Regenerator
s	Liquid desiccant
se	Air in equilibrium with desiccant

Questions and Answers:

Pascal Stabat*:*

What is the regeneration temperature of the liquid desiccant?

Ying Xie:

The regeneration temperature is 24.5°C. And the condensing temperature is 30.2°C. Even under more extreme outdoor conditions the condensing temperature will be above 30°C. It can work under winter conditions.

***

Assaad Zoughaib:

System applicability for old houses vs new ones well insulated? Ventilation load rate?

Ying Xie:

The applicability of this system has been discussed in the introduction that the system can use heat pump as an effective mean without available low-grade heat for desiccant refrigeration and the system should use the indoor exhaust air as the dehumidification air to get the recovered heat.

***

Sébastien Thomas:

How to be sure that the liquid desiccant does not pollute the air?

Ying Xie:

Use liquid baffle to prevent the liquid desiccant entering the indoor environment along with air supply.

FIFTH SESSION
MODELING, SIMULATION AND TESTING OF HEAT PUMPS

Modelling of an exhaust air heat pump used for heating and domestic hot water production

Frédéric Ransy[1]*, Samuel Gendebien[1], Vincent lemort[1]

[(1)] Thermodynamics Laboratory, University of Liege, Liège, Belgium

ABSTRACT

Exhaust heat pump is a promising solution to heat and ventilate a building with a high energy efficiency, and a competitive investment cost. The authors presented in 2015 laboratory test results about an exhaust heat pump and showed a COP of 4.4 for the conditions A22W35. A simple annual extrapolation of the results showed a similar primary energy consumption than the conventional balanced ventilation system combined with an outside air heat pump. However, the authors presented in 2018 the performance of the same machine integrated in a demonstration building in Belgium. Due to the ultra-low heating capacity (1500 W), the measured overall COP of the system was 2.18. In order to increase the heating capacity of the system, this paper presents a semi-empirical model of the heat pump to study the impact of the design of the different elements of the machine on the performance.

Keywords: Exhaust air heat pump, modelling, experimental

1. INTRODUCTION AND CONTEXT

In Belgium, typical HVAC systems installed in highly efficient residential buildings consist of a centralized balanced ventilation with heat recovery, combined with a gas condensing boiler or a heat pump for space heating and domestic hot water production. In this combination of systems, the ventilation and the heating systems are decoupled, and are therefore easy to control. However, the balanced ventilation system with heat recovery is characterized by a high electrical consumption, due to the presence of the supply and the exhaust fans and the relatively high specific fan power (Laverge et al., 2012). Moreover, the condensing boiler technology is a fossil-fuel based technology and emits CO_2. The heat pump is a good environmental-friendly alternative. On the other hand, the heat pump technology remains expensive and the investment is sometimes hardly justifiable in residential construction projects because the building energy demand is very low.

The performance of typical HVAC systems can be improved through two different aspects: the ventilation and the heating system.

For example, Gendebien et al. presented in 2013 a single room ventilation device with heat recovery, characterized by a lower specific fan power than conventional centralized units. However, by definition, one decentralized unit must be installed in each room where a ventilation airflow is necessary. It can lead to a high investment cost in residential construction projects. The noise level in bedrooms during the nights can also be a problem. Recently, the concept of smart ventilation strategies was also introduced in the literature (Guyotab et al, 2017). The concept is to control the ventilation airflows based on the CO_2 and the humidity levels. Consequently, the fan electrical consumption is lower, and the overall energy consumption of the ventilation can be decreased by 50%. However, the use of sensors increases the complexity and the investment cost of the system.

Concerning the heating system, many researchers are currently developing technologies to increase the performance of actual heat pump systems, such as heat pumps with vapor

injection (Dechesne et al, 2017), the development of new fluids (Nawaz et al., 2017 and Zhang et al., 2015) or advanced multivariable fuzzy logic control (Underwood, 2015). In addition, other renewable energy technologies are currently available on the market: micro-CHP, biomass boiler, … The major disadvantage of these systems is the investment cost which is prohibitive for residential projects without government support.

This paper presents another technology used to ventilate and heat highly efficient residential buildings: the exhaust air heat pump. Figure 1 shows a typical integration of an exhaust air heat pump in a residential building.

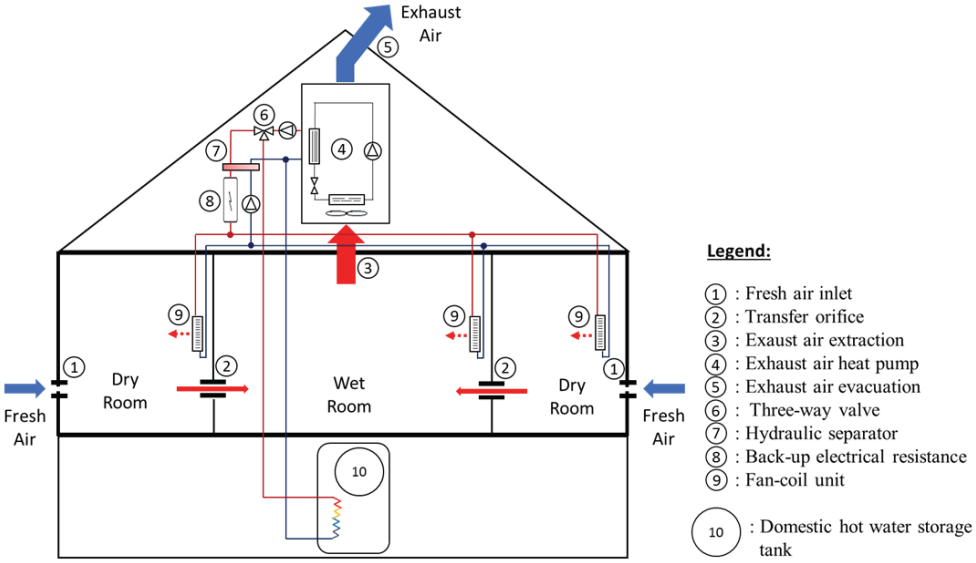

Figure 1: Typical integration of an exhaust air heat pump in residential buildings

In this system, the evaporator of the heat pump is located in the exhaust air flow of the mechanical exhaust ventilation system and the condenser is connected to the heating circuit of the house. The heat pump also provides the heat required for the hot water production, stored in a storage tank. The system can be coupled with fan-coil units or floor heating. If the heat pump cannot cover the whole building energy demand, an electrical resistance is activated.

The air temperature at the supply of the exhaust air heat pump is relatively constant over the year, i.e. between 18 and 23°C. By comparison, the cold source temperature of a conventional outside air heat pump varies from -10 to 15°C during winter. Consequently, the seasonal COP of an exhaust air heat pump is theoretically higher than conventional heat pump (Fracastoro et al., 2010). Moreover, the heating capacity, the COP and the operating conditions are constant over the year. For this reason, exhaust air heat pump can be cost-effective by keeping the design of the machine as simple as possible.

In the proposed building integration scheme (Figure 1), the exhaust air heat pump is combined with an exhaust ventilation system. Compared to the balanced (supply + exhaust) mechanical ventilation system, the fan electrical consumption is lower, because only one fan is required. The whole system performs a combination of three functions: ventilation, heating and domestic hot water production. For this reason, from an economic point of view, the system is a competitive alternative to conventional HVAC systems.

However, the system has two main disadvantages. Firstly, the heating demand of the building is much higher in the case of an exhaust mechanical ventilation, compared to a balanced ventilation system with heat recovery. Secondly, the heating capacity of the exhaust air heat pump is limited by the maximum ventilation airflow of the house. Consequently, if the heating capacity is not sufficient, the backup resistance is activated, and the COP of the whole system decreases.

In order to quantify the real performance of an exhaust air heat pump integrated in a typical residential building, several models of exhaust air heat pumps were tested experimentally in the thermodynamics laboratory of the University of Liege in Belgium. The results were presented for one machine in 2015 by the authors. The COP of the system for the conditions A22W35 (air supply temperature of 22°C and water exhaust temperature of 35°C) was equal to 4.4. A numerical model of the exhaust air heat pump was developed, and integrated into a numerical model of an apartment, representative of the Belgian building stock. The building model was presented in 2016 by the authors. The annual simulations of the system showed that the exhaust air heat pump and the balanced ventilation system coupled to an outside air heat pump were similar in terms of primary energy consumption.

To confirm these good results, an exhaust air heat pump was installed in 2016 in a demonstration building in Belgium. The heating capacity of the heat pump was 1500 Watts in nominal conditions (A20W35). The building was a new single-family freestanding house with two stories. The results were presented in 2018 by the authors.

The results showed good performance of the exhaust air heat pump. Indeed, in space heating mode with an average exhaust water temperature of 45°C, the average COP of the machine was equal to 3.55. In domestic hot water production mode, the average COP was equal to 3.44, with a domestic hot water set-point temperature of 50°C.

However, due to the limited heating capacity of 1500 W, the exhaust air heat pump was not able to provide the whole energy demand of the building, particularly in winter. Consequently, the electrical backup resistance was activated and the whole system efficiency decreases. A simple annual extrapolation of the results showed an annual coverage factor of 76 % and a seasonal COP of 2.18. This value is significantly lower than the theoretical value of 3.4 that could be achieved if the heat pump could cover the whole building energy demand.

In conclusion, the main problem of exhaust air heat pumps is the limited heating capacity, due to the limited ventilation airflow. The objective of this paper is to show what could be the maximum heating capacity of an exhaust air heat pump, if the ventilation airflow is fixed at a typical value for freestanding residential buildings. A second objective is also to show the impact on the design of the machine, and on the risk of frost formation on the evaporator.

For this purpose, a semi-empirical model of the heat pump is presented. For each component of the machine, the geometry is considered, in order to evaluate the impact of the design on the heating capacity and the performance. The model of each component is calibrated with experimental data from laboratory tests and the heat pump model is validated with five data set.

2. HEAT PUMP MODELLING

This section presents the semi-empirical model of the exhaust air heat pump developed in Matlab. In this type of model, the parameters have a physical meaning. The model can then be used to extrapolate the performance of the machine for non-tested conditions. The three main components of the system are the compressor, the condenser and the evaporator.

2.1 Compressor

The compressor is an air cooled and hermetic rolling piston compressor working with R134a. Rotary compressors are popular in low capacity air conditioning and refrigeration systems. Its control is a simple ON/OFF switch.

The semi-empirical model was initially developed for scroll, reciprocating, and screw compressors (Dardenne et al, 2015, Giuffrida, 2016, Li, 2013, Winandy et al, 2002, Lemort et al, 2009). The compression process from the suction to the discharge is described through elementary thermodynamic transformations that represent the thermodynamic processes accomplished by the refrigerant inside the compressor. The model considers the losses due to the internal heat exchanges, the heat losses to the environment, the internal leakage, the exhaust pressure drop and the electro-mechanical losses. A schematic representation of the compressor model is presented in Figure 2.

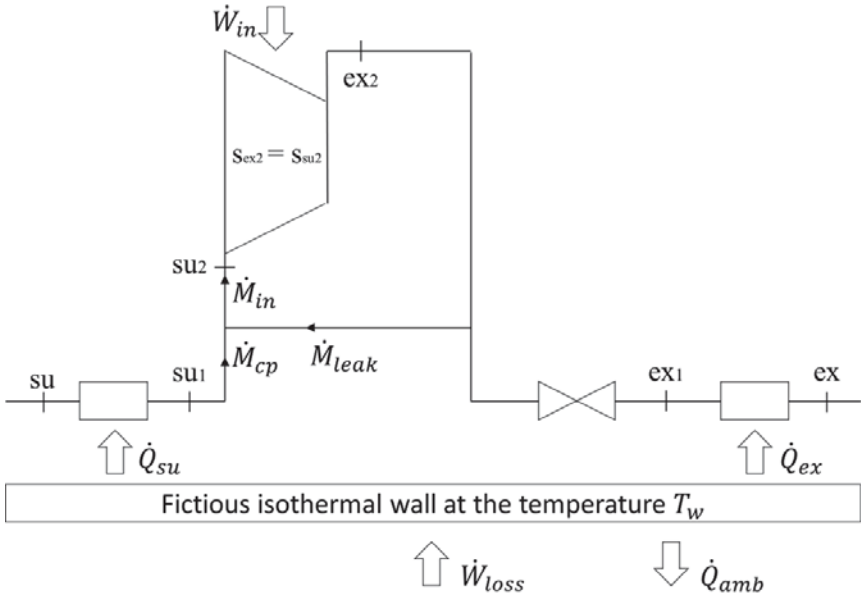

Figure 2: Schematic representation of the compressor model

In the model, the refrigerant is supposed to undergo the following transformations:

- su – su1: isobaric ($P_{su1} = P_{su}$) heating-up of the supply refrigerant mass flow rate,
- su1 – su2: isobaric ($P_{su2} = P_{su1}$) mixing of the supply mass flow with the internal leakage,
- su2 – ex2: isentropic ($s_{ex2} = s_{su2}$) compression,
- ex2 – ex1: isenthalpic ($h_{ex1} = h_{ex2}$) exhaust pressure drop through the discharge valve,
- ex1 – ex: isobaric ($P_{ex} = P_{ex1}$) cooling-down of the exhaust refrigerant mass flow rate.

The following sections describe the equations relative to the above-mentioned thermodynamic transformations.

Supply isobaric heat transfer

Internal heat transfers occur between the fluid, the compressor, the motor and the oil. In the present model, the internal heat transfers lead to a heating at the supply and a cooling at the

exhaust. To compute the heat transfers, a fictious isothermal wall at the temperature T_w is introduced. This isothermal wall exchanges thermal energy with the refrigerant, the motor (through the electro-mechanical losses, described in the following) and the ambient.
For the modelling of the heat exchange at the supply, a semi-isothermal heat exchanger is considered, and the ε-NTU method is used to determine the exchanger efficiency. The equations describing the heat transfer at the supply are the following:

$$\dot{Q}_{su} = \dot{M}_{cp}(h_{su1} - h_{su}) = \varepsilon_{su}\, \dot{M}_{cp} c_{p,su}(T_w - T_{su}) \quad (1)$$

$$\varepsilon_{su} = \left(1 - e^{\left(\frac{-AU_{su}}{\dot{M}_{cp}\, c_{p,su}}\right)}\right) \quad (2)$$

$$AU_{su} = AU_{su,n} \left(\frac{\dot{M}_{cp}}{\dot{M}_{cp,n}}\right)^{0.8} \quad (3)$$

The two parameters are the nominal overall heat transfer coefficient at the supply, $AU_{su,n}$, and the corresponding nominal mass flow rate, $\dot{M}_{cp,n}$.

Internal leakage and isobaric mixing with supply mass flow rate

In rolling piston compressors, due to clearance between the wall of the rolling piston and the cylinder, leakages occur from the compression to the suction chambers. In the model, the enthalpy of the leakage mass flow rate is supposed to be the enthalpy at the exhaust of the isentropic compression, h_{ex2}. The leakage mass flow rate is then mixed with the supply refrigerant mass flow rate, before the isentropic compression. The following equations are used for the mixing:

$$\dot{M}_{in} = \dot{M}_{cp} + \dot{M}_{leak} \quad (4)$$

$$\dot{M}_{in}\, h_{su2} = \dot{M}_{cp}\, h_{su1} + \dot{M}_{leak}\; h_{ex2} \quad (5)$$

An isentropic flow through a simply convergent nozzle is considered to calculate the leakage mass flow rate:

$$\dot{M}_{leak} = A_{leak}\, \rho(s_{ex2}, P_{thr}) \sqrt{2[h_{ex2} - h(s_{ex2}, P_{thr})]} \quad (6)$$

The nozzle throat A_{leak} is a parameter of the model to be identified. In Eq. 6, the throat pressure P_{thr} is the maximum between the throat outlet pressure and the critical low pressure corresponding to choked flow conditions, considering the refrigerant vapor as a perfect gas:

$$P_{thr} = \max\left(P_{su1}, P_{ex2}\, \left(\frac{2}{\gamma_{ex2}+1}\right)^{\frac{\gamma_{ex2}}{\gamma_{ex2}-1}}\right) \quad (7)$$

The internal mass flow rate $\dot{M}_{in}$ depends on the swept volume of the compressor, V_s, the rotational speed of the compressor, N, and on the density of the refrigerant after the mixing process:

$$\dot{M}_{in} = \rho_{su2}\, V_s\, \frac{N}{60} \quad (8)$$

The compressor swept volume V_s is parameter to be identified and is generally given by the manufacturer. In the following sections, the value given by the manufacturer is supposed to be

the good value. For a ON-OFF compressor, the rotational speed N is constant and generally equal to 3000 rpm.

Isentropic compression and isenthalpic exhaust pressure drop

In the model, the compression from the suction su2 to the exhaust ex2 is supposed to be isentropic. To determine the thermodynamic state at the end of the isentropic compression, the internal discharge pressure P_{ex2} needs to be determined. This pressure depends on the pressure drop at the exhaust of the compressor. Indeed, rolling piston compressors are manufactured with a discharge valve. Consequently, the internal discharge pressure is always higher than the actual exhaust pressure, to ensure a complete exhaust-gas discharge from the combustion chamber to the exhaust port. In the model, the exhaust refrigerant flow through the discharge valve is considered in the same way as for the leakage, i.e. an isentropic flow through a simply convergent nozzle. The same equations apply:

$$\dot{M}_{cp} = A_{dis}\,\rho\left(s_{ex2}, P_{thr,dis}\right)\sqrt{2[h_{ex2} - h\left(s_{ex2}, P_{thr,dis}\right)]} \tag{9}$$

$$P_{thr,dis} = \max\left(P_{ex}, P_{ex2}\left(\frac{2}{\gamma_{ex2}+1}\right)^{\frac{\gamma_{ex2}}{\gamma_{ex2}-1}}\right) \tag{10}$$

The parameter A_{dis} is the area of the discharge valve and is a parameter to be identified.

Exhaust isobaric heat transfer

The modelling approaches for the exhaust and the supply heat transfers are the same. Consequently, the equations are similar:

$$\dot{Q}_{ex} = \dot{M}_{cp}(h_{ex} - h_{ex1}) = \varepsilon_{ex}\,\dot{M}_{cp}c_{p,ex1}(T_w - T_{ex1}) \tag{11}$$

$$\varepsilon_{ex} = \left(1 - e^{\left(\frac{-AU_{ex}}{\dot{M}_{cp}\,c_{p,ex1}}\right)}\right) \tag{12}$$

$$AU_{ex} = AU_{ex,n}\left(\frac{\dot{M}_{cp}}{\dot{M}_{cp,n}}\right)^{0.8} \tag{13}$$

The two parameters are the nominal overall heat transfer coefficient at the exhaust, $AU_{ex,n}$, and the corresponding nominal mass flow rate, $\dot{M}_{cp,n}$.

Electrical consumption

The compressor electrical power input is the sum of the compressor internal power and the electro-mechanical losses. The electro-mechanical losses are split into two terms: constant losses and losses proportional to the internal power:

$$\dot{W}_{cp} = \dot{W}_{in} + \dot{W}_{loss} = \dot{M}_{in}\,(h_{ex2} - h_{su2}) + \dot{W}_{loss} \tag{14}$$

$$\dot{W}_{loss} = 2\,\pi\,N\,T_{loss} + \alpha\,\dot{W}_{in} \tag{15}$$

The two parameters to be identified are the constant mechanical loss torque T_{loss} and the factor of proportionality α for the electro-mechanical loss proportional to the internal power. The electro-mechanical losses are directly injected into the fictious envelope.

Fictitious envelope heat balance and heat losses to the environment

To close the system of equations, the heat balance applied on the fictious envelope on steady-state is written:

$$\dot{W}_{loss} - \dot{Q}_{ex} - \dot{Q}_{su} - \dot{Q}_{amb} = 0 \quad (16)$$

The last term in Eq. 16 is the heat losses to the environment. Different formulations exist in the literature to calculate the compressor ambient heat losses. For example, a simple constant overall heat transfer coefficient to the ambient can be used. In the case proposed in this paper, this modeling method is not sufficiently accurate. Indeed, the compressor is cooled down by the ventilation airflow. As a result, due to the important airflow around the compressor, the ambient heat losses can represent a non-negligible fraction of the compressor consumption (from 10 to 40%). The compressor performance can thus be largely influenced by the ventilation airflow. A mode detail model of ambient heat losses is consequently proposed in the following.

Figure 3 represents a 2-D top view of the relative positions the compressor and the evaporator in the heat pump casing. The airflow enters the heat pump and directly cools down the compressor. The heated air is then sent to the evaporator, is cooled down, and exits the heat pump. The air temperature at the supply of the evaporator directly depends on the convective heat losses. This temperature will influence the evaporator heat exchange, and the overall performance of the machine.

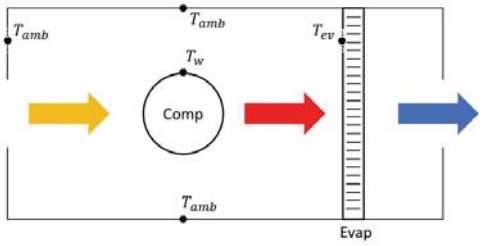

Figure 3: 2-D representation of the position of the compressor, the evaporator and the heat pump casing

The compressor heat losses $\dot{Q}_{amb}$ are divided in two terms: the radiative heat exchange with the surrounding surfaces, $\dot{Q}_{amb,r}$, and the convective heat transfer with the supply air, $\dot{Q}_{amb,c}$.

For the radiative heat exchange, the compressor is supposed to exchange energy with the casing of the heat pump, and with the surface of the evaporator, which is situated close to the compressor. The surface temperature of the casing is supposed to be the ambient temperature, T_{amb} , and the surface temperature of the evaporator is supposed to the evaporating temperature, T_{ev}. For the convective heat exchange, the heat flow depends on the convective heat transfer coefficient. The equations are the following:

$$\dot{Q}_{amb} = \dot{Q}_{amb,c} + \dot{Q}_{amb,r} \quad (17)$$

$$\dot{Q}_{amb,r} = \sigma\, \varepsilon_{cp}\, A_{ext,cp} \left(\left(F_{cp,ev} (T_w^4 - T_{ev}^4) + (1 - F_{cp,ev}) (T_w^4 - T_{amb}^4) \right) \right) \quad (18)$$

$$\dot{Q}_{amb,c} = A_{ext,cp}\, h_{c,cp} \left(T_w - T_{a,su} \right) \quad (19)$$

with σ the Stefan–Boltzmann constant, ε_{cp} the emissivity of the compressor casing, assumed to be 0.95, $A_{ext,cp}$ the outer surface of the compressor $\left(= \pi \frac{D_{ext,cp}^2}{4} + \pi D_{ext,cp} H_{cp}\right)$, $F_{cp,ev}$ the view factor from the compressor to the evaporator, T_w the surface temperature of the compressor casing, $T_{a,su}$ the air supply temperature and $h_{c,cp}$ the convective heat transfer coefficient. The following correlation is used to determine the heat transfer coefficient:

$$h_{c,cp} = \frac{Nu.k}{D_{ext,cp}} \tag{20}$$

$$Nu = C_{Nu} Re_{D_{ext,cp}}^{n_{Nu}} Pr^{1/3} \tag{21}$$

$$Re_{D_{ext,cp}} = \frac{V_{su} D_{ext,cp}\, \rho}{\mu} \tag{22}$$

The two constants C_{Nu} and n_{Nu} are two empirical parameters of the model to be identified.

Variation of the semi-empirical parameters with the compressor size

The semi-empirical parameters described in the previous sections are identified for one compressor size, i.e. one value of the swept volume V_s. However, the objective of the heat pump model is to predict the variation of the performance if the geometries of the constituting elements are changed. If the parameters are known for one compressor swept volume $V_{s,n}$, the parameters corresponding to another swept volume $V_{s,2}$ are calculated as followed:

$$AU_{su,n,V_s=V_s} = AU_{su,n,V_s=V_{s,n}} \left(\frac{V_s}{V_{s,n}}\right)^{n_1} \tag{23}$$

$$A_{leak,V_s=V_s} = A_{leak,V_s=V_{s,n}} \left(\frac{V_s}{V_{s,n}}\right)^{n_2} \tag{24}$$

$$A_{dis,V_s=V_s} = A_{dis,V_s=V_{s,n}} \left(\frac{V_s}{V_{s,n}}\right)^{n_3} \tag{25}$$

$$T_{loss,V_s=V_s} = T_{loss,V_s=V_{s,n}} \left(\frac{V_s}{V_{s,n}}\right)^{n_4} \tag{26}$$

The four constants n_1, n_2, n_3 and n_4 are identify with at least two set of experimental data from two compressors with a different swept volume. The two compressor technologies must be the same.

2.2 Condenser

The condenser consists of a brazed plate heat exchanger. The working fluid is the refrigerant R134a and the secondary fluid is liquid water. The principal geometric characteristics of the condenser are listed in Table 1.

L_{hex} $[m]$	W_{hex} $[m]$	p $[m]$	φ [°]	Φ [-]	th_p [mm]	N_p [-]
0.247	0.191	0.00152	30	1.22	0.4	24

Table 1: Geometric characteristics of the condenser

In the model, the condenser is divided in three zones: the superheated vapor, the two-phase flow and the subcooled liquid. The modelling principle is represented in Figure 4. The model supposes a counterflow heat exchange.

For each zone i, the two heat balances in steady state on the water side and on the refrigerant side are expressed as:

$$\dot{Q}_{cd,i} = \dot{M}_r \, (h_{r,su,i} - h_{r,ex,i}) \tag{27}$$

$$\dot{Q}_{cd,i} = \dot{M}_w \, cp_w \, (T_{w,ex,i} - T_{w,su,i}) \tag{28}$$

with $i = v, tp \; or \; l$.

To calculate the heat flow in each zone, the logarithmic mean temperature difference is calculated as followed:

$$\dot{Q}_{cd,i} = A_i \, U_i \, \Delta T_{log,i} \tag{29}$$

with A_i the heat transfer area of each zone, $\Delta T_{log,i}$ the logarithmic mean temperature difference between the working fluid and the secondary in each zone and U_i the overall heat transfer coefficient for each zone. This coefficient depends on the convective heat transfer coefficient on the water side, on the convective heat transfer coefficient on the refrigerant side and on the conductive thermal resistance of the plates. It is calculated as followed:

$$U_i = \frac{1}{\frac{1}{h_{i,sf}} + \frac{th_p}{k_p} + \frac{1}{h_{i,wf}}} \tag{30}$$

The heat transfer coefficient for the secondary fluid (water) and for the working fluid (refrigerant) in the superheated zone and the subcooled zone are calculated with the correlation proposed by Martin (1996). In this approach, the heat transfer coefficient depends only on geometrical characteristics of the exchanger. The heat transfer on the working fluid in the two-phase flow is determined with the correlation proposed by Longo (2015).

The total condenser heat flow rate is the sum of the heat flows in each zone:

$$\dot{Q}_{cd} = \dot{Q}_{cd,v} + \dot{Q}_{cd,tp} + \dot{Q}_{cd,l} \tag{31}$$

In the proposed model, it is not necessary to tune empirical parameters because all the calculations are based only on the geometrical characteristics of the exchanger.

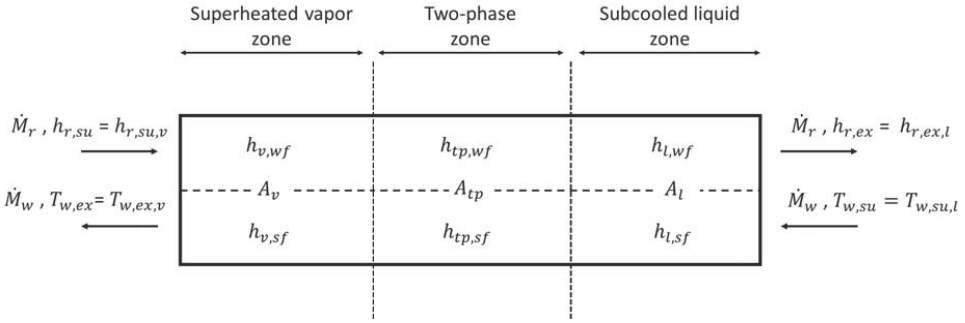

Figure 4: Three zones model of the condenser

2.3 Evaporator

The evaporator consists of a finned-tube heat exchanger. The working fluid is the refrigerant R134a and the secondary fluid is the air. The principal geometric characteristics of the condenser are listed in Table 2.

The modeling of the evaporator consists in assuming that the heat exchanger is semi-isothermal, with the constant temperature equal to the saturation temperature. It is assumed that the exchanger works in a completely dry regime, or a completely wet regime. The exchanger thermal output is the maximum of the heat exchange in the two regimes:

$$\dot{Q}_{ev} = \max\left(\dot{Q}_{ev,dry}, \dot{Q}_{ev,wet}\right) \tag{32}$$

The heat exchange in dry regime is calculated with the $\varepsilon - NTU$ method:

$$\dot{Q}_{ev,dry} = \varepsilon_{dry} \dot{M}_a cp_a (T_{a,su} - T_{ev,dry}) \tag{33}$$

The efficiency in dry regime depends on the overall heat transfer coefficient:

$$\varepsilon_{dry} = 1 - \exp\left(\frac{-AU_{dry}}{\dot{M}_a cp_a}\right) \tag{34}$$

The overall heat transfer coefficient depends on the wall thermal resistance, the total air heat transfer area, the fin efficiency, the air side convective heat transfer coefficient, the refrigerant convective heat transfer coefficient and the inside heat transfer area on the refrigerant side:

$$AU_{dry} = \frac{1}{\frac{1}{A_{a,tot}\,\eta_{f,dry} h_{a,dry}} + R_{cu} + \frac{1}{A_{r,in} h_{r,boiling}}} \tag{35}$$

The total air transfer area, the fin efficiency and the inside heat transfer area depends only on the geometrical characteristics of the evaporator. The air side convective heat transfer coefficient is determined with the correlation proposed by Wang et al. (2000). The refrigerant convective heat transfer coefficient inside the tube is determined with the Shah (1982) correlation.

To calculate the exhaust air temperature and the enthalpy of the refrigerant at the exhaust, the two heat balances apply:

$$\dot{Q}_{ev,dry} = \dot{M}_r \left(h_{r,ex,dry} - h_{r,su,ev}\right) \tag{36}$$

$$\dot{Q}_{ev,dry} = \dot{M}_a \, cp_a \left(T_{a,su} - T_{a,ex,dry}\right) \tag{37}$$

In wet regime, the moist air is replaced by a fictitious ideal gas with a specific heat cp_f given by:

$$cp_f = \frac{h_{a,su} - h_{a,ex}}{T_{wb,su} - T_{wb,ex}} \tag{38}$$

The equations 33, 34, 35, 36 still apply to calculate the heat exchange in wet regime, but with $cp_a = cp_f$ and $T_{a,su} = T_{wb,su}$. Moreover, the air side convective heat transfer coefficient is corrected as followed:

$$h_{a,wet} = h_{a,dry} \frac{cp_f}{cp_a} \tag{39}$$

It should be also noticed that the fin efficiency η_f is lower in wet regime than in dry regime.

To determine the exhaust air humidity ratio, the hypotheses proposed by ASHRAE (2000) are used.

$N_T[-]$	$N_L[-]$	$L[m]$	W[m]	H[m]	δ_f[mm]	P_L[m]	P_T[m]	F_p [m]
10	3	0.065	0.3	0.24	0.115	0.02	0.025	0.0025

Table 2: Geometric characteristics of the evaporator

2.4 Heat pump

The heat pump model associates the sub-models of the rolling piston compressor, the evaporator and the condenser. The information flow diagram is presented in Figure 5.

For given supply conditions and exhaust pressure, the compressor model imposes the refrigerant mass flow rate. The compressor rotational speed is fixed at 3000 rpm. The compressor heat losses are calculated based on the supply airflow and temperature.

For a given water mass flow rate, refrigerant mass flow rate, supply refrigerant temperature and supply water temperature, the condenser model imposes the condensing pressure. The liquid subcooling at the condenser exhaust is imposed at 5K.

The expansion valve model assumes that expansion is isenthalpic, which imposes the vapor enthalpy at the evaporator supply. It also imposes the vapor superheat at evaporator exhaust, fixed at 5K.

For a given supply refrigerant mass flow rate, given supply temperature and air humidity and a given air mass flow, the evaporator imposes the evaporating pressure. The air supply temperature depends on the compressor heat losses and air mass flow.

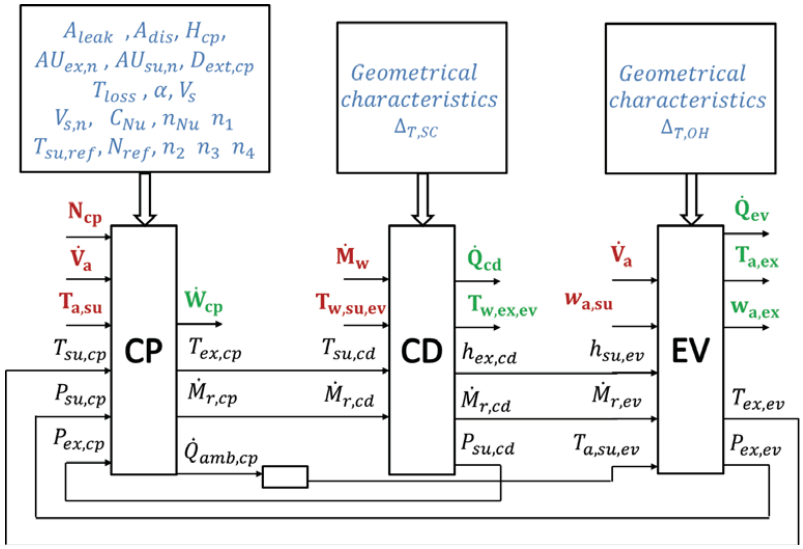

Figure 5: Schematic representation of the heat pump model

3. PARAMETERS IDENTIFICATION

This section describes the methodology used to identify the parameters of the compressor, the condenser and the evaporator. The predicted values with the model are compared with the experimental values obtained in laboratory conditions.

3.1 Methodology

The compressor model has 18 parameters. The three parameters $V_{s,n}$, $T_{su,ref}$ and N_{ref} are reference variables fixed at constant value, respectively 16.12 cm³, 5°C and 3000 rpm. The three parameters H_{cp}, $D_{ext,cp}$ and V_s are geometrical characteristics and do not have to be identified. The remaining parameters are A_{leak}, A_{dis} , $AU_{ex,n}$, $AU_{su,n}$, T_{loss}, α, C_{Nu} and n_{Nu}. These empirical parameters are valid for a fixed compressor swept volume $V_{s,n}$ and are identified with a set of experimental data obtained during laboratory tests. The last four parameters to be identified are the exponents n_1, n_2, n_3 and n_4. These parameters allow to extrapolate the performance for a different compressor swept volume using the same set of parameters.

The fmincon function of MATLAB is used to minimize the error between the measurement (mea index) and the prediction of the model (mod index). The error function is defined as:

$$E = \sqrt{\frac{\sum_{i=1}^{n}\left(\left(\frac{\dot{W}_{mod-}\dot{W}_{mea}}{\dot{W}_{mod}}\right)^2+\left(\frac{\dot{M}_{mod-}\dot{M}_{mea}}{\dot{M}_{mod}}\right)^2+\left(\frac{h_{ex,mod-}h_{ex,mea}}{h_{cex,mod}}\right)^2\right)}{n}} \quad (40)$$

The obtained results are listed in Table 3.

A_{leak} [mm²]	A_{dis} [mm²]	$AU_{ex,n}$ [W/K]	$AU_{su,n}$ [W/K]	T_{loss} [N.m]	α [-]	C_{Nu} [-]	n_{Nu} [-]	n_1 [-]	n_2 [-]	n_3 [-]	n_4 [-]
0.2	113	257	0	0.164	0.41	1.04	0.51	0.43	0	0.57	0.93

Table 3: Parameters of the compressor

The condenser and the evaporator models depend only on geometrical characteristics. Consequently, it is not necessary to identify empirical parameters with experimental data. However, a comparison between experimental and predicted data must be realized to validate the proposed model.

Three heat pumps with different heating capacities were tested over a large range of operating conditions. The condensers and the evaporators of the three machines were the same, for which the geometrical characteristics are given in Table 1 for the condenser and Table 2 for the evaporator. However, the compressor of each heat pump has a different swept volume, equals to 9.52 cm³, 12.75 cm³ and 16.12 cm³. In total, seven tests were performed. During the tests, the heat pumps were connected to a hot water storage tank, allowing the supply water temperature to vary from 15 to 60°C. The Table 4 shows the range of operating conditions for the 7 sets of experimental tests.

Test n°	V_s	$D_{ext,cp}$	H_{cp}	$\dot{M}_w$	$\dot{V}_{air}$	$T_{dp,su}$	$T_{a,su}$	$T_{w,su}$
1 - 1	9.52	0.12	0.22	300	200	9	21	35-55
2 - 1	12.75	0.12	0.23	400	210	10	22	39-57
3 - 1	16.12	0.12	0.24	576	350	10	23	33-57
3 - 2	16.12	0.12	0.24	576	300	10	21	28-55
3 - 3	16.12	0.12	0.24	596	250	10	21	33-57

3 - 4	16.12	0.12	0.24	336	340	9.5	20	21-40
3 - 5	16.12	0.12	0.24	334	350	16-18	22	16-42

Table 4: Range of operating conditions for the 7 sets of experimental tests

In the next sections, the performance predicted by the model are compared with the experimental data, for the compressor, the condenser and the evaporator.

3.2 Compressor

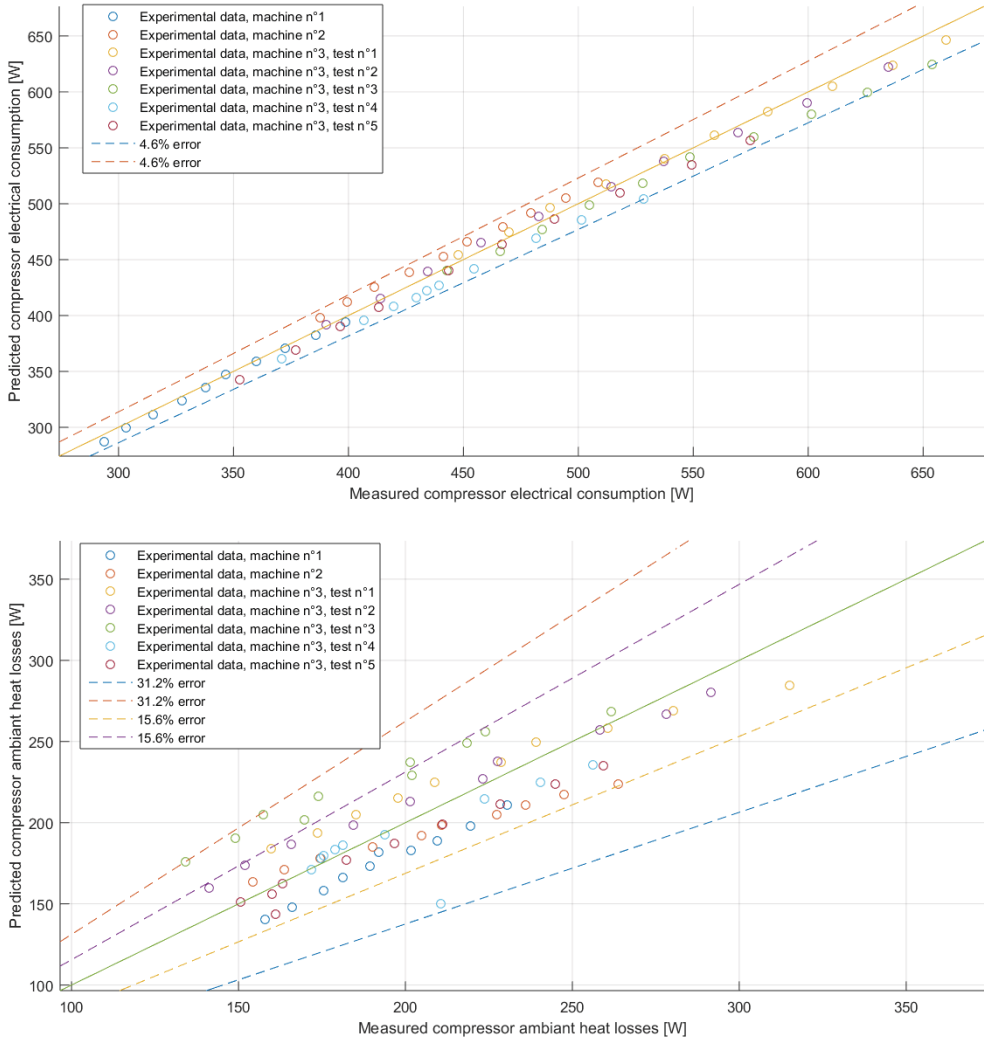

Figure 6: Comparison between simulated and experimental data for the compressor electrical consumption (top) and compressor ambient heat losses (bottom).

This section presents the comparison between simulated and experimental data for the compressor. Figure 6 shows the comparison for the electrical consumption and the ambient heat losses. For the electrical consumption, the maximum error between the prediction and the

experimental data is 5%. The results are very satisfactory considering that three compressors with three different swept volumes are modelled. Concerning the ambient heat losses, the maximum error is 31 % and the error is lower than 15 % for 90 % of the points. These results are considered satisfactory considering the large range of ventilation air values modelled (between 200 and 350 m³/h).

Figure 7 shows the comparison for the mass flow rate and the exhaust temperature. The maximum error is equal to 5 K. The mas flow rate is predicted with a lower accuracy. Indeed, the maximum error on the mass flow rate is equal to 20%.

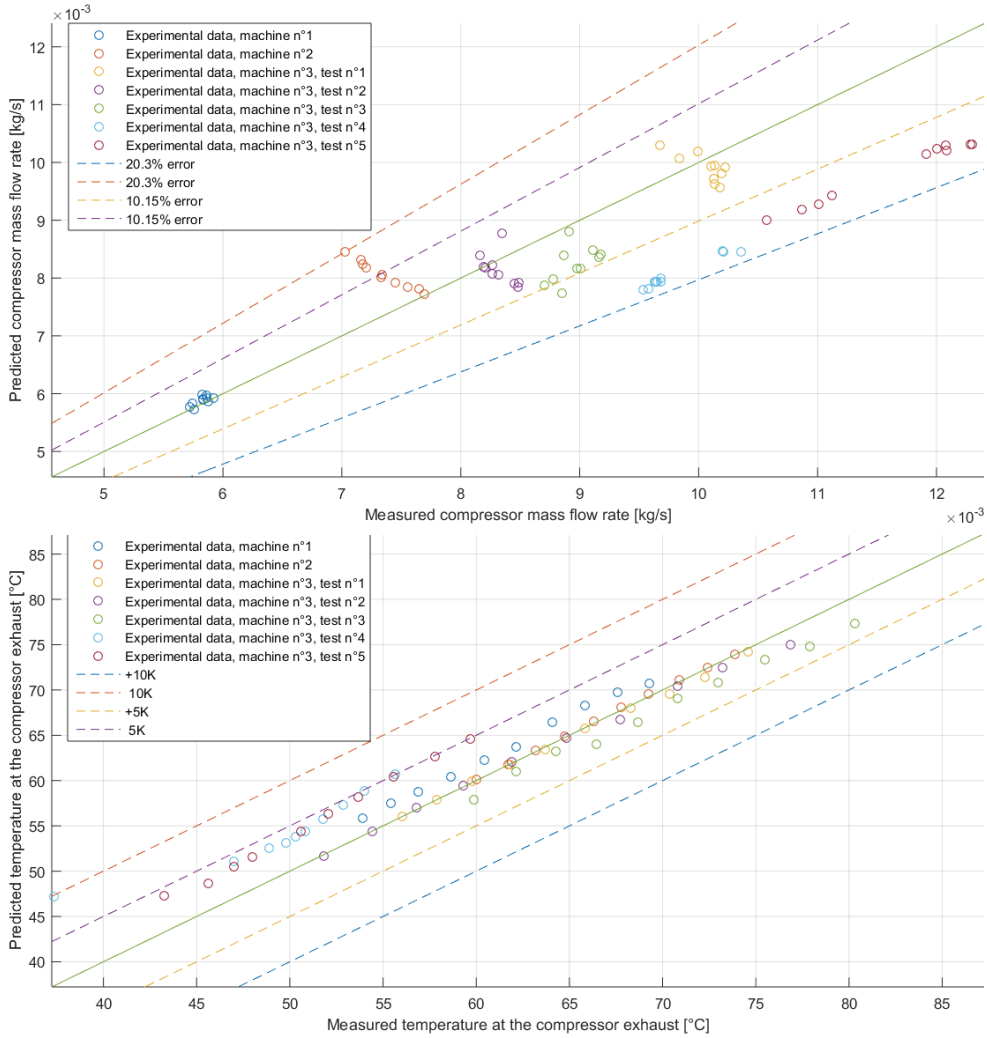

Figure 7: Comparison between simulated and experimental data for the compressor mass flow rate (top) and compressor exhaust temperature (bottom).

3.3 Condenser

This section presents the comparison between simulated and experimental data for the condenser. Figure 8 shows the comparison for the condensing pressure and the heat flow. The

heat flow is very well predicted with a maximum relative error of 4%. The prediction of the model is less accurate for the condensing pressure. In fact, the maximum error on the condensing pressure is 8%. It seems that the model overestimates the condensing pressure, meaning that the overall heat transfer coefficient is under-estimate.

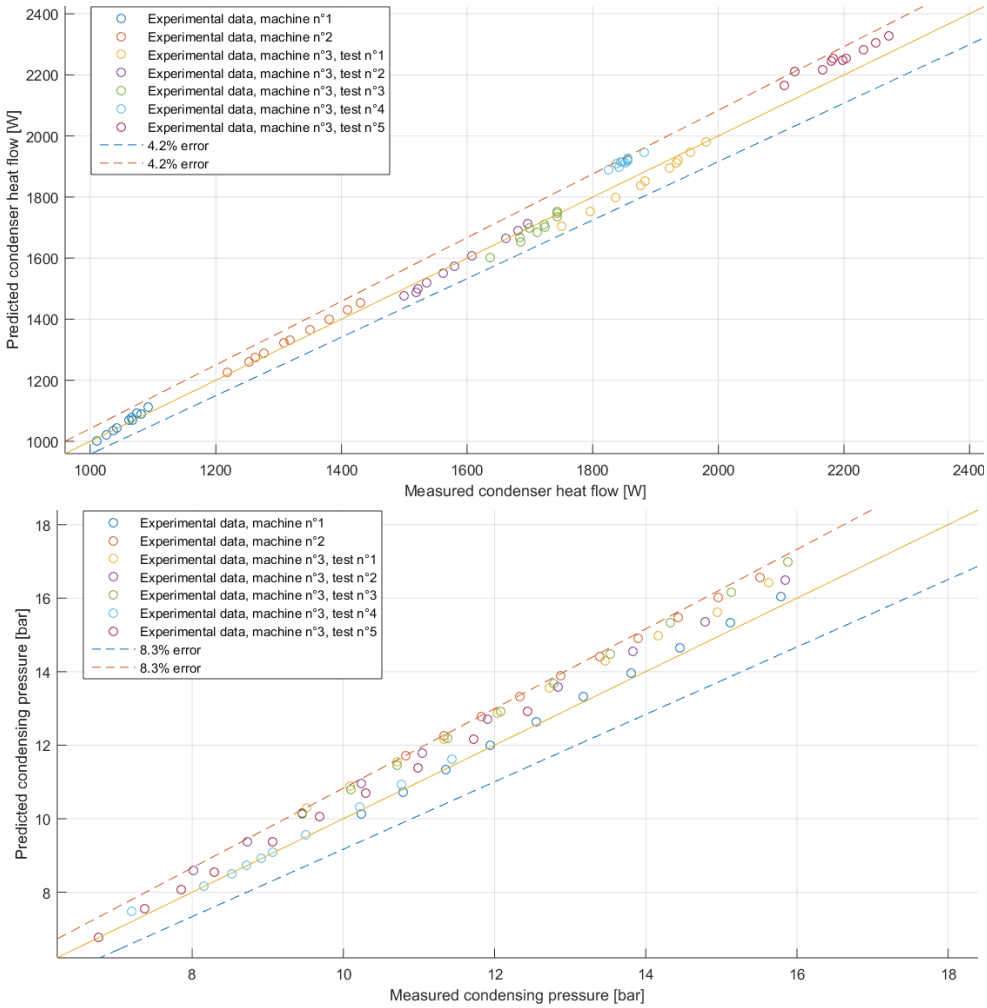

Figure 8: Comparison between simulated and experimental data for the condenser heat flow (top) and the condensing pressure (bottom).

3.4 Evaporator

This section presents the comparison between simulated and experimental data for the evaporator. The results are presented for the tests n°3-4 and n°3-5 because the temperature and the humidity at the exhaust were monitored for these cases only. Figure 9 shows the comparison for the evaporating pressure and the heat flow. The evaporating pressure is predicted with a good accuracy. The maximum relative error is 7%, and 90 % of the points are predicted with an error lower than 5%. The prediction of the heat flow is even better than the prediction of the evaporating pressure. Indeed, the maximum relative error is lower than 2%. Figure 10 shows the prediction of the humidity ratio and the dry bulb temperature at the

exhaust of the evaporator. Concerning the humidity ratio, the maximum relative error is 15 % and the dry bulb temperature is predicted with an error of 4K.

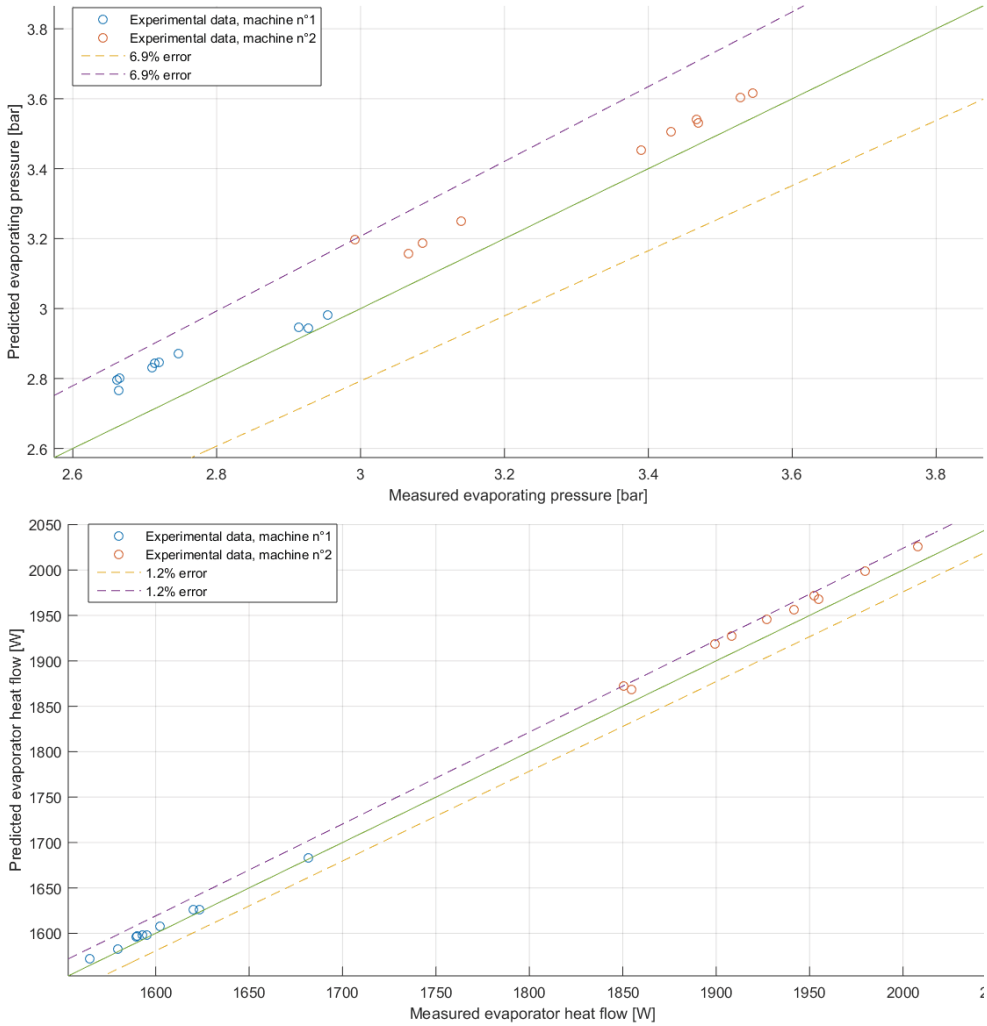

Figure 9: Comparison between simulated and experimental data for the evaporating pressure (top) and the evaporator heat flow (bottom).

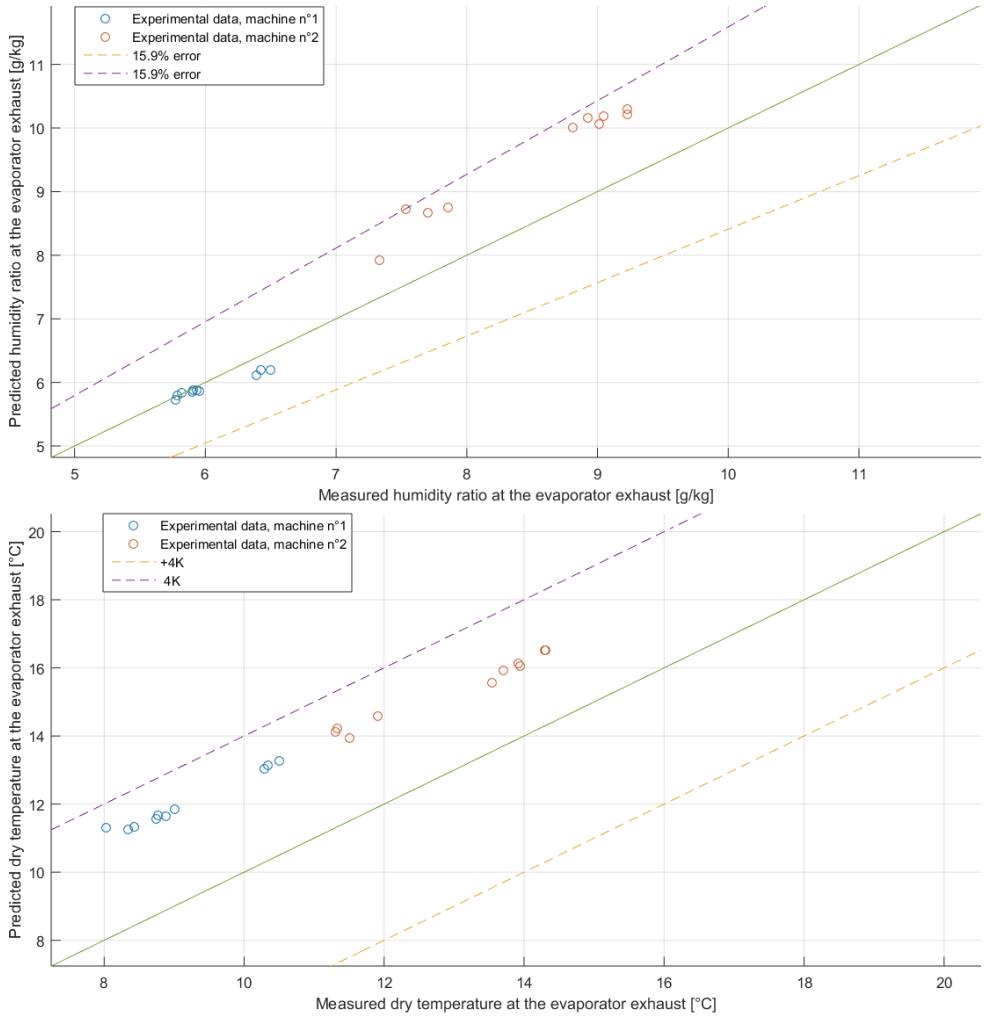

Figure 10: Comparison between simulated and experimental data for the exhaust humidity ratio (top) and the evaporator heat flow (bottom).

4. VALIDATION OF THE HEAT PUMP MODEL

This section presents the validation of the heat pump model and the errors between the predictions and the measurements when all the sub-models are connected. Figure 11 presents the comparison between simulated and experimental data for the compressor electrical consumption, the condenser heat flow and the COP. The maximum relative error for the compressor electrical consumption is 13%. The consumption seems to be over-estimate for the major part of the point. This is due to the over-estimated value of the condensing pressure. The maximum relative error for the condenser heat flow is 28 %. The predictions relative to the tests n° 1-1, 3-1, 3-3, 3-4 and 3-5 are well predicted, with a relative error lower than 10 %. The data sets n° 2 and 3-2 seems to be problematic and additional research will be undertaken to decrease these errors. The COP is predicted with a relative error of 16%.

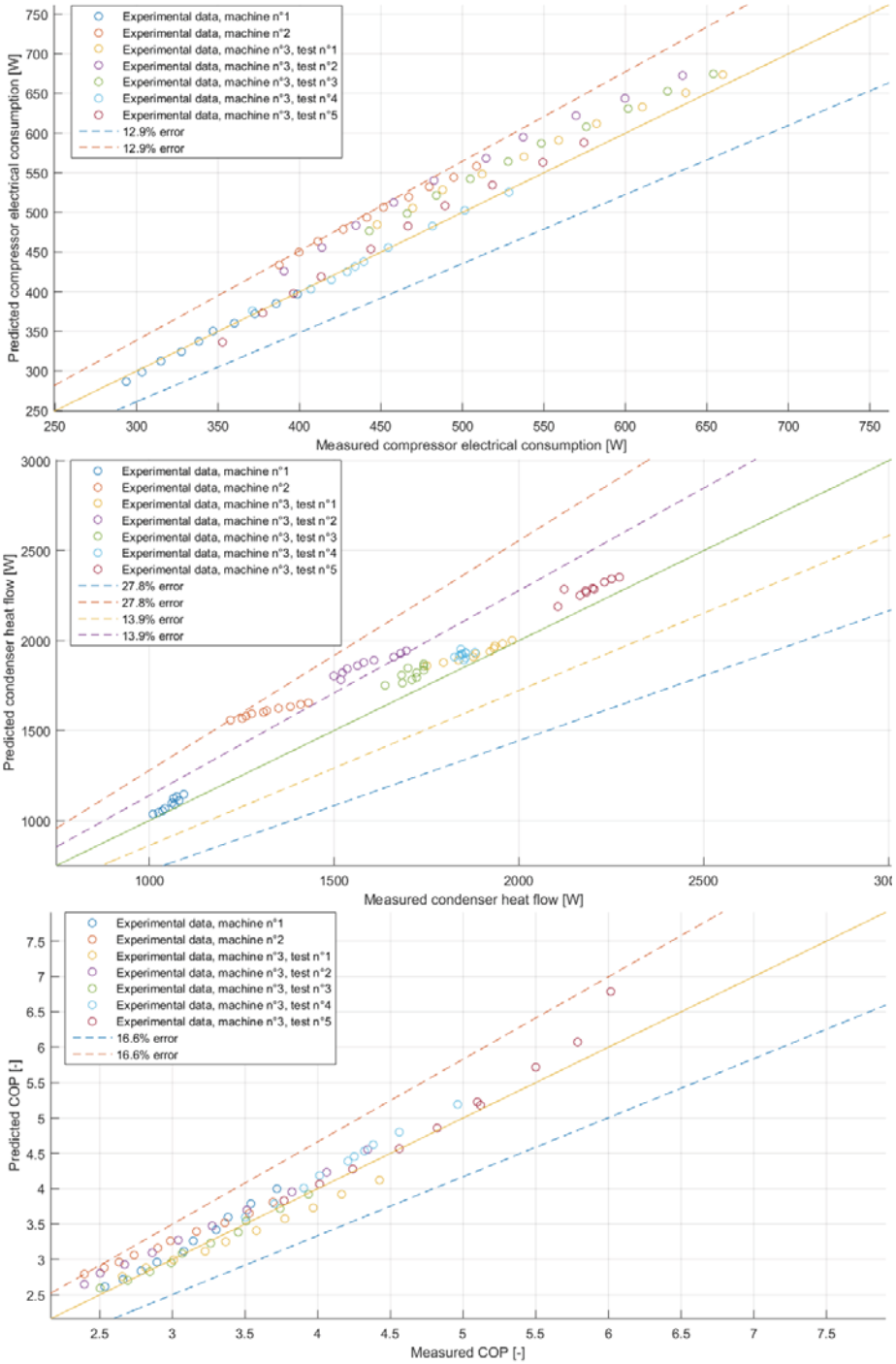

Figure 11: Comparison between simulated and experimental data for the compressor electrical consumption (top), the condenser heat flow (mid) and the COP (bottom).

5. DISCUSSION AND RESULTS

As explained in the introduction, the major drawback of the exhaust air heat pump technology is the limited heating capacity. It can be a problem in freestanding buildings in which a backup resistance is necessary. The objective of this section is to show the heating capacity that could be delivered by an exhaust air heat pump with a bigger compressor (higher compressor swept volume). Ideally, the machine should provide at least 3000 W of heating capacity. The following variables are fixed:

- Volume air flow: 200 m^3/h, corresponding to a typical ventilation airflow in freestanding residential buildings,
- Supply air temperature: 20°C,
- Supply dew-point temperature: 10°C,
- Water mass flow rate: 600 l/h.

Figure 12 shows the variation of the heating capacity of the heat pump with the compressor swept volume. The contact temperature is also represented. With a swept volume of 27 cm^3, the heating capacity could reach the value of 2600 W. However, the contact temperature on the evaporator falls below 0°C when the swept volume exceeds 18 cm^3. It is problem because frost can appear on the evaporator for a contact temperature lower than 0°C, and this phenomenon decreases the heating capacity and the COP of the machine. Moreover, defrosting strategies must be developed to ensure an optimal functioning of the machine. In conclusion, it is impossible to reach 3000 W of heating capacity with the actual evaporator geometry. Other geometries will be studied to reach the 3000 limit of heating capacity.

6. CONCLUSION

The objective of this paper was to develop a semi-empirical model of an exhaust air heat pump. This model can predict the performance of the heat pump if the geometries of the constituting elements are changed. The results show a relative error on the electrical consumption of 13%, a maximum relative error on the condenser heat flow of 28 % and a relative error on the COP of 17%. The prediction of the condenser heat flow still has to be improved.

The results showed that the actual evaporator geometry limits the heating capacity of the machine and it is difficult to reach 3000 W of heating capacity, even with a compressor swept volume of 27 cm^3. Other evaporators will be simulated to find the optimum geometry to reach the desired heating capacity, if possible.

Future research will deal with the new design of the machine and the test in laboratory. If necessary, different defrosting control strategies will be proposed and implemented.

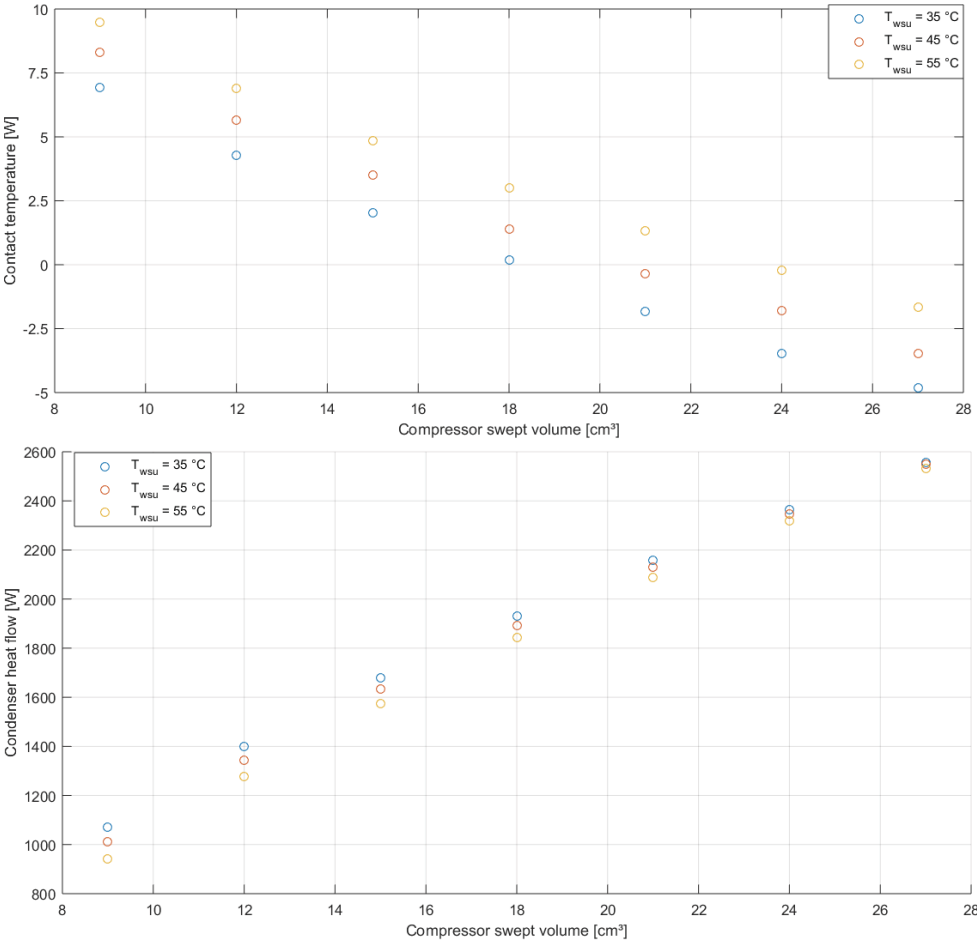

Figure 12: Influence of the compressor swept volume on the heat pump heating capacity

REFERENCES

Incropera, F.P., and DeWitt, D.P., 2002. *Fundamentals of Heat and Mass Transfer*. 5th ed. John Wiley & Sons, Hoboken, NJ.

Laverge, J., Janssens, A., 2012. *Heat recovery ventilation operation traded off against natural and simple exhaust ventilation in Europe by primary energy factor, carbon dioxide emission, household consumer price and exergy.* Energy and Buildings 50, pp 315–323.

Gendebien S., Georges E., Prieels L., Lemort V. 2013. *Experimental performance characterization of a new single room ventilation device with heat recovery.* Proceedings of the 34th AIVC conference.

Guyotab G., Shermanc M., Walkerc I. 2017. *Smart ventilation energy and indoor air quality performance in residential buildings: A review.* Energy and Buildings 165, pp 416-430.

Dechesne B., Gendebien S., Lemort V., Bertagnolio S. 2017. *Experimental investigation and dynamic modeling of an air-to-water residential heat pump with vapor injection and variable speed scroll compressor.* Proceedings of the 12th IEA Heat Pump Conference.

Nawaz K., Ahmed B., Elatar A., Baxter V., Abdelaziz O. 2017. *Performance optimization of CO2 heat pump water heater*. International Journal of Refrigeration, 85, pp 213-228.

Zhang J., Qin Y., Wang C. 2015. *Review on CO2 heat pump water heater for residential use in Japan.* Renewable and Sustainable Energy Reviews, 50, pp 1383-1391.

Underwood C.P. 2015. *Fuzzy multivariable control of domestic heat pumps.* Applied Thermal Engineering, 90, pp 957-969.

Fracastoro.V, Serraino.M. 2010. *Energy analyses of buildings equipped with exhaust air heat pumps (EAHP).* Energy and Buildings, 42 (8), pp 1283–1289.

Ransy F., Gendebien S., Lemort V. 2015. *Performances of a simple exhaust mechanical ventilation coupled to a mini heat pump: modeling and experimental investigations*. Proceedings of the 36th AIVC international conference.

Ransy F., Gendebien S., Lemort V. 2016. *Description of a Modelica-based thermal building model integrating multi-zone airflows calculation*. Proceedings of the 12th REHVA world congress CLIMA.

Ransy F., Sartor K., Gendebien S., Lemort V. 2018. *Performance analysis of a mini exhaust air heat pump integrated into a low energy detached house: experimental on-site performance.* Proceedings of the 5th International High Performance Building Conference.

Dardenne L., Fraccarib E., Maggioni A ., Molinaroli L., Proserpioc L., Winandy E. 2015. *Semi-empirical modelling of a variable speed scroll compressor with vapour injection.* International Journal of Refrigeration, 54, pp 76-87.

Giuffrida A. 2016. *A semi-empirical method for assessing the performance of an open-drive screw refrigeration compressor.* Applied Thermal Engineering, 93, pp 813-823.

Li W. 2013. *Simplified steady-state modeling for variable speed compressor.* Applied Thermal Engineering, 50, pp 318-326.

Winandy E., Saavedra C., Lebrun J. 2002. *Simplified modelling of an open-type reciprocating compressor.* International Journal of Thermal Sciences, 41, pp 183-192.

Lemort V., Quoilin S., Cuevas C., Lebrun J. 2009. *Testing and modeling a scroll expander integrated into an Organic Rankine Cycle.* Applied Thermal Engineering, 29, pp 3094-3102.

Martin H. 1996. *A theoretical approach to predict the performance of chevron-type plate heat exchangers.* Chemical Engineering and Processing, 35, pp 301-310.

Han, D., Lee, K., Kim, Y., 2003. *The characteristics of condensation in brazed plate heat exchangers with different chevron angles*. J. Korean Phys. Soc. 43 (1), 66–73.

Longo G., Righetti G., Zilio C. 2015. *A new computational procedure for refrigerant condensation inside herringbone-type Brazed Plate Heat Exchangers.* International Journal of Heat and Mass Transfer, 82, pp 530–536.

ASHRAE, 2000. *ASHRAE Handbook-HVAC Systems and Equipment*, Chapter 21. Atlanta: American Society of Heating, Refrigerating and Air-Conditioning Engineers, Inc.

Wang C., Chi K., Chang C. 2000. *Heat transfer and friction characteristics of plain fin-and-tube heat exchangers, part II: Correlation*. International Journal of Heat and Mass Transfer, 43, Issue 15, pp 2693-2700.

M.M. Shah. 1982. *Chart correlation for saturated boiling heat transfer: equations and further study*. ASHRAE Trans., Vol. 88, 185-196.

Questions and Answers:

Lieve Helsen:

Does it mean that your boundaries in the model are moving?

Frédéric Ransy:

Yes the condenser model is a moving boundary model.

***

Lieve Helsen:

Why don't you consider an additional heat pump to the system instead of increasing the heating capacity?

Frédéric Ransy:

Because the cost of the overall system would increase. To answer this question, a complete analysis will be conducted considering the different cost in the system and the combination with a complete building energy simulation software.

***

Jean Lebrun:

What about the actual subcooling in the condenser?

Frédéric Ransy:

The subcooling in the model is imposed. This approach is considered to be sufficient for the moment for design purpose. A complete void fraction model is necessary to determine the actual subcooling and this type of model is not considered for the moment.

***

Jean Lebrun:

What about the modelling of the expansion valve?

Frédéric Ransy:

The overheating at the exhaust of the evaporator is supposed to constant.

***

Jean Lebrun:

What about the effect of oil?

Frédéric Ransy:

For the moment the effect of oil on the properties of the refrigerant is not considered in the model.

Multi-criteria Air Source Heat Pump Water Heater optimization combining optimized thermodynamic performance and control

Kevin Ruben Deutz[a,b], Odile Cauret[b], Romuald Rullière[a], Philippe Haberschill[a]

[a]*Université de Lyon, CNRS, INSA-Lyon, CETHIL, UMR5008, Villeurbanne*
[b]*EDF R&D, Energy in Buildings and Territories Department, Moret-Sur-Loing*

ABSTRACT

Air Source Heat Pump Water Heaters (ASHPWH) are more efficient domestic hot water (DHW) systems compared to traditional electric water heaters. However, although these ASHPWH have reached an important level of maturity on the market, it seems that there is still room for improvement of their energy performance. Also for ASHPWH to increase their market penetration, other criteria such as end-user comfort level and economical payback should not be disregarded in an optimization process. Consequently, the main objective of the actual study is to search for optimization pathways leading to a multi-criteria optimized ASHPWH. This is done using a state of the art ASHPWH extensively validated Modelica model combined with a multi-criteria thermodynamic optimization algorithm and a model-based control. To validate the optimization process, an example of an ASHPWH resulting from this optimization process is simulated upon a large variety of real annual user draw-off profiles. This new ASHPWH design achieves a 37 % average annual energy saving and a 30 % reduction of the electrical bill while ensuring a same level of comfort for the end-users.

Keywords: Domestic Hot Water, Modeling and simulation, Optimization

1. INTRODUCTION

Domestic Hot Water (DHW) is representing an increasingly important share in the consumption of residential buildings. In France, it represents up to 10 % of the total final energy use of a building (ADEME, 2014). This share is expected to grow in the near future, especially considering decreasing thermal needs with respect to higher building performance. As such it is of great importance to develop new technologies and improve existing DHW production efficiencies.

Air Source Heat Pump Water Heaters (ASHPWH) are efficient DHW production systems. In Europe and particularly in France, they have reached a good level of maturity and market penetration with yearly increasing sales (EHPA, 2015). However according to the literature, there is still room for improvement both on the thermodynamic cycle performance and the heat pump water heater control (Willem, Lin, & Lekov, 2017).

In this paper, an optimization study conducted in several steps is presented. First, a validated thermodynamic model of an ASHPWH is used to perform design based optimization. Then, a simplified model is developed coupled with a model based controller. Using these tools, two optimization cases are studied for a wide range of real draw-off profiles. The first case considers a model based controller and a reference ASHPWH and the second one combines both the controller and an optimized ASHPWH.

2. MODEL DESCRIPTION

The model used in this study is a dynamic grey box modelica based model, developed with Dymola®, that was further presented in a previous paper (Deutz, Charles, Cauret, Rullière, & Haberschill, 2018). This model gathers a heat pump model developed thanks to the TIL® thermal component library and a storage tank model including a zonal model.

The reference model concerns a R134a ASHPWH with a mantle tank condenser (MHX) and a variable speed compressor with the specifications given in table 1. This model was validated experimentally and achieves an average error of 2 % on the Coefficient Of Performance (COP) on a dataset varying both air, tank temperatures and compressor speed.

Table 1: Reference ASHPWH design

Heat Pump Specifications ($T_t = 55\ °C, T_{air} = 7\ °C$)	
Total power (W)	2800
Heat Pump Maximum electric power (W)	1000
Electric auxiliary heater power (W)	1800
Type of compressor/ displacement volume (cm^3)	Rotary/13
Refrigerant type/mass (kg)	R134a / 1.1
Tank specifications	
Volume (l)	200
Dimensions H_t, D_t (m)	1.37, 0.53
Lower height of the MHX (m)	0.13
Upper height of the MHX (m)	0.73
Width of the wall (m)	0.0035
Width of the tank insulation wall – extremities (m)	0.039-0.025
Width of the tank insulation over the MHX (m)	0.028
Evaporator	
Length (m)	0.75
Internal tube diameter (m)	5.7×10^{-3}
Number of Rows	1
Number of hydraulics circuits	3
Number of tubes per circuit	8
Distance between tubes (m)	2.3×10^{-2}
Depth of fins (m)	1.5×10^{-2}
Fin thickness (m)	0.2×10^{-3}
Fin pitch (m)	2.0×10^{-3}
Condenser	
Type	« D » shaped
Number of coils	52
Inner diameter (m)	8.5×10^{-3}
Tube length (m)	73

This paper takes the advantage of two modeling approaches using a detailed model for thermodynamic optimization and a black box polynomial regression of the detailed model for annual simulations and control. The two variables of interest in the black box model are the heat power electric power and the heat pump condenser power that are obtained through least squared fitting with the detailed model as:

$$\dot{W}_{elec,ref} = a_0 + a_1 n + a_2 n^2 + a_3 T_t + a_4 {T_{water}}^2 + a_5 T_{air} + a_6 {T_{air}}^2 + a_7 T_{air} T_{water} + a_8 T_{air} n + a_9 T_{water} n \quad (1)$$

$$\dot{Q}_{cond,ref} = b_0 + b_1 n + b_2 n^2 + b_3 T_{water} + b_4 {T_{water}}^2 + b_5 T_{air} + b_6 {T_{air}}^2 + b_7 T_{air} T_{water} + b_8 T_{air} n + b_9 T_{water} n \quad (2)$$

3. SYSTEM OPTIMIZATION

3.1 Thermodynamic cycle

4.1.1. Model adaptation

ASHPWH manufacturers face multiple constraints such as: guaranteed user comfort, maximum energy performance, manufacturing costs, refrigerant choice and quantity, succeed normative tests. The importance set on each of the constraints has a particular impact on the product design ending up in a variety of possible ASHPWH designs. A way of solving the constraints can be done by weighing the importance of each in a multi criteria model based design approach and an iterative sequential tool chain such as presented in figure 1 considering that there is enough input data.

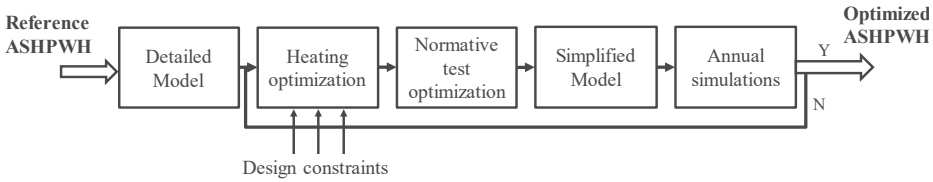

Figure 1. ASHPWH optimization tool chain

As shown in figure 1, the optimization process starts with a reference product described in table 1. However, it was shown by several authors that mini-tube condensers are good candidates to allow for refrigerant charge reduction (Ghoubali, Byrne, & Bazantay, 2017; Ibrahim, Fardoun, Younes, & Louahlia-Gualous, 2014; Peng, Li, & Zhang, 2016). Consequently, the reference model condenser presented in Deutz et al. (2017) is changed to a mini tube condenser for which the design is taken from Peng et al. (2016) (Figure 2). All the governing assumptions for this model are stated in Deutz et al. (2017).

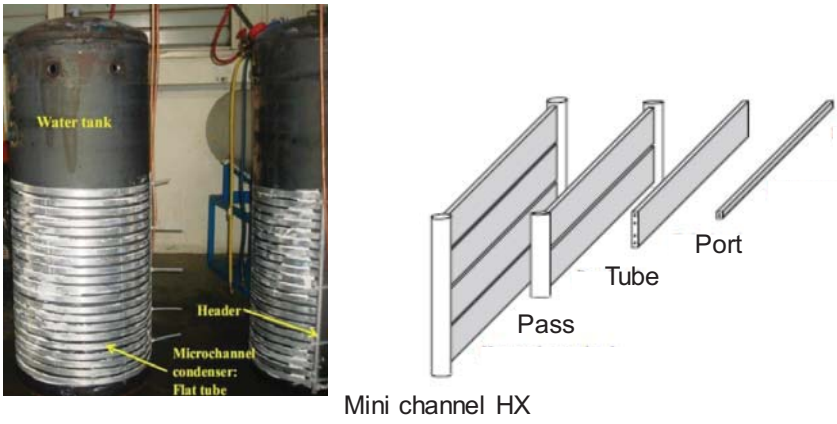

Figure 2. Mini channel condenser layout. Source: (Peng, Li, & Zhang, 2016)

For verification, in figure 3, the model is compared to Peng's experimental data and a good agreement is found for refrigerant operating pressures and electric compressor power (figure 3-left). In the same figure (figure 3- right), refrigerant charge is varied and presents similar optimal refrigerant charge of 0,95 kg which is close to the 0,96 kg found by Peng et al. (2016).

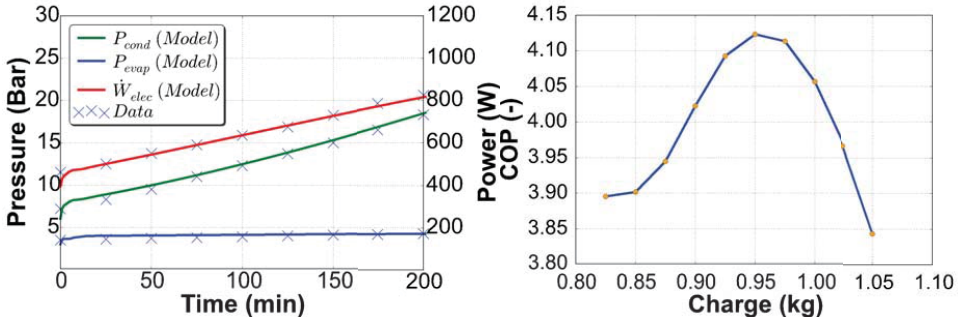

Figure 3. Mini channel model validation and optimal refrigerant charge for a 1.2 mm port diameter. Air temperature of 20 °C dry bulb and water temperatures from 15 to 55 °C. Source: (Peng et al., 2016)

4.1.2. Optimization results for R134a, R1234yf and R290

For the present paper, we focus on an illustration of the heating optimization from 10 °C to 55 °C at a 7 °C external air temperature. The thermodynamic cycle optimization problem is formulated in the 2.2.2. Modelica based Optimization library (Pfeiffer, 2012) using the following optimization criteria: minimize electric consumption, minimize refrigerant quantity and minimize heating time. An extra constraint is also set on the condenser height which should be sized according to the daily load pattern (Anderson & Morrison, 2007). This ensures higher heating energy performance because of the lower water temperature in front of the condenser at restart. Generally, ASHPWH are hysteresis controlled with a high hysteresis margin taken to ensure user comfort which results in the condenser situated in the lower parts of the tank. In the case of optimal control solution where the tank reheat is done at a lower thermal charge, the condenser size can be increased. Here the maximal height of the condenser is set to 1 m corresponding to about 75 % of the tank covered by the condenser.

Simulations are ended once they have reached the same stored energy as the baseline. The model used being zonal, the stored energy is calculated by integration over all elementary zone mass dm. And COP is calculated as:

$$COP = \frac{stored\ energy}{total\ electric\ energy} = \frac{\int c_p[T_t - (10 + 273.15)]dm}{\int(\dot{W}_{elec,comp} + \dot{W}_{elec,fan})dt} \quad (3)$$

The tuner parameters chosen are the following: condenser port diameter, number of total coils, number of parallel coils, number of rows at the evaporator and number of tubes per circuit, fin depths and pitch and refrigerant charge. The optimization is first performed for R134a which is the reference refrigerant and then repeated for R1234yf and propane which are potential candidates for substitution (Ghoubali et al., 2017; Nawaz, Shen, Elatar, Baxter, & Abdelaziz, 2017).

Propane compression is thermodynamically different to the two others, as such an extra compressor map is added for an 8.9 cm^3 compressor based on manufacturer data. Another exception for propane is its flammable nature, resulting in norm EN378:1 recommending a 150 g charge for safety reasons in domestic applications. Consequently propane ASHPWH optimization was repeated with an additional charge constraint of 150 g. It was soon noticed that such a charge constraint with the actual heat transfer surface lead to solutions with zero subcooling at the condenser. As such for propane, to reduce the refrigerant volume stored in non-active parts, the header diameter of the mini channel was also set as a design parameter that could be adapted for which values found in the literature range from 9.7 mm (Ghoubali et al., 2017) to 2.5 cm (Peng et al., 2016).

Consequently this results in a total of four design optimization examples, one for R134a, on for R1234yf and two for propane.

The optimization problem was solved heuristically using the optimization library's genetic algorithm that provides a close to optimal solution. Examples of optimal solutions fitting our criteria for every refrigerant are presented in table 2.

Table 2. ASHPWH criteria and parameter results

	R134a (reference)	**R134a optim.**	**R1234yf optim.**	**Propane optim.**	**Propane optim.**
Energy Performance					
COP	3.26	3.76	3.63	3.57	3.54
Mean global compressor efficiency (%)	67	66	66	55	55
Minimization Criteria					
Total electric consumption (kWh)	3.10	2.70	2.79	2.84	2.87
Refrigerant Charge (kg)	1.4	1.15	1	0.4	0.15
Heating time (s)	24960	24145	25389	26815	27240
Parameters					
Compressor size	13 cm^3	13 cm^3	13 cm^3	8.9 cm^3	8.9 cm^3
Total cond. heat exchange area (m^2)	0.85	1.38	1.38	1.38	1.39
Port diameter (mm)	8.5	2.15	2.15	2.15	1.15
Number of tubes or ports	52	120	120	120	138
Number of ports per pass	-	12	12	12	23
Condenser height(m)	0.6	1	1	1	1
Header diameter (cm)	-	2.5	2.5	2.5	1.5
Evaporator tubes	24	18	18	18	18
Number of rows	1	3	3	3	3
Fin pitch (mm)	2	1.2	1.2	1.2	1.2
Fin depth (cm)	1.5	1.8	1.8	1.8	1.8

In figure 4, the optimal cases are compared to the baseline R134a refrigerant. It can be seen that with the given investigated parameters, a 15 % COP increase can be achieved for R134a. This increase is mainly due to a better evaporator design allowing to reduce electric fan power by 60 % and to decrease compressor power by 5 % (Figure 4). This energy performance improvement is realized whilst minimizing refrigerant charge by 18 % thanks to the mini channel condenser design presented in table 2. For R1234yf, it is possible to achieve a 11 % increase in performance whilst decreasing refrigerant quantity by 29 %. This can be related to the lower specific latent heat of vaporization of R1234yf, inducing higher mass flow rates and electric consumption for an equivalent condenser thermal capacity.

For propane it can be seen that without a charge limit, a slightly lower COP can be reached with the optimization. This is due to the lower efficiency of the propane compressor used (Table 2). With the additional 150 g charge limit, COP is slightly reduced compared to the case without charge limit. This is due to lower heat transfer performance and increased pressure drop with the smaller hydraulic diameters obtained.

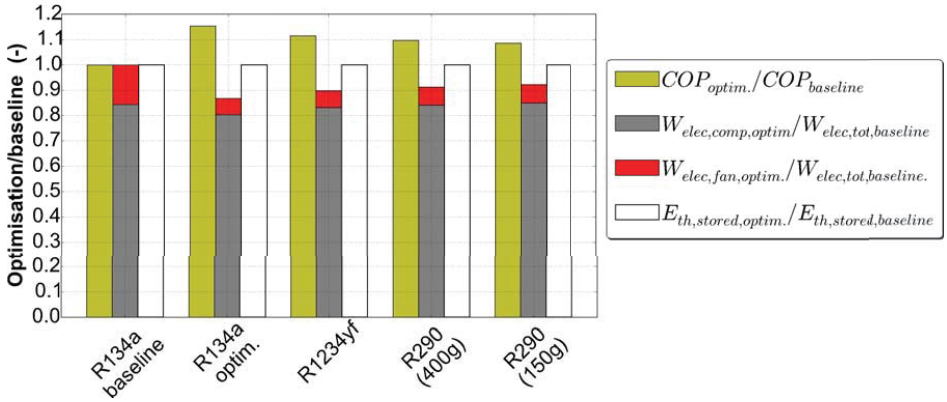

Figure 4. Optimization cases compared to baseline for R134a, R1234yf and R290

3.2 Control optimization algorithm

In this section we analyze the possible benefits of model based ASHPWH control coupled with DHW consumption prediction. It was shown by Ibrahim et al. (2014), that fractioning ASHPWH operation periods on a 10 minute to 60 minute interval could lead to more than 41 % energy saving. This is mainly due to the lower tank temperatures resulting in lower heat losses and a higher thermodynamic performance. However, the limit in achieving this potential is the exact knowledge of the DHW profiles and draw off events timing. This prediction is quite complicated for individual residential applications for which there is a pronounced randomness in intraday draw events (Fuentes, Arce, & Salom, 2018). As such in this section, we propose a model based control strategy that is in reasonable technical reach for residential ASHPWH application based on DHW prediction.

4.2.1 DHW prediction

Daily DHW consumptions based on past consumption has been extensively studied in the literature (Jin, Maguire, Christensen, & Renewable, 2014; Lomet, Suard, & Chèze, 2015). Hourly predictions have been tested by Gelažanskas and Gamage (2015) and it was shown that mathematical methods combining exponential smoothing or statistical methods such as ARIMA (Auto Regressive Integrated Moving Average) with seasonal decomposition showed the most accurate result. However although possibly more accurate, exact timing of draw events is still of concern. As such, as most generally the majority of the consumption happens during the morning or in the evening (Fuentes et al., 2018), the forecast is spitted on two prediction periods: the night/morning period from 10 P.M. to 12 A.M. and the afternoon/evening period from 12 A.M. to 10 P.M.

Although more advanced techniques exist, for simplicity, a sliding moving mean average was chosen with a 14 day historical consumption. To take into account the possible error in the prediction due to the intraday variability and the tank heat losses, the hot prediction is increased by 30 % for both periods.

4.2.2. The model based control set up

The ASPWH control is based upon three main bricks: a model based estimation of the heat pump capacity, a PID tuner and a hysteresis control. The hysteresis controller is given two authorized operating periods of a maximum 6 hour duration in which the energy set point is given by the DHW forecast for the two periods (Figure 5). The measured energy in the tank is based on 10 temperature sensors placed at an equidistant level in the tank and the tank is controlled with an 85 % of the set point energy hysteresis. The two operating periods were set to 10 P.M. to 4 A.M. and the second from 12 A.M to 6 P.M.. This allows to take profit of maximum temperature on the overday period and take

advantage of the minimum electricity tariff during the night whilst lowering the tank operating temperature.

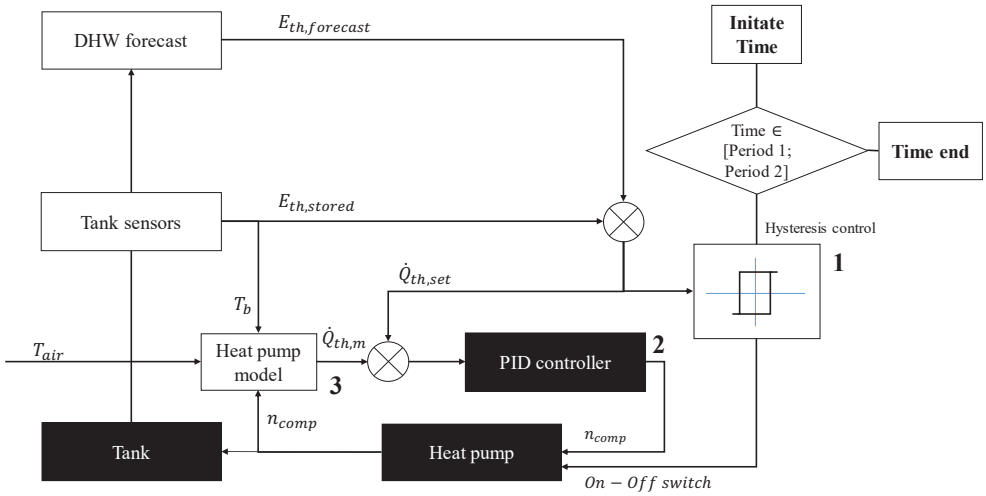

Figure 5. Control structure combining ASHPWH hysteresis (1), and model based (3) - PID control (2)

As the heat pump thermal power varies according to external air and water temperatures, this might lead to situations where if the ASHPWH's thermal capacity is not sufficient it might not achieve the desired set point in the given time period. As such an inverter compressor is used to vary compressor speed and a 50 % smaller capacity heat pump (Table 1) is used for it to achieve the given energy set point within the 6 hour period duration. This could also be achieved by oversizing the heat pump capacity for the extreme cases e.g. very low tank charge and minimum external operating temperatures. It is believed that for such cases an inverter compressor of smaller size can be more flexible.

One of the constraints using the control scheme presented in figure 5 is the condenser power measure, $\dot{Q}_{th,m}$. For now this is predicted by a simple heat pump characteristic represented by the polynomial model such as shown in equation (2). As previously discussed, the inverter controller allows to undersize the thermal capacity. Hence equation (1) and (2) are extrapolated to 50 % of their nominal capacity.

In figure 6, an illustration of the model based controller operation presented in figure 5 is given after a 14 day standard control learning period. For the comparison, a fixed 7 °C external air temperature is taken and a daily repetitive standard draw off test is performed. The profile used corresponds to 1.5 times scenario M of standard EN NF 16147 (about 9 kWh/day) at a 10 °C tank inlet temperature which is representative of a typical 4 person French family (Comité Scientifique et Technique des Industries Climatiques (COSTIC), 2016).

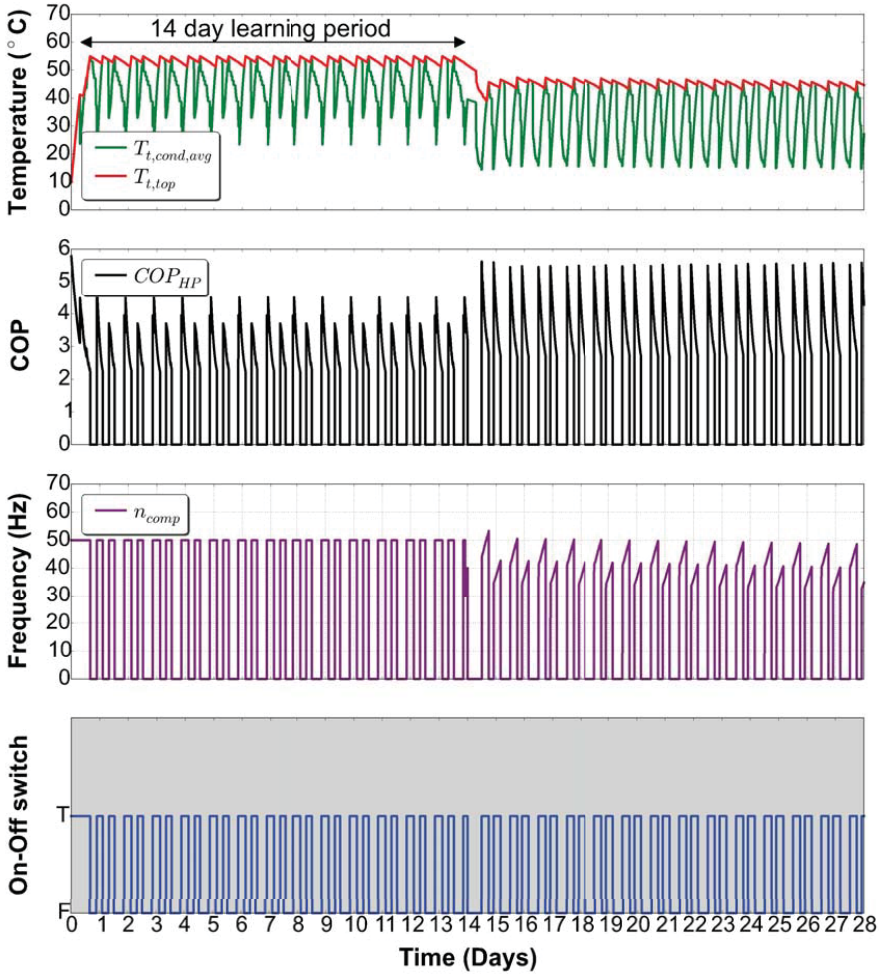

*Figure 6. 14 day Heat pump model based control illustration after a 14 day learning period on standard control. 7 °C external air and standard fixed draw off scenario 1.5*scenario M (NF EN 16147).*

From figure 6, it can be noticed, that after the 14 day learning period, the stored energy in the tank is adapted with a reduced tank temperature on two periods of 5 and 4 kWh each with some remaining energy at restart corresponding to the 30 % surplus instored. This model based control allows to start the heat pump at a lower average temperature in front of the condenser allowing for a 22 % increase in average COP from 3.17 to 3.87. The lower average tank temperature also allows reducing average tank heat losses by 38 % from 51 W to 32 W. Both heat pump COP and lower heat losses finally allow increasing ASHPWH COP by 31 % from 2.53 to 3.33.

4. RESULTS DURING ANNUAL SIMULATIONS

Following the methodology presented in figure 1, in this section, the combination of the thermodynamic optimization combined with the model based controller is assessed on a yearly basis, to assess three end-user criteria which are: comfort, cost and performance against real varying draw off profiles. To compare the benefits of each optimization, three cases are modeled based on equation (1) and (2) and the model based control previously developed:

- The reference R134a model using a standard thermostat on a measured temperature at 30 % of the height in the tank and a 10 °C hysteresis.
- Optimization 1: The reference R134a model with optimized control
- Optimization 2: The optimized thermodynamic R134a cycle with model based control

As presented in figure 1, the reference and the optimized thermodynamic cycle are simplified according to equation (1) & (2) and coefficients are presented in table 3. Both cycles are coupled with a simple 1D tank model such as in Drück (2006). The heat pump power given by equation 2 is supposed uniformly distributed under the thermocline level and the tank temperature in (2) is taken as the average temperature in front of the condenser.

Table 3. Heat pump model coefficients

Reference model coefficients		**Optimized model coefficients**	
$a_{i,ref}$	$b_{i,ref}$	$a_{i,optim}$	$b_{i,optim}$
3.83e+04	-1.93e+04	2,28e+04	-6,39e+03
-4.34e+01	-9.62e+01	-3,82e+01	-1,15e+02
3.26e-02	-9.94e-02	2,91e-02	-1,04e-01
-8.95e+01	1.37e+02	-7,49e+01	1,30e+02
4.11e-02	-9.70e-02	3,90e-02	-1,28e-01
-1.77e+02	-2.74e+01	-8,15e+01	-1,11e+02
1.84e-01	2.44e-01	3,93e-02	3,41e-01
2.36e-01	-2.96e-01	1,88e-01	-2,02e-01
8.13e-02	5.95e-01	7,36e-02	6,13e-01
8.68e-02	-9.68e-02	7,48e-02	-5,16e-02

Simulations are performed using the Dymola® simulation environment coupled with a Metonorm climate of Paris and varying the draw-off profiles. 28 draw off profiles are used issued from real DHW profiles measured on site ranging from 0.5 MWh to 3.5 MWh. Electricity tariffs have been taken as 15.9c€/kWh for base tariffs and 12.5c€/kWh for the Time of Use (TOU) tariffs occurring from 10 P.M. to 6 A.M..

In figure 7, as to illustrate, the annual tank temperature is compared to the reference for a real draw off scenario of 1.23 MWh. It can be seen that the tank temperature is varied according to the varying needs during the year. In the given case, the draw off profile has a marked seasonality with lower needs during the summer and higher needs during the winter period. Also, it can be seen that although the tank temperature is higher than the reference in winter, COP variation is not much affected in such periods because of the globally lower average tank temperature at restart due to the control splitting the two heat up phases. At a same tank temperature level, the COP of the optimized heat pump also has a higher magnitude because of the optimized design presented in section 3.1. These three factors (adaptation to seasonality, lower tank temperature at restart and optimized heat pump design) finally allow to increase annual COP by 35 % for this given case. This allows a reduction of electricity 26 % and a 29 % reduction in energy bill because of the better TOU valorization. As it can be seen in figure 7, this gain is achieved while maintaining the tank discharge temperature above 40 °C hence not compromising the end-user comfort.

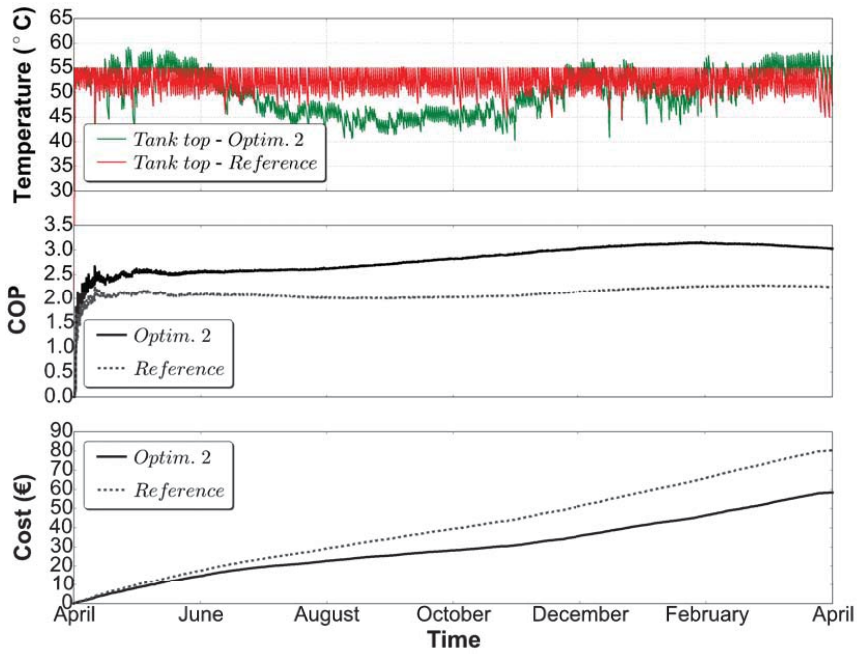

Figure 7. Annual variation of the tank top temperature, integral COP and cost for a 1.23 MWh scenario and a Paris climate

In figure 8-10, this simulation is repeated for different DHW needs using 28 different profiles. In terms of COP, a global 37 % yearly COP improvement can be achieved with a more stable end user COP average upon the different draw of profiles (Figure 8). This is particularly true for smaller draw off profiles because of the important heat losses and sub-optimal restart conditions for the reference heat pump with an oversized 200 l tank. In the case of control only (case 1), it can be seen that no more gains can be achieved after 2.5 MWh for which a fixed 200 l capacity tank is already well dimensioned for the needs. The only improvement potential left for higher DHW needs is a better thermodynamic design allowing to achieve in conjunction with the model based control an average 15 % improvement (Figure 8).

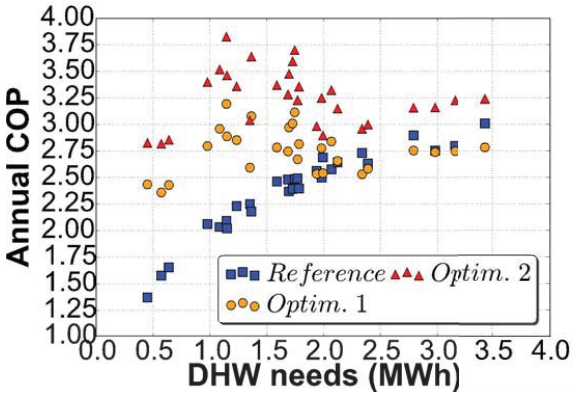

Figure 8. Annual COP variation for three ASHPWH design examples according to variable DHW needs and a fixed climate

In terms of comfort, in figure 9, it can be seen from the number of events where the tank temperature outlet falls below 40 °C that a similar level of comfort is achieved for the tested profiles from 0.5 MWh to 2.5 MWh (with some differences due to the higher variability of certain profiles). For higher tank needs, it can be seen that the comfort is globally better with the model based controller that adapts a higher tank temperature to the higher needs. This is achieved with a small tradeoff on performance as it was seen in figure 8. This would mean that with such a given control, a fixed tank size could be adopted by ASHPWH manufacturers for a larger DHW needs spread with a same level of energy performance.

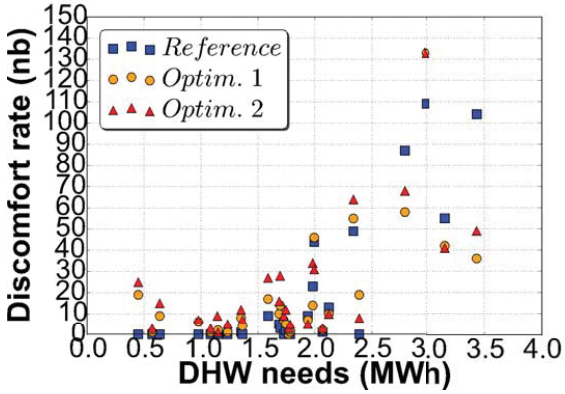

Figure 9. Annual discomfort rate for three ASHPWH design examples according to variable DHW needs and a fixed climate

Finally, in terms of cost, it can be seen in figure 10 that upon the tested profiles an average reduction of 30 % to an average 4,50 c€/kWh is achieved when combining an optimized ASHPWH with a model based controller. This can be related mainly to the increase in COP allowing to reduce electricity consumption by 27 % and the better TOU valorization allowing to further decrease the bill by an extra 3 % average.

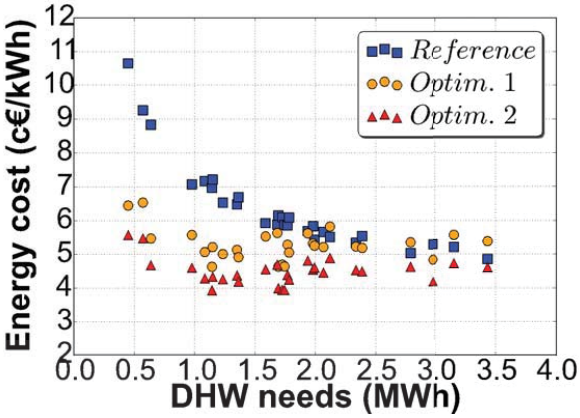

Figure 10. Annual energy cost for three ASHPWH design examples according to variable DHW needs and a fixed climate

5. CONCLUSION

In this paper, a previously developed detailed thermodynamic model was used to assess the energy performance improvement potential first based on ASHPWH design, then control and finally analyzing a combination of both. First, a multi criteria optimization potential was assessed and it was shown that on a given optimization example, heating COP could be improved by 15 % while minimizing refrigerant charge by 18 % by adopting mini channel condensers and adapting the evaporator design. Propane based ASHPWH optimization was repeated with a 150 g charge constraint and it was shown that although having a smaller thermodynamic performance, the constraint could be fulfilled by further adapting the mini channel condenser design. Then on the control side, a model based ASHPWH controller was presented that allows to vary tank thermal energy according to DHW needs on two operating periods (morning and evening) using a variable speed compressor. It was shown that on a standard fixed draw off profile, the heat pump COP improvement potential was of 22 % and the comfort was not deteriorated. In an ultimate part of the paper, the model based controller was coupled to the reference ASHPWH and an optimized design example. This combination was tested on a variety of 28 real draw off profile ranging from 0.5 to 3.5 MWh. The results indicate that the proposed optimization can reach an average 37 % end user annual COP increase with a more stable COP according to DHW needs and reducing electricity bill by 30 %. This performance was reached with a same level of comfort for small and mid-range DHW needs and an increased comfort for higher DHW needs. These two aspects make the proposed optimized ASHPWH more adaptable to a wide range of draw off profiles using a same ASHPWH design in terms of tank size and heat pump capacity.

REFERENCES

ADEME. (2014). *Climat, air et énergie édition 2015*.

Anderson, T. N., & Morrison, G. L. (2007). Effect of load pattern on solar-boosted heat pump water heater performance. *Solar Energy*, *81*(11), 1386–1395. https://doi.org/10.1016/j.solener.2007.01.018

Comité Scientifique et Technique des Industries Climatiques (COSTIC). (2016). *Les besoins d'eau chaude sanitaire en habitat individuel et collectif*.

Deutz, K. R., Charles, G.-L., Cauret, O., Rullière, R., & Haberschill, P. (2018). Detailed and dynamic variable speed air source heat pump water heater model: combining a zonal tank model approach with a grey box heat pump model. *International Journal of Refrigeration*, *In Press*. https://doi.org/10.1016/j.ijrefrig.2018.05.022

Drück, H. (2006). *MULTIPORT Store - Model for TRNSYS type 340 - Stratified fluid storage tank with four internal heat exchangers, ten connections for direct charge and discharge and an internal electrical heater*.

EHPA. (2015). *European Heat Pump Market and Statistics Report*.

Fuentes, E., Arce, L., & Salom, J. (2018). A review of domestic hot water consumption profiles for application in systems and buildings energy performance analysis. *Renewable and Sustainable Energy Reviews*. https://doi.org/10.1016/j.rser.2017.05.229

Gelažanskas, L., & Gamage, K. (2015). Forecasting HotWater Consumption in Residential Houses. *Energies*, *8*(11), 12702–12717. https://doi.org/10.3390/en81112336

Ghoubali, R., Byrne, P., & Bazantay, F. (2017). Refrigerant charge optimisation for propane heat pump water heaters. *International Journal of Refrigeration*, *76*, 230–244. https://doi.org/10.1016/j.ijrefrig.2017.02.017

Ibrahim, O., Fardoun, F., Younes, R., & Louahlia-Gualous, H. (2014). Air source heat pump water heater: Dynamic modeling, optimal energy management and mini-tubes condensers. *Energy*, *64*,

1102–1116. https://doi.org/10.1016/j.energy.2013.11.017

Jin, X., Maguire, J., Christensen, D., & Renewable, N. (2014). Model predictive control of heat pump water heaters for energy efficiency. In *Proceedings from the 18th ACEEE Summer Study on Energy Efficiency in Buildings* (pp. 133–145). Retrieved from https://pdfs.semanticscholar.org/be71/4482b1cf9097d51d4e5ed02e256a82521b29.pdf

Lomet, A., Suard, F., & Chèze, D. (2015). Statistical Modeling for Real Domestic Hot Water Consumption Forecasting. In *Energy Procedia* (Vol. 70, pp. 379–387). https://doi.org/10.1016/j.egypro.2015.02.138

Nawaz, K., Shen, B., Elatar, A., Baxter, V., & Abdelaziz, O. (2017). R290 (propane) and R600a (isobutane) as natural refrigerants for residential heat pump water heaters. *Applied Thermal Engineering*, *127*, 870–883. https://doi.org/10.1016/j.applthermaleng.2017.08.080

Peng, J. W., Li, H., & Zhang, C. L. (2016). Performance comparison of air-source heat pump water heater with different expansion devices. *Applied Thermal Engineering*, *99*, 1190–1200. https://doi.org/10.1016/j.applthermaleng.2016.01.113

Pfeiffer, A. (2012). Optimization Library for Interactive Multi-Criteria Optimization Tasks. *Proc. 9th International Modelica Conference*, 669–680. https://doi.org/10.3384/ecp12076669

Willem, H., Lin, Y., & Lekov, A. (2017). Review of energy efficiency and system performance of residential heat pump water heaters. *Energy and Buildings*. https://doi.org/10.1016/j.enbuild.2017.02.023

NOMENCLATURE

a, b	Fitting coefficients	(-)
c_p	Specific heat capacity per unit mass	($J.K^{-1}.kg^{-1}$)
m	Mass	(s^{-1})
E_{th}	Thermal energy	(J)
n	Rotational speed	(s^{-1})
p	Tank perimeter	(m)
P	Pressure	(Pa)
$\dot{Q}$	Heat Rate	(W)
t	Time	(s)
T, T_t	Temperature, Tank Temperature	(K)
$\dot{W}$	Power	(W)
x, y	Vapor quality or Horizontal axis and vertical axis coordinates	(–) - (m)

Questions and Answers:

Arno Dentel:

Which optimization library and simulation environment did you use for the optimization?

Kevin Ruben Deutz:

I used the Dymola "optimization" library that is developed by the TIL library.

***

Philippe André

Why did you select a 1-h time step for the PAC optimization?

Kevin Ruben Deutz:

Because the thermal inertia of the system is about 45 min.

***

Gabrielle Masy:

Why did you choose a set-point of 40°C? Isn't it a problem due to legionella risk?

Kevin Ruben Deutz:

40°C is the threshold in terms of available hot water for the user. We didn't include the legionella cycle which happens on a very short period over a day which energetically doesn't have a big impact.

Modelling of an air-to-water heat pump for heating and domestic hot water

Carlos Micolich[1], Néstor Fonseca[2], Cristian Cuevas[3]*

[(1,3)] Departamento de Ingeniería Mecánica, Universidad de Concepción, Concepción Chile

[(2)] Facultad de Ingeniería Mecánica, Universidad Tecnológica de Pereira, Pereira Colombia

ABSTRACT

In Chile, the use of heating systems based on wood combustion has generated several pollution problems in the central and southern Chilean regions. Several cities have been declared as saturated due to ambient air pollution. On the other hand, domestic hot water is mainly produced by combustion of liquefied petroleum gas, natural gas and in some few cases by electricity, which are very expensive energies in our country. These issues motivate the use of less contaminant and more energy efficient technologies, such as heat pumps. The use of this kind of technology is mainly evaluated through simulation during a representative period of time, which is in most of cases a year. The accuracy of the results for the annual simulations depends strongly on the approach used for the modelling of the heat pump. For this reason, a semi-empirical approach is proposed in this article to model and to simulate this kind of technology, which can be integrated to a more complex model, as for example the models proposed in TRNSYS. The approach proposed here consists of 3 sub-models: compressor, condenser and evaporator. The compressor model is validated with catalogue data for refrigerant R410A with good accuracies for refrigerant flow rate, compressor power and refrigerant exhaust temperature, which are predicted with errors lower than 1,4%, 1,2% and 1,1 K respectively. The overall model is then validated with catalogue data of heat pumps by obtaining satisfactory results (errors lower than 10%) on the heat pump power and COP.

Keywords: heat pump, modeling, heating, domestic hot water

1. INTRODUCTION

In central and southern Chile, residential heating is mainly supplied by wood stoves and domestic hot water by gas water heaters using natural gas or liquefied petroleum gas. Unfortunately, the use of wood stoves contributes enormously to the air pollution during the winter season. Wood as an energy resource represents 18% of the Chilean secondary energy consumption. In these last years, several cities in the central and southern Chile have been declared as saturated due mainly to the air pollution produced by the heating systems. These problems motivate this study, in order to evaluate the performance of heat pumps for heating and domestic hot water, which is a more efficient and less contaminant technology compared to conventional systems used in Chile. The performance of this technology can be analysed experimentally or by simulation. In particular, when the heat pump is evaluated with the overall heating system, this evaluation is mainly developed by simulation. Thus, the accuracy of the simulation depends strongly on the accuracy of each sub-model. In the case of the heat pump, most of modelling integrated in simulation software, such as TRNSYS, use a map performance approach, which is valid for a limited working domain. Furthermore, this approach does not determine some refrigerant properties that can be very important, such as the compressor refrigerant exhaust temperature. In conclusion, a more detailed model is necessary to include some physical phenomena occurring in each heat pump component. Thus, the heat pump model proposed in this study includes a semi-empirical approach for the compressor, condenser and evaporator model. The compressor is modelled using a semi-empirical approach, the condenser is modelled by considering a three zones approach and the evaporator is modelled by using a combined dry/wet approach in a one zone model.

The idea is to develop a database of heat pump models, by identifying their semi-empirical parameters for different heat pump sizes. Thus, this database shall be used to select the heat pump parameters according to the household heating demand in further system simulations. An air-to-water heat pump is considered, due to its relative low cost and to its better integration in the household. Besides, air-to-water heat pump allows to cover the building heating and domestic hot water demands. In this article, the procedure to develop the model and its validation is explained by taking an arbitrary heat pump size for household application.

2. HEAT PUMP MODELLING

The heat pump model is decomposed in three sub-models: compressor, condenser and evaporator model. In the modelling, a constant evaporator overheating is considered, by assuming that it is imposed by the expansion valve. The same hypothesis is assumed for the condenser subcooling, which is in this case imposed by the refrigerant charge.

The heat pump is modelled by using a modular approach, where each model is represented by a module, characterized by a certain number of parameters. Each model needs some inputs to generate some outputs. Inputs and outputs are interconnected between the different models to generate the heat pump model.

2.1 Compressor modeling

The compressor is modelled as proposed by Winandy et al. (2002). The semi-empirical model principle is shown in Figure 1 and its parameters are determined from a scroll compressor catalogue for heat pump application.

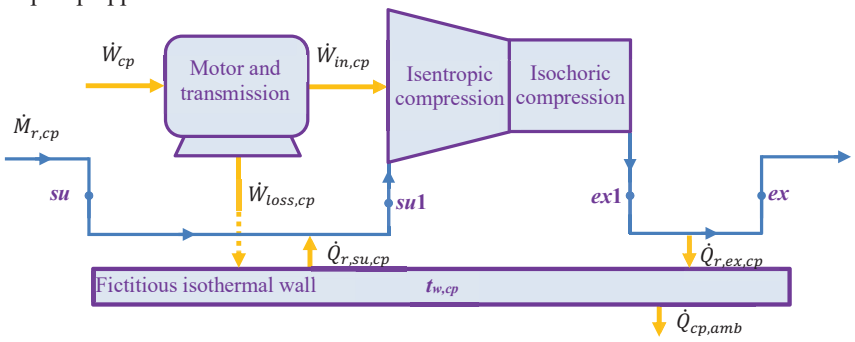

Figure 1: Compressor principle modelling.

The model is able to predict the refrigerant mass flow rate, the compressor power and the refrigerant exhaust temperature. The refrigerant mass flow rate is determined by the following equation:

$$\dot{M}_{r,cp} = \frac{N_{cp} \cdot V_s}{v_{r,su1}} \quad (1)$$

Where V_s is the compressor swept volume, which is a parameter of the model.

The compressor electric power is assumed to be equal to the sum of the internal power and the compressor loss:

$$\dot{W}_{cp} = \dot{W}_{in,cp} + \dot{W}_{loss,cp} \quad (2)$$

Where the compressor internal power is assumed to be equal to the sum of an isentropic power and an isochoric power. This consideration is assumed due to the specific characteristics in the compression process of the scroll compressor because of its fixed internal built-in volume ratio.

Where $r_{v,in}$ is the internal built-in volume ratio of the compressor, which is a parameter of the model.

The compressor loss is linearly dependent of the internal power, according to the following equation:

In this modelling, $\dot{W}_{loss,cp,0}$ is the constant electromechanical compressor loss and α is the proportional constant of the variable loss when the internal power varies, both $\dot{W}_{loss,cp,0}$ and α are parameters of the model.

The heat transfer between the refrigerant and the fictitious wall is determined by using the ε-*NTU* method:

According to previous studies developed by the author (Cuevas and Lebrun, 2009, Cuevas et al. 2010), at the supply heat exchange an effectiveness equal to 1 has been identified with experimental results. Thus, in this case a value of $\varepsilon_{su,cp} = 1$ is assumed. For the exhaust heat exchange, the following equations are used:

$$\varepsilon_{ex,cp} = 1 - e^{-(NTU_{ex,cp})} \quad (7)$$

In this case, the overall heat transfer coefficient is determined as:

Where $UA_{ex,cp,0}$ is a parameter of the compressor model.

2.2 Condenser modelling

The condenser is modelled by using a three zones model. A perfectly counterflow heat exchanger is assumed in the modelling, as shown in Figure 2. This modelling approach was proposed by Cuevas et al. (2009).

The heat flow in each zone is determined from the energy balance in steady state:

Where *zi* represents every zone: *sh*: superheated, *tp*: two phase, *sc*: subcooled.

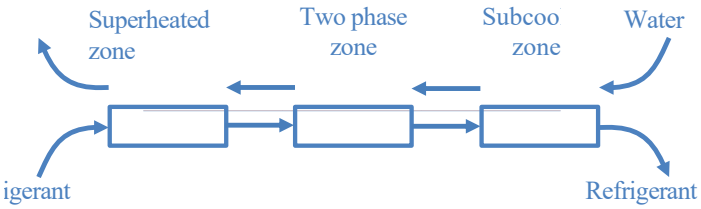

Figure 2: Condenser principle modelling.

The *ε-NTU* method is used to determine the heat transfer rate, which is decomposed in the following equations:

$$\dot{Q}_{cd,zi} = \varepsilon_{cd,zi} \cdot \dot{C}_{min,cd,zi} \cdot \left(t_{r,su,cd,zi} - t_{w,su,cd,zi}\right) \tag{11}$$

$$NTU_{zi,cd} = \frac{(U \cdot A)_{zi,cd}}{\dot{C}_{min,zi,cd}} \tag{12}$$

$$\frac{1}{(U \cdot A)_{zi,cd}} = \frac{1}{h_{i,zi,cd} \cdot A_{i,zi,cd}} + R_w + \frac{1}{h_{o,zi,cd} \cdot A_{o,zi,cd}} \tag{13}$$

The convective heat transfer coefficients are determined with an empirical relationship:

$$h = h_{ref} \cdot \left(\frac{\dot{M}}{\dot{M}_{ref}}\right)^n \tag{14}$$

Where h_{ref}, $\dot{M}_{ref}$ and n are parameters of the model. In the modelling, the wall thermal resistance is neglected.

By integrating the three zones, the heat flow of the condenser on the water and on the refrigerant sides are given by:

$$\dot{Q}_{cd} = \dot{Q}_{sh,cd} + \dot{Q}_{tp,cd} + \dot{Q}_{sc,cd} \tag{15}$$

The constraint for the heat transfer areas of each zone is given by:

$$A_{cd} = A_{sh,cd} + A_{tp,cd} + A_{sc,cd} \tag{16}$$

In this case, the area A_{cd} is a parameter of the model. The condenser model mainly predicts the condensing pressure, which allows then to determine the condenser heat transfer rates.

2.3 Evaporator modelling

The evaporator is modelled as proposed by Ding et al. (1990). In this case, a one zone approach is assumed, as shown in Figure 3. This model proposes to determine the evaporator heat transfer rate by assuming that it works in a purely dry regime or in a purely wet regime. Then, the evaporator actual working condition is determined as:

$$\dot{Q}_{a,ev} = MAX\left(\dot{Q}_{coil,dry}, \dot{Q}_{coil,wet}\right) \tag{17}$$

According to Braun et al. (1989), this hypothesis introduces an uncertainty lower than 5% on the predicted heat flow.

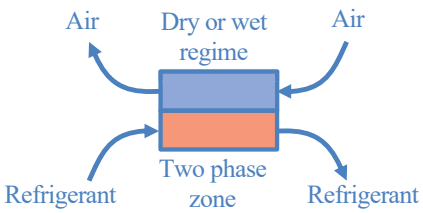

Figure 3: Evaporator principle modelling.

The refrigerant heat transfer rate is given by:

$$\dot{Q}_{r,ev} = \dot{M}_{r,ev} \cdot \left(h_{r,ex,ev} - h_{r,su,ev}\right) \quad (18)$$

On the air side the analysis is developed as follows.

Dry regime. In dry regime the global heat transfer coefficient is given by:

$$\frac{1}{(U \cdot A)_{coil,dry}} = R_{a,coil,dry} + R_{w,coil} + R_{r,coil} \quad (19)$$

The thermal resistances R are determined as indicated in Equations 20 and 21.

$$R_{a,coil,dry} = \frac{1}{h_{a,coil,dry} \cdot A_{a,coil}} \quad (20)$$

$$R_{r,coil} = \frac{1}{h_{r,coil} \cdot A_{r,coil}} \quad (21)$$

In this case, an area ratio $A_{a,coil}/A_{r,coil} = 23$ is assumed for the modelling.

The wall thermal resistance is also neglected in this case. The heat transfer rate is also determined by using the ε-NTU method.

$$\dot{Q}_{coil,dry} = \varepsilon_{coil,dry} \cdot \dot{C}_{min,coil,dry} \cdot \left(t_{a,su,coil} - t_{r,su,coil}\right) \quad (22)$$

The enthalpy flow from the air side is given by:

$$\dot{Q}_{coil,dry} = \dot{M}_{a,ev} \cdot \left(h_{a,su,coil} - h_{a,ex,coil,dry}\right) \quad (23)$$

Wet regime. When the evaporator works in wet regime, the moist air is replaced by a fictitious ideal gas with a specific heat given by:

$$c_{p,a,f,coil} = \frac{h_{a,su,coil} - h_{a,ex,coil,wet}}{t_{wb,su,coil} - t_{wb,ex,coil,wet}} \quad (24)$$

The thermal resistance on the air side is corrected as follows:

$$R_{a,f,coil,wet} = R_{a,coil,dry} \cdot \frac{c_{p,a,coil}}{c_{p,a,f,coil}} \quad (25)$$

The heat transfer rate is determined as:

$$\dot{Q}_{coil,wet} = \varepsilon_{coil,wet} \cdot \dot{C}_{min,coil,wet} \cdot \left(t_{wb,su,coil} - t_{r,su,coil}\right) \quad (26)$$

The heat exchanger effectiveness is determined as:

$$\varepsilon_{coil,wet} = 1 - exp\left(NTU_{coil,wet}\right) \quad (27)$$

In this calculation, only the thermal resistance on the air side of overall heat transfer coefficient changes in comparison to the dry regime:

$$\frac{1}{(U \cdot A)_{coil,wet}} = R_{a,f,coil,wet} + R_{w,coil} + R_{r,coil} \quad (28)$$

The exhaust air humidity and enthalpy are determined by using the hypotheses proposed by ASHRAE (2000). They assume that there are two driving potentials for the heat transfer in the cooling coil: A first one from the air to the heat exchanger surface given by the enthalpy difference h_a - h_s and a second one from the heat exchanger surface to the cooling fluid given by the temperature difference t_s - t_r. To simplify the simulation, the heat exchanger is assumed to have a constant surface temperature

throughout all its heat transfer area, which is called contact temperature $t_{c,coil,wet}$. Thus, the heat transfer from the air to the surface can be determined as:

$$\dot{Q}_{coil,wet} = \varepsilon_{c,coil,wet} \cdot \dot{M}_{a,ev} \cdot \left(h_{a,su,coil} - h_{c,coil,wet}\right) \quad (29)$$

Where the contact effectiveness is determined as:

$$\varepsilon_{c,coil,wet} = 1 - exp\left(NTU_{c,coil,wet}\right) \quad (30)$$

The $NTU_{c,coil,wet}$ is determined for the heat transfer from the air to the heat exchanger surface as:

$$NTU_{c,coil,wet} = \frac{1}{R_{a,f,coil,wet} \cdot \dot{C}_{a,coil}} \quad (31)$$

The enthalpy flow rate from the air is given by:

$$\dot{Q}_{coil,wet} = \dot{M}_{a,ev} \cdot \left(h_{a,su,coil} - h_{a,ex,coil,wet}\right) \quad (32)$$

The contact enthalpy is determined by combining equations 29 and 32:

$$h_{a,su,coil} - h_{a,ex,coil,wet} = \varepsilon_{c,coil,wet} \cdot \left(h_{a,su,coil} - h_{c,coil,wet}\right) \quad (33)$$

The contact temperature is determined by assuming that the air in contact with the heat exchanger surface is saturated.

Finally, assuming that the contact effectiveness is the same for the mass transfer allows to determine the air exhaust humidity ratio $W_{ex,coil,wet}$:

$$W_{su,coil} - W_{ex,coil,wet} = \varepsilon_{c,coil,wet} \cdot \left(W_{su,coil} - W_{c,coil,wet}\right) \quad (34)$$

Where $W_{c,coil,wet}$ is humidity ratio of the moist air determined at the contact temperature and at saturated conditions.

2.4 Heat pump modeling

The heat pump model is obtained by interconnecting the models described previously, by giving the result shown in Figure 4. The main outputs of the model are the condenser heat flow and the compressor power, both used to determine its instantaneous COP.

It is assumed that the heat pump produces hot water at a given temperature available in the heat pump catalogue.

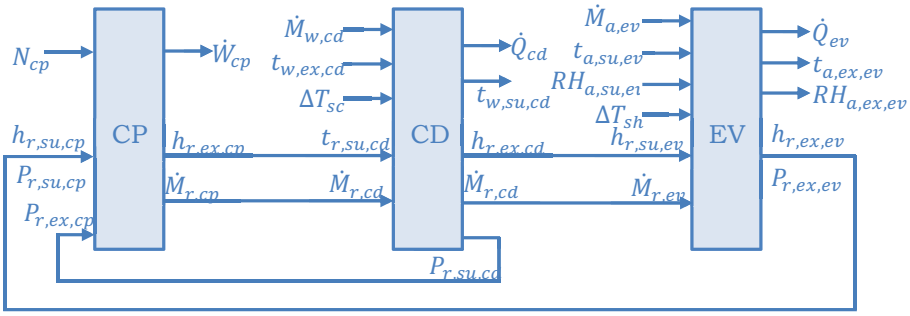

Figure 4: Heat pump principle modelling.

3. IDENTIFICATION AND DEFINITION OF THE PARAMETERS

Firstly, the parameters of the compressor model are identified by using catalogue data and then for the condenser and the evaporator some parameters for the heat transfer coefficient are assumed. Finally, their heat transfer areas are fitted by using heat pump catalogue datasheet.

3.1 Identification of the compressor parameters

This study is focused in air to water heat pumps of 230 V working with R410A. The compressor data are obtained for a superheating and a subcooling of 10 K respectively.

The parameters of the model are determined by comparing catalogue and simulated outputs of the model. In this case, an error function is defined:

$$\Phi = \sqrt{\frac{\sum_{i=1}^{n}\left[\left(\frac{\dot{W}_{cp,cat}-\dot{W}_{cp,sim}}{\dot{W}_{cp,cat}}\right)^2+\left(\frac{\dot{M}_{r,cp,cat}-\dot{M}_{r,cp,sim}}{\dot{M}_{r,cp,cat}}\right)^2+\left(\frac{t_{r,ex,cp,cat}-t_{r,ex,cp,sim}}{t_{r,ex,cp,cat}}\right)^2\right]}{n}} \quad (35)$$

The parameters of the model are identified in such a way that these are the values that minimize the function Φ. The method used to minimize this function is the Variable Metric Method available in EES [23]. The results obtained are shown in Table 1.

Table 1: Compressor parameters.

Parameter	Value
$\varepsilon_{su,cp}$	1
$UA_{ex,cp,0}$ [W/K]	9
$\dot{M}_{r,cp,ref}$ [kg/s]	0,085
V_s [cm^3]	29,463
$r_{v,in}$ [-]	2,489
α [-]	0,243
$\dot{W}_{loss,cp,0}$ [kW]	0,129

In order to have an idea about the error of the model, the simulated and catalogue values for refrigerant flow rate and compressor power are compared through the mean absolute percentage error (MAPE) and for the compressor exhaust temperature the comparison is developed with the mean absolute error (MAE):

$$MAPE = \sqrt{\frac{1}{n}\cdot\sum_{i=1}^{n}\left(\frac{V_{cat}-V_{sim}}{V_{cat}}\cdot 100\right)^2} \quad (36)$$

$$MAE = \sqrt{\frac{1}{n}\cdot\sum_{i=1}^{n}(V_{cat}-V_{sim})^2} \quad (37)$$

The main outputs of the compressor model: the compressor input power and the refrigerant flow rate are predicted with MAPEs of 1,35% and 1,16% respectively, and the refrigerant exhaust temperature with a MAE of 1,1 K. Figures 5 and 6 show a comparison between simulated and catalogue compressor refrigerant flow rate and compressor electric power respectively.

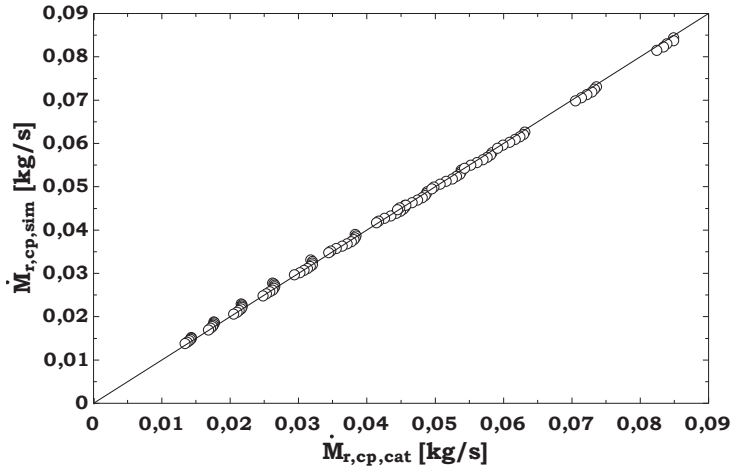

Figure 5: Comparison between simulated and catalogue compressor refrigerant flow rate.

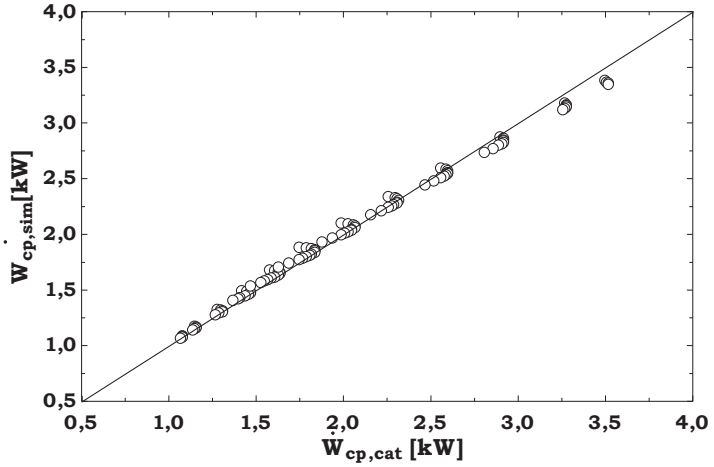

Figure 6: Comparison between simulated and catalogue compressor electric power.

The compressor power is slightly underestimated at high compressor powers. It is attributed to the function proposed here to identify the parameters, which use relative errors to identify the parameters.

In order to take into account the compressor ambient heat loss, which are not considered in the compressor catalogue, a constant overall *UA* value is estimated. An external compressor heat transfer area of 0,173 m^2 and an overall convective-radiative heat transfer coefficient of 15 W/m^2K are assumed for this compressor. Thus, an UA_{amb} of 2,6 W/K is considered in the further simulations.

3.2 Parameters of the condenser and evaporator model

To define the condenser and evaporator areas, as well as the water and air flow rates, a commercial heat pump is taken as reference, which works with R410A. Table 2 and Table 3 present the parameters used for the condenser and the evaporator respectively.

Table 2: Condenser parameters.

Parameter	Value
$h_{ref,w,cd}$ [W/m^{2}K]	2000
$h_{ref,r,sh,cd}$ [W/m^{2}K]	500
$h_{ref,r,tp,cd}$ [W/m^{2}K]	4000
$h_{ref,r,sc,cd}$ [W/m^{2}K]	2000
$\dot{M}_{w,ref,cd}$ [kg/s]	0,521
$\dot{M}_{r,ref,cd}$ [kg/s]	0,085

Table 3: Evaporator parameters.

Parameter	Value
$h_{ref,a,ev}$ [W/m^{2}K]	100
$h_{ref,r,tp,ev}$ [W/m^{2}K]	4000
$\dot{M}_{a,ref,ev}$ [kg/s]	1,449
$\dot{M}_{r,ref,ev}$ [kg/s]	0,085

Only the data without frosting are considered to validate the model, because the present model does not consider this phenomenon. Thus, 15 points are considered to identify the heat transfer areas of the heat exchangers. A heat transfer area of 1,25 m^2 was identified for the condenser and 1,3 m^2 for the evaporator on the refrigerant side. Figure 7 shows the comparison between simulated and catalogue heat pump heating power. A MAPE of 3,4% was obtained.

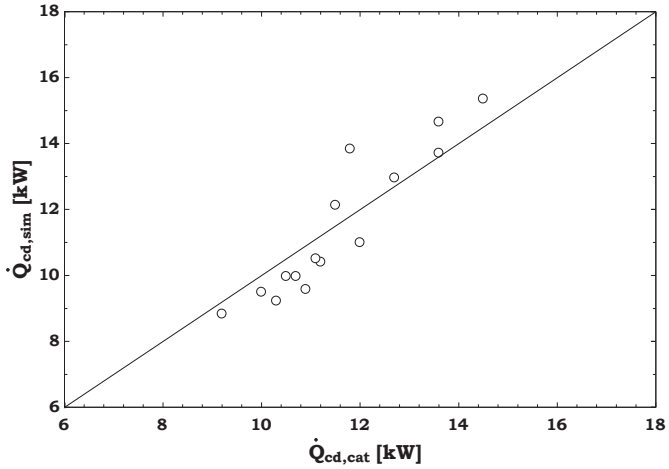

Figure 7: Comparison between simulated and catalogue heat pump heating power.

3.3 Validation of the heat pump model

Figure 8 presents the results of the model for the heating power for the heat pump supplying hot water at 45ºC. A good agreement is observed for the model when the evaporator is working in dry and in wet regimes. However, at low temperatures, when there is frosting, the difference increases, because the actual model does not consider this phenomenon.

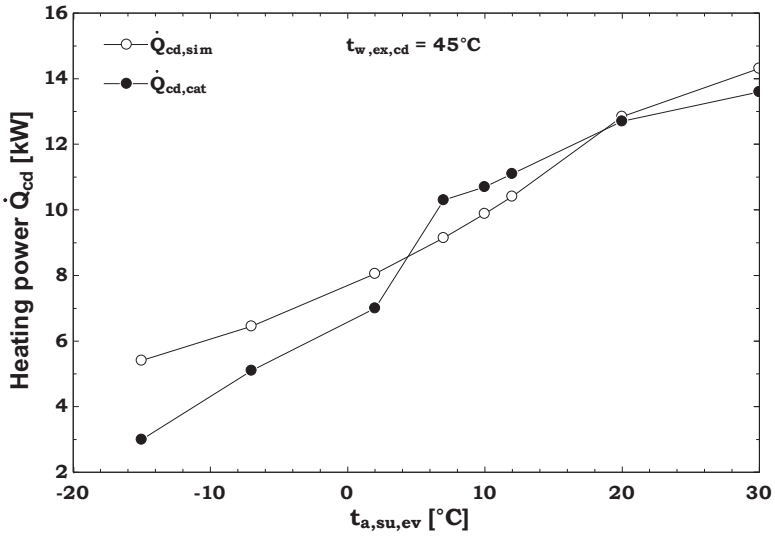

Figure 8: Comparison between simulated and catalogue heating power for different ambient temperatures.

3.4 Discussion

It was observed that the compressor model slightly overestimate the compressor power, which is attributed to the method used to identify the compressor parameters that uses relative errors to determine the error function. Thus, the minimization method tries to optimize three errors (flow, power and temperature) at the same time, by penalizing the variable with the lower errors. It could be improved, in a parametric analysis, by introducing weighting factors multiplying every error included in the error function.

The semi-empirical model developed in this study is able to predict with an acceptable uncertainty the heat pump performance in dry and in wet conditions. However, when the heat pump works under frosting conditions, the model over-predicts the heating power, because it does not consider that phenomenon. In a further study some improvements must be introduced to this model, such as the use of catalogue data from other compressor manufacturers and by including the frosting in the modelling. In spite of that, this model is able to include several improvements and it does not present any numerical problems during the resolution of the equations.

As mentioned previously, frosting will be included in a further analysis. As frosting is time depending, a further model should be implemented to determine the frost thickness growing through the time and then it shall be compared with a predefined frost thickness to stop the heat pump. The frost thickness will allow to determine the thermal resistance due to the ice layer and the heat transfer degradation. The predefined frost thickness to stop the heat pump will be estimated from the evaporator fin pitch for heat pump applications and tuned with the available heat pump catalogue data at air temperatures lower than 2ºC.

According to the information used as input to validate and to identify the models, it will be very useful to have more information about the heat pumps components. The heat pump manufacturers do not give enough information to develop ant to validate detailed models.

4. CONCLUSION

An air to water heat pump model has been developed. This model includes some physical improvements in comparison to the models used in long term simulation software such as TRNSYS. The model uses compressor catalogue data and heat pump catalogue data to validate the modelling approach. The compressor model shows an acceptable accuracy, with differences between the simulated and catalogue data lower than 1,4%, 1,2% and 1,1 K for the compressor power, refrigerant flow rate, and refrigerant exhaust temperature respectively. The model is validated with the heat pump catalogue, obtaining a difference between the predicted and catalogue data lower than 3,4%. The model can still be improved by including the frosting phenomenon and by improving the parameters identification process of the compressor, with more information given by the heat pump manufacturer.

REFERENCES

ASHRAE, 2000. ASHRAE Handbook-HVAC Systems and Equipment, Chapter 21. Atlanta: American Society of Heating, Refrigerating and Air-Conditioning Engineers, Inc.

Braun, J. E., Klein, S. A., Mitchell, J., 1989. Effectiveness models for cooling towers and cooling coils, ASHRAE Transaction 95, pp. 164-173.

Cuevas, C. and Lebrun, J., 2009. Testing and modelling of a variable speed scroll compressor. Applied Thermal Engineering, Volume 29, pp. 469-478.

Cuevas, C., Lebrun, J., Lemort, V., Ngendakumana, Ph., 2009. Development and validation of a condenser three zones model. Applied Thermal Engineering, Volume 29, pp. 3542-3551.

Cuevas, C., Lebrun, J., Lemort, V., Winandy, E., 2010. Characterization of a scroll compressor under extended operating conditions. Applied Thermal Engineering, Volume 30, pp. 605-615.

Ding, X., Lebrun, J., Eppe, J. P., Wasacz, M., 1990. Cooling coil models to be used in transient and/or wet regimes, theoretical analysis and experimental validation. Proceedings of SSB, Liège.

Winandy, E., Saavedra, C. and Lebrun, J., 2002. Experimental analysis and simplified modelling of a hermetic scroll refrigeration compressor. Applied Thermal Engineering, Volume 22, pp. 107-120.

NOMENCLATURE

A	area, m^2
$\dot{C}$	capacity flow, W/K
c	specific heat, J/kg-K
COP	Coefficient Of Performance
h	enthalpy, $J \cdot kg^{-1}$, or convective heat transfer coefficient, W/m^2-K
$\dot{M}$	mass flow rate, kg/s
N	rotational speed, 1/s
n	number of data or exponent
NTU	Number of Transfer Units
P	pressure, Pa
$\dot{Q}$	heat flow, W
R	thermal resistance, K/W

r	ratio
RH	relative humidity
t	temperature, ºC
U	heat transfer coefficient, W/m^2-K
V	volume, m^3, or value
v	specific volume, m^3/kg
W	humidity ratio, kg/kg
$\dot{W}$	power, W

Subscripts

0	constant value
a	air
amb	ambient
c	contact
cat	catalogue
cd	condenser
coil	heat exchanger
cp	compressor
dry	dry regime
ev	evaporator
ex, *ex*1	exhaust
f	fictitious
in	internal
loss	loss
min	minimum
p	at constant pressure
r	refrigerant
ref	reference
s	isentropic or swept
sc	subcooled
sh	superheated
sim	simulated
su, *su*1	supply
tp	two-phase
v	volumetric or isochoric or volume

w	water or wall
wb	wet bulb
wet	wet regime
zi	zone "*i*"

Greek symbols

α	power loss coefficient
Δ	difference
ε	effectiveness
Φ	error function

Questions and Answers:

Madjid Madjidi:

Couldn't we simplify the model of the compressor by taking into account that the polytropic process is similar to the isentropic (theoretical) process?

Cristian Cuevas:

The model considered here is based on manufacturer data and I wanted to have a physical-based model.

Experimental Characterization of Fault Impacts on the Functioning Variables of an Inverter Driven Heat Pump

D.Noël[1, 2], P. Rivière[2], C.Teuillières[1], O. Cauret[1], D. Marchio[2]

(1) EDF Lab Les Renardières, Ecuelles, France

(2) Centre for Energy Efficiency of Systems (CES), Mines ParisTech, PSL Research University, Paris, France

ABSTRACT

The heat pump technology answers to the three key targets of the European Union climate action by reducing greenhouse gas emissions, increasing renewable energy share and improving energy efficiency of buildings. In standard conditions, heat pumps can reach very high coefficients of performance (COPs). However, the in-situ COPs are poorly known and they depend on many factors such as sizing, climate, quality of installation, and can also be affected by some abnormal functioning caused by faults, such as heat exchanger fouling or incorrect refrigerant charge. This paper focuses on the characterization of these faults for an inverter driven residential heat pump, for which literature is very limited, in order to be able to detect those as early as possible, and thus to facilitate maintenance operation. A series of experimental tests has been conducted to generate correlations between faults and their impact on the main functioning variables and performances. The test results obtained are presented and discussed. Further steps required to develop an operational automated fault detection and diagnostic method for inverter driven heat pumps are finally discussed, as well as the possibility to associate it with a performance assessment method for heat pumps that was previously developed and validated.

Keywords: Heat pump, Inverter, Fault impact, Characterization

1. INTRODUCTION

Heat pumps (HP) contribute to reducing heating energy consumption in dwellings. But their performances depend on many external factors and can be impacted by different kinds of faults. These can be caused by a control issue, or by a physical deviation of the thermodynamic cycle as compared to its original or intended design. This study concerns this second kind of faults, which are difficult and expensive to diagnose (Li & Braun, 2009), like heat exchangers fouling and refrigerant under- and over-charging.

The impacts of these faults on the functioning and performance variables of heat pumps have been studied before, Mehrabi and Yuill (2017a & 2017b) made a very complete synthesis of these works by gathering the experimental data of many laboratory experiments. Their work provides generalized relationships between faults intensities (FI) and performance variables, and it shows that there is a remarkable similarity of results from different systems in many cases. Regression coefficients are provided for three different operating conditions in heating mode for charge variations and condenser fouling faults. These conditions are standard test conditions in heating mode (outdoor temperatures 8.33, 1.67 and -8.33 °C for an indoor temperature of 21.1 °C (H1, H2 and H3 from ANSI/AHRI Standard 210/240, 2008). This standard is for air to air and return inlet indoor temperature is fixed. There is little information on air to water and nothing on heat pumps with inverter and variable water loop temperature. This study concerned only fixed-speed HP with fixed orifice (FXO) or thermostatic (TXV) expansion valves. Thus, it is necessary to extend the knowledge of the impacts of faults on inverter-driven heat pumps using an electronic expansion valve (EEV).

Furthermore, a performance assessment method adapted to any type of residential HP has been identified (Tran et al., 2013), improved (Niznik, 2017) and widely validated (Noël et al., 2018). It was made to measure precisely and continuously the performances of heat pumps, particularly air-to-air, without interfering with the normal functioning of the system. It is based on a virtual mass flow sensor from the compressor energy balance, and uses only light instrumentation on the refrigerant side, in order to be easily implemented on-site. This method is able to measure the performances of residential heat pumps in a very large scale of operating conditions, and can thus measure the decrease of performance caused by faults. It measures continuously the refrigerant mass flow rate, which can be very useful in order to detect and/or discriminate between different faults.

This experimental study focuses on quantifying the normalized impacts of faults on different performance and functioning variables as a function of the fault intensity. In particular, the knowledge of the system behaviour under faulty conditions will lead to the identification of the necessary measurements to detect faults at an early stage. Then, this analysis will allow to evaluate in which way the in-situ performance assessment method can be used for fault detection process.

2. EXPERIMENTAL SETUP

2.1 Test bench

The test bench was an air-to-water HP with an inverter-driven rotary-type compressor using R134a as a working fluid, installed in adjacent climatic chambers, where temperature and humidity are controlled. It uses a plate heat exchanger as a condenser, and an electronic expansion valve (EEV). There is no liquid receiver after the condenser.

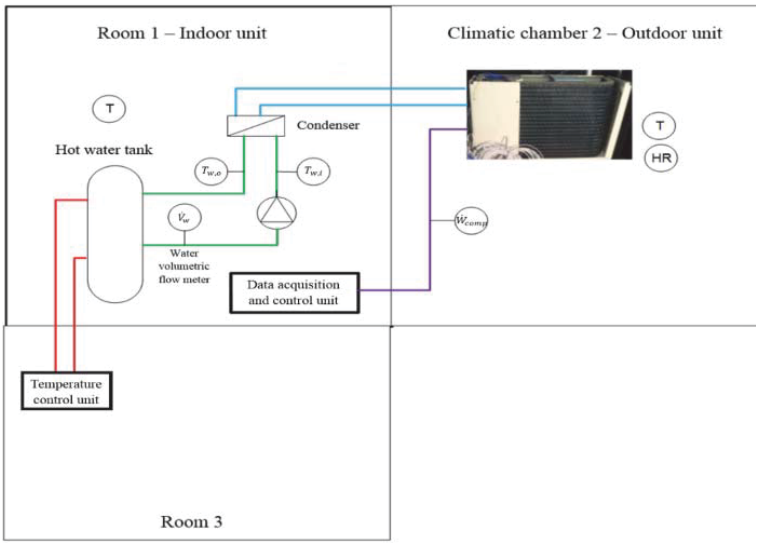

Figure 1: Air-to-water HP installed in climatic chambers

For each measurement condition, the acquisition lasted for two hours in order to be sure that the steady state was reached and to have a sufficient amount of data to analyse. The experimental set-up is described in figure 1.

2.2 Measurements

On the water-side, condenser inlet and outlet water temperatures ($T_{w,in}$ and $T_{w,out}$) were measured, as well as the water volumetric flow rate, $\dot{V}_w$. On the refrigerant side, condenser inlet and outlet temperatures ($T_{cond,in}$ and $T_{cond,out}$), compressor suction and discharge temperatures and pressures (T_{suc}, T_{dis} and P_{suc}, P_{dis}), as well as the compressor frequency (Freq) and EEV opening (EEV) were measured. Temperatures are measured with insulated contact Pt100. Evaporating and condensing temperatures (T_{evap} and T_{cond}) are calculated from P_{suc} and P_{dis}. The refrigerant mass flow rate ($\dot{m}$) is measured thanks to the virtual mass flow rate sensor used in the performance assessment method, using the energy balance of the compressor:

$$\dot{W}_{comp} = \dot{m}\left[(1 - C_{oil})\left(h_{r,comp,o} - h_{r,comp,i}\right) + C_{oil}.c_{p,oil}(T_{dis} - T_{suc})\right] + \dot{Q}_{losses} \quad (1)$$

Where $\dot{W}_{comp}$ is the compressor power input measured, and $\dot{Q}_{losses}$ the compressor heat losses that are estimated through a measurement of the temperature of the compressor shell surface (Niznik, 2017) and the ambient temperature. The working fluid is mainly composed of refrigerant fluid, but there is also a small part of oil, necessary to ensure the good working of the compressor, that migrates into the refrigerant cycle. The oil fraction, C_{oil}, is considered to be equal to 0.5 % of the total working fluid (Goossens, 2017). Therefore, the enthalpy variation is decomposed into the refrigerant variation of enthalpy and the oil variation of enthalpy. $h_{r,comp,i}$ and $h_{r,comp,o}$ are respectively the refrigerant compressor inlet and outlet enthalpies, $c_{p,oil}$ is the oil specific heat capacity, $T_{comp,i}$ and $T_{comp,o}$ are respectively the compressor inlet and outlet temperatures.

Goossens (2016 and 2017) and Niznik (2017) developed a method to estimate the heat losses of the compressor, based on CFD modelling of different types of compressors and experimental study. This work established the best locations for temperature sensors for the compressor shell and the ambient air and identified the best heat exchange correlations in order to estimate the compressor heat losses.

For rotary compressors, only one surface temperature sensor is necessary on the compressor shell, and only two for scroll compressors (one is used to check the validity of the correlation domain). The surface temperature is referred as T_{surf}. Niznik (2017) concluded that the best solution for the ambient air temperature T_{amb} as seen from the compressor is to measure $T_{amb} = T_{ext}$, with T_{ext} the air temperature outside the HP outdoor unit.

For example, the correlation used to calculate the compressor heat losses for a rotary type compressor is:

$$\dot{Q}_{losses} = \left(\frac{\overline{Nu}_L k}{L} A_L + \frac{\overline{Nu}_{D,1} k}{D} A_D + \frac{\overline{Nu}_{D,2} k}{D} A_D\right)\left(T_{surf} - T_{amb}\right) + \sigma A_{tot}\left(T_{surf}^4 - T_{amb}^4\right) \quad (2)$$

Where Nu is the Nusselt number for the different sides of the compressor, k is the thermal conductivity of the air, L, D and A stand for the different characteristic dimensions of the compressor, respectively length (height), diameter (1 and 2 for the top and the bottom surface respectively) and area for the lateral side, the top and the bottom of the compressor, σ is the Stefan-Boltzmann constant for radiative heat transfer.

Therefore, the refrigerant mass flow rate can be expressed as:

$$\dot{m} = \frac{\dot{W}_{comp} - \dot{Q}_{losses}}{(1 - C_{oil})\left(h_{r,comp,out} - h_{r,comp,in}\right) + C_{oil}.c_{p,oil}\left(T_{cond,in} - T_{cond,out}\right)} \quad (3)$$

To have the enthalpy values needed, pipe surface temperature measurements are monitored, and if there is no pressure sensor, low and high pressures can be determined from the temperature measurements where the fluid state is undoubtedly diphasic: the evaporator inlet for low pressure and the center of the condenser surface for high pressure. The pressure measurement error that could be caused by the temperature glide of zeotropic fluids classically used in residential HP (R410A, R407C) is very limited (Tran, 2012).

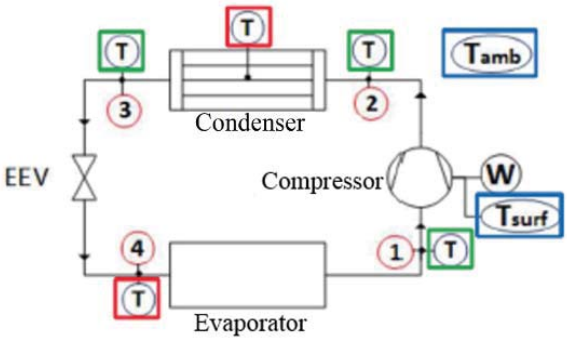

Figure 2: Required measurements for the in-situ performance assessment method

The measurement uncertainty of the refrigerant mass flow rate with this method is estimated to about 5 % maximum, taking into account that the measurement uncertainty for the temperatures is 0.8 K, for the electrical power measurement 0.2 %, for high and low pressures 0.25 %. From the pressure measurements, the absolute measurement uncertainties for condensing and evaporating temperatures are about 0.1 °C.

2.3 Control

The HP unit is controlled with a linear heating curve that sets the leaving water temperature as a function of the outdoor temperature (T_{ext}):

$$T_{w,out} = 45 - T_{ext}\ (°C) \tag{4}$$

The frequency of the compressor is thus controlled with a PI controller in order to provide enough power to maintain the outlet water temperature according to the heating curve.

In a real building, the water circulates through a heating circuit to heat the building, and the water temperature decreases according to the heat losses of the building. Here, these losses are simulated thanks to a water temperature control unit, so the condenser water inlet temperature is set according to the heat losses equation:

$$P_{th} = G.V.(T_{in} - T_{ext}) \tag{5}$$

G=0.6 W/m^{3}K is the overall heat loss coefficient of the virtual building, V=200 m^3 is its volume, T_{in} is the indoor ambient air temperature that would be set inside the building, it was set to 20°C. P_{th} is the heat lost by the building, but it is also the heating power that the HP should provide:

$$P_{th} = \rho_w.\dot{V}_w.c_{p,w}.(T_{w,out} - T_{w,in}) \tag{6}$$

Where ρ_w is the water density, $c_{p,w}$ is its specific heat. The HP provides the heat power needed to make the water temperature go from $T_{w,in}$ to $T_{w,out}$.

The EEV is controlled by a PI controller to maintain the suction superheat to a constant value of 10 °C.

T_{ext}	T_{in}	P_{th}	T_{wout}	T_{win}
10 °C	20 °C	1200 W	35 °C	32.2 °C
5 °C	20 °C	1800 W	40 °C	35.8 °C
0 °C	20 °C	2400 W	45 °C	39.4 °C
-3 °C	20 °C	2760 W	48 °C	41.6 °C

Table 1: Heat power and water temperatures for each outdoor temperature tested

2.4 Test program

Different refrigerant charge were adjusted to simulate over and under charge. Evaporator fouling faults were simulated by reducing the fan speed in order to reduce the air flow rate, as it would be the effect of a real fouling. In the same way, for condenser fouling faults, the water circulating pump was slowed down. Fault levels (i.e. the severity of the faults) are quantified using fault intensity (FI), defined by Yuill and Braun (2013):

$$FI_{CH} = \frac{m_{actual} - m_{nominal}}{m_{nominal}} \quad (7)$$

$$FI_{EA} = \frac{\dot{V}_{air,actual} - \dot{V}_{air,nominal}}{\dot{V}_{air,nominal}} \quad (8)$$

$$FI_{CA} = \frac{\dot{V}_{w,actual} - \dot{V}_{w,nominal}}{\dot{V}_{w,nominal}} \quad (9)$$

Where m is refrigerant mass, $\dot{V}_{air}$ is the air volumetric flow rate through the evaporator and $\dot{V}_w$ is the water volumetric flow rate through the condenser.

Three types of faults were studied:

Type of fault	FI tested [-]
Refrigerant mischarge	+0.1, 0, -0.1, -0.3, -0.5
Evaporator fouling	0, -0.1, -0.2, -0.3, -0.4, -0.5
Condenser fouling	0, -0.1, -0.2, -0.3, -0.4, -0.5

Table 2: Fault Intensities tested

The ranges of FI were chosen in order to be sure that a significant impact could be observed, at least for the strongest fault intensities.

Each FI was tested under 4 different outdoor temperatures: 10 °C, 5 °C, 0 °C and -3 °C.

3. RESULTS

The impacts of faults on the operating and performance variables are quantified using the fault impact ratio (FIR) defined by Yuill and Braun (2013), and extended to other variables: the coefficient of performance (COP), the discharge pressure (P_{dis}), refrigerant mass flow rate (m), compressor frequency (Freq), the EEV opening (EEV), subcooling (SC), condensing and evaporating temperatures (T_{cond} and T_{evap}), the air temperature at the evaporator outlet (T_{airout}).

The measurement uncertainties are represented with error bars on the graphs, slightly shifted from the data points when it improves readability, and not represented when negligible.

$$FIR_{COP} = \frac{COP_{actual}}{COP_{unfaulted}} \quad (10)$$

$$FIR_{m} = \frac{\dot{m}_{actual}}{\dot{m}_{unfaulted}} \quad (11)$$

$$FIR_{Freq} = \frac{Freq_{actual}}{Freq_{unfaulted}} \quad (12)$$

$$FIR_{EEV} = \frac{EEV_{actual}}{EEV_{unfaulted}} \quad (13)$$

$$Residual_{SC} = SC_{actual} - SC_{unfaulted} \quad (14)$$

$$Residual_{Tcond} = T_{cond,actual} - T_{cond,unfaulted} \quad (15)$$

$$Residual_{Tevap} = T_{evap,actual} - T_{evap,unfaulted} \quad (16)$$

$$Residual_{Tairout} = T_{airout,actual} - T_{airout,unfaulted} \quad (17)$$

3.1 Impact of the refrigerant charge

The mass of fluid chosen as “nominal” (FI_{CH} = 0) was not necessarily the optimal charge, as it can be observed in some following figures. It remains interesting to observe the impact of the variation of the refrigerant charge.

The results can partly be compared with those obtained by Mehrabi and Yuill (2017a), mentioned as MY2017 in the graphics, to see if there are similarities between fixed-speed and inverter driven HP.

For the strongest charge fault (FI_{CH} = -0.5), at 0 °C and -3 °C, the HP was only dealing with frost and defrosting cycles, thus those points are not always exploitable.

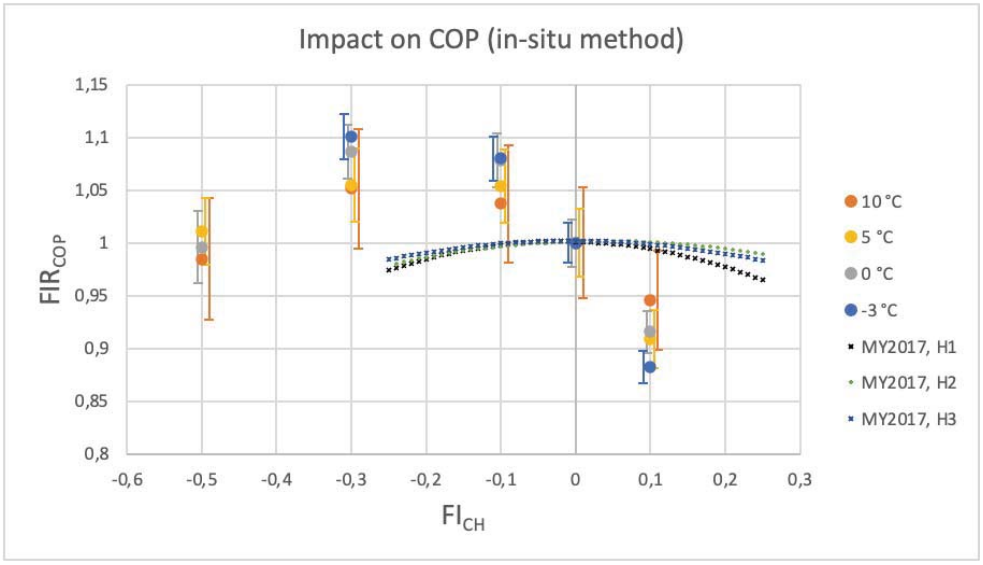

Figure 3: Refrigerant charge impact on the COP, compared with Mehrabi & Yuill (2017a)

In Figure 3, we can see that a refrigerant overcharge leads to a reduction of the performances, especially for low outdoor temperatures, as well as for a strong undercharge. The trends are the same for every outdoor temperature, but the measurement uncertainty at 10 °C is too high to observe a significant impact.

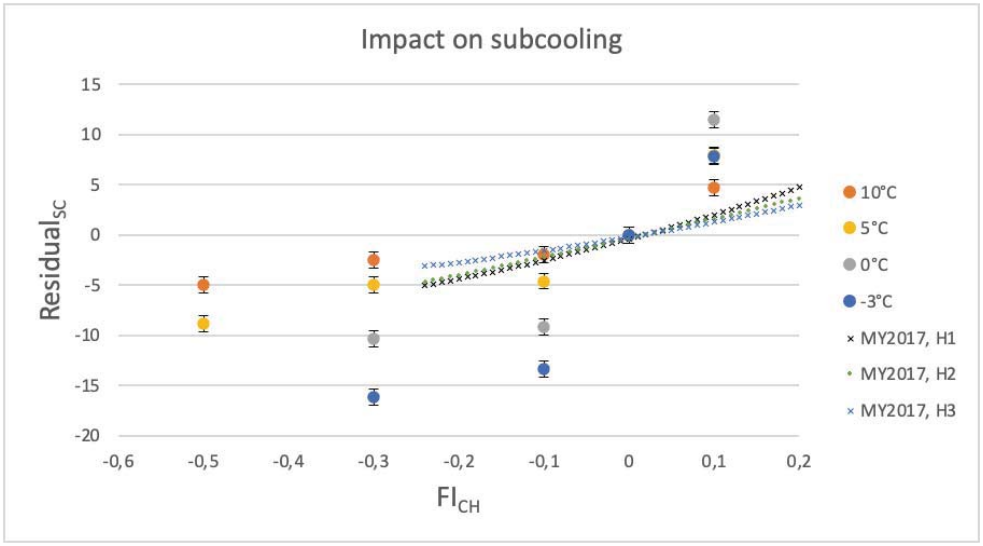

Figure 4: Refrigerant charge impact on subcooling, compared with Mehrabi & Yuill (2017a)

As figure 4 shows, subcooling is strongly and significantly impacted by refrigerant charge faults, for every climate condition tested. It decreases as the mass of refrigerant decreases. Actually, for the strongest fault (FI_{CH} = -0.5), the fluid is even diphasic at the condenser outlet, for every climate condition. The curves obtained from the regression coefficients given in Mehrabi & Yuill (2017a) show the same trends, even though the systems are different, with a fixed-speed compressor and a thermostatic expansion valve. The three conditions tested (H1, H2 and H3) are standard test conditions

(ANSI/AHRI Standard 210/240, 2008). The effect on subcooling is more pronounced for the variable speed HP. It can be explained looking at the evolution of other parameters. Figure 5 highlights the influence of refrigerant charge on condensing temperature, very similar to the influence on subcooling. Figures 6, 7 and 8 show how the HP reacts to a lack of refrigerant in order to compensate: the compressor speed increases, the EEV opens and thus the refrigerant mass flow rate increases. Then, the mass flow rate increase amplifies the impact of reducing high pressure on subcooling value. Conversely, in Mehrabi and Yuill (2017a), the effects are contradictory, as there is no action of the compressor in order to compensate the loss of heating power: the mass flow rate decreases in case of lack of refrigerant and limits the impact of reducing high pressure on subcooling.

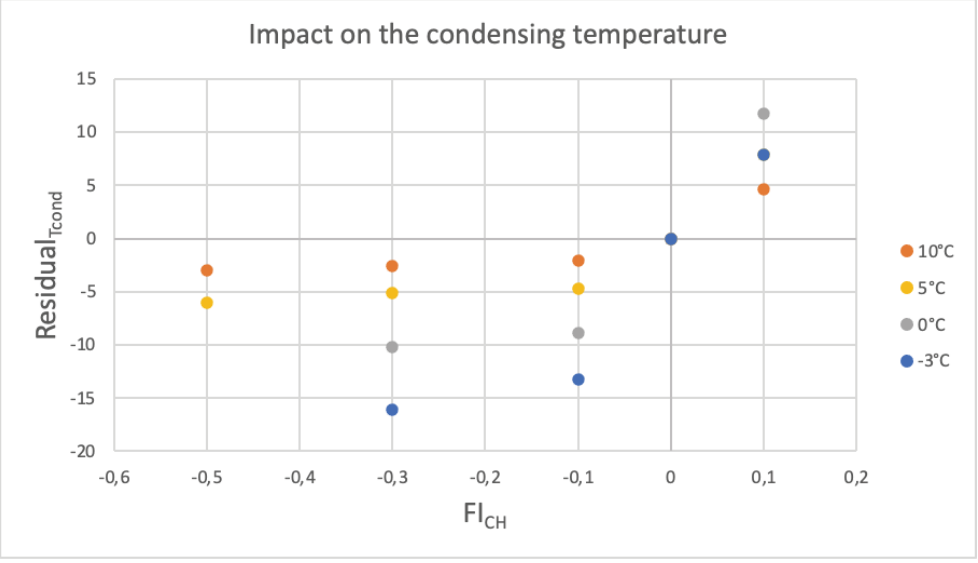

Figure 5: Impact of refrigerant charge on the condensing temperature

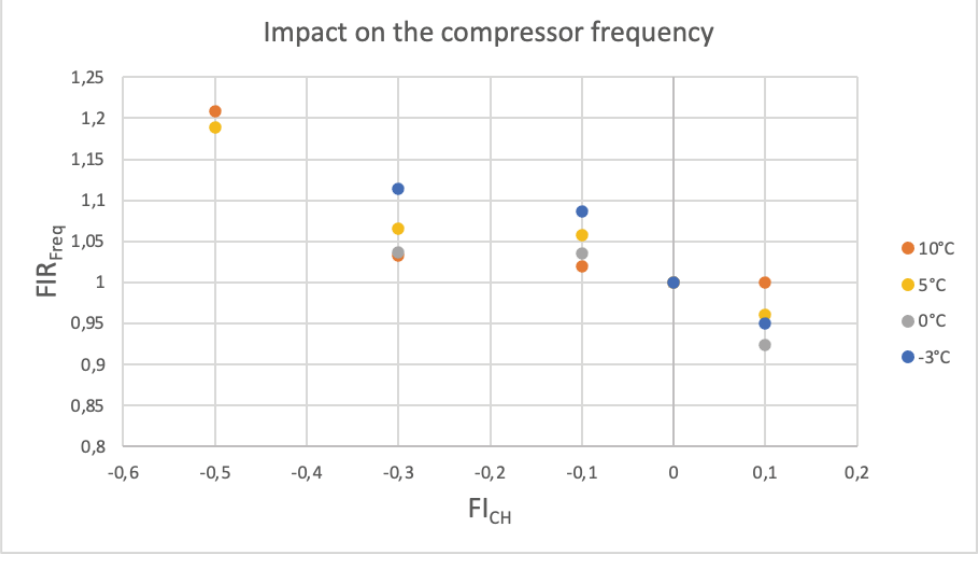

Figure 6: Impact of refrigerant charge on the compressor rotating frequency

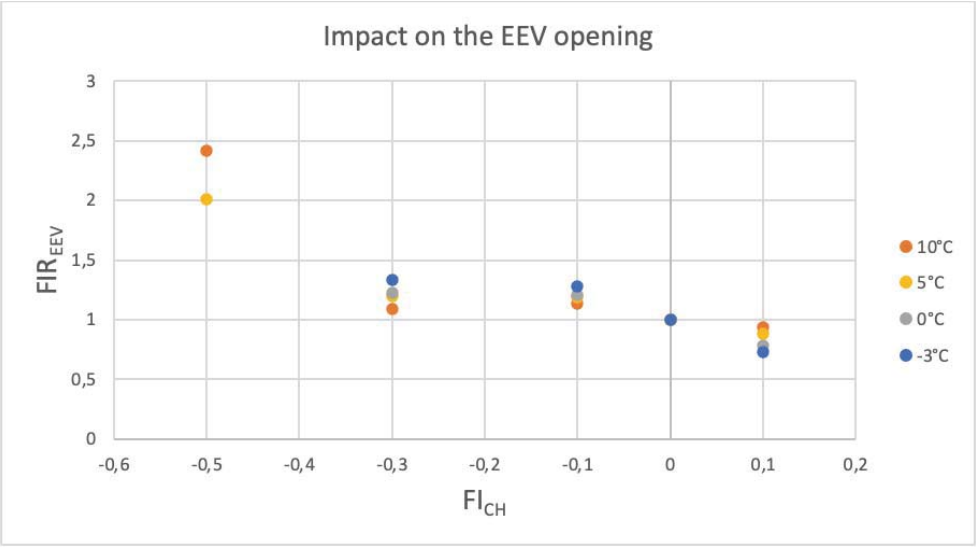

Figure 7: Impact of refrigerant charge on the EEV opening

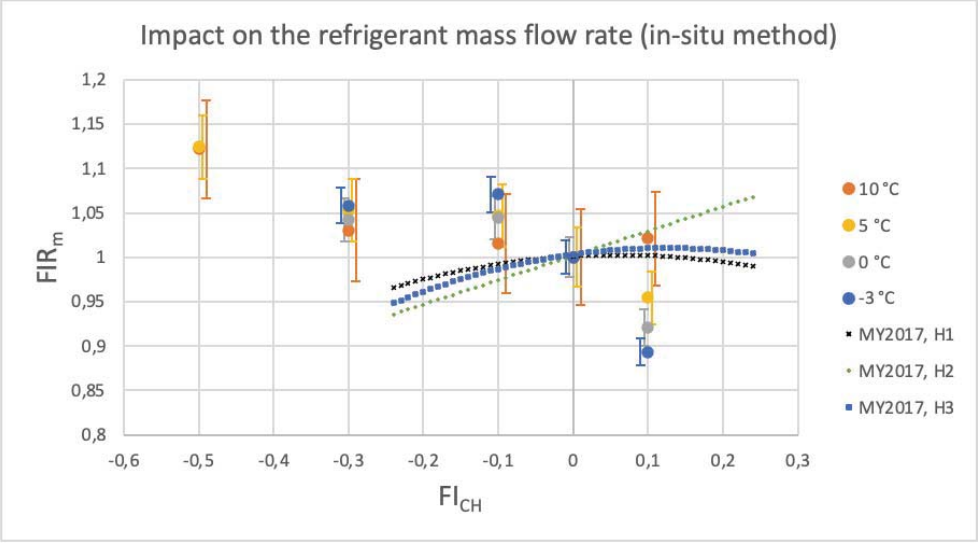

Figure 8: Impact of refrigerant charge on the refrigerant mass flow rate

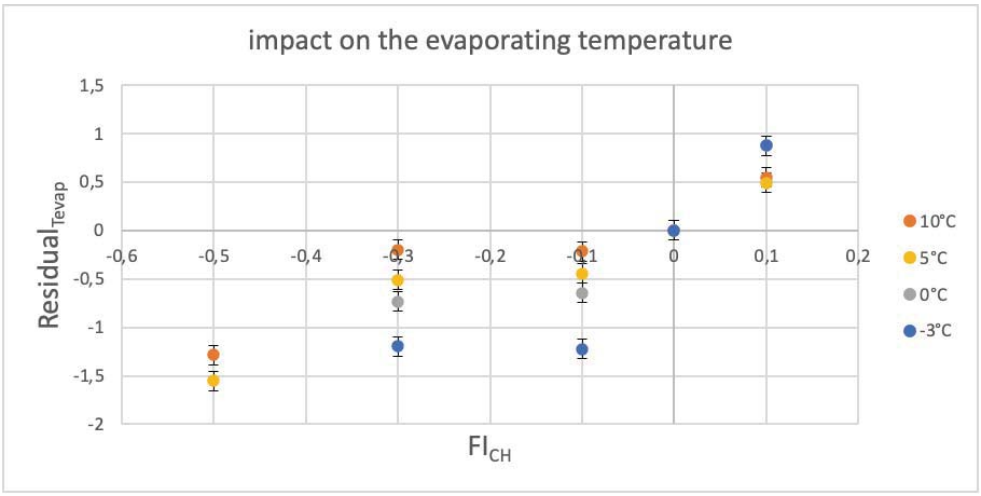

Figure 9: Impact of refrigerant charge on the evaporating temperature

The evaporating temperature increases a little as the refrigerant charge increases and conversely, decreases in case of lack of charge. It can explain why the tested heat pump was only dealing with frost and defrost cycles in case of low outside conditions.

It means that another interesting effect of refrigerant undercharge is that it can reduce the range of outdoor temperatures under which the HP can operate. Also, an overcharge leads to a higher discharge pressure and temperature and can reach safety limits at low outdoor temperatures.

3.2 Impact of evaporator fouling faults

The COP was calculated without taking into account the consumption of the fan, because it decreases as the fan speed decreases, which is not representative of a real fouling effect.

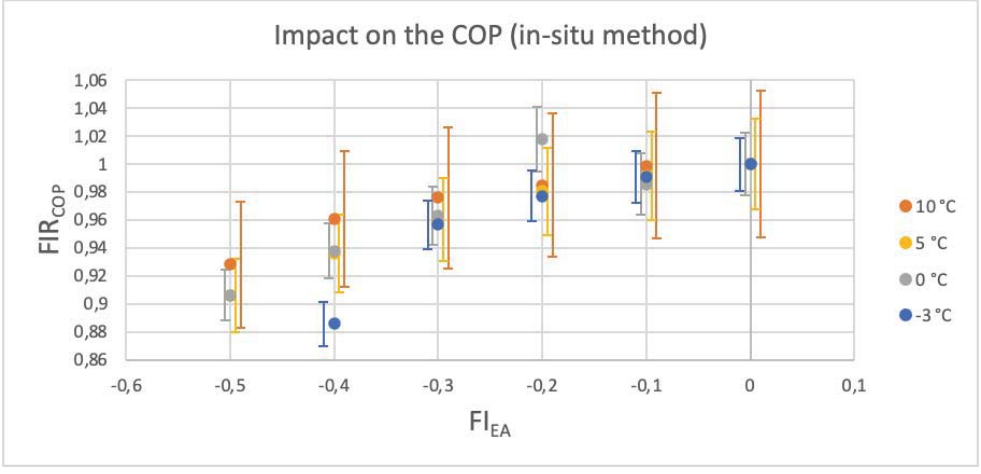

Figure 10: Impact of evaporator fouling on the COP

Figure 10 shows how reducing the air flow rate at the evaporator can affect the performances of the HP. The impact becomes significant only for the strongest FIs, especially at 10 °C for which the measurement uncertainty is not negligible.

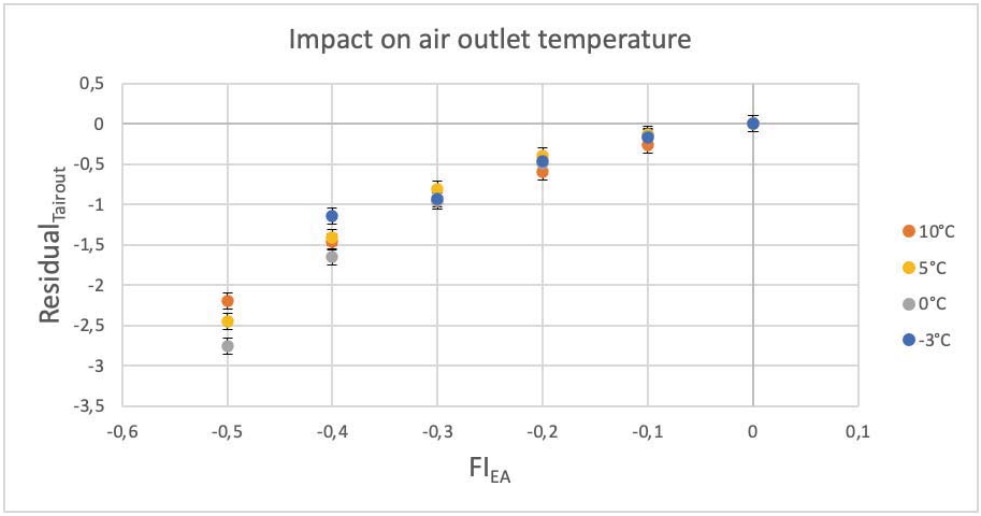

Figure 11: Impact of evaporator fouling on the air outlet temperature at the evaporator

Obviously, reducing the air flow rate at the evaporator has a direct impact on the air temperature at the evaporator outlet. This could be an easy and interesting measurement to make in order to detect this kind of fault.

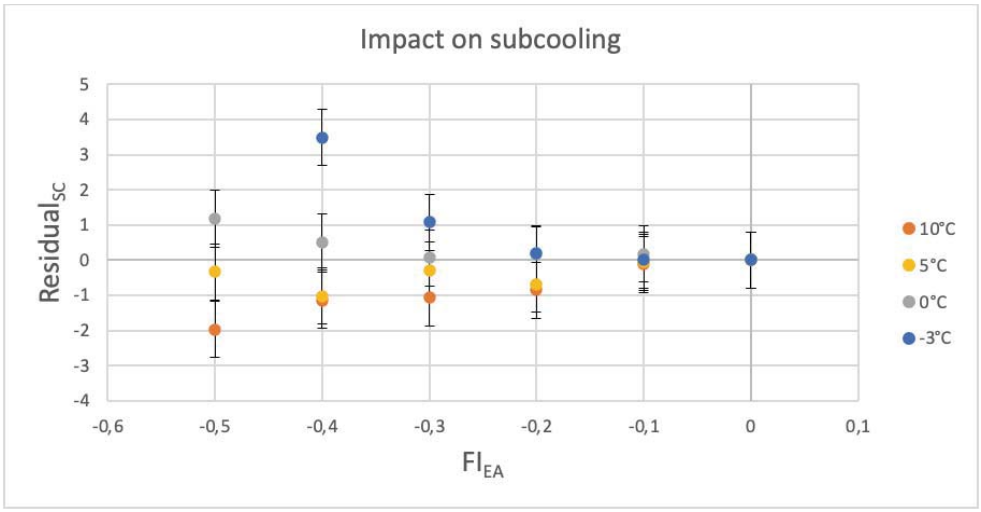

Figure 12: Impact of evaporator fouling on subcooling

As opposed to refrigerant charge variation, the effect of the reduction of the air flow rate at the evaporator on subcooling depends on the operating conditions. It increases with the reduction of air

flow rate at low outdoor temperatures and decreases for higher outdoor temperatures. It is almost not affected at 5°C.

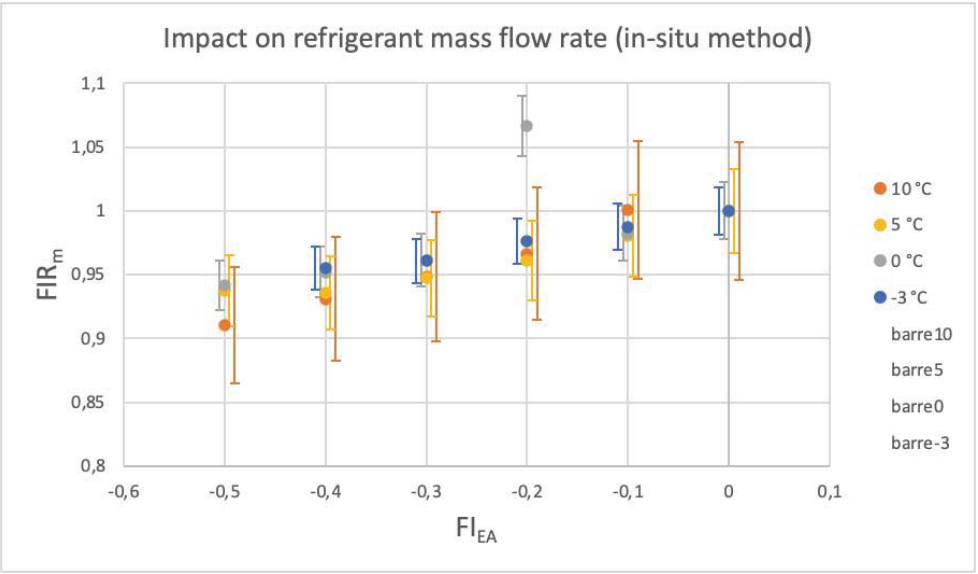

Figure 13: Impact of evaporator fouling on the refrigerant mass flow rate

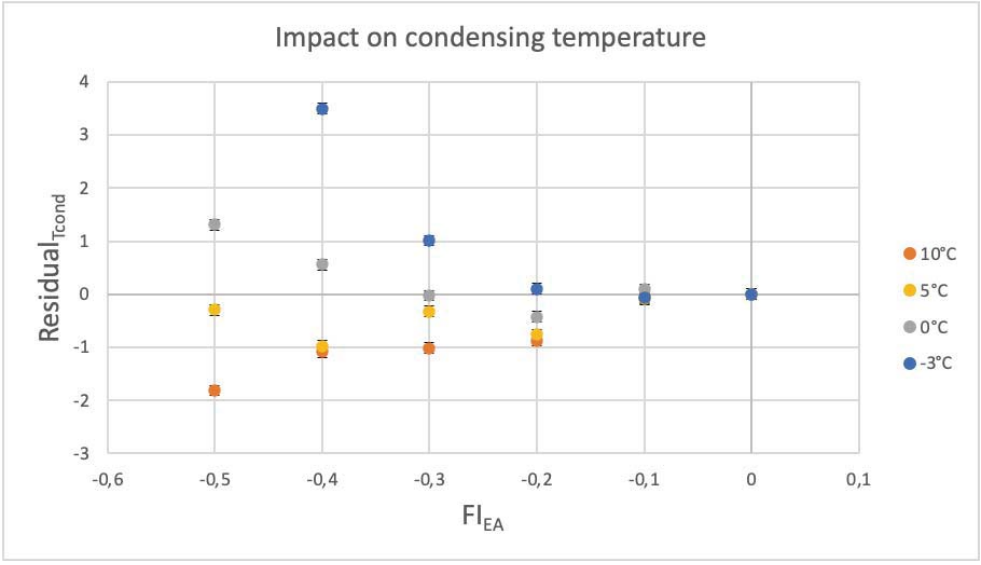

Figure 14: Impact of evaporator fouling on the condensing temperature

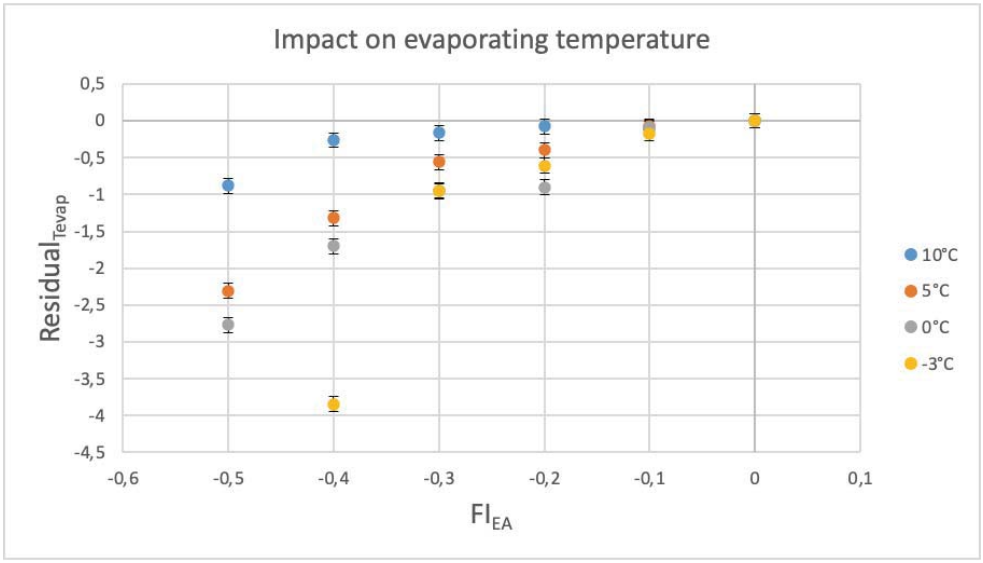

Figure 15: Impact of evaporator fouling on the evaporating temperature

As could be expected, evaporator fouling causes a decrease of the evaporating temperature for every climate condition tested.

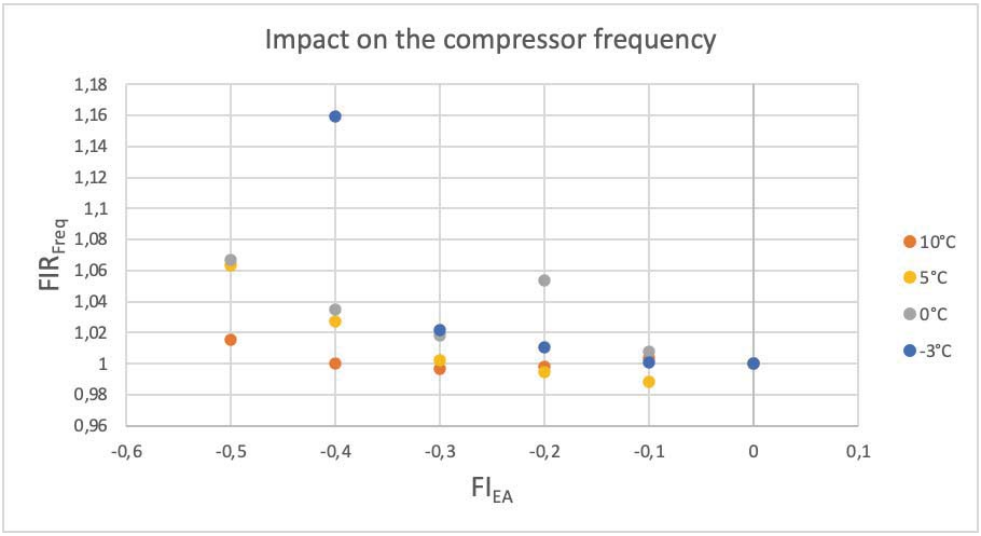

Figure 16: Impact of evaporator fouling on the compressor rotating frequency

The compressor frequency increases a little with the decrease of the air flow rate at the evaporator in order to maintain the heating power constant.

As the evaporating temperature decreases with the FI, the fluid density becomes lower. This explains the small decrease in refrigerant mass flow rate that is not fully compensated with the moderated increase in compressor frequency.

3.3 Impact of condenser fouling faults

The COP does not take into account the consumption of the circulating pump, because it decreases as the pump speed decreases, which is not representative of a real fouling effect.

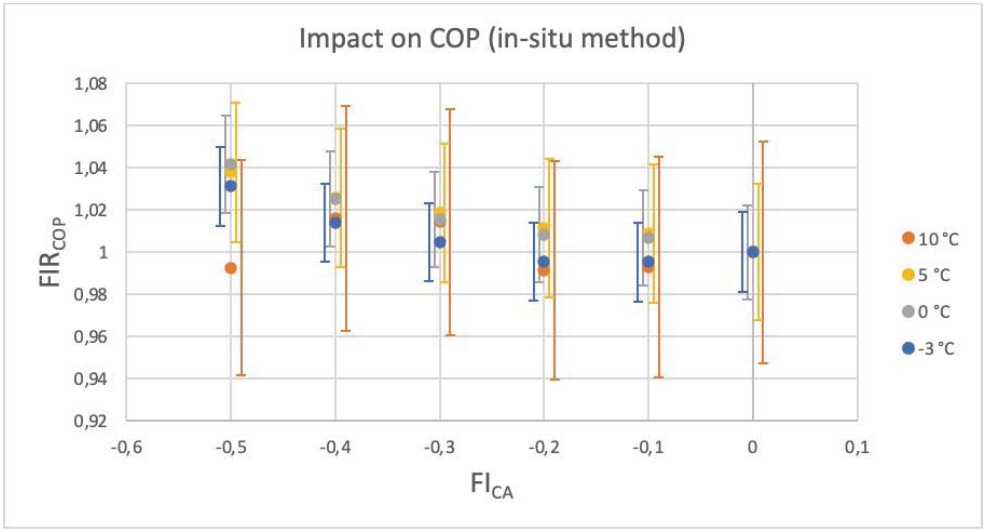

Figure 17: Impact of condenser fouling on the COP

The COP is only very lightly impacted by the condenser fouling, especially taking into account the measurement uncertainties. It shows that a variable speed HP can compensate faults to some extent. It also shows that maybe the circulating pump consumption could be reduced for high outdoor temperature and low load. Also, the small increase in the COP can be explained by the fact that in order to compare the results for the same heating capacity, as the circulating pump was slowed down, the condenser water inlet temperature was decreased. This lead to reduce the condensing temperature, as can be seen in figure 21, which contributes to a better value of COP. This is not necessarily representative of a real fouling effect, the results should then be taken carefully.

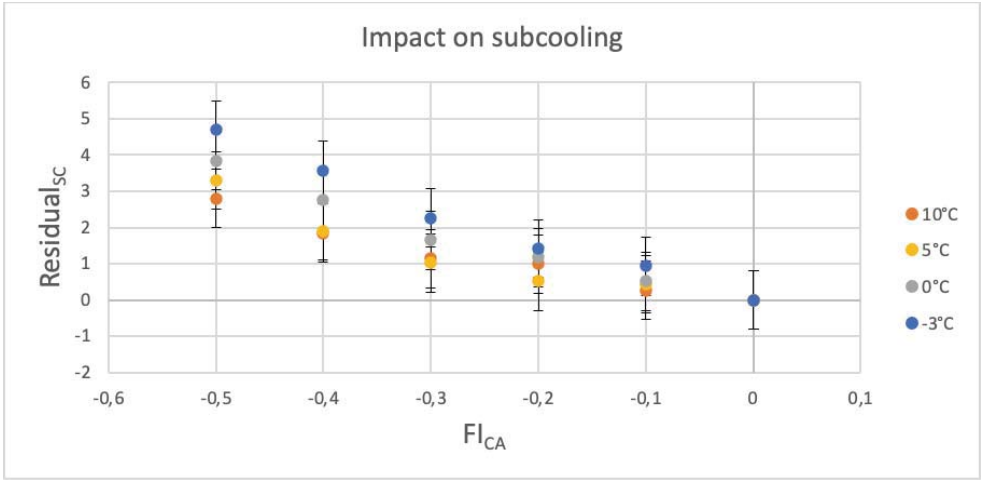

Figure 18: Impact of condenser fouling on subcooling

The effect of condenser fouling on subcooling is significant for every outdoor temperature. As opposed to the case of the lack of refrigerant, subcooling increases when the flow rate through the condenser decreases.

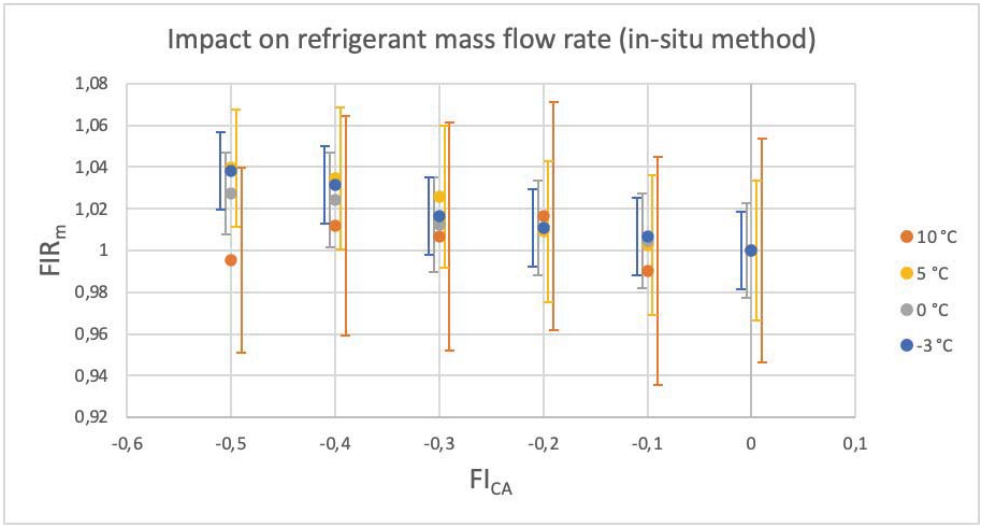

Figure 19: Impact of condenser fouling on the refrigerant mass flow rate

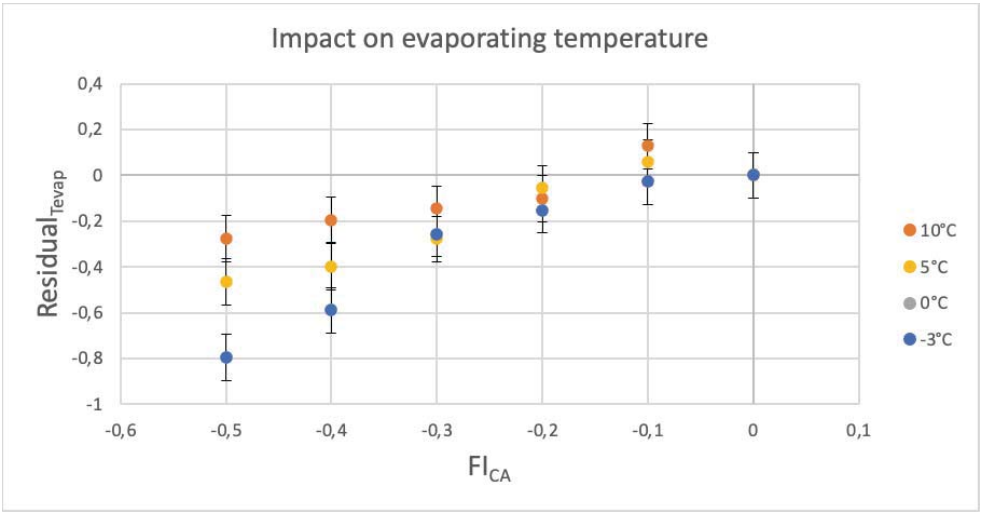

Figure 20: Impact of condenser fouling on the evaporating temperature

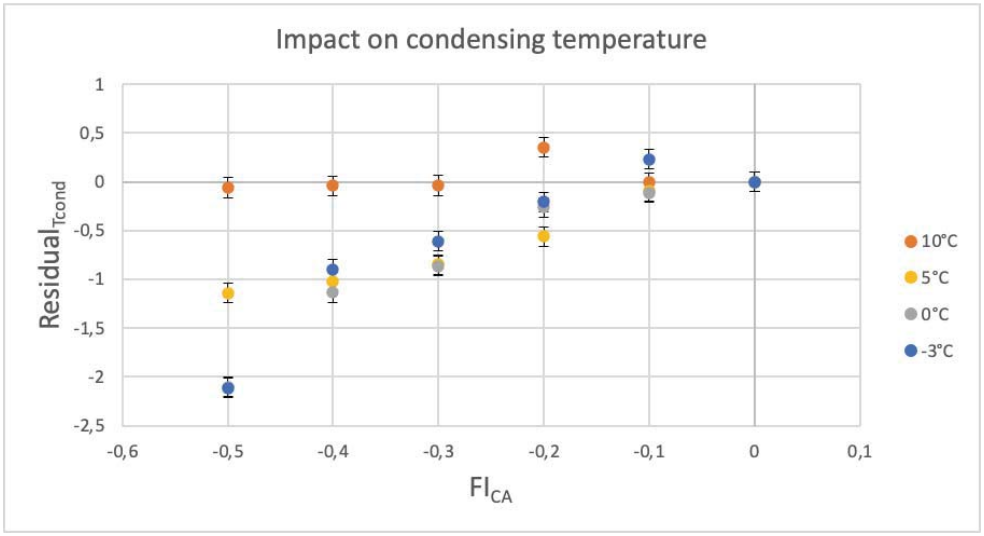

Figure 21: Impact of condenser fouling on the condensing temperature

Figure 20 shows that the reduction of the water flow rate through the condenser reduces the evaporating temperature, but not very significantly. However, figure 21 shows that the condensing temperature is strongly impacted for every temperature below 10°C.

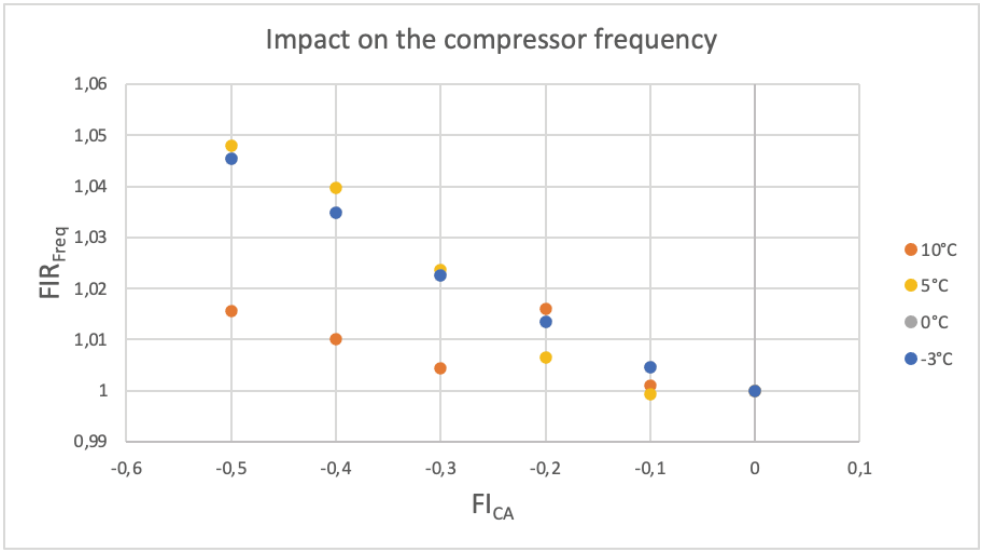

Figure 22: Impact of condenser fouling on the compressor rotating frequency

The compressor frequency increases a little with the decrease of water flow rate through the condenser as figure 22 shows, which is in accordance with the increase of refrigerant mass flow rate observed in figure 19, even though thos two effects are not very significant.

4. DISCUSSION

The following table is a short summary of the significant impacts of faults on the functioning variables of the inverter-driven HP studied, considering the measurement uncertainties:

	Refrigerant charge reduction	Evaporator air flow reduction	Condenser water flow reduction
Subcooling	Decrease	Not significant	Increase
T_{cond}	Decrease	Depends on T_{out}	Decrease, except for 10 °C
T_{evap}	Decrease	Decrease	Decrease
Freq	Increase	Increase	Small increase
EEV opening	Increase	Small increase	Not significant
$T_{air, out}$	-	Decrease	-

Table 3: Main effects of faults on the variables of the HP

Compared to fixed-speed HP, it is more difficult to characterize faults with variable speed because operating conditions affect a lot the evolution of the variables for a same fault. Also, the direct impact on the performances is reduced thanks to the compensation of the compressor. The effects in red are the ones that could allow to discriminate one fault from another. Subcooling is very interesting data to analyse as it reacts significantly and differently for condenser fouling and refrigerant charge reduction. This implies that a measurement of the condensing temperature should be made. Evaporating temperature and evaporator air outlet temperature seem very relevant in order to detect evaporator fouling. Having access to the compressor rotating frequency is very interesting in order to see how the HP reacts to faults. This measurement can be made when measuring the compressor power input.

Thus, it could be possible to detect and identify a fault from the measurements of some variables, as long as the impact is significant enough to be measurable. To go further and in order to implement an in-situ fault detection and diagnostics method, first it would be needed to make these measurements possible on field, and then, the reference values in any operating condition should be known, from physical or statistical modelling for example.

5. CONCLUSION

The experiments presented in this paper show that different faults have different impacts on the functioning variables of the HP tested. Observing a single variable might not be enough to characterize a particular fault, but a combination of the impacts on different variables can be useful to differentiate one fault from another. Therefore, the knowledge of these impacts is necessary to be able to detect faults.

This experimental work is a step towards the development of a fault detection and diagnostics (FDD) tool for residential inverter-driven HP, but it will require some other studies to make the correlations between the faults and their impacts compatible from one HP to another, especially because there can be some differences of control from one manufacturer to another, and for other types of heat pumps. Also, the HP studied uses a small plate heat exchanger as a condenser, which makes it very sensitive to refrigerant charge variations. A bigger HP or an air-to-air HP might not be as sensitive.

Moreover, for the implementation of an FDD tool on field, it will be necessary to identify what measurements can be made easily outside a laboratory. For example, measuring the refrigerant mass flow rate is challenging, that is why the in-situ refrigerant method (Tran et al. 2012 and Niznik 2017) can be very useful, to avoid the need of a heavy instrumentation.

The measured values must be compared with reference values, or unfaulted values. Knowing them can be quite challenging as the functioning variables depend on the operating conditions. A further study of existing faults detection and diagnostics algorithms, and the development of a tool to learn these values should be made, for example based on physical modelling or machine-learning.

REFERENCES

Bory, D. (2008). *Analysis and simulation of defects of operation for air conditioning audit.* (Doctoral dissertation, Mines ParisTech, Paris, France). Retrieved from https://pastel.archives-ouvertes.fr/pastel-00004297

Goossens, M., Teuillières, C., Rivière, P., Cauret, O. & Marchio, D. (2017). An Instrumented Method for the Evaluation of Compressor Heat Losses in Heat Pumps On-Field, *Proceedings of the 12th IEA Heat Pump Conference, Rotterdam, Netherlands.*

Kim, W., & Braun, J. E. (2012a). Evaluation of Virtual Refrigerant Mass Flow Sensors. *International Refrigeration and Air Conditioning Conference*. Retrieved from http://docs.lib.purdue.edu/iracc/1245

Kim, W., & Braun, J. E., (2012b). Virtual Refrigerant Mass Flow and Power Sensors for Variable-Speed Compressors. *International Refrigeration and Air Conditioning Conference*, 1–8.

Kim, W., & Braun, J. E. (2015). Extension of a virtual refrigerant charge sensor. *International Journal of Refrigeration*, *55*, 224–235.

Li, H., & Braun, J. E. (2007). Decoupling features and virtual sensors for diagnosis of faults in vapor compression air conditioners. *Int. J. of Refrig., 30*, 546-564.

Madani, H. (2016). Smart Fault Detection and Diagnosis for Heat Pump Systems, *Refrigeration Science and Technology*, International Institute of Refrigeration, 2015, p. 3703-3710

Madani, H. (2014). The common and costly faults in heat pump systems, *Proceedings of the 6th International Conference on Applied Energy – ICAE 2014* (pp. 1803-1806). Taipei City: Energy Procedia.

Mehrabi, M., & Yuill, D. (2017a). Generalized effects of refrigerant charge on normalized performance variables of air conditioners and heat pumps. *International Journal of Refrigeration*, *76*, 367–384.

Mehrabi, M., & Yuill, D. (2017b). Generalized effects of faults on normalized performance variables of air conditioners and heat pumps. *International Journal of Refrigeration*, *85*, 409–430.

Niznik, M. (2017). *Improvement and integration of the in-situ heat pump performance assessment method* (Doctoral dissertation, PSL Mines ParisTech, Center for Energy efficiency of Systems, Paris, France). Retrieved from https://pastel.archives-ouvertes.fr/tel-01753394

Noël, D., Teuillières, C., Rivière, P., Cauret, O., & Marchio, D. (2018). Non-Intrusive Performance Assessment Method for Heat Pumps: Experimental Validation and Robustness Evaluation Facing Faults. *International Refrigeration and Air Conditioning Conference*

Tran, C.T. (2012) Méthodes de mesure in situ des performances annuelles des pompes à chaleur air/air résidentielles (Doctoral dissertation, Mines ParisTech, Paris, France). Retrieved from https://hal.archives-ouvertes.fr/pastel-00765206

Tran, C. T., Rivière, P., Marchio, D., & Arzano-Daurelle, C. (2013). In situ measurement methods of air to air heat pump performance. *International Journal of Refrigeration*, *36*(5), 1442–1455.

Wichman, A., & Braun, J. E. (2009). Fault detection and diagnostics for commercial coolers and freezers. *HVAC and R Research*, *15*(1), 77–99.

Yuill, D. P., Cheung, H., & Braun, J. E. (2014). Evaluating Fault Detection and Diagnostics Tools with Simulations of Multiple Vapor Compression Systems. *Proceedings of the International Refrigeration and Air Conditioning Conference*.

NOMENCLATURE

A	area	(m²)
C_{oil}	oil concentration	
$c_{p,oil}$	oil specific heat	(J/(kg.K))
D	compressor diameter	(m)
h	enthalpy	(J/kg)
k	fluid thermal conductivity	(W/(m.K))
L	lateral compressor length	(m)
$\dot{m}$	mass flow rate	(kg/s)
$\overline{Nu}$	Nusselt number	
$\dot{Q}$	thermal power	(W)
T	temperature	(K)
$\dot{W}$	electric power	(W)
σ	Stefan-Boltzmann constant	(W/(m².K⁴))

Subscript

Amb	ambient air
avg	average
cond	condenser
comp	compressor
D,1	top surface of the compressor
D,2	bottom surface of the compressor
in	inlet
L	lateral side of the compressor
out	outlet
r	refrigerant
surf	surface of the compressor
tot	total

Abbreviations

CA	condenser fouling
CFD	computational fluid dynamics
CH	refrigerant charge fault
COP	coefficient of performance
EA	evaporator fouling
EEV	electronic expansion valve
FI	fault intensity
FIR	fault impact ratio
Freq	compressor frequency
FXO	fixed-orifice expansion valve
HP	heat pump
SC	subcooling
TXV	thermostatic expansion valve

Questions and Answers:

Abhinav Krishna:

How could you consider a liquid receiver in the system?

Derek Noël:

The studied system did not consider a liquid receiver, so the results could be a bit different, especially for the sub-cooling.

***

Abhinav Krishna:

How would you distinguish frost and evaporator fouling?

Derek Noël:

If we imagine that machine learning is used to determine reference values in every functioning conditions, the algorithm could detect whether the outdoor conditions correspond to frost conditions or not. But evaporator fouling combined with frost conditions could only be detected after a defrosting cycle, I guess.

SIXTH SESSION

INTEGRATION OF COLLECTIVE HEATING SYSTEMS IN BUILDINGS

An energetic comparison between collective heating systems and individual heating systems in apartment buildings.

M. De Pauw[1*], J. Van der Veken[3] ,F. Van Riet[2], J. De Schutter[1], I. Verhaert[2]

[(1)]Thomas More, Kenniscentrum Energie, Geel, Belgium
[(2)]University of Antwerp, Faculty of Applied Engineering, Antwerp, Belgium
[(3)]Belgian Building Research Institute, HVAC lab, Limelette, Belgium

ABSTRACT

To compare the energy efficiency of collective heating systems with individual heating systems, a simulation methodology was developed and implemented in Matlab. A branched pipe model is used to simulate the time delay and heat transfer to the environment in the distribution network. As start-up losses, part load and incoming water temperature are considered to have an influence on the efficiency of heat generation, this is also incorporated in the production model. Finally, reproducible and statistic representative domestic hot water (DHW) tap patterns, based on a survey in 600 households and verified with in situ measurements, are used as input for the simulations.

Simulations are made for apartment buildings of different scale. The energy performance and comfort level are compared for a collective 2-pipe heating system with substations and an individual heating system. Sensitivity analyses are performed on building insulation, pipe network and some other building and installation parameters.

Keywords: DHW, collective heating systems, heating efficiency

1. INTRODUCTION

Collective heating systems (CHS) make the integration of renewable energy much easier. Moreover, collective systems permit to reduce the installed power for domestic hot water (DHW). Finally, the heat production efficiency is expected to be higher compared to individual heating systems (IHS), but this can be counterbalanced by distribution losses, so that the final energy efficiency balance is difficult to assess. This paper aims to enable a comparison of the energy performance of both systems, quantifying the specific energy losses related to each system.

During the last years distribution heat losses in collective systems have been investigated. The heat losses in a collective distribution system are shown to be overestimated in the simplified calculations in the European Performance of Building standards in Europe by Himpe et al. [1]. An improved stationary calculation method based on dynamic simulations with TRNSYS, was developed by Himpe et al. [2] and was investigated by Vaillant Rebollar et al. [3]. The impact of the type of substation and different recirculation and control strategies on distribution losses was investigated by Vaillant Rebollar et al. [4a],[4b],[5].

An overall evaluation based on measurements was made by Cholewa et al. [2]. The energy performance of two different types of CHS was measured: the CHS as described above and a CHS with 2 separate distribution circuits for DWH and SH and without substations. The

efficiency was compared to a theoretical constant boiler efficiency of an IHS. Measurements inside the living units and an evaluation of the comfort level were missing.

A simulation based comparison between a CHS and an IHS in an apartment building, using the software 'Hysopt' was made by Van Riet et al. [6]. Results show that the CHS scores 6.9 percentage points lower on efficiency, compared to the IHS. Besides the CHS shows a higher controllability. However the results of the energy consumption are questionable. Fuel uptake and heat uptake at level of the apartments are higher for the IHS. Combined with large differences in temperature lack in the disadvantage of the IHS, this asks for some further research. Beside the software 'Hysopt' is primarily intended for hydraulic design purposes and has some restrictions for calculations of energy efficiency.

A new simulation methodology was developed and implemented in Matlab by De Pauw et al. [8] with focus on energy flows and time delay. The occupant behaviour is simulated with the 'Profile generator' (De Schutter et al. [7]) and consists of occupancy, internal heat gain and DHW profiles. The randomly generated DHW-profiles for each individual tapping point are based on a survey in 600 households and verified with in situ measurements. The assessment was illustrated on a case study, namely an apartment building with 6 apartments, based on a real building with an extended pipe network, but low heat demand due to a high compactness and well insulated envelope. In this particular case the IHS consumed less energy, but a general conclusion is difficult to take.

This paper aims to make an overall energetic comparison between a CHS and an IHS, including both heat losses in the distribution network and boiler efficiency. Moreover energy flows between installation components and zones are considered, which allows to determine a global efficiency on building level. The model-based approach allows to keep building and occupant parameters identical in both CHS and IHS. Starting from the model and case study described by De Pauw et al. [8], new cases are derived from the base case, varying building insulation, pipe network and building scale.

The paper starts with a short review of the simulation model, which was discusses in detail in [8] followed by a case description. The distribution heat losses and distribution efficiency of the CHS are quantified (§5.2) and the potential to improve energy efficiency of the CHS is investigated (§5.2). The boiler efficiency in an IHS and in a CHS with increasing building size is determined (§5.3). Finally the annual energy performance of both systems is compared (§5.4).

2. SIMULATION METHOD

The simulation method and Matlab component models are described by De Pauw et al. [8]. In summary the simulation model consists of Matlab functions representing boiler, pipe network, thermostatic control valves, substations, mixing valves and zones. The model of the distribution network is based on the approach as described by Van Riet et al. [10]. For each timestep water temperature and flow are calculated for every component. Since the aim of the model is to enable a comparison of energy use and comfort level of different heating systems, focus of the model is on heat losses and time delay. Hence hydraulic behaviour is simplified: the desired flows are imposed as such in the installation and the influence of pressure variation in the circuit is not taken into account. The boiler efficiency depends on the combustion efficiency, calculated skin losses and start/stop losses. The combustion efficiency is predefined as a function of the return water temperature, mass flow rate and part load ratio, based on technical data and measurements (Van der Veken et al. 2005, [9]). Start/stop losses are difficult to measure, but at each start of the boiler, a negative power equal to 1% of the maximum capacity is imposed during 1 sec.

Beside solar and internal gains from occupants, system gains are considered in the apartments, namely distribution losses from primary pipe network (through the pipe ducts of the CHS), distribution losses from tapping ducts (IHS and CHS), heat losses from substations (CHS) and skin losses from boiler (IHS).

Beside energy use, also the comfort levels are compared between the different cases. Discomfort for space heating (in Kh) is defined as $\int_{t_1}^{t_2}(T_{sp} - T_{op})dt$ for Top<19°C (Tsp is the setpoint temperature and Top the operative temperature of the apartment). To assess the DHW comfort, the response time to reach the comfort temperature (e.g. 38°C) is calculated for each tapping and the instances are counted where this waiting time exceeds 30sec.

3. CASE DESCRIPTION

The different cases are based on an existing apartment building, as described by De Pauw et al. [8], from which only 6 apartments on 3 floors are considered to limit simulation lead times. Basically all building parameters and most of the installation characteristics are retained from the real building, except for the boiler size since it would be oversized for our 6 apartments and except for the main piping length, which was optimized.
From this base case other variants are derived, adapting:

- the building size (6-18-36 apartments in one block).
- the compactness of the distribution network for the collective systems
- the heat demand for space heating of the building (by adapting the insulation level and ventilation system)

The variants with 18 and 36 apartments are obtained by concatenating the base case a multiple times in horizontal or vertical direction. The building envelope is assumed to be the same for each block of 6 apartments, which is a theoretical hypothesis to enable a straight forward comparison.

The horizontally and vertically extended distribution network are schematically represented in Figure1. The average pipe length per apartment is independent of the building size, and equal to 6m (single) per apartment for the horizontal (‘6m/aprt’) and 2m (single) per apartment for the vertical network (‘2m/aprt’).

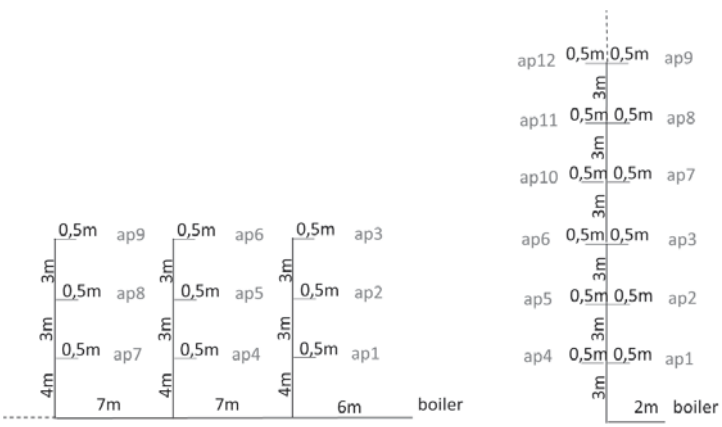

Figure 1: Horizontal and vertical pipe network

In the bas case (‘B1’) all apartments are well insulated, airtight and very compact. Emitters are a bit oversized, nominal power of the emitters in 1 apartment is 3.3kW (1.4kW compensating for transmission and ventilation losses and 1.4 kW for warming up). To investigate the impact of heat demand of the building, but restricting our research to recent buildings meeting the actual building standards, building envelope and ventilation system are adapted (‘B2’) in such a way that a nominal power of 4.4kW (3 kW transmission and ventilation losses) is required in each apartment.

The boiler size in the CHS is based on DIN4708. This standard prescribes a method to determine the boiler size to provide DHW in collective buildings considering the simultaneity for DHW. For the case with 18 apartments a boiler of 90kW was derived based on this standard. Also the simulations didn’t show any comfort issues (as defined in §3). The 36 apartments case, however, would need a boiler of 150 kW according to the standard, but the simulations show a slight discomfort for DHW. Indeed, with increasing building size the heat capacity for space heating becomes more important in relation to the heat capacity for DHW. Although in this case the required power for DHW (150kW) is still greater than the required power for space heating (circa 120kW), the increased relative importance of the latter can explain why sizing the boiler based on DHW alone might not be satisfying. Therefore a boiler of 180kW was selected for the building with 36 apartments. In the IHS the boiler is a lightweight combi-boiler of 30kW, which is required for DHW but oversized for SH.

Table 1 gives an overview of the different boiler parameters for the cases with 1, 6, 18 and 36 apartments. The parameters are based on manufacturer data.

Table 1: boiler parameters.

#aprts	P_{max} (kW)	P_{min} (kW)	C_{boiler} (kJ/K)	$T_{setpoint}$ (°C)	UA (W/K)	T_{max} (°C)	ΔT_{max} (°C)	$t_{run,min}$ (s)	$t_{off,min}$ (s)
36	180	45	600	70	11	95	-	300	0
18	90	22.5	600	70	6	95	-	300	0
6	60	15	360	70	6	95	-	300	0
1	30	7.5	20	70	4	95	50	300	0

The occupant behaviour is generated with a tool based on [7] (De Schutter et al. 2018). Each apartment is coupled with one of the possible family types and occupancy and DHW-profiles are generated for that type. To create enough spread on the demand profiles, and thus a realistic simultaneity, the family types are maximally distributed.

4. RESULTS AND DISCUSSION

First the results for the base case are compared to the results of the simulation in EES (§5.1). Afterwards an evaluation is made of the distribution efficiency in a collective heating system (§5.2), and of the boiler efficiency in the CHS and in the IHS (§5.3). Finally the overall energy efficiency of both systems is compared in §5.4.

4.1 Comparison with EES.

In contrast to the Matlab model, the EES model contains pumps and primary valves with proportional control laws; pressure drops in the different components are considered. The case with 6 apartments was simulated in EES for a period of one day. The radiator flow rates

and the secondary flow rates of the heat exchangers in the substations, as identified by the Matlab model, are input variables in EES. Figure 2 represents the integrated energy flow rates identified in the Matlab and the EES model.

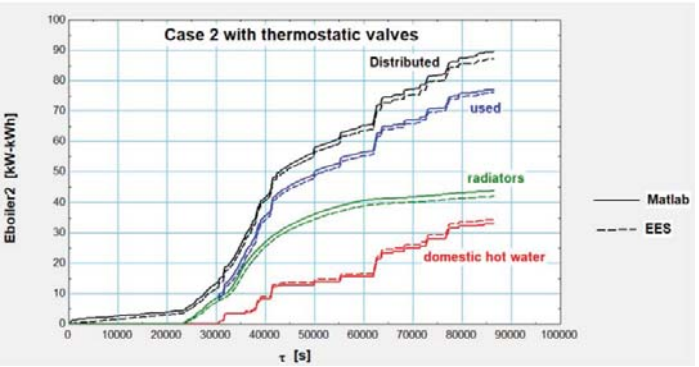

Figure 2: Comparison Matlab-EES

4.2 Distribution efficiency in a collective 2-pipe heating system.

Basically the distribution efficiency is investigated for the case with 6 apartments. Since the cases with more apartments are obtained by copying the 6 apartments horizontally or vertically, the distribution losses are expected to change approximately proportional.

4.2.1 Quantification of distribution losses.

Simulations are made for different pipe length (2 and 6m/aprt, single) and insulation (0 and 3cm) and for different heat demand (building 'B1' and 'B2' as described in §4.).

The boiler setpoint temperature is 70°C, emitters for space heating are dimensioned on a 65/30 regime and the DHW heat exchangers in the substations with variable flow control have a set_point of 50°C. The temperature in the shaft is supposed to be constant at 20°C. The average temperatures during the simulation period in the distribution supply network Tm,sup and in the distribution retour network Tm,ret are calculated from the simulation results. In January Tm,sup is circa 65°C and Tm,ret depends on the heat demand of the building, varying between 33°C in B1 and 28°C in B2. In July Tm,sup is 59°C, as a result of a lower average boiler temperature, and Tm,ret is 43°C, mainly determined by recirculation.

The distribution losses for the different simulations are represented in Figure3. It is clear that the amount of distribution losses depends principally on the pipe insulation, and to a lesser extent on the distribution network form: the horizontal distribution network is longer and will show more distribution heat losses in total, but the pipe diameters (based on the real building) are smaller, for the same insulation thickness, which causes less distribution losses per m.

In July distribution losses are greater than in January because of the higher retour temperatures due to the working of the thermostatic valves: retour temperatures in July seem on average 12°C higher than in January. In January the retour temperatures are lower with increasing demand for space heating. The average temperature in the retour network is circa 5°C lower in B2 compared to B1. Effect on distribution losses is negligible, except for the case 6m/aprt without insulation.

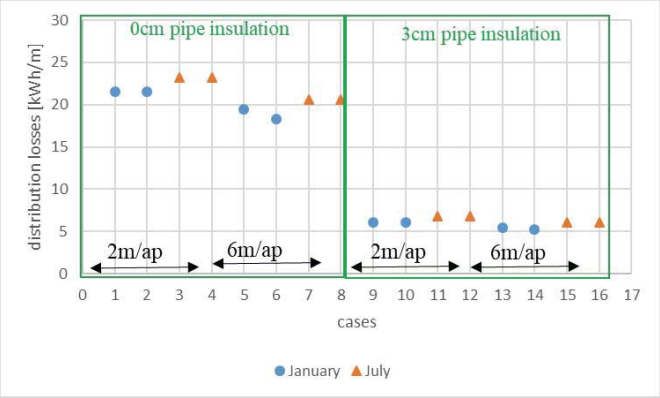

Figure 3: distribution losses per meter pipe length for building B1 and B2.

4.2.2 Reducing distribution losses.

With a given length and insulation of the distribution network, distribution losses can be reduced in different ways. Some variants are made on the reference case as described in §4.

1. Substations are used with variable primary flow ('VF') instead of a constant primary flow: the primary flow is adjusted to the hot water temperature at the secondary side of the heat exchanger.
2. Parameters of the thermostatic control valves (temperature, flow, working time) ('THV') are changed: temperature from which they open (40°C and 35°C instead of 45°C), the maximum flow (0.01l/s instead of 0.1l/s), the working time (not at night or not at all instead of continuously)
3. Smaller pipe diameters ('D') are used, since the diameters of the reference case are based on 'Ecodroom' and approx. 5mm larger than prescribed in the standard DIN1988 and based on an imposed water speed. It was verified with simulations in EES that the smaller diameters didn't cause hydraulic problems in the installation.
4. The installation is operating at lower temperatures ('LT'). To investigate the impact of an installation at lower temperature, the setpoint temperature of the boiler was set to 50°C (instead of 70°C). This might be inadequate to reach the required temperatures at the mixing valves. As if focus is on distribution losses, this problem was resolved in a very simplified way by adding an electrical resistance in order to obtain the setpoint temperature for DHW of the substation.

In what follows, measures are represented by the abbreviation above. The impact of a combination of measures is investigated too, namely 'VF', 'THV' and 'D', and referred to as 'C'. To evaluate the impact of the aforementioned measures different cases are simulated, all with an insulated pipe network, and varying the heat demand (building B1 and B2), the pipe length (2m/aprt and 6m/aprt) and the period of the year (January and July). In Figure4 the distribution heat losses resulting from those simulations, are represented as a percentage of the distribution heat losses in the reference case (without any measures).

Concerning the thermostatic valves at the top of the risers, it was verified that the modifications of the control parameters as described above, didn't cause any time delay >30sec at the tapping points. If this was the case, the measures were not included in the results shown in Figure4.

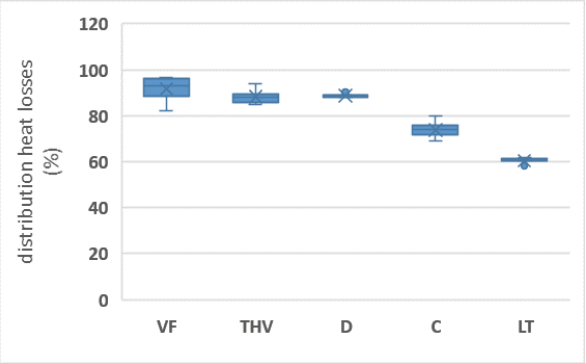

Figure 4: distribution heat losses as percentage of reference case

The most profit is taken from an installation at low temperature ('LT'). For a boiler setpoint of 50°C instead of 70°C, distribution losses decrease with about 40%.

Other measures have each individually limited impact on distribution losses (between -2% and -18%), when combined distribution losses can be reduced with circa 30%. There is a higher variability in the effect of measures causing a decreasing return temperature from heat exchanger of the substation ('VF','C') or from the thermostatic control valves ('THV','C'). They have more impact with decreasing importance of space heating, for instance in July and in building B1. But when there is an important flow for space heating (like in building B2), return temperatures are primarily determined by SH and the impact of these measures is less pronounced. Hence variable flow has more impact on the distribution losses in July, less in January in building B2.

At last it should be noted that the emitter regime has impact on the distribution losses too. In the simulations performed, the retour temperature in January is low (25 to 35°C) due to the SH-regime of 65/30 and the fact that the emitters work mostly at <50% of their full power (3.3kW) (see§4). If emitters of 1.5kW are selected for a regime 65/55, retour temperatures increase to 40°C and distribution losses with 15 to 20% (depending on building and pipe network). The impact of the emitter regime could be further investigated, but it is not part of this article.

4.2.3 Distribution efficiency

The distribution efficiency can be defined as the amount of energy leaving the substations (to emitter or mixing valves) related to the total energy entering the distribution network (Eq(1)). This definition takes the distribution pipes as the system boundary and the heat leaked towards the shaft as a loss, which could also be regarded as a ventilated shaft with no heat flowing towards the building.

$$\eta_{distr,syst} = \frac{energy\ leaving\ substations}{energy\ entering\ distribution\ network} \quad (1)$$

The total amount of distribution losses during the simulation period of 1 month and the distribution efficiency as defined in (1), for the simulations discussed in 5.2.1 and 5.2.2, is represented in Figure5 (no pipe insulation) and in Figure6 (3cm pipe insulation). 'C' represents the combined case with reduced distribution losses as described in §5.2.2.

The distribution efficiency depends on the total amount of useful energy for SH and DHW. It is clear that for the same distribution network, the distribution efficiency is higher in January in B2, with the most heat demand, and lower in July, when heat demand is lowest.

Figure 5: distribution heat losses and distribution efficiency (no pipe insulation)

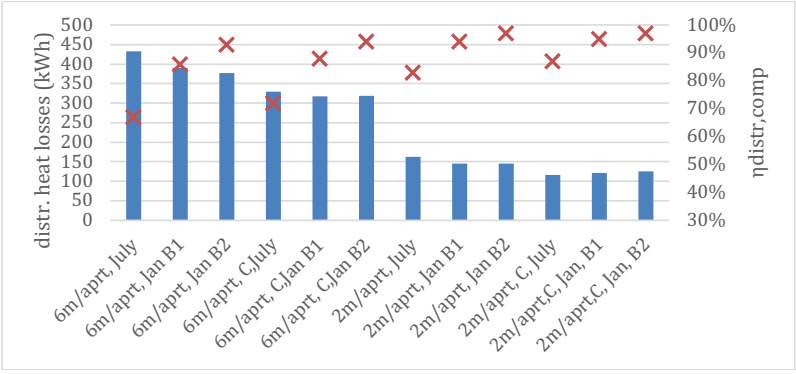

Figure 6: distribution heat losses and distribution efficiency (3cm pipe insulation)

With 3cm pipe insulation distribution efficiency is always higher than 80% and going up to 98%, except in July and for the horizontal (less compact) distribution network (67% and 72%). With a compact network efficiency in July is between 83% and 89%, in January in B1 94% to 95%, and in B2 97%. It is clear that the impact on efficiency of the measures described in 5.2.2 is not significant during the heating season.

Without pipe insulation the distribution efficiency drops below 80% and even towards 38% in July for the horizontal network. In January the distribution efficiency can exceptionally rise above 80% for the compact distribution form.

4.2.4 Impact of distribution losses on energy use.

When the technical shaft is not or only partly ventilated, and with a limited thermal insulation between shaft and protected volume, the distribution losses become partly internal 'system' gains in the apartments. They can lower energy use for space heating, depending on the

immediate heat demand and the thermal mass of the apartments. The definition of distribution efficiency as in Eq(1) does not consider this recuperation of distribution losses at building level. Hence a new definition Eq(2) is used, comparing the energy use without any distribution losses to the energy use including the pipe losses, but neglecting boiler losses in both cases.

$$\eta_{distr,build} = \frac{energy\ use\ without\ distribution\ losses}{energy\ use} \quad (2)$$

The numerator in Eq (2) is determined by simulations with infinite pipe insulation. In Table2 the results of a simulation for B1 with pipe length 6m/aprt are represented for both 3cm and almost infinite pipe insulation. In January the distribution of the base case leaks 390kWh heat towards the shaft, from which 90% is assumed to be recovered in the apartments. Thanks to this heat flow the energy demand for SH is lowered with 303 kWh (1565kWh instead of 1868kWh). Due to the recuperation of the heat losses, the distribution efficiency at building level is thus 97%, compared to 86% at system level.

Table 2: simulation results with 3cm and with infinite pipe insulation

pipe insulation	**pipe insulation**	
[m]	**3cm**	**infinite**
net energy use SH (kWh)	1565	1868
net energy use DHW (kWh)	914	915
distribution efficiency at system level ()	0.86	1.0
distribution heat losses (kWh)	390	0
energy entering distribution network (kWh)	2889	2804
boiler efficiency()	0.85	0.86
fuel consumption (kWh)	3384	3279

Table 3 illustrates the difference between the distribution efficiency at system and building level for simulations where it is relevant, namely during periods with a heat demand (January) and when distribution losses can be regained (shaft is part of the protected volume). Distribution efficiency at building level is mostly better than 95%, except for the (extreme) case with an extended distribution network, without insulation and a building with very low heat demand, so that the pipe losses often exceed the heat demands. Concerning the measures to reduce distribution losses, it is noticeable that, despite the reduction of distribution losses (5.2.2) , there is not much room for improvement of the efficiency at building level.

Table 3: distribution efficiency at system and building level (January)

pipe insulation	**pipe length**	**building env.**	**distribution efficiency**	
[m]	**[m/app]**		**system**	**building**
0	6	B1	55%	87%
0	6	B2	78%	96%
0	2	B1	82%	95%
0	2	B2	91%	98%
0,03	6	B1	86%	97%
0,03	6	B2	93%	99%
0,03	2	B1	94%	98%
0,03	2	B2	97%	99%
0.03	2 (*1)	B1	95%	99%

0.03	2 (*1)	B2	97%	99%
0.03	2 (*2)	B1	96%	99%
0.03	2 (*2)	B2	98%	99%

(*1) with combined measures 'C' as described in 5.2.2
(*2) low temperature 'LT' as described in 5.2.2

If there's no heat demand, outside the heating season, distribution losses can't be regained as useful gains, and distribution efficiency at system level applies. Moreover, the simulations show that the summer discomfort increases with increasing distribution losses in the protected volume.

4.3 Boiler efficiency in a collective 2-pipe heating system and in an individual heating system.

As described in §3, the boiler efficiency depends principally on the combustion efficiency ($\eta_{combust}$) and the skin losses (η_{skin}), which will be discussed separately. In fact, both skin losses and start/stop losses are included in the water-side boiler efficiency η_{skin}, but start/stop losses turned out to be negligible compared to the skin losses.

In analogy to §5.1.2, recuperation of heat losses from the boiler as internal gains in the apartments, insofar the boiler is situated in the protected volume, is considered. As well as for the distribution efficiency, a new definition is used for the boiler efficiency, comparing the energy use without boiler losses to the real energy use. The energy use without boiler losses is calculated based on a simulation with infinite boiler insulation.

$$\eta_{boiler,build} = \frac{energy\ use\ without\ boiler\ losses}{energy\ use} \quad (4)$$

It should be noted that the boiler of the CHS is assumed to be outside the protected volume, while the individual boilers are situated in the protected volume.

4.3.1 Skin losses in a CHS.

For the collective heating system, the impact of building size is investigated based on simulation results for a building with 6, 18 and 36 apartments. The installation is conceived as described in §4 and option 'C' in §5.2.2 (with a variable primary flow, diameters according to DIN, and thermal valves with max flow 0.01kg/s).

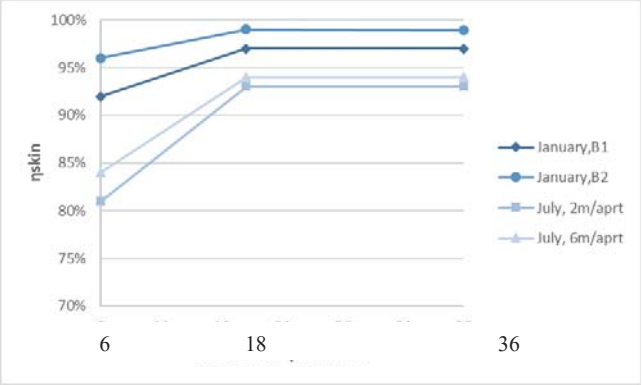

Figure 7: water-side boiler efficiency in CHS

Figure 7 shows an improvement of the water-side boiler efficiency η_{skin} in larger buildings, which is caused by a decreasing relative amount of skin losses. This is most pronounced in cases with lower heat demand, as in January in building1, where water-side boiler efficiency increases from 92% to 97%, or certainly in July, where boiler efficiency increases from 81% to 93% (2m/app) and from 84% to 94% (6m/app). It should be noted that these percentages give just an indication and depend on the assumed value for the specific skin losses of the boiler (see § 4).

In fact, since the mean boiler temperature is similar in all cases, the difference in efficiency depends on the relative amount of specific skin losses (kW/K) for the different boilers. When interpreting the results, it should be considered that the link between specific skin losses and power is not straight forward for all types of boiler (Figure 8), and the boiler for 36 apartments might be a bit oversized.

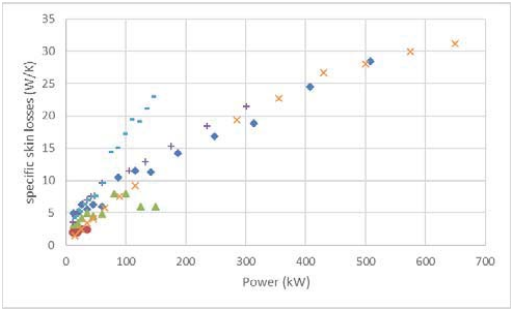

Figure 8:specific skin losses boiler

However, since in general boiler size is not increasing proportional to building size, due to simultaneity, and skin losses are not increasing proportional to boiler power (Figure 8), the amount of skin losses compared to the total heat demand will anyway decrease with increasing building size.

4.3.2 Skin losses in an IHS.

In case of an IHS, skin losses of the individual boilers in each apartment are added up, resulting in a lower efficiency compared with a CHS. On the other hand, the individual boilers are located in the protected volume, which allows to recuperate the skin losses.

During the heating season, water-side efficiency at building level is higher than 97% for the IHS (89% and 93% at system level for respectively B1 and B2). Outside the heating season the skin losses have no useful contribution and water-side boiler efficiency is lower. Beside, since heat demand only consists of the scattered DHW demand of a single dwelling, the total amount of skin losses of an individual boiler is affected by the capacity of the boiler. A lightweight boiler can cool down rapidly between different tappings. On the one hand this has positive effect for the skin losses. Indeed, the mean boiler temperature of the IHS is quite low in July, circa 30°C (see Table 4). On the other hand it must be noticed that the time delay of the tappings depends on the boiler start-up delay. In the simulations the latter was assumed to be 10 sec, which is probably a positive assumption, leading to a mean time delay of 30 sec. For a heavy boiler (150kJ/K instead of 20kJ/K), mean boiler temperature is increasing from 28°C to 37°C, leading to a water-side boiler efficiency of 71% instead of 84% for the lightweight boiler. Hence, looking at Table 5, there is apparently a problem with discomfort. 34 tappings per apartment have a time delay >30sec. At first sight this seems better than with a lightweight boiler, but the heavy boiler leads to more unacceptable extrema: 18 tappings are interrupted (§3), the maximum waiting time is 348sec. Hence it seems necessary to impose a function to keep the boiler warm ('WF'). This leads to a mean boiler temperature of 50°C and a boiler efficiency of 61% (Table 4), but comfort is significantly improved (Table 5). Although, best comfort is still attained with a collective system (Table 5).

Table 4:building1, individual, July

	Tboiler	**Qskin loss**	**ηwater-side**
	°C	kWh	%
lightweight boiler	28	201	**84**
heavy boiler	37	369	**71**
heavy boiler WF	50	537	**61**

Table 5:discomfort DHW per aprt, individual, July

	mean time delay	**max time delay**	**# >30sec**	**# interrupted**
	sec/aprt	sec/aprt	#/aprt	#/aprt
lightweight boiler	30	265	76	2
heavy boiler	32	348	34	18
heavy boiler WF	10	144	7	1
CHS	13	25	0	0

4.3.3 Combustion efficiency.

The simulations of the CHS show that in January, return temperature (circa 25°C), mass flow rate (circa 0.0026 kg/kJ) and PLR (30 a 40%) are not significantly influenced by building size, building insulation or pipe network. Combustion efficiency is always circa 95%. In July return temperatures can be higher, especially in the case of a short pipe network, and this results in decreasing combustion efficiency. The worst case is the building with 6 apartments

and a pipe network of 2m/aprt, where return temperature is 44°C, but even there combustion efficiency is still 92%.

In the IHS the part load ratio is higher, but also return temperatures are higher, both having an opposite effect, and thus resulting in similar combustion efficiencies (91%-95%).

The fact that in the CHS the mean PLR seems independent of the number of apartments is investigated in Figures 9 and 10. Figure 9 represents the PLR of the boiler and the total demand at the substations for 1 day of the simulation for the case with 6 and with 36 apartments in January in B1. In both cases the mean PLR resulting from the simulations is 30% and indeed, in both cases the boiler works mostly at minimum power (PLR=25%).

- The total heat demand for space heating is mostly lower than Pmin (3 to 4kW versus 15kW for 6 apartments and 20kW or less versus 45kW for 36 apartments), so during periods with only space heating the boiler is going on and off to its min power.
- When there is a demand for DHW, the required power is mostly 20 to 30 kW, so just for one tapping. PLR is then going to 1 for a few seconds, returning to Pmin during the rest of the tapping.
- In the case with 36 apartments, there is a short period in the morning (circa 0.5h between 7h and 8h) with multiple tappings occurring simultaneously, where the boiler is working permanently.

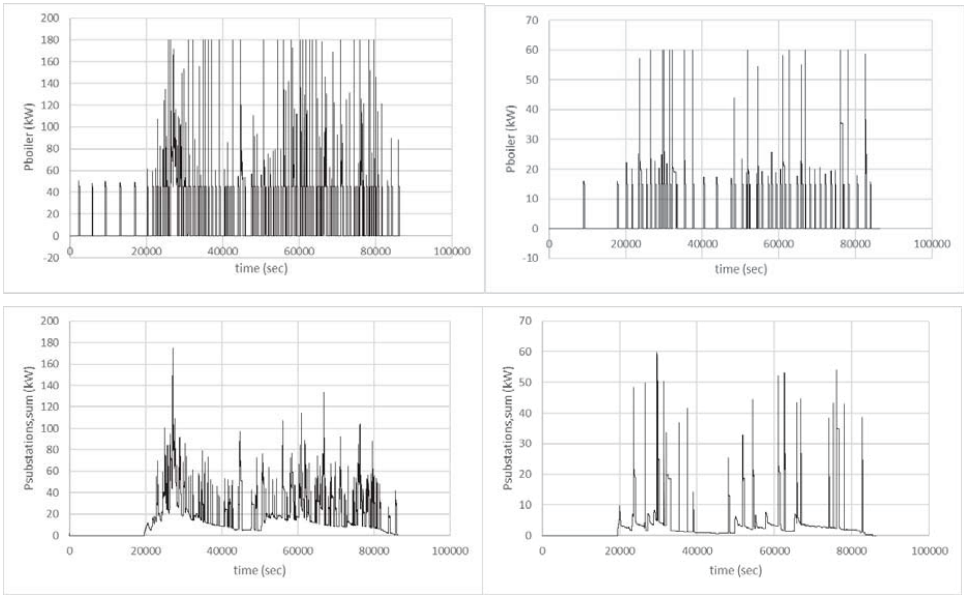

Figure 9: power of boiler and sum of substations, for 36 apartments (left) and 6 apartments (right), B1, January, 1 day

In B2 total demand for space heating will be higher (up to 60kW, see Figure 8), causing a higher PLR. In Figure 10 it can be seen that the boiler is evolving to a more permanent working.

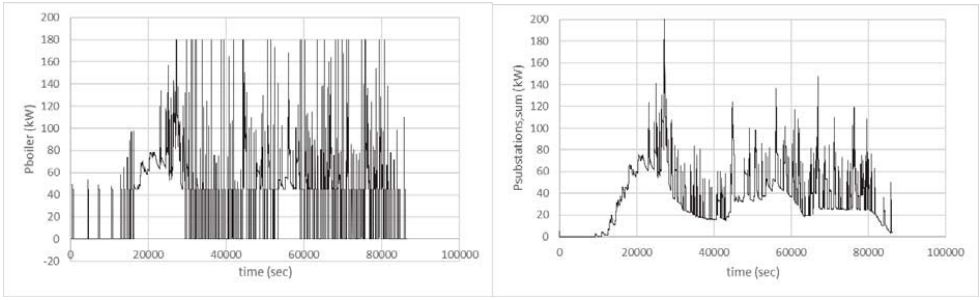

Figure 10: power of boiler and sum of substations, for 36 apartments, B2, January

A PLR > 40% can be expected in buildings with increasing relative demand for space heating, so less insulated buildings or buildings with more apartments. Due to simulation lead time buildings with more than 36 apartments are not yet simulated.

In the building with 36 apartments, the relative (to the total energy use) number of start stops is reduced significantly (with a factor 3.6) , but this is not reflected in the results: the energy losses at each start of the boiler are assumed very low (see§3) and have therefore no influence on total energy use.

4.3.4 Total boiler efficiency

Table 6 and 7 provide an overview of the total boiler efficiency (at component and at building level) as a result of the different simulations, as discussed in 5.3.1-5.3.3. Since the building envelope (B1 or B2) has no significant influence, only the results for B1 are shown.

Table 6:building B1, 2m/app, January

	IHS light	**IHS heavy**	**IHS heavy WF**	**CHS 6 aprt**	**CHS 18 aprt**	**CHS 36 aprt**
ηskin (syst)	89%	75%	74%	92%	97%	97%
ηcombust	95%	94%	94%	96%	95%	96%
ηboiler (syst)	84%	71%	70%	88%	93%	93%
ηboiler (building)	**93%**	**91%**	**91%**	**88%**	**93%**	**93%**

Table 7:building B1, 2m/app, July

	IHS light	**IHS heavy**	**IHS heavy WF**	**CHS 6 aprt**	**CHS 18 aprt**	**CHS 36 aprt**
ηskin (syst)	84%	71%	61%	81%	93%	93%
ηcombust	93%	92%	91%	92%	93%	94%
ηboiler (syst = building)	**78%**	**65%**	**56%**	**75%**	**86%**	**87%**

If the efficiencies at building level are considered, the differences between the CHS and the IHS are mainly situated outside the heating season. As discussed above, the skin losses are the principal parameter influencing the boiler efficiency, working to the detriment of the IHS, especially if a boiler is used with a function to keep it warm. In the building with 36 apartments this results in a boiler efficiency of 56% (IHS) compared to 87% (CHS).

4.4 Results of annual simulations for CHS and IHS

A comparison is made between the annual results of the CHS and the IHS for different building size and for building B1. The CHS is conceived as option 'C' in §5.2.2 (with a variable primary flow, diameters according to DIN, and thermal valves with max flow 0.01kg/s) and with pipe length of 2m/aprt and 6m/aprt.

The boiler efficiency, the distribution efficiency and the total efficiency on a monthly and on an annual basis are represented in Table8 and 9. The efficiencies are all determined at building level. The total efficiency consists of the boiler efficiency and the distribution efficiency of the primary distribution network (only for the CHS). This means that control efficiency is not taken into account.

Table 8:CHS, building B1

		January			**July**			**1 year**		
# aprt	distr. network	**6**	**18**	**36**	**6**	**18**	**36**	**6**	**18**	**36**
η_{boiler}	2m/aprt (*)	88%	93%	93%	75%	86%	87%	82%	90%	91%
η_{distr}		99%	99%	99%	87%	88%	88%	94%	94%	94%
$\boldsymbol{\eta_{tot}}$		**88%**	**91%**	**92%**	**65%**	**76%**	**76%**	**77%**	**85%**	**85%**
η_{boiler}	6m/aprt(*)	88%	93%	93%	78%	89%	90%	83%	91%	91%
η_{distr}		97%	97%	97%	72%	72%	71%	87%	86%	85%
$\boldsymbol{\eta_{tot}}$		**86%**	**90%**	**91%**	**56%**	**64%**	**64%**	**72%**	**78%**	**78%**

(*) single

Table 9:IHS, building B1

	January			**July**			**1 year**		
	light	heavy	heavy,WF	light	heavy	heavy,WF	light	heavy	heavy, WF
η_{boiler}	93%	91%	91%	78%	65%	56%	82%	79%	75%

Due to the recuperation of skin losses (IHS) and distribution heat losses (CHS) at building level, the total efficiency of both systems is similar during the heating season. Outside the heating season, the influence of system losses is more pronounced. On the one hand the distribution heat losses in the CHS result in a distribution efficiency of circa 88% (2m/aprt) and circa 72% (6m/aprt) . On the other hand the boiler efficiency of the CHS compared to the IHS is improving with increasing building size. For the CHS and a building with 18 or 36

apartments, it is varying from 86% to 90%, while it is between 56% and 78% for the IHS, depending on the type of boiler.

These findings are reflected in the graphical representation of the annual results in Figure 11. The efficiencies of the building with 60 apartments are extrapolated from the simulation results of the smaller buildings.

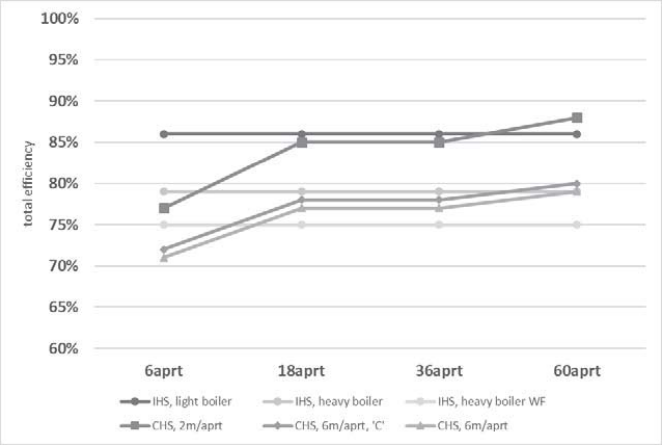

Figure 11: total efficiency of CHS and IHS for different building size

If we assume a similar level of comfort, the collective heating systems have to be compared to the individual heating system with a boiler of high capacity with a function to keep it warm. It appears from Figure 11 that a CHS, with the considered pipe networks (2m/aprt and 6m/aprt, single) can perform better from about 6 to 15 apartments. Obviously, if distribution efficiency of the CHS is lower (more length,…), the point from which CHS achieves better, will be at greater building size.

As a remark, individual systems with the same emitter, regime and preheating time, can have a lower comfort for SH because of the lower boiler temperatures (the lightweight boiler for instance is oversized for SH, so it has many start stops and temperature is fluctuating). It was verified that the same comfort level as for the CHS could be attained by increasing the preheating time. The difference in fuel consumption was less than 1% and impact on the total energy efficiency was negligible.

Finally the impact on annual fuel consumption of a heating system operating at low temperature is investigated. In §5.2.2 it was demonstrated that distribution heat losses could be reduced with 40%. Moreover boiler efficiency increases because of lower incoming temperatures and lower mean boiler temperature, especially in July (circa 82% compared to circa 74%). It should be noted that an installation at low temperature requires an additional temperature increase at the substations, which was simplified in this model (§5.2.2) adding an electrical resistance in each substation. In Figure 12 the total annual energy use, including the electrical energy at the substations and converted to primary energy, is represented for a system operating at 70°C, 50°C and at 40°C. A CHS at low temperature seems to have potential, but the electrical heating at the substations is penalized for the system at 40°C. Further research into systems at low temperature, for instance with local heat pumps, seems interesting.

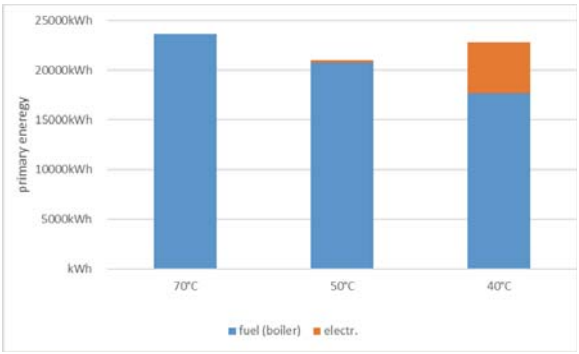

Figure 12: annual primary energy use for CHS at low temperature

5. CONCLUSION

An assessment of energy use and comfort of collective and individual heating systems was made, using a model based approach. In this paper simulations are performed on monthly and annual basis for different cases, all derived from an existing building, varying building size, building insulation and pipe network.

First distribution losses are quantified. For the considered cases (with boiler setpoint temperature 70°C and regime 65/30 for space heating) distribution losses are varying between 5 to 7 kWh/m pipe length (with 3cm pipe insulation) and between 18 to 24 kWh/m pipe length (with no pipe insulation), depending on the structure of the pipe network and heat demand for space heating. This leads to a distribution efficiency at system level varying from 38% (not insulated extended network in July) to 97% (insulated compact network in the least insulated building). The impact of some measures to reduce the distribution losses are investigated. A variable primary flow, smaller pipe diameters and a lower flow at the thermostatic control valves cause approx. 30% less distribution losses. However most profit is taken from an installation at low temperature (50°C instead of 70°C): distribution losses decrease with 40%.

Next impact of distribution losses on total energy use is investigated. In January, with a shaft part of the protected volume, distribution losses can be recovered as useful gains, leading to efficiencies at building level of 95% to 99% in all cases, except the case with an uninsulated extended network in the best insulated building (87%). Of course, impact of distribution losses on energy use remains more important outside the heating season (or with a ventilated shaft). In July and with an insulated network, distribution efficiencies vary between 67% to 87%.

In greater buildings (up to 36 apartments) boiler efficiency of the CHS is improving mainly due to a decreasing relative amount of skin losses: from 82% (6aprt) to 91% (36aprt) on an annual basis. Energy efficiency of an individual heating (IHS) system depends on the type of boiler (boiler mass), boiler control and the desired comfort level and vaies between 75% to 82%.

The IHS with a heavy boiler that is kept continuously at high temperature, uses more energy than the well-designed compact collective heating system of 2m/aprt (single), independent from the building size. When the primary distribution network of a collective heating system can be limited to 6m/aprt (single), it performs better than an IHS from a building size of circa 15 apartments, assumed that comfort should be similar. On the other hand, an IHS with a

lightweight boiler is favourable in the small size buildings, at least as far as energy consumption is concerned.

In the preceding conclusion, a well-designed and executed collective heating system is assumed, which is not always easy in practice. Due to a bad positioning of the shafts, structure of the pipe network or execution of insulation and hydraulics of the installation, performance of a CHS can decrease significantly, making a IHS more energy-efficient. On the other hand, a CHS makes a building future-proof, leaving open the possibility of using renewable energy or connecting it to a district heating network.

In future work focus will be put on installations at low temperature. The impact of boiler parameters and boiler control needs to be investigated, especially the start-stop losses which could influence the results in favour of the CHS in case they are underestimated in this paper. Furthermore, in a global comparison, pump energy should be considered.

6. ACKNOWLEDGMENT

This research is a part of the INSTAL2020 project (www.instal2020.be) sponsored by the Flemish government (www.vlaio.be).

REFERENCES

[1] Himpe E., Vaillant J., Janssens A.. 'Heat losses in collective heat distribution systems: comparing simplified calculation methods with dynamic simulations.' In: Proceedings of the 13th international conference of the international building performance simulation association, chambéry: IBPSA; 2013. P. 3432-9

[2] Himpe E., Vaillant Rebollar, J.E., and A. Janssens,., 'Heat losses in collective heat distribution systems: an improved method for EPBD calculations' , Proceedings of the 14th International Symposium on District Heating and Cooling, Stockholm, Sweden, 2014.

[3] Vaillant J., Himpe E., Laverge J., Janssens A.. 'Sensitivity analysis of heat losses in collective heat distribution system using an improved method of EPBD calculations.'

[4a] Vaillant Rebollar, J.E., E. Himpe, and A. Janssens, "Performance assessment of district heating substations based on dynamic simulations", Proceedings of the 14th International Symposium on District Heating and Cooling, Stockholm, Sweden, 2014.

[4b] Vaillant Rebollar, J.E., E. Himpe, and A. Janssens, " Simulation models and performance assessment of district heating substations", Proceedings of the 17 Convencion cientifica de ingenieria y arquitectura, La Habana, Cuba , 2014.

[5] Influence of recirculation strategies in collective heat distribution system on the performance of dwelling heating substations. Julio Vaillant Rebollar (UGent), Eline Himpe (UGent), Jelle Laverge (UGent) and Arnold Janssens (UGent) (2015) VIII International Conference for Renewable Energy, Energy Saving and Energy Education, Proceedings.

[6] Exploring the novel software Hysopt: a comparison of hydronic heat distribution systems of an apartment building. Van Riet F.,El Khaoui H.,Hulsbosch F., Steenackers G., Verhaert I. CLIMA 2016: proceedings of the 12th REHVA World Congress

[7] J. De Schutter, I. Verhaert, M. De Pauw, 2018. A methodology to generate realistic random behavior profiles for space heating and domestic hot water simulations. Proceedings of the REHVA Annual Meeting Conference.

[8] De Pauw M., Van Riet F., De Schutter J., Binnemans S., Van der Veken J.,Verhaert I., 2018. A methodology to compare collective heating systems with individual heating systems in buildings. Proceedings of the REHVA Annual Meeting Conference.

[9] Jeroen Van Der Veken, Veerle De Meulenaer, and Hugo Hens. "How Efficient Are Residential Heating Systems ?" In CLIMA 2005 proceedings, page 6, 2005.

[10] Van Riet Freek, Steenackers Gunther, Verhaert Ivan. "A new approach to model transport delay in branched pipes." Proceedings of the 10th SSB conference in Liege (in press).

Questions and Answers:

Wolfram Stephan:

You showed that boiler efficiency depends on the thermal mass. How are the boilers controlled? Is there a constant temperature in stand by operation?

Margot De Pauw:

A distinction is made between low and high mass boilers concerning the boiler control too.

For the low mass boiler, the boiler control allows the boiler to cool down during periods without any heat demand, so temperature must not remain constant in stand by operation. This results in the best water-side boiler efficiency according to the simulations.

For the high mass boiler, this kind of boiler control results in some unacceptable tapping delays, especially outside the heating season. Hence a second option is evaluated for the boiler control of the high mass boiler, with a function to keep it warm, maintaining a high boiler temperature during stand-by. This improves DHW comfort, but results in significantly lower water-side boiler-efficiencies.

Hydronic integration of ground-coupled heat pumps in collective heating system of buildings

Van Riet Freek[1,*], Steenackers Gunther[1], Verhaert Ivan[1]

[(1)]University of Antwerp, Faculty of Applied Engineering, Belgium
[(*)]Corresponding Author: freek.vanriet@uantwerpen.be

1 ABSTRACT

Ground-coupled heat pumps have a great potential to save primary energy in collective heating systems of buildings. However, these savings and their associated financial benefits are affected by the design of the complete heat production system, which often includes an auxiliary boiler and a storage tank. The hydronic configuration is a crucial aspect of that design, but it is overlooked in both scientific and technical literature. Therefore, this paper investigates which hydronic configuration should be selected for a given set of boundary conditions. First of all, the configurations (*serial*, *parallel* and *shunt*) and their control strategies that are used in practice are identified and described. Then, these design options are evaluated based on dynamic building simulations of an apartment block with 24 apartments. To generalise the findings of this paper, a sensitivity analysis of different boundary conditions is performed on the storage tank size, the heat pump size and the heat emitter systems characteristics (radiators and floor heating with different design temperature regimes). Results indicate that, if a shunt-type design is set as a design boundary condition, a variable flow control to discharge the storage tank is strongly recommended. If it is not set as a boundary condition, a serial configuration should be preferred over a parallel or shunt design. The sensitivity analysis reveals that these statements are true, regardless of tank size, heat pump size and the heat emitter characteristics.

Keywords: hydronic design, ground coupled heat pump, GCHP, building system simulations, hybrid heat production

2 INTRODUCTION

2.1 Problem statement and scope

In buildings, electrically driven heat pumps can help reach climate and energy targets by saving green house gas emissions directly (Bayer et al., 2012) and by facilitating renewable electricity production through demand response (Baeten et al., 2017). In collective heating systems, such as in apartment blocks, heat pumps are often supported by two other components: a thermal storage tank and an auxiliary heater. A thermal storage tank reduces the number of start-ups of a heat pump, which are known to decrease the efficiency (Fuentes et al., 2016). An auxiliary heater, e.g. a condensing boiler, reduces the investment of the production system (Hackel & Pertzborn, 2011; Di Perna et al., 2015) because a smaller heat pump can be installed.

The combination of these three components (heat pump, storage tank and auxiliary heater) increases the complexity of the design. Off course, the ecological and financial benefits of the installation depend on the quality of that design, for which three main design choices can be identified: the size of each component, the intended control strategy and finally the hydronic

configuration, which defines how the components are connected by pipes, pumps and valves.

The first aspect, choosing the heat pump size, is mainly based on initial investment cost, electricity price and the yearly energy demand of the building. The second aspect, choosing a control strategy, has frequently been subject of research. E.g., the control of a GSHP's compressor speed was compared with an ON/OFF strategy (Madani et al., 2011), the effect of supply water temperature on the efficiency of capacity control (Gasser et al., 2017) was examined, and the benefits of demand response by using a model predictive control-strategy (Fischer et al., 2014; Baeten et al., 2017) or weather and occupancy prediction (Rolando et al., 2017) have been investigated. However, for the third aspect, choosing the hydronic configuration, little information is available in literature. Based on research about the integration of cogeneration devices in collective heating systems (also in combination with an auxiliary boiler and storage tank) (Van Riet et al., 2019, 2018), a substantial effect on the performance of the production system can be expected. Indeed, latter cited research has shown that a proper selection of the hydronic configuration can increase relative primary energy savings with up to 35 percentage points. While these conclusions cannot be generalised for heat pumps because of the difference in characteristics of the technology, the results highlight the need for research on hydronic configurations.

Therefore, this paper aims to formulate guidelines about the hydronic integration of a ground-coupled heat pump (GCHP), auxiliary boiler and storage tank in a collective heating system. Note that this research is limited to a single type of heat pump technology (GCHP), as this is, based on its energetic performance, the most convenient one for large-scale applications such as collective housing. First (Section 2.2), the state-of-the-art hydronic configurations are discussed. Also control strategies will be described, since the performance of each particular configuration obviously depends on it. This paper focusses on control strategies which are applied in practice, and not on the advanced ones such as discussed in the previous paragraph. The methodology to evaluate each hydronic design (i.e. each hydronic configuration with its control strategy) is given in Section 3. This evaluation is based on simulations of a case study of an apartment block equipped with a collective heating system. Sensitivity analyses were performed on different boundary conditions: heat pump size, storage tank size, emitter system type (radiator or floor heating) and design temperatures of the emitters. The sensitivity analyses enable to generalise the results, i.e. to draw conclusions about which hydronic design should be selected for a given set of boundary conditions. Finally, in Section 4, the results of the case study and its sensitivity analyses are described and discussed.

3.1 Hydronic design: configurations and control strategies

Based on a review of technical literature and oral sources from industry (both heat pump manufacturers and design engineers), the hydronc designs that are applied in practice were identified. The results are shown in Figure 1. First, the hydronic design of the heat pump and storage tank is given and after that, the hydronic integration of the boiler is discussed. With exception of the shunt-type configuration (see below), the hydronic design concepts are similar to those used for heat production systems with cogeneration as descibed in (Van Riet et al., 2018).

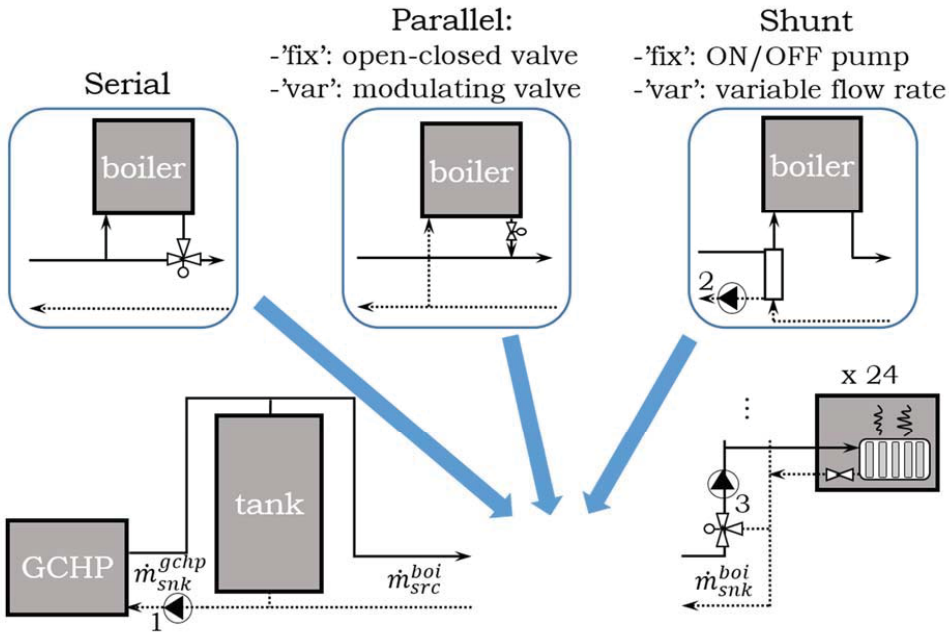

Figure 1: Schematic representation of three hydronic designs: a serial, a parallel and a shunt-type configuration. Balancing valves are not shown. In the shown example of an apartment unit, only a case with a radiator is shown and not one with floor heating.

3.1.1 Heat pump and storage tank

As stated in Subsection 2.1, a heat pump is often connected with a storage tank in collective heating systems (see Figure 1). The ON/OFF control of the heat pump depends on the state of charge of that tank, which is quantified by temperature sensors. Ideally, the tank is equipped with at least two sensors (not shown on Figure 1): one at the top and one at the bottom. If the temperature measured by the lower sensor exceeds the set point temperature of the supply water ($T_{sup,sp}$), the storage tank is assumed to be fully charged and hence the heat pump is shut down. It only starts up again if the temperature measured by the upper sensor drops below $T_{sup,sp}$.

If the heat pump is ON or still at a high temperature after a shut-down, pump '1' in Figure 1 should be activated. The resulting water flow rate through the sink side of the heat pump is typically constant and should ensure a maximal temperature difference between the inlet and outlet water. Note that the outlet water temperature is also limited, typically to 60°C.

3.1.2 Auxiliary boiler

Serial

The boiler can be integrated in different ways. The first option is to connect it in series with the supply pipe from the storage tank. In that case, the three-way valve shown on Figure 1 opens

completely when the boiler is ON (or OFF but still warm) and closes fully if the boiler is OFF. The main disadvantage that can be expected from this configuration is that the water going into the boiler has already been heated by the GCHP. In turn, this increase in temperature will result in a lower efficiency of the boiler.

Parallel

The second option is to connect the boiler in parallel, which results in colder water entering the boiler. In that case, two control strategies for the two-way valve exist: open-closed (will be referred to as 'parallel - fix') and a modulating one (will be referred to as 'parallel - var'). Both strategies open the two-way valve when the boiler is ON. However, the opening position of that valve is controlled differently:

– The open-closed control ('parallel - fix'): if the two-way valve opens, it always opens completely. The ratio of the water flow rate through the boiler, $(\dot{m}^{boi}_{snk} - \dot{m}^{boi}_{src})/\dot{m}^{boi}_{snk}$(Figure 1) depends then entirely on the settings of balancing valves. The opening position of these type of valves cannot be adjusted during operation (it is set only once: at installation). A typical setting for the balancing valves is to ensure the ratio $(\dot{m}^{boi}_{snk} - \dot{m}^{boi}_{src})/\dot{m}^{boi}_{snk}$ to be equal to the ratio 'nominal heat production of only boiler'/'nominal heat production of heat pump + boiler'. This strategy was already shown to decrease the discharging rate of the tank in a hybrid production system with a CHP device (Van Riet et al., 2018), resulting in less CHP operating hours. It is expected that the same issues will occur with a hybrid production system with a heat pump.

– Instead of opening completely, the modulating valve control ('parallel - var') adjusts the two-way valve if a flow through the boiler is required. The flow through the boiler is minimised, while a minimum is ensured to prevent the boiler from overheating. For a hybrid CHP production system, this strategy resulted in an increased discharging of the storage tank (Van Riet et al., 2018). Again, it is expected that this effect is also true for the heat production system that is considered in this paper.

Shunt

The third hydronic design, 'shunt', is often applied in renovations of heat production systems. The original heating system, i.e. only a boiler which is connected to distribution pipes, is then extended by inserting an hydraulic separator in the central return pipe. This separator ensures that the extension does not influence the hydraulics of the original heating system. Indeed, as the pressure drop along the network is not affected, flow rates are ensured with the original pump ('3' in Figure 1). This is not true if a serial or parallel extension is made, due to the increased pressure drop caused by the inlet and outlet of the storage tank. The hydraulic separator implies that an extra pump should be installed ('2' in Figure 1) to discharge the tank. This pump should be sized in order to guarantee a flow rate $\dot{m}^{boi}_{src}$ equal to the one through the heat pump, $\dot{m}^{gchp}_{snk}$. Indeed, if a smaller pump is selected, the tank would always be discharged at a lower rate than it is charged. Two different strategies can control that pump:

– ON/OFF control (will be referred to as 'shunt - fix'): pump '2' is ON whenever the building requires heat, i.e. whenever pump '3' is ON. If pump '2' is ON, the flow rate $\dot{m}^{boi}_{src}$ will be fixed. $\dot{m}^{boi}_{snk}$, on the contrary, varies in time if pump '3' is ON because of the central

mixing valve at the risers and because of the thermostatic radiator valves in the apartments. This means that $\dot{m}_{src}^{boi}$ can increase above $\dot{m}_{snk}^{boi}$, which increases the temperature of the water going into the heat pump and hence also of the water going out the heat pump. This will decrease the Coefficient Of Performance (COP) of the heat pump.

– Variable flow control (will be referred to as 'shunt - var'): to avoid the decrease of COP, $\dot{m}_{src}^{boi}$ is controlled in order to be equal to $\dot{m}_{snk}^{boi}$. In practice, the variable flow can be obtained by a control valve, a pump with variable frequency drive or a combination of both. Note that still a difference with a serial configuration exists, since $\dot{m}_{src}^{boi}$ can be less than $\dot{m}_{snk}^{boi}$, if its upper limit of pump 2 is reached.

For all configurations and control strategies, the boiler typically controls the supply water temperature to reach its set point. An ON/OFF signal is generated by hysteresis and modulation is determined by a controller (e.g. PI).

4 METHODOLOGY

4.1 Model descriptions

4.1.1 Heat pump

The condenser of the heat pump is considered as a lumped capacitance with capacity C^{gchp} and at temperature T_{out}^{gchp}. The dynamic thermal behaviour of the heat pump is therefore described by:

$$C^{gchp} * \frac{\mathrm{d}T_{out}^{gchp}}{\mathrm{d}t} = \dot{Q}_{con}^{gchp} - UA^{gchp} * (T_{out}^{gchp} - T_{env}) - c * \dot{m}_{snk}^{gchp} * (T_{out}^{gchp} - T_{in}^{gchp}) \quad (1)$$

C^{gchp} is calculated as:

$$C^{gchp} = c * \dot{m}_{snk,nom}^{gchp} * \tau \quad (2)$$

with τ [s] a time constant taken as $30s$ (Tassou & Votsis, 1992; Pärisch et al., 2014; Fuentes et al., 2016) and c the specific heat capacity of water, considered constant at $4187J/kgK$.

The first term of the right hand side of Equation 1, $\dot{Q}_{con}^{gchp}$ [W], represents the heat taken up by the condenser. A part of it is lost to surrounding (second term, see further) and a part of it is transferred to the hydronic system (third term). To calculate $\dot{Q}_{con}^{gchp}$ and the corresponding consumed power of the heat pump, P^{gchp}, empirical formulas based on steady-state performance were used.

The use of two dimensional second order polynomials is widespread as a model structure for these so called *performance maps* (Afjei & Dott, 2011; Haller et al., 2012; Cimmino & Wetter, 2017). In this paper, the performance map as defined by Equations 3 and 4 was used, based on a fit of data from 10 heat pumps between $25kW$ and $200kW$ (at conditions defined by NBN EN 14511 for brine-water heat pumps):

$$\frac{\dot{Q}^{gchp}_{con}}{\dot{Q}^{gchp}_{con,nom}} = -47 - 375 * T \quad + 411 * T \quad - 26 * T \quad \$rd$$
$$+ 416 * T_{src}^2 - 333 * T_{snk}^2 + 370 * T_{snk} * T_{src}^2 + 326 * T_{src} * T_{snk}^2 \tag{3}$$

$$\frac{P^{gchp}}{P^{gchp}_{nom}} = 11 - 63 * T_{src} + 32 * T_{snk} + 5 * T_{src} * T_{snk}$$
$$+ 59 * T_{src}^2 - 36 * T_{snk}^2 - 51 * T_{snk} * T_{src}^2 + 42 * T_{src} * T_{snk}^2 \tag{4}$$

with subscript 'nom' referring to nominal operating conditions. T_{snk} and T_{src} are the scaled temperatures at the sink (condenser) and source (evaporator) side of the heat pump, respectively:

$$T_{snk} = (T^{gchp}_{out} + 273)/273$$
$$T_{src} = (T^{brine}_{in} + 273)/273 \tag{5}$$

with T^{gchp}_{out} [°C] as explained before and T^{brine}_{in} [°C] the temperature of the brine entering the evaporator. In general, T_{snk} and T_{src} are scaled because of two reasons. First, by converting the units from Celsius to Kelvin, Equations 3 and 4 can also be used for source temperatures lower than 0°C (note the squares). Seconds, while it has no physical meaning, dividing by 273 prevents the parameters of Equations 3 and 4 from becoming small numbers. T^{brine}_{in} is considered constant at 10°C, which means that yearly ground temperature variations are neglected.

The second term of the right hand side of Equation 1 represents the heat loss to the environment (envelope losses) at temperature T_{env}. T_{env} was defined constant at 20°C, thereby assuming a constant temperature of the room the heat pump is located it. It is assumed that the condenser temperature T^{gchp}_{out} is representative for the envelope losses. UA^{gchp} [W/K] is the overall heat transfer coefficient of the heat pump's casing. It was fit on manufacturer's data of 10 heat pumps (the same ones as described above), resulting in the following equation:

$$UA_{loss} = 0.0164 * \left(\dot{Q}^{gchp}_{con,nom}\right)^{2/3} \tag{6}$$

3.1.2 Other models and case study description

The models described by Van Riet et al. (2018) were used to simulate the boiler, (stratified) storage tank, pipes and control valves. It should be mentioned that the storage tank model does not take buoyant yet mixing into account. Hence it is assumed that the storage tanks considered in this paper are able to maintain their thermal stratification.

In the case study, a weather compensation was applied to determine the set point supply water temperature, $T_{sup,sp}$, during the simulations. The building consists of six floors with four apartment units on each floor (24 apartment units in total) for which only space heating is considered. It is assumed that domestic hot water is produced in each individual apartment unit separately. That production is not taken into account in the analysis provided in this paper. All apartment units are considered identical, with exception of their solar orientation, and characterised by $5kW$ heat loss at design conditions (22°C indoor and −8°C outdoor). This means that extra

losses of the upper and lower apartments are neglected.

The same building model was used as the one from Van Riet et al. (2018). The only aspect of the model not discussed in that reference is the heat capacity of the emitter system, C^{emi}. It is calculated here as $C^{emi} = 900J/kgK * 2240kg/m^3 * 0.075m * 100m^2$, determined by the quantity and characteristics of screed.

The building model aims to reflect realistic dynamic thermal behaviour of the building only in order compare the different hydronic designs of the heat production system. It is not intended to estimate the exact energy consumption of a building. In fact, the building's thermal characteristics are not based on an existing building.

4.2 Sensitivity analyses of the case study

Five hydronic design concepts of the heat production system are examined in this paper: three hydronic configurations of which two with two different control strategies. These five design concepts are evaluated for different design boundary conditions (the heat pump size, storage tank size and heat emitter system):

– Two sizes of heat pump are considered. The "size" of the heat pump, $p^{gchp}_{\dot{Q}}$, is defined here relative to the peak load demand of the building, $\dot{Q}^{dem}_{nom}$, as:

$$p^{gchp}_{\dot{Q}} = \dot{Q}^{gchp}_{con,nom} / \dot{Q}^{dem}_{nom} \tag{7}$$

with $\dot{Q}^{dem}_{nom} = 24 * 5kW = 120kW$ (24 apartments with $5kW$ heat loss each) and $\dot{Q}^{gchp}_{con,nom}$ the heat load of the heat pump's condenser at design conditions. $p^{gchp}_{\dot{Q}} = 10\%$ and $p^{gchp}_{\dot{Q}} = 30\%$ are considered.

– The storage tank size is expressed as a minimal operating time, t^{sto} [h], of the GCHP at a load $\dot{Q}^{gchp}_{con,nom}$. To translate this time into a volume, it is assumed that the tank is filled with water at a temperature equal to the design return temperature of the emitter systems, $T^{emi}_{ret,des}$, and is heated completely to the design supply temperature, $T^{emi}_{sup,des}$. The formula:

$$\dot{Q}^{gchp}_{con,nom} * t_{sto} * 3600 = c * 1000kg/m^3 * V^{sto} * (T^{emi}_{sup,des} - T^{emi}_{ret,des}) \tag{8}$$

gives this relation, assuming a constant density and heat capacity. Loading times of $30min$ and of $60min$ are considered.

– Two types of heat emitter system are considered: radiators and floor heating systems. For each type, different design temperature regimes ($T^{emi}_{sup,des}$ and $T^{emi}_{ret,des}$) are examined as given in Table 1. Here, ΔT^{emi}_{des} is defined as $\Delta T^{emi}_{des} = T^{emi}_{sup,des} - T^{emi}_{ret,des}$, i.e. the design temperature difference of the emitter system. In the section covering the results (more specific Tables 2, 3 and 4), the highest and lowest ΔT^{emi}_{des} for all $T^{emi}_{sup,des}$ are referred to as 'high' and 'low', respectively.

To conclude, $(2 * 2 * 4 * 2 =) 32$ variations of the case study were considered and simulated for all five design concepts of the production system. Hence, 160 simulations of a full year were performed.

Table 1: Overview of the considered design temperatures (in °C) of the heat emitter systems. An 'r' refers to 'radiator', an 'f' to 'floor heating' and an empty cell means that its corresponding temperatures were not considered.

ΔT^{emi}_{des} \ $T^{emi}_{sup,des}$	75	50	45	35
10		r	f	f
15	r	r	f	
20	r			

4.3 Metrics

The following metrics were used to quantify the performance of the production system:

- t^{gchp}_{cyc}: the mean continuous operating time of the GCHP in hours
- *SPF*: the Seasonal Performance Factor of the heat pump over a full year
- η^{boi}: the yearly efficiency of the boiler in %
- t^{boi}_{cyc}: analogue to t^{gchp}_{cyc} but for boiler
- $p^{gchp}_{\dot{Q}}$: the percentage of thermal energy consumed by the building that is covered by the GCHP over a year. The remaining share is, obviously, covered by the boiler. Note the difference in meaning with $p^{gchp}_{\dot{Q}}$, which is defined in Equation 7.
- *RPES*: the yearly Relative Primary Energy Savings (in %), as defined by Verhaert, Mulder, and De Paepe (2016) with a boiler reference efficiency of 90% and an efficiency of the electric production of 40%.

5 RESULTS AND DISCUSSION

In this section, the results of the simulations are shown and discussed. The first subsection provides insight in the different hydronic configurations and controls by analysing the dynamic behaviour of the heat production systems. This analysis is based on a single day of the full year simulations. The second subsection elaborates on the yearly performance.

5.1 Dynamic behaviour

Figure 2 shows the dynamic behaviour of a single day (12 hours) and of a single set of boundary conditions: $T^{emi}_{sup,des} = 75$ °C, $T^{emi}_{ret,des} = 60$°C, $t^{sto} = 60min$ and $p^{gchp}_{\dot{Q}} = 30\%$. The figure consists of five columns, each with a different hydronic design, and four rows, each with different groups of variables. The first row shows the evolution of the different mass flow rates. The temperatures at the storage tank, indicating the state of charge of the tank, are given in the second row. The third row present the consumption of both the heat pump (electricity) and boiler (gas).

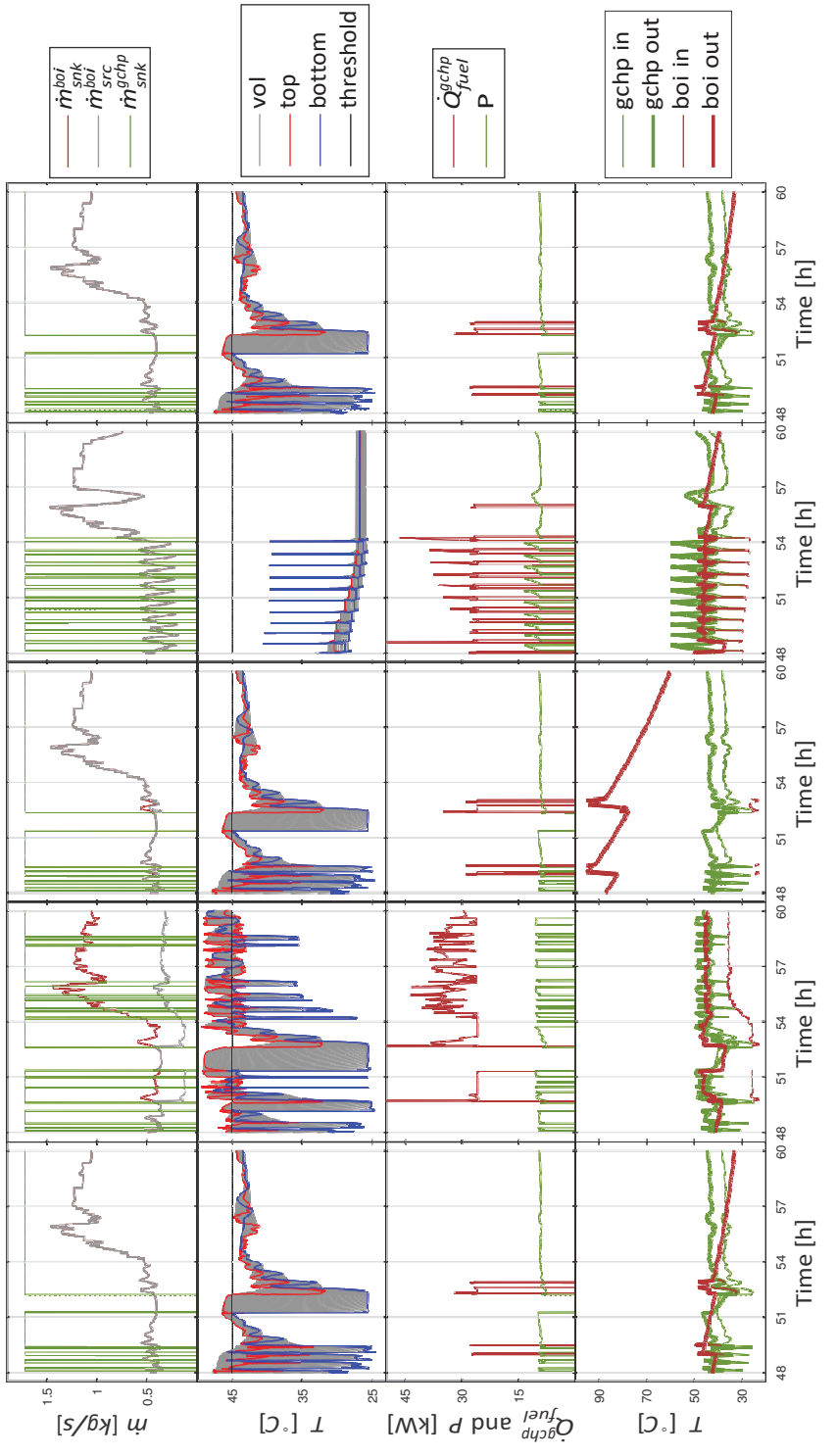

Figure 2: Examples of dynamic data for 12 hours for a case with $T^{emi}_{sup,des}$ = 75 C, $T^{emi}_{ret,des}$ = 60°C, t^{sto} = 60min and $p^{gchp}_{\dot{Q}}$ = 30%. Time is given in hours since the first of January at midnight. 'vol', 'top', 'bottom' and 'threshold' in the legend of the second row of plots refer to the temperatures of the different layers, of the top (sensed by upper sensor), of the bottom (sensed by lower sensor) and of the threshold value for shutting down/starting up the GCHP, respectively.

Finally, the fourth row shows the inlet and outlet temperatures of the heat pump and boiler.

The following three parts discuss the columns corresponding to the serial, two parallel and two shunt-type designs separately.

5.1.1 Serial: first column of Figure 2

The data of the serial configuration will be discussed to introduce Figure 2 and used as a reference for the other designs. Obviously, $\dot{m}^{boi}_{src}$ always equals $\dot{m}^{boi}_{snk}$ for a serial configuration and hence no distinction can be made between them in Figure 2 (first row). $\dot{m}^{boi}_{src}$ is always smaller than $\dot{m}^{gchp}_{snk}$ during the 12 hours shown (when not equal to zero), which means that the storage tank is charged. Indeed, it is charged above the threshold, $T_{sup,sp}$, four times (blue line increases above black one in second row). This results in shut-downs of the GCHP, as can be seen by the electrical consumption of the GCHP that decreases to zero (third row, green line). The boiler starts-up four times, which can be seen by its fuel consumption, and has limited operating time (red line, third row). Each time the boiler or GCHP shut-down, they cool down and their temperatures drop towards the temperature of the environment (fourth row).

5.1.2 Parallel: second and third columns of Figure 2

Because of the parallel connection of the boiler, $\dot{m}^{boi}_{src}$ will always be lower than $\dot{m}^{boi}_{snk}$ if the boiler is ON. Especially for the 'parallel - fix' design, $\dot{m}^{boi}_{src}$ is much lower compared to the serial configuration. Hence, the tank is discharged less (second row), resulting in more frequent shut-downs of the GCHP (third row, 18 in shown period). As expected, the temperature of the water going in the boiler is lower, compared to the serial configuration (fourth row, thin red line).

For the control with modulation ('parallel - var'), the flow through the boiler is minimised (as discussed in Section 2.2) and hence only a little difference between $\dot{m}^{boi}_{src}$ and $\dot{m}^{boi}_{snk}$ can be noticed. Therefore, the discharging rate of the tank comes close to that of the serial design (second row). Indeed, the number of GCHP shut-downs is limited to four (third row). The drawback of the modulating control is clearly shown in the fourth row: the boiler temperature is high, because of the low flow rate.

5.1.3 Shunt: fourth and fifth columns of Figure 2

In the second row of the 'shunt - fix' column, it can be seen that the shunt design with an ON/OFF pump control does not charge the tank above its temperature set point. And yet, the heat pump shuts down 10 times during the shown period. The reason for that is because the difference between $\dot{m}^{boi}_{src}$ and $\dot{m}^{boi}_{snk}$ is bypassed by the hydraulic separator. As a result, the water between heat pump and hydraulic separator circulates partially, for which its temperature increases. As a result, the temperature of the water going out the heat pump exceeds it maximum of 60°C (fourth row), shutting down the GCHP (third row). This occurs 10 times, all in the first six hours shown in the figure.

It should be noted that the 'shunt - fix' design is not able to charge and discharge the tank as intended. This is because whenever both pump 1 and pump 2 are running, $\dot{m}^{boi}_{src}$ will be equal to $\dot{m}^{gchp}_{snk}$. In fact, this control strategy results in behaviour similar to what would be expected from

a design without a storage tank.

A variable flow control of pump 2 ('shunt - var'), which limits $\dot{m}^{boi}_{src}$ to $\dot{m}^{boi}_{snk}$, can prevent this behaviour. Indeed, the water between heat pump and hydraulic separator is not bypassed and hence not heated above the heat pump's maximum. Also the charging and discharging of the storage tank are enabled. By using the 'shunt - var' design, the dynamics are actually similar to those of the serial configuration.

5.2 Yearly performance

In this subsection the full-year performance of all five hydronic designs are discussed for all different boundary conditions, based on Tables 2, 3 and 4.

In order to learn to interpret Tables 2, 3 and 4, the reader is advised to search in Table 2.b for *SPF*-values for all five hydronic designs with the following boundary conditions: $t^{sto} = 60min$, $T^{emi}_{ret,des} = 30°C$, $p^{gchp}_{\dot{Q}} = 30\%$ and $T^{emi}_{sup,des} = 35°C$. Table 1 reveals that $T^{emi}_{ret,des} = 30°C$ corresponds to a 'low' ΔT^{emi}_{des} ($\Delta T^{emi}_{des} = T^{emi}_{ret,des} - T^{emi}_{sup,des} = 5°C$) and that a floor heating system is considered. The values for 'Serial', 'Parallel - fix', 'Parallel - var', 'Shunt - fix', 'Shunt - var' are 6.7, 6.6, 6.7, 5.9 and 6.7, respectively. This means that, for the given set of boundary conditions, all hydronic designs perform similar in terms of *SPF*, with exception of the 'Shunt - fix' design. This can also be seen qualitatively by the background colors of the cells these five values are in: the lower value, 5.9, has a lighter color and the four other values have a similar, darker color. Within this group of five values, these background colors depends on the distribution of the five values.

For a set of five results (five different hydronic design with the same boundary conditions) with a less uniform distribution (i.e. larger difference between the results of the different hydronic designs) compared to the previous example, the colors will show more variation. This can be seen, for instance, in the upper left group of Table 2.a, which shows the variable t^{gchp}_{cyc}. The boundary conditions are: $t^{sto} = 30min$, ΔT^{emi}_{des} ='high', $p^{gchp}_{\dot{Q}} = 10\%$ and $T^{emi}_{sup,des} = 35°C$. The values for 'Serial', 'Parallel - fix', 'Parallel - var', 'Shunt - fix', 'Shunt - var' are 10.2, 2.4, 10.1, 3.2 and 9.5, respectively.

To conclude these examples, the results should be interpreted in groups of five values, each corresponding to five hydronic design and having the same set of boundary conditions. The background colors are intended to assist the reader to search for trends in the relative differences between the hydronic designs of the production system for the different boundary conditions, without focussing on the absoluut effect of the boundary conditions themselves. In fact, the influence of these boundary conditions as such, will not be a subject of the discussion.

In what follows, the heat pump, boiler and overall performs will be discussed.

5.2.1 Heat pump performance

For all design boundary conditions, both the 'parallel - fix' and 'shunt - fix' design have a lower t^{gchp}_{cyc} compared to the serial configuration (1.6 to 9.9 with a mean of 3.9 and 1.2 to 4.7 with a

mean of 2.1 times lower, respectively), meaning that the heat pump starts up more often (Table 2.a). This can be explained by the decreased discharging rate of the tank ('parallel - fix') and by the frequent increase in heat pump temperature above its maximal allowed value ('shunt - fix').

A modulating control for the parallel configuration ('parallel - var') solves this, as it increases the discharging rate to close to a serial configuration: t_{cyc}^{gchp} is for all boundary conditions maximum 2.5% (1.03 times) lower compared to the serial configuration. Also the shunt configuration benefits from a more advanced control ('shunt - var'): t_{cyc}^{gchp} was found to be maximal 13.5% (1.16 times) lower than the serial configuration. The fact that the storage tank can be discharged at a maximal rate of only $\dot{m}_{src}^{boi} = \dot{m}_{snk}^{gchp}$ might explain the limitations of this control strategy to reduce that maximum of 13.5% closer to 0% for the shunt design. This reasoning makes, obviously, only sense for $\dot{m}_{snk}^{boi} > \dot{m}_{src}^{boi}$, which is not discussed in the previous section and not shown in Figure 2.

Table 2.b shows analogue results for the *SPF*. Indeed, both the 'parallel - fix' and 'shunt - fix' design have a lower value than the serial configuration (0.2% to 12.8% with a mean of 5.8% and 2.7% to 13.7% with a mean of 6.9% lower, respectively). This can be explained by a higher heat pump temperature because of an increased charging of the tank (i.e. overall at a higher temperature, for 'parallel - fix') and because of the recirculation between heat pump and hydraulic separator ('shunt - fix'). The high heat pump temperature decreases the *COP* during operation and increases the losses to surrounding during stand-by mode.

Other control strategies for the parallel ('parallel - var') and shunt ('shunt - var') design can compensate for the lower *SPF* (maximum difference 0.6% and 0.2%, respectively).

5.2.2 Boiler performance

The 'parallel - fix' design scores the best on the stability of operation of the boiler (Table 3.a): t_{cyc}^{boi} is 1.2 to 17.2, with a mean of 5.0, times higher than the serial configuration, while t_{cyc}^{boi} of other hydronic designs vary between 0.4 and 1.9 times that of the serial design. This makes sense, as in the 'parallel - fix' design the boiler does not only serves as an auxiliary heater but it also produces a part of the base load of the building heat demand. Indeed, this occurs in situations at which the GCHP is shut down because of the inadequate discharging management.

Also in terms of boiler efficiency (Table 3.b), η^{boi}, the 'parallel - fix' design performs the best (up to 4.4 percentage points, with a mean of 0.9 percentage points more than the serial design). This is because the water that enters the boiler has a low temperature. On the contrary, the 'parallel - var' design, which has the same low inlet temperature, scores the worst in terms of η^{boi}. This is caused by the increased boiler temperature: it results in a decreased efficiency during operation as well as in high losses when cooling down to the temperature of the environment.

The two shunt type designs ('shunt - fix' and 'shunt -var') do not affect the boiler efficiency substantially, i.e. they show less than 1 percentage point difference with the serial configuration for all boundary conditions.

5.2.3 Overall energetic performance

The 'parallel - fix' design decreases the yearly heat demand covered by the GCHP, p_Q^{gchp} (Table 4.a). Depending on the boundary conditions, it is 4.7% to 37.7% (mean of 17.8%) lower than that of a serial design, while p_Q^{gchp} is maximum 3.5% lower than the serial design for the three other hydronic designs ('Parallel - var', 'Shunt - fix' and 'Shunt - var'). Again, the inadequate discharging of the 'parallel - fix' design causes this aspect of performance to decrease: during periods at which the tank is fully charged, the GCHP does not operate.

The *RPES* integrates three performance criteria that were discussed before: p_Q^{gchp}, η^{boi} and *SPF*. As a results, in the following two paragraphs these three criteria are used to explain the differences in *RPES* given in Table 4.b.

The 'parallel - fix' design shows a *RPES* 10.2% to 42.2% (mean 27.5%) lower than the serial one. This makes sense, as the GCHP covers a lower share of the heat production (see p_Q^{gchp}) and when it operates, it runs at a lower efficiency (see *SPF*). The increase in η^{boi} is not able to compensate that. A modulating control ('parallel - var') copes with the decreased operation time and efficiency of the GCHP, but lowers the boiler efficiency. Overall, this results in *RPES* close to those of a serial design, with a maximum of 4.3% lower.

Also the low *RPES* of a 'shunt -fix' design can be explained by the lower *SPF* and, to a lesser extend, a lower p_Q^{gchp}. The *RPES* are 1.6% to 11.3% (mean 5.2%) lower than a serial design. By implementing a variable flow control ('shunt -var'), this decrease in *RPES* can be limited to 2.5%.

Table 2: Yearly heat pump performance: a) t_{cyc}^{gchp} and b) SPF.

a) t_{cyc}^{gchp}			$p_{\dot{Q}}^{gchp}$ = 10%				$p_{\dot{Q}}^{gchp}$ = 30%			
	ΛT_{des}^{emi} ↓	$T_{sup,des}^{emi}$ →	35°C	45°C	50°C	75°C	35°C	45°C	50°C	75°C
t_{des}^{sto}=30 min	high	Serial	10.2	6.2	5.5	3.9	4.0	2.4	1.3	1.1
		Parallel - fix	2.4	0.8	0.7	0.4	2.2	0.9	0.4	0.3
		Parallel - var	10.1	6.1	5.6	4.0	3.9	2.4	1.3	1.1
		Shunt - fix	3.2	3.3	2.9	2.7	1.1	1.1	0.7	0.6
		Shunt - var	9.5	5.8	5.3	3.8	3.8	2.3	1.3	1.1
	low	Serial	5.2	3.9	3.6	2.9	1.9	1.5	1.0	0.9
		Parallel - fix	0.7	0.4	0.4	0.3	0.8	0.5	0.3	0.2
		Parallel - var	5.1	3.8	3.6	3.0	2.0	1.6	1.0	0.9
		Shunt - fix	2.7	3.1	2.7	2.5	0.9	0.9	0.6	0.6
		Shunt - var	4.7	3.7	3.5	2.9	1.8	1.5	1.0	0.9
t_{des}^{sto}=60 min	high	Serial	14.0	10.0	9.4	7.4	5.4	3.7	1.9	1.6
		Parallel - fix	4.4	1.7	1.5	0.9	3.5	1.5	0.7	0.4
		Parallel - var	13.8	10.0	9.6	7.5	5.4	3.8	1.8	1.5
		Shunt - fix	3.3	3.4	3.1	2.9	1.1	1.2	0.7	0.6
		Shunt - var	12.2	9.3	9.0	7.2	5.0	3.3	1.8	1.5
	low	Serial	9.5	7.8	6.8	5.7	3.2	2.4	1.4	1.3
		Parallel - fix	1.6	1.0	0.9	0.6	1.5	0.8	0.4	0.3
		Parallel - var	9.6	7.7	6.9	5.8	3.2	2.5	1.4	1.3
		Shunt - fix	2.7	3.2	2.8	2.7	0.9	1.0	0.6	0.6
		Shunt - var	8.5	7.3	6.5	5.5	2.8	2.4	1.4	1.3
b) *SPF*			$p_{\dot{Q}}^{gchp}$ = 10%				$p_{\dot{Q}}^{gchp}$ = 30%			
	ΛT_{des}^{emi} ↓	$T_{sup,des}^{emi}$ →	35°C	45°C	50°C	75°C	35°C	45°C	50°C	75°C
t_{des}^{sto}=30 min	high	Serial	6.4	6.2	6.1	5.3	6.4	6.1	5.7	4.9
		Parallel - fix	6.4	5.8	5.6	4.8	6.4	5.9	5.5	4.6
		Parallel - var	6.4	6.2	6.1	5.3	6.4	6.1	5.7	4.9
		Shunt - fix	6.2	6.0	5.8	5.1	5.9	5.6	5.0	4.5
		Shunt - var	6.4	6.2	6.1	5.3	6.4	6.1	5.7	4.9
	low	Serial	6.7	6.5	6.3	5.5	6.7	6.3	5.9	5.0
		Parallel - fix	6.5	5.9	5.7	4.8	6.6	6.0	5.5	4.6
		Parallel - var	6.7	6.5	6.3	5.6	6.7	6.3	5.8	4.9
		Shunt - fix	6.4	6.2	6.1	5.3	5.9	5.6	5.1	4.5
		Shunt - var	6.7	6.5	6.3	5.5	6.7	6.3	5.9	5.0
t_{des}^{sto}=60 min	high	Serial	6.4	6.2	6.1	5.3	6.4	6.1	5.7	4.9
		Parallel - fix	6.4	5.9	5.7	4.8	6.4	5.9	5.5	4.6
		Parallel - var	6.4	6.2	6.1	5.3	6.4	6.1	5.7	4.9
		Shunt - fix	6.2	6.0	5.8	5.1	6.0	5.6	5.0	4.5
		Shunt - var	6.4	6.2	6.1	5.3	6.4	6.1	5.7	4.9
	low	Serial	6.7	6.5	6.3	5.5	6.7	6.3	5.9	5.0
		Parallel - fix	6.5	6.0	5.7	4.8	6.6	6.0	5.6	4.6
		Parallel - var	6.7	6.5	6.3	5.5	6.7	6.3	5.8	5.0
		Shunt - fix	6.4	6.2	6.1	5.3	5.9	5.6	5.1	4.5
		Shunt - var	6.7	6.5	6.3	5.5	6.7	6.3	5.9	5.0

Table 3: Yearly boiler performance: a) t_{cyc}^{boi} and b) η^{boi}.

a) t_{cyc}^{boi}			$p_{\dot{Q}}^{gchp}$ = 10%				$p_{\dot{Q}}^{gchp}$ = 30%			
	ΔT_{des}^{emi} ↓	$T_{sup,des}^{emi}$ →	35°C	45°C	50°C	75°C	35°C	45°C	50°C	75°C
t_{des}^{sto}=30 min	high	Serial	5.7	3.0	0.7	0.5	5.0	5.9	0.9	0.4
		Parallel - fix	7.1	7.9	2.4	1.7	8.1	9.1	6.4	5.0
		Parallel - var	5.8	2.8	0.7	0.4	4.5	3.9	0.9	0.5
		Shunt - fix	5.8	2.9	0.7	0.5	4.9	3.3	0.6	0.3
		Shunt - var	5.8	2.9	0.7	0.5	5.1	5.6	0.8	0.4
	low	Serial	3.2	1.5	0.6	0.5	6.3	5.5	0.7	0.3
		Parallel - fix	8.5	6.8	2.2	1.5	10.9	12.7	6.4	4.4
		Parallel - var	3.1	1.5	0.6	0.3	4.5	3.4	0.8	0.4
		Shunt - fix	3.1	1.6	0.6	0.5	4.2	2.1	0.5	0.2
		Shunt - var	3.1	1.5	0.6	0.5	6.0	5.1	0.7	0.3
t_{des}^{sto}=60 min	high	Serial	5.8	3.1	0.7	0.5	4.8	5.9	0.9	0.4
		Parallel - fix	7.2	8.0	2.5	1.7	8.4	9.6	7.7	6.0
		Parallel - var	5.5	2.7	0.7	0.4	4.4	3.5	0.9	0.5
		Shunt - fix	5.7	2.9	0.7	0.5	4.8	3.6	0.6	0.3
		Shunt - var	5.8	2.8	0.7	0.5	5.1	5.8	0.8	0.4
	low	Serial	3.2	1.5	0.6	0.4	6.2	4.9	0.8	0.4
		Parallel - fix	8.7	6.9	2.3	1.6	11.1	11.8	6.9	5.1
		Parallel - var	3.0	1.5	0.6	0.4	4.1	3.2	0.8	0.4
		Shunt - fix	3.1	1.6	0.6	0.5	4.2	2.2	0.5	0.2
		Shunt - var	3.1	1.5	0.6	0.4	6.1	4.6	0.8	0.4
b) η^{boi}			$p_{\dot{Q}}^{gchp}$ = 10%				$p_{\dot{Q}}^{gchp}$ = 30%			
	ΔT_{des}^{emi} ↓	$T_{sup,des}^{emi}$ →	35°C	45°C	50°C	75°C	35°C	45°C	50°C	75°C
t_{des}^{sto}=30 min	high	Serial	96.9	96.5	96.0	94.6	96.2	95.5	94.1	91.1
		Parallel - fix	96.9	96.6	96.3	95.3	96.2	95.8	95.4	94.7
		Parallel - var	96.9	96.1	94.8	92.9	95.5	92.9	89.7	84.9
		Shunt - fix	96.9	96.5	96.1	94.8	96.3	95.5	94.1	91.8
		Shunt - var	96.9	96.5	96.0	94.7	96.3	95.6	94.1	91.1
	low	Serial	98.0	97.2	96.8	95.2	97.5	96.4	94.7	91.2
		Parallel - fix	98.1	97.5	97.3	96.2	97.4	96.8	96.5	95.5
		Parallel - var	97.9	96.5	94.8	92.6	94.4	91.5	89.7	85.4
		Shunt - fix	98.0	97.3	96.9	95.4	97.5	96.2	94.5	92.2
		Shunt - var	98.0	97.3	96.8	95.3	97.5	96.4	94.7	91.2
t_{des}^{sto}=60 min	high	Serial	96.9	96.5	96.0	94.6	96.1	95.5	94.1	91.5
		Parallel - fix	96.9	96.6	96.3	95.3	96.2	95.8	95.3	94.8
		Parallel - var	96.9	96.1	94.7	93.0	95.5	92.8	89.9	85.3
		Shunt - fix	96.8	96.5	96.1	94.8	96.3	95.5	94.1	91.7
		Shunt - var	96.9	96.5	96.0	94.7	96.3	95.6	94.2	91.5
	low	Serial	98.0	97.3	96.8	95.3	97.4	96.4	94.8	91.4
		Parallel - fix	98.1	97.5	97.2	96.2	97.4	96.8	96.5	95.6
		Parallel - var	97.9	96.5	94.7	93.2	94.4	91.6	89.8	85.5
		Shunt - fix	98.0	97.3	96.9	95.4	97.5	96.2	94.6	92.1
		Shunt - var	98.0	97.3	96.9	95.3	97.5	96.4	94.8	91.4

Table 4: Yearly overall performance: a) $p_{\dot{Q}}^{gchp}$ and b) RPES.

a) $p_{\dot{Q}}^{gchp}$			$p_{\dot{Q}}^{gchp}$ = 10%				$p_{\dot{Q}}^{gchp}$ = 30%			
	ΔT_{des}^{emi} ↓	$T_{sup,des}^{emi}$ →	35°C	45°C	50°C	75°C	35°C	45°C	50°C	75°C
t_{des}^{sto}=30 min	high	Serial	27.8	26.7	36.0	37.8	71.4	68.3	80.4	87.0
		Parallel - fix	22.6	18.0	22.8	22.3	62.9	52.7	54.4	52.0
		Parallel - var	27.8	26.7	36.1	38.4	71.7	68.8	80.6	86.8
		Shunt - fix	27.6	26.7	35.9	37.8	70.5	67.9	79.6	83.6
		Shunt - var	27.5	26.6	35.8	37.8	70.5	67.6	80.1	87.0
	low	Serial	31.2	29.7	36.7	38.4	76.1	72.7	80.9	87.4
		Parallel - fix	20.4	17.7	21.5	21.1	59.9	51.7	51.4	49.7
		Parallel - var	31.1	29.6	36.8	39.7	76.6	73.0	80.8	86.9
		Shunt - fix	31.1	29.7	36.7	38.5	75.8	72.8	80.2	84.0
		Shunt - var	31.0	29.5	36.6	38.4	75.5	72.6	80.9	87.4
t_{des}^{sto}=60 min	high	Serial	28.1	26.9	36.1	37.9	72.7	69.0	80.5	86.4
		Parallel - fix	23.4	18.6	23.6	23.3	64.2	53.4	55.3	51.6
		Parallel - var	28.2	26.9	36.3	38.4	72.9	69.7	80.7	86.4
		Shunt - fix	27.6	26.7	35.9	37.8	70.5	68.0	79.7	83.8
		Shunt - var	27.5	26.6	35.8	37.8	70.5	67.4	79.9	86.5
	low	Serial	31.4	29.8	36.9	38.6	77.0	72.5	80.4	87.0
		Parallel - fix	21.0	18.2	22.4	22.5	60.9	50.7	51.3	49.4
		Parallel - var	31.3	29.7	37.0	39.0	77.4	72.9	80.3	86.6
		Shunt - fix	31.1	29.7	36.7	38.5	75.8	72.8	80.3	84.2
		Shunt - var	31.0	29.5	36.7	38.4	75.4	72.4	80.4	87.0

b) *RPES*			$p_{\dot{Q}}^{gchp}$ = 10%				$p_{\dot{Q}}^{gchp}$ = 30%			
	ΔT_{des}^{emi} ↓	$T_{sup,des}^{emi}$ →	35°C	45°C	50°C	75°C	35°C	45°C	50°C	75°C
t_{des}^{sto}=30 min	high	Serial	23.2	21.9	26.6	24.7	48.2	45.0	49.6	47.3
		Parallel - fix	20.2	16.7	18.8	16.1	43.2	35.5	34.7	28.8
		Parallel - var	23.2	21.6	25.9	24.0	48.2	44.4	48.8	46.2
		Shunt - fix	22.7	21.6	26.1	24.3	45.6	42.5	44.7	42.1
		Shunt - var	23.0	21.8	26.5	24.7	47.7	44.5	49.5	47.4
	low	Serial	26.3	24.6	28.2	26.1	52.4	48.5	50.8	48.0
		Parallel - fix	19.9	17.2	18.8	16.3	42.4	35.6	33.7	28.2
		Parallel - var	26.2	24.0	27.0	25.4	51.9	47.2	49.5	46.7
		Shunt - fix	25.8	24.2	27.6	25.7	48.7	45.4	45.5	42.6
		Shunt - var	26.2	24.5	28.1	26.1	52.0	48.4	50.8	48.0
t_{des}^{sto}=60 min	high	Serial	23.4	22.0	26.7	24.7	49.0	45.4	49.8	47.1
		Parallel - fix	20.6	17.0	19.3	16.7	44.0	36.0	35.3	28.7
		Parallel - var	23.4	21.7	26.0	24.0	49.0	45.0	49.0	46.1
		Shunt - fix	22.7	21.6	26.1	24.3	45.8	42.6	44.9	42.3
		Shunt - var	23.0	21.8	26.5	24.7	47.8	44.4	49.4	47.2
	low	Serial	26.5	24.7	28.3	26.2	52.9	48.4	50.6	47.9
		Parallel - fix	20.3	17.6	19.4	17.0				28.2
		Parallel - var	26.4	24.1	27.0	25.2				46.6
		Shunt - fix	25.8	24.2	27.6	25.7				42.7
		Shunt - var	26.2	24.5	28.1	26.1		48.3	50.6	47.9

6 CONCLUSION

In this paper, three hydronic configurations of a collective heat production system consisting of a ground-coupled heat pump, an auxiliary boiler and a storage tank were investigated. Based on dynamic building simulations of an apartment block of 24 apartments units, including 32 variations of design boundary conditions (regarding heat emitter type, emitter design temperatures, storage tank size and heat pump size), the following can be concluded:

- Depending on the considered boundary conditions, a 'parallel - fix' design scores 10.2% to 41.2% (mean 27.5%) less on *RPES*, compared to a serial configuration. Also, the performance of a 'shunt - fix' design is less than the serial one in terms of that criteria: 1.6% to 11.3% (mean 5.2%).

- The mean continuous heat pump operating time, which gives an indication of live time and maintenance costs, for a 'parallel - fix' design is 1.6 to 9.9 (mean 3.8) times less compared to the serial, and 1.2 to 4.7 (mean 2.1) less for the 'shunt - fix'.

- For both the 'parallel - fix' and 'shunt - fix' design, disadvantages concerning *RPES* and stability of operation can be solved by implementing other strategies to control the flow rates at the production system. Indeed, the maximal percentual difference in *RPES* is only 4.3% for the 'parallel - var' design and 2.5% for the 'shunt - var' design. The decrease in mean continuous operating time can be reduced to lower than 1.03 and 1.2 for the parallel and shunt-type, respectively.

Based on these conclusions, the following design guidelines are suggested:

- While a parallel configuration can approximate the performance of a serial configuration, it requires a complex control strategy to do so. Hence, a serial configuration should be preferred to a parallel one.

- If a shunt-type configuration is set as a design boundary condition to ensure hydraulic separation between the original heating system and the extension with heat pump and tank, the discharging of the tank should be controlled with a variable flow rate. If it is not set as a boundary condition, a serial design should be selected.

NOMENCLATURE

c	specific heat capacity of water, considered as a constant of 4187 J/kgK
C^{gchp}	overall heat capacity of the heat pump (condenser) in J/K
CHP	Combined Heat and Power device/cogeneration
GCHP	Ground Coupled Heat Pump, in this paper meaning a brine-water heat pump
$\dot{m}_{snk}^{boi}$	mass flow rate as shown in Figure 1
$\dot{m}_{src}^{boi}$	mass flow rate as shown in Figure 1
$\dot{m}_{snk}^{gchp}$	mass flow rate as shown in Figure 1
nom	used as a subscript to refer to nominal conditions
η^{boi}	the efficiency of the boiler in higher heating value (in %)
p_Q^{gchp}	the percentage of thermal energy consumed by the building that is covered by the GCHP over a year
$p_{\dot{Q}}^{gchp}$	the GCHP nominal load relative to the peak load demand of the building, in %
P^{gchp}	the electric power consumed by the GCHP
$\dot{Q}_{nom}^{dem}$	the nominal required heat load of the building in W
$\dot{Q}_{con}^{gchp}$	the heat load that the condenser of the heat pump takes up from its internal cooling cycle in W
$RPES$	yearly Relative Primary Energy Savings
SPF	yearly Seasonal Performance Factor
t_{cyc}^{boi}	the mean continuous operating time of the boiler in hours
t_{cyc}^{gchp}	the mean continuous operating time of the GCHP in hours
t^{sto}	the size of the storage tank expressed in minutes of minimal continuous operation of the GCHP at design conditions
T_{in}^{brine}	the temperature in °C of the water entering the evaporator of the GCHP. In this paper it is assumed to be constant at 10°C
T_{in}^{gchp}	the temperature of the water going in the GCHP in °C
T_{out}^{gchp}	the temperature of the water going out the GCHP in °C
T_{env}	the temperature of the environment surrounding the production system (boiler room)
$T_{ret,des}^{emi}$	the design temperature of the water going out the emitter
$T_{sup,des}^{emi}$	the design temperature of the water going in the emitter
T_{snk}	scaled temperature of the condenser of the GCHP in K/K
T_{src}	scaled temperature of the evaporator of the GCHP in K/K
$T_{sup,sp}$	the set point of the supply water temperature, depends on outdoor temperature
ΔT_{des}^{emi}	the design temperature difference between in- and outgoing water of the emitter ($= T_{sup,des}^{emi} - T_{ret,des}^{emi}$)
τ	time constant in seconds that characterises the thermal inertia of the GCHP
UA^{gchp}	overall heat transfer coefficient in W/K of the GCHP envelope losses

REFERENCES

Afjei, T., & Dott, R. (2011). Heat Pump Modelling for Annual Performance, Design and New Technologies. *12th Conference of International Building Performance Simulation Association*, 14–16.

Baeten, B., Rogiers, F., & Helsen, L. (2017, jun). Reduction of heat pump induced peak electricity use and required generation capacity through thermal energy storage and demand response. *Applied Energy*, *195*, 184–195.

Bayer, P., Saner, D., Bolay, S., Rybach, L., & Blum, P. (2012, feb). Greenhouse gas emission savings of ground source heat pump systems in Europe: A review. *Renewable and Sustainable Energy Reviews*, *16*(2), 1256–1267.

Cimmino, M., & Wetter, M. (2017). Modelling of heat pumps with calibrated parameters based on manufacturer data. *Proceedings of the 12th International Modelica Conference 2017*(July), 219–226.

Di Perna, C., Magri, G., Giuliani, G., & Serenelli, G. (2015). Experimental assessment and dynamic analysis of a hybrid generator composed of an air source heat pump coupled with a condensing gas boiler in a residential building. *Applied Thermal Engineering*, *76*, 86–97.

Fischer, D., Toral, T. R., Lindberg, K., Wille-Haussmann, B., & Madani, H. (2014). Investigation of Thermal Storage Operation Strategies with Heat Pumps in German Multi Family Houses. *Energy Procedia*, *58*, 137–144.

Fuentes, E., Waddicor, D., & Salom, J. (2016, oct). Improvements in the characterization of the efficiency degradation of water-to-water heat pumps under cyclic conditions. *Applied Energy*, *179*, 778–789.

Gasser, L., Flück, S., Kleingries, M., & Wellig, B. (2017). Efficiency Improvements of Brine / Water Heat Pumps through Capacity Control. In *12th iea heat pump conference 2017*.

Hackel, S., & Pertzborn, A. (2011). Effective design and operation of hybrid ground-source heat pumps: Three case studies. *Energy and Buildings*, *43*(12), 3497–3504.

Haller, M. Y., Bertram, E., Dott, R., Afjei, T., Ochs, F., & Hadorn, J.-C. (2012). Review of Component Models for the Simulation of Combined Solar and Heat Pump Heating Systems. *Energy Procedia*, *30*, 611–622.

Madani, H., Claesson, J., & Lundqvist, P. (2011, dec). Capacity control in ground source heat pump systems part II: Comparative analysis between on/off controlled and variable capacity systems. *International Journal of Refrigeration*, *34*(8), 1934–1942.

Pärisch, P., Mercker, O., Warmuth, J., Tepe, R., Bertram, E., & Rockendorf, G. (2014, jan). Investigations and model validation of a ground-coupled heat pump for the combination with solar collectors. *Applied Thermal Engineering*, *62*(2), 375–381.

Rolando, D., Madani, H., Braida, G., & Tomasetig, R. (2017). Heat pump system control : the potential improvement based on perfect prediction of weather forecast and user occupancy. *12th IEA Heat Pump Conference 2017*, 1–9.

Tassou, S., & Votsis, P. (1992, mar). Transient response and cycling losses of air-to-water heat pump systems. *Heat Recovery Systems and CHP*, *12*(2), 123–129.

Van Riet, F., Janssen, E., Steenackers, G., & Verhaert, I. (2019, feb). Hydronic design of cogeneration in collective residential heating systems: state-of-the-art, comparison and improvements. *Applied Thermal Engineering*, *148*, 1246–1257.

Van Riet, F., Steenackers, G., & Verhaert, I. (2018). Design of Cogeneration : a Case Study of an Apartment Block. In *Proceedings of the rehva annual meeting conference: Low*

carbon technologies in hvac (www.rehvam2018atic.eu).
Verhaert, I., Mulder, G., & De Paepe, M. (2016). Evaluation of an alkaline fuel cell system as a micro-CHP. *Energy Conversion and Management*, *126*, 434–445.

Questions and Answers:

Wolfram Stephan:

Which kind of models do you use? (Heat pump, storage tank…)

Freek Van Reit:

In the paper, references are given and the heat pump model is described.

Solar and Heat Pump Systems: parallel vs series configurations analysis

J. Vega[1]*, C. Cuevas[2]

[(1)]Departamento de Ingeniería Mecánica - Universidad de Concepción

Edmundo Larenas 219 - Concepción – Chile

[(2)]Departamento de Ingeniería Mecánica - Universidad de Concepción

Edmundo Larenas 219 - Concepción – Chile

ABSTRACT

This paper presents simulations of a Solar and Heat pump System (SHP) system for Domestic Hot Water (DHW) preparation. Two system configurations are designed for covering the heat demand. These, can switch between parallel and series operation. Thus, Configuration "A" consists in using a heat pump with two evaporators that alternate: one to work as an air-to-water heat pump (HP) and the other to operate as a water-to-water HP using the solar collector's (SC) heat. Configuration "B" implements a heat exchanger in the air-to-water HP that can pre-heat the air, using solar energy. These system configurations are modelled in the TRNSYS 17 environment for evaluating system's performance in different climates and with different SCs. The control system applies a switching criterion between parallel or series operation modes, based primarily on the available solar irradiation. Results show that individual performance figures of the HP and the SCs increase. Nonetheless, the Seasonal Performance Factor (SPF) of the overall system decreases in most case studies (5.58 to 4.55 in the worst case). It is emphasized that the applied switching criterion does not force the SCs to increase their operational time by cooling them with the HP. In consequence, there is still potential solar energy unused that the series operation could seize.

Keywords: Solar and heat pump systems, series configuration, parallel configuration, control systems

1. INTRODUCTION

In central and southern Chile, residential heating systems are mainly based on wood, paraffin or liquefied petroleum gas stoves. Among these, wood is the most frequently used fuel because of its lower price and wide availability. Unfortunately, the combustion of wood is the main source of air pollution during the winter period, with several cities declared as *saturated* by airborne *pollution. In the case of the* domestic hot water, it is mainly heated by the combustion of liquefied petroleum gas or natural gas. Even if for this case the pollution concernf is less severe, there is still a constraint related to the cost of the fuels, proven to be highly sensitive to past energy crises. These problems motivate the present study to evaluate the performance of alternative, more efficient, and less contaminant technologies like heat pumps combined with solar collectors. These are known as Solar and Heat Pump Systems (SHP systems).

SHP systems have been widely studied in the literature, especially by IEA SHC Task 44. As said, they combine heat pumps with solar thermal technology, typically solar thermal collectors, to supply energy demands on Domestic Hot Water (DHW) and Space Heating (SH). To achieve this , these systems usually need an energy storage: hot water stratified storage tanks appear as the more frequent and market available for this function. Nonetheless, multiple systems architectures can result in combining these components. One way to categorize them, used by

Task 44, is according to the interaction of their components, which was fully described by Ruschenburg et al. (2013). Thus, three main configurations are defined: parallel, series and regenerative. The configuration is denoted as parallel if the SC and the HP independently supply useful energy. Second, when collectors act as the heat source for the heat pump, either as exclusive or additional source, the configuration is denoted as series. Last, if the solar energy is used to warm and maintain the main source of the heat pump, usually the ground, it is denoted as regenerative. The energy performance of the SHP systems depends on several variables such as the building characteristics, the heat pump components, the solar radiation, the ambient conditions, the energy demand schedules, and of course, the overall systems components interaction. Regarding the last, series configuration concept is of interest. It has been created to boost the individual performance of both solar collectors and heat pump. In fact, if solar collectors are the HP's heat source, then they are chilled by it. Thus, at lower operational temperatures, they improve their performance by reducing their convection heat losses to the ambient. On its side, heat pump's Coefficient of Performance (COP) benefits from working with a higher temperature heat source than the air or ground would be. These are the foundations that motivate the present paper.

Most of the SHP systems performance analyses are developed using modelling and simulations during a representative period. For the modelling, different kinds of approaches are proposed in the literature, classified by Hadorn J.C (2015). Semi-empirical black box models are the most popular approaches used to model conventional systems by giving sufficiently accurate results. These models are executed in programs like TRNSYS, Energy-Plus, ESP-r, Insel or Matlab, among others. Most of these component models are validated and it is assumed that the simulation of the overall system is thus correct. Nonetheless, some authors warn that these SHP systems simulated performance is rarely validated experimentally. This is remarked by Banister C. and Collins M. (2015) in their literature survey. This may be explained by the complexity of the systems and the costs associated to the instrumentation and to the measurements campaign. Nonetheless, some studies are found with in-field measurements and good model validation. For example, Fraga et al. (2017) validated the simulations for a SHP system including an ice storage using one-year measurements from a pilot plant. On their side, Liu et al. (2014) have done in-field measurements to determine a high-capacity SHP system performance for an office building, and then used TRNSYS simulations to optimize its operational behaviour.

Regarding the expected results of a SHP simulation, sizing of the equipment is fundamental. In particular, solar energy contribution will have great impact on the system Seasonal Performance Factor (SPF_{syst}), the most important figure to compare. It is found that increasing the total solar collector area is most likely going to increase SPF_{syst}, although the decrease of the total electric consumption is asymptotic as a function of the SPF_{syst} increase, as shown by Fraga et al. (2017). Then, in reasonably sized systems, the limit to the total solar collar collector's area will always respond to an economic criterion. For the evaluated systems in the climate of Geneva, the mentioned author concluded that for Geneva's weather, 3 m^2 of solar collector per kW of heat pump capacity is a good compromise between system size and system performance.

There is abundant literature regarding parallel systems. Systematic work was done by Carbonell et al. (2014) to analyse potential electricity savings of parallel SHP systems compared to simple Air-Source Heat Pumps (ASHP) and Ground-Source Heat Pumps (GSHP). Work has also been done to investigate parallel SHP systems performance with improvements in the heat pump's cycle, such as the case of ASHP studied by Poppi et al. (2016). They developed a theoretical analysis using TRNSYS for two different climates, using variable speed heat pumps, vapour injection compressors, condensers integrated in the storage tank, between others.

Regarding the study of series configuration systems, some are just heat-pump-focused. Sun et al. (2015) compared an air-source heat pump with a solar source heat pump in the highly heterogeneous climate of Shanghai, China. In their case study, SPF_{HP} was higher using series configuration, which is what should be expected. Others focus their conclusions more in SC's performance increase when chilled by the heat pump, such as Sterling et al. (2012). They also studied solar source heat pumps for DHW, predicting a solar fraction increase from 58% to 67%. Tzivanidis et al. (2016) developed a parametric analysis in TRNSYS for three different heating systems: a solar system, an ASHP and a solar source heat pump. They concluded the solar source heat pump was more convenient than the air-source one. Nonetheless, no parallel configuration was evaluated to compare its performance. Other complex systems using solar source heat pumps have been evaluated with measurements and simulations, but with no direct comparison between parallel and series configuration (Liu et al., 2014). Then, there are some innovative studies on series SHP systems. Banister and Collins [13] proposed to improve a classical series system with a dual tank solar source heat pump, which allowed to reduce the energy consumption from 60% to 69% when this system was used with a solar collector area of 7.5 m^2. They also noticed in their literature survey that the general conclusion of solar assisted heat pump systems is that energy savings exist in comparison to traditional solar domestic hot water systems. Other novel system was developed by He et al. [14] in which a solar façade loop-heat-pipe was used as source for a HP. The authors simulated the performance and compared their results with a test rig, concluding an average thermal efficiency of the solar façade of 71% and an average COP of 4.93 that could reach up to 6.14.

There is few but existing literature that compares parallel and series configuration directly. Lerch et al. (2015) compared several SHP systems for heating and DHW; studying different kinds of series configurations, including ice storages, air preheating by solar energy and refrigerant heating by solar energy after the heat pump's evaporator. Compared to a classical parallel configuration, the results showed little system performance increase. In addition, using unglazed collectors as source for the heat pumps, the system required to double the collector's aperture area to achieve a similar system performance.

Systems that work in a series configuration only have a disadvantage: if there is a heat demand when there is not enough solar radiation, the heat pump's performance would be low because of poor heat exchange between the solar collectors and ambient air. Thus, dual source heat pumps are interesting since they search to combine the best features of parallel and series configuration SHP systems. In these, the heat pump can switch between using solar energy or, for example, air source energy. Then, the control system for the heat pump's operation mode switching criterion is of high interest. Kaygusus K. (1995), managed to improve the overall system performance using an air-source and solar-source heat pump in the climate of Trabzon, Turkey. For this, the author implemented an operation mode switch criterion based on the collector's outlet temperature. Lazarrin M. (2012) deepened Kaygusus's work stufdying ground source heat pumps coupled with solar collectors, both systems with the capability to work in a series mode. He concluded that in series mode, as expected, higher COP can be achieved, but there is often a lower free (air+solar or ground+solar) energy fraction, requiring auxiliary energy more frequently. On the other hand, Haller et al. (2011) described the potential of these dual source configurations. The authors also focused in comparing a dual air-source and solar-source heat pump. It is shown by theoretical analysis and dynamic system simulations that, there is a limit for the solar irradiation on the collector field above which using collector heat for the evaporator of the heat pump instead of using it directly is not advantageous. This irradiation limit (G_{lim}) depends on the characteristic performance curves of the solar collector and of the heat pump, as well as on the temperature conditions of the heat sources and sinks. This can be used as a criterion for switching between parallel and series operation mode. Thus, the authors concluded

there is a high potential in improving the system's performance taking advantage of the additional running times the collectors gain when chilled by the heat pump. It is important to notice that Haller's criteria for switching between parallel and series is based on idealized and steady state conditions. Hadorn J.C (2015) warned that this does not consider the transient effect of thermal capacitances.

The present work is inspired by these last conclusions. The objective is to study SHP systems that can conmute between parallel and series mode of operation. The hypothesis, derived from Haller et al., consists in assuming that there exists a solar irradiation value G_{lim} below which a SHP system benefits the most if it operates in series mode exclusively. This is assumed valid for every combination of flow temperature of the heat demand and ambient temperature. This hypothesis is applied to two different system configurations. The hypothesis also implies that if in any of the previous mentioned SHP systems a control system could switch between parallel and series operation based on the available solar irradiation, then the SPF_{syst} would be optimized. On the other side, a certain parallel system will have a determined amount of time in which solar collectors effectively use available solar energy. So, could such the beforementioned control strategy be beneficial without modifying the solar collectors runtimes? For testing this thesis, SHP systems capable of switching its operation mode will be designed, modelled and simulated in TRNSYS to assess their performance in typical meteorological years in 3 Chilean cities. The case studies are derived from the heat demand of DHW and SH a medium rise Chilean residential building that has already been used by Vega et al. (2018) for assessing SHP systems performance for simple parallel systems. Nonetheless, the present paper focus its study just in the DHW heat demand.

2. METHODOLOGY

A system for DHW coverage of a mid-rise residential building is assessed. The selected heat demand to cover permits to evaluate the thesis in a somewhat high temperature load and with high component's thermal capacitance. High thermal capacitance on the Hot Water Storage Tank (HWST) and SCs, allows covering Hadorn's concerns on transient effects in the operation mode switching criterion. The system is tested in two different configurations, denoted as A and B, each of them capable of operating in parallel or series mode. Configuration A consists in a double evaporator HP, that can use as its energy source ambient air or solar energy from the SC. On the other hand, B configuration's series operation consists in using solar heat to warm the air passing though the heat pump. A simple solar radiation based criterion is applied based on different fixed solar irradiations value, $G_{lim,control}$, below which series operation will be activated. Thus, several numerical simulation to determine system's performance are carried on with different values of $G_{lim,control}$ set aiming to find an irradiation value that would switch parallel and series operation in an beneficial way.

2.1. Simulations boundary conditions

Regarding the boundary conditions of the simulations to test the studied systems, they can be divided in two: climate conditions and heat demand profiles. It is aimed to get valuable conclusions and performance indicators for the Chilean context. Then, to fully describe simulations boundary conditions, selected city weathers will first be presented, then, the heat loads and profiles that the SHP system seek to cover.

2.1.1. Climate boundary conditions.

The system covering the heat demand is evaluated in 3 different Chilean cities. First, Santiago is chosen for being the most populated city in Chile. Then, two cities are selected in the southern, and thus colder, regions of Chile: Concepcion, and Puerto Montt. Using different climate conditions is of interest because an ideal $G_{lim,control}$ will depend on ambient temperature and will also be reached at lower frequencies in southern cities. The characteristics of selected climate data are summarized in Table 1.

Table 1: Chilean thermal zone classification (MINVU, 2007), Köppen climate classification (Weatherbase, 2018) and climate data (Meteonorm, 2017) that characterize the selected weather

	Santiago	**Concepción**	**Puerto Montt**
Chilean thermal zone classification	Zone 1	Zone 4	Zone 6
Köppen climate classification	Csb (Mediterranean climate) bordering BSk (semi-arid climate)	Csb (mediterranean climate)	Cfb (marine west coast climate)
Average annual temperature	14.7 °C	12.5 °C	10.2 °C
Anual solar irradiation on a horizontal surface	1739 *kWh/m2*	1493 *kWh/m2*	1166 *kWh/m2*

2.1.2. Heat loads and energy demand profile.

A typical mid-rise building of Concepcion, Chile, is chosen for modelling its DHW heat load. The residential building with a total of 78 apartments, 13.2 m total high and located in Concepción, southern Chile. More details concerning its design and space heating related data are presented by Vega et al. (2018). The DHW profile demand used in this analysis is the one recommended by the ASHRAE Standard 90.2, while the total daily water consumption is estimated in 25270 litters according to ASPE. The DHW consumption temperature is defined as 48 °C. The resulting daily consumption is shown in Figure 1. Using the selected meteorological data, the heat load required to keep the internal energy of a DHW hot water storage tank during the whole year is presented in Table 2.

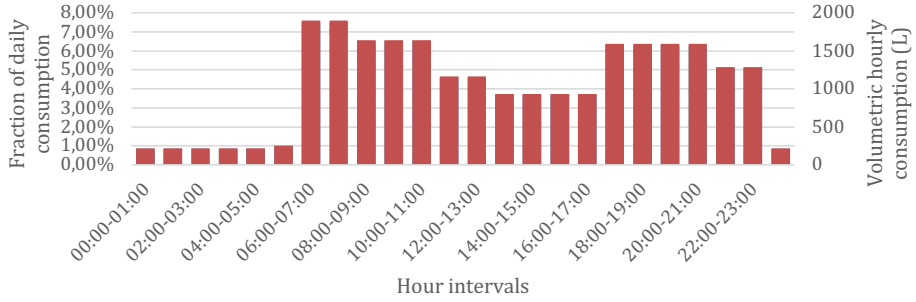

Figure 1: Daily consumption of DHW of the studied residential building.

Table 2: Heat load for DHW preparation in each assesed climate.

	Santiago	***Concepción***	***Puerto Montt***

Maximum capacity demand	*73.5 kW*	*76.6 kW*	*84.0 kW*
Annual energy demand	*315 890 kWh*	*350 720 kWh*	*388 610 kWh*

3. DESIGN AND MODELLING OF THE SHP SYSTEMS.

3.1. Overall design and system configurations.

Two different SHP system layouts are designed and modelled in TRNSYS: the SHP system in its A and B configurations. Besides testing these layouts in different climates and control system configurations, the use of two different types of solar collectors is proposed: Evacuated Tubes Collectors (ETCs) and Unglazed Collectors (UC). From a certain point of view, these collectors' performance profiles are opposed. ETC have a low optic performance, but low convective heat losses when they operate at higher temperatures. In contrary, UC can have a higher thermal efficiency if they are work at low temperatures, but this performance drops rapidly at higher operating temperatures.

In the system, SCs and a HP deliver heat to a hot water storage tank via submerged helical heat exchangers. The final consumer flow results in the controlled mixing by a thermostatic valve of cold tap water with hot water from the storage tank. The storage temperature is maintained at 48 (°C) at the top by the solar collectors and the heat pump. SCs are active if they can gain energy with the current conditions. On the other side, the heat pump's control system is set to be active if the solar collectors are not capable to maintain the HWST temperature.

Configuration A characterize itself for having a double evaporator HP, of which it can use just one at the time. The first evaporator allows the HP to use air as its heat source. On the other side, the second evaporator allows the HP to work as a water-water HP where the heat source fluid corresponds to the SC's working water. Then, configuration A has two modes of operation:

- Parallel operation: heat from the SCs is used directly in the HWST. If the HP is activated, it uses its air-source evaporator.
- Series operation: heat from the SCs is used indirectly, as a heat source for the HP. Thus, the HP uses its water source evaporator. In this mode, collectors are chilled, and the HP works with a higher temperature source.

It is important to notice that no simultaneous mode of operation can occur; the system works either as in parallel or in series mode. Configuration A's architecture and overall control strategy of each individual component is shown in Figure 2.

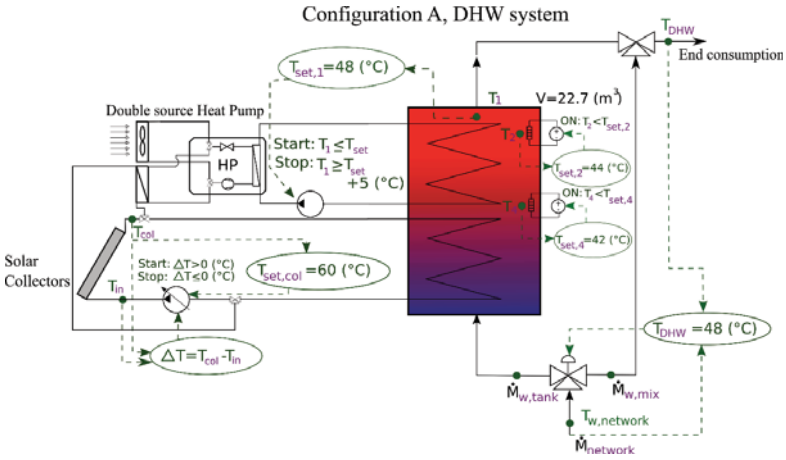

Figure 2: Simplified scheme of the components and hydronics of the DHW system in A configuration.

On its side, B configuration replaces the double source HP by a more conventional air-source HP. This time, the HP has a heat exchanger that can warm its heat source air using the SC's heat. Thus, two modes of operation can commute. As in A configuration, no partial parallel/series operation is permitted. Configuration B's architecture and overall control strategy of each individual component is shown in Figure 3.

- Parallel in B configuration: The system operates in the exact same way that the parallel operation of the A configuration.
- Series in B configuration: The collector's flow is redirected towards the heat exchanger to pre-heat the air passing through the HP evaporator.

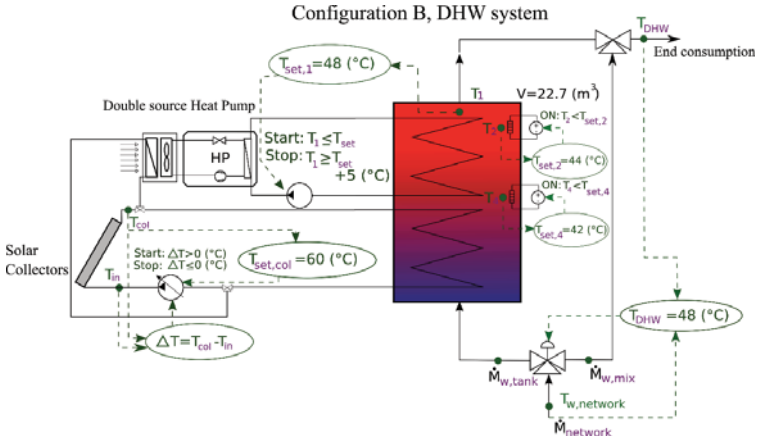

Figure 3: Simplified scheme of the components and hydronics of the DHW system in B configuration.

3.2. Equipment sizing.

DHW system has been designed based on the heat loads of the mid-rise residential building. It has been established than the maximum capacity required to maintain the internal energy of a

HWST is of 84 kW for the climate of Puerto Montt. Then, the system in its A and B configuration is designed with a HP somewhat oversized that can supply the heat demand in case there is no heat contribution by the SCs. A 90 kW HP is chosen and a total SC area in the range of t. Nonetheless, preliminary simulations, not shown in this paper for the sake of brevity, show that at some times desired DHW is not in the desired temperature, so two auxiliary heaters are installed. The auxiliary heaters capacities are chosen to diminish considerably this problem. On the other hand, the HWST volume sizing is chosen so it can store approximately the total daily consumption of the mid-rise residential building. The geometry of the tank is taken from the most suitable commercially available equipment found.

Table 3: Main components sizing of the DHW SHP system.

Nominal A7W30 heat pump's capacity (parallel mode)	Collectors-area/heat-pump-capacity ratio	Total solar collectors área	HWST volume	Auxiliary electric heaters capacity
90 kW	2.5	225 m^2	22.7 m^3	6 kW (x2)

3.3. System components modelling

3.3.1. Particularities on the Heat Pump modelling

A detailed physical model of heat pump is developed for TRNSYS 17. Its objective is to permit the authors further work in modelling SHP systems that require to simulate the refrigerant thermodynamical states in dynamic simulations. Nonetheless, this model is not finally implemented in the presented TRNSYS simulations and a black-box model whose performance map is obtained by testing the physical model in steady-state conditions replaces it.

The physical model code compiled in 4 TRNSYS modules that interact in its kernel: a condenser model, an air source evaporator model, a water source evaporator model and a compressor model.

The compressor model is based on its volumetic and isentropic efficiencies. Thus, the mass flow rate and the power consumption by the compressor are described in equations (1) and (2).

$$\dot{m}_{ref} = \dot{V}_{swept} * \rho_{in,comp} * \eta_{vol} \quad (1)$$

$$\dot{W}_{el,comp} = \dot{m}_{ref} * \frac{h_{out,comp,s} - h_{in,comp}}{\eta_s} \quad (2)$$

On the other side, the volumetric and isentropic efficiencies depend mainly on the pressure ratio of the compressor. The efficiencies are modelled as in equations (3) and (4).

$$\eta_s = K_1 + K_2\left(r_p - R_1\right)^2 - \frac{K_3}{r_p - R_2} \quad (3)$$

$$\eta_{vol} = a_0 - \alpha * r_p \quad (4)$$

Where K_1, K_2, K_3, R_1, R_2, a_0 and α are constants calculated from data from a compressor's catalogue.

On the other hand, heat exchangers are modeled accordingly to algorithms found in the literature survey, such as Type 877 described by Heinz & Haller (2013). Each heat exchanger working conditions are calculated with the inlet flow rates, inlet temperatures and total area of heat exchange. Global heat transference coefficient U is calculated with correlations that uses mass flow rate. UA_{HXis} then determined. Then, the HX is divided into sections accordingly to different refrigerant states: superheated gas, liquid-gas mixture and subcooled liquid. In each section, a local UA_i coefficient is calculated according to equation (5).

$$UA_i = \frac{\dot{Q}_i}{\Delta T_{log,i}} \quad (5)$$

Subcooling and superheating temperatures are assumed constant. The total heat transferred in the gas-liquide mixture section of the HX is calculated iterating the condensation or evaporation pressures, accordingly to the type of HX. Thus, convergence on the iteration of condensation or evaporation pressure is reached when equation (6) is fulfilled.

$$\sum UA_i = UA_{HX} \quad (6)$$

This physical model is not yet optimized at the time of writing this article. Nonetheless, the authors used this model to design a heat pump. Aiming for future work in the Space Heating simulations based in the residential building case study, 9 kW of nominal capacity is aimed. The selected compressor for designing and modelling the heat pump of the SH system is Copeland ZH38K4E, whose working fluid is R134a. The heat exchangers characteristics were chosen in order to maximize COP at nominal conditions, reaching 4.31. After design, the heat pump model is tested in steady state conditions to create a performance map under different heat source and heat sink temperatures, using both an air source evaporator and a water source evaporator. Thus, the performance data is used with commercial black box heat pump models that simulate the heat pump's energy consumption and heating capacity.

Table 4: Adjusted parameters to calculate the isentropic and volumetric efficiencies of the Copeland ZH38K4E compressor in the physical model.

K_1	K_2	K_3	R_1	R_2
0,388402	0,0011285	0,147789	20	1,3
a_0	α	V_{swept} (cm^3)	RPM (1/s)	
1,03195	0,0155827	82,76	2900	

For modelling the DHW system heat pump, the same performance map is used, but with a scale factor of 10 to adjust the heating capacity and power consumption for a 90 kW heat pump.

3.3.2. Modules used in each SHP system component.

For the system modelling, several modules available in TRNSYS and from Thermal Energy System Specialists [23-28] have been used. The most important components used in the system model are listed in Table 5.

Table 5: Models used in TRNSYS for the SHP systems simulation. Corresponding documentation is mentioned in references.

Type number	Description	Description/Parameters
538	Evacuated Tubes Collector Model	Quadratic efficiency curve model. Parameters: η_0=0.642; a_1=0.885; a_2=0.001. Bi-angular IAM's extracted from TESS library.
1290	Unglazed solar collector	Quadratic efficiency curve model. Parameters: η_0=0.828; a_1=18.52; a_2=0. b_0=0.1.
941	Air-to-Water Heat Pump	This model is based on an user-supplied performance map of the modelled heat pump containing the capacity and power consumption for various operating temperatures.
927	Water-to-Water HP. Used when the system works in	This model is based on an user-supplied performance map of the modelled heat pump containing the capacity and power consumption for various

	series operation in configuration A	operating temperatures.
534	Cylindrical Storage Tank (with immersed heat exchangers in the DHW system)	Constant volume, fluid filled tank model. The stratification is modelled through isothermal nodes. 10 vertical nodes. In the DHW system, there are internal coiled tubes HXs. Heat loss coefficient on every surface of 3 [$kJ \cdot h^{-1} \cdot m^{-2} \cdot K^{-1}$].

The solar collector's coefficients for their modelling are obtained from commercially available catalogue data of Wolf CRK-12 (ETC) and Heliocol HC-30 (UC). Their efficiency curves are shown in Figure 4. It can be seen the UC has more efficiency potential but a reduced operational range.

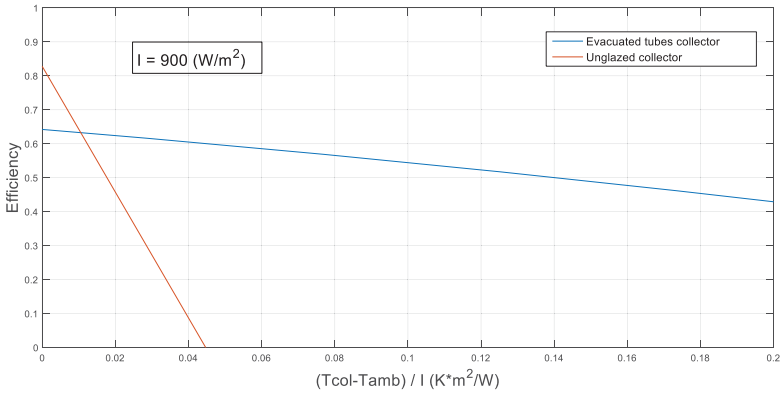

Figure 4: Efficiency curves of both evacuated tubes collector and unglazed collector used.

3.4. Control system for the mode of operation mode switching.

The control system designed switches the operation mode of each system mainly according to the total solar radiation available on the collectors' surface G_{col}. Thus, the control system of both system in A configuration requires 4 conditions for the system to operate in series, presented in Table 6.

Table 6: Conditions of the control system for activating series operation mode for systems in A configuration.

If the available solar radiation on the collector's surface fulfills	**If the solar collectors are running:**	**If the inlet water temperature of the heat pump's evaporator fulfills:**	**If the heat pump is activated :**
$G_{col} < G_{lim,control}$	$T_{out,col} > T_{in,col}$	$T_{in,evap,HP} > 2$ (°C)	*$T_1 < T_{1,set}$

T_1 is the top tank temperature, as shown in Figures 2&3.

The control system for both systems in B configuration also needs 4 conditions to switch to indirect solar use, showed in Table 7.

Table 7: Conditions of the control system for activating series operation mode for systems in B configuration.

If the vailable solar radiation on the collector's surface fulfills:	**If the solar collectors are running:**	**If the solar collectors are running:**	**If the heat pump is activated:**

$G_{col} < G_{lim,control}$	$T_{out,col} > T_{in,col}$	$T_{out,col} > T_{amb} + 1\ (°C)$	$*T_1 < T_{1,set}$

T_1 is the top tank temperature, as shown in Figures 2&3.

Both systems layouts are simulated through a whole TMY with different setups of $G_{lim,control}$, in order to search for a value that could improve SPF_{syst}. For every case study, 6 $G_{lim,control}$ values are tested, ranging from 0 and 500 W/m^2 with an increasing pace of 100 W/m^2. Notice that at $G_{lim,control}$= 0 W/m^2, the system operates exclusively in parallel mode.

4. SIMULATION RESULTS AND DISCUSSION.

4.1. Performance figures definitions.

Every simulation is performed within a timestep of 2 minutes for a period of one TMY. Analysis will be carried according to the following performance figures and definitions.

$$SPF_{syst} = \frac{\int \dot{Q}_{DHW} \cdot d\tau}{\int (\dot{W}_{el,tot,pp} + \dot{W}_{el,tot,HP} + \dot{W}_{el,tot,aux}) \cdot d\tau} \quad (7)$$

$$SPF_{HP} = \frac{\int \dot{Q}_{u,HP} \cdot d\tau}{\int \dot{W}_{el,tot,HP} \cdot d\tau} \quad (8)$$

$$F_{sol} = \frac{\int \dot{Q}_{u,col,HWST} \cdot d\tau}{\int (\dot{Q}_{u,col} + \dot{Q}_{u,HP} + \dot{W}_{el,tot,aux}) \cdot d\tau} \quad (9)$$

$$\eta_{ave,col} = \frac{\int \dot{Q}_{u,col} \cdot d\tau}{\int G_{col} \cdot A_{col} \cdot d\tau} \quad (10)$$

Notice F_{sol} consider solar heat when in direct use and $\eta_{ave,col}$ in both parallel and series operation. Also, the free energy fraction, defined as the renewable energy heat fraction delivered to the HWST can be calculated as in equation (11).

$$F_{free} = \frac{\int \dot{Q}_{free} \cdot d\tau}{\int (\dot{Q}_{u,HP} + \dot{Q}_{u,col,HWST} + \dot{W}_{el,tot,aux}) \cdot d\tau} = \frac{\int \dot{Q}_{free} \cdot d\tau}{} \quad (11)$$

$$\int \dot{Q}_{free} \cdot d\tau = \int (\dot{Q}_{u,col} + \dot{Q}_{airHP}) \cdot d\tau = \int (\dot{Q}_{u,col,HWST} + \dot{Q}_{HP,evaps}) \cdot d\tau = \int (\dot{Q}_{u,col,HWST} + \dot{Q}_{u,HP} - \dot{W}_{el,tot,HP}) \quad (12)$$

4.2. DHW system results.

Thirty-six simulations are executed for assessing A and B configurations in the 3 selected cities and for diferent $G_{lim,control}$ sets. SPF_{syst} is the most relevant parameter to conclude and compare system performance. Its predicted values are presented in Figure 5. It is important to notice that for a set of $G_{lim,control}$=0, A and B configuration work exclusively in parallel and with the same components sizing. Thus, for the same city weather and assessed type of solar collector both simulation should show the same results. This is not the case, and slightly different SPF_{syst} are encountered in each couple of theoretically equal results. The average difference in SPF_{syst} is of 0.15, while the largest relative difference is 4.84%; thus, the authors consider it is not a relevant matter because the true interest is in the figure dependence with $G_{lim,control}$. The authors attribute this to numerical deviations in the TRNSYS kernel because of different modules connections.

4.2.1. Components analysis.

Component analysis is essential to understand the overall system behaviour. First, it is important to notice that in every case study the SPF_{HP} figure increases with $G_{lim,control}$. These results are to

be expected for A and B configurations, because the HP works more frequently with a higher temperature source if series mode is activated more often. Also, it is important to notice that in A configuration, for the same operating temperatures, the water source evaporator improves heat pump's COP because of better heat transfer efficiency than with air.

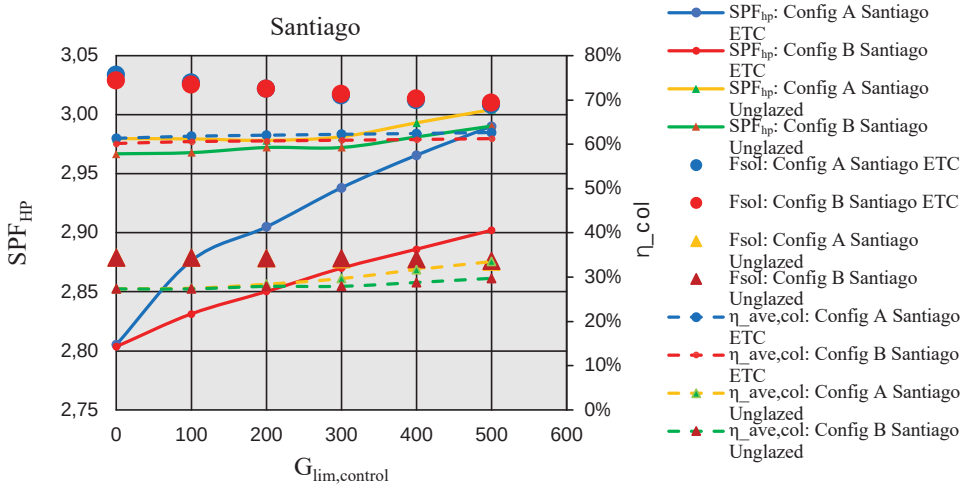

(a)

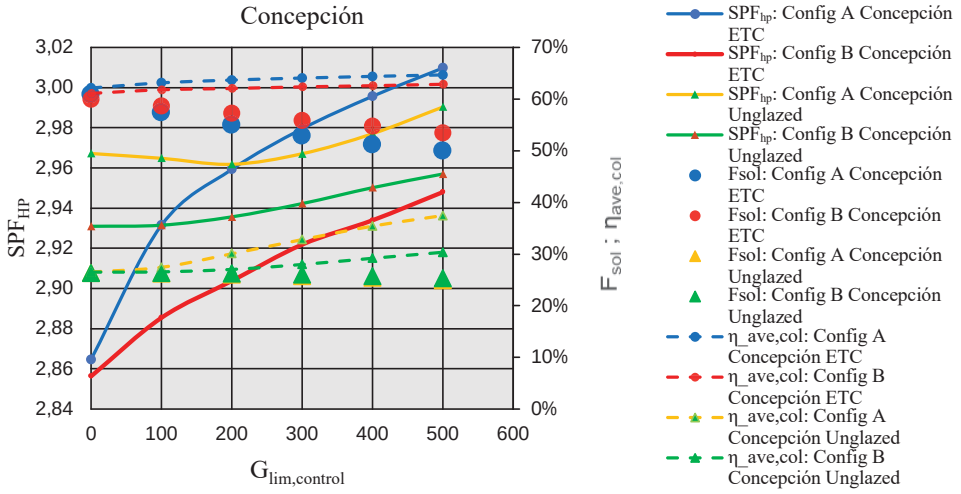

(b)

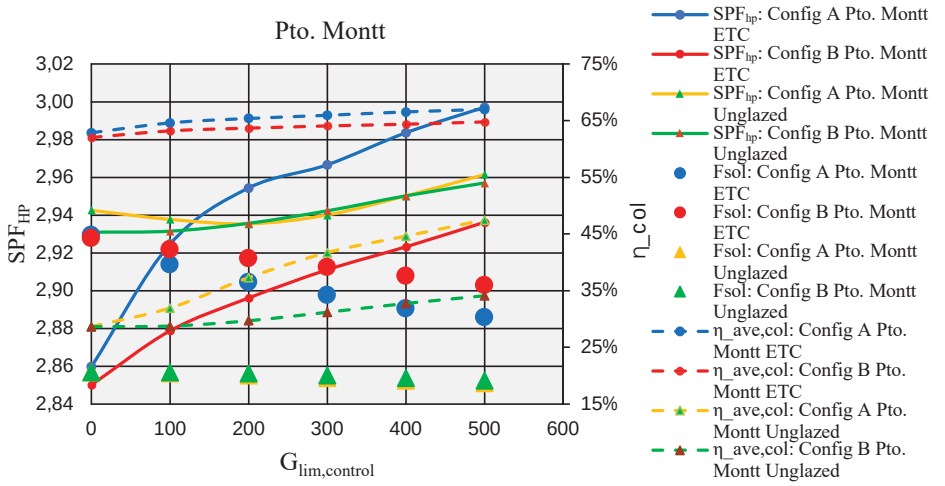

(c)

Figure 5: PF_{HP} , F_{sol} and $\eta_{ave,col}$ for each case study in the climates of (a) Santiago, (b) Concepción and (c) Puerto Montt in the DHW system.

A comparative analysis between SPF_{HP} tendencies show that A configuration has the better relative increase of this figure, reaching a 6.6% rise for Santiago's climate using ETCs. On its side, B configuration only manages to improve SPF_{HP} in 3.5% for the same climate and SCs. For each scenario, as expected, the double source HP appears as the best option to improve the component's performance, as shown in Table 8.

Table 8: Relative increase of each SPF_{HP} in the DHW system. Base value is obtained with $G_{lim,control} = 0$.

Configuration	SC	Santiago	Concepción	Puerto Montt
A	ETC	6.6%	5.1%	4.8%
	UC	0.82%	0.78%	0.64%
B	ETC	3.5%	3.2%	3.0%
	UC	0.79%	0.84%	0.89%

Regarding the SPF_{HP} improvement with each SC type, it is found that ETCs are the ones that increases the most the performance figure. This is explained by two factors. First, as seen in Figure 5, ETC have a wider range of operation; thus, they can support the HP more often since possible additional runtimes than UCs are covered. Second, contrary to what may be expected, $\eta_{ave,col}$ of UC did not surpassed ETC's even if the purpose of the system was to seize their low temperature potential efficiency.

Nonetheless, performance figures of both type of SCs did improve with $G_{lim,control}$. However, ETCs didn't show considerable relative improvement of $\eta_{ave,col}$. For this type of SCs, they consistently improve more their performance in A configuration, reaching a maximum increase of 4.13% for Puerto Montt's climate. As it is expected, UCs improve considerably more they performance, but not surpassing the ETC's. Again, A configuration is the one who achieves better improvement, reaching 18.8% in Puerto Montt. It is also important to notice that the

performance increases more if the climate is colder because greater convectional heat losses are avoided, especially with UCs. Results are shown in Table 9.

Table 9: Maximum increase of $\eta_{ave,col}$ for each case study in the DHW system.

Configuration	SC	Santiago	Concepción	Puerto Montt
A	ETC	1.31%	2.53%	4.13%
	UC	6.16%	10.93%	18.80%
B	ETC	1.09%	1.77%	2.75%
	UC	2.4%	3.84%	5.44%

The second figure that describes collectors' behaviour is F_{sol}. When increasing series mode operation range, less solar heat is used directly for charging the HWST. Thus, the figure is expected to decrease with $G_{lim,control}$, as shown in Table 10.

Table 10: Maximum decrease of F_{sol} for eachcase study in the DHW system.

Configuration	SC	Santiago	Concepción	Puerto Montt
A	ETC	-6.86%	-10.93%	-14.55%
	UC	-0.97%	-1.4%	-1.9%
B	ETC	-5.04%	-6.55%	-8.25%
	UC	-0.71%	-1.07%	-1.45%

4.2.2. Global system analysis.

SPF_{syst} results for each of the simulations are presented in Figure 6.

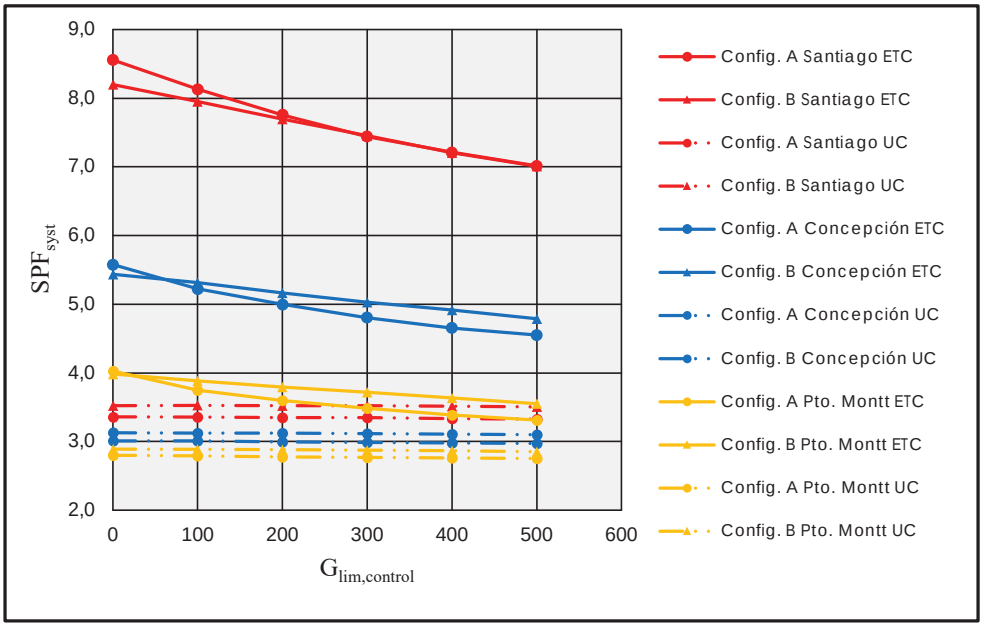

Figure 6: SPF_{syst} of A and B configurations of the DHW system in function of $G_{lim,control}$ set

On the main facts to notice, Puerto Montt is the city where constantly SPF_{syst} is the lowest for each configuration and SC type assessed. This is to be expected because it's the climate with the least solar irradiation and the lowest average ambient temperature, thus affecting negatively the SCs performance and the HP's COP. Lowest system performance figure for $G_{lim,control}$=0 W/m^2

is obtained in Puerto Montt with A configuration and UC, reaching a 2.8 value. The lowest SPF_{syst} of all is predicted for the same conditions with $G_{lim,control}$=500 W/m^2.

On the contrary, for the inverse reasons, the best SPF_{syst} are found in the Santiago climate. For the system operating exclusively in parallel, best results are found in A configuration using ETC, reaching a value of 8.56. In the surveyed literature, such high figures where never found. This is partly explained by the fact that most literature's case studies are in colder cities with least solar irradiation. Nonetheless, the main reason of this is that the SC total area has not been adjusted according to each climate and it is probably more economically reasonable to lower it for Santiago's climate. Even if a sensibility analysis for determining economically optimal SC areas is not relevant for testing this paper's thesis, it is seen as a work perspective.

Regarding the thesis put to test, it is observed that for each assessed configuration, type of SC used and climate, SPF_{syst} decreases with increasing $G_{lim,control}$. In other words, if the control system sets a wider range of operation conditions for the series mode, the system performs worst. Thus, it is verified that the control system, cannot improve the DHW system performance even if it based on the available solar irradiation. But, if individual performance figures of both SC and HP increases with $G_{lim,control}$, what explains the decrease of SPF_{syst}? In the case of A configuration, the increase of $\eta_{ave,col}$ and SPF_{HP} do not compensate the fact that when the system operates in series mode, it uses just one energy source (solar), when it could be using two energy sources at the same time (solar and air) in parallel mode. On its side, when B configuration operates in series it uses free energy from both air and solar collectors. Nonetheless, when this happens, the solar heat transferred to the HP's evaporator is done in expense of an energy quota that otherwise would be extracted from surrounding air. This is translated in a decrease of the free energy fraction in most case studies, as shown in Figure 7. On the other hand, Figure 8 shows that in both A and B configuration, the sum of total annual energy transferred to the HWST from the SCs and the heat pump tends to decrease up to 2.51%.

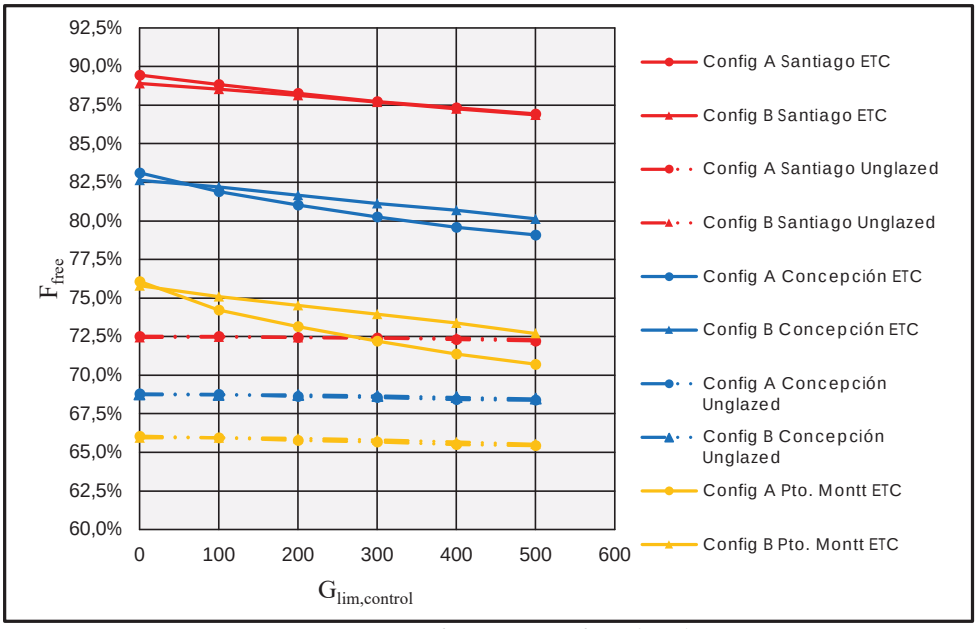

Figure 7: Free energy fraction transferred to the HWST

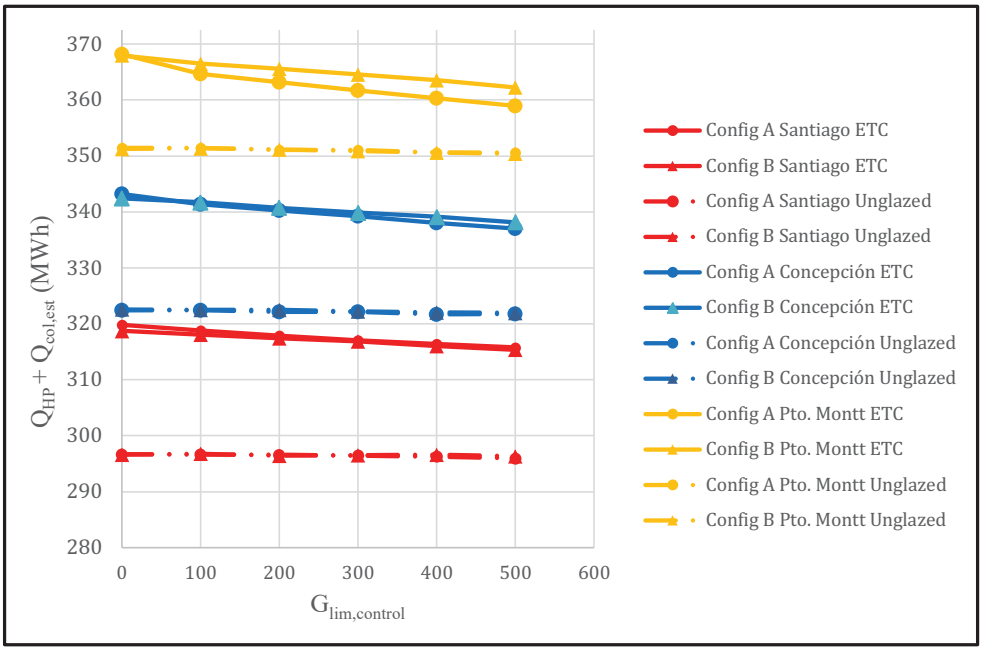

Figure 8: Total annual energy transferred to the HWST from the heat pump and the solar solar collectors in the DHW system.

This decrease on energy quota from the main system components is enough to set the auxiliary heaters running more often to maintain the defined minimum temperatures on the HWST. Thus, increasing $G_{lim,control}$ rises the amount of electric consumption, decreasing SPF_{syst}. These results are shown in Figure 9. Combined effects shown in Figure 7 and Figure 9 explain why the applied control system decreases SPF_{syst} in the DHW system.

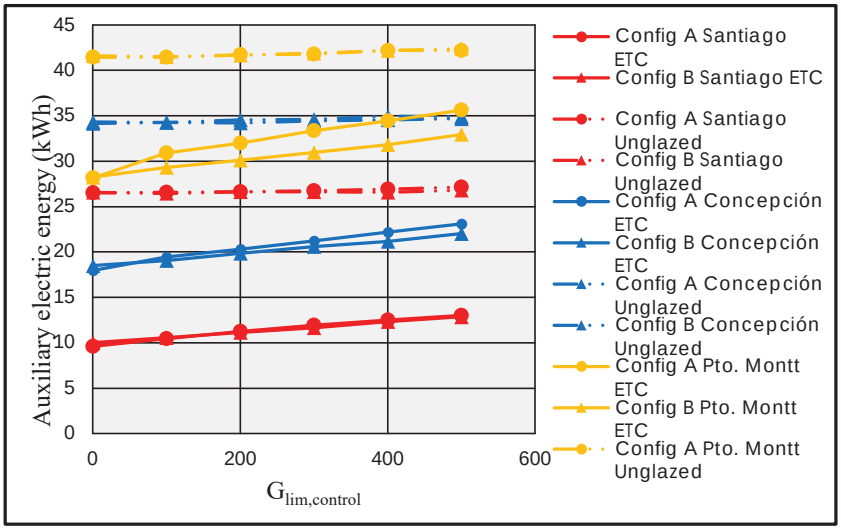

Figure 9: Total annual heat supplied by the auxiliary electric heaters of the DHW system for each case study.

It is also important to notice that for each case studied, the DHW system has better SPF_{syst} when using ETCs than with UCs. According to literature, it was expected to find a considerable performance increase on UCs when operating in series more frequently and this was not achieved. Results can be explained by the fact that the control of operation mode still has unused solar radiation potential. In other words, solar collectors' runtimes could be increased furthermore by turning ON the series mode of operation when the collectors are not previously working. This would chill them and force them into operating conditions with positive efficiency.

5. CONCLUSIONS AND WORK PERSPECTIVES.

The ability to commute between parallel and series operation, meaning direct or indirect use of solar heat, has been assessed in a solar and heat pump system with two different configurations. On one hand, a dual source (air and solar) heat pump layout has been implemented. According to literature, this configuration is beneficial if the control system decides which heat source to use in function of the available solar irradiation. In the present work, focus has been put in testing the configuration using a control system of this nature. The same is applied to a second configuration, denoted B, where the solar collectors can be used to warm the working fluid of an air source heat pump. The chosen methodology permits to test the thesis in different load temperatures, climates, magnitude order of the heat demand, heat demand profile and used solar collector type. Results show that individual performance figures increase of both heat pump and solar collectors is not a sufficient condition to improve the overall system performance figure SPF_{syst}. The reason for this is that the free energy fraction diminishes when increasing the series mode range of operation because the extra solar energy gained is lower than the air source energy the heat pump would extract in parallel operation. In other words, in evaluated systems, for both A and B configurations, there is not a limit solar irradiation below which series operation is beneficial. In fact, SPF_{syst} tends to decrease in most case studies.

Special discussion is done regarding the fact that there is still unused solar irradiation available than the series mode of operation could seize. Thus, the most important work perspective that arise in this work is the execution of numerical simulations of the same system layouts, in the same climates, using a control system that switches the mode of operation allowing the SCs to achieve all their potential runtimes. This would be done by forcing them to lower their temperature by chilling them with the HP when they were not previously working. Then, the SCs would be driven to reach a temperature where they meet a positive efficiency. Care should be taken to not allow this when there is no available solar energy, as in that condition the heat pump would perform better just taking heat from the air. A secondary work perspective is the economical and sensitivity analysis of the sizing of every main component implemented in the modelling. SHP systems are sensible to climate conditions and heat loads; thus, having additional information of the performance of these systems whose implementation is on the arise in Chile would be of interest.

Acknowledgements

This study was funded by the Chilean research agency CONICYT through the research project FONDECYT 1150965.

NOMENCLATURE

SHP	Solar and heat pump	**Subscripts**	
DHW	Domestic hot water	*lim*	Limit
COP	Coefficient of performance	*control*	Control system
F	Fraction	*syst*	System
HP	Heat pump	*ref*	Refrigerant
SC	Solar collector	*swept*	Swept

SPF	Seasonal performance factor
IEA	International energy agency
SHC	Solar heating and cooling
SH	Space heating
HWST	Hot water storage tank
ASHRAE	American society of heating, refrigerating and air-conditioning engineers
ASPE	American society of plumbing engineers
ETC	Evacuated tubes collector
UC	Unglazed collector
IAM	Incidence angle modifier
HX	Heat exchanger
TMY	Typical meteorological year
G	Solar radiation, $W \cdot m^{-2}$
$\dot{m}$	Flow rate, $kg \cdot s^{-1}$
ρ	Density, $kg \cdot m^{-3}$
$\dot{V}$	Volumetric flow rate, $m^3 \cdot s^{-1}$
$\dot{W}$	Power, W
h	Enthalpy
r	Ratio
K, R, a	Constant coefficient
U	Global heat transference coefficient, $W \cdot K^{-1} \cdot m^{-2}$
A	Area, m^2
$\dot{Q}$	Heat flow, $W \cdot s^{-1}$
T	Temperature, K
vol	Volumetric
el	Electric
comp	Compressor
out	Outlet
in	Inlet
s	Isentropic
p	Pressure
i	inth therm
log	Logarithmic
HX	Heat exchanger
col	Collector, collectors
evap	Evaporator
HP	Heat pump
Set	Set on the control system
amb	Ambient
u	Useful
tot	Total
aux	Auxiliary
sol	Solar
DHW	Domestic hot water
ave	Average
free	Free renewable energy
Greek symbols	
Δ	Delta, difference
η	Efficiency
α	Constant coefficient
τ	Time, s

REFERENCES

Vega J., Cuevas C. Simulation study of a combined solar and heat pump system for heating and domestic hot water in a medium rise residential building at Concepción in Chile. Applied Thermal Engineering 2018; 141:565-578.

Ruschenburg J, Herkel S, Henning H. A statistical analysis on market-available solar thermal heat pump systems. Solar Energy 2013; 95:79-89.

Carbonell D., Philippen D., Granzotto M., Haller M.Y. Simulation of a solar-ice system for heatin applications. System validation with one-year of monitoring data. Energy and Buildings 126 (2016) 846-858.

Hadorn J. Solar and heat pump systems for residential buildings. First edition. Berlin: Ernst & Sohn GmbH & Co; 2015.

Fraga C., Hollmuller P., Mermoud F., Lachal B. Solar assisted heat pump system for multifamily buildings: Towards a seasonal performance factor of 5? Numerical sensitivity analysis based on a monitored case study. Solar Energy 146 (2017) 543-564.

Sun X., Dai Y., Novakovic V., Wu J., Wang R. Performance comparison of direct expansion solar-assisted heat pump and conventional air source heat pump for domestic hot water. Energy Procedia 70 (2015) 394-401.

Sterling S.J., Collins M.R. Feasibility analysis of an indirect heat pump assisted solar domestic hot water system. Applied Energy 93 (2012) 11-17.

Liu H., Jiang Y., Yao Y. The field test and optimization of a solar assisted heat pump system for space heating in extremely cold area. Sustainable Cities and Society 13 (2014) 97-104.

Poppi S, Bales C, Heinz A, Hengel F, Chèze D, Mojic I, Cialani C. Analysis of system improvements in solar thermal and air source heat pump combisystems. Applied Energy 2016; 173:606-623.

Tzivanidis C, Bellos E, Mitsopoulos G, Antonopoulos K, Delis A. Energetic and financial evaluation of a solar assisted heat pump heating system with other usual heating systems in Athens. Applied Thermal Engineering 2016; 106:87-97.

Kamil Kaygusuz. Performance of Solar-Assisted Heat-Pump Systems. Applied Energy (1995) 93-109.

Lerch W., Heinz A., Heimrath R. Direct use of solar energy as heat source for a heat pump in comparison to a conventional parallel solar air heat pump system. Energy and Buildings 100 (2015) 34-42.

Renato M. Lazarrin. Dual source heat pump systems: Operation and performance. Energy and Buildings 52 (2012) 77-85.

Haller M, Frank E. On the potential of using heat from solar thermal collectors for heat pump evaporators. ISES Solar World Congress, 28. August-2 September 2011, Kassel, Germany.

Heinz A., Haller M. Model of Sub-components and Validation for the IEA SHC Tas 44/HPP Annex 38; A3 Description of TRNSYS Type 877 by IWT and SPF. Solar Heating & Cooling Programme (SHC), International Energy Agency (IEA).

Banister C, Collins M. Development and performance of a dual tank solar-assisted heat pump system. Applied Energy 2015; 149: 125-132.

He W, Hong X, Zhao X, Zhang X, Shen J, Ji J. Operational performance of a novel heat pump assisted solar façade loop-heat-pipe water heating system. Applied Energy 2015; 146: 371-382.

Meteotest, Meteonorm Version 7, Bern, Switzerland, http://www.meteonorm.com/, 2015.

ASHRAE Standard 90.2, Energy efficient design of low-rise residential buildings. American Society of Heating, Refrigerating and Air Conditioning Engineers, Atlanta, USA, 2007.

Domestic Water Heating Design Manual, American Society of Plumbing Engineers (ASPE), 2003.

TRNSYS 17 Mathematical Reference, TRNSYS 17 Documentation, Madison, Wisconsin, USA.

Thermal Energy Systems Specialists, Solar Library Mathematical Reference, Component Libraries for the TRNSYS Simulation Environment, Madison, Wisconsin, USA, Madison, Wisconsin, USA, 2012.

Thermal Energy Systems Specialists, HVAC Library Mathematical Reference, Component Libraries for the TRNSYS Simulation Environment, Madison, Wisconsin, USA, 2012.

Thermal Energy Systems Specialists, Storage Tank Library Mathematical Reference, Component Libraries for the TRNSYS Simulation Environment, Madison, Wisconsin, USA, 2012.

Questions and Answers:

Jean Lebrun:

What about the wind affecting solar collectors' performance? Is it considered?

Javier Vega:

Wind is not considered in the models used for these simulations. It is true that it could decrease performance especially for the Unglazed Solar Collectors. That said, one could think that when including the wind effect, simulations may show that series do boost system's Seasonal Performance Factor, in contrary to what current models showed.

Preliminary simulations were done to verify this. Type 1290 was used to describe unglazed collector's performance considering wind effect. This model is simpler than Type 553, it models the collectors with just 1 node. To consider wind, Type 1290 needs empirical coefficients that were not provided by the manufacturer of the selected collectors. Specific coefficients from another collector model were taken from literature and included. Simulations were performed with and without wind, for $G_{lim,control}$ *0 and 500* $(W \cdot m^{-2})$ *for Concepcion's climate, the most windy. It was found that for Configuration A with Unglazed Collectors,* SPF_{syst} *increases in just 0.04 and for Configuration B it stays invariable. In summary, this preliminary work suggest that overall conclusions of the article are not changing. Nonetheless, more detailed work could be done on the subject to confirm.*

SEVENTH SESSION
BUILDING ENERGY SIMULATION 2

Assessment of the Energy Performance of building facades through different testing conditions and analysis techniques

G. Masy[1]*, S. Hincque[1], A. Dawans[2]

(1) UCLouvain, Louvain-la-Neuve, Belgium

(2) Jacques Delens s.a., Brussels, Belgium

CAM(B)BRIDGE research Project is supported by Innoviris, the Brussels Institute for Research and Innovation.

ABSTRACT

The building envelope interacts with its HVAC equipment and control, as well as with the electric grid. As the energy performance of the building envelope has a large impact on the energy costs and on the thermal comfort, being able to confirm that the predicted performance of the envelope is really achieved is an important issue.

In that context, UCL is developing methods to characterize the performance of building facades, in collaboration with Jacques Delens s.a.. Those methods can be applied on site during the construction phase, requiring a maximum of 9 days monitoring period, without occupancy.

Parallel experiments were conducted during summer 2017 on two pair of south oriented identical building units, including two types of boundary conditions: insulation or no insulation added on the internal side of the party walls, as well as two types of solicitations: co-heating with electric radiators at a constant set point, or free-floating internal temperature. The data are analyzed through stationary and dynamic methods in order to assess the external façade Heat Transfer Coefficient.

The results highlight the relevancy of the placement of internal insulation on the party walls. Such a boundary condition do not only allows to reach higher levels of indoor temperatures. It also reduces the heat losses to neighboring units and allows to reach faster the stationary state. Without placement of internal insulation on the party walls, the stationary state cannot be reached within the imposed time period of 9 days for the experiment.

When performed in apartment units, co-heating tests tend to magnify the influence of the internal thermal bridges effect, thereby leading to an overestimation of the external façade Heat Transfer Coefficient.

Keywords: Building Physics, Parameters Identification, Experimental Design

1. INTRODUCTION

A relevant characterization of the energy performance of a building envelope is important not only for taking into account the building's interactions with its heating, ventilation, air-conditioning and heating equipment, but also when considering the interactions potential between the building and the electricity grid. The design of an efficient building envelope is an important issue for three reasons. First, an efficient envelope reduces the energy and

operating costs of the facility. Second, it provides comfortable environments at the building perimeter areas where the interface between the building envelope and the HVAC systems is crucial. Last, an efficiently integrated building envelope provides emerging opportunities of efficiency gains related to smart grid connectivity.

To ensure the positive impact of a well-designed energy efficient building envelope, it is crucial to verify that its predicted energy performance is really achieved. Bad workmanship for instance can result in difference between theoretical and achieved building performance which in turn induces higher energy cost as well as lower thermal comfort due to undersized equipment.

A common indicator to characterize the thermal performance of a building envelope is its Heat Transfer Coefficient, HTC (or Heat Loss Coefficient HLC), defined as the rate of heat loss from the whole envelope of a building, expressed in Watts per Kelvin of temperature differential between the internal and external environments.

A commonly referred method used to assess the building HTC is the co-heating test. In order for the co-heating method to be effective, there must be a significant internal-external temperature difference, a difference of at least 10 K is recommended (Bauwens & Roels, 2014; Jack, 2015; Janssens, 2016). This has restricted practical application of the co-heating test to the winter heating season (Johnston D., 2013; Wingfield J., 2010). The testing in building with attached spaces (such as semi-detached, terraced or apartment buildings) presents a problem in co-heating, particularly if it is not possible to access the adjacent space in order to install sensors (Stamp, 2016).

To overcome those restrictions, alternate measurement processes could be proposed, that should be suitable to summer weather conditions, and to building units that include common shared walls and floors.

Solar heat gains can be used as sole solicitation generating a free floating indoor temperature profile that can be dynamically analysed.

Internal insulation panels can be temporarily placed on the vertical and horizontal party walls in order to cut off the thermal mass effect, thereby increasing the internal-external temperature difference at the boundaries of the external facade. The later proposal also reduces the heat exchanges to the neighboring units.

Such alternate measurement methods have been tested on four south oriented building units, during the summer 2017. The data are analyzed through stationary methods and through dynamic grey-box modelling methods in order to assess the measured external façade Heat Transfer Coefficient. The HTC resulting from the data analysis are compared to the predicted HTC. When discrepancies are observed, investigations are made to determine if they are due to defects regarding the data analysis, such as underestimation of specific effects, or from real performance gap, i.e. a lower performance due to bad workmanship.

2. METHODOLOGY

The assessment of the HTC of a building unit requires the establishment of its complete heat balance, including the solar heat gains. Solar gains are the source of the most uncertainty, particularly in urban context where effects of mask and reflections occur. They must therefore be measured or carefully evaluated (Everett, 1985; Jack, 2015).

As measurements can be made on pairs of identical units, a methodology is adopted to get a reference value of the HTC that should not be affected by uncertainties related to the

estimation of solar heat gains. This *reference HTC* can be obtained by considering the data collected on two identical units, with one submitted to a co-heating test and the other left in free floating temperature mode. A fictitious experiment then can be deduced from both experiments by subtracting the results of the free floating temperature experiment from the results of the co-heating experiment, provided the solar heat gains are assumed to be the same in both units (Fig. 1).

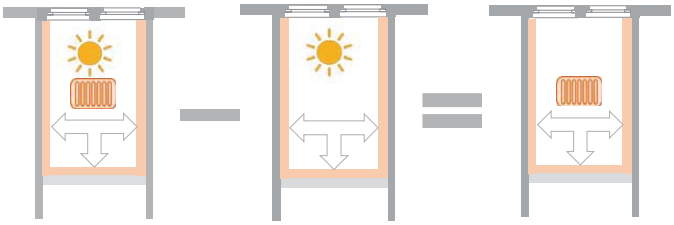

Figure 1: subtraction of the results related to the free floating temperature experiment from the results related to the co-heating test.

A second evaluation of the HTC can be obtained by analyzing the data collected on each separate unit. This step requires a reliable assessment of the solar heat gains inputs in the units.The HTC estimated by this way are called *confirmed HTC* as they are expected to confirm the reference value of the HTC. Results from the analysis of the units that are left in free-floating temperature mode are compared to the results from the units that are submitted to co-heating experiment.

3. EXPERIMENT

The experiment includes 9 days monitoring without occupancy. Ventilation inlets/outlets are sealed during the experiment. The ventilation system is off. Solar protections are removed when possible.

A difficulty is related to the presence of common walls and floors shared by adjacent units as it is not possible to gain access to all of the surrounding apartments or spaces when undertaking the tests. The temporarily placement of internal insulation on the party walls allows to overcome that difficulty in order to focus on the determination of the overall heat loss coefficient of the external facades (Fig. 2).

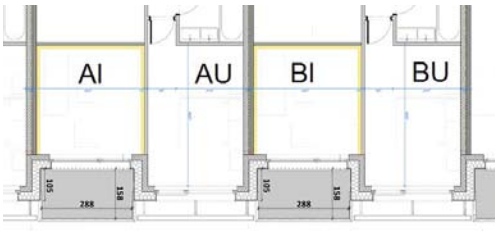

Figure 2: Layout (left) and perspective (right) of the apartments.

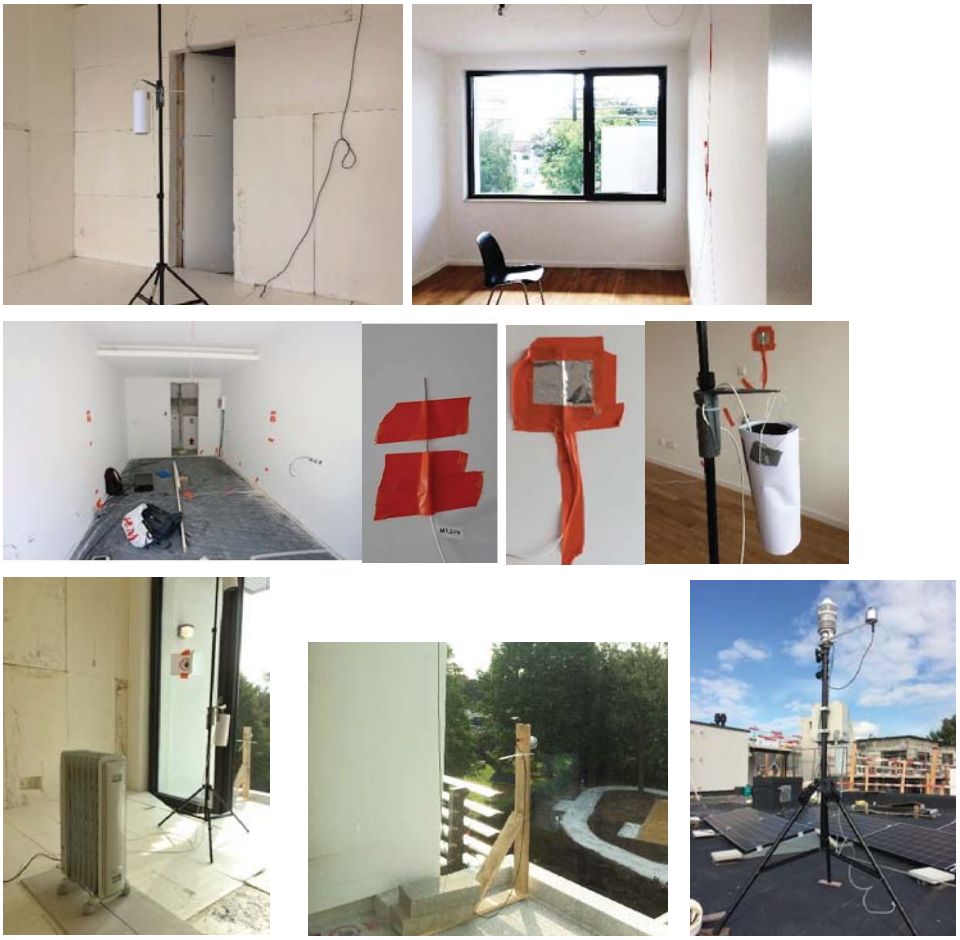

Figure 3: Experimental setup.
Row 1: Units covered or not covered with insulation panels.
Row 2: Temperature sensors at the interface of insulation layer before the placement of insulation panels (left and center left), at the surface of uninsulated walls (center right) and air temperature sensor protected from radiation (right).
Row 4: Experimental set-up for co-heating test (down left), external pyranometer (down middle), weather station located on the roof (down right).

A measurement campaign is performed on two South oriented apartments located in Brussels, from August to September 2017. The results concern two pairs of identical units, with one covered by inside insulation panels while the other is not (Fig. 2).

4. REFERENCE HTC

4.1 Results from stationary analysis

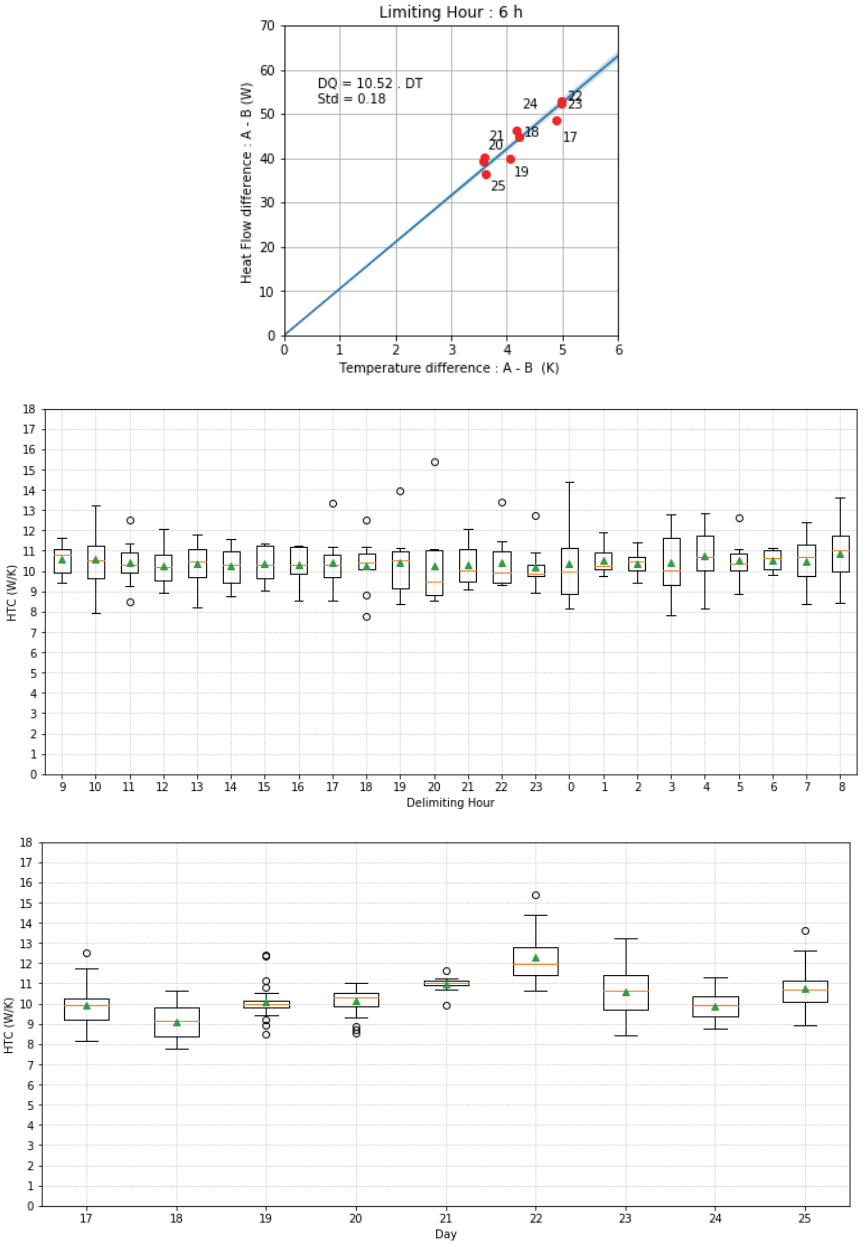

Figure 4: Correlation between daily means of heating powers and temperature differences between two identical insulated units (up), HTC obtained by shifting the aggregation intervals with delimiting hours ranging from 9 AM to 8 AM (middle), and daily average HTC values

obtained by shifting the aggregation intervals (down). Averages represented by green triangles.

Stationary analysis uses time-averaged data inputs in order to remove the influence of the thermal mass. The values of the heat input rate and temperature difference are averaged over a period of 24 hours (Jack, 2015).

The average heating powers used for the analysis are corrected by the heat transfers through the party walls. Those transfer heat flows are computed from the measured temperatures either at the interface of the insulation panels, when the party wall are internally insulated, or at the party wall surface, when the party wall are not covered by internal insulation. The heat transfer coefficient of the boundary layer is assumed to be equal to 8 W/m2-K. This assumption strongly influences the estimated heat flows when the party walls are not internally insulated. When the party wall are not insulated, the thermal resistance of the insulation equals 2.80 m2-K/W so that the assumption regarding the boundary layer heat transfer coefficient has a little influence on the estimated heat flows.

The HTC can be visualized as the slope of the regression line representing the average heating powers as function of the average temperature differences between the two units (Fig. 4). The intercept of the regression line with the power axis is forced to a zero value.

The linear regression method ideally requires a spread of temperature difference conditions during the test, otherwise the data points are clustered together, limiting the accuracy with which the regression can be carried out. Such a spread of temperature differences is not reached for all the tests and that is the reason why the intercept of the regression line with the power axis is forced to a zero value.

The HTC is estimated from the heating power divided by the difference of temperature between the units. The error associated to the HTC decreases as the difference of temperature between the units increases, provided the errors related to the heating power and to the temperature difference are constant as function of the temperature difference. The reliability of the HTC resulting from a co-heating test thus increases as the temperature difference between the units increases.

An average $\Delta T > 10$ K is recommended for co-heating test. Such a temperature difference between the units is difficult to reach because a maximum temperature of 30°C was set in the tested units to avoid damaging them. A temperature difference of 4 to 5 K is observed during the experiment (fig. 4, up).

If there is any fraction of stored solar energy remaining in the heat balance, the stored solar contributions can be better captured by shifting the aggregation interval used to compute the 24 hours average values. A box plot showing the HTC obtained by regressions on 9 daily average values, for different delimiting hours, shows a stability of the HTC as well as the robustness of a dawn-dawn aggregation approach (fig. 4, middle). Day by day values of the HTC can also be plotted considering samples associated to different delimiting hours, for each day (fig. 4, down).

The linear regression between average heat power inputs and average temperature difference only holds in the stationary case, when no heat is being charged/discharged by building components.

Dynamic effect due to a step of internal temperature set point may be observed by considering the day by day evolution of the HTC, either when the party walls of the tested units are not internally covered by insulation or in presence of a massive external roof that is not internally covered with insulation (fig. 5). When such a day by day evolution of the HTC is detected,

results from the stationary analysis should be considered as irrelevant and a dynamic analysis approach should be undertaken.

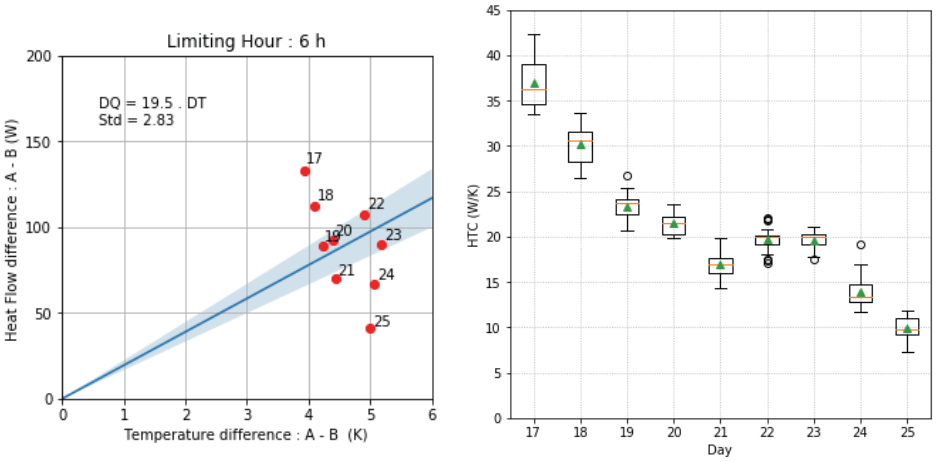

Figure 5: Correlation between daily mean heating power differences and temperature differences (left) and day by day evolution of the HTC (right), when party walls are not internally insulated.

4.2 Results from dynamic analysis

A literature review regarding dynamic heating experiments is included in Bauwens PhD Thesis (Bauwens, 2015). A common approach for analysis of dynamic data is to perform identification of the parameters of a grey-box model, constructed as lumped capacitance models, incorporating resistances and capacitances as well as introducing heat sources such as heating powers and solar gains (if any).

Application of grey-box modelling is based on prior physical knowledge of the building behaviour. The modeller starts from a simple model involving one capacity and interatively selects models of increasing complexity (fig. 6). The performance of the model is measured at each step through a given indicator, and the models are validated in both a statistical and physical context (Bacher & Madsen, 2010). Such an approach delivers a value of the HTC expressed as an equivalent resistance between internal and external temperature nodes.

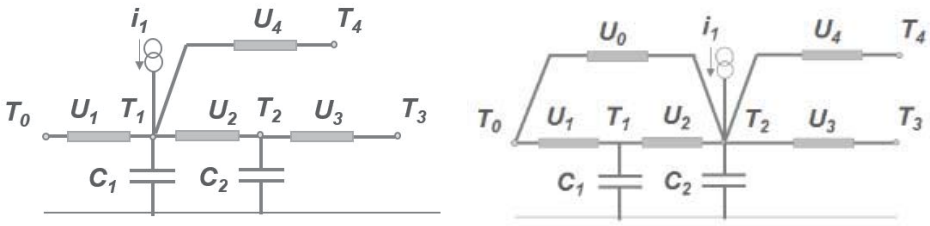

Figure 6: RC models used for insulated units (left) and uninsulated units (right). Temperature T3 is the temperature measured at the party wall surface and temperature T4 is measured in the adjacent zone of the same apartment.

The grey-box modelling approach is used to reproduce the time varying temperature difference between two identical units, when introducing the measured values of the heating powers differences. The performance of the model is quantified by the Root Mean Square of the error between the measured and the calculated temperature profiles (fig. 7). The corresponding RC networks are displayed on Fig. 6, where U represent conductance values. Table 1 displays the corresponding parameters of the RC models as well as their related HTC values.

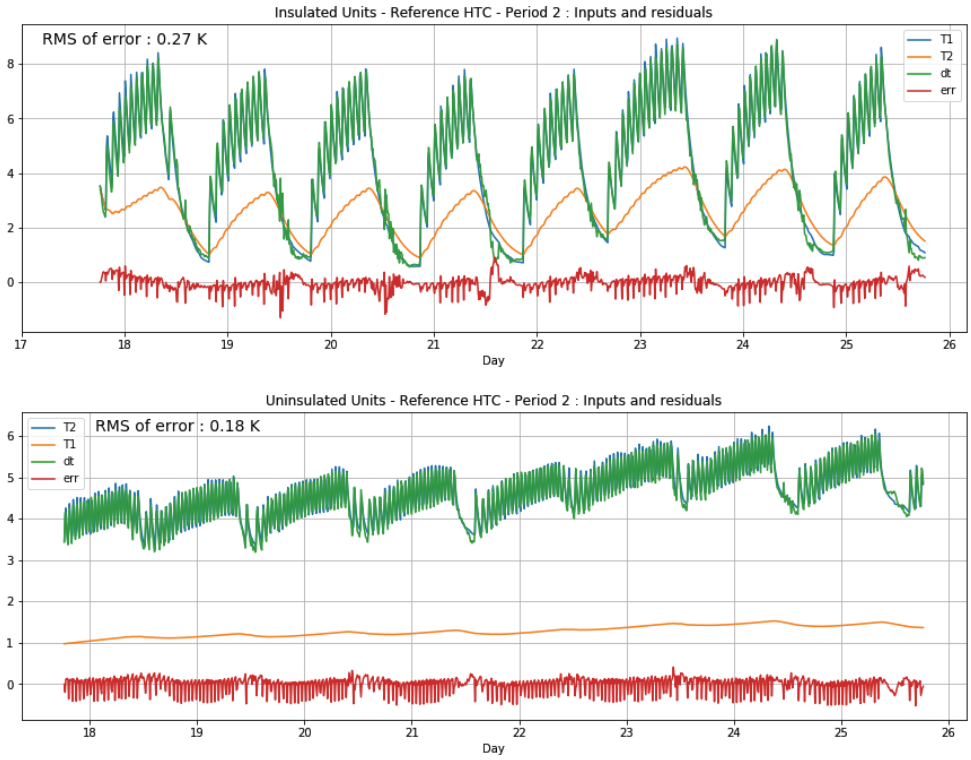

Figure 7: Measured indoor temperature difference between two identical units (green curve) and corresponding profile generated by grey box modelling (blue curve), in insulated units (up) and uninsulated units (down).

Tableœ 1: RC models conductances and related values of the HTC in W/K.

Units	U0	U1	U2	U3	U4	HTC
Insulated	-	7.56	26.02	32.26	5.47	7.56 W/K
Uninsulated	10.59	20.36	8.08	485.45	82.23	16.37 W/K

The grey box modelling approach gives a HTC value of 7.56 W/K for insulated units, close to the predicted HTC of 6.58 W/K (Table 2). The HTC obtained for uninsulated units is 16.37

W/K. That value is close to the day by day evolution of the HTC displayed on fig. 5, but far from the predicted HTC of 7.40 W/K (Table 2).

5. PREDICTED HTC

The predicted values of the façade HTC are 6.58 W/K for insulated units and 7.40 W/K for uninsulated units (Table 2). The corresponding measured values are respectively 7.56 W/K and 16.37 W/K, showing a difference that can be explained by considering the heat transfers due to internal thermal bridges towards adjacent units (Fig. 8 and Table 3).

Table 2: Predicted HTC of the tested units.

	Through the facade				
Units	External walls	AU	Thermal Bridges	ψL	Infiltration
				W/K	Heat losses
	W/K				
Insulated	Glazing	3.09	Parapet	0.81	
	Frame	1.61	Screen anchorages	0.35	
	Opaque vertical walls	0.30	Balcony	0.10	
			Inward angles	- 0.15	
	Total	*5.00*	*Total*	*1.11*	*0.47 W/K*
Uninsulated	Glazing	1.99	Parapet	1.25	
	Frame	1.27	Screen anchorages	0.47	
	Opaque vertical walls	1.06	Outward angles	0.31	
	Roof	0.88	Inward angles	- 0.21	
	Total	*5.20*	*Total*	*1.82*	*0.38 W/K*

Table 3: Thermal bridges towards the adjacent zones.

	Towards adjacent zones	
Units	Thermal Bridges	ψL
Insulated	Single party wall	2.65
	Double party wall	1.83
Uninsulated	Single party wall	2.65
	Double party wall	1.83
	Ceiling-North party wall	1.30
	Ceiling-single party wall	1.56
	Ceiling-double party wall	2.11
	Ceiling-North party wall	1.12
	Ceiling-single party wall	0.93
	Ceiling-double party wall	1.63

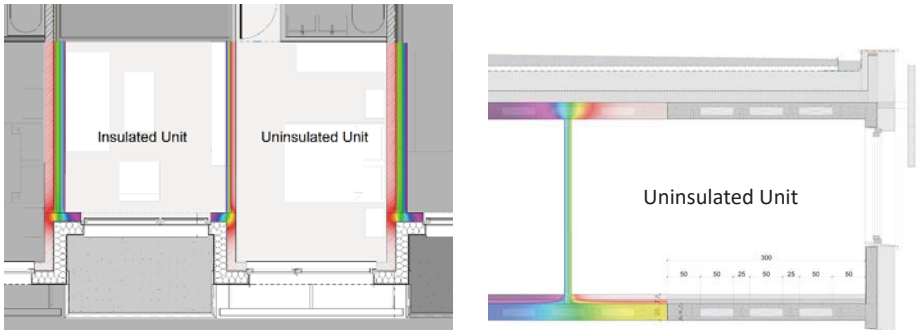

Figure 8: Thermal bridges towards adjacent zones.

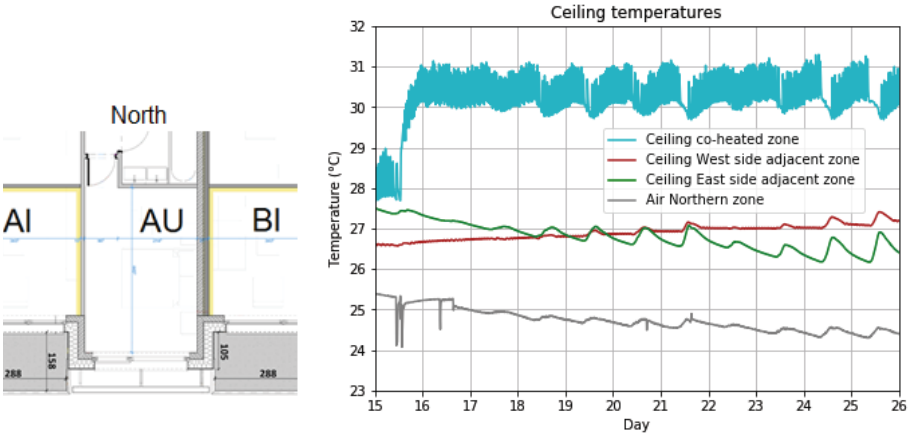

Figure 9: Temperature of the uninsulated unit at the ceiling (blue curve), at the ceilings of the adjacent zones (red and green curves), and in the Northern zone (grey curve), during a co-heating test.

An updated value of the HTC can be computed by including the extra heat flows due to the internal thermal bridges in the heat balance of the tested units. Those extra heat flows are evaluated from the predicted ψL values of the thermal bridges and considering the measured temperatures at their boundaries (Table 4). When a co-heating test is performed in one unit surrounded by unheated units, the temperature differences occurring at the connections of the vertical party walls with the ceiling is magnified by the stratification effect due to the co-heating (Fig. 9).

Dividing the difference of internal thermal bridges heat flows by the average temperature difference measured between both identical uninsulated units (4.60 K) during the co-heating test performed in one of them, the impact of the internal thermal bridges heat flows on the reference HTC is 8.72 W/K for the uninsulated units.

A similar approach applied to insulated units gives an impact of 3.59 W/K on the reference HTC, due to internal thermal bridges.

Table 4: Internal thermal bridges heat flows towards adjacent zones (Saints Pierre & Paul).

Units		Co-heated		Free floating temperature	
	Thermal bridges	ΔT *K*	Φ *W*	ΔT *K*	Φ *W*
Insulated	Single party wall	1.9	5	2.3	6
	Double party wall	6.5 (assumption)	12	-2.3	-4
	Total		*17 W*		*2 W*
Uninsulated	Single party wall	-1.9	-5	-2.3	-6
	Double party wall	2.3	4	0 (assumption)	0
	Ceiling-North party wall	4.9	6	0.5	1
	Ceiling-single party wall	3.4	5	-1.5	-2
	Ceiling-double party wall	3.7	8	0 (assumption)	0
	Floor-North party wall	4.9	5	0.5	1
	Floor-single party wall	3.1	3	0.1	0
	Floor-double party wall	4.7	8	0 (assumption)	0
	Total		*34 W*		*-7 W*

The difference between the predicted and the reference value of the HTC observed in uninsulated units (7.40 W/K and 16.38 W/K) is mostly explained by the effect of internal thermal bridges (8.72 W/K).

6. CONFIRMED HTC

The confirmation of the HTC by analyzing the data measured on the separate units requires a reliable estimation of the solar heat gains.

6.1 Solar heat gains assessment

Direct and diffuse solar irradiations are measured on a horizontal plane, with a pyranometer located on the roof of the building. Global irradiation is measured on a vertical plane parallel to the façade (Fig. 10).

Figure 10: Weather station, measurement of vertical irradiation and urban masks.

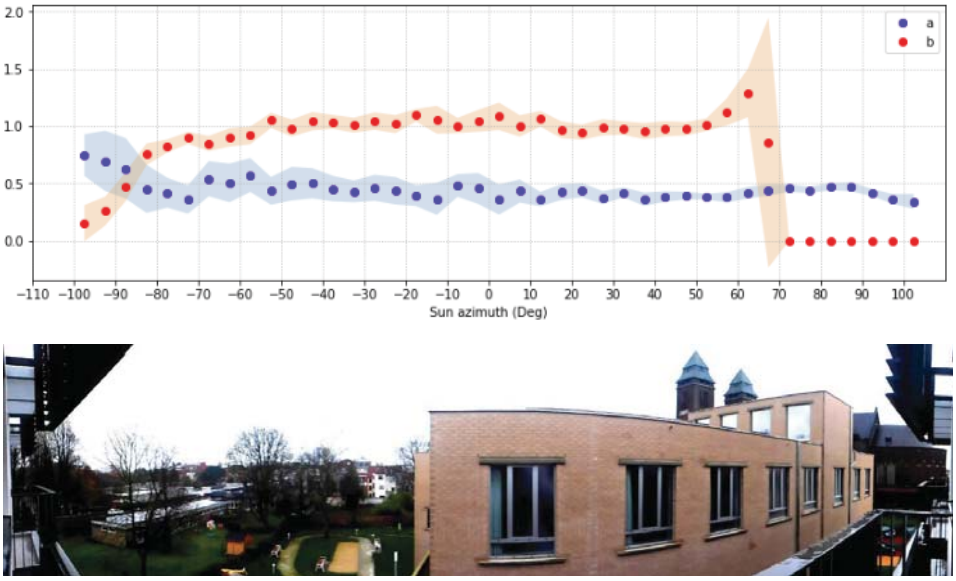

Figure 11: Decomposition of the vertical solar irradiation into its diffuse (a) and direct (b) components, with façade Azimuth = - 22°.

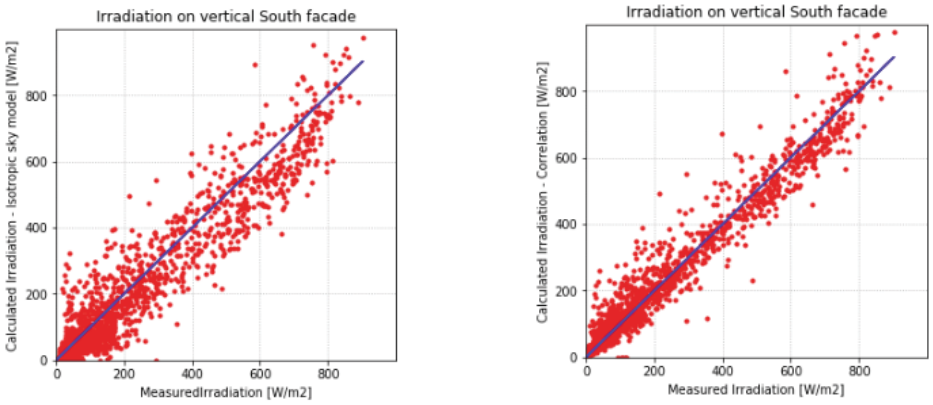

Figure 12: Vertical solar irradiation predicted by a conventional isotropic sky model (left) and by correlations (right), compared to measured values, with façade Azimuth = - 22°.

As measurement occurs in an urban site, the effect of the masks surrounding the building must be considered. The effect of the shading due to the screens surrounding the windows must be calculated as well.

The global solar irradiation measured on a vertical plane is shared into its direct and diffuse components by the following correlation, involving both horizontal diffuse and direct irradiations, with the direct component being projected from the horizontal to the vertical plane:

$$I_v = a(\gamma)\, I_{dh} + b(\gamma)\, I_b \qquad (1)$$

I_v Global irradiation on a vertical plane facing surrounding masks *W/m²*
I_{dh} Diffuse irradiation on a horizontal plane located in an open space *W/m²*
I_b Direct irradiation on a vertical plane, computed from the direct irradiation measured on an horizontal plane located in an open space *W/m²*
γ Sun azimuth *degree*

The correlations are done for given ranges of the sun azimuth (Fig. 11).

The vertical irradiations predicted by the correlations (1) can be compared to the vertical irradiations predicted by a conventional isotropic sky model (2):

$$I_v = \frac{1+\cos p}{2} I_{dh} + \frac{1-\cos p}{2} \rho I_{th} + I_b \quad (2)$$

I_{dh} Diffuse irradiation on a horizontal plane located in an open space *W/m*
I_{th} Global irradiation on a horizontal plane located in an open space *W/m²²*
ρ Ground refection factor (ρ set to 0 to fit better with the measured values).
p Slope of the plane *degree* (90° for a vertical plane).

The agreement provided by the correlations is better than that provided by the conventional isotropic sky model (Fig. 12). The RMS of the predicted irradiation error drops from 50.2 W/m² for the isotropic model until 31.9 W/m² for the correlation model. In an urban context, the correlation model is more likely to capture the effect of masks due to the elements facing each other (buildings, trees).

Figure 13: Effect of shading screens surrounding windows.

The calculation of solar heat gains includes the assessment of the solar factors from the sky (diffuse solar radiation), the assessment of all the shadings on the glazing (direct solar irradiation) and the assessment of reflected radiation (balconies and lateral walls). The assessment of the shading due to the screens surrounding the windows is an important issue (Fig. 13).

Considering the previously calculated reference HTC, a comparison can be made between the daily average values of the calculated solar heat gains and the average solar heat gains required to balance the heat losses of the units when computed from the units reference HTC. Such a comparison is shown on fig. 14 for the two insulated units with stationary reference HTC equal to 10.52 W/K.

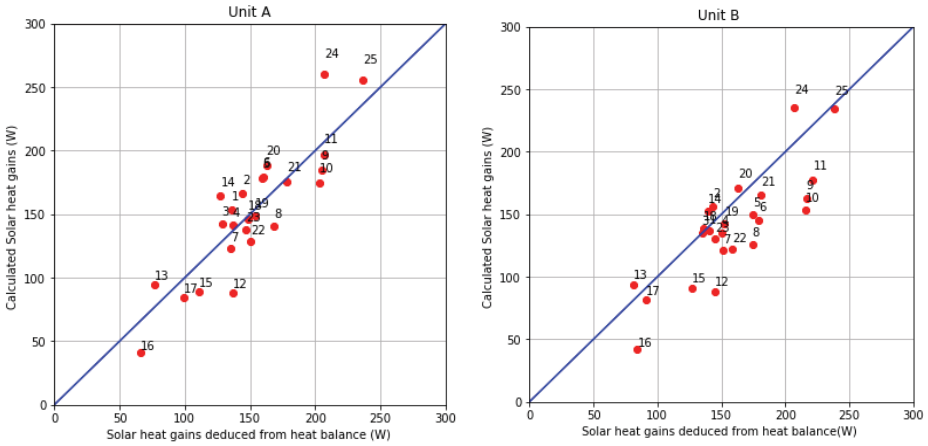

Figure 14: Calculated solar heat gains compared to the heat gains required to balance the heat losses associated to the reference HTC of insulted units.

6.2 Uncertainty assessment

The probable uncertainty of the HTC is calculated on the basis of the chi-square merit function, defined for a unitary standard deviation. A confidence interval of the HTC is calculated by considering the variation of the chi-square as function of the HTC, around its minimum, with the rest of the parameters being chosen to minimize the chi-square. The asymmetric limits of a confidence interval are defined for a variation of chi-square (fig. 5):

$$\Delta\chi^2 = \chi^2 - \chi^2_{min} = \chi^2_{min} \qquad (3)$$

6.3 Results from stationary analysis on separate units

Results from stationary analysis on separate units are presented on fig. 15 and 16 and summarized on Table 5.

Table 5: Results from stationary analysis on separate units

Unit	Test	HTC *W/K*	INTERVAL *W/K*
Insulated	T° 29°C	10.46 ± 0.37	–0.72 + 1.12
Insulated	Floating T°	9.68 ± 0.39	–0.74 + 1.26
Uninsulated	T° 29°C	10.54 ± 0.29	–0.65 + 0.78
Uninsulated	Floating T°	6.82 ± 0.79	–1.19 + 3.31

The HTC values obtained in the identical insulated units are similar (HTC values of 10.46 and 9.68 W/K) while the values obtained for identical uninsulated units are different (HTC values of 10.54 and 6.82 W/K). Co-heating test results show increasing HTC values, particularly when performed in uninsulated units.

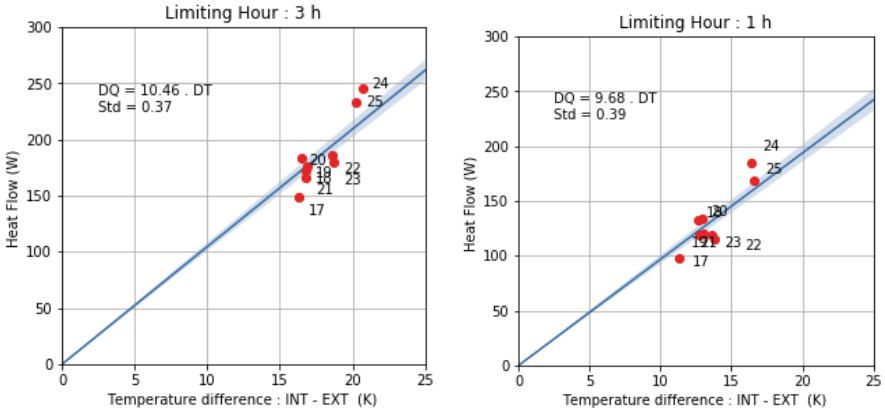

Figure 15: HTC obtained for two identical insulated units tested in parallel, with one co-heated at 30°C (left), and the other left in free floating temperature (right).

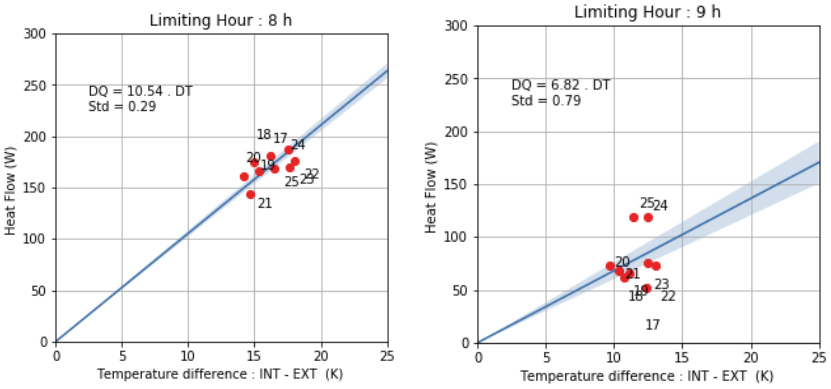

Figure 16: HTC obtained for identical uninsulated units tested in parallel, with one co-heated at 30°C (left), and the other left in free floating temperature (right).

6.4 Results from dynamic analysis on separate units

Results from dynamic analysis on separate units are presented on fig. 17 and summarized on Table 6.

Table 6: Results from dynamic analysis on separate units.

Unit	**Test**	**HTC** *W/K*	**INTERVAL** *W/K*
Insulated	T° 29°C	6.43	– 1.05+ 1.14
Insulated	Floating T°	7.55	– 0.90 + 1.17
Uninsulated	T° 29°C	10.93	– 4.10 + 4.74
Uninsulated	Floating T°	7.00	– 3.54 + 4.04

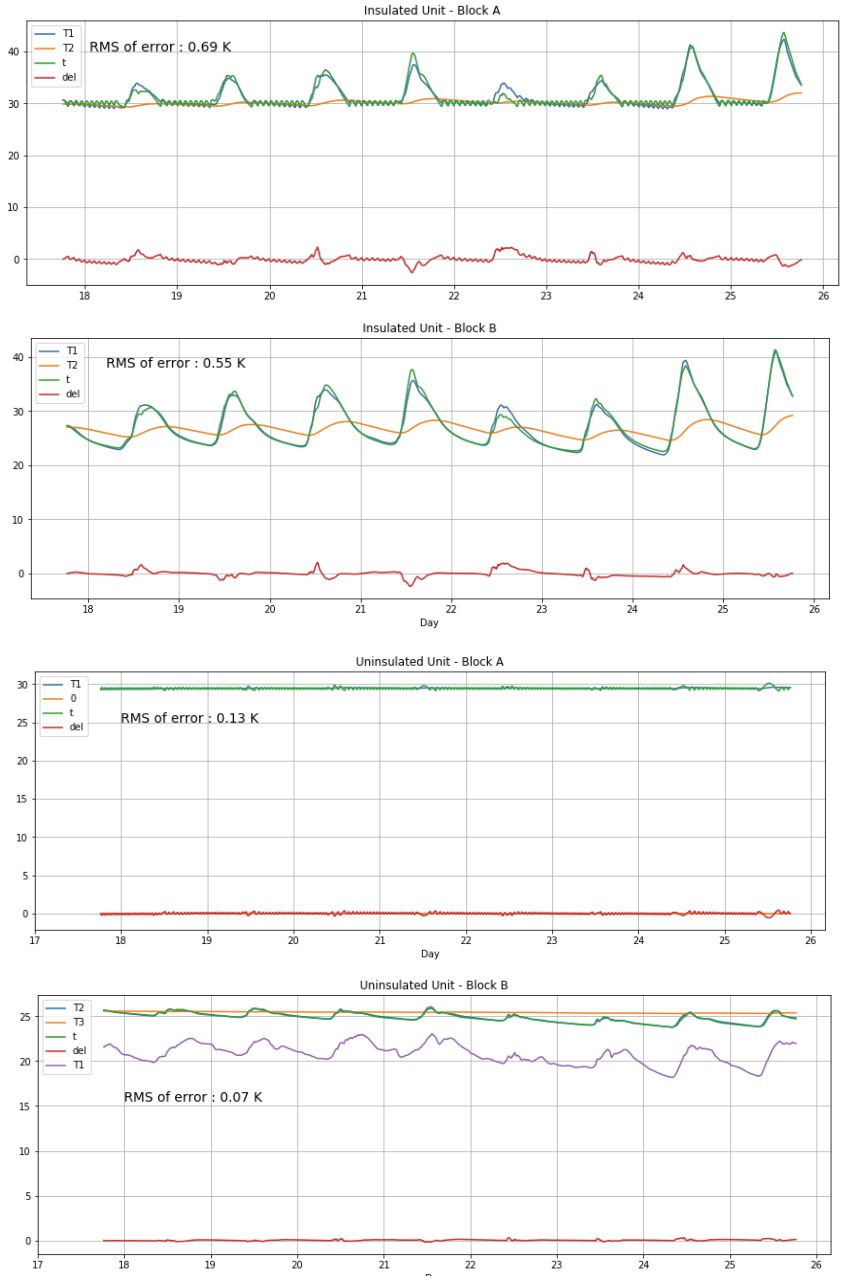

*Figure 17: Indoor temperature profiles generated by grey-box modelling (blue curves) compared to measured temperatures (green curves) for identical **insulated** units tested in parallel with one co-heated at 30°C (up), and the other in free floating temperature (up middle), and for identical **uninsulated** units tested in parallel with one co-heated at 30°C (down middle), and the other in free floating temperature (down).*

The HTC values obtained in the identical insulated units are similar (HTC values of 6.43 and 7.55 W/K) while the values obtained for identical uninsulated units are different (HTC values of 10.93 and 7.00 W/K). Co-heating test results show increasing HTC values, particularly when performed in uninsulated units. The associated confidence interval indicates more reliable results when the units are internally insulated.

Fig. 18 shows a comparison of the resulting HTC with the confidence intervals.

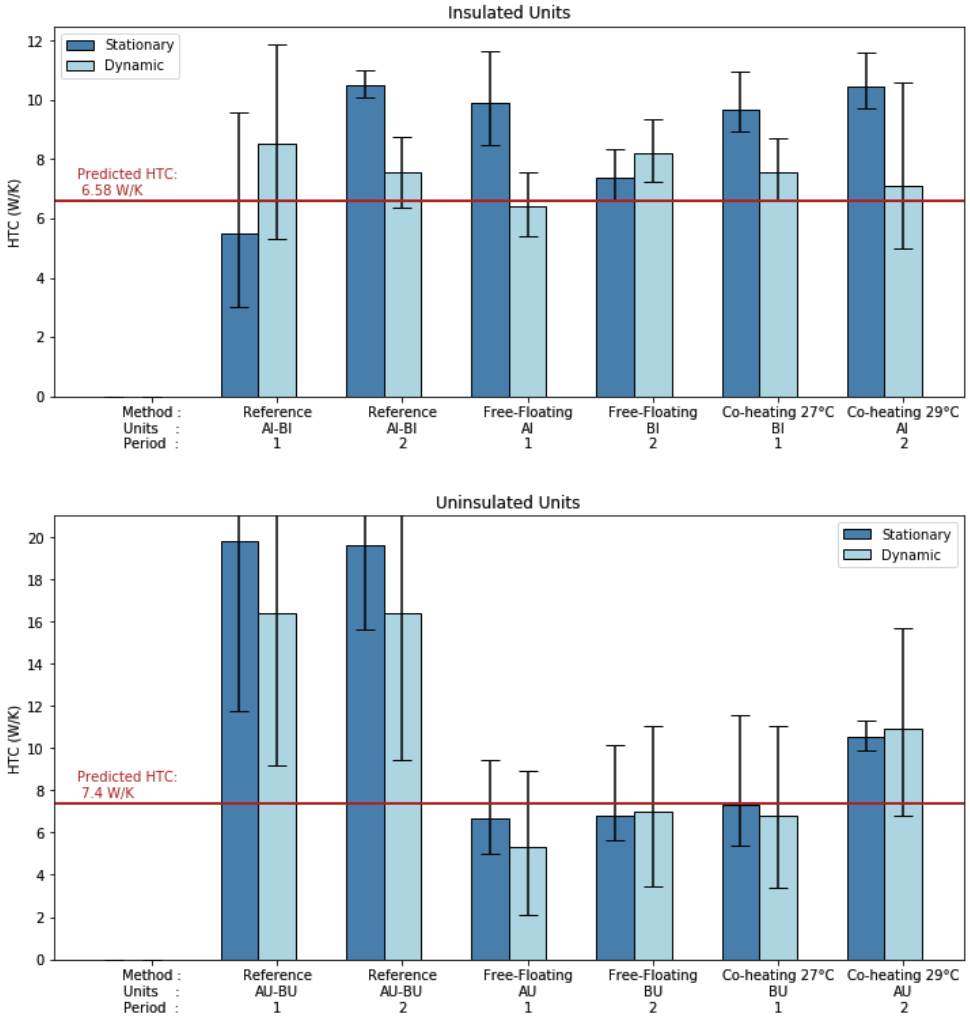

Figure 18: Predicted HTC, Reference HTC and confirmed HTC values obtained by stationary and dynamic analysis on insulated (up) and uninsulated units (down).

For the insulated units: The mean values of the HTC are close to the predicted value when obtained by dynamic approach, showing a maximum gap of -1 W/K (-13%). This gap increases up to +3 W/K (+41 %) when the analysis is performed trough a stationary approach.

For the uninsulated units: The mean values of the HTC obtained by either stationary or dynamic approaches confirm the predicted HTC, provided the test is performed in floating temperature mode (maximum difference of 19 %). This is also true for the co-heating test performed at 27°C as this set point was too low to start the heating system.

The uncertainty associated to the HTC is much higher when the tested units are not covered by inside insulation panels, whatever the testing method (free floating temperature vs co-heating) or the analysis method (stationary vs dynamic).

When using internal insulation panels to perform the test, the uncertainty is divided by 2 on average in case of stationary analysis of the data (interval reduced from 63 to 30% of the HTC), and by 3 in case of dynamic grey-box modelling approach (interval reduced from 117 to 41% of the HTC). The placement of inside insulation on party walls is a relevant solution to increase the reliability of the assessed HTC.

7. CONCLUSION

A methodology is proposed to identify a reference value of the HLC in case of parallel experiment on identical units. Data measured in parallel on identical units can be used to generate fictitious experiments by subtracting the results of the free floating temperature experiment from the results of the co-heating experiment, in order to asses a reference HTC.

Confirmed values of the HTC are then obtained by considering the heat balance of each unit separately, each of them being provided both with the heat inputs due to the calculated solar heat gains and the measured powers from electric radiators.

The methodology is applied on 4 apartments units. Two solicitations are used (free floating temperature due to solar gains vs co-heating at constant set point) with two types of boundary conditions (with and without placement of internal insulation panels on common party walls) . The data are analyzed by stationary and dynamic approaches. The stationary approach uses 24 h average data while the dynamic approach is based on grey-box modelling. An uncertainty indicator is used to provide a confidence interval to the results.

When coupled with the placement of internal insulation on party walls, the grey-box modelling approach is able to predict the HTC with a maximum discrepancy of 13 %, according to our uncertainty indicator. The discrepancy increases until 41 % when a stationary analysis is performed on the same measurement data.

When the party walls are not covered by internal insulation panels, a reliable assessment of the HTC can only be performed for free floating temperature conditions, either by a stationary or by a dynamic approach. A reliable assessment of the HTC is not possible in case of a co-heating test, whatever the analysis method, either stationary or dynamic. This lack of reliability is due to the effect of internal thermal bridges. The heat exchanges through those thermal bridges are magnified by the increase of temperature differences at their boundaries, due to the co-heating experiment.

The methodology used to obtain a reference value of the HTC on basis of the results with and without co-heating on identical units, is corrupted by the effect of internal thermal bridges. This effect entails an overestimation of the reference HTC. It mostly explains the discrepancy observed in insulated units (10.5 W/ instead of 6.58 W/K, K by stationary approach) and in uninsulated units (16.4W/K instead of 7.40 W/K, by dynamic analysis).

The relevancy of the placement of inside insulation on common party walls is assessed on basis of our uncertainty indicator. With the use of inside insulation panels to perform the test, the uncertainty indicator is divided by 2 on average in case of stationary analysis of the data, and by 3 in case of dynamic grey-box modelling approach. The placement of inside insulation on party walls can be considered as a relevant solution to increase the reliability of the HTC assessment. A rough estimation of the cost related to the placement and the removal of the insulation panels including repair (patching of the ceiling) is about 2000 EUR per tested unit including VAT.

ACKNOWLEDGEMENT

Innoviris, the Brussels Institute for Research and Innovation, is gratefully acknowledged for their financial support to CAMB(B)RIDGE research Project. RMI, the Royal Meteorological Institute of Belgium is gratefully acknowledged for providing weather data.

REFERENCES

Bacher, P., & Madsen, H. (2010). *Procedure for identifying models for the heat dynamics of buildings: Financed by The Danish Electricity Saving Trust and Vind i Øresund-Interreg 4A*. Retrieved from

Bauwens, G. (2015). In Situ Testing of a Building's Overall Heat Loss Coefficient-Embedding Quasi-stationary and Dynamic Tests in a Building Physical and Statistical Framework.

Bauwens, G., & Roels, S. (2014). Co-heating test: A state-of-the-art. *Energy and Buildings, 82*, 163-172. doi:10.1016/j.enbuild.2014.04.039

Everett, A. (1985). *RAPID THERMAL CALIBRATION OF HOUSES*. Retrieved from

Jack, R. (2015). *Building diagnostics: practical measurement of the fabric thermal performance of houses.* © Richard Jack,

Janssens, A. (2016). *International Energy Agency, EBC Annex 58, Reliable building energy performance characterisation based on full scale dynamic measurements, Report of Subtask 1b: Overview of methods to analyse dynamic data*. Retrieved from

Johnston D., M.-S. D., Farmer D., Wingfield J., Miles-Shenton D., Bell M. (2013). *Whole House Heat Loss Test Method (Coheating)*. Retrieved from

Stamp, S. (2016). *Assessing uncertainty in co-heating tests: Calibrating a whole building steady state heat loss measurement method.* UCL (University College London),

Wingfield J., J. D., Miles-Shenton D., Bell M. (2010). *Whole House Heat Loss Test Method (Coheating)*. Retrieved from CeBE Centre for the Built Environment:

Questions and Answers:

Sebastian Gonzato:

This would appear to be a very complicated setup – what modifications do you envisage to make it more user friendly? Are there alternative ways of calculating HTC for the façade and what are the benefits of your method?

Gabrielle Masy:

We intend to develop a simplified version of the setup using a temporary wall made of self-supporting insulation panel. There are ways to measure the U value of a wall but we intend to measure the global heat transfer coefficient of the whole façade.

***

Madjid Madjidi:

Does your result for measurement of radiation come from a non-isotropic sky or from surrounding?

Gabrielle Masy:

The horizontal irradiations (global and diffused) measured on site are similar to those measured in a nearby weather station. It means that the sky is isotropic but the radiation measured on site on a vertical plane are affected by the surroundings mask effects.

Impact of air-conditioning waste heat on air temperature in Paris during heat waves

Brice Tremeac[1]

[(1)]Laboratoire de Chimie Moléculaire, Génie des Procédés Chimiques et Energétiques (EA 7341), Conservatoire National des Arts et Métiers, HESAM Université, 292 rue Saint Martin 75003 Paris

ABSTRACT

This communication presents some results from Clim² project included two French laboratories: CNAM/CMGPCE (Dr B. Tremeac and Pr F.Meunier) and CNRM/GAME, Météo France (Dr C. DeMunck, Dr G. Pigeon, Dr V. Masson and C. Marchadier) and an urban cooling network company in Paris Climespace (Dr M. Merchat and P. Poeuf). This project studied influence of air-conditioning waste heat on air temperatures in Paris during heat waves (9-13 August 2003). Results of a meso-scale meteorological model coupled to an urban energy balance model including a simplified building model, are used. Simulations based on a realistic spatial cartography of air-cooled chillers and cooling towers in the city of Paris and surroundings have been performed. Five scenarios will be discussed: firstly, a baseline without air-conditioning (REF scenario); secondly the actual situation including individual air-dry coolers, wet cooling towers and an urban cooling network relying on free-cooling (water-cooled A/C with the river Seine) (REAL scenario). A third scenario will assume that all the heat is rejected as sensible heat in the atmosphere (DRY AC scenario). Two other scenarios correspond to a prospective where A/C is doubled: all the heat is rejected as sensible heat in the atmosphere (DRY ACx2 scenario); all the heat is rejected underground or in the river Seine (NOREJ scenario). The first three scenarios show that the heat island effect is enhanced by A/C management whereas the fifth scenario is neutral and even slightly decreases the heat island.

Keywords: Air-conditioning, heat waves, heat island mitigation, urban heat island

1. INTRODUCTION

As a result of climate change, many cities including Paris are expected to face a strong increase in the frequency and intensity of heat-waves by the end of the 21st Century. In Paris, the frequency of heat-waves could rise from an average one day per year to 14-26 days per year (Lemonsu *et al.*, 2013). The most worrying consequence is certainly the risk for heat waves since heat wave is becoming a “major summer killer”. The 2003 heat wave in Europe killed 14 802 persons in France (Billiard, 2004). Air-conditioning (A/C) is a well-known technic to mitigate the effect of heat waves in buildings. The use of energy for space cooling is tripling between 1990 (about 600 TWh) and 2016 (about 2000 TWh) (IEA, 2018). In big cities like Paris, Tokyo or Doha for example, the waste heat discharged by air conditioners into the urban atmosphere is significant, especially during summer. When air-cooled chillers are used, A/C creates indoor comfort but as it rejects heat to the surroundings, it contributes to increase outdoor air temperatures.

Wen and Lian (2009) developed a box model to quantitatively determine the rise in outdoor air temperature caused by using domestic air conditioners in Wuhan, China. The variation in temperature may reach 2.56 °C. Hsieh *et al.* (2007) discussed the penalty of heat rejection to

the cooling load during the night-time, in Taipei city. The temperature rise obtained through numerical modelling, was found to reach 1.89 °C. In Tokyo, the heat resulting from air conditioners usage increased the air temperature by 1-2 °C or more on weekdays, in the office district (Ohashi *et al.*, 2007).

These results demonstrate the importance of considering the heat resulting from energy consumption with air-conditioning on the energy balance. Beside individual A/C, there are urban cooling networks that manage the heat rejection differently, as is the case for Climespace in Paris which use either wet cooling towers or the river Seine. The consequences of such managements on the street temperatures in Paris and the 25km surroundings in the case of the severe heat wave which occurred in August 2003 will be discussed in this communication.

This paper presents a summary of some results from CLIM² project included two French laboratories: CNAM/CMGPCE (Dr B. Tremeac and Pr F.Meunier) and CNRM/GAME, Météo France (Dr C. DeMunck, Dr G. Pigeon, Dr V. Masson and C. Marchadier) and an urban cooling network company in Paris Climespace (Dr M. Merchat and P. Poeuf).

2. MODEL AND METHODOLOGY

MESO-NH, a meso-scale meteorological model developed by Lafore *et al.* 1998 and Stein *et al.* 2000 was used to reproduce meteorological conditions for the 2003 heat wave (9-13 August). The general methodology is shown Figure 1. The exchanges of energy (momentum, convection, radiation) are computed using a tiling approach splitting the surface between 4 major types of land use that are natural or agricultural covers, seas, inland water and urban areas. For the latter surfaces, the Town Energy Balance (TEB) is used (Masson, 2000). It is a single layer urban canopy model that has been evaluated on various cities and climate. Within TEB, the urban landscape is simplified as an isotropic network of street canyons. TEB simulates exchanges of momentum, heat and water for three generic surfaces: road, wall and roof that interacts directly for radiative fluxes and with the street canyon air volume for convection fluxes. Implementation of A/C within TEB was based on the heat released by A/C and an indoor target temperature of 26°C for buildings with A/C (Figure 2). The other inputs for the model are the surface building fraction, the ratio between the buildings' height and the streets width (H/W), the building height, the thermal and radiative properties of roads, walls and roofs. The simulations realized for this study use specific parameters computed for the urban area of Paris by the Urban planning agency of Paris-APUR, Agence Parisienne d'Urbanisme-from digital maps.

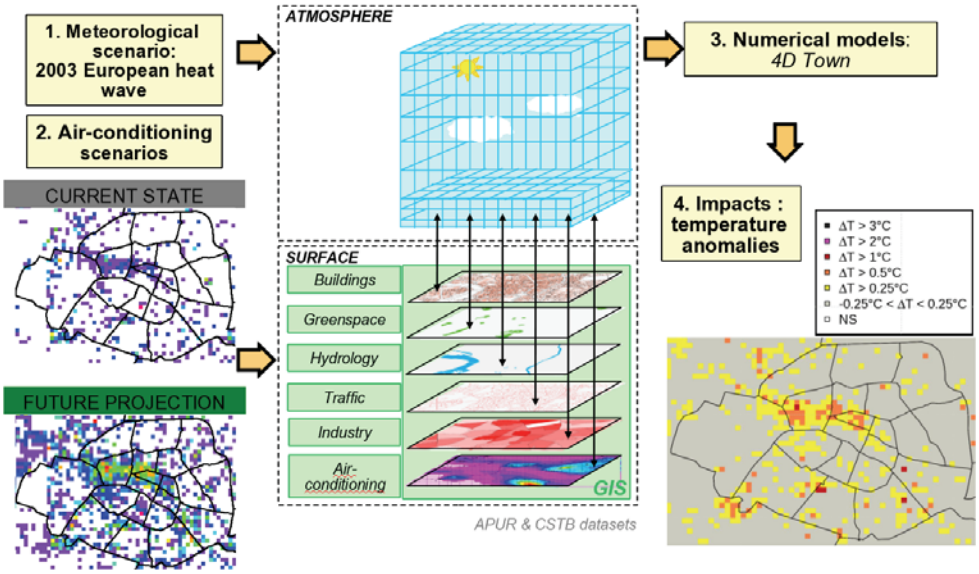

Figure 1: General methodology for simulation (de Munck et al., 2010)

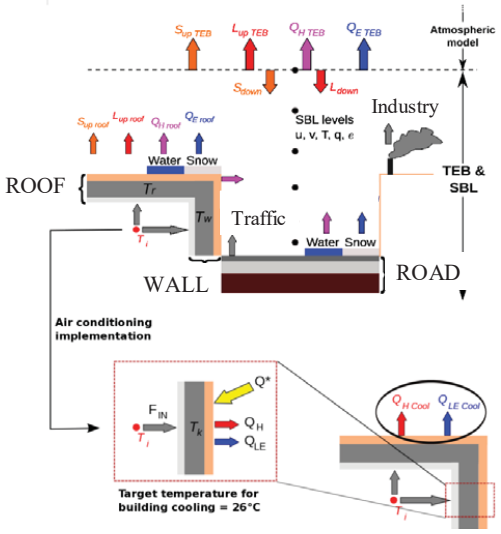

Figure 2: Simplified description of TEB model implemented with A/C (de Munck et al., 2010).

Simulations based on a realistic spatial cartography of air-cooled chillers and cooling towers in the city of Paris and its surroundings (simulation domain, 125 km x 125 km with Paris as center with 250 m x 250 m mesh for Paris and 1.5 km x1.5 km for surroundings) have been performed.

For the estimation of heat released, A/C systems are classified in three categories:

(1) evaporative cooling towers discharging latent waste heat to air. Their inventory was facilitated by the legal requirement imposed on them to declare their power and localisation to the authorities. In terms of heat discharge, the waste heat is assumed partitioned into 95% latent heat and 5% sensible heat (based on the manufacturers' data);

(2) large dry cooling towers (data center, commercial center, hotels …). The estimation of the heat released was undertaken based on a visual inventory via open source satellite images (using Google Earth for example) for roof condensers;

(3) small dry cooling systems (from 6 to 70 kW per unit). Visual inventory of these small condensers was first carried out within inner Paris on a sub sample of five districts (ground surfaces between 742.103 and 260.103 m^2) representative in building type and dwellings or business diversity, using both open source satellite images for roof condensers and Google Street View for front condensers. The cooling power of the small dry condensers observed yielded two levels (i.e. baseline ratio) of dry waste heat intensity for these five districts: 8 and 34 W/m^2_{land} (in this case "land" is used for mesh's area and not for building area).

An example of visualization using online tools is shown Figure 3.

Figure 3: Example of visualization of condensers using online tools

Based on this inventory, about 5.6 GW of heat released from A/C for Paris and its surroundings has been implemented in the model according to the types of air-conditioning systems existing in the city: dry air cooling for individual systems, wet towers and a district cooling network using either wet towers or water-cooled A/C with the river Seine (technique known as free-cooling). This is the REAL scenario.

Another present-time scenario is the DRY AC scenario: all the heat released is converted to sensible heat. The overall heat released over the simulation domain is the same as for the REAL scenario.

Two other scenarios correspond to a future situation where A/C is doubled: one assumes that all the heat is rejected as sensible heat in the atmosphere (DRY ACx2 scenario), the other, on the contrary, even if based on the DRY ACx2 scenario, assumes that all the heat is rejected underground or in the river Seine (NOREJ scenario). In this study, impact on ground or river temperature is not taken account. The NOREJ scenario is quite complicated to implant in an old city like Paris. This ideal scenario could give some informations for a new city with an optimal management of A/C waste heat.

For the DRY ACx2 scenario, to avoid a non-realistic case, a heat rejection limit of 126 W/m^2_{floor} (corresponding to a ratio of 90 W_{cold}/m^2_{floor}) [1] is imposed into the model. Furthermore, the 10.32 GW of sensible heat reject is distributed with 68% in Paris and 32% outside of central Paris.

All scenarios are compared to a baseline (NO-AC scenario) referring to a situation without air-conditioning. All results of temperatures are for pedestrian height: 2 m from the ground.

3. RESULTS

3.1 Impact on street temperatures

When compared to the baseline without A/C, the three scenarios considered in Figure 4 show an increase in 2 m street temperatures which is greater at night than day time (airflow is lower at night than during the day). Compared to the baseline, temperature elevation at night in Paris is about 0.5 °C, 1 °C and 2 °C for the REAL, DRY AC and DRY ACx2 scenarios respectively. The average temperature variation is about +0.25 °C, +0.5 °C and +1 °C outside of Paris.

As expected, temperature in central Paris is more influenced by A/C than outside, due to a strong concentration of air-conditioned buildings in Paris. The future projection scenario (DRY ACx2) impacts wider zones in the city.

[1] "floor" is used for building area and not for the mesh's area

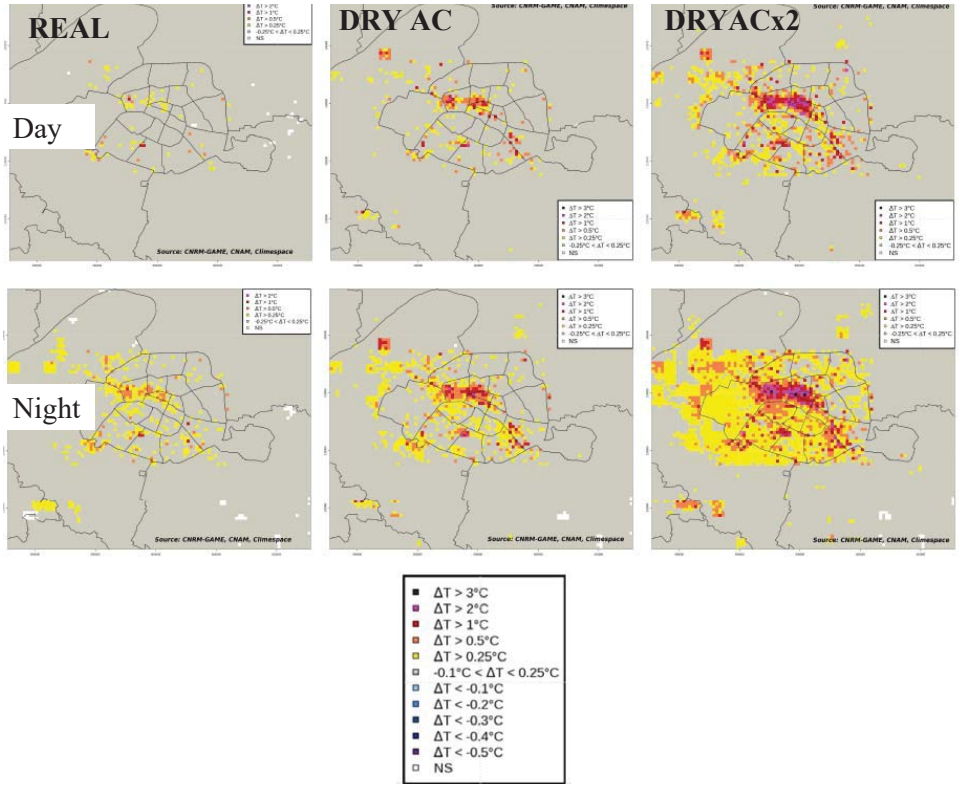

Figure 4: Average variation of temperature at 2 m for 3 A/C scenarios at daytime and night-time (de Munck et al., 2010)

3.2 Impact on Urban Heat Island (UHI)

Figure 5 represents for a cross section an average night-time street temperature profile for the four scenarios including the baseline (NO-AC). This figure shows the influence of air-conditioning on the heat island in Paris, especially on the spatial expansion and the intensity. For the NO-AC scenario UHI (Urban Heat Island) amplitude reaches 3.75 °C and it increases to 4.5 °C for DRY AC and 5.5 °C for DRY ACx2.

For the REAL scenario corresponding to an actual situation of the air-conditioning development in Paris and its surroundings, the amplitude of the UHI is not modified notably compared to the baseline. However, this scenario shows that A/C still influences the temperature profile with an increase in temperature in the hottest areas in central Paris.

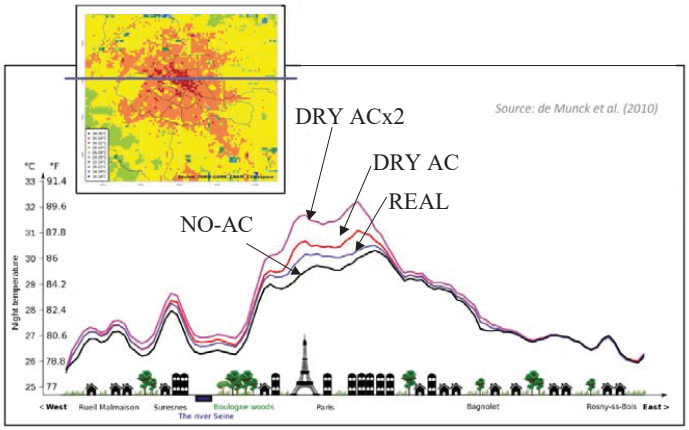

Figure 5: Temperature profiles at night-time for a West-to-East cross section (de Munck et al., 2010)

3.3 Evolution of the maximum variation in street temperature

From the total 9000 meshes in Paris simulation domain, 12 have been selected, based on their representativeness, for a local analysis. The maximum variation in street air temperatures due to A/C for those meshes is reported versus the heat rejected by A/C on Figure 6. Locally, the temperature increase due to A/C appears to be proportional to the heat rejected by A/C. That means that districts highly equipped with air cooled A/C will much more suffer from heat waves than those not equipped with A/C and those equipped with A/C which does not reject sensible heat.

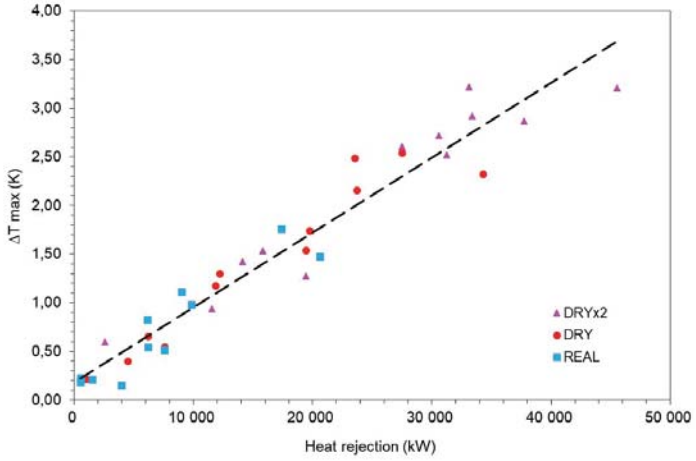

Figure 6: Variation of local temperature as a function of sensible heat rejection for a subset of 12 meshes (Tremeac et al, 2012)

Calculated as a function of the ground surface (surface occupied by building), the ratio of maximal street temperature variation is about 5 $K.m^2_{ground}.kW^{-1}_{heat}$.

3.4 Local variation of temperature for 2 districts

Some districts in Paris have been selected to look at the influence of the local management of A/C on the street temperatures: type of air-conditioning (dry or wet unit, individual or connected to the Climespace network, the urban cooling network in Paris), density of A/C, type of building etc. For a local comparison of the influence of AC management in this communication, three meshes of 250x250 m² localized in 3 different districts in central Paris are studied. Descriptions of these meshes for the REAL scenario can be found below (Table 1):

Table 1: Description of the three studied meshes (250x250 m²)

	Localisation	Main Description	Sensible/Latent heat releases (kW)	A/C ratio (W_{heat}/m^2_{floor} ; W_{heat}/m^2_{ground})	$\%_{power}$ of buildings connected to the Climespace network
Mesh A	North East	Residential	549 / 427	6.5; 15.6	0
Mesh B	West Paris	Commercial district, top-of-the-range hotels	6 131/ 1 843	24.9; 127	<1%
Mesh C	Center	Commercial district, museum	580 / 926	5.7; 24	91

Figures 7, 8 and 9 present local variations of air temperatures at 2m during five days in August 2003 for meshes A, B and C respectively and for the four scenarios. NO-AC scenario is the baseline and all other scenario are compared to this baseline. Be careful, graphs are not at the same scale allow shown clearly results.

For all districts (*i.e.* meshes), the maximum temperature variation is around the 11 August 2003 and reaches up to +3.5 °C for the mesh B and the DRY ACx2 scenario.

For mesh A, with a low A/C ratio, the impact of A/C is not marked except on the 11 August afternoon at 16 pm, with a maximum of +1.5 °C (DRY ACx2 scenario).

In the case of mesh B with high density of dry air A/C, the temperature increases in the REAL case reaches 2.3 °C and not be much affected by the DRY AC management but the DRY ACx2 case would yield a strong enhancement of the local temperatures. In that case, A/C management without heat rejection in the ambient air (NOREJ) results with a small mitigation of the heat island (negative effect on the temperature variation).

For mesh C, the large part of district cooling present in the REAL scenario avoids the temperature increase which is observed with the DRY scenario (Figure 8). Consequently, the districts which can use district cooling are less affected by heat waves than those which use air cooled A/C.

In districts with a lot of air-conditioned buildings, if all buildings use units discharging dry waste heat to air, temperatures could be impacted and should increase between 0.7 °C and 2.5 °C (Figures 7 and 8, DRY scenario). The impact could be as high as 3.5 °C/4 °C for the DRY ACx2 scenario.

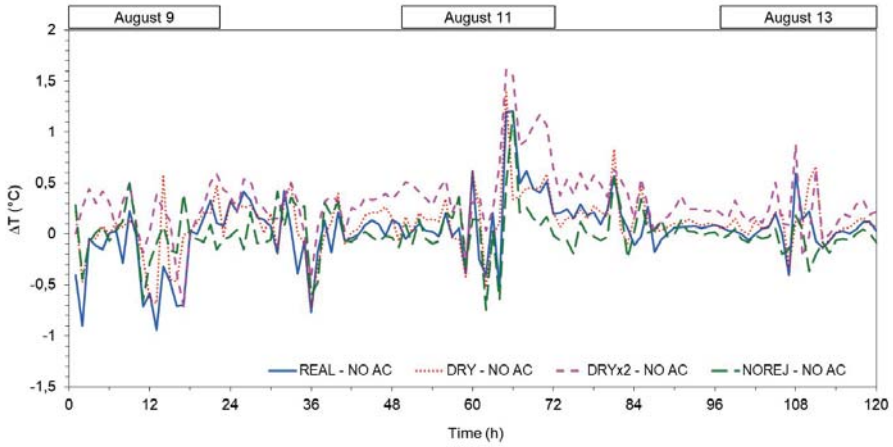

Figure 7: Local temperature variation between each A/C scenario and the baseline (NO AC scenario) for mesh A (Tremeac et al, 2012)

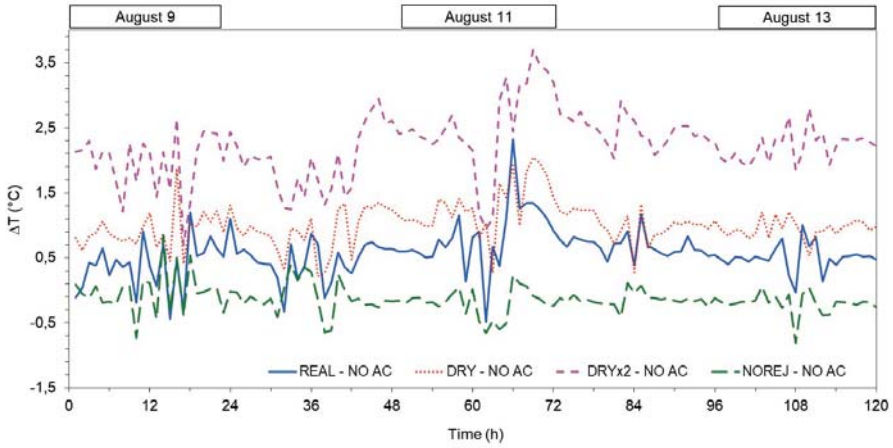

Figure 8: Local temperature variation between each A/C scenario and the baseline (NO AC scenario) for mesh B (Tremeac et al, 2012)

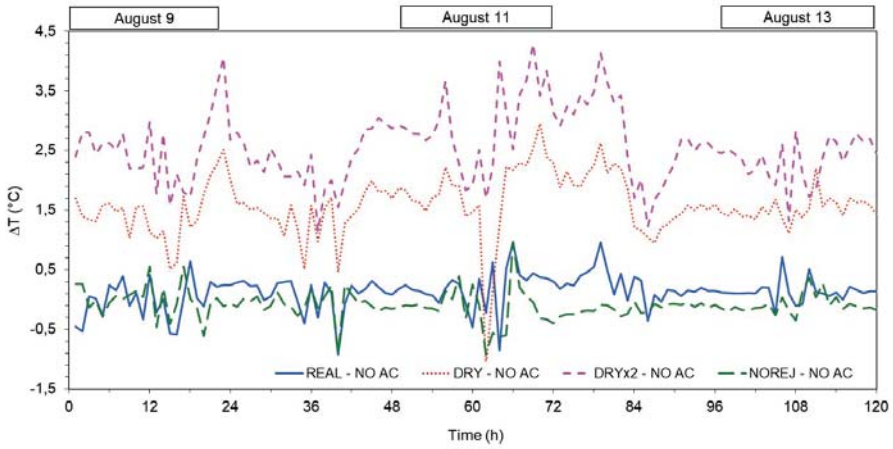

Figure 9: Local temperature variation between each A/C scenario and the baseline (NO AC scenario) for mesh C (Tremeac et al, 2012)

For all meshes, the NOREJ scenario (buildings are air-conditioned and A/C waste heat is released to ground or the Seine river) cancels temperature increase and, punctually and locally, decreases air temperatures and slightly the heat island.

4. CONCLUSION

Air conditioning is necessary for comfort and health security especially in a dense city like Paris. However, a vicious circle is created if A/C waste heat is released in the streets. Results of this communication show the influence of A/C management in Paris and its surroundings during a heat wave like the one of August 2003. Local temperature variations compared to a baseline without A/C can reach about +3.6°C in a high-density district under the future projection scenario DRY ACx2. This local variation is equivalent to the UHI amplitude of 4.5°C in the baseline case without air-conditioning.

Clearly, wet cooling towers or district cooling with either wet cooling towers or heat rejection underground or in water (river, lake, sea…) is a good solution to preserve comfort without affecting street temperatures. Ultimately A/C with heat rejection underground or in water allows to slightly mitigate heat waves.

REFERENCES

Billiard F. 2004, *Europe's heat waven* Int. J. Refrig. 27(1): 1-3.

de Munck C., Pigeon G., Masson V., Marchadier C., Meunier F., Tremeac B., Bousquet P., Merchat M., Poeuf P. 2010, *The influence of air-conditioning on street temperatures in the city of Paris*, AGU Fall Meeting, 13-17 December 2010

Hsieh C-M., Aramaki T. and Hanaki K. 2007. *The feedback of heat rejection to air conditioning load during the nighttime in subtropical climate*, Energy Build. 39: 1175-1182

IEA (International Energy Agency), 2018, *The Future of Cooling – Opportunities for energy-efficient air conditioning*

Lafore, J. P.; Stein, J.; Asencio, N.; Bougeault, P.; Ducrocq, V.; Duron, J.; Fischer, C.; Héreil, P.; Mascart, P.; Masson, V.; Pinty, J. P.; Redelsperger, J. L.; Richard, E. & de Arellano, J. V.-G. 1998. *The Méso-NH atmospheric simulation system. Part I: adiabatic formulation and control simulation*, Ann. Geophys. 16: 90-109.

Lemonsu A., Kounkou-Arnaud R., Desplat J., Salagnac J.L.and Masson V, 2013. *Evolution of the Parisian urban climate under a global changing climate*, Clim. Change 116(3-4): 679–692.

Masson, V. 2000, *A physically-based scheme for the urban energy budget in atmospheric models*, Boundary-Layer Meteorol. 94: 357-397.

Ohashi Y., Genchi Y., Kondo H., Kikegawa Y., Yoshikado H. and Hirano Y. 2007, *Influence of air-conditioning waste heat on air temperature in Tokyo during summer: numerical experiments using an urban canopy model coupled with a building energy model*, J. Appl. Meteorol. Climatol. 46: 66-81.

Stein, J.; Richard, E.; Lafore, J.; Pinty, J.; Asencio, N. & Cosma, S. 2000, *High -resolution non-hydrostatic simulations of flash-flood episodes with grid-nesting and ice-phase parametrization,* Meteorol. Atmos. Phys. 72: 101-110.

Tremeac B., Bousquet P., De Munck C., Pigeon G., Masson V., Marchadier C., Merchat M., Poeuf P., Meunier F. 2012, *Influence of air-conditioning management on heat island in Paris air street temperatures*. Applied Energy. 95:102-110

Wen Y. and Lian Z. 2009, *Influence of air conditioners utilization on urban thermal environment*, Appl. Therm. Eng. 29(4): 670-675

Questions and Answers:

Rémi Dickes:

Since you are concerned about the impact of HVAC systems on the temperature of the air in the cities, do you account for the influence of all the other parameters?

Brice Tremeac:

For city and surroundings, all parameters like traffic, industries, greenspace, hydrology, are taking into account.

***

Sébastien Thomas:

The use of absorption chiller driven by solar heat, will finally increase the outside air temperature?

Brice Tremeac:

In our study for prospective scenario (NOREJ DRY ACx2), waste heat is not released in the air. With this assumption, using solar AC system reduces the impact of solar radiation on air temperature.

***

Madjid Madjidi:

Where does the heat disappear, if it is not gone to the air?

Brice Tremeac:

In our model, for the prospective scenario (NOREJ DRY ACx2), waste heat from A/C are equal to 0 and the cooling power inside the buildings is kept identical to that of scenario DRY-ACx2.

VALIDATION OF A BES MODEL OF AN ALL-AIR HVAC SYSTEM IN AN EDUCATIONAL BUILDING

Bart Merema*[1], Hilde Breesch[1], Dirk Saelens[2]

(1) KU Leuven , Department of Civil Engineering, Construction Technology Cluster, Technology Campus Ghent, Gebroeders De Smetstraat 1, 9000 Gent, Belgium

(2) KU Leuven, Department of Civil Engineering, Building Physics, Kasteelpark Arenberg 40, 3001 Leuven, Belgium

ABSTRACT

To make an accurate prediction of the operation for the building and its systems, building energy simulation (BES) programs need to include detailed control strategies. However, in most simulation programs the dynamics of the HVAC systems are difficult to implement (e.g. VAV damper which controls both CO_2 and operative temperature) since idealized controllers are used in the component model. Simulation of control is of importance for all-air systems, since it reacts fast to changes. The aim of this paper is to demonstrate the process of validation for a Modelica model of an educational building.
The simulation model is validated using building monitoring data of two consecutive weeks of room temperature, CO_2-concentration, fan power consumption and heating energy for the heating coil. Room temperatures were simulated with a RMSE of 0.6°C and for CO_2 138 ppm compared to measurements. Results for validation of heating and fan power improved after adjusting the radiative fraction for the thermostat, the air capacity of the zone and the air tightness. The simulated data of fan and heating power fit within the set requirements for hourly calibration data $C_vRMSE \leq 30\%$ and $MBE \leq 10\%$.

Keywords: validation, Modelica, all-air HVAC system, Building Energy Simulation

1. INTRODUCTION

By the end of 2020 all newly constructed buildings have to be nearly Zero Energy Buildings (nZEB). In schools and office buildings the ventilation system has a significant impact on the total energy use. A smart control strategy that adjusts the operation of the ventilation to the actual demand can significantly reduce this energy use (Maripuu, 2009; Merema et al. 2018; Wachenfeldt, Mysen, & Schild, 2007). Consequently, control systems are becoming an important part of the ventilation system in these nZEB buildings. To make an accurate prediction of the operation for the building and its systems, Building Energy Simulation (BES) programs need to include detailed control strategies and predict the behaviour of the HVAC system. However, in most simulation programs the dynamics of the heating, ventilation and air-conditioning (HVAC) systems are difficult to implement. For example a VAV damper controlling both CO_2 and operative temperature) since idealized controllers are used in the component model (Wetter, 2009).

Modelica is an object oriented equation based language allowing simpler schematic modelling and generating code for both simulation and optimization (Wetter, Bonvini, & Nouidui, 2016). It is a continuous time system simulation contrary to widely used BES tools such as EnergyPlus that calculates solutions at discrete time intervals. Open source libraries have

been developed to include building and HVAC components inside Modelica. One of the available libraries for Modelica is IDEAS integrating both building envelope and HVAC systems as well as electric system simulations (Baetens et al., 2012; Baetens et al., 2015, Jorissen et al., 2018). Recently, the focus of the development of IDEAS extended to detailed simulations at the building level. Therefore, more detailed multi-zone models are required while at the same time reducing the computation time. Jorissen, et al., (2018) demonstrated that the accuracy of a BES model created in Modelica using the IDEAS library is comparable to EnergyPlus models based on BESTEST series 600 and 900 regarding results for heating and cooling loads. A second library that is developed, is the Buildings library (Wetter et al., 2014). This library offers the ability to implement component and system models for building energy and control systems inside Modelica.

To make a reliable prediction of the energy consumption of an all-air system, the BES model has to be validated to detailed monitoring data of the building and the HVAC system. Buildings do not usually perform during operation as well as predicted during the design stage. Disagreement between simulated and metered energy consumption represents a common issue in building simulation. For this purpose, validation of the BES model is needed. For validation, the mean bias error (MBE) and the coefficient of variance of the root mean square error (C_vRMSE) are used as described in ASHRAE guidelines 14 (ASHRAE, 2002). Recent studies have shown the importance of validation for BES models. Coakley (2014) showed that detailed building and HVAC system information could produce an accurate representation of the building by using hourly measured data. The EnergyPlus model of the case study building, described in this paper, has already been validated (Merema et al. 2017). Yang & Becerik-Gerber (2015) calibrated a BES model for a multi-level building. In this study measured energy consumption for an all-air HVAC system was compared to simulated energy consumption at building and zone level. Royapoor & Roskilly (2015) deployed a calibration study for a 5-storey office building by using hourly based measurement data to demonstrate that an accurate simulation model could be created.

The aim of this study is to demonstrate the validation process of a BES model of an all-air HVAC system in an educational building in Modelica, including the control for the HVAC system. Currently, studies focussing on validation for BES, by using Modelica, of complete HVAC systems in “real use” buildings are still missing. Jorissen, Boydens & Helsen (2018) already demonstrated, by validating an air handling unit (AHU), that Modelica is a suitable language for simulating complex HVAC models. The study demonstrates that the simulated AHU showed an average normalized absolute error of approximately 1% for the electrical power consumption. Furthermore, pressure drops in airflow networks in most BES tools are neglected or modelled in function of the mass flow rate. In most cases the air flow rate is used as an input for HVAC components. Modelica includes pressure-driven airflow networks. To construct these networks in Modelica in a fast and efficient manner a comprehensive overview is given by Jorissen, Wetter, and Helsen (2018), presenting solutions to reduce the number of equations in Modelica.

The paper is outlined as followed. First the case study building and its systems, and the simulation model are described. Afterwards, a description of the method used for the validation process is presented. Section 4 presents the results of the sensitivity analysis for the room temperature and CO_2-concentration. In addition, the validation results are shown for the heating power and the fan power. Finally, a discussion and conclusion are given for the study including recommendations concerning validation studies for BES.

2. METHOD

2.1 Case study: Test lecture rooms KU Leuven Ghent Technology Campus

2.1.1 Building properties

The case study building is an educational building, built according to the Passive House standard, shown in Figure 1 and located in Ghent, Belgium. The building is built on top of an existing university building and contains 4 zones: 2 large lecture rooms, a staircase and a technical room. The floor area of the lecture rooms is 140 m² with a volume 380 m³ and a maximum capacity of 80 students each. A floor plan and a cross section of the building is illustrated in Figure 2. The building is in use but at the same time it is a test facility for research on building energy-efficiency strategies in a "real use" environment. Therefore, the lecture rooms are thermally insulated from the outside, to the adjacent zones and each other. The U-value of the construction parts are listed in Table 1. The solar heat gain coefficient for the glazing is 0,52. The window to wall ratio is 26% for NE and 27% for SW façade. Air tightness at 50 Pa of the lecture rooms is 0,29 1/h for the first floor and 0,47 1/h for the second floor. Moveable external blinds are applied on the windows on the south-west side. Blinds are closed when the incident solar radiation exceeds 250 W/m² with a deadband of 50 W/m^2, this reduces the g-value to 0,08. More information about the design process can be found in Breesch et al. (2016).

Table 1, U-value of the building construction

Construction part	U-Value (W/m^{2}K)
Wall	0,15
Roof	0,14
Floor	0,15
Glazing (glazing)	0,60
Glazing (frame)	0,90

2.1.2 HVAC properties

A demand controlled, balanced mechanical ventilation (DCV) system is provided with an air-to-air heat exchanger (efficiency is 78%). VAV-boxes are placed in the supply and extract openings in each room controlling the air flow rate based on measurements of CO_2-concentration and operative temperature in the lecture rooms. The maximum air flow rate per room is set at 2200 m^3/h and the minimum at 400 m^3/h. Fan speed is variable and based on a constant pressure control inside the ducts of 200 Pa. The location of the supply- and extract air grills is shown in Figure 2. Two heating coils of 8 kW are integrated in the supply ducts to control the supply air temperature. The heating production system consists of a condensing wood pellet boiler with an internal storage of 600 l. The maximum heating power is 8 kW with a maximum efficiency of 106 %. The supply and extract fan have a maximum power of 1,57 kW respectively 1,33 kW with an efficiency of 71%. The efficiency of the fan motors is 85%. Indirect evaporative cooling (IEC) with a maximum capacity of 13.1 kW is provided. The opening of the windows is controlled to allow ventilative cooling. For the operation of the night-time ventilation an extensive description is given in Breesch, Merema, Versele (2018).

Figure 1; Outside view (left) and inside view (right) of the educational building

Figure 2; (Left) Floor plan of the lecture room evaluated, blue is supply air and red extract air (Right) Cross-section of the building (1) lecture room (2) lecture room (3) staircase (4) technical room

2.1.3 Use and control

The lecture rooms are used during the academic year, which counts 124 days with courses and 53 days with exams (in January, June and August-September). Holiday periods are in April (2 weeks), July and the first half of August (6 weeks) and December-January (2 weeks). The lecture rooms are in use from Monday to Friday between 8:15h and 17:30h with a maximum occupancy of 80 persons.

The air handling unit (AHU) is operating from 07:30-17:30h during weekdays. The CO_2 set point for the DCV system in use is set at 1000 ppm, which corresponds to IDA class 3 with an air flow of 28 m^3/h.pers (EN 13779, 2007) or 16 $m^3/(h.m^2)$. The heating set point for the heating system is set at 22°C with a deadband of ± 0,5°C to avoid oscillating of the heating. Standby temperature during non-operating hours is set at 15°C. The air flow rate and/or supply temperature is increased when the set point for CO_2 or room temperature is not met. The operation of the bypass and the IEC are controlled by the indoor and outdoor temperature and is demonstrated in Figure 3.

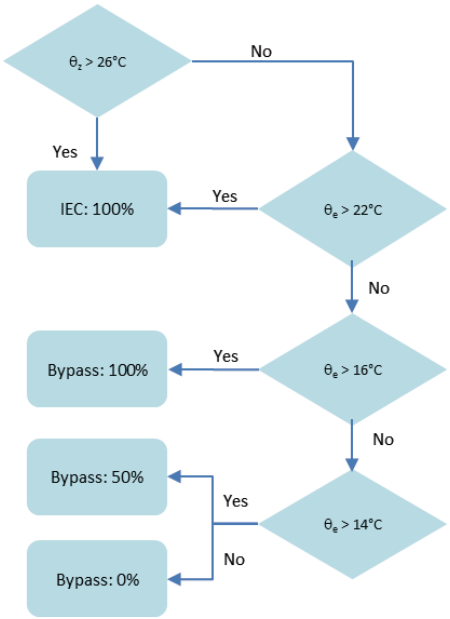

Figure 3; Control strategy of AHU during operation hours with (θ_z) zone temperature, (θ_e) external temperature

2.1.4 Monitoring data

A set of sensors has been permanently installed in the lecture room and ventilation system to monitor indoor and outdoor conditions. A short overview of the properties of the used sensors in this study is summarized in Table 2. The building contains a weather station monitoring the main outdoor parameters: global horizontal radiation, outdoor temperature, relative humidity, wind speed and wind direction. For the indoor conditions, the indoor temperature, the CO_2-concentration and the relative humidity are continuously monitored. The number of people present in the lecture room is measured by using a counting camera installed near the entrance of the lecture room.

Table 2; Properties of the sensors

Parameter	Type sensor	Accuracy
CO_2-concentration	VAISALA GMW83	±30 ppm + 3% reading
Room temperature	SE CSTHR PT1000	± 0.1 °C
Supply temperature	SE CSTHK HX	± 0.4 °C
Occupancy	Acurity Crosscan Camera	± 5%
Outdoor temperature	Vaisala HMS82	± 0.3 °C at 20°C
Wind velocity	Ultrasonic 2D Anemometer	± 0.1 m/s (0-5 m/s)
Wind direction	Ultrasonic 2D Anemometer	± 1 °
Solar radiation	SP Lite2 Silicon Pyranometer	4.5% of reading

For the weather data, as shown in Figure 4, used in the simulation model outdoor dry bulb temperatures, relative humidity and incident horizontal solar radiation are monitored by the weather station. A Python-script is used for the transformation of global horizontal solar radiation into direct normal and diffuse solar radiation based on the methods described by Perez et al. (1992) and Maxwell (1987). This data is used to create a .TMY weather file with the local air temperature, relative humidity, diffuse solar radiation and direct normal radiation. The occupancy profile of the week from 18-22 of April is shown in Figure 5. In this week, the lecture room is used for approximately 30 hours. The maximum number of people present was 60 and a minimum of 12 during the monitored period.

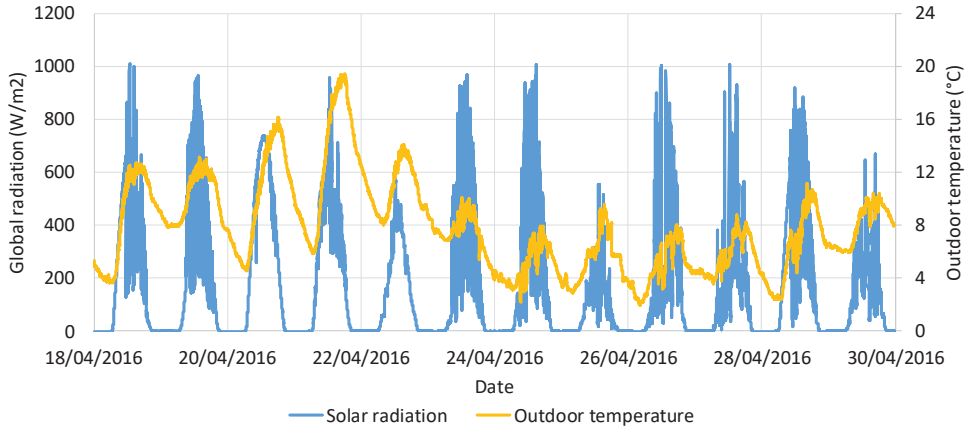

Figure 4; Outdoor weather conditions during measurement period 18-29th of April 2016

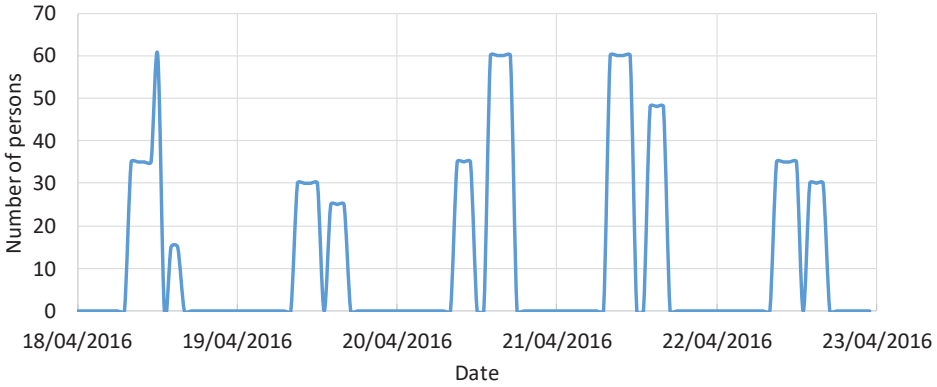

Figure 5; Occupancy of the lecture room during validation period

2.2 Simulation model

The simulation model is created in Modelica (Dymola 2018) using the existing models derived from the IDEAS and Buildings open source libraries. Modelica allows to include detailed control for the HVAC system, therefore the dynamics of the systems are included. A short overview of the used simulation models is displayed in table 3. These models have been used in Modelica to simulate specific components related to this study. These separate simulation models are connected to create the complete Modelica model for the case study building as shown in Figure 6. Output for the results in Modelica is set at a 1 minute time-interval to compare results with the 1 minute measurement results. Properties for the internal heat gains for the occupants and the lighting are listed in Table 4. The simulation period is from evaluated is 18-30 of April 2016.

Table 3; Simulation models used in Modelica

Component	Simulation model	Part of model
VAV	IDEAS.Fluid.actuators.dampers.exponential	Air loop
Fans	IDEAS.fluid.movers.flowcontrolled_dp	Air loop
Heat exchanger	Buildings.fluid.heatexchanger.constanteffectiveness	Air loop
Dampers AHU	Buildings.Fluid.Actuators.Valves.TwoWayLinear	Air loop
Building zone model	IDEAS.buildings.components.zone IDEAS.buildings.components.window IDEAS.buildings.components.outerwall IDEAS.buildings.components.boundarywall	Building
Weather data	IDEAS.BoundaryConditions.WeatherData.ReaderTMY3	Weather
CO_2 generation	Buildings.Fluid.Sources.TraceSubstancesFlowSource	Schedule

In Modelica the damper position of the VAV is controlled by a PI controller, one based on temperature and one based on CO_2-concentration. The integration time and the gain factor for the PI control are respectively set at 120 seconds and 0.1. The actual position of the VAV damper is the maximum output value of the two PI controllers. In addition, a deadband of 1°C on the heating set point of 22°C is included to avoid oscillating of the damper. The reheat coil integrated with the VAV is controlled by the measured room temperature. The supply

temperature will be increased to the maximum when the zone temperature is below the heating set point. The fans are regulated by a PI control, based on a constant pressure set point inside the duct in Modelica. For the complete air loop the pressure drop is set at 250 Pa as to account for pressure drops by VAVs, duct and filters. The control for the heat exchanger uses a PI-controller based on the outdoor temperature in order to activate the bypass.

Table 4; Internal heat gain settings used in simulations

Source	Internal heat gains	Convection/Radiation
Lighting	1100 W/room	50/50
People	73 W/person	60/40

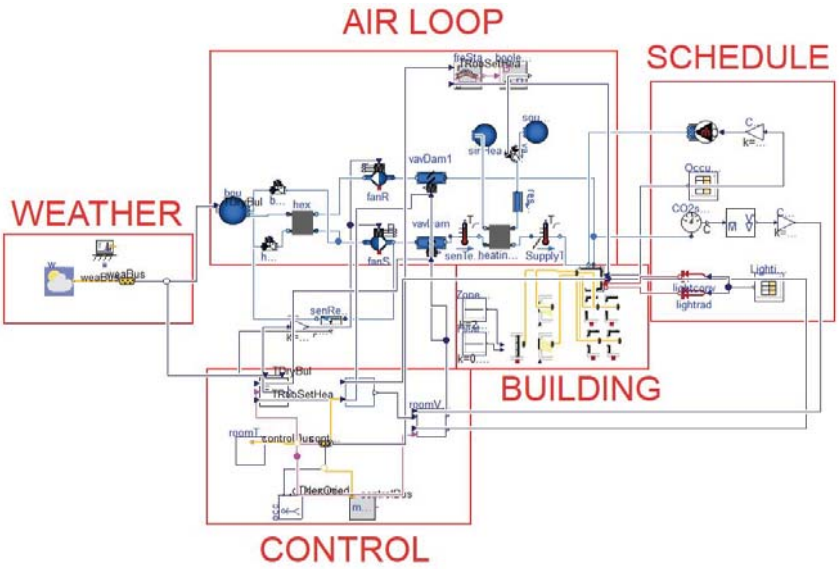

Figure 6; Modelica model of the case study building

The control of the bypass of the heat exchanger as well as the IEC in the model are based on the measured data of the outdoor air (OA) temperature by the AHU and not on the outdoor temperature sensed by the weather station. In addition, the internal air temperature (IA) AHU is used as input air temperature for the ventilation system. This is due high deviances, noticed between the outdoor temperature sensed by the weather station and the outdoor air (OA) temperature by the AHU. Figure 7 suggests that there is not a good agreement between these two temperature sensors. The AHU sensor is affected by solar radiation and is measuring temperatures up to 8°C higher compared to the weather station sensor on the 20th of April. The AHU sensor is used for the control for both the bypass of the heat exchanger and the IEC. Therefore, during validation the OA AHU temperature is used for control of the HVAC system and the internal air (IA) AHU is used as input air temperature for the ventilation system. These changes are implemented in the simulation model for the validation process.

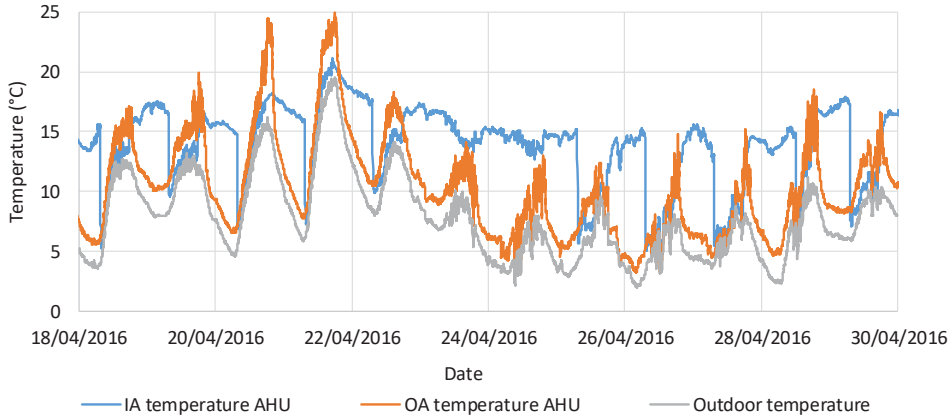

Figure 7; Monitoring data of the outdoor and internal temperature for the AHU and out temperature of the weather station

2.3 Validation process

The process of validation in this research involves an analysis based on an iterative approach (Coakley, Raftery & Keane, 2014; Reddy, 2006). This includes trial and error approaches to manually adapt model input parameters based on knowledge about the building and user experience. To set up the simulation model, the following steps are performed:

(i) connect the building and system parts from the available libraries in Modelica
(ii) assign thermal properties to the construction
(iii) obtain weather data for implementation in simulation model
(iv) define properties and control algorithms according to the as-built file for all modelled HVAC system parts
(v) assign activity schedules for equipment and occupancy
(vi) error check
(vii) test criteria for validation
(viii) trial and error of validation if criteria are not in agreement.

The validation of the simulation model is performed according to the ASHRAE Guideline 14 (2002). The guideline uses the mean bias error (MBE), given in equation 1, and the coefficient of variation of the root mean square error (C_vRMSE), shown in equation 2-4, to assess the uncertainty of the simulation data compared to monitoring data.

To validate the model, monitoring data of room temperature and energy use, logged on a one-minute time interval by the building monitoring system (BMS) is used. Requirements for the MBE are ≤ 10% for hourly data and for the C_vRMSE ≤ 30% for hourly data regarding the energy use. For monthly data the requirements are respectively ≤5 and ≤10%. Since for daily data no requirements are specified in the guidelines the same requirements as for hourly data are used. For room temperature, simulation results are regarded validated within a magnitude of ±0.5°C compared to measurements.

$$MBE\ (\%) = \frac{\sum(S-M)_{interval}}{\sum M_{interval}} * 100 \quad (1)$$

$$RMSE_{Period} = \sqrt{\sum \frac{(S-M)_{interval}{}^2}{N_{interval}}} \quad (2)$$

$$A_{period} = \frac{\sum M_{interval}}{N_{interval}} \quad (3)$$

$$C_v RMSE\ (\%) = \frac{RMSE_{Period}}{A_{Period}} * 100 \quad (4)$$

S = Simulated data
M = Measured data
N = Number

The following parameters of the system will be analysed during the verification process: radiative fraction for the room temperature, capacity of the zone air and air tightness. Finally, the simulation results will be validated for the fan power (supply and extract) and the heating power.

3. RESULTS

This section presents results for the sensitivity analysis performed for the room temperature and CO_2-concentration. Afterwards, the validation results for both the fan power and the heating power are presented.

3.1 Room temperature

To evaluate if the results for room temperature are in agreement with the measurement results, a sensitivity analysis is performed for the radiative fraction, the air capacity of the zone and the air tightness. In the first simulation, the fraction of the air and the radiant temperature is set at the default value (T50/50). The air capacity of the zone air (AC) is set to the default value of 5, meaning that the mass of air in the simulation model is 5 times higher than normal to account for furniture and internal walls. The air tightness (AT) of the building envelope is set at 1 ACH. Since previous results obtained in EnergyPlus (Merema et al. 2017) showed good results regarding the temperature decay at night and in the weekend. In addition, a blower door test was performed indicating that an air tightness of 1 is a better estimation of the real air tightness. The value of 0,29 for air tightness given in the description was a result of a test performed in 2012 during construction. However, it is noticed that in the current situation the windows are not locked which affects the air tightness. Figure 8, compares the simulated room temperatures to the measurements. It is shown that with these settings, the simulated temperature overestimates the measured temperature. Especially the room temperature on the 21st and 22nd of April is not in agreement with the measurement results. Differences between the simulated and measured room temperatures are 1 to 1.5K. During these two days there are high solar heat gains in the afternoon. This indicates that the room thermostat might be more sensible to the air temperature than the radiant temperature. Adjusting the radiative fraction to 80/20 (T80/20) seems to results in a better agreement to the measurement results. Maximum difference noticed is 1K during the afternoon on the 21st of April.

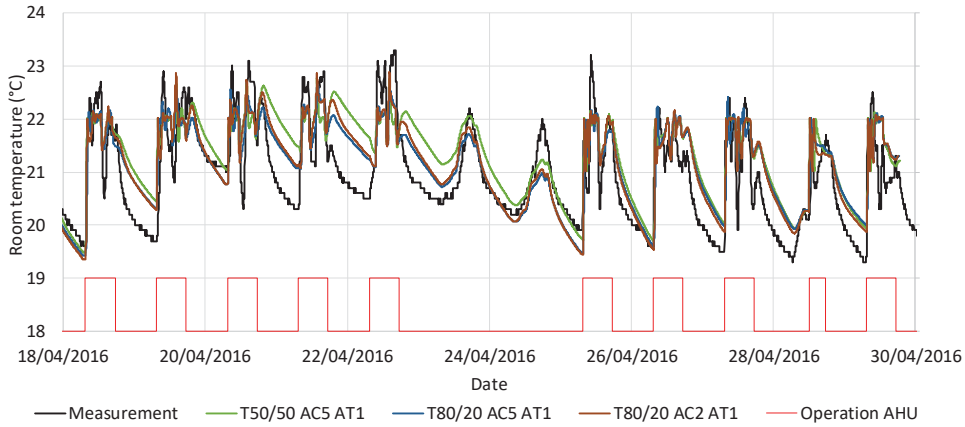

Figure 8; Manual sensitivity analysis of the radiative fraction for room temperature

The second parameter that is adjusted is the capacity of the zone air. In simulation, a thermal capacity can be assigned to the zone air to account for the lack of homogeneity of the indoor temperature. However, from the room temperature results, depicted in Figure 8, it is hard to notice differences between a capacity of 2, and 5 for the zone air. However, the factor 2 is probably a better approximation because the induction effect of the air outlet improves the homogeneity of the zone air temperature. Therefore, for the validation the value is set to 2. Furthermore, it is noticed from the results displayed in Figure 8 that the temperature difference during the decay at night is at maximum 0.5K. The decrease for room temperature during the night and in the weekends is in the same order of magnitude compared to the measurement results. Therefore, it can be concluded that an air tightness of 1 is a good approximation of the real air tightness of the building envelope.

The results of the sensitivity analysis are also tested for the validation requirements for the fans and heating coil. Table 5 suggest that the first three settings did not results in an accurate model, especially regarding the heating coil. In all the first three settings there was always one day where no heating was needed compared to the measurements resulting in high differences for the heating coil for both the MBE and the C_VRMSE. The last change in settings for the radiative fraction from 80 to 85 resulted in a higher heating demand for the 21st of April, lowering the MBE and the C_VRMSE.

Table 5; Results for MBE and C_VRMSE during the sensitivity analysis

	Setting	**T50/50 AC5 AT1**	**T80/20 AC5 AT1**	**T80/20 AC2 AT1**	**T85/15 AC2 AT1**
Fan	*MBE*	8,4	-0,5	1,7	-1,8
	C_VRMSE	29,7	28,3	30,2	28,4
Heating coil	*MBE*	36	-12	25,3	4,8
	C_VRMSE	52,3	47.3	43,7	28,3

The room temperature results for the setting (T85/15 AC2 AT1) are illustrated in Figure 9 including a boundary of ± 0.5°C. Overall, the results for room temperature are in good

agreement when comparing with the measurement results the root mean square error (RMSE) error is 0.6K. Some higher deviances are found on the 21st and the 24th of April with a maximum of 1K.

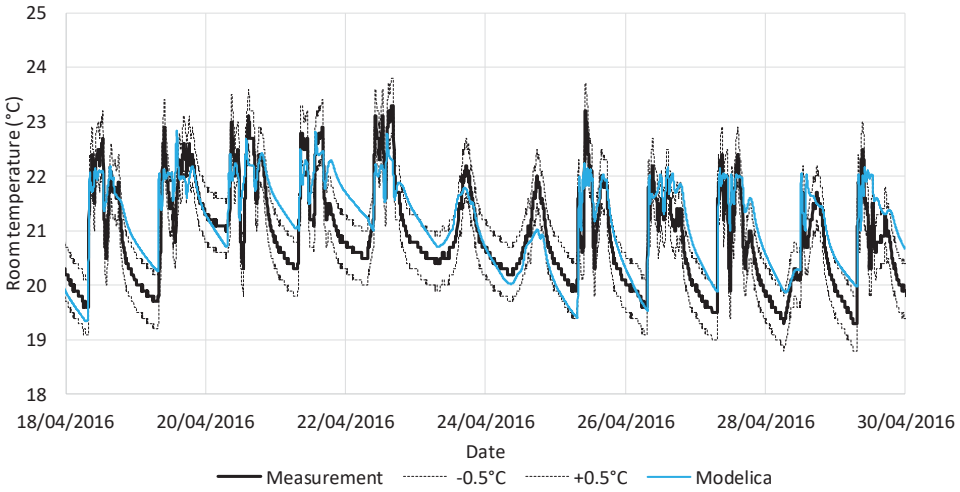

Figure 9; Result for the room temperature with setting (T85/15 AC2 AT1)

3.2 CO_2-concentration

Next parameter validated is the CO_2-concentration inside the lecture room. The impact of the CO_2 generation rate per person on the CO_2-concentration in the room is analyzed. In literature values can be found ranging from 0.25 – 0.45 l/min (ASHRAE 62.1, 2007; Persily & de Jonge, 2017) depending on the level of activity and age of the persons. Three different generation rates have been tested: 0.31, 0.38 and 0.45 l/min. The outdoor CO_2-concentration is set to 500 ppm, based on the measurement results. Figure 10 suggest that at night during no air flow the CO_2-concentration decreases to approximately 500 ppm. Figure 9 shows the impact of the CO_2 generation rate of persons on the room CO_2-concentration. The differences between the three generation rates is approximately 100 ppm during a period with a high occupancy of 50 persons. With smaller groups as in the afternoon (25 persons) the difference is only 70 ppm. Both results are below 100 ppm difference indicating that the impact of variation for CO_2 generation is not that significant. In addition, the results are within the measurement accuracy of most commercially available CO_2 sensors.

From the CO_2 measurement results the air tightness can be obtained using the night decay of the CO_2 concentration. For this the decay in CO_2 concentration in the night of 18 to 19 April is used. The obtained ACH using the decay is 1.10 which is close to the results obtained by the blower door test (1.0 ACH).

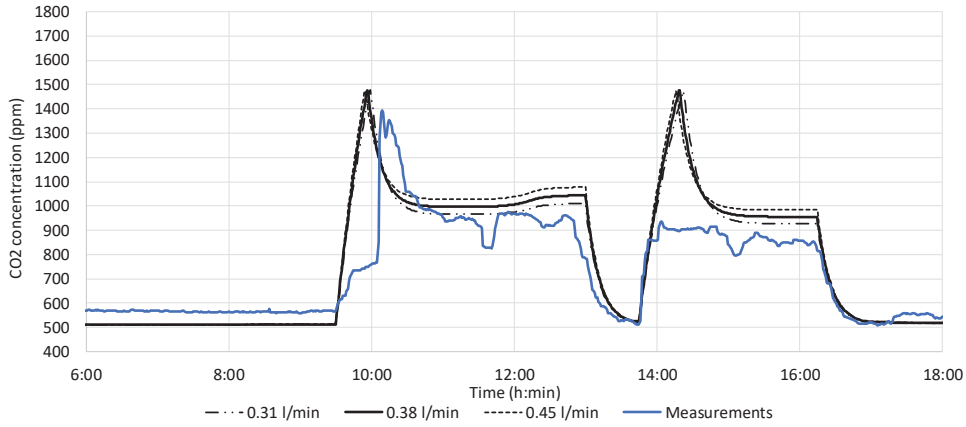

Figure 10; CO_2-concentration at varying CO_2 generation rates, respectively 0.31, 0.38 and 0.45 l/min on the 22nd of April 2016

As the impact of the generation rate is low, the generation rate is set at 0.31 l/min, which is the default value recommended in ASHRAE 62.1 (2007) and is compared to the measurement results. Figure 11 depicts the CO_2-concentrations during measurements and simulations. In general, the simulated CO_2-concentration is in good agreement with the measurements since the results are within the accuracy of the sensor (see table 2). The RMSE for the zone CO_2-concentration is approximately 138 ppm. Only on the third day in the morning and the fourth day during occupancy differences are noticed up to 200 ppm. Measurement results might be affected by opening the door to the staircase by the users allowing fresh air to enter the room and mix with the zone air resulting in a lower CO_2-concentration than measured.

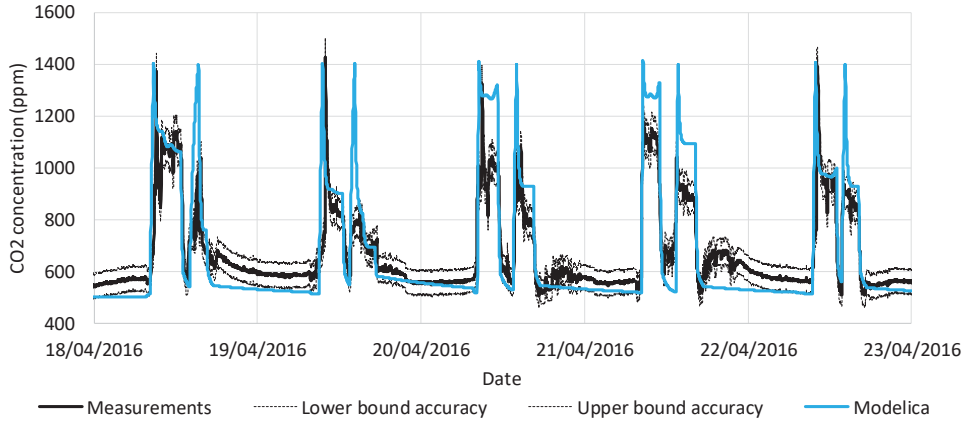

Figure 11; CO_2-concentration for measurements and simulations including the sensor accuracy (± 30 ppm +3% reading)

3.3 Operation of the ventilation system: supply air temperature and air flowrate

Figure 12 and 13 illustrate the operation of the DCV system for the simulation (T85/15 AC2 AT1). In general there is a good agreement between the simulation and measurement results. However, when looking into the details differences are noticed. For supply temperature it is demonstrated on Figure 12 that on the 22nd of April in measurements heating was needed. Contrary, in simulations the supply temperature is maintained at 18°C compared to 30°C for measurements.

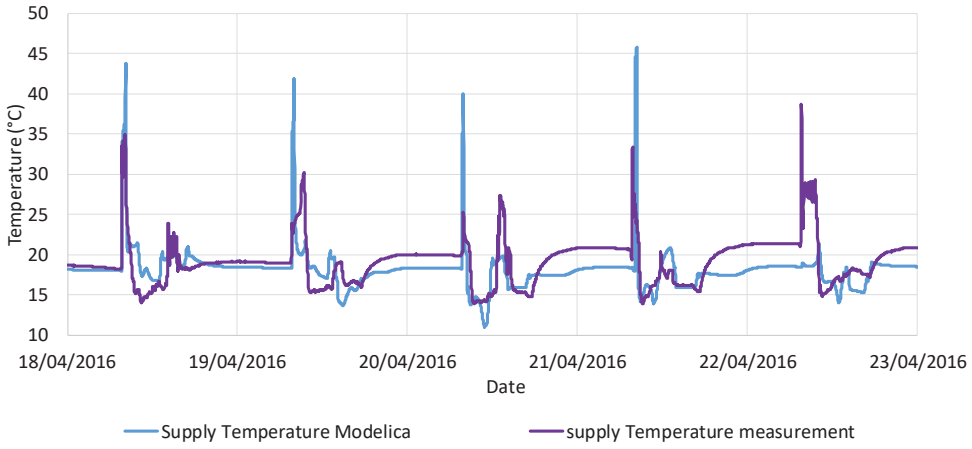

Figure 12; Supply air temperature for simulation and measurements

For the supply air flow rate it is shown in Figure 13 that generally for both measurements and simulations the results are in the same magnitude. The profile of minimum and maximum air flow rate is comparable. However, on the second and fifth day is it noticed that at noon the measured air flow is maintained at maximum flow rate of 2200 m^3/h while the simulated airflow rate is decreased to the minimum air flow rate of 400 m^3/h. Furthermore, in measurements the air flow rate is maintained at a maximum flow for a longer time compared to the simulations at the end of each day. This is most likely due to the influence of the settings used in the PI control for CO_2.

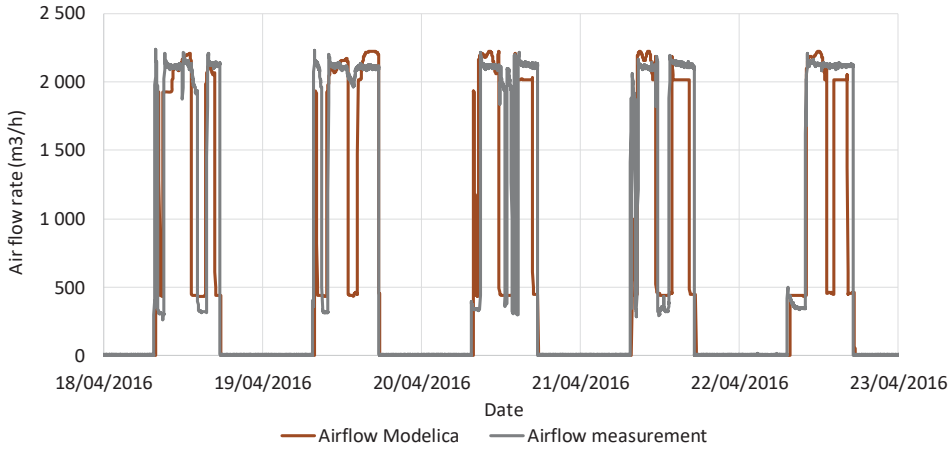

Figure 13; Supply air flow rate during measurement and simulation

3.4 Heating coil power and fan power

As a final step in the verification process, the heating power and fan power were compared against the measurement results of a 2 week test period. The data is averaged over a 1 hour time interval. Overall, it is shown in Figure 14 that there is a good agreement with the measurement results for both heating power and fan power. Heating power is in the same order of magnitude as in the measurements. On the 22nd of April in Modelica no heating is needed on this day since the room temperature during startup is already in the heating set point deadband. Furthermore, the heating peak on the third day is in Modelica noticed during the morning while in measurements the heating peak was at 12:00h. For the fan it is shown that the power is overall in good agreement with the measurement results. Some deviances are found in the first week during the mornings with a difference up to 500W.

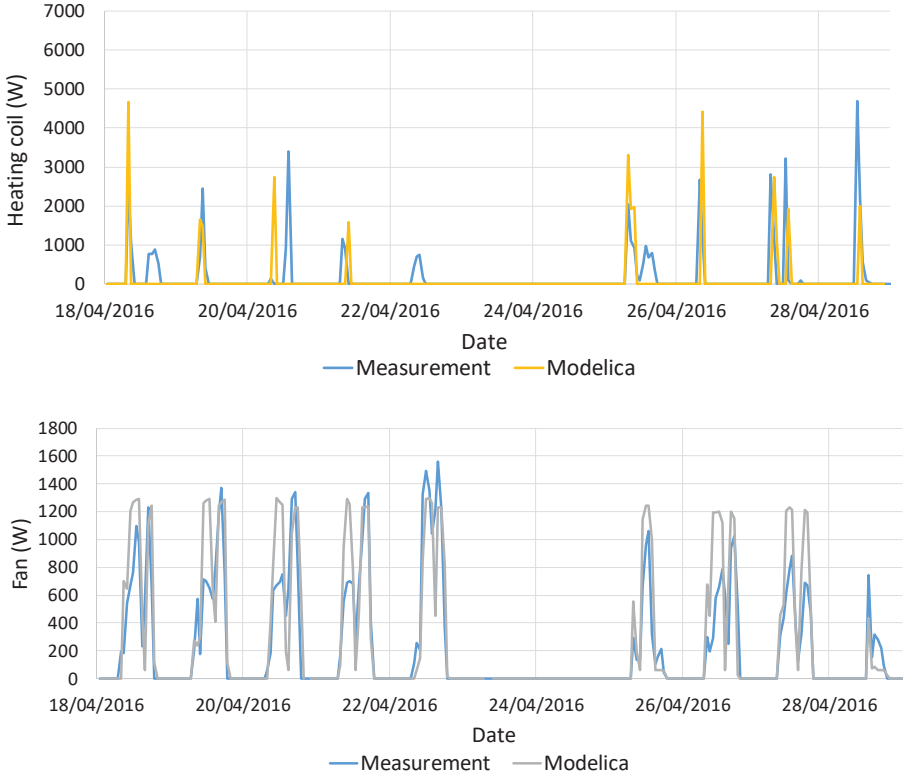

Figure 14; Validation results for heating coil capacity (above) and fan power (below)

Table 6 summarises the energy use for the fans and heating coil during the measurements and the simulation for the analysed period. It is illustrated that the absolute difference is relatively small, for the fans just 1 kWh (1.8%) and for the heating coil 2 kWh (4.8%).

Table 6; Total energy consumption during validation period (18-29 April, 2016)

	Measured energy use (kWh)	**Simulated energy use (kWh)**
Fans	57,0	58,0
Heating coil	44,9	42,8

The results for validation as listed in Table 7 shows that the MBE for both the heating and the fans, respectively 4,8% and -1,8%, is in good agreement with the measurement results. The C_vRMSE shows larger differences with values of approximately 28% for both the heating and fan power, but still below the maximum of 30% as defined in ASHRAE guidelines 14 (2002). For the energy use of the heating and fan, the high C_vRMSE of approximately 30% can be attributed to the deviations that we see during the fifth day, as depicted in Figure 14. Here no heating was needed during simulations contrary to the measurement results. In the table the values of an earlier validated model created with Designbuilder/EnergyPlus (Merema et al. 2017) are included. Compared to the previously validated model in EnergyPlus it can be noticed that the results for both heating and fans are in the same order of magnitude. A high CvRMSE of just under 30% for both the heating and fan power and a low MBE. Only the MBE for heating shows a difference of approximately 5% attributed by the heating demand needed on the 22nd of April.

Table 7; Validation results for both Modelica and EnergyPlus

	C_vRMSE	**MBE**
Heating – Modelica	28,3	4,8
Fans – Modelica	28,4	-1,8
Heating - EnergyPlus	31,7	-0,1
Fans – EnergyPlus	27,3	-2,8

4. DISCUSSION

The results indicate that the radiative fraction used in the thermostat for room temperature has a large impact on both room temperature and the heating coil power. Simulation software allows to alter the values for the radiative fraction for the thermostat, at default this value is set to 50/50. In the case study building, the operative temperature seems to be more affected by the air temperature than the radiant temperature. Since, the heating system is controlled by the ventilation system and the room temperature sensor is installed on a cable tray just below the ceiling. Changing the radiative fraction by lowering the value from 50 to 15 resulted in a more accurate simulation model than the default setting. However further research is needed before it can be concluded that the room temperature sensor is affected more by the air temperature. The air capacity of the zone had a small effect on the room temperature. However, the impact on the heating demand was more significant as indicated by the change in the MBE for the heating coil.

The results also show that the CO_2-generation rate per person does not affect the CO_2-concentration in the lecture room considerably. Values found in literature resulted in differences for CO_2-concentrations within the accuracy bound of most CO_2 sensors, approximately 100 ppm. While the air flow rate in all simulations was similar, with differences just under 50 m^3/h. In general good results were found for the simulated room CO_2-concentration. Most simulated values were within the accuracy of the installed room sensor during operating hours. The RMSE for the zone CO_2-concentration during the complete evaluated period is approximately 138 ppm. The CO_2-concentration was overestimated on three occasions by at maximum 200 ppm in the simulations. This might be affected by persons opening the door to the staircase allowing fresh air to mix with the zone air. For future studies, a sensor has been installed on the door to monitor opening and closing.

During analysis of the monitoring data it was noticed that the external AHU temperature sensor, that controls operation for the bypass and cooling, is sensing too high temperatures compared to the actual outdoor temperature of the weather station. The external AHU sensor is affected by solar radiation. This indicates that for simulation studies the choice for the outdoor sensor is of importance.

By using Modelica a more complex control strategy could be implemented. In Modelica the gain factor and the integration time for PI controllers can be included, hereby the control strategy can be implemented with a high level of detail. This enables Modelica to have more control for each specific HVAC component and to simulate the specific dynamics for each individual component of the complete HVAC system.

5. CONCLUSION

With the future requirements for building energy consumption, the effect of control of HVAC systems on the energy consumption is increasing. For an educational building with an all-air HVAC system, a simulation model made in Modelica is validated with use of real monitoring data. A sensitivity analysis using an iterative approach for the parameters: air tightness, air capacity of the zone and room thermostat resulted in an accurate BES model. A good agreement is shown between the simulations and the measurements, room temperatures were simulated with a RMSE of 0.6°C and for CO_2 138 ppm compared to measurements. The simulated data of fan and heating power fit within the set requirements for hourly calibration

data $C_vRMSE \leq 30\%$ and $MBE \leq 10\%$. The results for the MBE for both the heating (4,8%) and the fans (-1,8%) is in good agreement with the measurement results. The C_vRMSE for both the fans and heating is just acceptable with approximately 28%. However, when evaluating all the results for room temperature, CO_2-concentration and air flow it can be concluded that the simulation model is able to predict these quantities with good accuracy. It will serve as basis for evaluating the energy use and indoor air quality within future research.

6. ACKNOWLEDGEMENTS

This research is funded by a PhD scholarship of KU Leuven: IOF BAM.

7. REFERENCES

ASHRAE Standard 62.1 (2007) Ventilation for acceptable indoor air quality, *Health Care 1-4*

ASHRAE. (2002). Measurement of energy and demand savings. *ASHARE Guidelines 14-2002*, *8400*, 1–165.

Baetens, R., De Coninck, R., Jorissen, F., Picard, D., Helsen, L., & Saelens, D. (2015). OpenIDEAS – an Open Framework for Integrated District Energy Simulations. *BS2015, 14th Conference of International Building Performance Simulation Association*, 347–354.

Baetens, R., De Coninck, R., Van Roy, J., Verbruggen, B., Driesen, J., Helsen, L., & Saelens, D. (2012). Assessing electrical bottlenecks at feeder level for residential net zero-energy buildings by integrated system simulation. *Applied Energy*, *96*, 74–83. https://doi.org/10.1016/j.apenergy.2011.12.098

Breesch, H., Wauman, B., Klein, R., Versele, A., (2016). Design of a new nZEB test school building, *The REHVA European HVAC Journal 53 (1), 17-20*

Breesch, Merema, Versele (2018). Ventilative cooling in a school building: evaluation of the measured performances, *39th AIVC - 7th TightVent & 5th venticool Conference*

Coakley, D., Raftery, P., Keane, M., (2014). Calibration of Detailed Building Energy Simulation Models to Measured Data using Uncertainty Analysis, 299. Retrieved from http://vmserver14.nuigalway.ie/xmlui/handle/10379/4421%5Cnhttp://hdl.handle.net/10379/4421

EN 13779. (2007). Ventilatie voor niet-residentiële gebouwen - Prestatie-eisen voor ventilatie- en luchtbehandelingssystemen. *Work*, (april), 0–90.

Jorissen, F., Boydens, W., & Helsen, L. (2018). Validated air handling unit model using indirect evaporative cooling. *Journal of Building Performance Simulation*, *11*(1), 48–64. https://doi.org/10.1080/19401493.2016.1273391

Jorissen, F., Reynders, G., Baetens, R., Picard, D., Saelens, D., & Helsen, L. (2018). Implementation and verification of the IDEAS building energy simulation library. *Journal of Building Performance Simulation*, *1493*, 1–20. https://doi.org/10.1080/19401493.2018.1428361

Jorissen, F., Wetter, M., & Helsen, L. (2018). Simplifications for hydronic system models in modelica. *Journal of Building Performance Simulation*, *0*(0), 1–16. https://doi.org/10.1080/19401493.2017.1421263

Maripuu, M. (2009). *DEMAND CONTROLLED VENTILATION State-of-the-art review*. *PhD*. Chalmers University of Technology.

Maxwell, E. L (1987). A Quasi-Physical Model for Converting Hourly Global Horizontal to *Direct Normal Insolation, Technical Report No. SERI/TR-215-3087*, Golden, CO: Solar Energy Research Institute, 1987

Merema, B., Delwati, M., Sourbron, M., Breesch, H., (2017), Calibration of a BES model of an educational building with demand controlled ventilation, *15th conference of IBPSA 43-51*

Merema, B., Delwati, M., Sourbron, M., & Breesch, H. (2018). Demand controlled ventilation (DCV) in school and office buildings: Lessons learnt from case studies. *Energy and Buildings*, *172*, 349–360. https://doi.org/10.1016/j.enbuild.2018.04.065

Perez, R., P. Ineichen, E. Maxwell, R. Seals and A. Zelenka, (1992). Dynamic Global-to-Direct Irradiance Conversion Models, *ASHRAE Transactions-Research Series,* pp. 354-369

Persily, A., & de Jonge, L. (2017). Carbon dioxide generation rates for building occupants. *Indoor Air*, *27*(5), 868–879. https://doi.org/10.1111/ina.12383

Reddy, T. A. (2006). Literature Review on Calibration of Building Energy Simulation Programs. *ASHRAE Transactions*, *112*(1), 226–240. https://doi.org/Article

Royapoor, M., & Roskilly, T. (2015). Building model calibration using energy and environmental data. *Energy and Buildings*, *94*, 109–120. https://doi.org/10.1016/j.enbuild.2015.02.050

Wachenfeldt, B. J., Mysen, M., & Schild, P. G. (2007). Air flow rates and energy saving potential in schools with demand-controlled displacement ventilation. *Energy and Buildings*, *39*(10), 1073–1079. https://doi.org/10.1016/j.enbuild.2006.10.018

Wetter, M. (2009). Modelica-based modelling and simulation to support research and development in building energy and control systems. *Journal of Building Performance Simulation*, *2*(2), 143–161. https://doi.org/10.1080/19401490902818259

Wetter, M., Bonvini, M., & Nouidui, T. S. (2016). Equation-based languages - A new paradigm for building energy modeling, simulation and optimization. *Energy and Buildings*, *117*, 290–300. https://doi.org/10.1016/j.enbuild.2015.10.017

Wetter, M., Zuo, W., Nouidui, T. S., & Pang, X. (2014). Modelica Buildings library. *Journal of Building Performance Simulation*, *7*(4), 253–270. https://doi.org/10.1080/19401493.2013.765506

Yang, Z., & Becerik-Gerber, B. (2015). A model calibration framework for simultaneous multi-level building energy simulation. *Applied Energy*, *149*, 415–431. https://doi.org/10.1016/j.apenergy.2015.03.048

Questions and Answers:

Filip Jorissen:

What four curves did you use? Try to use all surface temperature instead of zone sensor in validation?

Bart Merema:

We did measurements on the AHU where the active power of the fan is measured at varying airflow rates. Yes the surface temperature might be a better approach.

***

Lieve Helsen:

Slide 15, where do the peaks in supply air temperature come from?

Bart Merema:

The peaks are caused by the fact that the supply air temperature is increased first. When the heating demand is still not met, the airflow rate is increased.

***

Madjid Madjidi:

Perhaps the deviation between simulation and measurement comes from different parameters for the PID controller?

Bart Merema:

Indeed the deviation can be caused by different parameters for the PID controller. However, manufacturers don't give the true values for the PID parameters used in control for HVAC components. Therefore we analysed the measurement data and try to obtain the PI parameters as close to the true values. The simulation results indicate that the values are close to the measurements results (regarding the uncertainty of measurement results).

EIGHTH SESSION
BUILDING ENERGY SIMULATION 3

Connecting Thermal Building Simulation to Computational Fluid Dynamics - an experience report for TRNSYS and FDS

M. Madjidi *, E. Moldovan **

University of Applied Sciences Munich

* Prof. Dr.-Ing., Department of Building Services Engineering

** B. Eng., Student in Master of Building Technology

ABSTRACT

This paper shows the occasional need for connecting thermal building simulations to computational fluid dynamics for the estimation of airflow distribution within building zones and for the estimation of wall surface temperatures. An approach based on reading and converting of input and output files is presented for the simulation packages TRNSYS and FDS. Some additional software has been programmed in Python for the converting procedures. Simulation results for an application example are shown and approach limits and further work for parallel simulations are discussed.

Keywords

natural ventilation, mechanical ventilation, airflow distribution, wall surface temperatures, thermal building simulation, computational fluid dynamics, numerical definition of walls and outlet geometry, file parser, text converter, TRNSYS, FDS, Python, co-simulation, HVAC, ice hockey arena.

1. INTRODUCTION

Buildings with natural ventilation concepts or large building zones involving mechanical ventilation might be a challenge for thermal building simulations. In both cases the simulation engineer should consider the horizontal air movement between the zones driven by air pressure differences and the vertical air movement driven by stack effect or supply airflow momentum of the air outlet. For example, in an ice hockey arena as shown in Figure 1 different indoor climate spaces should be conditioned within the same encapsulated air volume. Figure 2 shows a scheme of sub-zones and air movements for such an application. Zone A is the ice hockey playground. The required air temperature is 8 °C. The surface temperature of the ice is -5 °C. The visitors sit in the Zones D, E and F which should have an air temperature of 15 °C. So, different air supply systems provide the arena and air enters and leaves the indoor space from air-conditioning ducts close to the ceiling. But not all of the supply air does reach the arena bottom. It might be helpful to estimate the sub-airflows

shown in Figure 2 (a,b,c, ...) by running pre-simulations based on Computational Fluid Dynamics (CFD). This requires additional information such as indoor surface temperatures of external walls. This information can be achieved with thermal building simulations considering the dynamic thermal behaviour of building constructions. So, it might be even necessary to run iteration loops as shown in Figure 3. This paper shows how such a loop can be realized and even automated by using the simulation packages TRNSYS /1/ and FDS /2/. Furthermore, it is shown, how some FDS objects are generated automatically by parsing and converting TRNSYS 3D /3/ data.

2. SELECTED SIMULATION PACKAGES

2.1 FDS

Fire Dynamics Simulator (FDS) /1/ is a freeware package for transient CFD simulations based on fire-driven air flow. Focused on the Large Eddy method the program solves the Navier-Stokes equations for thermally-driven transient flow at low speed. The large Eddy method applies a lowpass filter to involve turbulence within the fluid dynamics but FDS does not resolve boundary layers on walls. Instead, air velocity dependent empirical heat transfer functions are implemented for the calculation of convection between walls and air. Furthermore, three dimensional exchange of radiative heat can be considered and the computation mesh can be divided into groups with different resolution. In comparison to commercial CFD packages FDS requires less training time but it has no graphical user interface for pre-processing in the original package and the geometry of objects and meshes is limited to rectangular shapes. Test cases show /4/ that FDS is also capable of simulating indoor air movements without any fire modeling. Therefore, it is also a good tool for

introducing students to CFD.

2.2 TRNSYS

TRNSYS /1/ is a software package used to simulate the transient behavior of thermal and electrical energy systems. But the standard package includes also a well-tested multi-zone building model based on the response factor method. This model can be pre-processed by running a special Plugin within SketchUp™ /5/. The TRNSYS 3D plugin exports the geometry including building selfshading and internal view factors for radiation exchange directly into the building editor, the TRNSYS building environment (TRNBuild). Although TRNSYS is not the main building simulation tool, especially in the USA and GB, and after 40 years of commercial availability of TRNSYS, today a large number of more convenient building simulation packages might exist in the market, but the modular concept, the free access to any input and output data and the capability of including user-written modules to the simulation model keep TRNSYS still to be a flexible engineering tool in practice and a didactic teaching tool for students in the field of engineering and modelling of building energy systems.

3. CONNECTION PROCEDURE

TRNSYS, TRNSYS 3D and FDS read and write input and output data files which can be opened as text files. Figure 4 shows some text lines of a FDS input file linked to their corresponding objects. In FDS any object is described by two vectors as shown in Figure 7. TRNSY 3D allows the user to describe walls and windows graphically based on mouse movements on the computer monitor. Furthermore, CAD data files can be imported to SketchUp™ and be used for definition of building zones. TRNSYS 3D exports the building description to a text file called IDF. Figure 5 shows an extract of such a data file. TRNSYS can read external files via TYPE 9 (Data Reader) and export data via TYPE 25 (Data Printer). So, only two additional components are needed to run a loop as shown in Figure 6. They are converters which have been written in Python /6/ and are described in the following sections.

3.1 CONV1

CONV1 converts the geometrical information written by TRNSYS 3D in SketchUp™ (see example in Figure 5) to FDS input text lines (see example in Figure 4) and combines them with wall surface temperatures computed by TRNSYS and written by TRNSYS TYPE 25 in the SUT-file. Figure 8 shows an extract of CONV1. The extract shows the IDF-parser part of the code. This part identifies the coordinates of walls and windows (12 values per object) and converts them to the FDS vector format XB (6 values per object) as shown in Figure 7. The information described by XB is embedded in the FDS command line &OBST. Further parts of CONV1 read the surface temperatures coming from TYPE 25 and add this information to the &OBST lines of the FDS input file.

3.2 CONV2

CONV2 converts the airflow information computed and written by FDS in the DEVC-file and it writes the AIR-file. This file is then opened by TRNSYS TYPE 9. CONV2 is needed because FDS writes into the DEVC-file from the start of the transient CFD simulation. It writes values for the airflow crossing pre-defined rectangular areas within the model. These areas can be defined by the user in the FDS input file using the command line which starts with &DEVC. The user can define any computed variable to be estimated for a specific point in the computed space (mesh cell) or for a group of cells within rectangular areas defined by the user. But as FDS simulations are transient these values change during the simulation until a certain simulation time has been reached. The duration of this period is usually corresponding to the air exchange rate. The CFD simulation time should be set to be equal or higher than the air exchange rate. CONV2 calculates the average of 50 to 100 values from the last time steps before the end of the simulation and provides TRNSYS with constant values to be set as inputs (instead of constant or scheduled) in TRNSYS TYPE 56 (multi-zone building model).

4. APPLICATION EXAMPLE

The concept has been applied on the simulation of an ice hockey arena as shown in Figure 1 and 9. The ice hockey arena has a ground area of 110 m x 80 m and an average height of 20 m. The building encapsulates approx. 150 000 m3 of air. 10 000 visitors are expected. The calculated supply air volume is 300 000 m3/h. For the simulations only a section of the building has been modeled with TRNSYS and FDS by taking into account the whole height of the building, the whole visitors area within the section and a part of the playground. The depth of the section shown in Figure 9 is 20 m, the length is 42 m and the height is 20 m. The supply air temperatures vary between 8 and 20 °C. The U-value of the ceiling is 0,2 W/m2K. The U-value for external walls is 0,35 W/m2K. Window areas have been neglected. The pink box in Figure 9 represents video screen, the white boxes represent artificial light and the blue boxes represent the exhaust air inlets. The model has been used to find out the adequate distribution of supply air flow between outlet for the playground area (green box in Figure 9) and the visitors area (seat outlets). The ice temperature of the playground surface is a simulation boundary condition and set to -5 °C. The simulation results show that the playground area must be covered by 15 % of the supply total air flow to be able to

keep an air temperature of 8 °C in the playground (height 0 to 2 m) during the whole year. The result of the CFD simulation is shown in the upper part of Figure 9 for the worst summer case but the results for other seasons are nearly identical. The simulations show that the air movement can be kept steady, even though different outdoor conditions appear. The supply air temperatures have been set by the controllers observing the air temperatures in the playground and visitors area. This leads to nearly constant air conditions during the whole year as shown in the lower part of Figure 9. The only surprising result is that the air mass in the arena is not stratified as it might be expected which is a good news for the visitors of an ice hockey game.

5. RESULTS AND POTENTIALS

Student projects at the Munich University of Applied Sciences show that the concept works well for simple, rectangular zone descriptions. But furniture, people and other objects which cannot be described by TRNSYS 3D must be added manually. Furthermore, the loop between TRNSYS and FDS is not fully automated yet. Type 9 and Type 25 should be replaced by user-written TYPES which could communicate with the converters directly during both simulations (instead of after and before).

6. CONCLUSION

The need and feasibility for connecting thermal building simulations to computational fluid

dynamics has been demonstrated. An approach based on reading and converting of input and output files is now available for the simulation packages TRNSYS and FDS. The concept works well for simple zone descriptions. The loop between TRNSYS and FDS is not fully automated yet. Type 9 and Type 25 should be replaced by user-written TYPES which would communicate with the converters directly. This work is in progress now. Furthermore, FDS limits the building description to combinations of rectangular objects. Additional investigations have been just started to replace FDS by OpenFoam /7/.

7. REFERENCES

/1/ Klein, S.A. et al, 2017, TRNSYS 18: A Transient System Simulation Program, Solar Energy Laboratory, University of Wisconsin, Madison, USA. http://sel.me.wisc.edu/trnsys.

/2/ McGrattan, K. B. et al, Fire Dynamics Simulator Technical Reference Guide. 6th edition, NIST Special publication 1018-1. National Institute of Standards and Technology, USA.

http://dx.doi.org/10.6028/NIST.SP.1018

/3/ Trnsys3d Tutorial, TRANSSOLAR Energietechnik GmbH, March 2012

/4/ McGrattan, K. B. et al, Fire Dynamics Simulator Technical Reference Guide - Volume 3: Validation. 6th edition. NIST Special Publication 1018-1. National Institute of Standards and Technology, USA. http://dx.doi.org/10.6028/NIST.SP.1018-3

/5/ SketchUp™, https://www.sketchup.com

/6/ Python, https://www.python.org/

/7/ OpenFOAM, https://openfoam.org/

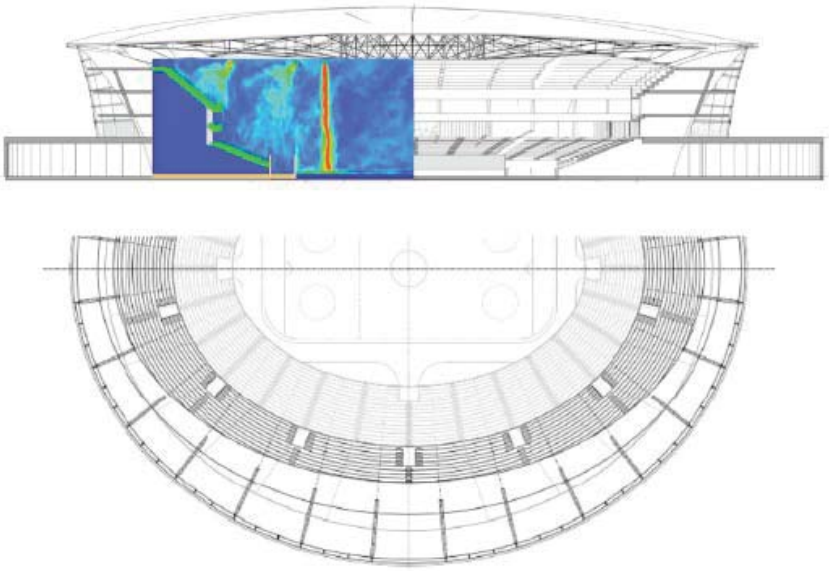

Figure 1: Application example (fictitious icehockey arena)

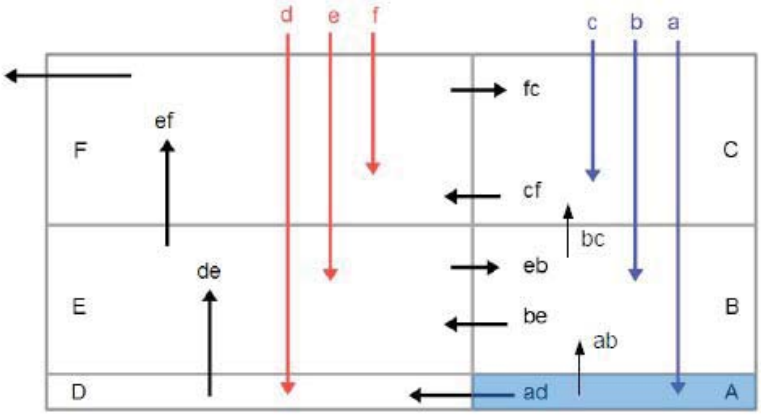

Figure 2: Airflow distribution scheme for icehockey arena

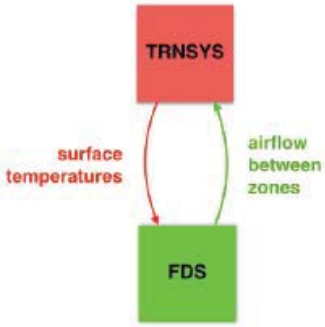

Figure 3: Information loop between TRNSYS and FDS

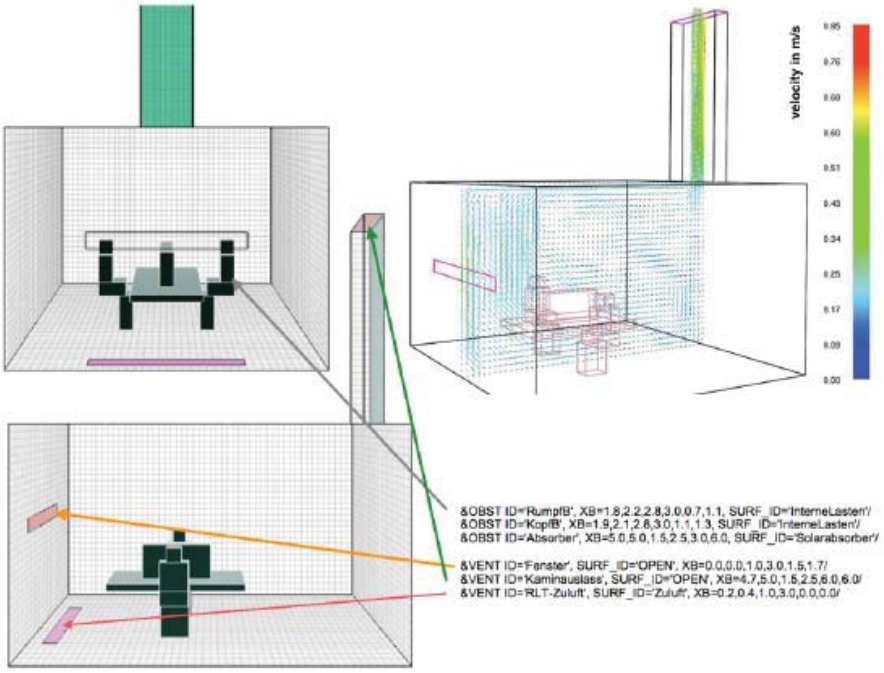

Figure 4: Definition of outlets and obstacles in FDS

```
BuildingSurface:Detailed,
  41FE42,  !- Name
  Wall,  !- Surface Type
  EXT_WALL,  !- Construction Name
  EDF028,  !- Zone Name
  Outdoors,  !- Outside Boundary Condition
  ,  !- Outside Boundary Condition Object
  SunExposed,  !- Sun Exposure
  WindExposed,  !- Wind Exposure
  ,  !- TRNSYS 17 - additional surface data
  4,  !- Number of Vertices
  5.030000000000,  !- Vertex 1 X-coordinate {m}
  0.000000000000,  !- Vertex 1 Y-coordinate {m}
  2.720000000000,  !- Vertex 1 Z-coordinate {m}
  5.030000000000,  !- Vertex 2 X-coordinate {m}
  0.000000000000,  !- Vertex 2 Y-coordinate {m}
  0.000000000000,  !- Vertex 2 Z-coordinate {m}
  7.150000000000,  !- Vertex 3 X-coordinate {m}
  0.000000000000,  !- Vertex 3 Y-coordinate {m}
  0.000000000000,  !- Vertex 3 Z-coordinate {m}
  7.150000000000,  !- Vertex 4 X-coordinate {m}
  0.000000000000,  !- Vertex 4 Y-coordinate {m}
  2.720000000000;  !- Vertex 4 Z-coordinate {m}

BuildingSurface:Detailed,
  FF27F8,  !- Name
  Wall,  !- Surface Type
  EXT_WALL,  !- Construction Name
  EDF028,  !- Zone Name
  Outdoors,  !- Outside Boundary Condition
  ,  !- Outside Boundary Condition Object
  SunExposed,  !- Sun Exposure
```

Figure 5: Wall coordinates in IDF-File (TRNSYS-3D)

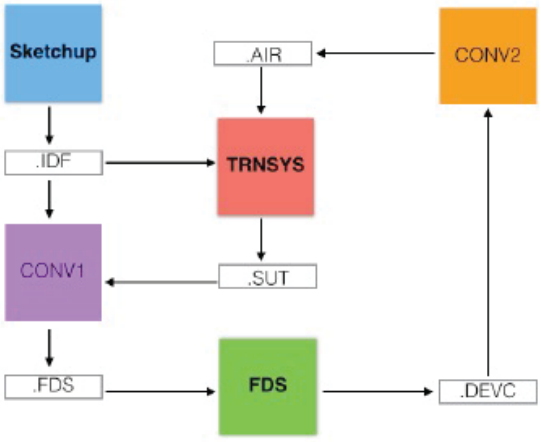

Figure 6: Loop management with converters in Python

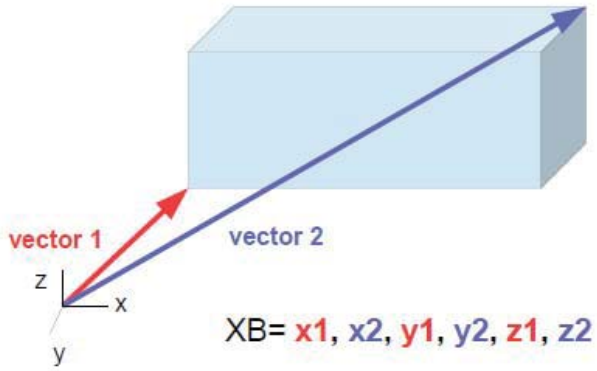

Figure 7: Definition of objects in FDS with only two vectors

```
if "1 X-coordinate" in Zeile and Shading == False:

    X1ersterSplit = re.split("[0-9][0-9][0-9][0-9][0-9][0-9][0-9][0-9][0-9][0-9][0-9],  !- Vertex 1 X-coordinate {m}", Zeile)
    X1mitLeer = X1ersterSplit[0]
    X1zweiterSplit = re.split("    ", X1mitLeer)
    PerfekterX1 = X1zweiterSplit[1]
    AusgabeInhalt.write(", XB=")

if "3 X-coordinate" in Zeile and Shading == False:
    X3ersterSplit = re.split("[0-9][0-9][0-9][0-9][0-9][0-9][0-9][0-9][0-9][0-9][0-9],  !- Vertex 3 X-coordinate {m}", Zeile)
    X3mitLeer = X3ersterSplit[0]
    X3zweiterSplit = re.split("    ", X3mitLeer)
    PerfekterX3 = X3zweiterSplit[1]
    if float(PerfekterX3) > float(MaximalX3):
        MaximalX3 = PerfekterX3

if "1 Y-coordinate" in Zeile and Shading == False:
    Y1ersterSplit = re.split("[0-9][0-9][0-9][0-9][0-9][0-9][0-9][0-9][0-9][0-9][0-9],  !- Vertex 1 Y-coordinate {m}", Zeile)
    Y1mitLeer = Y1ersterSplit[0]
    Y1zweiterSplit = re.split("    ", Y1mitLeer)
    PerfekterY1 = Y1zweiterSplit[1]

if "3 Y-coordinate" in Zeile and Shading == False:
    Y3ersterSplit = re.split("[0-9][0-9][0-9][0-9][0-9][0-9][0-9][0-9][0-9][0-9][0-9],  !- Vertex 3 Y-coordinate {m}", Zeile)
    Y3mitLeer = Y3ersterSplit[0]
    Y3zweiterSplit = re.split("    ", Y3mitLeer)
    PerfekterY3 = Y3zweiterSplit[1]
    if float(PerfekterY3) > float(MaximalY3):
        MaximalY3 = PerfekterY3

if "1 Z-coordinate" in Zeile and Shading == False:
    Z1ersterSplit = re.split("[0-9][0-9][0-9][0-9][0-9][0-9][0-9][0-9][0-9][0-9][0-9],  !- Vertex 1 Z-coordinate {m}", Zeile)
    Z1mitLeer = Z1ersterSplit[0]
    Z1zweiterSplit = re.split("    ", Z1mitLeer)
    PerfekterZ1 = Z1zweiterSplit[1]

if "3 Z-coordinate" in Zeile and Shading == False:
    Z3ersterSplit = re.split("[0-9][0-9][0-9][0-9][0-9][0-9][0-9][0-9][0-9][0-9][0-9],  !- Vertex 3 Z-coordinate {m}", Zeile)
    Z3mitLeer = Z3ersterSplit[0]
    Z3zweiterSplit = re.split("    ", Z3mitLeer)
    PerfekterZ3 = Z3zweiterSplit[1]
    if float(PerfekterZ3) > float(MaximalZ3):
        MaximalZ3 = PerfekterZ3

    AusgabeInhalt.write("{},{},{},{},{},{}".format(PerfekterX1,
    PerfekterX3, PerfekterY1, PerfekterY3, PerfekterZ1,PerfekterZ3))

    AusgabeInhalt.write("\n")
```

Figure 8: Python code section converting IDF data to FDS vectors

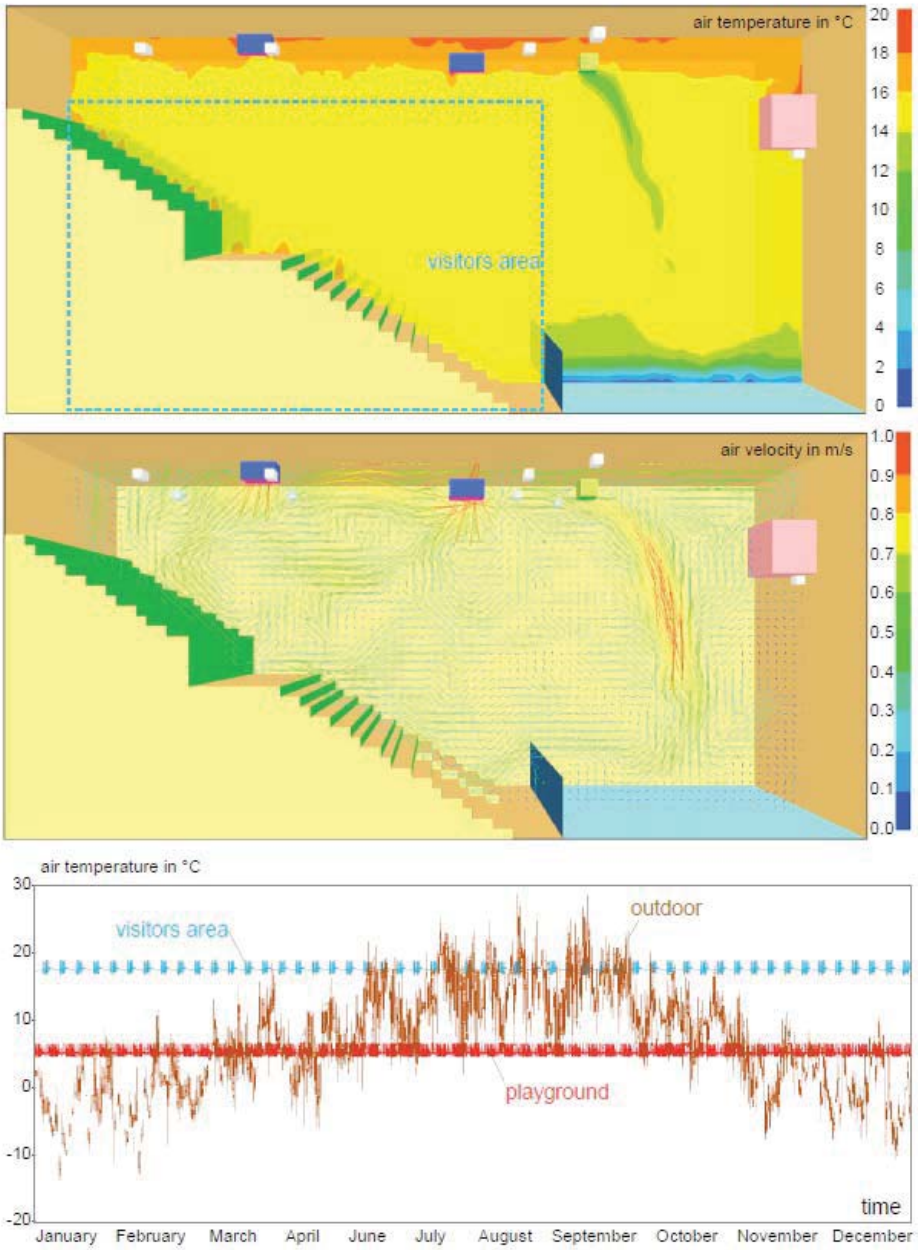

Figure 9: Simulation results for an icehockey arena

Questions and Answers:

Michaël Kummert:

Could you explain how the surface temperature and airflows are exchanged between TRNSYS and FDS for each time step? Do you run long simulations in each program separately or do you iterate at each time step?

Madjid Madjidi:

We did just few simulations in FDS for typical weather conditions (winter, mid-season, summer), then, we sent the results to TRNSYS and we repeated the simulation; yet there is no link for each time step but it would be possible.

***

Jean Lebrun:

What is the energy issue?

Madjid Madjidi:

With such a study, we get the zone temperature near the exhaust outlet; this temperature is an input for the computation of the heat recovery.

***

Jean Lebrun:

Is the flow pattern whanging a lot along the year?

Madjid Madjidi:

Not a lot but it is observable. Therefore, we simulated the indoor air movement for winter, mid-season and summer by running TRNSYS.

***

Jean Lebrun:

Why extracting the air from above? Why blowing air in the cold zone? Why not calculating CO2 concentration?

Madjid Madjidi:

The air ducts are placed in the ceiling by the responsibility of the architects. According to CO2 you are right. It makes the need for extra fresh air for the playground clearer. At the playground, 8°C is a requirement.

A new approach to model transport delay in branched pipes

Van Riet Freek[1,*], Steenackers Gunther[1], Verhaert Ivan[1]

[(1)]University of Antwerp, Faculty of Applied Engineering, Belgium
[(*)]Corresponding Author: freek.vanriet@uantwerpen.be

1 ABSTRACT

Pipe networks are ubiquitous in both space heating systems and domestic hot water systems of buildings. The thermal and hydraulic behaviour of such networks can be simulated in several energy performance simulation programs. Conventionally, this is done by calling multiple individual pipe models and defining their interconnections. However, especially in script-based programs, this is labour-intensive and prone to scripting errors for large pipe networks. Therefore, this paper proposes a new way to improve this part of simulation processes. More specifically, an algorithmic approach is presented to model the thermal behaviour of flow in branched pipes as a whole, rather than of that in an assembly of multiple single pipes. A branched pipe was defined here as a network having one main pipe and multiple branches. The algorithm contains two steps. In the first, the pipe with n branches is separated into n fictitious single pipes from inlet to all outlets. In the second, the thermal behaviour is calculated for every fictitious pipe, based on a plug-flow model. The developed approach enables faster and more robust scripting in simulations of systems containing pipe networks.
Keywords: branched pipes, pipe transport delay, script-based programming

2 INTRODUCTION

2.1 Problem Statement

Space heating and domestic hot water (DHW) production account for, respectively, 32% and 24% of the global final energy consumption in residential buildings (Berardi, 2016). Various authors (Cholewa & Siuta-Olcha, 2010; Cholewa et al., 2011; Van Riet et al., 2016; De Pauw et al., 2018) have shown that, especially when considering apartment blocks, the type of heat distribution system (individual systems or collective systems, and its many variations) is one of the main factors affecting that consumption. Comparing the findings of these authors reveals that the energetic and comfort-related performance of a specific distribution system depends on the building it is implemented in.

This means that, when designing a building, a large amount of design concepts have to be evaluated and compared in order to find an optimal distribution system. In the project 'Instal2020: Integraal ontwerp van installaties voor sanitair en verwarming (Dutch)' (www.instal2020.be), a methodology was proposed (De Pauw et al., 2018) to find that optimum, thereby decreasing the duration and increasing the quality of a design process of heating and DHW systems in apartment blocks. This methodology is based on dynamic building simulations, for which a script-based program was developed in Matlab (i.e. without Graphical User Interface).

In script-based simulation programmes, the number of code lines that should be written determines how labour-intensive and how prone to scripting errors a particular simulation is. The

number of lines increases with increasing size of the distribution system, because of the expanding pipe network. Indeed, a pipe network consists of multiple pipe segments*, and each single segment requires multiple code lines: first, the connections with other pipe segments at junctions should be defined (i.e. mass balances), and second, a function that includes the mathematical model which describes the behaviour of the fluid in the pipe has to be called. As a result, scripting for the simulation of large apartment blocks become impractical.

2.2 Scope and Outline

This paper proposes an algorithmic approach to facilitate the time-consuming scripting of large pipe networks: it allows to reduce the number of code lines. This approach was already successfully implemented in the methodology discussed above (De Pauw et al., 2018). The main idea is to use a function which has to be called only once in a simulation script for a branched pipe†, rather than for each single pipe segment (which is the conventional approach).

In order to do so, the function contains two algorithms. In the first, the network with n branches is separated into n fictitious single pipes from inlet to the outlets (section 4). In the second, the thermal behaviour is calculated for every single fictitious pipe (section 3). Although the proposed approach is applicable for multiple types of pipe models (see e.g. (Duquette et al., 2016) for a discussion on model types), it is elaborated for a plug-flow model type (see TRNSYS 17 Mathematical Reference, Type 31: Pipe or Duct) only. The advantage of a plug-flow model is that it allows to reflect sudden changes in inlet temperature in the outlet temperature, while taking into account the transport delay. This is a crucial aspect to assess comfort-related performance of a distribution system, especially when considering DHW consumption at the level of the end-user. In a final section, the approach is verified by means of a case study. The results are therefore compared with the conventional approach.

The algorithmic approach, presented in this paper, speed-ups scripting processes for simulations of flow in large pipe networks, while making the scripting less prone to errors. This was already proofed by implementing it in the methodology developed in 'Instal2020'. The proposed approach is not limited to apartment buildings: also simulations of other large pipe networks, such as district heating and cooling systems, can benefit from it.

3 MODEL DESCRIPTION OF A SINGLE PIPE

While the principle of a plug-flow model of a single pipe is not new, the concept is crucial to understand the branched pipe approach. Therefore, it will be introduced briefly. For further information, the reader is referred to TRNSYS documentation, type 31.

*In this paper, a pipe segment is defined as a piece of a pipe network between two pipe junctions, see e.g. Figure 2

†A branched pipe is considered here as a pipe network having one main pipe with a single inlet and multiple branches (the outlets), see e.g. Figure 2

In this paper, it is assumed that the (varying) flow rate through the pipe is known at all times. This information might originate from an hydraulic model of the pipe network or directly from a process with known flow rates, such as when simulating DHW consumption. This makes it possible to characterise the pipe with only two parameters: its total volume and the overall heat transfer coefficient of its wall and insulation. However, as this paper focusses on transport delay, the heat loss to surroundings, and hence also the heat transfer coefficient will not be considered.

The principle of a plug-flow pipe model is shown in Figure 1. Initially (at $t = t$), the pipe is filled with n_{plug} 'plugs' (three in example) of which its volumes are represented by vector $\mathbf{V}(t)$ and their corresponding uniform temperatures by a vector $\mathbf{T}(t)$, both vectors having n_{plug} elements:

$$\begin{matrix} \cdot & & \cdot \\ \cdot \boldsymbol{V}(t) = & \left[V_1(t) \quad V_2(t) \quad V_3(t) \right] & \cdot \\ \cdot \boldsymbol{T}(t) = & \left[T_1(t) \quad T_2(t) \quad T_3(t) \right] & \cdot \end{matrix} \tag{1}$$

During a time-step Δt, the fluid flows through the pipe with a mass flow rate $\dot{m}$. Two possible situation after the time-step $t = t + \Delta t$ are shown as an example in the figure, each characterised by a different mass flow rate (see $\dot{m}_1$ and $\dot{m}_2$). From an algorithmic point of view, two steps should be performed to model the transport delay: finding and storing the new content of the pipe (e.g. $\boldsymbol{V}(t+\Delta t) = \left[V_1(t+\Delta t) \quad V_2(t+\Delta t) \quad V_3(t+\Delta t) \right]$, $\boldsymbol{T}(t+\Delta t) = \left[T_1(t+\Delta t) \quad T_2(t+\Delta t) \quad T_3(t+\Delta t) \right]$ for the situation $\dot{m} = \dot{m}_1$), and calculating the mean outgoing temperature. For the first step, the following items should be implemented in an algorithm:

1. Concatenate the volume of the ingoing plug, $V_1(t+\Delta t)$, and $\boldsymbol{V}(t)$ into an extended vector $\boldsymbol{V}_{ex}(t+\Delta t)$ with $n_{plug}+1$ elements.
2. Take the cumulative sum of the elements in $\boldsymbol{V}_{ex}(t+\Delta t)$, $\boldsymbol{V}_{cu}(t+\Delta t)$ with $n_{plug}+1$ elements.
3. Concatenate the value of the total volume of the pipe and store this vector into a new one having $n_{plug}+2$ elements.
4. Sort that latter vector and find the position i_{tot} of the element containing the value of the total volume.
5. Reverse the cumulative sum.
6. Assign the resulting elements with positions one to i_{tot} to a new state vector $\boldsymbol{V}(t+\Delta t)$, and analogue for $\boldsymbol{T}(t+\Delta t)$.

For the second step, the remaining elements starting from $i_{tot}+1$ are used to calculate the mean outgoing temperature according to an energy balance.

4 MODEL DESCRIPTION OF A BRANCHED PIPE

4.1 Defining the Branched Pipe and its States

The main challenge of the developed approach is accessing and storing data (temperatures and volumes) effectively. A first step in order to do so, is to define the branched pipe unambiguously. The upper part of Figure 2 shows an example of a branched pipe with one inlet and three

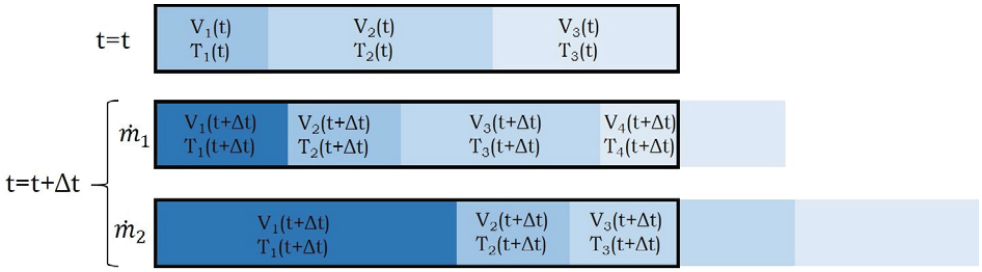

Figure 1: Schematic overview of water flowing through a pipe during a time-step Δt using a plug-flow model. After the time-step ($t = t + \Delta t$), two possible situations are shown: each with a different mass flow rate ($\dot{m}_2 > \dot{m}_1$).

outlets. The main pipe consists of three pipe segments and all branches consist of one pipe segment. Each pipe segment is characterised by its total volume $V_{i,j}$ (and its overall heat transfer coefficient $UA_{i,j}$ if heat losses are taken into account), as indicated with curly brackets on the figure.

The complete branched pipe can than be characterised by a matrix $\boldsymbol{V}_t$ and, optionally, a matrix **UA**. Slashes represent positions in the matrices without reference to any pipe segment.

$$\boldsymbol{V}_t = \begin{matrix} V_{1,1} & V_{1,2} & V_{1,3} & V_{1,4} \\ / & V_{2,2} & V_{2,3} & / \end{matrix} \quad (2)$$

$$\mathbf{UA} = \begin{matrix} UA_{1,1} & UA_{1,2} & UA_{1,3} & UA_{1,4} \\ / & UA_{2,2} & UA_{2,3} & / \end{matrix} \quad (3)$$

Besides these parameters, the algorithm needs to know how to 'move' in these matrices. Therefore, for all outlets, a unique path has to be defined between the inlet and the corresponding outlet by means of a matrix $\boldsymbol{p_k}$. These paths indicate which pipe segments are flown through from the inlet to the outlets. Hence, $\boldsymbol{p_k}$ should contain the indices to locate the characteristics of the pipe segments involved, corresponding to each outlet. For the example in Figure 2, the paths of the three outlets are given as:

$$\boldsymbol{p}_1 = \begin{matrix} 1 & 2 \\ 1 & 2 \end{matrix}, \quad \boldsymbol{p}_2 = \begin{matrix} 1 & 2 & 3 \\ 1 & 1 & 2 \end{matrix}, \quad \boldsymbol{p}_3 = \begin{matrix} 1 & 1 & 1 & 1 \\ 1 & 2 & 3 & 4 \end{matrix} \quad (4)$$

Each column of $\boldsymbol{p}_k$ (for all k) contains two indexes, i and j, that refer to a pipe segment, as defined by $\boldsymbol{V}_t$ and **UA**. The order of the columns in a path is consistent with the order of the pipe segments that would be be flown through when 'moving' from inlet to the outlet associated to that path.

Up to this point, the pipe network itself has been defined by $\boldsymbol{V}_t$, **UA** and $\boldsymbol{p_k}$. However, the content of the network should also be defined as each pipe segment may contain more than one

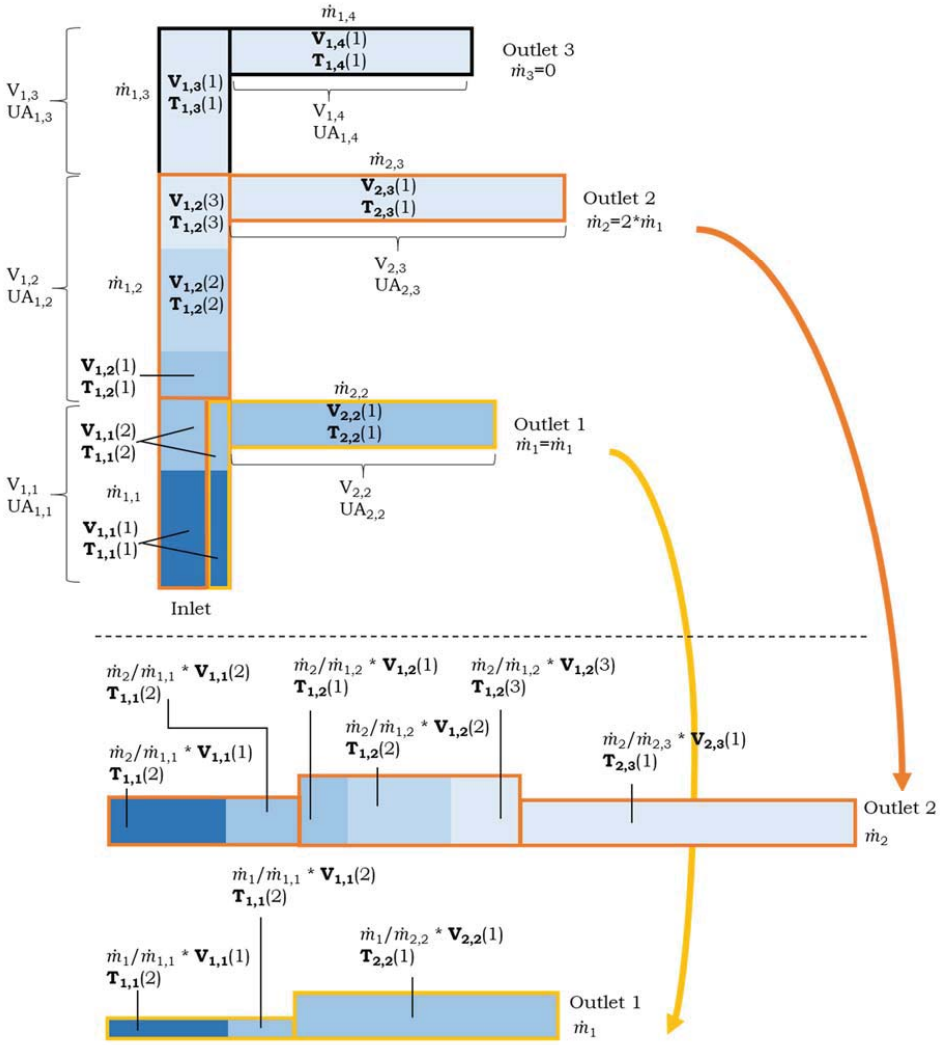

Figure 2: Upper part: Schematic representation of the flows in each pipe segment. Each outlet flow 'divides' the partial volumes in the segments. The volumes which will flow to outlet 1 are framed by yellow rectangles. The volumes which will flow to outlet 2 are framed by orange rectangles. It can be seen that the first pipe segment $(1,\ 1)$ *is divided in two sections. The orange rectangle is twice as wide as the yellow one. Indeed, it is stated that* $\dot{m}_2 = 2 * \dot{m}_2$*. The flow to outlet 3 is not framed separately as it is stated that* $\dot{m}_3 = 0$*. Lower part: The translation from the branched pipe network to multiple fictitious single pipes. Each segment of a fictitious single pipe contains a share of the content of the corresponding original ('real') segment. For further interpretation, the reader is referred to the text.*

plug. E.g. pipe segment (1,2) in the upper part of Figure 2 contains three plugs, and all branches contain only one plug. The state of each pipe segment (i, j) can be defined by two vectors: $\boldsymbol{V}_{i,\,j}(t)$ and $\boldsymbol{T}_{i,j}(t)$. Again for pipe segment (1 ,2), this gives $\boldsymbol{V}_{1,2}(t) = \boldsymbol{V}_{1,2}(1)\ \ \boldsymbol{V}_{1,2}(2)\ \ \boldsymbol{V}_{1,2}(3)$ and $\boldsymbol{T}_{1,2}(t) = \boldsymbol{T}_{1,2}(1)\ \ \boldsymbol{T}_{1,2}(2)\ \ \boldsymbol{T}_{1,2}(3)$. In this section, the numbers in parentheses at the right hand side of the equations represent the number of the plug in the pipe segment (and not the time, as is the case at the left hand side of the equations).

$\boldsymbol{V}_{i,\,j}(t)$ for all combinations of (i,j) is stored in a three-dimensional tensor $\boldsymbol{V}_{bp}(t)$ according to $\boldsymbol{p_k}$, for all k. Analogously, all temperature states are stored in a three-dimensional tensor $\boldsymbol{T}_{bp}(t)$. The number of elements in the third dimension of these two tensors depends on the highest number of plugs contained in a single pipe segment. In the example given in the upper part of Figure 2, the number of elements would be determined by pipe segment (1,2) and would be equal to three:

$\boldsymbol{V}_{bp}(t) =$

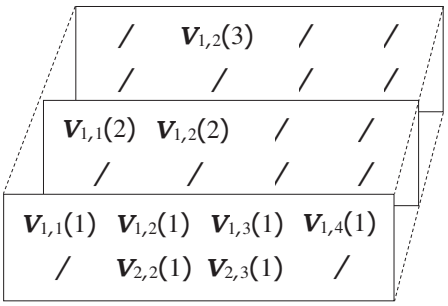

The slashes represent zero-volume plugs, that only fill empty array elements.

4.2 Calculating the Transport Delay

The transport delay is inherently taken into account when the outgoing temperature of a plug-flow model is calculated. In order to do that, the following three action were implemented in an algorithm:

1. Split the branched pipe with n outlets into n fictitious single pipes from the inlet to the outlets. The scope of this action is to create state vectors for all fictitious pipes, analogue to the example given by Eq. 1. This section will describe this approach.

2. Calculate the outgoing temperature for each single fictitious pipe. For this step a conventional single pipe model can be used, as described in the previous section 'model description of a single pipe'. It will not be discussed further in this section.

3. Store the new states of the pipe network. This will be mentioned shortly, as it requires a slightly different approach compared to the one discussed for the single pipe.

The splitting of the pipe network into fictitious single pipes is possible under the assumption that flow rates are known at the outlets. While these rates are considered to be constant during one discrete simulation time-step, they may vary over time. The density of the fluid will be assumed to be constant in the rest of this paper.

In order to create a fictitious pipe that corresponds to a particular outlet k, all subsequent plugs from inlet to that outlet are extracted from $\boldsymbol{V}_{bp}(t)$. Therefore, a two-dimensional 'masking-matrix' is applied on $\boldsymbol{V}_{bp}(t)$, defined by the path indices $\boldsymbol{p_k}$. All elements in the third dimension of $\boldsymbol{V}_{bp}(t)$ are then extracted.

However, the volumes of the plugs in a pipe segment might flow towards multiple outlets. In e.g. the upper part of Figure 2 this is true for the pipe segment (1,1). Therefore, only a share of the plug volumes in a segment should be assigned to a fictitious pipe. The extend of that share depends on the flow rate at the different outlets the plugs flow to. This is graphically explained in the upper and lower part of Figure 2. The fictitious pipes corresponding to outlet 1 and 2 are framed by yellow and orange rectangles, respectively. For outlet 3, no fictitious pipe is shown, as the flow rate through it is assumed to be zero ($\dot{m}_3 = 0$). $\dot{m}_2$ is assumed to be twice $\dot{m}_1$, which can be seen in the upper part of the figure: a double share of the volumes of the plugs in segment (1,1) is framed is orange. Only one third is framed in yellow. Indeed, whatever the absolute values of the mass flow rates are, outlet 2 has a double share in the total mass flow rate in segment (1,1): $\dot{m}_2 / \dot{m}_{1,1} = 2 * \dot{m}_1 / \dot{m}_{1,1}$.

In general, this means that the algorithm should determine the total mass flow rate in each segment. This is straightforward, as the path from inlet to all outlets are given by $\boldsymbol{p_k}$. Thereafter, the share of mass flow rate in each pipe segment for all outlets should be determined. All elements extracted in the third dimension of $\boldsymbol{V}_{bp}(t)$, as previously discussed, should than be multiplied by the corresponding fraction. This principle can also be seen in the lower part of Figure 2, in which two fictitious pipes (corresponding to outlet 1 and 2) are shown 'unfolded'. The temperatures of the plugs of the fictitious pipes should be extracted from $\boldsymbol{T}_{bp}(t)$ analogously to the extraction of the volumes. However, the temperatures should, obviously, not be multiplied with the fraction the volumes are multiplied with.

Next, all fictitious pipes can be treated as a single pipes to calculate the outgoing the temperature (and, optionally, heat losses), as already mentioned.

Finally, the new states of the complete pipe network should be saved in the tensors $\boldsymbol{V}_{bp}(t + \Delta t)$ and $\boldsymbol{T}_{bp}(t + \Delta t)$. It is comparable to the protocol explained in the section covering the single pipe model. However, the fictitious pipes should not just be separated into a part that is flushed out and one that is not. Indeed, they should be separated into multiple parts in order to fit the data back into all corresponding pipe segments. The resulting pipe segments should then contain a number of plugs, of which the volume of each plug is the sum taken over all fictitious pipes related to that segment.

5 ILLUSTRATION AND COMPARISON

In this section, the method discussed above is illustrated and compared with the conventional method (i.e. defining one pipe model for every single pipe segments) by means of predefined inputs. Both methods were implemented in Matlab (R2015a).

For a period of ten minutes and a step size of 10 seconds, a branched pipe network having one main pipe (inlet) and three branches (outlets) is simulated. This network is represented by the

one shown in the upper part of Figure 2. By filling in Equation 2 (in litre with a density of $1 kg/l$) the network is defined by:

$$\boldsymbol{V_t} = \begin{matrix} 6 & 6 & 6 & 2 \\ / & 2 & 2 & / \end{matrix} \tag{5}$$

and Equation 4. Heat losses to surroundings are calculated identically by the new and conventional approach. Therefore, it is not considered and hence it is not required to define **UA**.

To illustrate the transport delay, the temperature of the water going in the inlet and the mass flow rates of the outlets were varied with step-functions (upper two plots of Figure 3). First, a mass flow rate of $0.19 kg/s$ is applied for two minutes for the third outlet, while no flow is assumed for the other ones. This is subsequently repeated for the two other outlets. At the end, the same mass flow rate is considered for all outlets at the same time. The ingoing temperature varies each two minutes with steps of $10°C$. Since heat losses were neglected, the difference in temperature between inlet and outlets depends on the transport delay only, thereby enabling an unambiguous interpretation of the results. The outgoing temperatures are shown in the lower plot of Figure 3. The initial temperature of the complete pipe network was set at $20°C$ (not shown on the figure).

Figure 3 shows clearly the transport delay. Two examples will be discussed:

- During the first two minutes, water flows only through outlet 3 (as already mentioned above) while water flows into the inlet at the same rate with a temperature of $30°C$. This means that after 100 seconds (10th simulation point) the 'active' space (i.e. flowing water) between the inlet and outlet 3 is occupied with 19 litres of water at $20°C$ and 1 litre at $30°C$ (20 litres in total: 6+6+6+2, see Equation 5). During the 11th simulation time-step, 1 litre at $20°C$ and 0.9 litre at $30°C$ flows through the outlet. The model gives the mean temperature, being $((1 * 20 + 0.9 * 30)/1.9) = 24.74°C$. One time-step further, water at exactly $30°C$ flows through the outlet.
- Again, the reaction of outlet 3 will be discussed. At 360 seconds, a flow rate occurs through all outlets at the same time (again, as mentioned above). Before that moment, pipe segments $(1, 1)$, $(1, 2)$, $(1, 3)$ and $(1, 4)$ are at a temperature of $50°C$, $40°C$, $30°C$ and $30°C$, respectively. Hence, at 360 second, 8 litres of water at $30°C$ awaits before the third outlet. This means that during 40 seconds (four time-steps), 7.6 litres of that 8 litres leaves at $30°C$. During the same period, half of the 6 litre from segment $(1, 2)$ flows through segment $(1, 3)$ and partially (1.6 litre) into segment $(1, 4)$ (the other half flows out outlet 2). Therefore, at the next time-step, water leaves outlet 3 at a mean temperature of $((0.4 * 30 + 1.5 * 40)/1.9) = 37.89°C$. Then 2 litres of the water that was in segment $(1, 1)$ at 360 seconds reach segment $(1, 3)$ and $(1, 4)$ (again, the other shares leave via the other outlets). At 410 seconds 0.4 litre of it, along with the remaining 1.5 litre at $40°C$, flow through outlet three with a mean temperature of $((1.5 * 40 + 0.4 * 50)/1.9 =) 42.11°C$. The next time-step, the ingoing water at $60°C$ has reached segment $(1, 4)$, resulting in an outlet temperature of $((1.6 * 50 + 0.3 * 60)/1.9 =) 52.58°C$.

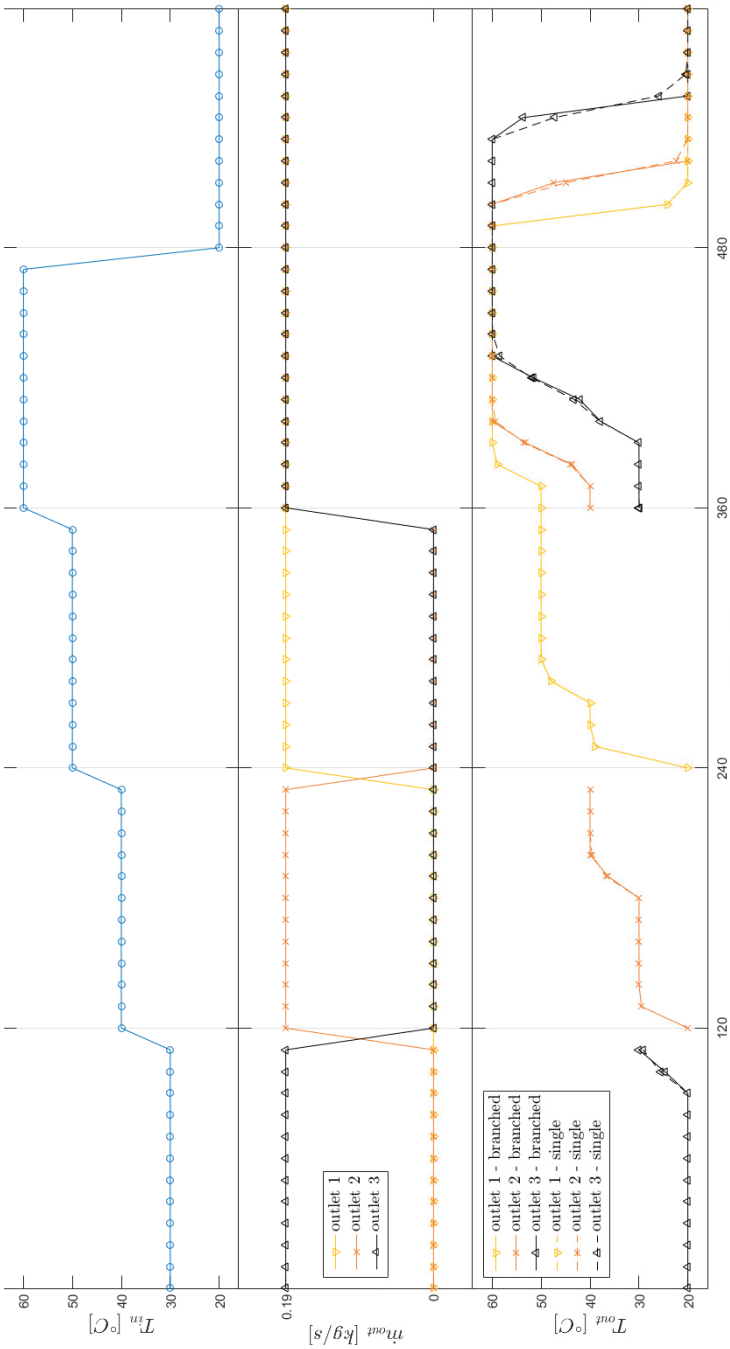

Figure 3: Simulation results of the branched pipe approach ('branched') and comparison with the conventional method ('single'). The two upper plots are the inputs that were applied: the temperature of the ingoing water T_{in} and the outgoing mass flow rates at the different outlets $\dot{m}_{out}$. The lower plot shows the transport delay for both the branched pipe approach (solid lines) and the conventional approach (dashed lines). This delay is clearly larger for an outlet further away from the inlet (e.g. outlet 3). While the two methods give similar results, the branched-pipe method can reflect sudden changes in inlet temperature even better, as explained in the text of this paper. The complete network is initially at a temperature of 20°C. Each symbol represents the data for a complete time-step (i.e. the simulations are discretised in time). Hence, lines represent only connections between values and not data itself.

After that, the temperature of the outlet is, obviously, exactly $60°C$, at least up to the point at which the water of $20°C$ reaches the third outlet. This is after 7 time-steps after the ingoing temperature switches to $20°C$. Indeed, the volume of the fictitious pipe between inlet and outlet 3 is - at a moment on which all outlets have the same flow rate - (6/3+6/2+6+2)=13 litre. In 70 seconds (=7 time-steps), $(70 * 0.19 =) 13.3$ litre is flushed through that fictitious pipe. This mean that at 540 seconds, still $(1.9 - (13.3 - 13)) = 1.6$ litre of water at $60°C$ outlet 3 leaves. This corresponds to a mean temperature of $(1.6 * 60 + 0.3 * 20)/1.9 =) 53.68°C$.

While these particular examples are meant to help the reader interpret the figure, all outgoing temperatures were checked for all data of the branched pipe method, showing the reliability of the proposed method. The conventional method, on the contrary, deviates for some data points from the outgoing temperatures as would be expected (and hence also from the branched pipe method): in the lower part of Figure 3, the dashed lines do not follow the solid lines exactly. The reason for that is because each pipe segment passes a uniform outgoing temperature (equal to the mean) to the next pipe segment. This can smooth the temperature variations. Indeed, a sudden changing temperature front at the inlet will go e.g. through three pipe segments before it flows through outlet 3. Hence, it can be concluded that the suggested method has, advantage over the conventional method, as the data is not smoothed between subsequent pipe segments but at the outlets only.

However, the main scope of the proposed approach was to facilitate scripting. It was experienced by the authors of this paper that this goal was reached: the difference in number of code lines between the two approaches to be written decreases proportional with the number of outlets. The scripting was therefore speeded-up and the probability of scripting errors was substantially decreased.

6 CONCLUSION

In this paper, a new method to model the transport delay in branched pipes has been proposed. The main idea is to split a branched pipe with n branches into n fictitious pipes from inlet to all outlets. This is in contrast with the conventional simulation method in which each pipe segment is treated as a separate pipe.

The main advantage of the proposed approach is elaborated on in this paper: it facilitates the scripting process in script-based simulation programs. Indeed, the duration of scripting of large pipe networks and the corresponding probability on scripting errors was substantially improved. On top of that, another advantage was found: changes in inlet temperature propagate through the network without being smoothed by each pipe segment, as is the case for the conventional method.

The new approach has been developed in Matlab as an algorithmic code, rather than a set of acausal equations. This means that it can be implemented in other simulation software, both with and without equation solvers.

ACKNOWLEDGMENT

We would like to express our gratitude to the partners of *INSTAL2020* (www.instal2020.be), a project sponsored by the Flemish government (www.vlaio.be), for their collaboration.

NOMENCLATURE

Parameters

n	number of outlets of the branched pipe
$\boldsymbol{p_k}$	matrix defining the order of pipe segments between inlet and outlet k, corresponding to $\boldsymbol{V_t}$ and **UA**
UA	matrix containing the overall heat transfer coefficients of the pipe walls of all the pipe segments of the branched pipe
$\boldsymbol{V_t}$	matrix containing the total volumes of all the pipe segments of the branched pipe

Variables

$n_{plug}(t)$	number of plugs in a single pipe
t	time (s)
$\boldsymbol{T}_{i,j}(t)$	vector containing the uniform temperatures of all plugs in pipe segment (i, j)
$\boldsymbol{T}_{bp}(t)$	3D tensor containing the uniform temperatures of all plugs in the branched pipe
$\boldsymbol{V}_{i,j}(t)$	vector containing the volumes of all plugs in pipe segment (i, j)
$\boldsymbol{V}_{bp}(t)$	3D tensor containing the volumes of all plugs of the branched pipe

REFERENCES

Berardi, U. (2016). A cross-country comparison of the building energy consumptions and their trends. *Resources, Conservation and Recycling*, *123*, 230–241.

Cholewa, T., & Siuta-Olcha, A. (2010). Experimental investigations of a decentralized system for heating and hot water generation in a residential building. *Energy and Buildings*, *42*(2), 183–188.

Cholewa, T., Siuta-Olcha, A., & Skwarczyński, M. A. (2011). Experimental evaluation of three heating systems commonly used in the residential sector. *Energy and Buildings*, *43*(9), 2140–2144.

De Pauw, M., Van Riet, F., De Schutter, J., Binnemans, S., Van Der Veken, J., & Verhaert, I. (2018). A methogology to compare collective heating systems with individual heating systems in buildings. In *Proceedings of the rehva annual meeting conference: Low carbon technologies in hvac (www.rehvam2018atic.eu)* (pp. 1–8).

Duquette, J., Rowe, A., & Wild, P. (2016). Thermal performance of a steady state physical pipe model for simulating district heating grids with variable flow. *Applied Energy*, *178*, 383–393.

Van Riet, F., El Khaoui, H., Hulsbosch, F., Steenackers, G., & Verhaert, I. (2016). Exploring the novel software Hysopt: a comparison of hydronic heat distribution systems of an apartment building. In *Clima 2016 - proceedings of the 12th rehva world congress.*

NINTH SESSION

ENERGY STORAGE IN BUILDINGS

Thermodynamic simulation of quasi-isothermal air compression/expansion for energy storage

Ghady DIB[12*], Philippe HABERSCHILL[1], Romuald RULLIERE[1], Rémi REVELLIN[1], Simon DAVIES[2]

[(1)]Univ Lyon, CNRS, INSA-Lyon, Université Claude Bernard Lyon 1, CETHIL UMR5008 Villeurbanne, 69621 France
[(2)]AIA Life Designers - AIA environnement
20, rue Lortet – 69007 Lyon, France
[*](Ghady Dib: ghady.dib@insa-lyon.fr)

ABSTRACT

In the context of developing renewable energies, storing energy improves energy efficiency and promotes the insertion of intermittent renewable energies. It consists of accumulating energy for later use in a place that may be the same or different from the place of production. Converting electrical energy to high-pressure air seems a promising solution in the energy storage field: it is characterized by a high reliability, low environmental impact and a remarkable energy density. This article carries out a numerical model based on thermodynamic and energy analysis of two technologies for quasi-isothermal air compression: liquid piston (with integrated heat exchanger) and mechanical piston (with water injection). High isothermal efficiency was scored with liquid piston air compressor compared to mechanical piston air compressor. A second numerical model based on thermodynamic analysis is presented in order to study the air expansion by the liquid piston technology. Heat transfer coefficient has a big impact on air temperature and system efficiency during the air compression/expansion modes. Currently, a global storage model for building applications is under development. This model propose multiple scenarios for electrical, heat and cold energy management based on energy production (RE, grid) and energy storage technology.

Keywords: Energy storage, quasi-isothermal, compression/expansion, numerical model

1. INTRODUCTION

While the world energy demand is growing, the transition from fossil resources to clean, durable and renewable resources is essential. Renewable resources intermittency presents a major obstacle and challenge to their extensive penetration into the grid. The energy storage technology can be a solution for stabilizing the fluctuating energy production and so the energy demand. This energy balance is achieved by allowing excess energy production to be saved for periods of higher customer demand.

These days high electricity demand is answered through the import of electricity, the use of gas/fuel power and hydraulic storage (STEP) plants. The deployment of other storage systems would lower the cost of imported electricity and significantly reduce the CO2

emissions generated by the use of thermal power plants and the dependence on fossil resources. The compressed air energy storage system (CAES) is one of the most promising technologies of the field of smart grid and poly-generation in the near future. CAES presents several significant advantages due to its reliability, economic feasibility and low environmental impact (Venkataramani et al., 2016). Energy storage technologies have been the subject of research document published by “French Alternative Energies and Atomic Energy Commission” (CEA) where CAES technology presents between the lowest investment cost per power and energy unit (€/kW, €/kWh) compared to Li-ion batteries and STEP energy storage technology. (CEA, 2012).

Nowadays, only two power plants with compressed air storage systems operate in the world: Huntorf plant in Germany built in 1978 with a capacity of 290 MW, and the AEC plant at McIntosh, Alabama, in the United States with a capacity of 110 MW (Ter-Gazarian, 1994). Compressed air is stored in former salt cavities or coal mines. These plants (classical CAES system) use an external heat source to raise the air temperature before entering the turbine (Crotogino, 2001). Compressed air storage systems allow an electrical efficiency ranging from 40 to 70% depending on the heat management resulting from air compression. Thus, if the heat of compression is stored for reuse during compressed air expansion, the storage system is said adiabatic and its electrical efficiency can reach up to 70% according to INERIS (INERIS, 2016).

While large-scale (>50 MW) CAES systems depend on various geological factors (underground storage) that are difficult to control for air storage, micro-CAES systems (<1 MW) with specifically developed reservoirs may be more adaptable and effective solution in meeting the electricity, heat and cold needs. These systems allow storing potential energy, generating electrical energy and integrating a heating and cooling cycle. The quasi-isothermal micro-CAES system answers the problem of the heat releasing during the air compression and the cold during the air expansion in order to make the storage or the use of compressed air possible. In fact, it allows to reduce the compensated work during the air compression and to increase the work recovered during the air expansion. This system requires a continuous release of heat during the air compression and to reuse it to the compressed air during the expansion phase. Two important innovative technologies were developed in order to compress/expand air with a quasi-isothermal transformation and to produce heat and cold energy: mechanical piston with water injection developed by LighSail Energy (Crane et al., 2012) and liquid piston with integrated heat exchanger developed by Enairys (Lemofouet, 2006).

LightSail Energy proposed the water injection in the compression/expansion chamber in order to create an air-water direct contact heat exchanger. The mechanical piston used is connected to a crankshaft related to a motor. Also, they installed air-water separator after the chamber that allows to collect compressed air and heated water. The same method is applicable during expansion phase. LightSail Energy uses carbon fiber tanks to store compressed air (Crane et al., 2012).

The energy storage concept of the HyPES (Hydro-pneumatic energy storage) system is based on the thesis work of S. Lemofouet (Lemofouet, 2006). In this system, water is used as a "liquid piston" to compress the air by cooling it and expand the air by heating it simultaneously. For this, an exchanger (cylindrical tubes) is placed in the compression/expansion chamber to ensure an exchange surface between air and water. Reversible pump and electric motor are connected to the chamber to convert electrical energy into mechanical in order to let the water circulate in the tubes. In expansion mode, the motor

is used as a generator to recover the mechanical energy from the pump and convert it into electricity (Lemofouet et al., 2013).

This study focuses on the development of a numerical model that simulate three stages of air compression using the two quasi-isothermal storage technologies described above. Furthermore, the study focuses on the liquid piston air expansion technology.

2. CASE STUDY

In order to simulate air compression/expansion modes, a numerical code was developed in FORTRAN that presents iterative calculations based on the principles of energy and mass conservation and heat transfer equation (described below). Dichotomy method is used in this code where the air temperature at the end of the compression/expansion is taken as a convergence parameter (MIT, 2012). This outlet temperature is limited by the inlet and adiabatic air temperature.

The numerical model consists in modeling three air compression/expansion stages whose pressures are:

- Low pressure (LP): 1 bar ⇔ 6 bar
- Middle pressure (MP): 6 bar ⇔ 36 bar
- High pressure (HP): 36 bar ⇔ 216 bar

The calculated outputs and fixed inputs for the two fluids (air/water) that pass through the air compressor/expander are shown below in Table 1.

Table 1: Inputs/outputs for the two fluids (air/water) that pass through two air compressors: Mechanical piston (Me.Pi) and liquid piston (Li.Pi)

<table>
<tr><th></th><th colspan="3">INLET (fixed)</th><th colspan="3">OUTPUT (calculated)</th></tr>
<tr><td>Air</td><td colspan="3">Inlet/outlet pressure
(Me.Pi/Li.Pi)</td><td colspan="3">Outlet temperature
(Me.Pi/Li.Pi)</td></tr>
<tr><td>Water</td><td>Inlet temperature
(Me.Pi/Li.Pi)</td><td>Tube diameter
(Li.Pi)</td><td>Droplet radius
(Me.Pi)</td><td colspan="3">Outlet temperature
(Me.Pi/Li.Pi)</td></tr>
<tr><td>Other Parameters</td><td colspan="3">Heat transfer coefficient
(Me.Pi/Li.Pi)</td><td>Polytropic index
(Me.Pi/Li.Pi)</td><td>Technical work
(Me.Pi/Li.Pi)</td><td>Thermal power exchanged between air and water
(Me.Pi/Li.Pi)</td></tr>
</table>

In this article we focus on two cases:

- Liquid and mechanical piston compressors comparison (compression mode)
- Liquid piston air expander/compressor study (expansion/compression mode)

2.1 Liquid and mechanical piston compressors comparison (compression mode)

Two air compressor technologies are compared in this study: Liquid and mechanical air piston compressors. Air compression mode is shown in figure 1 below. Air aspiration and exhaust phases (Phase A→B and phase C→D) are considered isobaric and polytropic processes respectively in this study. The volume flow rate is set in order to compare the two air compression technologies.

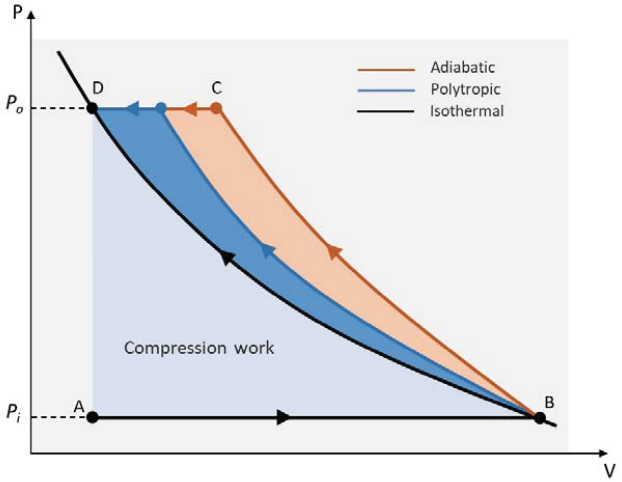

Figure 1: PV diagram of the air passing through the compressor (liquid and mechanical)

2.2 Liquid piston air expander/compressor study (expansion/compression mode)

In addition to the compression mode studied in the previous case, the expansion mode for the liquid piston technology is analyzed. Also, to note that in expansion mode, the air aspiration phase (A'→B') and exhaust phase (C'→D') are considered isobaric and polytropic processes (figure 2).

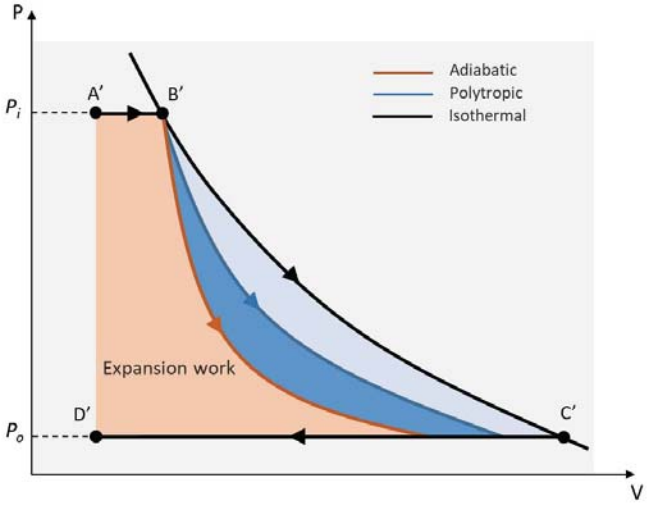

Figure 2: PV diagram of the air passing through the expander

3. THEORITICAL MODEL

The thermodynamic and heat transfer equations used for the two air compressors technologies (mechanical and liquid piston) during the air aspiration, compression and exhaust phases are developed in this section below. In addition the air expansion mode (aspiration, expansion and exhaust phases) for liquid piston technology is described in the next section.

Air intake and exhaust strokes for all compressors and expander are considered isobaric/polytropic processes.

3.1 Air compression by mechanical piston with water injection

3.1.1 Energy conservation

a) Energy conservation for moist air running through the compressor:

$$\dot{m}_{DA}(h_o - h_i) = \dot{m}_{DA}\frac{1}{\eta_p}\frac{k}{k-1}(P_o v_o - P_i v_i) - \dot{Q} + \alpha S\left(T_{wa} - T_{a,av}\right) + \dot{m}_{DA}\,(x_o - x_i)\,h_v \quad (1)$$

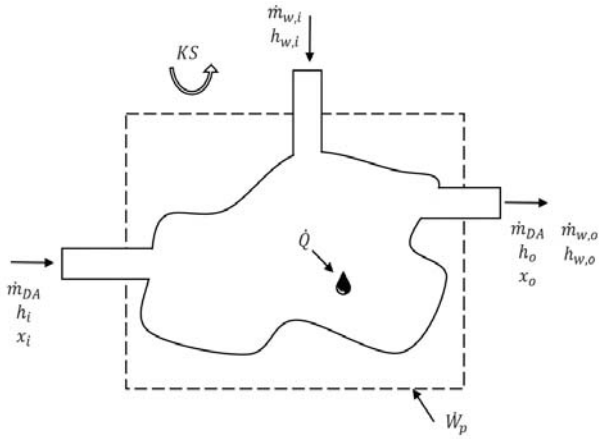

Figure 3: Conservation of energy for a steady-flow, open system

Absolute humidity x of the moist air is function of the temperature and of the air relative humidity at the compressor inlet. At the compressor outlet, considering the wet temperature equal to that of water:

$$x_o = d\frac{P_{w0}(T_{wo})}{P_o - P_{w0}(T_{wo})} \quad (2)$$

With $d = 0,62198$ *density of water vapor (relative to the air);*

$$ln(P_{w0}) = \frac{a_{-1}}{T} + a_0 + a_1 T + a_2 T^2 + a_l ln(T) \quad (3)$$

Where P_{w0} corresponds to the saturation vapor pressure of the water at temperature T. The a_i values are given in Table 2.

Table 2: Coefficient of correlation for the calculation of the saturation vapor pressure of water (Cretinon, 2004)

a_{-1}/(K)	a_0	$a_1/(K^{-1})$	$a_2/(K^{-2})$	a_l
−6 096,938 5	21,240 964 2	$-2{,}711\ 193\ 10^{-2}$	$1{,}673\ 952\ 10^{-2}$	2,433 502

b) Water injected energy conservation:

$$\dot{m}_{w,o}h_{w,o} - \dot{m}_{w,i}h_{w,i} = \dot{Q} - \dot{m}_{DA}\,(x_o - x_i)\,(h_v) \tag{4}$$

3.1.2 Mass conservation

Water injected mass conservation:

$$\dot{m}_{w,i} = \rho_w\,\dot{n}'\,\frac{4}{3}\pi\,r_i'^{\,3} = \dot{m}_{DA}\,(x_i - x_o) + \dot{m}_{w,o} \tag{5}$$

3.1.3 Complementary equations

The heat transfer exchanged between water and air is given by:

$$\dot{Q} = \alpha_w 4\,\pi\,r_{av}'^{\,2}\,n'\left(T_{a,av} - T_{w,av}\right) \tag{6}$$

And α_w calculated according to Ranz-Marshall (Laminar phase) (Qin et al., 2016):

$$Nu = 2 + 0.6Re^{\frac{1}{2}}Pr^{\frac{1}{2}} \tag{7}$$

Furthermore:

$$n' = \dot{n}'\,\mathrm{t_{st}} \tag{8}$$

It is also necessary to write the energy conservation for the compressor wall (wall conduction neglected due the assumption of low wall thermal resistance with respect to the thermal resistance between the ambient air and the outer wall of the compressor):

$$0 = -\alpha\,\mathrm{S}\left(\mathrm{T}_{wa} - \mathrm{T}_{a,av}\right) + \alpha_{ext}\,\mathrm{S}_{ext}\,(T_\infty - T_{wa}) \tag{9}$$

With $\alpha_{ext}\,\mathrm{S}_{ext}$ external conductance of the machine and T_∞ external temperature;

This equation makes it possible to replace in the equation (1) the energy losses by:

$$\dot{Q}_{ext} = \alpha\,\mathrm{S}\left(\mathrm{T}_{wa} - \mathrm{T}_{a,av}\right) = KS\left(\mathrm{T}_\infty - \mathrm{T}_{a,av}\right) \tag{10}$$

With KS global conductance: $KS = [1/(\alpha S) + 1/(\alpha_{ext}\,\mathrm{S}_{ext})]^{-1}$. Equation (1) becomes

$$\dot{\mathrm{m}}_{\mathrm{AS}}(\mathrm{h}_o - \mathrm{h}_\mathrm{i}) = \dot{W}_p - \dot{\mathrm{Q}} + \dot{\mathrm{m}}_{\mathrm{DA}}\,(x_i - x_o)\,\mathrm{h_v} + \dot{Q}_{ext} \tag{11}$$

The dry air flow sucked by the compressor is deduced from the volumetric efficiency by:

$$\dot{m}_{DA} = \frac{\dot{V}_c}{v_i}\,\eta_{v\prime} \tag{12}$$

With $\dot{V}_c$ the volume flow generated ($\frac{Volume\ of\ air\ sucked}{Cycle\ time}$).

3.2 Air compression by liquid piston with integrated heat exchanger

3.2.1 Energy conservation

a) The total energy conservation equation for the studied system "air" is :

$$\dot{m}_{DA}(h_o - h_i) = \dot{W}_t - \dot{Q} \tag{13}$$

- The energy equation written for the air aspiration phase (A→B, figure 1) is:

$$\frac{dU}{dt} = \dot{m}_{DA}h_e + \dot{Q} - P\frac{dV}{dt} \tag{14}$$

From equation (14) we developed an analytical expression in order to calculate the air temperature at state B (end of air aspiration phase):

$$\dot{m}c_p\, t\, \frac{dT}{dt} + \left(\dot{m}c_p + h\, S(t)\right)T(t) = \dot{m}c_p T_{a,i} + hS(t)T_w \tag{15}$$

With the exchange surface “S” is:

$$S(t) = \frac{4}{D}V_B = \frac{4}{D}\frac{\pi D^2}{4}L(t)n = \pi\, D\, n\, a\, t$$

Equation 15 becomes:

$$\dot{m}c_p\, t\, \frac{dT}{dt} + \left(\dot{m}c_p + h\,\pi\, D\, a\, n\, t\,\right)T(t) = \dot{m}c_p T_{a,i} + h\,\pi\, D\, n\, a\, t\, T_w \tag{16}$$

Equation (16) can be simplified to:

$$\frac{\tau\, t}{\tau + t}\frac{dT}{dt} + T = \frac{\tau\, T_{a,i}}{\tau + t} + \frac{t\, T_w}{\tau + t} \tag{17}$$

With $NTU = \frac{\dot{m}\, c_p}{a\, n\, h\, D\pi}$;

Using the average air flow we demonstrate that: $= \frac{t_c}{NTU}$;

With the transfer unit number equals to: $= \frac{hn\pi DL_0}{\dot{m}_{av}\, c_p}$;

The air temperature (at the end of air aspiration phase) solution is written:

$$T = T_w + \frac{\tau}{t}\left(T_{a,i} - T_w\right)\left(1 - e^{-t/\tau}\right) \tag{18}$$

By considering that the air aspiration time is equal to half the air compression cycle time (Enairys Powertech, 2012), the air temperature at states B is found to be:

$$T_B = T_w + \frac{\tau}{\frac{t_c}{2}}\left(T_{a,i} - T_w\right)\left(1 - e^{-\frac{t_c}{2}/\tau}\right) \tag{19}$$

- The energy equation written for the air exhaust phase (C→D) is:

$$\frac{dH}{dt} = \dot{m}h + hS(t)\left(T_{w,i} - T\right) \tag{20}$$

$$M\frac{dh}{dt} + h\frac{dM}{dt} = h\frac{dM}{dt} + hS(t)(T_{w,i} - T) \tag{21}$$

$$M\frac{dh}{dt} = hS(t)(T_{w,i} - T) \tag{22}$$

$$Mc_p\frac{dT}{dt} = hS(t)(T_{w,i} - T) \tag{23}$$

From equation (23), the air temperature at states D (end of air exhaust phase) is found to be:

$$T_{\mathrm{D}} = T_{w,i} + (T_{\mathrm{C}} - T_{w,i})\, e^{-NTU\left(\frac{1}{2}-\frac{t_C}{tcy}\right)} \tag{24}$$

- The total work is defined by (figure 1):

$$W_{tot} = (W_{asp} + W_{comp} + W_{ex})\frac{1}{\eta_p\, t_c} \tag{25}$$

With:

$$W_{asp} = -P_i V_B \tag{26}$$

$$W_{comp} = \frac{1}{k-1}(P_o V_C - P_i V_B) \tag{27}$$

$$W_{exh} = P_o V_C \tag{28}$$

b) The water energy balance is then given by:

$$\dot{m}_w\left(h_{w,o} - h_{w,i}\right)t_c = W_{tot} + Q_{A\to B} + Q_{\mathrm{B}\to\mathrm{C}} + Q_{\mathrm{C}\to\mathrm{D}} \tag{29}$$

To calculate the outlet water temperature it is necessary to express its enthalpy as a function of its pressure and its temperature, by separating the internal energy from the mechanical content of the enthalpy (neglecting the kinetic and gravitational energies):

$$h_w = C_w T + \frac{P}{\rho_w} \tag{30}$$

To simplify the problem, the transfer of mechanical energy is supposed to be isothermal; In this case the water outlet temperature is given by the following expression:

$$T_{w,o} = T_{w,i} + \frac{\dot{Q}}{c_w \dot{m}_w} \tag{31}$$

3.2.2 Mass conservation

a) Air mass conservation:

The flow of dry air sucked during a cycle is given by:

$$\dot{m}_{DA} = \frac{V_B\, \rho_a\, \eta_{v\prime}}{t_c} \tag{32}$$

The displacement volume in all the compression chambers is given by:

$$V_B = n\,\frac{\pi\, D^2}{4} L \tag{33}$$

b) Water mass conservation:

$$\dot{m}_{w,i} = \dot{m}_{w,o} = \frac{V_B\, \rho_w}{t_c} \tag{34}$$

$$\dot{m}_{w,i} t_c = V_{\mathrm{B}}\, \rho_i \tag{35}$$

3.2.3 Complementary equations

The heat transfer exchanged between water and air is given by:

$$\dot{Q}_{\text{tot}} = \dot{Q}_{asp} + \dot{Q}_{comp} + \dot{Q}_{exh} \tag{36}$$

With:

$$\dot{Q}_{asp} = \dot{m}_{DA}\, c_p\, (T_{\text{B}} - T_A) \tag{37}$$

$$\dot{Q}_{comp} = \text{h}\left(\frac{V_B + V_C}{0{,}5\, D}\right)\left(T_{w,i} - \left(\frac{T_{\text{C}} + T_{\text{B}}}{2}\right)\right) \tag{38}$$

$$\dot{Q}_{exh} = \dot{m}_{DA}\, c_p\, (T_{\text{D}} - T_{\text{C}}) \tag{39}$$

And h is calculated from the correlation developed for a laminar flow in a tube ($Nu = \frac{hD}{k} = 4.36$).

3.3 Air expansion by liquid piston with integrated heat exchanger

The expansion mode is similar to the compression mode developed in the previous section. The mass conservation and the complementary equations are the same used for the compression mode. Equation (14) is also applicable for the air aspiration phase (A'→B'). Equation (18) is solved in this case and the air temperature at state B' (end of air aspiration phase) is:

$$T_{B\prime} = T_{w,o} + \frac{\tau}{t}\left(T_{a,i} - T_{w,o}\right)\left(1 - e^{-t/\tau}\right) \tag{40}$$

The air exhaust phase is also similar to that developed for the compression mode. Equation (23) is solved to calculate the air temperature at state D' (end of air exhaust phase):

$$T_{\text{D}\prime} = T_{w,i} + (T_{\text{C}} - T_{w,i})\, e^{\frac{-NTU}{2}} \tag{41}$$

4. RESULTS AND DISCUSSION

4.1 Liquid and mechanical piston compressors comparison (compression mode)

4.1.1 Influence of convective heat transfer coefficient on air/water temperature

The influence of the heat transfer variation during the air compression is analyzed for the two technolo since the compression is almost isothermal when the heat transfer coefficient is high.

The heat transfer coefficient between 5 and 40 W.m^2.K^{-1} has a strong influence on the air temperature (at the end of the compression phase: T_C) for the second and third stages of the liquid piston compressor. Regarding the mechanical piston compressor, the air temperatures with a low heat transfer coefficient show similar values for the three stages. The higher the heat transfer coefficient in the mechanical piston compressor, the more the difference between the temperatures remains constant.

The main conclusion is that the heat transfer coefficient has a strong influence on the results. In addition, liquid piston compression provides a process closer to the isothermal than mechanical piston compression with water injection. These results show a good agreement between the numerical results and the data given by Enairys Powertech (Enairys Powertech, 2012).

To note that in the case of the liquid piston compressor, the air temperature at state B (end of the air aspiration phase) is slightly increased due to the contact with warm water that is exiting the compressor but remains close the inlet air temperature (20 °C) for all the stages. Also the air temperature at state D (end of the air exhaust phase) is equal to 20 °C for the all the stages and heat transfer coefficient variation and this due to the contact of the air with fresh water pumped into the liquid air compressor at 20 °C. The time cycle fixed for liquid piston compression phase is equal to 20 s (Enairys Powertech, 2012).

It is important to note that these compressor/expander proposed by LightSail Energy and Enairys are not well described in the literature (geometry, dimensions, air/water exchange surface, droplet radius). For this reason, the heat transfer coefficient range used in this study are magnitudes with respect to future accurate system sizing.

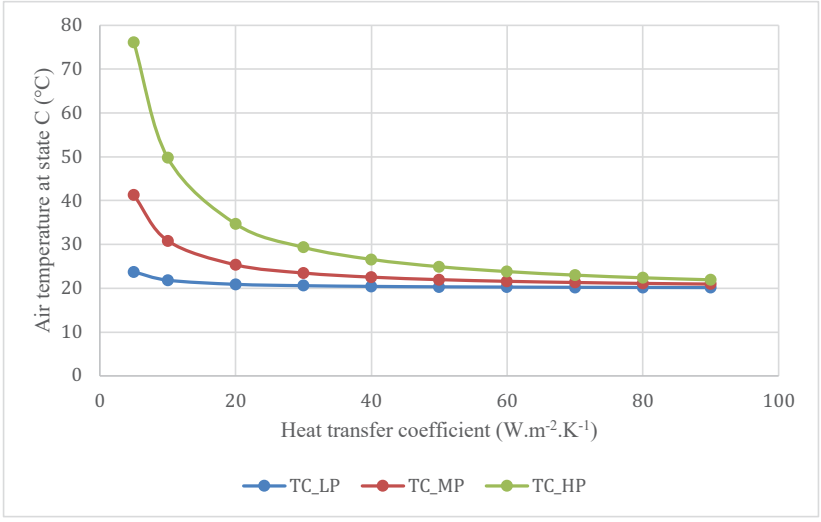

Figure 4: Air temperature at thermodynamic state C (figure 1) for three air compression stages according to heat transfer coefficient (liquid piston)

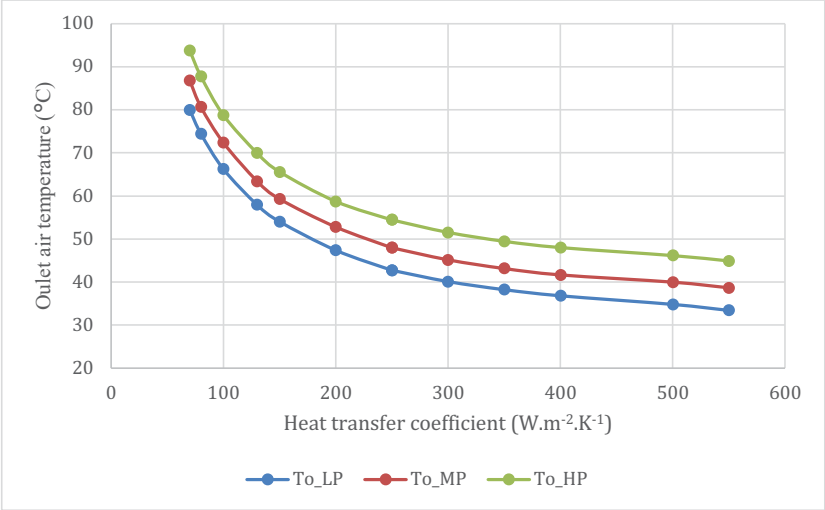

Figure 5: Outlet air temperature for the three air compression stages according to heat transfer coefficient (mechanical piston)

It should be noted that for the case of the liquid piston compressor, water is introduced into each stage at the same inlet temperature (20 °C). Whereas for the mechanical piston, the compression stages are cooled in series. For the liquid piston, the water volume flow rate correspond to the volume swept by each stage. This flow is important and imposed by the system and the difference in water temperature is low. In contrast, the series cooling of the air compressors allows a high rise in the water temperature. The flow rate is adjustable to a certain extent and could be used to regulate the air temperature.

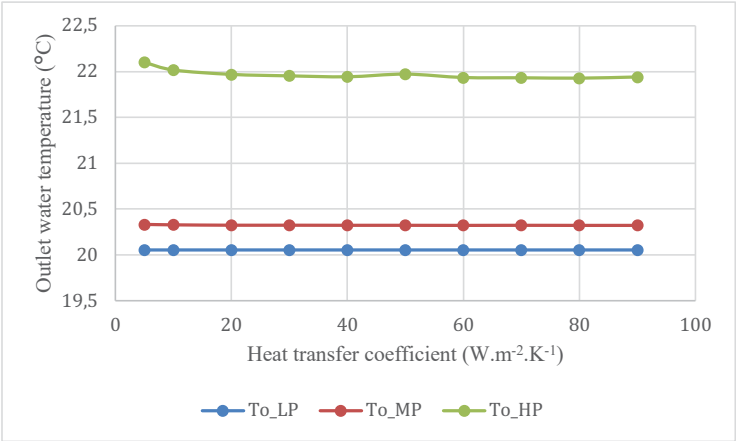

Figure 6: Outlet water temperature for the three air compression stages according to heat transfer coefficient (liquid piston)

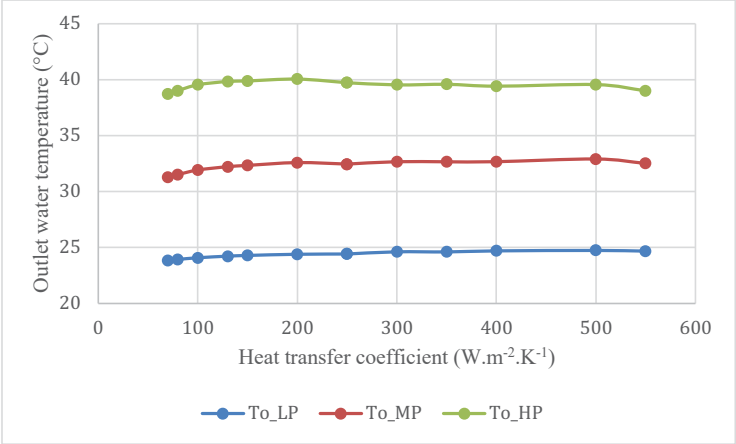

Figure 7: Outlet water temperature for the three air compression stages according to heat transfer coefficient (mechanical piston)

4.1.2 Influence of convective heat transfer coefficient on isothermal efficiency

Isothermal efficiency is defined as follows:

$$\eta_{isot} = \frac{W_{isot}}{W_{comp}} = \frac{r\ T\ ln\ (\frac{P_o}{P_i})}{W_{comp}} \tag{42}$$

Figure 8 shows the isothermal efficiency for both air compression technologies (mechanical piston and liquid piston). For both technologies, increasing heat transfer coefficient helps to increase the heat transfer and therefore the compression process will be closer to isothermal process which yield to decreasing in the compression work (figure 1). It is clear that the liquid piston has a better isothermal efficiency on the total heat coefficient range. Also, it should be noted that the higher heat transfer coefficient the better isothermal efficiency for both technologies.

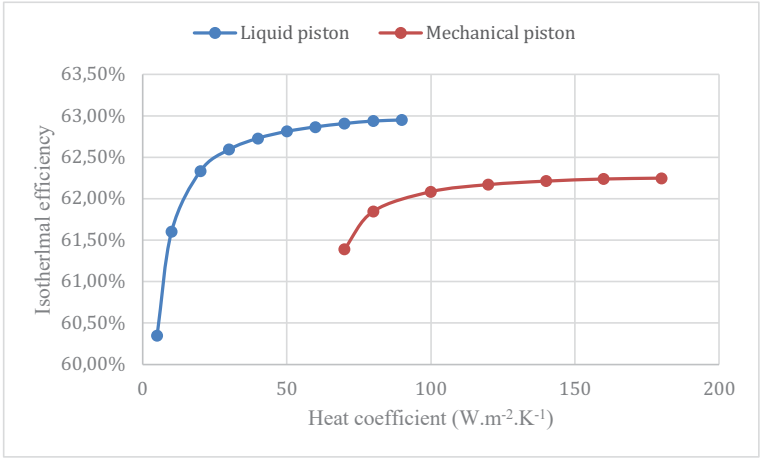

Figure 8: Isothermal efficiency according to heat transfer coefficient (liquid and mechanical piston compressor)

4.2 Liquid piston air expander/compressor study (expansion/compression mode)

4.2.1 Influence of convective heat transfer coefficient on air/water outlet temperature during expansion mode

The influence of the heat transfer variation during the air expansion is analyzed for the liquid piston technology. Figures 9 and 10 show the variation of the water temperature at different thermodynamic states of expansion stages (HP, MP and LP).

Air is introduced at 20°C in the expander chamber (state A') for the high pressure stage. Air temperature at state B' (end of air aspiration phase) is slightly increased due to the contact with

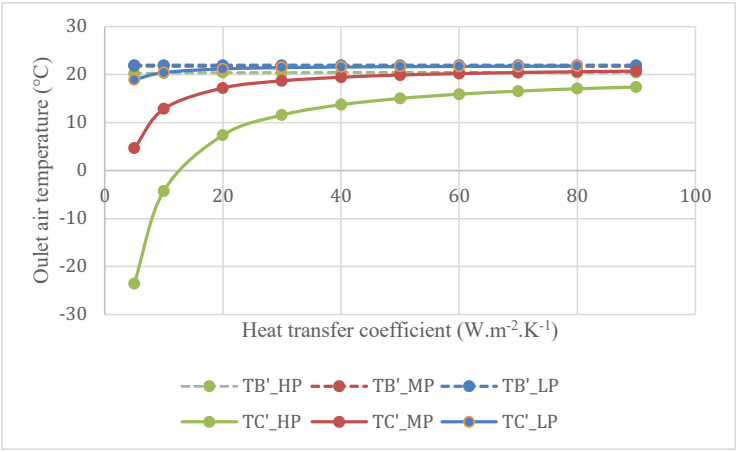

Figure 9: Air temperature at states B' (end of air aspiration phase) and C' (end of air expansion phase) for the three air expansion stages according to heat transfer coefficient

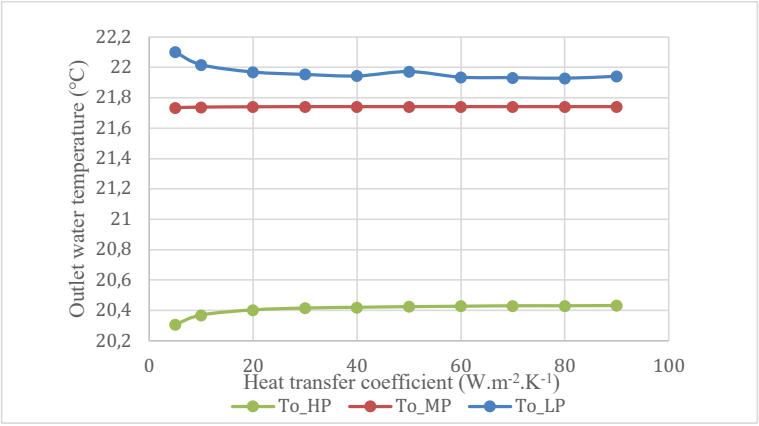

Figure 10: Outlet water temperature for the three air expansion stages according to heat transfer coefficient

warm air that is exiting the expander. In fact water is pumped at 22°C and exiting the expander around 21°C. The heat transfer coefficient has a big impact on the air temperature at state C (end of the expansion phase). As the heat transfer coefficient increases, the air temperature after the expansion process also increases (figure 9). It can be noticed that the high pressure stage has the lowest air temperature after air expanding process. The air is exiting the expander at all stages at 22°C because of the contact with the pumped water.

The outlet water temperature is shown in the figure 10. Water is pumped at 22 °C at each air expansion stage. It can be noticed that the heat transfer coefficient does not have a big impact on the water temperature. The water exists the high pressure stage at the lowest temperature whereas the lower pressure stage scores the highest outlet water temperature.

4.2.2 Influence of convective heat transfer coefficient on power (compression/expansion mode)

The power consumed during air compression phase and recovered during air expansion phase is shown in the figure 11. After 40 $W.m^2.K^{-1}$, the heat transfer coefficient has a lower

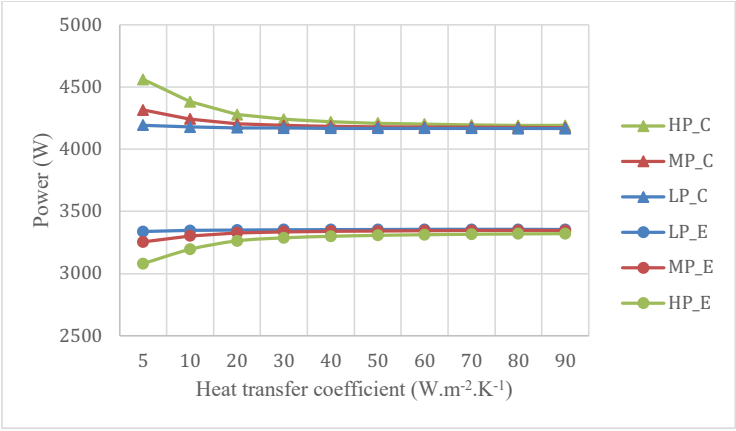

Figure 11: Power consumed and recovered for the three air compression/expansion stages according to heat transfer coefficient

influence on consumed and recovered power for the three compression/expansion stages. It is noticed that, for a range between 5 and 40 $W.m^2.K^{-1}$, the lower pressure stage consumed the less compression power while the high pressure stage scored the most important compression power. Also for the same range of heat transfer coefficient, the most recovered power was noticed during the lower pressure stage.

4.2.3 Influence of convective heat transfer coefficient on system efficiency (compression/ expansion mode)

System efficiency is defined as follow:

$$System\ efficiency = \frac{Power_{expansion}}{Power_{compression}} \tag{43}$$

Figure 12 shows that the increasing of the heat transfer coefficient has a positive effect on the system by reaching an 80% efficiency (> 60 $W.m^2.K^{-1}$). Lower heat transfer coefficient have a big impact on the compression/expansion work (excluding mechanical losses).

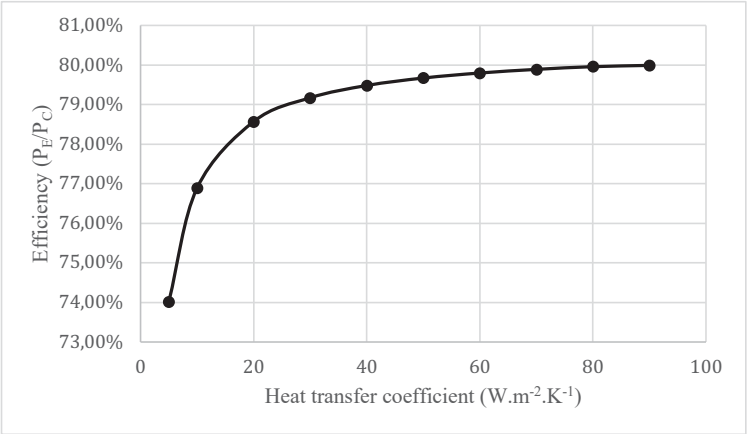

Figure 12: System efficiency according to heat transfer coefficient

5. GLOBAL STORAGE MODEL – BUILDING APPLICATION

The previous numerical models are integrated in a global storage model (Excel/VBA) where three interacting modules are developed (figure 13):

- AIR4POWER application module:

Numerical model that takes into account the different building typologies program and several geographical locations in order to specify the building energy needs (heat, cold, electricity).

- System module:

Dynamic calculation of various energy storage system: compressed air, hot and cold water. The different input data identified previously (storage volume, consumption and production of renewable energy) are used in this module to calculate the electric, heat and cooling energy storage. Many efficiencies required for these calculations are obtained from the numerical models presented in this article (electrical compression/expansion and heat/cold recovery during compression efficiencies.

In this section, different functions are proposed for the storage system:

• Self-consumption renewable energy produced
• Energy storage from the electric grid
• Sell stored energy to the electric grid
• Stored energy consumption

- Post processing module:

An overall energy and economic balance is established in this module. This assessment is based on hourly/monthly energy (autonomy, valued energy) and economic analyses (energy costs) for the three studied energies (electrical, heat and refrigeration). In addition, this module presents a life cycle analysis and economic interest over a determined period of operation.

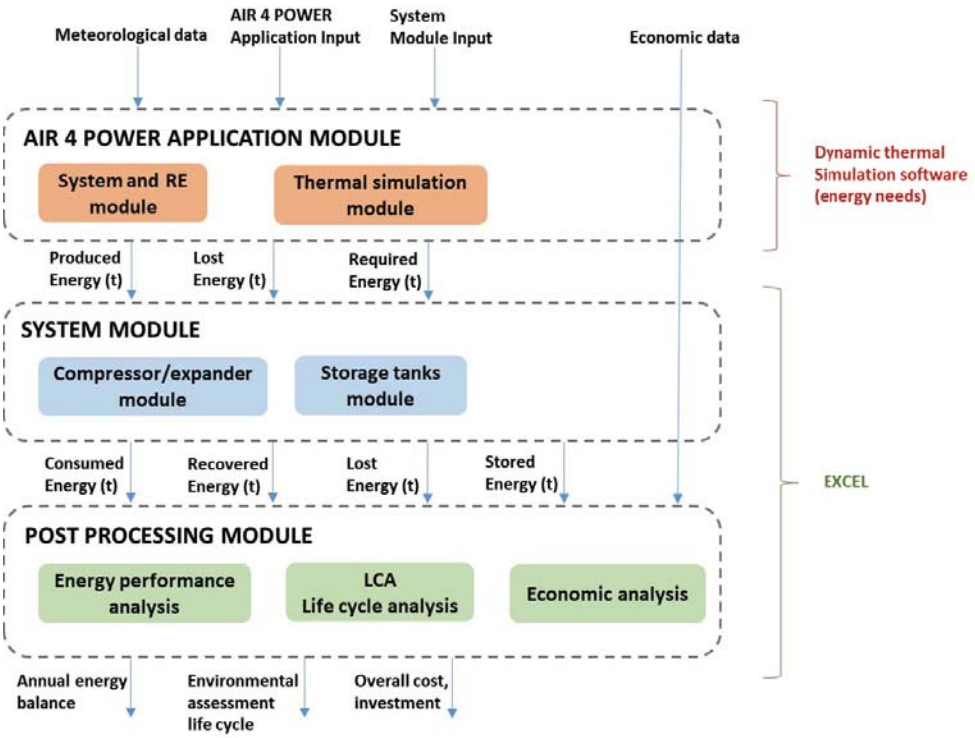

Figure 13: Diagram of the dynamic tool - global model

6. CONCLUSION

By representing the air and water temperature distributions for the two types of compressor, it can be deduced that the mechanical piston with water injection is more favorable to the production of heat (or cold in the case of expansion). In addition, it was noticed that the isothermal efficiency is higher in the liquid piston air compressor technology. We have been also able to highlight the strong and minor influences of the heat transfer coefficient on the air/water temperature and system efficiency (liquid piston air compression/expansion mode). The results obtained defend the quasi-isothermal compression/expansion hypothesis with the liquid piston air compressor/expander.

This study allowed us to compare two different air compression technologies and to understand the air compression/expansion mode with liquid piston technology. In addition, this work allowed us to obtain calculated system efficiencies that are essential for a global storage model. The next step is to study multiple scenarios for building applications (for different geographical locations):

- Self-consumption system
- Grid-connecting system (sale the extra produced/stored energy to the grid)

REFERENCES

CEA, 2012. *Le stockage stationnaire de l'énergie*, p. 41.

Crane, S., Fong, D., & Berlin, E., 2012. *US 8,247,915 B2.*

Cretinon, B., 2004. *Paramètres hygrométriques*. Techniques de l'Ingénieur. ref. R3047 v1.

Crotogino, F., 2001. *Le stockage d'air comprimé de HUNTORF : plus de 20 ans de succès dans l'exploitation*, p. 4.

Enairys Powertech., 2012. *Réalisation et caractérisation étendue d'un prototype de système de stockage hydropneumatique d'énergie*. École polytechnique fédérale de Lausanne, Lausanne.

INERIS, 2016. *Stockage souterrain de l'air comprimé dans le contexte de la transition énergétique*. (Rapport d'étude No. DRS-16-149645-00148A).

Lemofouet, S., 2006. *Investigation and optimization of hybrid electricity storage systems based on compressed air and supercapacitors* (PhD thesis). École polytechnique fédérale de Lausanne, Lausanne.

Lemofouet, S., & Rufer, A., 2013. *US 5 567 183 B2*.

MIT, 2012. *Introduction to numerical analysis*. Retrieved from https://ocw.mit.edu/courses/mathematics/18-330-introduction-to-numerical-analysis-spring-2012/lecture-notes/MIT18_330S12_Chapter4.pdf.

Qin, C., Loth, E., 2016. *Efficient Compressed Air Energy Storage through Spray-Cooling.* 9th International Conference on Multiphase Flow.

Ter-Gazarian, A., 1994. *Energy storage for power systems.*

Venkataramani, G., & Wang, J., 2016. *A review on compressed air energy storage – A path way for smart grid and polygeneration*. Renewable and Sustainable Energy Reviews, p.13.

NOMENCLATURE

a	air/water interface velocity, m/s
C	specific heat, $J.kg^{-1}.K^{-1}$
D	diameter, m
h	specific enthalpy, $J.kg^{-1}$
k	polytropic index
L	length, m
Li	liquid
M	air mass, kg
Me	mechanical
$\dot{m}$	mass flow, $kg.s^{-1}$
n	tube number
n'	water droplets number
Nu	Nusselt number
NTU	number of transfer units
Pi	piston
P	pressure, Pa
Pr	Prandtl number
$\dot{Q}$	heat transfer between water/air, $J.s^{-1}$
r	gas constant, J/kg.K
r'	droplet radius, m
Re	Reynolds number
S	exchange surface, m^2
T	temperature, K
t	time, s
U	internal energy, J
v	specific volume, $m^3.kg^{-1}$
V	volume, m^3
W	work, J

x absolute humidity

Greek letters

α heat transfer coefficient, $W.m^{-2}.K^{-1}$
ρ density, $kg.m^{-3}$
η efficiency
τ characteristic time

Subscripts

0 saturated vapor
a air
asp aspiration
av average
c cycle
comp compression
DA dry air
ex exhaust
i *inlet*
isot *isothermal*
o outlet
p polytropic
st stay
t technical
tu tubes
v vapor
v' volumetric
w water
wa wal

Question and Answers:

What is the round trip effinciency?

Ghady Dib:

The roundtrip efficiency is around 60%.

Development and Evaluation of a Generalized Rule-Based Heuristic Control Strategy for Ice Storage Systems in Residential Buildings

A. Tam, D. Ziviani*, J. E. Braun, N. Jain

Ray W. Herrick Laboratories, School of Mechanical Engineering, Purdue University,
177 S. Russell Street, West Lafayette, IN 47907-2099, USA

ABSTRACT

In recent years, variable electricity pricing has become available to residential consumers to incentivize demand reductions during traditional midday peak hours. This is especially important in hot climates where the use of air-conditioning (A/C) equipment is the primary cause for peak electricity demand. Thermal energy storage (TES) systems enable consumers to store cooling energy when demand is low and assist the operation of the A/C during peak demand periods. However, the cost savings achievable using integrated TES are highly dependent on how the system is operated for a given utility rate structure. Therefore, this paper investigates control strategies for a packaged A/C unit integrated with ice storage that leverage available residential utility rate structures in the U.S. to reduce electricity cost to the consumer. In particular, the present work describes the development and evaluation of a rule-based heuristic control strategy. The evaluation is performed in comparison to a minimum cost benchmark. The rule-based heuristic control strategy is designed based on a unique combination of different heuristic strategies for charging and discharging of TES that are typically applied to commercial-scale A/C systems with integrated TES. The benchmark optimal controller minimizes the monthly electricity cost considering both time-of-use energy and demand charges. The total electricity cost associated with each control strategy is determined using an hourly system simulation model that includes models for the cooling equipment, ice storage tank, and secondary loop components along with a relatively simple load model. The performance of the heuristic strategy is evaluated in relation to the benchmark for a range of equipment cooling capacities, TES sizes, geographic locations, and residential utility rates. The results show that the heuristic strategy works well with operating costs that are within 15% of those of the minimum cost benchmark but with orders of magnitude less computational requirement.

Keywords: Thermal energy storage, residential cooling systems, demand response, system control, operating cost minimization

1. INTRODUCTION

Thermal energy storage (TES) has been a popular option for reducing operating costs in commercial cooling systems; however, it is rarely considered in residential applications (Kung et al., 2013). One of the major factors is the structure of utility rates. Commercial utility rates typically have on-peak energy charges that incentivize off-peak energy use as well as demand charges that penalize high peak power consumption. By integrating TES with building chillers, cooling (e.g. in the form of ice) can be generated and stored during off-peak hours when electricity rates are low and then provide cooling to the building during on-peak

hours. Historically, residential utility rates have had a flat rate structure, so the inclusion of TES with residential cooling systems has not enabled significant operating cost savings. However, in recent years, variable rates have become more available to residential customers, thereby changing the potential for cost savings (NREL, 2018). Beyond operational cost savings, cooling systems with integrated TES also offer other benefits. High penetration of renewable electricity generation in California and other states is leading to utility incentives that promote systems with better demand responsiveness, which can be achieved with TES (NREL, 2018). The primary cooling equipment can also be downsized due to the additional cooling capacity provided by the TES, which provides an additional economic advantage for TES systems.

The system under consideration is a residential-scale cooling system with integrated ice storage that is depicted in Figure 1. It consists of a packaged chiller, a water-ethylene glycol secondary loop, and an internal melt ice-on-pipe storage tank. Points 1-4 in the dotted area represent the packaged chiller and points 5-8 represent the secondary loop. The secondary loop connects the outdoor packaged chiller to the ice storage tank and an indoor air handling unit. A three-way valve at point 6 is used to control the charging and discharging rate of the storage.

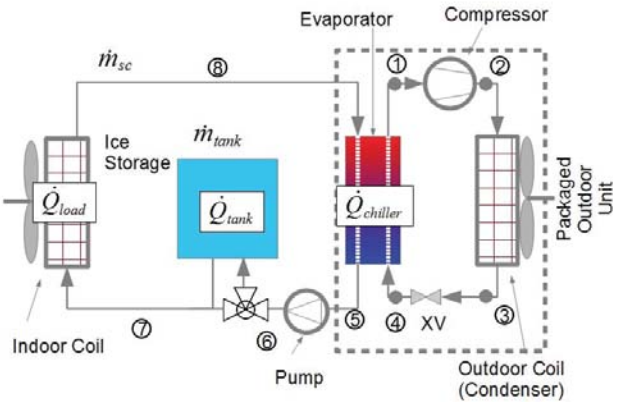

Figure 1. Schematic of the proposed cooling system with secondary loop and ice storage.

Many heuristic control strategies have been developed for managing charging and discharging of storage for TES systems applied to commercial buildings (Braun, 2007; Drees and Braun, 1996; Henze, 2003; Kung et al., 2013; Lo et al., 2016, p.; Sun et al., 2006). The simpler strategies prioritize use of either the chiller or the storage to meet cooling loads during on-peak periods. For chiller-priority control, the operating cost savings compared to no storage are primarily due to a reduction in on-peak demand and energy use that results from downsizing of the chiller through the use of storage. Strategies that tend to prioritize the use of storage generally have greater cost savings opportunities, but require load-forecasting to predict the amount of cooling needed during the peak hours. One of the most effective control strategies for TES in commercial buildings is a hybrid strategy that alternates between the chiller-priority and storage-priority strategies based on a set of rules and operating conditions (Drees and Braun, 1996). This strategy was developed and evaluated for commercial buildings but has never been evaluated for residential applications.

Two important differences between residential and commercial building applications that impact the performance of existing control strategies are the *schedule* and *intensity* of power consumption apart from heating, ventilation, and air conditioning (HVAC). Commercial

buildings have very high daytime occupant and non-HVAC related power density (lights, computers, and other plug loads) that mostly disappear outside of normal working hours. On the other hand, residential buildings have much lower overall occupant and non-HVAC power density that are more evenly distributed over time. For commercial buildings, the relatively low unoccupied non-HVAC power consumption means that high storage charging rates do not result in peak power demand occurring outside of occupied periods. However, applying existing control strategies that employ simple charging strategies to residential buildings can lead to high demand costs when there are anytime or off-peak residential demand charges. As variable utility rates become more available for residential buildings, there is a need for a control strategy for cooling systems with integrated TES that can minimize the total utility costs under *any* residential utility rate structure. In this study, we extend the rule-based control strategy of Drees and Braun (1996) to explicitly handle anytime and off-peak demand charges and evaluate its performance against an optimal controller for different geographic locations and utility rates.

In Section 3, we review existing heuristic control strategies and present sample residential utility rates acquired from a survey of available rates. The system model is described in Section 4. The generalized rule-based controller is presented in Section 5, and a benchmark optimal controller is presented in Section 6. We compare the different control strategies through a set of simulated case studies in Section 7 and summarize conclusions in Section 8.

2. BACKGROUND

2.1 Heuristic Control Strategies

The typical chiller-priority control strategy has two distinct operating modes: charging and discharging. The charging mode begins during the off-peak period when the building is unoccupied. The chiller then operates at full cooling capacity until the storage is fully charged. In discharging mode, the chiller is operated to meet the building cooling load. If the load exceeds the chiller capacity, then storage discharge occurs at a rate sufficient to meet the load. Although chiller-priority is far from optimal, it is simple to implement and doesn't require load forecasting. The primary operating cost savings are achieved by reductions in on-peak energy use and peak demand that occur for days with high cooling loads. These savings are possible in comparison to a conventional system because the chiller and storage are sized such that the chiller must operate nearly continuously at maximum capacity for the design day. This leads to significant downsizing in capacity relative to a conventional system.

Drees and Braun (1996) presented a rule-based controller that combines elements of chiller-priority and storage-priority strategies, along with a demand-limiting algorithm. The demand-limiting algorithm requires a measurement of the total building electrical use. A simpler version of this strategy that doesn't require the power measurement is described in the ASHRAE Handbook of HVAC Applications (2011) and is a starting point for the strategy presented in the current paper. The rule-based control strategy uses the chiller-priority charging strategy during the unoccupied period, but employs different discharging strategies during the occupied period depending on economic considerations. The strategy minimizes the use of storage (i.e., chiller-priority) if it would not be cost effective to replenish the discharged energy (e.g., off-peak utility rates) and if the current chiller load is less than a target load limit. Alternatively, if the use of storage would lower daily energy costs and there is sufficient storage to meet the remainder of the load for the occupied period without operating the chillers, then the chillers are turned off and the load is met by storage alone (full-storage control strategy). However, if there isn't sufficient storage to meet the remainder of the integrated loads over the discharge period then the control switches to a load-limiting

control strategy where the chiller operates at the minimum constant load necessary to fully discharge the storage over the discharge period. Finally, if the use of storage is not economical but the chiller load would be greater than a target limit, the chiller load is restricted to the maximum of this limit and the load-limiting value necessary to avoid premature storage discharge. The target load limit is reset to zero for each new billing period (i.e., month) and then reset over time as the maximum of the previous target and the current load. Compared to a simple chiller-priority control, the rule-based control requires forecasting of future loads but results in significantly greater savings opportunities.

2.2 Residential Utility Rates

Utility rate structures play a significant role in how cooling systems with integrated storage are controlled. We surveyed the different rate structures currently available to residential customers across the United States using a database (OpenEI.org) maintained by the National Renewable Energy Laboratory (NREL, 2018). Based on information from OpenEI.org, there were only 25 states that had some form of variable rates for residential buildings in 2012. This number has increased significantly in recent years, and variable rates are currently available in all 50 states, with more companies incorporating demand charges as well. All variable utility rates are optional for customers. We identified six different structures based on combinations of energy and demand charges:

1) flat energy only
2) flat energy with flat demand
3) flat energy with on-peak and off-peak demand
4) time-of-use (TOU) energy only
5) TOU energy with flat demand
6) TOU energy with on-peak and off-peak demand.

Note that demand charges are based on the highest average power over a 15-minute window throughout the month; this is an additional cost to the cost computed based on the total energy consumed. In this paper we specifically consider the TOU rates mentioned above. These rates vary the price of electricity based on the time of day, usually separating the day into on-peak, off-peak, and in some cases mid-peak periods. This structure encourages customers to shift their power consumption to off-peak periods when the price of electricity is lower. The main features of TOU pricing are the duration of the price periods and the difference in price between different periods.

3. SYSTEM MODEL

In this section we describe the models used for evaluating the performance of different control strategies in this study.

3.1 Ice Storage Model

An internal melt, ice-on-pipe storage model is derived for the secondary loop following the approach described by West and Braun (1999) in which the heat transfer effectiveness of the storage is used to calculate the limit on the rate of change of energy in the ice storage tank. The model only considers latent charging and discharging. The rate at which energy is removed from the storage tank is calculated by

$$\dot{Q}_{tank} = \varepsilon \dot{m}_{tank} c_f (T_s - T_{chw}), \quad (1)$$

where $\dot{Q}_{tank}$ is the storage charging (+) or discharging (-) rate (kW), ε is the heat transfer effectiveness (-), $\dot{m}_{tank}$ is the secondary fluid flow rate through the storage tank (kg/s), c_f is the secondary fluid specific heat (kJ/kg-ºC), T_s is the phase change temperature (ºC), and T_{chw} is the inlet temperature of the secondary fluid (ºC). The limit of the rate at which energy can be removed or added to the storage tank is reached when $\dot{m}_{tank}$ equals the total flow rate in the secondary loop. At each time step, the state of charge is calculated by

$$x_k = x_{k-1} + \frac{\dot{Q}_{tank}\Delta t}{L}, \tag{2}$$

where x_k is the state of charge (-), k is the time index, Δt is the time step (h), and L is the maximum change in internal energy that can occur during charge or discharge (kWh). The outlet temperature of the tank at time k is then calculated by

$$T_{f,o} = T_{chw} + \left(\frac{\dot{Q}_{tank}}{\dot{m}_{tank} c_f}\right). \tag{3}$$

West and Braun (1999) developed correlations between the state of charge and the heat transfer effectiveness by curve-fitting polynomial functions to test data of charging and discharging cycles, given by

$$\varepsilon_C = 0.92 - 0.62x + 4.93x^2 - 17.05x^3 + 24.02x^4 - 12.12x^5, \tag{4}$$

$$\varepsilon_D = 0.49 + 0.81x - 0.98x^2 + 0.67x^3. \tag{5}$$

The subscript C represents charging and D represents discharging. As shown in Figure 2, there is a significant decrease in heat transfer effectiveness as the storage tank reaches full charge due to a loss in surface area of the ice and water interface caused by the intersecting ice formations. Because of this decrease in heat transfer effectiveness, the ice storage tank is oversized in this study so that 80% of the TES can be used to meet design day loads. There is also a decrease in effectiveness in discharging mode as the TES is depleted, but the effect is smaller than for charging. Here we only consider the latent capacity of the storage tank, so a state of charge of 0 denotes a full tank of water at 0 °C, and a state of charge of 1 denotes a full tank of ice at 0 °C.

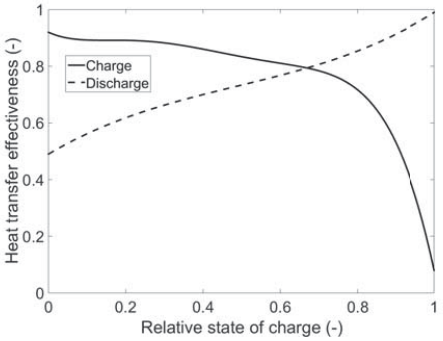

Figure 2. Ice storage charging and discharging heat transfer effectiveness curves.

3.2 Chiller Model

A residential-scale fixed-speed packaged chiller unit is modeled using the open-source ACHP (Air Conditioning/Heat Pump) tool (Bell, 2012). ACHP uses detailed mechanistic models and includes thermo-physical properties of working fluids from the CoolProp and REFPROP

libraries (Bell et al., 2014; Lemmon et al., 2018). ACHP calculates chiller performance and capacity at different operating conditions. A performance map for this packaged unit was developed using linear regression on the data generated from ACHP. The map determines the chiller's maximum capacity and coefficient of performance (COP) at any given ambient temperature and chilled water supply temperature as shown in Eqs. (6)-(7).

$$\frac{\dot{Q}_{max}}{\dot{Q}_{rated}} = 6.82 - (1.43\times10^{-2})T_{chw} + (5.38\times10^{-5})T_{chw}^2 - (3.61\times10^{-3})T_{amb} - (1.11\times10^{-5})T_{amb}^2 \quad (6)$$

$$\frac{COP_{actual}}{COP_{rated}} = 1.73 + (2.43\times10^{-2})T_{chw} - (7.01\times10^{-5})T_{chw}^2 - (2.01\times10^{-2})T_{amb} + (2.49\times10^{-5})T_{amb}^2 \quad (7)$$

The variable $\dot{Q}_{chiller,max}$ is the chiller maximum capacity (kW), $\dot{Q}_{rated}$ is the chiller rated capacity (kW), T_{chw} is the chilled water supply temperature (˚C), T_{amb} is the ambient temperature (˚C), COP_{actual} is the chiller's coefficient of performance at the specified operating conditions (-), and COP_{rated} is the chiller's rated coefficient of performance (-). The effect of chiller part-load conditions on the COP is neglected in this model. The map is normalized so that different chiller sizes and efficiencies can be easily modeled. The chiller model considered in this study is based on a rated capacity of 10.55 kW (3 tons) and a COP of 3 with a rating condition of 35 ºC (95 ºF) ambient temperature and 7 °C (45 ºF) chilled water supply temperature. Figure 3 shows cooling capacity and COP as a function of ambient and chilled water temperatures. As the chilled water supply temperature decreases, the system loses capacity and efficiency because of a lower evaporating temperature. Similarly, efficiency and capacity decrease with increasing ambient temperature due to a higher condenser temperature. There is an energy penalty for charging storage that must be considered when evaluating the performance of cooling systems integrated with TES.

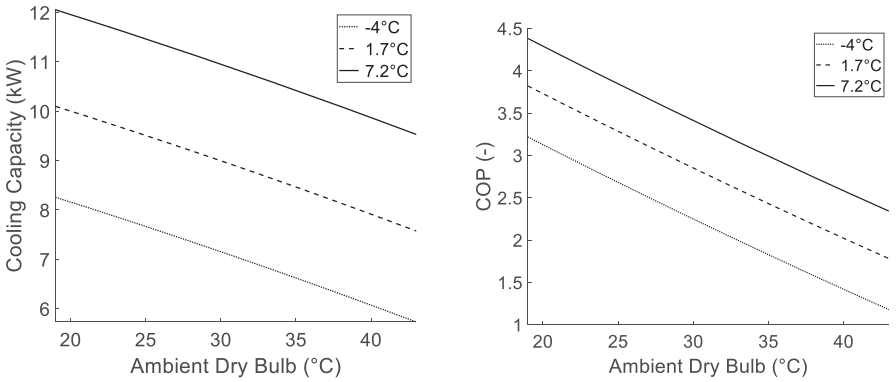

Figure 3. Capacity and COP of the modeled packaged A/C at different ambient conditions and chilled water supply temperatures.

3.3 Building Load Model

A simple conductance model with an internal gain was utilized to generate building load profiles based on ambient temperatures. Weather data for the typical meteorological year (TMY) was obtained from the data set TMY3 provided by the National Solar Radiation Data Base (Wilcox and Marion, 2008). Building load profiles were then calculated according to

$$\dot{Q}_{load} = UA_{house}(T_{amb} - T_{zone}) + \dot{g}, \tag{8}$$

where $\dot{Q}_{load}$ is the hourly cooling load (kW), UA_{house} is the heat transfer coefficient (kW/ ºC), T_{amb} is the ambient temperature (ºC), T_{zone} is the indoor temperature set-point (ºC), and $\dot{g}$ is the internal gain of the house (kW), which is assumed to be a constant 1 kW (Mitchell and Braun, 2013). UA_{house} is assumed to be constant and calculated by using a design point ($\dot{Q}_{load}$) of 10.55 kW (3 tons) at an ambient temperature (T_{amb}) of 35 ºC (95 ºF), indoor temperature set-point (T_{zone}) of 22 ºC (72 ºF), and internal gain ($\dot{g}$) of 1 kW.

3.4 Secondary Loop Model

The secondary loop employs a mixture of 70% water and 30% ethylene glycol by mass as the working fluid. Energy balances are applied to the indoor coil and chiller evaporator to relate the heat transfer rates to temperature changes across the secondary fluid according to

$$\dot{Q}_{load} = \dot{m}_{sc} c_f (T_{cc,out} - T_{cc,in}), \tag{9}$$

$$\dot{Q}_{chiller} = \dot{m}_{sc} c_f (T_{cc,out} - T_{chw}), \tag{10}$$

where $\dot{Q}_{load}$ is the hourly cooling load (kW), $\dot{Q}_{chiller}$ is the chiller cooling rate (kW), $\dot{m}_{sc}$ is the mass flow rate in the secondary loop (kg/s), $T_{cc,in}$ is the supply temperature to the indoor coil (ºC), and $T_{cc,out}$ is the return temperature from the indoor coil (ºC).

The storage charging (-) or discharging (+) rate, $\dot{Q}_{tank}$, is related to the load and chiller cooling rates using an overall energy balance on the secondary loop according to Eq. (11) . The storage charging and discharging rates are limited by the heat transfer effectiveness model presented in Eq. (1) and change over time with the state of charge. These rates also depend on the flow rate through the storage tank, which is controlled to maintain a constant temperature entering the indoor coil (state point 7 in Figure 1) as shown in Eq. (12). The mass flow rate through the storage tank is constrained to be less than or equal to the secondary loop flow rate as shown in Eq. (13). The chilled water supply temperature provided by the chiller is -4 ºC (25 ºF) for storage charging and 7 ºC (45 ºF) for storage discharging. The water glycol temperature supplied to the indoor coils is set to be 2.8 ºC (5 ºF) above the chilled water supply temperature to the storage tank during charging, and 2.8 ºC (5 ºF) below the chilled water supply temperature to the storage tank during discharging.

$$\dot{Q}_{tank} = \dot{Q}_{load} - \dot{Q}_{chiller} \tag{11}$$

$$\dot{m}_{sc} T_{cc,in} = (\dot{m}_{sc} - \dot{m}_{tank}) T_{chw} + \dot{m}_{tank} T_{f,o} \tag{12}$$

$$\dot{m}_{tank} \le \dot{m}_{sc} \tag{13}$$

The total power consumption of the system can be separated into power consumption of the chiller and the pump. The chiller power consumption is calculated using the performance map developed from ACHP as shown in Eq. (14), while the pump power consumption is calculated based on the maximum flow of the pump as shown in Eq. (15). This study assumes a pump efficiency of 60%, a maximum pump flow rate of 1 kg/s, and a maximum delivery head of 5 m based on products available on the market.

$$\dot{W}_{chiller} = \frac{\dot{Q}_{chiller}}{COP_{actual}} \tag{14}$$

$$\frac{\dot{W}_{pump}}{\dot{W}_{pump,max}} = \left(\frac{\dot{m}_{sc}}{\dot{m}_{max}} \right)^3 \tag{15}$$

$$\dot{W}_{pump,max} = \eta_{pump} \dot{m}_{max} g h_{max} \tag{16}$$

$$P = (\dot{W}_{chiller} + \dot{W}_{pump}) \tag{17}$$

The variable P is the power consumption of the system (kW), $\dot{W}_{chiller}$ is the power consumption of the chiller (kW), $\dot{W}_{pump}$ is the power consumption of the pump (kW), $\dot{W}_{pump,max}$ is the maximum power consumption of the pump (kW), $\dot{m}_{max}$ is the maximum mass flow rate of the pump, η_{pump} is the pump efficiency (-), g is the acceleration due to gravity (m/s^2), and h is the maximum delivery head (m).

3.5 Integrated System Model

The ice storage, chiller, and building load models are integrated with the secondary loop equations to form a system model. For a given building load, chiller cooling rate or tank charging rate, and state of charge, the pump flow rate and indoor coil return temperature are determined by iterative solution of the secondary loop energy balance equations (Eqs. (9) – (11)) along with the constraint of Eq. (13) and component performance models. The building load varies with time as a result of ambient temperature variations, with hourly temperatures obtained from TMY3 data (Wilcox and Marion, 2008). The ambient temperature also influences the COP of chiller. In order to run a dynamic simulation, it is necessary to specify an initial state of the storage tank and a control strategy for varying the chiller cooling rate over time in response to varying building loads and utility rates. For each time step, the system of equations are solved and then the state of charge is updated according to Eq. (2). The system power consumption for each time step in the simulation period is calculated using Eqs. (14) - (17). A solution flow diagram which shows an inner loop solution scheme for the secondary loop energy balance and an outer loop for each step in time is shown in Figure 4. R_e is the energy charge rate (\$/kWh), and R_d is the demand charge rate (\$/kW), both of which changes based on the TOU utility rate structure.

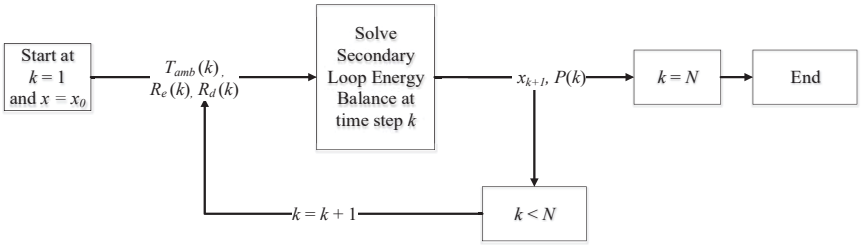

Figure 4. Ice storage system solution flow diagram with inner loop solution using energy balance equations.

4. GENERALIZED RULE-BASED CONTROLLER

4.1 Generalized Rule-based Controller Logic

The proposed control logic is designed to accommodate different utility rate structures and is loosely based on the method presented in the ASHRAE Handbook of HVAC Applications (2011). The strategy switches between the full storage, load-limiting storage-priority, and

chiller-priority strategies for *discharging* the ice storage, and it switches between the full-capacity and load-limiting strategies for *charging* the ice storage. The proposed control logic first determines the utility rate period: on-peak, off-peak, or mid-peak. For utility rates that have a flat rate, an "effective" on-peak period is determined as the hours during which the cooling load exceeds 0.75 of the chiller's maximum capacity. As mentioned in the description of the model, we set the maximum allowable state of charge of the storage tank to be 0.9 and the minimum allowable state of charge to be 0.1 to avoid decreases in heat transfer effectiveness.

The control logic for discharging the storage is depicted in Figure 5. If there is a demand charge in the off-peak period, then the chiller operates with a load-limiting strategy to prevent a large demand cost from being incurred. In the absence of a demand charge during the off-peak period, the system uses chiller-priority to preserve the storage for the on-peak period. During the on-peak period, the system operates under a load-limiting strategy regardless of the demand charge. If there is a mid-peak period, the system prioritizes the use of storage during the on-peak period, and the remaining capacity is discharged for the mid-peak period using load-limiting storage-priority. For the load-limiting discharge strategy, the chiller loading during an on-peak period and during a mid-peak period are given by

$$\dot{Q}_{chiller,on} = \frac{\sum_{i=1}^{t_{on-peak}} \dot{Q}_{on,i}\Delta t - Q_{storage}}{t_{on}} \tag{18}$$

and

$$\dot{Q}_{chiller,mid} = \frac{\sum_{i=1}^{t_{mid}} \dot{Q}_{mid,i}\Delta t + \sum_{j=1}^{t_{on}} \dot{Q}_{on,j}\Delta t - Q_{storage}}{t_{mid}} \tag{19}$$

respectively, where $\dot{Q}_{chiller,on}$ is the on-peak rate of cooling from the chiller (kW), $\dot{Q}_{on}$ is the cooling load during the on-peak period (kW), Δt is the time interval (h), $Q_{storage}$ is the maximum possible energy discharged from storage (kWh), and t is the duration of the peak period (h), $\dot{Q}_{chiller,mid}$ is the on-peak rate of cooling from the chiller (kW), and $\dot{Q}_{mid}$ is the cooling load during the mid-peak period (kW).

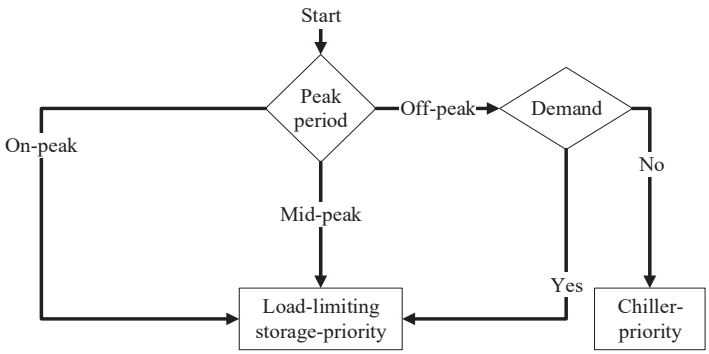

Figure 5. Control logic for discharging storage in the generalized rule-based controller.

The control logic for charging the storage tank is depicted in Figure 6. The storage tank is charged during off-peak hours for all utility rates. If there is a demand charge during the off-peak period, the chiller operates using a load-limiting charging strategy. This means the chiller charges the storage at a constant rate that is *just sufficient* to charge the storage to a 0.9 state of charge at the end of the off-peak period. If there is no off-peak demand charge, the chiller charges the storage using a full-capacity charging strategy. This means the chiller operates at maximum capacity until the storage reaches the desired charged level and *then* meets any loads with only the chiller. For the load-limiting charging strategy, the chiller charging rate is calculated by

$$\dot{Q}_{chiller,off} = \frac{\sum_{i=1}^{t_{off}} \dot{Q}_{off,i} \Delta t + Q_{charge}}{t_{off}}, \tag{20}$$

where $\dot{Q}_{chiller,off}$ is the off-peak rate of cooling from the chiller (kW), $\dot{Q}_{off}$ is the building cooling load during the off-peak period (kW), Q_{charge} is the energy required to charge the storage to the desired state of charge (kWh) and t_{off} is the duration of the off-peak period (h).

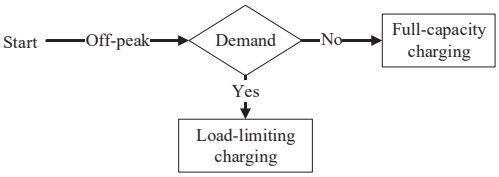

Figure 6. Control logic for charging storage in the generalized rule-based controller.

5. OPTIMAL CONTROLLER

In order to further evaluate the generalized rule-based controller, we benchmark it against an optimal controller. The optimal controller is designed to minimize the consumer's utility costs for providing cooling over a monthly billing period assuming that there are time-of-use energy charges along with on-peak, off-peak, and anytime demand charges. The problem is mathematically stated as

$$\min_{\substack{D_{on}, D_{off}, D_{any}, \\ \dot{Q}_{tank,k} \text{ for } k=1,\ldots,N}} J = D_{on} + D_{off} + D_{any} + \sum_{k=1}^{N} R_{e,k} P_k \Delta t \tag{21}$$

s.t.

$$\dot{Q}_{tank,min,k} \le \dot{Q}_{tank,k} \le \dot{Q}_{tank,max,k} \tag{22}$$

$$0 \le \dot{Q}_{chiller,k} \le \dot{Q}_{chiller,max,k} \tag{23}$$

$$x_{min} \le x_k \le x_{max} \tag{24}$$

$$x_0 = x_N \quad (25)$$

$$P_k R_{d,on} \gamma_{on} \leq D_{on} \quad (26)$$

$$P_k R_{d,off} \gamma_{off} \leq D_{off} \quad (27)$$

$$P_k R_{d,any} \gamma_{any} \leq D_{any} \quad (28)$$

where J is the monthly utility cost for cooling ($), k is the stage, N is the number of stages in the monthly billing period, $\dot{Q}_{tank}$ is the charging/discharging (+/-) rate of storage (kW), R_e is the energy charge rate ($/kWh), P is the power consumption (kW), Δt is the time interval (h), D is the target demand cost for the monthly billing period ($), R_d is the demand charge rate ($/kW), x is the state of charge of the storage tank (-), $\dot{Q}_{chiller}$ is the chiller cooling rate (kW), $\dot{Q}_{chiller,max}$ is the maximum capacity of the chiller (kW), x_0 is the storage state of charge in the beginning of the simulation (-), x_N is the storage state of charge at the end of the simulation (-), and γ is a binary switch for demand charge (-) with a value of 1 when the demand charge is applied for a time step and a value of 0 when the demand charge is not applied for a time step. Note that the power consumption at stage k, P_k, is itself a function of the storage charging/discharging rate at that stage, $\dot{Q}_{tank,k}$.

The subscripts "on", "off", and "any" in this formulation refer to on-peak, off-peak, and anytime demand charges. The variable D is used to place limits on the hourly power consumption at each stage in the optimization as shown in Eqs. (26) - (28). For utility rates without any demand charges, there are no limits on the demand cost and so the demand charge R_d and D are set to zero for all 3 cases. For utility rates with only an on-peak demand, the terms with subscripts "off" and "any" are zero (i.e. there is no limit), and so on for the cases of an anytime demand or separate on and off-peak demand charges. The constraints on the charge/discharge rate of storage in Eq. (22) are determined by the mass flow rate as shown in Eq. (1). This limit is also a function of the heat transfer effectiveness of the storage, which is determined through the state of charge and mode of operation shown in Figure 2. The cooling provided by the chiller is constrained between zero and the chiller capacity as shown in Eq. (23). The lower and upper limits on storage state of charge in Eq. (24), x_{min} and x_{max}, are assumed to be 0 and 1 such that only the latent capacity of the storage tank is considered. Finally, Eq. (25) ensures a steady periodic solution.

The decision variables of this optimization problem are the charging/discharging rate of the storage for all stages of the optimization period and the three target demand costs. The optimization is performed using a monthly optimization that begins at 0:00 on the first day and ends at 24:00 on the last day of the month (day 30). The problem is solved using a hybrid method of dynamic programming (Bellman, 1957) and non-linear optimization. Dynamic programming utilizes Bellman's principle of optimality and guarantees a global minimum. At any time stage k, there are multiple paths to reach the previous time stage k-1. Each stage represents an hour time step in the simulation period, and the state variable is defined as the state of charge of the storage tank. This state variable is discretized between 0 and 1 by intervals of 0.01 to establish a grid of possible paths between consecutive stages. Penalty

functions are utilized to handle constraints that would not allow transitions between states within the grid. Dynamic programming calculates the cost of all possible paths to find the least cost solution for each consecutive stage in time. This process is used recursively to determine the minimum cost for the entire simulation period. Eq. (25) is satisfied by considering a specified state of charge at the beginning and end of the time period over which the optimization is conducted. The remaining constraints are enforced using penalty functions, which assign a very large cost to a path if the constraints are violated. For utility rates with demand charges, the optimal utility cost J^* is determined by solving the N variable optimization problem for each iteration of an outer loop optimization problem to determine the optimal values of $D_{on,}$ $D_{off,}$ and D_{any} as shown in Figure 7. This study uses the *fmincon* function in MATLAB to solve the outer loop nonlinear optimization problem.

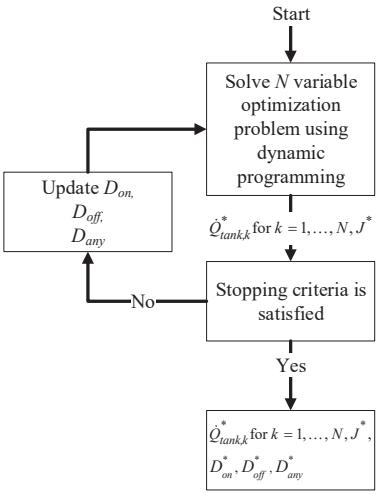

Figure 7. Schematic describing the optimal control problem.

6. SIMULATION RESULTS

In this section, we evaluate the performance of the generalized rule-based controller against that of the optimal controller for a cooling system with a 10.55 kW (3-ton) chiller and 473 L (125 gallons) of ice storage. Daily comparisons of the two controllers are used to highlight the differences in system operation that result from the two approaches. We then present monthly cost comparisons based on system operation using each of the controllers.

The simulations assume a perfect weather forecast and use weather data from TMY3 for determining ambient conditions and building loads (Wilcox and Marion, 2008). An hour long time step is considered for both control strategies. The indoor set-point temperature (T_{zone}) is 24.4 °C (76 °F) from 10 am to 4 pm on weekdays and 22.2 °F (72 °F) the rest of the time. The results are generated using three sample utility rates and weather data for the month of May at the location where each utility rate is offered. The sample rates used in the comparisons are provided in Table 1. The first two utility rates represent TOU energy rate structures with no demand charges, and the second two utility rates represent TOU energy rates with anytime demand charges.

The first utility rate is a TOU energy only rate from Miami, Florida. This utility rate has an off-peak energy charge of $0.035/kWh, an on-peak energy charge of $0.184/kWh, and no demand charge. The results for Miami, Florida are shown in Figures 8 and 9. Figure 8 presents the difference in chiller operation between the two controllers and an overlay of the cooling load profile, and Figure 9 presents the difference in storage state of charge. The black bars represent the generalized rule-based controller and the white bars represent the optimal controller. Two consecutive days are shown to highlight the differences in controller behavior, and the second day shown is the hottest day of the month. The shaded areas in the figures denote the on-peak period of each day.

Table 1: Sample Residential Utility Rates

TOU energy with no demand			
	On-peak energy ($/kWh)	Mid peak energy ($/kWh)	Off-peak energy ($/kWh)
Florida Power & Light (FL)	0.184 (<1000 kWh) 0.204 (>1000 kWh) (12-8pm)	n/a	0.035(<1000 kWh) 0.055(>1000 kWh)
Sacramento Municipal Utility District (CA)	0.316 (4-7pm)	0.149 (9am-4pm & 7-9pm)	0.087
TOU energy with anytime demand			
	On-peak energy ($/kWh)	Off-peak energy ($/kWh)	Anytime demand ($/kW)
Alabama Power (AL)	0.221 (1-6pm)	0.072	1.5

As shown in Figure 8, the two controllers follow a similar pattern for chiller operation, which minimizes the use of the chiller during the on-peak period and charges the storage at a high capacity during the off-peak period. While the generalized rule-based controller charges the storage at full capacity at the start of the off-peak period (see hour 20 in Figure 8), the optimal controller chooses to charge the storage in the early morning (i.e. hours 24-31 in this example). The optimal controller optimizes the charging scheme by charging the storage when the ambient temperature is lower and the chiller has higher efficiency. When discharging the storage on the hottest day (i.e. hours 24-48), the optimal controller operates the chiller at very low capacities at the start of the on-peak period instead of operating the chiller at a constant capacity. While both controllers minimize the use of chiller during the on-peak period, the optimal controller also minimizes the use of chiller during the hottest hour of this on-peak period. The operating cost for this comparison is shown in Table 2, in which the generalized rule-based controller achieved an operating cost within 15% of the optimal controller.

The optimal controller and the generalized rule-based controller both try to maximize the use of storage so that most of the storage is discharged by the end of each day. The generalized rule-based controller is limited to discharging to a 0.1 state of charge to avoid a decrease in heat transfer effectiveness, while the optimal controller is allowed to discharge the storage completely to 0 charge. This is shown in Figure 9 by the absence of white bars after both on-peak periods. The optimal controller also has the option of charging the storage completely, even though there is a significant decrease in the heat transfer effectiveness as the storage reaches full charge. The generalized rule-based controller avoids this penalty and limits the state of charge to 0.9. Despite this penalty, though, the optimal controller charges the storage completely to reduce chiller operation during the on-peak period on the hottest day. In this way, the optimal controller is able to optimally evaluate the trade-off between the heat transfer effectiveness penalty and additional storage capacity for the hottest day.

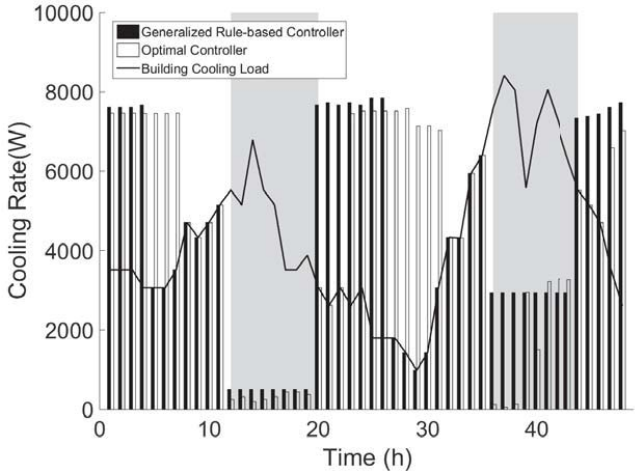

Figure 8. Comparison of chiller operation under generalized rule-based and optimal controller over two consecutive days using a TOU energy only utility rate from Miami, Florida.

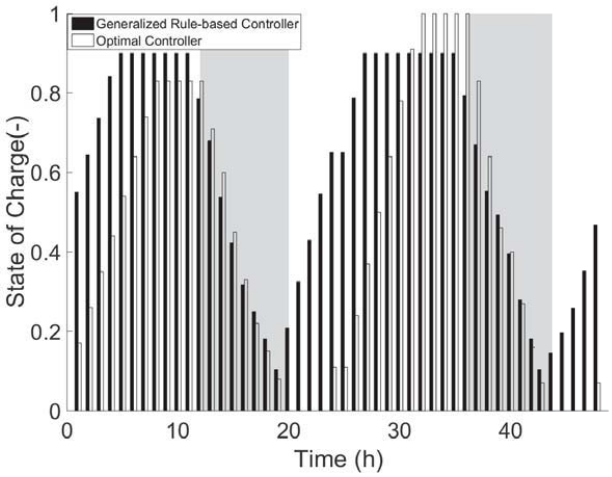

Figure 9. Comparison of state of charge under generalized rule-based and optimal controller over two consecutive days using a TOU energy only utility rate from Miami, Florida.

The second utility rate is a TOU energy rate with mid-peak period from Sacramento, California. This utility rate has an off-peak energy charge of $0.087/kWh, a mid-peak energy charge of $0.149/kWh, an on-peak energy charge of $0.316/kWh, and no demand charge. The results for Sacramento, California are shown in Figures 10 and 11 in a similar format as the results for Miami, Florida. The lighter shade area represents the mid-peak period, and the darker shade area represents the on-peak period.

Table 2. One month cost comparison between controllers simulated in Miami, Florida.

	Optimal Controller	Generalized Rule-based Controller	Relative Cost
Energy Cost ($/MW-h)	21.15	24.14	1.14

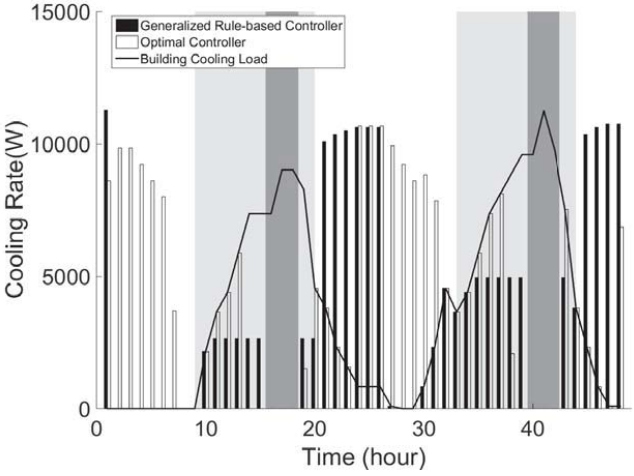

Figure 10. Comparison of chiller operation under generalized rule-based and optimal controller over two consecutive days using a TOU energy with mid-peak utility rate from Sacramento, California.

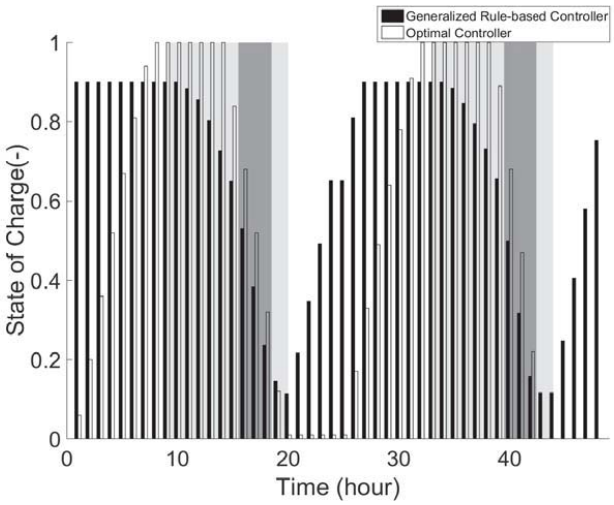

Figure 11. Comparison of state of charge under generalized rule-based and optimal controller over two consecutive days using TOU energy with mid-peak utility rate from Sacramento, California.

The daily comparison of Sacramento, California is similar to that of Miami, Florida. The optimal controller once again chooses to charge the storage later than the generalized rule-based controller to take advantage of lower ambient conditions. When discharging the storage, the optimal controller reduces the chiller cooling rate when the building cooling load is higher. This is because the chiller has a lower COP when the ambient temperature is higher. Both controllers maximize the use of storage during the on-peak period. This can be seen in Figure 10, where there are no bars within the darker shaded area.

When considering the storage state of charge, the optimal controller chooses to fully charge the storage on both days. The optimal controller discharges most of the storage on the first day, and discharges it completely on the hottest day. The Sacramento utility rate has a very long mid-peak period, so additional storage capacity can provide more operating cost savings that in turn can compensate for the penalty in heat transfer effectiveness. Table 3 shows the monthly operating cost comparison between the two controllers. The generalized rule-based controller performs very well under this utility rate and is able to achieve operating cost within 5% of the minimal cost. This is mainly because the utility rate has an on-peak energy charge that is very expensive but short in duration. The generalized rule-based controller uses a load-limiting discharge strategy, which becomes full storage control when the storage capacity is sufficient to meet the total on-peak cooling load. Since the on-peak period is relatively short, the generalized rule-based controller meets the on-peak load without operating the chiller. The difference in operating cost is mainly due to the charging strategies, where the optimal controller chooses cooler hours to charge the storage. This does not lead to a significant difference in operating cost because the off-peak energy charge is inexpensive, and the off-peak cooling load is low.

Table 3. One month cost comparison between controllers simulated in Sacramento, California.

	Optimal Controller	Generalized Rule-based Controller	Relative Cost
Energy Cost ($/MW-h)	27.30	28.29	1.04

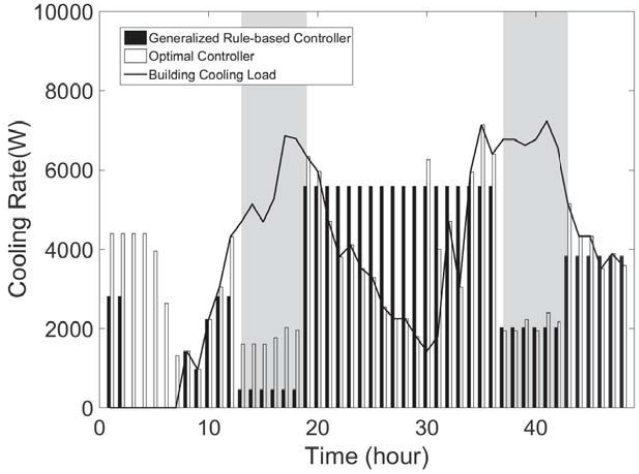

Figure 12. Comparison of chiller operation under generalized rule-based and optimal controller over two consecutive days using a TOU energy with anytime demand utility rate from Birmingham, Alabama.

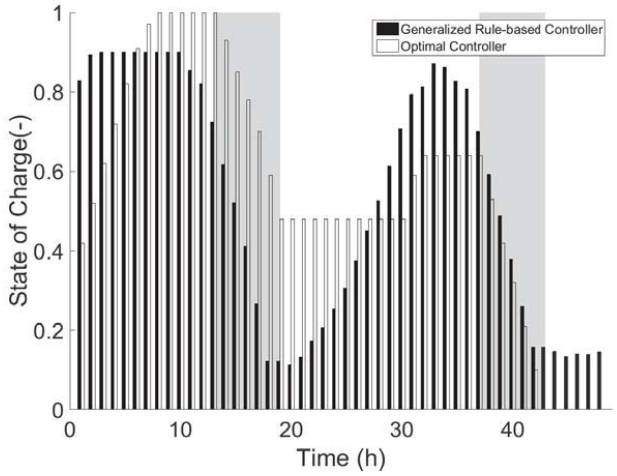

Figure 13. Comparison of state of charge under generalized rule-based and optimal controller over two consecutive days using a TOU energy with anytime demand utility rate from Birmingham, Alabama.

The third comparison uses a utility rate that has a TOU energy rate with anytime demand from Birmingham, Alabama. This utility rate has an off-peak energy charge of $0.072/kWh, an on-peak energy charge of $0.221/kWh, and an anytime demand charge of $1.5/kW. The results for Birmingham, Alabama are shown in Figures 12 and 13 in a similar format as the previous results.

The two controllers have more differences in chiller operation under this utility rate structure than were seen using the utility rates from Miami and Sacramento. Since there is an *anytime* demand for this utility rate structure, the generalized rule-based controller tries to minimize the demand for each on-peak and off-peak period. Figure 12 shows that the optimal controller actually operates the chiller at a higher rate on the hottest day when compared to the generalized rule-based controller. While the generalized rule-based controller is able to achieve a lower demand charge on the hottest day, the optimal controller outperforms the generalized rule-based controller over the entire month. In particular, the optimal controller is able to weigh the trade-off between incurring high demand costs versus high energy cost as shown in Table 4. The optimal controller has a higher demand cost but a much lower energy cost when compared to the generalized rule-based controller. This shows that minimizing the demand of each day is not always the optimal strategy, especially under utility rates with lower demand charges.

Figure 13 shows that the optimal controller does not charge the storage completely before the hottest day. The optimal controller charges the storage on the coolest hour in that off-peak period, but only to a 0.7 state of charge. The optimal controller instead charges the storage pre-emptively on the day before the hottest day, since the cooling loads between the two days are relatively high. This means that the optimal controller avoids operating the chiller in charging mode while the ambient temperature is high, because that leads to very low system efficiency. The generalized rule-based controller is able to charge the storage before the end of the off-peak period on the first day because the storage was not depleted during the previous on-peak period. It assumes the storage is depleted to 0.1 at the end of each on-peak period and charges the storage with a load-limiting charging strategy. This allows the system to achieve a minimum demand during each off-peak period, but is unnecessary for days when the power consumption does not reach the peak demand. Unlike the generalized rule-based controller, the optimal controller utilizes perfect load forecasts for the entire month. Therefore, the optimal controller can charge the storage at a constant rate that is limited by the forecasted maximum power consumption instead of the minimum demand for every off-peak period. The optimal controller can charge the storage at a higher rate on days where the minimum demand of the off-peak period is less than this maximum limit. The optimal controller can then meet the remaining loads during the off-peak period at a higher chilled water supply temperature, which increases the system efficiency.

Table *4. One month cost comparison between controllers simulated in Birmingham, Alabama.*

	Optimal Controller	Generalized Rule-based Controller	Relative Cost
Energy Cost ($/MW-h)	21.61	26.41	1.22
Demand Cost ($/MW-h)	5.20	3.53	0.68
Total ($/MW-h)	26.81	29.94	1.11

7. CONCLUSION

In this study, we defined a generalized rule-based control strategy for thermal storage systems applied to cooling in residential buildings that works well for residential utility rates structures that are available today. The rule-based strategy switches between three different heuristic strategies traditionally used in commercial building systems in order to leverage the best features of each one. A system consisting of an ice storage tank and a packaged chiller was modeled along with the building load in order to evaluate, in simulation, controller performance under different residential variable utility rates. The generalized rule-based

control strategy was compared in simulations against an optimal controller designed to minimize monthly total operating cost. The controllers were evaluated using three different residential utility rate structures in different climates. The generalized rule-based controller was able to achieve operating costs within 15% of the minimal cost achieved by the optimal controller. The optimal controller was able to evaluate the trade-off between energy and demand charge, and between storage capacity and heat transfer effectiveness penalty. The results also showed the utility rate structure can influence performance of the controllers, and the generalized rule-based controller performed better under rates with shorter on-peak periods. Future work will consider the effect that uncertainty in the building load and ambient temperature forecast has on each controller.

NOMENCLATURE

c	Specific heat	(kJ/kg-ºC)
g	Internal gain	(kW)
J	Integrated utility costs	($)
L	Latent capacity	(kW)
m	Mass flow rate	(kg/s)
P	Power consumption	(kW)
Q	Heat transfer rate	(kW)
R	Utility charge	($/kWh) / ($/kW)
T	Temperature	(ºC)
t	Time period	(hour)
UA	Heat transfer coefficient	(W/ºC)
x	State of charge	(-)
ε	Heat transfer effectiveness	(-)

Subscript

amb	Ambient
C	Charge mode
chw	Chilled water supply
D	Discharge mode
d	Demand charge
e	Energy charge
f	Secondary fluid
f,i	Secondary fluid at storage inlet
f,o	Secondary fluid at storage outlet
k	Time index
max	Maximum
mid	Mid-peak period
min	Minimum
off	Off-peak period
on	On-peak period
return	Secondary fluid return temperature
s	Phase change temperature
sc	Secondary loop
tank	Storage tank
zone	Indoor set-point

REFERENCES

Bell, I.H., 2012. ACHP Documentation. 1.4 [WWW Document]. URL http://achp.sourceforge.net/index.html.

Bellman, R., 1957. Dynamic Programming. Princeton University Press, Princeton, N.J.

Drees, K., Braun, J., 1996. Development and Evaluation of a Rule-Based Control Strategy for Ice Storage Systems. HVACR Res. 2, 312–334. https://doi.org/10.1080/10789669.1996.10391352

Henze, G.P., 2003. Parametric Study of a Simplified Ice Storage Model Operating Under Conventional and Optimal Control Strategies. J. Sol. Energy Eng. 125, 2. https://doi.org/10.1115/1.1530629

Kung, F., Deru, M., Bonnema, E., 2013. Evaluation Framework and Analyses for Thermal Energy Storage Integrated with Packaged Air Conditioning. National Renewable Energy Laboratory (NREL), Golden, CO.

Lo, C.-C., Tsai, S.-H., Lin, B.-S., 2016. Ice Storage Air-Conditioning System Simulation with Dynamic Electricity Pricing: A Demand Response Study. Energies 9, 113. https://doi.org/10.3390/en9020113

Mitchell, J., Braun, J.E., n.d. Principles of heating, ventilation, and air conditioning in buildings. Wiley, 2013. Print., Hoboken, NJ.

NREL, 2018. U.S. Utility Rate Database [WWW Document]. URL https://openei.org/apps/USURDB/

Sun, C., Temple, K., Rossi, T., Braun, J.E., 2006. Interaction between dynamic electric rates and thermal energy storage control, Final Report for RP-1252.

Supervisory Control Strategies and Optimization, 2011. , in: ASHRAE Handbook of HVAC Applications. pp. 42.1-42.39.

West, J., Braun, J., 1999. Modeling Partial Charging and Discharging of Area-Constrained Ice Storage Tanks. HVACR Res. 5, 209–228. https://doi.org/10.1080/10789669.1999.10391234

Wilcox, S., Marion, W., 2008. Users Manual for TMY3 Data Sets (Revised). National Renewable Energy Lab.(NREL), Golden, CO (United States).

Questions and Answers:

What is the additional energy consumption to operate the load shifting?

Davide Ziviani:

Not known

***

If you do not melt all the ice at the end of the discharge, there will be ice remaining in the tank at the begining of the new ice building phase. Would it impact the performance during charging?

Davide Ziviani:

The control strategy avoids this kind of problems.

***

Does the 100% faster simulation include the time for inputs variations?

Davide Ziviani:

Yes, the initialization procedure needs to be run only when design parameters are changed.

***

Do you have information about the deviation between the original model and the simplified model?

Davide Ziviani:

No but we are confident in the accuracy.

Towards a subsurface predictive-model environment to simulate aquifer thermal energy storage for demand-side management applications

T. Robert[1,2]*, T. Hermans[3], N. Lesparre[4], G. De Schepper[5], F. Nguyen[2], A. Defourny[2], P. Jamin[2], P. Orban[2], S. Brouyère[2], A. Dassargues[2]

[(1)] F.R.S.-FNRS (Fonds de la Recherche Scientifique), Brussels, Belgium

[(2)] University of Liege, Department of Urban & Environmental Engineering, Liege, Belgium

[(3)] Ghent University, Department of Geology, Ghent, Belgium

[(4)] University of Strasbourg, Laboratoire d'Hydrologie et de Géochimie, Strasbourg, France

[(5)] AQUALE SPRL, Department of R&D, Noville-les-Bois, Belgium

ABSTRACT

Considering that coupling electrically-driven heating, ventilation, and air-conditioning (HVAC) systems with thermal energy storage (TES) in buildings is seen as a promising tool for demand-side management (DSM) in the low-voltage grid, we propose to study high and low temperature aquifer thermal energy storage (ATES) for DSM applications and to improve the overall energy efficiency of an open-loop geothermal system connected to a building and a smart-grid.

To do so, we present a detailed review of short-term ATES experiments conducted in alluvial aquifers of Belgium with the scope of defining the best prior information to design and construct a predictive-model environment to simulate subsurface ATES scenarios at different DSM frequencies: real time, intraday, interday, and interseasonal. This environment is built upon HydroGeoSphere (HGS): a three-dimensional numerical model describing fully-integrated subsurface and surface flow and solute and heat transport inside porous and fractured media.

We focused on shallow and productive alluvial aquifers by summarizing the key parameters from several study sites of Wallonia (Belgium). The predictive-model environment is built in Matlab and allows to easily adapt the subsurface model to a specific alluvial aquifer as well as to predict any specific responses of the aquifer linked to energy storage and recovery cycles.

Keywords: Aquifer Thermal Energy Storage (ATES), Demand-Side Management (DSM), Predictive modeling

1. INTRODUCTION

Coupling electrically-driven heating, ventilation, and air-conditioning (HVAC) systems with thermal energy storage (TES) in buildings is seen as a promising tool for demand-side management (DSM) in the low-voltage grid (e.g. Arteconi et al., 2012; 2013). In particular, space heating and cooling as well as domestic hot water (DHW) production with heat pumps (HP) can be combined with different TES strategies for flexibility purposes (e.g. Fisher and Madani, 2017 and references therein; Georges et al., 2017). Among them, thermostatically-controlled load-shifting using the thermal envelope of the building or using water tanks is often considered (Arteconi et al., 2012; 2013; Lund et al., 2015). With this work, we further consider using subsurface TES to offer a new potential flexibility tool as well as to improve the overall energy efficiency of groundwater heat pump (GWHP) systems.

A GWHP (or open-loop geothermal) system is connected to an aquifer with a well doublet (Figure 1) made of a production well used to pump groundwater and a distinct injection well used to infiltrate groundwater back in the aquifer at a distance far enough to avoid any thermal feedback and/or thermal recycling (e.g. Milnes and Perrochet, 2012). Groundwater is delivered to a GWHP or to a heat exchanger where it acts as a heat source or sink for space heating and DHW production while it is chilled for space (free) cooling (e.g. Sanner et al., 2003; Banks, 2009; Vanhoudt et al., 2011).

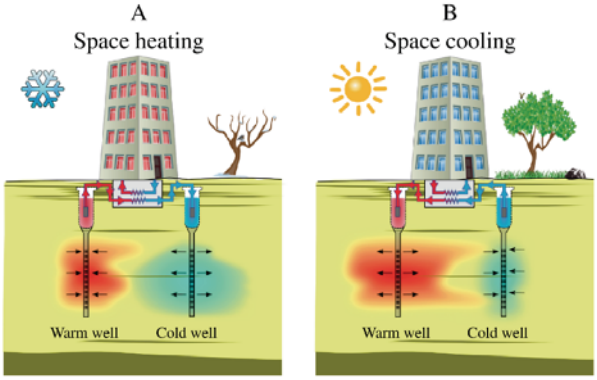

Figure 1: ATES system during space heating mode (A) and during space cooling mode (B) (modified after Bonte, 2013).

Aquifer thermal energy storage (ATES) systems further use GWHP to perform TES in the subsurface with heat being stored in the so-called warm well during space cooling (summer) and cold being stored in the so-called cold well during space heating (winter) (Figure 1). Such seasonal storage theoretically leads to an improvement in the overall performance of the system (Saner et al., 2010; Vanhoudt et al., 2011; Bayer et al. 2013). So far, ATES is mainly seasonal (Hesaraki et al., 2015) and not optimized in space nor in time (Bloemendal et al., 2014) because the heat storage potential is often considered as a bonus of the basic functioning of an open-loop geothermal system.

In this context, and provided that a productive aquifer is present, ATES systems offer a significant decentralised potential of flexibility when we consider their thermal and electrical powers (up to MW) and/or the thermal inertia of the building(s) to which they are connected. However, the design and functioning of such ATES systems have strong interconnections with the geology and hydrogeology of the site which may be complex and heterogeneous, making robust predictions on thermal energy storage and recovery cycles difficult (Hermans et al., 2018).

Thermal energy recovery rate depends on different processes, namely thermal conduction and dispersion, regional groundwater flow, and density-dependent flow (at higher temperature) (e.g. Doughty et al., 1982). Regional groundwater flow is further related to the regional hydraulic gradient (driving force) and the hydraulic conductivities (K in m/s) of the area of interest. Therefore, the porous media heterogeneity (in terms of hydraulic conductivity for example) can significantly impact thermal energy storage. Short-term storage appears to be better in high permeability media than in low permeability media, with higher recovery rates, while long-term storage gives poorer recovery rates in high permeability media compared to low permeable ones (Bridger and Allen, 2010; 2014; Ferguson, 2007; Paulus et al., 2016; Hermans et al., 2018).

Moreover, the heterogeneity in the groundwater flow parameters has a much stronger effect than the heterogeneity in the thermal parameters of the same model (Ferguson, 2007; Hermans et al., 2018). The above-mentioned features prove that using simple analytical models to homogeneous 3D numerical models is not enough to fully study heat storage and recovery cycles in aquifers.

Our wish with this work is to propose a library of ATES predictive numerical models based on real-world shallow alluvial aquifers (including their heterogeneity) associated with a user-friendly Matlab interface to compute any heat storage and recovery simulations related to the functioning of any HVAC system connected to a building and a low-voltage grid. To do so, we will first present all the prior information on alluvial aquifers compiled from many studies involving them in Wallonia (Belgium) (**section 3**). We will then focus on the design and construction of our predictive-model environment (**section 4**) and how to use the latter to simulate ATES scenarios at different DSM frequencies: real time, intraday, interday, and interseasonal or to couple it with other building and HVAC systems simulation codes (**section 5**) before discussing some results to rapidly assess the perspective of using ATES for DSM applications (**section 6**) and concluding (**section 7**). This ongoing work offers plenty of perspectives which are listed in **section 8**.

2. PRIOR INFORMATION ON ALLUVIAL AQUIFERS

Major cities in Wallonia (Belgium) (but also worldwide) are built above alluvial deposits: sands and gravels which generally constitute productive aquifers (Dassargues et al., 2014) and clay lenses which can be locally responsible of low productive areas (Fossoul et al., 2011). Low-enthalpy geothermal energy can then be generated from this easily available shallow groundwater (Fossoul et al., 2011; Dassargues and Wildemeersch, 2014; Paulus et al., 2016). Allen and Milenic (2003) demonstrated that for flow rates of 20 l s^{-1} (or 72 m^3 h^{-1} which can for example be achieved with one or two production wells in Walloon alluvial aquifers), and a temperature reduction of 8 K in the GWHP, enough heating resource (672 kW) can be generated to heat buildings of 11,000 m^2 floor area. In Wallonia, ATES or more generally GWHP systems struggle to find their place and alluvial aquifers should be considered as the primary target because of the reduced installation costs (mostly related to shallower drillings). Given the above-mentioned reasons, alluvial aquifers constitute our first subsurface model library.

In the following subsections, we will present different study sites (all located in Wallonia, Belgium) that will progressively compose our library. We will focus our detailed discussion on the Hermalle-sous-Argenteau (HSSA) and Jemeppe-sur-Sambre (JSS) sites because they present different hydrogeological characteristics and heat storage behaviours and possess already a rich database (e.g. heat storage and recovery tests) as well as the Colonster (COL) site located in the Campus of the University of Liège and currently under construction. Other sites might be included later in the library (e.g. Fossoul et al., 2011; De Schepper et al., 2018).

2.1 Hermalle-sous-Argenteau (HSSA) site

The HSSA site, an experimental site of the University of Liège, is located in Hermalle-sous-Argenteau near the Liège Trilogiport, in a meadow lying on the alluvial deposits of the Meuse River (Figure 2). This site has now been investigated for decades and probably constitutes the most documented experimental site in Walloon alluvial deposits with a strong database composed of results of hydrogeological tests, geophysical surveys and monitoring, and thermal tracer tests (Brouyère, 2001; 2003; Wildemeersch et al., 2014; Hermans et al., 2015a; 2015b; Klepikova et al., 2016; Hermans and Irving, 2017, Lesparre et al., 2019; Hermans et al., 2018; Jamin and Brouyère, 2018).

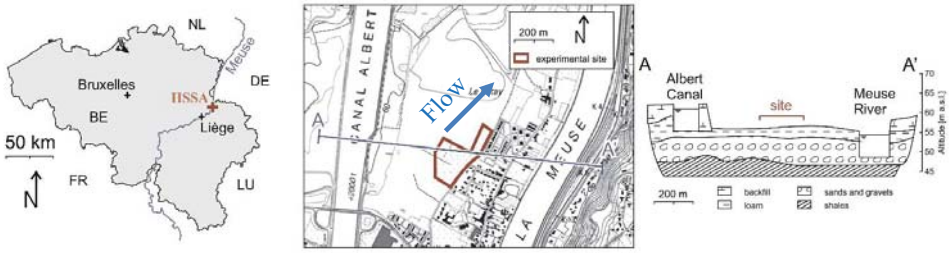

Figure 2: Location of the HSSA site in Belgium (left) and in the town of Hermalle-sous-Argenteau (middle) and (hydro)geological cross section of the alluvial plain (right) (modified after Wildemeersch et al., 2014).

As shown in Figure 3, the Meuse alluvial plain lies on top of a low permeable Carboniferous shaly bedrock which constitutes the basement of the alluvial aquifer. Geologically, alluvial deposits are composed of three layers (from the ground surface): a first unit composed of loam and clay lenses between 0 and 1.5 m.b.s.; sandy loam with an increasing proportion of millimetre gravels at the end of this second unit (still unsaturated) between 1.5 and 3 m.b.s.; alluvial sand and gravel between 3 and 10 m.b.s., with a progressive increasing proportion (and size) of gravels in depth (Wildemeersch et al., 2014). This unit is fully saturated and constitutes the main (mostly) unconfined aquifer in this work. Hydrogeologically, the water table is about 3.2 m.b.s. with a maximum annual fluctuation of half a meter. The main aquifer can be subdivided into two layers of different hydraulic characteristics: the upper aquifer (sandy gravels) between 3 and 7 m.b.s. and the lower aquifer (coarse clean gravels, with frequent clean pebbles of more than 0.2 m in diameter) between 7 and 10 m.b.s.

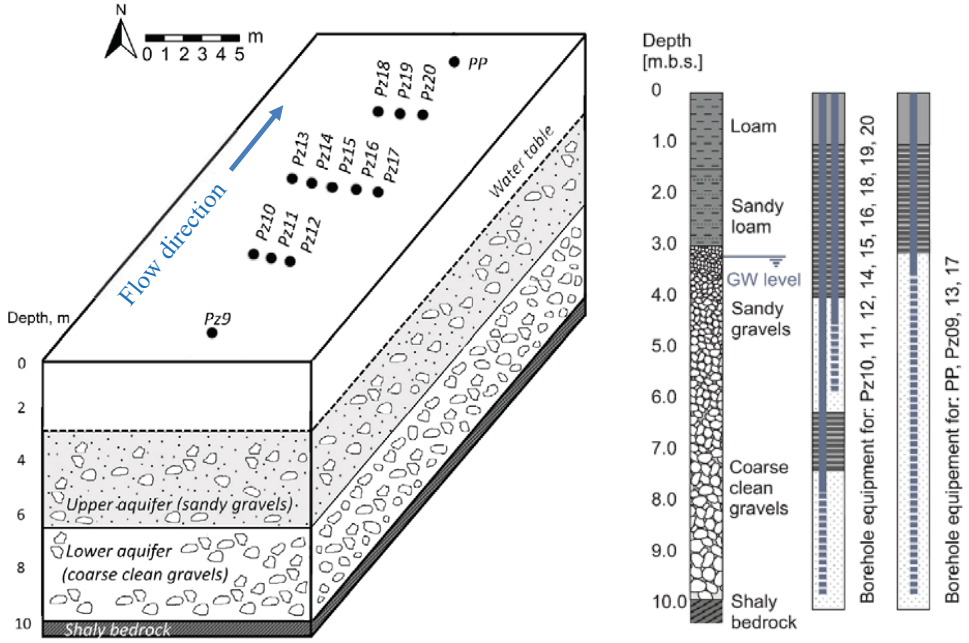

Figure 3: (Hydro) geological conceptual model of the alluvial aquifer around the area of interest (left, modified after Klepikova et al., 2016) and associated boreholes information (right, modified after Wildemeersch et al., 2014).

The recharge of the alluvial aquifer comes from two sources: direct infiltration from rainfall events and surface water from the Albert Canal whose basement is not impervious. The hydraulic gradient (driving force of groundwater flow) is about 0.06 % towards NE and the draining Meuse River that imposes the base water level as the principal outflow of the alluvial aquifer. In terms of hydraulic conductivity, Brouyère (2001; 2003) showed with the help of pumping tests that the mean hydraulic conductivity of the alluvial aquifer is in the order of 2 to 7×10^{-2} m/s.

Table 1: Hydraulic and thermal parameters in the HSSA model deduced from experiments (Brouyère, 2001; Wildemeersch et al., 2014) and model calibration (Klepikova et al., 2016).

Parameters	Upper aquifer	Lower aquifer
Mean hydraulic conductivity [m/s]	5×10^{-4}	5×10^{-2}
Range of hydraulic conductivity [m/s]	1×10^{-4} to 5×10^{-3}	1×10^{-2} to 1×10^{-1}
Effective porosity [-]	0.04	0.08
Hydraulic gradient [%]	0.06 but varies with the Meuse River level	
Mean Darcy fluxes [m/d]	~0.03	~3
FVPDM Darcy fluxes [m/d]	~0.1	~20
Maximum pumping rate [m³/h]	> 80	
Bulk density [kg/m³]	1800	1500
Thermal conductivity [$Wm^{-1}K^{-1}$]	1.37	1.86
Volumetric heat capacity [$MJm^{-3}K^{-1}$]	2.24	2.34
Thermal retardation factor [-]	5	
Longitudinal dispersivity [m]	3	
Transverse dispersivity [m]	0.3	
Groundwater temperature [°C]	10 to 13 depending on the season	

The site has been reequipped in 2012 with a full set of twelve new (2 inches) piezometers, some being double screened in the upper and the lower aquifers, others being screened over the entire aquifer (Figure 3). Thanks to this new set-up combined with an existing well, Wildemeersch et al. (2014) conducted and interpreted a multiple tracer test (including heated water) to characterise solute and heat transport parameters in the site. Hermans et al. (2015a) showed with electrical resistivity tomography monitoring that preferential flow and heat transport occurred during this multiple tracer test, especially in the lower aquifer. Jamin and Brouyère (2018) further demonstrated with the *finite volume point-dilution method* (*FVPDM*, see Brouyère et al., 2008) that the Darcy fluxes of the upper aquifer is in average 200 times lower than the Darcy fluxes of the lower layer. Parameters relevant to groundwater flow and heat transport were therefore deduced from all these experiments but also from a numerical model inversion performed by Klepikova et al. (2016) (see Table 1). More recently, Lesparre et al. (2019) and Hermans et al. (2018) conducted two heat storage and recovery experiments by specifically targeting the upper layer (where Darcy fluxes are lower) showing that a high energy recovery rate (associated with a high exergy) is only possible (in the HSSA site) in the upper layer and for short-term frequencies: real time and intraday. Interday frequencies still allow a fair energy recovery but exergy is drastically lowered with an increasing storage duration (see section 6 for a full thermal energy recovery rate and exergy analysis).

2.2 Colonster (COL) site

The COL site, another experimental site of the University of Liège, is located in Colonster below the Sart-Tilman Campus of the University of Liège, in a meadow lying on the alluvial deposits of the Ourthe River (Figure 4). This experimental site is already equipped with five (two inches) piezometers in the form of a dice of five but two new (four inches) wells will be drilled and equipped in fall 2018 allowing new hydrogeological, geophysical, and geothermal experiments in the near future.

Geologically, the site has all the characteristics of alluvial deposits (Figure 4, right). From the ground surface, we can find a 6 m thick layer mainly composed of clay and then, a 6 to 7 m thick layer composed of gravel lying on top of the sandstone bedrock (at about 13.5 m.b.s.). Hydrogeologically, the gravel layer constitutes the main aquifer of the alluvial plain of the Ourthe River. This aquifer is captive since the water table is situated between 3 and 4 m.b.s. depending on the season, so 2 to 3 m above the upper limit of the gravel layer. The recharge of the aquifer comes from two different sources: groundwater flow from the sandstone aquifer of the Sart-Tilman hill (in the SW limit of the site) and direct infiltration from rainfall events. A small stream creating an inundated area (thanks to a beaver family living nearby) and a pond might also favour vertical recharge.

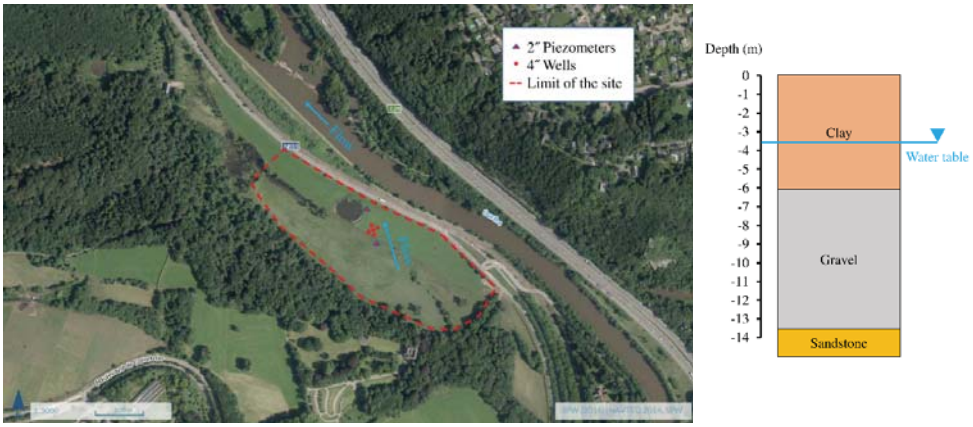

Figure 4: The Colonster site is located below the Sart-Tilman Campus of the University of Liège, near the Ourthe River, and equipped with wells (soon) and piezometers.

So far, the site has been studied by Borgers (2018) with geophysical surveys and by Defourny (2018) with pumping tests, FVPDM experiments, and finally push-pull tests (a push-pull test is equivalent to heat storage and recovery but with solute and/or heat tracers, see Haggerty et al. (1998) for more details) to determine the heterogeneity of the aquifer regarding groundwater flow and solute transport parameters. More experiments are planned in the near future.

Defourny (2018) demonstrated that the site was quite productive with a mean hydraulic conductivity value of 2 to 4×10^{-4} m/s and locally higher values ($\sim10^{-3}$ m/s) in the vicinity of the tested piezometer. EM39 logging (Defourny, 2018) and electrical resistivity tomography surveys (Borgers, 2018) showed that the gravel layer has a homogeneous behaviour in terms of electrical resistivity and consequently, potentially a homogeneous behaviour in terms of hydraulic conductivity. The hydraulic gradient seems to be higher than in HSSA, with estimated values in the range of 2 % towards NW and the draining Ourthe River. New wells will help us to calculate a more precise value of this important parameter (driving force of

groundwater flow). Other hydraulic and solute transport parameters (Defourny, 2018) are given in Table 2.

Table 2: Hydraulic and thermal parameters in the COL model deduced (or estimated) from experiments (Defourny, 2018).

Parameters	COL alluvial aquifer
Mean hydraulic conductivity [m/s]	2×10^{-4}
Range of hydraulic conductivity [m/s]	5×10^{-4} to 5×10^{-3}
Effective porosity [-]	0.08
Hydraulic gradient [%]	(2)
Mean Darcy fluxes [m/d]	0.35
FVPDM Darcy fluxes [m/d]	2.34
Maximum pumping rate [m³/h]	?
Retardation factor [-]	2.3
Longitudinal dispersivity [m]	0.4
Groundwater temperature [°C]	8

2.3 Jemeppe-sur-Sambre (JSS) site

The JSS site is located in an old alluvial plain of the Sambre River near Charleroi, in Wallonia, Belgium. The topography of the study site is roughly flat. The area of interest is located in sparse woods, that extend from east to west, and that is bordered by a dirt track (north; 0.75 m higher than the rest of the site) and a grass field (south) (Figure 5). The investigated area possess three 4" wells (W1, W2, and W3) and two 2" piezometers (PzA and PzB).

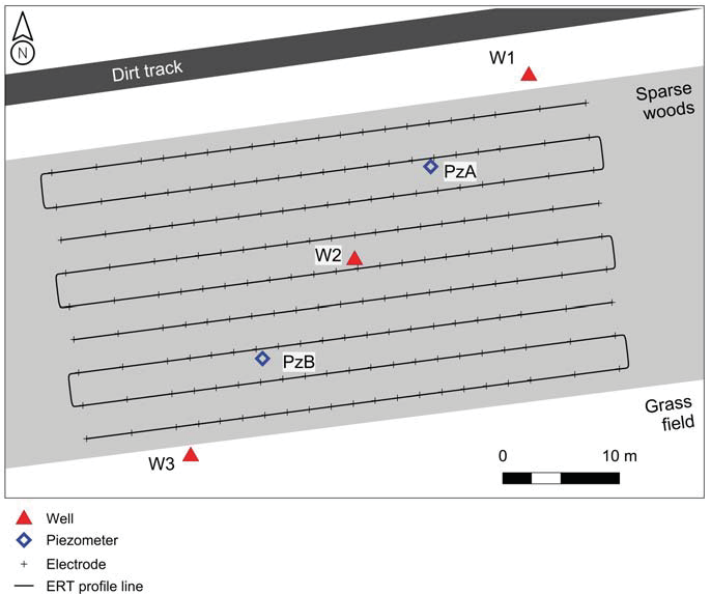

Figure 5: The JSS site (fully equipped with wells and piezometers) is no longer available for experiments (wells are now in an operating mode for the site owner).

The local geological setting is typical of an alluvial plain: a 2 to 4 m thick layer of Quaternary clayey loam soils, partially mixed with backfill soils at the top, is underlain by about 3 to 6 m thick Quaternary sandy gravel alluvial deposits. A NE-SW (hydro) geological cross section (sketched based on the geological logs from the 5 boreholes located in the investigated area; see Figure 6) also demonstrates some heterogeneity in the thickness of these Quaternary sandy gravel alluvial deposits which constitute the studied aquifer. Deeper (about 7.5 m.b.s.) is found a several meters thick clay layer, originating from the weathering of the subjacent Carboniferous coal shales from the regional scale Hainaut coalfield (Piessens and Dusar, 2004; Ruthy and Dassargues, 2014).

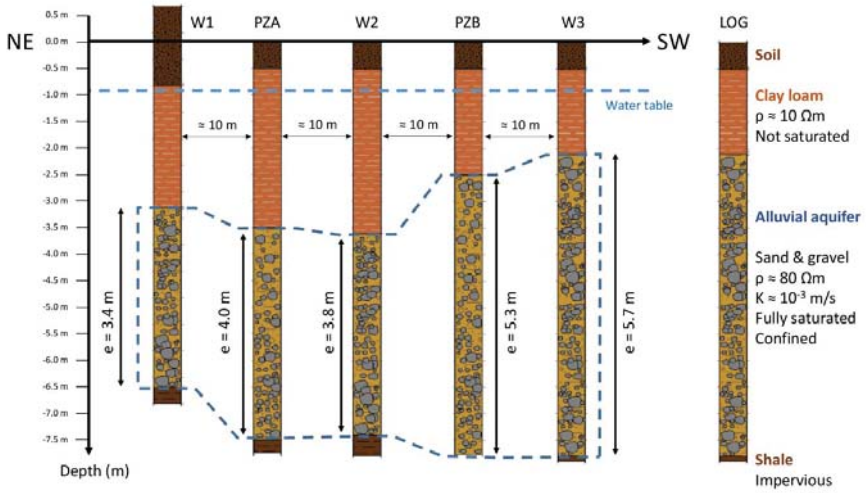

Figure 6: (Hydro) geological cross section of the JSS site.

On a hydrogeological perspective, the shallow clayey loam layer constitutes an aquitard unit (here partially saturated) confining the subjacent fully saturated alluvial aquifer. Hydraulic conductivities in the aquifer were estimated to be 10^{-3} m/s on average over the entire site (not only the area of interest presented here), by means of pumping tests (De Schepper et al., 2018). Nevertheless, pumping tests that Paulus et al. (2016) conducted specifically in W1 & W2 demonstrated that hydraulic conductivity values are heterogeneous inside the area of interest, with a difference of one order of magnitude: 4×10^{-4} m/s in the vicinity of W1 (SW part of the study site) and 4×10^{-3} m/s in the vicinity of W2 (middle part of the study site). The deeper clay layer is almost impervious, acting as an aquiclude unit. The local hydraulic gradient in the aquifer is extremely low (0.01%) with a very slow groundwater flow from north to south. Estimated groundwater fluxes in the main aquifer range therefore between 0.0035 and 0.035 m/d constituting a perfect target for ATES since thermal transport with groundwater flow is expected to be very low.

Paulus et al. (2016) performed an aquifer thermal energy storage and recovery experiment with a storage frequency of 72 hours (mimicking interday frequencies; see section 6 for a detailed discussion of their results in terms of DSM applications). With the collected data set of Paulus et al. (2016), De Schepper et al. (2018) conceptualised, constructed, and calibrated a groundwater flow and heat transport model of the area of interest. This model, transposed in HydroGeoSphere, constitutes the basis of the JSS site model in our library. Table 3 presents most of the hydraulic and thermal parameters of the JSS site.

Table 3: Hydraulic and thermal parameters in the JSS model deduced from experiments (Paulus et al., 2016) and model calibration (De Schepper et al., 2018).

Parameters	JSS alluvial aquifer
Mean hydraulic conductivity [m/s]	$\sim10^{-3}$
Range of hydraulic conductivity [m/s]	4×10^{-4} to 4×10^{-3}
Effective porosity [-]	10
Hydraulic gradient [%]	0.01
Mean Darcy fluxes [m/d]	0.035

Maximum pumping rate [m^3/h]	15 to 20
Thermal conductivity [$Wm^{-1}K^{-1}$]	3.94
Volumetric heat capacity [$MJm^{-3}K^{-1}$]	2
Longitudinal dispersivity [m]	5
Transverse dispersivity [m]	0.5
Groundwater temperature [°C]	9.5 to 11.5

3. DESIGN AND CONSTRUCTION OF THE PREDICTIVE-MODEL ENVIRONMENT

The predictive-model environment is built upon HydroGeoSphere or HGS (Therrien et al., 2010) which is a three-dimensional numerical model describing fully-integrated subsurface and surface flow and solute and heat transport inside porous and fractured media. Our predictive-model environment comprises several numerical models of shallow alluvial aquifers forming a library. Among them, we can find the model of the HSSA site (Figure 7) updated from Klepikova et al. (2016) with new data sets reviewed in this work and in a second step, the model of the JSS site (after De Schepper et al., 2018) as well as the model of the COL site. For the latter, new wells will be available in fall 2018 allowing new experiments, including heat storage and transport. All these models represent then real-world examples.

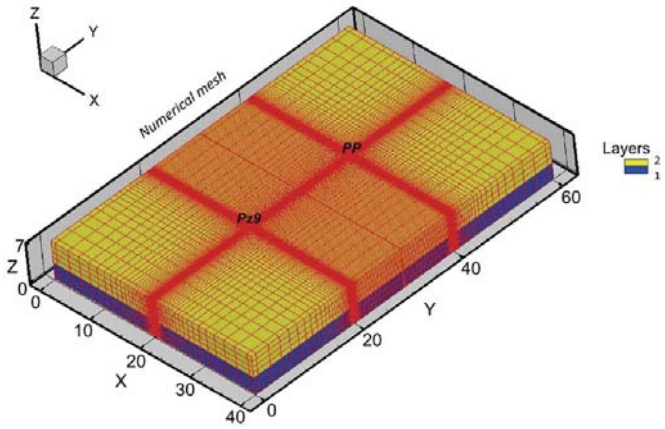

Figure 7: Example of a numerical mesh (from Klepikova et al., 2016) refined around some well positions of the HSSA site.

Our library also comprises a synthetic numerical model representative of typical shallow alluvial aquifers which can be modified as required by the end-user (e.g. to adapt it to a specific case study). Conceptually, this groundwater flow and heat transport model takes all the typical characteristics of previously mentioned aquifers (Figure 8). First, the aquifer is viewed as a rectangular parallelepiped with a length, width, and thickness of L × l × H, presupposing a constant thickness. This rectangular parallelepiped is oriented towards the draining river that prescribes the base water level in the aquifer. Let's assume that the river is in the northern part of the aquifer and that it flows from east to west.

In terms of boundary conditions, we choose to represent a groundwater flow direction towards N (and the draining river) with a hydraulic gradient i that can be modified by changing the prescribed hydraulic heads in the northern and southern limits of the model. By default, we prescribe a constant hydraulic head value per limit. Western and eastern limits are set with a no-flow boundary conditions as a corollary. The model then knows that groundwater flows in by the southern limit (e.g. mimicking the COL site) and flows out by the northern limit (in the river). Vertical recharge is also applied but its use is constrained by the rainfall events that the end-user wants to take into account.

The user can choose to set the model in a confined or unconfined mode, to run simulations under steady or transient states but only in a fully saturated configuration. Since density effects occur because of the nature of this work, density-dependent flow is set by default. The user can use the default hydraulic and thermal parameters or others if data are available for the specific case study in mind. Some options exist to create a heterogeneous distribution of the most sensitive parameters (e.g. the hydraulic conductivity).

The mesh of the numerical model is alterable, allowing layering (e.g. see HSSA site), and can be refined around wells / piezometers positions. Wells / piezometers / observation points can be added easily since all it needs is to specify their position in the model.

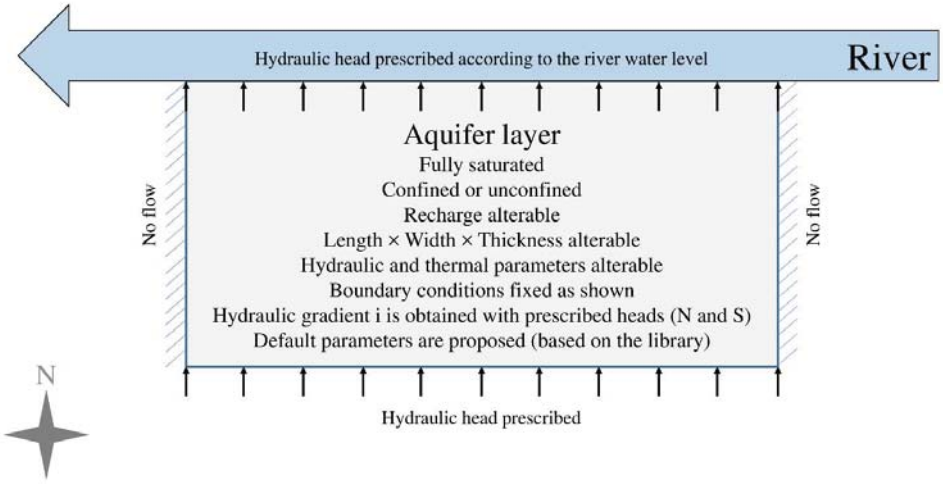

Figure 8: Synthetic shallow alluvial aquifer conceptual model.

4. HOW TO USE THE PREDICTIVE-MODEL ENVIRONMENT

The predictive-model environment is built upon HydroGeoSphere or HGS (Therrien et al., 2010 and https://www.aquanty.com/hydrogeosphere/) which is a three-dimensional numerical model describing fully-integrated subsurface and surface flow and solute/heat transport inside porous and fractured media. To use our toolbox, one must first acquire a valid license of this model.

HGS uses a pre-processor called “grok” that generates all input data files required to run HGS which then solves the problem and generate output data files. Post-processing can then be done to visualise and analyse the data or to import them in another working environment (e.g. numerical models linked to building).

Our toolbox, written in Matlab, is used as a user-friendly interface to create all the necessary files to run grok and then HGS. This work is still ongoing and we will profit from the 10th International Conference on System Simulation in Buildings, Liege, December 10-12, 2018 to adapt our toolbox to specific needs of the building, HVAC, and DSM communities. After that, a tutorial / manual of the toolbox will be written and the predictive-model environment will be available in open-access.

5. DISCUSSION

In this section, we will take another perspective on the heat storage and recovery experiments performed in the HSSA and JSS sites, respectively by Lesparre et al. (2019), Hermans et al. (2018), and Paulus et al. (2016). Indeed, these experiments were first designed to modify the bulk electrical resistivity in the subsurface (with heated water) to monitor with 4D electrical resistivity tomography the dynamics of physical processes occurring in the subsurface (Paulus et al., 2016; Lesparre et al., 2019) or as a way to validate a prediction-focused approach with two different experiments (one being used as data to predict the second, and vice-versa) (Hermans et al., 2018). Taking another look at the results with a specific focus on thermal energy recovery rate and exergy can be instructive when considering high or low temperature ATES for DSM applications.

Paulus et al. (2016) conducted a standard push-pull test (single well test) consisting in injecting heated water (difference of temperature $\Delta T = 30$ K, 16 m³ in total) in the JSS aquifer for 5.33 hours, and after a storage phase of 3 days, to pump it back and measure the amount of recovered energy. Figure 9 gives all the details and data of this experiment. The JSS site is productive (medium hydraulic conductivity) and groundwater flow is very slow (low hydraulic gradient). In such conditions, one can demonstrate that a high amount of energy (up to 75 %) could be easily retrieved after 72 hours of storage. Obviously, exergy has lowered a lot (ΔT was still 12 K at the start of the recovery phase but only 5 K at the end of it) but such ΔT would still improve significantly the GWHP efficiency. As an estimation, the authors consider that up to 90-95 % of the stored energy could have been retrieved by pumping much longer.

Lesparre et al. (2019) conducted the same kind of experiment in the upper aquifer of the HSSA site. The authors injected heated water ($\Delta T = 30$ K, 18 m³ in total) during 6 hours and cold water during 20 minutes ($\Delta T = 0$ K, 1 m³ in total) right after due to a technical failure of the water flow heater. After a storage phase of 91 hours, they pumped it back and measured the amount of recovered energy. Figure 10 gives all the details and data of this experiment. The HSSA site is productive and the upper aquifer has a medium hydraulic conductivity similar to the one in JSS. However, groundwater flow is much significant (the hydraulic gradient is 6 times higher than in JSS).

For this experiment, one can show that only a medium-to-low amount of energy (< 40 % at the maximum) can be retrieved by pumping for a long time (~16 h compared to ~5 h for JSS) and much more groundwater (~78 m³ in total compared to ~37 m³ for JSS, so twice the volume). If we consider equivalent pumped volumes (37 m³) (and considering that the stored energy is similar between both experiments), only 25 % of the stored energy is retrieved in the upper aquifer of the HSSA site (compared to 75 % in JSS). We must highlight that the storage phase lasted longer here (91 h compared to 72 h in JSS, but it is less than a day) and that 1 m³ of cold water pushed heated water farther from the well. Even so, we can conclude

that lower recovery rates are expected when groundwater flow is significant as well as lower exergy (ΔT was here 7 K at the start of the recovery phase but less than 2 K at the end of it). Nevertheless, such ΔT would still improve the GWHP efficiency. To fully compare the two sites, one must redo the same exact experiment performed by Paulus et al. (2016) in HSSA, upper aquifer and test the lower aquifer in the same time. Such experiments are planned in the future.

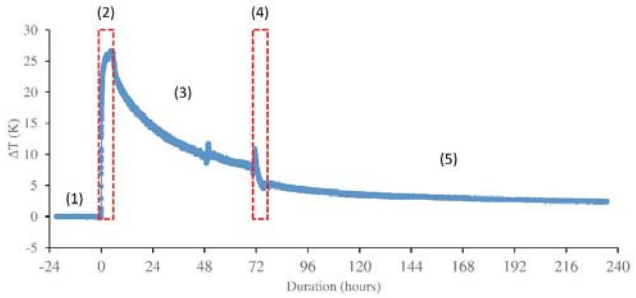

Figure 9: Experiment performed by Paulus et al. (2016): (1) temperature monitoring before injection; (2) injection of heated water (3 m³/h during 5.33 h with a ΔT = 30 K); (3) storage phase (72 h); (4) recovery of heated water (~7 m³/h during 4.5 h, 75 % of the total energy recovered); (5) temperature monitoring after the recovery phase showing that some energy is still stored in the aquifer.

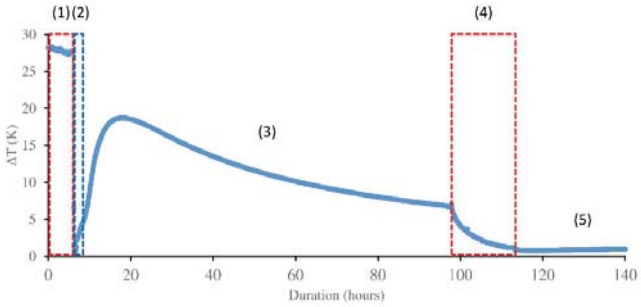

Figure 10: Experiment performed by Lesparre et al. (2019): (1) injection of heated water (3 m³/h during 6 h with a ΔT = 30 K); (2) due to a technical failure of the mobile water flow heater, cold water (ΔT = 0 K) was injected during 0.33 h (1 m³ in total); (3) storage phase (91 h); (4) recovery of heated water (5 m³/h during 15.5 h, 37 % of the total energy recovered); (5) temperature monitoring after the recovery phase showing that almost no more energy recovery is possible.

Hermans et al. (2018) conducted a cyclic push-pull test in the same well as Lesparre et al. (2019), so still in the upper aquifer of the HSSA site. This test consisted in injecting heated water (ΔT = 30 K, 15 m³ in total) for 5 hours, and after a storage phase of 19 hours, to pump it back for 5 hours and measure the amount of recovered energy. After another resting phase of 19 hours, the authors started another cycle. Figure 11 gives all the details and data of this experiment.

After recalculating energy recovery rates, one can demonstrate that for shorter storage periods (less than a day), a medium amount of energy (35 % for cycle 1 and 43 % for cycle 2) is easily retrieved after 5 hours of pumping (45 m³ in total). Exergy is however higher this time. Indeed, ΔT was still 18 K at the start of the recovery phase and 3 K at the end of it for both cycles. Such ΔT would have a significant impact on the GWHP efficiency. If we speak in absolute temperature, a ΔT of 18 K means a temperature of 31°C (the initial groundwater temperature being ~13°C) at the start of the recovery. It misses only a few degree (e.g. to reach 40 – 45°C) to perform space heating for short periods (a quarter to an hour maybe) without the use of a GWHP. Knowing that the system improves with increasing cycles until a full equilibrium is reached between groundwater temperature and the bulk temperature, and knowing that the HSSA site does not present the best characteristics for heat storage (at least for interday and interseasonal frequencies), more experiments need to be performed in the future (and are planned both in HSSA, considered as the worst case scenario, and in COL, which seems to have a behaviour in between JSS and the upper layer of HSSA).

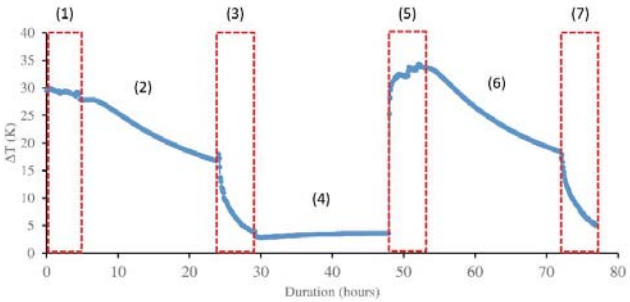

Figure 11: Experiment performed by Hermans et al. (2018): (1) injection of heated water (3 m³/h during 5 h with a ΔT = 30 K); (2) storage phase (19 h); (3) recovery of heated water (5 m³/h during 5 h, 35 % of the total energy recovered); (4) another storage phase before the second cycle; (5) injection of heated water (3 m³/h during 5 h with a ΔT = 35 K); (6) storage phase (19 h); (7) recovery of heated water (5 m³/h during 5 h, 43 % of the total energy recovered); some energy is still available in the aquifer.

6. CONCLUSIONS

We demonstrated that storing thermal energy in the subsurface, and more specifically in shallow alluvial aquifers with ATES systems, has the potential to become a DSM tool in the future by combining the positive effects on flexibility of the low-voltage grid and on the overall GWHP system connected to a building. Experiments reported in this work showed that Walloon shallow alluvial aquifers (along the Ourthe, the Sambre, and the Meuse Rivers) are productive enough to consider the installation of GWHP systems.

In terms of ATES, some aquifers characterised by high (HSSA, lower layer) or medium (HSSA, upper layer and COL) Darcy fluxes are not suited for seasonal DSM frequencies because thermal energy transport with groundwater flow is too prominent. Nevertheless, real time, intraday, and interday (to a certain point) frequencies may be suited since high thermal energy recovery rates can be achieved and to certain point, high-to-medium exergy as well. Other aquifers characterised by lower Darcy fluxes (JSS site) seem suited for all frequencies, including seasonal ones. The rate of thermal energy recovery (and exergy) is then strongly

dependent on groundwater fluxes and on the duration of the storage phase (Table 4; Table 5). Increasing rates come with shorter storage durations and lower groundwater fluxes.

Table 4: Comparison of thermal energy recovery rates for different experiments.

Storage duration → Site	19 hours	72 hours	91 hours
JSS	-	75 % (16 m³ injected, 37 m³ pumped) Up to 90 % with higher pumped volume	-
HSSA, upper layer	35 % for cycle 1 (15 m³ injected, 25 m³ pumped) 43 % for cycle 2 (15 m³ injected, 25 m³ pumped)	-	25 % (18 m³ injected, 37 m³ pumped) 37 % (18 m³ injected, 78 m³ pumped)

Table 5: Comparison of exergy for different experiments.

Storage duration → Site	19 hours	72 hours	91 hours
JSS	-	ΔT from 12 to 5 K T from 22 to 15°C	-
HSSA, upper layer	ΔT from 18 to 7 K T from 31 to 20°C	-	ΔT from 7 to 2 K T from 20 to 15°C

This work also presents a predictive-model environment, composed of a library of real-world subsurface numerical models of shallow alluvial aquifers of Wallonia and a synthetic but representative and flexible numerical model that can be modified easily by the end-user. This toolbox can then be used to "Assess THermal ENergy storage in Aquifers". For this reason, we will call it the ATHENA toolbox.

7. PERSPECTIVES

So far, the ATHENA toolbox only contains the HSSA numerical model in its library but we are working to add both COL and JSS numerical models soon. Concerning the COL site, many experiments are planned in the near future (once the two new 4 inches wells are drilled and equipped, hopefully in fall 2018) including pumping, solute and heat tracer, and push-pull tests monitored or not with geophysical imaging. We will therefore wait for the new data set to construct and calibrate the best model for COL. On the contrary, the JSS site is no longer available for new experiments. Its associated numerical model will be made available once it is published (De Schepper et al., 2018).

New thermal energy storage and recovery experiments are planned in HSSA and COL. Among them, we want to reproduce exactly the same experiment that Paulus et al. (2016) performed in JSS order to compare rigorously the energy recovery rate (and exergy) over different sites presenting different hydraulic and thermal parameters.

REFERENCES

Allen, A., and Milenic, D., 2003. *Low-enthalpy geothermal energy resources from groundwater in fluvioglacial gravels of buried valleys*. Applied Energy 74, 9–19. https://doi.org/10.1016/S0306-2619(02)00126-5

Arteconi, A., Hewitt, N.J., and Polonara, F., 2012. *State of the art of thermal storage for demand-side management*. Applied Energy 93, 371–389. https://doi.org/10.1016/j.apenergy.2011.12.045

Arteconi, A., Hewitt, N.J., and Polonara, F., 2013. *Domestic demand-side management (DSM): Role of heat pumps and thermal energy storage (TES) systems*. Applied Thermal Engineering 51 (1-2), 155-165. https://doi.org/10.1016/j.applthermaleng.2012.09.023

Banks, D., 2009. *Thermogeological assessment of open-loop well-doublet schemes: A review and synthesis of analytical approaches*. Hydrogeology Journal 17 (5), 1149-1155. https://doi.org/10.1007/s10040-008-0427-6

Bayer, P., Rybach, L., Blum, P., and Brauchler, R., 2013. *Review on life cycle environmental effects of geothermal power generation*. Renewable and Sustainable Energy Reviews 26, 446-463. https://doi.org/10.1016/j.rser.2013.05.039

Bloemendal, M., Olsthoorn, T., and Boons, F., 2014. *How to achieve optimal and sustainable use of the subsurface for Aquifer Thermal Energy Storage*. Energy Policy 66, 104-114. https://doi.org/10.1016/j.enpol.2013.11.034

Bonte, M., 2013. *Impacts of shallow geothermal energy on groundwater quality: a hydrochemical and geomicrobial study of the effects of ground source heat pumps and aquifer thermal energy storage*. PhD thesis, Vrije Universiteit Amsterdam, Amsterdam, the Netherlands.

Borgers, R., 2018. *In-depth interpretation of the Ourthe river aquifer*. Bachelor thesis, KULeuven, Leuven, Belgium, 37 p.

Bridger, D.W., and Allen, D.M., 2010. *Heat transport simulations in a heterogeneous aquifer used for aquifer thermal energy storage (ATES)*. Canadian Geotechnical Journal 47 (1), 96-115. https://doi.org/10.1139/T09-078

Bridger, D.W., and Allen, D.M., 2014. *Influence of geologic layering on heat transport and storage in an aquifer thermal energy storage system*. Hydrogeology Journal 22, 233-250. https://doi.org/10.1007/s10040-013-1049-1

Brouyère, S., 2001. *Etude et modélisation du transport et du piégeage de solutés en milieu variablement saturés*. PhD thesis, University of Liège, Belgium (In French).

Brouyère, S., 2003. *Modeling tracer injection and well-aquifer interactions: a new mathematical and numerical approach*. Water Resources Research 39 (3), 1070. https://doi.org/10.1029/2002WR001813

Brouyère, S., Batlle-Aguilar, J., Goderniaux, P., and Dassargues, A., 2008. *A new tracer technique for monitoring groundwater fluxes: the finite volume point dilution method*.

Journal of Contaminant Hydrology 95 (3-4), 121-140. https://doi.org/10.1016/j.jconhyd.2007.09.001

Dassargues, A., Wildemeersch, S., and Rentier, C., 2014. *Graviers de la Meuse (alluvions modernes et anciennes) en Wallonie*. 37-46 (In French). In: Dassargues, A., and Walraevens, K. (ed.), 2014. *Watervoerende lagen & grondwater in België / Aquifères & eaux souterraines de Belgique*. Academia Press, Gent, Belgium, XXIV + 455 p.

Dassargues, A., and Wildemeersch, S., 2014. *Géothermie de très basse température*. 375-381 (In French). In: Dassargues, A., and Walraevens, K. (ed.), 2014. *Watervoerende lagen & grondwater in België / Aquifères & eaux souterraines de Belgique*. Academia Press, Gent, Belgium, XXIV + 455 p.

Defourny, A., 2018. *Push-pull tests for the characterisation of heterogeneity in alluvial aquifers*. Master thesis, University of Liège, Liège, Belgium, 86 p.

De Schepper, G., Bolly, P.-Y., Nguyen, F., and Lesparre, N. 2018. *Hydrothermal management of an urban shallow alluvial aquifer by numerical modelling*. Geophysical Research Abstracts. Vol. 20, EGU2018-12607-1

De Schepper, G., Paulus, C., Bolly, P.-Y., Hermans, T., Lesparre, N., and Robert, T. 2018. *Assessment of short-term aquifer thermal energy storage for demand-side management perspectives: experimental & numerical developments*. Submitted to Applied Energy

Doughty, C., Hellström, G., Tsang, C.F., and Claesson, J., 1982. A dimensionless parameter approach to the thermal behavior of an aquifer thermal energy storage system. Water Resources Research 18 (3), 571-587. http://dx.doi.org/10.1029/WR018i003p00571

Ferguson, G., 2007. *Heterogeneity and thermal modeling of ground water*. Ground Water 45 (4), 485-490. https://doi.org/10.1111/j.1745-6584.2007.00323.x

Fisher, D., and Madani, H., 2017. *On heat pumps in smart grids: A review*. Renewable and Sustainable Energy Reviews 70, 342-357. https://doi.org/10.1016/j.rser.2016.11.182

Fossoul, F., Orban, P., and Dassargues, A., 2011. *Numerical simulation of heat transfer associated with low enthalpy geothermal pumping in an alluvial aquifer*. GEOLOGICA BELGICA, 14 (1-2), 45-54. https://popups.uliege.be:443/1374-8505/index.php?id=3212

Georges, E., Cornélusse, B., Ernst, D., Lemort, V., and Mathieu, S. 2017. *Residential heat pump as flexible load for direct control service with parametrized duration and rebound effect*. Applied Energy 187, 140–153. https://doi.org/10.1016/j.apenergy.2016.11.012

Haggerty, R., Schroth, M.H., and Istok, J.D., 1998. *Simplified Method of "Push-Pull" Test Data Analysis for Determining In Situ Reaction Rate Coefficients*. Ground Water 36 (2), 314-324. https://doi.org/10.1111/j.1745-6584.1998.tb01097.x

Hermans, T., Nguyen, F., and Caers, J., 2015a. *Uncertainty in training image-based inversion of hydraulic head data constrained to ERT data: Workflow and case study*. Water Resources Research 51, 5332-5352. https://doi.org/10.1002/2014WR016460

Hermans, T., Wildemeersch, S., Jamin, P., Orban, P., Brouyère, S., Dassargues, A., and Nguyen, F., 2015b. *Quantitative temperature monitoring of a heat tracing experiment using cross-borehole ERT*. Geothermics 53, 14-26. https://doi.org/10.1016/j.geothermics.2014.03.013

Hermans, T., and Irving, J., 2017. *Facies discrimination with ERT using a probabilistic methodology: effect of sensitivity and regularization*. Near Surface Geophysics 15 (1), 13-25. https://doi.org/10.3997/1873-0604.2016047

Hermans, T., Lesparre, N., De Schepper, G., and Robert, T., 2018. *Bayesian Evidential Learning: a field validation using push-pull tests*. Submitted to Hydrogeology Journal.

Hesaraki, A., Holmberg, S., and Haghighat, F., 2015. *Seasonal thermal energy storage with heat pumps and low temperatures in building projects – A comparative review*. Renewable and Sustainable Energy Reviews 43, 1199-1213. https://doi.org/10.1016/j.rser.2014.12.002

Jamin, P., and Brouyère, S., 2018. *Monitoring transient groundwater fluxes using the Finite Volume Point Dilution Method*. Journal of Contaminant Hydrology 218, 10-18. https://doi.org/10.1016/j.jconhyd.2018.07.005

Klepikova, M., Wildemeersch, S., Hermans, T., Jamin, P., Orban, P., Nguyen, F., Brouyère, S., and Dassargues, A., 2016. *Heat tracer test in an alluvial aquifer: Field experiment and inverse modelling*. Journal of Hydrology 540, 812-823. https://doi.org/10.1016/j.jhydrol.2016.06.066

Lesparre, N., Robert, T., Nguyen, F., Boyle, A., and Hermans, T., 2019. *4D electrical resistivity tomography (ERT) for aquifer thermal energy storage monitoring*. Geothermics, 77, 368-382, https://doi.org/10.1016/j.geothermics.2018.10.011

Lund, J.W., Freeston, D.H., and Boyd, T.L., 2015. *Direct utilization of geothermal energy 2015 worldwide review*. In Proceedings of the World Geothermal Congress 2015, Melbourne, Australia, 31 p. https://doi.org/10.1016/j.geothermics.2015.11.004

Milnes, E., and Perrochet, P., 2013. *Assessing the impact of thermal feedback and recycling in open-loop groundwater heat pump (GWHP) systems: A complementary design tool*. Hydrogeology Journal 21 (2), 505-514. https://doi.org/10.1007/s10040-012-0902-y

Paulus, C., Bolly, P.-Y., Hermans, T., Koo Seen Lin, E., and Robert, T., 2016. *Stockage de chaleur en aquifère et flexibilité de la demande électrique : quelles possibilités ?* 34èmes Rencontres de l'AUGC, Université de Liège, Belgique, 8 p. (In French)

Piessens, K., and Dusar, M., 2004. *Feasibility of CO2 sequestration in abandoned coal mines in Belgium*. Geologica Belgica 7 (3), 165-180

Ruthy, I., and Dassargues, A., 2014. *Carte hydrogéologique de Wallonie, Fleurus-Spy 47/1-2 : Notice explicative* (In French). SPW Editions, Namur, Belgium. Available online at: http://environnement.wallonie.be/cartosig/cartehydrogeo/utilisation_carte.htm

Saner, D., Juraske, R., Kuebert, M., Blum, P., Hellweg, S., and Bayer, P., 2010. *Is it only CO2 that matters? A life cycle perspective on shallow geothermal systems*. Renewable and Sustainable Energy Reviews 14, 1798-1813. https://doi.org/10.1016/j.rser.2010.04.002

Sanner, B., Karytsas, C., Mendrinos, D., and Rybach, L. (2003). *Current status of ground source heat pumps and underground thermal energy storage in Europe*. Geothermics 32 (4), 579-588. https://doi.org/10.1016/S0375-6505(03)00060-9

Therrien, R., McLaren, R., Sudicky, E., and Panday, S., 2010. *HydroGeoSphere: A three-dimensional numerical model describing fully-integrated subsurface and surface flow and solute transport*. Groundwater Simulation Group, Waterloo, ON, Canada.

Vanhoudt, D., Desmedt, J., Van Bael, J., Robeyn, N., and Hoes, H., 2011. *An aquifer thermal storage system in a Belgian hospital: Long-term experimental evaluation of energy and cost savings*. Energy and Buildings, 43 (12), 3657-3665. doi:10.1016/j.enbuild.2011.09.040

Wildemeersch, S., Jamin, P., Orban, P., Hermans, T., Klepikova, M., Nguyen, F., Brouyère, S., and Dassargues, A., 2014. *Coupling heat and chemical tracer experiments for*

estimating heat transfer parameters in shallow alluvial aquifers. Journal of Contaminant Hydrology 169, 90-99. https://doi.org/10.1016/j.jconhyd.2014.08.001

Questions and Answers:

Is there any legal constraint regarding the temperature of aquifer storage?

Tanguy Robert:

Yes, but they are different from one country to another. Regulations are either on absolute temperature or on DT or both. In some countries, however, there is still a possibility to use high temperature (>45°C) but with impact studies to do before the obtention of the permit.

***

What is the impact of pump on COP?

Tanguy Robert:

Submersible pumps have a low impact expecially for system of high capacity (MW).

***

Is the groundwater flow constant?

Tanguy Robert:

Yes because forecasting the subsurface is challenging because of the heterogeinity and of the lack of information. We are working on it.

Optimized control for standing column wells in cold climate

C. Beurcq[1], M. Kummert[1], P. Pasquier[2]

(1) Polytechnique Montréal, dept. of Mechanical Engineering, Montréal (Québec), Canada

(2) Polytechnique Montréal, dept. of Civil, Geological and Mining Engineering, Montréal (Québec), Canada

ABSTRACT

This paper aims at developing and assessing control strategies for Standing Column Well (SCW) ground-source heat pump systems. Pumping flowrate and bleeding ratio (fraction of the flowrate which is not directly reinjected in the SCW) are controlled to minimize the operating cost and risks, while reducing the peak demand and yearly energy use. The building is modelled in TRNSYS and coupled to a Matlab model of the SCW. The SCW model is based on a thermal resistance and capacity model and includes the impact of bleeding and hydrogeological conditions on thermal performance. Some "reactive" control strategies recommended in the literature are assessed and compared to new strategies that use information on the building loads. Results show that different control strategies can have a large impact on operation costs. The load-dependent strategies investigated in this paper can deliver savings from 4% to 8% compared to a well-tuned best-practice control strategy. Optimized control strategies for bleeding ratio can also reduce the total diverted flowrate, reducing environmental risks and maintenance costs. System sizing also has a large impact on performance, and both sizing and operation guidelines are required to ensure the success of SCW systems in cold climates.

Keywords: Standing Column Well, ground-source heat pump, Bleed control strategies, Geoexchange

1. INTRODUCTION

In Canada, cooling and heating energy represents two thirds of the energy used in the commercial and institutional sector while it is almost 80 % in the residential sector. Ground-source heat pumps (GSHPs) can provide heating and cooling efficiently using renewable energy from the ground, benefiting from the constant temperature of the soil beyond a certain depth.

Standing Column Wells (SCWs) are ground heat exchangers that use groundwater to transfer heat from and to the ground and can lead to significant capital cost savings compared to conventional closed-loop geothermal systems if installed in suitable hydrogeological environments. According to recent studies, for a similar installed thermal power, SCWs can show savings on construction costs between 49% to 78% when compared to closed-loop systems (Deng O'Neill et al., 2006). A 9-year monitoring study in the United States showed that six SCWs of 455 m were are able to generate energy savings of more than 685,000 kWh per year in a relatively cold climate (Orio et al., 2006). These large savings with a relatively small number of wells were possible due to the significant thermal power supported by each well (more than 110 kW per SCW).

The real potential of SCWs lies in their capacity of being installed in dense urban areas or in historic districts where a lack of land area impedes the installation of a wide closed-loop system (Pasquier et al., 2016). Another advantage of SCWs is their ability to operate

efficiently in porous or rocky geological formation having a low permeability, where an open-loop system would not be a viable option. Despite a significant potential, SCWs are not widely used outside the north-east of the United States. This is mainly due to a lack of technical expertise outside the geographical areas where SCWs initially emerged.

Figure 1 shows a typical SCW system where a building loop (heat sink or source for decentralized heat pumps) and a loop are connected by a plate heat exchanger. The performance of the decentralized heat pumps connected to the building loop is directly impacted by the fluid temperature at their inlet, i.e. by the temperature at the load side of the heat exchanger. The ground loop consists of a submersible pump immersed in the SCW and a return pipe which is typically inserted within the well. Before reinjecting the groundwater into the SCW, part of the flowrate can be diverted into a separate injection well. This process is called “bleed” and normally improves the system performance by attracting water from the undisturbed neighbouring ground through aquifer fractures. The maximum bleed fraction is dictated by ground conditions and is usually in the order of 10 % to 30 % (Pasquier et al., 2016). This means that 90 % to 70 % of the well flowrate is reinjected directly in the SCW, while the rest is diverted to a nearby sewer, river or injection well. Note that some jurisdictions require to reinject the bleed water to its original aquifer, which is usually achieved by an injection well.

The bleed flowrate cannot usually be maintained at high levels for long periods of time, due to the risk of bringing the water level down too much in the SCW or overflowing the injection well in low permeability aquifers. Bleeding continuously the SCW also increases the risk of clogging the fracture network around the injection well. The total pumping flowrate also influences the residence time of water in the well, which impacts the SCW performance. The pumping power can represent a significant share of the operational costs, and is influenced by two parameters: total flowrate in the ground loop and pumping head. The latter is caused by the activation of the bleed which lowers the groundwater level in the SCW and increases the pumping head.

The total flowrate and the ‘’bleed ratio’’ (fraction of the flowrate diverted) are two control variables important for SCWs installed in cold climate because of the low available margin between the ground undisturbed temperature (typically around or below 10 °C) and the minimum acceptable temperature (above freezing). Auxiliary heating devices with a lower efficiency (e.g. electric resistance heating, natural gas furnaces and conventional chillers for cooling) are typically used when the SCW cannot insure acceptable temperature conditions in the building loop. The setpoints for these auxiliary devices and the control strategy for total flowrate and bleeding will have a significant impact on annual energy use, peak demand, and costs.

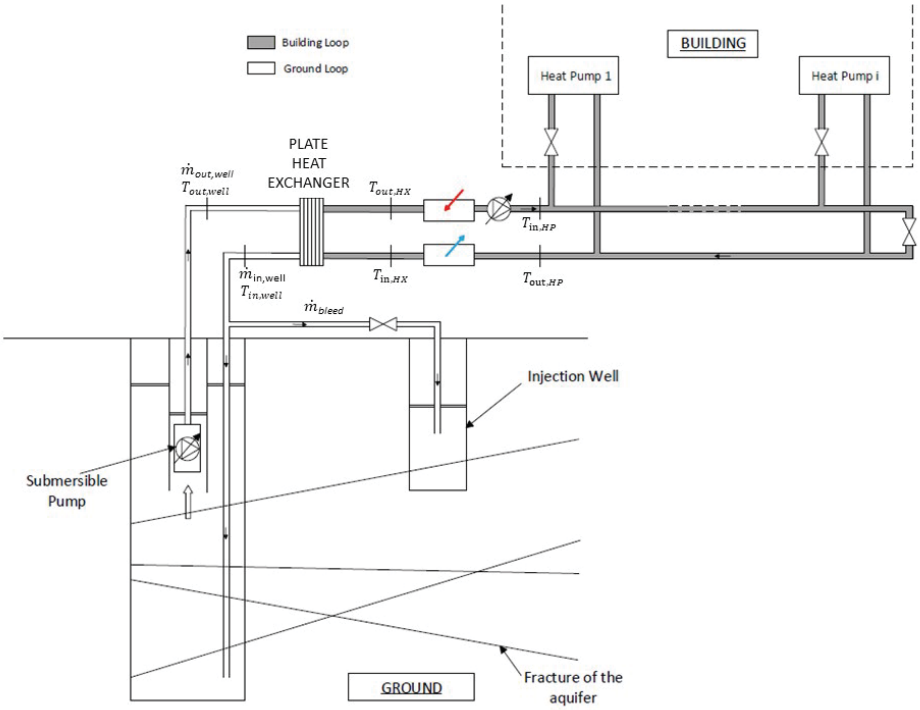

Figure 1:Schematic of the SCW system.

1.1. Control strategies: literature review

Only a few papers investigating bleed control strategies for SCWs were found in the literature. Rees et al. (2004) proposed the following logic:

- Temperature difference: if the difference between the temperature entering and leaving the well is above a given threshold, bleeding is used. The authors use the value of 5.6 °C and a constant 10% bleed ratio.
- Dead-band on well leaving temperature: under a certain temperature coming out of the well, bleeding is used. Bleeding stops when the return temperature from the well has returned above the initial value plus a dead-band. The authors use a level of 5.83 °C to start using bleed and a level of 8.6 °C to stop bleeding, in heating mode (other values are used in cooling mode). Again, a constant 10% bleed ratio is used.

Minea (2013) suggests initiating a 10% bleed in heating mode when the temperature of the groundwater drops below 4.6 °C.

Nguyen et al. (2013) implemented an off-loading sequence of the GSHPs with a three-level bleed control (10%, 20% and 30% of the total flowrate) triggered when the temperature leaving the SCW falls below a prescribed temperature. The control sequence was also designed to start an auxiliary heating system when the groundwater was approaching 4 °C in heating. The main goal of this work was to prevent any risk of groundwater freezing and operational problems with the GSHP while increasing the running time of the heat pumps.

The reviewed control strategies were shown to perform adequately in simulation by their respective authors, but none of the studies presented an explicit optimization of the strategies themselves or their parameters (i.e. thresholds and dead-bands).

2. OBJECTIVES AND METHODOLOGY

The aim of this paper is to investigate control strategies for SCW systems, addressing both the modulation of the (total) pumping flowrate and the modulation of the bleed ratio. Control strategies will be compared to the ones found in the literature in terms of energy use, peak demand, and electricity cost. Conclusions will then be drawn on recommendations for cold-climate SCW control strategies.

The system presented in Figure 1 is modeled in TRNSYS, except for the SCW model, which is implemented in Matlab. The two software programs communicate through a TRNSYS component that allows the user to exchange inputs and outputs (Type 155).

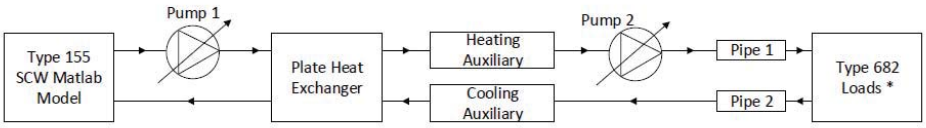

Figure 2: Pattern of the system implemented in TRNSYS.

* The load imposed by Type 682 on the building loop corresponds to the heat transfer on the source-side of decentralized heat pumps in the building, as explained in section 2.2.1.

2.1 Building Loads

A medium three-storey office inspired by the U.S. Department of Energy Prototype Buildings (USDOE-BTO, 2017) is modeled in TRNSYS using the 3D Sketchup plugin and the TRNBuild interface.

Performance parameters and simulation assumptions (e.g. internal gains) follow the ASHRAE Standard 90.1 – 2010 specifications (ASHRAE, 2010). The simulation uses a typical weather file for Montreal, QC (EnvironmentCanada, 2010). The simulated building is artificially scaled up or down to result in peak building loads of 25, 50 and 75 kW as detailed below. Daily average and peak heating and cooling loads are shown in Figure 3. Plotted values represent the heat that must be added to or removed from the building to maintain the desired temperature setpoint. Figure 3 includes the load corresponding to service water heating. No efficiency or coefficient of performance are included.

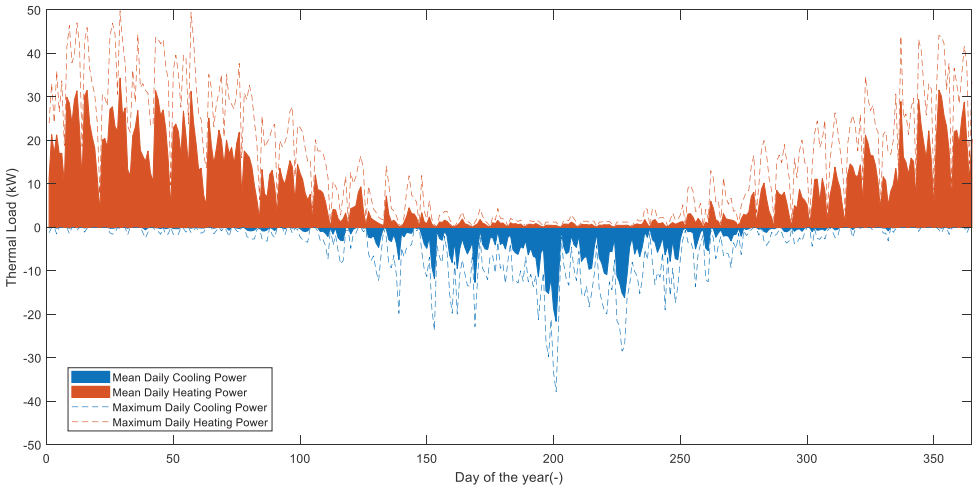

Figure 3: Building thermal load (heating and cooling)

2.2 Building loop

2.2.1 Load

The calculated building thermal load (heating or cooling) is converted into a thermal load on the building loop by a simple heat pump model. Figure 4 presents the method implemented in TRNSYS. To keep the simulation simple, hourly building loads for space heating, service hot water, and space cooling are pre-calculated and read-in by a data reader (Type 9c). Figure 4 and 5 shows the calculation of the thermal load on the building loop using a simple heat pump model.

Some of the heat pumps provide heat to the loop while some others extract heat from it. It is assumed that the actual extra heating or cooling load needed by the loop is provided either by the SCW or the auxiliary system. In the end, the calculated building loop load is sent to a component (Type 682) that imposes the load on its incoming flow stream.

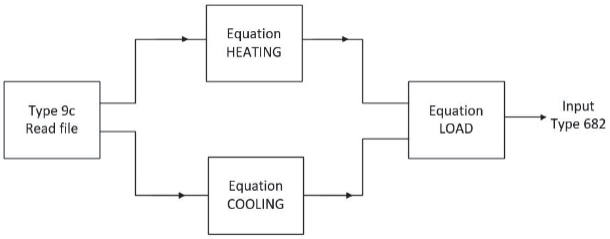

Figure 4: Converting building loads to thermal loads on the building loop.

The TRNSYS equations blocks used in Figure 3 implement the following relationships for the heating and cooling cases (see the nomenclature at the end for a variable description):

$$Q_{loop} = Q_{bldg} - W_c \qquad Q_{loop} = Q_{bldg} + W_c$$

$$\text{with } COP_{heat} = \frac{Q_{bldg}}{W_c} \qquad \text{with } COP_{cool} = \frac{Q_{bldg}}{W_c}$$

$$Q_{loop} = Q_{bldg}\left(1 - \frac{1}{COP_{heat}}\right) \qquad Q_{loop} = Q_{bldg}\left(1 + \frac{1}{COP_{cool}}\right)$$

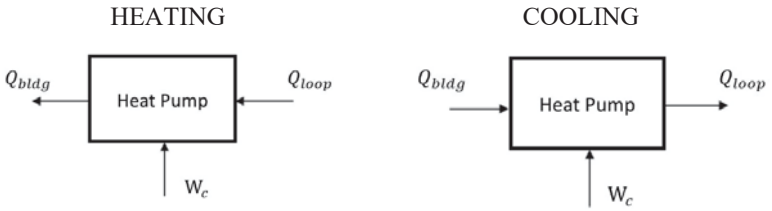

Figure 5: Heat pump in heating mode (left) and cooling mode (right)

In the previous equations, the coefficients of performance (COP) are evaluated with the following equations. Typical values are taken from (Bernier et al., 2007) for heating and cooling and adapted for service water heating (which requires a higher temperature for the delivered heat):

$$COP_{heat} = 3.49 + 0.061 \times T_{in,HP}$$

$$COP_{cool} = 7.92 - 0.117 \times T_{in,HP}$$

$$COP_{swh} = 1 + 0.061 \times T_{in,HP}$$

Figure 6 shows the load on the building loop after calculation. The curves above the horizontal axe represents heating loads while the one under are for cooling loads. Also, the colored areas show the daily mean loads whereas the dotted curves show the maximum load reached during the considered day.

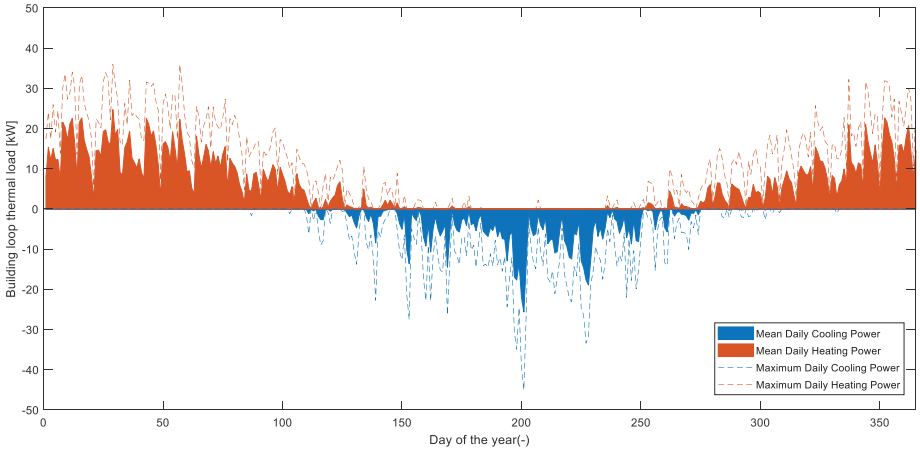

Figure 6: Daily loads on the building loop. A negative value corresponds to cooling mode.

As shown in the equations above, the electrical power used by the heat pump is subtracted from the heating building load but added to the building cooling load to calculate the load on the building loop, which changes slightly the balance between heating and cooling. It also results in a peak cooling load on the building loop which is higher than the peak heating load, while the situation was reversed for the "pure" building loads. Heat pump COPs depend on their inlet temperatures, and the values plotted in Figure 6 were obtained reference scenario 2 described below. Values of the building loop loads will vary slightly for each case.

2.2.2 Pump control in the building loop

In the building loop, the fluid can experience a slightly negative temperature, so a mix of water and glycol is needed to prevent freezing of the fluid in the heat pumps during their operation in heating mode. A fluid composed of 25% of propylene glycol and 75% of water was then selected. The fluid properties were adjusted according to this concentration of propylene glycol.

The pump on the building loop is set to provide a maximum temperature difference of 3 °C at the maximum load on the loop. Figure 7 shows the control of the pump as a function of the load. In this figure, the maximum load for the simulation is 50 kW.

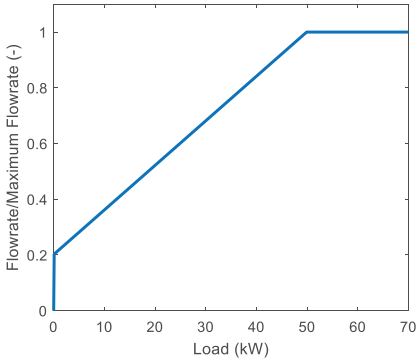

Figure 7: Control Strategy for the pump on the building loop for a 50 kW maximum load.

2.2.3 Auxiliary heating and cooling

In the building loop there are two auxiliary systems for cooling and heating. They operate when the well cannot maintain the building loop within acceptable levels by itself. The auxiliary heating system helps maintaining a minimum temperature of 3 °C in the building loop if the temperature coming back from the well is less than 5 °C with a 1 °C dead-band. This dead-band means that the auxiliary system will start when the temperature coming out from the well is under 4.5 °C and stops when it is above 5.5 °C. For heating, the auxiliary is an electrical resistance with a coefficient of performance set at 1.

For the cooling mode, the same dead-band is applied for a set point temperature of 35 °C if the groundwater comes back at more than 30.5 °C. The cooling auxiliary is conventional chiller that has a performance coefficient of 3.

The power and capacity are supposed to be sufficient to maintain the set point temperature at all time. The consumption of the auxiliary system is studied and part of the cost calculation.

2.2.4 Pipes

The heating and cooling system used for the building includes a piping network that connects the water-to-air heat pumps to the plate heat exchanger as illustrated in Figure 2. The simulation model includes the TRNSYS type 31 for pipes before and after the location of the Load type that simulates the action of the water-to-air heat pumps on the loop. The size of the pipes was adapted to represent a reasonable approximation of the system's thermal mass. The selected value also ensures that the volume of fluid in the pipes is larger than the volume that can be displaced within one time step (1 h) at the maximum flowrate (this helps avoid numerical oscillations). This led to 50-m long pipes with a 0.45-m diameter.

2.3 Ground loop

2.3.1 Matlab Model for the SCW

The SCW model used to perform the simulations is the Thermal Resistance and Capacity Model (TRCM) developed in A. Nguyen et al. (2015b) and A. Nguyen et al. (2015a). The model is written in Matlab and integrates the geometry, thermal conductivity and diffusivity of the surrounding ground, vertical pipes and groundwater through a network of interconnected thermal resistances and capacities. Solution of the model also takes into account the vertical displacement of the groundwater in the SCW and the groundwater flow in the aquifer induced by the bleed. Bleeding results in a reduction of the water level in the extraction well (drawdown D) and in an increase of the water level in the injection well (impression I). The various formulae used to evaluate the resistances and capacities of the network are presented in the original paper describing the model. Note that the model has been validated against several numerical reference solutions.

Table 1: Parameters of the SCW.

Parameter	Value
Borehole Length	300 (m)
Hydraulic conductivity	5.7e-7 (m/s)
Borehole diameter	0.15 (m)
Pump pipe diameter	77.5 (mm)
Porosity	2 (%)

The Matlab model is linked to the simulation via the TRNSYS Type 155. The main parameters of the SCW used are shown in Table 2 and were obtained from the experimental system described by Beaudry et al. (2018). During the simulations, the model receives inputs from TRNSYS and gives back the outputs summarized in Table 3.

Table 2: Inputs and outputs of type 155.

No	Input		Output	
	Name	**Unit**	**Name**	**Unit**
1	Inlet Temperature to the well - $T_{in,well}$	°C	Outlet Temperature of the well - $T_{out,well}$ T_{out}	°C
2	Inlet Flowrate to the well - $\dot{m}_{in,well}$	kg/hr	Outlet Flowrate of the well - $\dot{m}_{out,well}$	kg/hr
3	Bleed flowrate - $\dot{m}_{bleed}$	kg/hr	Bleed flowrate - $\dot{m}_{bleed}$	kg/hr
4	-	-	Drawdown – D	m
5	-	-	Pressure Drop	kPa
6	-	-	Impression in the injection well	m

2.3.2 Submersible Pump (SP)

The submersible pump is responsible for the flowrate on the source side of the plate heat exchanger. The pump is designed with a variable frequency drive that is meant to provide the best efficiency at every time step. The efficiency of the motor and the pump are then set to constant values for our simulation.

Table 3: Parameters for the submersible pump.

Parameter	Value (unit)
Pump efficiency	0.6 (-)
Motor efficiency	0.76 (-)

The simulation of the submersible pump is a key component in the simulation because the electrical consumption of the submersible pump has a significant impact on the overall consumption of the system. The pump consumption is function of the flowrate and pressure drop in the ground loop. The latter includes the pressure drops caused by the drawdown of the dynamical water level in the SCW and pressure drops in the piping network. The pump is modeled by Type 742, which takes an externally calculated pressure drop as an input as well as the flowrate.

The pressure drop is calculated and returned by the Matlab model. It is a function of the temperature and the flowrate, and represents the sum of the pressure drops in: the pipes, the heat exchanger, the elbows and valves of the system. It also considers the drawdown induced by bleeding of the SCW. Table 5 sums up the parameters used for each component included in the total pressure drop.

Table 4:Parameters for the calculation of pressure drop in the ground loop.

Parameter	Units	Length (m)	Diameter (mm)
Rising pipes	1	28	77.5
Reinjection pipe	1	225	48.68
Elbows	6	-	77.5 (3)/ 48.68(3)
Valves	2	-	77.5 (1)/ 48.68(1)

The pressure drop for the plate heat exchanger is a combination of a computation based on Thulukkanam (2013) and manufacturer data of the heat exchanger used in Varennes. The roughness of the pipes used is 0.0000212 and corresponds to the roughness of HDPE pipes.

2.3.3 Bleed and injection well

Different bleeding control strategies are implemented in the simulations. For instance, to prevent the injection well from overflowing, the bleed ratio is set to zero if the water level in the injection well is less than 5 m from the surface. This threshold was chosen based on observations made by Orio et al. (2005) that observed a static water level for commercial buildings that are usually between 5 to 12 m from the surface, with a median value of 6 m. Setting the threshold at 5 m gives a safety margin of 1 m.

2.4 Computation of energy costs

To analyze the simulations, the electricity bill is calculated according to the M rate of the local electricity provider (Hydro-Québec). The billing is divided in two parts for energy and power. The output of the simulation is treated to provide monthly results for energy and power considering heating and cooling provided by the heat pumps and by the auxiliary systems, and the energy used by the submersible pump. The Rate M structure is as follows (units are Canadian Dollars, abbreviated as $ here):

- 14.46 $ per kW for the monthly peak power demand;
- 4.99 ¢/kWh (0.05 $/kWh) for the first 210,000 kWh of the month; and
- 3.70 ¢/kWh (0.037 $/kWh) for the remaining consumption of the month.

The billing demand is the maximum power used by the system during the current month, but is at least 65% of the power used between the 1st of December and 31st of march. For example, if the yearly peak demand occurring in January is 100 kW, and the peak monthly demand for August is 50 kW, the monthly bill for August will use a value of 65 kW (65 % of the winter maximum) and not 50 kW.

3. SIMULATED CASES

We implemented a model that allows us to control the pumping and bleeding flowrates with various control strategies. To obtain consistent results, we compared eight control strategies (Scenarios 1 to 8) to two reference scenarios (Reference 1 and 2). The first reference scenario implements the same building loop without the ground heat exchanger, and relies on auxiliary heating and cooling only. This reference scenario aims at identifying the gain of using a ground heat exchanger. The second reference scenario combines the control strategies usually implemented according to a literature review (dead-band of 3 °C, pumping flowrate of 3GPM/ton (54 L/s-MW) and a 10% bleed ratio). Note that the pump is switched off when there is no load on the building loop. Also, as the temperature thresholds are location dependent, we simulated different cases to derive the best auxiliary heating and cooling set points for our case, which correspond to temperatures of 5 °C and 29 °C, respectively. This was done to ensure that the reference scenario presents a good level of performance with well-tuned simple control strategies.

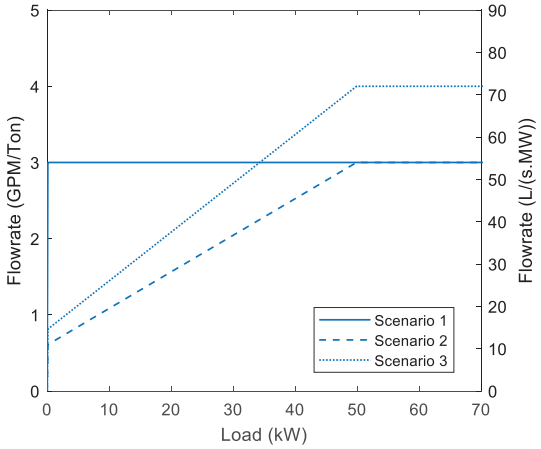

Figure 8: Pumping flowrate control strategies

Scenarios 1 to 3 investigate the control strategies for the total pumping flowrate of the ground loop. These control strategies are shown in Figure 8 and were selected after performing a few preliminary tests. We selected a constant pumping flowrate of 3 GPM/ton (Scenario1) and a linear control of the pumping flowrate as a function of the load applied on the building loop (Scenario 2 and 3). The linear controls have a minimum flowrate corresponding to 20% of the maximum flowrate to account for practical limitations of variable speed drives. Note that these scenarios consider no bleed and a maximum peak load of 50 kW.

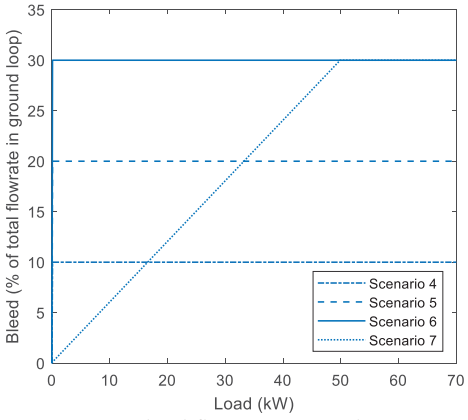

Figure 9: Bleed flowrate control strategies

Scenarios 4 to 7 aim at comparing various control strategies for the bleed and are illustrated in Figure 9. These control strategies are based on the scenario 3 for the pumping flowrate and will be adding a control over bleeding with a constant bleed ratio (Scenario 4 to 6) or a bleed ratio that varies linearly from 0 to 30% as a function of the load applied on the loop.

In Figure 9, the bleed ratio is controlled based on the ratio between the current load and the maximum absolute load, whether the current load is positive (heating) or negative (cooling). Comparing with Figure 7 shows that, since the maximum heating and cooling loads are

different, the maximum flowrate will never be reached in one of the modes. With the situation illustrated in Figure 7, the maximum cooling load on the building loop is about 45 kW and the maximum heating load is about 35 kW. The control law in Figure 9 would calculate the bleed ratio based on the ratio between the current load and 45 kW, therefore only reaching 78 % (=35/45) in heating.

In a last variant (scenario 8), the law represented in Figure 9 is implemented separately for heating and cooling, with their respective maximum values. Using the same example as above, the bleed ratio in heating would be proportional to the ratio between the current heating load and 35 kW, while the bleed ratio in cooling would be proportional to the ratio between the current load and 45 kW.

4. RESULTS AND DISCUSSION

The simulated temperatures on each side of the plate heat exchanger for a peak demand day both in cooling and heating mode are illustrated in Figure 10. In cooling mode, the temperatures remain below 30 °C, which means that the cooling auxiliary (AC) is not used. As the building is designed for a heating-dominated climate, it is not surprising to observe cooling is covered entirely by the geothermal system. We can observe a 3 °C temperature difference between entering and leaving water temperature on the load side of the plate heat exchanger. This observation is consistent with the settings of the simulation as the peak demand of the year is presented in Figure 10. In heating mode, we can observe a temperature close to zero, the freezing point. On that day, the auxiliary heating (AH) system is always operating because the temperature leaving the SCW is always lower than the setpoint of 5 °C mentioned in Section 3. It should be mentioned that the temperature difference is less than 3 °C because the peak demand in heating is lower than in cooling.

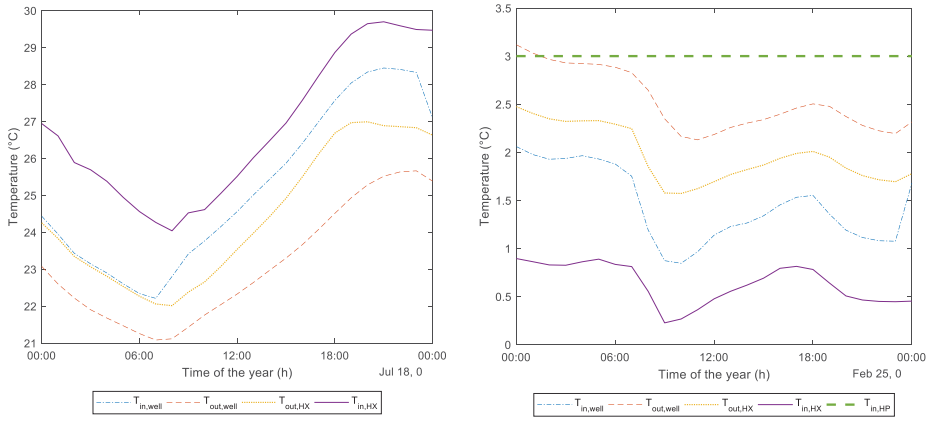

Figure 10: Temperature at the plate heat exchanger for (left) a peak day in cooling mode and (right) a peak day in heating

Looking at figure 9, it is important to note that in cooling mode, $T_{out,HX}$ is equal to $T_{in,HP}$, $T_{out,HP}$, $T_{in,HX}$ because none of the auxiliaries are working. In heating mode, the auxiliary heating is working so $T_{in,HP}$ is different from $T_{out,HX}$ while $T_{out,HP}$ and $T_{in,HX}$ are the same.

4.1 Control of the total pumping flowrate

In this section, the energy consumption and the maximum power demand corresponding to the first three scenarios are compared to the first reference case where no SCW is used to

exchange heat with the building loop. Figure 11 summarizes the results and also shows the portion of the energy or power demand associated to the operation of the heat pumps (HP), auxiliary cooling (AC), auxiliary heating (AH) and submersible pump (SP).

Our results indicate that using a SCW halve the energy consumption and reduce by approximately 30% the power demand (compare Scenario 1 to 3 to Reference 1). This first result confirms the potential of ground heat exchangers to reduce the energy bill. We also observed that using a linear control for the pumping flowrate (Scenario 2 and 3) decreases the total energy consumption and the pumping energy significantly by comparison to the use of a constant flowrate (Scenario 1). Indeed, using a linear control reduces the pumping energy even though the off-peak flowrates lead to less heat exchange and therefore to a higher use of the auxiliary systems.

Comparing the results of Scenario 2 and 3 shows a slight reduction of the energy consumption and power demand when using a maximum flowrate of 4 GPM/ton (Scenario 3). Indeed, a higher flowrate increases the heat exchanged by the SCW, which in turn will help reducing the operation of the auxiliary systems. On the basis of this result, a maximum flowrate of 4 GPM/ton will be used for Scenarios 4 to 8.

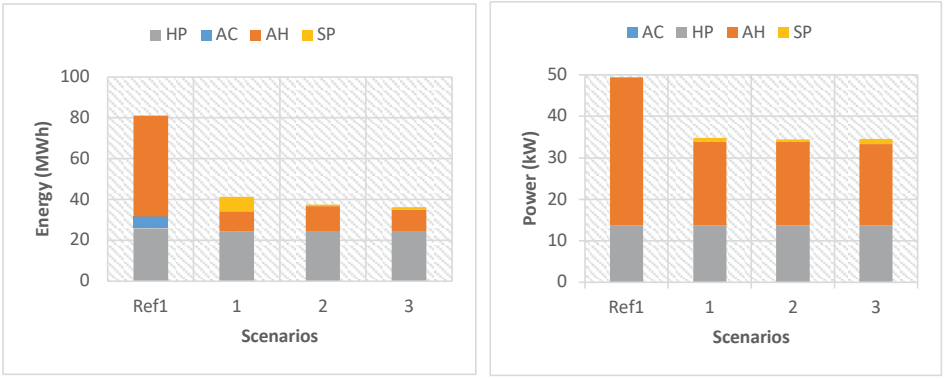

Figure 11: Energy consumption (left) and power demand (right) for Scenario 1,2 and 3.

4.2 Control of the bleed ratio

Figure 12 shows the impact of the control strategy of the bleed flowrate on the energy consumption and the maximum power demand. Our results indicate that using the more complex control strategy of Scenario 4 to 8 helps reducing the energy consumption of approximately 15 to 20% by comparison to the reference scenario 2. The impact on the power demand is however limited and a small variation of only 1.25 kW is observed between the studied cases.

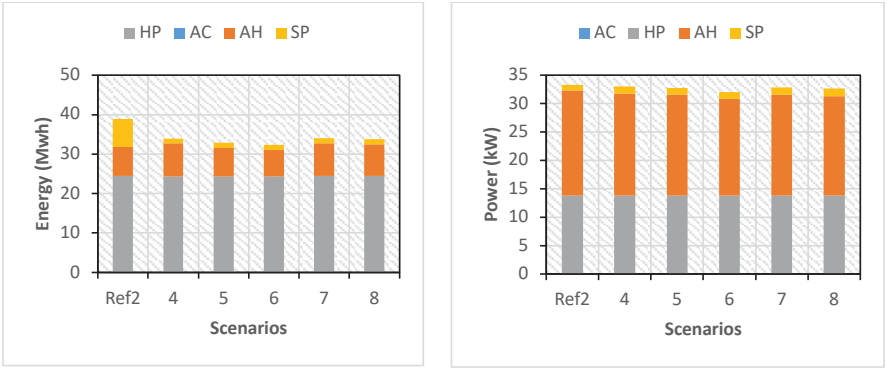

Figure 12: Energy (left) and maximum power (right) for simulations bleeding control

Figure 13 shows the amount of groundwater bled during a year with the control strategies used for the simulations. The volume of groundwater discharged to the injection well varies from 2480 to 7640 m^3 per year for Scenario 4 to 8, with a minimum for Scenario 7 and 8. This is an interesting result because discharging groundwater in the injection well oxygenates the water, which in turn promotes mineral and biological clogging of the injection well. Reducing the volume of groundwater bled is then desirable for the operation of SCW systems. Consequently, the energy consumption and power demand being similar for Scenario 4 to 8, the controls of Scenario 7 and 8 should be preferred since they show a significantly smaller discharged volume of groundwater.

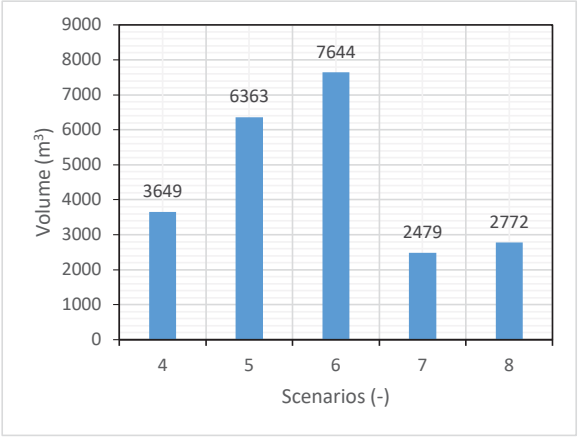

Figure 13: Volume of groundwater bled for different bleed controls

4.3 Financial savings

Table 6 shows the financial savings achieved in comparison to the reference scenarios. Our results indicate that the SCW system provides savings ranging between 39% and 46% with respect to a system having no ground heat exchanger. The savings achieved by improving control strategies are in the range of 4 to 8%, but it should be stressed that the Reference 2 scenario has been tuned by trial and error to the simulated case and represents an “optimized best practice” case.

Table 5: Savings on costs compared to the reference cases

	Reference scenarios		Scenarios Without Bleed control			Scenarios With Bleed control				
	1	2	1	2	3	4	5	6	7	8
Operational Costs ($)	10370	6050	6370	6160	6090	5790	5690	5580	5770	5730
Savings compared to Reference 1 (%)	-	-	38.6	40.6	41.2	44.2	45.1	46.2	44.3	44.8
Savings compared to Reference 2 (%)	-	-	-	-	-	4.3	5.9	7.8	4.6	5.3

4.4 Influence of system sizing (fraction of the building load covered by the SCW)

Figure 14 shows the operating costs for buildings having different peak loads but connected to a single SCW. Unsurprisingly, we can see that as the peak load diminishes, the operating cost also diminishes. The reduction is however much more interesting for the geothermal system since the load covered by the SCW increases with a smaller building.

The non-geothermal references show a total cost divided in 40% for energy and 60% for power costs. For the 50 and 75 kW cases, power is responsible for 70% of the total cost. Regarding the billing rates, it is better to give priority on lowering the peak power and then the energy.

These figures also show how important it is to size SCW systems (as all types of geothermal systems) properly to match their capacity to the building needs. Proper sizing allows to limit the use of auxiliary heating and cooling and to maximize the savings of ground-source systems.

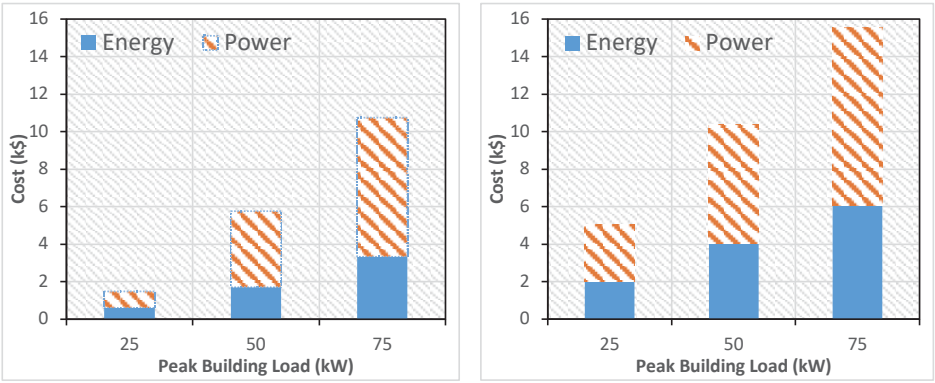

Figure 14: Comparison of the power and energy costs for the different peak power demand (25, 50 and 75 kW) with (left) a SCW system and (right) no geothermal system

5. CONCLUSION

The operation of SCW systems involves two major control variables: the total pumping flowrate (water extracted from the SCW) and bleeding ratio (fraction of the flowrate which is not directly reinjected in the same well).

The results presented in this paper show that using a linear control on the pumping flowrate has a major influence on the pumping energy required. The control strategy must achieve a balance between pumping energy use and using more auxiliary energy for heating or cooling. The control of bleeding ratio shows cost savings from 4 to 8% compared to bleed control strategies found in the (scarce) literature on SCW systems. The most important point about bleed control is the reduction of the volume of groundwater bled which will have a significant impact on operational cost of the SCW system especially concerning the injection well maintenance.

It seems necessary to develop design guidelines for SCW system to help sizing underground components compared to building loads. Guidelines are also lacking to select control strategies for the total pumping flowrate and the bleeding ratio, and the authors help that this paper will be a first step towards developing such guidelines for cold climate operation.

Further work should address more complex control strategies such as predictive control, and assess system performance for different combinations of building types, control strategies, and climates.

6. REFERENCES

ASHRAE. (2010). *Energy Standard for buildings except low-rise residential buildings (Standard 90.1-2010)*. Paper presented at the Atlanta, GA, USA: American Society of Heating, Refrigerating and Air-conditioning Engineers.

Beaudry, G., Pasquier, P., & Marcotte, D. (2018). *Hydrogeothermal Characterization and Modelling of a Standing Column Well Experimental Installation*. Paper presented at the International Ground Source Heat Pump Association (IGSHPA), Conference 2018.

Bernier, M., Kummert, M., & Bertagnolio, S. (2007). *Development and application of test cases for comparing vertical ground heat exchanger models.* Paper presented at the International Building Performance Simulation Association (IBPSA) Conference 2007.

Deng O'Neill, Z., Spitler, J. D., & Rees, S. J. (2006). Performance Analysis of Standing Column Well Ground Heat Exchanger Systems. *ASHRAE Transactions, 112*(2).

EnvironmentCanada. (2010). *Canadian Weather Energy and Engineering Data Sets (CWEEDS files) and Canadian Weather for Energy Calculations (CWEC files) updated user's manual.* Paper presented at the Ottawa, ON, CAN: Environment Canada. Retrieved from http://climate.weather.gc.ca/prods_servs/engineering_e.html.

Minea, V. (2013). Experimental investigation of the reliability of residential standing column heat pump systems without bleed in cold climates. *Applied Thermal Engineering, 52*(1), 230-243.

Nguyen, Pasquier, P., & Marcotte, D. (2013). Development of an ODE model featuring a three level bleed control and an off-loading sequence for standing column wells. *Proceedings of BS2013, Chambéry, France*, 26-28.

Nguyen, A., Pasquier, P., & Marcotte, D. (2015a). Influence of groundwater flow in fractured aquifers on standing column wells performance. *Geothermics, 58*, 39-48.

Nguyen, A., Pasquier, P., & Marcotte, D. (2015b). Thermal resistance and capacity model for standing column wells operating under a bleed control. *Renewable Energy, 76*, 743-756.

Orio, C. D., Chiasson, A., Johnson, C. N., Deng, Z., Rees, S. J., & Spitler, J. D. (2005). A Survey of Standing Column Well Installations in North America. *ASHRAE Transactions, 111*(2).

Orio, C. D., Johnson, C. N., & Poor, K. D. (2006). Geothermal Standing Column Wells: Ten Years in a New England School. *ASHRAE Transactions, 112*(2).

Pasquier, P., Nguyen, A., Eppner, F., Marcotte, D., & Baudron, P. (2016). Standing column wells *Advances in Ground-Source Heat Pump Systems* (pp. 269-294): Elsevier.

Rees, S. J., Spitler, J., Deng, Z., Orio, C., & Johnson, C. (2004). A study of geothermal heat pump and standing column well performance. *ASHRAE Transactions, 110*(1), 3-13.

Thulukkanam, K. (2013). *Heat exchanger design handbook*: CRC press.

USDOE-BTO. (2017). Commercial Prototype Building Models. Retrieved February 28, 2017, from https://www.energycodes.gov/development/commercial/prototype_models.

7. NOMENCLATURE

AC – Auxiliary Cooling

AH – Auxiliary Heating

COP – Coefficient of performance (subscript will indicate if it is for cooling, heating or service water heating)

D – Drawdown (lowering of the water level in the extraction well due to bleeding)

GPM – Gallons Per Minute

GSHP – Ground Source Heat Pump

HDPE – High-Density Polyethylene

HP – Heat Pump

I – Impression (water level rise in injection well due to bleeding)

$\dot{m}_{bleed}$ – Bleed Flowrate

$\dot{m}_{in,well}$ – Flowrate entering the well (= flowrate leaving the well minus the bled flowrate)

$\dot{m}_{out,well}$ – Flowrate leaving the well

Q_{bldg} – Building thermal load

Q_{loop} – Thermal load on the building loop

SCW – Standing Column Well

SP – Submersible Pump

SWH – Service Water Heating

$T_{in,well}$ – Temperature of groundwater entering the well

$T_{out,well}$ – Temperature of groundwater leaving the well

$T_{in,HX}$ – Temperature entering the heat exchanger on load side

$T_{out,HX}$ – Temperature leaving the heat exchanger on load side

$T_{in,HP}$ – Temperature entering the heat pumps on building loop

$T_{out,HP}$ – Temperature leaving the heat pumps on building loop

TRNSYS – Transient System Simulation tool

W_c – Energy consumption of the heat pump (energy required by the compressor)

Questions and Answers:

Isn't the supply temperature of the floor heating too high? Why?

Camille Beurcq:

It is just a given study case, for sure, using a lower temperature would improve the performance of the system.

Development of sophisticated heat pump heating systems considering different storage technologies: A comparative simulation study

Christian Vering[1], Lars Schellhas[1], Moritz Lauster[1], Dirk Müller[1]

[(1)]RWTH Aachen University, E.ON Energy Research Center, Institute for Energy Efficient Buildings and Indoor Climate, Mathieustraße 10, 52074 Aachen, Germany

ABSTRACT

Achieving national climate goals is a major challenge of the energy sector in Germany. The building stock obtains about 30 % of overall energy consumption, which is mostly related to provision of buildings with residential heat and domestic hot water. In order to develop a climate-neutral building stock until 2050, a transition of chain of heat supply has to be both climate-neutral and efficient. In this context, heat pump heating systems are awarded to be a key technology by utilizing ambient heat and electricity to provide useful heat. The efficiency of heat pumps strongly depends on both design and operation. Using storage systems, operational efficiency can be increased.

Within this work, we contribute to the understanding of storage system integration in heat pump heating systems. Therefore, we precisely model thermal behaviour of a typical existing building and link it to a heat supply system consisting of heat pump, heat storage and electrical backup heater. The heat storage can be a sensible water tank, a PCM-storage or an adsorption storage. Each storage is integrated in the heat supply system by adapting simple control strategies, which are developed using finite automata.

Applying yearly simulations, a relative comparison of different heat storages is conducted in the context of heat pump heating systems. The simulation results show, that all systems are operable and ensure permanent heat supply. Furthermore, the system efficiency is utilized to assess energetic performance of the presented systems. We show, that the PCM-storage does not improve system efficiency compared to the hot water tank. However, the adsorption storage exhibits an increase of this reference value by about 10 %.

Keywords: Storage system integration, heat pump heating systems, efficiency comparison

1. INTRODUCTION

New technical solutions reducing global greenhouse gas emissions are required to match stated climate goals. In Germany about 30 % of energy consumption belongs to the building stock mostly providing buildings with residential heat and domestic hot water (Energiebilanzen AG 2018). Fossil fuel fired boilers still are the most widely used residential heating technology. Therefore, an exchange of this technology, that emits carbon dioxide by burning fuel, offers the potential to reduce emissions systematically.

Compression heat pumps are awarded as key technology in this context. They utilize low temperature ambient heat by pumping it to higher temperatures using an electrical driven compressor. Hence, covering this ambient heat reduces emissions of this technology.

Enabling high heat pump efficiencies, thermal storage systems need to be integrated in the heating system. However, many storage systems are available, the most common ones are hot water storage tanks (HWS). Although the hot water tanks are sophisticated and have been widely used for decades, alternative heat storage technologies might offer better overall efficiency. (Sharma und et al. 2009), (Cabeza 2017)

In the context of heating systems, alternative storage systems are phase change material storages (PCM) or adsorption storage systems (AS). Both have higher energy densities compared to HWSs. Thus, it is possible to design these storages to be smaller than HWSs. Concurrently, heat losses dissipating to the environment are reduced based on smaller storage surfaces. In addition, both technologies imply different advantages. Regarding PCM storage, utilizing the phase change on a well-defined use case distinguished PCM temperature level, heat can be stored within a close range around phase change temperature. Thereby, average storing temperature can be reduced compared to HWS which increases efficiencies of heat pumps. Furthermore, a lower temperature level decreases dissipation loss to the environment. Considering AS, vacuum sorption technology allows a nearly lossless storage system. Related to discontinuous charge and discharge process, an AS is a highly complex system that needs to be sophisticatedly controlled to ensure high system efficiencies. Additionally, due to high heating powers, an AS can be an option to replace the heat pumps' electrical backup heater in order to reduce electricity consumption. (Sharma und et al. 2009), (Cabeza 2017)

Within this paper, we contribute in three main chapters to the investigation of different thermal storage systems using detailed building energy system simulation studies:

- In Chapter 2 we present our simulation model setup containing models of heat generation technology, storage system and building physics.
- We show in Chapter 3 HWS and PCM intended control setups. Furthermore, we present a control strategy allowing the use of AS storage systems. First commissioning results complement this Chapter.
- Finally, Chapter 4 shows different results of energetic performance of all systems including thermal losses, charging behaviour and Seasonal Coefficient of Performance (SCOP).

Summarising all results, we discuss our simulation study in detail including advantages and drawbacks of the presented systems. In the end, we will give an outlook on future work that needs to be done.

2. VALUATION AND MODELLING OF HEAT PUMP HEATING SYSTEMS

Heat pumps and refrigerators are the most common applications of vapour refrigeration processes. Their inner efficiency is defined by the Coefficient of Performance (COP), which describes the ratio of useful heat $\dot{Q}_{\mathrm{Use}}$ and expended electricity P_{el}:

$$COP = \frac{\dot{Q}_{\mathrm{Use}}}{P_{\mathrm{el}}} \tag{1}$$

Simplifying this equation by idealizing assumptions, COP is entirely related to the temperature of the heat source T_{Evap} and the heat sink T_{Cond} of the system:

$$COP = \frac{T_{\mathrm{Cond}}}{T_{\mathrm{Cond}} - T_{\mathrm{Evap}}} \tag{2}$$

Comparing different storage technologies within this work, we set up a heat source of ambient heat and leave it unchanged. Hence, the evaporation temperature T_{Evap} of all systems will be the same. Due to different charging processes, heat source related efficiency increases occur coincidental because of heat absorption at times of higher evaporation temperatures. This means we do not consider demand side management strategies to charge the storage systems at preferably high evaporation temperatures. However, we show effects of different storage technologies on the condenser temperature $T_{\mathrm{Cond}}$and its consequences on efficiency.

Assessing the whole impact of the storage on the system efficiency for one year, a wider energy balance limit needs to be intended. Therefore, we use the Seasonal Coefficient of Performance ($SCOP$) following the normative standard DIN EN 14825 (Deutsches Institut für Normung 2016):

$$SCOP = \frac{\dot{Q}_{\mathrm{Use}} + \dot{Q}_{\mathrm{Backup}}}{P_{\mathrm{el}} + P_{\mathrm{el,Backupdate}}} \tag{3}$$

Compared to Equation 1, we calculate the integral of both thermal and electrical powers and divide them for a period of one year. Additionally, to fulfil comfort requirements, an electrical backup heater is set up to support the heat pump, if the heat provision is too low.

This implies an estimation of storage losses that need to be balanced by higher or lower heating demands within the whole period.

2.1 Model development of the residential heating system

The modelled system consists of a reference house, an air-to-water heat pump and the examined heat storage technologies in between as shown in Figure 1. The house is represented by its heating demand throughout one year (Mehrfeld 2016). Heat is provided by an air-water heat pump, which is modelled as a black box model using the theoretical maximum coefficient of performance (COP) multiplied with a constant efficiency factor for air-water heat pumps of 0.35, which is typical for On-/Off-controlled heat pumps (Kaltschmitt, Streicher und Wiese 2013). The electrical backup heater has an efficiency of 1. For the calculation of the COP the same ambient temperature data is used which was used to perform the heating demand analysis for the reference building (Mehrfeld 2016), (Deutscher Wetterdienst 2004). It is a typical building for the German building stock with a year of construction about 1960. It has an insulation standard following WSchV84 and a net area of 250 m².

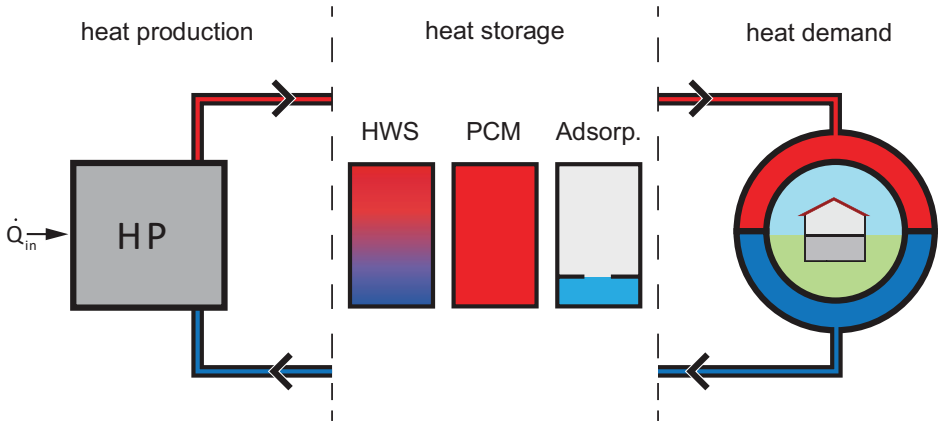

Figure 1 - Schematic representation of the relevant components of the heating system.

Since the heating set temperature range of the system influences the heat pump efficiency, all systems were tested for both radiator and underfloor heating, respectively using a temperature range of 25 °C to 35 °C for underfloor heating and 40 to 60 °C regarding the radiator heating system.

To be able to easily exchange storage simulation models a common basic interface of four fluid ports for the heating medium and one heat port covering heat losses are implemented.

2.2 Model development of the Considered Heat Storages

To examine the influence of the heat storage technology on the system efficiency three models for different storage technologies are tested. In the following part the heat storage mechanisms and the model development of the individual storage models is covered. All storages share the same basic interface with the residential heating system.

2.2.1 Sensible Heat Storage

The hot water storage represents as of today the standard technology for buffer storages in residential heating systems. Therefore, a hot water storage system was used as reference case for comparison. Based on the buffer storage model of the open-source Modelica library AixLib (Müller, et al. 2016), the hot water storage was modelled. It contains five layers of different temperatures, considering static buoyancy and conduction as described by Viskanta et al. (1977). All geometric and material properties were taken from the values deposited in the library for a 500 l storage. The properties of the hot water storage, regarding insulation and total heat capacity have been adopted for all investigated storages to directly compare the storage technology influence on heating systems SCOP.

2.2.2 Latent Heat Storage

To use latent heat as a heat storage a storage with phase change material (PCM) is needed. Based on a model described by Leonhardt (2016), (2009), (2010) the phase change is represented by a temperature dependent specific heat capacity, using the derivation of the arctic tangent. In the liquid as in the solid state the heat capacity is approximately 2.5 kJ / (kg K), while in a range of 10 K around the melting temperature the phase change enthalpy of Δh_{PCM} = 165 kJ / kg is absorbed. These values are taken from the model for paraffins by Leonhardt (2016), (2009), (2010).

The amount of PCM was chosen in a way that the total latent heat would match the heat capacity of the hot water storage within a range from 20 °C to 60 °C, which is approximately 24 kWh. To take the different heating temperatures into account, the phase change temperature was defined to be 318 K for the radiator system and 313 K for the floor heating system.

A challenge of PCM storages often is the low heat conductivity of solid PCMs. To provide heat demand higher temperature gradients or larger heat exchangers are required, which is thermodynamically and economically not favourable. This heat conductivity behaviour was included in the analysis by using a model of the heat transfer in PCMs by Leonhardt (2016), (2009), (2010).

2.2.3 Adsorption Heat Storage

A model for the adsorption process of the adsorption pair silica-gel-123/water was provided by the Institute of Technical Thermodynamics of the RWTH Aachen University. It´s based on

the TIL Suite (TLK-Thermo GmbH 2012) and the adsorption library SorpLib (Lehrstuhl für Technische Thermodynamik - RWTH Aachen 2017) for Modelica.

The adsorption storage consists of

- adsorbent,
- condenser and
- evaporator.

Though condenser and evaporator could be realised as a single combined part, they are split in this work. That way the condensation heat, which occurs during the charging process, can be used within the water-based heating circle, while the evaporator uses ambient air to provide the required heat to discharge the adsorption storage.

Condenser and evaporator are modelled as phase separators, based on the phase equilibrium of water regarding temperature and pressure. Both are connected by one-way valves so that water from the condenser can be returned and vice versa. Through a heat port in the phase separator model, the charging and discharging process can be realized. The connections of condenser and evaporator to the adsorbent is implemented as diffuse mass transfer model.

3. MODEL DEVELOPMENT OF THE SYSTEM CONTROLS

In order to perform yearly simulation of the presented system, control strategies for the technologies need to be implemented. Both the HWS and the PCM storage are controlled with a typical state of the art ambient temperature dependent two-point hysteresis control. Compared with this, the AS needs a more sophisticated control strategy to ensure continuous system control.

In Figure 2 a two-point hysteresis control is schematically depicted by a hybrid automata with the states s_0 and s_1 and its transition conditions e_1 and e_2. State s_0 describes a working heat pump. An exceed of the hysteresis temperature above a well-defined level turns of the heat pump (s_0), which is state s_1. Falling below a new temperature level, the heat pump is turned on (e_2) again.

Regarding temperature levels, we implemented a heating curve that linearly determines the set temperature depending on ambient temperature. Using normative standards, the maximum (minimum) set temperature at an ambient temperature of $T_{\mathrm{Amb}} = -15\ °C$ is $T_{\mathrm{set,max}} = 60\ °C$ ($T_{\mathrm{set,min}} = 55\ °C$) considering both underfloor and radiator heating systems. However, the slope of the heating curves differs for each heating system. On the one hand, underfloor heating maximum temperature is linearly decreased to 40 °C at an ambient temperature of 25 °C. The slope of the minimum temperature development is the same. The Radiator heating system has a maximum set temperature at 25 °C of 45 °C on the other hand. The minimum temperature slope equals the maximum slope, too.

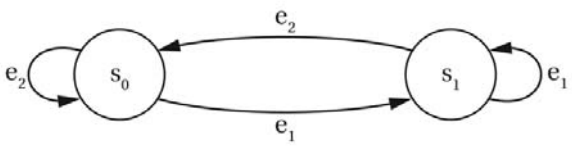

Figure 2 - Schematic representation of the 2-point control of hot water and PCM storage systems.

As mentioned before, AS systems work discontinuously. To ensure continuous operation conditions, two adsorber beds are required. Therefore, a different control strategy needs to be implemented.

The control of the AS is more complex than a two-point hysteresis control as shown in Figure 3. Herein, nine states (from state s_0 to s_8) are depicted with different transition conditions (e_1 to e_{14}).

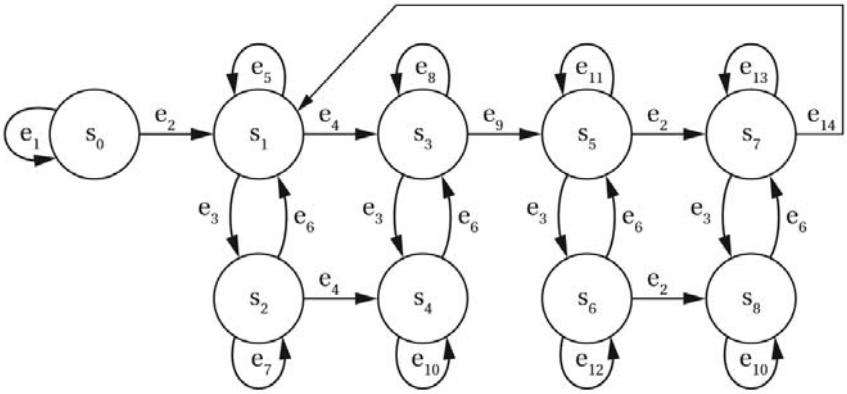

Figure 3 - Schematic representation of the on/off control of examined adsorption storage systems.

In general, each simulation starts in state s_0. Thereby both adsorber beds are charged. After that, four columns are possible system states with different system transitions. All states and transitions are explained in Table 1 and Table 2.

Table 1 - States of heat pump and adsorber beds.

State	Charge Bed 1	Charge Bed 2	Discharge Bed 1	Discharge Bed 2	Heat Pump on
s_0	1	1	0	0	1
s_1	0	1	1	0	1
s_2	0	1	0	0	1
s_3	0	0	1	0	0
s_4	0	0	0	0	0
s_5	1	0	0	1	1
s_6	1	0	0	0	1
s_7	0	0	0	0	0
s_8	0	0	0	1	0

Table 2 - Transition condition of charging and discharging the adsorber beds.

Transition	Condition
e_1	$T_1 \leq T_{\mathrm{max,des}}$
e_2	$T_1 > T_{\mathrm{max,des}}$

e_3	$T_{\text{Buffer}} > T_{\text{max}}$
e_4	$T_2 > T_{\text{max,des}}$
e_5	$[T_{\text{Buffer}} \leq T_{\text{max}}] \cap [T_2 \leq T_{\text{max,des}}]$
e_6	$T_{\text{Buffer}} < T_{\text{min}}$
e_7	$[T_{\text{Buffer}} \geq T_{\text{min}}] \cap [T_2 \leq T_{\text{max,des}}]$
e_8	$[T_{\text{Buffer}} \leq T_{\text{max}}] \cap [T_1 - T_{\text{min}} \geq \Delta T]$
e_9	$T_1 - T_{\text{min}} < \Delta T$
e_{10}	$T_{\text{Buffer}} \geq T_{\text{min}}$
e_{11}	$[T_1 \leq T_{\text{max,des}}] \cap [T_{\text{Buffer}} \leq T_{\text{max}}]$
e_{12}	$[T_1 \leq T_{\text{max,des}}] \cap [T_{\text{Buffer}} \geq T_{\text{min}}]$
e_{13}	$[T_{\text{Buffer}} \leq T_{\text{max}}] \cap [T_2 - T_{\text{min}} \geq \Delta T]$
e_{14}	$T_2 - T_{\text{min}} < \Delta T$

Within a commissioning test, the functionality of all storage systems is proved. This test is depicted in Figure 4. For a period of one year, the relevant storage temperatures are presented. One can see the different heating temperature levels regarding winter time (~ first 100 days and last 50 days) and summer time (~ centred 200 days). This indicated a successful implementation of the heating curve in the controller.

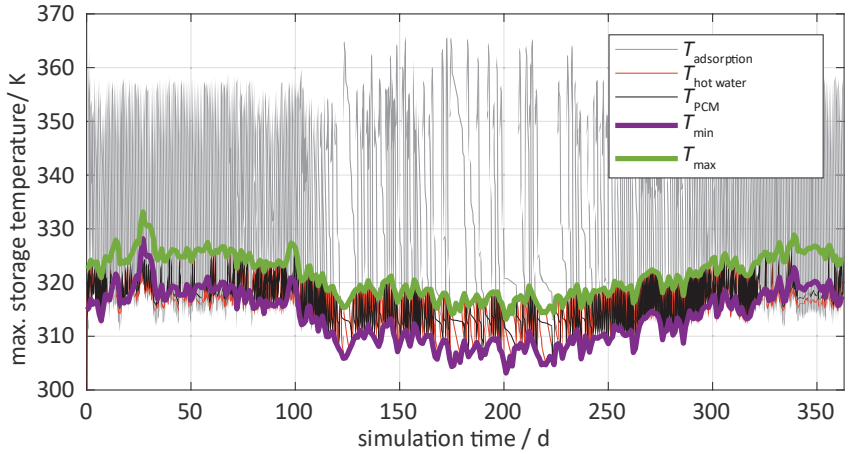

Figure 4 - Annual course of the storage tank temperature in the floor heating system.

In addition, one can see that the PCM storage temperature T_{PCM} as well as the hot water temperature $T_{\text{Hot water}}$ is within the band of minimum and maximum temperature. This indicates a well-implemented two-point hysteresis control strategy for both heating systems. Due to highly nonlinear performance of adsorption processes, the AS temperature $T_{\text{Adsorption}}$ exceeds the maximum temperature level in each charging process. Few fall downs of lower temperature level indicate, that the sophisticated control strategy is successfully implemented so that detailed analysis of all three systems can be done.

4. ENERGETIC COMPARISON OF HEAT STORAGE SYSTEMS

Within this paper we discuss effects on two energetic indicators that are revealed by our simulation studies. These are storage heat losses and $SCOP$. Besides these, other factors like

electrical backup heater demand and power consumption of the heat pump are investigated. These results will be published within the extended paper version.

In Figure 5 storage heat losses for one year of each technology are shown for underfloor and radiator heating. Due to higher set temperatures the radiator system heat losses are slightly higher than the underfloor system ones, respectively.

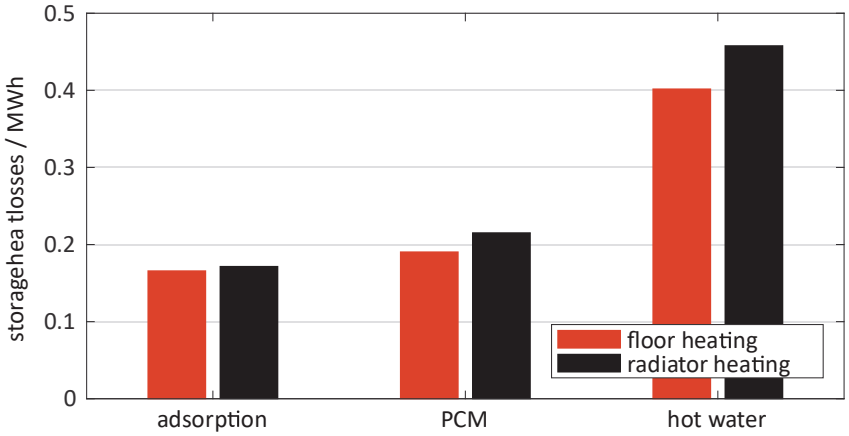

Figure 5 - Cumulative heat losses of the storage variants.

Additionally, Figure 5 reveals that adsorption storage heat losses are about 20 % lower than PCM storage losses and about a factor of 2.5 lower compared to HWS. These losses are about 180 kWh. These mainly indicates a more compact design because of higher energy densities and a lower heat loss transferred to the environment.

This has an impact on system overall efficiency as shown in Figure 6. It can be seen that the efficiency of the HWS system nearly equals the efficiency of the PCM storage system with an $SCOP$ of about 2.2 for underfloor heating and 2.1 for radiator heating.

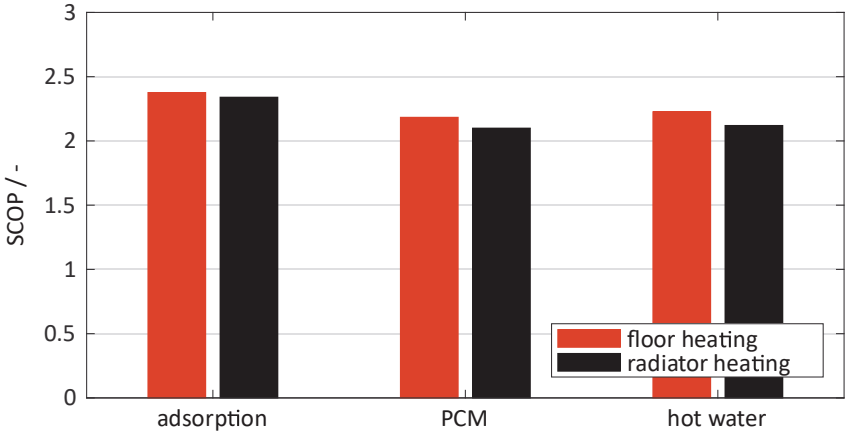

Figure 6 - Seasonal Coefficients of Performance of the systems examined.

The AS system outperforms the other technologies with an efficiency about 2.45 for underfloor heating and 2.4 for radiator heating which is an increase by about 10 %.

Comparing PCM and HWS technology regarding residential heating systems, the HWS is preferable for these temperature levels because it is a cheaper and a fully developed technology compared to a PCM storage. Considering the increase of SCOP by using an AS system, the AS system is an interesting technology that needs to be investigated for sophisticated heat pump heating systems with high efficiencies.

5. DISCUSSION AND CONCLUSION

Within this work, we present a simulation model, mainly based on open source libraries, for yearly energy building simulations comparing different storage technologies in combination with a non-modulating heat pump.

An overview over modelling approaches and further literature is given and the development of typical control strategies is shown.

The commissioning tests show, that all three storage technologies can be successfully integrated in the building energy system simulation.

Evaluating yearly simulations, one can see that the AS outperforms the HWS and the PCM storage. Due to its high complexity, further research must be done, to include AS technology economically in building energy systems. Comparing PCM and HWS, the energetic performance nearly equals. Considering economic effects, the HWS is preferable to a PCM storage.

6. REFERENCES

Arteconi, A., N.J. Hewitt, and F. Polonara. “Domestic demand-side management (DSM): Role of theat pumps and thermal energy storage (TES) systems.” *Applied Thermal Engineering* 51, no. 1-2 (2013): 155-165.

Ashrae Handbook. New-York, 1977.

AST, H. "IEA Annex 10 - System simultaion : Thermostactic Valve." Stuttgart, Germany, n.d.

Baetens, R., and D. Saelens. “Modelling uncertainty in district energy simulations by stochastic residential occupant behaviour.” *Journal of Building Performance Simulation* 9, no. 4 (2015): 431-447.

Baetens, R., R. De Coninck, F. Jorissen, D. Picard, L. Helsen, and D. Saelens. “OpenIDEAS - an open framework for integrated district energy simulations.” *14th Conference of International Building Performance Simulation Association.* Hyderabad, India, 2015. 347-354.

Bouvenot, J.-B, et al. “Gas Stirling engine - CHP boiler experimental data driven model for building energy simulation.” *Energy and Buildings 84*, 2014: 117-131.

Brandemuehl, M.J., S. Gabel, and I. Andersen. “A toolkit for secondary HVAC System Energy Calculations.” *ASHRAE*, 1993.

Braun, J. E. & Lee, K.-H. “Assessment of demand limiting using building thermal mass in small commercial buildings.” *ASHRAE Transactions*, 2006: 112 PART 1, 547-558.

Cabeza, L. F. “Review on sorption materials and technologies for heat pumps and thermal energy storage.” *Renewable and Sustainable Energy Reviews* 110 (2017): 3-39.

Candanedo, José A., Vahid R. Dehkordi, and Phylroy Lopez. “A multi-level architecture to facilitate MPC implementation in commercial buildings: basic principles and case study.” *Proceedings of eSim 2014 conference.* 2014.

Claeys, B., and M. Sourbron. “Pas het elektriciteitstarief aan voor meer groene warmte (in Dutch).” *De Tijd, Opinion piece.* 24 May 2017.

“Code van goede praktijk voor de toepassing van warmtepompsystemen in de woningbouw (in Dutch).” *Computer software manual.* 2004.

Coffey, Edward Brian. “Approximating model predictive control with existing building simulation tools and offline optimization.” *Journal of Building Performance Simulation* 6, no. 3 (2013): 220-235.

Commission des Communautés Européennes. “"Etude CIEL" : Maîtrise de la Demande Electrique Campagne de Mesures par usage dans le secteur domestique.” n.d.

CSTB. *Règlementation Thermique 2012 - Règles d'application Th-Bât.* CSTB Edition, 2012.

Cyx, W., N. Renders, and M. Van Holm. “IEE TABULA - Typology Approach for Building Stock Energy Assessment.” Technical report, VITO, Vlaamse instelling voor technologisch onderzoek, 2011.

Cyx, W., N. Renders, M. Van Holm, and S. Verbeke. “IEE TABULA - Typology Approach for Building Stock Energy Assessment.” 2011.

Daikin Europe N.V. "Technical data sheets for Altherma EVLQ-CV3, Multisplit 4MXS, Split FTXM35+RXM25." Brussels, 2018.

Deutscher Wetterdienst. “Testreferenzjahr 2004.” 2004. https://www.dwd.de/DE/leistungen/testreferenzjahre/testreferenzjahre.html (accessed 08 02, 2016).

Deutsches Institut für Normung. “DIN EN 14825 - Luftkonditionierer, Flüssigkeitskühlsätze und Wärmepumpen mit elektrisch angetriebenen Verdichtern zur Raumbeheizung und -kühlung - Prüfung und Leistungsbemessung unter Teillastbedingungen und Berechnung der saisonalen Arbeitszahl.” 2016.

Dugaria, S., L. Moro, and D. Del Col. “Modelling heat and mass transfer in a membrane-based air-to-air enthalpy exchanger.” *33rd UIT (Italian Union of Thermo-fluid-dynamics) Heat Transfer Conference.* 2015.

Elia. *Déséquilibre actuel du système.* 6 July 2018. http://www.elia.be/fr/grid-data/balancing/desequilibre-actuel-du-systeme.

Energiebilanzen AG. “Evaluation tables from 1990-2017.” 2018.

Enertech, ADEME, and Union Européenne. “Projet REMODECE : Mesure de la consommation des usages domestiques de l’audiovisuel et de l'informatique - Rapport final.” 2008.

Engie. "Engie Easy Fixed 1y tariffs for electricity and gas." May 2018.

Entsoe Transparancy Platform. “Day-ahead electricity prices.” n.d.

Euroheat & Power. "Ecoheatcool project - Workpackage 3: Guidelines for assessing the efficiency of district heating and district cooling systems." Technical report, Euroheat & Power, 2005-2006.

European Comission. “Smarter, greener, more inclusive? Indicators to support the Europe 2020 strategy.” Luxembourg (LU), 2013.

European Parliament. “The primary energy factor for renewables.” *Parliamentary questions.* 19 November 2016.

Forsén, Martin. “Heat pumps - technology and environmental impact.” Technical report, Swedisch Heat Pump Association, European Heat Pump Association, 2005.

Gendebien, S, S Bertagnolio, and V Lemort. “Investigation on a ventilation heat recovery exchanger: Modeling and.” *Energy and Buildings* 62 (2013): 176-189.

Georges, E., S. Gendebien, S. Bertagnolio, B. Dechesne, and V. Lemort. “Evolution des profils de consommations énergétiques des bâtiments résidentiels en Belgique, suite à l'introduction de nouvelles technologies de chauffage, climatisation et cogénération.” Liège (Belgium), 2013.

Händel, Claus. “Ventilation with heat recovery.” *Rheva Journal*, 2001.

Henze, Gregor P, Clemens Felsmann, and Gottfried Knabe. “Evaluation of optimal control for active and passive building thermal storage.” *International Journal of Thermal Sciences* 43, no. 2 (2004): 173–183.

Henze, Gregor P, Thoi H Le, Anthony R Florita, and Clemens Felsmann. “Sensitivity Analysis of Optimal Building Thermal Mass Control.” *Journal of Solar Energy Engineering* 129, no. 4 (2006): 473-485.

Huchuk, Brent , Cynthia A. Cruickshank, William O’Brien, and H.Burak Gunay. “Recursive thermal building model training using Ensemble.” *Proceedings of eSim 2014 conference.* 2014.

Hydro-Québec. “Hydro-Québec demande à ses clients de poursuivre leurs efforts de réduction de la consommation d'électricité en période de pointe et les remercie de leur collaboration.” 22 01 2014. http://cnw.ca/ONjV5 (accessed August 01, 2014).

IBPSA-Canada. “Model predictive control in buildings workshop.” 2011. http://www.ibpsa.us/conferences (accessed September 10, 2014).

IEA, and IPEEC. “Building energy performance metrics - Supporting energy efficiency progress in major economies.” Technical report, IEA, IPEEC, 2015.

ISO-1. “ISO 10211:2008 - Thermal bridges in building construction - Heat flows and surface temperatures - Detailed calculations.” 2008.

ISO-2. “ISO 10456: 2008 - Building materials and products - Hygrothermal properties - Tabulated design values and procedures for determining declared and design thermal values.” June 2008.

ISO-3. “ISO 13370: 2008 - Thermal performance of buildings - Heat transfer via the groung - Calculation methods.” April 2008.

ISO-4. “ISO 13790: 2013 - Energy performance of buildings - Calculation of energy use for space heating and cooling.” *Energy performance of buildings - Calculation of energy use for space heating and cooling.* 2013.

ISO-5. “ISO 6946:2008 - Building components and building elements - Thermal resistance and thermal transmittance - Calculation method.” 2008.

Jespers, Kaat, Jad Al Koussa, Yoko Dams, Nele Renders, and Pieter Vingerhoets. “Inventaris hernieuwbare energiebronnen Vlaanderen 2005-2016 (in Dutch).” Technical report, VITO, Vlaams instituut voor technologisch onderzoek, 2017.

Kaltschmitt, Martin, Wolfgang Streicher, and Andreas Wiese. *Erneuerbare Energien: Systemtechnik, Wirtschaftlichkeit, Umweltaspekte.* Heidelberg: Springer Verlag, 2013.

Kelly, George E. “Control system simulation in North America.” *Energy and Buildings* 10, no. 3 (1988): 193–202.

Keys, William Morrow, and Michael E Crawford. *Convective heat and mass transfer* . 1980.

Knight, I. “IEA Annex 42 - The simulation of Building-Integrated Fuel Cell and other cogeneration systems (FC+COGEN-SIM) : Domestic Energy Profiles.” Cardiff (UK), 2007.

Koester, S., M. Falkenberg, M. Logemann, and M. Wessling. “Modeling heat and mass transfer in cross-counterflow enthalpy exchangers.” *Journal of Membrane Science*, 2017: 68-76.

Kummert, Michaël , Marie-Andrée Leduc , and Alain Moreau . “Using MPC to reduce the peak demand associated with electric heating.” *Model Predictive Control in Buildings Workshop.* Montréal, Quebec, 2011.

Lebrun, J., X. Ding, J.-P. Eppe, and M. Wasac. “Cooling Coil Models to be used in Transient and/or Wet Regimes. Theoretical Analysis and Experimental Validation.” *Proceedings of SSB.* Liège, 1990. 405-411.

Lehmann, B, D Gyalistras, M Gwerder, K Wirth, and S Carl. “Intermediate complexity model for Model Predictive Control of Integrated Room.” *Energy and Buildings* (Elsevier), no. 58 (2013): 250–262.

Lehrstuhl für Technische Thermodynamik - RWTH Aachen. “SorpLib 3: Adsorption Energy System Library.” Aachen, 2017.

Leonhardt, Corinna. *Thermische Speicher mit Phasenwechselmaterialien im Heizsystem.* Aachen, 2016.

Leonhardt, Corinna, and Dirk Müller. “Latent Heat Storage Devices for Heat Pump and Solar Heating Systems.” 2010.

—. “Modelling of Residential Heating Systems using a Phase Change Material Storage System.” *Proceedings of the 7th International Modelica Conference.* Como, 2009.

Liang, C.H. “Experiments Investigation of the Parallel-plates Enthalpy Exchangers.” *The 6th International Conference on Applied Energy.* 2014. 2699 – 2703.

Luminus. “Luminus #BeGreenFix tariffs for electricity and gas.” May 2018.

Müller, D., M. Lauster, A. Constantin, M. Fuchs, and P. Remmen. “AixLib - An Open-Source Modelica Library within the IEA-EBC Annex 60 Framework.” *BauSIM*, September 2016: 3-9.

Ma, Y, and F. Borrelli. “Hierarchical Predictive Control Energy Efficient Buildings.” *Model Predictive Control in Buildings Workshop.* Montreal, 2011.

Madson, H, and J Holst. “Estimation of continuous-time models for the heat dynamics.” *Energy and Buildings* (ELSEVIER), 1995: 67-79.

May-Ostendorp, Peter , Gregor P Henze, Charles D Corbin, Balaji Rajagopalan, and Clemens Felsmann. “Model-predictive control of mixed-mode buildings with rule extraction.” *Building and Environment* 46, no. 2 (2011): 428–437.

May-Ostendorp, Peter T, Gregor P Henze, Balaji Rajagopalan, and Charles D Corbin. “Extraction of supervisory building control rules from model predictive control of windows in a mixed mode building.” *Journal of Building Performance Simulation* 6, no. 3 (2013): 199-219.

Mehrfeld, Philipp. *Reference Building Model.* Aachen: E.ON Energy Research Center, Institute for Energy Efficient Buildings and Indoor Climate, 2016.

Morari, Manfred, and Jay H. Lee. “Model predictive control: past, present and future.” *Computers & Chemical Engineering*, 1999: 667–682.

Morisot, O., and D. Marchio. “Simplified Model for the Operation of Chilled Water Cooling Coils Under Nonnominal Conditions.” *HVAC&R Research*, 2002: 135-158.

Nasif, M., R. AL-Waked, G. Morrison, and M. Behinia. “Membrane heat exchanger in HVAC energy recovery systems, systems energy analysis.” *Energy and buildings* , 2010: 1833-1840.

Nasif, Mohammad Shakir, Ra’fat Al-Waked, Masud Behnia, and Graham Morrison. “Modeling of Air to Air Enthalpy Heat Exchanger.” *Heat Transfer Engineering*, 2012: 1010-1023.

Nassif, N, S Kajl, and R Sabourin. “Simplified model-based optimal control of VAV air conditioning system.” Montreal: Proceedings of the 9th international building performance simulation association (IBPSA) conference, 2005a.

Nassif, N, K Stainslaw , and R Sabourin. “Optimization of HVAC control system strategy using two-objective genetic algorithm.” *International Journal of HVAC&R Research* 11, no. 3 (2005b): 459-486.

Niu, J.L., and L.Z. Zhang. “Membrane-based Enthalpy Exchanger: material considerations and clarification of moisture resistance.” *Journal of Membrane Science*, 2001: 179-191.

Oldewurtel, F, A Parisio, C.N Jones, and M Morari. “Energy efficient building climate control using Stochastic Model Predictive Control and weather predictions.” *American Control Conference (ACC).* Baltimore, MD , 2010. 5100 - 5105.

Oldewurtel, Frauke, et al. “Use of model predictive control and weather forecasts for energy efficient building climate control.” *Energy and Buildings* , no. 45 (2012): 15–27.

Patteeuw, D. “Demand response for residential heat pumps in interaction with the electricity generation system.” PhD Thesis, KU Leuven, Belgium, 2016.

Prívara, Samuel , Jiří Cigler, Zdeněk Váňa, Frauke Oldewurtel, Carina Sagerschnig, and Eva Žáčeková. “Building modeling as a crucial part for building predictive control.” *Energy and Buildings* 56 (2013): 8–22.

Reynders, G. “Quantifying the impact of building design on the potential of structural storage for active demand response in residential buildings.” PhD Thesis, KU Leuven, Belgium, 2015.

Rosato, A., and S. Sibilio. “Calibration and validation of a model for simulating thermal and electric performance of an internal combustion engine-based micro-cogeneration device.” *Applied Thermal Engineering 45-46*, 2012: 79-98.

Roulet, C.-A, F.D Heidt, F Foradini, and M.-C Pibiri. “Real heat recovery with air handling units.” *Energy and Buildings* 33, no. 5 (2001): 495-502.

Sebai, R., R. Chouikh, and A. Guizani. “Cross-flow membrane-based enthalpy exchanger balanced and unbalanced flow.” *Energy Conversion and Management*, 2014: 19-28.

Sharma, A., and et al. “Review on thermal energy storage with phase change materials and applications.” *Renewable and Sustainable Energy Reviews* 13, no. 2 (2009): 318-345.

Six, Daan, Johan Desmedt, Dirk Vanhoudt, and John Van Bael. “Exploring the flexibility potential of residential heat pumps combined with thermal energy storage for smart grids.” *21st International Conference on Electricity Distribution.* Frankfurt, Germany, 2011. 1-4.

Stephan, W. “IEA Annex 10 - System simulation : Radiator.” Stuttgart (Germany), n.d.

Sturzenegger, David, Dimitrios Gyalistras, Vito Semeraro, Manfred Morari, and Roy S Smith. “BRCM Matlab Toolbox: Model Generation for Model Predictive Building Control.” *American Control Conference.* 2014.

Sweetnam, T., M. Fell, E. Oikonomou, and T. Oreszczyn. “Domestic demand-side response with heat pumps: controls and tariffs.” *Building Research & Information*, 2018: 1-18.

Swinton, Michael C, Hussein Moussa, and Roger J Marchand. *Commissioning Twin Houses for Assessing the Performance of Energy-Conserving Technologies.* Thermal Performance of the Exterior Envelopes of Whole Buildings VIII, 2001.

TLK-Thermo GmbH. “TIL Suite.” 2012. https://www.tlk-thermo.com/index.php/de/softwareprodukte/til-suite (accessed 11 14, 2018).

Verhelst, C., F. Logist, J. Van Impe, and L. Helsen. “Study of the optimal control problem formulation for modulating air-to-water heat pumps connected to a residential floor heating system.” *Energy and Buildings* 45 (2012): 43-53.

Verhelst, Clara, Maarten Sourbron, Stefan Antonov, and Lieve Helsen . “Towards MPC for office buildings with TABS connected to a GCHP system controller model.” *Model Predictive Control in Buildings Workshop.* Montreal, 2011.

Viskanta, R., M. Behnia, and A. Karalis. “Interferometric observations of the temperatur estructure in water cooled or heated from above.” *Advances in Water Resources*, Nr. 2 1977: 57-59.

VREG. “Hoeveel kost 1 kWh elektriciteit/aardgas? Prijzen voor huishoudelijke afnemers (all in, incl. BTW) (in Dutch).” 2018.

Wang , Shengwei, and Xinhua Xu. “Simplified building model for transient thermal performance estimation.” *International Journal of Thermal Sciences*, no. 45 (2006): 419–432.

Wang, Shengwei , and Xinqiao Jin. “Model-based optimal control of VAV air-conditioning system using genetic algorithm.” *Building and Environment* 35, no. 6 (2000): 471–487.

Wetter, Michael. “GenOpt® -- A Generic Optimization Program.” Proceedings of the 7th IBPSA Conference, 2001.

—. “GenOpt, Generic Optimization Program, User Manual Version 3.1.0.” 2011. http://gundog.lbl.gov/GO/ (accessed July 01, 2014).

Wystrcil, et al. “Model-based optimization of control strategies for low-exergy space heating systems using an environmental heat source.” *13th Conference of International Building Performance Simulation Association.* Chambéry: BS2013, 2013.

Zeng, Cheng, Shuli Liu, and Ashish Shukla. “A review on the air-to-air heat and mass exchanger technologies for building applications.” *Renewable and Sustainable Energy Reviews*, 2017: 753-774.

Zhang, Li-Zhi. “Heat and mass transfer in plate-fin enthalpy exchangers with different plate and fin materials.” *International Journal of Heat and Mass Transfer*, 2009: 2704-2713.

TENTH SESSION
NON-CONVENTIONAL HVAC SYSTEMS

NUMERICAL INVESTIGATION OF ENERGY POTENTIAL AND PERFORMANCE OF A RESIDENTIAL BUILDING-INTEGRATED SOLAR μCHP SYTEM

Simon Martinez[1]*, Ghislain Michaux[1], Patrick Salagnac[1], Jean-Luc Faure[2]

(1) LaSIE, UMR-CNRS 7356, Université de La Rochelle, av. Michel Crépeau, 17 042 la Rochelle Cedex 1, France

(2) Département de Génie Civil, Faculté des Sciences et Technologie, Université de La Rochelle, av. Michel Crépeau, 17 042 la Rochelle Cedex 1, France

ABSTRACT

The studied micro-CHP unit converts concentrated solar energy into electricity and heat by coupling a 46.5 m² parabolic trough collector with an oil-free single-cylinder steam engine operating according to the Hirn cycle. Originalities of this system are two axis solar tracking and direct steam generation. The exhaust heat of the cycle is recovered to cover building's heat needs, while the electricity is either self-consumed or fed back into the electricity grid. Experimental studies have shown that it is impossible to achieve continuous operation of the facility without an additional heat source. Thus, we are studying solutions for integrating a backup heating system from dynamic thermal simulations performed with TRNSYS© software One of them consists in adding a 30 kW boiler to the primary circuit in order to ensure daily electricity production. However, this is restricted by the considered storage tank. A parametric study on the volume of the storage tank makes it possible to propose an optimal solution for heat recovery. The results indicate that a storage volume of 3 m^3 meets the needs of the building and limits the heat losses due to heat storage. In order to optimize the use of such a micro-CHP unit, a heat sharing between several buildings equipped with 3 m^3 storage seems therefore to be a coherent solution.

Keywords: micro-CHP, distributed generation, solar energy, concentrating solar power, direct steam generation, building, numerical simulation

1. INTRODUCTION

Micro-CHP is a distributed generation of electricity and heat for low electrical power (<50 kWel) [1] [2]. The principle is to recover waste heat during electrical production using a thermodynamic cycle. This heat can then be used to cover heating and domestic hot water needs of a building.

Micro-CHP reduces primary energy consumption and greenhouse gas emissions with higher efficiency than separate production of electricity and heat [3]. It should also be noted that in Europe, the recent "Climate Energy Package" agreements signed in 2014 aim to increase renewable energies in the energy mix by up to 27 %, reduce greenhouse gas emissions by at least 40 % and improve the energy efficiency of systems by at least 27 % by 2030 [4]. A micro-CHP unit operating from concentrated solar energy can therefore meet the objectives previously mentioned. In this context of integrating renewable energies into the energy mix and improving the efficiency of energy production systems, many micro-CHP units using renewable energies are currently under study [5].

The solar micro-CHP unit studied here converts concentrated solar energy into electricity and heat by coupling a 46.5 m² parabolic trough collector with an oil-free single-cylinder steam engine operating according to a Hirn cycle. This system has been the subject of several previous works [6] [7] [8] dealing with the evaluation of performances of the solar concentrator, the steam engine and the whole system. Experimental studies have shown that it is impossible to ensure continuous operation of the installation without an additional heat source [9].

Studies on the integration of micro-CHP units into buildings have already been conducted. Concerning a SenerTech's DACH micro-CHP unit, Campos-Celador *et al.* [10] proposed a thermo-economic study of the integration into a 160 kW boiler room supplying a group of residential buildings. Thanks to annual simulations carried out with TRNSYS16© software, the building's needs have been determined. From a comprehensive study [11], it is possible to define the main advantages and difficulties of integrating a micro-CHP unit into a boiler room. Interesting notions about thermal storage to ensure a continuous electrical production have been highlighted.

Habibi and Varmazyar [10] have conducted an experimental study in order to investigate the behavior of a gas micro-CHP unit generating 14 kW electrical power and 35 kW thermal power. Authors pointed out the influence of heating network's supply temperature to ensure the performance of the installation. The lower the supply temperature is, the better the performance of the system is. It also appeared that an increase in the electrical power generated leads to better overall performances.

For an installation using biofuel, Chen *et al.* [12] proposed a dynamic optimization of an electrical storage installation to meet the electricity and heat needs of a residential building. The originality of this study is installation controlled by a decision tree. However, uncertainties about the performance of the engine powered by biofuel remain under investigation.

In general, it seems that there is a real enthusiasm for micro-cogeneration systems integrated into the building. Several studies [13] [14] [15] [16] and policy proposals [17] [18] illustrate the interest on cogeneration, and specifically micro-cogeneration in buildings [19] [20] [21] [22] [23].

2. SOLAR-MICRO CHP UNIT MODEL

In this section, we describe the main components of the studied solar micro-CHP unit as well as the models used to simulate its operation. For additional technical information on these various components, one can refer to published experimental works previously mentioned.

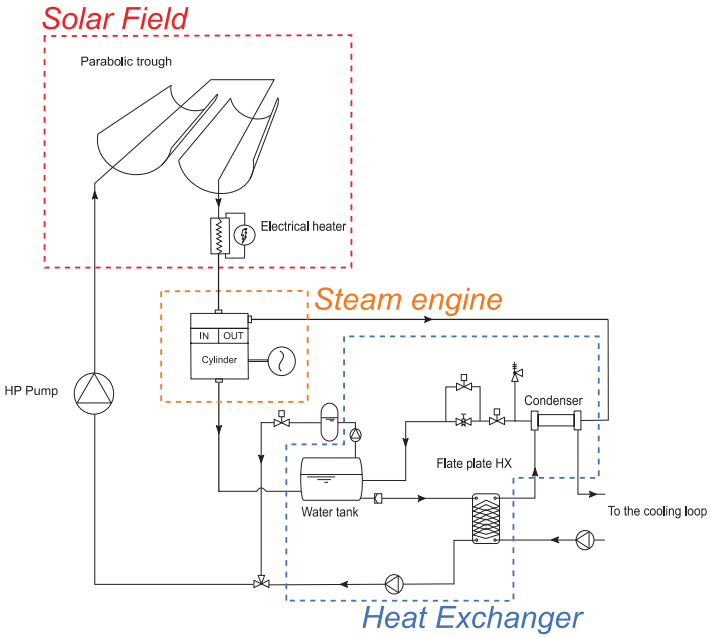

Figure 1 : Schematic diagram of the studied solar micro-CHP unit

Two lines of parabolic trough collectors with a collection area of 46,5 m² following the solar position thanks to a two-axis tracking system compose the solar field. Within the steel absorber tube located at the focal point of the mirror, water circulates at low flow and high pressure to be vaporized. An additional electrical heater ensures good engine intake conditions even in order to compensate solar intermittencies (5 kW). The steam engine converts thermal energy into electrical one using an alternator. The hydraulic skid called « heat exchanger » in Figure 1 is composed by various components providing the interface between the primary loop and a cooling one. Finally, a high pressure pump is used to reach pressure and flowrate set points (25 bars and 30 kg/hr respectively).

2.1 Parabolic trough collector model

A model to characterize the efficiency of the solar concentrator has been defined. It consists of determining the optical efficiency and the convective loss coefficient. Thus, ratio of thermal energy transmitted to the fluid divided per total solar energy received by the mirrors surface can be calculated:

$$\eta_{sol} = \frac{P_{th,sol}}{P_{tot,sol}} = \frac{\dot{m}(h_{out,sol} - h_{in,sol})}{S_{sol} I} = 0.60 - 0.81\left(\frac{\left(\frac{T_{sat} + T_{in,sol}}{2}\right) - T_{ext}}{I}\right) \quad (1)$$

Where, $\dot{m}$ corresponds to the mass flow in the concentrator, $h_{out,sol}$ is the enthalpy at the outlet of the solar field, $h_{in,sol}$ is the enthalpy at the inlet of the solar field, S_{sol} corresponds to the surface of the mirrors, I corresponds to the irradiance, T_{sat} is the saturation temperature, $T_{in,sol}$ is the water temperature at the inlet of the solar field and T_{ext} represents the external temperature

This polynomial form of efficiency is usually defined for solar thermal systems [24]. Note that an accurate description of direct steam generation generally leads to more complex models [25] [26] [27] [28] that are incompatible with dynamic thermal modelling.

2.2 Steam engine model

The model used for the steam engine has also been based on experimental data obtained on a test bench with a controllable heat source [8]. This model allows to express the filling factor as well as the isentropic efficiency of the engine as a function of the pressure ratio, the intake water density and the engine rotation speed [29] :

$$FF = \sum_{i=0}^{n-1}\sum_{j=0}^{n-1}\sum_{k=0}^{n-1} b_{ijk}\,\ln(r_p)^i\,\rho_{in}^{\,j}\,\ln(N)^k + b_{n00}\ln(r_p)^n + b_{0n0}{\rho_{in}}^n + b_{0n0}\ln(N)^n \quad (2)$$

$$\eta_{\exp} = \sum_{i=0}^{n-1}\sum_{j=0}^{n-1}\sum_{k=0}^{n-1} a_{ijk}\ln(r_p)^i\,\rho_{in}^{\,j}N^k + a_{n00}\ln(r_p)^n + a_{0n0}{\rho_{in}}^n + a_{0n0}N^n \quad (3)$$

Where, r_p corresponds to the pressure ratio between the intake and exhaust of the engine, N is the rotational speed of the engine, ρ_{in} is the density at the intake and the coefficients a and b are calibrated from experimental measurements.

In practice, only the first order terms are considered. Once the motor characteristics have been determined, it is possible to calculate the enthalpy of the output fluid as well as the electric production thanks to the following relations:

$$FF = \frac{\dot{m}_{admis}}{\rho_{in}\dot{V}_{swept}} = \frac{\dot{m}_{admis}}{\rho_{in}\left(\frac{N}{60}\right)V_{swept}} \quad (4)$$

$$\eta_{\exp} = \frac{P_{el}}{\dot{m}_{admis}(h_{in} - h_{out,is})} \quad (5)$$

Where P_{el} corresponds to the electrical power, $\dot{m}_{admis}$ is the actual flowrate admitted into the steam engine, V_{swept} is the volume swept by the piston, h_{in} corresponds to the admission steam enthalpy and $h_{out,is}$ is the isentropic steam enthalpy at the outlet of the steam engine.

As described in equation (4), the filling factor therefore corresponds to the ratio of the mass admitted into the engine to the theoretical mass contained in the intake volume.

A stationary balance assuming constant exchange efficiency models heat exchanges between the primary and secondary loops. In accordance with the experimental data, it is assumed that the water flow temperature to the solar field is fixed. Thus, one can write:

$$\begin{aligned} P_{HX} &= \dot{m}(h_{in,HX} - h_{out,HX}) \\ &= \frac{P_{cooling}}{\varepsilon_{HX}} = \frac{\dot{m}_{cooling}C_p(T_{out,cooling} - T_{in,cooling})}{\varepsilon_{HX}} \end{aligned} \quad (6)$$

The efficiency of the exchanger, ε_{HX}, is assumed constant and equal to 80 %. Thus, the thermal power obtained on the secondary loop is deduced from an enthalpy balance and is about 15 kW, which is in agreement with measured experimental values.

2.3 Boiler model

The used model here, defined by its overall efficiency and its combustion efficiency, is a model available in the TRNSYS© TESS library (Type 638). The maximum boiler power output is fixed and the power required to reach the enthalpy set point at the boiler outlet is calculated by:

$$\dot{Q}_{needed} = \dot{m}(h_{obj} - h_{out,PTC}) \tag{7}$$

Where h_{obj} corresponds to the enthalpy aimed at the inlet of the steam engine and $h_{out,PTC}$ corresponds to the enthalpy at the outlet of the solar field.

Once the necessary power is determined, the boiler power output can be defined as follows:

$$\dot{Q}_{boiler} = \min(\dot{Q}_{needed}, \dot{Q}_{\max}) \tag{8}$$

For the boiler model, a total efficiency of 0.78 is defined. The value of the combustion efficiency is 0.85.

2.4 Other models

Pump and hot water tank models come from the TRNSYS library (Type 114 and Type 534 respectively).

3. THE BUILDING MODEL

The building model has been carefully defined because it determine heating requirements according to the envelope, indoor temperature set point, outdoor temperature and internal gains.

3.1 Description

The modelled building is located on the INCAS platform of the INES site located in Chambéry, France. It is a two floors house with a net floor area of 97.5 m². It includes a kitchen, a dining room / living room, a laundry room, an entrance hall and a toilet on the ground floor. On the first floor, there are three bedrooms, a bathroom and a toilet. For the modelling, we consider the following rooms as heated: the bathroom, the kitchen/living room, and the three bedrooms upstairs. Plans of the INCAS house are provided by Figure 2.

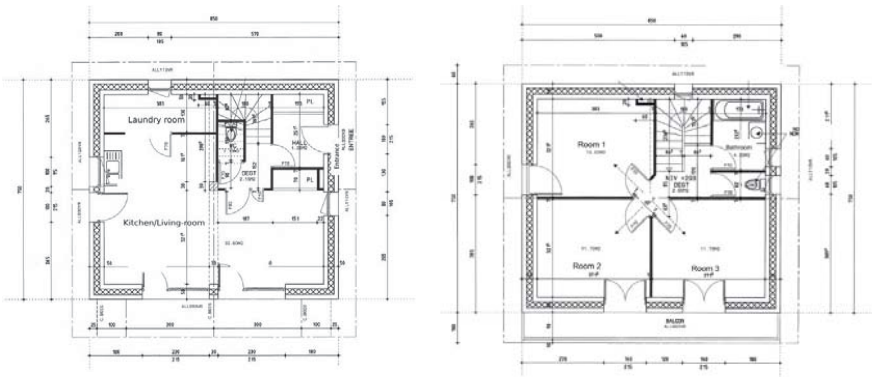

Figure 2: Plans of the INCAS house, ground floor (left) and first floor (right)

3.2 Building heating

The heating contribution of the micro-CHP unit has to ensure the thermal comfort into the house. Thus, set point temperatures are defined in each heated room. Figure 3 shows temperature profiles defined for weekdays and weekends. These temperature levels are essential for calculating losses and heating requirements.

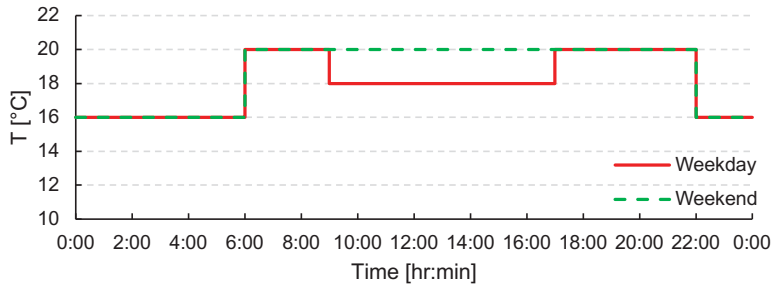

Figure 3 : Set temperatures in heated rooms of the building

Therefore, the heat requirements of the building can be calculated from dynamic thermal simulations performed with TRNSYS© software. For one year, Figure 4 shows the heating capacity required to reach the set point temperature in the heated zones.

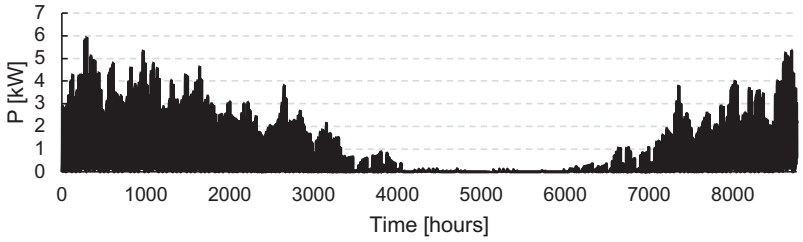

Figure 4 : Annual power profile for heating

3.3 Withdrawal of domestic hot water

The domestic hot water drawing profile is defined for one week and is derived from the open access model developed by McKenna *et al.* [30]. The profile shown by Figure 5 is representative of a consumption of four people. Water is assumed to be consumed at 60°C.

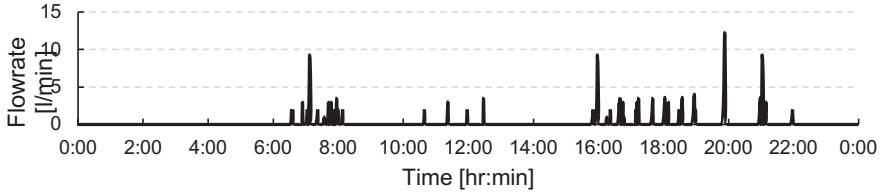

Figure 5: Hot domestic water withdrawal profile

3.4 Electrical requirements

Electrical requirements are based on the McKenna's model [30]. The electricity consumption profile is defined for one day and four occupants. This profile provides the electrical power

consumed by the building (Figure 6). Note that the model distinguishes electrical consumption from lighting and household appliances. Total consumption is considered in this study.

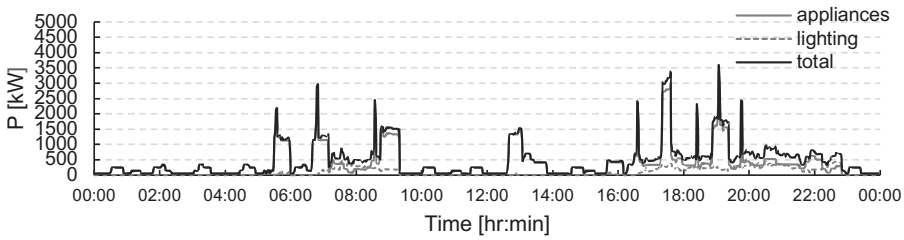

Figure 6: Daily electrical power consumption

4. INTEGRATION OF MICRO-CHP UNIT INTO THE BUILDING

We propose in this numerical work to replace the electrical heater at the solar field outlet by a boiler of greater power (30 kW) in order to ensure the water evaporation even in the absence of sunlight. For the modeling considered, the time step used is 15 min. It results from a compromise between the need for a small time step to represent the control of the micro-generator and a large time step to perform annual reviews. Figure 7 presents a schematic diagram of the coupling between the micro-CHP unit and the building.

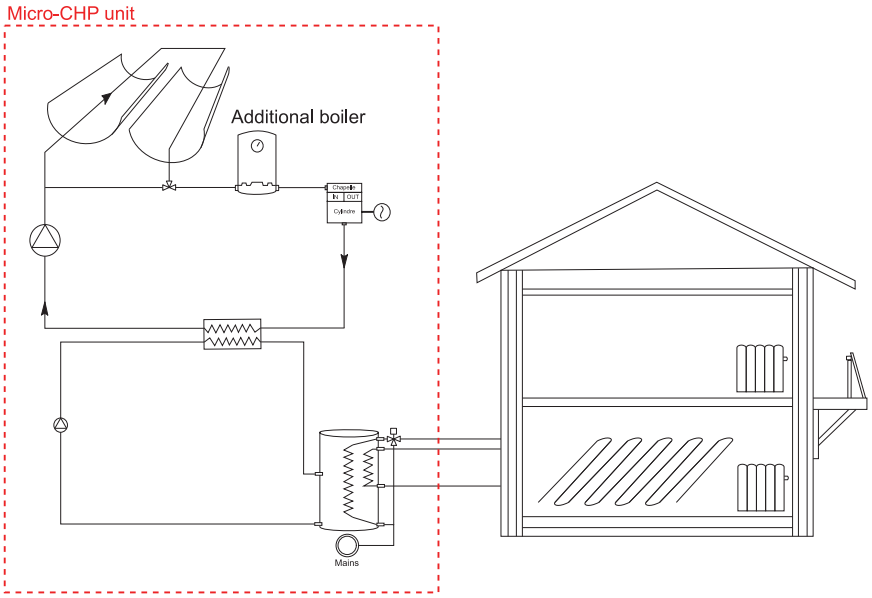

Figure 7: Coupling between the micro-CHP unit and the building

According to the numerical modeling, the micro-CHP unit produces electricity and stores heat in the storage tank regardless of the amount of sunlight, and this in order to provide heating and domestic hot water production for the building.

The objective of this integration is to produce electricity and heat in order to cover building's needs while promoting the use of solar energy. For this purpose, it is assumed that the system

operates during the day and as long as the storage tank is not fully charged (average storage tank temperature below 85 °C).

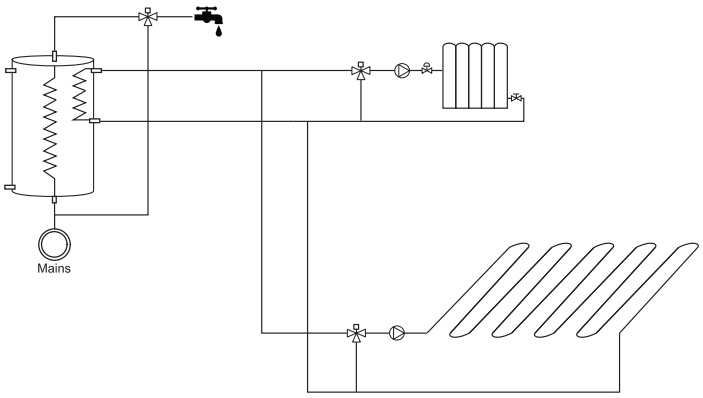

Figure 8: Hydraulic diagram corresponding to the case study

Figure 8 shows the domestic hot water, radiator and underfloor heating distribution networks. For each circuit, solenoid valves ensure the flow temperature of the circuits according to a heating curve.

In this section, we present the architecture of the TRNSys modelling. This study is based on the modelling of the micro-CHP unit, its hydraulic integration and the building.

4.1 The primary loop

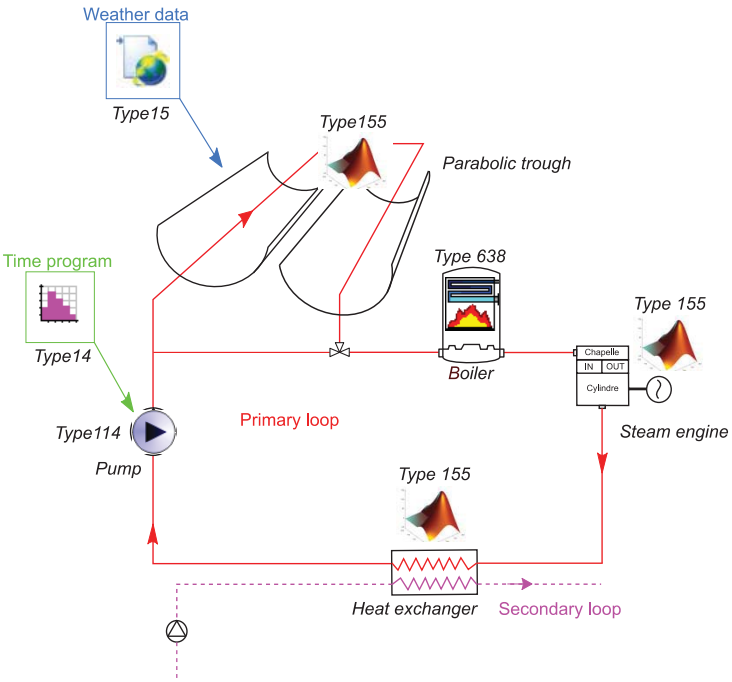

Figure 9: TRNSYS modelling of the primary loop

The primary loop is one of the most difficult elements to model. In particular, unsteady phenomena in the solar field can lead to variations in the output steam flow. To our knowledge, there is no similar installation already studied. Thus, the originality of the studied solar micro-CHP unit prevents the use of model already existing in the TRNSys library. In order to implement the experimentally determined correlations and to have access to a database of the thermo-physical properties of water, Matlab© software has been used.

In Figure 9 the main Types used to model the primary circuit are shown. Between each of these Types, main information characteristics are the flow rate, enthalpy and pressure, which make it possible to carry out energy balances. The time schedule is the main control presented in green. The operating period of the micro-CHP unit is between 10h and 18h in order to benefit from the solar resource. It should be noted that the charging of the thermal storage tank is a determining factor in the control of the installation. Finally, the meteorological data, represented in blue, provide access to the evolution of sunshine and outdoor temperature according to the geographical location of the building. We consider in this study that it is located in La Rochelle, France. Note that Figure 9 shows an integration proposal for which the additional heat source (boiler) is located on the primary loop.

4.2 The secondary loop

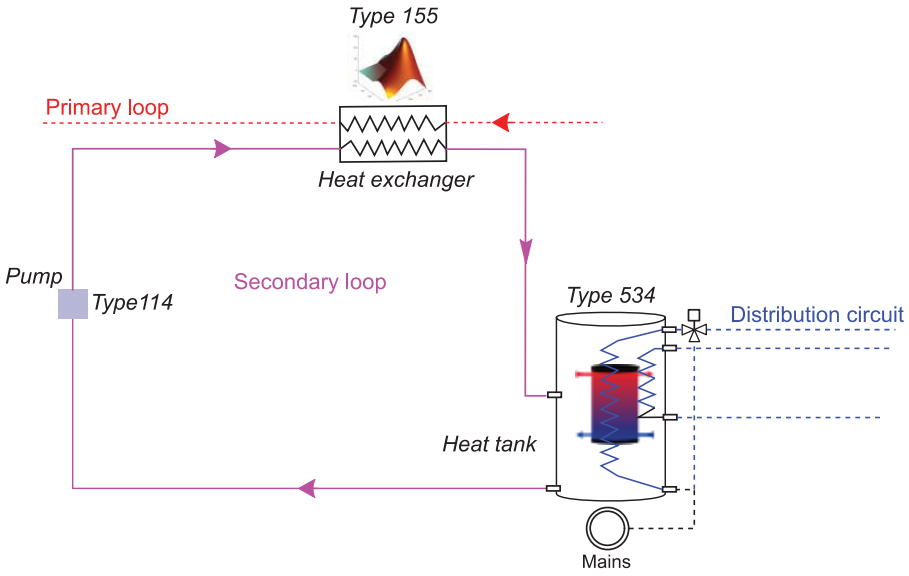

Figure 10: TRNSys modelling of the secondary loop

Figure 10 shows the secondary loop. Characteristics transmitted between the different types are mainly the flow rate, temperature and pressure of the water in the system.

Main parameters of this loop are the flowrate and storage tank characteristics. We considered a heat tank with two internal exchangers to meet the needs of the heating and DHW network.

4.3 The distribution loop and the coupling to the building

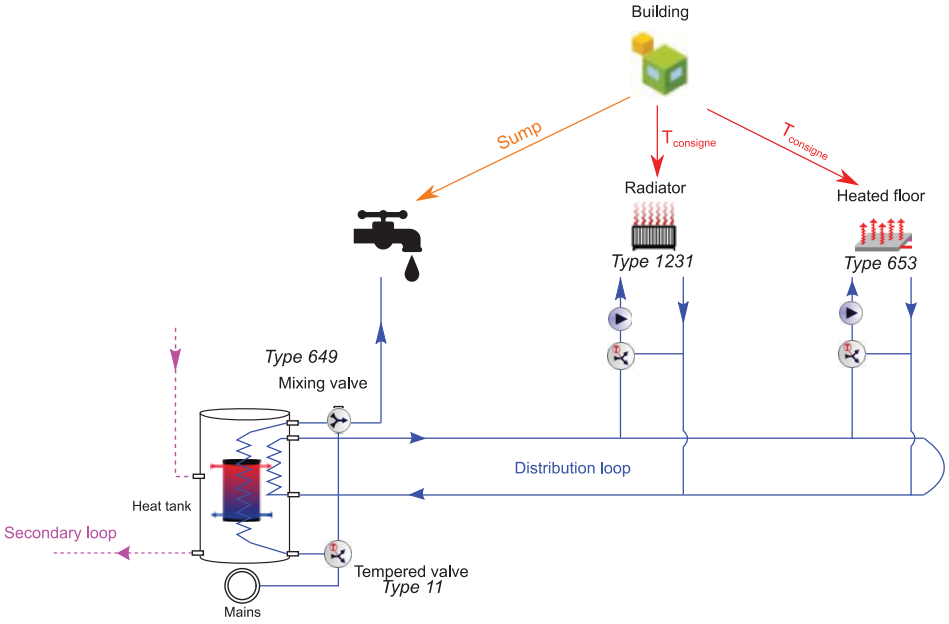

Figure 11: TRNSys modelling of the distribution loop

Finally, Figure 11 shows the distribution loop. For the DHW network, a tempering valve distributes the flow to the storage tank and to a mixing valve according to the set point temperature of 60 °C on the DHW withdrawal. It should be noted that heat losses located in the piping system were not taken in account here.

The pumps are located at the start of each hydraulic network. There are two heating networks in this installation: a radiator network composed by five radiators and a network for the underfloor heating. For clarity reasons, we represent only one radiator network in Figure 11.

For each emitter, tempering valves are used to adapt the supply temperature of the networks according to heating curve. The heating capacities are then injected into the building via the Type 56 in the form of gains for each zone of the building. The calculation of the thermal power emitted in each heated room takes into account its ambient temperature value.

4.3.1 Emitter modeling

The water regime of the radiators is determined in order to reach a temperature difference of 55/40 °C between inlet and outlet for outdoor conditions of -5 °C. The latter allows the sizing of emitters. For the underfloor heating system, the temperature difference between inlet and outlet is set to 35/28°C considering a flow rate of 120 kg/h.

It should be noted that a time schedule carries out the activation of the pump that supplies the radiator network, safety devices on the outside temperature and the ambient temperature. This means that the heating network is supplied according to a time schedule, but also if the outside temperature falls below -5 °C or if the ambient temperature in main rooms drops below 15 °C.

4.3.2 The distribution network

We detail in Figure 12 the radiator network operating principle. For underfloor heating, the control strategy is similar, without change in flowrate.

The achievement of the set point temperature in each room of the building is mainly ensured by:

- The flow temperature of the network, which is calculated using a heating curve depending on the outdoor temperature;
- The sizing of emitters, determined from usual laws;
- The flowrate control in each radiator, which is carried out by building occupants in practice, using thermostatic valves. A proportional flow control law based on the temperature difference between the set point and the ambient temperature was considered here. This law provides an opening signal in 0 and 1 calculated from the temperature difference between the ambient temperature and the set point (Figure 12).

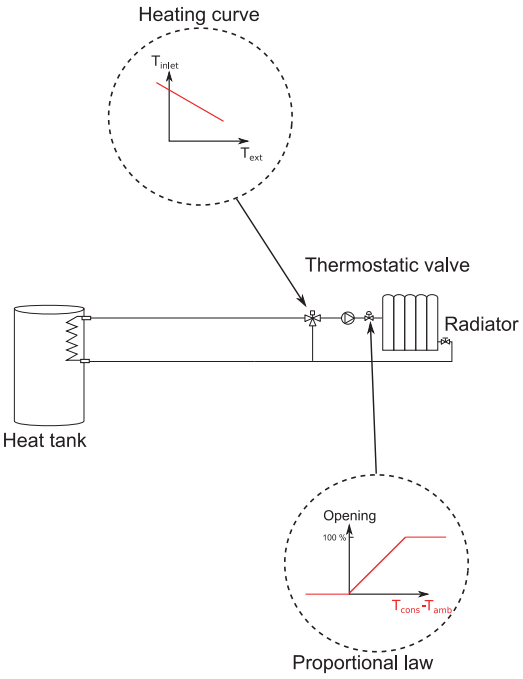

Figure 12: Schematic diagram of the radiator network

Thereafter, the radiator power is calculated by the emission law (12) and then taken into account in the heat balance of each heated room as a gain:

$$\dot{Q}_{radiator} = c(T_s - T_{amb})^n = \dot{m}C_p(T_{water,in} - T_{water,out}) \quad (12)$$

where c and n are constants depending on the type of radiator considered and the nominal operating conditions. The constant c is defined by the nominal conditions of operation while n corresponds to the type of radiator considered. For this simulation, the n value is equal to 1,4.

5. RESULTS

This section presents the main results from numerical simulations. For a week with heating needs (cold period), external conditions and powers generated by the micro-CHP units are plotted on Figure 13 and Figure 14 respectively. The weather data come from the Meteonorm database for the city of La Rochelle. Figure 14 confirms the need of an additional heat source (boiler) to ensure the continuous operation of the system.

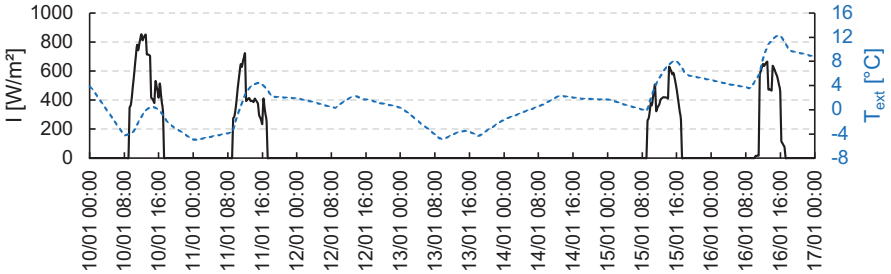

Figure 13: Evolution of solar irradiation and outside temperature

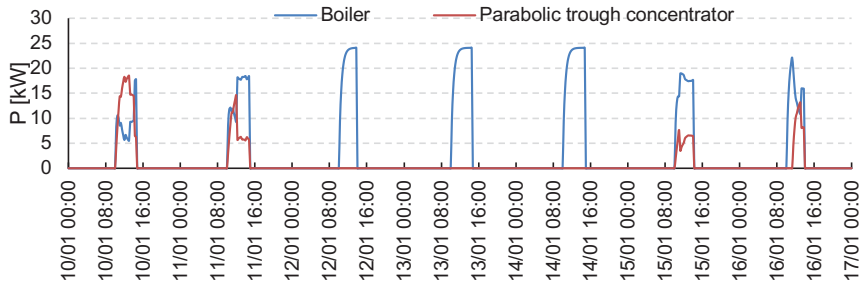

Figure 14: Evolution of the micro-CHP unit and boiler power

The boiler therefore supplements the concentrator's energy input and ensures constant inlet conditions to the steam engine. However, the system operation time is restricted by the storage tank load. Indeed, the micro-CHP unit is stopped while it is in its operating period. This is due to the fact that the average temperature of the storage tank has reached 85 °C. Figure 15 shows the evolution of the average temperature within the storage tank.

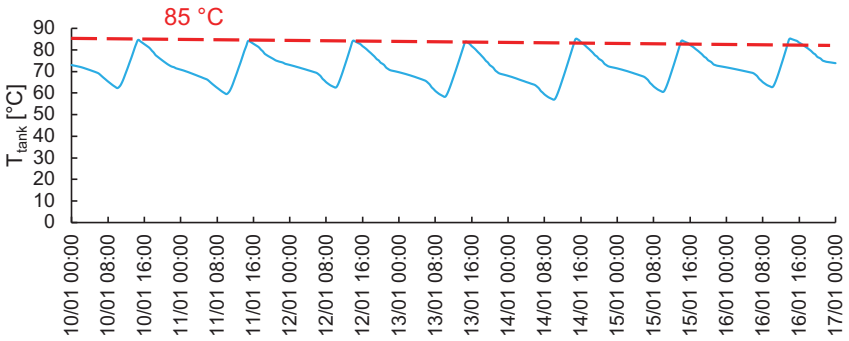

Figure 15: Average temperature within the storage tank

The average temperature in the storage tank must remain high enough to ensure temperature supply of domestic hot water, radiator and underfloor heating networks. The DHW and heating loads are presented by Figure 16.

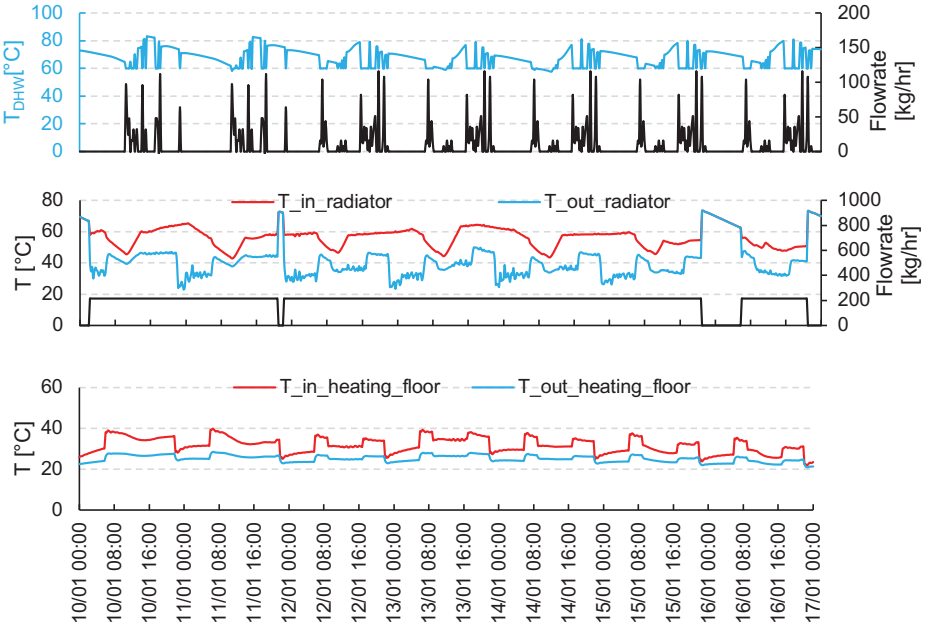

Figure 16: Details of the different water draws from the storage tank

The first graph in Figure 16 corresponds to the domestic hot water draws. The mixing valve outlet temperature is shown in blue. Thus, each time the withdrawal flow is not zero, this temperature must be equal to the set point temperature (60 °C). In other words, in order to meet the DHW requirements, the system must provide a temperature above 60 °C at the storage tank tap. The two others correspond to the radiator and underfloor heating network. For the radiators, a water regime of 55/40 °C for an outside temperature of -5 °C was chosen

to determine the network power. For the underfloor heating, a 35/28°C regime was chosen. The flow rate in the underfloor heating is constant, equal to 120 kg/hr.

Finally, power generation and consumption are shown by Figure 17. The superposition of these two curves makes it possible to quantify the self-consumed electricity as well as the electricity surplus and the imported electricity from the grid.

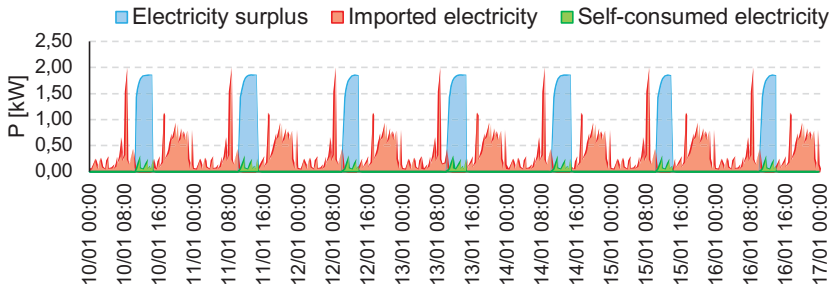

Figure 17: Electrical balance of the installation

Figure 17 points out the low self-consumption rate of the installation for the considered electricity consumption profile. Two observations can explain this low rate of electricity needs coverage. Firstly, the operation of the system between 10am and 6pm prevents production during the high evening demand. However, this is classical for solar systems. Secondly, it has already been mentioned that the system operation is limited by the storage tank load. Thus, the use of electrical storage and the increase in thermal requirements are two ways to improve performances of the micro-CHP unit. This second point will be discussed in section 8.

5.1 Summary

First of all an operating balance (illustrated by Figure 18) of the installation gives an account of the electrical and thermal energies produced by the installation from the energies consumed in order to obtain the output of the installation.

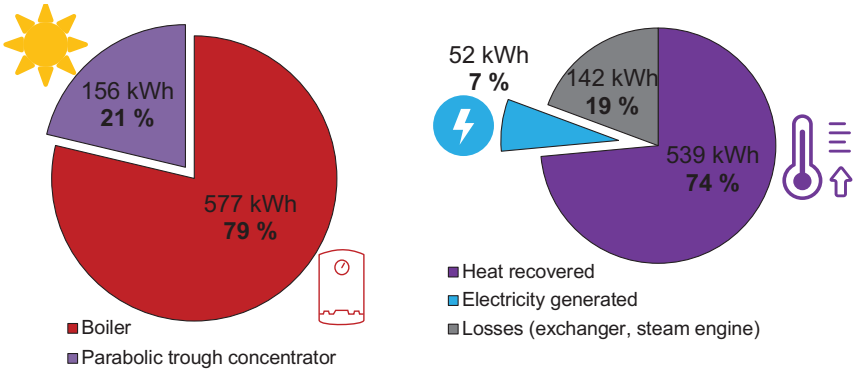

Figure 18: Balance of heat and electricity production by the micro-CHP unit for a cold week

During the heating period, the heating requirements are much higher than the requirements for DHW and electricity. The overall efficiency of the system is 81 % and it appears to be similar

to that determined experimentally. A second assessment quantifies the final heat used by the consumer.

During the winter period heat needs are divided in DHW and heating needs. The latter is much greater than the first one, according to Figure 19. This was expected as in France, the DHW need represents 12.1% of the total average energy consumption, while it is 61.3% for heating [31].

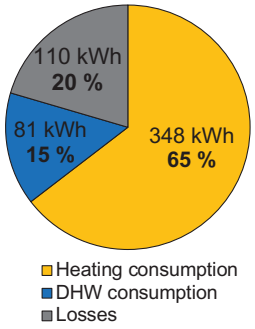

Figure 19: Balance of heat provided by the distribution loop

Finally, an overall assessment of the production by the micro-CHP unit has been carried out and shown by Figure 20. Note the importance of heat needs that represents 89% of the building's energy needs during the heating period.

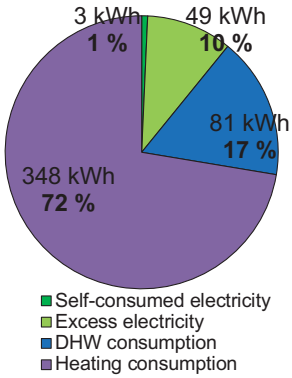

Figure 20: Balance of the production by the micro-CHP unit

5.2 Annual summary

For an entire year, production and consumption have been summed monthly and results are plotted in Figure 21. These results constitute an interesting synthesis of the operation of the micro-CHP unit during the whole year.

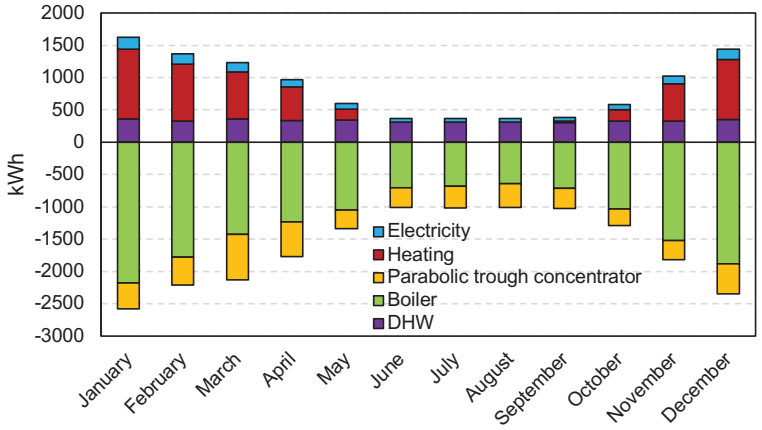

Figure 21: Balance of production and monthly consumption of the micro-CHP unit

It can be seen that DHW consumption remains constant while heating needs vary. Electricity is produced less in summer than in winter. This is due to the fact that the micro-CHP unit operates less in summer because it is limited by the load of the storage tank. Overall, the boiler's heat production remains majoritary in comparison to solar gains.

Finally, the overall efficiency decreases during the summer (63% in January and 37% in July). This is logical because the low heat consumption in summer means that the tank does not discharge much. Thus, the thermal losses of the storage tank are greater during the summer period.

6. IMPACT OF THE HEAT STORAGE VOLUME INCREASE ON THE SYSTEM PERFORMANCE

It has been shown that the charge of the storage tank is the limiting factor for the operation of the micro-CHP unit throughout the day. Indeed, the micro-CHP unit studied produces ten times more heat than electricity. It is therefore necessary to adapt the heat storage for such a system and we propose in this Section an investigation on the impact of the storage volume on its performance. For a whole year, we considered heat storage volumes ranging from 1 m^3 to 50 m^3 as shown by Figure 23.

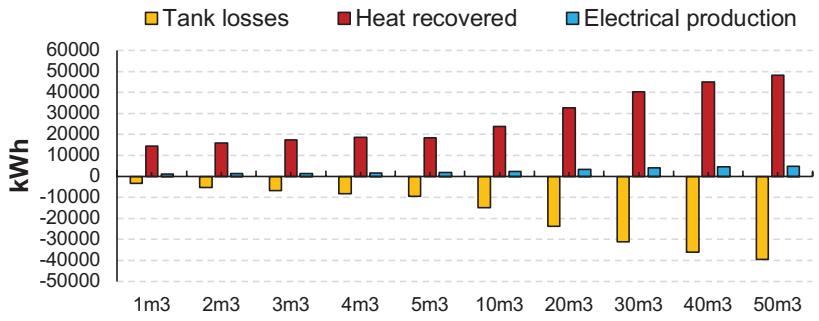

(a)

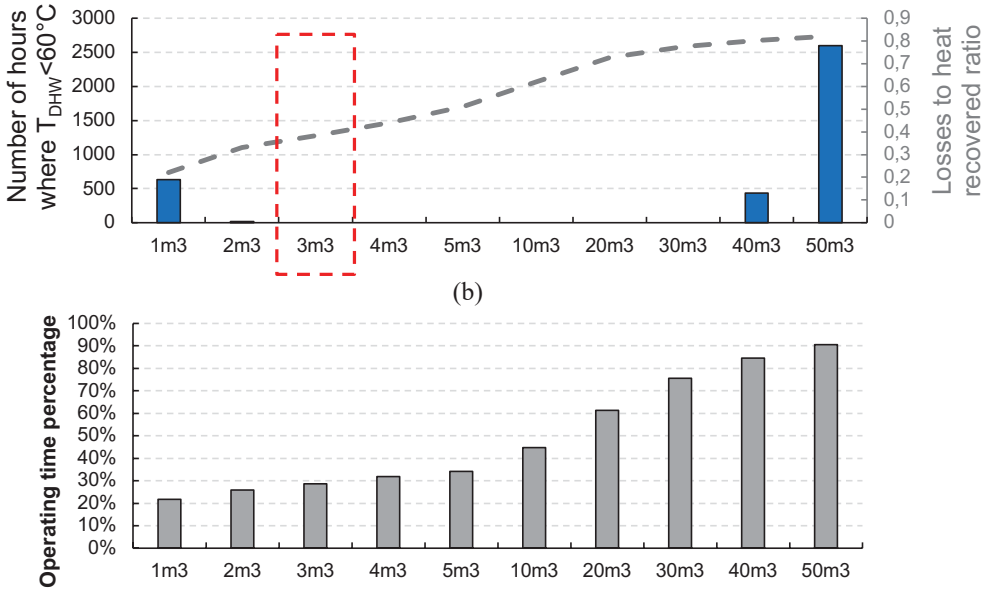

(b)

(c)

Figure 22: Effect of the heat storage volume on the system performance

Figure 23 points out that an increase in the storage volume has a small impact on the electrical production of the micro-CHP unit. A ten-fold increase in volume, from 1 to 10 m^3, leads to only a twofold rise in electrical production. A tank volume leading to the lowest loss ratio and ensuring heat requirements seems therefore to be the most relevant solution (Figure 23 (b)).

Not surprisingly, the system operating time is longer when the heat storage volume increases (20% of the maximum operating time for a volume of 1 m^3, 90% for a volume of 50 m^3). On one hand, such increase in heat storage volume leads to a more continuous operation but, on the other hand, it significantly increases heat losses.

The results suggest that preference should be given to the use of a 3 m^3 storage tank for this micro-CHP unit. To make the best use of the available heat, several houses with heat storage volumes could be connected. Indeed, low storage tanks volume limits heat losses while an increase in the number of consumers, and thus buildings, allows highest operating time of the system, and electricity production too.

7. CONCLUSIONS

In this article, we propose a solution for integrating a solar micro-CHP unit into a residential building. The system operates according to Hirn's thermodynamic cycle for electricity generation. It is based on direct steam generation within the absorber tube of a parabolic trough collector equipped with a two-axis solar tracking system.

Previous experimental works have pointed out the difficulty for the solar micro-CHP unit to operate without additional heater. We have therefore proposed a numerical model for integration of the micro-CHP unit to a building with backup on the primary loop.

Technically, the feasibility of adding such an additional heat source has to be studied. The results for a winter week and for a whole year show that the overall efficiency of the system can be interesting (up to 81 %). However, since it is oversized for a single building, it appears that its operation is limited by the storage tank load. An increase in the thermal load leads to an increase in the production by the system.

Finally, a parametrical study on the impact of the storage volume has been carried out. As the system produces a large amount of heat compared to its electrical production, it is necessary to propose an optimal heat use management strategy. Results suggest to share the heat between several dwellings with storage volumes of 3 m^3.

REFERENCES

[1] *Directive 2004/8/EC of the european parliament and of the council*.

[2] J.-B. Bouvenot, B. Latour, M. Siroux, B. Flament, P. Stabat, et D. Marchio, « Dynamic model based on experimental investigations of a wood pellet steam engine micro CHP for building energy simulation », *Applied Thermal Engineering*, vol. 73, nº 1, p. 1041-1054, 2014.

[3] R. Beith, Éd., *Small and micro-combined heat and power (CHP) systems*. CRC Press, 2011.

[4] Anonymous, « 2030 climate & energy framework », *Climate Action - European Commission*, 23-nov-2016. [En ligne]. Disponible sur: https://ec.europa.eu/clima/policies/strategies/2030_en. [Consulté le: 19-sept-2018].

[5] S. Martinez, G. Michaux, P. Salagnac, et J.-L. Bouvier, « Micro-combined heat and power systems (micro-CHP) based on renewable energy sources », *Energy Conversion and Management*, vol. 154, p. 262-285, 2017.

[6] J.-L. Bouvier, G. Michaux, P. Salagnac, F. Nepveu, D. Rochier, et T. Kientz, « Experimental characterisation of a solar parabolic trough collector used in a micro-CHP (micro-cogeneration) system with direct steam generation », *Energy*, vol. 83, p. 474-485, 2015.

[7] J.-L. Bouvier, G. Michaux, P. Salagnac, T. Kientz, et D. Rochier, « Experimental study of a micro combined heat and power system with a solar parabolic trough collector coupled to a steam Rankine cycle expander », *Solar Energy*, vol. 134, p. 180-192, 2016.

[8] J.-L. Bouvier, V. Lemort, G. Michaux, P. Salagnac, et T. Kientz, « Experimental study of an oil-free steam piston expander for micro-combined heat and power systems », *Applied Energy*, vol. 169, nº Supplement C, p. 788-798, 2016.

[9] J.-L. Bouvier, « Étude expérimentale d'une installation de micro-cogénération solaire couplant un concentrateur cylindro-parabolique et un moteur à cycle de Hirn », Thèse de doctorat, La Rochelle, 2014.

[10] Á. Campos-Celador, E. Pérez-Iribarren, J. M. Sala, et L. A. del Portillo-Valdés, « Thermoeconomic analysis of a micro-CHP installation in a tertiary sector building through dynamic simulation », *Energy*, vol. 45, nº 1, p. 228-236, sept. 2012.

[11] Y. Lebbe et D. Darimont, « Réussir l'intégration de l'hydraulique et de la régulation d'une cogénération dans une chaufferie », Guide technique, 2014.

[12] X. P. Chen, N. Hewitt, Z. T. Li, Q. M. Wu, X. Yuan, et T. Roskilly, « Dynamic programming for optimal operation of a biofuel micro CHP-HES system », *Applied Energy*, vol. 208, p. 132-141, déc. 2017.

[13] M. A. Rosen, M. N. Le, et I. Dincer, « Efficiency analysis of a cogeneration and district energy system », *Applied Thermal Engineering*, vol. 25, nº 1, p. 147-159, janv. 2005.

[14] V. Havelský, « Energetic efficiency of cogeneration systems for combined heat, cold and power production », *International Journal of Refrigeration*, vol. 22, nº 6, p. 479-485, sept. 1999.

[15] T. Nuytten, B. Claessens, K. Paredis, J. Van Bael, et D. Six, « Flexibility of a combined heat and power system with thermal energy storage for district heating », *Applied Energy*, vol. 104, p. 583-591, avr. 2013.

[16] S. Sanaye, M. A. Meybodi, et S. Shokrollahi, « Selecting the prime movers and nominal powers in combined heat and power systems », *Applied Thermal Engineering*, vol. 28, nº 10, p. 1177-1188, juill. 2008.

[17] A. Williams, « Micro-CHP in buildings », *Build Up*, 21-juin-2011. [En ligne]. Disponible sur: http://www.buildup.eu/en/topics/micro-chp-buildings. [Consulté le: 19-sept-2018].

[18] « Cogeneration of heat and power - Energy - European Commission », *Energy*. [En ligne]. Disponible sur: /energy/en/topics/energy-efficiency/cogeneration-heat-and-power. [Consulté le: 19-sept-2018].

[19] H. I. Onovwiona et V. I. Ugursal, « Residential cogeneration systems: review of the current technology », *Renewable and Sustainable Energy Reviews*, vol. 10, nº 5, p. 389-431, oct. 2006.

[20] « European and Canadian non-HVAC electric and DHW load profiles for use in simulating the performance of residential cogeneration systems[A report of Subtask A of FC+COGEN-SIM : The simulation of building-integrated fuel cell and other cogeneration systems : Annex 42 of the International Energy Agency, Energy Conservation in Buildings and Community Systems Programme] (Book) | ETDEWEB ». [En ligne]. Disponible sur: https://www.osti.gov/etdeweb/biblio/20987338. [Consulté le: 19-sept-2018].

[21] M. Dentice d'Accadia, M. Sasso, S. Sibilio, et L. Vanoli, « Micro-combined heat and power in residential and light commercial applications », *Applied Thermal Engineering*, vol. 23, nº 10, p. 1247-1259, juill. 2003.

[22] R. J. Braun, S. A. Klein, et D. T. Reindl, « Evaluation of system configurations for solid oxide fuel cell-based micro-combined heat and power generators in residential applications », *Journal of Power Sources*, vol. 158, nº 2, p. 1290-1305, août 2006.

[23] A. D. Hawkes et M. A. Leach, « Cost-effective operating strategy for residential micro-combined heat and power », *Energy*, vol. 32, nº 5, p. 711-723, mai 2007.

[24] S. A. Kalogirou, « Solar thermal collectors and applications », *Progress in Energy and Combustion Science*, vol. 30, nº 3, p. 231-295, 2004.

[25] S. Bendapudi, J. E. Braun, et E. A. Groll, « A comparison of moving-boundary and finite-volume formulations for transients in centrifugal chillers », *International Journal of Refrigeration*, vol. 31, nº 8, p. 1437-1452, déc. 2008.

[26] E. Zarza *et al.*, « Direct steam generation in parabolic troughs: Final results and conclusions of the DISS project », *Energy*, vol. 29, nº 5–6, p. 635-644, 2004.

[27] M. Eck et T. Hirsch, « Dynamics and control of parabolic trough collector loops with direct steam generation », *Solar Energy*, vol. 81, nº 2, p. 268-279, 2007.

[28] R. Xu et T. F. Wiesner, « Closed-form modeling of direct steam generation in a parabolic trough solar receiver », *Energy*, vol. 79, p. 163-176, janv. 2015.

[29] S. Quoilin, V. Lemort, et J. Lebrun, « Experimental study and modeling of an Organic Rankine Cycle using scroll expander », *Applied Energy*, vol. 87, nº 4, p. 1260-1268, avr. 2010.

[30] E. McKenna et M. Thomson, « High-resolution stochastic integrated thermal–electrical domestic demand model », *Applied Energy*, vol. 165, p. 445-461, 2016.

[31] ADEME, « L'eau chaude sanitaire », *ADEME*. [En ligne]. Disponible sur: https://www.ademe.fr/expertises/batiment/passer-a-laction/elements-dequipement/leau-chaude-sanitaire. [Consulté le: 06-août-2018].

Questions and Answers:

Sylvain Quoilin:

What is comparison of presented system against PV?

Simon Martinez:

The presented system is a prototype. When it comes to compare its solar to electricity efficiency with the photovoltaic technology, it seems that solar thermodynamic technologies get a lower efficiency (about 20% for photovoltaic, 5 % for our technology). The main advantage of the presented technology is its high overall efficiency thanks to the heat recovery and the high level of temperature of the working fluid (about 200 °C) that enables thermal storage.

***

Van Riet Freek:

Why did you use a (spiral) heat exchanger in the tank for space heating?

Simon Martinez:

Indeed, the heat exchanger used in the model is not mandatory. We use it only if there is a risk of freezing (i.e. when the working fluid in the space heating network is not pure water). In some cases, it can be deleted.

***

Jean Lebrun:

What about instability inside the evaporator?

Simon Martinez:

There are a lot of instabilities in the evaporator, in particular concerning the mass flow rate. This is mainly due to the boundary conditions that are variable (direct normal radiation,

temperature,...). This particularity has been widely studied for direct steam generation technologies (see Zarza, Eck,...) and makes the system regulation more complex.

***

Jean Lebrun:

What about mechanical losses (friction) of the cylinder?

Simon Martinez:

There are some mechanical losses of the cyclinder due to the piston ring that are made in ceramic. As an order of magnitude, note that the isentropic efficiency of the steam engine is about 30 %.

Cascading implementation of a magnetocaloric heat pump for building space heating applications

H. Johra[1]*, K. Filonenko[2], P. Heiselberg[1], C. Veje[2], S. Dall'Olio[3], K. Engelbrecht[3], C. Bahl[3]

[(1)] Aalborg University, Division of Architectural Engineering, Department of Civil Engineering

Thomas Manns Vej 23, DK-9220 Aalborg Øst, Denmark

[(2)] University of Southern Denmark, Center for Energy Informatics

Campusvej 55, DK-5230 Odense M, Denmark

[(3)] Technical University of Denmark, Department of Energy Conversion and Storage

Frederiksborgvej 399, DK-4000 Roskilde, Denmark

ABSTRACT

The main objective of the ENOVHEAT project is to develop, build and test the prototype of an innovative and efficient heat pump system based on the active magnetic regenerator technology and to demonstrate that it can be used for building space heating applications. The numerical investigation presented in this article tested different configurations of single magnetocaloric heating systems and cascaded magnetocaloric heating networks. It has been shown that the magnetocaloric heat pump can provide for the heating need of a single family house under Danish winter weather condition and presents appreciable coefficient of performance. At optimum fluid flow rate, certain magnetocaloric heat pump configurations could generate fluid temperature outlet of up to 35.3 °C and COPs of up to 4.45. When integrated and operating in a multi-zone dwelling, magnetocaloric heat pump presented average seasonal COPs of up to 1.84 and 2.63 for single unit systems and cascaded magnetocaloric heating networks, respectively. These results are encouraging to continue investigating further the magnetocaloric heat pump technology.

Keywords: Magnetocaloric heat pump, magnetic heating, active magnetic regenerator, innovative heating system, cascading configuration.

1. INTRODUCTION

To tackle the problems of CO_2 emissions and pollution, mitigate the effects of climate change, and meet crucial energy and environmental goals, our modern industrial societies must operate a transition towards decarbonized and renewable energy sources. However, a global decrease of our energy usage is also necessary, which implies a sharp efficiency improvement of the different energy systems.

The building sector has clearly been identified as the main target for energy savings as it is the largest energy end-user in the world. In Europe, for example, the buildings represent 40% of the total energy demand, among which 75% is used for indoor space heating (BPIE, 2011). A large share of this heating need can be cut down by enhancing the thermal performance of the building's envelope and improving the energy efficiency of the heating systems (IEA, 2013). In regards to the latter, heat pumps were found to be an excellent cost-effective heating supply helping to establish a sustainable building stock with low greenhouse gas emissions,

and facilitating the integration of a large share of renewable energy sources (Cockroft and Kelly, 2006; Lund et al., 2010; Palzer and Henning, 2014). Consequently, heat pump systems became a key component of the energy development planning of many countries and their market has shown continuous growth over the last decade.

Currently, the heat pump market is dominated by conventional systems based on a vapour-compression thermodynamic cycle to transfer heat from a cold reservoir (heat source) to a hot reservoir (heat sink). This mature technology has proved its cost-effectiveness in industrial and building applications with high coefficient of performance (COP), typically ranging from 3 to 5 (Self et al., 2013; Fischer and Madani, 2017).

Promising alternatives to conventional vapour-compression heat pumps are devices based on the active magnetic regenerator (AMR) cycle employing the magnetocaloric effect (MCE). Because of the reversible nature of the MCE, AMR-based systems have a great potential for high COP. Moreover, they can operate with low vibration and noise level, have the possibility of recycling their components, and do not employ any toxic or greenhouse gases (Smith et al., 2012). The latest magnetocaloric prototypes developed by different research team present encouraging performance for cooling applications. The rotary AMR device of Engelbrecht et al. (2012) has a cooling capacity of 1010 W and a 25.4 K no-load temperature span. The magnetic cooling machine of Okamura and Hirano (2013) was operating at a COP of 2.5 with a 5 K temperature span. Jacobs et al. (2014) reported a prototype with 2502 W of cooling power at a COP above 2 and a temperature span of 12 K. The magnetocaloric device of Eriksen et al. (2016) has a cooling power of 81.5 W with a COP of 3.6 and a temperature span of 15.5 K.

The ENOVHEAT project (Bahl, 2015) aims at demonstrating that AMR-based systems can be integrated in buildings as a magnetocaloric heat pump (MCHP) and be able to provide for the indoor space heating needs. A previous publication from Johra et al. (2018) has presented a numerical study showing that the MCHP of the ENOVHEAT project can be integrated in a low-energy single family house under Danish winter weather conditions. However, the limited temperature span of this MCHP prototype restricts its application to low-temperature under-floor heating system for well-insulated buildings.

The objective of this article is to present the results of a numerical investigation testing innovative cascading implementations of AMR systems in order to increase the MCHP temperature span and provide for the indoor space heating of poorly-insulated buildings. Firstly, the operational principle and characteristics of the MCHP prototype are described. Details about the building study case and numerical models are then presented. The performances of two types of MCHP with and without cascading implementation are then compared in the case of poorly-insulated and well insulated buildings. Finally, a conclusion and suggestions for further research close this article.

2. THE MAGNETOCALORIC HEAT PUMP

2.1 The magnetocaloric effect and the active magnetic regenerator cycle

The magnetocaloric effect is a reversible temperature change that occurs in a magnetocaloric material (MCM) when subjected to an adiabatic magnetization or demagnetization. When a magnetic field is applied to the MCM, its magnetic entropy decreases and, consequently, its temperature increases. Reciprocally, when the MCM is demagnetized, its magnetic entropy increases and its temperature decreases (Smith et al., 2012).

The magnetocaloric effect was discovered a century ago by Weiss and Piccard (1918). At first, the MCE was only used for laboratory cooling purposes at absolute temperatures below 1 K (Giauque and MacDougall, 1935).

In 1982, Barclay and Steyert (1982) developed the active magnetic regenerator cycle (see *Figure 1*) which employs the MCM as a thermal regenerator. It allows to generate temperature spans which are much larger than the adiabatic temperature change of the MCE alone. The solid refrigerant MCM is contained as a porous media in a regenerator which is alternatively magnetized and demagnetized with an external magnetic field source (e.g., a rotating permanent magnet). The bi-directional circulation of a coolant fluid through the MCM exhibiting a magnetocaloric response performs the heat transfer from a heat source (cold side) to a heat sink (hot side) (Johra, 2018). The AMR technology is considered to be the most thermodynamically efficient principle for magnetocaloric heat pumps (Chen et al., 1992). AMR-based devices are therefore the most common MCHP systems for near room-temperature magnetic heating and cooling applications.

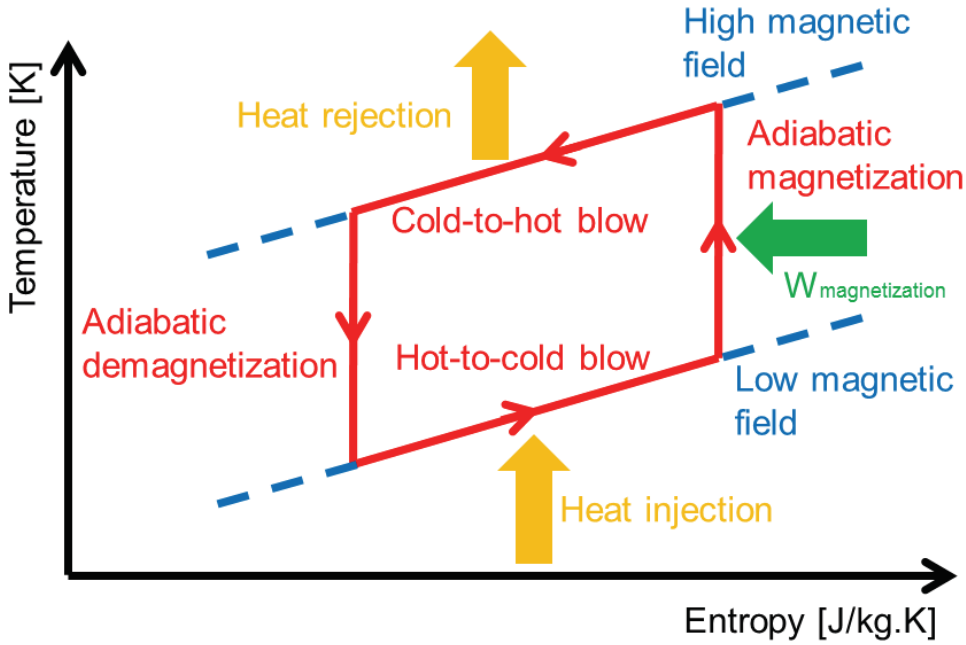

Figure 1: Temperature–entropy diagram of the AMR cycle (Johra, 2018).

Gadolinium (Gd) is considered to be the reference material for MCE at near room-temperature (Smith et al., 2012). As an alternative to this rare earth element, intermetallic compounds such as $La(Fe,Mn,Si)_{13}H_y$ have shown very interesting magnetocaloric properties. These compounds can also exhibit a large MCE at near-room-temperature but are composed of chemical elements which are more abundant and low-cost than Gadolinium (Smith et al., 2012). In addition, the Curie temperature of these MCMs can be adjusted precisely to optimize the MCE inside the AMR (graded or multi-layered regenerator) according to the inherent temperature gradient inside the latter (Navickaitė et al., 2018).

Extensive explanations of the magnetocaloric effect and active magnetic regenerator devices can be found in Smith et al. (2012), Kitanovski et al. (2015) and Engelbrecth et al. (2012).

2.2 Characteristics of the magnetocaloric heat pump

The MCHP prototype developed by the ENOVHEAT project and currently under testing at the Technical University of Denmark (DTU) is a rotary AMR system (see *Figure 2*). 13 active magnetic regenerators mounted on an iron ring compose the vertical stator. The vertical rotor is composed of a two-pole magnet assembly attached to a shaft which is driven by an electrical motor. The rotation of the magnets (rotation frequency ranging from 0.5 Hz to 4 Hz) creates a varying magnetic field (maximum value of 1.46 Tesla) in the regenerators which alternately magnetizes and demagnetizes the MCM. The 13 AMRs are connected to 2 manifold collectors and 2 manifold distributors, one of each for the heat source and similarly for the heat sink. 26 synchronized valves control the bi-directional flow of the heat transfer fluid (20%vol ethylene glycol; 80%vol water) through the individual regenerators (Johra et al., 2018).

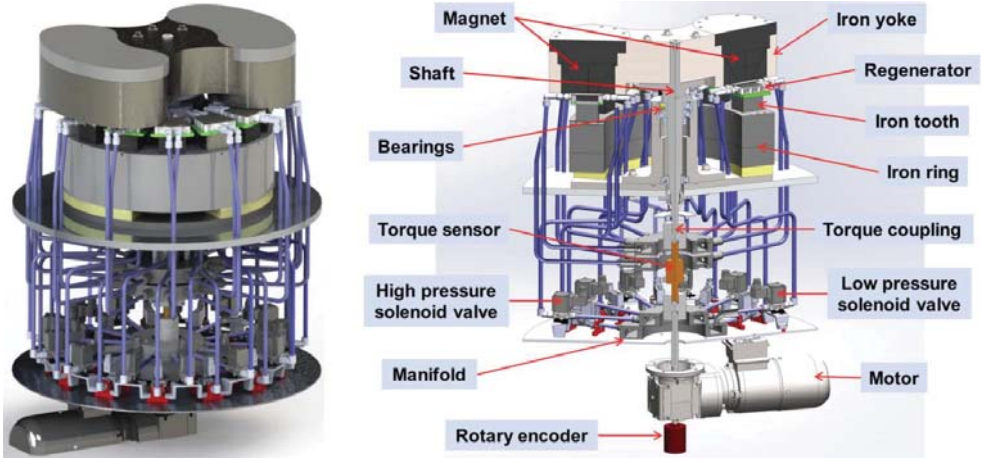

Figure 2: Full view CAD model (left) and detailed description (right) of the magnetocaloric heat pump prototype of the ENOVHEAT project: "MagQueen".

The magnetocaloric material is placed inside the trapezoidal shaped-cassette regenerators as packed bed spheres. In the current numerical investigation, two types of MCM are tested: Gadolinium and $La(Fe,Mn,Si)_{13}H_y$. In the case of $La(Fe,Mn,Si)_{13}H_y$, the Curie temperature of the MCM is adjusted so that 10 layers in the AMR are formed with optimized operational temperatures for maximizing the MCE.

2.3 Modelling of the magnetocaloric heat pump

The original detailed numerical model of the AMR prototype was created by Engelbrecht (2008), then further developed by Lei et al. (2017), and validated with experimental data of different AMR prototypes. With reasonable assumptions on regenerator's geometry, external heat losses and demagnetization losses, the time-dependent fluid temperature distribution in the AMR can be calculated with the two following coupled partial differential equations:

$$\frac{\partial}{\partial x}\left(k_{\text{disp}} A_c \frac{\partial T_f}{\partial x}\right) - \dot{m}_f c_f \frac{\partial T_f}{\partial x} - \frac{Nuk_f}{d_h} a_s A_c \left(T_f - T_s\right) + \left|\frac{\partial P}{\partial x}\frac{\dot{m}_f}{\rho_f}\right| = A_c \varepsilon \rho_f c_f \frac{\partial T_f}{\partial t} \quad (1)$$

$$\frac{\partial}{\partial x}\left(k_{\text{stat}} A_c \frac{\partial T_s}{\partial x}\right)+\frac{\text{Nu}k_f}{d_h} a_s A_c \left(T_f - T_s\right) = A_c \left(1-\varepsilon\right)\rho_s \times \left[c_H \frac{\partial T_s}{\partial t} + T_s \left(\frac{\partial s_s}{\partial H}\right)_{T_s} \frac{\partial H}{\partial t}\right] \quad (2)$$

Where k, T, ρ, c and s are the thermal conductivity, temperature, density, specific heat, and specific entropy; A_c, d_h, a_s, ε, x, t, $\dot{m}_f$, and H are the cross sectional area, hydraulic diameter, specific surface area, porosity of the regenerator bed, axial position, time, fluid mass flow rate and internal magnetic field; $\partial P / \partial x$ and Nu are the pressure drop and the Nusselt number. The subscripts f and s represent fluid and solid refrigerant, respectively. k_{disp} is the thermal conductivity of the fluid due to axial dispersion, k_{stat} is the static thermal conductivity of regenerator and fluid, and c_H is the specific heat capacity of the MCM at constant magnetic field.

These partial differential equations are originally solved with an implicit finite volume method scheme. However, this detailed model is too computationally demanding for a direct use in a building simulation tool. It is therefore approximated by 5-dimentional interpolation lookup table functions containing around 1600 output points generated by the detailed model with the parameters of the ENOVHEAT MCHP prototype.

The other components of the MCHP (valves, motor, circulation pump) are modelled with simple functions fitting data from measurements on the prototype and from manufacturers documentation (Johra et al., 2018).

3. THE BUILDING SYSTEM

3.1 Building study cases

Two versions of the same building with different envelope thermal performances are chosen for testing the MCHP configurations. The building study cases are based on a typical Danish single-story single family house (4 occupants) with 126 m² of heated floor surface area. One house is a well-insulated building with a yearly heating need of 16 kWh/m². The other house is a poorly-insulated building with a yearly heating need of 160 kWh/m². The dwellings are equipped with a hydronic radiant under-floor heating (UFH) system which is the heat sink of the MCHP. In the case of the well-insulated dwelling, the heat source of the heating system is a single collector vertical borehole ground source heat exchanger (VBGSHE) with a depth of 100 m. For the poorly-insulated house, the heat source consists of two VBGSHE of 100 m depth each. The outdoor boundary conditions are extracted from weather file of the national Danish Reference Year 2013 (Johra, 2018).

3.2 Building modelling

Thermodynamic multi-zone models of the building study cases have been created within the MATLAB-Simulink software environment. The heat transfer through the different planar construction elements is calculated with a one-dimensional finite volume method formulation comprising a limited number of control volumes (also known as Resistance-Capacitance or RC thermal network model). Each building model has 10 thermal zones. The UFH system and the VBGSHE are modelled by coupling a "plug flow" model with the ε-NTU method which accounts for the thermal interactions between the adjacent legs of the hydronic circuits. The simulation time step size is set constant to 60 seconds which ensures numerical stability. The entire building model and its sub-components have been validated against well-known commercial software (BSim and COMSOL Multiphysics), experimental data, and with a BESTEST procedure (Johra, 2018).

4. INTEGRATION OF THE MAGNETOCALORIC HEAT PUMP IN BUILDINGS

4.1 Single hydronic loop implementation

The different MCHP configurations can operate at temperatures and fluid flow rates which are compatible with a direct use in the UFH emitters. The MCHP is therefore integrated in the building heating system within a single hydronic loop connecting the VBGSHE and the UFH circuits (see *Figure 3*). There is no intermediate heat exchanger or water storage tank in the circuit and the same heat transfer fluid is circulated through the VBGSHE, the UFH and the MCHP by a single circulation pump (Johra, 2018).

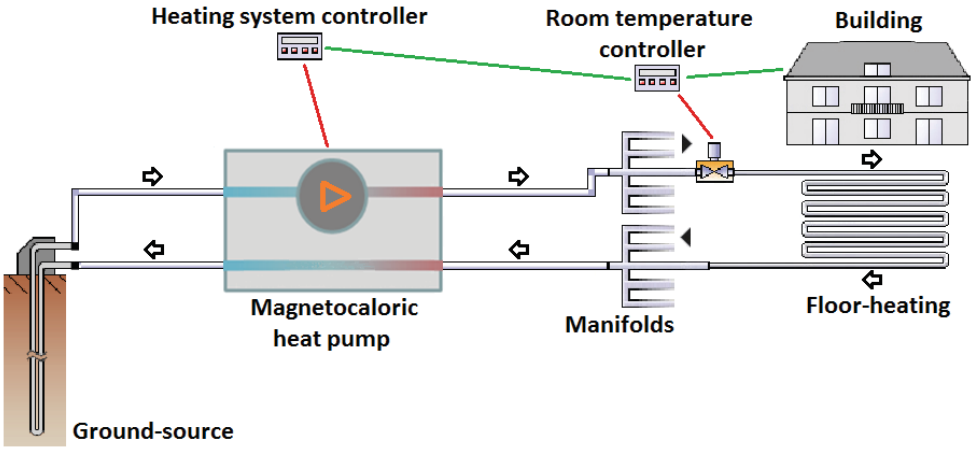

Figure 3: Integration of a magnetocaloric heat pump in a single hydronic loop with vertical borehole ground source heat exchanger and under-floor heating system.

4.2 Cascading of magnetocaloric heat pumps

The inability to generate large temperature span between the heat source and the heat sink is a primary limitation of the current MCHP technology for building heating applications. As shown by Johra et al., (2018), a Gadolinium MCHP connected to a VBGSHE can provide a fluid outlet temperature of up to 27.6 °C, which is sufficient to heat up to 22 °C a well-insulated house equipped with a low-temperature UFH system. However, this fluid outlet temperature is not sufficient for space heating of a poorly-insulated dwelling.

One possible solution to overcome this limitation and increase the outlet fluid temperature of MCHPs lies in establishing cold-to-cold and hot-to-hot connections of the AMRs inside a cascaded magnetocaloric heating network (Tahavori et al., 2017; Filonenko et al., 2018a; Filonenko et al., 2018b). Cascading has the potential for increasing the AMR temperature span ΔT_{AMR}, based on the principle explained in *Figure 4*. The hot (cold) outlet of the n^{th} magnetocaloric heat pump MCHP#n with temperature $T^{o(n)}{}_H$ (temperature $T^{o(n)}{}_C$) is connected to the hot (cold) inlet of the $(n+1)^{th}$ magnetocaloric heat pump MCHP#(n+1) with temperature $T^{i(n+1)}{}_H$ (temperature $T^{i(n+1)}{}_C$). Since it is expected that the MCHP will heat the hot fluid, $T^{i(n)}{}_H < T^{i(n+1)}{}_H$, and cool down the cold fluid, $T^{i(n)}{}_C > T^{i(n+1)}{}_C$, the hot (cold) fluid will be heated up (cooled down) more and more as it progresses through the cascade. As a result, the temperature difference between the outlet and the inlet on both sides ($\Delta T_H = T^{o(N)}{}_H - T^{i(1)}{}_H$ and

$\Delta T_C = T^{i(1)}_C - T^{o(N)}_C$) must increase with each added MCHP. This leads to an augmentation of the total temperature span according to the following equation:

$$\Delta T_{AMR} \equiv T^{o(N)}_H - T^{o(N)}_C = T^{i(1)}_H - T^{i(1)}_C + \Delta T_H + \Delta T_C \quad (3)$$

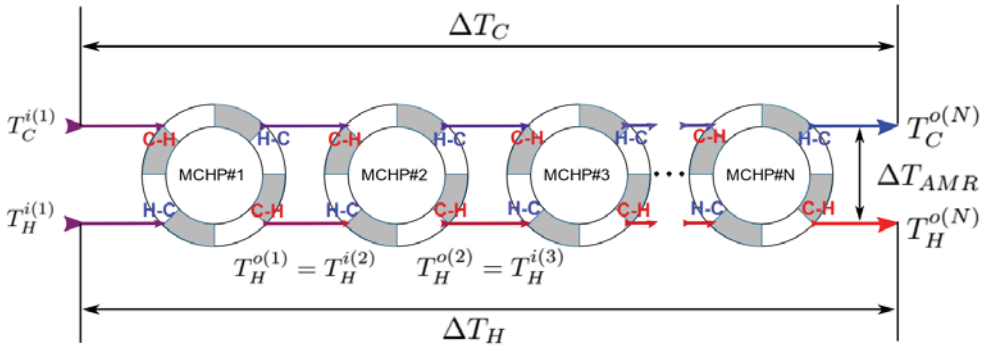

Figure 4: Cascading connection diagram (hot-to-hot and cold-to-cold rule).

Equation (3) defines the temperature span of the cascade as a difference between the hot and the cold outlet of the system, which coincide with the hot and the cold outlets of the last heat pump, MCHP#N. As one can see, the hot and cold temperature spans, ΔT_H and ΔT_C, are the main characteristics of the cascaded network, which relate its "outlet" and "inlet" temperature spans (ΔT_{AMR} and $T^{i(1)}_H - T^{i(1)}_C$).

The flows of fluid in and out of each heat pump during the hot-to-cold and the cold-to-hot blows are denoted in *Figure 4* by C-H and H-C, respectively. From a dynamic point of view, all hot-to-cold blows in the network occur simultaneously during a low field period accepting heat from the heat source at the cold end of the MCHP#1. In the same way, all cold-to-hot blows in the network occur simultaneously during the high-field period rejecting heat at the hot end of the MCHP#N. The coupling of the inlet and outlet temperatures of different heat pumps happens through Dirichlet boundary conditions imposed in individual MCHP models. It is important to keep in mind that because the boundary conditions are obtained under quasi-steady state approximation, the cascading model is an approximation. The latter should be verified in future work against fully transient simulations.

The magnetocaloric network properties established in previous studies (Filonenko et al., 2018a) give a way to simulate and compare the temperature span enhancement in various configurations of cascaded magnetocaloric heating networks (cascades). For simplicity, it is assumed that all MCHP blocks in *Figure 4* contain the same number of AMR beds N_{bed}. When comparing cascades with different number of MCHPs N_{MCHP}, the total MCM mass $m_T = m_{MCHP} \times N_{MCHP}$ of the network is kept constant, forcing a single heat pump mass m_{MCHP} to be inversely proportional to N_{MCHP}. Since the MCHP prototypes have almost identical AMRs, this mass can be found as $m_{MCHP} = m_{bed} \times N_{bed}$. The relationship between different scaling factors can, therefore, be written as:

$$N_{MCHP} \times N_{bed} = m_T/m_{bed} \quad (4)$$

It is required that N_{bed} and N_{MCHP} are both integers, therefore, the AMR mass cannot be chosen freely, but must be a divisor of the total cascade mass. In all simulations, m_T and m_{bed} are both set constant according to a scaling factor $N_{MCHP} \times N_{bed} = 24$. A single MCHP consisting of 24 AMRs connected separately to a common heat source and a common heat

load (parallel connection) is used as reference case. Several cascades are then constructed by grouping these AMRs inside several identical heat pumps without changing their total number or their individual properties, as illustrated in *Figure 5*. The connections between different heat pumps in each cascade correspond to the diagram in *Figure 4*. The detailed numerical model of the AMR system is firstly used to generate the output data for a single MCHP with cold side temperatures ranging from 0 °C to 15 °C, and hot side temperatures ranging from 20 °C to 40 °C. Lookup tables containing operation data are then generated and scaled to calculate the models for each of the heat pumps presented in *Figure 5*:

1. Single MCHP with $N_{bed} = 24$ AMRs connected in parallel ($N_{MCHP}=1$).
2. Two cascaded (hot-to-hot and cold-to-cold connected) MCHPs consisting of $N_{bed} = 12$ AMRs connected in parallel ($N_{MCHP}=2$).
3. Three cascaded MCHPs consisting of $N_{bed} = 8$ AMRs connected in parallel. ($N_{MCHP}=3$)
4. Four cascaded MCHPs consisting of $N_{bed} = 6$ AMRs connected in parallel ($N_{MCHP}=4$).
5. Six cascaded MCHPs consisting of $N_{bed} = 4$ AMRs connected in parallel ($N_{MCHP}=6$).
6. Eight cascaded MCHPs consisting of $N_{bed} = 3$ AMRs connected in parallel ($N_{MCHP}=8$).
7. Twelve cascaded MCHPs consisting of $N_{bed} = 2$ AMRs connected in parallel ($N_{MCHP}=12$).
8. Twenty-four cascaded MCHPs consisting of $N_{bed} = 1$ AMRs ($N_{MCHP}=24$). In this case it would not be practical to use the design described in previous sections, because the individual AMRs are cascaded, which is reflected in the *Figure 5*.

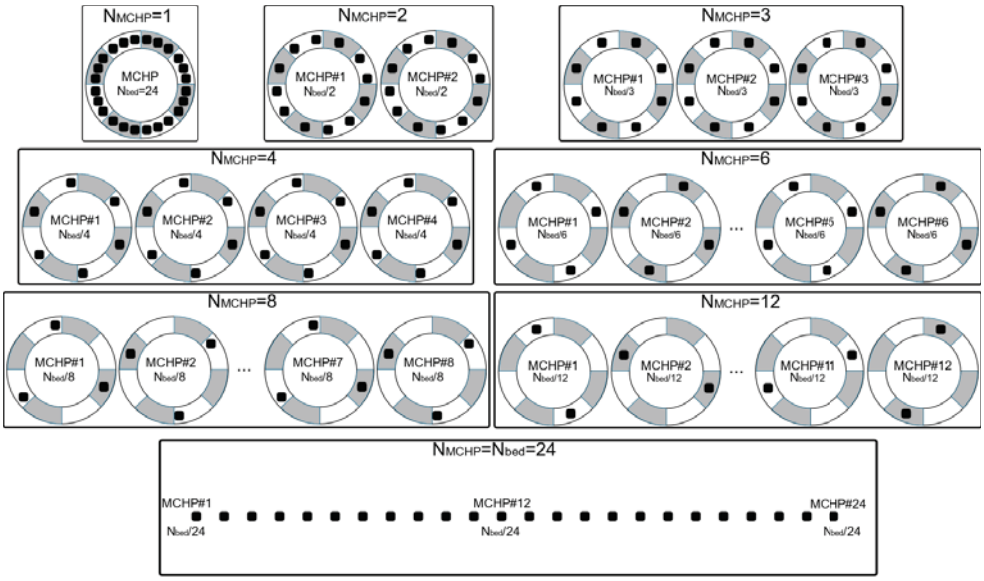

Figure 5: Cascade configurations produced by reconnecting the 24 regenerators of a single MCHP into identical MCHPs in all possible ways.

The cascading was implemented by equating the inlet temperatures of each next MCHP to the outlet of the previous, e.g. $T_o^{(n)}{}_H = T_i^{(n+1)}{}_H$. The cooling and heating powers were calculated as:

$$Q_C = \Sigma\, Q_{Cn,HP}(m_{MCHP}) = N_{bed}\,(Q_{C1} + Q_{C2} + \ldots + Q_{CN}) \quad (5)$$

$$Q_H = \Sigma\, Q_{Hn,HP}(m_{MCHP}) = N_{bed}\,(Q_{H1} + Q_{H2} + \ldots + Q_{HN}) \quad (6)$$

Eqations (5) and (6) assume that all of the cascaded heat pumps contain the same amount of AMRs connected in parallel. Q_{H1}, Q_{H2}, …, Q_{HN}, $Q_{Cn,HP}$ denote the heating powers of AMRs

belonging to different heat pumps MCHP#1, MCHP#2, …, MCHP#N and the total n^{th} heat pumps power, respectively.

5. RESULTS

This section compares the results of numerical tests performed with different configurations of MCHPs and cascaded implementations. The 2 cascaded configurations have been selected among the aforementioned ones for their ability to deliver higher outlet fluid temperature:

- Single MCHP with Gadolinium as MCM.
- Single MCHP with $La(Fe,Mn,Si)_{13}H_y$ as MCM (layered regenerator).
- 12 cascaded MCHPs with Gadolinium as MCM comprising 2 AMRs each connected in parallel.
- 4 cascaded MCHPs with $La(Fe,Mn,Si)_{13}H_y$ as MCM comprising 6 AMRs each connected in parallel (layered regenerators).

All the results are calculated for a four-month test heating period (1st of January to 30th of April). Two coefficients of performance are used here to assess the MCHP efficiency: COP_{AMR} is calculated with the useful heating power delivered by the MCHP and only considering the work due to the AMR internal operation (regenerator hydraulic pressure losses and magnetic work); The COP_{system} is calculated with the useful heating power and considering all the work power usage of the heating system including circulation pump work, motor work and valves work (Johra et al., 2018). The rotation frequency of the MCHP system is always kept constant at 1 Hz.

5.1 Nominal performance tests of the magnetocaloric heat pumps

The initial numerical tests are performed with the MCHPs running at constant fluid flow rate and heating up only one thermal zone of the well-insulated house (living room) during the four-month heating test period.

One can see in *Figure 6* the useful heating power outputs of the different MCHP configurations. When the fluid flow rate is increasing, the power output of the MCHP is increasing almost linearly until a certain point. The higher the flow rate passing through each AMR and the more heat energy can be exchanged between the regenerator bed and the fluid. However, above an optimum point, further increase of the fluid flow rate disturbs the temperature profile of the AMR, causing a drop of the temperature output. Consequently, the MCHP heating power decreases rapidly (Li et al. 2006). In addition, higher fluid flow rate increases pumping work due to pressure losses in the hydraulic system, which decreases the system's COP even more. To improve the heating power output of the AMR system with higher fluid flow rates, the operational rotation frequency of the MCHP has to be increased, which brings other technical challenges.

With a maximum average heating power of 158 W, the Layered $La(Fe,Mn,Si)_{13}H_y$ single MCHP has a very limited power compared to the other configurations. The Gadolinium single MCHP presents a linear increase of its power output with a maximum average value of 2560 W at maximum fluid flow rate. The cascade systems present a heating power peak at 2935 W and 3652 W for the Gadolinium cascaded MCHPs and the Layered $La(Fe,Mn,Si)_{13}H_y$ cascaded MCHPs, respectively. However, one can notice that the maximum heating power output of the cascaded configurations occurs at lower fluid flow rate than the Gadolinium single MCHP, especially in the case of the Gadolinium cascaded MCHPs.

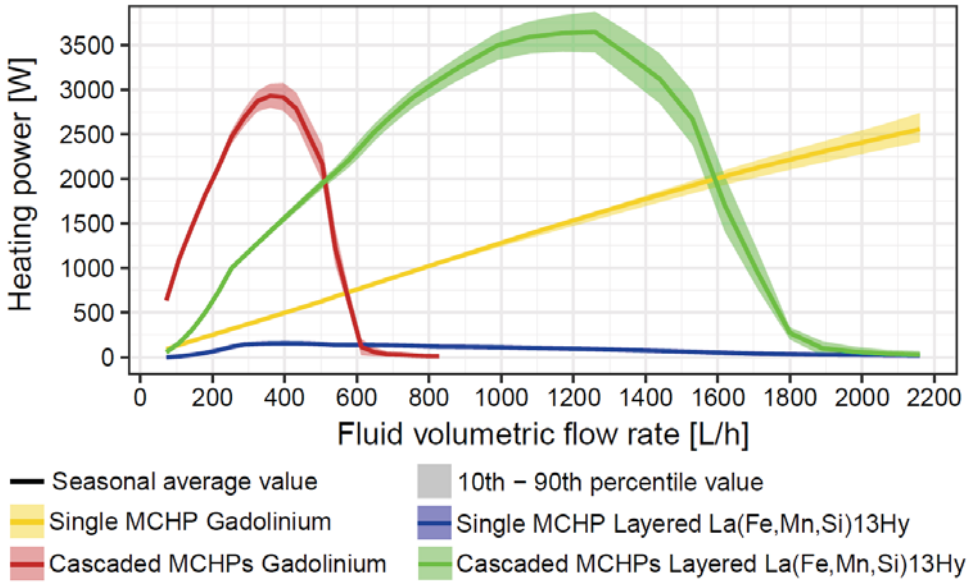

Figure 6: Heating power production of the MCHP as function of fluid volumetric flow rate.

Similar trends can be seen in *Figure 7* concerning the MCHP outlet fluid temperature. The maximum average outlet fluid temperature of the Layered $La(Fe,Mn,Si)_{13}H_y$ single MCHP is 22.3 °C (12 K temperature span), which is very critical for indoor space heating purpose. The other configurations manage to produce more appreciable fluid temperature outlet with a maximum average value of 27.6 °C (19.9 K temperature span), 35.3 °C (26.7 K temperature span) and 30.3 °C (23.8 K temperature span) for the Gadolinium single MCHP, the Gadolinium cascaded MCHPs and the Layered $La(Fe,Mn,Si)_{13}H_y$ cascaded MCHPs, respectively.

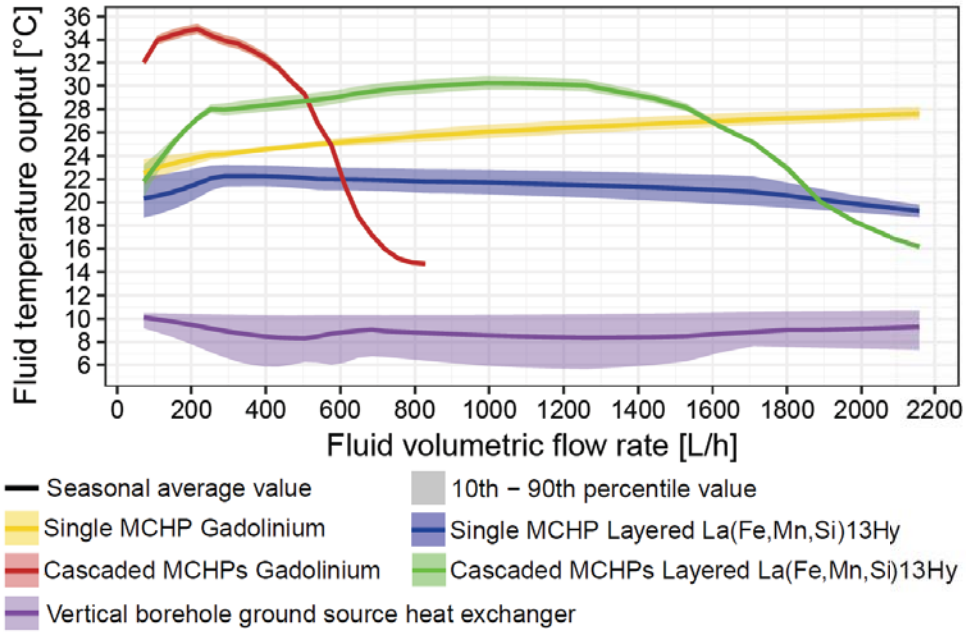

Figure 7: Fluid temperature output of the MCHP as function of fluid volumetric flow rate.

Concerning the systems energy efficiency, one can see in *Figure 8* that the COP_{AMR} (only considering the AMR internal operation efficiency) of the Gadolinium single MCHP, the Gadolinium cascaded MCHPs and the Layered $La(Fe,Mn,Si)_{13}H_y$ cascaded MCHPs reaches high values for low fluid flow rates. For these cases, the maximum average COP_{AMR} is 12.1, 6.9 and 12.3, respectively. Because the Layered $La(Fe,Mn,Si)_{13}H_y$ single MCHP has a much lower heating power output but has similar operational hydraulic pressure losses and magnetic work, its COP_{AMR} is much lower with a maximum average value of 3.3.

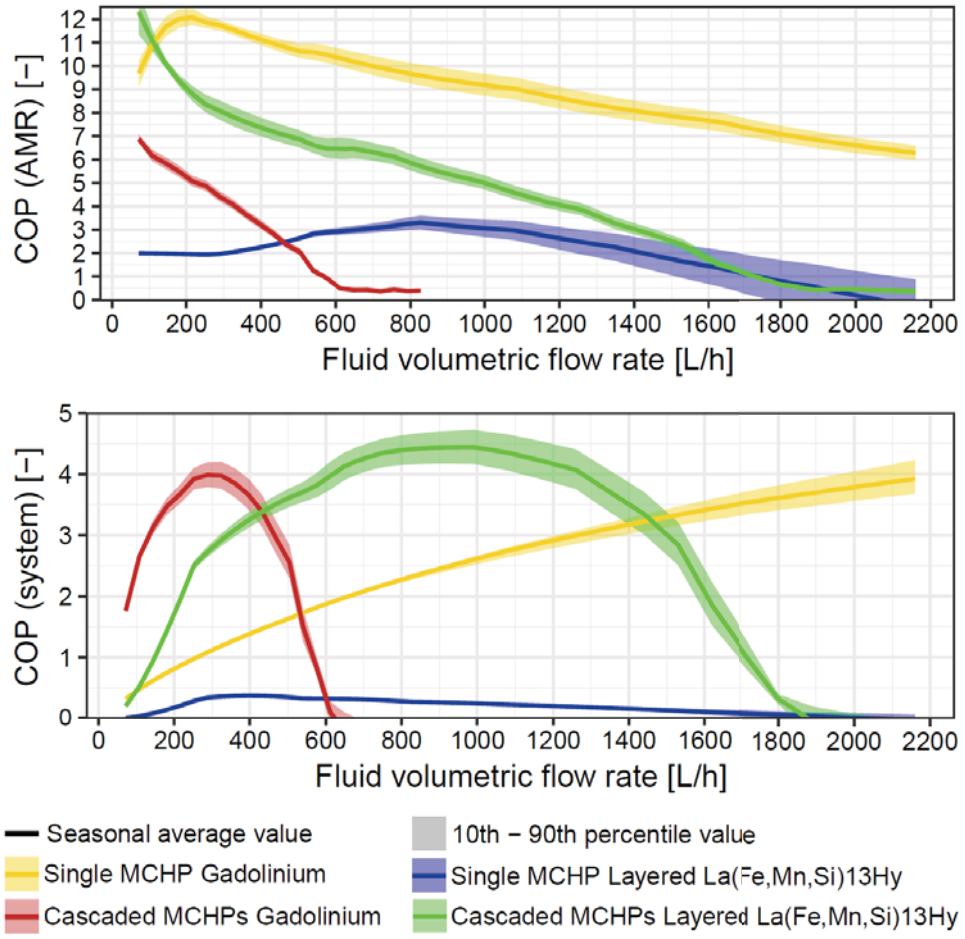

Figure 8: COP_{AMR} (top figure) and COP_{system} (bottom figure) of the MCHP as function of fluid volumetric flow rate.

The COP_{system} profiles of the different MCHP configurations is very similar to the heating power output curves because the work input needs of the entire heating system is rather stable over the whole range of fluid flow rates. The maximum average COP_{system} is 3.92, 0.37, 3.99 and 4.45 for the Gadolinium single MCHP, the Layered $La(Fe,Mn,Si)_{13}H_y$ single MCHP, the Gadolinium cascaded MCHPs and the Layered $La(Fe,Mn,Si)_{13}H_y$ cascaded MCHPs, respectively. One can observe that the Gadolinium single MCHP and the Layered cascaded MCHPs have very appreciable COP_{system} which are within the 3 - 5 range of typical COPs for conventional vapor-compression heat pumps (Self et al., 2013; Fischer and Madani, 2017). However, the significant difference between the COP_{AMR} and the COP_{system} indicates that a large part of the system's inefficiency is due to energy losses associated to the pump, the motor and the valves. The reduction of the latter constitutes a compelling engineering challenge for the development of this technology.

5.2 Test of a well-insulated house with a single MCHP

In this section, the 2 single MCHPs are tested numerically to provide for the indoor space heating needs of the entire building study case: a well-insulated single family house with a low-temperature UFH system. As shown previously, the Gadolinium single MCHP can provide enough heating power output to warm up the entire building. Therefore, only one of it is integrated in the well-insulated dwelling. On the other hand, the Layered La(Fe,Mn,Si)$_{13}$H$_y$ single MCHP has a very limited heating power output. Therefore in that case, one MCHP is integrated in each of the thermal zone UFH sub-circuits.

The controller of the Gadolinium MCHP is an ON/OFF controller connected to individual thermostats in each room of the house. Similarly, each of the Layered La(Fe,Mn,Si)$_{13}$H$_y$ MCHP is controlled with an ON/OFF controller connected to the thermostat of the corresponding thermal zone. In this case, the operational MCHP fluid flow rate is set to 400 L/h for optimum performance (according to previous section's tests).

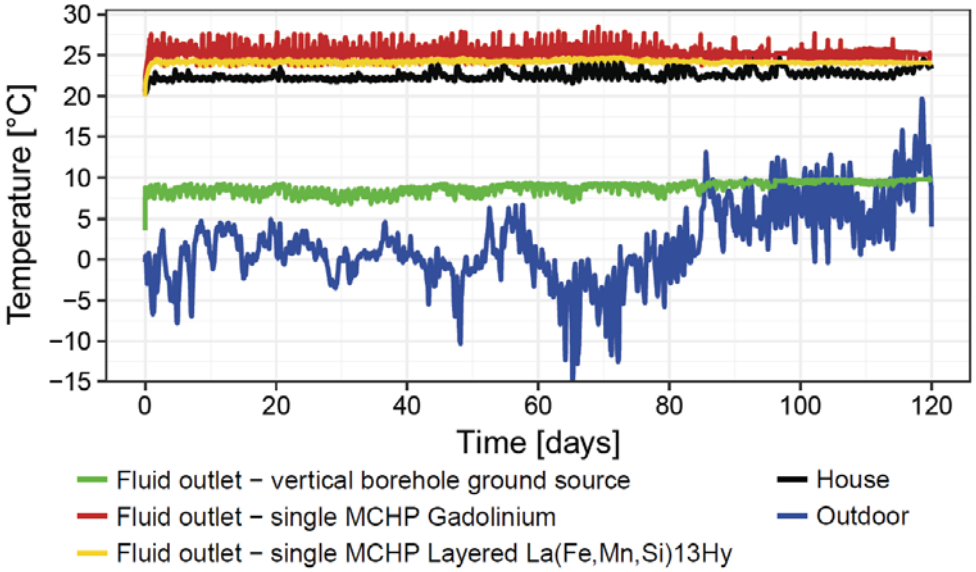

Figure 9: Temperatures of the building system as function of time during the four-month heating test period for the well-insulated house cases with single MCHPs.

Both the Gadolinium and the Layered La(Fe,Mn,Si)$_{13}$H$_y$ single MCHPs manage to provide enough heating power to keep the well-insulated house at an indoor temperature set point of 22 °C during the four-month heating test period. One can see in *Figure 9* that the Gadolinium system provides a higher fluid temperature outlet (25.4 °C in average) compared to the Layered La(Fe,Mn,Si)$_{13}$H$_y$ one (24.2 °C in average). The oscillations of fluid temperature in the hydronic systems are induced by the start-and-stop cycles of the MCHP.

However, one can clearly observe in *Figure 10* that the Gadolinium heating system has a much higher energy efficiency (average seasonal COP$_{system}$ of 1.84) compared to the Layered La(Fe,Mn,Si)$_{13}$H$_y$ one (average seasonal COP$_{system}$ of 0.57). In the full-house heating test, the COP of the Gadolinium system is much lower than the maximum COP achieved in the previous section's test. This is due to the fact that the controller of the Gadolinium single MCHP does not manage to operate the heating system at optimum (maximum) fluid flow rate

most of the time. On the other hand, the average seasonal COP of the Layered $La(Fe,Mn,Si)_{13}H_y$ system is higher than the maximum COP achieved in the previous section's test. This is because implementing one MCHP per UFH sub-loop induces a significant increase of the total heating power production while the pumping work (which holds a large share of the total system's inefficiency) remains relatively stable.

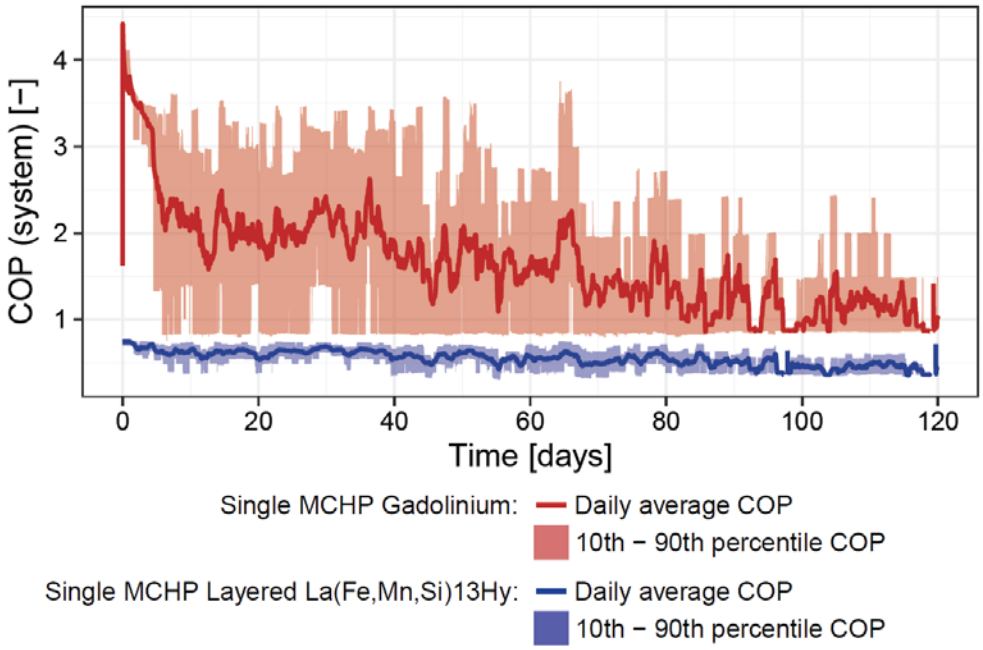

Figure 10: COP of the entire heating system as function of time during the four-month heating test period for the well-insulated house cases with single MCHPs.

5.3 Test of a poorly-insulated house with cascaded MCHPs

In this section, the 2 cascaded MCHPs systems are tested to provide for the indoor space heating needs of the entire building study case: a poorly-insulated single family house with a high-temperature UFH system. Because the envelope thermal performance of this building is lower than in the previous section's test, the usage of cascaded MCHPs systems is required to provide higher heating power output and warmer fluid inlet to each room in the house. Similarly to the Layered $La(Fe,Mn,Si)_{13}H_y$ single MCHP case, there is one cascaded MCHPs system integrated in each of the thermal zone UFH sub-circuits. It is therefore ensured that enough heating power is provided to all rooms in the dwelling.

For both cascaded heating systems, the MCHPs are controlled with an ON/OFF controller connected to the thermostat of the corresponding thermal zone. To ensure optimum performance (according to previous section's tests), the operational MCHP fluid flow rate is set to 300 L/h and 1000 L/h for the Gadolinium and the Layered $La(Fe,Mn,Si)_{13}H_y$ system, respectively.

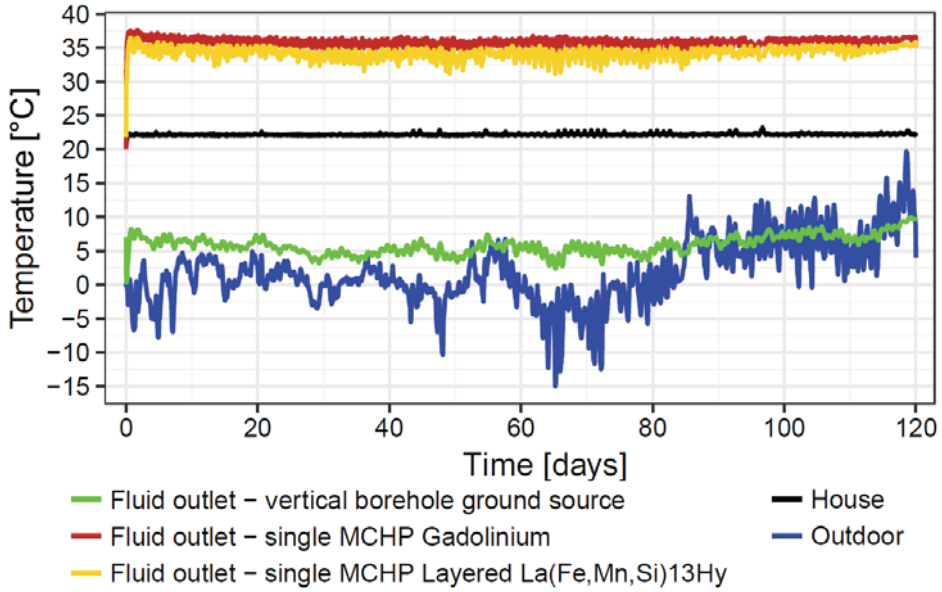

Figure 11: Temperatures of the building system as function of time during the four-month heating test period for the poorly-insulated house cases with cascaded MCHPs.

Both the Gadolinium and the Layered $La(Fe,Mn,Si)_{13}H_y$ cascaded MCHPs manage to provide enough heating power to keep the poorly-insulated house at an indoor temperature set point of 22 °C during the four-month heating test period. One can see in *Figure 11* that the Gadolinium system provides a higher fluid temperature outlet (36.0 °C in average) compared to the Layered $La(Fe,Mn,Si)_{13}H_y$ one (34.3 °C in average).

However, one can observe in *Figure 12* that both systems have an appreciable and very similar energy efficiency. The average seasonal COP_{system} is 2.62 and 2.63 for the cascaded MCHPs Gadolinium and the cascaded MCHPs Layered $La(Fe,Mn,Si)_{13}H_y$, respectively. This result is coherent with the previous nominal performance tests indicating that both cascaded systems have similar COP_{system} at optimum fluid flow rate.

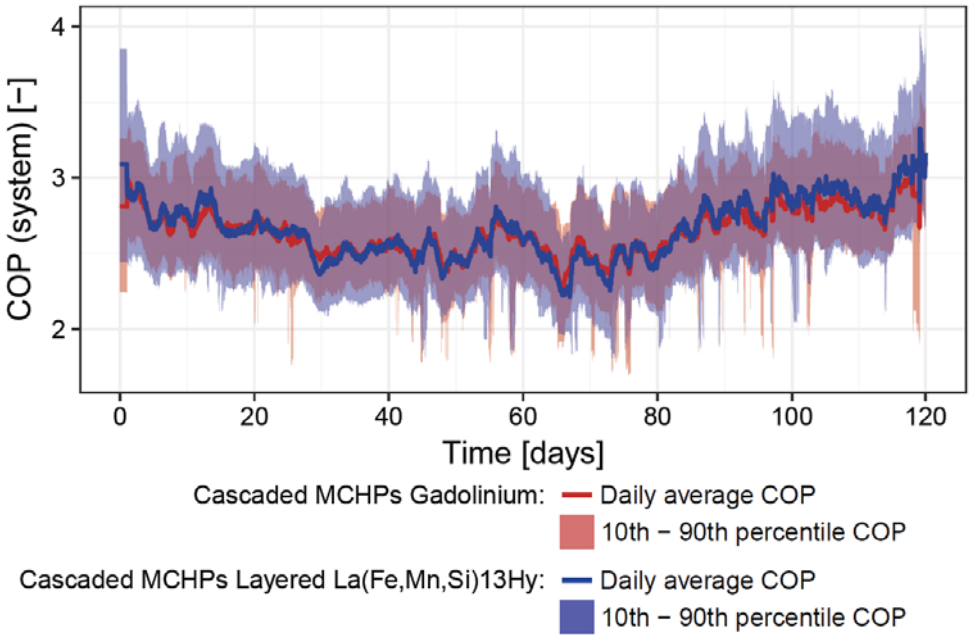

Figure 12: COP of the entire heating system as function of time during the four-month heating test period for the poorly-insulated house cases with cascaded MCHPs.

6. CONCLUSION

This article presented an innovative heat pump system based on the magnetocaloric effect and showed that it can be used for building heating applications. The active magnetic regenerator technology for magnetocaloric heat pump systems has the potential for high coefficient of performance but has yet to prove its competitiveness in comparison to vapor-compression devices. Currently, the main limitation of the magnetocaloric heat pump systems is the small temperature span they can generate between heat source and heat sink. To overcome this problem, the creation of cascaded magnetocaloric heating networks appears to be an interesting solution.

This numerical investigation has shown that different configurations of magnetocaloric heating system can provide enough heating power output for building applications. At nominal fluid flow rate, the magnetocaloric heat pumps could provide fluid temperature outlet at up to 35.3 °C and presents nominal coefficient of performance of up to 4.45.

When integrated in a single family house equipped with an under-floor heating system and a ground source heat exchanger, the magnetocaloric heating system was able to keep the dwelling at a set point temperature of 22 °C during the entire heating test period under Danish winter conditions. For well-insulated houses, single magnetocaloric heat pump systems were sufficient to operate with low-temperature under-floor heating systems. However, average seasonal COPs were not higher than 1.84. In the case of poorly-insulated houses, cascaded magnetocaloric heating networks were able to provide higher fluid temperature output to the under-floor heating system while operating at appreciable average seasonal COPs of up to 2.63.

Further research in the field of magnetocaloric technology is necessary to make the latter cost-effective and able to compete with conventional heat pump system. New magnetocaloric materials should be developed and characterized. More numerical and experimental test should be conducted on magnetic heating system and the different configurations of cascaded magnetocaloric heating networks.

ACKNOWLEDGEMENT

This work was financed by the ENOVHEAT project, which is funded by Innovation Fund Denmark (contract no 12-132673).

REFERENCES

Bahl, C.R.H., 2015. *ENOVHEAT project summary: development of efficient novel magnetocaloric heat pumps*. http://www.enovheat.dk/Research/ProjectSummary

Barclay, J.A., and Steyert, W.A., 1982. *US Patent US4332135*.

Building Performance Institute Europe (BPIE), 2011. *Europe's Buildings under the Microscope, Executive Summary 2011*.

Chen, F. C., Murphy, R. W., Mei, V. C., and Chen, G. L., 1992. *Thermodynamic Analysis of Four Magnetic Heat-Pump Cycles*. Journal of Engineering for Gas Turbines and Power, 114(4), 715-720.

Cockroft, J., and Kelly, N., 2006. *A comparative assessment of future heat and power sources for the UK domestic sector*. Energy Conversion and Management, 47, 2349-2360.

Engelbrecht, K. 2008. *A Numerical Model of an Active Magnetic Regenerator Refrigerator with Experimental Validation.* Ph.D. thesis, University of Wisconsin, Madison.

Engelbrecht, K., Eriksen, D., Bahl, C.R.H., Bjørk, R., Geyti, J., Lozano, J.A., Nielsen, K.K., Saxild, F., Smith, A., and Pryds, N., 2012. *Experimental results for a novel rotary active magnetic regenerator*. International Journal of Refrigeration 35, 1498-1505.

Filonenko, K., Johra, H., Dall'Olio, S., Engelbrecht, K., Heiselberg, P., Bahl, C., and Veje, C. T., 2018a. *Simulation of a magnetocaloric heating network*. Submitted to 8th International Conference on Magnetic Refrigeration at Room Temperature.

Filonenko, K., Lei, T., Veje, C., Engelbrecht, K., Johra, H., Heiselberg, P. K., and Bahl, C. R. H., 2018b. *Magnetocaloric heating modules for scalable and efficient heating*. Submitted to International Journal of Thermal Sciences.

Fischer, D., and Madani, H., 2017. *On heat pumps in smart grids: A review*. Renewable and Sustainable Energy Reviews, 70, 342-357.

Giauque, W.F., and MacDougall, D.P., 1935. *The production of temperatures below one degree absolute by adiabatic demagnetization of gadolinium sulfate*. Journal of the American Chemical Society 57, 1175-1185.

International Energy Agency (IEA), 2013. *Transition to Sustainable Buildings: Strategies and Opportunities to 2050*.

Jacobs, S., Auringer, J., Boeder, A., Chell, J., Komorowski, L., Leonard, J., Russek, S., and Zimm, C., 2014. *The performance of a large-scale rotary magnetic refrigerator*. International Journal of Refrigeration 37(1), 84-91.

Johra, H., Filonenko, K., Heiselberg, P., Veje, C., Lei, T., Dall'Olio, S., Engelbrecht, K., and Bahl, C., 2018. *Integration of a magnetocaloric heat pump in a low-energy residential building*. Building Simulation: An International Journal.

Johra, H., 2018. *Integration of a magnetocaloric heat pump in energy flexible buildings*. Ph.D. thesis, Aalborg University, Aalborg.

Kitanovski, A., Tušek, J., Tomc, U., Plaznik, U., Ožbolt, M., and Poredoš, A., 2015. *Magnetocaloric Energy Conversion: From Theory to Applications*. New York: Springer International Publisher, New York.

Lei, T., Engelbrecht, K., Nielsen, K. K., and Veje, C. T., 2017. *Study of the geometries of active magnetic regenerators for room temperature magnetocaloric refrigeration*. Applied Thermal Engineering, 111, 1232-1243.

Li, P., Gong, M., Yao, G., and Wu, J., 2006. *A practical model for analysis of active magnetic regenerative refrigerators for room temperature applications*, International Journal of Refrigeration, 29, 1259-1266.

Lund, H., Möller, B., Mathiesen, B. V., and Dyrelund, A., 2010. *The role of district heating in future renewable energy systems*. Energy, 35(3), 1381-90.

Navickaitė, K., Neves Bez, H., Lei, T., Barcza, A., Vieyra, H., Bahl, C.R.H., and Engelbrecht, K., 2018. *Experimental and numerical comparison of multi-layered La(Fe,Si,Mn)13Hy active magnetic regenerators*. International Journal of Refrigeration 86, 322-330.

Okamura, T., and Hirano, N., 2013. *Improvement of the performance of a room temperature magnetic refrigerator using Gd-alloy*. Journal of the Japan Society of Applied Electromagnetics and Mechanics 21 (1), 10-14.

Palzer, A., and Henning, H. M., 2014. *A comprehensive model for the German electricity and heat sector in a future energy system with a dominant contribution from renewable energy technologies – Part II: Results*. Renewable and Sustainable Energy Reviews, 30, 1019-1034.

Self, S. J., Reddy, B. V., and Rosen, M. A., 2013. *Geothermal heat pump systems: Status review and comparison with other heating options*. Applied Energy, 111, 341-348.

Smith, A., Bahl, C.R.H., Bjørk, R., Engelbrecht, K., Nielsen, K.K., and Pryds, N., 2012. *Materials challenges for high performance magnetocaloric refrigeration devices*. Advances Energy Materials 2, 1288-1318.

Tahavori, M., Filonenko, K., Veje, C. T., Lei, T., Engelbrecht, K., and Bahl, C., 2017. *A Cascading Model Of An Active Magnetic Regenerator System*. Proceedings of the 7th International Conference on Magnetic Refrigeration at Room Temperature, Turin, Italy, IIF/IIR, 248-251.

Weiss, P., and Piccard, A., 1918. *Sur un nouveau phénomène magnétocalorique*. Comptes Rendus Acad. Sci. (Paris) 166, 352-354.

Questions and Answers:

Madjidi Madjid

What does mean COP < 1?

Hicham Johra:

It means that the device produces less useful heating power than it uses electrical power: COP = useful heating power / (pumping work + valve work + motor work).

***

Vincent Lemort

What is the intensity of the magnetic field?

Hicham Johra:

1.46 Tesla inside the regenerator.

***

Vincent Lemort

What is the frequency of rotation (in Hz)? And what is limiting it? Is it the time needed to heat up and cool down the material?

Hicham Johra:

1 Hz rotation operation. Commonly 0.2-4 Hz operation. Larger operation frequency can bring problem for time to perform heat transfer between material and the fluid, but also creation of Eddy currents in the iron yoke of the machine with parasitic heat losses and counter torque which decrease COP and causes technical problems.

Simulation of solar collectors with two low temperature heat engines for buildings applications

V. Novotny[1, 2,3]*, D.J. Szűcs, M. Kolovratnik[2], T. Matuska[2]

(1) Faculty of Mechanical Engineering, Czech Technical University in Prague, Technická 4, 16607 Prague 6, Czech Republic

(2) University Centre for Energy Efficient Buildings, Czech Technical University in Prague, Trinecka 1024, 27343 Bustehrad, Czech Republic

(3) Thermodynamics Laboratory, Faculty of Applied Sciences, University of Liège, Allée de la Découverte 17, B-4000, Liège, Belgium

ABSTRACT

Previous theoretical work identified the absorption power cycles (APC) working with LiBr-H_2O solution as a working fluid, as an alternative to ORC. For low temperature waste heat recovery, it may offer a higher utilization efficiency. The APC similarly as zeotropic ORC has an advantage of higher exergy efficiency of heat exchangers by smoother temperature match of hot and cold fluids provided by temperature glide of the working fluid.

This work explores application to another low temperature heat sources, which are solar thermal collectors, particularly evacuated tube collectors. Such configuration may be interesting for buildings application, offering to use excess of thermal energy for electricity production and taking advantage of APC and ORC feasibility for low power systems.

A model is developed coupling performance of the heat engine (APC and ORC) with the collectors. Behaviour and overall performance of such system is estimated based on experimental solar irradiation and temperature data for one year. The results are compared to performance of photovoltaic modules (PV). The models show significantly lower potential for power production, but the APC system could find application in suggested alternative, hybrid and combined cooling and power configurations integrated into buildings' systems for supply of these energies.

Keywords: solar collector, Absorption power cycle, LiBr, Kalina cycle, ORC, Cogeneration

1. INTRODUCTION

Current world tries to focus its future in the energy field into new, renewable and environmentally friendly resources and energy savings as well as better utilization of current resources. Various works highlight a potential of waste heat recovery together a note, that most of the untacked potential lies within low temperature domain, especially below 200°C, such as (Chan, Ling-Chin, & Roskilly, 2013; Johnson, William, Choate, & Amber Davidson, 2008). Commonly considered technology for tapping low temperature sources is based on ORC units. Problem is that capital cost of such unit is for low temperature applications rather high and a net efficiency of such units as well as exergetic efficiency is often deep below the thermodynamic limits, mainly due to high exergetic losses during isothermal boiling and condensation and high parasitic load for heat rejection. A range of processes has been proposed to decrease the losses by improving the temperature match within the heat exchangers, but they have been commercialized very little or not at all. These cycles include transcritical ORC, trilateral cycles, ORC with zeotropic fluid mixtures and also absorption

power cycles (Chan et al., 2013; Chen, Goswami, & Stefanakos, 2010; Lecompte, Huisseune, van den Broek, Vanslambrouck, & De Paepe, 2015; Novotny & Kolovratnik, 2017).

Absorption power cycles (APC) use, similarly as zeotropic ORC, a working fluid mixed from multiple (typically two) components with different boiling points. During the evaporation (desorption) process the less volatile component evaporates first, gradually decreasing its concentration in the liquid content and thus increasing the mixture boiling point. Similarly during condensation (absorption) the liquid concentration of less volatile component gradually decreases and so does the saturation temperature. With a counter-current heat exchanger we can achieve a good temperature match between the fluids and thus decrease the exergy losses. Compared to the ORC where all fluid evaporates, the APC provides one another degree of freedom as the evaporation is only partial, the two phase mixture is split into a vapour stream going to turbine and a liquid stream going through a recuperator and mixing with the vapour at the beginning of an absorber. A principle of the operation is obvious from a schematic diagram in Fig. 1 together with an example of a Q-T diagrams for the absorber and desorber.

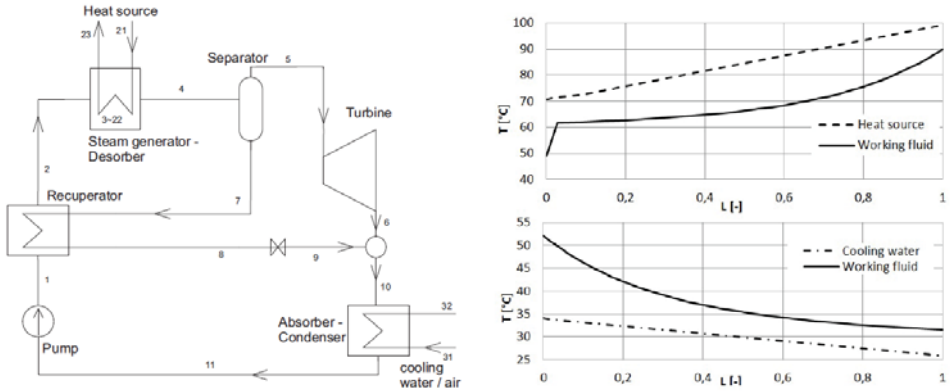

Figure 1: (a) Schematic diagram of an absorption power cycle; (b) Example of the $\dot{Q} - T$ diagram for heat addition and rejection.

The most common and best known APC is the Kalina cycle, which uses an ammonia-water mixture. There is however a large range of possibilities for using other working fluids (Sun, Fu, & Zhang, 2012). Recently in few works as (Garcia-Hernando, de Vega, Soria-Verdugo, & Sanchez-Delgado, 2013; Rogdakis & Lolos, 2015; Shokati, Ranjbar, & Yari, 2014), there have been explored possibilities, features and identified some advantages of LiBr solution APC mostly in terms of cycle efficiency. Comparison has been done with both with water, organic fluids and typical Kalina cycle with ammonia-water mixture. Utilization efficiency of APC has been further explored in (Novotny & Kolovratnik, 2017), comparing aqueous salt solutions (LiBr, LiCl and $CaCl_2$ considered for absorption cooling), ammonia-water mixture and ORCs with different working fluids, further in (Eller, Heberle, & Brüggemann, 2017; Novotny, Vitvarova, & Kolovratnik, 2017) comparing alcohol mixtures, ammonia-water mixture, ORCs both pure fluid and mixtures at both sub- and super-critical conditions. Results partly differ based on selected boundary conditions and whether parasitic load for heat rejection (pumps, fans) was included or not. In overall the APC, especially with salt mixtures, appears as the most perspective for applications to very low temperature heat sources, namely below 100-120°C. Zeotropic mixture ORC results as more efficient choice for higher temperatures, then follows the APC with alcohol mixture and water-ammonia Kalina cycle.

Performance of an ORC with a range of explored working fluids (also with supercritical working fluids) is significantly worse. Note that as the heat source temperature decreases the potential advantage of the APC compared to alternatives increases.

Current energy goals in electricity production also require large utilization of renewable energy sources. Solar energy is widely abundant and available. The most common conversion technology to electricity is by PV panels, which is rather simple and already also on a cost competitive level and for grid connection easily scalable to units even in order of 100s Watts. Major disadvantage is however the intermittency of such source with possible change between nearly 100% of the output in less than a minute. Contrary to that are concentrated solar plants heating working fluid to temperatures 300-600°C (typically with intermediate heat transfer fluids) using different mirrors configurations with power output ranging typically in 10s-100s MW (except for parabolic mirrors with Stirling engine in the focus with ~10 kW). These are efficient (20+%) commercial systems, typically with integrated thermal energy storage for hours of full load power production, but applicable only for large scale. For lower temperatures and plant scale, ORC is often considered. Solar ORC plants were investigated both theoretically and experimentally, can work with various types of solar collectors but most of the built units are still only for research and demonstration purposes (Aboelwafa, Fateen, Soliman, & Ismail, 2018; Dickes, 2016; Modi, Bühler, Andreasen, & Haglind, 2017) .

Given the potential of the APC with LiBr solution in waste heat recovery and given the presence of much cheaper lower temperature solar collectors for heating on the market, a suggestion to combine these two system emerges, extending the scope of possible APC applications. This work explores the option of coupling the heat engines (ORC and APC) and solar collectors (evacuated tube type). Overall performance is then analysed for changing ambient conditions based on experimental data for one year and finally a brief comparison of power produced is done with respect to PV modules.

2. MODELLING

Models of all equipment are based on mass (for each of the fluid component) and energy conservation with standard notations, as is shown in Eq. (1) and (2). Specific models are described separately below. The solar model and all subsequently related have a time step of 1 h for a time period of one year, based on the experimental data available for this work. Performance characteristics of heat engines are modelled in EES (Hans-Joachim Kretzschmar, Ines Stoecker, Matthias Kunick, S. Hasch, 2015), rest of the models and result processing are made in MS Excel.

$$\sum \xi_i \dot{m}_i = 0 \tag{1}$$

$$\sum h_i \dot{m}_i + \dot{Q}_j - \dot{W}_j = 0 \tag{2}$$

In the analysis, there will be used following performance metrics of various components. Gross and net efficiency of heat engine (thermodynamic cycle alone or with auxiliaries) in Eq. (3) and Eq. (4) respectively. Net efficiency of the system with heat engine is then described by Eq. (5), which is also applied for the PV modules used for comparison.

$$\eta_{cycle,gross} = \frac{\dot{W}_{cycle}}{\dot{Q}_{col,net}} = \frac{\dot{W}_{exp} - \dot{W}_{pump}}{\dot{Q}_{col,net}} \quad (3)$$

$$\eta_{cycle,net} = \frac{\dot{W}_{net}}{\dot{Q}_{col,net}} = \frac{\dot{W}_{exp} - \dot{W}_{pump} - \dot{W}_{colpump} - \dot{W}_{DC\ pump} - \dot{W}_{DC\ fan}}{\dot{Q}_{col,net}} \quad (4)$$

$$\eta_{net} = \frac{\dot{W}_{net}}{G_T\ A_a} \quad (5)$$

2.1.1 Assumptions and boundary conditions

The solar model uses normalized experimental data of temperatures and solar irradiation of horizontal plane measured for location of UCEEB, Czech Technical University in Prague (see also Fig. 2). Other ambient conditions (pressure, relative humidity) are considered constant. Within the models are assumed steady state conditions and all transient effects are neglected. Heat loss and pressure drop is considered only where explicitly stated, otherwise neglected. Heat transfer is limited by minimal temperature differences (pinch points), which are kept constant. Numerically the constant assumptions and boundary conditions are summarized in Tab. 1, where subscripts $_{amb}$ stand for ambient, $_{liq}$ stand for liquid phase of fluid, $_{wf}$ for working fluid, $_{DC}$ for dry cooler, $_{exp}$ for expander. Included are main collector parameters of the selected collector *Eurosun Sunstar DF 100/6* obtained from the *Solar Keymark Database*[1]. The collector was selected to be among the more efficient among vacuum tube collectors on the market.

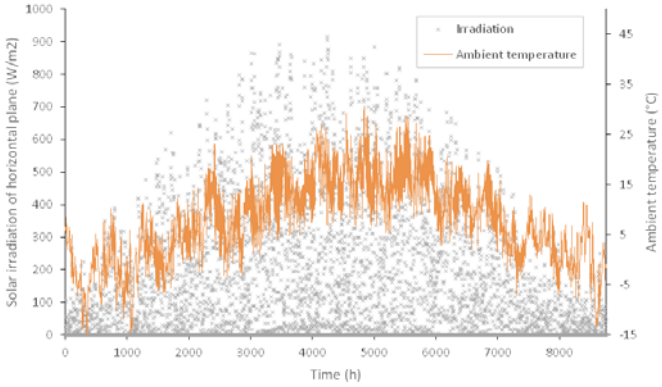

Figure 2: Illustration of used experimental data for solar irradiation of horizontal surface and ambient temperature.

Table 1: Boundary conditions and parameters of the models.

p_{amb}	RH_{amb}	$\Delta T_{min,liq\text{-}wf}$	$\Delta T_{min,wf\text{-}wf}$	$\Delta T_{min,DC}$	$\Delta p_{cool\ loop}$	Δp_{DC}	η_{exp}	η_{pump}	η_{fan}
[kPa]	[%]	[°C]	[°C]	[°C]	[kPa]	[Pa]	[%]	[%]	[%]

[1] http://www.solarkeymark.dk/CollectorCertificates

101	70	5	5	10	80	200	80	70	70
β_{surf}	γ	ρ	φ	$\eta_{col,0}$	a_1	a_2	A_a		
[°]	[°]	[-]	[°]	(%)	(W/m^2 K)	(W/m^2 K^2)	(m^2)		
30	0	0.2	50	79.2	1.62	0.0021	1.114		

2.1.2 Solar model

Solar model follows a general model described for example by (Cihelka, 1994) and here will be described only briefly. In the model there are following inputs:

- Day of the year
- Solar time *ST* (1 hour resolution, adjusted to measured data from UCEEB, CTU in Prague)
- Experimental solar irradiance to horizontal surface *G=f(ST)* for each hour from above
- Collector slope
- Collector azimuth
- Location latitude

The output of the solar model is then irradiance of a specified surface with its distribution to direct, diffuse and reflected light. The model first describes geometry of Sun movement with respect to given position and surface on Earth with horizontal irradiation determined from solar constant G_{sc} from Eq. (6). Then is used a correlation (Orgill & Hollands, 1977) using sky clearness index relating solar irradiation out of the Earth's atmosphere G_0 and measured value G to obtain diffuse light, Eq. (7). Following that is evaluated the diffuse radiation and direct radiation contents. Finally, for a surface that is not horizontal there is additional (though small) content of reflected light.

$$G_0 = G_{sc}\left(1 + 0.033 \cdot \cos\frac{360 \cdot DR}{365}\right)\sin h \tag{6}$$

$$k_T = \frac{G}{G_0} \approx \frac{G_d}{G} = \begin{cases} 1.0 - 0.249k_T & for\ k_T < 0.35 \\ 1.557 - 1.84k_T & for\ 0.35 < k_T < 0.75 \\ 0.177 & for\ k_T > 0.75 \end{cases} \tag{7}$$

Irradiation of specific surface is then determined by trigonometric functions. Note that the trigonometric functions in the relations might cause incorrect values near incidence angles very close to and above 90°. Therefore, the irradiance values are limited to incidence angles only to 85° (actual power obtainable between 85°and 90° is anyway negligible and below the model accuracy).

Also note that the solar time provided with experimental data has to be adjusted to fit the actual longitude. It can be done either knowing a time zone and time of measurement. Other option (useful when these data are not available) is to plot the average irradiation and find the time of solar noon as a maximum of the smooth curve running through these points.

2.1.3 Collector model

The collector model provides a portion of irradiation that is absorbed by the collector, heat losses that are a function of ambient temperature and finally its output and efficiency. The inputs of the collector model are following:

- Irradiation per given surface (from solar model in direct, diffuse and reflected components)

- Ambient temperature T_{amb}
- Collector transversal and longitudinal incidence angle modifiers (IAM) from reported measurements
- Collector mean fluid temperature

A 6th order polynomial fit using function *LINEST* is applied to the IAM so that these can be used as a function. Subsequently is obtained transversal, longitudinal direction and overall IAM for direct irradiation (changing with each value), diffuse and reflected light. Note that the diffuse and reflected light IAM are constant for single surface setting with respect to effective diffuse and reflected angles of incidence obtained from correlations (Brandemuehl & Beckman, 1980) in Eq. (8) and (9).

$$\theta_d = 59.7 - 0.1388\,\beta + 0.001497\,\beta^2 \tag{8}$$

$$\theta_r = 90 - 0.5788\,\beta + 0.002693\,\beta^2 \tag{9}$$

Finally, for a given collector aperture area the energy input to the collector is expressed by Eq. (10). The collector has thermal losses which are evaluated from reported efficiency curve coefficients a_1 and a_2, mean temperature of collector medium and ambient temperature. These losses are described by Eq. (11). Net collector output is obviously a difference between the two heats and taken are only cases of positive output. When the output would be negative, no operation is assumed. Collector output then relates to fluid mass flow rate based on inlet and outlet temperatures according to Eq. (12). Note that the mass flow rate is a function of input parameters.

$$\dot{Q}_{col,in} = A_a\left[K_{\theta,b}G_{bT} + K_{\theta,d}G_{dT} + K_{\theta,r}G_{rT}\right]\eta_0 \tag{10}$$

$$\dot{Q}_{col,loss} = A_a[a_1(t_m - t_{amb}) + a_2(t_m - t_{amb})^2] \tag{11}$$

$$\dot{Q}_{col,net} = \dot{Q}_{col,in} - \dot{Q}_{col,loss} = \dot{m}\left(h_{fluid,out} - h_{fluid,in}\right) \tag{12}$$

2.1.4 Collector efficiency

The collector efficiency is defined by Eq. (13) and it is just a ratio of energy output in heat transfer fluid to irradiation of collector aperture area. Obviously, it is a function of efficiency characteristics, ambient temperature, effective angles (through IAM) and energy incident to the collector aperture area in one of the three forms.

$$\eta_{col} = \frac{\dot{Q}_{col,net}}{(G_b + G_d + G_r)\,A_a} = \frac{\dot{Q}_{col,net}}{G_T\,A_a} \tag{13}$$

2.1.5 Heat engine and equipment models

Two types of heat engines are considered in this study. The first one is a simple (non-recuperated) ORC (configuration in Fig. 3, number of nodes 2 and 5 correspond to pinch-points). Within the assumed minimum temperature difference constrains the recuperated amount of heat would be very small or even none. The working fluid was chosen as R245fa, which is rather standard fluid in ORC and in many studies and actual plant has proven to be an efficient well usable working fluid. The second type of the heat engine selected is the mentioned APC with aqueous salt solution as a working fluid. The models of the cycles and its components are based on mass and energy equations (Eq. (1) and (2)) for each fluid stream (and fluid component for APC) of each component. Regarding minimum temperature differences, it is kept in mind, that some of them appear as pinch point within the heat

exchangers and not in their ends. No subcooling of liquid at the end of condenser / absorber is considered and for ORC is not considered superheating (APC at the end of heat input has two phase fluid). Reason is that it typically doesn't bring significant thermodynamic benefit. For a detailed description of the models and calculation principles of the cycles is the reader referred to (Novotny & Kolovratnik, 2017), from where is the calculation method of the cycles adopted.

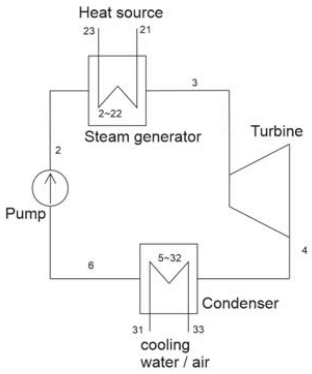

Figure 3: Simple Rankine cycle

2.2 Auxiliaries

Auxiliary systems necessary to operate the system are pumps for the heat transfer fluid between collector and the APCC (and eventually thermal storage) which need to overcome mainly friction losses. Second, however very significant for plant's parasitic load, is system for heat rejection. Overall configuration of the system is in Fig. 4. Note that for conversion of heat to power from low temperature heat sources the parasitic load related to heat rejection can be significant. Particularly with dry cooler it is circulation pump for intermediate loop and especially fans for induced draft.

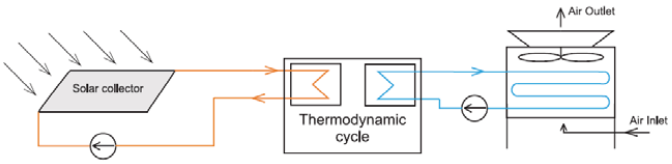

Figure 4: Configuration of power system using solar collectors.

Here we consider intermediate pressurized water loop between the collector and the heat engine to have pressure drop driven by quadratic law according to Eq. (15) with the constant $k_{\Delta p}$ (neglecting change in density) determined from reference flow and pressure loss, according to Eq. (14). Reference values are estimated from manufacturer's datasheets as 5 mbar for 100 l/h = 0.02778 kg/s flow[2] and pressure loss for entire system (piping and input heat exchanger) in a reference state of flow is assumed to be ten times as much.

$$\Delta p = \xi \frac{\rho u^2}{2} = \xi \frac{\rho \dot{m}^2}{2\rho^2 A} = k_{\Delta p} \cdot \dot{m}^2 \tag{14}$$

[2] http://www.eurosunsolar.de/en/sunstar-df-100/

$$k_{\Delta p} = \frac{\Delta p_{ref}}{\dot{m}_{ref}^2} \tag{15}$$

In the heat rejection system is considered a constant pressure drop of intermediate water loop as well as constant pressure drop of the cooling air in the dry cooler (as a particular reference size of any piece of equipment isn't a priori given and detailed sizing isn't for this elementary evaluation taken). Power consumption of each auxiliary equipment (pump or fan) is then, neglecting change of density across it, given by Eq. (16). With the power input of the auxiliary equipment there can be obtained cycle and net system power output.

$$\dot{W} = \frac{\dot{m} \cdot \Delta p}{\rho \cdot \eta} \tag{16}$$

2.3 Photovoltaic module model

Photovoltaic module is taken as a reference to the power cycles. The first step of the PV model is to obtain reflectance ρ of the panels. For each time step of the model for given incidence angle θ there is estimated reflectance of the panels from Eq. (17), where estimated values of constants[3] are $\rho_{ref}=0.05$ and $b_0=0.11$. Following that is estimated a temperature of the modules. If the absolute value of the incidence angle θ is larger than 85°, the temperature is assumed to be equal to ambient. When this angle is smaller, approximate relation from Eq. (18) is used (neglects electrical energy output of the module), where heat transfer coefficient α is estimated from Eq. (19) for assumed average windspeed u of 2 m/s.

$$\rho = 1 - (1 - \rho_{ref}) \left[1 - b_0 \left(\frac{1}{cos\theta} - 1 \right) \right] \tag{17}$$

$$t_{PV,module} = t_{amb} + \frac{(1-\rho) G_T}{\alpha} \tag{18}$$

$$\alpha = 5.7 + 3.8u \ \ [W/m^2] \tag{19}$$

Lastly an efficiency of the module can be calculated with thermal coefficient β and reference state efficiency η_{ref} from Eq. (20). Note that the PV module model is directly related to 1 m^2 of the panels while the thermal collector is calculated with respect to aperture area of a single collector. Two types of PV modules were considered, polycrystaline and amorphous Si modules. Values of constants adopted in PV model are summarized in Tab. 2.

$$\eta_{PV,module} = \eta_{ref}(1 + \beta(t_{PV,module} + 25)) \left(1 + 0.03 ln \frac{G_T}{1000} \right) \tag{20}$$

[3] http://users.fs.cvut.cz/tomas.matuska/wordpress/wp-content/uploads/2015/02/AZE2-P7_FV_produkce_FVT_panely.pdf

Table 2: Boundary conditions and parameters of the PV modules models.

cell type	η_{ref} [%]	β [% / K]	ρ_{ref} [-]	b_0 [-]	$u_{wind,aver}$ [m/s]
polycrystalline	15	-0.4	0.05	0.11	2
amorphous	6	-0.2	0.05	0.11	2

2.4 Models interconnection

The PV models can be directly coupled with the solar model and power produced is evaluated for model each time step and given the simplification of neglecting produced electricity in thermal energy balance, no iteration is needed. Power produced is simply evaluated from Eq. (21) with surface area for further analyses taken as 1 m^2.

$$\dot{W}_{PV,net} = \eta_{PV,module} G_T A \tag{21}$$

For the heat engines, net power is evaluated after obtaining expander power production and power consumption of all components as shown in Eq. (4). Obtaining parameters of the heat engines with thermal collectors is not so straight forward. Disregarding eventual iteration loops in the heat engines themselves (non-regenerated ORC has almost issues but APC is computationally more complex). There are also imposed additional limits as following only the pinch points, in winter months with very low temperature the condensation (or absorption) pressure would enormously decrease but also the cooling circuit water could get below freezing point. To mitigate this issue the operation of the heat engine was split into two regimes, first as defined above with pinch point limits which goes down to ambient air temperature of -5°C (cooling water return temperature +5°C). For temperatures below this point is condensation (absorption) pressure and thus condenser (absorber) outlet temperature and the cooling circuit return temperature are further kept constant.

An input and control value of for the heat engine models are heat source inlet temperature. Outlet temperature is a function of heat engine parameters, thus the mean temperature to evaluate collector efficiency can be obtained only after the cycle parameters are given. The calculation methods used in the presented analyses are for clarity schematically shown in Fig. 5. The reason of creating the intermediate functions representing the heat engine in issues of model convergence with the entire inputs array as an input in the EES.

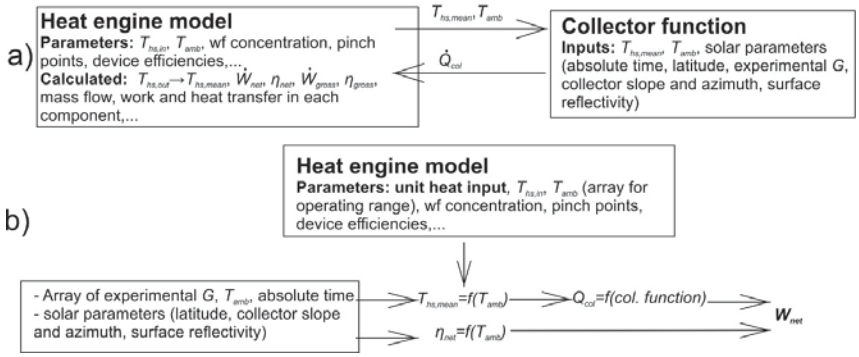

Figure 5: Diagram of principle of the two calculation procedures used, a) completely in EES, b) in MS Excel based on functions of heat engine operation obtained from heat engine models in EES.

An approach taken is to obtain a net efficiency of the power cycle and collector mean temperature (change of mean temperature can be rather small) as a function of ambient temperature with other parameters of the cycle fixed. This was done by fitting a suitable polynomial in MS excel using a LINEST function on the data from the EES models. Example of the net cycle efficiency and temperature functions are in Fig. 6. Note that the change of the mean collector temperature is very small, in case of APC less than 0.5°C, in case of ORC is this change several °C. Using these functions the models can be coupled and power production potential can be estimated for the system in each time step of the model.

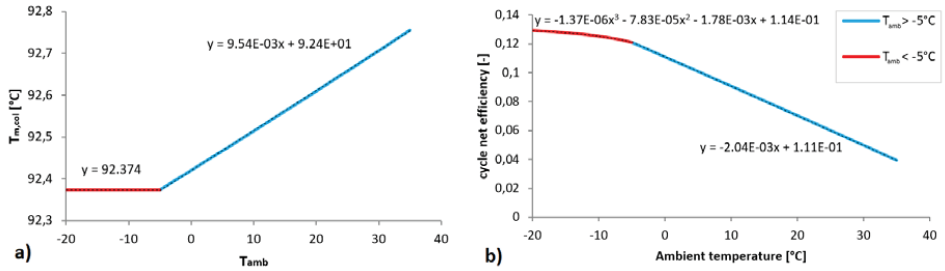

Figure 6: Mean collector temperature and cycle net efficiency for APC with collector outlet temperature 100°C.

3. RESULTS

At first the parameters of the ORC and APC cycles are presented. A starting reference point for the cycle parameters was taken from parameters of the cycles optimized for highest net electricity production with respect to conditions for 1st May around 3 pm (time=2919.46 *h*). Solar and ambient parameters for this point are summarized in Tab. 3.

Table 3: Parameters for chosen (reference / design) point at the time of the year 2919.5 h.

ST [h]	θ [°]	T_{amb} [°C]	G_{horiz} [W/m^2]
15,5	49,5	14,2	321
G_{bT} [W/m^2]	G_{dT} [W/m^2]	G_{rT} [W/m^2]	G_{Tsum} [W/m^2]
70,5	240,5	4,3	315,3

Resulting parameters of the cycle are for the boundary regimes of their operation, i.e. for the cases of ambient temperature 35°C and -5°C to -20°C are presented in Tab. 4 for ORC and Tab. 5 for APC. Node numbers correspond to Fig. 1 for ORC and Fig. 3 for APC. All results are calculated with reference heat input of 1 kW.

To further show the regimes of operation, Fig. 7 shows a $\dot{Q} - T$ diagrams of heat addition and heat rejection for the cases of ambient temperature 35°C, -5°C and -20°C. A different cycle efficiency is obvious from different rejected heat at different temperature levels. Non-isothermal boiling and absorption (condensation) is also apparent for the APC.

Table 4: Parameters of APC operating at limits of the regimes. (Node numbers – see Fig. 1)

	T_{amb} = 35°C						T_{amb} = -5°C to -20°C					
node	T_i [°C]	h_i [kJ/kg]	m_i [kg/s]	p_i [bar]	s_i [kJ/kgK]	ξ_{LiBr} [kg$_{LiBr}$/kg$_{sol}$]	T_i [°C]	h_i [kJ/kg]	m_i [g/s]	p_i [bar]	s_i [kJ/kgK]	ξ_{LiBr} [kg$_{LiBr}$/kg$_{sol}$]
1	52.3	115	1.70	0.25	0.49	0.378	14.0	20	1.62	0.25	0.17	0.378
2	75.4	175	1.70	0.25	0.66	0.378	63.4	144	1.62	0.25	0.57	0.378
3	77.3	180	1.70	0.25	0.68	0.378	77.3	180	1.62	0.25	0.68	0.378
4	91.4	762	1.70	0.25	2.31	0.378	91.4	763	1.62	0.25	2.31	0.378
5	91.4	2669	0.39	0.25	7.97	0.000	91.4	2669	0.37	0.25	7.97	0.000
6	41.7	2531	0.39	0.08	8.08	0.000	5.5	2310	0.37	0.01	8.29	0.000
7	91.4	197	1.31	0.25	0.63	0.490	91.4	197.9	1.25	0.25	0.63	0.490
8	57.3	121	1.31	0.25	0.41	0.490	19.0	37	1.25	0.25	0.14	0.490
9	57.3	121	1.31	0.08	0.41	0.490	19.0	37	1.25	0.01	0.14	0.490
10	64.1	672	1.70	0.08	2.17	0.476	23.1	557	1.62	0.01	2.02	0.476
11	52.3	115	1.70	0.08	0.49	0.378	14.0	20	1.62	0.01	0.17	0.378

Table 5: Parameters of ORC operating at limits of the regimes. (Node numbers – see Fig. 3)

	T_{amb} = 35°C					T_{amb} = -5°C to -20°C				
node	T_i [°C]	h_i [kJ/kg]	m_i [kg/s]	p_i [bar]	s_i [kJ/kgK]	T_i [°C]	h_i [kJ/kg]	m_i [kg/s]	p_i [bar]	s_i [kJ/kgK]
1	62.0	283	5.52	4.89	1.27	21.5	228	4.23	1.30	1.10
2	62.3	284	5.52	8.92	1.27	22.0	229	4.23	8.92	1.10
3	84.9	317	5.52	8.92	1.37	84.9	317	4.23	8.92	1.37
4	84.9	465	5.52	8.92	1.78	84.9	465	4.23	8.92	1.78
5	68.1	456	5.52	4.89	1.79	39.0	437	4.23	1.30	1.81
6	62.0	450	5.52	4.89	1.77	21.5	420	4.23	1.30	1.75

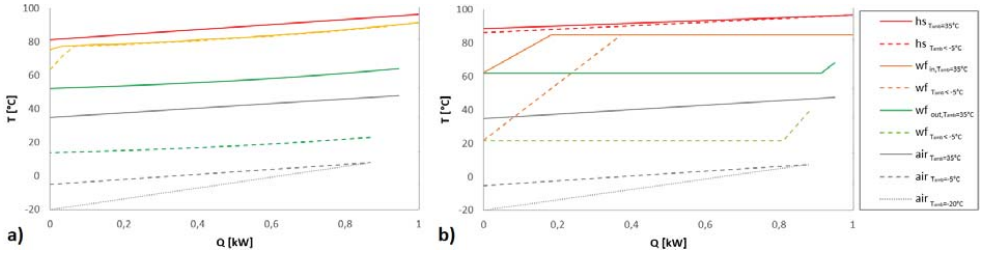

Figure 7: $\dot{Q} - T$ diagrams of heat addition and heat rejection from the cycles for limiting cases of operating conditions depending on ambient temperature for a) APC and b) ORC.

To see a behaviour of different settings, effect of intensity of cooling (ΔT of cooling air) and case of fixed condensing temperature for different ambient temperatures are explored and depicted in Fig. 8. An optimal point for the selected conditions is apparent. Also it can be seen that operating the cycle with given pinch points even for different ΔT_{air} gives higher efficiency than keeping condensing (final absorption) temperature constant.

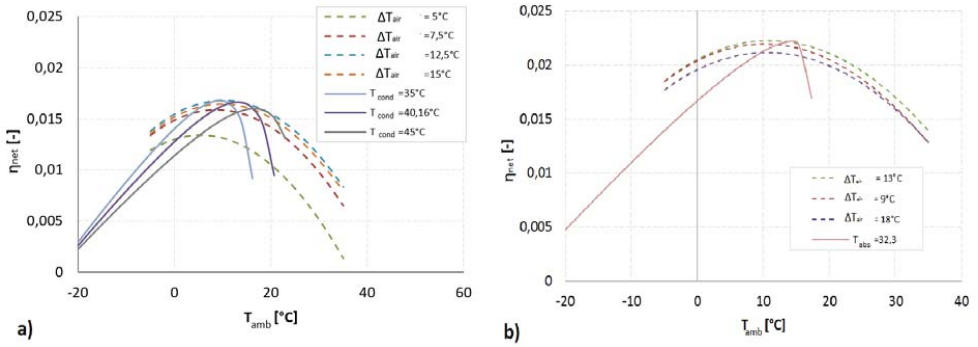

Figure 8: Effect of ambient temperature and different types of condenser / absorber operation regime on net system efficiency for a) ORC and b) APC.

To give more insight into behaviour of the system, Fig. 9 shows system efficiency under the considered mode of operation and collector efficiency for various cases of collector irradiation G_T based on cases of total time 2919 h (G_T =315 W/m^2), 4355 h (G_T =725 W/m^2), 5745 h (G_T =446 W/m^2). Note that due to different ratios between direct, diffuse and reflected light and angle / azimuth of incidence, the results can't be entirely generalized as there are different IAMs. The collector efficiency difference between ORC and APC case is very small as the mean temperature is on a similar value, only slightly higher temperature for ORC causes its slightly lower efficiency. Note that the magnitude of coefficients a_1 and a_2 makes the collector efficiency trend to appear nearly linear.

Cycle efficiency (same for different G_T as it is a function of temperature levels) is obviously increasing with available temperature difference according to the 2nd law of thermodynamics and is noticeably higher for APC, causing higher net system efficiency. The trend of overall efficiency is dependent on the cycle and collector efficiency and a breaking point in operation regime below -5°C has a negative effect.

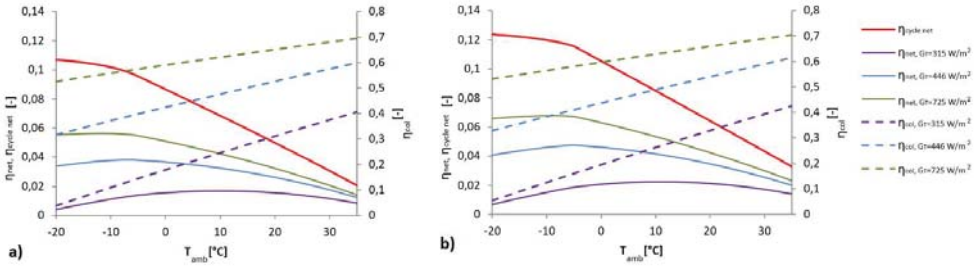

Figure 9: Effect of ambient temperature and different irradiation (for total time 2919 h, G_T =315 W/m²; 4355 h, G_T =725 W/m²; 5745 h, G_T =446 W/m²) on collector and overall system efficiency for a) ORC and b) APC.

Similar charts can be generated to explore different settings in heat source side - collector outlet temperature, evaporation (end of desorption) temperature. To keep this work concise these results aren't shown here.

The most important result is however a net power production potential throughout the year. Figure 10 shows a cumulative power production per aperture area for the system with power cycles with their parameters based on the selected case and on boundary conditions while varying heat input (collector outlet) temperature. For the ORC there was kept according to the reference case 12°C temperature difference between evaporation temperature and collector outlet temperature. APC isn't limited by a pinch point within the exchanger and therefore the temperature difference comes directly from the boundary conditions. In the APC is however kept constant the concentration change of the liquid LiBr solution in the evaporator. Results clearly show higher power production coming from the APC. Note that the maximum points still might not represent the most optimized situation even within the assumptions of an operation regime. Additionally to have a more accurate information and optimization possibilities, there should be developed model based on fixed dimensions of the equipment and accounting for a thermal storage as well. Development of such model and detailed optimization however exceeds a scope of this paper.

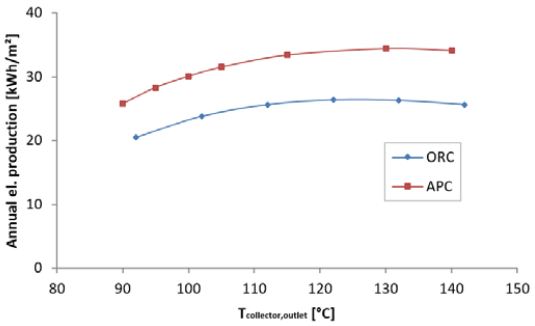

Figure 10: Annual potential of electricity production from ORC and APC.

Finally a comparison of maximal power production values from the heat engines is in Tab. 6 compared to the results of photovoltaic modules. These values show nearly double potential of amorphous PV and about five times higher potential for polycrystaline PV systems which only hardly justifies direct application of heat engine systems in this configuration. There are however further considerations outlined further.

Table 6: Annual maximal potential of power production potential for the analysed systems.

system	max ORC	max APC	$PV_{amorphous}$	$PV_{polycrystaline}$
kWh/(m^{2}year)	26.3	34.4	61.8	153.8

4. DISCUSSION

The results for heat engines has to be taken as initial estimates with possibilities for some efficiency increase. These are in detailed optimization and controlling for adjusting to a maximal power point for each time period. However major production increase (so that to surpass PV systems) is anyway not expected.

The results are preliminary assuming constant minimum temperature differences in the heat exchangers, constant pressure drop on heat rejection side equipment and constant efficiency of pumps, turbine (assumed turbine for rather lower sensitivity to changing pressure ration than volumetric expanders) and fan. For actual power production evaluation a system of specific sizing of the equipment in a single operating mode would need to be made. This is particularly for APC rather complicated as the details of heat transfer mechanism for detailed sizing are still a subject of research and has large uncertainties on heat transfer change with different operation modes. This shows a research potential towards off-design models (first assuming constant UA value in exchangers and expanders and pump performance curves) followed eventually by dynamic models.

Even though the results show lower overall efficiency and power production than for the photovoltaic modules, ORC and especially APC systems may find niche applications and have certain advantages. The first one is possibility of integration thermal energy storage. Power production thus can have smooth supply and can be available when needed. The APC can be further combined with typical absorption cooling cycle into a single-device absorption power and cooling cycle (APCC) as shown in Fig. 11.

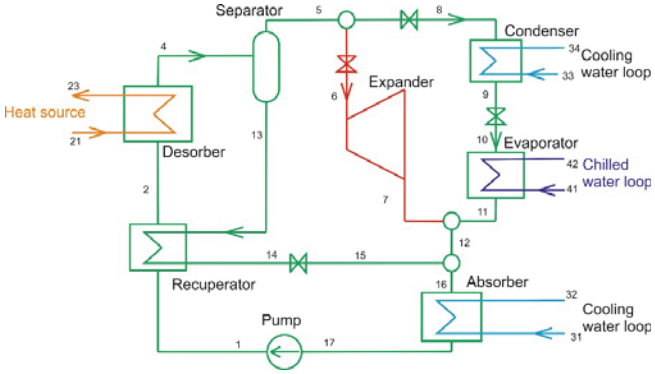

Figure 11: Schematic diagram of the absorption combined cooling and power system (APCC).

Other option (possibly also combined with previous) is a comprehensive integration into a building energy systems, where the system could utilize also heat from other (biomass, fossil...) sources. Considering the temperature range of heat source between 80°C – 120°C, APCC can find application in buildings and small industries as both topping and bottoming cycle. Example of use as a topping cycle in a heating system is in Fig. 12. The trend is to have heating systems requiring lower temperatures while for the boiler systems are the limits

around 90°C-95°C. APCC in this configuration could not only produce power or cooling from excess thermal energy from solar collectors, but also from using the boiler as a standard CHP configuration, thus maximizing its capacity factor and providing certain savings of primary energy resources. Note that the solar collectors are only optional.

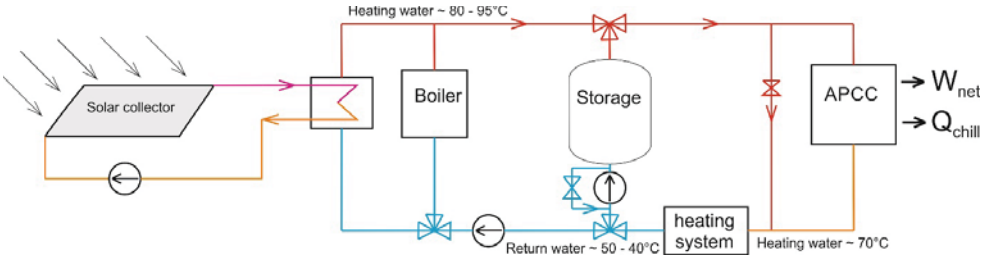

Figure 12: Proposed configuration of heating system with APCC as a topping system.

Bottoming option is then illustrated in Fig. 13 where the APCC is at the return line of water (eventually condensate) from other processes as can be found in small industries. This return water may have typically temperature of 95-120°C (depending on process parameters) and normally there might not be any other use for it (like significantly larger amount than necessary for heating and hot water). Cooling it down thus might have negligible effect on the rest of the system as it would be balanced by increased boiler efficiency (lower chimney loss). Integration of solar collectors into such system would however not be straight forward and two options are proposed for different regimes and both depicted integrations of them are only optional.

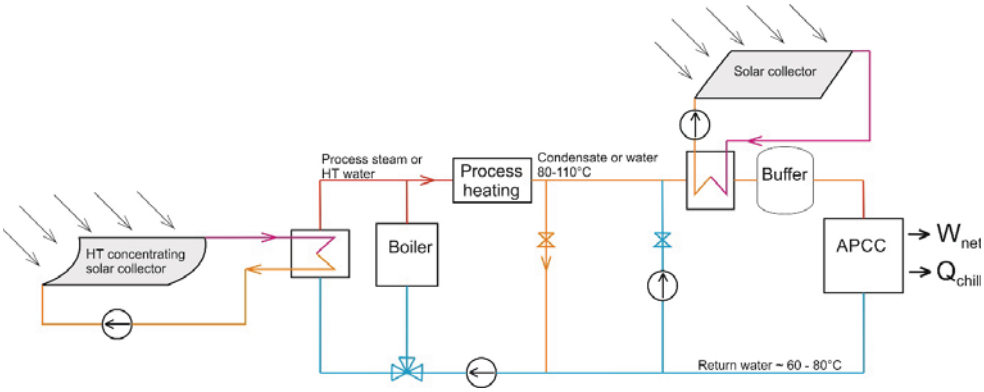

Figure 13: Proposed configuration of industrial heating system with APCC as a bottoming cycle.

5. CONCLUSION

A solar model based on annual experimental data and solar thermal collector models were set up and coupled to models of ORC, absorption power cycle (APC) and PV systems. A behaviour of the collector - heat engine systems was analysed, considering entire system including collector fluid circulation, cooling circuit water circulation and air fan power.

Starting from a selected operation point, there was explored behaviour with different heat rejection regimes. For selected design point as well as for overall annual power production (considering regime of operation based on ambient temperature), APC significantly outperformed ORC. However, when comparison was made against PV modules, there was nearly double potential of amorphous PV and about five times higher potential for polycrystaline PV systems. Particularly within the limits of assumptions and considered mode of operation, ORC can provide 26.3 kWh/m^2/year of electricity, APC 34.5 kWh/m^2/year, amorphous PV 61.8 kWh/m^2/year and poly-crystalline PV 153.8 kWh/m^2/year.

Advantages for systems with heat engines are however possibility of thermal energy storage, complex integration into building heating systems or for APC possibility of combined solar power and cooling production systems within a single machine.

ACKNOWLEDGEMENTS

This work was supported by the Grant Agency of the Czech Technical University in Prague, grant No. SGS OHK2-032/18 and by project OPVVV mobility of junior researchers, no.: CZ.02.2.69/0.0/0.0/16_027/0008465.

NOMENCLATURE

A	Surface area (m^2)
a	Collector losses coefficients (1)
APC	Absorption power cycle
APCC	Absorption power and cooling cycle
b_0	PV module coefficient for reflectivity (1)
DC	Dry cooler (for heat rejection)
DR	Day of a year (for obtaining declination)
G	Solar radiation (W/m^2)
G_0	Solar irradiation outside of atmosphere (W/m^2)
h	Enthalpy (kJ/kg), sun height above horizon (°)
IAM	Incidence angle modifier
k_T	Index of sky clarity (1)
$k_{\Delta p}$	Lumped pressure loss coefficient (1/(kg m))
K	Evaluated IAM (-)
$\dot{m}$	Mass flow (kg/s)
ORC	Organic Rankine cycle
p	Pressure (Pa)
PV	Photovoltaic
$\dot{Q}$	Heat flow (kW)
RH	Relative humidity (1)
ST	Solar time (1)

T,t	Temperature (°C)
u	Windspeed (m/s)
$\dot{W}$	Work (kW)

Greek letters

α	Heat transfer coefficient (W/m2K)
β	Collector slope(°), PV module thermal coefficient (1/K)
γ	Collector azimuth (°)
Δ	Difference
η	Efficiency (1)
ρ	Reflectance (1), density (kg/m3)
ξ	Mass concentration (1), minor pressure loss coefficient (1)
θ	Radiation incidence angle (°)

Index

0	Collector for zero heating up of the fluid
a	Aperture
abs	Absorber
Amb	Ambient
Aver	Average
b	Beam, direct (radiation)
col	Collector
cond	Condenser
cool	Cooling, heat rejection
d	Diffuse (radiation)
DC	Dry cooler
Exp	Expander
g	Surroundings (for reflectivity)
horiz	Horizontal (surface)
i	Node number
in	Input, inlet
j	Component number
liq	Liquid
m	mean
r	Reflected (radiation)
ref	Reference

surf	Surface
T	Perpendicular to the surface
wf	Working fluid

REFERENCES

Aboelwafa, O., Fateen, S. E. K., Soliman, A., & Ismail, I. M. (2018, February). A review on solar Rankine cycles: Working fluids, applications, and cycle modifications. *Renewable and Sustainable Energy Reviews*. Pergamon. https://doi.org/10.1016/j.rser.2017.09.097

Brandemuehl, M. J., & Beckman, W. A. (1980). Transmission of diffuse radiation through CPC and flat plate collector glazings. *Solar Energy*, *24*(5), 511–513. https://doi.org/10.1016/0038-092X(80)90320-5

Chan, C. W., Ling-Chin, J., & Roskilly, A. P. (2013). A review of chemical heat pumps, thermodynamic cycles and thermal energy storage technologies for low grade heat utilisation. *Applied Thermal Engineering*, *50*(1), 1257–1273.

Chen, H., Goswami, D. Y., & Stefanakos, E. K. (2010). A review of thermodynamic cycles and working fluids for the conversion of low-grade heat. *Renewable and Sustainable Energy Reviews*, *14*(9), 3059–3067. https://doi.org/10.1016/j.rser.2010.07.006

Cihelka, J. (1994). *Solar Thermal Technique*. *Publishing house T. Malina, Prague*.

Dickes, R. (2016). *Solar-based ORC power systems*. Retrieved from https://orbi.uliege.be/bitstream/2268/197155/1/Presentation_RDickes_ORC-Plus_workshop_OSV.pdf

Eller, T., Heberle, F., & Brüggemann, D. (2017). Second law analysis of novel working fluid pairs for waste heat recovery by the Kalina cycle. *Energy*, *119*, 188–198. https://doi.org/10.1016/j.energy.2016.12.081

Garcia-Hernando, N., de Vega, M., Soria-Verdugo, A., & Sanchez-Delgado, S. (2013). Energy and exergy analysis of an absorption power cycle. *Applied Thermal Engineering*, *55*(1), 69–77.

Hans-Joachim Kretzschmar, Ines Stoecker, Matthias Kunick, S. Hasch,. (2015). Engineering Equation Solver.

Johnson, I., William, T., Choate, W. T., & Amber Davidson, A. (2008). *Waste heat recovery: technology and opportunities in US industry*. *Waste Heat Recovery: Technology Opportunities in the US Industry*. Retrieved from http://www1.eere.energy.gov/manufacturing/intensiveprocesses/pdfs/waste_heat_recovery.pdf

Lecompte, S., Huisseune, H., van den Broek, M., Vanslambrouck, B., & De Paepe, M. (2015). Review of organic {R}ankine cycle ({ORC}) architectures for waste heat recovery. *Renewable and Sustainable Energy Reviews*, *47*, 448–461.

Modi, A., Bühler, F., Andreasen, J. G., & Haglind, F. (2017). A review of solar energy based heat and power generation systems. *Renewable and Sustainable Energy Reviews*, *67*, 1047–1064. https://doi.org/10.1016/J.RSER.2016.09.075

Novotny, V., & Kolovratnik, M. (2017). Absorption power cycles for low-temperature heat sources using aqueous salt solutions as working fluids. *International Journal of Energy Research*, *41*(7), 952–975. https://doi.org/10.1002/er.3671

Novotny, V., Vitvarova, M., & Kolovratnik, M. (2017). Absorption power cycle for low temperature waste heat recovery - performance comparison of different working fluids. In *9th International Exergy, Energy and Environment Symposium (IEEES-9), Split, Croatia*. Split.

Orgill, J. F., & Hollands, K. G. T. (1977). Correlation equation for hourly diffuse radiation on a horizontal surface. *Solar Energy*, *19*(4), 357–359. https://doi.org/10.1016/0038-

092X(77)90006-8
Rogdakis, E., & Lolos, P. (2015). Kalina Cycles for Power Generation. *Handbook of Clean Energy Systems*, 1–25. https://doi.org/10.1002/9781118991978.hces014
Shokati, N., Ranjbar, F., & Yari, M. (2014). A comparative analysis of {R}ankine and absorption power cycles from exergoeconomic viewpoint. *Energy Conversion and Management*, *88*, 657–668.
Sun, J., Fu, L., & Zhang, S. (2012). A review of working fluids of absorption cycles. *Renewable and Sustainable Energy Reviews*, *16*(4), 1899–1906.

Questions and Answers:

Sylvain Quoilin:

Why do you focus at such low temperature levels?

Vaclav Novotny:

Low temperature systems have potential to be significantly cheaper than concentrating systems for higher temperatures. Additionally this temperature level is interesting domain of absorption power cycle, while for higher temperatures, ORC is directly the best choice.

***

Remi Dickes:

What type of expander do you plan for your proof-of-concept absorption power cycle system?

Vaclav Novotny:

As the volumetric flow rate is high and temperatures are low, we are developing a turboexpander made partly by 3D printed plastics.

Dynamic modelling and control strategy of a heating system based on wood pellet boiler-stove

Van Long Le[1]*, Arnaud Candaele[1], Kévin Siau[1], Jean-Dominique Thomassin[2], Thomas Duquesne[2], Olivier Fontaine de Ghélin[1]

(1) Cenaero absl, Gosselies, Belgium

(2) Stûv, Namur, Belgium

ABSTRACT

The present study, carried out within the framework of the PCC80 project (PCC80 stands for the Development of a New Generation of Condensing Boiler Stove with recovery rate over 80 %), aims at modelling the behaviour and the performance of a heating system in a transient condition. The system is based on a wood pellet boiler-stove, which is equipped in a single-family detached-house in Belgium for the space heating and the Domestic Hot Water (DHW) production. As such a heating device is meant to be located in a living room, a challenge rises in terms of control to avoid over-heating, especially during Summer.

From available results of high-fidelity simulation (i.e. detailed 3D CFD simulation) and the experimental data, a simplified (0D) model of boiler-stove was developed. This model is then used within TRNSYS (Klein, S.A. et al, 2017) environment to perform the thermal dynamic simulation of the stove and its surrounding (i.e. the building). The multi-zone building simulation is carried out by using Type 56 component being available in the standard library of TRNSYS. The transient system simulation approach allows to determine the performance gain on the annual basis and to optimize the global concept.

Keywords: Wood pellet boiler-stove, space heating, domestic hot water production, thermal dynamic simulation, optimization

1. INTRODUCTION

In Europe, among the different energy consuming sectors, residential one accounts for about 27 % of the total final energy consumption (Capros et al., 2016). The two thirds of this energy consumption come from the heating demand (Capros et al., 2016). It is therefore a promising sector to intervene through for a more sustainable future. Regarding the building sector, beside of well-insulated building envelopes, the implementation of high-efficiency energy systems is essential and contributes to reduce the consumption of primary energy.

Furthermore, the economic, ecological and geopolitical as well as the normative frameworks such as the Energy Performance of Building Directive (EU, 2010), the Renewable Energy Directive (The European Parliament and the Council of the European Union, 2009) and the EU 2030 Framework for Climate and Energy (European Commission, 2014) require Member States to evolve technologies and behaviours towards a more rational use of renewable energies, reducing the dependency on energy imports as well as the environmental footprint. Indeed, within just several decades, renewable energy has developed from an alternative energy source in a niche market to one of the most important energy sources worldwide and a driving force for a sustainable 21st century economy (Zervos et al., 2010). Renewable energy is currently on its way to becoming the mainstream source of Europe's energy system. Recently, the European Commission, the Parliament and the Council reached a political

agreement which includes a binding renewable energy target of 32 % by 2030 (Commision, 2018). As aforementioned, the heating demand presents an important part of the overall final energy demand in the EU and will most likely remain a high share of the final energy demand in the future. Therefore, without a major shift towards heating and cooling from renewable energy, the EU will continue to import an ever-larger share of fossil fuels, while damaging the environment and putting the health of its citizens at risk (Zervos et al., 2010). To meet the overall target of at least 20 % by 2020, the share of renewable heating and cooling could, as estimated by the EREC (European Renewable Energy Council), almost triple compared to the share by 2007 of about 10 %. Most of the growth could be provided by biomass. By 2050, the biomass could contribute 214.5 Mtoe for renewable heating and cooling consumption.

Within this context, the development of efficient wood heating systems, which is adapted to the specific technical characteristics of dwellings and the financial constraints of their occupants, seems particularly relevant. Among the wood fuels, the pellet of compressed wood (or pellet) presents a set of assets that constitutes one of the fuels of the future. It is a fuel that can be produced locally, whose production and logistics chains have been structured and professionalised for a number of years and whose quality is better and better mastered, thanks in particular to the introduction of standards and quality labels at the international level. Moreover, it can be used in fully automated systems, to conciliate user comfort, energy performance and combustion hygiene. These features enable the individual wood-pellet heating systems, among the most suitable systems, to economically meet the new building energy efficiency requirements imposed on the European market.

Today, the demand of direct heating is progressively reduced, the major part of supplied heat must be able to be valorised under other mode that the heat directly released in the room where the heating device (e.g. traditional wood stove) is placed. Indeed, the fact of converting most of the heat produced during the combustion into hot water makes it possible to upgrade this energy in various ways such as distribution in other pieces by radiators, production of DHW, etc. Actually, gas and oil boilers are often used within residential building for space heating and domestic hot water preparation. With the incentives for renewable energy of the EU, the wood pellet boiler is becoming one of the most potential renewable-based alternatives for this traditional fossil fuel boiler.

The PCC80 project aims at developing a wood pellet boiler-stove that is aesthetic, user-friendly, efficient and adapted to the specific technical characteristics of dwellings as well as to the requirement of their occupants. The such heating device must meet a double objective:

- The stove, on the one hand, offers a broad vision on the flame for the warm and friendly character expected by this type of product.
- The boiler, on the other hand, must have a high efficiency.

A particular attention of the project will be paid to the technical integration of the product (boiler-stove) into the building. Indeed, the solution will not be designed as a monolithic closed and frozen system but as a preponderant element of a global and evolutionary heating solution, allowing an optimal valorisation of the different sources of energy available in a house. In this respect, the regulation of system, its opened characteristics and the possibilities of the communication with other energy system such as photovoltaic panels, heat pumps, and with outside world (e.g. weather database) will be a significant part of the development effort.

This study presents the result of the simulation for integrating a pellet boiler-stove within a single-family house for rooms heating and producing domestic hot water. The simulation is carried out by using TRNSYS kernel. Two new non-standard components, i.e. pellet boiler-stove and hydronic radiator, are developed within the framework of the project. The other

components from standard and TESS library of TRNSYS are employed to perform the simulation. The dynamic behaviour and the performance of the boiler-stove are investigated for its operation in Summer and Winter including extreme cold period (i.e. outdoor temperature is lower than -3 °C). The potential over-heating of the building provoked by device utilisation, especially during Summer, with different measures on device control strategy is also considered. Only the room and tap water temperature are considered for the occupants' thermal comfort. The one-year complete simulation is also performed to determine the annual power consumption for room heating and DHW demand.

2. SYSTEM MODELLING

A very first (simple) hydraulic concept (cf. Figure 1) for the space heating and the domestic hot water preparation is in this study used for investigating the transient behaviour and the performance of the wood pellet boiler-stove. The latter will be the only main heating device of the building, i.e. none other auxiliary heat production system than the pellet boiler is needed for making the heat carrier (hot water) flow at about 70 °C. This hot liquid, coming from the boiler, goes through the radiators for heating up the rooms, and also feeds the thermal storage tank of the DHW loop. The water exiting the radiators or the hot water tank at lower temperature is then driven back to the boiler for increasing again its temperature up to the set-point one (e.g. 70 °C). For the present hydraulic architecture, the hot water exiting the stove can only either feed the room heat emitters (radiators) or the storage tank at a time. Moreover, when the boiler-stove is needed for the sanitary hot water preparation, it cannot be used for the space heating (i.e. there is no hot fluid goes through the radiators). In other words, the use of pellet boiler-stove for hot water production/ space heating is in master/slave mode. Therefore, the room temperature could potentially fall down below the room's set-point temperature when the stove is needed for rising the temperature of water inside tank.

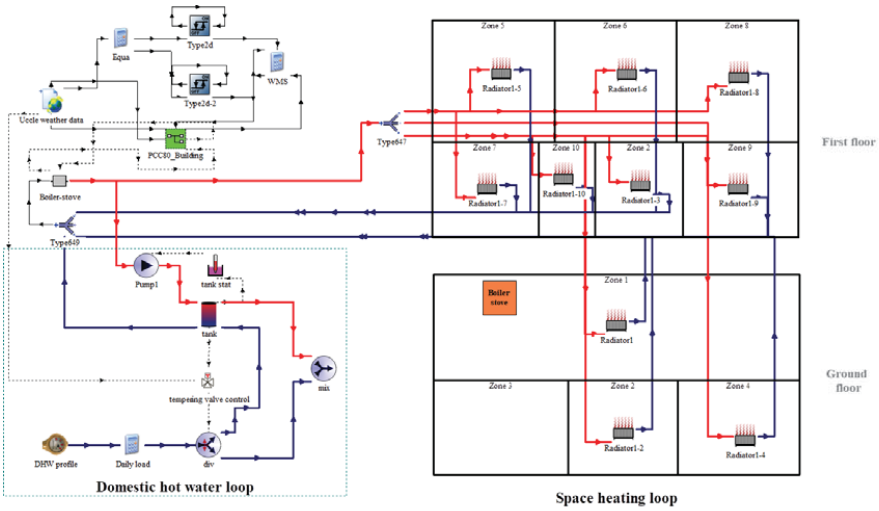

Figure 1: Hydraulic concept for space heating and domestic hot water production

The mass flow rate of the water going through the boiler-stove is either determined as the hot water mass flow rate required for the sanitary hot water preparation (via the Pump1) or by the total mass flow rate needed for the space heating, i.e. the sum of mass flow rates of the water going through the radiators controlled by the thermostatic valves (described later in the text).

For the current study, the stove must be located in the living-room (combined with the kitchen) of the building for maximizing the vision of stove's flame, an amount of heat will be released by the natural convection and the radiation to stove's surrounding when it is in operation (cf. Figure 2). This causes eventually the building over-heating, especially during Summer. Several control measures are therefore implemented for inspecting the occupants' thermal comfort.

Figure 2: Pellet stove is placed in living-room (zone 1) (courtesy of Stûv)

2.1 3.1 Building model

The house is simulated using the multi-zone building model of TRNSYS (i.e. Type 56). The building is a typical Belgian detached (4 facades) single-family (5 persons) house whose benchmark geometry has been established in (Massart & De Herde, 2010). The building is also used and well described in the study of (Georges et al., 2014). The house has a total floor area of 152 m^2. The envelope presents a protected volume of 420 m^3, 360 m^2 of opaque surfaces and 35 m^2 of windows. The house's internal organization is displayed in Figure 3 (Massart & De Herde, 2010):

- The building is partitioned into two stages, relief between them by a corridor (zone 2).
- Each zone is modelled by only one thermal node, including zone 2 spreading on both stages.
- The living-room (zone 1) is oriented towards the South and contained the pellets boiler-stove.

To take into account the ventilation and the circulation of air inside the building, TRNFLOW (Weber et al., 2003) will be used. This module is coupled to TRNSYS allowing to model simultaneously the balanced whole-house mechanical ventilation by the air-intake within living-room and bedrooms and the extraction of the air from wet pieces (bathroom, laundry, toilets), but also to integrate different doors between the pieces, and to consider the house

tightness by means of appropriated mathematical model. For the present study, the door of living-room is always opened while the doors of other pieces (bedrooms, office and the bathroom) are always closed.

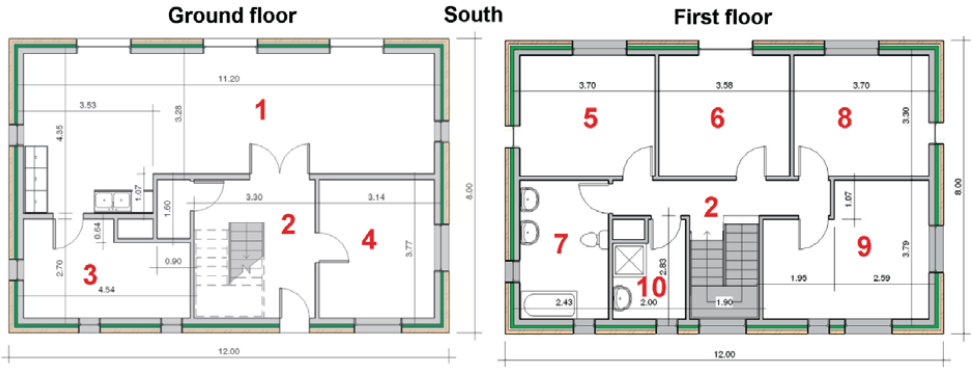

Figure 3: Sketches of ground and first floor of building: kitchen coupled living-room (1), corridor (2), laundry (3), office (4), bedrooms (5, 6, 8, 9) and bathroom (7,10)

A summary of main building properties is given in Table 1.

Table 1: Building properties

	External wall	**Adjacent wall**	**Adjacent ceiling**	**Roof**	**Ground slab**	**Glazing/ window**
Thickness [m]	0.465	0.13	0.248	0.419	0.495	-
U-value [W/m^2-K]	0.114	2.963	1.873	0.111	0.155	0.81

Some other features of the building model such as solar protection, internal heat gain are also implemented as described in (Massart & De Herde, 2010).

2.2 3.2 Boiler-stove model

The boiler-stove model in this study has been developed on the basis of an existing pellet boiler-stove model (Nordlander, 2003) with appropriate adaptations and modifications.

The stove combustion power, P_{cmb}, is controlled between the minimum and maximum one and by the control signal γ:

$$P_{cmb} = \gamma \cdot P_{cmb,max} \quad (1)$$

The device maximum combustion power is in the present study of 9.37 kW. The control signal, γ, varies from 0 to 1. During the normal operation, P_{cmb} is limited to $P_{cmb,min} \leq P_{cmb} \leq P_{cmb,max}$. Being similar to the model of (Nordlander, 2003), the stove operation has two-step start phase, burning phase and two-step stop phase. The description of the start and stop phases as well as the minimum operating and cooling time of the heating device are given in Table 2. The start and stop phases are initiated by switches of control function at current (γ) and previous (γ_{pr}) time step, and by the constraints of the operating and cooling time.

In fact, the heating device will be turned on if these following conditions are simultaneously satisfied:

- $\gamma_{pr} = 0$
- $\gamma > 0$
- Cooling time ≥ minimum cooling duration

The stove will be turned off if three conditions below are at the same time fulfilled

- $\gamma_{pr} > 0$
- $\gamma = 0$
- Operating time ≥ minimum operating duration

Table 2: Boiler-stove characteristics

Operation	Duration (hour)	Description
First start phase duration	dt_{sta1}	Duration between start signal and first flame vision of the stove, no combustion power is assumed.
Second start phase duration	dt_{sta2}	Duration in which the stove operates with a combustion power P_{cmbsta} (e.g. $P_{cmbsta} = P_{cmb,min}$)
Stop phase duration	dt_{fstp}	After stop sign, duration in which the stove continues to generate a decreasing power.
Minimum cooling duration	$dt_{cool,\ min}$	In addition to stop phase duration, the minimum time before the device can be switched on again.
Minimum operating duration	$dt_{op,min}$	Minimum operating time between obtaining first flame and the stop sign

As described in (Persson et al., 2006), A typical pellet stove has a preset stop phase lasting for a certain time after the pellet feeder has been turned off. For venting out the gases from the after-burning phase the fan is active for a certain time (i.e. stop phase duration in Table 2). After the fan stops, the gas flow is driven by buoyancy forces only. The boiler-stove model in the present study performs the similar two-step start and stop phases as described in (Persson et al., 2006).

The mathematical equations of the boiler-stove model have been developed and implemented as a new non-standard component in TRNYS using C++ programming language. The differential ordinary equations of the model are solved using Rosenbrock 4 implicit method being available in Boost C++ library. The model calibration is carried out by means of an optimization process and the experimental data including the outlet water temperature and the combustion efficiency. For the optimization, the generic optimization program GenOpt (Wetter, 2001) is used with the GPS (Global Pattern Search) Hooke-Jeeves method. The optimization algorithm tries to find out the global minima of the cost function, *CF*, described as follows:

$$CF = (T_{w,out,cal} - T_{w,out,ex})^2 + (\eta_{cmb,cal} - \eta_{cmb,ex})^2 \quad (2)$$

Where

$T_{wo,cal}$ and $T_{wo,ex}$ is the water outlet temperature calculated by the numerical model and from the experimental data, respectively.

$\eta_{cmb,cal}$ and $\eta_{cmb,ex}$ is the combustion efficiency calculated by the numerical model and provided by the manufacturer.

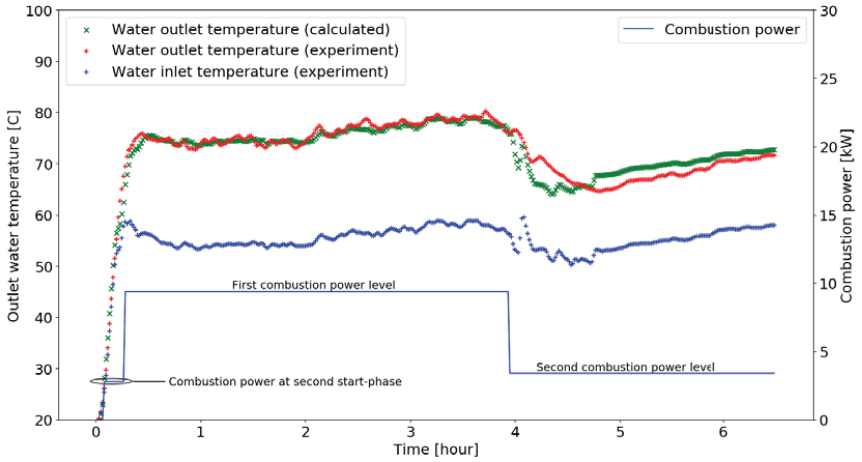

Figure 4: Water outlet temperature (simulation vs. experiment)

The difference between the numerical calculation and experimental values of water outlet temperature is shown in Figure 4. The differences between the simulation and the experiment for the combustion efficiency and the heat rate absorbed by water are presented in Figure 5. For the calibration process, the experiment was carried out for about 8 hours. Two combustion power levels were applied for investigating the dynamic behaviour of the stove. The figures show a good agreement between the simulation results and the experimental data.

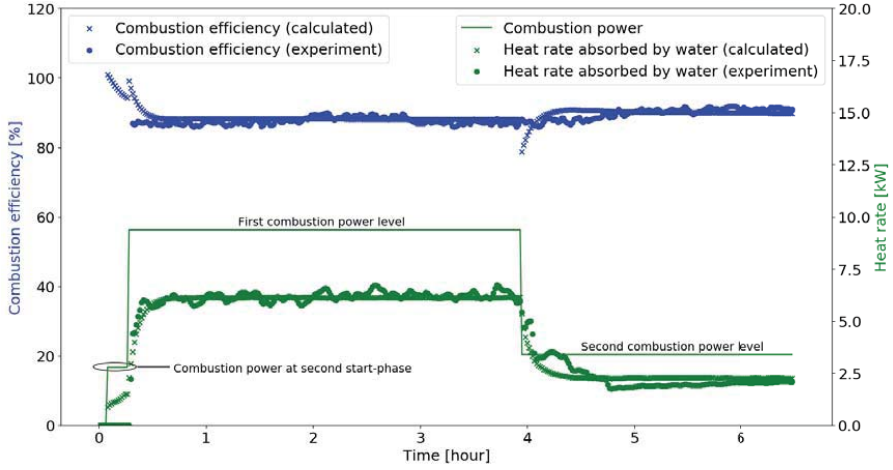

Figure 5: Combustion efficiency and heat rate absorbed by water (simulation vs. experiment)

2.3 3.3 DHW loop

Concerning DHW production, the water comes from the tank bottom at lower temperature is heated up by the stove to a temperature of 70 °C and stored in the thermal storage tank. The

hot water drawn from the top of storage tank will then be mixed with the cooling water to produce tap water at desired temperature (i.e. 45°C for this study). The load profile of tap water (cf. Figure 6) is in this work specified by a daily repeating forcing function using Type 14 of TRNSYS standard library. The value specified for each time period of the forcing function is the fraction of the total daily water draw that is drawn during that time period. The forcing function value is then multiplied by a daily total water draw of 250 L (50 L/person) to arrive at the flow rate (in kg/h) of domestic water.

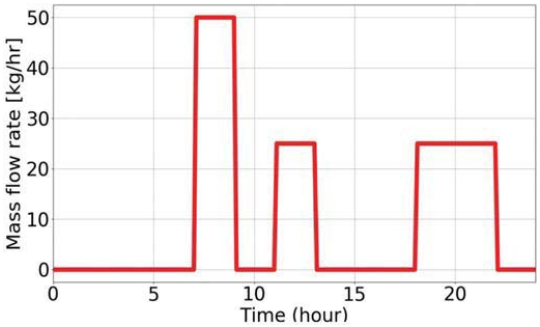

Figure 6: Simple DHW load profile

The hot water tank is simulated using Type 158 (TRNSYS standard library) which is a constant volume tank model. The tank volume is of 0.3 m³. The tank model accounts for thermal stratification by breaking the tank into a user specified number of isothermal nodes. The water at the bottom of the tank is sent to the boiler depending on the water temperature at the thermostat position and the set-point temperature value as given in Table 3. Furthermore, the additional heat generated by mismatch (explained further in the text) between stove's operating cycle and thermostat signals (room and tank) will also be stored in hot water tank. Therefore, temperature of water at thermostat position is sometime greater that the set-point one.

Table 3: Set-point temperature for hot water storage tank

	Night (22 h – 6 h)	**Day** (6 h – 22 h)
Summer mode	60 [°C]	45 [°C]
Winter mode	45 [°C]	60 [°C]
Extreme cold mode	60 [°C]	45 [°C]

In summer it is preferred to produce hot water between 22 h – 6 h for avoiding the overheating caused by pellet stove utilisation. Otherwise, the boiler is forced to work during daytime for the hot water preparation to maximize the vision on the flame in Winter out of extreme cold period (i.e. outdoor temperature below -3 °C). When the outdoor temperature is below -3 °C, the heating device is, once again, adopted to run during night-time for the DHW production as more power will be needed during daytime for space heating.

2.4 3.4 The space heating loop

The space heating will be automatically triggered during heating season by means of hydronic radiators installed in different rooms of the house except for the laundry room (zone 3). The operation of the boiler-stove for the room heating is activated depending on the temperature of living-room (where the thermostat is located) and the room's set-point temperature specified in Table 4. The room's set-point temperature varies in function of the occupation period of the building, which is also different for weekdays and weekend.

Table 4: Set-point temperature for space heating

Time interval [h]	0 – 6	6 – 8	8 – 9	9 – 16	16 – 22	22 – 24
Week-day [°C]	16	22	22	16	22	16
Week-end [°C]	16	16	22	22	22	16

2.4.1 3.4.1 Radiator

The radiator is simulated using the first order radiator model (i.e. the total radiator heat capacitance is concentrated at the exhaust node) as described in (Holst, 1996). The basic equations for radiator model are given as follows:

The heat balance equation:

$$\dot{M}_w \cdot Cp_w \cdot (T_{w,\text{in}} - T_{w,out}) = C_{radiator} \cdot \frac{dT_{w,out}}{dt} + \dot{Q}_{radiator,nom}\left(\frac{\Delta T_{lg}}{\Delta T_{lg,nom}}\right)^n \quad (3)$$

The actual logarithmic mean temperature difference:

$$\Delta T_{lg} = \frac{T_{w,\text{in}} - T_{w,out}}{\ln \frac{T_{w,\text{in}} - T_{amb}}{T_{w,\text{out}} - T_{amb}}} \quad (4)$$

Similarly, the nominal logarithmic mean temperature difference, $\Delta T_{lg,nom}$, is calculated with with nominal value of water inlet, $T_{w,in,nom}$, and outlet, $T_{w,out,nom}$, temperature and nominal value of ambient temperature, $T_{amb,nom.}$ For the current study, these nominal values of temperature are respectively set of 70°C, 50°C and 20°C.

The lumped radiator capacitance of fluid and metal:

$$C_{radiator} = m_w \cdot Cp_w + m_{met} \cdot Cp_{met} \quad (5)$$

The emitted radiator power is transferred to the room by convective and radiative heat exchange. Knowing the radiative fraction of the emitted power at nominal operating condition (s_{nom}), the radiative fraction at other operating condition (s), is obtained by the following equation:

$$s = \frac{s_{nom} \cdot (T_{amb}^K + \Delta T_{lg})^4 - (T_{amb}^K)^4}{\left(\frac{\Delta T_{lg}}{\Delta T_{lg,nom}}\right)^n \cdot [(T_{amb}^K + \Delta T_{lg,nom})^4 - (T_{amb}^K)^4]} \quad (6)$$

The superscript n in the equation (3) is the radiator exponent with a value of 1.3 for this study.

The water mass flow ($\dot{M}_{radiator}$) entering the radiator is controlled by a thermostatic radiator valve. The flow rate is regulated between zero and the designed mass flow rate ($\dot{M}_{radiator,nom}$). When the room ambient temperature (T_{amb}) is greater than the upper limit, e.g. 24°C, i.e. heating is no longer required, the controller delivers zero flow. Conversely, the radiator receives the designed mass flow rate when the room temperature is below the lower limit, e.g. 14°C. The mass flow fluctuation goes through the heat emitter can be expressed by the following equation:

$$\dot{M}_{radiator} = \begin{cases} 0 if T_{amb} \geq T_{upper} \\ \dot{M}_{radiator,nom}\left(1 - \frac{T_{amb} - T_{lower}}{K_p}\right) if T_{lower} < T_{amb} < T_{upper} \\ \dot{M}_{radiator,nom} if T_{amb} \leq T_{lower} \end{cases} \quad (7)$$

Where K_p is the proportional band, e.g. 10.

3. CONTROL STRATEGIES

During heating season, the stove will be automatically launched when the temperature of room or tank thermostat is below corresponding set-point temperature. The temperature of water exiting the heat exchanger is regulated by a PI (proportional integral) controller with a variable set-point temperature:

- When the stove is needed for space heating or domestic hot water production, the set-point temperature of water exiting the heat exchanger is set to be of 70 °C. The combustion power of the stove is regulated to keep water outlet temperature as close as possible to the set-point temperature value.
- When the stove is no longer needed to produce hot water (for space heating or DHW production) but still in operation because of the constraint of minimum operating duration, the heating device will operate with a minimum power output until satisfying the minimum operating time and turning off or receiving another signal for hot water production and operating again with normal operation mode. The exceed energy generated during this period will be stored in thermal storage tank. Therefore, the temperature of water inside tank at thermostat position is sometime greater than the set-point temperature specified in Table 3.

The parameters of PI controller are determined using Cohen Coon tuning method (Cohen & Coon, 1953).

4. RESULTS AND DISCUSSIONS

4.1 5.1 Heating season

During the heating season (October – May), the boiler-stove is employed to make hot water for room heating and domestic water preparation. The upper part of Figure 7 exhibits the combustion power and its useful capacity (i.e. the heat transferred to the building through the stove wall and the heat shifted to the water over the heat exchanger wall) as well as the combustion loss (light blue area) with the flue gas for two-day operation of the heating device in Winter. The stove is regulated at maximum, partial and minimum load. Every phase from the start to the stop of the device's operating cycle is named from 0 to 5 (i.e. 0 – the stove is inactive; 1, 2 – first and second start phases; 3 – burning phase; 4, 5 – stop phases with and without fan operation respectively) in the lower part of the figure. During two-day operation, three operating cycles per day are observed. For the first day, out of extreme cold period, the

stove is active between 6 a.m. to 10 p.m. for the demands of both space heating and DHW. However, next day when the outdoor temperature is below -3 °C, from 6 a.m. to 10 p.m., this device is only used for room heating requirement. The preparations of DHW are shifted to the night-time. Because of the constraint of minimum cooling and operating time, there is the case that the stove cannot turn on/off right after receiving the room/tank thermostat signal, e.g. the case between second and third or fourth and fifth operating cycle. The results have been obtained from the simulation with 1-minutes time step.

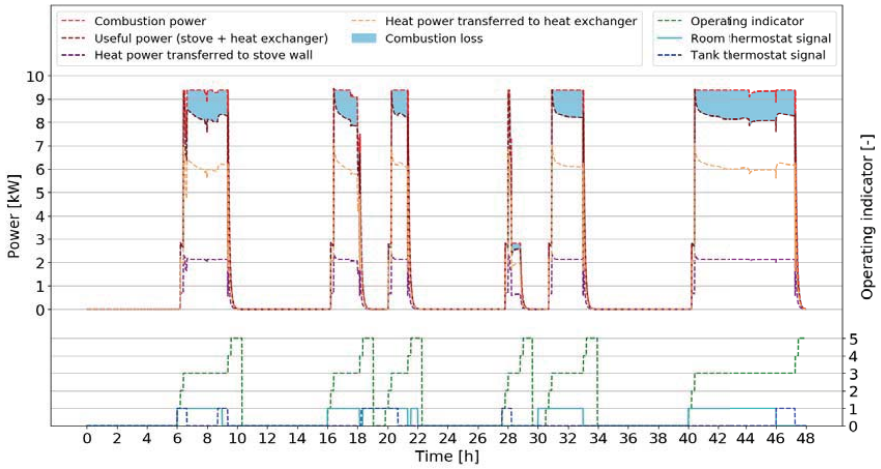

Figure 7: Boiler-stove operation for two chosen days in Winter (11-13 January)

The variation of rooms and outdoor temperature is reported in the middle and lower part of Figure 8. In fact, the living-room set-point temperature during occupation periods (i.e. from 6 a.m. to 9 a.m. and from 4 p.m. to 10 p.m.) is of 22 °C, while during the remaining hours of the day, it is set to be of 16 °C. Thanks to the pellet boiler-stove, the living-room is maintained at the desired temperatures. However, the temperature in other rooms are slightly lower than the one of living-room. Furthermore, the living-room temperature is sometime below or above its set-point. This fact can be explained by:

- The mismatch between stove's operating cycle and room/tank thermostat signals as explained before.
- The priority of the DHW production over the space heating when the overlap between room and tank thermostat signal occurs.
- The room thermal inertia and the controller hysteresis.

The air is brought into the living-zoom and the bedrooms from outside and extracted from the wet pieces (bathrooms, laundry) to outside by a double flow mechanical ventilation system with a heat exchanger. The by-pass of heat exchanger is triggered depending on the outdoor temperature, the scheduled set-point temperature, and the actual temperature of the living-room. The bedrooms temperature falls at certain moment as found in the Figure 8 (e.g. at about 6 a.m.) can be explained by the fact that the fresh-air get into the house without goes through the heat exchanger and the boiler-stove is not used for space heating, i.e. it is turned off or needed for sanitary hot water preparation.

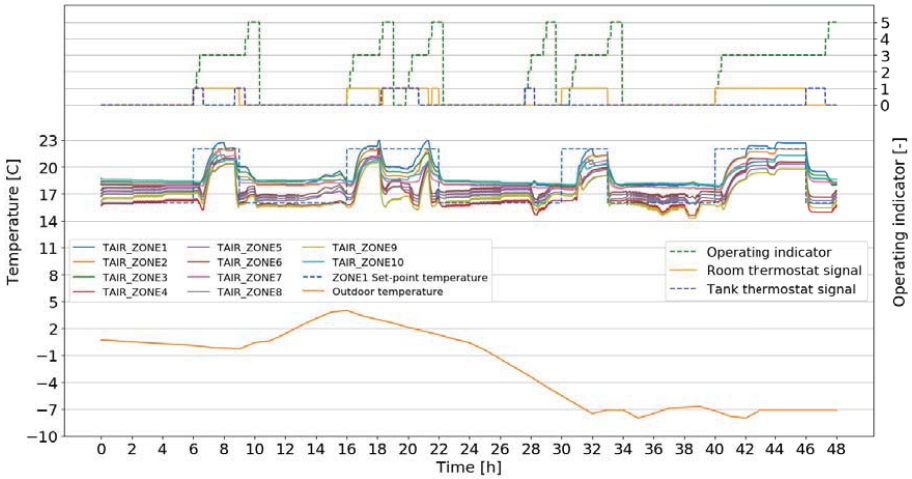

Figure 8: Temperature at different rooms of the house for two-day operation of the stove in Winter (11-13 January)

The temperature fluctuation of water at different positions inside thermal storage tank (top, bottom and at the position of thermostat) and at tap outlet is given in Figure 9. The current control strategies and power output allow the boiler-stove to produce enough hot water for family requirements with specified DHW-load profile at desired temperature (e.g. 45°C).

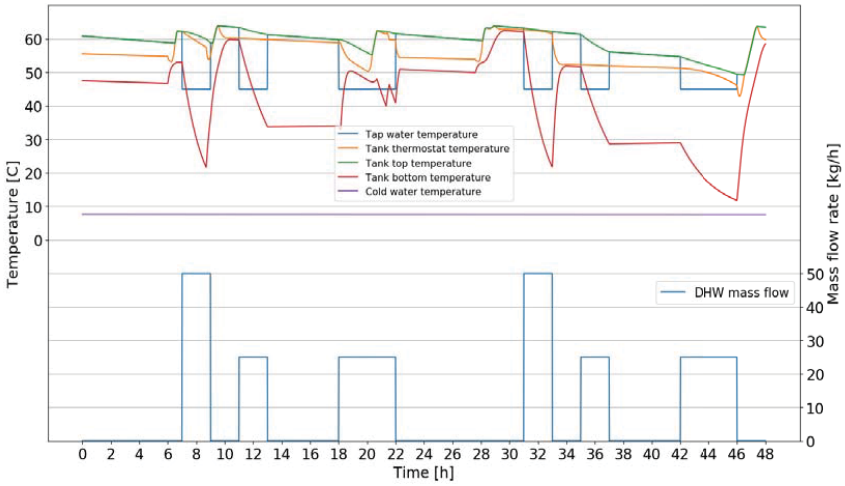

Figure 9: Temperature of water inside thermal storage tank and at tap outlet in winter (11-13 January)

4.2 5.2 Cooling season

During summer, the stove is only activated for domestic hot water preparation. For avoiding the room over-heating caused by natural convection and the radiation from stove wall to its surrounding, the hot water at 60 °C inside tank can only be prepared after 22 h and before 6 h. During the remaining time of the day, the stove will only be turned on if the temperature of

water at the position of tank thermostat is lower than 45 °C. As found in Figure 10, the boiler-stove is in operation only once per day for the two-day operation in Summer. As different building doors except the ones of living and laundry room are set to be closed at all time for the simulation in this paper, the additional heat generated by the natural convection and the radiation from the stove wall to the building when the device is used for making hot water causes only slightly over-heating in the pieces 1, 2 and 3 of the house as can be found in Figure 11. The temperature increasing is highest for living-room where the boiler in installed. Since the objective of the paper is to investigate the dynamic behaviour and the performance of the pellet boiler-stove for heating space and DHW demands, there is no cooling device/solution, including night and day ventilation by doors/windows opening, is implemented for the simulation. Consequently, the room temperatures are quite high during summer.

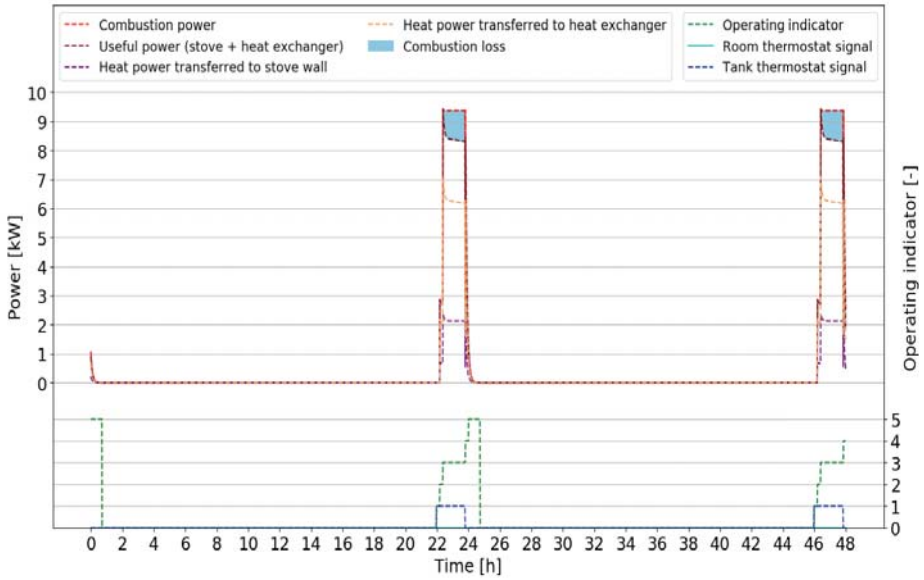

Figure 10: Boiler-stove operation for two choosen days in Summer (23-25 July)

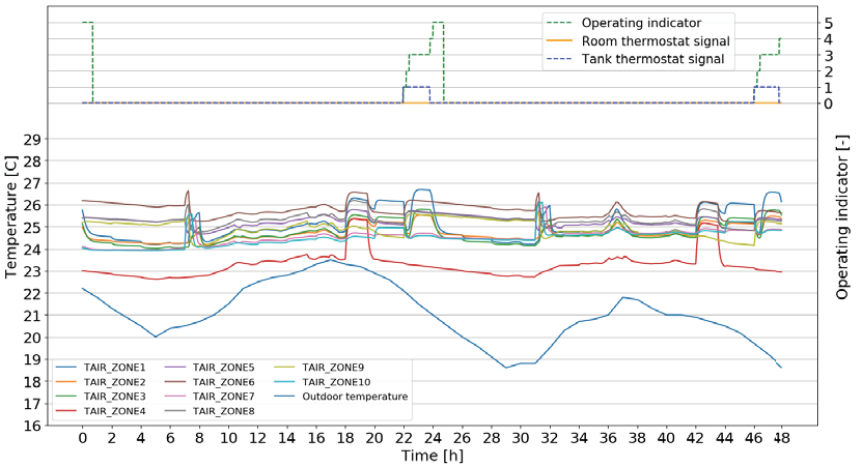

Figure 11: Temperature at different building rooms for two-day operation of the stove in Summer (23-25 July)

The family requirement of DHW with specified load profile at desired temperature is always satisfied as reported in Figure 12.

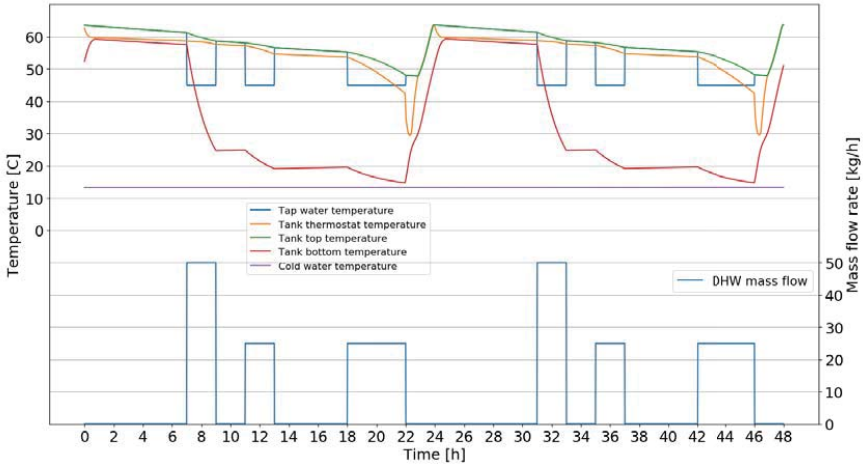

Figure 12: Temperature of water inside thermal storage tank and at tap outlet for two-day stove operation in Summer (23-25 July)

4.3 5.3 Annual power consumption

The annual power consumption for space heating and DHW preparation using only the pellet boiler-stove is presented in Figure 13. The integral combustion power is calculated based on the simulation result with 1-hour time step for the whole year. The annual consumption of the heating device for both space heating and DHW preparation is of 9153 kWh.

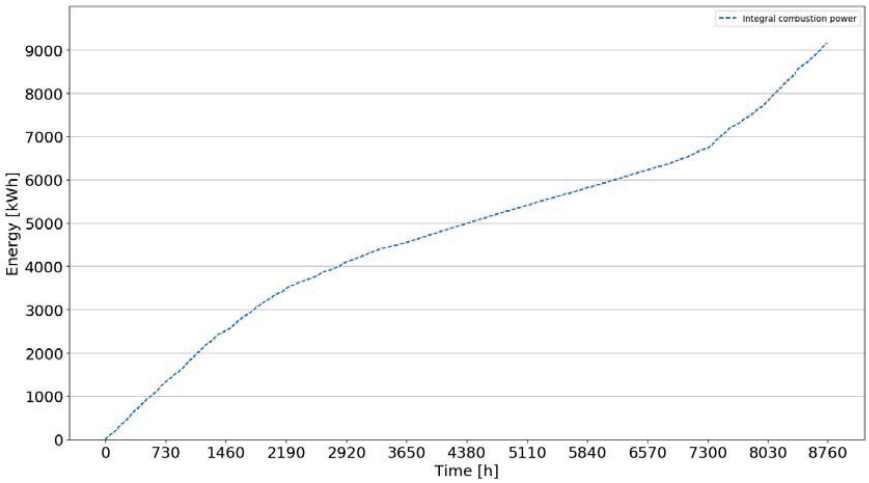

Figure 13: Annual power consumption of pellet boiler-stove for space heating and DHW requirements

The greatest slop is observed at two ends of the power consumption curve which represents the period when the heating device is used for both space heating and DHW. The curve is less inclined in the middle when the heating space is no longer required.

5. CONCLUSIONS

The present study performs the dynamic simulation of a heating system based on wood pellet boiler-stove implemented in a residential building for space heating and DHW preparation. The multi-zone building simulation is performed using component Type 56 of TRNSYS coupled with TRNFLOW. The building is a typical Walloon detached single-family house. The system simulation is carried out using different components from standard and TESS library of TRNSYS as well as the ones developed within the framework of project. Indeed, the pellet boiler-stove is developed from the basis of an existing model in the literature with the appropriate adaptations and modifications. Several heat transfer parameters of the model are determined by the calibration between the model and experimental data using an optimization process. Different measures on the control strategy of the heating device are also implemented for assessing device performance and occupant thermal comfort. The simulation results show that even the pellet boiler-stove has several drawbacks concerning the operating constraints and thermal inertia, it could be a good renewable alternative-solution for the traditional gas and oil boiler which cost probably expensive for the environment and the health of the citizens. In addition, the pellet stove comes with not only the performance features but also the aesthetic one as a residential heating device. The results also demonstrate that pellet device drawback can be eventually minimized or eliminated with an appropriate and smart control system.

The further works will be focus on the improvement of the regulation system and the combination between the pellet boiler-stove with other heating system device such as solar water heater, gas-and-oil boiler, etc.

6. ACKNOWLEDGEMENTS

The authors would like to thank the Walloon Public Service for funding this research.

7. NOMENCLATURE

A	[m^2]	area
AF_r	[-]	air-fuel ratio
C	[kJ/K]	thermal mass
CF	[-]	cost function
Cp	[$kJ.kg^{-1}.K^{-1}$]	specific heat
m	[kg]	mass
M	[kg/kmol]	molar mass
$\dot{M}$	[kg/h]	mass flow rate
MF	[-]	mass fraction
P	[kJ/h]	power
$\dot{Q}$	[kJ/h]	heat power
T	[°C]	temperature
t	[h]	time
UA	[$kJ.h^{-1}.K^{-1}$]	thermal conductance

subscript/ superscript

amb	ambient (room)
cal	calculated
cmb	combustion
ex	experimental
f	fumes
hex	heat exchanger
in/out	inlet/outlet
K	Kelvin degree
lg	logarithmic
met	metal
Moist	moisture
nom	nominal (or design) condition
pr	previous time step
rad	radiative part of heat power
stv	stove
w	water
wall	wall

8. REFERENCES

Bell, I. H., Wronski, J., Quoilin, S., & Lemort, V. (2014). Pure and pseudo-pure fluid thermophysical property evaluation and the open-source thermophysical property library coolprop. *Industrial and Engineering Chemistry Research*. https://doi.org/10.1021/ie4033999

Capros, P., De Vita, A., Tasios, N., Siskos, P., Kannavou, M., Petropoulos, A., … Kesting, M. (2016). *EU Reference Scenario 2016: Energy, Transport and GHG emissions trends to 2050*. *European Commission*. https://doi.org/10.2833/9127

Cohen, G. H., & Coon, G. A. (1953). Theoretical considerations of retarded control. *Transactions of the ASME*, 827–834.

Commision, E. (2018). Europe leads the global clean energy transition: Commission welcomes ambitious agreement on further renewable energy development in the EU. Retrieved June 29, 2018, from http://europa.eu/rapid/press-release_STATEMENT-18-4155_en.htm

EU. (2010). Directive 2010/31/EU of the European Parliament and of the Council of 19 May 2010 on the energy performance of buildings (recast). *Official Journal of the European Union*. https://doi.org/doi:10.3000/17252555.L_2010.153.eng

European Commission. (2014). *A policy framework for climate and energy in the period from 2020 to 2030*. *https://ec.europa.eu/energy/en/topics/energy-strategy/2030-energy-strategy*. https://doi.org/10.1007/s13398-014-0173-7.2

Georges, L., & Novakovic, V. (2012). On the Integration of Wood Stoves for the Space-Heating of Passive Houses: Assessment Using Dynamic Simulation. *Proceedings of the First Building Simulation and Optimization Conference*, (September), 157–164.

Georges, L., Skreiberg, Ø., & Novakovic, V. (2014). On the proper integration of wood stoves in passive houses under cold climates. *Energy and Buildings*, *72*, 87–95. https://doi.org/10.1016/j.enbuild.2013.12.023

Holst, S. (1996). TRNSYS - Models for Radiator Heating Systems.

Klein, S.A. et al. (2017). TRNSYS 18: A Transient System Simulation Program. Solar Energy Laboratory, University of Wisconsin. Retrieved from http://sel.me.wisc.edu/trnsys

Massart, C., & De Herde, A. (2010). Conception de maisons neuves durables.

Nordlander, S. (2003). *TRNSYS model for Type 210 Pellet stove with liquid heat exchanger: Documentation of model and parameter identification*. *Solar Energy Research Center*.

Persson, T., Nordlander, S., Fiedler, F., Rönnelid, M., & Bales, C. (2006). Computer modelling of wood pellet stoves and boilers connected to solar heating systems. In *Proc on USB ofPellets 2006, 30 May - 1 June, Jönköping, Sweden* (pp. 207–211).

Quoilin, S. (2011). Sustainable energy conversion through the use of Organic Rankine Cycles for waste heat recovery and solar applications, (October), 1–183. https://doi.org/10.1016/j.fsc.2004.06.001

Sawerysyn, J. (2012). La Combustion Du Bois Et Ses Impacts Sur La Qualité De L ' Air. *Air Pur*, *81*(2009), 7–16.

The European Parliament and the Council of the European Union. (2009). Renewable Energy Directive. *Official Journal of the European Union*.

Weber, A., Koschenz, M., Dorer, V., Hiller, M., & Holst, S. (2003). TRNFLOW, a new tool for the modelling of heat, air and pollutant transport in buildings within TRNSYS. *8th International IBPSA Conference*.

Wetter, M. (2001). GenOpt - A Generic Optimization Program. *Seventh International IBPSA Conference*. https://doi.org/10.2172/962948

Zervos, A., Lins, C., & Muth, J. (2010). RE-thinking 2050: a 100% renewable energy vision for the European Union. *Erec*. https://doi.org/https://www2.warwick.ac.uk/fac/soc/pais/research/researchcentres/csgr/green/foresight/energyenvironment/2010_erec_rethinkhing_2050.pdf

Questions and Andswers:

Vincent Lemort:

Is the combustion power the theoretical one? (Based on LHV [J/kg])? Or does it account for unburnt fuel losses? What is the combustion efficiency?

Long Van Lê:

Indeed the combustion power is imposed and controlled between maximum and minimum value using a PI controller. No unburnt fuel loss is taken into account. Combustion efficiency is supposed to be 100%.

***

Jean Lebrun:

Is the combustion power stable? No initial drying of the pellets?

Long Van Lê:

The combustion process is not simulated for this study. The combustion power is assumed stable and there is no initial drying of the pellets.

***

Jean Lebrun:

HEX in parallel. How are you evaluating the heat transfer? (towards water and towards stove) Is it in series or parallel?

Long Van Lê:

Yes, HEX is in parallel. Heat towards water and stove are in parallel as well. Heat partitions (towards water and towards stove) are calculated from the product of heat transfer coefficient and heat transfer surface area (UA) for each side. Indeed, the value of UA at transient conditions is determined from the following equation

UA = UA_nom(Mdot/Mdot_nom)^n

The values of UA_nom and n are determined using a calibration process by optimisation while Mdot_nom is provided by the manufacturer.

Evaluation of micro combined heat and power systems in the Walloon residential sector through dynamic simulation

V. Cousin[1*], E. Davin[1], P. André[1]

[1]BEMS Université de Liège, Arlon Campus Environnement, Belgique

ABSTRACT

Combined Heat and Power (CHP) systems are known for a long time and are well established especially in the industrial sector where they allow interesting energy savings. However, the application of this technology in the residential and small tertiary sectors remains difficult due to the irregularity and the low heat demand during certain months of the year. The "Smart Micro Cogen" project focused on evaluating the potential of micro CHP systems ($\leq 50kW_e$) in the Belgian building stock (residential and small tertiary sector) by means of dynamic simulation using TRNSYS 17 software.

This work provides the hypotheses allowing representing the Belgian residential building stock and the different elements taken into account in the modelling and simulation of a complex HVAC system including a micro CHP system.

Some results of the various simulations performed will be presented to show the robustness of the proposed modeling.

Keywords: Combined Heat and Power, CHP, Complex HVAC system simulation, Dynamic simulation, TRNSYS

1. INTRODUCTION

According to the European Commission (2013), buildings are responsible for 40% of primary energy consumption in the EU. Improvements of the buildings energy efficiency are therefore crucial to ensure that EU meets its energy and climate ambitious targets by 2020.

One target of the 2020 Climate & Energy package is a 20% improvement of energy efficiency. In this context, the 2012 Energy Directive establishes measures to help countries to reach this target. One of them is to achieve an equivalent level of savings through alternative heating systems reaching the same level of efficiency.

Combined Heat and Power (CHP) is one of the option available within these measures in order to help the EU to achieve his goal of energy efficiency improvement. These systems are known for a long time and are well established especially in the industrial sector where it allows interesting energy savings. However, the application of this technology in the residential and small tertiary sectors remains difficult due to the low and intermittent heating demand during certain months of the year. Nevertheless, this technology is being continuously improved and new options are now available. Micro-CHP systems ($\leq 50kW_e$) are entering the residential heating market and seem to be an attractive solution with both environmental and economical potential benefits.

The Smart Micro Cogen (SMC) took place in this context with the funding of the main belgian electricity producer. The aim of this project was to evaluate the potential of the micro cogeneration in the Belgian existing real estate in the current and future context of smart grids. CHP products electricity that, injected on the grid atthe right moment could help to balance grid. The aim of the SMC project was to evaluate the impact on the grid of this technology

and the cost for all actors in stake. This paper focuses on the only Energy aspect in residential buildings.

A state of the art of CHP technologies and a state of the market in Wallonia was carried out. Four buildings and two CHP technologies considered as the most interesting and mature were selected. The selected cases were simulated in order to evaluate their performance. The use of TRNSYS 17 allowed the modelling of the complex HVAC system (CHP system, storage tank, emission systems, DHW,...). In these first simulations, two CHP systems (Internal Combustion Engine (ICE) and Stirling) were controlled according to the heat demand. The electrical storage use was also studied.

In a second set of simulations, the analysis took into account the control of the CHP system in order to minimize its impact on the grid by allowing electricity production only at the appropriate times.

As CHP is often presented as a solution to reduce primary energy consumption, this criterion was evaluated as well as other relevant criteria: the cost of use, electricity self-consumption, electricity coverage, injection on the grid... For bothCHP technologies (ICE, Stirling) simulations were carried out.

2. HYPOTHESES AND MODELLING

2.1 Buildings

Four relevant buildings were selected in order to be the most representative of the Belgian real estate according to the TABULA (Cyx, Renders, et al., IEE TABULA - Typology Approach for Building Stock Energy Assessment 2011) and PROCEBAR (Georges, et al. 2013) studies. The buildings in Figure 1 -are considered as the the most interesting for the use of CHP technology (with sufficient heat demand and sufficient potential electric production). They represent a total of 40% of the Belgian building stock with consequently a large potential impact.

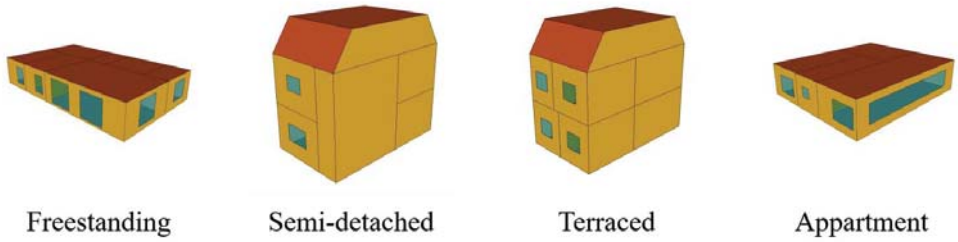

Figure 1 : Sketchup models of the selected buildings

General characteristics of buildings are described in table 1

Table 1: General characteristics of buildings

	Freestanding	Semi-detached	Terraced	Appartment
Building U-values (W/m²K)	Uwall = 1.771 Uroof = 0.435 Ufloor = 0.729	Uwall = 2.259 Uroof = 3.995 Ufloor = 3.379	Uwall = 2.259 Uroof = 3.995 Ufloor = 3.379	Uwall = 0.491 Uroof = 0.435 Ufloor = 0.729
Area (m²) :	112	113	133	171
Number of occupants	4	4	4	4

Rooms were divided in three types in order to apply different heating schedules: day occupied room, night occupied room and bathroom. In each room type, different temperature set points were applied corresponding to three types of consumers: low, medium and high consumer.

In each building, the internal gains and occupation rate were taken into account. It was considered that a family of four people with one full time working parents lived in the buildings.

These hypotheses led to three heating demands for each building as shown in Table 2.

Table 2: Yearly heating demands

Building	**Low consumer**	**Medium consumer**	**High consumer**
Freestanding	24 913 kWh	33 570 kWh	48 425 kWh
Semi-detached	23 409 kWh	32 609 kWh	39 442 kWh
Terraced	19 152 kWh	26 258 kWh	31 758 kWh
Apartment	10 823 kWh	13 791 kWh	16 627 kWh

Note that assumption in specifications of the project was that buildings envelope were not changed. Only the heat production system could changed (from boiler to CHP)

2.2 Weather data

Weather data used in the TRNSYS simulations are Meteonorm data from Uccle (Belgium).

2.3 Electrical consumption

Scenarios of the building's electrical consumption has been established on the basis of the "CIEL"1 (Commission des Communautés Européennes n.d.) and "REMODECE"2 (Enertech, ADEME et Union Européenne 2008) studies which include the hourly consumptions (in Wh/h) for each electrical appliance.

From these curves, daily usage profiles for each month and for each electrical appliance were determined. A method was then used to re-establish annual scenarios on a stochastic basis.

When the profiles of the various elements are aggregated they should match a profile similar to the total home consumption profile obtained from “Synthetic Load Profiles” curves leading to three electrical consumptions as shown in Table .

Table 3: Yearly electrical consumptions

	Low consumer	**Medium consumer**	**High consumer**

Yearly electrical consumption	2 600 kWh	3 500 kWh	4 400 kWh

2.4 DHW consumption

Hot water consumption is an important assumption for the simulation of a residential house or a rest home. Statistical values were produced by IEA Annex 42 (Knight 2007) with a time base of 15 minutes.

Consumption of water at 60 °C from mains water at approx. 10 °C (ΔT = 50°C)) is assumed.

For the three consumers types, the values are shown in Table .

Table 4: Hot water consumption

	Low consumer	**Medium consumer**	**High consumer**
Hot water consumption	25 L/person.day (2 100 kWh/year)	37.5 L/person.day (3 200 kWh/year)	50 L/person.day (4 400 kWh/year)

2.5 HVAC system

The most important part of this work was to model the HVAC system of the buildings in order to correctly assess the impact of the CHP systems integration.

After a state of the art of micro-CHP technologies, two of them were selected that could be qualified as mature in terms of both their development and their presence on the Belgian market for the residential sector: ICE and the Stirling engine. Two dynamic models of these technologies were calibrated and used in the different simulated cases for comparison with a conventional boiler.

Based upon these technologies, two configurations of the HVAC system were modelled as shown in Figure 2 where it can be observed that the ICE did not internally include an auxiliary boiler. This is due to the model of CHP (see below "CHP model"). CHP models were not developed in the project and some adaptations between existing CHP models and HVAC system were mandatory.

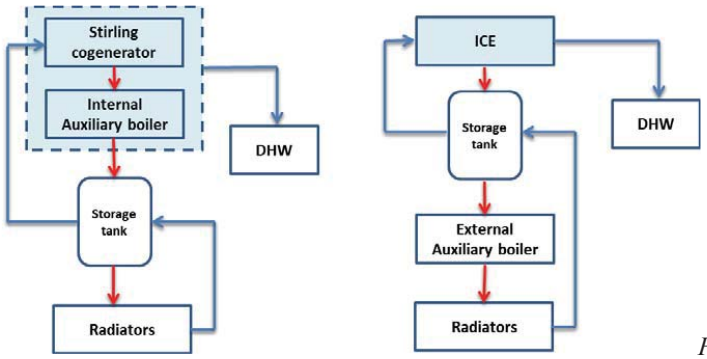

Figure 2: Configurations of the HVAC system according to the CHP technology

A choice has been made not to include pipes, pumps and heat exchangers in the modelling of the HVAC system.In order to optimise the use of the electricity produced, the use of a battery was also evaluated.

2.5.1 CHP models

Three models of CHPs were studied in order to choose those that would best show the impact of such technologies.

Two TRNSYS types were choosen and both of them took into account the transient states of cogeneration systems (ignition, full speed operation and shutdown).

The ICE model was developed by Rosato & Sibilio (2012) and the Stirling model was developed by Bouvenot, et al. (2014).

The three CHP engines characteristics are the following (Table).

Table 5: CHP parameters

Technology	**Stirling**	**ICE**	**ICE**
P_{elec}	0.9 kW_e	5.6 kW_e	1 kW_e
P_{therm}	5.3 kW_{th}	14 kW_{th}	2.5 kW_{th}
Nominal Efficiency (electrical, global)	$\eta_e = 0.13$ $\eta_g = 0.93$	$\eta_e = 0.25$ $\eta_g = 0.93$	$\eta_e = 0.25$ $\eta_g = 0.93$
Auxiliary boiler	Integrated in the model	Not integrated in the model	Not integrated in the model
Power modulation	No	No	No
Market product	Hybris Power DE DIETRICH	AISIN System	-

Note that model of ICE 1kWe is adapted from ICE 5.6 kWe with reduced power (flanged motor). No commercial product indeed corresponds to this model.

Time step of simulation is 1 min. This is imposed by model of Stirling with time step of 1 min maximum.

2.5.2 Radiators

The objective of the SMC project was to study only the choice of cogeneration over a boiler without changing the building. With this in mind, the emission system has not been changed between the "boiler" case and the "CHP" cases.

The radiators were sized in each zone of building according to the following temperature set points:

- Inlet temperature: 80°C (controlled temperature for heat supply)
- Outlet temperature: 60°C

- Room temperature set point: 20°C

In simulation, a heating curve was also taken into account to adjust the water temperature to the different radiators taking into account the outside temperature.

The choice of the different radiators was made by calculating the maximum demand for each room of the different dwellings.

In TRNSYS, the first approach was to use the Radiator Type 1231 (TESS library). However as shown in Figure 3, two problems with the return temperature of the radiators appeared. The calculated value was lower than the temperature in the rooms when the temperature set point decreased and was at certain times bellow 0°C.

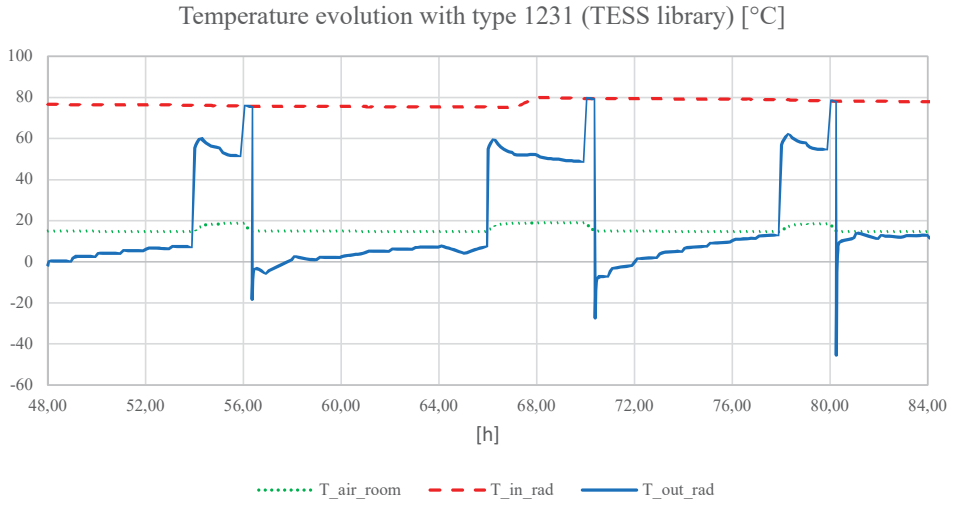

Figure 3: Temperature evolution with type 1231 (TESS library)

Following this, an analysis of the internal code of the type was performed. It appeared that the heat flow was correctly calculated according to the following equations:

$$\phi = \dot{m}.c_P.(t_{in} - t_{out}) \quad (1)$$

$$\phi = \frac{Q_N}{(\Delta T_N)^n}.(\Delta T)^n \text{ with } \Delta T = \frac{t_{in}-t_{out}}{\ln\left(\frac{t_{in}-t_{room}}{t_{out}-t_{room}}\right)} \quad (2)$$

where ϕ is the heat flow, $\dot{m}$ is the water flow rate, c_P is the water heat capacity, t_{in} is the temperature of the water entering in the radiator, t_{out} is the temperature of the water leaving the radiator, Q_N is the heat emission of the radiator under nominal conditions, ΔT_N is the mean arithmetic temperature difference under nominal conditions, t_{room} is the air temperature in the room and n is the radiator exponent.

However, it appeared that the particular cases corresponding to low and high flow rates were not taken into account. Indeed, ΔT must be calculated differently when the flow is smaller than 2% of the nominal flow and when it is larger than 98% of the nominal flow (Ast H, 1986).

The following additional equations were therefore implemented in the Type 1231:

$$\text{If } \dot{m} \geq 0{,}98.\dot{m}_N : \Delta T = \frac{t_{in}+t_{out}}{2} - t_{room} \quad (3)$$

$$\text{If } 0{,}02.\dot{m}_N < \dot{m} < 0{,}98.\dot{m}_N : \Delta T = \frac{t_{in}-t_{out}}{ln\left(\frac{t_{in}-t_{room}}{t_{out}-t_{room}}\right)} \quad (4)$$

$$\text{If } \dot{m} \leq 0{,}02.\dot{m}_N : t_{out} = t_{room} \quad (5)$$

where $\dot{m}_N$ is the nominal flow rate.

2.5.3 Thermostatic valves

The thermostatic valves were implemented in TRNSYS after the creation of a new type based on the physical equations (Stephan n.d.):

$$\text{If } \Delta t_c \geq \Delta t_{C,P} \text{ then } \frac{\dot{m}}{\dot{m}_N} = \frac{\Delta t_{C,P}}{\Delta t_{C,N}}\left(a_v + \left(\frac{\Delta t_{C,P}}{\Delta t_{C,N}}\right)^2 . (1-a_v)\right)^{\frac{-1}{2}} \quad (6)$$

$$\text{If } 0 < \Delta t_c < \Delta t_{C,P} \text{ then } \frac{\dot{m}}{\dot{m}_N} = \frac{\Delta t_C}{\Delta t_{C,N}}\left(a_v + \left(\frac{\Delta t_C}{\Delta t_{C,N}}\right)^2 . (1-a_v)\right)^{\frac{-1}{2}} \quad (7)$$

$$\text{If } \Delta t_c \leq 0 \text{ then } \frac{\dot{m}}{\dot{m}_N} = 0 \quad (8)$$

where Δt_C is the temperature difference between the instantaneous temperature of the thermostat and the temperature, when the valve is just closed, $\Delta t_{C,N}$ is the nominal range of temperature difference t_c, $\Delta t_{C,P}$ is the proportional range of temperature difference t_c and a_v is the valve authority.

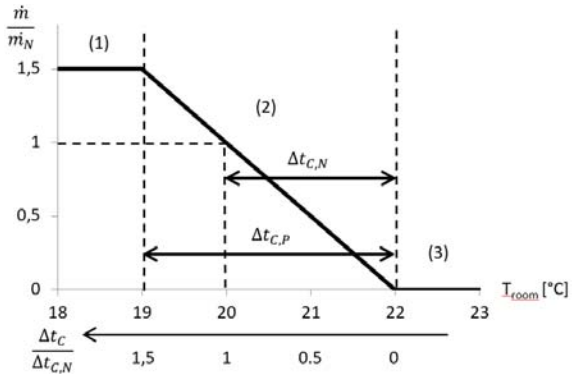

Figure 4: Evolution of the relative flow rate trough a thermostatic valve

2.5.4 Hot water tank

The type 543-NOHX (TESS library) was used for the hot water tank. The tank was divided in 7 nodes in order to consider the temperature stratification and the parametrization was made according to an existing model(VPS ALL-STORE from Vaillant).

A preliminary study was conducted in order to determine to ideal tank size. Three volumes were selected: 300L, 800L and 1000L. This study was conducted with the CHP Stirling model.

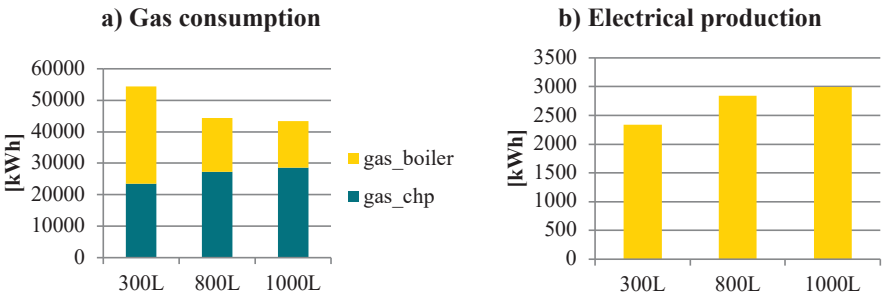

Figure 5: a) CHP and boiler gas consumption for different hot water tank sizes; b) CHP Power output for different hot water tank sizes

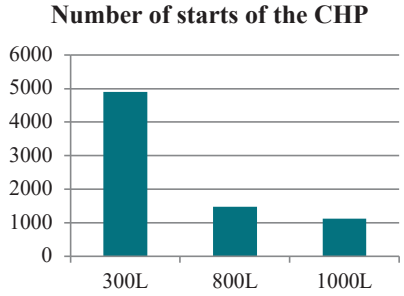

Figure 6: Number of starts of the CHP for different hot water tank sizes

The study showed that the best choice was the 1000L hot water tank for multiple reasons:

- The total gas consumption decreases when the tank size increases (Figure 5a).

-

- The part of gas consumption from CHP increases while part of gas consumption from boiler decreases when the tank size increases as shown on figure 5a. That means that production from CHP increases. This is also highlighted by Figure 5b "Electrical production from CHP"

- The number of starts of the CHP module decreases when the tank size increases (Figure 6).

Those observations lead to a better use of the CHP with the 1000L hot water tank. Indeed, longer heating periods increase the number of working hour and improve the electrical production efficiency .

2.5.5 DHW tank

The DHW tank was also modelled using the type 543-NOHX (TESS library) and parametrized like the hot water tank.

A preliminary study was conducted in order to determine the best way to produce DHW. Two methods were evaluated: using the heat produced by the CHP and using the electricity produced by the CHP. Second method allows to increase the self-consumption.

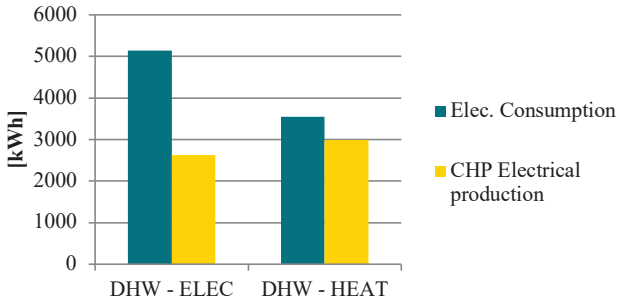

Figure 7: Comparison of electricity consumption and CHP power output according to the DHW production method

The study showed that using the heat produced by the CHP was the best way since it implies a higher production of electricity and a lower electrical consumption (Figure 7).

2.5.6 Controls

Strategies for steering cogeneration are a key point of the work. In this study, different management strategies were compared. These strategies include controls to optimize production of heat, electricity, grid assistance...

It should be noted that in all types of control, there was never waste of heat produced by cogeneration. This means that CHP was only allowed to start up when sufficient heat was required (possibly coupled with other conditions).

Moreover, the house was never considered as a “mini power plant”. There was no power generation strategy for the sole purpose of rejecting to the grid.

It should also be noted that all simulations take place at "equal comfort". All simulations include a CHP system paired with an auxiliary boiler.

Where cogeneration does not produce enough heat to fill all the needs of the building (for different reasons of sizing choice, control...), the auxiliary boiler brings the necessary supplement to satisfy the thermal comfort of the dwelling.

Three controls were implemented to the HVAC system using hysteresis.

It must be noticed that DHW heating needs are the priority. If the cogenerator is not sufficient to heat the DHW tank, an electrical resistance is present as an extra device to ensure that the temperature set point is reached.

2.5.7 Battery

Modelling an electric storage battery was not really planned or envisaged at the start of the project. Batteries remained a very marginal technology in the residential sector due to the lack of technological maturity, the cost of such systems and the lack of product available on the market.

However, quick evolution of the market lead to foresee this system

The electrical storage model used in the simulations was relatively simplified: the electrical storage was charged and discharged like a “water reservoir” without taking into account transient effects nor losses.

Capacity of the battery was set to 10 kWh. This value was chosen according to available product on market.

2.6 Controls description :

2.6.1 Heat driven

If no heat is required for the DHW tank, the CHP can feed the storage loop. The control temperature is the one at the outlet of the storage tank to the radiators (Tin_rad):

- If Tin_rad < 75°C: the CHP is turned on.
- If Tin_rad > 80°C: the CHP is turned off.

If the CHP is not sufficient to meet the storage heating needs, the auxiliary boiler can fill the gap. The controlled temperature is still the one at the outlet of the storage tank:

- If Tin_rad < 73°C: the auxiliary boiler is turned on.
- If Tin_rad > 78°C: the auxiliary boiler is turned off.

The electricity produced by cogeneration is first self-consumed to meet the electrical needs of the building. If the electricity produced by the CHP is not consumed, it is rejected to the network.

2.6.2 Grid control

In order to integrate the buildings in smart grids, the CHP is controlled according to the grid status.

In this case, the CHP will only be allowed to operate and inject electricity to the grid when the grid needs it.

In order to control the state of the grid, the choice was made to use the Belgian “NRV” (Net Regulation Volume) indicator which is the difference between the sum of volumes of all control action “upwards” and the sum of volumes of all control actions “downwards” requested by Elia (Belgian network operator) in order to balance the electrical network, (Elia 2018).

The CHP is then allowed to be turned on only if NRV is positive (when Elia had to request more actions upward than downward).

2.6.3 Battery control

This control is focused on self-consumption and “islanding” of buildings. In this configuration, CHP switches ON when heating needs are sufficient AND battery loading is minimum (minimum load was fixed to 20% of maximal load). This ensures a minimum duration to CHP work and avoid high frequency in cycle of load/unload of the battery.CHP switches OFF if heat needs are not sufficient any more OR if battery is fully charged.

3. SIMULATIONS AND RESULT ANALYSIS

3.1 Simulations

Simulations were carried out for the four buildings and the three consumer profiles. In addition, the three technologies (ICE 1kW$_e$, ICE 5.6kW$_e$ and Stirling 1kW$_e$) were studied for each strategy (heat-driven (HEAT), network control (NRV) and battery).The results obtained for the terraced house and a medium consumer will be presented. The results for the other cases are similar to the following ones.

3.2 Results

Total heat production results (Figure 8) are similar with or without CHP (compared to boiler) whatever CHP technologies or controls considered. The use of a cogeneration system will not penalise the consumer. If the cogenerator power is not sufficient to satisfy the thermal demand, the auxiliary boiler allows for each technology considered to fill the gap.

This result appears for all residential buildings and all consumption profiles (low, mdium, high consumer) considered.

The use of a cogeneration system and its control allows equal comfort compared to a boiler.

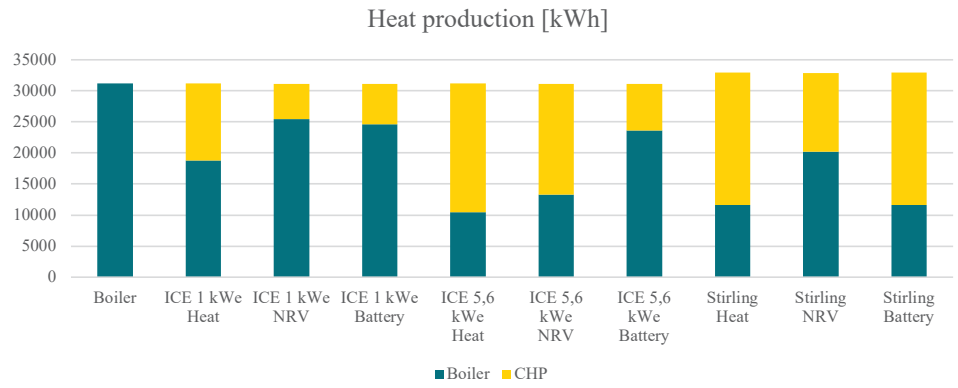

Figure 8: Heat production comparison

It also appeared that the Stirling system is better suited than the ICE 1kWe and equivalent to the ICE 5.6 kWe. Indeed, if scenario with heat driven ("ICE 1kWe Heat", "ICE 5.6kWe Heat" and "Stirling Heat") are compared, part of heat production from CHP is higher in the case of Stirling (equivalent to ICE 5.6kWe) than ICE 1KWe.

By analyzing the gas consumption of the complete system (Figure 9), it is clear that, whatever the technology considered, an excess of gas is always necessary in order to satisfy the criterion of equal comfort (boiler vs all CHP configurations). A cogeneration system always needs more gas than a boiler to produce 1kW th as a part of the energy consumed will be converted into electricity (the thermal efficiency of CHP is lower than the one of the boiler).

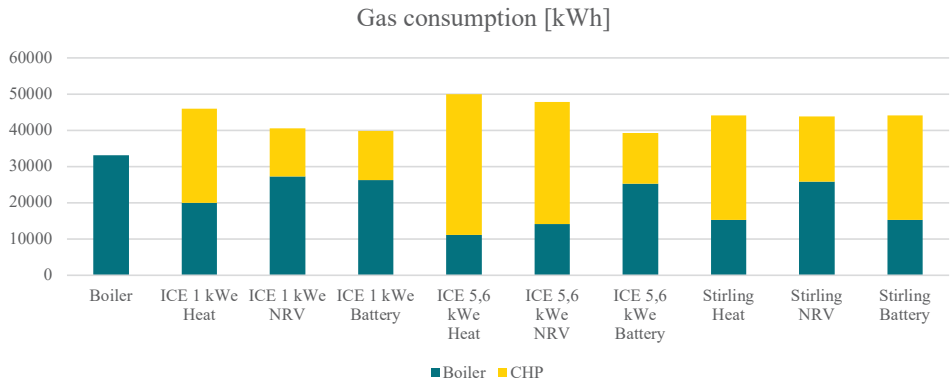

Figure 9: Gas consumption comparison

Cogeneration therefore requires more gas but produces electricity that can be consumed directly by the owner or sold to reduce his electrical bill. It is therefore important to analyse in detail this electricity production (Figure 10). The first analysis that can be made aims at looking if the production is directly carried out for the benefit of the owner of the system (in-situ valorisation).

Regarding to the technologies, a smaller engine seems most suitable. Although electricity production is lower, it is more constant and can therefore be better consumed in-situ than for a larger engine.

Regarding the strategies, the network control seems to have a small impact on self-consumption ("Heat" compares to "NRV" in the 3 technologies) even though it decreases the production but has more impact on self-sufficiency and the quantity of electricity bought (Figure 11). The use of a battery increases the self-consumption (Figure 10) as well as self-sufficiency (Figure 11 "Battery" compared to "Heat" and "NRV" for the 3 technologies) in all cases.

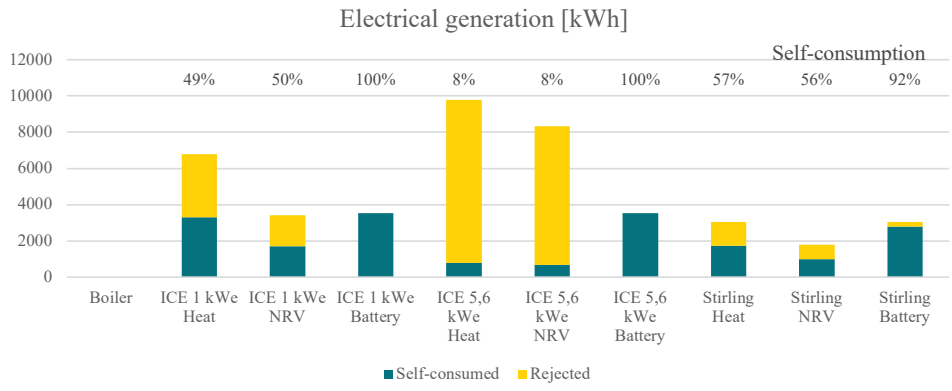

Figure 10: Electrical generation comparison

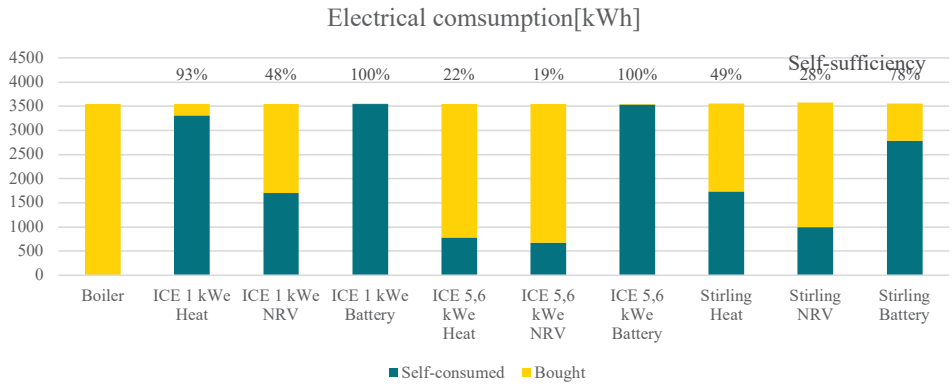

Figure 11: Electrical consumption comparison

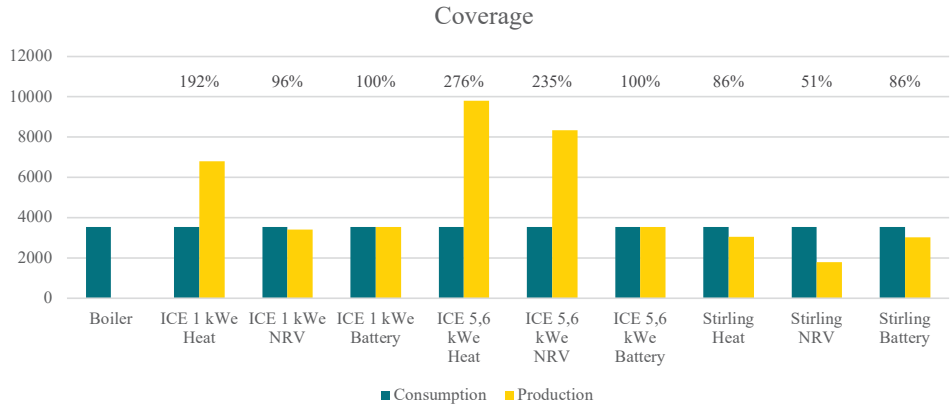

Figure 12: Electrical coverage analysis

Regarding electrical consumption, the ICE 1kW$_e$ seems more interesting since the self-consumption is higher (Figure 11 "ICE 1KWe heat" compares to "ICE 5.6kWe Heat" and "Stirling Heat", "ICE 1KWe NRV" compares to "ICE 5.6kWe NRV" and "Stirling NRV", "ICE 1KWe Battery" compares to "ICE 5.6kWe Battery" and "Stirling Battery") but when comparing the total production to the total needs it appears that the ICE technologies are oversized (Figure 12).

4. CONCLUSION

The modelling of a complex HVAC system including two micro-CHP technologies with very different thermal and electrical efficiencies allowed assessing the potential of these systems in the current Belgian residential real estate according to three different strategies.

This work did not only look at the micro-CHP models but allowed to evaluate the different models of storage, DHW production and emission systems. Since some models were inexistent or incorrect in TRNSYS, the physical models were studied and implemented in the program.

Size of storage tank has been studied. Results show that a bigger tank is more interesting. Electrical efficiency is improved since longer periods of heat production occur for CHP. 1000l tank appeared to be the best solution.

In buildings, since the objective was to compare results with equivalent comfort, heat production is similar whatever CHP technologies or strategies of control. A surplus of gas is required in case of CHP since electricity is produced. This electrical consumption could be either consumed in situ or rejected to the grid.

Regarding self-consumption, a smaller engine seems most suitable. Although electricity production is lower, it is more constant and can therefore be better consumed in-situ than for a larger engine.

Regarding the strategies, the “grid control” seems to have a small impact on self-consumption even though it decreases the production but has more impact on self-sufficiency and the quantity of electricity bought (Figure 11).

The use of a battery increases the self-consumption (Figure 10) as well as self-sufficiency.

5. *ACKNOWLEDGEMENTS*

This work was carried out within the framework of the Smart Micro Cogen project which was funded by ENGIE Electrabel, between 2013 and 2016.

6. NOMENCLATURE

SMC: Smart Micro Cogen

CHP: Combined Heat and Power

HVAC: Heating, Ventilation and Air-Conditioning

DHW: Domestic Hot Water

ICE: Internal Combustion Engine

NRV: Net Regulation Volume

7. REFERENCES

Arteconi, A., N.J. Hewitt, and F. Polonara. “Domestic demand-side management (DSM): Role of theat pumps and thermal energy storage (TES) systems.” *Applied Thermal Engineering* 51, no. 1-2 (2013): 155-165.

Ashrae Handbook. New-York, 1977.

AST, H. "IEA Annex 10 - System simultaion : Thermostactic Valve." Stuttgart, Germany, n.d.

Baetens, R., and D. Saelens. “Modelling uncertainty in district energy simulations by stochastic residential occupant behaviour.” *Journal of Building Performance Simulation* 9, no. 4 (2015): 431-447.

Baetens, R., R. De Coninck, F. Jorissen, D. Picard, L. Helsen, and D. Saelens. “OpenIDEAS - an open framework for integrated district energy simulations.” *14th Conference of*

International Building Performance Simulation Association. Hyderabad, India, 2015. 347-354.

Bouvenot, J.-B, et al. “Gas Stirling engine - CHP boiler experimental data driven model for building energy simulation.” *Energy and Buildings 84*, 2014: 117-131.

Brandemuehl, M.J., S. Gabel, and I. Andersen. “A toolkit for secondary HVAC System Energy Calculations.” *ASHRAE*, 1993.

Braun, J. E. & Lee, K.-H. “Assessment of demand limiting using building thermal mass in small commercial buildings.” *ASHRAE Transactions*, 2006: 112 PART 1, 547-558.

Cabeza, L. F. “Review on sorption materials and technologies for heat pumps and thermal energy storage.” *Renewable and Sustainable Energy Reviews* 110 (2017): 3-39.

Candanedo, José A., Vahid R. Dehkordi, and Phylroy Lopez. “A multi-level architecture to facilitate MPC implementation in commercial buildings: basic principles and case study.” *Proceedings of eSim 2014 conference.* 2014.

Claeys, B., and M. Sourbron. “Pas het elektriciteitstarief aan voor meer groene warmte (in Dutch).” *De Tijd, Opinion piece.* 24 May 2017.

“Code van goede praktijk voor de toepassing van warmtepompsystemen in de woningbouw (in Dutch).” *Computer software manual.* 2004.

Coffey, Edward Brian. “Approximating model predictive control with existing building simulation tools and offline optimization.” *Journal of Building Performance Simulation* 6, no. 3 (2013): 220-235.

Commission des Communautés Européennes. “"Etude CIEL" : Maîtrise de la Demande Electrique Campagne de Mesures par usage dans le secteur domestique.” n.d.

CSTB. *Règlementation Thermique 2012 - Règles d'application Th-Bât.* CSTB Edition, 2012.

Cyx, W., N. Renders, and M. Van Holm. “IEE TABULA - Typology Approach for Building Stock Energy Assessment.” Technical report, VITO, Vlaamse instelling voor technologisch onderzoek, 2011.

Cyx, W., N. Renders, M. Van Holm, and S. Verbeke. “IEE TABULA - Typology Approach for Building Stock Energy Assessment.” 2011.

Daikin Europe N.V. "Technical data sheets for Altherma EVLQ-CV3, Multisplit 4MXS, Split FTXM35+RXM25." Brussels, 2018.

Deutscher Wetterdienst. “Testreferenzjahr 2004.” 2004. https://www.dwd.de/DE/leistungen/testreferenzjahre/testreferenzjahre.html (accessed 08 02, 2016).

Deutsches Institut für Normung. “DIN EN 14825 - Luftkonditionierer, Flüssigkeitskühlsätze und Wärmepumpen mit elektrisch angetriebenen Verdichtern zur Raumbeheizung und -kühlung - Prüfung und Leistungsbemessung unter Teillastbedingungen und Berechnung der saisonalen Arbeitszahl.” 2016.

Dugaria, S., L. Moro, and D. Del Col. “Modelling heat and mass transfer in a membrane-based air-to-air enthalpy exchanger.” *33rd UIT (Italian Union of Thermo-fluid-dynamics) Heat Transfer Conference.* 2015.

Elia. *Déséquilibre actuel du système.* 6 July 2018. http://www.elia.be/fr/grid-data/balancing/desequilibre-actuel-du-systeme.

Energiebilanzen AG. “Evaluation tables from 1990-2017.” 2018.

Enertech, ADEME, and Union Européenne. “Projet REMODECE : Mesure de la consommation des usages domestiques de l’audiovisuel et de l'informatique - Rapport final.” 2008.

Engie. "Engie Easy Fixed 1y tariffs for electricity and gas." May 2018.

Entsoe Transparancy Platform. “Day-ahead electricity prices.” n.d.

Euroheat & Power. "Ecoheatcool project - Workpackage 3: Guidelines for assessing the efficiency of district heating and district cooling systems." Technical report, Euroheat & Power, 2005-2006.

European Comission. “Smarter, greener, more inclusive? Indicators to support the Europe 2020 strategy.” Luxembourg (LU), 2013.

European Parliament. “The primary energy factor for renewables.” *Parliamentary questions.* 19 November 2016.

Forsén, Martin. “Heat pumps - technology and environmental impact.” Technical report, Swedisch Heat Pump Association, European Heat Pump Association, 2005.

Gendebien, S, S Bertagnolio, and V Lemort. “Investigation on a ventilation heat recovery exchanger: Modeling and.” *Energy and Buildings* 62 (2013): 176-189.

Georges, E., S. Gendebien, S. Bertagnolio, B. Dechesne, and V. Lemort. “Evolution des profils de consommations énergétiques des bâtiments résidentiels en Belgique, suite à l'introduction de nouvelles technologies de chauffage, climatisation et cogénération.” Liège (Belgium), 2013.

Händel, Claus. “Ventilation with heat recovery.” *Rheva Journal*, 2001.

Henze, Gregor P, Clemens Felsmann, and Gottfried Knabe. “Evaluation of optimal control for active and passive building thermal storage.” *International Journal of Thermal Sciences* 43, no. 2 (2004): 173–183.

Henze, Gregor P, Thoi H Le, Anthony R Florita, and Clemens Felsmann. “Sensitivity Analysis of Optimal Building Thermal Mass Control.” *Journal of Solar Energy Engineering* 129, no. 4 (2006): 473-485.

Huchuk, Brent , Cynthia A. Cruickshank, William O’Brien, and H.Burak Gunay. “Recursive thermal building model training using Ensemble.” *Proceedings of eSim 2014 conference.* 2014.

Hydro-Québec. “Hydro-Québec demande à ses clients de poursuivre leurs efforts de réduction de la consommation d'électricité en période de pointe et les remercie de leur collaboration.” 22 01 2014. http://cnw.ca/ONjV5 (accessed August 01, 2014).

IBPSA-Canada. “Model predictive control in buildings workshop.” 2011. http://www.ibpsa.us/conferences (accessed September 10, 2014).

IEA, and IPEEC. “Building energy performance metrics - Supporting energy efficiency progress in major economies.” Technical report, IEA, IPEEC, 2015.

ISO-1. “ISO 10211:2008 - Thermal bridges in building construction - Heat flows and surface temperatures - Detailed calculations.” 2008.

ISO-2. “ISO 10456: 2008 - Building materials and products - Hygrothermal properties - Tabulated design values and procedures for determining declared and design thermal values.” June 2008.

ISO-3. “ISO 13370: 2008 - Thermal performance of buildings - Heat transfer via the groung - Calculation methods.” April 2008.

ISO-4. “ISO 13790: 2013 - Energy performance of buildings - Calculation of energy use for space heating and cooling.” *Energy performance of buildings - Calculation of energy use for space heating and cooling.* 2013.

ISO-5. “ISO 6946:2008 - Building components and building elements - Thermal resistance and thermal transmittance - Calculation method.” 2008.

Jespers, Kaat, Jad Al Koussa, Yoko Dams, Nele Renders, and Pieter Vingerhoets. “Inventaris hernieuwbare energiebronnen Vlaanderen 2005-2016 (in Dutch).” Technical report, VITO, Vlaams instituut voor technologisch onderzoek, 2017.

Kaltschmitt, Martin, Wolfgang Streicher, and Andreas Wiese. *Erneuerbare Energien: Systemtechnik, Wirtschaftlichkeit, Umweltaspekte.* Heidelberg: Springer Verlag, 2013.

Kelly, George E. “Control system simulation in North America.” *Energy and Buildings* 10, no. 3 (1988): 193–202.

Keys, William Morrow, and Michael E Crawford. *Convective heat and mass transfer* . 1980.

Knight, I. “IEA Annex 42 - The simulation of Building-Integrated Fuel Cell and other cogeneration systems (FC+COGEN-SIM) : Domestic Energy Profiles.” Cardiff (UK), 2007.

Koester, S., M. Falkenberg, M. Logemann, and M. Wessling. “Modeling heat and mass transfer in cross-counterflow enthalpy exchangers.” *Journal of Membrane Science*, 2017: 68-76.

Kummert, Michaël , Marie-Andrée Leduc , and Alain Moreau . “Using MPC to reduce the peak demand associated with electric heating.” *Model Predictive Control in Buildings Workshop.* Montréal, Quebec, 2011.

Lebrun, J., X. Ding, J.-P. Eppe, and M. Wasac. “Cooling Coil Models to be used in Transient and/or Wet Regimes. Theoretical Analysis and Experimental Validation.” *Proceedings of SSB.* Liège, 1990. 405-411.

Lehmann, B, D Gyalistras, M Gwerder, K Wirth, and S Carl. “Intermediate complexity model for Model Predictive Control of Integrated Room.” *Energy and Buildings* (Elsevier), no. 58 (2013): 250–262.

Lehrstuhl für Technische Thermodynamik - RWTH Aachen. “SorpLib 3: Adsorption Energy System Library.” Aachen, 2017.

Leonhardt, Corinna. *Thermische Speicher mit Phasenwechselmaterialien im Heizsystem.* Aachen, 2016.

Leonhardt, Corinna, and Dirk Müller. “Latent Heat Storage Devices for Heat Pump and Solar Heating Systems.” 2010.

—. “Modelling of Residential Heating Systems using a Phase Change Material Storage System.” *Proceedings of the 7th International Modelica Conference.* Como, 2009.

Liang, C.H. “Experiments Investigation of the Parallel-plates Enthalpy Exchangers.” *The 6th International Conference on Applied Energy.* 2014. 2699 – 2703.

Luminus. “Luminus #BeGreenFix tariffs for electricity and gas.” May 2018.

Müller, D., M. Lauster, A. Constantin, M. Fuchs, and P. Remmen. “AixLib - An Open-Source Modelica Library within the IEA-EBC Annex 60 Framework.” *BauSIM*, September 2016: 3-9.

Ma, Y, and F. Borrelli. “Hierarchical Predictive Control Energy Efficient Buildings.” *Model Predictive Control in Buildings Workshop.* Montreal, 2011.

Madson, H, and J Holst. “Estimation of continuous-time models for the heat dynamics.” *Energy and Buildings* (ELSEVIER), 1995: 67-79.

May-Ostendorp, Peter , Gregor P Henze, Charles D Corbin, Balaji Rajagopalan, and Clemens Felsmann. “Model-predictive control of mixed-mode buildings with rule extraction.” *Building and Environment* 46, no. 2 (2011): 428–437.

May-Ostendorp, Peter T, Gregor P Henze, Balaji Rajagopalan, and Charles D Corbin. “Extraction of supervisory building control rules from model predictive control of windows in a mixed mode building.” *Journal of Building Performance Simulation* 6, no. 3 (2013): 199-219.

Mehrfeld, Philipp. *Reference Building Model.* Aachen: E.ON Energy Research Center, Institute for Energy Efficient Buildings and Indoor Climate, 2016.

Morari, Manfred, and Jay H. Lee. “Model predictive control: past, present and future.” *Computers & Chemical Engineering*, 1999: 667–682.

Morisot, O., and D. Marchio. “Simplified Model for the Operation of Chilled Water Cooling Coils Under Nonnominal Conditions.” *HVAC&R Research*, 2002: 135-158.

Nasif, M., R. AL-Waked, G. Morrison, and M. Behinia. “Membrane heat exchanger in HVAC energy recovery systems, systems energy analysis.” *Energy and buildings* , 2010: 1833-1840.

Nasif, Mohammad Shakir, Ra’fat Al-Waked, Masud Behnia, and Graham Morrison. “Modeling of Air to Air Enthalpy Heat Exchanger.” *Heat Transfer Engineering*, 2012: 1010-1023.

Nassif, N, S Kajl, and R Sabourin. “Simplified model-based optimal control of VAV air conditioning system.” Montreal: Proceedings of the 9th international building performance simulation association (IBPSA) conference, 2005a.

Nassif, N, K Stainslaw , and R Sabourin. “Optimization of HVAC control system strategy using two-objective genetic algorithm.” *International Journal of HVAC&R Research* 11, no. 3 (2005b): 459-486.

Niu, J.L., and L.Z. Zhang. “Membrane-based Enthalpy Exchanger: material considerations and clarification of moisture resistance.” *Journal of Membrane Science*, 2001: 179-191.

Oldewurtel, F, A Parisio, C.N Jones, and M Morari. “Energy efficient building climate control using Stochastic Model Predictive Control and weather predictions.” *American Control Conference (ACC).* Baltimore, MD , 2010. 5100 - 5105.

Oldewurtel, Frauke, et al. “Use of model predictive control and weather forecasts for energy efficient building climate control.” *Energy and Buildings* , no. 45 (2012): 15–27.

Patteeuw, D. “Demand response for residential heat pumps in interaction with the electricity generation system.” PhD Thesis, KU Leuven, Belgium, 2016.

Prívara, Samuel , Jiří Cigler, Zdeněk Váňa, Frauke Oldewurtel, Carina Sagerschnig, and Eva Žáčeková. “Building modeling as a crucial part for building predictive control.” *Energy and Buildings* 56 (2013): 8–22.

Reynders, G. “Quantifying the impact of building design on the potential of structural storage for active demand response in residential buildings.” PhD Thesis, KU Leuven, Belgium, 2015.

Rosato, A., and S. Sibilio. “Calibration and validation of a model for simulating thermal and electric performance of an internal combustion engine-based micro-cogeneration device.” *Applied Thermal Engineering 45-46*, 2012: 79-98.

Roulet, C.-A, F.D Heidt, F Foradini, and M.-C Pibiri. “Real heat recovery with air handling units.” *Energy and Buildings* 33, no. 5 (2001): 495-502.

Sebai, R., R. Chouikh, and A. Guizani. “Cross-flow membrane-based enthalpy exchanger balanced and unbalanced flow.” *Energy Conversion and Management*, 2014: 19-28.

Sharma, A., and et al. “Review on thermal energy storage with phase change materials and applications.” *Renewable and Sustainable Energy Reviews* 13, no. 2 (2009): 318-345.

Six, Daan, Johan Desmedt, Dirk Vanhoudt, and John Van Bael. “Exploring the flexibility potential of residential heat pumps combined with thermal energy storage for smart grids.” *21st International Conference on Electricity Distribution.* Frankfurt, Germany, 2011. 1-4.

Stephan, W. “IEA Annex 10 - System simulation : Radiator.” Stuttgart (Germany), n.d.

Sturzenegger, David, Dimitrios Gyalistras, Vito Semeraro, Manfred Morari, and Roy S Smith. “BRCM Matlab Toolbox: Model Generation for Model Predictive Building Control.” *American Control Conference.* 2014.

Sweetnam, T., M. Fell, E. Oikonomou, and T. Oreszczyn. “Domestic demand-side response with heat pumps: controls and tariffs.” *Building Research & Information*, 2018: 1-18.

Swinton, Michael C, Hussein Moussa, and Roger J Marchand. *Commissioning Twin Houses for Assessing the Performance of Energy-Conserving Technologies.* Thermal Performance of the Exterior Envelopes of Whole Buildings VIII, 2001.

TLK-Thermo GmbH. “TIL Suite.” 2012. https://www.tlk-thermo.com/index.php/de/softwareprodukte/til-suite (accessed 11 14, 2018).

Verhelst, C., F. Logist, J. Van Impe, and L. Helsen. “Study of the optimal control problem formulation for modulating air-to-water heat pumps connected to a residential floor heating system.” *Energy and Buildings* 45 (2012): 43-53.

Verhelst, Clara, Maarten Sourbron, Stefan Antonov, and Lieve Helsen . “Towards MPC for office buildings with TABS connected to a GCHP system controller model.” *Model Predictive Control in Buildings Workshop.* Montreal, 2011.

Viskanta, R., M. Behnia, and A. Karalis. “Interferometric observations of the temperatur estructure in water cooled or heated from above.” *Advances in Water Resources*, Nr. 2 1977: 57-59.

VREG. “Hoeveel kost 1 kWh elektriciteit/aardgas? Prijzen voor huishoudelijke afnemers (all in, incl. BTW) (in Dutch).” 2018.

Wang , Shengwei, and Xinhua Xu. “Simplified building model for transient thermal performance estimation.” *International Journal of Thermal Sciences*, no. 45 (2006): 419–432.

Wang, Shengwei , and Xinqiao Jin. “Model-based optimal control of VAV air-conditioning system using genetic algorithm.” *Building and Environment* 35, no. 6 (2000): 471–487.

Wetter, Michael. “GenOpt® -- A Generic Optimization Program.” Proceedings of the 7th IBPSA Conference, 2001.

—. “GenOpt, Generic Optimization Program, User Manual Version 3.1.0.” 2011. http://gundog.lbl.gov/GO/ (accessed July 01, 2014).

Wystrcil, et al. “Model-based optimization of control strategies for low-exergy space heating systems using an environmental heat source.” *13th Conference of International Building Performance Simulation Association.* Chambéry: BS2013, 2013.

Zeng, Cheng, Shuli Liu, and Ashish Shukla. “A review on the air-to-air heat and mass exchanger technologies for building applications.” *Renewable and Sustainable Energy Reviews*, 2017: 753-774.

Zhang, Li-Zhi. “Heat and mass transfer in plate-fin enthalpy exchangers with different plate and fin materials.” *International Journal of Heat and Mass Transfer*, 2009: 2704-2713.

Questions and answers:

Jean Lebrun:

What was the actual efficiency of electricity storage (battery and conversion)?

Philippe André:

Battery: 92%, Inverter: 92%

***

Jean Lebrun :

Why imposing 73°C of water temperature all the time? Why not adjusting it to actual weather conditions? Look to actual heating demand.

Philippe André:

You are right.

***

Van Riet Freek:

Was the occupancy (i.e. heat demand profiles) correlated with the electricity consumption? It will affect the level of self-consumption.

Philippe André:

The occupancy profiles were synchronized with the electricity power consumption.

CONCLUSIONS

The 36 papers presented during the SSB 2018 conference may lead a to a number of outcomes or conclusions, which can be summarized as follows:

- Demonstration of maturation of the modelling process in different areas
- The optimization concept takes an increasing place in the research activities of the scientific community
- A move to a more global scale (urban, district, grid) is observed in many simulation works
- A trend to the simulation of more complex systems is also observed
- The conference offered to possibility to present innovative applications of the simulation models

Matured modelling:

Less « classical » modelling developments were presented while more applications to complex systems (one exception: the modelling of a « wet heat exchanger », now applied to dessicant heat exchangers)

Would this be the sign of a maturing modelling activity (except for very innovative concepts) or of the growing demand to solve society problems?

Optimization

This appears as a key concept for the future. Optimization is implemented in all phases of the building Life-Cycle: design, sizing, operation, control and is also used for model calibration and parameters identification. A preliminary conclusion is that design optimization may not be separated from operation optimization. But, on the other hand, a global optimization of the whole building energy system may still be difficult to reach.

Networks and grids:

Simulations go out of the buildings to address network scale problems

- District heating
- Electricity grids
- Urban scale

Consequence: the simulations are moving to « multiphysics » approaches (thermal, electrical, magnetic, chemical, agricultural, etc.)

Complex system simulations

The debate about the selection of the most adapted tool to building and system simulation is still open: Modelica, TRNSYS and MatLab/Simulink offer more or less the same capabilities. Nevertheless, Modelica is getting more and more interest from the scientific community while the flexibility and resistance of TRNSYS is observed and the genericity of MatLab/Simulink is highly appreciated. But is such a debate really worthwhile?

Innovative applications

The conference was the opportunity to learn about new applications of simulation tools: dynamic thermal bridges, air compression, standing column well, liquid dessicants, combination of solar and micro-cogeneration, caloric heat pumps to name just a few…This demonstrates that the domain of building and system simulations is still very living and open to innovation.

Atelier des Presses

LABORATOIRE DE
THERMO
DYNAMIQUE
UNIVERSITE DE LIEGE